Matthew J. Budoff
Jerold S. Shinbane
Editors

Cardiac CT Imaging

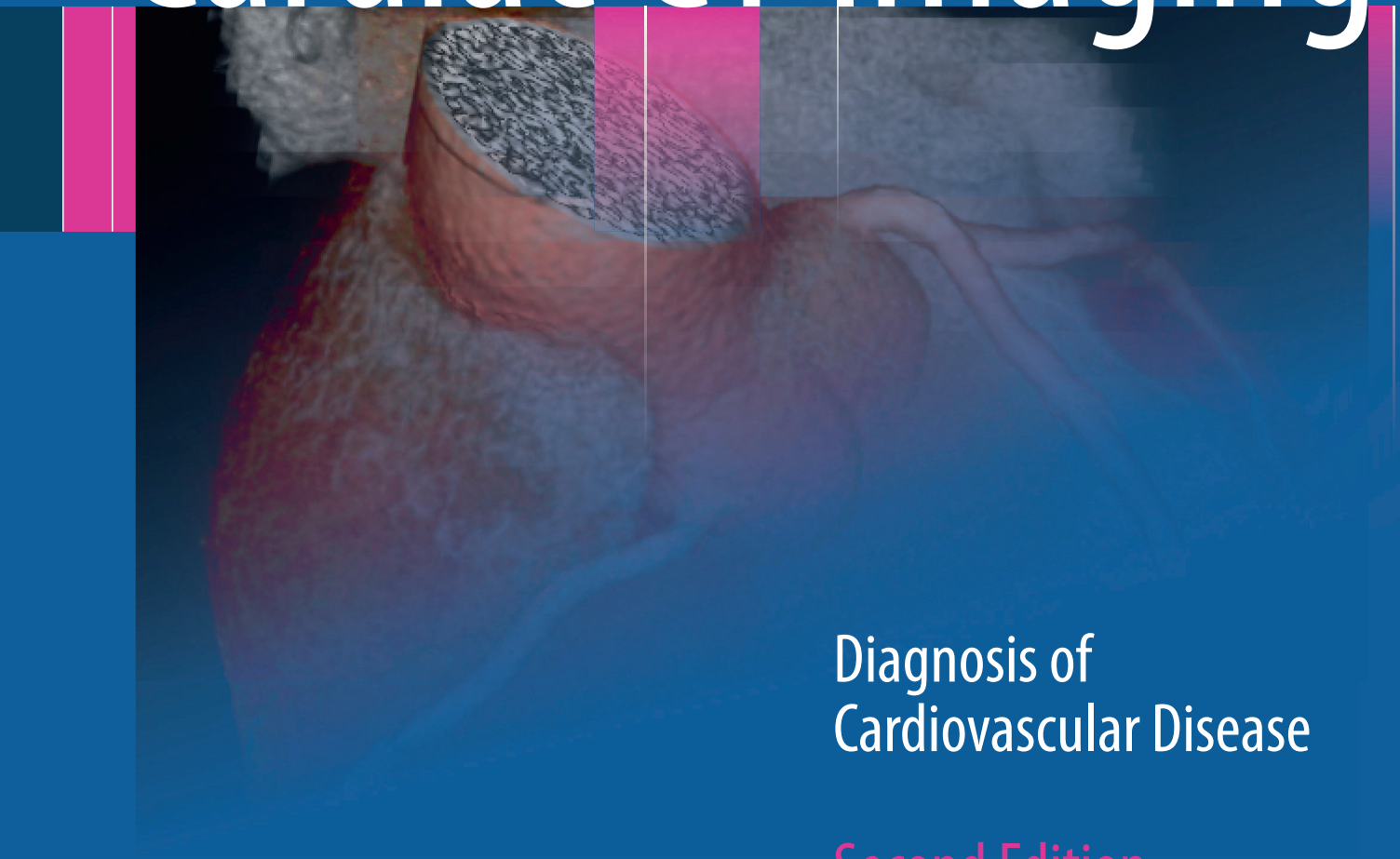

Diagnosis of Cardiovascular Disease

Second Edition

CD-ROM
INCLUDED

Springer

Cardiac CT Imaging

Second Edition

Matthew J. Budoff
Jerold S. Shinbane
Editors

Cardiac CT Imaging

Diagnosis of Cardiovascular Disease

Second Edition

Springer

Dr. Matthew Budoff MD, FSCCT, FACC, FAHA
Professor of Medicine,
David Geffen School of Medicine at UCLA
Director of Cardiac CT
Los Angeles Biomedical Research Institute at Harbor-UCLA
Torrance
CA USA
mbudoff@labiomed.org

Dr. Jerold S. Shinbane
Division of Cardiovasular Medicine
Keck School of Medicine at USC
Los Angeles
CA USA
shinbane@usc.edu

ISBN: 978-1-84882-649-6 e-ISBN: 978-1-84882-650-2
DOI: 10.1007/978-1-84882-650-2
Springer Dordrecht Heidelberg London New York

Library of Congress Control Number: 2010929048

Cover design: eStudio Calamar, Figueres/Berlin

Printed on acid-free paper

Springer is part of Springer Science+Business Media (www.springer.com)

Foreword to the First Edition

Cardiac CT has finally come of age. After nearly 30 years of development and growth, tomographic X-ray is being embraced by cardiologists as a useful imaging technology. Thirty years ago, Doug Boyd envisioned a unique CT scanner that would have sufficient temporal resolution to permit motion-artifact-free images of the heart. In the late 1970s, I had the good fortune to work closely with Dr. Boyd, Marty Lipton, and Bob Herkens who had the vision to recognize the potential of CT imaging for the diagnosis of heart disease. In the early 1980s, when electron beam CT became available, others, including Mel Marcus, John Rumberger (deceased), Arthur Agatston, and Dave King (deceased), were instrumental in making clinical cardiologists aware of the potential of cardiac CT.

In 1985, several investigators recognized the potential of cardiac CT for identifying and quantifying coronary artery calcium. Now, 20 years later, there is wide recognition of the value of coronary calcium quantification for the prediction of future coronary events in asymptomatic people. It has been a long and arduous road, but finally, wide-spread screening may significantly reduce the 150,000 sudden deaths and 300,000 myocardial infarctions that occur each year in the United States as the first symptom of heart disease.

In the late 1970s, it was thought that a 2.4-s scan time was very fast CT scanning. With the development of electron beam technology, scan times of 50 ms became possible, giving rise to terms such as fast CT, ultrafast CT, and RACAT (rapid acquisition computed axial tomography). Now, with the development of multidetector scanners capable of 64, 128, 256, and beyond simultaneous slices, spatial resolution is approaching that of conventional cineangiography, and the holy grail, noninvasive coronary arteriography, appears attainable.

In this book, Drs. Matthew Budoff and Jerold Shinbane, preeminent leaders in the field of cardiac CT, have described the many and varied uses of the technology in the diagnosis of cardiovascular disease. The book clearly documents that cardiac CT has not only arrived but has become a very valuable and potent diagnostic tool.

Bruce H. Brundage MD, MACC
Medical Director
Heart Institute of the Cascades
Professor of Medicine Emeritus
UCLA School of Medicine

Preface to the Second Edition

It is a testament to the intellect and diligence of the physician-scientists and engineers involved in the field of Cardiovascular Computed Tomography that a second edition of this text was necessary only four short years after the introduction of the first edition. In the Preface to the First Edition of this text, the long pathway to acceptance of cardiac CT was described as reminiscent of a quote by the philosopher Arthur Schopenhauer:

> All truth passes through three stages.
> First, it is ridiculed.
> Second, it is violently opposed.
> Third, it is accepted as being self-evident.

Cardiovascular CT has now matured into a firmly established subspecialty of radiology and cardiovascular medicine with a multidisciplinary society, a board examination, dedicated journals, numerous scientific statements from leading national societies, focused national and international meetings, and clear education and training pathways. The foundation has been provided by a sound medical literature, which continues to grow at an astounding pace. We hope that research maintains the same forward momentum fueled by the intellectual curiosity and passion to increase the understanding of the cardiovascular system and improve patient care. As we look ahead, we also continue to look back and acknowledge our debt to the pioneers of this technology who dedicated their careers to forwarding this discipline.

Cardiovascular CT has become a powerful risk stratifying tool for the early detection of atherosclerosis, a substitute for coronary angiography or noninvasive exercise testing in certain clinical situations, and a powerful tool to image the heart for congenital heart disease. There has been a paradigm shift in its role related to cardiovascular therapies, with progress from pre and postprocedure assessment to use in the actual guidance of a variety of invasive procedures.

Advances in CT scanners, imaging techniques, postprocessing workstations, and interpretation for diagnostic and therapeutic applications have now made the field relevant to the entire spectrum of physicians who diagnose and treat cardiovascular disease. As such, a thorough knowledge of cardiovascular CT is required for the thoughtful and individualized application in patient care. We hope that this text will provide the substrate for a detailed understanding of the art and science of this technology.

Los Angeles, CA, USA

Matthew J. Budoff, MD, FACC, FAHA, FSCCT
Jerold S. Shinbane, MD, FACC, FHRS, FSCCT

Preface to the First Edition

Since its introduction in the early 1970s, computed tomography (CT) has become a robust modality to evaluate extracranial, thoracic, and abdominal vascular distributions. It has become a gold standard to noninvasively image the aorta, pulmonary arteries, great vessels, and renal and peripheral arteries. However, cardiac anatomy evaluation with this modality was not possible, due to rapid cardiac motion and slow image acquisition times. Since the introduction of the first dedicated cardiac CT scanner, the electron beam CT (EBCT), the diagnosis and workup of cardiac structures has become possible. The lack of movement of the X-ray source allowed for images at a rate of 20 per second – 100 times faster than conventional CT at that time. Dr. Douglas Boyd, the inventor of EBCT, created this technology specifically with cardiac imaging in mind, and first published clinical data in 1982 [1]. However, limited reimbursement, high cost of acquisition, and very limited industry support kept this technology from expanding. The number of EBCT scanners in operation at any time never exceeded 100 worldwide, and physician exposure to the technology was very limited. Despite these hurdles, functional cardiac analysis (wall motion, cardiac output, wall thickening, and ejection fraction), perfusion imaging, noninvasive angiography, and coronary calcium assessment were validated, each with at least 10 years of experience. To date, over 1,000 scientific papers have been published in English, and three scientific statements from the American Heart Association have been written specifically on this modality. With the advent of helical CT in the mid-1990s and multidetector CT (MDCT) in 1999, the widespread availability of scanners to thousands of centers created a marked increase in utilization of and interest in cardiac CT. By 2004, three professional societies were vying for membership of potential cardiac CT physicians, and guidelines and credentialing standards were developed at a record pace.

Despite coronary calcium reports since 1989, and noninvasive coronary angiographic imaging reports with EBCT since 1995 [2], these applications did not gain widespread appeal until studies with MDCT became available. The preliminary studies (with subsecond single slice "helical" CT) had very limited cardiac applications and significant motion artifacts. The comparisons to EBCT were modest at best, and most investigators were quite concerned about applying the results of helical CT to clinical patients [3]. The early exposure MDCT, specifically the 4-slice scanner, was also disappointing with limited temporal resolution, volume coverage, collimation, and *z*-axis imaging. Due to the rapid coronary motion and limited scan speeds available with these early scanners, accurate and reliable imaging of the heart and coronary arteries has been significantly limited [4]. Diagnostic accuracy for cardiac 4-slice MDCT angiography, the most promising new application of these machines, was severely limited. Several studies reported diagnostic rates of only 30%, mostly due to cardiac motion [5]. However, evolution of MDCT with increased detectors, allowing for thinner slices and improved spatial resolution, has made this the most robust technology. Cardiac CT (with either MDCT or EBCT) offers several advantages over other diagnostic methodologies and is quite complementary to more common or traditional tests performed today. Clearly, the ability to see the lumen and vessel wall adds quite a lot to the assessment of the cardiac patient. Yet, cardiac CT does not readily afford functional assessment of the patient under stress (exercise), and that information, garnered most commonly with treadmill testing,

stress thallium, or echocardiography, adds vital information to the cardiac assessment. Thus, cardiac CT has been seen as a mostly complementary modality, adding anatomic information to the functional data acquired with stress testing.

Magnetic resonance imaging garnered quite a bit of interest in the early 1990s with the promise of a noninvasive angiogram with high accuracy. However, the next decade brought little improvement in the diagnostic accuracy of this technique, most likely due to limitations in slice thickness, and temporal and spatial resolution. As compared to MRI, EBCT and MDCT allow for higher spatial and temporal resolution. The ease of use and robustness allow for fairly easy application to a variety of cardiac diagnoses. This book will highlight the vast array of cardiac (and vascular) applications of CT, updating the reader on the methodology employed by a variety of experts with a cumulative 100 or more years of cardiac CT experience.

We are forever indebted to the experts (both cardiologists and radiologists) who have spent the last 10–20 years of their lives dedicated to studying and publishing in this particular field of interest. Some of the experts who originated this work in the mid-1980s and allowed us to progress to where we are today include Bruce Brundage, William Stanford, Ralph Haberl, Geoff Rubin, Robert Detrano, Warren Janowitz, Arthur Agatston, John Rumberger, Marty Lipton, and Ruping Dai. This is clearly a very incomplete list, yet these are some of the early investigators who had to literally fight against a medical community that thought cardiac CT posed a threat to their more traditional tests. There has been significant controversy regarding cardiac CT over the years, with raging debates at national meetings, and policies by the professional organizations sometimes swayed against the technology more by emotion than science.

The pathway that cardiac CT had to endure over the last 20 years is reminiscent of a quote by Arthur Schopenhauer. He stated:

> All truth passes through three stages.
> First, it is ridiculed.
> Second, it is violently opposed.
> Third, it is accepted as being self-evident.

A prominent cardiologist and past president of the American College of Cardiology recently told me that he thought some of the early investigators in the 1980s were clearly out of their mind when suggesting the widespread use of cardiac CT, whether for coronary calcium assessment as a "mammogram of the heart," or CT angiography as a possible replacement for some conventional angiograms (ridicule stage). Violent opposition to this modality came in the late 1990s, when debates at the American College of Cardiology and AHA centered on the inappropriate advertising of these tests, rather than the science. Today, we are approaching the third stage, with the acceptance that cardiac CT has an important role in risk stratification (coronary artery calcification) and diagnosis of obstructive coronary artery disease (CT angiography).

As you will see, cardiac CT has matured significantly. It has become a powerful risk stratifying tool for the early detection of atherosclerosis, a possible substitute for coronary angiography or noninvasive exercise testing in certain clinical situations, and a powerful tool to image the heart for congenital heart disease, pre and postelectrophysiologic testing, and peripheral angiography. Future directions include possibly replacing some conventional catheterizations and noninvasive tracking of atherosclerosis (progression/regression of either calcified plaque or noncalcified or "soft plaque"). The promise of CT includes noninvasive coronary plaque characterization, as well as accurate stenosis identification. It is highly likely that, if these goals are obtained, CT coronary angiography may become the most valuable tool to evaluate the coronary arteries noninvasively. It is possible that direct noninvasive CT visualization of the arteries will partially replace both nuclear cardiology and diagnostic angiography in certain clinical situations, with a subsequent increase in coronary revascularizations.

Los Angeles, CA, USA

Matthew J. Budoff, MD, FACC, FAHA, FSCCT
Jerold S. Shinbane, MD, FACC, FHRS

References

1. Boyd DP, Lipton MJ. Cardiac computed tomography. *Proc IEEE*. 1982;71;298–307.
2. Moshage WEL, Achenbach S, Seese B, Bachmann K, Kirchgeorg M. Coronary artery stenoses: three-dimensional imaging with electrocardiographically triggered, contrast agent-enhanced, electron beam CT. *Radiology*. 1995; 196:707–714.
3. Budoff MJ, Mao SS, Zalace CP, Bakhsheshi H, Oudiz RJ. Comparison of spiral and electron beam tomography in the evaluation of coronary calcification in asymptomatic persons. *Int J Cardiol*. 2001;77:181–188.
4. Budoff MJ, Achenbach S, Duerinckx A. Clinical utility of computed tomography and magnetic resonance techniques for noninvasive coronary angiography. *J Am Coll Cardiol*. 2003;42;1867–1878.
5. Achenbach S, Ulzheimer S, Baum U, et al. Non-invasive coronary angiography by retrospectively EcG-gated multislice spiral CT. *Circulation*. 2000;102:2823–2828.

Acknowledgments for the Second Edition

I would like to thank the authors of the chapters not only for their excellent and concise contributions, but also for their innovations that continue to move this field forward. Thanks to my family, especially Victoria, Daniel, and Garrett, who put up with my long hours in front of my laptop while creating this book. Thanks to Jerold, who cajoled me to undertake this project, for without his encouragement and assistance, this would never have come to be.

Matthew J. Budoff, MD, FACC, FAHA, FSCCT

I would like to thank Matthew Budoff for his collaboration on this second edition of the text and for his continued enthusiasm in advancing the field of cardiovascular CT. Thanks to the authors for their excellence in writing chapters that make cardiovascular CT accessible to the reader. Most of all, thanks to my family, especially Rosemary, Anna and Laura, for their encouragement, love and support.

Jerold S. Shinbane, MD, FACC, FHRS, FSCCT

Cardiovascular CT CD

Enclosed in this book is a CD with images and videos providing orientation to cardiovascular anatomy and pathology. The editors wish to acknowledge and thank the chapter authors for additional images provided in this CD.

Contents

CD Table of Contents

Enclosed in this book is a CD with images and videos providing orientation to cardiovascular anatomy and pathology.

Orientation to Axial Images: Serial labeled and unlabeled CT angiography images in the axial plane.

Orientation to Sagittal Images: Serial labeled and unlabeled CT angiography images in the sagittal plane.

Orientation to Coronal Images: Serial labeled and unlabeled CT angiography images in the coronal plane.

Coronary Artery Calcium Images: Serial non-contrast axial images demonstrating identification of coronary artery calcium

3-D Cardiovascular Anatomy: Video loops demonstrating 3-Dimensional cardiovascular anatomy and pathology.

- CT coronary angiography – volume rendered, MIP and angio emulation, 2D and 3D views of cases including normal coronaries, RCA stenosis, LAD stenosis, left main disease, left dominant circulation, apical infarction, bypass grafts, coronary ectasia, apical pseudoaneurysm and LV thrombus
- Function imaging including 3D Wall Motion, Short Axis and volume rendered short and long axis views
- Electrophysiology including 3D visualization of left atrium and pulmonary veins, endocardial views of atria and veins, fly throughs of pulmonary arteries and left atrial appendage, segmentation and editing for atrial fibrillation ablation, integration of CT with electroanatomic map, arrhythmia propagation map integration with CT, integration with ablation lesions and intracardiac echo, coronary venous system
- Congenital views including anomalous coronary arteries, dual ostia, atrial septal defects, subclavian vein views, bicuspid aortic valves, bicuspid pulmonic valve, coarctation
- CT Peripheral imaging including native vessels, fem-fem and iliac graft cases including stenting
- CMR for function and evaluation of ischemic cardiomyopathy and post-aneruysmectomy

Contributors

Aiden Abidov, MD, PhD Sarver Heart Center, University of Arizona College of Medicine, Tucson, AZ, USA
aabidov@shc.arizona.edu

Stephan Achenbach, MD, FACC, FESC, FSCCT Department of Cardiology, University of Erlangen, Erlangen, Germany
stephan.achenbach@uk-erlangen.de

Craig J. Baker, MD Department of Surgery, CardioVascular Thoracic Institute, University of Southern California, Keck School of Medicine, Los Angeles, CA, USA
cbaker@surgery.usc.edu

Daniel S. Berman, MD Cardiac Imaging, Cedars-Sinai Medical Center, Los Angeles, CA, USA
bermand@cshs.org

William D. Boswell, Jr., MD Department of Radiology, University of Southern California, Keck School of Medicine, Los Angeles, CA, USA
wbosw@usc.edu

Matthew J. Budoff, MD, FACC, FAHA, FSCCT Department of Internal Medicine, David Geffen School of Medicine at UCLA, Torrance, CA, USA
mbudoff@labiomed.org

Michael K. Cao, MD Division of Cardiovascular Medicine, University of Southern California, Keck School of Medicine, Los Angeles, CA, USA
caom@usc.edu

David A. Cesario, MD, PhD Division of Cardiovascular Medicine, University of Southern California, Keck School of Medicine, Los Angeles, CA, USA
cesario@usc.edu

Tae Young Choi, MD Los Angeles Biomedical Research Institute, Harbor-UCLA Medical Center, Los Angeles, CA, USA
youngchoi71@hanmail.net

Leonardo C. Clavijo, MD, PhD Division of Cardiovascular Medicine, University of Southern California, Keck School of Medicine, CA, USA
lclavijo@usc.edu

Patrick M. Colletti, MD Department of Radiology, University of Southern California, Keck School of Medicine, Los Angeles, CA, USA
colletti@usc.edu

Stephen C. Cook, MD Adolescent and Adult Congenital Heart Disease Program, Department of Cardiology, The Heart Center, Nationwide Children's Hospital, Columbus, OH, USA
stephen.cook@nationwidechildrens.org

Mark J. Cunningham, MD Department of Surgery, CardioVascular Thoracic Institute, University of Southern California, Keck School of Medicine, Los Angeles, CA, USA
mcunningham@surgery.usc.edu

Leticia Fernández-Friera, MD Department of Cardiology, Mount Sinai School of Medicine, New York, NY, USA
leticiaffriera@yahoo.es

John D. Friedman, MD Department of Imaging/Nuclear Medicine, Cedars-Sinai Medical Center, Los Angeles, CA, USA
FriedmanJ@cshs.org

Mario J. Garcia, MD, FACC, FACP Cardiovascular Division, Mount Sinai School of Medicine, New York, NY, USA and Department of Medicine, Mount Sinai Hospital, New York, NY, USA
mario.garcia@mountsinai.org

Guido Germano, PhD, FACC Artifical Intelligence Program, Department of Medicine, UCLA/Cedars-Sinai Medical Center, Los Angeles, CA, USA
germano@aim.csmc.edu

Marc J. Girsky, MD Department of Cardiology, Geffen School of Medicine of UCLA, Los Angeles, CA, USA
marc@drgirsky.com

Ilan Gottlieb, MD Department of Cardiology, Johns Hopkins University, Baltimore, MD, USA
ilangottlieb@gmail.com

Mohit Gupta, MD Department of Cardiology, Harbor-UCLA Medical Center, Torrance, CA, USA
mohit_gupta13@yahoo.com

Swaminatha V. Gurudevan, MD, FACC, FSCCT, FASE Cedars-Sinai Heart Institute, UCLA David Geffen School of Medicine, Los Angeles, CA, USA
gurudevans@cshs.org

Yasmin S. Hamirani, MBBS, MD Division of Cardiology, Harbor-UCLA Medical Center, Torrance, CA, USA
yasminshamshuddin@yahoo.com

Sean W. Hayes, MD Department of Imaging/Nuclear Medicine, Cedars-Sinai Medical Center, Los Angeles, CA, USA
HayesS@cshs.org

Harvey S. Hecht, MD, FACC, FSCCT Lenox Hill Heart & Vascular Institute, New York, NY, USA
hhecht@aol.com

Antreas Hindoyan, MD Department of Medicine, University of Southern California, Keck School of Medicine, Los Angeles, CA, USA
hindoyaa@usc.edu

Xingping Kang, MD Department of Cardiac Imaging, Cedars-Sinai Medical Center, Los Angeles, CA, USA
kangx@cshs.org

Christopher P. Learn, MD Adolescent and Adult Congenital Heart Disease Program, Department of Cardiology, Nationwide Children's Hospital, Columbus, OH, USA
christopher.learn@nationwidechildrens.org

Kai H. Lee, PhD Department of Radiology, University of Southern California, Keck School of Medicine, Los Angeles, CA, USA
kailee@usc.edu

Joao A.C. Lima, MD Department of Medicine/Cardiology, Johns Hopkins University, Baltimore, MD, USA
jlima@jhmi.edu

Annett Magedanz, MD Cardioangiologisches Centrum Bethanien, Frankfurt-Am-Main, Germany
a.magedanz@ccb.de

Songshao Mao, MD Department of Internal Medicine, David Geffen School of Medicine at UCLA, Torrance, CA, USA
smao@labiomed.org

James K. Min, MD Department of Medicine/Cardiology, Weill Cornell Medical College, New York, NY, USA
jkm2001@med.cornell.edu

Khurram Nasir, MD, MPH Division of Cardiology, Johns Hopkins University, Baltimore, MD, USA
knasir1@jhmi.edu

Ronald J. Oudiz, MD Department of Medicine, Division of Cardiology, Harbor-UCLA Medical Center, Torrance, CA, USA
roudiz@labiomed.org

Paolo Raggi, MD Department of Cardiology and Radiology, Emory University School of Medicine, Atlanta, GA, USA
praggi@emory.edu

Alan Rozanski, MD Department of Cardiology, St. Lukes Roosevelt Hospital Center, New York, NY, USA
arozanski@chpnet.org

John A. Rumberger, MD, PhD Department of Cardiovascular CT, The Princeton Longevity Center, Princeton, NJ, USA
jrumberger@theplc.net

Javier Sanz, MD Department of Cardiology, Mount Sinai School of Medicine, New York, NY, USA
javier.sanz@mssm.edu

Ammar Sarwar, MD Department of Radiology, Beth Israel Deaconess Medical Center, Harvard Medical School, Boston, MA, USA
asarwar@bidmc.harvard.edu

Leslie A. Saxon, MD Division of Cardiovascular Medicine, University of Southern California, Keck School of Medicine, Los Angeles, CA, USA
saxon@usc.edu

Thomas Schlosser, MD Department of Diagnostic and Interventional Radiology and Neuroradiology, University Hospital Essen, Essen, Germany
thomas.schlosser@uni-due.de

Axel Schmermund, MD Cardioangiologisches Centrum Bethanien, Frankfurt-Am-MainGermany
a.schmermund@ccb.de

Marco J. M. Schmidt, MD Cardioangiologisches Centrum Bethanien,
Frankfurt-Am-Main, Germany
m.schmidt@ccb.de

Jeffrey M. Schussler, MD, FACC, FSCAI, FSCCT Department of Cardiology,
Baylor University Medical Center, Hamilton Heart and Vascular Hospital,
Dallas, TX, USA
jeffrey.schussler@baylorhealth.edu

Michael D. Shapiro, DO Division of Cardiovascular Medicine,
Oregon Health and Science University, Portland, OR, USA
shapirmi@ohsu.edu

David M. Shavelle, MD, FACC, FACAI Division of Cardiovascular Medicine,
Department of Internal Medicine, Los Angeles County/USC Medical Center,
USC Cardiovascular Medicine, 1510 San Pablo Street, Suite 322

Los Angeles, CA 90033 USA
shavelle@usc.edu

Leslee J. Shaw, PhD, FACC, FAHA Department of Medicine, Emory University,
Atlanta, GA, USA
lshaw3@emory.edu

Jerold S. Shinbane, MD, FACC, FHRS, FSCCT Division of Cardiovascular Medicine,
USC Keck School of Medicine, Los Angeles, CA, USA
shinbane@usc.edu

Jabi E. Shriki, MD Department of Radiology, University of Southern California,
Keck School of Medicine, Los Angeles, CA, USA
jshriki@gmail.com

Piotr J. Slomka, PhD Department of Medicine/Imaging,
UCLA/Cedars-Sinai Medical Center, Los Angeles, CA, USA
piotr.slomka@cshs.org

Vaughn A. Starnes, MD Department of Surgery, Cardiovascular Thoracic Institute,
University of Southern California, Keck School of Medicine, Los Angeles, CA, USA
starnes@usc.edu

Louise E. J. Thomson, MBChB, FRACP Department of Imaging/Nuclear Medicine,
Cedars-Sinai Medical Center, Los Angeles, CA, USA
ThomsonL@cshs.org

Thomas-Duythuc To, MD Department of Medicine, University of Southern California,
Keck School of Medicine,
Los Angeles, CA, USA
thomasdt@usc.edu

Thomas Voigtländer, MD Cardioangiologisches Centrum Bethanien,
Frankfurt-Am-Main, Germany
t.voigtlaender@ccb.de

Wm. Guy Weigold, MD Department of Medicine (Cardiology),
Washington Hospital Center, Washington, DC, USA
guy.weigold@medstar.net

Common CT Abbreviations

CAC	Coronary artery calcium
CAD	Coronary artery disease
CCS	Coronary calcium score
CCTA	Coronary computed tomographic angiography
CT	Computed tomography
CVD	Cardiovascular disease
EBCT	Electron beam computed tomography
EBT	Electron beam tomography
HU	Hounsfield unit
ICA	Invasive coronary angiography
Kv	Kilovoltage
mA	milliAmpere/milliAmperage
MDCT	Multirow detector computed tomography
MPS	Myocardial perfusion scintigraphy
MSCT	Multislice computed tomography
PET	Positron emission tomography
SPECT	Single photon emission computed tomography

CT Glossary

ALARA (As Low As Reasonably Achievable) A concept to keep the radiation dose low but one should make sure the test remains diagnostic.

Attenuation Brightness of an object, based upon density. Typically measured by use of the Hounsfield unit (HU), which is a scale developed by Sir Godfrey Hounsfield that attributes brightness of water as a HU of 0, and less dense objects being negative (i.e., air is typically −1000 HU), and more dense objects being positive (i.e., metal is typically +1000 HU).

Beam Hardening An artifact with effects on image accuracy primarily due to high–density metal or calcium situated near a low-density structure (i.e., soft-tissue or lumen), which attenuates the X-ray signal from disproportionately low-energy X-rays.

Blooming An artifact on CT which is caused by severe calcification or metal, which causes the bright object to appear larger than it is (due to partial voluming).

Collimation The amount of tissue imaged on one rotation of the detectors, calculated as the number of detectors multiplied by the slice thickness (i.e., 64 detectors at 0.625 = 40 mm).

Collimator Shapes the X-ray beam. This controls the width, detector configuration, quality, and position of the X-ray beam.

Contrast to Noise Ratio A marker of image quality on CT, with a goal of high contrast enhancement to low noise. The worse the ratio, the harder the study is to interpret. Similar to signal to noise ratios.

Convolution kernel Defined as the image processing filter applied to the raw data to yield a final scan image. The sharpness of the final image is most directly influenced by the type of filter employed.

CT Dose Index (CTDI) Dose delivered to a standard reference phantom.

Dissipation How fast the tube can cool down, which is a limiting factor for image quality.

Effective Dose Reported in millisieverts (mSv), is a measure of the overall detrimental biological effect of a given radiation exposure. It is calculated by weighting the concentrations of energy deposited in each organ from a given radiation exposure, taking into account type of radiation and the potential for organ-specific damage in a reference individual.

Field of View The *scanned field of view* represents the entire object scanned within the gantry; the *displayed field of view* is defined as the angular size of the displayed scan on the three-dimensional matrix.

Negative Predictive Value The percentage of patients with negative results that are actually negative (i.e., free of the disease or condition). The higher the negative predictive value, the more accurate the test is at excluding patients that do not have the disease or condition.

Partial Volume Averaging An artifact on CT caused by objects being incompletely imaged on an individual slice of data. A small object (i.e., 0.3 mm foci of fat in the vessel) may be seen on an individual slice (0.6 mm), but may be somewhat obscured due to averaging with higher

density objects around it. Thus, since most imaging on CT is based upon maximal intensity projection, the brightest objects (calcium, metal) tend to dominate lower density objects (lumen, non-calcified plaque). Newer scanners with the ability to obtain thinner slices therefore have less problems with partial voluming.

Peak Tube Voltage (kVp) Is the energy of the X-rays produced, measured in kilovolts.

Pitch Is defined as the ratio of table travel to the beam collimation.

Pixel A two dimensional measure describing the x- and y-axis resolution of an individual datapoint. Using a 512 × 512 matrix, current CT scanners can achieve resolution of an individual datapoint of 0.35 × 0.35 mm.

Positive Predictive Value The percentage of patients with positive test results who are actually positive (i.e., have the disease or condition). The higher the positive predictive value, the more accurate the test is at detecting/diagnosing the disease of interest.

Prospective ECG Gating Relies on the scanner initiating imaging only during a pre-specified interval of the cardiac cycle (otherwise known as step and shoot).

Retrospective ECG Gating Involves a continuous spiral (helical) feed and scan wherein the entire heart volume is covered continuously. Data acquisition occurs from all phases of the cardiac cycle.

Sensitivity The percentage of actual positives which are correctly identified by the test (or the ability of the test to detect disease at a particular level).

Signal to Noise Ratio A marker of image quality on CT, describing the ratio of the image signal (attenuation or brightness) to the background noise level. Increasing radiation doses (especially kVp) will increase the signal and decrease the noise.

Spatial Resolution Refers to the ability of an imaging modality to detect two distinct objects in space as separate objects, and is expressed in units of distance.

Specificity The percentage of negatives which are correctly identified (or the ability of the test to detect the disease or condition of interest).

Temporal Resolution Refers to the ability of an imaging modality to detect two distinct events in time as separate events, and is expressed in units of time.

Tube Capacity How much heat a tube can store safely.

Tube Current It is the number of X-rays produced, measured as milliAmperes (mA).

Voxel A three dimensional datapoint on CT (pixel with z axis added). An isotropic voxel describes the ability to have all three dimensions with equal spatial resolution (i.e., 0.35 × 0.35 × 0.35 mm), allowing free rotation of the three-dimensional image without distortion.

Part I

Overview

1

Computed Tomography: Overview

Matthew J. Budoff

Overview of X-Ray Computed Tomography

Sir Godfrey Hounsfield is credited with the invention of the CT scanner in late 1960s. Since CT uses X-ray absorption to create images, the differences in the image brightness at any point will depend on physical density and the presence of atoms with a high difference in anatomic number like calcium, and soft tissue and water. The absorption of the X-ray beam by different atoms will cause differences in CT brightness on the resulting image (contrast resolution). Blood and soft tissue (in the absence of vascular contrast enhancement) have similar density and consist of similar proportions of the same atoms (hydrogen, oxygen, carbon). Bone has an abundance of calcium and is thus brighter on CT. Fat has an abundance of hydrogen. Lung contains air, which is of extremely low physical density and appears black on CT (HU -1,000). The higher the density, the brighter the structure on CT. Calcium is bright white, air is black, and muscle or blood is gray. There are over 5,000 shades of this gray scale represented on CT, centered around zero (water). CT, therefore, can distinguish blood from air, fat, and bone, but not readily from muscle or other soft tissue. The densities of blood, myocardium, thrombus, and fibrous tissues are so similar in their CT number that non-enhanced CT cannot distinguish these structures. Thus, the ventricles and other cardiac chambers can be seen on non-enhanced CT, but delineating the wall from the blood pool is not possible (Figure 1.1). Investigators have validated the measurement of "LV size" with cardiac CT, which is the sum of both left ventricle (LV) mass and volume [1]. Due to the thin wall, which does not contribute significantly to the total measured volume, the left and right atrial volumes can be accurately measured on noncontrast CT [2].

The basic principle of CT is that a fan-shaped, thin X-ray beam passes through the body at many angles to allow for cross-sectional imaging. The corresponding X-ray transmission measurements are collected by a detector array. Information entering the detector array and X-ray beam itself is collimated to produce thin sections while avoiding unnecessary photon scatter (to keep radiation exposure and image noise to a minimum). The x-ray tube and detector array rotate around the patient separated by 180°, allowing continuous acquisition of data. The data recorded by the detectors are digitized into picture elements (pixels) with known dimensions. The gray-scale information contained in each individual pixel is reconstructed according to the attenuation of the X-ray tube along its path using a standardized technique termed "filtered back projection." Gray-scale values for pixels within the reconstructed tomo-gram are defined with reference to the value for water and are called "Hounsfield units" (HU; for the 1979 Nobel Prize winner, Sir Godfrey N. Hounsfield), or simply "CT numbers." These CT numbers are the attenuation or brightness of the individual pixel (smallest definable unit on CT) of data. A 3D pixel is called a voxel. Typical pixel values for studies commonly seen on cardiac CT are listed in Table 1.1.

Because contrast resolution uses attenuation or density to visualize structures in gray scale, limitations of contrast resolution exist even on contrast enhanced studies. These include differentiating the cardiac vessels from cardiac cavities with same density (such as when the arteries run become intra-myocardial) and differentiating non-calcified plaque from surrounding low density structures, including thrombus. Even with good contrast enhancement, differentiating different types of plaque (lipid-laden and fibrous) can sometimes be challenging, although it is always easy to differentiate the bright white plaques (calcified) from non-calcific plaques.

The higher spatial resolution of CT allows visualization of coronary arteries both with and without contrast enhancement. The ability to see the coronary arteries on a non-contrast study depends upon the fat surrounding the artery (of lower density, thus more black on images), providing a natural contrast between the myocardium and the epicardial artery (Figure 1.1). Usually, the entire course of each coronary artery is visible on non-enhanced scans (Figure 1.2). The major exception is bridging, when the coronary artery delves into the myocardium and cannot be distinguished without contrast. The distinction of blood and soft tissue (such as the left ventricle, where there is no

Table 1.1. Typical Hounsfield unit values

Air ~ −1,000 HU
Fat −100 to −40
Water – zero
Non-enhanced myocardium and blood 40–60
Contrast enhanced myocardium 80–140
Calcium >130 (to about 1,000)
Enhanced blood pools (lumen, aorta, LV) 300–500
Metal >1,000

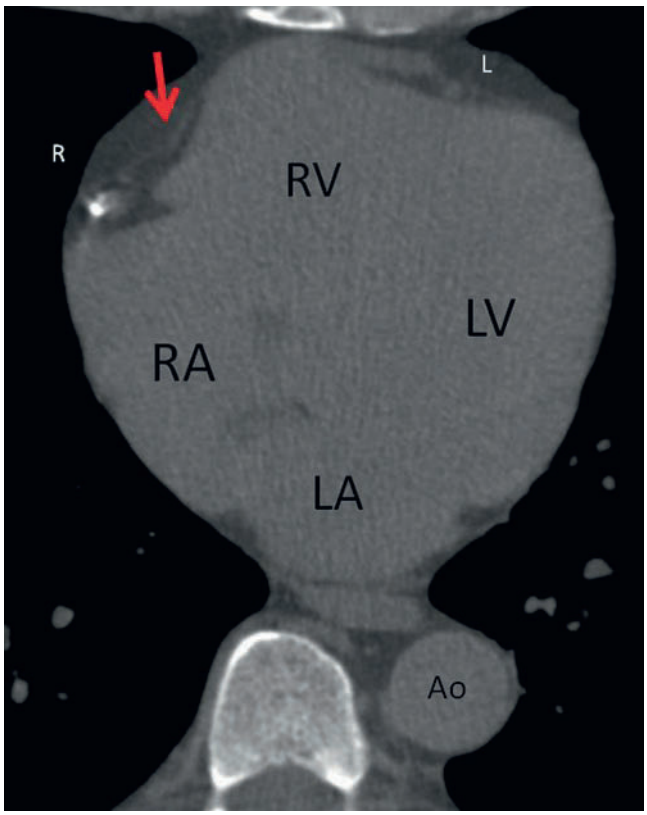

Figure 1.1. A non-contrast CT scan of the heart. Quite a bit of information can be garnered without contrast. The pericardium is visible as a thin line (*red arrow*). The coronary arteries can be seen, and diameters and calcifications are present (R). The right coronary artery is seen near the R, and the left anterior at the L. The four chambers of the heart are also seen, and relative sizes can be measured from this non-contrast study. The descending aorta is also present on this image and can be evaluated and measured. Higher levels would allow visualization of the ascending aorta, pulmonary artery and superior vena cava on the same study. *Ao* aorta, *L* left anterior descending artery, *LA* left atrium, *LV* left ventricle, *RA* right atrium, *RV* right ventricle.

air or fat to act as a natural contrast agent) requires injection of contrast with CT. Similarly, distinguishing the lumen and wall of the coronary artery also requires contrast enhancement. The accentuated absorption of X-rays by elements of high atomic number like calcium and iodine allows excellent visualization of small amounts of coronary calcium as well as the contrast-enhanced lumen of medium-size coronary arteries (Figure 1.3). Air attenuates the X-ray less than water, and bone attenuates it more than water, so that in a given patient, Hounsfield units may range from −1,000 HU (air) through 0 HU (water) to above +1,000 HU (bone cortex) (Table 1.1). Coronary artery calcium in coronary atherosclerosis (consisting of the same calcium phosphate as in bone) has CT number >130 HU, typically going as high as +1,000 HU. It does not go as high as the bony cortex of the spine due to the smaller quantity and mostly inhomogeneous distribution in the coronary artery plaque. Metal, such as that found in valves, wires, stents, and surgical clips, typically have densities of +1,000 HU or higher.

Cardiac CT

Cardiac computed tomography (CT) provides image slices or tomograms of the heart. CT technology has significantly improved since its introduction into clinical practice in 1972. Current conventional scanners used for cardiac and cardiovascular imaging now employ either a rotating X-ray source with a circular, stationary detector array (spiral or helical CT) or a rotating electron beam (EBCT). The attenuation map recorded by the detectors is then transformed through a filtered back-projection into the CT image used for diagnosis. The biggest issue with cardiac imaging is the need for both spatial and temporal resolution. Cardiac magnetic resonance (MR) has been an emerging technique for almost 2 decades, making little progress toward widespread utilization over this time. Temporal resolution (how long it takes to obtain an image) is inversely related to spatial resolution with cardiac MR. Improving the MR spatial resolution requires prolonging the imaging time. This greatly limits the ability to focus with precision on moving objects, as the viewer needs to settle for either a high resolution image plagued by cardiac motion, or a low resolution image with no motion artifacts. Cardiac CT does not suffer from this inverse relationship, and allows for both high spatial and temporal resolution simultaneously. Electron beam CT (EBCT – described in detail in text to come) allows for high resolution imaging at 50–100 milliseconds (ms). Multidetector CT (MDCT), with improved spatial resolution, allows for rotation speeds now on the order of 260–350 ms. The most distinct advantage of cardiac CT over cardiac MR is the improved spatial resolution and thinner slice thickness achievable with current systems. CT has the ability to image every 0.5 mm (submillimeter slices), providing high z-axis (through plane resolution). In-plane resolution is dependent upon the number of pixels that can be seen by a given detector array. Resolution of current CT systems uses a matrix of 512×512, allowing x- and y-axis (in plane) resolution down to 0.35 mm. MR systems use a matrix of 256×256, and flat plate technology currently used in advanced fluoroscopy labs and cardiac catheterization labs use $1{,}024 \times 1{,}024$ matrix resolution. The best resolution reported by a cardiac MR study (using the 3 Tesla magnet) demonstrated resolution in the x-, y- and z-axes of $0.6 \times 0.6 \times 3$ mm [3]. The best resolution offered by cardiac CT is $0.35 \times 0.35 \times 0.5$ mm, which is almost a factor of 10 better spatial resolution and approaching the ultimate for 3D tomography of nearly cubic (isotropic))

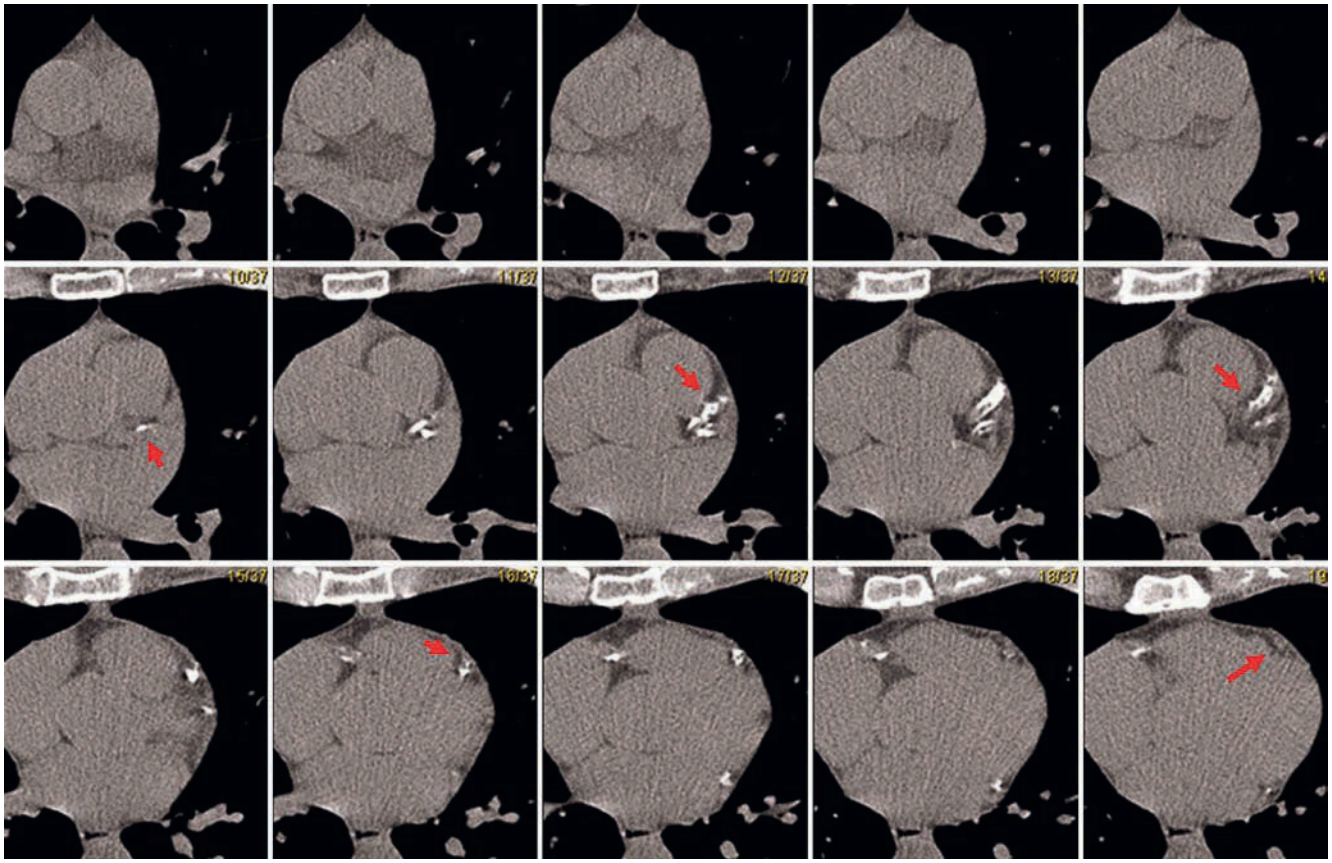

Figure 1.2. Sequential 3 mm slices from a non-contrast CT scan study (calcium scan). This study depicts the course and calcifications of the left anterior descending (LAD) artery. The white calcifications are easily seen (*red arrows*) and quantitated by the computer to derive a calcium score, volume or mass with high inter-reader reproducibility.

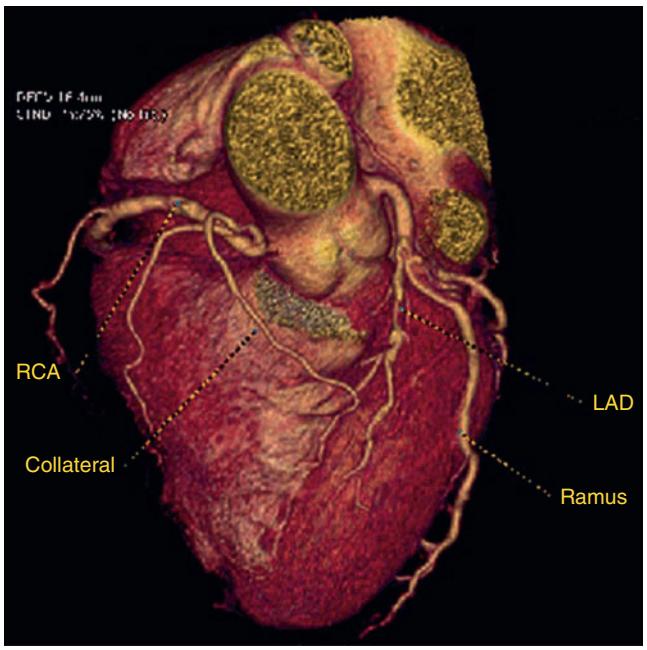

Figure 1.3. A contrast-enhanced CT of the coronary arteries, with excellent visualization of a highgrade stenosis in the mid-portion of the LAD. A large collateral vessel is seen from the RCA, but this is quite rare, as usually the collaterals are too small to be well seen on cardiac CT. A large ramus intermedius is well visualized, and the dominant RCA is present. This is but one view of many that can be visualized with cardiac CT, allowing for near-complete visualizations of the coronary tree.

"voxels" – or volume elements (a 3D pixel). As we consider noninvasive angiography with either CT or MR, we need to remember that both spatial and temporal resolution is much higher with traditional invasive angiography (discussed in more detail later in this chapter).

Reconstruction algorithms and multi-"head" detectors common to both current electron beam and spiral/helical CT have been implemented enabling volumetric imaging, and multiple high-quality reconstructions of various volumes of interest can be done either prospectively or retrospectively, depending on the method. The details of each type of scanner and principles of use will be described in detail.

MDCT Methods

Sub-second MDCT scanners use a rapidly rotating X-ray tube and several rows of detectors, also rotating. The tube and detectors are fitted with slip rings that allow them to continuously move through multiple 360° rotations. The "helical" or "spiral" mode is possible secondary to the development of this slip-ring interconnect. This allows the X-ray tube and detectors to rotate continuously during image acquisition since no wires directly connect the

rotating and stationary components of the system (i.e., no need to unwind the wires). This slip-ring technology was considered the most fundamental breakthrough for CT, allowing advancement from conventional CT performing single slice scanning in the 1980s to rapid multislice scanning in the 1990s. With the gantry continuously rotating, the table moves the patient through the imaging plane at a predetermined speed (table speed). The speed of the gantry relative to the rotation of the detectors is the scan pitch. Pitch is calculated as table speed divided by collimator width. The collimator width is simply the number of detectors multiplied by the individual detector width. A typical 64 detector system with 0.625 mm detectors will thus have a collimation width of 64×0.625 mm $= 40$ mm. Thus, each rotation of the detector array will "cover" 40 mm of the body. If the pitch is 1, than the table is moving at 40 mm and the coverage is 40 mm, allowing for no overlapping data and acquisition of 0.625 mm data per slice. Moving the table faster will lead to wider slices, as a pitch of 1.5 will infer that the table is moving at 60 mm, while the detector array only covers 40 mm, so each of the 64 detectors will be responsible for almost 1 mm of the 60 mm that was covered during the rotation. A low pitch (low table speed, typically used in cardiac imaging) allows for over-lapping data from adjacent detectors. A typical pitch for cardiac CT is 0.25, meaning that the table is moved at 10 mm per rotation, while the detectors cover 40 mm, allowing thin slice acquisition and overlapping datasets. The heart is literally moved only one fourth of the way through the detector array each rotation, so it takes four rotations to completely cover any portion of the heart. The pitch is varied based upon the heart rate of the patient, to allow optimal timing of image acquisition. Most commonly, physicians use a low table speed and thin imaging, leading to a lot of images, each very thin axial slices, which are of great value for visualizing the heart with the highest resolution. The downside is that the slower the table movement (while still rotating the X-ray tube), the higher the radiation exposure (See chapter 3).

The smooth rapid table motion or pitch in helical scanning allows complete coverage of the cardiac anatomy in 5–25 s, depending on the actual number of multi-row detectors. The current generation of MDCT systems complete a 360° rotation in about three tenths of a second (300 ms) and are capable of acquiring 64–320 sections of the heart simultaneously with electrocardiographic (ECG) gating in either a prospective or retrospective mode. MDCT differs from single detector-row helical or spiral CT systems principally by the design of the detector arrays and data acquisition systems, which allow the detector arrays to be configured electronically to acquire multiple adjacent sections simultaneously. For example, in 64-row MDCT systems, 64 sections can be acquired at either 0.5–0.75 or 1–1.5 mm section widths or 16 sections 2.5 mm thick (commonly used for calcium scoring).

In MDCT systems, like the preceding generation of single-detector-row helical scanners, the X-ray photons are generated within a specialized X-ray tube mounted on a rotating gantry. The patient is centered within the bore of the gantry such that the array of detectors is positioned to record incident photons after traversing the patient. Within the X-ray tube, a tungsten filament allows the tube current to be increased (mA), which proportionately increases the number of X-ray photons for producing an image. Thus, heavier patients can have increased mA, allowing for better tissue penetration and decreased image noise. One of the advantages of MDCT over EBCT is the variability of the mA settings, thus increasing the versatility for general diagnostic CT in nearly all patients and nearly all body segments. The other variable on the acquisition is the voltage, commonly expressed as kilovoltage (kv or kVp). The voltage was not varied on cardiac CT for the first 20 years of use, but recently it has been noted that by reducing the kV, exponential reduction in radiation exposure can be achieved. As the kV goes down, image noise goes up, so it is important that the kV only be reduced on thinner patients. While 120 kV was most typical, now increasingly 100 kV and even 80 kV studies are being reported, especially in children, where radiation issues are much more acute.

For example, the calcium scanning protocol employed in the National Institutes of Health (NIH) Multi-Ethnic Study of Atherosclerosis is complex [4]. Scans were performed using prospective ECG gating at 50% of the cardiac cycle, 120 kV, 106 mAs, 2.5 mm slice collimation, 0.5 s gantry rotation, and a partial scan reconstruction resulting in a temporal resolution of 300 ms. Images were reconstructed using the standard algorithm into a 35 cm display field of view. For participants weighing 100 kg (220 lb) or greater, the milliampere (mA) setting was increased by 25%.

However, the kV is typically not currently reduced for calcium scoring for two reasons. First, the radiation dose of calcium scoring is generally low (approximately 0.7 mSv), similar to mammography (0.75 mSv) and lower than annual background radiation (3–6 mSv per year). Secondly, as the kV is lowered, calcium and contrast appear brighter, and this would change the calcium scores, which up until this point, have only been obtained using 120 kV acquisitions. As more data are available on the algorithms for scoring with lower kV scans, calcium scoring may undergo a radiation reduction of up to 40% by lowering the kV from 120 to 100 for the acquisition.

MDCT systems can operate in either the sequential (prospective triggered) or helical mode (retrospective gating). These modes of scanning are dependent upon whether the patient on the CT couch is stationary (axial, or sequential mode) or moved at a fixed speed relative to the gantry rotation (helical mode). The sequential mode utilizes prospective ECG triggering at predetermined offset from the ECG-detected R wave analogous to EBCT and is the current mode for measuring coronary calcium at most centers using MDCT, and increasingly being used for CT angiography when heart rates are stable and slow. This mode utilizes a "step and shoot modality," which reduces radiation exposure by "prospectively" acquiring images, as compared to the helical mode, where continuous radiation is applied

(and thousands of images created) and images are "retrospectively" aligned to the ECG tracing. In the sequential mode, a 64-slice scanner can acquire 64 simultaneous data channels of image information gated prospectively to the ECG. Thus, a 64-channel system (with 0.625 mm detectors) can acquire, within the same cardiac cycle, 40 mm in coverage per heartbeat (collimation). The promise of improved cardiac imaging from the 64-, 256 or 320 slice scanners is mostly larger volumes of coverage simultaneously (up to 160 mm of coverage per rotation with a 320 slice scanner with 0.5 mm detectors), allowing for less *z*-axis alignment issues (cranial–caudal), and improved 3D modeling with only 2–5 s of imaging, although each vendor has a different array of detectors, with different slice widths and capabilities (Table 1.2). As coverage speeds increase, breath-hold and contrast requirements will also diminish.

Modern MDCT systems have currently an X-ray gantry rotation time of less than 500 ms. The fastest available rotation time is 260 ms. This remains suboptimal in faster heart rates (>80 bpm), as imaging during systole (or atrial contraction during late diastole) will be plagued by motion artifacts. Reconstruction algorithms have been developed that permit the use of data acquired during a limited part of the X-ray tube rotation (e.g., little more than one half of one rotation or smaller sections of several subsequent rotations) to reconstruct one cross-sectional image (described later in this chapter). Simultaneous recording of the patient ECG permits the assignment of reconstructed images to certain time instants in the cardiac cycle. Image acquisition windows of approximately 200 ms can be achieved without the necessity to average data acquired over more than one heartbeat (Figure 1.4). This may be sufficient to obtain images free of motion artifacts in many patients if the data reconstruction window is positioned in suitable phases of the cardiac cycle and the patient has a sufficiently low heart rate. Motion-free segments on four-slice MDCT decrease from approximately 80 to 54% with increasing heart rates [5], and similar observations have been made with both 16- and 64-detector systems. Dual source CT, utilizing two X-ray tubes and two detector arrays moving simultaneously around the body, can utilize partial images from each detector array to effectively "half" the temporal resolution, allowing motion free images up to heart rates of 70 bpm or more. However, the system is limited by 32 detectors, so collimation or coverage is only 19.2 mm per rotation (32 × 0.6 mm).

Table 1.2. Sample protocols for MDCT angiography: contrast-enhanced retrospectively ECG-gated scan

4-Slice scanner: 4 × 1.0 mm collimation, table feed 1.5 mm/rotation, effective tube current 400 mAs at 120 kV. Pitch = 1.5/4.0 collimation = 0.375. Average scan time = 35 s

16-Slice scanner (1.5 mm slices): 16 × 1.5 mm collimation, table feed 3.8 mm/rotation, effective tube current 133 mAs at 120 kV. Pitch = 3.8/24 mm collimation = 0.16. Averagescan time = 15–20 s

16-Slice scanner (0.75 mm slices): 16 ¥ 0.75 mm collimation, table feed 3.4 mm/rotation, effective tube current 550–650 mAs at 120 kV. Pitch = 3.4/12 mm collimation = 0.28. Average scan time = 15–20 s

64-Slice scanner (0.625 mm slices): 64 ¥ 0.6.25 mm collimation, table feed 10 mm/rotation, effective tube current 685 mAs at 120 kV. Pitch = 10/40 mm collimation = 0.25. Average scan time = 5 s

Dual source scanner (0.6 mm slices): 32 × 0.6 mm collimation, table feed 6 mm/rotation, effective tube current 685 mAs at 120 kV. Pitch = 6/19.2 mm collimation = 0.3. Average scan time = 10–12 s

320-Slice scanner (0.5 mm slices): 320 × 0.5 mm collimation, table feed 12 mm/rotation, effective tube current 685 mAs at 120 kV. Pitch = 12/40 mm collimation = 0.3. Average scan time = 2–3 s

MDCT Terminology

Isotropic Data Acquisition. The biggest advance that the newest systems provide is thinner slices, important for improving image quality as well as diminishing partial volume effects. The current systems allow for slice thick-nesses between 0.5 and 0.625 mm (depending on manufacturer and scan model). Thus, the imaging voxel is virtually equal

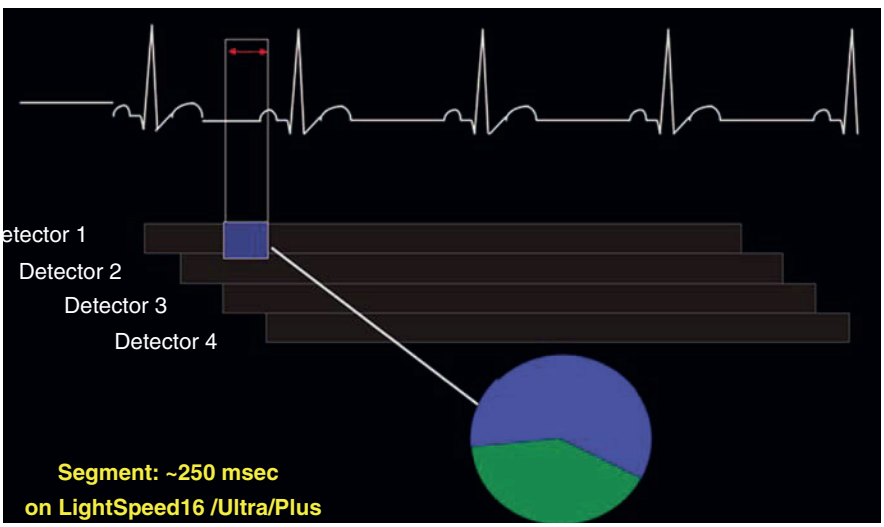

Figure 1.4. A typical acquisition using the "halfscan" method on multidetector CT (MDCT) (Light-Speed16, GE Medical Systems, Milwaukee, Wisconsin). This demonstrates an acquisition starting at approximately 50% of the R-R interval. A scanner with a rotation speed of 200 ms takes approximately 250 ms to complete an image, as depicted.

in size in all dimensions (isotropic). The spatial resolution of current CT systems is 0.35 × 0.35 mm, and has always been limited by the *z*-axis (slice thickness). Current systems theoretically allow for isotropic resolution (as reconstructed images can be seen at 0.4 mm), allowing for no loss of data by reconstructing the data in a different plane. This is very important for imaging the coronary, peripheral, and carotid arteries, as they run perpendicular to the imaging plane – each slice only encompasses a small amount of data – and to follow these arteries, one must add multiple slices together in the *z*-axis. The old limitations of CT (better interpretation for structures that run within the plane it was imaged, i.e., parallel to the imaging plane) are no longer present. There is now no loss of data with reformatting the data with multiplanar reformation (MPR) or volume rendering (VR). This differs significantly from MR, which due to thick slice acquisition (still >1 mm), does not allow free rotation of the resultant in-plane images. Thus, acquisition for CT is quite simple, obtaining axial slices through the area of interest, with the ability to reconstruct a 3D image that can be freely rotated. MR requires acquisition of data within the plane of interest, so if a short axis image of the left ventricle is required, it must be obtained in that plane, not reconstructed from the axial data. Furthermore, the thinner slice imaging allows for less partial volume artifacts (different densities overlying one another, causing a mixed picture of brightness on the resultant scan) and less streaking and shadowing, prevalent from dense calcifications and metal objects (such as bypass clips, pace-maker wires, and stents).

Pitch. In the helical or spiral mode of operation, a 64-MDCT system can acquire 64 simultaneous data channels while there is continuous motion of the CT table. The relative motion of the rotating X-ray tube to the table speed is called the scan pitch and is particularly important for cardiac gating in the helical mode. Increased collimator coverage allows for decreasing the pitch, without losing spatial resolution. The definition of pitch for the multidetector systems is the distance the table travels per 360° rotation of the gantry, divided by the dimension of the exposed detector array (the collimation, which is the slice thickness times the number of imaging channels). For example, a 64-slice system, with 64 equal detectors each of 0.625 mm, gives a collimation of 40 mm. Thus, if the table is moving at 40 mm/rotation, the pitch is 1.0. The pitch remains 1.0 if the table moves at 60 mm/rotation and the slices are thicker (0.975 mm each), or if the number of channels (detectors utilized) increases. Moving the table faster will lead to thicker slices, which will decrease resolution and lead to partial volume effects. If there is no overlap, the pitch is 1. If 50% overlap is desired, the pitch is 0.5, as the table is moved slower to allow for overlapping images. This is necessary with multisector reconstruction. Typical pitch values for cardiac work are 0.25–0.4, allowing for up to a 4-fold overlap of images. If the collimation with 64-row scanners increases to 40 mm, the table can move four times faster than the 16-slice scanner, without affecting slice thickness. Thus, the coverage with increased numbers of detectors can go up dramatically over a short period of scanning time, by imaging more detectors and increasing the speed of table movement in concert.

Field of View. Another method to improve image quality of the CT angiograph (CCTA) is to keep the field of view small. The matrix for CT is 512 × 512, meaning that there are 512 voxels in the *x* and *y* plane for a given field of view. If the field of view is 15 cm (small enough to encompass the whole heart, but only allows visualization of perhaps 4% of the lung field on average), than each pixel is 0.3 mm, which maximizes the spatial resolution of the current detector systems. Increasing the field of view to 45 cm (typical for encompassing the entire chest) increases each pixel dimension to 0.9 mm, effectively reducing the spatial resolution of each data-point 3-fold. Thus, there is a strong need to keep the field of view small, to both improve spatial resolution of the resultant image for interpretation, and decrease liability by having less lung, breast, and bone visualized on the interpreted scan. This is significantly better than current MR scanners (which utilize a 256 × 256 matrix), effectively 50% the spatial resolution compared to CT for each the *x* and *y* plane. Current flat plate technology for fluoroscopy allows for 1,024 × 1,024 resolution, 2-fold better than CT and 4-fold better than MR in each plane.

Contrast. Finally, the high scan speed allows substantial reduction in the amount of contrast material. The high speed of the scan allows one to decrease the amount of contrast administered; by using a 64-channel unit with a detector collimation of 0.625 mm and a tube rotation of 0.35 s (typical values for a 64-detector CCTA), the acquisition interval is around 5–6 s, which allows one to reduce the contrast load to approximately 50 mL. For a faster acquisition protocol, the contrast delivery strategy needs to be optimized according to the scan duration time. Use of a 320 detector scanner (which currently has 0.5 mm slices), covers the entire heart with one rotation, further reducing the contrast needs (although some minimal amount of contrast will be required to fill the heart and arteries in question). The general rule is the duration of scanning (scan acquisition time) equals the contrast infusion. So, if an average rate of 5 mL/s is used, a 15-s scan acquisition (typical 16 slice scanner) would require 75 mL of contrast. With volume scanners (64+ detector systems), the scan times are reduced to 2–6 s, and contrast doses are subsequently reduced as well.

Slip Ring. Allows continuous imaging, by transmitting power to the rotating frame from the stationary frame, and acquiring scan data, and allowing the gantry to rotate continuously as signals are received from the detector array (DAS) assembly, and then passes data from the rotating side to the stationary side of the slip ring.

X-ray Tube. CT X-ray tubes are similar to conventional X-ray tubes, with some issues related to anode heat capacity and dissipation. More slices and higher mA capacity lead to more heat generation by the tube. The tube is limited by its capacity (how much heat a tube can store safely) and its dissipation (how fast the tube can cool down). Most

systems use air cooling, while one uses water cooling to dissipate the heat.

Temporal Resolution. When performing typical cardiac imaging, the temporal resolution of a MDCT system is proportional to the gantry speed, which determines the time to complete one 360° rotation. To reconstruct each slice, data from a minimum of 180° plus the angle of the fan beam are required (half scan reconstruction), typically 210° of the total 360° rotation. For a 16-row system with 0.40-s rotation, the temporal resolution is approximately 0.25 s or 250 ms for a 50 cm display field of view. By reducing the display field of view to the 20 cm to encompass the heart, the number of views can be reduced to further improve temporal resolution to approximately 200 ms per slice (focusing on the central resolution of the image). The majority of MDCT systems currently have gantry speeds of 330–420 ms and thus resultant temporal resolution of 180–300 ms per image when used for measuring coronary calcium or creating individual images for CT angiography, as compared to 50–100 ms for EBCT. The newest scanners now have rotation gantry speeds down to 270 ms for a 360° rotation.

Although physically faster rotational times may be possible in the future, this is still rotation of an X-ray source (with attached detectors) that must rotate around the patient. This is subject to the forces and limitations of momentum. It is estimated that a conventional CT system generates 18 G of force (18 times the force of gravity) and weighs over 1 ton currently. It is doubtful that great strides will be made on significantly faster rotation speeds, but with dual (and potentially more detector arrays), temporal resolution of cardiac CT may continue to improve.

Halfscan Reconstruction

A multislice helical CT halfscan (HS) reconstruction algorithm is most commonly employed for cardiac applications. Halfscan reconstruction theoretically uses scan data from a 180° gantry rotation (180–250 ms) for generating one single axial image (Figure 1.4). However, more than 50% of the scan is required to obtain the data for an individual slice. Most vendors report their half-scan acquisition times as 50% of their rotation speed (for example, a 330 ms scanner reporting temporal resolution of 165 ms). This is not true resolution of the entire image, as the fan beam must be excluded, requiring longer acquisition times to complete the image. Half of the rotation speed is the "central time resolution," or the time needed to create only the center of the image. In traditional or single-source systems, the single X-ray tube rotates around the patient opposite the detector array, allowing for images to be created continuously (thanks to the slip ring technology described earlier). Dual source scanners take two sets of images simultaneously, and "add" the data together, creating an image in half the required time (similar to multi-segment reconstruction described in text to come, available with single source scanners, but images are taken over two successive heart beats instead of two sets of images acquired during the same heart beat). Either technique (multi-segment reconstruction or dual source imaging) effectively lowers the temporal resolution by a factor of two: thus, central time resolution drops from 165 to 83 ms.

The imaging performances (in terms of the temporal resolution, *z*-axis resolution, image noise, and image artifacts) of the heartscan algorithm have demonstrated improvement over utilizing the entire rotation (full scan). It has been shown that the halfscan reconstruction results in improved image temporal resolution and is more immune to the inconsistent data problem induced by cardiac motions. The temporal resolution of multislice helical CT with the halfscan algorithm is approximately 60% of the rotation speed of the scanner. The reason it is not 50% of the rotation speed is that slightly more than 180° is required to create an image, as the fan beam width (usually 30°) must be excluded from the window (Figure 1.4). Thus, approximately 210° of a rotation is needed to reconstruct an entire image as described. MDCT using the standard halfscan reconstruction method permits reliable assessment of the main coronary branches (those in the center of the image field) in patients with heart rates below 70 beats/min [6, 7]. The necessity of a low heart rate is a limitation of MDCT coronary angiography using this methodology.

With halfscan reconstruction, the proportion of the acquisition time per heartbeat is linearly rising from 20% at 60 beats/min to 33% at 100 beats/min. When evaluating the diastolic time, the proportion is much greater. Slower heart rates have longer diastolic imaging. The diastolic time useful for imaging for a heart rate of 60 beats/min is on the order of 500 ms (excluding systole and atrial contraction). Thus, a 250 ms scan will take up 50% of the diastolic imaging time. Increase the heart rate to 100 beats/min (systole remains relatively fixed) and the biggest change is shortening of diastole. Optimal diastolic imaging times are reduced to approximately 100 ms, clearly far too short for a motion-free MDCT scan acquisition of 250 ms (Figure 1.5, left panel). Thus, heart rate reduction remains a central limitation for motion-free imaging of the heart using MDCT. This can be partially overcome by multisegment reconstruction, described in text to come.

Multisegment Reconstruction

The scan window refers to the time when the volume of interest is present in the scan field and is therefore "seen" by the detector. It is the limiting factor for temporal resolution. In multisegment reconstruction, it defines the number of cardiac cycles available and hence the maximum number of segments that can be used to reconstruct one slice. Multisegment reconstruction utilizes a helical scanning technique coupled with ECG synchronization. (Images are retrospectively aligned to the ECG data acquired to keep track of systolic and diastolic images.) Multisegment

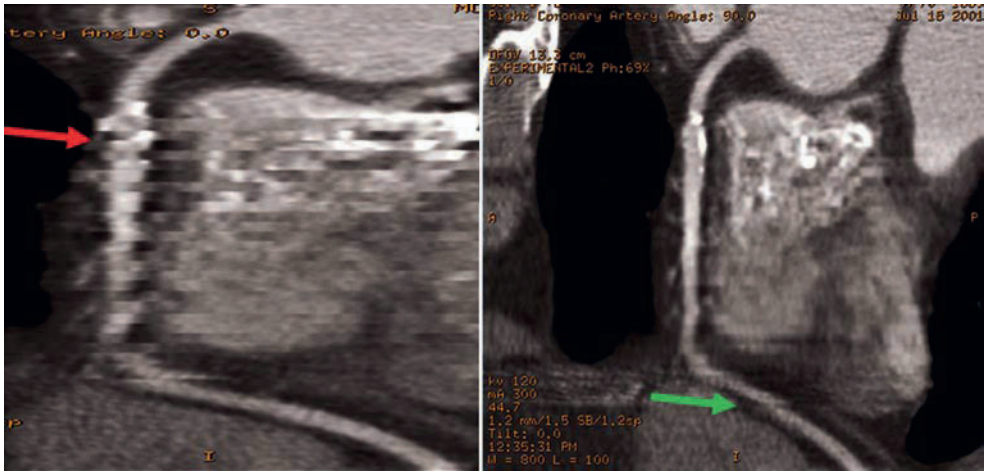

Figure 1.5. LightSpeed16 CT angiography images. On the left is the halfscan reconstruction. On the right is a reconstructed image using the same dataset, using multisegment reconstruction. There are still some motion artifacts in the distal right (*green arrow*), but much improved over the halfscan image, which is not interpretable (*red arrow*).

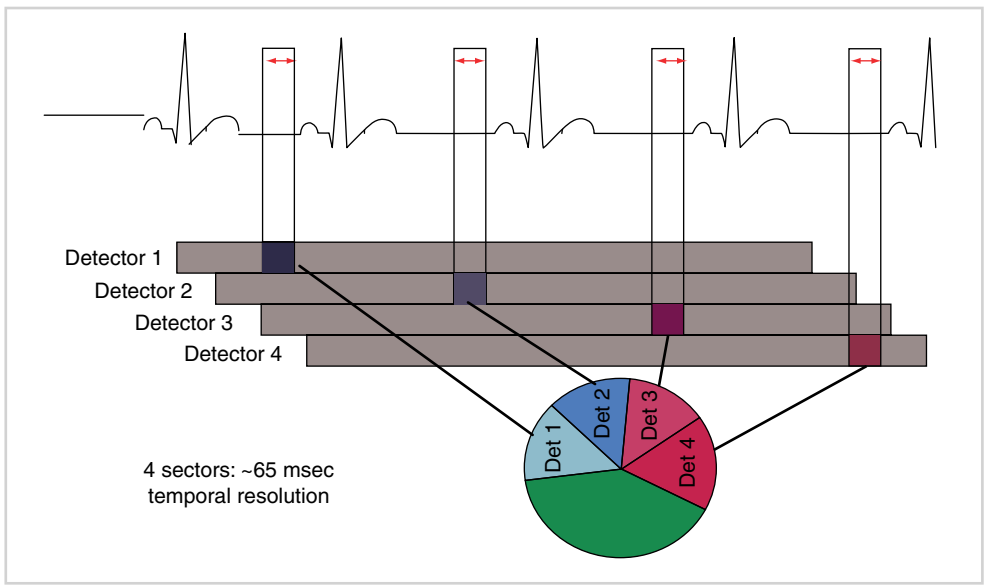

Figure 1.6. A demonstration of a theoretical image using multisegment reconstruction. The resulting image is constructed of four equal segments from four different detectors. Each is reconstructed from the same point in the cardiac cycle (approximately 50% in this depiction). Four different detectors, each visualizing the same portion of the heart in the same portion of the cardiac cycle, can be used to add together to create one image. In practice, the segments are not always of equal length, and four images are not always avail-able for reconstruction.

reconstruction can typically use up 2–4 different segments correlated to the raw data. By using four heartbeats to create an image, the acquisition time can be reduced to a minimum of 65 ms (Figure 1.6).

During retrospective segmented reconstruction, views from different rotations are combined to simulate one halfscan rotation (approximately 210° of data is needed to create an image). To calculate the number of segments that can be extracted from a scan window, the number of positions available for reconstruction is determined automatically by a workstation. Each position is extended into a wedge so that the combination of all wedges simulates a halfscan tube rotation. The raw data acquired in this virtual halfscan rotation is sufficient for the reconstruction of one slice. The size of the largest wedge (largest segment) defines the temporal resolution within the image (Figure 1.6). In other words, the subsegment with the longest temporal data acquisition determines the temporal resolution of the overall image. If the four segments used to create an image were of the following size (65, 65, 50, and 100 ms), then the temporal resolution of the reconstructed image is 100 ms (Figure 1.7).

This method of segmenting the information of one image into several heartbeats is quite similar to the established prospective triggering techniques used for MRI of the coronary arteries [8, 9]. With multisegment reconstruction, the length of the acquisition time varies between 10 and 20% of the R-R interval. Since the reconstruction algorithm is only capable of handling a limited number of segments, the pitch (table speed) is often increased for patients with higher heart rates. Thus, fewer images are available with higher heart rates, decreasing the potential success rate with this methodology.

The use of multisegment reconstruction has allowed for markedly improved effective temporal resolution and image quality, and is the basis of the Dual Source Scanner (Siemens, Erlangen, Germany). Just to be clear about how this works, let us use an analogy of a pie. Imagine needing just over half of a pie for a picture. To create an image, you can either add together one small slice from several pies

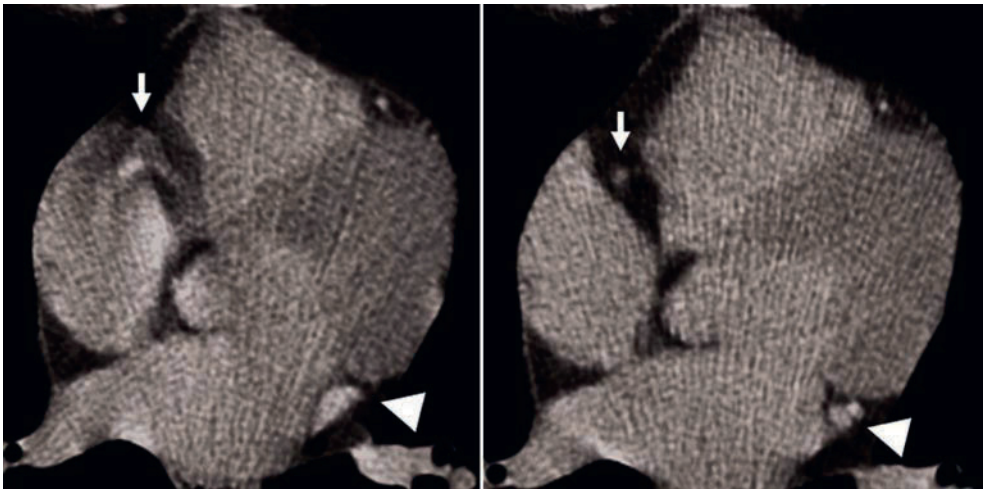

Figure 1.7. The figure on the left demonstrates a standard halfscan reconstruction with a rotation speed of 400 ms (approximate 260 ms image temporal resolution), with image data acquired on a four-channel MDCT system, 1.25 mm slice collimation, 0.6 gantry speed, and a heart rate of 72 beats/min. The image to the right demonstrates the same helical scan data, but processed with a two-sector reconstruction algorithm, resulting in an effective temporal resolution of 180 ms. Note how the proximal RCA (*white arrows*), as well as the left circumflex and great coronary vein, are now distinguishable (*white arrowhead*) and motion-free on the multisector reconstructed image.

(Figure 1.6) or you can take one large piece from one pie (Figure 1.4). The advantage of taking small pieces from each heartbeat is that the temporal resolution goes down proportionally. The difficulty in using this technique is that the pieces of the pie must align properly. Patients with even very slight arrhythmias (especially atrial fibrillation, sinus arrhythmia, or multifocal atrial rhythms), changing heart rates (increased vagal tone during breath-holding, catecholamine response after getting a contrast flush, etc.), or premature beats will cause misregistration to occur. If the heartbeats used are not perfectly regular, the computer will inadvertently add different portions of the cardiac cycle together, making a non-diagnostic image. Thus, there is still need for regular rhythms with CT angiography, although with higher detector systems (i.e., 64 detectors), the number of heartbeats needed to cover the entire heart goes down to 4–8, reducing the chance of significant changes in heart rates due to premature beats, breath-holding, vagal or sympathetic tone. As the detector arrays cover the entire heart with one heartbeat (320 Scanner, Toshiba), the possibility of imaging patients with arrhythmias and variable heart rates becomes a reality.

Multisegment reconstruction has been shown to improve depiction of the coronary arteries as compared to halfscan reconstruction [10, 11] (Figure 1.5). This methodology will improve temporal resolution, but high heart rates will still increase the motion of the coronaries, increasing the likelihood of image blurring and non-diagnostic images (Figure 1.5, right panel still demonstrating some blurring of the mid-distal right coronary artery with heart rates of 70–75 beats/min). It is fairly common for patients with low heart rates at rest to increase the heart rate significantly at the time of CT angiography. This can occur due to three factors: anxiety about the examination, the breath-hold, or the warmth of the contrast infusion to the patient. Thus, there is still a need for somewhat reduced heart rates during MDCT angiography with all current reconstruction systems.

Studies examining the image quality of multisegment and halfscan reconstruction in CT with four [12] and eight [11] detector rows showed similar image quality in both phantoms and patients. However, Dewey et al. [13] demonstrated that the accuracy, sensitivity, specificity, and rate of non-assessable coronary branches were significantly better using multisegment reconstruction in a 16-slice MDCT scanner. The authors attributed the difference to the higher image quality and resulting longer vessel length free of motion artifacts with multisegment reconstruction. The obvious advantage of multisegment reconstruction is achieved by reducing the acquisition window per heartbeat to approximately 160 ms on average, particularly useful for diagnostic images of the right coronary artery and circumflex artery (the two arteries that suffer the most from motion artifacts) [14]. Therefore, MDCT in combination with multisegment reconstruction does not always require administration of beta blockers to reduce heart rate. This improvement simplifies the procedure and expands the group of patients who can be examined with noninvasive coronary angiography using MDCT. The potential is for even greater application with aligning these multiple segments together with 64-slice scanners, further improving the diagnostic rate with MDCT angiography. If the heart rate is unexpectedly irregular (i.e., premature ventricular contractions (PVCs) or stress reaction to the dye causing increased heart rate during imaging), multisegment reconstruction will not be successful and the diagnostic image quality will have to rely on the halfscan reconstruction.

Retrospective Gating. The ECG is used to add R peak markers to the raw data set. A simultaneous ECG is recorded during the acquisition of cardiac images. The ECG is retrospectively used to assign source images to the respective phases of the cardiac cycle (ECG gating). The best imaging time to minimize coronary motion is from 40 to 80% of the cardiac cycle (early to mid-diastole). The interval between markers determines the time of each scanned cardiac cycle. Retrospective, phase-specific, short time segments of several R-R intervals are combined to reconstruct a "frozen axial slice." During helical scanning, the patient is moved through the CT scanner to cover a body volume (i.e., the heart). An advantage of the helical acquisition mode is that

there is a continuous model of the volume of interest from base to apex, as opposed to the sequential/cine mode in which there are discrete slabs of slices which have been obtained in a "step and shoot" prospective fashion. The obvious detriment to the helical acquisition is the increase in radiation dose delivered to the patient, as continuous images are created, and then "retrospectively" aligned to the ECG tracing to create images at any point of the R-R interval (cardiac cycle).

Prospective Triggering. The prospectively triggered image uses a "step and shoot" system, similar to EBCT. This obtains images at a certain time of the cardiac cycle (see Chapter 2), which can be chosen in advance, and then only one image per detector per cardiac cycle is obtained. This greatly reduces radiation dose, as the scanner is not on continuously (such as retrospective gating above). This has been used for quite a while with coronary calcium scanning, as multiple phases were not required to derive a calcium score. Only recently has this allowed for CT angiographic images, as there is markedly less data available to perform reconstructions. With retrospective gating, thousands of images are obtained as the detectors continuously acquire data. The resultant images are then 'retrospectively' aligned with the ECG, to create multiple datasets at each portion of the cardiac cycle. With prospective imaging, only images at a certain phase (for example 70% of the R-R interval, or mid-diastole) would be obtained, and then the scanner would move the patient (step), await another heart beat (R wave), and then trigger again (shoot) at 70% to obtain another set of images (64 images with a 64 MDCT). This would continue for 3–5 beats until the entire heart is covered. With 320 detector scanners, the volume is covered within 1 heart beat, at the predetermined phase, saving possible reconstruction artifacts when lining up volumes of data from subsequent heart beats (step or collimation artifacts). However, motion artifacts can still occur with more detector arrays, as the motion of the right coronary artery is dependent on the rotation speed (temporal resolution), not the number of detectors.

EBCT Methods

EBCT (GE Healthcare, Waukegan, WI) is a tomographic-imaging device developed over 20 years ago specifically for cardiac imaging. To date, and specifically over the past decade, there has been a huge increase in diagnostic and prognostic data regarding EBCT and coronary artery imaging. In order to achieve rapid acquisition times useful for cardiac imaging, these fourth-generation CT scanners have been developed with a nonmechanical X-ray source. This allows for image acquisition on the order of 50–100 ms, and with prospective ECG triggering, the ability to "freeze" the heart. Electron beam scanners use a fixed X-ray source, which consists of a 210° arc ring of tungsten, activated by bombardment from a magnetically focused beam of electrons fired from an electron source "gun" behind the scanner ring. The patient is positioned inside the X-ray tube, obviating the need to move any part of the scanner during image acquisition (Figure 1.8). EBCT is distinguished by its use of a scanning electron beam rather than the traditional X-ray tube and mechanical rotation device used in current "spiral" single and multiple detector scanners (requiring a physically moving X-ray source around the patient). EBCT requires only that the electron beam is swept across the tungsten targets to create a fan beam of X-ray, possible in as short as 50 ms per image (20 frames/s). The electron beam is emitted from the cathode, which is several feet superior to the patient's head, and then passes through a magnetic coil, which bends the beam so that it will strike one of four tungsten anode targets. The magnetic coil also steers the beam through an arc of 210°. The X-rays are generated when the electron beam strikes the tungsten anode target, then passes through the patient in a fan-shaped X-ray and strikes the detector array positioned opposite the anodes. This stationary multisource/split-detector combination is coupled to a rotating electron beam and produces serial, contiguous, thin section tomographic scans in synchrony with the heart cycle.

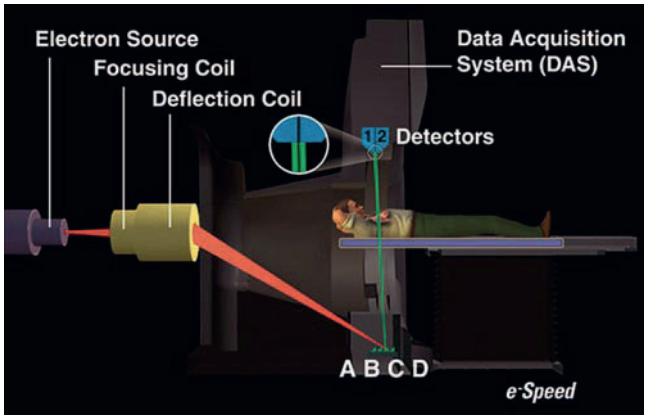

Figure 1.8. Depiction of the e-Speed electron beam computed tomography scanner. The electron source emits a beam, which is steered magnetically through the detection coil, then reflected to tungsten targets (A B C D), where a fan-shaped X-ray beam is created and, after passing through the area of interest, seen by the detectors.

There have been four iterations for EBCT since it was introduced clinically in the early 1980s. Since its initial introduction in 1982, it has been known as "rapid CT," "cine CT," "Ultrafast CT©," EBCT, and "Electron Beam Tomography©." The overall imaging methods have remained unchanged, but there have been improvements in data storage, data manipulation and management, data display, and spatial resolution. The original C-100 scanner was replaced in 1993 by the C-150, which was replaced by the C-300 in 2000. The current EBCT scanner, the e-Speed (GE/Imatron) was introduced in 2003. The e-Speed is a multislice scanner and currently can perform a heart or vascular study in one half the total examination time required by the C-150 and C-300 scanners. The e-Speed, in addition to the standard 50 and 100 ms scan modes common to all EBCT scanners, is capable of imaging speeds as fast as 33 ms. A major limitation of this modality currently is the slice width, which is limited

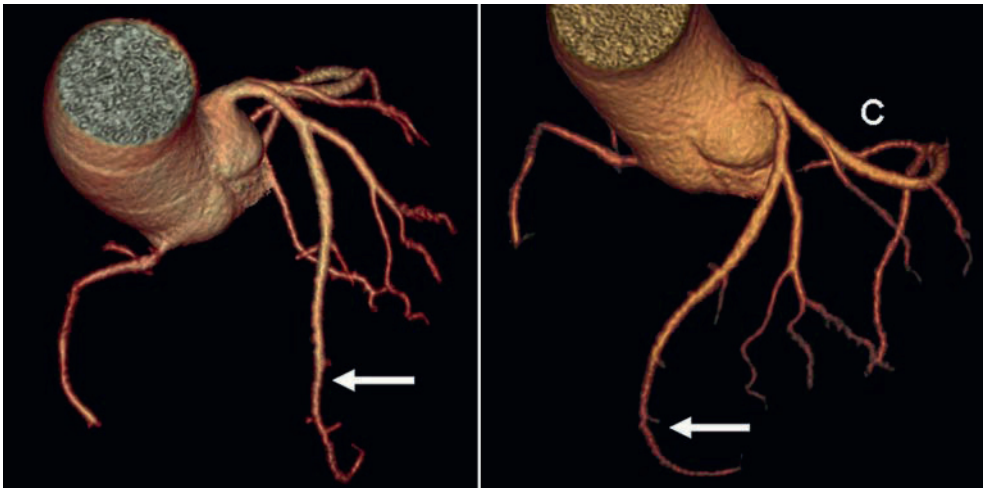

Figure 1.9. A contrast-enhanced CT angiogram demonstrating long segments of the LAD (*arrow*). Images such as seen here can be created which are much more similar to a conventional coronary angiogram, if desired.

to 1.5 mm. Current MDCT scanners can obtain images in 0.5–0.75 mm per slice. See Figure 1.9.

CT allows for imaging beyond the coronary arteries. Assessing wall motion, myocardial mass (utilizing the known specific gravity of cardiac tissue), and global and regional ejection fraction is easily done [15]. Importantly, since blood is being injected into the venous system, simultaneous enhancement of the right and left ventricle allows for excellent visualization of all cardiac chambers simultaneously, and measure of both right and left ventricular function and structure [16]. Early work with perfusion has shown that time to enhancement can be assessed, and actual measurement of myocardial perfusion is now possible. Images can be obtained for every cardiac cycle to allow for perfusion measures. Scanning is initiated before the arrival of a contrast bolus at an area of interest (e.g., left ventricular (LV) myocardium) and is continued until the contrast has washed in and out of the area. Time density curves from the region of interest can be created for quantitative analysis of flow (Figure 1.10). The filling of different chambers (and segments of the myocardial walls) can be visualized sequentially, allowing for visualization of flow into and out of any area of interest. It should be noted that early studies dating back to 1983 have demonstrated saphenous vein graft patency with this technique, achieving an accuracy of approximately 90% as compared to invasive angiography [17]. This technique is still commonly employed to detect shunts (see Chapter 21), as well as to determine the length of time it takes for contrast to travel from the arm vein at the site of injection to the central aortic root (allowing for accurate image acquisition of the high resolution contrast-enhanced images).

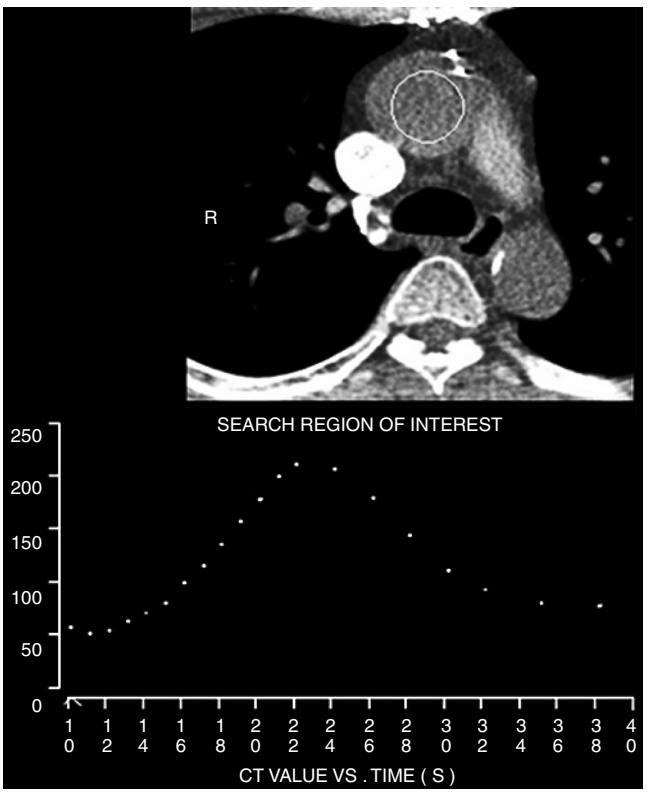

Figure 1.10. A flow or timing study. This study images the same level over time. A region of interest (in this study, the circle is placed in the ascending aorta) defines the anatomy to be measured. The graph below measures the Hounsfield units (HU) of that region of interest on each subsequent image. Initially, there is no contrast enhancement, and the measures are of non-enhanced tissue, around 50–60 HU. Contrast starts to arrive on this study around 16 s, and peaks at 22 s. The bright white structure next to the ascending aorta is the superior vena cava, filled with unmixed contrast.

Importance of Spatial Resolution

Spatial resolution compares the ability of the scanners to delineate fine detail within an image. Spatial resolution is important in all three dimensions when measuring coronary plaque. Even if limited to the proximal coronary arteries, the left system courses obliquely within the x–y imaging planes, while the right coronary artery courses through the z imaging plane. Simply put, one axial image may demonstrate five or more centimeters of the left anterior descending, while most images will demonstrate only a cross-section of the right coronary artery. The in-plane resolution of current CT systems is superior to magnetic resonance imaging, echocardiography and nuclear testing, but

lower than invasive angiography. The resolution in *z* dimension is determined by the detector width in MDCT (slice width). This is a "voxel" or volume element and it has the potential to be nearly cubic using MDCT but will always be "rectanguloid" or a "rectangular prism" for MRI (slice width greater than *x*–*y* pixel width), which precludes 3D manipulation of the MR data. Current coronary artery calcification (CAC) scanning protocols use 3 mm thickness for EBCT and vary between manufacturers from 2.5 to 3.0 mm for MDCT. For CT angiography, EBCT utilizes 1.5 mm slices, and MDCT obtains images with 0.5–0.625 mm per axial slice (submillimeter). Thus, MDCT has a significant advantage in terms of spatial resolution, and results in less partial volume averaging. Also the principles of resolution of a 1 mm vessel require that the slice width be 1 mm or less. Partial volume averaging occurs when a small plaque has dramatically different CT numbers related to whether it is centered within one slice or divided between two adjacent slices. Thus, thinner slices will have less partial volume averaging. The visualization of smaller lesions is only possible with smaller slice widths. For MRI and EBCT, the slice thickness is 2–3.0 mm, with an in-plane resolution of approximately 7–9 line pairs/cm (Figure 1.11). Modern MDCT systems permit simultaneous data acquisition in 64–320 parallel cross-sections with 0.5–0.625 mm collimation each. The in-plane spatial resolution is now as high as 14 line pairs/cm, increasing further with new High Definition CT (General Electric, Milwaulkee, WI). However, conventional CT angiography still has higher temporal and spatial resolution, allowing for better visualization of the smaller arteries and collateral vessels. Modern angiographic equipment has a resolution of 40 line pairs per centimeter with a six-inch field of view, the usual image magnification for coronary angiography [18]. Thus, invasive coronary angiography still has a three to fourfold better resolution than current MDCT systems. It is likely to remain this way until the perfection of flat panel detectors for CT – which would be akin to the current state of the art in conventional angiography devices and under development currently.

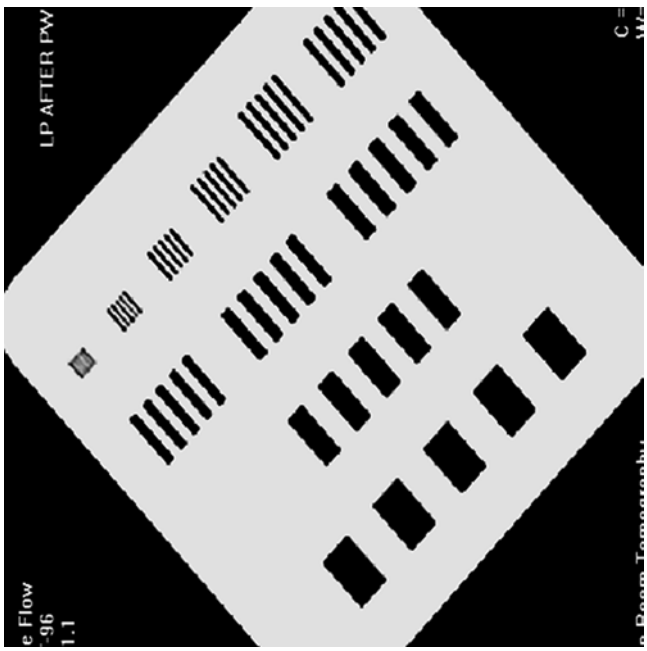

Figure 1.11. Spatial resolution as measured on computed tomography. A phantom is imaged, and the smaller line pairs per centimeter are evaluated. Somewhat similar to an eye chart, the thinnest lines clearly seen define the spatial resolution of the scanner.

Generally, the higher X-ray flux (mAs = tube current ¥ scan time) and greater number and efficiency of X-ray detectors available with MDCT devices leads to images with better signal-to-noise ratio and higher spatial resolution when compared to other imaging modalities. Early detection of calcified plaque is dependent upon distinguishing the plaque from image noise. Current MDCT systems have reduced image noise compared to older CT systems (8–18 noise/HU vs. 24 noise/HU). Typical values for mA for MDCT angiography is on the order of 300–700. While both EBCT and MRI have difficulties with the morbidly obese patient, MDCT can increase the mAs (and kV) to help with tissue penetration, while MRI is more limited in this clinical setting.

Speed/Temporal Resolution

Cardiac CT is dependent upon having a high temporal resolution to minimize coronary motion-related imaging artifacts. By coupling rapid image acquisition with ECG gating, images can be acquired in specific phases of the cardiac cycle. Studies have indicated that temporal resolutions of 19 ms are needed to suppress all pulmonary and cardiac motion [19]. Interestingly, temporal resolution needs to be faster to suppress motion of the pulmonary arteries than for cardiac imaging. The study by Ritchie et al. demonstrated the need for 19 ms imaging to suppress pulmonary motion (despite breath-holding), while needing 35 ms imaging to fully suppress motion for cardiac structures. This is most likely due to the accordion motion of the pulmonary arteries, whereby the motion of the heart causes the surrounding pulmonary arteries to be pulled in and out with each beat. This has led some physicians to use cardiac gating during pulmonary embolism studies to improve resolution down to fourth and fifth generation branches of the pulmonary system.

Cardiac MR motion studies of the coronary arteries demonstrate that the rest period of the coronary artery (optimal diastolic imaging time) varies significantly between individuals with a range of 66–333 ms for the left coronary artery and 66–200 ms for the right coronary artery [20], and that for mapping coronary flow, temporal resolution of 23 ms may be required for segments of the right coronary artery [21, 22]. Current generation cardiac CT systems create images with temporal resolution as low as 50–100 ms (EBCT) and 200–300 ms for prospectively gated MDCT and 100–150 ms for Dual Source CT. These systems cannot totally eliminate coronary artery motion in all individuals. Motion artifacts are especially prominent in the mid-right coronary artery, where

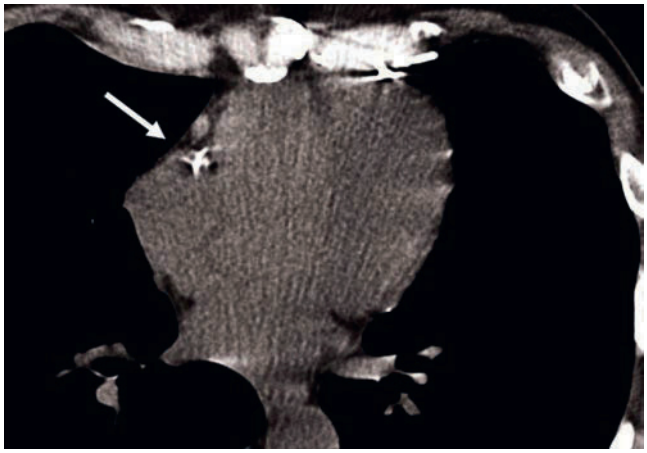

Figure 1.12. A typical motion artifact seen with calcium scans on MDCT images. The limited reproducibility of this technique is due to the star artifacts seen on this image (RCA, *white arrow*). Prospective gating is done, with halfscan reconstruction techniques. In cases of faster heart rates, motion artifacts seen here are commonplace. To limit radiation to a reasonable level for this screening text, no overlap or retrospective images are obtained, so multisegment reconstruction is not possible.

the ballistic movement of the vessel may be five times its diameter during the twisting and torsion of the heart during the cardiac cycle (thus, a 4 mm RCA may move up to 20 mm per cycle) (Figure 1.12). It should be remembered that the motion of the coronary artery during the cardiac cycle is a 3D event with translation, rotation, and accordion type movements. Thus, portions of the coronary artery pass within and through adjacent tomographic planes during each R-R cycle. Blurring of plaques secondary to coronary motion increases in systems with slower acquisition speeds. The resulting artifacts tend to increase plaque area and decrease plaque density and thus alter the calcium measurements. The artifacts may make those segments of the CT angiogram non-diagnostic, a problem that plagued up to 70% of the early four-slice MDCT system studies [5, 12], and perhaps 1–5% of current 64+ MDCT studies.

The image quality achieved with cardiac CT is determined not only by the 3D spatial resolution but also by the temporal resolution. The spatial resolution is directly related to the scan slice thickness and the reconstruction matrix. The temporal resolution, which determines the degree of motion suppression, is dependent on the pitch factor (which is determined by the table speed), the gantry rotation time, and the patient's heart rate during the examination. As stated above, utilizing more detectors (i.e., 16- vs. 64- vs. 256 or 320-detector/channel systems) will not improve the temporal resolution of the images (to lower motion artifacts on an individual slice), but will reduce scan time (i.e., breath-hold time) and section misregistration.

Radiation Dose

Computed tomography utilizes X-rays, a form of ionizing radiation, to produce the information required for generating CT images. Although ionizing radiation from natural sources is part of our daily existence (background radiation including air travel, ground sources, and television), a role of healthcare professionals involved in medical imaging is to understand potential risks of a test and balance those against the potential benefits. This is particularly true for diagnostic tests that will be applied to healthy individuals as part of a disease screening or risk stratification program. In order for healthcare professionals to effectively advise individuals, they must have an understanding of the exposure involved. The use of radiological investigations is an accepted part of medical practice, justified in terms of clear clinical benefits to the patient which should far outweigh the small radiation risks. Diagnostic medical exposures, being the major source of man-made radiation exposure of the population, add up to 50% of the radiation exposure to the population. However, even small radiation doses are not entirely without risk. A small fraction of the genetic mutations and malignant diseases occurring in the population can be attributed to natural background radiation. The concept of "effective dose" was introduced in 1975 to provide a mechanism for assessing the radiation detriment from partial body irradiations in terms of data derived from whole-body irradiations. The effective dose for a radiological investigation is the weighted sum of the doses to a number of body tissues, where the weighting factor for each tissue depends upon its relative sensitivity to radiation-induced cancer or severe hereditary effects. It thus provides a single dose estimate related to the total radiation risk, no matter how the radiation dose is distributed around the body. Adoption of the *effective dose* as a standard measure of dose allows comparability across the spectrum of medical and non-medical exposures:

> The effective dose is, by definition, an estimate of the uniform, whole-body equivalent dose that would produce the same level of risk for adverse effects that results from the non-uniform partial body irradiation. The unit for the effective dose is the sievert (Sv). (www.fda.gov/cdrh/ct/rqu.html).

Although it has many limitations, the effective dose is often used to compare the dose from a CT examination, a fluoroscopic examination, and the background radiation one experiences in a year. Units are either millirem (mrem) or millisievert (mSv); 100 mrem equals 1 mSv. The estimated dose from chest X-ray is 0.04 mSv, and the average annual back-ground radiation in the United States is about 300 mrem or 3 mSv [23], increasing as high as 6 mSv per year at places at elevation (such as Denver, CO). Table 1.3 shows the estimated radiation doses of some commonly used tests.

The Food and Drug Administration (FDA) in describing the radiation risks from CT screening in general used the following language (www.fda.gov/cdrh/ct/risks.html):

> In the field of radiation protection, it is commonly assumed that the risk for adverse health effects from cancer is proportional to the amount of radiation dose absorbed and the amount of dose depends on the type of

Table 1.3. Common tests with estimated radiation exposures

Test	Radiation dose (mSv)	
1 Stress MIBI	9 (technetium), 41 (thallium)	
1 LC spine	1.3	
1 Barium enema	7	
1 Upper GI	3	
1 Abdominal X-ray	1	
1 Dental X-ray	0.7	
1 Cardiac catheterization	2.5–10	
	Radiation dose for MDCT (mSv)	Radiation dose for EBC (mSv)
Calcium scan	1–1.5	0.6
CT angiography	8–13	1–1.5
CCTA, prospective triggering	2–4	–
Lung CT	8	1.5
Abdomen/Pelvis	10	2
Body scan	12	2.6
Virtual colon	8–14	2–3

X-ray examination. A CT examination with an effective dose of 10 mSv (abbreviated mSv; 1 mSv=1 mGy in the case of X rays) may be associated with an increase in the possibility of fatal cancer of approximately 1 chance in 2,000. This increase in the possibility of a fatal cancer from radiation can be compared to the natural incidence of fatal cancer in the US population, about 1 chance in 5. In other words, for any one person the risk of radiation-induced cancer is much smaller than the natural risk of cancer. Nevertheless, this small increase in radiation-associated cancer risk for an individual can become a public health concern if large numbers of the population undergo increased numbers of CT procedures for screening purposes.

Since CT is the most important source of ionizing radiation for the general population, dose reduction and avoidance is of the utmost importance, especially for the asymptomatic person undergoing risk stratification, rather than diagnostic workup. Already, 50% of a person's lifetime radiation exposure is due to medical testing, and this is expected to go up with increased exposure to nuclear tests and CT scanning. Used as a tool in preventive cardiology, cardiac CT is increasingly being performed in the population of asymptomatic persons, a priori healthier individuals, where use of excessive radiation is of special concern.

The other variable involved in dose is the protocol used. EBCT protocols are fairly fixed; the only variable is the use, if any, of overlap. All data are acquired by prospective triggering; that is, the X-rays are only on during the acquisition of data that will be used for the image. MDCT, however, can use prospective triggering or retrospective gating, 100–140 kilovolts (kV) (with protocols now possible with lower kV depending upon future research and tube current improvements), and a wide range of mA. Retrospective gating means that the X-rays are on throughout the heart cycle. One drawback of MDCT as compared to EBCT is the potential for higher radiation exposure to the patient, depending on the tube current selected for the examination. The X-ray photon flux expressed by the product of X-ray tube current and exposure time (mAs) is generally higher with MDCT. For example, 200 mA with 0.5 s exposure time yields 100 mAs in MDCT, whereas 614 mA (fixed tube current) with 0.1 s exposure time yields 61.4 mAs in EBCT. Hunold et al. [24] reported a study of radiation doses during cardiac examinations. In millisieverts, calcium scanning leads to an approximate dose of 1–1.2 mSv for MDCT, and 0.7 mSv for EBCT [24]. This is in comparison to a conventional coronary angiogram, with effective doses of 2–5 mSv for men and women respectively, and background radiation of 3–6 mSv annually, depending on the altitude at which one lives.

There are primary three factors that go into radiation dosimetry: the X-ray energy (kV), tube current (mA), and exposure time. The distance of the X-ray source from the patient is a fourth source, but, unlike fluoroscopy, this distance is fixed in CT. In females, the effective radiation doses is another 25% higher than in males due to increased radiation sensitivity in both the breast tissue and lung tissue [25]. When MDCT angiography utilizes retrospective imaging, radiation is continuously applied while only a fraction of the acquired data is utilized, higher radiation doses (doses of 8–15 mSv/study) still play a role in decisions to utilize this modality [24, 26].

Theoretically, since narrow collimation (beam widths) causes "overbeaming," the dose efficiency is lower with four-slice scanners than with more detectors. Estimated efficiency goes from 67% with 4 slices (1.25 mm, 5 mm cov-erage) to 97% with 16 slices (at 1.25 mm, covering 20 mm). However, obtaining thinner slices will offset this gain, as obtaining more images will lead to higher radiation doses. Furthermore, wider collimations (more detectors) will cause less efficiency, as the detector must have enough photons to hit each detector. Thus, each increment in detectors will lead to an increment in radiation dose (for the same protocol). Typical studies with four-slice MDCT scanners obtained 600 images, while 16-slice scanners typically produce about 1,200 scans, and 64-detector scanners are reporting over 2,000 images produced per study. Newer MDCT studies report that radiation doses continue to increase with high levels of multidetector scanners [26, 27], and the highest doses will be with the 320 scanner (widest collimation, least efficient). Of course, use of prospective imaging, will lower doses, but the 320 scanner using prospective imaging will be a higher radiation dose on average than the 64 detector using prospective imaging [27].

The energy (killivolt or kV) used can be altered in MDCT studies, and while typical imaging is done in the range of 100–120 kV, this can be varied with MDCT [27]. The attenuation (densities) of calcium and iodine contrast agents increases with reduced X-ray energy (reduced kV settings). This can reduce the X-ray exposure, as the X-ray power emitted by the tube decreases considerably with reduced kV settings. To compensate for the lower power (and resultant increased noise of the image), the tube current (mA) can be increased. Scans with less than 120 kV tube voltage (i.e., 80 kV) can potentially maintain contrast-to-noise ratios that

have been established for coronary calcium and CT angiography images, and significant lower radiation exposure. Preliminary experiments have demonstrated a reduction in radiation exposures of up to 50% with use of 80 kV. Jakobs et al. demonstrated that the radiation dose for CAC scoring with use of 80 kV may be as low as 0.6 mSv (similar to EBCT data) [28]. As the noise will go up with 80 kV imaging, this may be too low for CT angiography, except in thin adults and children. However, lower kV will cause the contrast to appear brighter (raising the contrast or C), and at the same time raising the noise (or N), so the net C/N ratio may not change much, until heavier or thicker patients are imaged. This allows the dose to be reduced without resultant loss of image quality [27]. CT angiography protocols are now commonly performed with 100 kV protocols, providing a reduction in radiation of 30–40%. The reduction of kV leads to an exponential reduction of radiation dose, so a 20% reduction of kV will lead to a 40% reduction in dose [27]. There is only emerging research on the clinical diagnostic accuracy utilizing these radiation-dose-reducing options routinely. A lower kV is most often used for pediatric patients. Similarly, for obese patients, where penetration is important, a kV of 135 or even 140 can be utilized, but one must keep in mind the dose will go up exponentially as kV goes up. The power (mAs) used is directly proportional to the radiation dose. Higher mAs results in lower image noise, following the relationship: noise is inversely proportional to the square root of the mAs. Thus, limiting mAs can result in lower radiation, but higher noise. It is important to remember that reducing mAs too much to save radiation will increase noise to the point where the scan is non-diagnostic. Most centers use either an "automatic" mAs system, which adjusts the mAs based upon the image quality, or leave the mAs relatively fixed.

Prospective triggering or "sequential" mode is typically used and strongly recommended for coronary calcium assessment with MDCT, due to the lower radiation doses to which the patient is exposed. However, the drawback of using MDCT prospective triggering is the inability to perform overlapping images, and longer image acquisition times. Thus, it is still common for CCTA to be done with retrospective image acquisition, despite the higher radiation doses. This is due to the requirement during retrospective imaging for slower table movement to allow for oversampling, for gap-less and motion-reduced imaging, as well as the possibility of multisegment reconstruction. Retrospective imaging allows the clinician to have multiple phases of the cardiac cycle available for reconstruction, to find the portion of the study with the least coronary motion. Many clinicians utilize multiple phases for reconstruction, with different phases used for different coronary arteries (depending on heart rate). However, constant irradiation is redundant, as most images are reconstructed during the diastolic phases of the heart cycle. Thus, a new method for reducing radiation dose with MDCT is to implement tube current modulation. Tube current is reduced during systole, when images are not utilized for reconstruction of images for MDCT angiography, by 80%, and then full dose is utilized during diastole. Depending upon the heart rate, this may reduce radiation exposure by as much as 47% [28], but with slower heart rates, this reduction will be less, as systole encompasses a shorter and shorter fraction of the cardiac cycle. Dose modulation protocols reduce radiation doses with MDCT by attempting to decrease beam current during systole, when images are not used for interpretation, and should be employed whenever possible [29]. Most of these protocols turn down the beam current (mA) during systole, so that diagnostic images are still available from roughly 40–80% of the R-R interval (cardiac cycle).

Dose modulation is not universally employed, as it is harder to use it with fast heart rates, as the time to ramp up and ramp down the radiation dose becomes significant, and the ever shortening diastole becomes a smaller target. The routine use of beta blockers makes even more sense in this setting, given the increased ability to use dose modulation with lower heart rates, thus lowering the radiation dose [26, 27, 29]. Clinically, dose modulation is used less than expected, as many clinicians, nervous about not having a portion of the cardiac cycle available for analysis, choose to leave the dose modulation feature off. Another issue is the potential loss of wall motion and other functional data. If tube current modulation is used, systolic images are obtained with less energy, thus have more noise per image. Some investigators have reported that no functional information can be obtained while using dose modulation. This is probably not correct, as an image from end-systole (early diastole) and end-diastole can be compared to calculated wall thickening, ejection fraction, and cardiac motion. Most CT angiography studies performed today reported to date have utilized dose modulation routinely.

One must be careful and cognizant of the dose being given. In one study using 16-slice MDCT, the pitch was reduced based upon the patient being able to hold their breath for 20 s, so very high overlap was obtained (very low pitch). The mean irradiation dose received by the patients during this MDCT angiography study was 24.2 mSv [30]. Understanding the physics and implications of higher mAs and kV and thinner slices will help the clinician choose the necessary parameters, without over-irradiating the patient. This concept, called "information/milliSv," causes one to think about the benefit garnered from each mSv given.

Clinical Applications of Cardiovascular CT

Cardiac CT has several unique diagnostic capabilities applicable to the many facets of CAD, worth the radiation exposures and time needed to learn these applications. Each will be discussed at length in chapters throughout this book. The presence of coronary calcium is invariably an indicator of atherosclerosis [31, 32]. Non-contrast studies can accurately identify and quantify coronary calcification (a marker of total plaque burden) [33], while contrast-enhanced studies can define ventricular volumes, ejection fraction, and

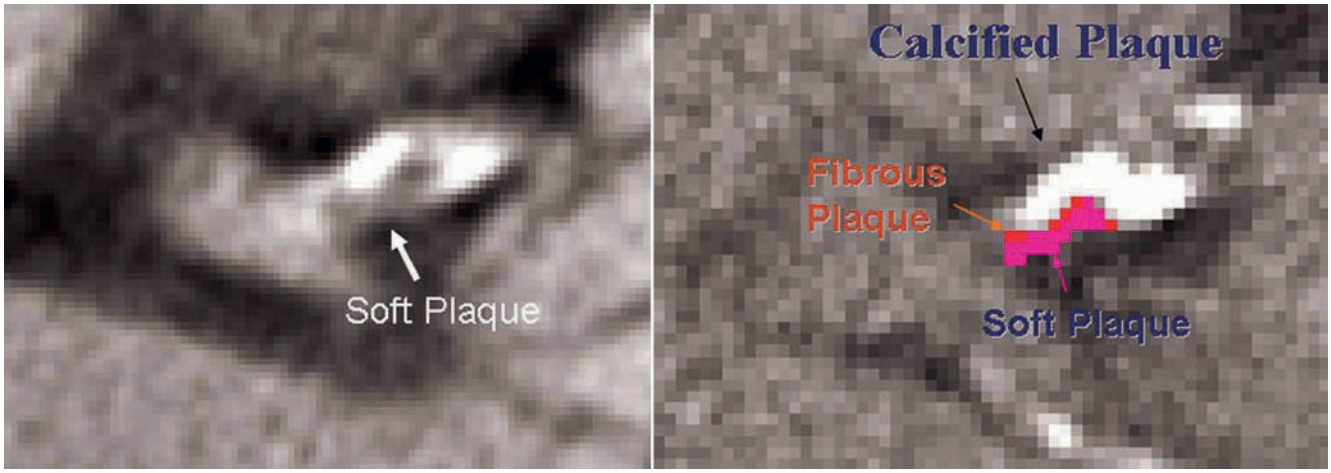

Figure 1.13. A contrast-enhanced (*left image*) and non-contrast study (*right image*) of the left main and proximal LAD. The soft plaque is visible (*dark region*, representing fat density) with calcified plaque (*white regions*). A computer program can be applied (AcuImage, San Francisco, CA) to the individual pixels to measure lower density (*pink squares*, fat density), intermediate density (*red squares*, fibrous density), and high density (*white squares*, calcified plaque). This can theoretically quantitate the volume of soft plaque, fibrous plaque, and calcified plaque in any given CT image.

wall motion and wall thickening with high accuracy [34]. Studies can be performed at rest, and during exercise can identify reversible ischemia [35].

Coronary angiography during cardiac catheterization is the clinical gold standard for definitive diagnosis and determination of coronary lesions. Pathologic studies have demonstrated that the severity of coronary stenoses is underestimated by visual analysis during clinical coronary angiography [36–39]. This may result from the limitations of resolution based upon fluoroscopy and the 2D imaging inherent in coronary angiography, as well as the inability to see beyond the lumen with conventional angiography. The true promise of cardiovascular CT is to visualize the coronary artery, including the lumen and wall. Three-dimensional digital coronary images may provide more accurate representation of coronary artery anatomy and be more amenable to quantitation, thereby improving the diagnosis and treatment of CAD [40]. There is rapidly accumulating data with both MDCT and EBCT to visualize the coronary arteries accurately and reliably (CT angiography) [41–44]. Looking beyond the lumen by visualizing the wall and its constituents (including fat, calcium, and fibrous tissue) is now possible with cardiac CT (Figure 1.13). Coronary plaque composition evaluation is being actively investigated [45–47]. This so-called "soft plaque" evaluation may prove to have prognostic significance over coronary calcium or risk factors alone, as well as helping to target revascularization better than luminography alone.

Future of CT and MR

The strengths of magnetic resonance cardiovascular imaging include greater definition of tissue characteristics, perfusion, valvular function, lack of X-ray radiation, and lack of need for potentially nephrotoxic contrast media, compared to CT technologies. Several studies have been reported comparing this modality to coronary angiography [48–50]. Limited temporal and spatial resolution [51], partial volume artifacts (due to slice thickness limitations) [52], reliance on multiple breath-holds, and poor visualization of the left main coronary artery [53] all reduce the clinical applicability of MR angiography. Reported sensitivities for MR angiography range from 0 to 90% [9, 47]. MR angiography remains a technically challenging technique with certain limitations hindering its clinical use. CT angiography offers advantages over MR angiography, including single breath-hold to reduce respiratory motion, higher spatial resolution, reduced slice thickness and overall study time of 35–50 s with CT techniques as compared to 45–90 min for MR angiography [9]. The rapidity and ease with which CT coronary angiography can be performed suggest possible cost advantages compared with MR angiography and selective coronary angiography [6, 54]. Thus, for most applications (in the absence of renal insufficiency or contrast allergy), CT will be the preferred method to evaluate anatomy, be it coronary, renal, carotid, or peripheral vascular beds (Figure 1.14). MR, in the foreseeable future, will remain a better test for intercranial imaging, as the bony structures cause some scatter with CT imaging.

For cardiovascular CT in general, better workstations (ease of use and diagnostic capabilities), as well as improvements in both spatial and temporal resolution will continue to push this diagnostic tool to the forefront of cardiology. For MDCT, increased numbers of detectors (64-320 slice systems are now available) will allow for better collimation and spatial reconstructions. Having more of the heart visualized simultaneously will also allow for reductions in the contrast requirements and breath-holding, further improving the methodology. Multi-sector reconstruction (combining images from consecutive heart beats) and dose modulation (to reduce radiation exposure during systole,

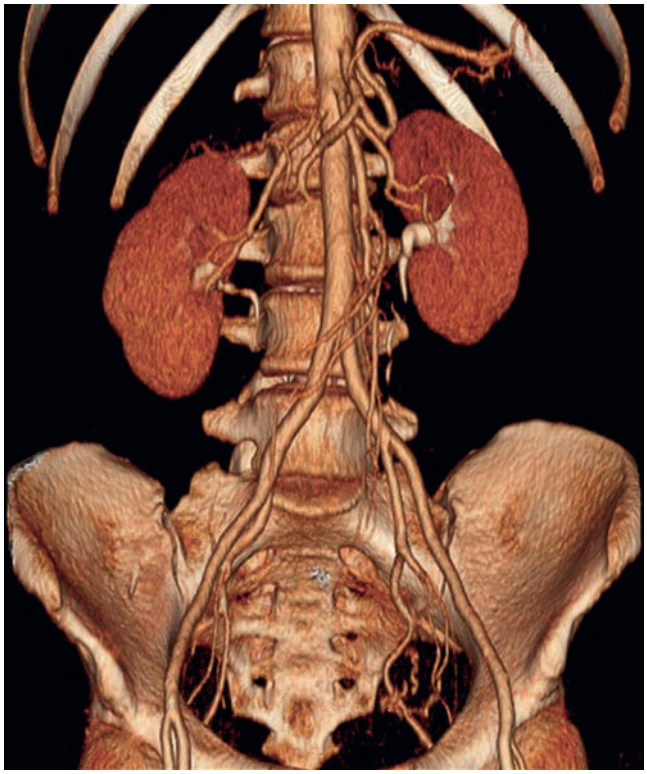

Figure 1.14. A constrast-enhanced study demonstrating the abdominal aorta, renal arteries and kidneys, and iliac circulation. This study can be done with 40 cm^3 of iodinated contrast, taking between 5 and 10 s depending on the scanner used. Highly diagnostic vascular imaging is quite routine with EBCT and MDCT scanners.

when images are not used for reconstruction) are increasingly being applied, which will continue to improve the image quality and diagnostic rate of these machines, while lowering the risks.

References

1. Mao S, Budoff MJ, Oudiz RJ, Bakhsheshi H, Wang S, Brundage BH. A simple single slice method for measurement of left and right ventricular enlargement by electron beam tomography. *Int J Card Imaging*. 2000;16:383–390.
2. Budoff MJ, Mao SS, Wang S, Bakhsheshi H, Brundage BH. A Simple single slice method for measurement of left and right atrial volume by electron beam computed tomography. *Acad Radiol*. 1999;6:481–486.
3. Stuber M, Botnar RM, Fischer SE, et al. Preliminary report of in-vivo coronary MRA at 3 Tesla in humans. *Magn Reson Med*. 2002;48: 425–428.
4. Carr JJ, Nelson JC, Wong ND, et al. Calcified coronary artery plaque measurement with cardiac CT in population-based studies: standardized protocol of Multi-Ethnic Study of Atherosclerosis (MESA) and Coronary Artery Risk Development in Young Adults (CARDIA) study. *Radiology*. 2005;234:35–43.
5. Nieman K, Rensing BJ, van Geuns RJ, et al. Non-invasive coronary angiography with multislice spiral computed tomography: impact of heart rate. *Heart*. 2002;88(5):470–474.
6. Budoff MJ, Achenbach S, Blumenthal RS, et al. Assessment of coronary artery disease by cardiac computed tomography, a scientific statement from the American Heart Association Committee on Cardiovascular Imaging and Intervention, Council on Cardiovascular Radiology and Intervention, and Committee on Cardiac Imaging, Council on Clinical Cardiology. *Circulation*. 2006;114(16):1761–1791.
7. Leber AW, Knez A, von Ziegler F, et al. Quantification of obstructive and nonobstructive coronary lesions by 64-slice computed tomography: a comparative study with quantitative coronary angiography and intravascular ultrasound. *J Am Coll Cardiol*. 2005;46:147–154.
8. Regenfus M, Ropers D, Achenbach S, et al. Noninvasive detection of coronary artery stenosis using contrast-enhanced three-dimensional breath-hold magnetic resonance coronary angiography. *J Am Coll Cardiol*. 2000;36:44–50.
9. Kim WY, Danias PG, Stuber M, et al. Coronary magnetic resonance angiography for the detection of coronary stenoses. *N Engl J Med*. 2001;345:1863–1869.
10. Blobel J, Baartman H, Rogalla P, Mews J, Lembcke A. Spatial and temporal resolution with 16-slice computed tomography for cardiac imaging. *Fortschr Roentgenstr*. 2003;175:1264–1271.
11. Lembcke A, Rogalla P, Mews J, et al. Imaging of the coronary arteries by means of multislice helical CT: optimization of image quality with multisegmental reconstruction and variable gantry rotation time. *Fortschr Roentgenstr*. 2003;175:780–785.
12. Wicky S, Rosol M, Hoffmann U, Graziano M, Yucel KE, Brady TJ. Comparative study with a moving heart phantom of the impact of temporal resolution on image quality with two multidetector electrocardiography-gated computed tomography units. *J Comput Assist Tomogr*. 2003;27:392–398.
13. Dewey M, Laule M, Krug L, et al. Multisegment and halfscan reconstruction of 16-slice computed tomography for detection of coronary artery stenosis. *Invest Radiol*. 2004;39:223–229.
14. Mao S, Lu B, Oudiz RJ, Bakhsheshi H, Liu SCK, Budoff MJ. Coronary artery motion in electron beam tomography. *J Comput Assist Tomogr*. 2000;24:253–258.
15. Orakzai SH, Orakzai RH, Nasir K, Budoff MJ. Assessment of cardiac function using multidetector row computed tomography. *J Comput Assist Tomogr*. 2006;30(4):555–563.
16. Mao SS, Budoff MJ, Oudiz RJ, et al. Effect of exercise on left and right ventricular ejection fraction and wall motion in patients with coronary artery disease: an electron beam computed tomography study. *Int J Cardiol*. 1999;71:23–31.
17. McKay CR, Brundage BH, Ullyot DJ, et al. Evaluation of early postoperative coronary artery bypass grafts patency by contrast-enhanced computed tomography. *J Am Coll Cardiol*. 1983;2:312–317.
18. Nissen SE, Gurley GL. Assessment of coronary angioplasty results by intravascular ultrasound. In: Serruys PW, Straus BH, King SB III, eds. *Restenosis After Intervention with New Mechanical Devices*. Dordrecht, Netherlands: Kluwer; 1992:73–96.
19. Ritchie CJ, Godwin JD. Minimum scan speeds for suppression of motion artifacts in CT. *Radiology*. 1992;185:37–42.
20. Wang Y, Vidan E. Cardiac motion of coronary arteries: variability in the rest period and implications for coronary MR angiography. *Radiology*. 1999;213(3):751–758.
21. Hofman MB, Wickline SA. Quantification of in-plane motion of the coronary arteries during the cardiac cycle: implications for acquisition window duration for MR flow quantification. *J Magn Reson Imaging*. 1998;8(3):568–576.
22. Marcus JT, Smeenk HG. Flow profiles in the left anterior descending and the right coronary artery assessed by MR velocity quantification: effects of through-plane and in-plane motion of the heart. *J Comput Assist Tomogr*. 1999;23(4):567–576.
23. Morin RL, Gerber TC, McCollough CH. Radiation dose in computed tomography of the heart. *Circulation*. 2003;107:917–922.
24. Hunold P, Vogt FM, Schmermund A, et al. Radiation exposure during cardiac CT: effective doses at multi-detector row CT and electron-beam CT. *Radiology*. 2003;226:145–152.
25. ICRP (ICoRP). The 2007 recommendations of the International Commission on Radiological Protection (ICRP Publication 103). *Ann ICRP*. 2007;37:1–332.
26. Gerber TC, Carr JJ, Arai AE, et al. Ionizing radiation in cardiac imaging: a science advisory from the American Heart Association Committee on Cardiac Imaging of the Council on Clinical Cardiology and Committee on Cardiovascular Imaging and Intervention of the

Council on Cardiovascular Radiology and Intervention. *Circulation*. 2009;119(7):1056–1065. epub.
27. Budoff MJ. Maximizing dose reductions with cardiac CT. *Int J Cardiovasc Imaging*. 2008; PMID: 19115082.
28. Jakobs TF, Becker CR, Ohnesorge B, et al. Multislice helical CT of the heart with retrospective ECG gating: reduction of radiation exposure by ECG-controlled tube current modulation. *Eur Radiol*. 2002;12:1081–1086.
29. Trabold T, Buchgeister M, Kuttner A, et al. Estimation of radiation exposure in 16-detector row computed tomography of the heart with retrospective ECG-gating. *Rofo*. 2003;175:1051–1055.
30. Gopal A, Mao SS, Karlsberg D, et al. Radiation reduction with prospective ECG-triggering acquisition using 64-multidetector computed tomographic angiography. *Int J Cardiovasc Imaging*. 2009;25 (4):405–416.
31. Budoff MJ, Nasir K, McClelland RL, et al. Coronary calcium predicts events better with absolute calcium scores than age-gender-race percentiles – The Multi-Ethnic Study of Atherosclerosis (MESA). *J Am Coll Cardiol*. 2009;53:345–352.
32. Blankenhorn DH. Coronary artery calcification: a review. *Am J Med Sci*. 1961;242:1–9.
33. Breen JF, Sheedy PF, Schwartz RS, et al. Coronary artery calcification detected with ultrafast CT as an indication of coronary artery disease. *Radiology*. 1992;185:435–439.
34. Lipton MJ, Higgins CB, Boyd DP. Computed tomography of the heart: evaluation of anatomy and function. *J Am Coll Cardiol*. 1985;5: 555–595.
35. Wu YW, Tadamura E, Yamamuro M, et al. Estimation of global and regional cardiac function using 64-slice computed tomography: a comparison study with echocardiography, gated-SPECT and cardiovascular magnetic resonance. *Int J Cardiol*. 2008;128:69–76.
36. Lessick J, Dragu R, Mutlak D, et al. Is functional improvement after myocardial infarction predicted with myocardial enhancement patterns at multidetector CT? *Radiology*. 2007;244:736–744.
37. Grondin CM, Dyrda I, Pasternac A, Campeau L, Bourassa MG, Lesperance J. Discrepancies between cineangiographic and postmortem findings in patients with coronary artery disease and recent myocardial revascularization. *Circulation*. 1974;49:703–708.
38. Thomas AC, Daview MJ, Dilly S, Dilly N, Franc F. Potential errors in estimation of coronary arterial stenoses from clinical coronary arteriography with reference to the shape of the coronary arterial lumen. *Br Heart J*. 1986;55:129–139.
39. Mintz GS, Painter JA, Pichard AD, et al. Atherosclerosis in angiographically normal coronary artery reference segments: an intravascular ultrasound study with clinical correlations. *J Am Coll Cardiol*. 1995;25:1479–1485.
40. Van den Broek JGM, Slump CH, Storm CJ, Van Benthem AC, Buis B. Three-dimensional densitometric reconstruction and visualization of stenosed coronary artery segments. *Comput Med Imaging Graph*. 1995;19:207–217.
41. Napel S, Rubin GD, Jeffrey RB Jr. STS-MIP: A new reconstruction technique for CT of the chest. *J Comput Assist Tomogr*. 1993;17(5): 832–838.
42. Budoff MJ, Dowe D, Jollis JG, et al. Diagnostic performance of 64-detector row coronary computed tomographic angiography of individuals undergoing invasive coronary prospective multicenter ACCURACY (Assessment by Coronary Computed Individuals Without Known Coronary Artery Disease: Results From the Tomographic Angiography for Evaluation of Coronary Artery Stenosis in Angiography) trial. *J Am Coll Cardiol*. 2008;52(21):1724–1732.
43. Budoff MJ, Rasouli ML, Shavelle DM, et al. Cardiac CT angiography (CCTA) and nuclear myocardial perfusion imaging (MPI)-a comparison in detecting significant coronary artery disease. *Acad Radiol*. 2007;14(3):252–257.
44. Bluemke DA, Achenbach S, Budoff M, et al. Noninvasive coronary artery imaging: magnetic resonance angiography and multidetector computed tomography angiography: a scientific statement from the american heart association committee on cardiovascular imaging and intervention of the council on cardiovascular radiology and intervention, and the councils on clinical cardiology and cardiovascular disease in the young. *Circulation*. 2008;118(5):586–606.
45. Hoffmann U, Bamberg F, Chae CU, et al. Coronary computed tomography angiography for early triage of patients with acute chest pain - the Rule Out Myocardial Infarction using Computer Assisted Tomography (ROMICAT) trial. *J Am Coll Cardiol*. 2009;53(18):1642–1650.
46. Schroeder S, Kopp AF, Baumbach A, et al. Noninvasive detection and evaluation of atherosclerotic coronary plaques with multislice computed tomography. *J Am Coll Cardiol*. 2001;37:1430–1435.
47. Leber AW, Knez A, White CW, et al. Composition of coronary atherosclerotic plaques in patients with acute myocardial infarction and stable angina pectoris determined by contrast-enhanced multislice computed tomography. *Am J Cardiol*. 2003;91:714–718.
48. Manning WJ, Li W, Edelman RR. A preliminary report comparing magnetic resonance imaging with conventional angiography. *N Engl J Med*. 1993;328:828–832.
49. Pennell DJ, Keegan J, Firmin DN, Gatehouse PD, Underwood SR, Longmore DB. Magnetic resonance imaging of coronary arteries: technique and preliminary results. *Br Heart J*. 1993;70:315–326.
50. Paschal CB, Haache EM, Adler LP. Coronary arteries: three-dimensional MR imaging of the coronary arteries: preliminary clinical experience. *J Magn Reson Imaging*. 1993;3:491–501.
51. Duerinckx AJ, Urman MK. Two dimensional coronary MR angiography: analysis of initial clinical results. *Radiology*. 1994;193:731–738.
52. Duerinckx AJ, Urman MK, Atkinson DJ, Simonetti OP, Sinha U, Lewis B. Limitations of MR coronary angiography. *J Magn Reson Imaging*. 1994;4:81.
53. Duerinckx AJ, Atkinson DP, Mintorovitch J, Simonetti OP, Urman MK. Two-dimensional coronary MRA: limitations and artifacts. *Eur Radiol*. 1996;6:312–325.
54. Chernoff DM, Ritchie CJ, Higgins CB. Evaluation of electron beam CT coronary angiography in healthy subjects. *AJR Am J Roentgenol*. 1997;169:93–99.

2

Cardiovascular Computed Tomography: Current and Future Scanning System Design

Wm. Guy Weigold

Introduction

The heart can be visualized in gross form on any standard chest computed tomography (CT), but for detailed evaluation of cardiac anatomy exacting specifications of scanner hardware and software must be in place because: the heart is continually in motion, the structures of interest (i.e., coronary arteries) are small, and their curvilinear course requires multiplanar reformatting for analysis.

For these specifications to be met, the scanner hardware must be robust, the scanner must be fitted with ECG-monitoring equipment, and cardiac-specific software and image reconstruction servers must be installed.

Elements of Scanner Design

The general design of a CT scanner equipped for cardiac imaging is the same as that of any modern scanner: an X-ray tube mounted on a rotating gantry opposite a detector array generates X-rays which are emitted across the bore, are attenuated as they pass through the patient's chest, and are scintillated by the detectors as the gantry rotates around the patient obtaining attenuation data from multiple view angles. These data are transmitted to an image reconstruction server which then computes the axial images. To perform cardiac CT, however, a number of additional capabilities are required, [1, 2] namely, high spatial resolution, high temporal resolution, and fast scan speed, while delivering an acceptable radiation exposure.

Special Design Considerations for Cardiac CT

Spatial Resolution

Spatial resolution is the product of multiple variables including detector characteristics and collimation, sampling rate, and reconstruction methods. State of the art scanners use thin 0.5–0.625 mm collimation. This reduces volume averaging thus increasing image detail of small objects, and allows reconstruction of isotropic datasets, thereby preserving *z*-axis resolution and permitting multiplanar reformatting necessary for analysis of cardiac anatomy.

GE Healthcare has focused their system development on spatial resolution, developing a new detector scintillation material with a fast decay time (30 ns), minimal afterglow (one-quarter that of conventional Gd_2O_2S crystals), and increased efficiency [3]. This new detector is one element of a multipronged approach to increasing image resolution, which also includes new electronics that permit increased sampling,[4] and a new iterative reconstruction algorithm [5, 6] (Figure 2.1). These innovations increase spatial resolution by 3–4.5 line pairs per centimeter (lp/cm), which is substantial given that current resolution of systems is approximately 12–15 lp/cm. The enhanced resolution is particularly useful for imaging stented and/or calcified coronary arteries.

Temporal Resolution

In order to reconstruct an axial image, attenuation data from multiple view angles that encompass half a rotation around the patient are required. The amount of time needed to obtain these data is the nominal, heart-rate independent temporal resolution of the scanner. Hence, a gantry that requires 330 ms to make one complete rotation has a baseline temporal resolution of 165 ms. This is analogous to shutter speed: just as shutter speed must be sufficiently fast to capture motion-free images of a moving subject, temporal resolution must be sufficiently fast to capture the data needed for image reconstruction within the relatively brief period of cardiac diastasis. If temporal resolution is insufficient, motion artifact occurs (Figure 2.2). A temporal resolution of 165 ms is relatively slow for cardiac imaging, so systems overcome this by various means: faster gantry rotation, multicycle reconstruction, and a second X-ray tube.

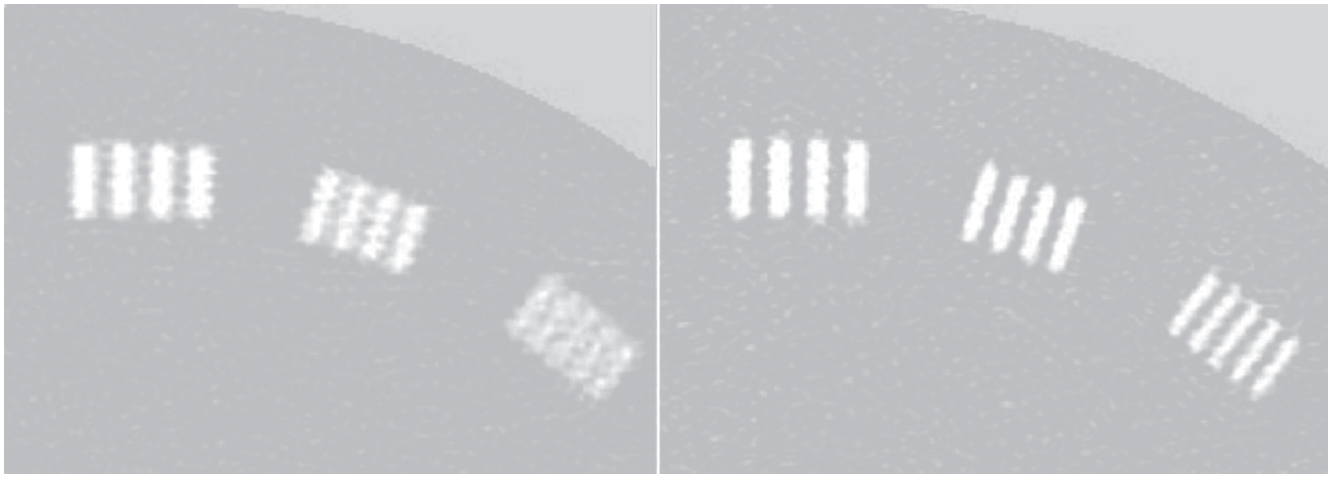

Figure 2.1. Increased sampling improves image quality. Axial images of line-pair phantom demonstrating improved spatial resolution using increased sampling density (*on the right*) compared to standard sampling frequency (*on the left*). Note the improved edge detail and resolution of the line pairs of the image derived from the high density sampling dataset. (Reproduced with permission from Chandra [4]).

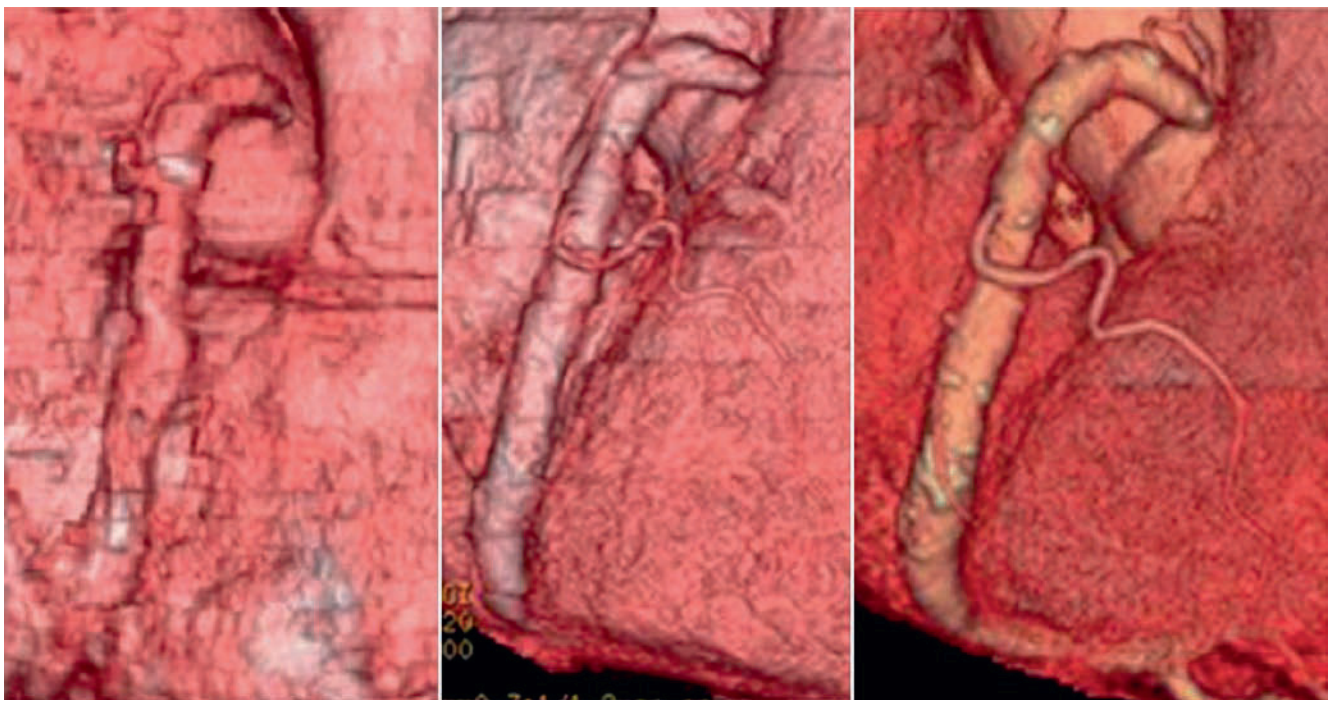

Figure 2.2. Better temporal resolution improves image quality of moving structures. 3D volume reconstructions of the right coronary artery in three CT scans representing three generations of CT scanner (4-, 16-, and 64-slice, from *left to right*, respectively), possessing temporal resolution of 400, 250, and 180 ms from *left to right*, respectively. Note that the vessel appears distorted and disjointed, due to motion artifact, when temporal resolution is insufficient (*far left*), while motion artifact is minimally present, and small anatomic details are clearly imaged when temporal resolution is improved (*far right*). (Reproduced with the kind permission from Springer Science + Business Media from Hurlock et al [2]).

Currently, the fastest gantry on the market resides in the Philips iCT, which has a rotation time of 270 ms using an innovative frictionless design in which the gantry is actually suspended in air [7]. As this design has only recently been released, it is likely that future iterations will allow even faster rotation.

Multicycle reconstruction combines data from multiple contiguous heart beats to complete the half-scan of views (Figure 2.3). This technique is heart-rate dependent: it can only be used within certain ranges of heart rates, since the cardiac cycle and gantry rotation must be asynchronous.

An approach adopted by Siemens in 2006 uses two X-ray tubes mounted on the gantry at 90° angles; therefore, only a quarter turn of the gantry is required to collect the 180° of attenuation data (Figure 2.4). Hence, a dual-source system with a gantry rotation time of 330 ms has a baseline central temporal resolution of approximately 85 ms. This obviates the need for multicycle reconstruction, making the system less susceptible to variation in heart rate, and providing high heart rate independent temporal resolution. Initial reports demonstrated very good image quality, [8] and, in a comparison of 64 MDCT and DSCT scans, the dual-source

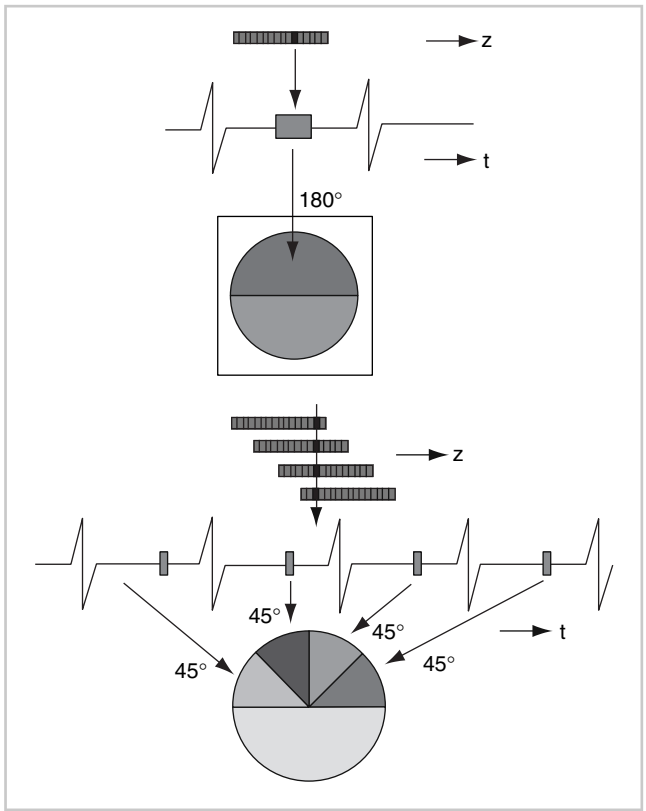

Figure 2.3. Multicycle reconstruction. Single cycle recon (**a**) the duration of the acquisition window (*gray bar*) is approximately equivalent to one-half the gantry rotation time, since this is the time required to obtain 180° of attenuation data. Multicycle recon (**b**) When multiple detector rows are present, the axial slice position in the *z*-position can be imaged at multiple different times, using multiple, shorter, acquisition windows distributed across multiple contiguous beats. These data can then be combined to provide 180° of attenuation data and used to reconstruct the axial image. Temporal resolution of the image is improved because the duration of the each acquisition window is shorter. (Reproduced with permission from Wolters Kluwer from Vembar et al [1]).

system produced better image quality at higher heart rates [9]. Image quality is still improved, however, by reducing heart rate before scanning. Siemens recently announced a new scanner with an even faster (280 ms) gantry which is capable of a central temporal resolution of 75 ms [10].

Detector Coverage and Scan Speed

Since the advent of multislice CT, manufacturers have increased *z*-axis coverage by the addition of more rows of detectors. By increasing coverage, scan times have been reduced to just a few seconds, and even to single-beat scanning. This has been achieved by Toshiba's Aquilion One scanner, which currently has the largest *z*-axis coverage [11]. This scanner has 320 rows of detectors, with 0.5 mm collimation, 16 cm of coverage, and can perform an axial 1-beat acquisition of the entire heart when the rate is well controlled.

The Philips iCT is a 128-row scanner with 8 cm of coverage, which allows axial acquisition of the entire heart in 2 beats [7]. GE offers a 64-row scanner with 4 cm of

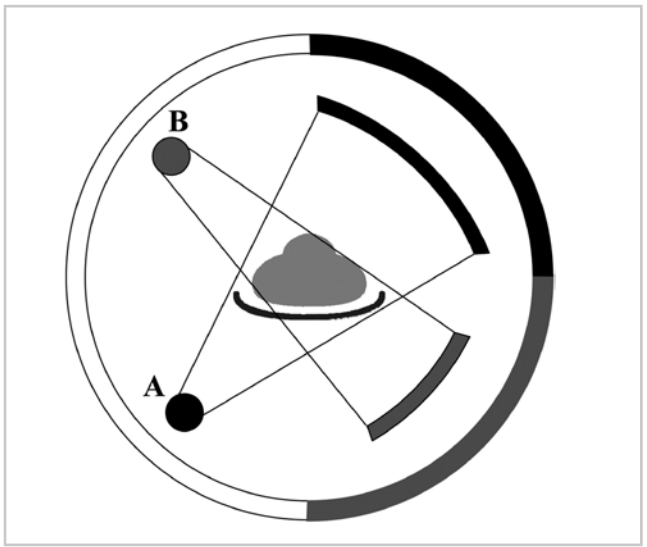

Figure 2.4. Dual source CT. Schematic diagram of dual-source CT scanner: two X-ray source and corresponding detector arrays are offset by approximately 90°. In this way, the half-scan of data required for axial image reconstruction can be acquired over a quarter-rotation of the gantry, thereby halving the nominal heart rate independent temporal resolution of the scan. (Reproduced with permission from the RSNA from McCollough et al [22]).

coverage. The current Siemens system is a 32-row scanner, with approximately 2 cm of coverage, but Siemens has recently announced a new 64-row scanner offering approximately 3.8 cm of coverage.

Radiation Exposure

Traditional cardiac CT uses a helical scan mode and very low pitch to perform retrospective ECG-gated reconstructions. This delivers an undesirably high radiation exposure, so various methods have been designed to reduce radiation exposure.

One of the first was ECG-based tube current modulation, which fluctuates tube current in sync with the heart rate, maintaining high tube current during diastasis and providing best image quality in that phase, then lowering tube current during other phases when high-resolution detail is not required (Figure 2.5). This results in a dose savings of approximately 40%.

A great advance in dose reduction was made with the advent of prospective, ECG-triggered, axial cardiac CT (Figure 2.6). By keeping the X-ray tube off during most of the scan, and only turning it on during diastasis, as triggered by the ECG, radiation exposure is dramatically reduced (Figure 2.7). GE first published results using this method [12] with good clinical results and radiation doses of 1–2 mSv, [13] and this approach is now offered by all manufacturers. Using a 64-slice system, the entire heart can be covered in 3–4 acquisitions; however this leaves the system vulnerable to fluctuations in heart rate and rhythm during the scan. Larger coverage mitigates this vulnerability by reducing the number of beats

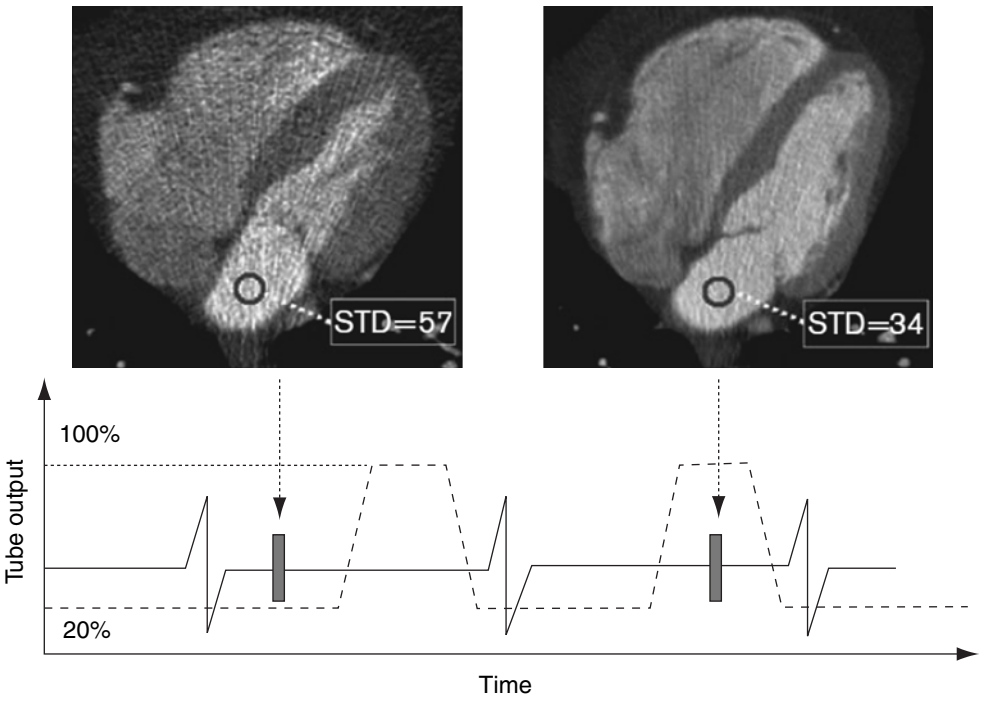

Figure 2.5. ECG-based tube current modulation reduces radiation exposure. Once the desired acquisition phase is determined, based on heart rate, in this case 75% phase, scanning proceeds with maintenance of 100% tube output during that phase, while tube current is reduced outside of that phase. This can reduce effective radiation dose by 40% or more; however, note that images reconstructed from the low tube output phases (*left image*) will be excessively noisy, and are usually considered unusable for coronary interpretation. (Reproduced with permission from Wolters Klower from Vembar et al [1]).

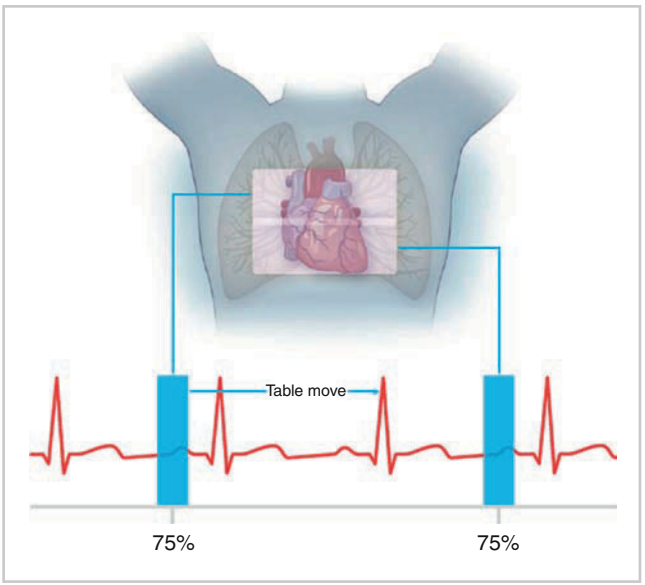

Figure 2.6. Prospective ECG-triggered acquisition method. Cardiac rhythm is monitored while table remains stationary. When cardiac cycle reaches predetermined acquisition phase (in this case 75%, diastolic, phase), X-ray source is briefly turned on (<1 s, *blue bars*) and acquires attenuation data of a length equivalent to the craniocaudal coverage of the detector array, and is then turned off. The table is advanced almost the length of craniocaudal coverage (minus a small amount of overlap), and the process repeats again. Depending on the craniocaudal coverage of the scanner, the entire heart can be scanned in 1–4 acquisitions. (Reproduced with the kind permission from Springer Science + Business Media from Weigold et al [7]).

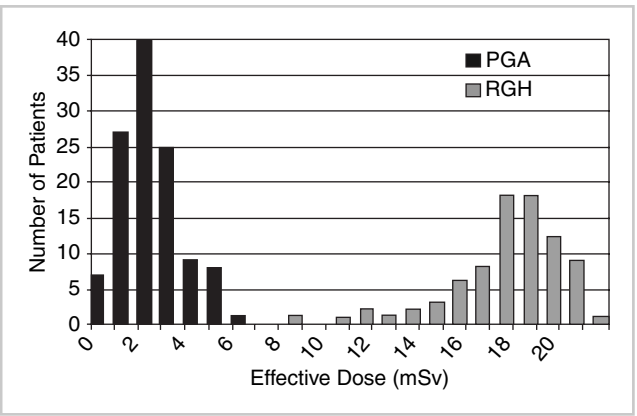

Figure 2.7. Prospective cardiovascular computer tomographic angiography (CCTA) reduces radiation dose. Histogram of effective radiation dose, grouped by acquisition method. Using prospectively gated axial scanning, average effective dose is dramatically reduced to 2–3 mSv. Even the highest dose PGA scan still delivers a lower effective dose than the lowest-dose RGH scan. *PGA* prospectively gated axial; *RGH* retrospectively gated helical. (Reproduced with permission from RSNA from Earls et al [13]).

required for data acquisition. However, larger coverage lends to higher radiation doses, as the detectors are less efficient when having to expose a wider detector array. Hence, Philips' 128-row iCT system can cover the entire heart in 2 beats, with a reported radiation exposure of 3–5 mSv [7]. Toshiba's 320-row Aquilion One scanner can cover the entire heart in one beat, with a reported radiation exposure of approximately 6 mSv. However, lower radiation doses and dependable coronary scanning using 1-beat acquisition requires heart rate reduction. At higher heart rates (>65 bpm), optimal image quality requires a 2- or 3-beat acquisition (and use of multicycle recon) which increases radiation exposure to approximately 13 (2-beat) to 19 (3-beat) mSv [14, 15]. Acquiring with a wide exposure window ("padding") can ensure the capture

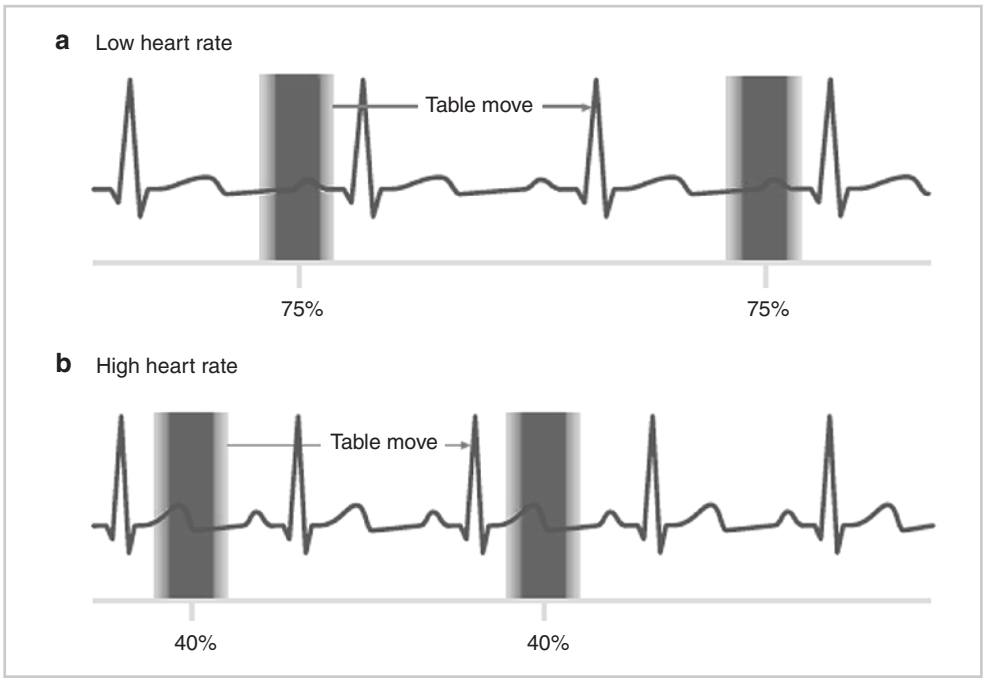

Figure 2.8. Prospective CCTA phase selection and padding. Acquisition phase and padding depend on heart rate: For low heart rates (**a**), target late diastole (75% phase) for prospective acquisition, but if heart rate is high (**b**) (>75 bpm), target end-systole (40% phase) which is more likely to produce motion-free images. By restricting acquisition to the minimum exposure window (*dark gray*), radiation dose is minimized, but ability to reconstruct adjacent cardiac phases is obliterated. Widening the acquisition window ("padding," *light gray shading*) allows reconstruction of a small number of additional phases, which can help interpretation of motion artifact, but increases the radiation dose. (Reproduced with the kind permission from Springer Science + Business Media from Weigold et al [7]).

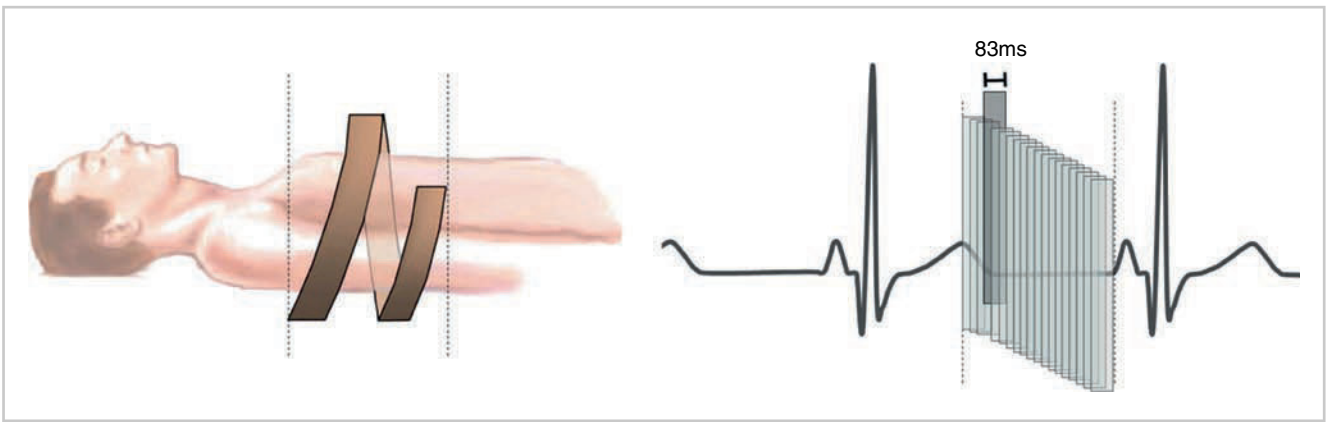

Figure 2.9. Method of high-pitch coronary CCTA. Single source helical CT requires a pitch ≤1.5; a faster pitch results in gaps in the data (*left panel*). A dual-source system can scan at a higher pitch (up to 3.2), using the second X-ray source-detector system to fill in what would otherwise be gaps in the data. Since the table speed is so high, the entire heart can be imaged in a fraction of a second, from data derived from a single heartbeat (*right panel*). If the image acquisition is triggered appropriately to synchronize acquisition with diastasis, and the heart rate is sufficiently low, motion-free images can be obtained with a very low radiation dose. (Reproduced with permission from Elsevier from Achenbach et al [18]).

of motion-free data, but increases radiation exposure (Figure 2.8). A narrower exposure window can be used with preservation of image quality if heart rate is controlled [16] and reduces radiation exposure.

Siemens has recently introduced a new innovative scanning method using a high pitch helical mode which takes advantage of the dual-source design [17, 18] (Figure 2.9). The high pitch (3.2–3.4) would normally produce gaps in the attenuation data using a single-source system, but, in a dual-source system, these are compensated for by data gathered from the second detector. Scan time is less than 1 s, with a radiation exposure of approximately 2 mSv. Initial studies performed on the first-generation dual-source system proved the feasibility of the method, though the authors noted that these first-generation systems are not suitable for this high pitch technique. High pitch scanning with their new scanner, with faster gantry rotation (280 ms) and larger coverage (64 rows), has been reported to produce very good coronary image quality with radiation exposure of approximately 1 mSv [10]. Of note, in this initial investigational phase, low heart rates (<60 bpm) are absolutely required, as the entire data collection takes place

within a 250–270 ms acquisition window of one heart beat; hence diastasis must be at least this long to provide motion free data acquisition, and therefore the requirement for a very low heart rate.

The previously described new detector and reconstruction system offered by GE aims to lower radiation exposure by preserving image quality while scanning with less radiation (<1 mSv), because images are of higher resolution and lower noise than would otherwise be achievable with a low-exposure scan.

Future Directions

Future scanner designs are closely guarded industry secrets, but some concepts have been openly discussed. Flat-panel volume CT systems replace detector rows with a large area detector, and provide coverage of the entire heart in one axial acquisition and extremely high spatial resolution of up to 26 lp/cm, comparable to invasive angiography [19] (Figure 2.10). However, the contrast resolution is inferior to that of multidetector CT, a high radiation exposure is needed to achieve a sufficient contrast-to-noise ratio, and scintillation times are slow and temporal resolution insufficient for cardiac imaging.

Dual energy scanning is being developed by all vendors by various means, including rapid fluctuation of tube energy, stacked detectors, or the dual-tube design in which each tube emits photons of different energy levels. Dual energy CT could take the field to a new level of diagnostic power if it can be used for refined tissue characterization, such as differentiating plaque characteristics. This is difficult to do in the coronary arteries, and initial studies have not yielded any breakthroughs, but at the least it has the potential to enhance coronary lumen visualization in heavily calcified vessels by differentiating calcium and iodine [20] (Figure 2.11). Dual-energy CT may also yield new applications for noncoronary imaging, such as imaging of myocardial perfusion [21].

Conclusions

Since the turn of the twenty-first century, there has been an explosion in technological development of cardiac CT systems, with concomitant gain in reliability and accuracy, especially of coronary imaging. The theme has been one of progressively improved spatial and temporal resolution, reduced scan time, and, most recently, a focus on driving down radiation exposure. In appropriately selected patients, using careful technique, it is easily achievable to perform a cardiac CT using less radiation exposure than that of a standard chest CT or an invasive coronary angiogram. The goal of future systems will be to make this more widely achievable in a larger group of patients without requiring patient selection or stringent patient prep. Given the history of rapid technological advancement, we can expect to see this goal achieved in the near future.

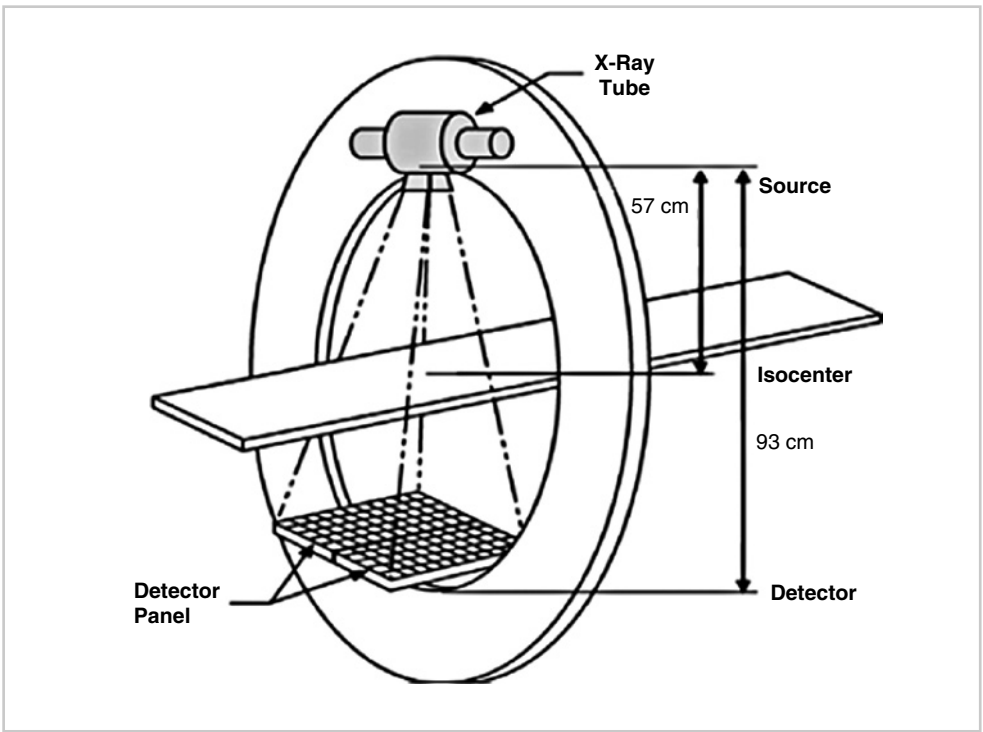

Figure 2.10. Flat panel CT. Schematic of flat panel scanner: In a flat panel system, the traditional multirow detector array is replaced by an area detector consisting of millions of detector elements, each with dimensions <0.2 × 0.2 mm. Large coverage allows whole-organ imaging with tremendous spatial resolution (up to 150 μm). Limiting factors of these prototypes for cardiac imaging have been insufficient temporal resolution, and requirement of high radiation dose. (Reproduced with permission from the RSNA from Gupta et al [19]).

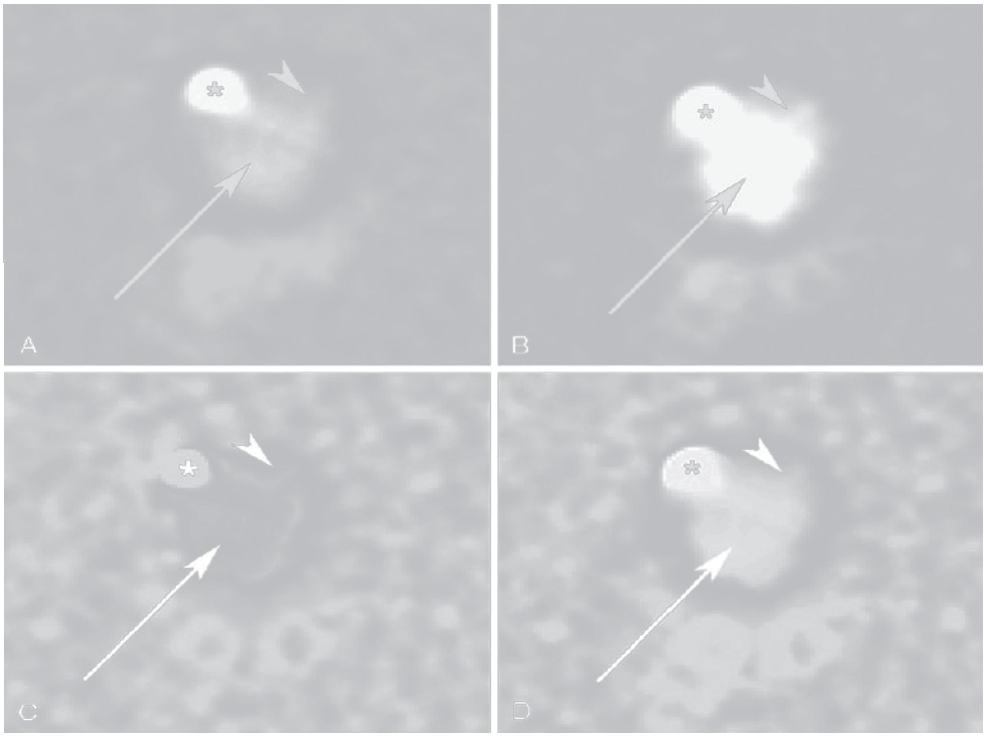

Figure 2.11. Dual energy CT. Dual energy CT can be used to characterize tissue: vessel cross-sectional images derived from high- (140 keV) and low-energy (90 keV) attenuation profiles (**a**, **b**) demonstrate the influence of photon energy on photoattenuation. The contrast-filled lumen (*arrow*) exerts greater photoattenuation on low-energy photons, and hence appears brighter in (**b**), while calcification (*asterisk*) appears high-density in both images. In the subtracted image (**c**), dense calcification has been "removed." By adding in the low-energy (90 keV) attenuation data to this subtracted image, depiction of the lumen edge is enhanced (because of reduced contrast blooming), and visualization of a small side branch (*arrowhead*) is improved (**d**). (Reproduced with permission from Wolters Kluwer from Boll et al [23]).

References

1. Vembar M, Walker MJ, Johnson PC. Cardiac imaging using multislice computed tomography scanners: technical considerations. *Coron Artery Dis*. 2006;17:115–123.
2. Hurlock GS, Higashino H, Mochizuki T. History of cardiac computed tomography: single to 320-detector row multislice computed tomography [Review] [50 refs]. *Int J Cardiovasc Imaging*. 2009;25:31–42.
3. Jiang H. *Gemstone – The Ultimate Scintillator for Computed Tomography [White Paper]*. Waukesha, WI: GE Healthcare; 2008.
4. Chandra N. *CT Sampling Technology [White Paper]*. Waukesha, WI: GE Healthcare; 2008.
5. Thibault JB, Sauer KD, Bouman CA, Hsieh J. A three-dimensional statistical approach to improved image quality for multislice helical CT. *Med Phys*. 2007;34:4526–4544.
6. Hsieh J. *Adaptive Statistical Iterative Reconstruction [White Paper]*. Waukesha, WI: GE Healthcare; 2008.
7. Weigold W, Olszewski M, Walker MJ. Low-dose prospectively gated 256-slice coronary computed tomographic angiography. *Int J Cardiovasc Imaging*. 2009;25(suppl 2):217–230.
8. Achenbach S, Ropers D, Kuettner A, et al. Contrast-enhanced coronary artery visualization by dual-source computed tomography–initial experience. *Eur J Radiol*. 2006;57:331–335.
9. Achenbach S, Ropers U, Kuettner A, et al. Randomized comparison of 64-slice single- and dual-source computed tomography coronary angiography for the detection of coronary artery disease. *JACC Cardiovas Imaging*. 2008;1:177–186 [see comment].
10. Lell M, Marwan M, Schepis T, et al. Prospectively ECG-triggered high-pitch spiral acquisition for coronary CT angiography using dual-source CT: technique and initial experience. *Eur Radiol*. 2009; 19:2576–2583.
11. Mather R. *Dynamic Volume CT [White Paper]*. Tustin, CA: Toshiba America Medical Systems; 2007.
12. Hsieh J, Londt JH, Vass M, Li J, Tang X, Okerlund D. Step and shoot data acquisition and reconstruction for cardiac x-ray computed tomography. *Med Phys*. 2006;33:4236–4248.
13. Earls JP, Berman EL, Urban BA, et al. Prospectively gated transverse coronary CT angiography versus retrospectively gated helical technique: improved image quality and reduced radiation dose. *Radiology*. 2008;246:742–753.
14. Hoe J, Toh KH. First experience with 320-row multidetector CT coronary angiography scanning with prospective electrocardiogram gating to reduce radiation dose. *J Cardiovasc Comput Tomogr*. 2009;3:257–261.
15. Rybicki FJ, Otero HJ, Steigner ML, et al. Initial evaluation of coronary images from 320-detector row computed tomography. *Int J Cardiovasc Imaging*. 2008;24:535–546 [see comment].
16. Steigner ML, Otero HJ, Cai T, et al. Narrowing the phase window width in prospectively ECG-gated single heart beat 320-detector row coronary CT angiography. *Int J Cardiovasc Imaging*. 2009;25:85–90.
17. Hausleiter J, Bischoff B, Hein F, et al. Feasibility of dual-source cardiac CT angiography with high-pitch scan protocols. *J Cardiovasc Comput Tomogr*. 2009;3:236–242 [see comment].
18. Achenbach S, Marwan M, Schepis T, et al. High-pitch spiral acquisition: a new scan mode for coronary CT angiography. *J Cardiovasc Comput Tomogr*. 2009;3:117–121.
19. Gupta R, Cheung AC, Bartling SH, et al. Flat-panel volume CT: fundamental principles, technology, and applications. *Radiographics*. 2008; 28:2009–2022.
20. Barreto M, Schoenhagen P, Nair A, et al. Potential of dual-energy computed tomography to characterize atherosclerotic plaque: ex vivo assessment of human coronary arteries in comparison to histology. *J Cardiovasc Comput Tomogr*. 2008;2:234–242 [see comment].
21. Ruzsics B, Schwarz F, Schoepf UJ, et al. Comparison of dual-energy computed tomography of the heart with single photon emission computed tomography for assessment of coronary artery stenosis and of the myocardial blood supply. *Am J Cardiol*. 2009;104:318–326.
22. McCollough CH, Primak AN, Saba O, et al. Dose performance of a 64-channel dual-source CT scanner. *Radiology*. 2007;243:775–784.
23. Boll DT, Hoffmann MH, Huber N, Bossert AS, Aschoff AJ, Fleiter TR. Spectral coronary multidetector computed tomography angiography: dual benefit by facilitating plaque characterization and enhancing lumen depiction. *J Comput Assist Tomogr*. 2006;30(5):804–811.

3

Radiation Safety: Radiation Dosimetry and CT Dose Reduction Techniques

Kai H. Lee

Introduction

The ability of modern multidetector CT scanners with submillimeter resolution, subsecond rotation time, and large volume imaging has resulted in widespread utilization of cardiovascular computed tomographic angiography (CCTA) [1]. However, the widespread use of CCTA has also raised concerns about the radiation dose to the patients. The National Council on Radiation Protection, NCRP Report No. 160, reported that the radiation exposure to the United States population due to medical sources increased more than 7 times in the 20 years between 1986 and 2006 [2]. Although in 2006 CT constituted about 10% of the diagnostic examinations that utilize X-rays, it contributed to nearly 50% of the population dose [2–4]. Based on our current knowledge of radiation biology, the deleterious effects of radiation are cumulative and medical radiation is increasingly a significant contributor to the amount of radiation accumulated in a person's lifetime [1, 2, 5]. The risk of cancer from radiation exposure is especially worrisome in children and young women who received multiple CT examinations early in their lives. For example, studies found that one CT examination of the female chest gives as much radiation as 10 mammograms to each breast [6]. Therefore, the practitioners of CT must be constantly aware of the risks of radiation and strive toward applying the lowest dose to the patient consistent with the clinical study.

One of the difficulties confronting physicians when evaluating the radiation safety of a CT procedure is the plethora of terms used to quantify the amount of radiation given to the patient. Thus, this chapter has two aims. The first aim is to explain the fundamental concepts of radiation dosimetry relevant to cardiac CT examinations. The second aim is to describe the techniques that physicians may exercise to control radiation dose to their patients.

Fundamentals of Radiation Dosimetry

Absorbed Dose

The International System unit (SI units) of radiation dose measurement is the *Gray* (Gy) [7]. However, Gray is a large unit of radiation. When evaluating radiation dose from CT examinations, two smaller divisions of the Gray are commonly used. The two subunits of Gray are the milliGray (mGy) and the centiGray (cGy):

$$1\,\text{mGy} = 10^{-3}\,\text{Gy}$$
$$1\,\text{cGy} = 10^{-2}\,\text{Gy}.$$

In the United States, the SI units are quoted in the literature, but the traditional unit *rad* is utilized in routine radiation safety practice [7]. The unit *rad* is an acronym for *r*adiation *a*bsorbed *d*ose. The conversion between the traditional and the international systems of radiation dose measurements is simple: 1 Gy = 100 rad. It follows that 1 cGy = 1 rad.

Equivalent Dose

The severity of biological damage depends not only on the amount of radiation absorbed. It also depends on the type of radiation absorbed. For example, 1 Gy of neutron radiation is 10 times more damaging than 1 Gy of X-rays [8]. A unit of measurement is required that takes into account the effectiveness of different types of the radiation in producing biological damages. The biological equivalent unit used in radiation protection is the Sievert (Sv), and the traditional unit is the rem (acronym for radiation equivalent man). In SI units, the biological equivalent dose H is equal

to the radiation absorbed dose D measured in Gy multiplied by the radiation damage weighting factor W_r, i.e.,:

$$H(\text{Sv}) = D(\text{Gy}) \times W_r,$$

when using the traditionally units, the biological equivalent dose in rem is equal to the absorbed dose in rad multiplied by the quality factor Q, i.e.,:

$$H(\text{rem}) = D(\text{rad}) \times Q,$$

where the quality factor Q serves the same function as W_r to account for the relative effectiveness of different types of radiation in producing biological damage. The numerical values of Q and W_r are in fact identical for the same type of radiation. Some typical weight factors are given in Table 3.1.

The values of W_r or Q are proportional to the density of ionization created by the incident radiation along its path of travel in tissue. For X-rays, gamma rays, beta particles, and electrons from radioactive materials, the density of ionization created in tissue is relatively low. The weighting factor W_r equals to 1. Thus, when working with X-rays from CT, the equivalent dose and absorbed dose are numerically equal, i.e., 1 Sv = 1 Gy, and 1 rem = 1 rad. For neutrons, the weighting factor $W_r = 10$. The equivalent dose for 1 Gy of neutron absorbed dose equals to:

$$H(\text{Sv}) = 1(\text{Gy}) \times 10 = 10\,\text{Sv}.$$

This example shows that neutrons are 10 times more damaging to the human body than X-rays for the same absorbed dose. In other words, 1 Gy of neutron produces 10 times greater risk than 1 Gy of X-ray.

For radiation protection purposes, subunits of Sievert and rem are used. Subunits of Sievert and rem are the milliSievert (mSv), and millirem (mrem), respectively. Since both the traditional and SI units are used in the US, it should be noted that 1 mSv = 100 mrem. A convenient method to convert an equivalent dose given in SI unit to the traditional unit is to multiply the SI values by 100 and change the unit name from Sv to rem but leave the numeric prefix unchanged.

In summary, *absorbed dose* is the quantity of radiation energy deposited per unit volume of tissue. The equivalent *dose* is a measure of biological damage equal to the absorbed dose modified by a weighting factor according the relative effectiveness of the incident radiation to produce biological damage.

Table 3.1. Radiation weighting factors

Type of radiation	Weighting factor
X- and gamma rays, electrons, positrons	1
Neutrons	10
Protons	2
Alpha particles	20

Table 3.2. Typical annual whole body radiation dose

	mSv	mrem
Nuclear medicine technologists	1.2	120
Airline flight crews	2.2	220
Nuclear power plant workers	5.5	550
Interventional radiologists	18	1,800
Interventional cardiologists	16	1,600
Natural background radiation	2.5	250
Regulatory limit on the occupational workers	50	5,000
Regulatory limit on the general public	1	100

Given this metric to quantify radiation, Table 3.2 lists the average equivalent dose received annually to the total body by workers in the various occupations [9–12]. The table also gives the natural background radiation and the regulatory limits on radiation exposure as reference to occupational exposures. It is interesting to note that airline flight crews, who are not classified as occupational radiation workers, receive annual equivalent dose from the cosmic rays of nearly twice as much as the nuclear medicine technologists who routinely handle radioactive materials on the job.

Effective Dose

Unlike the absorbed dose and the equivalent dose, the effective dose is not a physically measurable quantity. The effective dose is an imaginary total body dose. It is calculated from the absorbed dose given to any part or parts of the body. That is, the effective dose is the equivalent whole body dose if the radiation given to a partial body exposure such as a CCTA study was spread uniformly across the entire body. The purpose of the effective dose is to translate a partial body exposure such as a cardiac CT scan to an equivalent uniform total body dose to assess the risk of carcinogenesis and genetic defects.

It is important to calculate the effective dose from a given medical procedure, such as CCTA, because our current knowledge of the risk of radiation-induced carcinogenesis and genetic defects is based on data collected from the total body exposed uniformly to certain doses of radiation. In order to estimate the risk resulting from CT of the chest for example, one must translate the partial body irradiation to an equivalent whole body exposure in order to utilize the database for risk estimates. To do so, a mathematical model is used to compute the doses to all other organs resulting from radiation scattered from CT of the chest. These computed organ doses are then multiplied by a risk factor according to the sensitivity of each organ to radiation. Summation of the product of these computed organ doses and their associated risk weighting factor is called the effective dose. That is, the effective dose E is computed using the equation:

$$E = \Sigma H_i w_i,$$

where E is the effective dose, H_i is the dose equivalent to a given organ, and w_i is the risk weighting factor for that organ.

The effective dose is thus a weighted sum of the computed doses to all organs in the body. A table of weighting factors for different body organs is given in a report by the International Commission on Radiation Protection [8, 13].

One may interpret the effective dose as a calculated equivalent dose of radiation given to the entire body that would be required to produce the same risk of cancer and genetic damages as a dose of radiation delivered to a localized region of the body as in a CT examination. In other words, the risk from a part of the body exposed to a given dose of radiation is the same as the total body uniformly receiving the effective dose. Thus, the effective dose is an extrapolated whole body dose from a partial body dose. As such, the effective dose is a computed value rather than a physically measurable quantity. The effective dose is calculated to serve as a common denominator for comparison of stochastic risk between different medical or nonmedical exposures to radiation.

With an understanding of the concept of the absorbed dose, equivalent dose, and effective dose, the next step is to learn how to calculate the effective dose from CT examinations.

CT Dosimetry

Special dosimetric techniques have to be developed for measuring CT doses because the geometry of the X-ray field employed in CT scans is very different from the conditions of conventional radiographic exposures [14, 15]. The fundamental parameter developed for CT dosimetry is the Computed Tomography Dose Index (CTDI). From the CTDI, the dose-length product (DLP) is calculated and then used to derive the effective dose (E) for risk comparison.

CTDI

The CTDI, or specifically the $CTDI_{100}$, is measured using a dosimeter of 100 mm length in a cylindrical acrylic phantom of 16- or 32-cm diameter to simulate a head or body (Figure 3.1). Four measurements are made in the periphery and one in the center of the phantom. The four peripheral measurements and the central measurement are used to compute the weighted average of the $CTDI_{100}$ in the phantom as follows:

$$CTDI_W = 0.87 \times [2/3 CTDI_{100}(\text{periphery}) + 1/3\, CTDI_{100}(\text{center}),$$

where $CTDI_w$ is the weighted average of $CTDI_{100}$ in the phantom.

Figure 3.1. A 100-mm length cylindrical acrylic phantom used for measuring the $CTDI_{100}$.

The factor 0.87 is a conversion factor to relate dose measured in air to dose in soft tissues. The $CTDI_w$ can be interpreted as the average absorbed dose in the cross section of the patient from one axial scan.

For helical scans, the average dose may be greater than or less than the dose from an axial scan. If in a helical scan the table moves the patient slowly through the gantry, the average absorbed dose in a transverse section of the patient may be greater than that in an axial scan due to the X-ray beam overlapping on the patient in successive rotations of the X-ray tube. Conversely, if the table moves at a high speed, the X-ray beam passes through the patient in a non-overlapping helical path as shown in Figure 3.2. There would be less radiation delivered to the scan volume because of the gaps between tracks of the X-ray beam. That is, for CT scans done with a pitch of less than 1, there is overlapping of the X-ray beam as it passes through the patient, and the patient receives a higher dose. For scans done with a pitch greater than 1, the X-ray beam does not overlap, and the patient receives less radiation. Of course, there is greater image noise for scans done with pitch greater than 1. The clinicians will have to make a compromise between image noise and the patient dose.

The $CTDI_{vol}$ was therefore developed to compute the average absorbed dose in the scan volume taking into account the variable overlaps in the spiral path of the X-ray beam. The $CTDI_{vol}$ is calculated using the following equation:

$$CTDI_{vol} = CTDI_W / \text{pitch}.$$

Pitch is a dimensionless unit equal to the distance the table traveled during one complete rotation of the X-ray tube divided by the width of the X-ray beam at the axis of rotation. For a multislice CT, the pitch is defined as follows:

$$\text{Pitch} = D / nT,$$

where D is the distance the patient table moved in one rotation of the X-ray tube, n is the number of slices produced in

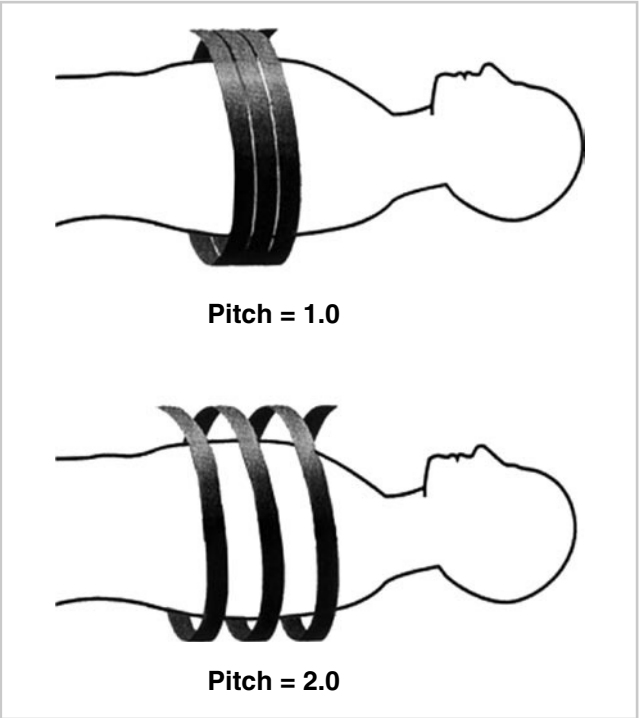

Figure 3.2. Schematic demonstrating the concept of pitch. With a pitch of 1, there is no overlap or gap. With a pitch of greater than 1, the X-ray beam passes through the patient in a nonoverlapping helical path with less radiation delivered to the scan volume, but with greater image noise. With a pitch of less than 1, there is overlap in the X-ray beam path, and the patient receives a higher radiation dose, but with less image noise.

one tube rotation, T is the thickness of each slice measured at the axis of rotation, and the product nT represents the width of the X-ray beam that sweeps around the patient during a CT scan.

Dose-Length Product

One final measurable dosimetric parameter for CT is the DLP. The DLP is proportional to the total amount of X-ray energy deposit in the scan volume. DLP is defined as:

$$\mathrm{DLP} = \mathrm{CTDI}_{\mathrm{vol}} \times \mathrm{scan\,length}$$

The cross-sectional area of the patient is implicitly included in $\mathrm{CTDI}_{\mathrm{vol}}$ by multiplying the $\mathrm{CTDI}_{\mathrm{vol}}$ by the scan length. DLP thus describes the volume of tissues irradiated and the total amount of X-ray energy deposited in that volume. DLP is an important risk indicator because the severity of biological damage from radiation depends not only on the quantity and type of radiation given, but on the volume of tissue irradiated as well. For example, a radiation oncologist could deliver 7,000 cGy of X-rays to a small region surrounding the prostate gland to cure a patient with prostate cancer. If 7,000 cGy was delivered over the entire body, the person would most certainly die from the absorbed dose. Thus, the risk of radiation increases with the volume of tissue irradiated. The two descriptors of CT dosimetry, $\mathrm{CTDI}_{\mathrm{vol}}$ and DLP, serve to quantify the amount of X-ray energy absorbed per unit mass of tissue, the volume of tissue exposed to radiation, and thus the total amount of energy deposited in the scan volume. Because $\mathrm{CTDI}_{\mathrm{vol}}$ and DLP are such important indicators of the risk from a CT procedure, the values of $\mathrm{CTDI}_{\mathrm{vol}}$ and DLP have been displayed on the control console in all CT systems manufactured since year 2000.

The Effective Dose from CT

For other imaging procedures, the effective dose has to be computed from an elaborate computer model. The effective dose from CT, however, can be calculated from the DLP using a simple formula developed by the ICRP [16, 17]. The effective dose is conveniently calculated by multiplying the DLP by the corresponding conversion factor shown in Table 3.3, i.e.,:

$$\mathrm{E(mSv)} = \mathrm{DLP} \times \mathrm{CF}$$

where CF is the conversion factor for the corresponding CT procedure.

By using the $\mathrm{CTDI}_{\mathrm{vol}}$, DLP, and conversion factors in Table 3.3, some typical values of the effective dose from different CT procedures are shown in Table 3.4. The effective doses from other radiologic examinations are also shown in the table for comparison [18, 19].

CT Dose Reduction Techniques

The effective doses in Table 3.4 show that CT is a high dose procedure compared with other X-ray examinations. As mentioned, CT examinations consisted of about 10% of all diagnostic examinations that utilize X-rays, but contributed to nearly 50% of the medical radiation to the population. The contribution of CT dose to the population is expected to continue to rise given the expanding use of CT. It is therefore imperative for the practitioners of CT to

Table 3.3. CT effective dose conversion factors

Region of body	Conversion factor
Head	0.0023
Neck	0.0054
Chest	0.0170
Abdomen	0.0150
Pelvis	0.0190

Table 3.4. Typical effective doses of radiological examinations

Radiologic examination	Typical effective dose (mSv)
Head/neck CT	2–5
Chest CT	5–7
Abdomen/pelvis CT	8–11
Coronary CT angiogram	5–15
Coronary bi-plane angiogram	3–10
PET cardiac viability per 370 MBq	4–7
MIBI cardiac stress/rest per 1.3 GBq	10.6
PA chest X-ray	0.02
Skull X-ray	0.07
Lumbar spine	1.3
I.V. urogram	2.5
Upper GI	3.0
Barium enema	7.0

obtain the desired diagnostic information using low dose techniques whenever possible.

Several recent studies reported that radiation dose in cardiac CT can be reduced by more than 50% simply by modifying the basic technical factors in their CT scanning protocols without having to invest in new equipment [20–24]. The technical factors available to nearly all CT scanners for dose reduction include limiting the scan length, lowering the tube voltage, modulating the X-ray tube current, minimizing scan time, and using prospective ECG gating.

Limiting the Scan Length

The effective dose to a patient is proportional to the dose-length-product DLP, which in turn is proportional to the craniocaudal length being scanned. One study reported the use of the calcium score protocol as a guide to determine the minimum scan length for each individual patient in a CCTA examination [25]. Prior to CCTA, the patient was given a prescan using the calcium score protocol. The start of the scan was then determined from the calcium score images at 1 cm above the visualized top of the coronary arteries and stopped at 1 cm below the posterior descending artery. The dose savings from limiting the scan length more than offset the dose from the calcium score scan. The effective dose was reduced by as much as 30%.

Reducing the Tube Voltage

Coronary CT angiography protocols commonly use a tube voltage of 120 kV for all patients. Reducing the tube voltage from 120 to 100 kV for patients weighing 185 pounds or less has been reported to reduce the effective dose by 30–40% to the range 5–12 mSv from 9 to 17 mSv [20, 21, 24]. Other studies showed that, for thin patients, the tube voltage can be further reduced to 80 kV without degrading the diagnostic accuracy, and the dose savings was as high as 80% [26]. Although the tube voltage affects the image contrast, the above studies showed that the overall image quality was preserved when matching the size of the patient with the reduced tube voltage.

Modulating the Tube Current and Time Product

Radiation dose to the patient is approximately directly proportional to the product of the tube current measured in mA and the tube rotation time in seconds. While options for varying the tube rotation time are limited for CCTA, there is great latitude in the choice of tube current. Similar to reducing the tube voltage, there is a delicate balance between the desire to lower the mA for dose reduction, and the need to apply sufficient mA to keep the image noise from degrading the image quality. When the mA is reduced, the intensity of the X-ray beam passing through the patient is decreased, therefore reducing the patient dose. But by reducing the mA, the image noise is increased and the overall quality of the images is reduced because fewer photons, less data, are available to reconstruct the images.

The question becomes one of deciding the optimum mA to minimize dose to the patient while still producing images of acceptable quality for diagnosis. CT manufacturers have responded to this question by incorporating dose reduction options into their system. The various dose reduction techniques available in modern CT scanners are actually different implementations of automatic exposure control (AEC) that have been in use for decades in fluoroscopy and radiography. The AEC controls dose to the patient by modulating the X-ray beam intensity according to the patient's anatomy to produce the desired image quality. The intensity of the X-ray beam emitted from the X-ray tube and subsequently sent towards the patient is directly proportional to the mA across the tube. By modulating the electron current mA according to the thickness of tissues that the X-ray beam must pass through, the desired image quality can be maintained without imparting unnecessary radiation to the patient. For example, the CT scanner can automatically raise the mA to produce a more intense X-ray beam to pass through the abdomen, and reduce the mA to produce a less intense X-ray beam when passing through the lungs.

There are three conditions under which the AEC can modulate the tube current (mA) to produce the desire image quality, and in the process reduce the unnecessary radiation to the patient. First, the AEC can be programmed to adjust the mA along the long axis of the patient so that the mA is reduced when the X-ray beam passes through large volume of air in the thorax, and is raised when the beam goes through the more attenuating soft tissues in the abdomen and pelvis. Second, the mA can be adjusted in the transverse plane of the patient according to the tube angle during its rotation around the patient. That is, the mA is reduced when the X-ray beam passes through the patient in the thinner AP and PA directions, and increased in the thicker lateral directions. Third, the overall tube

current can be adjusted according to the patient's size such that a lower mA would be used on pediatric patients and thinner adult patients.

There are three general methods used by the manufacturers in their dose reduction options [18, 27, 28], each with their own advantages and disadvantages. Implementation of the dose reduction option changes frequently with changes in the technology, but the principles behind the methodology remain essentially the same. The three common algorithms employed by manufacturers of CT scanners are AEC guided by image noise, AEC guided by reference image, and AEC guided by reference mAs.

AEC Guided by Image Noise

Image noise can be described qualitatively as the graininess of the image. Low noise images appear smooth with continuous shades of gray from the darkest to the lightest portions of the image. High noise images show characteristic salt and pepper grains interspersed throughout the image. Resolution of low contrast objects can be greatly impaired by image noise. Image noise is influenced by a number of factors, but is ultimately determined by the number of X-ray photons that contribute to the image. A simple way to quantify noise in an image is to calculate the percentage standard deviation. The standard deviation of an image is the square root of the total number of counts or dots that make up the image. The resulting standard deviation is then divided by the total counts in the image to arrive at the percentage standard deviation. The standard deviation of the number of counts in an image is an expression of the fraction of noise in an image. The percentage standard deviation as computed by the ratio of the standard deviation to the total number of counts in the image indicates what fraction of the image is occupied by noise. Low contrast objects are often obscured by the image noise.

The number of counts in a given CT image is directly proportional to the number of X-ray photons available for image formation, which in turn depends on the intensity of the X-ray beam striking the detectors and the length of time that the X-ray beam is on. The AEC modulates the beam intensity by varying the tube current. The exposure time is determined by the speed of the X-ray tube to make one rotation around the patient. The product of the tube current in mA and the rotation time in seconds is commonly called the mAs. The mAs selected for a CT scan determines the number of X-ray photons striking the patient. The higher the mAs, the greater the number of photons available to pass through the patient to reach the detectors, and therefore the lower the noise in the reconstructed images. When all the other technical factors are held constant, the image noise is inversely proportional to the square root of the mAs, i.e.,:

$$\text{Noise} \sim 1/\sqrt{\text{mAs}}.$$

During CT scans, the tube rotation time is fixed. The image noise guided AEC continually adjusts the mAs by varying the mA to maintain the same number of photons reaching the detectors, and hence keeping the image noise at a preselected level. For example, the AEC reduces the mA when the beam is passing through in the thinner anterior–posterior direction of the patient, and increases the mA when passing through laterally.

Patient dose optimization can be achieved by selecting a target image noise level appropriate for the particular CT procedure. The disadvantage is that the target noise level selected by the user may be lower than necessary for obtaining the diagnostic information, and result in giving unnecessary dose to the patient. A simple rule to remember is that reducing the mAs and hence the patient dose by a factor of 4 increases the image noise only by a factor of 2.

AEC Guided by Reference Image

This method of AEC is an extension of the constant image noise algorithm. Here, the target image noise is set on the AEC using a clinical image that is selected by the reader as of adequate quality for the given CT procedure. During scan, the mA at each tube position is adjusted by the AEC to yield an image noise approximating the noise in the reference image. The advantage of the reference image approach is that the target image noise is derived from a database of clinical images rather than some abstract percentage standard deviation. The major disadvantage of the reference image approach is the user inclination to select the most esthetic image as the reference image even though a less esthetic image will allow diagnosis. This results in the patient receiving a larger radiation dose than necessary.

AEC Guided by Reference mAs

This approach uses the mAs of a reference patient as a guide to modulate the mA for the actual patient. For a given CT procedure, a certain mAs that was found to produce images of acceptable quality on a reference patient is used as the standard of reference. From the attenuation profile measured on a scout view of the actual patient, the AEC adjusts the tube current at each tube position to compensate for the difference in attenuation between the actual and reference patient. The image noise is not maintained for different patient sizes. The technique relies on the experience of the user to select the proper level of tube current modulation for a given patient and CT procedure.

ECG Gating

Prospective ECG gating is based on the finding that least motion artifacts were found in the images reconstructed

from data in the ventricular diastolic phase. The X-ray beam is turned on only during middiastole to acquire the image data, and turned off during the other phases of the cardiac cycle. Prospective gating is also known as an ECG gated step-and-shoot technique. The most dramatic reduction of dose has been reported by using a prospective gating technique in combination with tube voltage reduction [24, 27, 29].

With prospective gating, the tube current is modulated by the ECG tracings to synchronize with the patient's cardiac cycle. Signals from the ECG monitor trigger the X-ray beam to turn on for data acquisition during diastole, and turn off when not acquiring data during the systolic and early diastolic phases. The table is then stepped to the next position for scanning in the predefined phase of the cardiac cycle. The heart is thus scanned in a sequential step-and-shoot fashion as shown in Figure 3.3.

Immediately before the scan, a sample of the ECG tracing is taken to measure the average R–R time interval. When the CT is set to scan, the AEC sets the clock to zero upon receiving an R-wave from the ECG monitor. The tube current is turned off until 70–75% of the cardiac cycle has elapsed. After this initial delay, the tube current is turned on to the maximum and maintains the maximum output for the next 10% of the cardiac cycle, corresponding to the time during which the heart is in the diastolic phase. The AEC subsequently turns off the tube current at the 80–85% mark that approximates the end of the diastolic phase to stop data acquisition. The time marker is reset to zero upon receiving the next R-wave. While the X-ray beam is off, the table moves the patient to the next scanning position. By activating the X-ray beam during only 10% of the cardiac cycle for data acquisition, the patient dose was reduced by 50–70% in comparison with retrospective gating that requires that the X-ray beam on continuously throughout the scan [22].

Although the advantage of prospective gating is dose reduction, images are only obtained at a certain percentage of the R–R interval. If there is motion artifact of the coronary arteries at this phase of the cardiac cycle, images may not be diagnostic. Retrospective gating can somewhat limit dose through dose modulation. With this technique, the tube current is ramped down during a certain portion of the cardiac cycle. Although the phases of the R–R interval during the phases of dose reduction may not be useful for coronary artery assessment, they may still be used for cardiac functional assessment. Both prospective gating and retrospective gating with dose modulation are problematic in patients with rapid or irregular heart rates.

Rapidly advances in MSCT technology have brought drastic changes to cardiovascular imaging techniques and lowering of radiation dose to the patient. Of particular interest to cardiologists is the introduction of 320-slice MSCT. Preliminary studies [27] using the 320-slice CT found that image data for the entire heart volume could be acquired in a single rotation, and obviates helical scans and bed indexing to acquire data over several cardiac cycles. When using a combination of kV reduction, prospective gating, and elimination of scan overlap of the X-ray path, dramatic reduction of the patient dose can be achieved without compromising the image quality.

Conclusion

High speed multislice CT with its high temporal and spatial resolution is increasingly applied for a wide spectrum of cardiac studies. Because of the high radiation dose associated with cardiac CT examinations, it is necessary for clinicians to become familiar with the dosimetric principles and to adopt dose reduction techniques in their clinical practice. This chapter reviewed the basic dosimetry parameters necessary to understand the terms and concepts invariably brought up in any discussion of radiation dose optimization methods. The abstract concept of effective dose should be well understood in order to explain to the patients the relative risks of different medical procedures that involve the use of radiation, e.g., the comparative risks of coronary CT angiography, chest X-rays, and radionuclide perfusion studies.

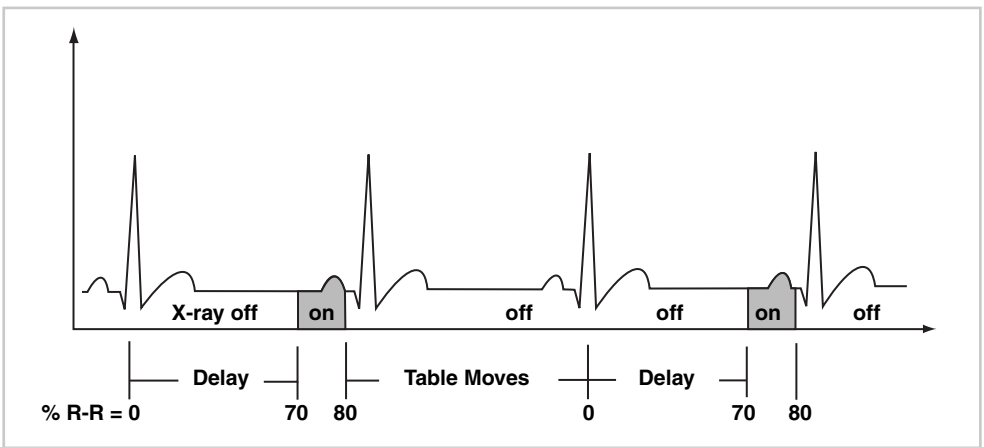

Figure 3.3. Schematic demonstrating prospective gating. When the CT is set to scan, the AEC sets the clock to zero upon receiving an R-wave from the ECG monitor. The tube current is turned off until 70% of the cardiac cycle has elapsed. After this initial delay, the tube current is turned on to the maximum and maintains the maximum output for the next 10% of the cardiac cycle. The AEC subsequently turns off the tube current at 80% of the R–R interval.

References

1. Einstein AJ, Henzlova MJ, Rajagopalan S. Estimating risk of cancer associated with radiation exposure from 654-slice computed tomography coronary angiography. *JAMA*. 2007;298(3):317–323.
2. NCRP Report No. 160. *Ionizing Radiation Exposure of the Population of the United States*; 2009.
3. Kalendar W. *Computed Tomography: Fundamentals, System Technology, Image Quality, Applications*. Erlangen: Publicis Corporate; 2005.
4. Watson SJ, Jones AL, Oatway WB, Hughes JS. *Ionizing radiation exposure of the UK population: 2005 review*. Health Protection Agency, Report HPA-RPD-001; 2005.
5. National Research Council. *BEIR report VII. Health risks from exposure to low levels of ionizing radiation*. Washington, DC: The National Academies Press; 2006.
6. Parker MS, Hui FK, Camacho MA, et al. Female breast radiation exposure during CT pulmonary angiography. *Am J Roentgenol*. 2005; 185(5):1228–1233.
7. NCRP Report No. 82. *SI Units in Radiation Protection and Measurements*; 1985.
8. ICRP. *ICRP publication 92: Relative Biological Effectiveness (RBE), Quality Factor (Q), and Radiation Weighting Factor (wR)*. Oxford, UK: Elsevier; 2003.
9. Health Canada. 2007 Report on occupational radiation exposures in Canada. http://www.hc-sc.gc.ca/ewh-semt/alt_formats/hecs-sesc/pdf/pubs/occup-travail/2007-report-rapport-eng.pdf; 2007
10. Feng YJ, Chen WR, Sun TP, Duan SY, Jia BS, Zhang HL. Estimated cosmic radiation doses for flight personnel. *Space Med Med Eng*. 2002;15(4):265–269.
11. Department of Transportation Report – DOT/FAA/AM-03/16. Friedberg W and Copeland K. *What Aircrews Should Know About Their Occupational Exposure to Ionizing Radiation;* 2003.
12. NCRP. *NCRP Report No. 101. Exposure of the U.S. Population From Occupational Radiation;* 1989.
13. ICRP. *ICRP Publication 60: 1990 Recommendations of the International Commission on Radiological Protection*. Oxford, UK: Elsevier; 1991. ISBN 0-08-041144–4.
14. Morin RL, Gerber TC, McCollough CH. Radiation dose in computed tomography of the heart. *Circulation*. 2003;107:917–922.
15. AAPM. *AAPM Report No. 96. The measurement, Reporting, and Management of Radiation Dose in CT*. College Park, MD: American Association of Physicists in Medicine; 2008.
16. Impact CT patient dosimetry calculator. http://www.impactscan.org/download/ctdosimetrydownload.htm. Accessed 7.08.2009.
17. European guidelines on quality criteria for computed tomography. http://www.drs.dk/guidelines/ct/quality/index.htm. Accessed 7.08.2009.
18. Goodman TR, Brink JA. Adult CT: Controlling Dose and Image Quality. In: *From Invisible to Visible – The Science and Practice of X-Ray Imaging and Radiation Dose Optimization*. 2006 Categorical Course Syllabus, Radiologicqal Society of North America; 2006.
19. Prokop M, Galanski M, eds. *Spiral and Multislice Computed Tomography of the Body*. New York: Thieme; 2003.
20. Raff GL, Chinnaiyan KM, Share DA, et al. Radiation dose from cardiac computed tomography before and after implementation of radiation dose reduction techniques. *JAMA*. 2009;301: 2340–2348.
21. Pflederer T, Rudofsky L, Ropers D, et al. Image quality in a low radiation exposure protocol for retrospective ECG-gated coronary CT angiography. *Am J Roentgenol*. 2009;192:1045–1050.
22. Takakuwa KM et al. Radiation dose in a "Triple Rule-Out" coronary CT angiography protocol of emergency department patients using 64-MDCT: the impact of ECG-based tube current modulation on age, sex, and body mass index. *Am J Roentgenol*. 2009;192:866–872.
23. Gopal A, Budoff MJ. A new method to reduce radiation exposure during multi-row detector cardiac computed tomographic angiography. *Int J Cardiol*. 2009;132:435–436.
24. Budoff MJ, et al. Substantial radiation dose reduction in 64-multidetector cardiac computed tomography by using lower X-ray energy during scanning. *J Am Coll Cardiol*. 2008;51:A148.
25. Hausleiter J et al. Radiation dose estimates from cardiac multislice computed tomography in daily practice. *Circulation*. 2006;113: 1305–1310.
26. Gopal A, et al. Radiation reduction with prospective ECG-triggering acquisition using 64-multidetector computed tomographic angiography. *Int J Cardiovasc Imaging*. 2009;25:405–416.
27. McCollough CH, Bruesewitz MR, Kofler JM. CT dose reduction and dose management tools: overview of available options. *Radiographics*. 2006;26:503–512.
28. http://www.impactscan.org/slides/ecr2005/index.htm as of 18 May 2007.
29. Steigner ML et al. Narrowing the phase window width in prospectively ECG-gated single heart beat 320-detector row coronary CT angiography. *Int J Cardiovasc Imaging*. 2009;25:85–90.

Part II

Coronary Artery Calcium

4

Assessment of Cardiovascular Calcium: Interpretation, Prognostic Value, and Relationship to Lipids and Other Cardiovascular Risk Factors

Harvey S. Hecht

Cardiac risk assessment has traditionally been based on conventional risk factors; the shortcomings of this approach are all too often highlighted by major cardiac events occurring in presumably low-risk people. The annual presentation of 650,000 previously asymptomatic patients with an acute coronary event as the initial manifestation of coronary artery disease (CAD) [1] is a testimony to the failure of our current risk assessment model. Consequently, there has been a focus on markers of subclinical atherosclerosis that may be utilized for risk assessment of individuals, rather than extrapolating from risk factors that reflect trends in large groups of patients in epidemiologic studies. The most powerful of these subclinical markers is coronary artery calcium (CAC).

Background

CAC is pathognomonic for atherosclerosis [2–4]. Mönckeberg's calcific medial sclerosis does not occur in the coronary arteries [5]; atherosclerosis is the only vascular disease known to be associated with coronary calcification. Calcium phosphate (in the hydroxyapatite form) and cholesterol accumulate in atherosclerotic lesions. Circulating proteins that are normally associated with bone remodeling play an important role in coronary calcification, and arterial calcium in atherosclerosis is a regulated active process similar to bone formation, rather than a passive precipitation of calcium phosphate crystals [6–9]. Rumberger et al. [10] demonstrated that the total area of coronary artery calcification is highly correlated ($r = 0.9$) in a linear fashion with the total area of coronary artery plaque on a segmental, individual, and whole coronary artery system basis (Figure 4.1), and the areas of coronary calcification comprise approximately one-fifth that of the associated coronary plaque. Additionally, there were plaque areas without associated coronary calcium, suggesting that there may be a coronary plaque size most commonly associated with coronary calcium but, in the smaller plaques, the calcium is either not present or is undetectable.

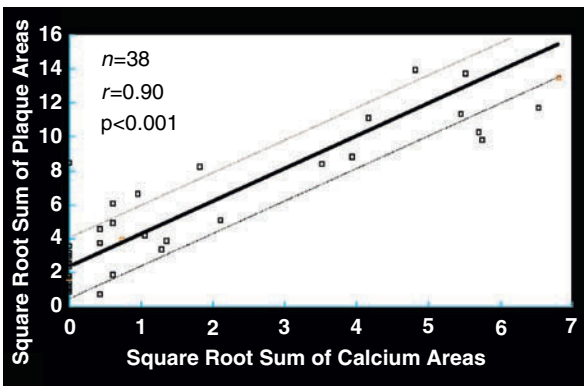

Figure 4.1. Correlation between calcified and total plaque burden in histopathologic coronary artery specimens (reproduced with permission of Wolters Kluwer from Rumberger et al. [10]).

Intravascular ultrasound [11, 12] measures of combined calcified and noncalcified plaque confirm the strong relationship (Figure 4.2).

Methodology

Technical

Until recently, the data substantiating the importance of CAC have been derived almost exclusively through the use of electron beam tomography (EBT), utilizing a rotating electron beam to acquire prospectively triggered, tomographic 100-ms X-ray images at 3 mm intervals in the space of a 30- to 40-s breathhold. The multidetector computed tomography (MDCT) technology is a more recent development and employs a rotating gantry with a special X-ray tube and variable number of detectors (from 4 to 64), with 165–375-ms images at 0.5, 1.5, 2.0, or 3.0 mm intervals, depending on the protocol and manufacturer.

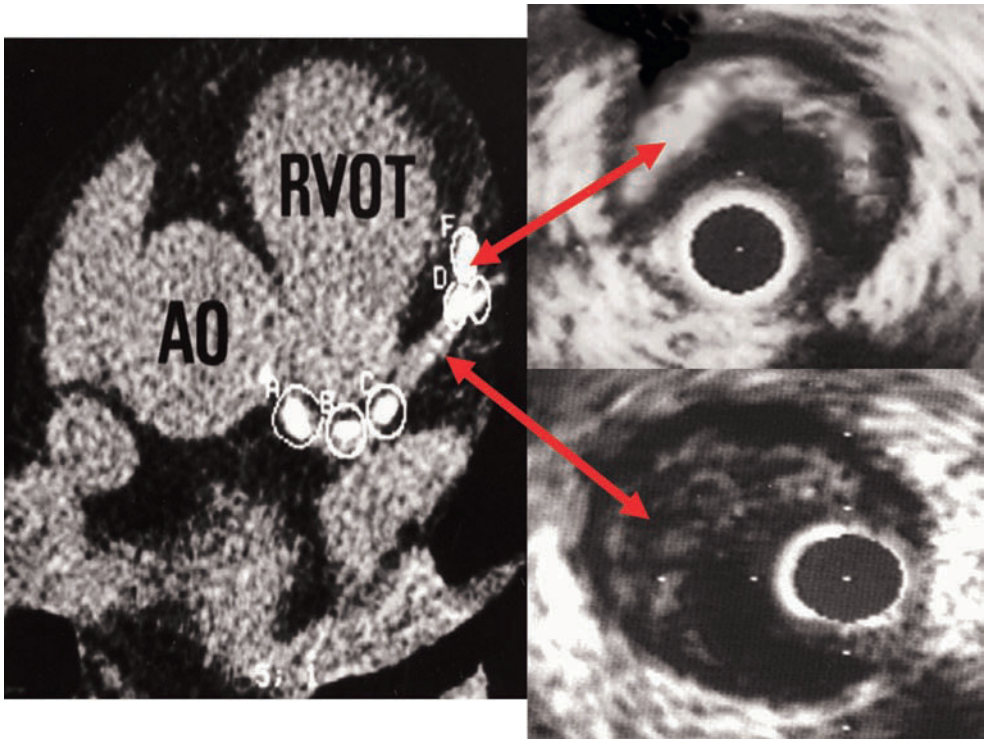

Figure 4.2. Electron beam tomography (EBT) scan (*left*) demonstrating areas of extensive calcification corresponding to heavily calcified plaque on intravascular ultrasound (*upper right*), and less extensive calcification corresponding to less heavily calcified plaque on intravascular ultrasound (*lower right*).

Scoring

The presence of coronary calcium is sequentially quantified through the entire epicardial coronary system. Coronary calcium is defined as a lesion above a threshold of 130 Hounsfield units (which range from −1,000 (air), through 0 (water), and up to +1,000 (dense cortical bone)), with an area of three or more adjacent pixels (at least 1 mm^2). The original calcium score developed by Agatston et al [13] is determined by the product of the calcified plaque area and maximum calcium lesion density (from 1 to 4 based upon Hounsfield units). Standardized categories for the calcium score have been developed with scores of 1–10 considered minimal, 11–100 mild, 101–400 moderate, and >400 severe. Examples are shown in Figure 4.1. The calcium volume score [14] is a more reproducible parameter that is independent of calcium density and is considered to be the parameter of choice for serial studies to track progression or regression of atherosclerosis. Phantom-based calcium mass scores are being developed that will be applicable to any CT scanner [15], but have yet to be validated. Examples of CAC scans are shown in Figure 4.3.

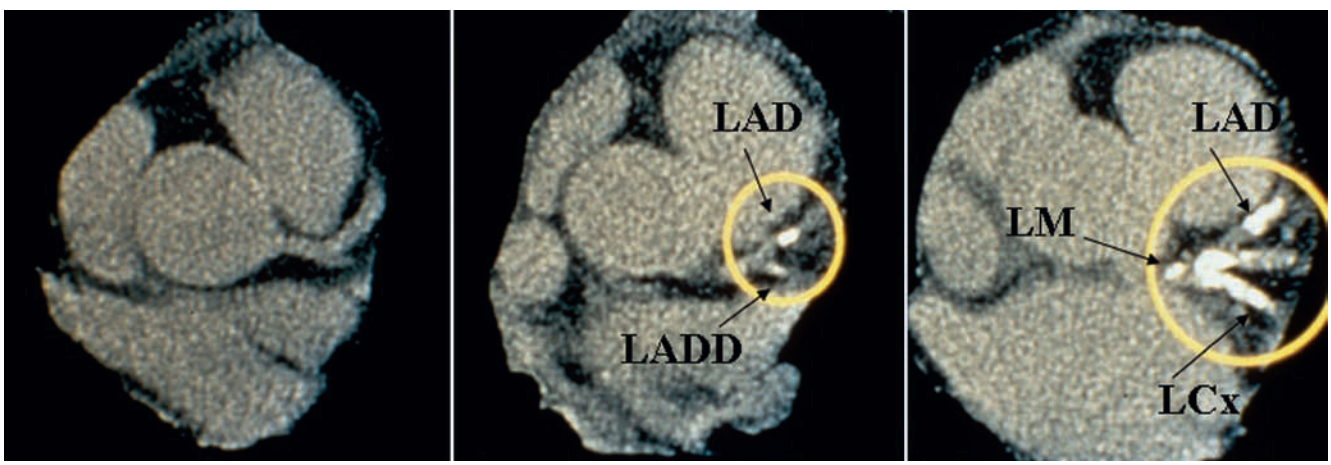

Figure 4.3. Examples of EBT coronary artery calcium (CAC) scans. *Left*: Normal without CAC. *Center*: Moderate CAC involving the left anterior descending (LAD) and circumflex (LCx) coronary arteries. *Right*: Extensive CAC involving the left main (LM), anterior descending, and circumflex coronary arteries.

Epidemiology

By comparing a person's calcium score to others of the same age and gender through the use of large databases of asymptomatic subjects, a *calcium percentile* is generated [16]. This is an index of the prematurity of atherosclerosis; for example, a 50-year-old man in the 76th percentile has more plaque than 75% but less plaque than 24% of asymptomatic 50-year-old men. Although there is an increasing incidence of coronary calcification with increasing age (Figure 4.4), this simply parallels the development of coronary atherosclerosis.

Table 4.1 shows coronary calcification incidence by EBT in an unselected patient population of men and women [17]. The amount of CAC in women is similar to that in men a decade younger, paralleling the 10-year lag in women of the development of clinical atherosclerosis.

Useful though these current nomograms are, variations according to ethnicity have been described, and data regarding these variations are still being collected and separated. In earlier studies, Blacks were noted to have either lower [18, 19] or similar [20, 21] amounts of CAC as Caucasians of the same age; Hispanics had less CAC than Caucasians [18]. In the more recent Multi-Ethnic Study of Atherosclerosis (MESA) of 6,110 asymptomatic patients with 53% female and an average age of 62 years, men had greater calcium levels than women, and calcium amount and prevalence continually increased with increasing age [22]. In men, Caucasians and Hispanics were the first and second highest respectively; Blacks were lowest at the younger ages, and Chinese were lowest at the older ages. In women, whites were highest, Chinese and Black were intermediate, and Hispanics were the lowest except for Chinese in the oldest age group. Thus, predictive indices should be extrapolated to non-whites with caution. However, MESA demonstrated very strong CAC predictive for all groups [23].

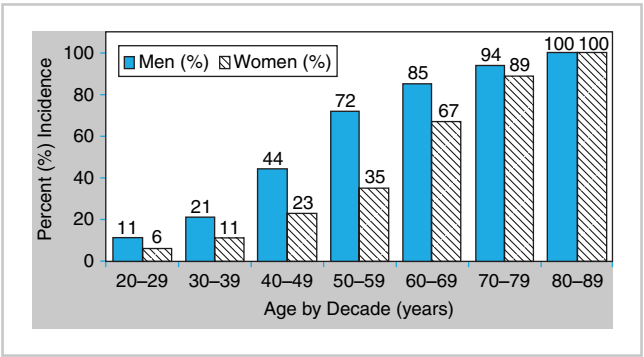

Figure 4.4. Prevalence of CAC in men and women by decades (reproduced with permission of Elsevier from Janowitz et al [16]).

Younger patients with a family history of premature CAD have significantly higher CAC scores than similar aged individuals without this risk factor, particularly if there is a sibling history of premature CAD [24]. In MESA, the odds ratios for the presence of CAC independent of all risk factors in those with compared to those without a family history of premature CAD were 2.74 with premature CAD in both a parent and a sibling, 2.06 in a sibling alone, and 1.52 in a parent alone [25].

Radiation

The vast majority of CAC scanning is being performed on MDCT scanners; in the future it will be the exclusive technology as electron beam computed tomography (EBCT) scanners disappear. The radiation exposure is 1.0 mSv [26]: appropriate perspective is obtained by comparing this exposure to the 0.75 mSv of the annual mammographic examination recommended for women 45 years and older.

Coronary Artery Calcium and Obstructive Disease

The relationship of CAC to obstructive disease has been extensively investigated, and was misunderstood by the 2000 ACC/AHA Consensus Document on EBT [27], which focused on the low specificity as a critical flaw. While the

Table 4.1. Calcium percentile database for asymptomatic men and women: EBT coronary calcium scores as a function of patient age at the time of examination

Percentiles	40–45 years	46–50 years	51–55 years	56–60 years	61–65 years	66–70 years	71–75 years
Men ($n = 28,250$)							
10	0	0	0	1	1	3	3
25	0	1	2	5	12	30	69
50	2	3	15	54	117	166	350
75	11	36	110	229	386	538	844
90	69	151	346	588	933	1,151	1,650
Women ($n = 14,540$)							
10	0	0	0	0	0	0	0
25	0	0	0	0	0	1	4
50	0	0	1	1	3	25	51
75	1	2	6	22	68	148	231
90	4	21	61	127	208	327	698

presence of CAC is nearly 100% specific for atherosclerosis, it is not specific for obstructive disease since both obstructive and nonobstructive lesions have calcification present in the intima. Comparisons with pathology specimens have shown that the degree of luminal narrowing is weakly correlated with the amount of calcification on a site-by-site basis [28–30], whereas the likelihood of significant obstruction increases with the total CAC score [4, 31, 32]. Shavelle et al. [33] reported a 96% sensitivity and 47% specificity for a calcium score >0, with a relative risk for obstructive disease of 4.5, compared to a 76% sensitivity and 60% specificity for treadmill testing, with a relative risk of 1.7. Bielak et al [34] noted a sensitivity and specificity of 99.1 and 38.6% for a calcium score >0. However, when corrected for verification bias, the specificity improved to 72.4%, without loss of sensitivity (97%). The likelihood ratio for obstruction ranged from 0.03 to 0.07 in men and women ≥50 years of age for 0 scores to 12.85 for scores >200. In the <50 years cohort, the likelihood ratios ranged from 0.1 to 0.29 for 0 scores to 54–189 for scores >100.

Rumberger et al [35] demonstrated that higher calcium scores are associated with a greater specificity for obstructive disease at the expense of sensitivity; for example, a threshold score of 368 was 95% specific for the presence of obstructive CAD. In 1,764 persons undergoing angiography, the sensitivity and negative predictive value in men and women were >99% [36]; a score of 0 virtually excluded patients with obstructive CAD. In a separate study of 1,851 patients undergoing CAC scanning and angiography [37], CAC scanning by EBT in conjunction with pretest probability of disease derived by a combination of age, gender, and risk factors, facilitated prediction of the severity and extent of angiographically significant CAD in symptomatic patients.

In a recent meta-analysis of 10,355 symptomatic patients who underwent cardiac catheterization and CAC, 0 CAC was noted in 1941. Significant obstructive disease, defined as >50% diameter stenosis, was noted in 5,805 (56%). For CAC > 0 and the presence of >50% diameter stenosis, the following were reported: sensitivity 98%, specificity 40%, positive predictive value 68%, and negative predictive value 93% [38].

Prognostic Studies in Symptomatic Patients

The prognostic value of extensive coronary calcium (>1,000) in symptomatic males with established advanced CAD was demonstrated in a 5-year follow-up study of 150 patients [39]. More recently, in a meta-analysis of 3,924 symptomatic patients with a 3.5 year follow-up, the cardiac event rate was 2.6% per year in those with CAC > 0 and 0.5% per year in 0 CAC patients [38]. However, with the development of coronary computed tomographic angiography (CCTA), CAC alone is not justified in the symptomatic population; CCTA will identify the noncalcified plaque and even obstructive disease that may be noted in these patients, even with 0 CAC.

Clarification

Despite the apparently reasonable specificities, which are similar to those of stress testing, it must be understood that the purpose of CAC scanning is not to detect obstructive disease and, therefore, it is inappropriate to even use "specificity" in the context of obstruction. Rather, its purpose is to detect subclinical atherosclerosis in its early stages, for which it is virtually 100% specific.

Key Prognostic Studies in Primary Prevention

The utility of CAC for risk evaluation in the asymptomatic primary prevention population is dependent on prognostic studies documenting the relative risk conferred by calcified plaque quantitation compared to conventional risk factors. Raggi et al [40] demonstrated, in 632 asymptomatic patients followed for 32 months, an annualized event rate of 0.1% per year in patients with 0 scores, compared to 2.1% per year with scores of 1–99, 4.1% per year with scores of 100–400, and 4.8% per year with scores >400. Thus, the annualized event rates associated with coronary calcium were in the range considered to warrant secondary prevention classification by the Framingham Risk Score (Figure 4.5).

The odds ratio conferred by a calcium percentile >75% was 21.5 times greater than for the lowest 25%, compared to an odds ratio of 7 for the highest vs. lowest quartiles of National Cholesterol Education Program (NCEP) risk factors (Figure 4.6).

Wong et al [41], in 926 asymptomatic patients followed for 3.3 years, noted a relative risk of 8 for scores >270, after adjusting for age, gender, hypertension, high cholesterol, smoking, and diabetes. Arad et al [42], in 1,132 subjects followed for 3.6 years, reported odds ratios of 14.3–20.2 for scores ranging from >80 to >600; these were three to seven

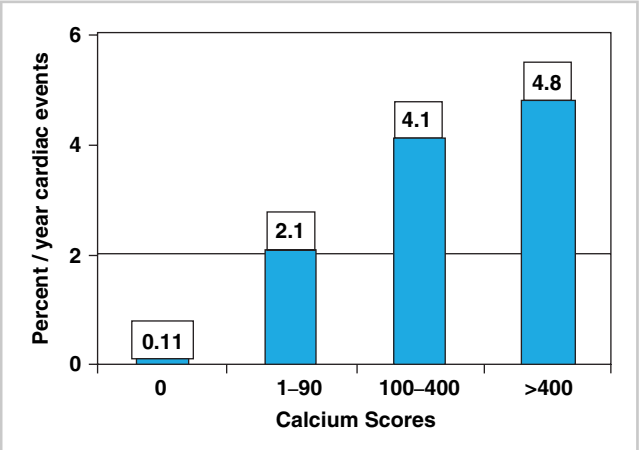

Figure 4.5. Relationship of CAC score to annual hard cardiac event rates in 632 asymptomatic patients undergoing EBT calcified plaque imaging. The solid line indicates the 2% per year event rate consistent with secondary prevention risk.

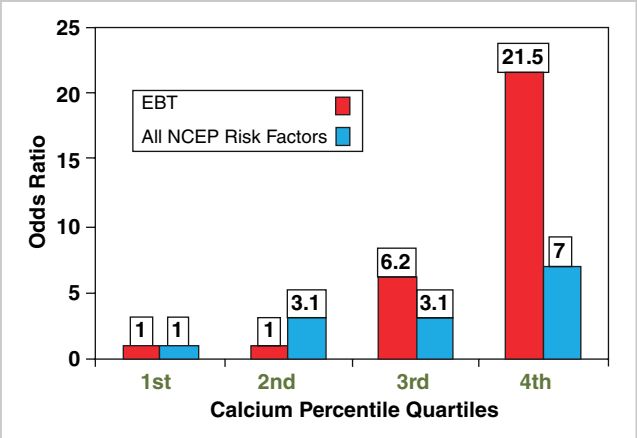

Figure 4.6. Odds ratios of CAC and National Cholesterol Education Program (NCEP) risk factor quartiles for annual hard cardiac event rates in asymptomatic patients undergoing EBT calcified plaque imaging.

times greater than for the NCEP risk factors. In a retrospective analysis of 5,635 asymptomatic, predominantly low to moderate risk, largely middle-aged patients followed for 37 ± 12 months, Kondos et al. [43] found that the presence of any CAC by EBT was associated with a relative risk for events of 10.5, compared to 1.98 and 1.4 for diabetes and smoking, respectively. In women, only CAC was linked to events, with a relative risk of 2.6; risk factors were not related. The presence of CAC provided prognostic information incremental to age and other risk factors.

Shaw et al [44] retrospectively analyzed 10,377 asymptomatic patients with a 5-year follow-up after an initial EBT evaluation. All-cause mortality increased proportional to CAC (Figure 4.7), which was an independent predictor of risk after adjusting for all of the Framingham risk factors ($p < 0.001$).

Superiority of CAC to conventional Framingham risk factor assessment was demonstrated by a significantly greater area under the ROC curves (0.73 vs. 0.67, $p < 0.001$). Incremental value of CAC to Framingham risk was also established by a significant increase of the area under the ROC curves, from 0.72 for Framingham risk to 0.78 with the addition of CAC ($p < 0.001$). Risk stratification was present in each risk group, and was particularly strong in the 10–20% 10-year Framingham risk group. Stratification of mortality risk by CAC score was as effective in women as in men.

Greenland et al [45] analyzed a population-based study of 1,461 prospectively followed, asymptomatic subjects who were predominantly moderate to high risk, and found that CAC scores >300 significantly added prognostic information to Framingham risk analysis in the 10–20% Framingham risk category. The results of the St Francis Heart Study by Arad et al [46] in a prospective, population-based study of 5,585 asymptomatic, predominantly moderate- to moderately-high-risk men and women, mirrored previous retrospective studies [7, 18–20], and confirmed the higher event rates associated with increasing CAC scores. CAC scores >100 were associated with relative risks of from 12 to 32, and were secondary prevention equivalent, with event rates>2% per year (Figure 4.8).

Incremental information over Framingham scores was documented with areas under the ROC curves of 0.81 for CAC and 0.71 for Framingham ($p < 0.01$). Importantly, classification by CAC tertiles changed the risk group of approximately 67% of patients classified in the Framingham 10–20% 10-year event rate group to either lower or higher risk. The appropriateness of this change was confirmed by outcome measures of cardiac events. Furthermore, in the Framingham high-risk category (>20% 10-year event rate), 45% were correctly moved to lower-risk categories by CAC tertile reclassification. Finally, in the Framingham <10% 10-year risk group, 29% had scores >100 with an associated 1.7% per year event rate (Figure 4.9).

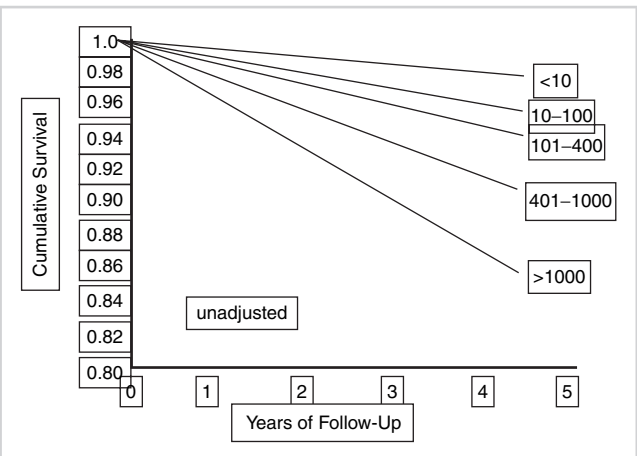

Figure 4.7. Cumulative survival of 10,377 patients from the National Death Registry according to CAC categories (reproduced with permission of the RSNA from Shaw et al [45], p. 831).

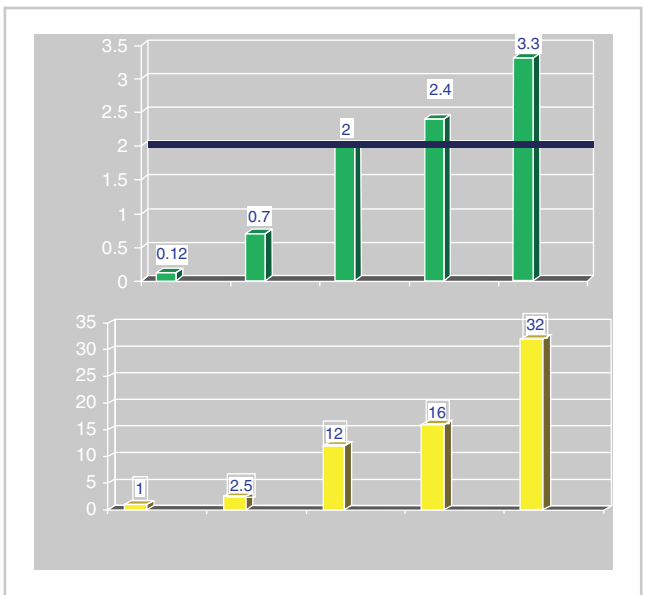

Figure 4.8. Annual event rates and relative risks for cardiac events in 5,585 asymptomatic patients at different levels of CAC (St. Francis Heart Study). The solid line indicates the 2% per year event rate consistent with secondary prevention risk.

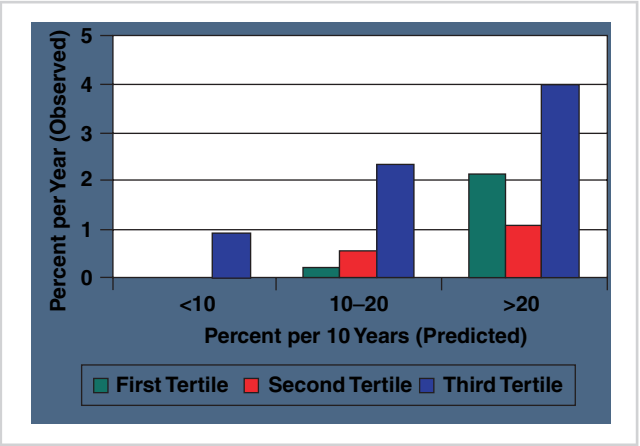

Figure 4.9. Annual event rates in asymptomatic patients in the different Framingham 10-year risk groups according to the tertile of CAC score (St. Francis Heart Study).

The prognostic significance of very high calcium scores was provided in a study of 98 asymptomatic patients with a CAC score >1,000 who were followed for 17 months [47] during which 35 patients (36%) suffered a hard cardiac event (myocardial infarction (MI) or cardiac death). The annualized event rate of 25% refuted the erroneous concept that extensive calcified plaque may confer protection against plaque rupture and events.

In a younger cohort of 2,000 asymptomatic Army personnel, Taylor et al [48] demonstrated the powerful predictive value of CAC. There was a relative risk of 11.8 in patients with CAC > 44 compared to those with 0 CAC, after correcting for the Framingham Risk Score. In a much more elderly population (71 years), Vliegenthart et al [49] found a hazard ratio of 4.6 for CAC 400–1,000 compared to <100 after 3.3 years of follow-up.

Subsequently, even more powerful data have emerged. Budoff et al [50] in another all-cause mortality study, with retrospective analysis of 25,203 asymptomatic patients after 6.8 years, found that CAC > 400 was associated with a hazard ratio of 9.2. In the largest study using coronary calcium percentile rather than absolute scores, Becker et al. [51] in 1,724 patients followed prospectively for 3.4 years, reported hazard ratios for CAC percentile >75% vs. 0% of 6.8 for men and 7.9 for women. The area under the ROC curve for CAC percentile (0.81) was significantly superior to the Framingham (0.66), European Society of Cardiology (0.65), and PROCAM risk scores (0.63). Eighty-two percent of patients who developed MI or cardiac death were correctly classified as high risk by CAC percentile, compared to only 30% by Framingham, 36% by the European Society of Cardiology, and 32% by PROCAM.

Perhaps the most important study is the MESA, an NHLBI sponsored prospective evaluation of 6,814 patients followed for 3.8 years [23]. Compared to patients with 0 CAC, the hazard ratios for a coronary event were 7.73 for those with CAC 101–300, and 9.67 among participants for CAC > 300 ($p < 0.001$) (Table 4.2; Figure 4.10).

Table 4.2. Risk of coronary events associated with increasing CAC after adjusting for standard risk factors in MESA

CAC	Annual rate (%)	Events/no at risk	HR	*p*
0	0.11	15/3,409	1.0	<0.001
1–100	0.59	39/1,728	3.61	<0.001
101–300	1.43	41/752	7.73	<0.001
>300	2.87	67/833	9.67	<0.001
Doubling			1.26	<0.001

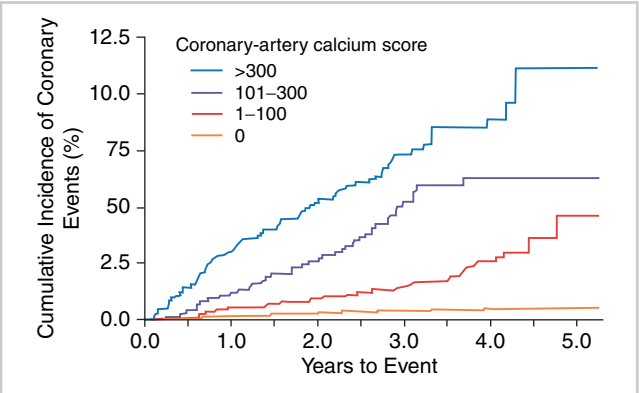

Figure 4.10. Coronary events at different CAC levels in multi-ethnic study of atherosclerosis (MESA).

Among the four racial and ethnic groups (Caucasian, Chinese, Hispanic, Black), doubling the CAC increased risk of any coronary event by 18–39%. The ROC curve areas were significantly higher ($p < 0.001$) with the addition of CAC to standard risk factors. CAC was more predictive of coronary disease than carotid intima-media thickness; the hazard ratios per 1-SD increment increased 2.5-fold (95% CI, 2.1–3.1) for CAC and 1.2-fold (95% CI, 1.0–1.4) for IMT [52].

In the 2,684 patients in the female component of MESA [53], Lagoski et al. reported a 6.5 hazard ratio for the 32% with a CAC > 0 vs. the 68% with 0 CAC, even though 90% were low risk by Framingham. In an analysis of all-cause mortality in 44,052 asymptomatic patients followed for 5.6 years [54], the deaths/1,000 patient years were 7.48 for CAC > 10, compared to 1.92 for CAC 1–10, and 0.87 for 0 CAC. Finally, in a meta-analysis of 64,873 patients followed for 4.2 years, the coronary event rate was 1% per year for the 42,283 with CAC > 0, compared to 0.13% per year in the 25,903 patients with 0 CAC [38].

Finally, in the Heinz Nixdorf Recall Study [55], 4,487 subjects without CAD were followed for 5 years. Low ATP III risk was noted in 51.5%, while 28.8 and 19.7% were at intermediate and high risk, respectively. The prevalence of low (<100), intermediate (100–399) and high (≥400) CAC scores was 72.9, 16.8, and 10.3%, respectively ($p < 0.0001$). The relative risk of CAC >75th vs. ≤25th percentile was 11.1 ($p < 0.0001$) for men and 3.2 ($p = 0.006$) for women. Adding CAC to the ATP III categories improved the AUC from 0.602 to 0.727 in men and from 0.660 to 0.723 in women, and led to a reclassification of 77.1% of intermediate risk individuals (62.9% into low risk, and 14.1% into high risk group). The

relative risk associated with doubling of the CAC score was 1.32 (95% CI: 1.20–1.45, $p < 0.001$) in men and 1.25 (95% CI: 1.11–1.42, $p < 0.0001$) in women.

In all of these studies, receiver operator characteristic curves for CAC were superior to the Framingham Risk Score and the annual event rate for CAC > 100–400 exceeded the CAD equivalent of >2% per year. Table 4.3 summarizes the relative risk results of the largest published outcome studies.

Zero Coronary Artery Calcium Scores

Individuals with zero CAC scores have not yet developed detectable, calcified coronary plaque but they may have fatty streaking and early stages of plaque. Noncalcified plaques are present in many young adults. Nonetheless, the event rate in patients with CAC score 0 is very low [40, 45, 46]. Raggi et al. [40] demonstrated an annual event rate of 0.11% in asymptomatic subjects with 0 scores (amounting to a 10-year risk of only 1.1%), and in the St Francis Heart Study [46], scores of 0 were associated with a 0.12% annual event rate over the ensuing 4.3 years. Greenland et al. [45], in a higher-risk asymptomatic cohort, noted a higher annual event rate (0.62%) with 0 CAC scores; a less sensitive CAC detection technique and marked ethnic heterogeneity may have contributed to their findings [56]. In the definitive MESA study [23], 0 CAC was associated with a 0.11% annual event rate. In a meta-analysis of 64,873 patients followed for 4.2 years [54], the coronary event rate was 0.13% per year in the 25,903 patients with 0 CAC compared to 1% per year for the 42,283 with CAC > 0. In an analysis of all-cause mortality in 44,052 asymptomatic patients followed for 5.6 years [54], the deaths/1,000 patient years for the 19,898 with 0 CAC was 0.87, compared to 1.92 for CAC 1–10, and 7.48 for CAC > 10.

While noncalcified, potentially "vulnerable" plaque is by definition not detected by CAC testing, CAC can identify the pool of higher-risk asymptomatic patients out of which will emerge approximately 95% of the patients presenting each year with sudden death or an acute MI. While the culprit lesion contains calcified plaque in only 80% of the acute events [57], of greater importance is the observation that exclusively soft, noncalcified plaque has been seen in only 5% of acute ischemic syndromes in both younger and older populations [12, 58]. In a more recent meta-analysis [38], only 2 of 183 (1.1%) 0 CAC patients were ultimately diagnosed with an acute coronary syndrome after presenting with acute chest pain, normal troponin, and equivocal EKG findings. CAC > 0 had 99% sensitivity, 57% specificity, 24% positive predictive value, and 99% negative predictive value for ACS. Thus, while it is uncommon that a patient with an imminent acute ischemic syndrome would have had a 0 CAC score, further evaluation, particularly with CCTA, is recommended.

Compliance with Therapeutic Interventions

With the exception of a single study flawed by insufficient power [59], CAC has been shown to have a positive effect on compliance and initiation of and adherence to medication and life style changes. In 505 asymptomatic patients, statin adherence 3.6 years after visualizing their CAC scan was 90% in those with CAC > 400 compared to 75% for 100–399, 63% for 1–99, and 44% for 0 CAC ($p < 0.0001$) [60]. Similarly, in 980 asymptomatic subjects followed for 3 years, ASA initiation, dietary changes, and exercise increased significantly from those with 0 CAC (29, 33, 44%, respectively) and was lowest (29%) in those with CAC > 400 (61, 67, 56%, respectively [61]. Finally, after a 6 year follow-up in 1,640

Table 4.3. Characteristics and risk ratio for follow-up studies using electron beam computed tomography (EBCT) in asymptomatic persons

Author	*n*	Mean age (years)	Follow-up duration (years)	Calcium score cutoff	Comparator group for RR calculation	Relative risk ratio
Arad et al [42]	1,173	53	3.6	CAC > 160	CAC < 160	20.2
Park et al [77]	967	67	6.4	CAC > 142.1	CAC < 3.7	4.9
Raggi et al [40]	632	52	2.7	Top quartile	Lowest quartile	13
Wong et al [41]	926	54	3.3	Top quartile (>270)	First quartile	8.8
Kondos et al [43]	5,635	51	3.1	CAC	No CAC	10.5
Greenland et al [45]	1,312	66	7.0	CAC > 300	No CAC	3.9
Shaw et al [44]	10,377	53	5	CAC ≥ 400	CAC ≤ 10	8.4
Arad et al [46]	5,585	59	4.3	CAC ≥ 100	CAC < 100	10.7
Taylor et al [48]	2,000	40–50	3.0	CAC > 44	CAC = 0	11.8
Vliegenthart et al [49]	1,795	71	3.3	CAC > 1,000	CAC < 100	8.3
				CAC 400–1,000	CAC < 100	4.6
Budoff et al [50]	25,503	56	6.8	CAC > 400	CAC 0	9.2
Lagoski et al [53]	3,601	45–84	3.75	CAC > 0	CAC 0	6.5
Becker et al [51]	1,726	57.7	3.4	CAC > 400		6.8 men
						7.9 women
Detrano et al [23]	6,814	62.2	3.8	CAC > 300	CAC > 0	14.1
Erbel et al [55]	4,487	45–75	5	>75th%	<25th%	11.1 men
						3.2 women

CAC Coronary Artery Calcium Score

asymptomatic subjects, the odds ratios for those with CAC > 0 compared to 0 CAC for usage of statins, ASA, and statin + ASA were 3.53, 3.05 and 6.97, respectively [62].

Coronary Artery Calcium and Guidelines

Guidelines have been increasingly positive regarding the value of CAC scanning. The American College of Cardiology/American Heart Association expert consensus document (2000) concluded that:

1. A negative EBCT test makes the presence of atherosclerotic plaque, including unstable plaque, very unlikely.
2. A negative test is highly unlikely in the presence of significant luminal obstructive disease.
3. Negative tests occur in the majority of patients who have angiographically normal coronary arteries.
4. A negative test may be consistent with a low risk of a cardiovascular event in the next 2–5 years.
5. A positive EBCT confirms the presence of a coronary atherosclerotic plaque.
6. The greater the amount of calcium, the greater the likelihood of occlusive CAD, but there is not a 1-to-1 relationship, and findings may not be site specific.
7. The total amount of calcium correlates best with the total amount of atherosclerotic plaque, although the true "plaque burden" is underestimated.
8. A high calcium score may be consistent with moderate to high risk of a cardiovascular event within the next 2–5 years [27].

The American Heart Association Prevention V Update (2000) suggested that CAC be considered for risk assessment in the 6–20% Framingham 10-year risk category [63]. The final report of the NCEP guidelines [64] made the following recommendation on the basis of existing data at the time of publication (2002):

> Therefore, measurement of coronary calcium is an option for advanced risk assessment in appropriately selected persons. In persons with multiple risk factors, high coronary calcium scores (e.g., >75th percentile for age and sex) denotes advanced coronary atherosclerosis and provides a rationale for intensified LDL-lowering therapy.

The European Guidelines on Cardiovascular Disease Prevention in Clinical Practice (2003) state "Coronary calcium scanning is thus especially suited for patients at medium risk," and use CAC to qualify conventional risk analysis [65]. The American Heart Association Guidelines for Cardiovascular Disease Prevention in Women (2004) listed coronary calcification as an example of subclinical cardiovascular disease (CVD) placing patients in the 10–20% Framingham 10-year risk category and acknowledged that "some patients with subclinical CVD will have >20% 10-year CHD risk and should be elevated to the high-risk category" [66].

In 2006, the SHAPE guidelines (Figure 4.11) recommended CAC or carotid intima-media thickening for all but the lowest risk asymptomatic men >45 and women >55 years, with subsequent treatment based upon the amount of CAC [67].

Based upon the accumulated evidence at the time, which did not yet include the MESA [23] and Becker [51] data, the ACCF/AHA 2007 Clinical Expert Consensus Document [68] judged that in the intermediate risk population "it may be reasonable to consider use of CAC measurement in such patients based on available evidence that demonstrates incremental risk prediction information in this selected (intermediate risk) patient group." A more robust endorsement is anticipated in future recommendations.

Correlation with Risk Factors

Correlation in Individual Patients

Conventional risk factors do correlate with CAC [69–71], even though CAC is superior to conventional risk factors in predicting outcomes. There is a clear association of CAC with a premature family history of CAD, diabetes, and lipid values in large groups of patients. However, the difficulty equating risk factors with CAC in individual patients has been highlighted by the work of Hecht et al in 930 consecutive primary prevention subjects undergoing EBT [70]. They found increasing likelihoods of CAC with increasing levels of low-density lipoprotein cholesterol (LDL-C) and decreasing levels of high-density lipoprotein cholesterol (HDL-C) in the population as a whole, but found no differences in the amount of plaque between groups and demonstrated a total lack of correlation in *individual* patients between the EBT calcium percentile and the levels of total, LDL- and HDL-cholesterol, total/HDL-cholesterol, triglycerides, lipoprotein(a) (Lp(a)), homocysteine, and LDL particle size (Figure 4.12).

Postmenopausal women presented a striking example of the inability of conventional risk analysis to predict the presence or absence of subclinical atherosclerosis [72]. There were no differences in any lipid parameters or in the Framingham Risk Scores between postmenopausal women with and without calcified plaque, rendering therapeutic decisions that are not plaque- imaging-based extremely problematic. Further support for the poor correlation of conventional risk factors with subclinical atherosclerosis was provided by Taylor et al in 630 active duty US Army personnel aged 39–45 years, undergoing EBT [73]. The area under the ROC curve was only 0.62 for the Framingham Risk Score and 0.61 for LDL-C alone. The authors conclude: "In this age homogeneous, low-risk screening cohort, conventional coronary risk factors significantly underestimated the presence of premature, subclinical calcified coronary atherosclerosis." *These discrepancies underscore the difficulties inherent in applying population based guidelines derived from statistical analyzes to decision-making in the real world of individual patient care.*

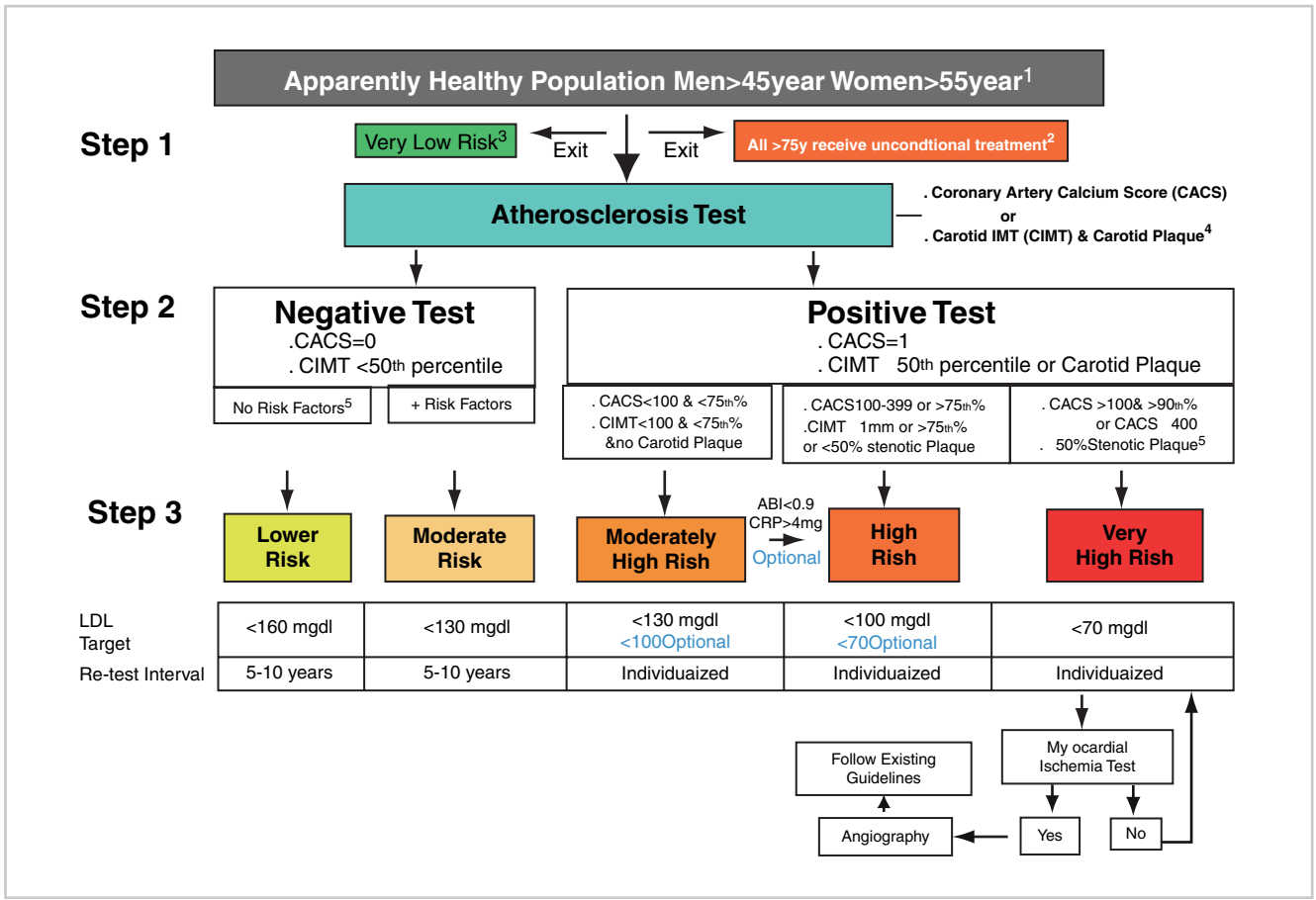

Figure 4.11. The SHAPE Guideline (towards the National Screening for Heart Attack Prevention and Education Program).

Advanced Metabolic Testing

The discovery of significant CAC in patients with ostensibly unremarkable lipid values has led to more extensive metabolic analysis in these patients in the search for treatable disorders. In 296 asymptomatic patients with CAC, Superko and Hecht [74] reported a 66% incidence of small, dense LDL; 27% had elevated Lp(a) and 7% had elevated homocysteine. While there is no clear-cut evidence for event reduction by treatment of these abnormalities, consideration should be given to the administration of niacin for small, dense LDL and Lp(a) elevations. The combination of tomographic plaque imaging with metabolic testing and aggressive treatment of identifiable abnormalities has been termed "interventional lipidology" [75].

Inflammation and Coronary Artery Calcium

hs-CRP

Although still controversial, high sensitivity C-reactive protein (hs-CRP) has been clearly linked to the inflammatory process inherent in CAD. Extensive investigations have led to the suggestion that it be used to screen large segments of the asymptomatic population [76] despite the absence of data demonstrating that hs-CRP is additive to standard risk factors in predicting events. There is, however, evidence that it is significantly inferior to CAC in this capacity. Park et al, in 967 asymptomatic patients, demonstrated that the relative risk of an MI or cardiac death, after adjustment for conventional risk factors, increased four to fivefold from low to high calcium scores at any hs-CRP level, and only 0.25–0.7-fold from low to high hs-CRP at any calcified plaque level (Figure 4.13).

In multivariate analysis after adjustment for risk factors, CAC was significantly predictive of events ($p < 0.005$); hs-CRP was not significantly predictive ($p = 0.09$) before or after adjustment for CAC [77]. In 323 Framingham Heart Study participants, there was a weak relationship between hs-CRP and CAC in men ($r = 0.19$, $p < 0.05$) in multivariate analysis, and no significant correlation in women [78]. There was no significant relationship between hs-CRP and CAC after multivariate analysis in 914 asymptomatic subjects in the Study of Inherited Risk of Coronary Atherosclerosis [79]. In 1,005 asymptomatic patients randomized to treatment with atorvastatin or placebo in the St Francis Heart Study [80], only the calcium score was significantly associated with disease events ($p < 0.0001$) in a multivariate analysis including standard coronary disease risk factors, hs-CRP,

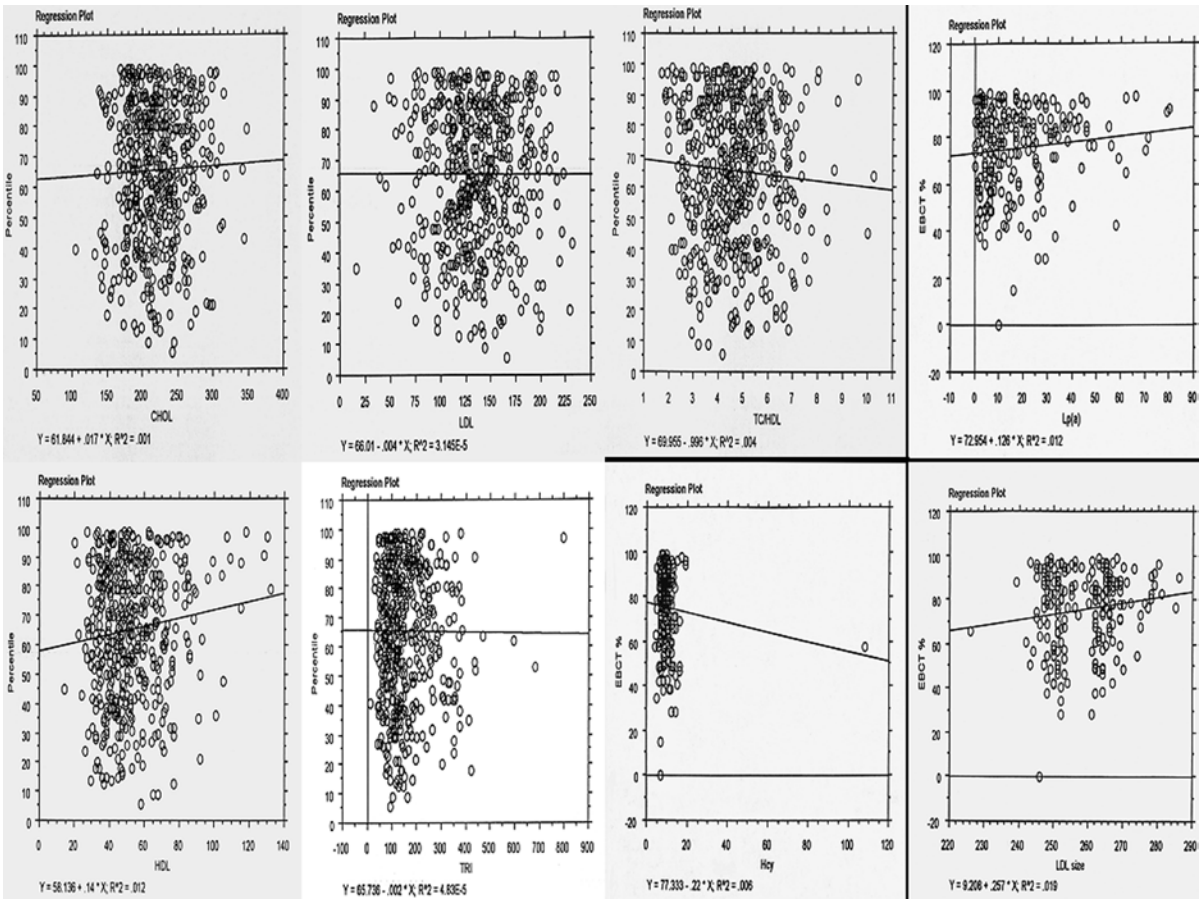

Figure 4.12. Correlation between CAC percentile and plasma levels of multiple lipid parameters in 930 asymptomatic patients. Not all correlations are significant (reproduced with permission of Elsevier from Hecht [104]).

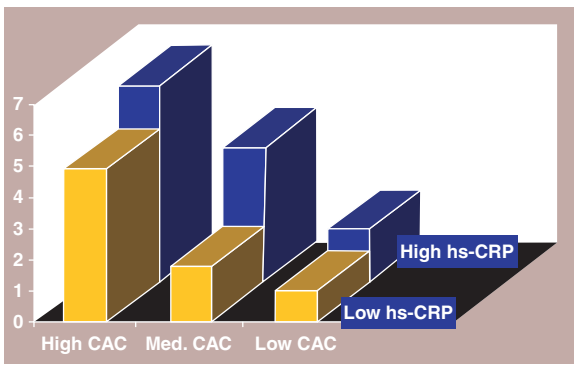

Figure 4.13. Relative risks (RR) of non-fatal myocardial infarction (MI) or coronary death associated with high (≥75th percentile = 4.05 mg/L) and low (<4.05 mg/L) levels of C-reactive protein (CRP) and high (>142.1), medium (3.7–142.1), and low (<3.7) tertiles of calcium scores (reproduced with permission of Wolters Kluwer from Park et al [78], p. 2076).

and baseline coronary calcium score. Hs-CRP did not predict events independently of the calcium score ($p = 0.47$). There were no correlations between CAC and hs-CRP in either study. In the Dallas Heart Study in 3,373 asymptomatic subjects, there was no significant relationship between hs-CRP and CAC by multivariate analysis [81].

The absence of additional predictive value of hs-CRP and its lack of correlation with CAC do not challenge the inflammatory aspects of the disease process. Rather, it emphasizes the greater value of evidence of the disease itself, namely CAC, compared to a risk marker, such as hs-CRP.

Lipoprotein-Associated Phospholipase A2 (Lp-PLA2)

There is much less data regarding Lp-PLA2. In a nested case-control study among 266 CARDIA participants [82],

Lp-PLA2 mass was significantly higher in subjects with CAC compared to those without CAC (OR 1.28). The numbers are too small to provide meaningful conclusions.

Unknown Factors

The lack of clear relationship between lipid levels and subclinical plaque in individual patients does not negate the atherogenic effect of these metabolic disorders. Rather, it highlights the variations in individual susceptibility to the atherogenic effects at a given plasma level, very likely mediated by as yet undetermined genetic factors. O'Donnell et al [83], in an analysis of abdominal aortic calcium in 2,151 patients in 1,159 families in the Framingham Study, noted a heritability component accounting for up to 49% of the variability in calcified plaque, and concluded that "AAC deposits are heritable atherosclerotic traits. A substantial portion of the variation is due to the additive effects of genes, which have yet to be characterized." Peyser et al. [84], analyzing coronary calcium in 698 patients in 302 families, found a variance of up to 48% associated with additive polygenes after adjustment for covariates. They concluded that there is a:

> substantial genetic component for subclinical CAD variation . . . even after accounting for effects of genes acting through measured risk factors. These genes may act through other measurable risk factors or through novel pathways that have not or cannot be measured in vivo. Identification of such genes will provide a better basis for prevention and treatment of subclinical CAD.

The inevitable conclusion of the consistent lack of relationship between risk factors and disease and the superiority of CAC in individual patients was summarized by Hecht [85]: "*The most important role of risk factors may be to identify the modifiable targets of risk reduction in patients with risk already established by clinical events or significant CAC.*"

Clinical Applications

Patient Selection

Moderately High Risk

Hecht et al. [86] have proposed recommendations for the application of CAC scanning. (Table 4.4). The Framingham Risk Score [87], incorporating both age and gender, is recommended as the initial step in selecting the appropriate test populations. Asymptomatic patients in the National Cholesterol Education Adult Treatment Program III [88] classified 10–20% Framingham 10-year risk category (moderately high risk) comprise the group that presents the greatest challenge to the treating physician, and are those in whom the application of CAC scoring is most appropriate; the CAC score can assist the physician in decisions regarding recommendations for the use of medications and the degree of emphasis to be placed on lifestyle modifications.

Lower Risk

Patients with less than moderately high Framingham risk may also benefit from CAC scoring to guide management decisions. For instance, most young patients with a family history of premature CAD will not have sufficient risk factors to even warrant Framingham scoring (lower NCEP risk) or will be in the moderate (1–10% 10-year Framingham risk group), since family history, while an NCEP risk factor, does not contribute points to the Framingham score. In 222 young patients presenting with an MI as the first sign of CAD (mean age 50 years), Akosah et al [89] demonstrated that 70% were in these lesser risk categories and would not have been started on a statin using NCEP guidelines. Data from Schmermund et al. [12]. and Pohle et al [58] indicate that 95% of acute MI patients would have been identified by EBT plaque imaging irrespective of age. On the basis of these observations, the use of CAC scoring should be considered in patients with a family history of premature CAD, even when their Framingham risk is moderate or even low.

Higher Risk

Since the Framingham Risk Score is not very accurate in the high risk population, as demonstrated by the St. Francis Heart Study [46], application of CAC scanning to this group is also warranted. In addition, some Framingham high-risk patients may be intolerant of statins or may strongly prefer alternative medicine approaches. In these patients, CAC evidence of high risk may be used to reinforce the necessity for finding a statin that can be tolerated and for persuading the refractory patient of the need for aggressive treatment. Conversely, the absence of significant CAC may permit relaxation of the treatment goals.

Initiation and Goals of Drug Therapy

New Paradigm

The presence or absence and the amount of CAC can be useful for clinical decision-making, as previously recommended in the AHA Prevention V Update [63]. As an extension of this report, based on recent data, Table 4.4 provides simple, easily implemented treatment paradigms for

Table 4.4. Guidelines for treatment in asymptomatic, NCEP classified moderately high-risk patients based upon CAC score

CAC score/percentile	Framingham risk group equivalent	LDL goal (mg/dL)	Drug therapy (mg/dL)
0	Lower risk; 0–1 risk factors; Framingham risk assessment not required	<160	≥190 160–189: drug optional
1–10 and ≤75th %	Moderate risk; 2 + risk factors (<10% Framingham 10-year risk)	<130	≥160
11–100 and ≤75th %	Moderately high risk; 2 + risk factors (10–20% Framingham 10-year risk)	<130	≥130 100–129: consider drug
101–400 or >75th %	High risk; CAD risk equivalent (>20% Framingham 10-year risk)	<100 Optional goal <70	≥100 <100: consider drug
>400 or >90th %	Highest risk[a]	<100 Optional goal <70	Any LDL level

[a]Based on CAC score; consider beta blockers

combining the risks of varying CAC scores with the most recent NCEP recommendations [88]. The SHAPE guidelines [67] go one step further and recommend CAC scanning irrespective of the Framingham Risk Score.

Conversion to Higher or Lower Risk

Patients in the moderately high (10–20% 10-year risk) category who are then identified to be at higher risk by CAC become candidates for secondary prevention lipid goals [87] irrespective of their baseline lipid level. This would apply even for patients with LDL-C <100 mg/dL, as implied by the Heart Protection Study [90] and stated in the most recent NCEP report [88]. Based on prognostic data, CAC >100 or >75th percentile defines a CAD equivalent. In the St Francis Heart Study [46], the CAC cutpoint for initiating secondary prevention therapy was a score >100, and the >75th percentile was suggested by the NCEP guidelines [44]. In this regard, CAC scores >400 [35] or >90th percentile [68] are associated with a very high annual risk (4.8 and 6.5% respectively) and are candidates for the most aggressive approach. These recommendations also apply to initiation of the NCEP guided therapeutic life changes [91] that are an essential component of aggressive prevention.

The transformation of a moderately high-risk to a high-risk patient is shown in Figure 4.14. A 57-year-old man with hypertension, total cholesterol 235 mg/dL, LDL-C 150 mg/dL, HDL-C 75 mg/dL, and a 10-year Framingham risk of 12%, was referred for CAC scanning. The CAC score was 1,872, in the >99th % for his age, placing him in the highest risk category with LDL-C treatment goal of <70 mg/dL.

In the Framingham 10–20% 10-year risk population, patients with CAC scores >100 and >75th percentile remain in the same risk group or are transformed to lower-risk categories depending on the score, and are treated accordingly. CAC scores from 10 to 100 and <75th percentile maintain the patient in the moderately high-risk group (10–20% 10-year risk). Patients with CAC scores from 1 to 10 and <75th percentile are reclassified as moderate risk (<10% 10-year risk), and CAC scores of 0 reclassify the patient to the lower-risk category. As noted above, some patients in the lower-risk groups based on Framingham scores, such as younger patients (35–45 years of age) with a strong family history of premature coronary heart disease, are appropriate candidates for CAC scanning. In such patients, the recommendations in Table 4.3 would also apply.

Figure 4.15a displays the CAC scan of a 41-year-old woman whose mother experienced a MI at age 55. The total cholesterol was 188 mg/dL, LDL-C 112 mg/dL, HDL-C 50 mg/dL and triglycerides 132 mg/dL. She was in the 0–1 risk factor group in which a Framingham Risk Score need not be calculated. The CAC score was 110, in the left anterior descending (LAD) and diagonal branch, in the >99th percentile for her age, placing her in a high-risk category. She underwent dual isotope nuclear stress testing (Figure 4.15b), which revealed severe anteroseptal ischemia, followed by angiography and placement of a stent to treat a 95% ostial LAD stenosis (Figure 4.15c). Statin therapy was implemented to reduce the LDL-C to <70 mg/dL.

Patients in the high-risk category (10-year Framingham risk >20%) may be downgraded if the CAC scores do not warrant the highest risk category. CAC scores <100, and, in particular, <10, imply a lower than expected risk and should reduce the intensity of therapy. For instance, a 65-year-old male hypertensive smoker, with an LDL-C of 140 mg/dL and a 10-year Framingham risk of 25%, was very reluctant to take a statin prescribed for his LDL-C. A CAC scan was performed (Figure 4.16), which demonstrated total absence of calcified plaque, despite the presumed high risk. Therapeutic life changes, rather than statins, were recommended.

Other Applications

Diabetes

Diabetic patients deserve special consideration. The NCEP ATP-III guidelines characterize diabetes as a CAD risk equivalent. Raggi et al [92] (Figure 4.17), however, have demonstrated that diabetic patients with 0 CAC scores have

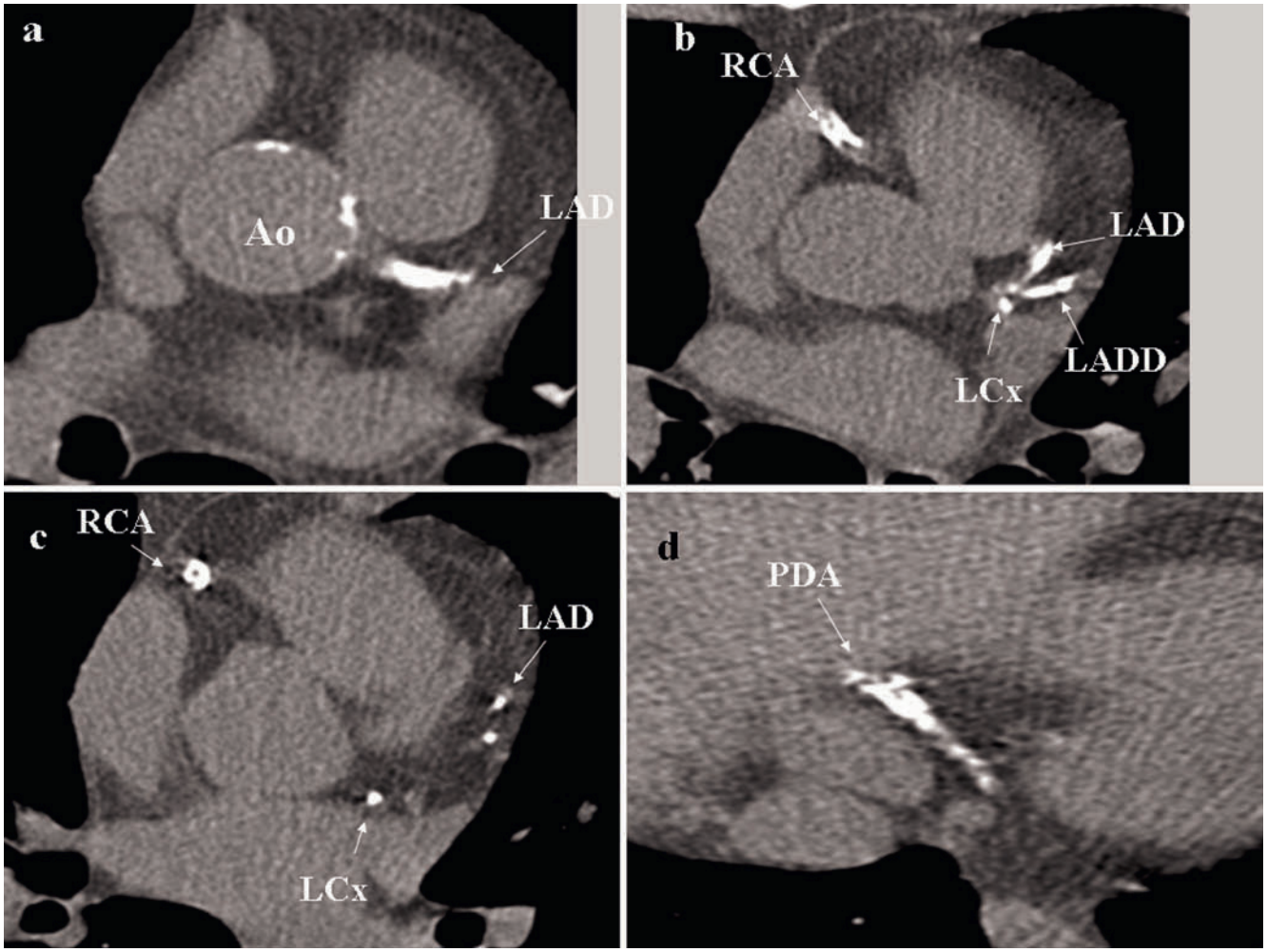

Figure 4.14. A 57-year-old man with hypertension, total cholesterol 235 mg/dL, low-density lipoprotein cholesterol (LDL-C) 150 mg/dL, high-density lipoprotein cholesterol (HDL-C) 75 mg/dL, and a 10-year Framingham risk of 12% referred for CAC scanning; CAC score was 1,872, in the >99th percentile. Slices from base (**a**) through apex (**d**) reveal significant CAC in all coronary arteries and the ascending aorta. *Ao* aorta; *LAD* left anterior descending coronary artery; *LADD* diagonal branch of left anterior descending coronary artery; *LCx* left circumflex coronary artery; *PDA* posterior descending branch of right coronary artery; *RCA* right coronary artery.

the same excellent prognosis as patients without diabetes; it is reasonable to treat those with 0 CAC scores less aggressively than would be dictated as a CAD risk equivalent.

At the same time, diabetic patients have CAC scores corresponding to older people [93, 94] and have a worse prognosis than those without diabetes and similar CAC scores [92], and should be treated more aggressively.

Evaluation of Therapy

The use of serial CAC scanning to evaluate the progression of disease and the effects of therapy will be covered in great detail in Chap. 5. For this purpose, patients with established CAD who would not ordinarily be candidates for CAC scanning may undergo evaluation as a baseline for future examinations. This may include patients who have had stent placement; the stented area must be excluded from the scoring. In Figure 4.18, the patient underwent stent placement in the right coronary artery. Calcified plaque was noted in the left main and LAD coronary arteries. The non-stented areas are suitable for tracking plaque progression.

Patients with coronary artery bypass grafting are not good candidates for CAC scanning; the profusion of surgical clips makes scoring difficult, and the importance of plaque progression in bypassed areas is unknown.

Stress Testing

The importance of the relationship of CAC scanning to stress testing has decreased with the growth of CCTA, which has developed as an alternative, and even as a preferential choice to stress testing [95]. While CAC scanning is almost always reserved for patients without symptoms, it has been employed following stress tests in equivocal

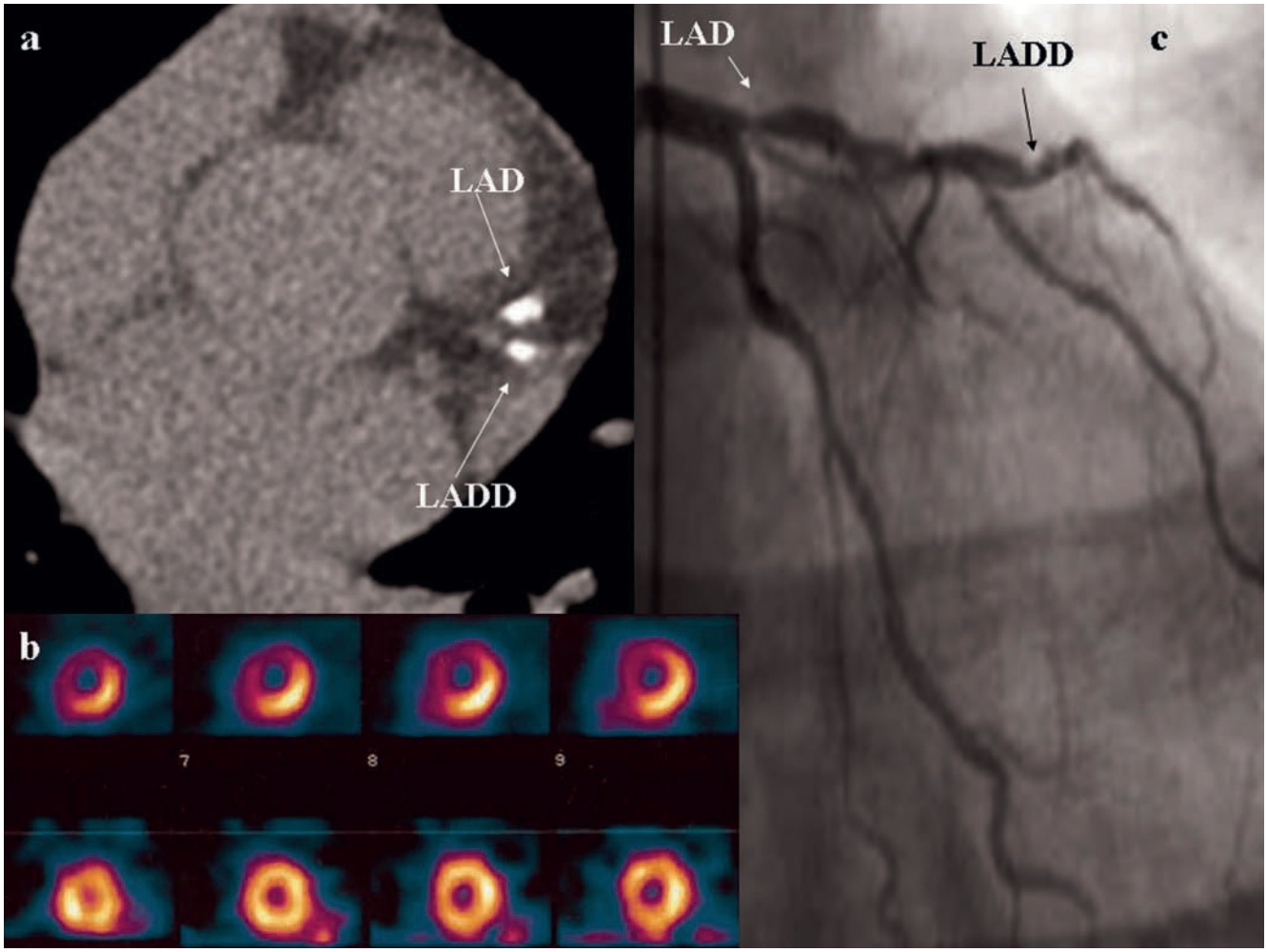

Figure 4.15. A 41-year-old woman with a premature family history of coronary artery disease (CAD), total cholesterol 188 mg/dL, LDL-C 112 mg/dL, HDL-C 50 mg/dL, and triglycerides 132 mg/dL, in the lowest Framingham risk group. (**a**) CAC score of 110, in the LAD and diagonal branch, in the >99th percentile. (**b**) Dual isotope nuclear stress testing revealing severe anteroseptal ischemia. (**c**) Angiography demonstrating 95% ostial LAD stenosis and severe LADD disease. *LAD* left anterior descending coronary artery; *LADD* diagonal branch of left anterior descending coronary artery.

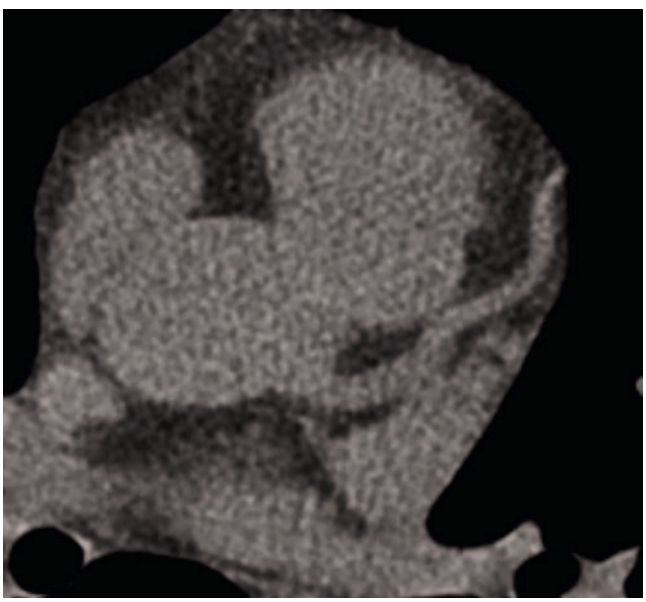

Figure 4.16. A 65-year-old male hypertensive smoker, LDL-C of 140 mg/dL and a 10-year Framingham risk of 25%. CAC scan demonstrated total absence of calcified plaque.

situations to determine the need for invasive evaluation, irrespective of the symptomatic status. In a series of 118 patients, the absence of coronary calcium accurately identified those with a false-positive treadmill test with a negative predictive value of 90% [96], suggesting that CAC may be useful to enhance the accuracy of abnormal stress tests in patients with a low clinical suspicion of obstructive disease, prior to recommending angiography. In 323 primary prevention patients referred for angiography who underwent electrocardiographic stress testing and calcified plaque imaging, Schmermund et al reported that CAC significantly improved angiographic classification of patients with an equivocal or normal stress evaluation, but not of those with abnormal tests [97]. Figure 4.19 displays the CAC scan of a 51-year-old male smoker with atypical chest pain, obtained after an equivocal nuclear stress test. Extensive plaque and aneurysmal dilatation were demonstrated in both the LAD and right coronary arteries. Subsequent coronary arteriography confirmed the coronary aneurysms and revealed critical LAD stenosis and thrombus.

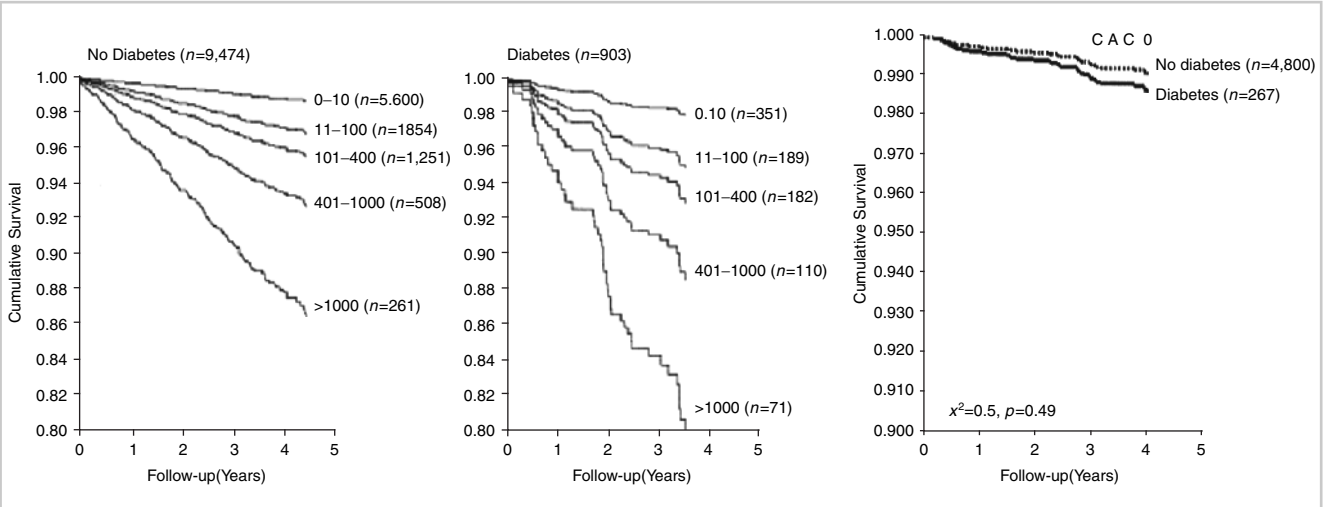

Figure 4.17. Cumulative survival in nondiabetic (*left*) and diabetics (*center*) in relation to CAC score, and in diabetics and nondiabetics with 0 CAC scores (*right*) (reproduced with permission of Elsevier from Raggi et al [93], p. 1663).

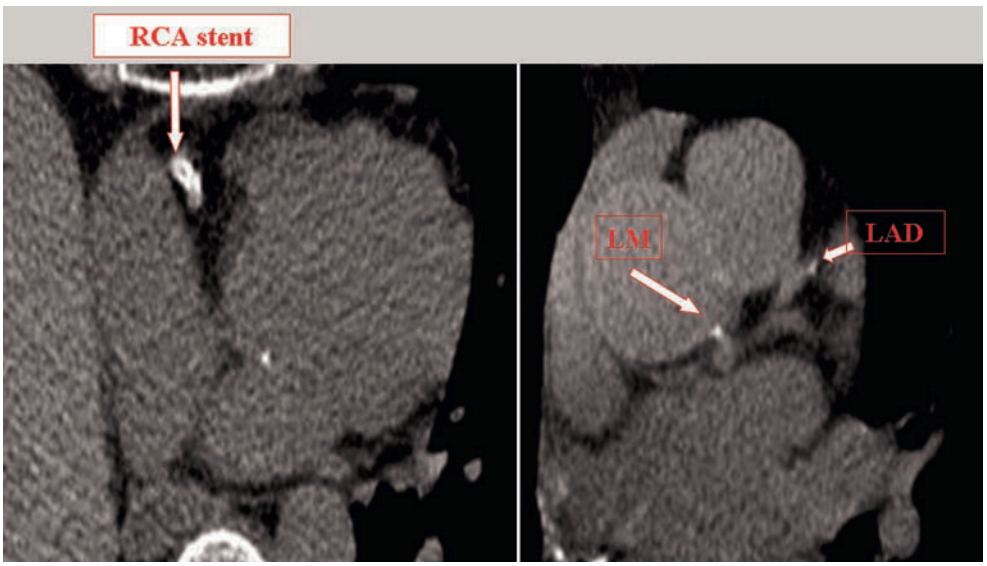

Figure 4.18. CAC scan demonstrating a stent in the right coronary artery (RCA) and calcified plaque in the LM and LAD. *LM* left main coronary artery; *LAD* left anterior descending coronary artery.

Cardiomyopathy

CAC may be used to differentiate ischemic from nonischemic cardiomyopathies. Budoff et al. [98] demonstrated in 120 patients with heart failure of unknown etiology that the presence of CAC was associated with a 99% sensitivity for ischemic cardiomyopathy.

Emergency Department Chest Pain Evaluation

Emergency department triage of chest pain patients by CAC has been totally supplanted by CCTA. Several early studies demonstrated potential application of CAC to the ED. Laudon et al [99] reported on 105 patients. Of the 46 with positive scores (>0), 14 had abnormal follow-up inpatient testing. Of the 59 with 0 calcium scores, stress evaluation and/or coronary arteriography were normal in the 54 who underwent further testing and all were free of cardiac events 4 months later (100% negative predictive value). Georgiou et al. [100] noted 41 cardiac events in 192 emergency room patients followed for 37 months; all but four were associated with calcium scores ≥4. However, CCTA data have clearly demonstrated a small (5%) but finite incidence of obstructive disease in 0 CAC patients with chest pain [101], mandating performance of CCTA rather than CAC alone in this setting.

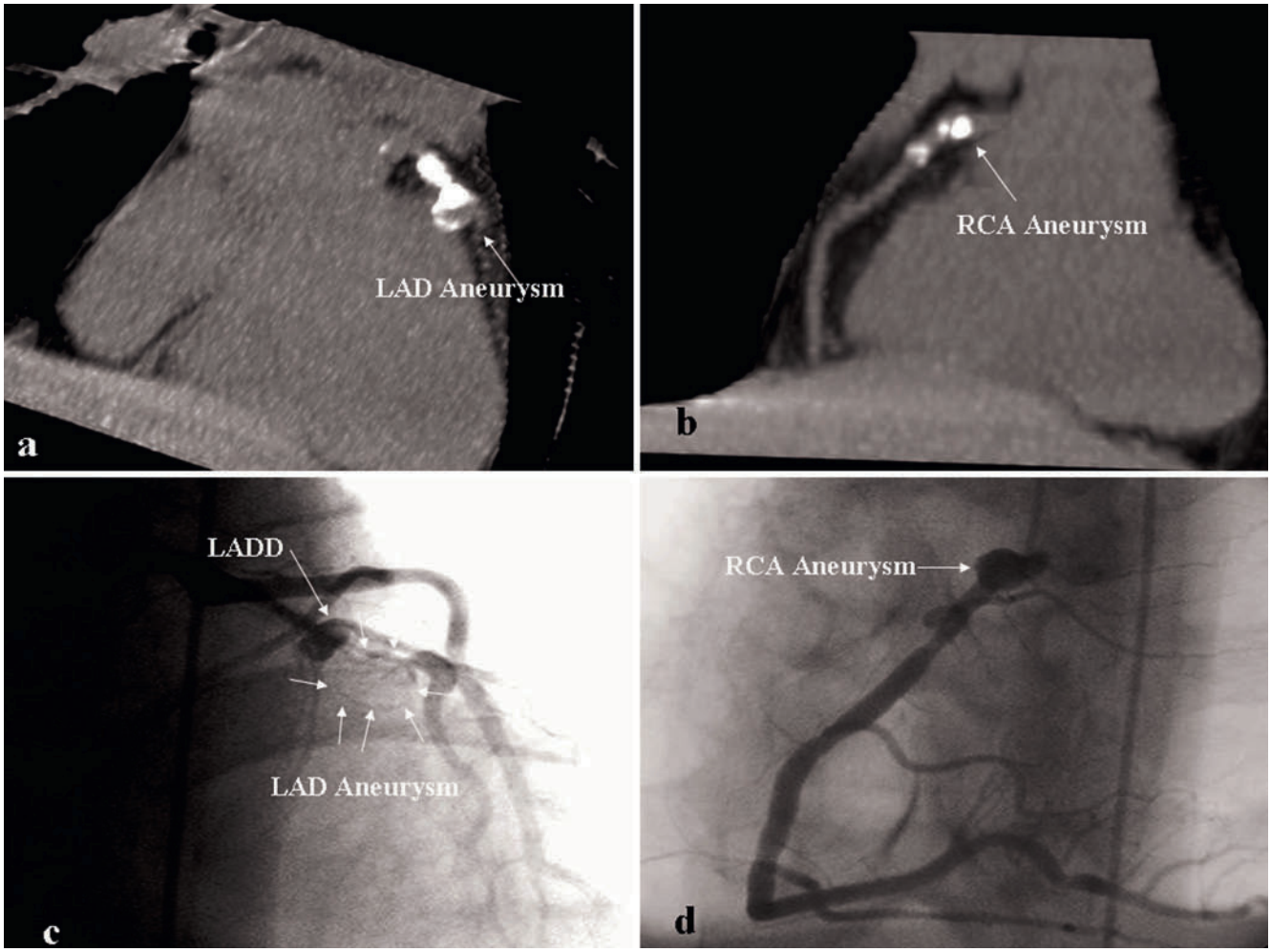

Figure 4.19. CAC imaging in a 51-year-old male smoker with atypical chest pain, post equivocal nuclear stress test. Extensive plaque and aneurysmal dilatation were demonstrated in both the LAD (**a**) and RCA (**b**). Subsequent coronary arteriography confirmed the coronary aneurysms (**c** and **d**) and revealed critical LAD stenosis and thrombus. *LAD* left anterior descending coronary artery; *LADD* diagonal branch of left anterior descending coronary artery; *RCA* right coronary artery.

Conclusions

The validation of CAC scanning as a risk assessment tool may well represent one of the most significant advances in the history of preventive medicine. It offers the possibility of accurately identifying the vast majority of patients destined to suffer acute cardiac events, and, in so doing, should allow for substantial reduction of cardiovascular mortality and morbidity by increasingly effective pharmacologic and lifestyle therapy of the underlying disease process. The sole remaining obstacle to widespread implementation:

> … is a double standard that demands randomized controlled (outcome) trials for CAC screening while ignoring their necessity for every other technology…. It is incumbent on the cardiology community to temper the inflexible need for randomized trials with the reality of 565,000 patients presenting with myocardial infarctions annually as their first symptoms, 95% of whom could be identified as at high risk by CAC screening and aggressively treated to significantly reduce events [102].

It is appropriate to conclude by quoting Dr. Scott Grundy [103]:

> The power of imaging for detecting subclinical atherosclerosis to predict future ASCVD events is increasingly being recognized. Imaging has at least three virtues. It individualizes risk assessment beyond use of age, which is a less reliable surrogate for atherosclerosis burden; it provides an integrated assessment of the lifetime exposure to risk factors; and it identifies individuals who are susceptible to developing atherosclerosis beyond established risk factors. Also of importance, in the absence of detectable atherosclerosis, short-term risk appears to be very low. Thus, for primary prevention, a recommendation could be established that detection of significant plaque burden is a preferred strategy for initiation of LDL-lowering drugs. With such

a recommendation, major risk factors and emerging risk factors could be used as a guide for selecting subjects for imaging more than as a primary guide for therapy. Once subclinical atherosclerosis is detected, intensity of drug therapy could be adjusted for plaque burden. This 2-step approach to risk assessment could provide a solution to the dilemma of patient selection for cholesterol-lowering drugs in primary prevention. In addition, it could be applied to all population subgroups. It could also be useful as a guide to low-dose aspirin prophylaxis and cholesterol-lowering therapy.

References

1. American Heart Association. *Heart and Stoke Statistical Update*. Dallas, TX: American Heart Association; 2001.
2. Blankenhorn DH, Stern D. Calcification of the coronary arteries. *Am J Roentgenol*. 1959;81:772–777.
3. Frink RJ, Achor RWP, Brown AL, et al. Significance of calcification of the coronary arteries. *Am J Cardiol*. 1970;26:241–247.
4. Wexler L, Brundage B, Crouse J, et al. Coronary artery calcification: pathophysiology, epidemiology, image methods and clinical implications. A scientific statement from the American Heart Association. *Circulation*. 1996;94:1175–1192.
5. Faber A. Die Arteriosklerose, from Pathologische Anatomie, from Pathogenese Und Actiologie. In: G. Fischer, ed; 1912.
6. Bostrom K, Watson KE, Horn S, et al. Bone morphogenetic protein expression in human atherosclerotic lesions. *J Clin Invest*. 1993;91:1800–1809.
7. Ideda T, Shirasawa T, Esaki Y, et al. Osteopontin mRNA is expressed by smooth muscle-derived foam cells in human atherosclerotic lesions of the aorta. *J Clin Invest*. 1993;92:2814–2820.
8. Hirota S, Imakita M, Kohri K, et al. Expression of osteopontin messenger RNA by macrophages in atherosclerotic plaques. A possible association with calcification. *Am J Pathol*. 1993;143:1003–1008.
9. Shanahan CM, Cary NR, Metcalfe JC, Weissberg PL. High expression of genes for calcification-regulating proteins in human atherosclerotic plaque. *J Clin Invest*. 1994;93:2393–2402.
10. Rumberger JA, Simons DB, Fitzpatrick LA, et al. Coronary artery calcium areas by electron beam computed tomography and coronary atherosclerotic plaque area: a histopathologic correlative study. *Circulation*. 1995;92:2157–2162.
11. Baumgart D, Schmermund A, Goerge G, et al. Comparison of electron beam computed tomography with intracoronary ultrasound and coronary angiography for detection of coronary atherosclerosis. *J Am Coll Cardiol*. 1997;30:57–64.
12. Schmermund A, Baumgart D, Gorge G, et al. Coronary artery calcium in acute coronary syndromes: a comparative study of electron beam CT, coronary angiography, and intracoronary ultrasound in survivors of acute myocardial infarction and unstable angina. *Circulation*. 1997;96:1461–1469.
13. Agatston AS, Janowitz WR, Hildner FJ, et al. Quantification of coronary artery calcium using ultrafast computed tomography. *J Am Coll Cardiol*. 1990;15:827–832.
14. Callister TQ, Cooil B, Raya SP, et al. Coronary artery disease: improved reproducibility of calcium scoring with an electron-beam CT volumetric method. *Radiology*. 1998;208:807–814.
15. Becker CR, Kleffel T, Crispin A, et al. Coronary artery calcium measurement. Agreement of multirow detector and electron beam CT. *Am J Roentgenol*. 2001;176:1295–1298.
16. Janowitz WR, Agatston AS, Kaplan G, Viamonte M. Differences in prevalence and extent of coronary artery calcium detected by ultrafast computed tomography in asymptomatic men and women. *Am J Cardiol*. 1993;72:247–254.
17. Hoff JA, Chomka EV, Krainik AJ, et al. Age and gender distributions of coronary artery calcium detected by electron beam tomography in 35,246 adults. *Am J Cardiol*. 2001;87:1335–1339.
18. Budoff MJ, Yang TP, Shavelle RM. Ethnic differences in coronary atherosclerosis. *J Am Coll Cardiol*. 2002;39:408–412.
19. Newman AB, Naydeck BL, Whittle J, et al. Racial differences in coronary artery calcification in adults. *Arterioscler Thromb Vasc Biol*. 2002;22:424–430.
20. Khuran C, Rosenbaum CG, Howard BV, et al. Coronary artery calcification in black women and white women. *Am Heart J*. 2003;145:724–729.
21. Jain T, Peshock R, Darren K, et al. African Americans and Caucasians have a similar prevalence of coronary calcium in the Dallas Heart Study. *J Am Coll Cardiol*. 2004;44:1011–1017.
22. McClelland RL, Chung H, Detrano R, et al. Distribution of coronary artery calcium by race, gender, and age. Results from the Multi-Ethnic Study of Atherosclerosis (MESA). *Circulation*. 2006;113:30–37.
23. Detrano R, Guerci AD, Carr JJ, et al. Coronary calcium as a predictor of coronary events in four racial or ethnic groups. *N Engl J Med*. 2008;358:1336–1345.
24. Nasir K, Michos ED, Rumberger JA, et al. Coronary artery calcification and family history of premature coronary heart disease: sibling history is more strongly associated than parental history. *Circulation*. 2004;110:2150–2156.
25. Khurram Nasir K, Budoff MJ, Wong ND, et al. Family history of premature coronary heart disease and coronary artery calcification. Multi-Ethnic Study of Atherosclerosis (MESA). *Circulation*. 2007;116:619–662.
26. Gerber TC, Carr JJ, Arai AE, et al. Ionizing radiation in cardiac imaging. A Science Advisory From the American Heart Association Committee on Cardiac Imaging of the Council on Clinical Cardiology and Committee on Cardiovascular Imaging and Intervention of the Council on Cardiovascular Radiology and Intervention. *Circulation*. 2009; 119:1056–1065.
27. O'Rourke RA, Brundage BH, Froelicher VF, et al. American College of Cardiology/American Heart Association expert consensus document on electron beam computed tomography for the diagnosis and prognosis of coronary artery disease. *Circulation*. 2000;102:126–140.
28. Simons DB, Schwartz RS, Edwards WD, et al. Noninvasive definition of anatomic coronary disease by ultrafast computed tomographic scanning: a quantitative pathologic comparison study. *J Am Coll Cardiol*. 1992;20:1118–1126.
29. Detrano R, Tang W, Kang X, et al. Accurate coronary calcium phosphate mass measurements from electron beam computed tomograms. *Am J Card Imaging*. 1995;9:167–173.
30. Mautner GC, Mautner SL, Froelich J, et al. Coronary artery calcification: assessment with electron beam CT and histomorphometric correlation. *Radiology*. 1994;192:619–623.
31. Budoff MJ, Georgiou D, Brody A, et al. Ultrafast computed tomography as a diagnostic modality in the detection of coronary artery disease-a multicenter study. *Circulation*. 1996;93:898–904.
32. Guerci AD, Spadaro LA, Popma JJ, et al. Electron beam tomography of the coronary arteries: relationship of coronary calcium score to arteriographic findings in asymptomatic and symptomatic adults. *Am J Cardiol*. 1997;79:128–133.
33. Shavelle DM, Budoff MJ, LaMont DH, et al. Exercise testing and electron beam computed tomography in the evaluation of coronary artery disease. *J Am Coll Cardiol*. 2000;36:32–38.
34. Bielak LF, Rumberger JA, Sheedy PF, et al. Probabilistic model for prediction of agiographically defined obstructive coronary artery disease using electron beam computed tomography calcium score strata. *Circulation*. 2000;102:380–385.
35. Rumberger JA, Sheedy PF, Breen FJ, et al. Electron beam CT coronary calcium score cutpoints and severity of associated angiography luminal stenosis. *J Am Coll Cardiol*. 1997;29:1542–1548.
36. Haberl R, Becker A, Leber A, et al. Correlation of coronary calcification and angiographically documented stenoses in patients with suspected coronary artery disease: results of 1,764 patients. *J Am Coll Cardiol*. 2001;37:451–457.

37. Budoff MJ, Raggi P, Berman D, et al. Continuous probabilistic prediction of angiographically significant coronary artery disease using electron beam tomography. *Circulation*. 2002;105(15):1791–1796.
38. Sarwar A, Shaw LJ, Shapiro MD, et al. Diagnostic and prognostic value of absence of coronary artery calcification. *JACC Cardiovasc Imaging*. 2009;2:675–688.
39. Mohlenkamp S, Lehmann N, Schmermund A, et al. Prognostic value of extensive coronary calcium quantities in symptomatic males – a 5-year follow-up study. *Eur Heart J*. 2003;24:845–854.
40. Raggi P, Callister TQ, Cooil B, et al. Identification of patients at increased risk of first unheralded acute myocardial infarction by electron beam computed tomography. *Circulation*. 2000;101:850–855.
41. Wong ND, Hsu JC, Detrano RC, et al. Coronary artery calcium evaluation by electron beam compute tomography and its relation to new cardiovascular events. *Am J Cardiol*. 2000;86:495–498.
42. Arad Y, Spadaro LA, Goodman K, et al. Prediction of coronary events with electron beam computed tomography. *J Am Coll Cardiol*. 2000; 36:1253–1260.
43. Kondos GT, Hoff JA, Sevrukov A, et al. Electron-beam tomography coronary artery calcium and cardiac events: a 37-month follow-up of 5,635 initially asymptomatic low to intermediate risk adults. *Circulation*. 2003;107:2571–2576.
44. Shaw LJ, Raggi P, Schisterman E, et al. Prognostic value of cardiac risk factors and coronary artery calcium screening for all-cause mortality. *Radiology*. 2003;28:826–833.
45. Greenland P, LaBree L, Azen SP, et al. Coronary artery calcium score combined with Framingham score for risk prediction in asymptomatic individuals. *JAMA*. 2004;291:210–215.
46. Arad Y, Goodman KJ, Roth M, et al. Coronary calcification, coronary risk factors, and atherosclerotic cardiovascular disease events. The St Francis Heart Study. *J Am Coll Cardiol*. 2005;46(1):158–165.
47. Wayhs R, Zelinger A, Raggi P. High coronary artery calcium scores pose an extremely elevated risk for hard events. *J Am Coll Cardiol*. 2002;39:225–230.
48. Taylor AJ, Bindeman J, Feuerstein I, et al. Coronary calcium independently predicts incident premature coronary heart disease over measured cardiovascular risk factors mean three-year outcomes in the prospective army C\coronary C\calcium (PACC) project. *J Am Coll Cardiol*. 2005;46:807–814.
49. Vliegenthart R, Oudkerk M, Song B, et al. Coronary calcification detected by electron-beam computed tomography and myocardial infarction. The Rotterdam Coronary Calcification Study. *Eur Heart J*. 2002;23:1596–1603.
50. Budoff MJ, Shaw LJ, Liu ST, et al. Long-term prognosis associated with coronary calcification. Observations from a registry of 25,253 patients. *J Am Coll Cardiol*. 2007;49:1860–1870.
51. Becker A, Leber A, Becker C, Knez A. Predictive value of coronary calcifications for future cardiac events in asymptomatic individuals. *Am Heart J*. 2008;155:154–160.
52. Folsom AR, Kronmal RA, Detrano RC, et al. Coronary artery calcification compared with carotid intima-media thickness in the prediction of cardiovascular disease incidence the multi-ethnic study of atherosclerosis (MESA). *Arch Intern Med*. 2008;168:1333–1339.
53. Lakoski SG, Greenland P, Wong ND, et al. Coronary artery calcium scores and risk for cardiovascular events in women classified as "Low Risk" based on Framingham risk score. The Multi-Ethnic Study of Atherosclerosis (MESA). *Arch Intern Med*. 2007;167(22):2437–2442.
54. Blaha M, Budoff MJ, Shaw LJ, et al. Absence of coronary artery calcification and all-cause mortality. *JACC Cardiovasc Imaging*. 2009; 2:692–700.
55. Erbel R, Möhlenkamp S, Moebus S, et al. Coronary Risk Stratification, Discrimination, and Reclassification Improvement Based on Quantification of Subclinical Coronary Atherosclerosis. *J Am Coll Cardiol*. 2010. In press.
56. Budoff MJ, Ehrlich J, Hecht HS, Rumberger JR. Letter to the editor. *JAMA*. 2004;291:1822.
57. Mascola A, Ko J, Bakhsheshi H, et al. Electron beam tomography comparison of culprit and non-culprit coronary arteries in patients with acute myocardial infarction. *Am J Cardiol*. 2000;85:1357–1359.
58. Pohle K, Ropers D, Mäffert R, et al. Coronary calcifications in young patients with first, unheralded myocardial infarction: a risk factor matched analysis by electron beam tomography. *Heart*. 2003; 89:625–628.
59. O'Malley PG, Feuerstein IM, Taylor AJ. Impact of electron beam tomography, with or without case management, on motivation, behavioral change, and cardiovascular risk profile: a randomized controlled trial. *JAMA*. 2003;289:2215–2223.
60. Kalia NK, Miller LG, Nasir K, et al. Visualizing coronary calcium is associated with improvements in adherence to statin therapy. *Atherosclerosis*. 2006;185:394–399.
61. Orakzai RH, Nasir K, Orakzai SH, et al. Effect of patient visualization of coronary calcium by electron beam computed tomography on changes in beneficial lifestyle behaviors. *Am J Cardiol*. 2008;101:999–1002.
62. Taylor AJ, Bindeman J, Feuerstein I, et al. Community-based provision of statin and aspirin after the detection of coronary artery calcium within a community-based screening cohort. *J Am Coll Cardiol*. 2008;51:1337–1341.
63. Smith SC, Greenland P, Grundy SM. Prevention Conference V: beyond secondary prevention: identifying the high-risk patient for primary prevention. Executive summary. *Circulation*. 2000;101:111–116.
64. *Third Report of the National Cholesterol Education Program (NCEP) Expert Panel on Detection, Evaluation, and Treatment of High Blood Cholesterol in Adults (Adult Treatment Panel III). Final Report*. NIH Publication No. 02–5215; September 2002.
65. De Backer G, Ambrosioni E, Borch-Johnson K, et al. European guidelines on cardiovascular disease prevention in clinical practice. Third joint task force of European and other societies in cardiovascular disease prevention in clinical practice. *Eur J Cardiovasc Prev Rehabil*. 2003;10(suppl 1):S1–S10.
66. Mosca L, Appel LJ, Benjamin EJ, et al.; Expert Panel/Writing Group. Evidence-based guidelines for cardiovascular disease prevention in women. *Circulation*. 2004;109:672–693.
67. Naghavi M, Falk E, Hecht HS, et al. From vulnerable plaque to vulnerable patient – part III: executive summary of the Screening for Heart Attack Prevention and Education (SHAPE) Task Force Report. *Am J Cardiol*. 2006;98(suppl):2H–15H.
68. Greenland P, Bonow RO, Brundage BH, et al. ACCF/AHA 2007 clinical expert consensus document on coronary artery calcium scoring by computed tomography in global cardiovascular risk assessment and in evaluation of patients with chest pain: a report of the American College of Cardiology Clinical Expert Consensus Task Force (ACCF/AHA Writing Committee to Update the 2000 Expert Consensus Document on Electron Beam Computed Tomography). *Circulation*. 2007;115:402–426.
69. Kuller LH, Matthews KA, Sutton-Tyrrell K, et al. Coronary and aortic calcification among women 8 years after menopause and their premenopausal risk factors: The Healthy Women Study. *Arterioscler Thromb Vasc Biol*. 1999;19:2189–2198.
70. Hecht HS, Superko HR, Smith LK, et al. Relation of coronary artery calcium identified by electron beam tomography to serum lipoprotein levels and implications for treatment. *Am J Cardiol*. 2001; 87:406–412.
71. Daviglus ML, Pirzada A, Liu K, et al. Comparison of low risk and higher risk profiles in middle age to frequency and quantity of coronary artery calcium years later. *Am J Cardiol*. 2004;94:367–369.
72. Hecht HS, Superko HR. Electron beam tomography and national cholesterol education program guidelines in asymptomatic women. *J Am Coll Cardiol*. 2001;37:1506–1511.
73. Taylor AJ, Feuerstein I, Wong H, et al. Do conventional risk factors predict subclinical coronary artery disease? Results from the Prospective Army Coronary Calcium Project. *Am Heart J*. 2001; 141:463–468.

74. Superko HR, Hecht HS. Metabolic disorders contribute to subclinical coronary atherosclerosis in patients with coronary calcification. *Am J Cardiol*. 2001;88:260–264.
75. Hecht HS. "Interventional lipidology": tomographic plaque imaging and aggressive treatment of metabolic disorders. *Am J Cardiol*. 2002;90:268–270.
76. Ridker PM, Wilson PW, Grundy SM. Should C-reactive protein be added to metabolic syndrome and to assessment of global cardiovascular risk? *Circulation*. 2004;109:2818–2825.
77. Park R, Detrano R, Xiang M, et al. Combined use of computed tomography coronary calcium scores and C-reactive protein levels in predicting cardiovascular events in nondiabetic individuals. *Circulation*. 2002;106:2073–2077.
78. Wang TJ, Larson MG, Levy D, et al. Epicardial coronary calcification in men and women. The Framingham Heart Study. *Circulation*. 2002;106:1189–1191.
79. Reilly MP, Wolfe ML, Localio AR, Rader DJ. C-reactive protein and coronary artery calcification: The Study of Inherited Risk of Coronary Atherosclerosis (SIRCA). *Arterioscler Thromb Vasc Biol*. 2003; 23:1851–1856.
80. Arad Y, Spadaro LA, Roth M, et al. Treatment of asymptomatic adults with elevated coronary calcium scores with atorvastatin, vitamin C, and vitamin E: The St Francis Heart Study randomized clinical trial. *J Am Coll Cardiol*. 2005;46(1):166–172.
81. Khera A, de Lemos JA, Peshock RM, et al. Relationship between C-reactive protein and subclinical atherosclerosis. The Dallas Heart Study. *Circulation*. 2006;113:38–43.
82. Iribarren C, Gross MD, Darbinian JA, et al. Association of lipoprotein-associated phospholipase A2 mass and activity with calcified coronary plaque in young adults. The CARDIA study. *Arterioscler Thromb Vasc Biol*. 2005;25:216–221.
83. O'Donnell CJ, Chazaro I, Wilson PWF, et al. Evidence for heritability of abdominal aortic calcific deposits in the Framingham Heart Study. *Circulation*. 2002;106:337–341.
84. Peyser PA, Bielak LF, Chu J, et al. Heritability of coronary artery calcium quantity measured by electron beam computed tomography in asymptomatic adults. *Circulation*. 2002;106:304–308.
85. Hecht HS. Risk factors revisited. *Am J Cardiol*. 2003;93:73–75.
86. Hecht HS, Budoff M, Ehrlich J, Rumberger J. Coronary artery calcium scanning: clinical recommendations for cardiac risk assessment and treatment. *Am Heart J*. 2006;151:1139–1146.
87. Wilson PWF, D'Agostino B, Levy D, et al. Prediction of coronary heart disease using risk factor categories. *Circulation*. 1998; 97:1837–1847.
88. Grundy SM, Cleeman JI, Merz CNB, et al. Implications of recent clinical trials for the National Cholesterol Education Program Adult Treatment Panel III guidelines. *Circulation*. 2004;110:227–239.
89. Akosah K, Schaper A, Cogbill C, Schoenfeld P. Preventing myocardial infarction in the young adult in the first place: how do the National Cholesterol Education Panel III guidelines perform? *J Am Coll Cardiol*. 2003;41:1475–1479.
90. Heart Protection Study Collaborative Group. MRC/BHF Heart Protection Study of cholesterol lowering with simvastatin in 20 536 high-risk individuals: a randomised placebo-controlled trial. *Lancet*. 2002;360:7–22.
91. Expert Panel on Detection, Evaluation, and Treatment of High Blood Cholesterol in Adults. Executive Summary of the Third Report of The National Cholesterol Education Program (NCEP) (Adult Treatment Panel III). *JAMA*. 2001;285:2486–2497.
92. Raggi P, Shaw LJ, Berman DS, Callister TQ. Prognostic value of coronary artery calcium screening in subjects with and without diabetes. *J Am Coll Cardiol*. 2004;43:1663–1669.
93. Kuller LH, Velentgas P, Barzilay J, et al. Diabetes mellitus, subclinical cardiovascular disease and risk of incident cardiovascular disease and all-cause mortality. *Arterioscler Thromb Vasc Biol*. 2000; 20:823–829.
94. Hoff JA, Quinn L, Sevrukov A, et al. The prevalence of coronary artery calcium among diabetic individuals without known coronary artery disease. *J Am Coll Cardiol*. 2003;41:1008–1012.
95. Hecht HS. A paradigm shift: coronary computed tomographic angiography before stress testing. *Am J Cardiol*. 2009;104(4):613–618.
96. LaMont DH, Budoff MJ, Shavelle DM, et al. Coronary calcium screening identifies patients with false positive stress tests [abstract]. *Circulation*. 1997;96:306–I.
97. Schmermund A, Baumgart D, Sack S, et al. Assessment of coronary calcification by electron-beam computed tomography in symptomatic patients with normal, abnormal or equivocal exercise stress test. *Eur Heart J*. 2000;21:1674–1682.
98. Budoff MJ, Shavelle DM, Lamont DH, et al. Usefulness of electron beam computed tomography scanning for distinguishing ischemic from non-ischemic cardiomyopathy. *J Am Coll Cardiol*. 1998;32:1173–1178.
99. Laudon DA, Vukov LF, Breen JF, et al. Use of electron-beam computed tomography in the evaluation of chest pain patients in the emergency department. *Ann Emerg Med*. 1999;33:15–21.
100. Georgiou D, Budoff MJ, Kaufer E, et al. Screening patients with chest pain in the emergency department using electron beam tomography: a follow-up study. *J Am Coll Cardiol*. 2001;38:105–110.
101. Rosen BD, Fernandes V, McClelland RL, et al. The prevalence of flow limiting stenoses in coronary arteries with previously documented zero calcium score: The Multi-Ethnic Study of Atherosclerosis (MESA). *J Am Coll Cardiol Img*. 2009;2:1175–1183.
102. Hecht HS. The deadly double standard: the saga of screening for subclinical atherosclerosis. *Am J Cardiol*. 2008;101:1085–1087.
103. Grundy SM. Is lowering low-density lipoprotein an effective strategy to reduce cardiac risk? Promise of low-density lipoprotein–lowering therapy for primary and secondary prevention. *Circulation*. 2008; 117:569–573.
104. Hecht HS. Translating tomographic plaque imaging into treatment: interventional lipidology. *Prog Cardiovasc Dis*. 2003;46(2):149–170.

5

Natural History and Impact of Interventions on Coronary Calcium

Paolo Raggi

Introduction

Coronary artery calcium (CAC) has long been known to be associated with atherosclerotic plaque development. Similarly, aortic valve degeneration and calcification appear to follow a pathophysiologic process very similar to atherosclerosis. Noninvasive imaging technologies such as electron beam tomography (EBT) and multi-detector computer tomography (MDCT) scanners allow the accurate detection and quantification of cardiovascular calcification, offering an opportunity to monitor progression of disease. It has recently become apparent that continued progression of CAC is associated with an increased risk of myocardial infarction and cardiac death, suggesting that there might be some utility for sequential imaging. Therefore, researchers have investigated the utilization of cardiac CT imaging to follow the progression of cardiovascular calcification in a variety of clinical settings. In this chapter, a review of the studies published to date on the use of CT technology to follow progression of CAC is presented.

Animal Studies of Plaque Calcification Development and Regression

In Western societies, changes in the arterial walls begin very early in life. Necropsy data from 2,876 subjects between the ages of 15 and 34 revealed intimal lesions in the aortas of all patients, and more than half of the right coronary arteries of the youngest age group (15–19-year old) showed increasing prevalence and extent of disease with advancing age [1]. Though CAC has long been known to be associated with atherosclerosis, it was only recently suggested that plaque calcification may be dependent upon an active process of mineralization resembling bone formation [2–5]. Several enzymes necessary for the assembly of normal bone have been found in the context of human atherosclerotic plaques [2–4], and cells normally found in the vessel wall, such as smooth muscle cells and macrophages, can transform in osteoblast-like cells with bone-generating potential [5]. As a result, in advanced stages of atherosclerotic disease, true ossification can be observed in pathological specimen. It is currently unknown if arterial calcification is a part of the ongoing inflammatory phenomena at the level of the plaque or an attempt at repairing the damage brought to the vascular wall by noxious stimuli. Indeed, some investigators have suggested that calcium deposition simply results from recurrent intralesional hemorrhage and thrombosis [6]. Nonetheless, as the process of calcification of a plaque appears to be dependent upon active phenomena of mineralization, it is plausible that formation and degradation of calcium deposits may be an ongoing dynamic phenomenon in the atherosclerotic plaque like in bone tissue, and that these processes may be activated or inhibited by external interventions. Several investigators conducted animal studies of atherosclerosis regression to analyze the morphological plaque changes induced by various treatments. In one such experiment, 59 Rhesus monkeys were fed a high cholesterol diet for several years and then exposed to a cholesterol restricted diet [7]. Animals were sacrificed at different times during the experimental period and findings revealed development of typical plaques with a lipid rich core and scattered calcific granules. As plaques expanded, more extensive calcific deposits became visible. However, after exposing the animals to 3 years of a severely cholesterol restricted diet, the plaques became more fibrotic, with a lower cholesterol content and, although the calcium did not disappear, its burden did not increase either [7].

In another experiment, Williams et al. [8] used a monkey model of atherosclerosis to study the effect of medical therapy in addition to diet on atherosclerosis progression and regression. Thirty-two adult (7–10 years of age) male cynomolgus monkeys were fed an atherogenic diet containing 0.61 mg of cholesterol per kilocalorie of diet for 2 years (progression phase). The monkeys were divided into two well-balanced groups as far as the baseline lipid levels were concerned. During the subsequent 2-year treatment

phase, a low cholesterol diet (0.11 mg of cholesterol per kilocalorie of diet) was begun. Additionally, 14 monkeys received pravastatin (20 mg/kg body weight per day), and the diet of the other 18 was adjusted over time to maintain equal plasma LDL levels between treatment groups. At the end of the treatment phase the total, low density and high-density lipoprotein cholesterol levels were similar in the two animal groups. However, histological analysis of the coronary, carotid, and iliac arteries revealed important differences between treatment groups. While the lumen area was not different, pravastatin treated animals showed a reduction in intimal neovascularization, plaque macrophage infiltration and a decrease in calcification of early as well as advanced plaques. These findings suggested that statins might benefit the arterial wall in more ways than just lowering serum lipoprotein levels.

Unlike the above investigators, Daoud et al. [9] and Clarkson et al. [10] did not find any reduction in atherosclerotic plaque calcium deposition with intervention in experiments conducted in swine and monkeys, respectively. Hence, although attractive, the histological proof that cardiovascular calcification may regress remains a matter of debate at this time.

Technical Considerations

CAC can be accurately detected by EBT and MDCT, but it usually becomes visible in the intermediate to late stages of development of an atherosclerotic plaque. The degree of calcification is assessed by means of quantitative calcium scores. Agatston et al. [11] developed a scoring system that correlates well with the underlying atherosclerotic plaque burden [12] and has been widely used in research and clinical trials. This score is a unitless number derived from the multiplication of the area of a calcified plaque by an arbitrarily chosen density coefficient rated 1–4. This scoring method was initially shown to have a limited interscan reproducibility, especially when used with the older CT technologies, and new scoring methods were therefore introduced for the performance of sequential studies [13–15]. The calcium volume score is derived using an isotropic interpolation principle and it represents a direct measurement of the volume of calcium in an atherosclerotic plaque (measured in picoliters). This score, found to be substantially more reproducible than the Agatston method [13], takes into consideration the likely pathophysiologic changes that occur in a plaque undergoing healing. In fact, it is conceivable that volumetric contraction and increase in density due to the loss of soft-core contents in the plaque would cause an increase in the Agatston score (dependent on density) rather than a decrease. More recently, a third type of score has been introduced, the mass score [14, 15]. Though reportedly more reliable and reproducible than the other scores, to date this measurement has not yet been employed in sequential studies of atherosclerosis.

Effect of Statins on Progression of Coronary Artery Calcium

Human studies of atherosclerosis progression and regression have mainly been conducted by means of quantitative coronary angiography [16, 17] and only recently with sequential measurements of coronary artery calcification and carotid artery intimal medial thickness [17–22]. The cardiovascular event reduction associated with luminal stenosis improvements seen on quantitative angiography far outweighed the magnitude of the minimal regression recorded over long-term follow-up periods [23]. This observation became germane to the concept that induction of plaque regression is an important surrogate marker worth achieving since it may translate in substantial cardiovascular risk reduction.

Nonetheless, the invasive nature of coronary angiography greatly limits the utility of this tool for sequential studies, especially in asymptomatic people. In this vein, several human studies have addressed the utility of CT technology, as well as that of several other technologies not discussed in this chapter, to assess the effect of various medical interventions on cardiovascular disease. This notion suffers from the inherent limitation that limiting the progression or inducing the regression of atherosclerosis in asymptomatic individuals will provide the same benefit observed in symptomatic patients studied with invasive modalities. Indeed, symptomatic patients may have a very different substrate for their ongoing atherosclerotic disease compared to asymptomatic subjects harboring subclinical disease.

Callister et al. [18] published the first report of sequential. EBT scanning in asymptomatic patients. They conducted an observational study on 149 patients referred by primary care physicians for CAC screening. Since the reproducibility of the calcium volume score is very high for scores above 30 [13], a minimum score of 30 was required for patients' inclusion in the study. Treatment with HMG-CoA reductase inhibitors (statins) was advised for all patients, but the initiation of such therapy was left to the discretion of the referring physician. Patients underwent a baseline and follow-up EBT scan at a minimum of 12-month interval (range 12–15 months), and serial LDL cholesterol measurements were obtained. Of the 149 patients, 105 received treatment with HMG-CoA reductase inhibitors and 44 did not. Progression of calcium volume score was seen in all untreated patients (mean LDL ± SD: 147 ± 22 mg/dL) and averaged 52 ± 36% per year (Figure 5.1). In contrast, the mean yearly calcium volume score change for all treated patients (mean LDL: 114 ± 23 mg/dL) was 5 ± 28% ($p < 0.001$ vs. untreated patients). Among the treated patients, 65 individuals attained a LDL level <120 mg/dL (mean LDL: 100 ± 17 mg/dL) and showed a net regression of their calcium volume score (−7 ± 22%, Figure 5.2). For the patients who received statins but maintained an average LDL >120 mg/dL (mean LDL: 139 ± 18 mg/dL), the mean yearly calcium volume score progression was 25 ± 22% (Figure 5.2). All intergroup comparisons were

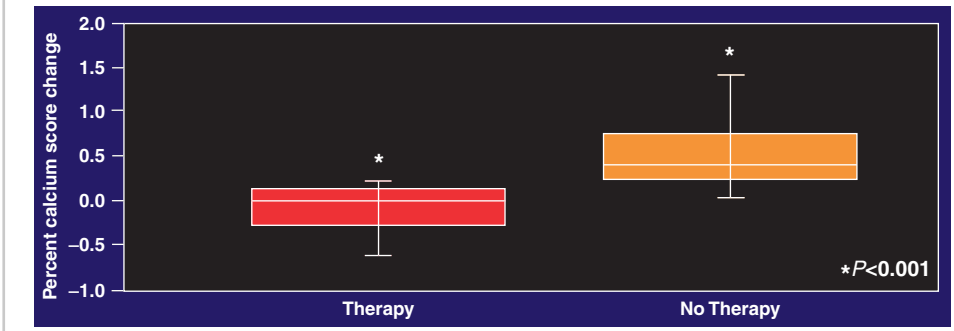

Figure 5.1. Progression of calcium volume score in 105 patients treated for a year with statins and 44 untreated patients. There was a significant difference in progression between the two groups. The *box plots* indicate median (line in the middle of the box), confidence intervals (*vertical lines*) as well as 25th and 75th percentile (lower and top border of the box) [18].

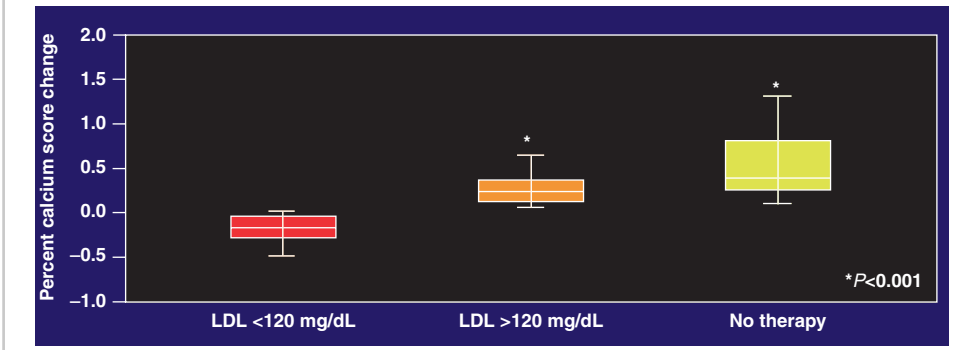

Figure 5.2. Progression of calcium volume score in 65 patients exposed to intensive treatment with statins for 1 year (mean LDL<120 mg/dL), 40 patients treated with a moderate statin regimen for a year (mean LDL>120 mg/dL on treatment), and 44 untreated patients. There was a significant difference in progression between the three groups. The box plots indicate median (line in the middle of the box), confidence intervals (vertical lines) as well as 25th and 75th percentile (lower and top border of the box) [18].

highly statistically significant ($p < 0.0001$). The study provided the first indication that there might be a direct correlation between the aggressiveness of LDL treatment and effectiveness with which the atherosclerotic process is halted as demonstrated by EBT imaging. An example of progression of coronary calcification in a patient who remained symptom free through time is shown in Figure 5.3. Other emerging lipid or nonlipid factors, such as Lp (a), low HDL levels, homocysteine, high CRP, etc., that could have affected the outcome of the analysis were not taken into consideration. This might help explain the apparent failure to treat a portion of the study cohort.

In the next published report, Budoff et al. [19] followed a total of 299 asymptomatic patients with various risk factors for atherosclerosis for 1–6.5 years. All patients underwent sequential EBT scans at a minimum of 12-month interval. The follow-up scans indicated a significant increase in calcium score of all untreated patients, regardless of the underlying risk factors. However, treatment with statins resulted in a statistically significant slowing of calcium score progression (15 ± 8% per year on treatment vs. 39 ± 12 % per year without treatment).

Achenbach et al. [20] conducted a small prospective cohort study and compared the rate of change in the amount of coronary calcium prior to and during lipid-lowering therapy with cerivastatin. A total of 66 patients with known coronary calcium and LDL levels >130 mg/dL were evaluated. An EBT scan was performed at baseline and repeated after a period of 14 months without therapy. Cerivastatin therapy was then initiated at a dose of 0.3 mg/day, and a final EBT scan was performed after 12 months of treatment. Therapy with cerivastatin lowered the cholesterol level from an average of 164 ± 30 to 107 ± 21 mg/dL. The median calcium volume score increase during the drug free period was 25%, but it slowed to 8.8% after 1 year of treatment with cerivastatin (Figure 5.4) ($p < 0.0001$). In 32 patients who attained an average LDL <100 mg/dL with treatment, the median annual calcium volume score change was −3.4% while the same patients had progressed 27% during the untreated period ($p = 0.0001$). Though small, this prospective cross-over study confirmed and expanded the findings of the earlier observational studies that suggested that a decline in the rate of progression in coronary calcification can be attained with aggressive medical treatment of hypercholesterolemia. A small trial of LDL apheresis and sequential CAC scoring was conducted in eight patients with familial hypercholesterolemia in whom diet and optimum pharmacotherapy had not resulted in the desired LDL levels [21]. The mean patient age was 46 ± 8 years. All patients had been on treatment with simvastatin 40 mg/day prior to initiation of LDL apheresis, but were switched to atorvastatin 80 mg/day during apheresis and continued treatment for an average period of 29 months. Total cholesterol, LDL, triglycerides, and HDL levels were

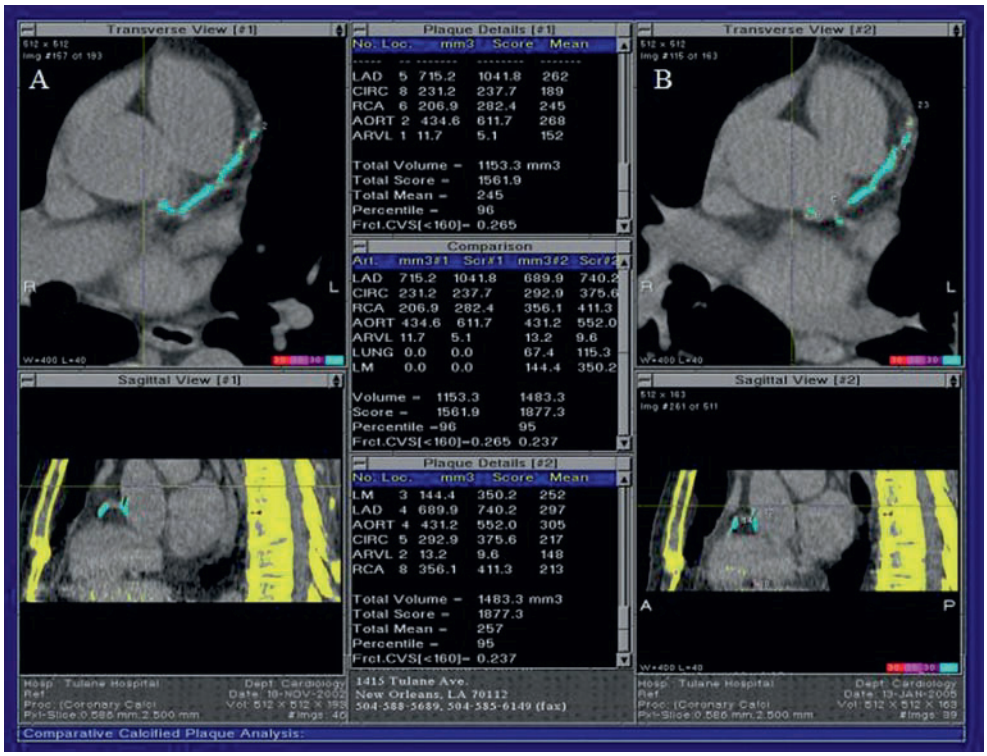

Figure 5.3. Asymptomatic patient with extensive coronary calcification (calcium volume score = 1153.3) at baseline (**a**). After 26 months of intensive treatment with lipid-lowering drugs and antihypertensive drugs (**b**), there was a mild progression of calcification (follow-up score = 1483.3). This corresponds to an annualized score increase of 12%, which is smaller than the 15% annual score increase necessary for the test to indicate actual progression. (**a, b**) Transverse sections of the heart with calcification in the proximal and midportion of the left anterior descending coronary artery. The central inset shows a comparison of baseline and follow-up volume scores and Agatston scores. Note that the calcium score percentile diminished from 96th at baseline to 95th at follow-up despite an increase in absolute score. This suggests a relative slowing of the progression of disease.

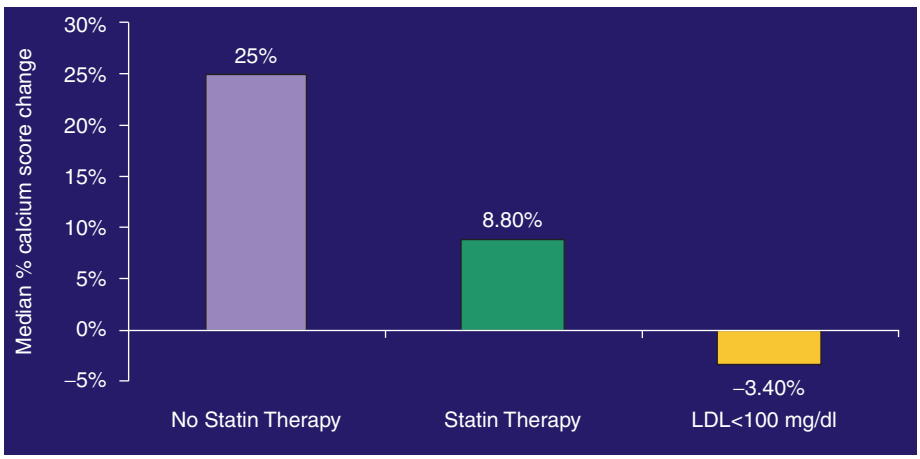

Figure 5.4. Median yearly progression of coronary calcium volume score in 66 hypercholesterolemic patients left untreated for 1 year (score increase = 25%), followed by 1 year of treatment with 0.3 mg of cerivastatin daily (score increase = 8.8%). Thirty-two patients attained a mean level of LDL < 100 mg/dL with treatment, and their median annual calcium score change was slightly negative (change: −3.4%) [20].

obtained at baseline and at several time points during the study period. Baseline imaging of the coronary arteries was performed by EBT and follow-up scans were done by means of multi-detector spiral CT scanning. CT measurements included calcium volume scores, mean plaque density, and Agatston scores. At the end of study, the calcium volume score decreased in all patients by an average of 23 ± 15% ($p < 0.01$). In contrast, the mean plaque density increased by 17 ± 11% ($p < 0.01$), suggesting that healing of the plaque may be associated with partial collapse of the plaque and further calcium accumulation.

Finally, Hsia et al. [24] conducted a subanalysis of the Women's Health Initiative (WHI) observational study, and evaluated prospectively the rate of progression of CAC in healthy postmenopausal women. Of 914 postmenopausal women enrolled in the main study, 305 women with a

baseline calcium score ≥10 were invited for a repeat scan. The progression analysis included the 94 women who agreed to undergo a second scan. The mean age of the study participants was 65 ± 9 years, and the mean interval between scans was 3.3 ± 0.7 years. A wide range of changes in CAC score was observed, with variations from −53 to +452 Agatston score units per year. Women with lower scores at baseline had smaller annual increases in CAC score. CAC scores increased 11, 31, and 79 units per year among women with baseline calcium score in the lowest, middle, and highest tertiles of score. In a multivariate analysis, age was not an independent predictor of change in CAC score. Statin use at baseline was a negative predictor ($p = 0.015$), whereas baseline score was a strong positive predictor ($p < 0.0001$) of progression of CAC.

Despite these favorable results, several observational [25–27] and randomized studies [28–30] failed to confirm an association between LDL lowering and progression of CAC. The Beyond Endorsed Lipid Lowering with EBT Scanning trial was a prospective, randomized study of postmenopausal and dyslipidemic women with a minimal calcium volume score of 30 at baseline [28]. After the initial EBT scan, the 615 women enrolled were randomized to treatment with atorvastatin 80 mg/day or pravastatin 40 mg/day, and a repeat second scan was performed 12 months later (Figure 5.5). The mean age of the 475 women who completed the study was 64 years. The attained mean LDL cholesterol level was significantly lower with atorvastatin (94 mg/dL) than pravastatin (129 mg/dL). Nonetheless, the median relative change in the calcium volume score was not different between the two treatment arms (15.1 and 14.3% for atorvastatin and pravastatin, respectively, p = NS). The St. Francis Heart Study [29] was a prospective, randomized study of 1,005 healthy individuals with a CAC score above the 80th percentile for age and sex at the time of CT screening. The study compared the effect of 20 mg/daily of atorvastatin along with vitamin C and E versus placebo on progression of CAC. At the end of a mean follow-up of 4.3 years, the progression was similar among treatment arms (~20% per year). Finally, Schmermund et al. [30] randomized 366 patients with no known cardiovascular disease to 10 mg vs. 80 mg of atorvastatin daily for 1 year. The mean LDL levels on treatment were 109 ± 28 and 87 ± 33 mg/dL, respectively. However, the mean calcium volume score progression was not different at the end of 12 months of follow-up (25 vs. 27%)

In conclusion, the results of randomized trials failed to confirm that lipid-lowering therapy may slow progression of CAC and indeed suggested an opposite effect. Of interest, in an observational study Wong et al. suggested that higher levels of HDL may be associated with a slower progression of CAC [27], but this association has not been studied prospectively to date.

Effect of Nonlipid Lowering Interventions on Progression of Coronary Artery Calcium

Besides medical therapy for dyslipidemia, other treatment modalities have been studied in relation to slowing of the progression of coronary artery calcification. An example of therapy of critical importance is represented by the effect of tight diabetic control on atherosclerotic disease progression. Snell-Bergeon et al. [31] assessed the importance of glycemic control in type 1 diabetes patients as a mean to reduce continued expansion of atherosclerosis and CAC. In 109 type 1 diabetic patients (22–50-year old), sequential EBT scans were performed at an interval of 2.7 years. Progression of CAC was noted in 21 patients, and it was associated with baseline hyperglycemia (odds ratio 7.11, 95% CI 1.38–36.6, $p = 0.02$), after adjustment for the presence of CAC at baseline, duration of diabetes, age, and sex. There was also a

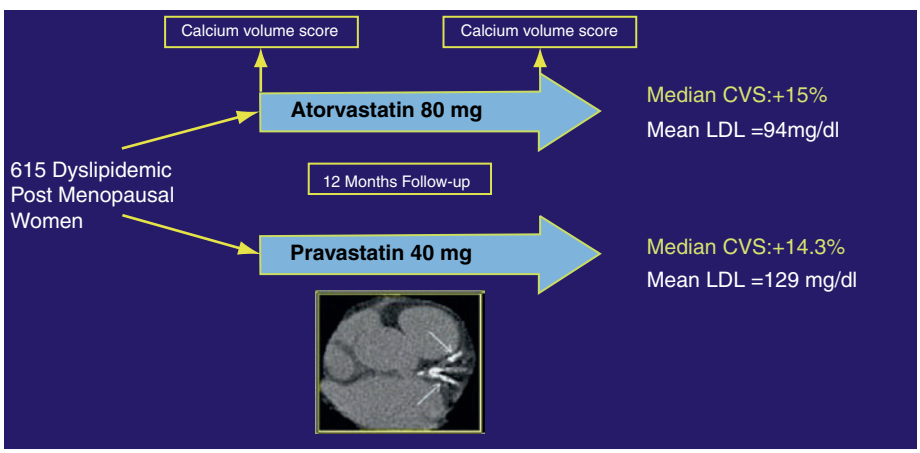

Figure 5.5. Design of the BELLES trial and main study results. Aggressive lipid-lowering therapy with atorvastatin did not slow progression of CAC more than moderate treatment with pravastatin [28].

significant interaction between higher insulin dose and higher body mass index ($p = 0.03$), suggesting that glycemic control and insulin resistance interact in determining progression of atherosclerosis in Type 1 diabetes.

In the WHI, menopausal women between the ages of 50–59 years were randomized to treatment with conjugated estrogens or placebo [32]. In a substudy of the WHI, 1064 women were submitted to CAC screening after 8.7 years from trial initiation. Women receiving estrogens showed a lower CAC score compared those receiving placebo (83.1 vs. 123.1, $p = 0.02$).

Several other approaches have been attempted to demonstrate slowing of CAC progression. In a small, randomized study, Rath et al. [33] assessed the progression rate of CAC in subjects treated with a combination of vitamins, minerals, and coenzymes. Untreated patients showed an average annual score increase of 44% as assessed by the Agatston method. The rate of progression was slowed to 15% yearly when patients were given nutritional supplements.

Budoff et al. [34] used aged garlic extract (AGE) to inhibit CAC progression. AGE was employed because it was previously shown to reduce multiple cardiovascular risk factors, including blood pressure, serum cholesterol levels, platelet aggregation, and adhesion, while stimulating nitric oxide generation in endothelial cells. In a placebo-controlled, double-blind, randomized pilot study, 23 patients were treated with 4 mL of oral AGE or the equivalent amount of placebo per day. Nineteen patients completed the 1-year study protocol. At the end of follow-up, the mean change in calcium volume score for the AGE group ($n = 9$) was significantly smaller ($7.5 \pm 9.4\%$) than for the placebo group ($n = 10$) that demonstrated an average increase of $22 \pm 18.5\%$ ($p = 0.046$). Throughout the study, there were no significant differences in individual cholesterol parameters or CRP between treatment group.

Nanobacteria have been implicated in the initiation process of atherosclerosis where they seem to operate as the trigger or nucleating factor for CAC. Concurrently, ethylenediaminetetraacetic acid (EDTA) disodium salt has been experimented with for a long time as a component of chelation therapy for the removal of calcium from soft tissue deposits with very variable results. In an attempt to address both the infectious as well as the chemical component of the calcified atherosclerotic plaque, a combination therapy composed of EDTA, tetracyclines, vitamins, and CoQ10 was administered to 77 volunteers with stable coronary artery disease [35]. EBT scans were performed at baseline and after a mere follow-up of 4 months from the initiation of therapy. Of the 77 patients, 44 (57%) showed CAC score regression (average −14%), while the remaining 33 showed either no change or an increase in score. Of interest, serum lipid levels were reduced in a large proportion of patients despite the baseline use of statins by the majority of the patients enrolled. No liver, renal, or hematological side effects were recorded.

Obviously, these studies based on nontraditional therapies were very small and mainly exploratory in nature, and the utility of such remedies will need to be confirmed in larger prospective studies.

Effect of Phosphate-Binding Therapies on Progression of Cardiovascular Calcification in End-Stage Renal Disease

The cardiovascular disease rates of end-stage renal disease (ESRD) patients are 30–50-fold higher than in the general population [36]. However, the cardiovascular mortality and morbidity of this patient group is only partially explained by traditional risk factors [37], and disorders of mineral metabolism may contribute substantially to the high incidence of events [38–44]. Hyperphosphatemia and its traditional management with calcium-based phosphate binders have been implicated in the development and progression of arterial and valvular calcification, and the dose of oral calcium has been correlated with the severity of calcification [39, 45]. Vascular and valvular calcifications are very extensive in ESRD disease (Figure 5.6), and they progress rapidly. In an attempt to curb the rapid progression of calcification, the Treat-to-Goal Study – a randomized, multicenter clinical trial – compared the calcium-free, nonabsorbable polymer sevelamer to traditional calcium-based phosphate binders [46]. Study outcomes included serum levels of phosphorus, calcium, intact parathyroid hormone (PTH), and lipids, as well as change in calcification of the coronary arteries and thoracic aorta quantified by EBT. Two hundred adult hemodialysis patients, who had received hemodialysis for a median of 3 years prior to study entry, were randomized in 15 medical centers in Europe and the United States. During the study period, phosphate binders were adjusted to maintain serum phosphorus levels between 3.0 and 5.0 mg/dL, serum calcium levels between 8.5 and 10.5 mg/dL, and serum PTH levels between 150 and 300 pg/mL. EBT was performed at the start of the study, and after 6 and 12 months of treatment. In spite of a similar control of serum phosphorus and calcium, coronary and aortic calcification progressed significantly in the calcium-treated patients while there was no statistically significant change from baseline in the sevelamer group. At 1-year follow-up (Figure 5.7), the median relative change in coronary and aorta scores were 25 and 28% and 6 and 5% in the calcium and sevelamer group, respectively ($p = 0.02$ for all intergroup comparisons). Of note, the mean LDL cholesterol was significantly lower in the sevelamer group than in patients treated with calcium salts, despite the fact that the latter received statins more often. However, the changes in calcium score severity seen at 52 weeks were independent of the levels of LDL cholesterol, HDL cholesterol and C-reactive protein. Additionally, sevelamer therapy was accompanied by a simultaneous improvement in bone mineral density [47]. Interestingly, an inverse relationship between CAC and bone mineral density has also been

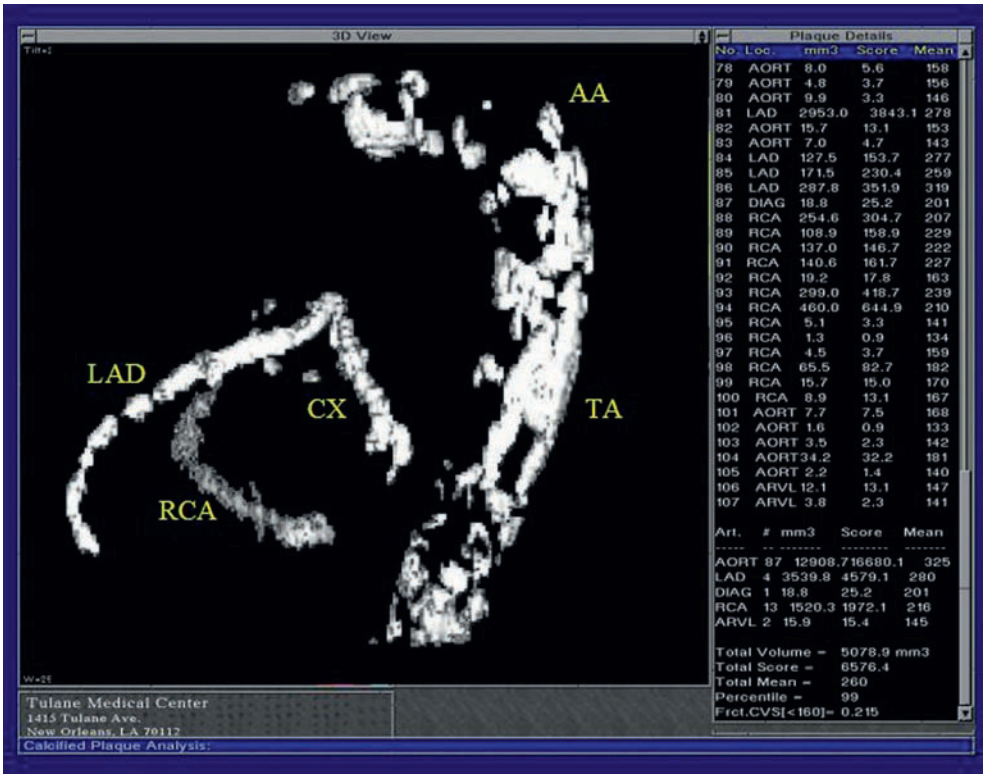

Figure 5.6. Extensive cardiovascular calcification in a patient suffering from end-stage renal disease. The soft tissues have been removed, and only the calcified portion of the aorta and coronary arteries are shown. *AA* aortic arch; *LAD* left anterior descending coronary artery; *CX* circumflex coronary artery; *RCA* right coronary artery; *TA* thoracic aorta.

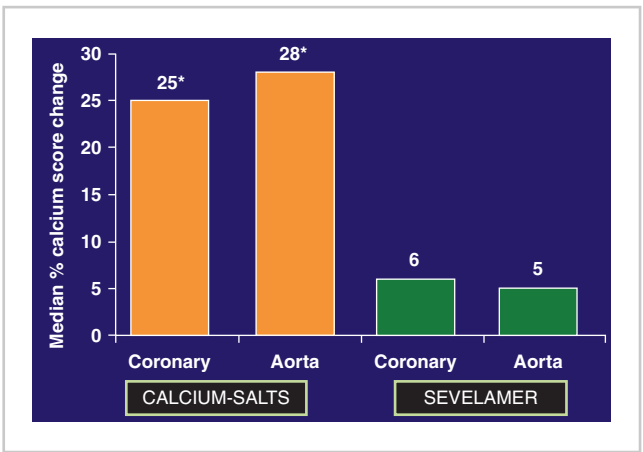

Figure 5.7. Median percentage calcium score change for coronary arteries and aorta in end-stage renal disease patients randomized to 1-year treatment with sevelamer or calcium-based salts. The progression was significant for both coronary arteries and aorta only in the calcium salt treated patients [46].

observed in nonuremic individuals [48, 49] and suggests an interaction between bone and vascular health.

A second randomized study was performed with the same primary end-point in patients referred for CAC screening and randomized to sevelamer or calcium-based phosphate binders within a few weeks of beginning hemodialysis [50]. At the end of 18 months of follow-up, calcium-treated patients again showed a significant increase in CAC from baseline and an 11-fold greater progression than sevelamer treated patients ($p < 0.002$). The secondary end-point of this study was long-term mortality; at the end of 4.5 years of follow-up the mortality of calcium-treated patients was double that of sevelamer treated subjects (hazard ratio: 2.2; $p < 0.02$) [51]. More recently, the investigators of the CARE-2 study were unable to confirm that sevelamer and calcium-acetate phosphate binders affect CAC progression differently and showed an approximate 30% progression at the end of 1 year for both treatment arms [52]. In this protocol, the investigators intended to compare the lipid-lowering ability of sevelamer to a combination of calcium salts and statins on CAC progression. However, 80% of the sevelamer treated patients also received statins and this may have caused progression in both arms as shown in the general population (see earlier discussion). Furthermore, the PTH level of sevelamer treated patients was double that of prior studies [46, 50], suggesting a very poor control of mineral metabolism.

Clinical Implications of Coronary Artery Calcium Progression

The clinical significance of progression of CAC has been addressed in several observational studies and one randomized trial to date. Raggi et al. [53] followed 817 asymptomatic individuals referred by primary care physicians for sequential EBT imaging at an average interval of 2.2 ± 1.3 years. Patients were treated with statins at the discretion of the treating physician. After several years from the initial EBT scan, telephone interviews were conducted to determine the occurrence of myocardial infarction, and

follow-up information was obtained in all subjects. Events were considered linked with CAC changes only if they occurred after the second EBT scan. The mean yearly CAC volume score change for the individuals who suffered a myocardial infarction was 47 ± 50%, while it averaged 26 ± 32% in those free of events ($p < 0.001$). Treatment of hyperlipidemia (a probable marker of greater baseline risk) and CAC score change were independent predictors of myocardial infarction.

In a second observation [54], the occurrence of myocardial infarction was estimated in a cohort of 495 asymptomatic individuals submitted to sequential EBT scanning while undergoing treatment with statins. The mean follow-up was 3 years, men and women were enrolled in equal proportions, and the mean age of the enrolled subjects was 57 ± 8 years. In spite of an identical average LDL level on treatment (~120 mg/dL in each group), the 41 patients who suffered a myocardial infarction showed a much greater yearly CAC score progression than the 454 event-free survivors (42 ± 23 vs. 17 ± 25%, $p < 0.001$, Figure 5.8). The subjects were further identified according to a relative CAC score increase greater than 15% per year. This value was identified in prior publications as representing a true score change as opposed to a measurement reproducibility error [13]. In a multivariable model, the best predictors of a yearly CAC score increase ≥15% were smoking ($p = 0.032$), male gender ($p = 0.014$), and baseline CAC score ($p = 0.002$). Independent of the baseline CAC score, patients demonstrating an increase smaller than 15% per year (i.e., no progression from baseline) suffered very few events ($n = 5$), and the events occurred late during follow-up. On the contrary, the majority of events ($n = 36$) occurred in patients showing a CAC score progression >15% per year and the events occurred early during follow-up. Figure 5.9 shows an example of rapid progression of CAC and the occurrence of an acute coronary event in a 64-year-old man.

In the St. Francis Heart Study [55], 4,613 patients (age 50–70) were followed prospectively with a repeat CT scan 2 years after screening. The median absolute CAC score increase was 4 units in patients without cardiovascular

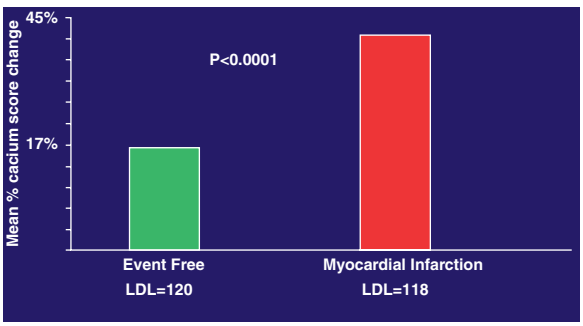

Figure 5.8. Mean coronary calcium volume score in patients treated with statins who suffered a myocardial infarction during follow-up and event-free subjects. Despite attaining a similar mean LDL level with treatment, the calcium score progression was significantly different between groups [54].

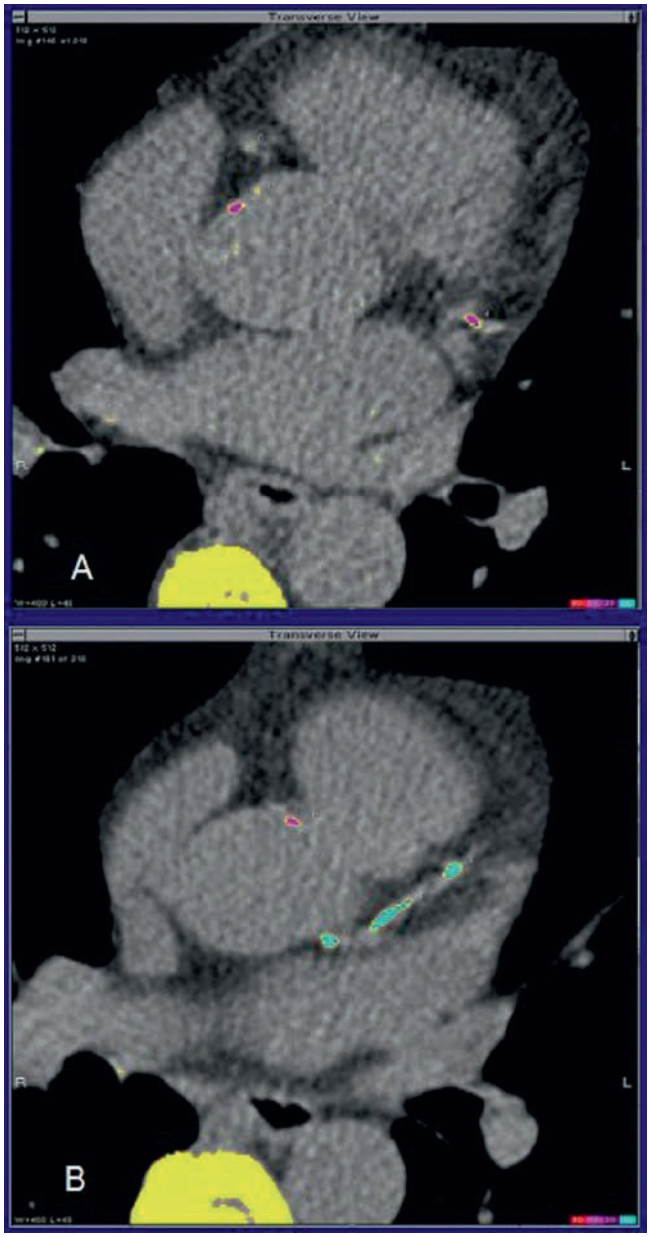

Figure 5.9. (**a**) This 64-year-old man at intermediate risk of cardiovascular events by Framingham categories had a baseline coronary artery calcium score of 106. (**b**) After 18 months from the first CT, his score increased to 296. Within 3 months of the second CT scan, he suffered a non-ST elevation myocardial infarction.

events during follow-up and 247 units in those with events ($p < 0.0001$). In multiple logistic regression analyses, age ($p = 0.03$), male gender ($p = 0.04$), LDL cholesterol ($p = 0.01$), HDL cholesterol ($p = 0.04$), and 2-year change in CAC score ($p = 0.0001$) were significantly associated with risk of events.

The studies we reviewed above clearly indicate that although several currently available therapies may not be effective in slowing the process, continued CAC progression poses a serious threat for the occurrence of future events. Nonetheless, whether sequential CAC screening should be recommended in clinical practice remains controversial [56, 57].

Conclusion

Despite a sound basic science construct, there has not been validation of the utility of CAC imaging with computer tomography to monitor the effectiveness of lipid-lowering therapy. On the other hand, the effects of calcium and non-calcium based therapies for phosphate-binding purposes in ESRD have been clearly shown with this technique. Additionally, a number of small and preliminary studies have shown that CT can be of potential use in monitoring the outcome of various therapies. Nonetheless, there are limitations inherent with the technology currently available. There is a strong need to standardize the scoring methods and assess the equivalence of the existing CT equipments [15, 56]. Additionally, the rigid application of a density threshold of 130 HU to define the presence of tissue calcification in all patients limits our ability to identify more recent and less densely calcified plaques and may be incorrectly applied to all the different CT models available on the market. Although there is a need for further prospective studies, the most interesting finding so far emerged is that the continued progression of CAC is associated with a greater risk of adverse events than lack of progression.

Future directions of research may include studying the effect of such therapies as HDL rising, reduction of HIV viral load [58], etc. If sequential CT imaging were confirmed to be useful in assessing the effectiveness of antiatherosclerotic therapies, it could greatly facilitate the conduction of prevention trials by allowing a reduction in the number of patients needed to treat. Furthermore, a physician's effort to implement preventive measures could be facilitated.

Screening for CAC in primary prevention has finally come of age and has become more readily accepted by a wide circle of physicians [57]. With continued improvements in CT technology and further reduction in radiation exposure, it is hoped that the role of sequential CT may become better defined either for follow-up of CAC changes or noncalcified plaque by CT angiography.

References

1. Strong JP, Malcom GT, McMahan A, et al. Prevalence and extent of atherosclerosis in adolescents and young adults. The Pathobiological Determinants of Atherosclerosis in Youth Study. *JAMA*. 1999;281: 727–735.
2. Bostrom K, Watson KE, Horn S, Wortham C, Herman IM, Demer LL. Bone morphogenic protein expression in human atherosclerotic lesions. *J Clin Invest*. 1993;91:1800–1809.
3. Fitzpatrick LA, Severson A, Edwards WD, Ingram RT. Diffuse calcification in human coronary arteries: association of osteopontin with atherosclerosis. *J Clin Invest*. 1994;94:1597–1604.
4. Shanahan CM, Cary NR, Metcalfe JC, Weissberg PL. High Expression of genes for calcification-regulating proteins in human atherosclerotic plaques. *J Clin Invest*. 1994;93:2393–2402.
5. Proudfoot D, Davies JD, Skepper JN, Weissberg PL, Shanahan CM. Acetylated low-density lipoprotein stimulates human vascular smooth muscle cell calcification by promoting osteoblastic differentiation and inhibiting phagocytosis. *Circulation*. 2002;106: 3044–3050.
6. Bini A, Mann KG, Kudryk BJ, Schen FJ. Noncollagenous bone matrix proteins, calcification and thrombosis in carotid artery atherosclerosis. *Arterioscl Thromb Vasc Biol*. 1999;19:1852–1861.
7. Stary HC. Natural history of calcium deposits in atherosclerosis progression and regression. *Z Kardiol*. 2000;89(suppl 2):28–35.
8. Williams JK, Sukhova GK, Herrington DM, Libby P. Pravastatin has cholesterol-lowering independent effects on the artery wall of atherosclerotic monkeys. *J Am Coll Cardiol*. 1998;31:684–91.
9. Daoud AS, Jarmolych J, Augustyn JM, et al. Sequential morphologic studies of regression of advanced atherosclerosis. *Arch Pathol*. 1981; 105:233–239.
10. Clarkson TB, Bond MG, Bullock BC, et al. A study of atherosclerosis regression in *Macaca mulatta*. IV. Changes in coronary arteries from animals with atherosclerosis induced for 19 months and then regressed for 24 months or 48 months at plasma cholesterol concentrations of 300 or 200 mg/dl. *Exp Mol Pathol*. 1981;34:345–368.
11. Agatston AS, Janowitz WR, Hildner JR, Zusmer NR, Viamonte M Jr, Detrano R. Quantification of coronary artery calcium using ultrafast computed tomography scanning. *J Am Coll Cardiol*. 1990;15: 827–832.
12. Sangiorgi G, Rumberger JA, Severson A, et al. Arterial calcification and not lumen stenosis is highly correlated with atherosclerotic plaque burden in humans: a histologic study of 723 coronary artery segements using non-decalcifying methodology. Electron beam computed tomography and coronary artery disease: scanning for coronary artery calcification. *J Am Coll Cardiology*. 1998;31:126–133.
13. Callister TQ, Cooil B, Raya S, Lippolis NJ, Russo DJ, Raggi P. Coronary artery disease: improved reproducibility of calcium scoring with electron-beam CT volumetric method. *Radiology*. 1998;208:807–814.
14. Rumberger JA, Kaufman L. A rosetta stone for coronary calcium risk stratification: agatston, volume, and mass scores in 11, 490 individuals. *AJR Am J Roentgenol*. 2003;181:743–748.
15. McCollough CH, Ulzheimer S, Halliburton SS, Shanneik K, White RD, Kalender WA. Coronary artery calcium: a multi-institutional, multimanufacturer international standard for quantification at cardiac CT. *Radiology*. 2007;243:527–538.
16. Jukema JW, Bruschke AV, van Boven AJ, et al. he Regression Growth Evaluation Statin Study (REGRESS). *Circulation*. 1995;91:2528–2540.
17. Brown G, Albers JJ, Fisher LD, et al. Regression of coronary artery disease as a result of intensive lipid-lowering therapy in men with high levels of apolipoprotein B. *N Engl J Med*. 1990;323:1289–1298.
18. Callister TQ, Raggi P, Cooil B. Effects of HMG-CoA reductase inhibitors on coronary artery disease. *N Engl J Med*. 1998;339:1972–1977.
19. Budoff MJ, Lane KL, Bakhsheshi H, et al. Rates of progression of coronary calcium by electron beam tomography. *Am J Cardiol*. 2000; 86:8–11.
20. Achenbach S, Dieter R, Pohle K, et al. Influence of lipid-lowering therapy on the progression of coronary artery calcification. *Circulation*. 2002;106:1077–1082.
21. Hoffmann U, Derfler K, Haas M, Stadler A, Brady TJ, Kostner K. Effects of combined low density lipoprotein apheresis and aggressive statin therapy on coronary calcified plaque as measured by computed tomography. *Am J Cardiol*. 2003;91:461–464.
22. Taylor AJ, Kent SM, Flaherty PJ, Coyle LC, Markwood TT, Vernalis MN. ARBITER: arterial biology for the investigation of the treatment effects of reducing cholesterol: a randomized trial comparing the effects of atorvastatin and pravastatin on carotid intima medial thickness. *Circulation*. 2002;106:2055–2060.
23. Levine GN, Keaney JF Jr, Vita JA. Cholesterol reduction in cardiovascular disease: clinical benefits and possible mechanisms. *N Engl J Med*. 1995;332:512–521.
24. Hsia J, Klouj A, Prasad A, Burt J, Adams-Campbell LL, Howard BV. Progression of coronary calcification in healthy postmenopausal women. *BMC Cardiovasc Disord*. 2004;4:21.
25. Hecht HS, Harman SM. Comparison of the effects of atorvastatin versus simvastatin on subclinical atherosclerosis in primary prevention as determined by electron beam tomography. *Am J Cardiol*. 2003; 91:42–45.

26. Hecht HS, Harman SM. Relation of aggressiveness of lipid-lowering treatment to changes in calcified plaque burden by electron beam tomography. *Am J Cardiol*. 2003;92:334–336.
27. Wong ND, Kawakubo M, LaBree L, Azen SP, Xiang M, Detrano R. Relation of coronary calcium progression and control of lipids according to the National Cholesterol Education Program guidelines. *Am J Cardiol*. 2004;94:431–436.
28. Raggi P, Davidson M, Callister TQ, et al. Aggressive versus moderate lipid-lowering therapy in hypercholesterolemic post-menopausal women: beyond Endorsed Lipid Lowering With EBT Scanning (BELLES). *Circulation*. 2005;112(4):563–571.
29. Arad Y, Spadaro LA, Roth M, Newstein D, Guerci A. Treatment of asymptomatic adults with elevated calcium scores with atorvastatin, vitamin C and vitamin E. The St. Francis Heart Study randomized clinical trial. *J Am Coll Cardiol*. 2005;46:166–172.
30. Schmermund A, Achenbach S, Budde T, et al. Effect of intensive versus standard lipid-lowering treatment with atorvastatin on the progression of calcified coronary atherosclerosis over 12 months: a multicenter, randomized, double-blind trial. *Circulation*. 2006; 113: 427–437.
31. Snell-Bergeon JK, Hokanson JE, Jensen L, et al. Progression of coronary artery calcification in type 1 diabetes: the importance of glycemic control. *Diabetes Care*. 2003;26:2923–2928.
32. Manson JE, Allison MA, Rossouw JE, et al. Estrogen therapy and coronary-artery calcification. *N Engl J Med*. 2007;356:2591–2602.
33. Rath M, Niedzwiecki A. Nutritional supplement program halts progression of early coronary atherosclerosis documented by ultrafast computed tomography. *J Appl Nutr*. 1996;48:67–78.
34. Budoff MJ, Takasu J, Flores FR, et al. Inhibiting progression of coronary calcification using aged garlic extract in patients receiving statin therapy: a preliminary study. *Prev Med*. 2004;39:985–991.
35. Maniscalco BS, Taylor KA. Calcification in coronary artery disease can be reversed by EDTA-tetracycline long-term chemotherapy. *Pathophysiology*. 2004;11:95–101.
36. US Renal Data System. *USRDS 2004 Annual Data Report: atlas of end-stage renal disease in the United States*. National Institute of Diabetes and Digestive and Kidney Diseases, Bethesda, MD: National Institutes of Health; 2004.
37. Longenecker JC, Coresh J, Powe NR, et al. Traditional cardiovascular disease risk factors in dialysis patients compared with the general population: the CHOICE Study. *J Am Soc Nephrol*. 2002; 13: 1918–1927.
38. Block G, Hulbert-Shearon T, Levin N, et al. Association of serum phosphorus and calcium x phosphate product with mortality risk in chronic hemodialysis patients: a national study. *Am J Kidney Dis*. 1998;31:607–617.
39. Guerin AP, London GM, Marchais SJ, et al. Arterial stiffening and vascular calcifications in end-stage renal disease. *Nephrol Dial Transplant*. 2000;15:1014–1021.
40. Blacher J, Guerin AP, Pannier B, et al. Arterial calcifications, arterial stiffness, and cardiovascular risk in end-stage renal disease. *Hypertension*. 2001;38:938–942.
41. Raggi P, Boulay A, Chasan-Taber S, et al. Cardiac calcification in adult hemodialysis patients. A link between end-stage renal disease and cardiovascular disease? *J Am Coll Cardiol*. 2002;39:695–701.
42. London GM, Guerin AP, Marchais SJ, et al. Arterial media calcification in end-stage renal disease: impact on all-cause and cardiovascular mortality. *Nephrol Dial Transplant*. 2003;18:1731–1740.
43. London GM. Cardiovascular calcifications in uremic patients: clinical impact on cardiovascular function. *J Am Soc Nephrol*. 2003; 14:S305–309.
44. Block GA, Klassen PS, Lazarus JM, et al. Mineral metabolism, mortality, and morbidity in maintenance hemodialysis. *J Am Soc Nephrol*. 2004;15:2208–2218.
45. Goodman WG, Goldin J, Kuizon BD, et al. Coronary-artery calcification in young adults with end-stage renal disease who are undergoing dialysis. *N Engl J Med*. 2000;342:1478–1483.
46. Chertow GM, Burke SK, Raggi P. Sevelamer attenuates the progression of coronary and aortic calcification in hemodialysis patients. *Kidney Int*. 2002;62:245–252.
47. Raggi P, James G, Burke S, et al. Paradoxical decrease in vertebral bone density with calcium-based phosphate binders in hemodialysis. *J Bone Miner Res*. 2005;20:762–772.
48. Barengolts EI, Berman M, Kukreja SC, Kouznetsova T, Lin C, Chomka EV. Osteoporosis and coronary atherosclerosis in asymptomatic postmenopausal women. *Calcif Tissue Int*. 1998;62:209–213.
49. Sirola J, Sirola J, Honkanen R, et al. Relation of statin use and bone loss: a prospective population-based cohort study in early postmenopausal women. *Osteoporos Int*. 2002;13:537–541.
50. Block GA, Spiegel DM, Ehrlich J, et al. Effects of sevelamer and calcium on coronary artery calcification in patients new to hemodialysis. *Kidney Int*. 2005;68(4):1815–24.
51. Block GA, Raggi P, Bellasi A, Kooienga L, Spiegel DM. Mortality effect of coronary calcification and phosphate binder choice in incident hemodialysis patients. *Kidney Int*. 2007;7:438–41.
52. Qunibi W, Moustafa M, Muenz LR, et al. A 1-year randomized trial of calcium acetate versus sevelamer on progression of coronary artery calcification in hemodialysis patients with comparable lipid control: the Calcium Acetate Renagel Evaluation-2 (CARE-2) study. *Am J Kidney Dis*. 2008;5:952–65.
53. Raggi P, Cooil B, Shaw LJ, et al. Progression of coronary calcification on serial electron beam tomography scanning is greater in patients with future myocardial infarction. *Am J Cardiol*. 2003;92:827–829.
54. Raggi P, Callister T, Budoff M, Shaw L. Progression of coronary artery calcium and risk of first myocardial infarction in patients receiving cholesterol-lowering therapy. *Arterioscler Thromb Vasc Biol*. 2004;24:1272–7.
55. Arad Y, Goodman KJ, Roth M, Newstein D, Guerci AD. Coronary calcification, coronary risk factors, and atherosclerotic cardiovascular disease events. The St. Francis Heart Study. *J Am Coll Cardiol*. 2005;46:158–165.
56. Oudkerk M, Stillman AE, Halliburton SS, et al. Coronary artery calcium screening: current status and recommendations from the European Society of Cardiac Radiology and North American Society for Cardiovascular Imaging. *Int J Cardiovasc Imaging*. 2008; 24(6): 645–71.
57. Greenland P, Bonow RO, Brundage BH, et al.; American College of Cardiology Foundation Clinical Expert Consensus Task Force (ACCF/AHA Writing Committee to Update the 2000 Expert Consensus Document on Electron Beam Computed Tomography); Society of Atherosclerosis Imaging and Prevention; Society of Cardiovascular Computed Tomography. ACCF/AHA 2007 clinical expert consensus document on coronary artery calcium scoring by computed tomography in global cardiovascular risk assessment and in evaluation of patients with chest pain: a report of the American College of Cardiology Foundation Clinical Expert Consensus Task Force (ACCF/AHA Writing Committee to Update the 2000 Expert Consensus Document on Electron Beam Computed Tomography). *J Am Coll Cardiol*. 2007;49:378–402.
58. Kingsley LA, Cuervo-Rojas J, Munoz A, et al. Subclinical coronary atherosclerosis, HIV infection and antiretroviral therapy: multicenter AIDS cohort study. *AIDS*. 2008;22:1589–99.

6

The Aorta and Great Vessels

David M. Shavelle

Introduction

Technological improvements with 64 multidetector computed tomography (MDCT) have greatly advanced its role for diagnostic imaging in patients with vascular disease. CT angiography has thus become a useful tool in evaluating patients with various diseases of the aorta and the great vessels such as aortic dissection, aortic aneurysm and carotid artery disease.

Normal Anatomy

The thoracic aortic is commonly divided into three anatomic segments: (1) the ascending aorta, (2) the aortic arch, and (3) the descending aorta. The aortic arch gives rise to three branches: (1) the brachiocephalic, (2) the left common carotid, and (3) the left subclavian artery. Approximately 35% of patients will have a variation in this normal branching pattern, such as the "bovine arch," where the left common carotid artery arises from the brachiocephalic trunk as opposed to the aortic arch (Figure 6.1a). In patients being evaluated for carotid artery stenting, it is also useful to classify the overall shape of the aortic arch as level I, II, or III. A horizontal line is drawn across the top of the aortic arch, and a second horizontal line that is 2-times the diameter of the common carotid artery is drawn inferior to this (Figure 6.1b). A level I arch describes each of the great vessels originating along this horizontal line. A level II arch has the great vessels originating below this line, and a level III arch has the origin of the great vessels arising more than 2-times the diameter of the common carotid artery below

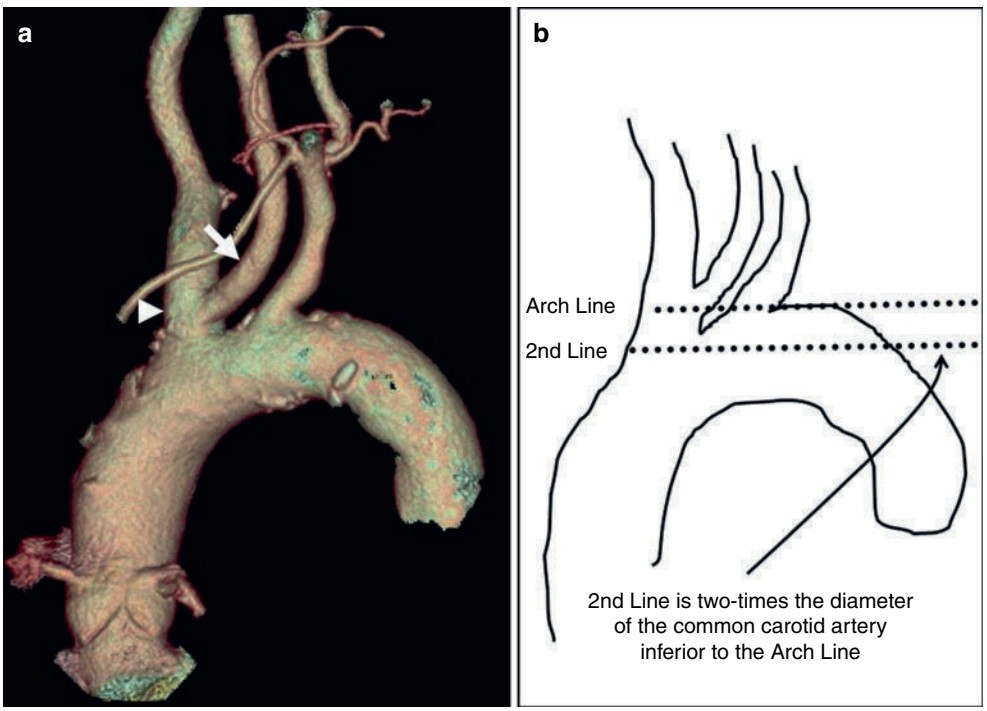

Figure 6.1. (**a**) Bovine aortic arch with left common carotid artery (*white arrow*) originating from the right brachiocephalic artery (*white arrowhead*). Volume rendering (VR). (**b**) To classify the shape of the aortic arch, a *horizontal line* is drawn along the top of the arch (*arch line*). A second line is drawn 2-times the diameter of the common carotid artery, inferior to the arch line. This is an example of a Level II arch.

Table 6.1. Normal diameters referenced to body surface area (m^2) of the ascending, descending and abdominal aorta

Location	Normal size	Comments
Ascending aorta	<2.1 cm/m^2	Surgery recommended for aneurysms >5.5 cm in those with Marfan's syndrome and >6.0 cm in those without connective tissue disease
Descending aorta	<1.6/m^2	
Abdominal aorta	<3.0 cm	

this line. Level III aortic arches increase the complexity of carotid artery stenting.

The normal size of the aorta varies at different anatomic locations and decreases in size with distance from the aortic valve (Table 6.1).

Diseases of the Aorta

Common diseases that involve the aorta include aneurysm, dissection, and atherosclerosis.

Aortic Aneurysm

Aneurysms commonly involve the abdominal and thoracic aorta. Aortic endovascular stenting is gaining acceptance as an alternative to traditional open surgical repair for abdominal aortic aneurysms. CT imaging is the predominant method used for preoperative planning to assess the feasibility of endovascular aortic stenting. Following endovascular aortic repair (EVAR), CT is commonly used to assess for device complications that include endoleaks, aneurysm expansion, rupture, endograft stent fracture, and graft migration that may occur in up to 10% of cases (Figure 6.2) [1].

CT imaging of abdominal and thoracic aneurysms should assess the proximal and distal extent of the aneurysm, the size of the aneurysm, and involvement of adjacent vessels. Axial CT images (raw data) should be the primary source to accurately size the aneurysm and obtain preoperative measurements for selecting the appropriate aortic stent graft (Table 6.2, Figure 6.3). The most accurate measurement of aneurysm size should be obtained in a plane perpendicular to the center line of the vessel. Maximum intensity projection (MIP) provides images similar to those obtained with

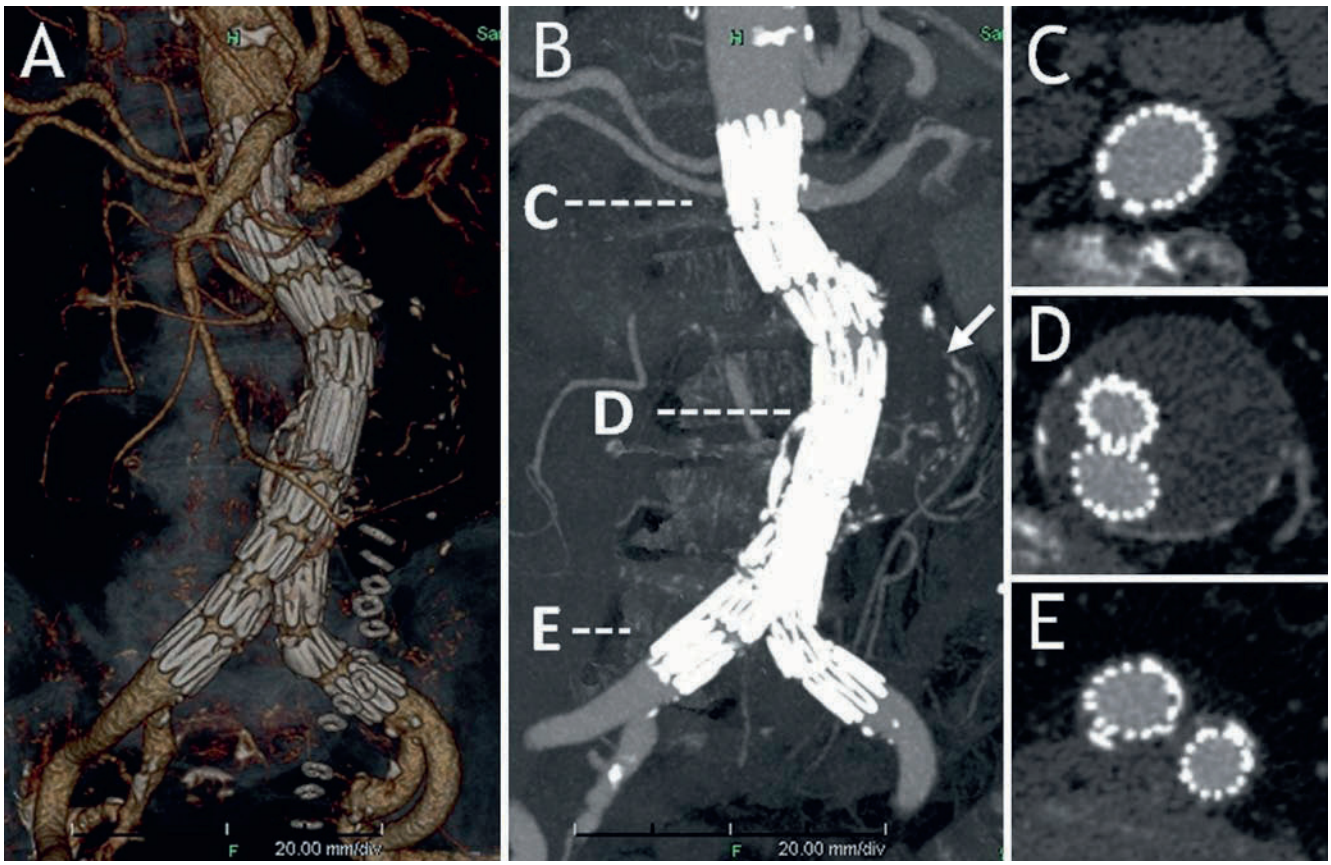

Figure 6.2. Aortic endograft. (**a**) VR image showing aortic endograft with stents extending into the right and left common iliac arteries. (**b**) Maximum intensity projection (MIP) showing aortic endograft and residual abdominal aortic aneurysm (*white arrow*). Location of the cross sectional axial images shown in (**c–e**). (**c**) Cross sectional axial image within the proximal portion of the abdominal aorta, proximal to the beginning of the aneurismal segment. (**d**) Cross sectional axial image at the location of the aneurismal segment. Note appearance of aortic endograft limbs. (**e**) Cross sectional axial image at the proximal right and left common iliac arteries.

Table 6.2. Essential CT measurements in the evaluation of an abdominal aortic aneurysm for possible endovascular aortic repair (EVAR), see Figure 6.3

Measurement	Description of measurement
D1	Aortic diameter at lowest renal artery
D2	Maximal aortic diameter
D3	Diameter at right iliac artery landing zone
D4	Diameter at left iliac artery landing zone
L1	Length of aortic neck below renal arteries
L2	Length of aorta from beginning of aneurysm to bifurcation
L3	Length of aneurysmal right iliac artery
L4	Length of nonaneurysmal right iliac artery
L5	Length of aneurysmal left iliac artery
L6	Length of nonaneurysmal left iliac artery

conventional angiography and is useful to visualize calcification and the relationship of the aneurysm to adjacent vessels. Volume rendering (VR) provides an accurate anatomic representation of the aneurysm in respect to adjacent vessels and helps to define vessel tortuosity (Figure 6.4).

Aortic Dissection

The main CT feature of an aortic dissection is the presence of an intimal flap that separates the true and false lumens (Figures. 6.5 and 6.6). The ability to establish this diagnosis relies heavily upon a good quality CT scan with optimal vascular enhancement. The extent of the dissection (proximal entry and distal re-entry sites), involvement of adjacent branch vessels, and potential compromise of the true lumen should be evaluated. Potential imaging artifacts include insufficient contrast enhancement of the lumen (improper timing of contrast), streak artifacts (adjacent surgical staples, vascular calcification), periaortic structures (soft tissue masses, residual thymus), and congenital aortic diverticulum (residual ductus tissue) [2]. Two disease processes that can be confused with an aortic dissection include intramural hematoma (focal dissection of blood within the aortic wall) and penetrating aortic ulcer.

Atherosclerosis

CT findings of aortic atherosclerosis include thickening or raised lesions of the aortic wall and the presence of calcification (Figure 6.7). The presence of thoracic aortic calcification by CT is associated with coronary calcification and both the severity and extent of angiographic coronary artery disease [3, 4].

Disease of the Great Vessels

The most common disease process that involves the great vessels is atherosclerosis. Atherosclerosis typically affects the carotid artery system at the bifurcation of the common carotid into the internal (ICA) and external carotid arteries (ECA).

The common carotid artery should be followed from its aortic origin, through the carotid bifurcation and into the skull base using the raw data in axial imaging cuts. The ECA can usually be easily differentiated from the ICA because of multiple side branches arising from the ECA within the neck region (the ICA lacks branches within the

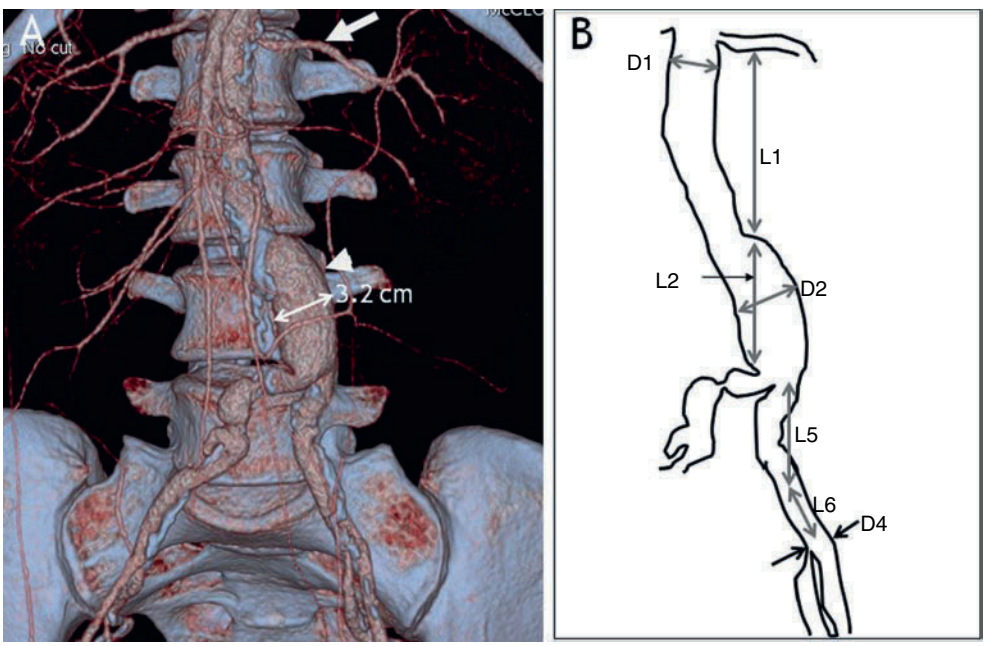

Figure 6.3. (**a**) Infra-renal abdominal aortic aneurysm (*white arrowhead*) measuring approximately 3.2 cm at the largest diameter. *White arrow* shows left renal artery. VR. (**b**) Essential measurements used in the evaluation of an abdominal aortic aneurysm for possible aortic stent graft placement. See Table 6.2.

Figure 6.4. (**a**) Lateral projection of the ascending aorta, aortic arch, and descending aorta. Calcification within the aortic arch (*white arrowhead*). Bovine arch with origin of the left common carotid artery (*white arrow*) from the right innominate artery. Moderate aneurysmal dilation of the ascending aorta that does not involve the aortic arch or descending aorta. VR. (**b**) Lateral projection, MIP mode. Calcification within the aortic arch (*white arrowhead*) and origin of the left common carotid artery (*white arrow*) from the right innominant artery. (**c**) Multiplanar reconstruction (MPR) mode showing moderate aneurysmal dilation of the ascending aorta that does not involve the aortic arch or the descending aorta. The proximal ascending aorta measured 4.5 by 4.6 cm in cross sectional axial imaging.

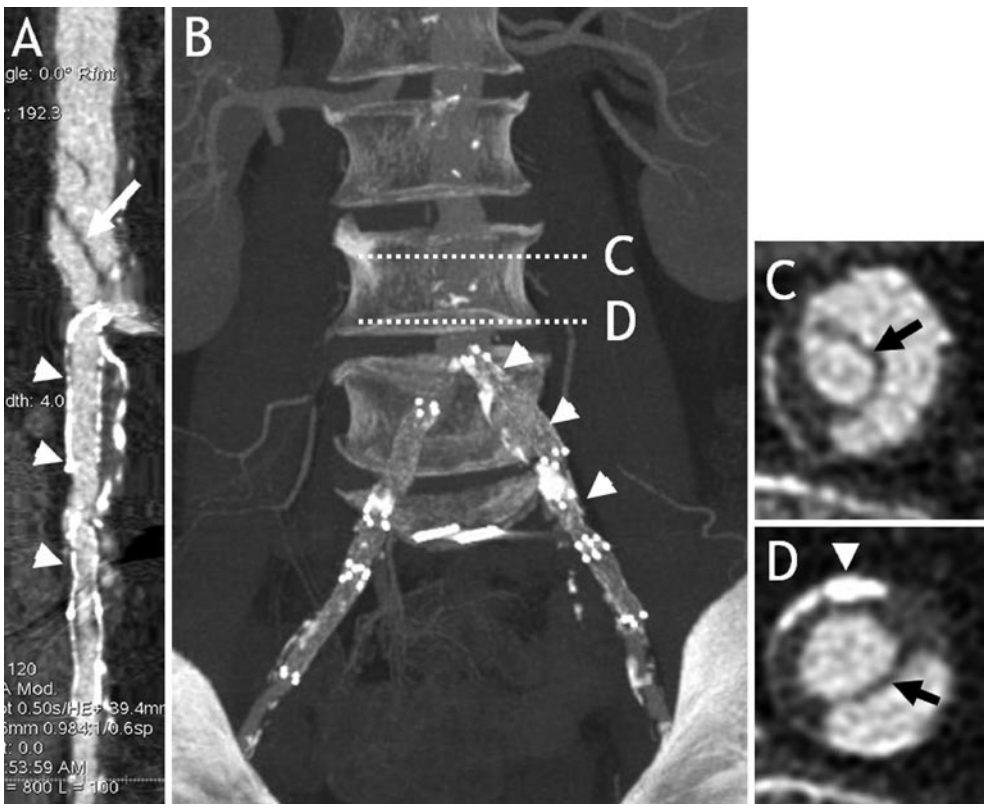

Figure 6.5. Dissection of the distal abdominal aorta. (**a**) A clear dissection flap is present (*white arrow*). Three stents are seen in the right and left iliac (*white arrowheads*) arteries. Curved multiplanar reformation (cMPR). (**b**) Frontal image showing the location of the left iliac stents (*white arrowheads*), and location of the cross-sections (axial cuts) shown in (**c**) and (**d**). (**c**) Cross-sectional image showing dissection (*black arrow*). (**d**) Cross-sectional image showing dissection (*black arrow*) with calcification within aortic wall (*white arrowhead*).

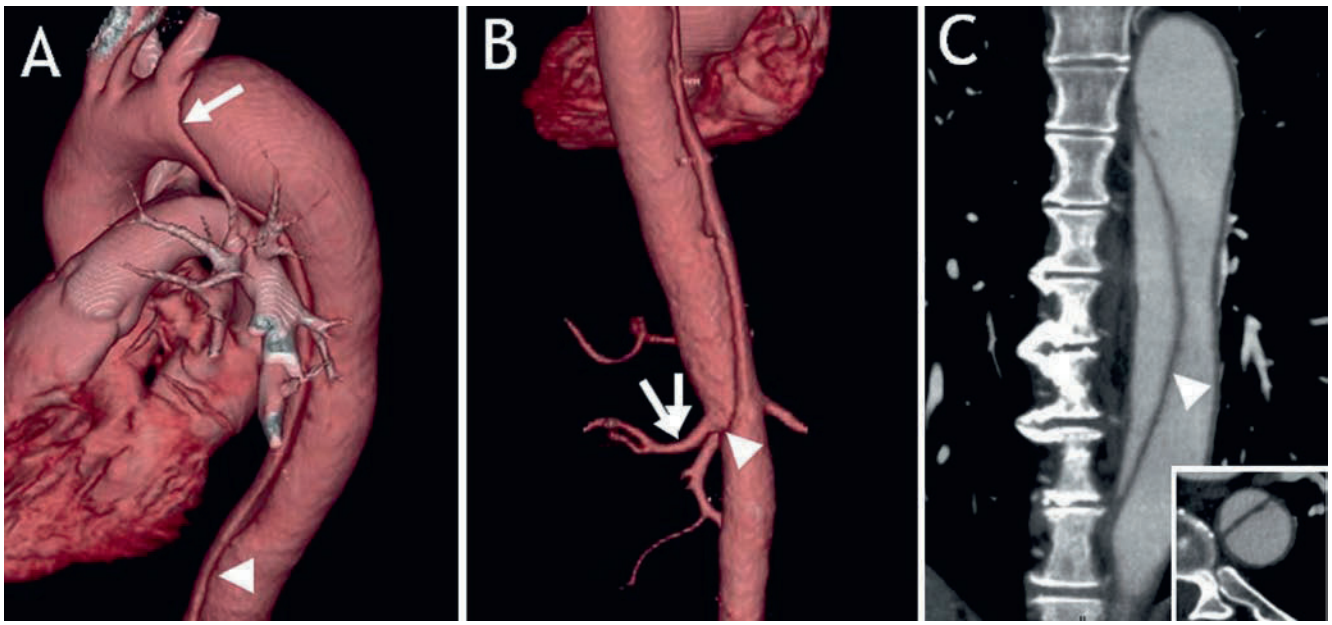

Figure 6.6 Type B aortic dissection. (**a**) The aortic dissection begins just distal to the origin of the left subclavian artery (*white arrow*) and extends into the abdominal aorta (*white arrowhead*). VR. (**b**) Dissection ends (*white arrowhead*) just inferior to the left renal artery (*white arrows*). Note this is a posterior projection, so the left renal artery is on the left side of the image. VR. (**c**) Maximum intensity projection (MIP) in a sagittal section through the dissection (*white arrowhead*) in the thoracic and abdominal aorta. The true and false lumens are clearly seen. Inset shows MIP axial cross section of dissection within the abdominal aorta.

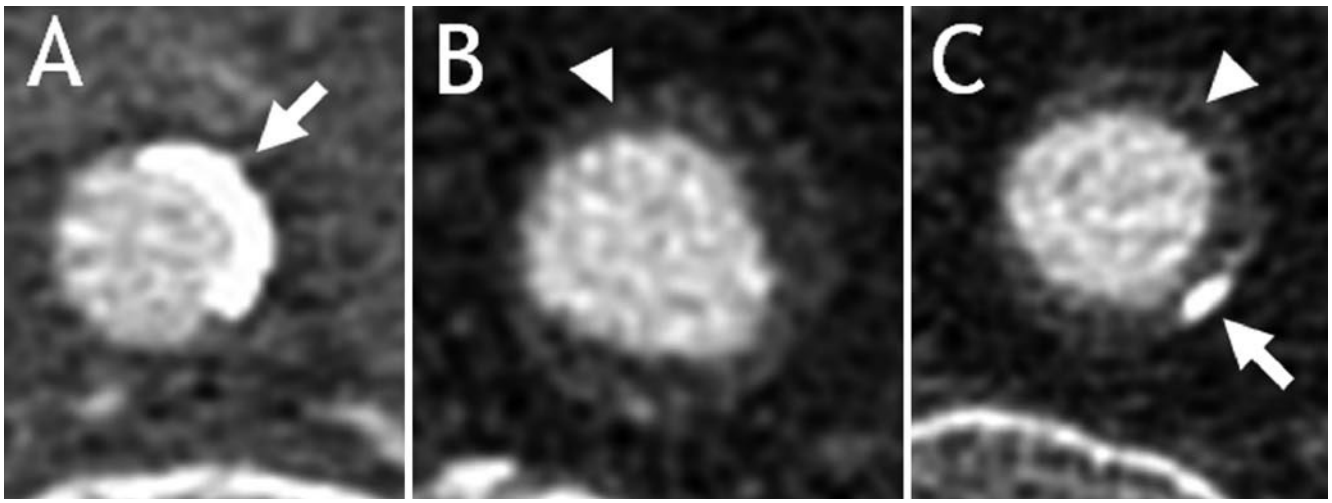

Figure 6.7. Aortic atherosclerosis. (**a**) Raw axial image showing calcification of the aortic wall (*white arrow*). (**b**) Raw axial image showing thickening of the aortic wall (*white arrowhead*). (**c**) Raw axial image showing both calcification of the aortic wall (*white arrow*) and thickening of the aortic wall (*white arrowhead*).

neck, Figure 6.8). In the setting of complete occlusion of the ICA, the external carotid artery may occasionally be mistaken for the ICA. The presence of near-occlusion of the ICA (the so-called angiographic "string sign") may result in a reduction in the caliber of the distal ICA relative to its expected size, and an increase in size of both the contralateral ICA and the ipsi-lateral ECA. The right ICA can be separated from the right ECA using a right anterior oblique or lateral projection. Similarly, the left ICA can be separated from the left ECA using a left anterior oblique or lateral projection.

To accurately evaluate the carotid arteries, a spacial position perpendicular to the carotid axis should be chosen. VR is useful as the initial postprocessing option to assess the general course of the carotid arteries and the shape and configuration of the aortic arch. Sagittal MIP with a slab thickness of 7–10 mm and multiplanar reconstruction (MRP) with a slice thickness of 1 mm should be applied to completely evaluate disease severity. Cross sectional images should be used to assess lumen diameters and stenosis severity [5]. MIP appears to be the most accurate reformatting technique to assess stenosis severity [6]. A step left

Figure 6.8. Normal left carotid artery. (**a**) Normal left carotid artery. The proximal common carotid artery is tortuous (*white arrow*), and there is no disease at the carotid bifurcation (*arrowhead*). The external carotid artery can be differentiated from the internal carotid artery because of its multiple branches (*curved arrow*). VR mode. (**b**) Maximum intensity projection (MIP) with a slice thickness of 7 mm in the same projection as shown in (**a**).

anterior oblique or left lateral, as opposed to an anterior, projection is useful to show the origins of the common carotid arteries (Figure 6.9). Although various window/level settings can be used based on operator preference, a setting of 700/200 HU will suffice in the majority of cases, and 1,100/200 HU can be used in the setting of significant calcification. Significant calcification often precludes the use of MIP formatting, and, in this setting, VR and axial raw data should be used.

Given that a large proportion of patients with carotid artery disease will be evaluated for potential carotid artery stenting, CT imaging should focus on assessment of: (1) stenosis severity using the NASCET criteria [7], (2) disease within the aortic arch and at the origin of the common carotid arteries, (3) size of common carotid artery at lesion location, (4) size of the distal internal carotid artery, and (5) the presence of contra-lateral disease (Table 6.3).

A recent meta-analysis found the sensitivity and specificity for CT angiography to detect severe carotid artery stenosis (>70%) to be 85% and 93%, respectively [8]. Visual estimation with CT angiography appears to be superior to caliper measurements [9]. CT angiography is also highly accurate in assessing carotid plaque morphology, particularly ulcerated plaques [10, 11].

Atherosclerosis can also involve the subclavian artery, commonly at its origin and therefore proximal to the origin of the internal thoracic arteries. CT imaging of the subclavian artery follows the same principles as outlined above for the carotid arteries. In patients being considered for endovascular treatment for subclavian artery stenosis, CT imaging can be useful to evaluate the reference vessel diameter and length of disease so that the appropriately sized stent can be chosen. For subclavian artery lesions that extend into the origin of the vertebral artery, endovascular treatment may pose significant risk because of compromise of the vertebral artery during stent placement and alternative forms of therapy (conservative vs. surgical) should be considered.

Carotid Artery Disease

To evaluate patients for possible carotid stenting, CT imaging should assess:

1. Stenosis severity (NASCET criteria).
2. Disease within the aortic arch and at the origin of the common carotid arteries.
3. Size of common carotid artery at lesion location.
4. Size of the distal internal carotid artery.
5. The presence of contra-lateral disease.

A window/level setting of 700/200 HU will suffice in the majority of cases, and 1,100/200 HU can be used in the setting of significant calcification.

VR and axial raw data can be useful in the setting of significant calcification.

Aortic Atherosclerosis

CT findings include thickening or raised lesions of the aortic wall and the presence of calcification.

Aortic Dissection

The main CT finding is an intimal flap that separates the true and false lumens.

CT imaging should assess:

1. Extent of the dissection (proximal entry and distal re-entry sites).
2. Involvement of adjacent branch vessels.
3. Potential compromise of the true lumen.

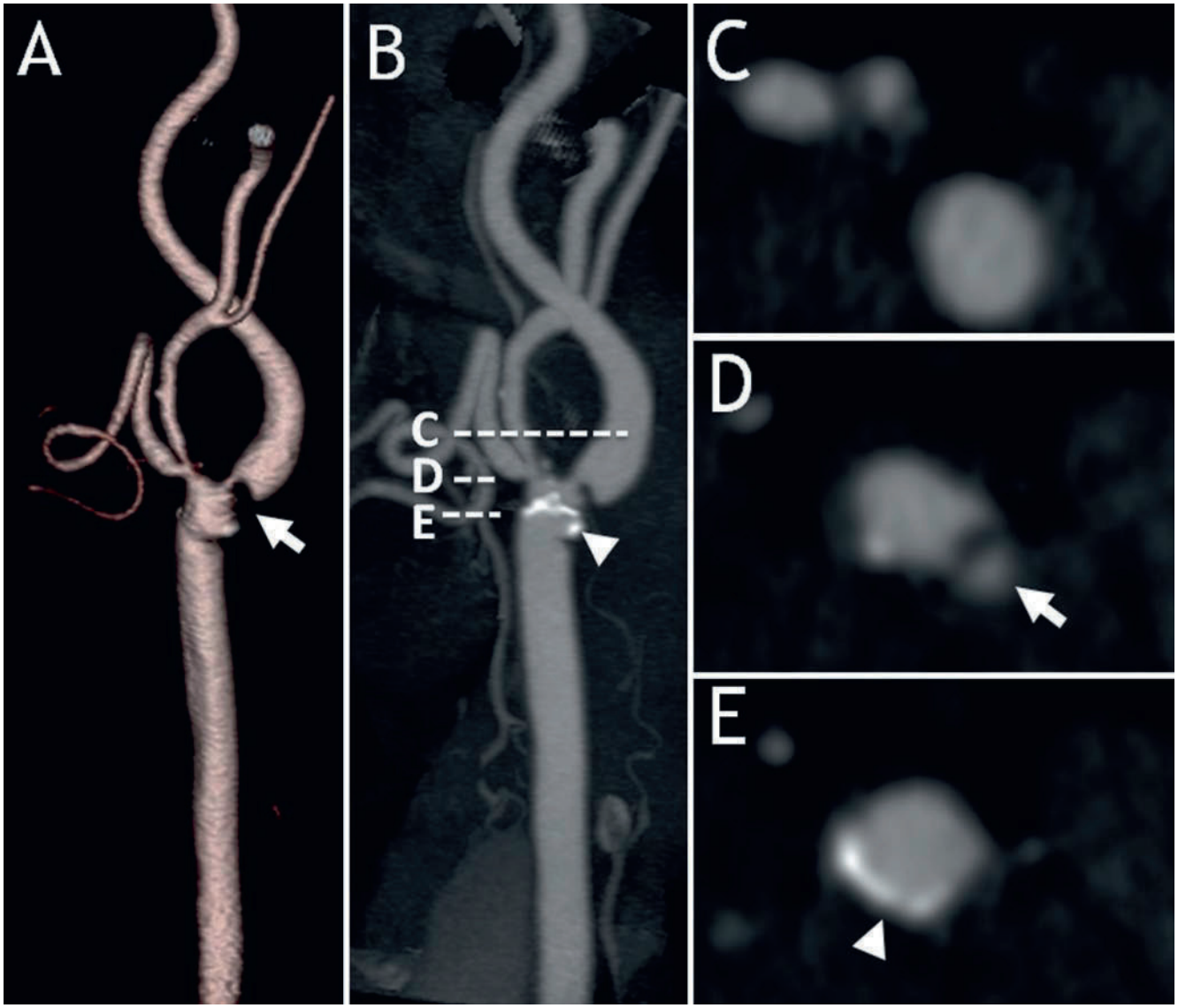

Figure 6.9. Severe left carotid artery disease. (**a**) VR mode showing severe disease of the proximal left internal carotid artery (*white arrow*), distal to the carotid artery bifurcation. (**b**) Maximum intensity projection (MIP) in the same projection as (**a**). Mild calcification within the distal common carotid artery (*white arrowhead*). Location of the cross sectional axial images shown in (**c–e**). (**c**) Cross sectional axial image of external and proximal internal carotid artery, distal to the area of stenosis. (**d**) Cross sectional axial image at the site of stenosis in the ostial internal carotid artery (*white arrow*). (**e**) Cross sectional axial image in the distal common carotid artery. *White arrowhead* shows mild calcification.

Table 6.3. Essential information to be obtained during CT imaging of carotid artery disease

	Comments
Stenosis severity	NASCET classification using the distal internal carotid artery as the reference segment to assess disease severity [7]
Disease within the aortic arch and origins of common carotid arteries	Placement of catheters and sheaths in diseased segments could result in embolic events to the central nervous system
Size of common carotid artery at lesion location	Useful for choosing correct size of endovascular stent
Size of distal internal carotid artery	Useful for choosing correct size of distal protection device

Imaging artifacts include insufficient contrast enhancement of the lumen, streak artifacts, peri-aortic structures, and congenital aortic diverticulum.

Aortic Aneurysm

CT imaging should focus on:

1. Proximal and distal extent of the aneurysm.
2. Size of the aneurysm: Axial CT images (raw data) should be the primary source to accurately size the aneurysm and obtain preoperative measurements for selecting the appropriate aortic stent graft.

Involvement of adjacent vessels:

1. Presence of thrombus within the aneurysm.
2. MIP provides images similar to those obtained with conventional angiography and is useful to visualize calcification and the relationship of the aneurysm to adjacent vessels.

3. VR provides an accurate anatomic representation of the aneurysm relative to adjacent vessels and helps to define vessel tortuosity.

References

1. Hobo R, Buth J. Secondary interventions following endovascular abdominal aortic aneurysm repair using current endografts. A EUROSTAR report. *J Vasc Surg*. 2006;43(5):896–902.
2. Batra P, Bigoni B, Manning J, et al. Pitfalls in the diagnosis of thoracic aortic dissection at CT angiography. *Radiographics*. 2000;20(2): 309–320.
3. Yamamoto H, Shavelle D, Takasu J, et al. Valvular and thoracic aortic calcium as a marker of the extent and severity of angiographic coronary artery disease. *Am Heart J*. 2003;146(1):153–159.
4. Wu MH, Chern MS, Chen LC, et al. Electron beam computed tomography evidence of aortic calcification as an independent determinant of coronary artery calcification. *J Chin Med Assoc*. 2006;69(9):409–414.
5. Lell M, Fellner C, Baum U, et al. Evaluation of carotid artery stenosis with multisection CT and MR imaging: influence of imaging modality and postprocessing. *AJNR Am J Neuroradiol*. 2007;28(1):104–110.
6. Sparacia G, Bencivinni F, Banco A, Sarno C, Bartolotta TV, Lagalla R. Imaging processing for CT angiography of the cervicocranial arteries: evaluation of reformatting technique. *Radiol Med (Torino)*. 2007;112(2):224–238.
7. Beneficial effect of carotid endarterectomy in symptomatic patients with high-grade carotid stenosis. North American Symptomatic Carotid Endarterectomy Trial Collaborators. *N Engl J Med*. 1991; 325(7):445–453.
8. Koelemay MJ, Nederkoorn PJ, Reitsma JB, Majoie CB. Systematic review of computed tomographic angiography for assessment of carotid artery disease. *Stroke*. 2004;35(10):2306–2312.
9. Waaifer A, Weber M, van Leeuwen MS, et al. Grading of carotid artery stenosis with multidetector-row CR angiography: visual estimation or caliper measurements? *Eur Radiol*. 2009;19(12):2809–2818.
10. Saba L, Sanfilippo R, Pirisi R, Pascalis L, Montisci R, Mallarini G. Multidetector-row CT angiography in the study of atherosclerotic carotid arteries. *Neuroradiology*. 2007;49(8):623–637.
11. Saba L, Caddeo G, Sanfilippo R, Montisci R, Mallarini G. CT and ultrasound in the study of ulcerated carotid plaque compared with surgical results: potentialities and advantages of multidetector row CT angiography. *AJNR Am J Neuroradiol*. 2007;28(6): 1061–1066.

Part III

CT Coronary Angiography

7

Methodology for CCTA Image Acquisition

Jerold S. Shinbane, Songshao Mao, and Matthew J. Budoff

Introduction

Cardiovascular computed tomographic angiography (CCTA) can assess cardiovascular pathology through visualization of gross anatomic abnormalities, characterization of tissue attenuation, and cardiac functional analysis. As cardiac structures are in constant motion, special attention to the methodology of image acquisition is essential to capturing high quality images during the most quiescent stage of cardiac and coronary artery motion. Successful imaging requires an understanding of the interplay of multiple motions, including the complexities of cardiac motion, motion related to variation in heart rate and rhythm, potential respiratory motion, potential patient movement, table motion, gantry rotation, and timing and movement of the intravenous contrast bolus through the structures of interest (Figure 7.1).

Optimization of image acquisition is achieved through localization of target structures, timing of scanning for capture of images during the segment of the R-R interval with relatively slow cardiac motion, and injection of contrast media to enhance opacification of structures throughout all slice levels. These techniques help to avoid or minimize motion artifacts and suboptimal opacification of structures of interest, which would make subsequent image reconstruction and diagnostic analysis a challenge. Imaging methodology must also focus on minimizing the exposure to radiation and the amount of intravenous contrast used. This chapter will focus on methods essential to acquisition of diagnostic images for the assessment of cardiovascular pathology.

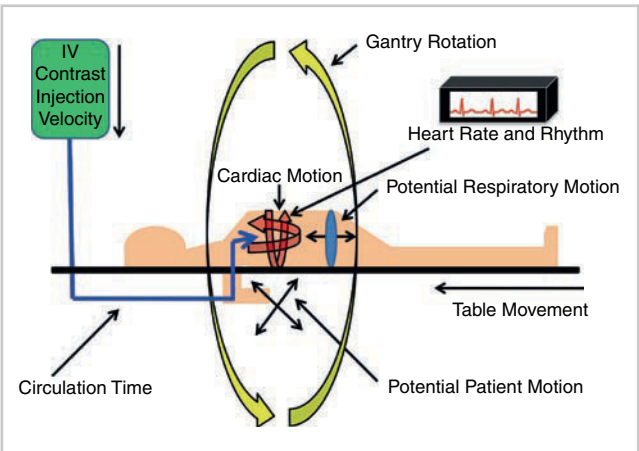

Figure 7.1. Schematic demonstrating multiple motion factors which must be accounted for during imaging, including the complexities of cardiac motion, motion related to variation in heart rate and rhythm, potential respiratory motion, potential patient movement, table motion, gantry rotation, and the movement of the intravenous contrast bolus to the structures of interest.

Image Acquisition Concepts

The ability to visualize the coronary vasculature is due to advances in spatial and temporal resolution of scanning technology. There are multiple factors that affect spatial and temporal resolution, many of which are interdependent. The goal of image acquisition is to visualize the target structures in their entirety while limiting the field of view to exclude additional structures, as a larger field of view will increase radiation exposure and may diminish image quality. The field of view defines the imaging boundaries important to ensuring visualization of structures of interest. As voxels are assigned to a particular field of view, a smaller field of view leads to greater spatial resolution. Structures are delineated by Hounsfield units (HU). Each voxel is assigned a unit of attenuation based on a scale, with the attenuation values of different substances represented by a different HU values [1]. Representative HU values include: air 1,000, fat 50–100, water 0, muscle 10–40, contrast 80–300, and calcium 130–1,500.

Scanner

Conceptually, multidetector computed tomography (MDCT) systems work using similar principles, but vary in regard to specific components and features. A MDCT

system has an X-ray tube/collimator and detector/collimator housed in a gantry capable of extremely rapid rotation. The X-ray tube provides radiation energy quantified through tube current (mAs) and tube voltage (kVP). Multidetector scanners have multiple rows of detectors arranged in a variety of arrays with the goal of covering a specified volume during each gantry rotation. Advances in detector number and arrangement have lead to increases in the volume of coverage per rotation, with imaging of the entire heart now achievable within one cardiac cycle [2].

The relationship between table movement, gantry rotation speed and beam collimation defines the degree volume coverage per rotation, as well as the degree of overlap between rotations. The concept of "pitch" quantifies this relationship, as pitch relates to coverage obtained by the X-ray beam, through beam width and table movement, during one rotation of the gantry. The pitch therefore defines the amount of overlap of the acquired data. Overlapping images allow for oversampling, permitting multisector image reconstruction, but also lead to greater radiation exposure. With a pitch value of less than 1, there is overlap between volumes of coverage. The definition of pitch has evolved with advancement of scanner technologies, and various equations have been proposed depending on the specific type of scanner [3]. Newer systems enable thinner slice thickness and collimation, allowing for an even lower pitch resulting in more images, thinner reconstruction intervals, and better visualization of the coronary anatomy. Systems which provide enough *z*-axis coverage for whole heart imaging in one gantry rotation eliminate the variable of pitch, by allowing for imaging without table movement [2].

ECG Triggering

ECG triggering is essential to minimize the effects of cardiac motion on image acquisition. Cardiac and coronary motion during a single cardiac cycle is extremely complex and can be analyzed in the context of the *x*, *y*, and *z* axis planes. Left ventricular contraction and relaxation are the main source of cardiac motion. Multiple types of cardiac motion have been noted including: inward or outward motion of the endocardium with systole and diastole, rotation, torsion or wringing, translocation, and "accordion-like" base to apex motion [4]. There is greater *x-y* direction motion at the mid-portion of the left ventricle and greater *z* direction motion at the base of the heart [5]. Left ventricular endocardial maximal motion speed has been reported at 41–100 mm/s [6, 7].

Specific motion issues also relate to individual coronary arteries. Since the right coronary artery is further from the center of the left ventricle than the left coronary artery, this artery exhibits faster motion, especially in its mid-section [8]. Atrial systole and diastole are important factors causing motion of the right coronary artery and the left circumflex cornary artery [9]. The right coronary artery has 50 mm/s motion speed by angiography [10]. The left main and proximal portion of left anterior descending coronary artery have greater *z* plane motion, and therefore *z*-axis motion can induces left main motion abnormalities [5, 7].

Given the imaging challenges caused by cardiac motion, appropriate collimation size and acquisition speed are factors important to minimizing CCTA motion artifact. Since the acquisition speed is insufficient to completely freeze heart motion, cardiac triggering is essential in order to capture and process images at times of minimal cardiac and coronary artery motion speed in order to avoid blurring of images.

Based on ventricular and atrial contraction and relaxation, there are six phases in a cardiac cycle (R-R interval). These include: isovolumic contraction time, ejection time, isovolumic relaxation time, left ventricular rapid filling, diatasis, and atrial contraction time. During ventricular systole, the motion of right coronary artery and left circumflex mid-segment are in an anterior and inner direction, which reverses in diastole. At end isovolemic contraction and relaxation, the motion speed is close zero, but the time interval for imaging is very short.

There are three relatively low speed motion segments: isovolumic contraction, isovolumic relaxation, and diastasis. The isovolumic contraction time (after the R wave) and relaxation time (after the T wave) are approximately 50–140 ms. Diastasis is the other slower motion segment, but the length is more variable following heart rate changes. In patient with heart rates of greater than 100–110 bpm, diastasis is minimal [11]. The diastasis segment is the optimal scan time in patient with a lower heart rate, and is the most common time period for assessment in patients with regular and controlled heart rates.

With image acquisition, an ECG signal is simultaneously recorded with the raw data set. Two ECG gating techniques are used for CCTA imaging, retrospective and prospective triggering. With retrospective ECG gating, images are acquired throughout the cardiac cycle (Figure 7.2 and 7.3) [12]. The strength of this approach is that images can be reconstructed using the most optimal timing for each coronary artery or arterial segment after image acquisition has occurred. Additionally, acquisition of images throughout the cardiac cycle allows for volumetric assessment of cardiac function. The major drawback of this approach is that radiation exposure is significantly greater than with a prospective ECG gated approach. Retrospective gating with current tube modulation leads to a significant decrease in radiation by decreasing radiation exposure during the systolic phase of the cardiac cycle [13].

With prospective triggering, images are obtained at a set percentage of the R-R interval. The advantage of this technique is the limitation to radiation exposure [14]. The disadvantage relates to the limited dataset obtained. If the images obtained demonstrate significant motion artifact, there are no other images to reconstruct. Given the variability of heart rate with arrhythmias, prospective gating

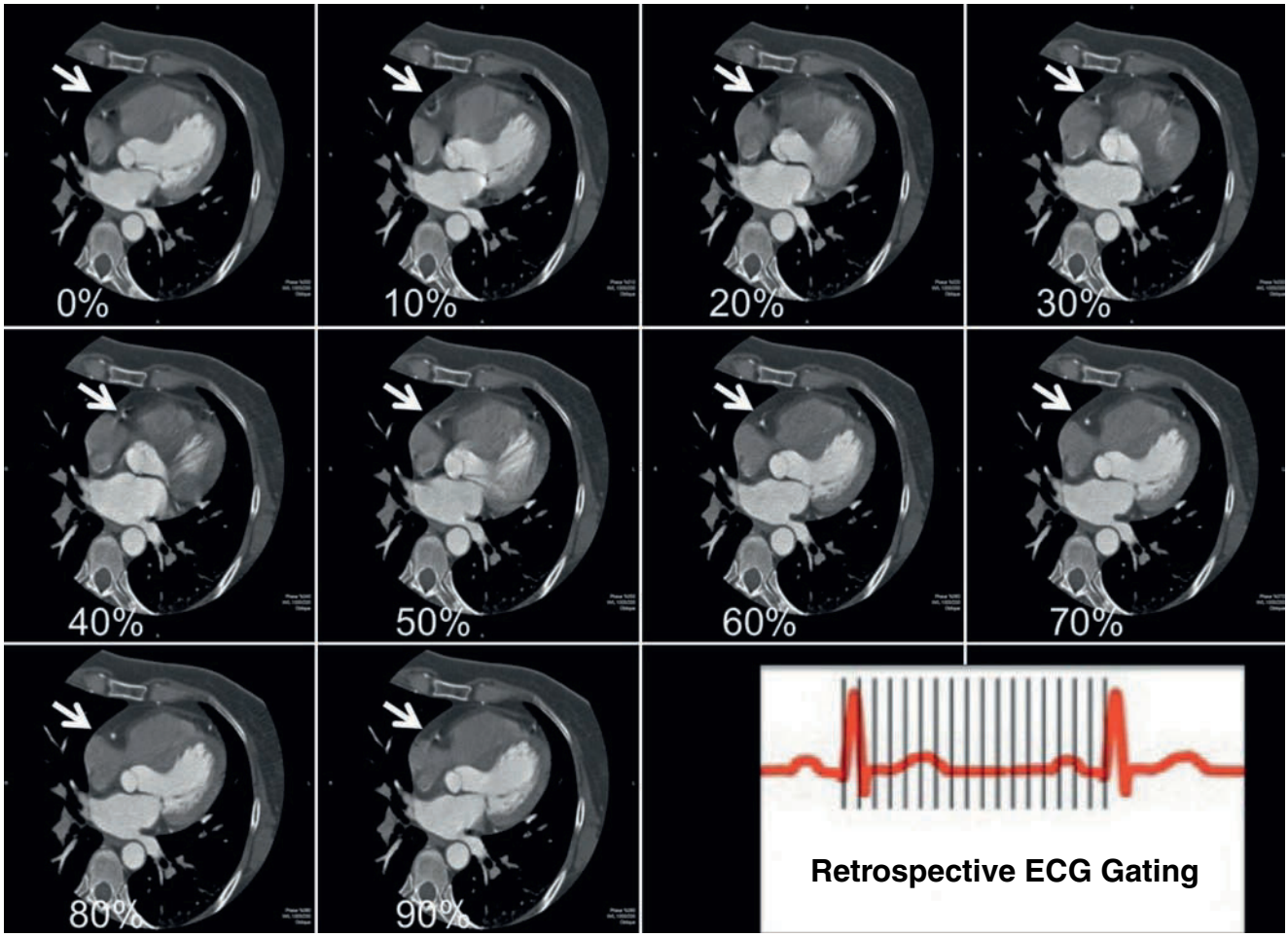

Figure 7.2. Demonstration of motion of the right coronary artery at serial decile percentages of the R-R interval during retrospective gating. The most optimal R-R percentage is 70%, as blurring of the right coronary artery is seen at other phases.

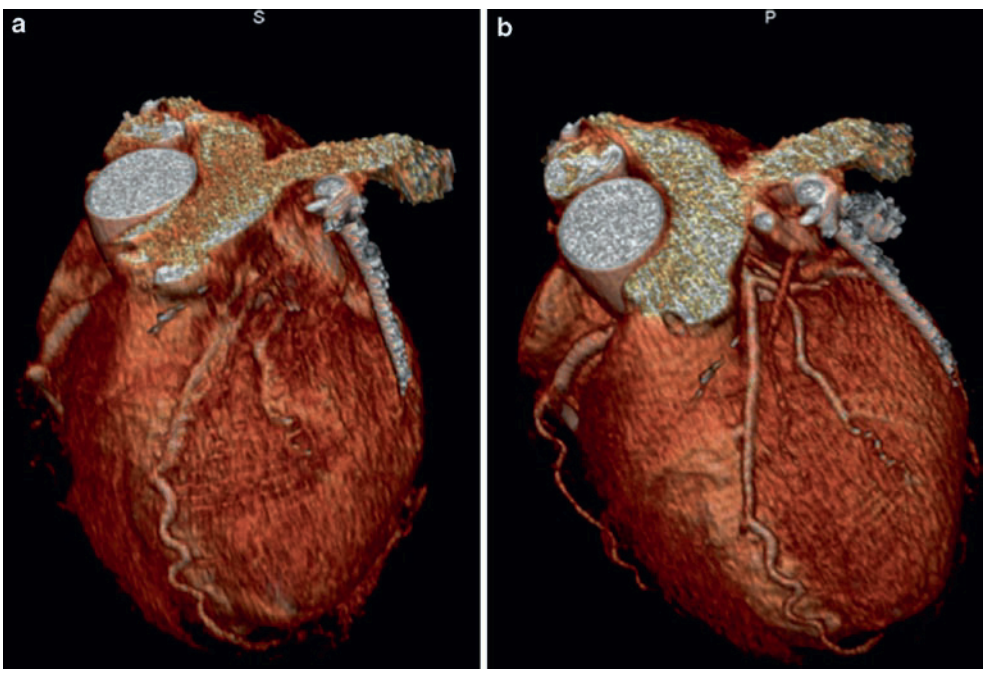

Figure 7.3. 3-D reconstructions of the LAD at different phases of the R-R interval, demonstrating reconstruction at a suboptimal phase and an optimal phase for artery visualization. (**a**) Reconstruction at 30% of the R-R interval. (**b**) Reconstruction at 70% of the R-R interval.

can be problematic with significant atrial or ventricular ectopy or atrial fibrillation.

In regard to variability of heart rate or rhythm, any change in heart rate or rhythm can alter chamber size, and therefore change of the spatial location of target structures in axial or 3-D images, even if the individual axial image is not blurred. All patients have some variability in heart rate, even those without atrial or ventricular ectopy. Scanning protocols exist which can withold imaging during short R-R intervals during image acquisition [15]. Post processing analysis includes editing and deletion of images from ectopic beats and analysis of mid-diastolic phases of the R-R interval with an absolute rather than relative time from the preceding R wave when the R-R interval is variable.

Heart rate control is essential for image optimization. Premedication with beta blockers, or calcium channel blockers when beta blockers are contrainidcated, is used to achieve sinus rates of 60 beats/min using most standard MDCT systems. With dual source MDCT systems, imaging can be performed with heart rates in a higher range [16,17]. Nitroglycerin is given sublingually prior to scanning to maximally dilate coronary arteries. Since there may be catecholamine stimulation with breath hold, the sound of the scanner, nitroglycerin administration, and the sensation of contrast administration, a resting sinus rate that appears to be controlled without medications prior to scanning may still increase during scanning. Special attention to monitoring of heart rate and blood pressure is important, as in some circumstances patients may not be able to tolerate medications for heart rate control and dilation of coronary arteries.

Breath hold is essential to limit motion of structures due to respiration during image acquisition. Breath hold times have decreased significantly with advances in technology and allow for cardiac imaging to be completed during a single breath hold. There is some controversy as to the optimal phase of respiration for breath hold. Regardless of the phase chosen in an individual lab, it is important to practice breath hold commands and exercises prior to the scan. As an end-inspiratory breath hold will move thoracic structures more caudally than an end-expiratory breath hold, consistent breath hold instructions need to be given for preview images and actual scans.

Contrast Media Injection

The aim of contrast media injection is to enhance the contrast differentiation between target structure and surrounding tissues, by increasing the CT Hounsfield Units (CT HU) of the structure of interest. Ideally, an injection protocol will achieve optimal enhancement with uniformity of contrast enhancement at all slice levels using as small a dose of contrast medium as possible. Important factors to consider in regard to contrast media injection are circulation time and injection methodology.

Assessment of the circulation time is important to timing the acquisition of images, and is defined as the time from contrast injection to the optimal enhancement of target structures. This sequence typically consists of repetitively imaging a single slice using low radiation serial scanning of the same slice to obtain the peak enhancement time through time density curve analysis (Figure 7.4 and 7.5). With CCTA, scans are obtained at the level of the takeoff of the left main coronary artery or descending aorta, to create a time–density curve to assess the time to peak opacification. The measured transit time is then used as the delay time from the start of the contrast injection to the start of imaging for the CCTA. It is important to use the same injection rate for the circulation time as for the subsequent CCTA study.

Another contrast timing method utilizes an automatic bolus-triggering technique. With this method, angiography imaging is automatically activated when the CT HU reaches a prespecified HU value [18]. Circulation times vary based on the cardiac output. Patients with low output states have increased times and high output states with decreased times. Many factors influence circulation time, including venous anatomy, cardiac output, and underlying cardiac and valvular function and therefore must be individually determined.

Low osmolar nonionic contrast media contrast medium is usually administered via an 18-gauge needle in the antecubital vein. Optimal enhancement depends on the contrast media dose and injection rate. The goal is to maintain the same level of vascular enhancement throughout image acquisition. The dose of contrast media is dependent on multiple factors, such as patient size, scan time, and desired enhancement level (CT HU). Multiphase contrast injectors with preset volumes and injection velocities are used to maintain uniformity of contrast enhancement throughout the study. A first injection stage with a high velocity, often 5 mL/s, is followed by saline injection using a multiphase injector. The use of a saline bolus after contrast injection moves the residual contrast in the intravenous tubing and arm veins into the heart and coronary vasculature. The timing of the saline bolus is important, as in some studies clearance of the venous circulation and right heart structures can help with visualization of arterial structures, while in other studies, these structures are important to analysis. A middle phase with diluted contrast can also be utilized for some opacification of right heart and venous structures. Specific injection protocols may be necessary for certain specialized indications including congenital heart disease.

Preview, Calcium, and Contrast Scans

CCTA is performed in the following sequence: planar scout images, a noncontrast coronary artery calcium scan, a timing scan for assessment of the circulation time, and a contrast scan. Planar scout images are obtained in order to define the most cranial and caudal scanning levels (z-axis) of the structures of interest. The scout images are obtained in anteroposterior and lateral views and aligned to the

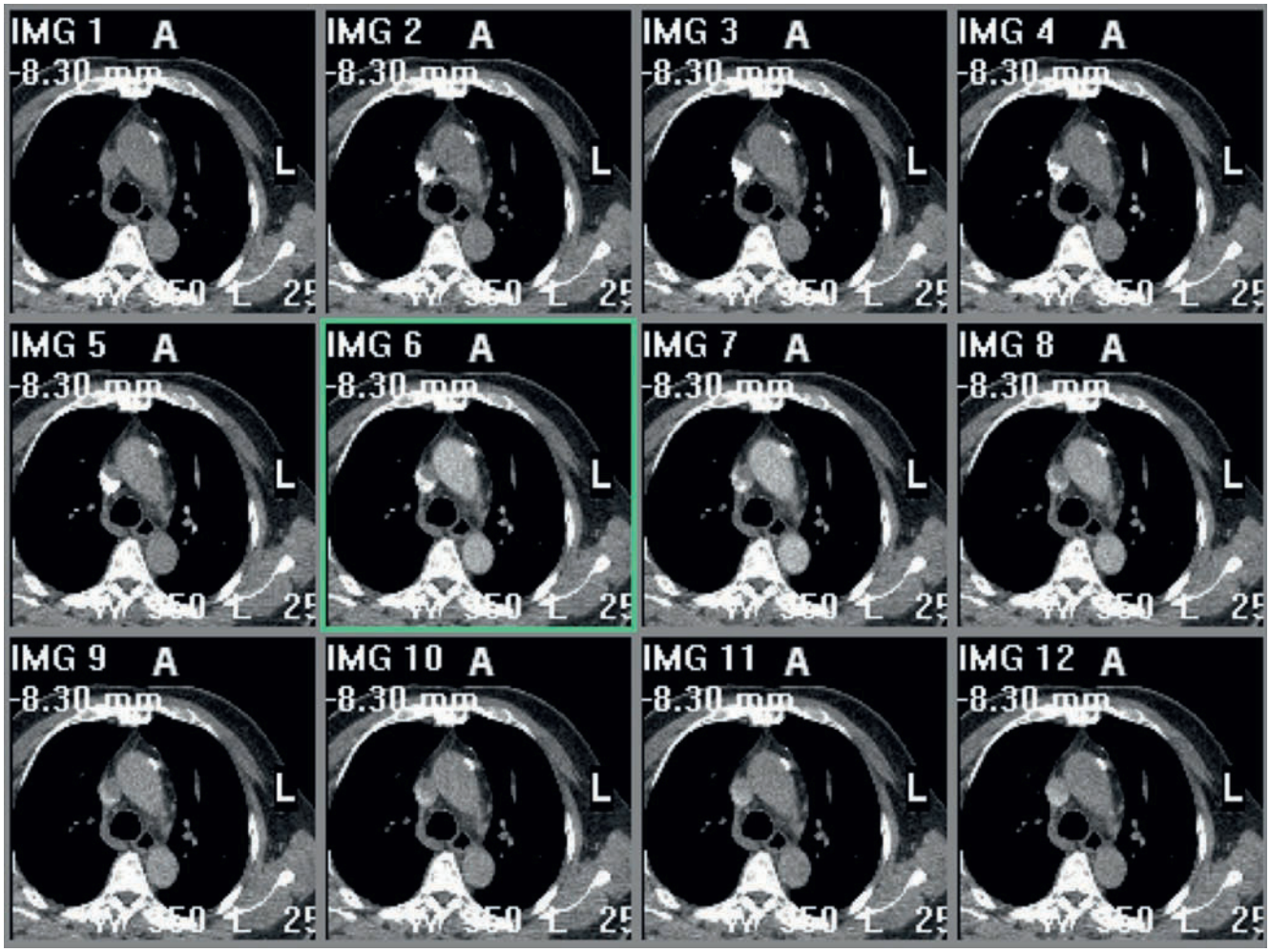

Figure 7.4. Serial axial images of the target slice demonstrating opacification for determination of the circulation time.

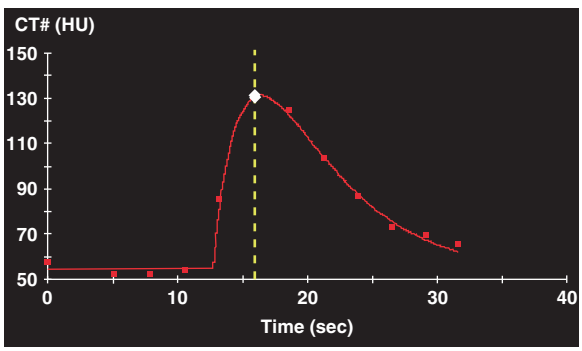

Figure 7.5. Graph of CT Hounsfield Units vs. time, demonstrating the time to maximal opacification of the region of interest.

patient by a laser system. The scan volume is selected with the structures of interest placed within the center of the scanning volume. Important landmarks can be identified including the left atrial appendage, which is usually the most cranial structure of the heart, and the ventricular apex, which is the most caudal structure. Although the carina had served as a marker to localize the most cranial aspect of the heart, the distance from carina to left main coronary artery is extremely variable [19]. Also, the left anterior descending coronary artery can course cranial to the left main coronary artery (Figure 7.6). For coronary artery imaging, scanning 10 mm cranial to the left main coronary artery and 10 mm caudal to the apex is subsequently performed with CCTA. In patients with coronary artery bypass grafts, the starting point is the top of the aortic arch or 10 mm higher than the surgical metal clips. The mid level of the right pulmonary artery can also be used as the beginning of the scan level, if it can be defined in preview images.

After the scout images, a calcium scan is performed (Figure 7.7). This is a high resolution noncontrast cardiac-gated study which provides important prognostic information regarding future cardiovascular risk. For the calcium scan, the 2-D axial images are analyzed with the identification of calcium either using manual or automated methods, with quantification of calcium score based on identification of HU units with an attenuation of at least 130 HU in the areas of identified calcium. There are two major methods of quantifying coronary artery calcium, the Agatston score and volumetric analysis. The Agatston score

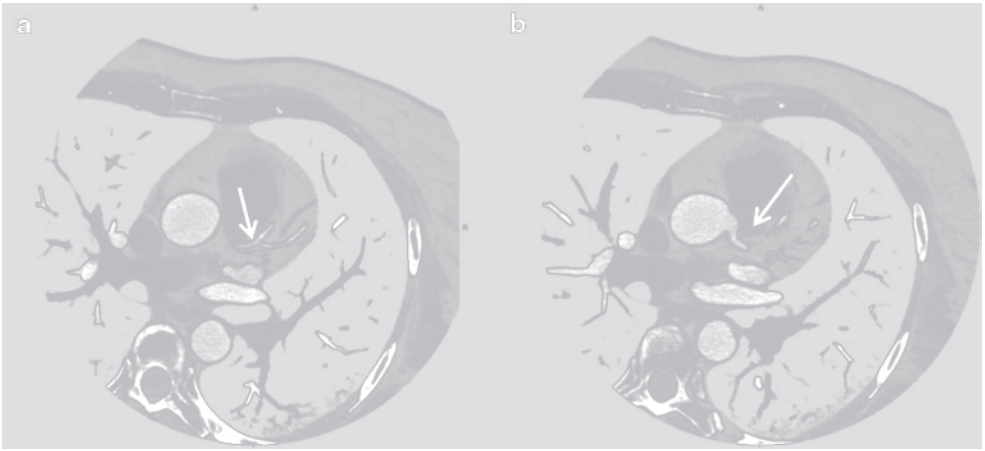

Figure 7.6. Axial views (cranial to caudal) showing the left anterior descending artery (**a**) (*arrow*) coursing cranial to the takeoff off the left main coronary artery (**b**) (*arrow*). If the cranial limit of the field of view were at the level of the left main, the left anterior descending could be out of the imaging field.

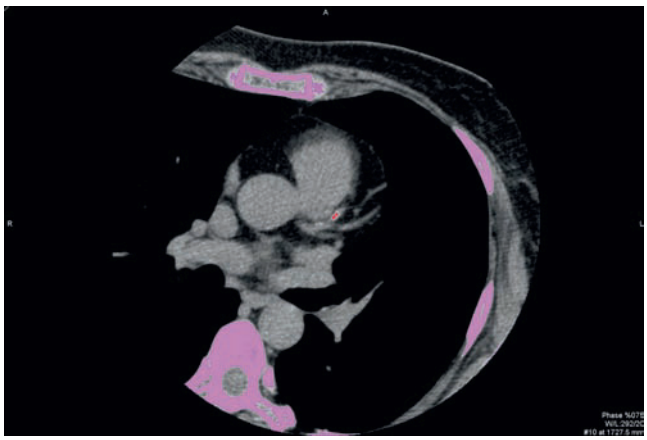

Figure 7.7. Coronary artery calcium score axial image showing a calcification of the left anterior descending coronary artery.

is based on the plaque number, and plaque area times a coefficient based on the peak HU units in the plaque [20]. Calcium volume score describes a volumetric analysis of calcium with calculation based on volumetric reconstruction and is more reproducible on serial study [21]. The calcium score is a marker of plaque burden and is an independent risk factor for coronary artery disease beyond traditional risk factors [22, 23].

The calcium scan is useful to the planning, performance, and interpretation of the CCTA. Assessment of the images can be used to ensure that there is complete coverage of the coronary anatomy in the image set prior to contrast angiography, as well as to determine the minimum volume to be covered to minimize radiation exposure [24]. The degree of coronary calcification may prohibit the accurate assessment of coronary artery stenoses.

The calcium score as well as the calcium distribution should be assessed prior to the performance of the CCTA to determine whether the contrast study should be performed. Different imaging centers use various cutoffs for the performance of CCTA in the setting of a significantly elevated calcium score, with some center using >500 or >1,000. It is important though to have an understanding of the specific goal of an individual study, as depending on the question asked and the location of calcium, some studies may still be performed in settings of an elevated calcium score. For example, in cases where the location and patency of coronary artery bypass grafts are the clinical questions, calcium in the native coronary arteries may still not necessarily prohibit the study from being performed. In addition to traditional cardiac risk factors, knowledge of the calcium score is helpful in assessing the pretest probability of coronary artery disease when interpreting the contrast angiography images.

After performance of the calcium scan, a contrast angiography study is performed, requiring the administration of iodinated contrast timed to enhance the structures of interest. This may vary by the type of study, with some studies performed specifically for assessment of coronary artery anatomy, while others are performed for additional assessment of thoracic vasculature, such as in the case of congenital heart disease.

Relation of Image Acquisition to Image Analysis

Image reconstruction is dependent on image acquisition, as the reconstructed images are only as good as the acquired data. The raw datasets are imported to workstations with software allowing the analysis of images in multiple 2-D and 3-D formats. Before reconstruction, there needs to be assessment of the 2-D images for adequacy of the dataset. The 2-D images are reviewed to assess whether the structures of interest have been visualized in their entirety and adequately opacified by contrast. For coronary arterial studies, assessment for the complete visualization of the coronary arterial system is necessary. The 2-D images must also be analyzed for the degree of contrast uniformity between slices, as a decrease in contrast in the distal vessels can appear as stenoses. Adequate and uniform enhancement of the distal aorta can be helpful in ensuring that distal coronary arteries have been adequately visualized.

Interpretation of CCTA requires reconstruction and analysis of multiple 2-D and 3-D formats so that findings can be confirmed on multiple views and artifacts related to image acquisition can be identified. Image reconstruction allows a 3-D understanding of cardiovascular anatomy from large vessel to small vessel. The serial axial 2-D images are reconstructed into a 3-D data cube with subsequent use of software to edit and analyze cardiovascular structure. Workstation software has dramatically reduced the time for image editing and reconstruction. Systematic reconstruction, serial automated editing, and analysis of this data cube allows one to glean information important to characterization of cardiovascular structures and relationship between structures essential to clinical diagnosis and planning and facilitation of procedures. These reconstructions include: assessment of thoracic structures in relation to skeletal structures, relation of large vessel vasculature and structures, cardiac chambers, valves, and coronary vasculature (Figure 7.8).

Reconstruction of coronary artery anatomy requires assessment of the phase of the cardiac cycle during which an artery or arterial segment is most quiescent. Retrospectively gated axial images can be reconstructed at different diastolic phases of the cardiac cycle and assessed for the most optimal images regarding minimizing cardiac motion (Figures. 7.2 and 7.3). As the optimal phase of the cardiac cycle may vary by artery and arterial segment, different arteries or segments may need to be analyzed using multiple modalities. Once the correct phase or phases have been chosen, 2-D images can be rapidly formatted in axial, sagittal, and coronal planes. Subsequent analysis is performed primarily from axial images with additional analysis with multiple modalities of image reconstruction (Figure 7.9a–g). Functional analysis for retrospectively gated scans can be formatted and assessed in standard echo views (Figure 7.10).

Although the 3-D reconstructed images are both aesthetic and intuitive regarding orientation, it is essential to recognize that the process of reconstruction has limitations. It is important to remember that the 2-D views provide an entire dataset whereas the 3-D techniques lead to loss of data and potential artifacts that adversely affect interpretation of images. Given the limitations of reconstruction techniques, it is essential to continually reference back to the 2-D images and view potential findings using multiple types of reconstructions before making a diagnosis.

There are many factors related to image acquisition that may affect image reconstruction and analysis. With volume rendering, pixels are assigned HU depending on their attenuation. With automated editing, pixels below a certain HU cutoff (lower threshold 80–100 HU) are edited out. Volume rendering and editing software allows creation of 3-D image with structures removed to adequately visualize structures of interest, but involves potential loss of data through over-editing of structures. If over-edited, the coronary arteries can appear as though stenoses are present.

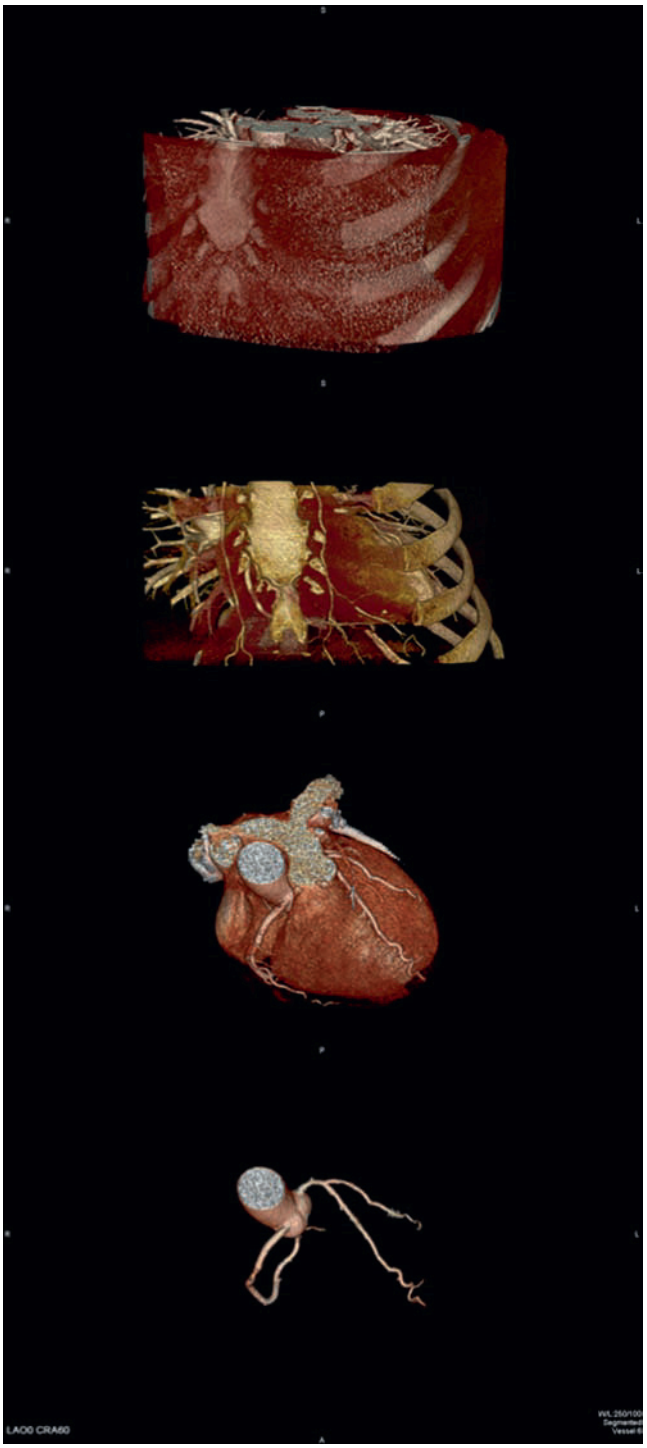

Figure 7.8. Reconstructions of thoracic structures in relation to skeletal structures, relation of large vessel vasculature and structures, cardiac chambers, valves, and coronary vasculature.

Construction of 3-D images from 2-D image sets with cardiac, respiratory, or patient motion between slices can lead to artifactually discontinuous arterial segments that could be misinterpreted as stenoses. Lack of uniformity of contrast enhancement on serial slices may also result in the artifactual appearance of stenoses. If only viewed on 3-D images, myocardial bridging can be misinterpreted as obstructive coronary artery disease.

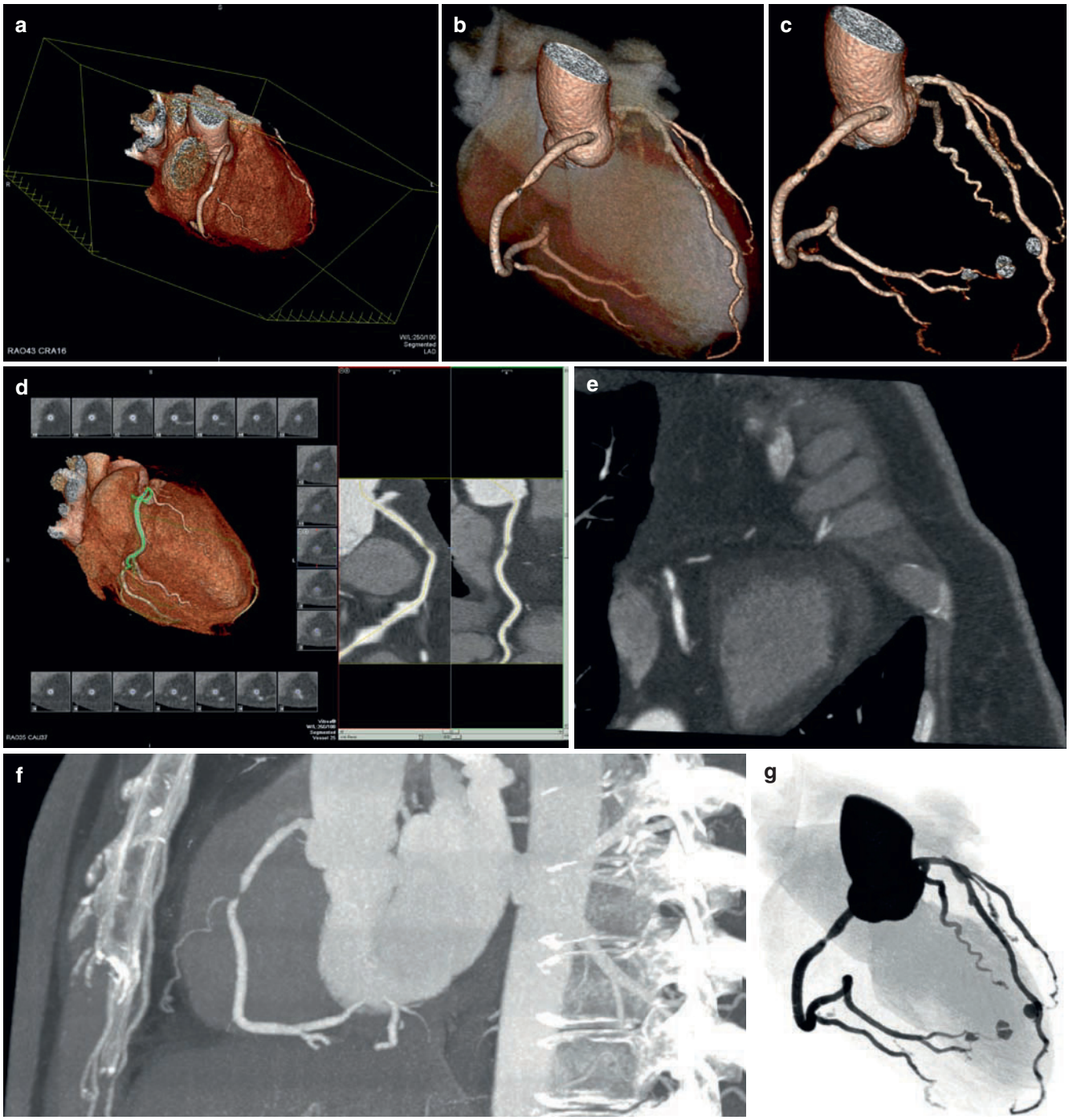

Figure 7.9. A significant right coronary artery noncalcified stenosis is shown using multiple reconstruction modalities. Multiple CCTA angiography views are demonstrated including (**a**) 3-D volume rendered view of the heart and coronary arteries; (**b**) 3-D volume rendered view of the heart and coronary arteries with semi- transparent cardiac background; (**c**) 3-D volume rendered view of only the coronary arteries; (**d**) Curved multiplanar reformatted view; (**e**) Double oblique reformat; (**f**) Sagittal view with a thick maximum intensity projection; (**g**) Cardiac catheterization angiography emulation.

Partial volume effects may limit reconstruction and analysis. The goal of scanning is to acquire isotropic data, where the spatial resolution is equal in the x, y, and z axes, allowing for accurate images with multiplane reconstructions [25]. As spatial resolution in the z-axis may not be truly isotropic, some volume averaging of data may with only a portion of the depth of the image being represented as present throughout the dataset.

Calcified plaques may also limit reconstruction and analysis of images. The purpose of contrast enhanced studies is to increase contrast between coronary vessel lumen and surrounding tissues. Greater lumen enhancement (represented by increased CT HU) will create greater contrast between the vessel lumen and noncalcified vessel wall, which is especially important for visualization of small vessels. Luminal enhancement though,

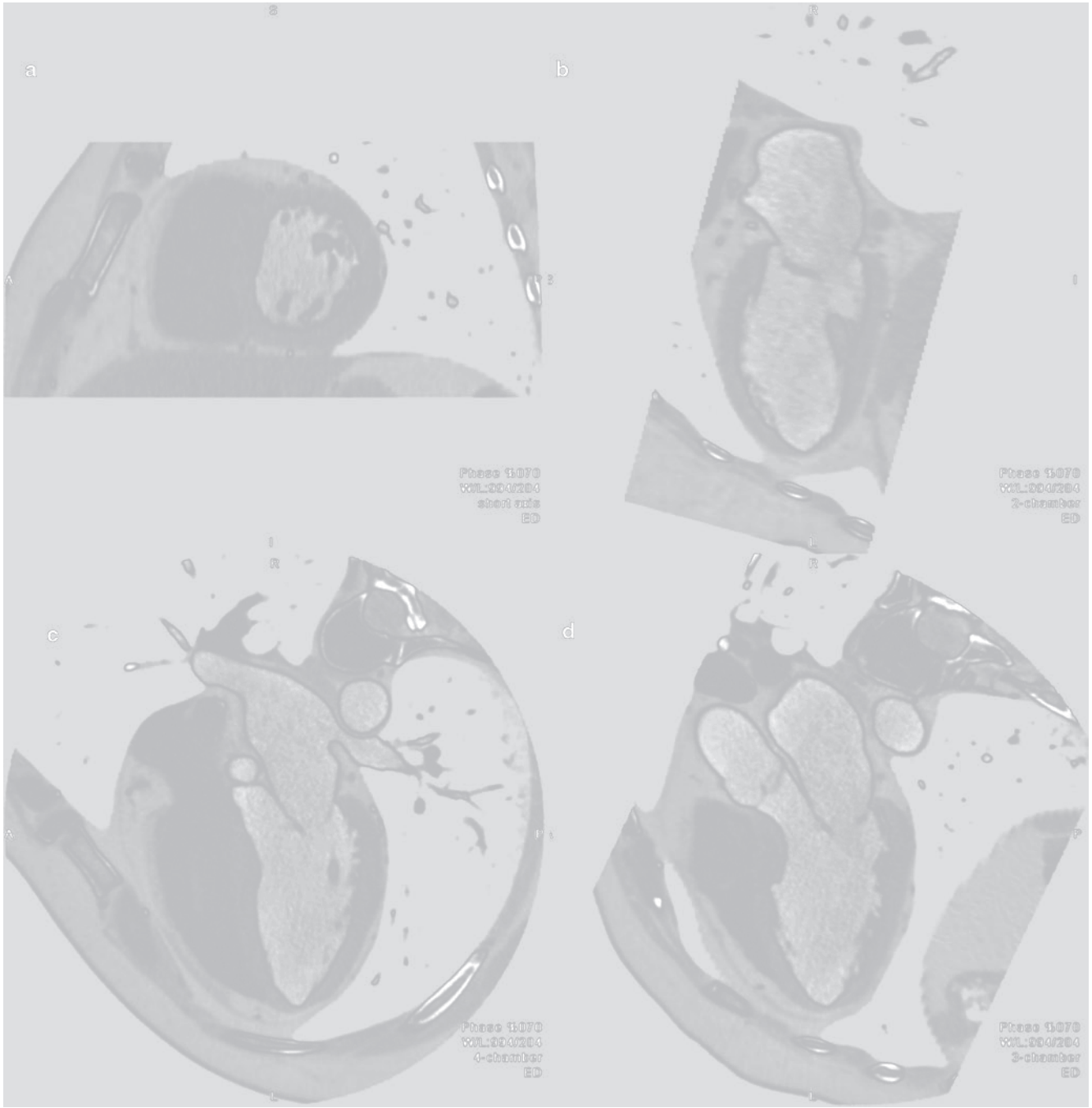

Figure 7.10. Functional views in standard echo planes. (**a**) Short axis view; (**b**) 2 chamber view; (**c**) 4 chamber view; (**d**) 3 chamber view.

will decrease the contrast between enhanced vessel lumen and calcified plaques.

Other reconstruction and viewing modalites are useful for analysis of images that are problematic due to issues related to image acquisition [26]. Maximal intensity projections demonstrate the maximal density point at each point in a 3-D volume. Conceptually, this provides the ability to move through the 3-D data cube with a thick slab focused on the maximum intensity of the images in the slab. The modality provides for assessment of small and distal vessels and is helpful for differentiating calcium, contrast, and metal in the coronary arteries and avoids issues of volume averaging of structures. As editing is not involved with this modality, there will be overlap of structures as one moves through the dataset.

Multiplanar curved reformatting allows for in plane analysis of an individual vessel (Figure 7.11) [27]. A reconstruction is performed orthogonal to vessel centerline and does not require editing. Vessels can be analyzed in a 360° rotation allowing for assessment of eccentricity of plaque in relation to the vessel lumen. The technique requires accurate vessel tracking and determination of the centerline

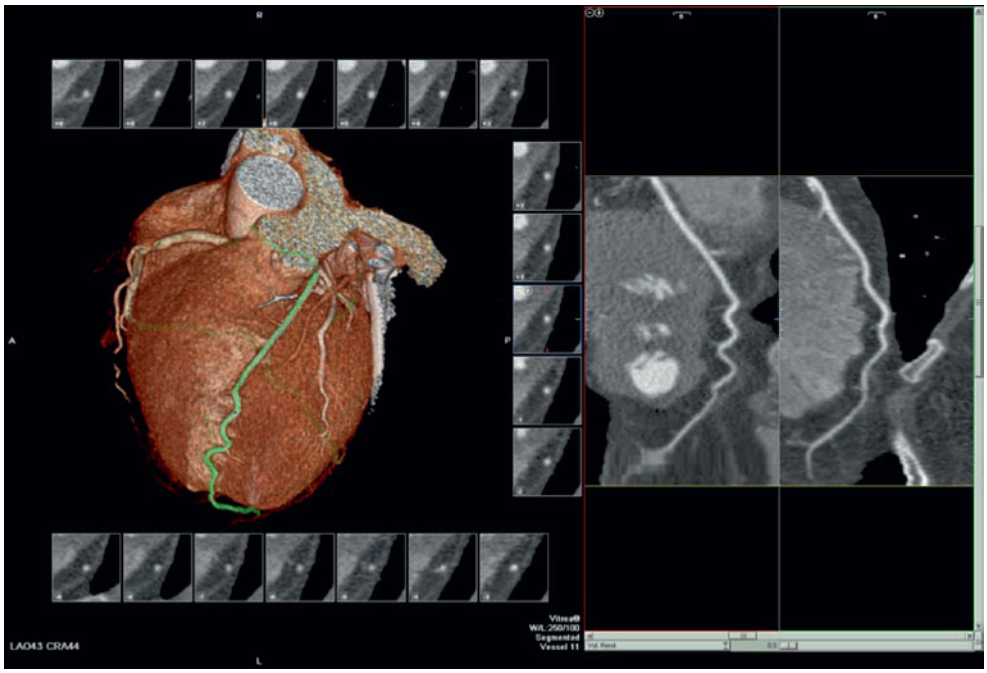

Figure 7.11. Curved multiplanar reformation of the left anterior descending coronary artery, allowing in plane analysis of the vessel.

of the vessel. Interactive display methods may provide greater diagnostic accuracy than prerendered images [26]. Virtual endoscopic views, which provide a perspective from inside a vessel or chamber have been developed, but are very dependent on filtering and smoothing techniques. Fluoroscopic views are helpful for assessment of metallic structures such as pacemaker leads.

Summary

The evolution of CT scanners and workstations has allowed for rapid acquisition and reconstructions of images for the characterization of cardiovascular disease processes. CCTA imaging poses challenges due to the complex motion of the heart, variation in heart rate and rhythm, and tissue characteristics of cardiovascular structures. An understanding of these factors and meticulous attention to triggering techniques, contrast injection methods, and preview methods can lead to images visualizing anatomy and function critical to the diagnosis and treatment of patients with cardiovascular disease.

References

1. Brooks RA. A quantitative theory of the Hounsfield unit and its application to dual energy scanning. *J Comput Assist Tomogr*. 1977; 1(4):487–493.
2. Dewey M, Zimmermann E, Deissenrieder F, et al. Noninvasive coronary angiography by 320-row computed tomography with lower radiation exposure and maintained diagnostic accuracy: comparison of results with cardiac catheterization in a head-to-head pilot investigation. *Circulation*. 2009;120(10):867–875.
3. Silverman PM, Kalender WA, Hazle JD. Common terminology for single and multislice helical CT. *AJR Am J Roentgenol*. 2001;176(5):1135–1136.
4. Marcus ML, Skorton DJ, Schelbert HR, Wolf GL. *Cardiac Imaging: A Companion to Braunwald's Heart Disease*. Philadelphia, PA: WB Saunders; 1991:671–731.
5. Mao S, Budoff MJ, Bin L, Liu SC. Optimal ECG trigger point in electron-beam CT studies: three methods for minimizing motion artifacts. *Acad Radiol*. 2001;8(11):1107–1115.
6. Ritchie CJ, Godwin JD, Crawford CR, Stanford W, Anno H, Kim Y. Minimum scan speeds for suppression of motion artifacts in CT. *Radiology*. 1992;185(1):37–42.
7. Rogers WJ Jr, Shapiro EP, Weiss JL, et al. Quantification of and correction for left ventricular systolic long-axis shortening by magnetic resonance tissue tagging and slice isolation. *Circulation*. 1991;84(2): 721–731.
8. Mao S, Lu B, Oudiz RJ, Bakhsheshi H, Liu SC, Budoff MJ. Coronary artery motion in electron beam tomography. *J Comput Assist Tomogr*. 2000;24(2):253–258.
9. Achenbach S, Ropers D, Holle J, Muschiol G, Daniel WG, Moshage W. In-plane coronary arterial motion velocity: measurement with electron-beam CT. *Radiology*. 2000;216(2):457–463.
10. Topol EJ, Nissen SE. Our preoccupation with coronary luminology. The dissociation between clinical and angiographic findings in ischemic heart disease. *Circulation*. 1995;92(8):2333–2342.
11. Weyman AE. *Principles and Practice of Echocardiography*. 2nd ed. Philadelphia: Lea and Febiger; 1994:721–741.
12. Becker CR, Knez A, Ohnesorge B, Schoepf UJ, Reiser MF. Imaging of noncalcified coronary plaques using helical CT with retrospective ECG gating. *AJR Am J Roentgenol*. 2000;175(2):423–424.
13. Abada HT, Larchez C, Daoud B, Sigal-Cinqualbre A, Paul JF. MDCT of the coronary arteries: feasibility of low-dose CT with ECG-pulsed tube current modulation to reduce radiation dose. *AJR Am J Roentgenol*. 2006;186(6 suppl 2):S387–S390.
14. Husmann L, Valenta I, Gaemperli O, et al. Feasibility of low-dose coronary CT angiography: first experience with prospective ECG-gating. *Eur Heart J*. 2008;29(2):191–197.
15. Matsutani H, Sano T, Kondo T, et al. ECG-edit function in multidetector-row computed tomography coronary arteriography for patients with arrhythmias. *Circ J*. 2008;72(7):1071–1078.

16. Brodoefel H, Burgstahler C, Tsiflikas I, et al. Dual-source CT: effect of heart rate, heart rate variability, and calcification on image quality and diagnostic accuracy. *Radiology*. 2008;247(2):346–355.
17. Ropers U, Ropers D, Pflederer T, et al. Influence of heart rate on the diagnostic accuracy of dual-source computed tomography coronary angiography. *J Am Coll Cardiol*. 2007;50(25):2393–2398.
18. Cademartiri F, Nieman K, van der Lugt A, et al. Intravenous contrast material administration at 16-detector row helical CT coronary angiography: test bolus versus bolus-tracking technique. *Radiology*. 2004;233(3):817–823.
19. Bakhsheshi H, Mao S, Budoff MJ, Bin L, Brundage BH. Preview method for electron-beam CT scanning of the coronary arteries. *Acad Radiol*. 2000;7(8):620–626.
20. Agatston AS, Janowitz WR, Hildner FJ, Zusmer NR, Viamonte M Jr, Detrano R. Quantification of coronary artery calcium using ultrafast computed tomography. *J Am Coll Cardiol*. 1990;15(4):827–832.
21. Callister TQ, Cooil B, Raya SP, Lippolis NJ, Russo DJ, Raggi P. Coronary artery disease: improved reproducibility of calcium scoring with an electron-beam CT volumetric method. *Radiology*. 1998;208(3): 807–814.
22. Greenland P, LaBree L, Azen SP, Doherty TM, Detrano RC. Coronary artery calcium score combined with Framingham score for risk prediction in asymptomatic individuals. *JAMA*. 2004;291(2):210–215.
23. Greenland P, Bonow RO, Brundage BH, et al. ACCF/AHA 2007 clinical expert consensus document on coronary artery calcium scoring by computed tomography in global cardiovascular risk assessment and in evaluation of patients with chest pain: a report of the American College of Cardiology Foundation Clinical Expert Consensus Task Force (ACCF/AHA Writing Committee to Update the 2000 Expert Consensus Document on Electron Beam Computed Tomography) developed in collaboration with the Society of Atherosclerosis Imaging and Prevention and the Society of Cardiovascular Computed Tomography. *J Am Coll Cardiol*. 2007;49(3):378–402.
24. Gopal A, Budoff MJ. A new method to reduce radiation exposure during multi-row detector cardiac computed tomographic angiography. *Int J Cardiol*. 2009;132(3):435–436.
25. Tsukagoshi S, Ota T, Fujii M, Kazama M, Okumura M, Johkoh T. Improvement of spatial resolution in the longitudinal direction for isotropic imaging in helical CT. *Phys Med Biol*. 2007;52(3):791–801.
26. Ferencik M, Ropers D, Abbara S, et al. Diagnostic accuracy of image postprocessing methods for the detection of coronary artery stenoses by using multidetector CT. *Radiology*. 2007;243(3):696–702.
27. Achenbach S, Moshage W, Ropers D, Bachmann K. Curved multiplanar reconstructions for the evaluation of contrast-enhanced electron beam CT of the coronary arteries. *AJR Am J Roentgenol*. 1998;170(4): 895–899.

8

Postprocessing and Reconstruction Techniques for the Coronary Arteries

Swaminatha V. Gurudevan

Introduction

With the advent of multidetector computed tomography, noninvasive imaging of the coronary arteries is now possible. Attention to detail in the postprocessing aspects of coronary artery imaging is crucial to obtaining high-quality, clinically diagnostic images. This chapter will review the scan-related and postscan related postprocessing parameters that, with careful adjustment, can greatly aid the reader in accurately interpreting cardiovascular CT images.

Scan-Related Postprocessing Parameters

Temporal and Spatial Resolution

Two important parameters to understand when evaluating an imaging modality are temporal and spatial resolution. *Temporal resolution* refers to the ability of an imaging modality to detect two distinct events in time as separate events, and is expressed in units of time. It can be likened to the shutter speed on a camera. Fast shutter speeds have superior temporal resolution to slow shutter speeds and produce superior images of rapidly moving subjects in action shots. Slow shutter speeds, on the other hand, will produce blurring artifacts when subjects move. The intrinsic temporal resolution of single source multidetector CT systems ranges from 135 to 210 ms, while dual source CT systems have a temporal resolution as low as 83 ms. Two approaches to optimize temporal resolution in cardiac CT include improving the imaging speed with ultrafast gantry rotation speeds and slowing the motion of the heart during the examination through effective beta blockade. Each technique is essential to produce motion-free images.

Spatial resolution, on the other hand, refers to the ability of an imaging modality to detect two distinct objects in space as separate objects, and is expressed in units of distance. Smaller objects such as coronary arteries require submillimeter spatial resolution to clearly define the vessel wall, lumen, and coronary plaque. The spatial resolution of multidetector CT ranges from 0.5 to 0.625 mm, and is most directly related to the width of the collimated beam.

Cardiac CT Gating

Coronary artery motion that occurs during the cardiac cycle remains the greatest challenge to effective imaging of the coronary arteries with cardiovascular CT [1,2]. Reconstruction algorithms target phases of the cardiac cycle where the coronary arteries move the least. Coronary artery motion occurs predictably in specific phases of the cardiac cycle. The two phases of the cardiac cycle in which the coronary arteries move the least are *mid-diastole*, during the diastasis period between early rapid ventricular filling (the E wave) and atrial contraction (the A wave), and *end-systole*, immediately prior to the E wave [3]. At slow heart rates (Figure 8.1), the diastasis period (between 70 and 80% of the R–R interval) is the most optimal imaging period. At faster heart rates (Figure 8.2), the diastasis period shrinks, making the end-systolic period (between 30 and 50% of the R–R interval) the period of least coronary motion [4].

Due to the motion of the beating heart, ECG gating is necessary to achieve consistent images of the heart that are free of motion artifacts. *Prospective ECG gating* relies on the scanner initiating imaging only during a prespecified interval of the cardiac cycle (Figure 8.3), usually the mid-diastolic interval. Systolic images are not obtained, and a slow, steady heart rate is necessary to avoid motion artifacts. The greatest advantage of prospective ECG gating is the use of a low radiation dose (as low as 1 mSv) [5].

Retrospective ECG gating involves a continuous spiral feed and scan wherein the entire heart volume is covered continuously. Data acquisition occurs from all phases of the cardiac cycle (Figure 8.4). The patient's ECG is recorded simultaneously with the CT data acquisition, and, from the raw scan data, specific phases of the cardiac cycle are reconstructed to create multiple data sets [6]. Data overlap is necessary to capture each table position at more than one cardiac cycle.

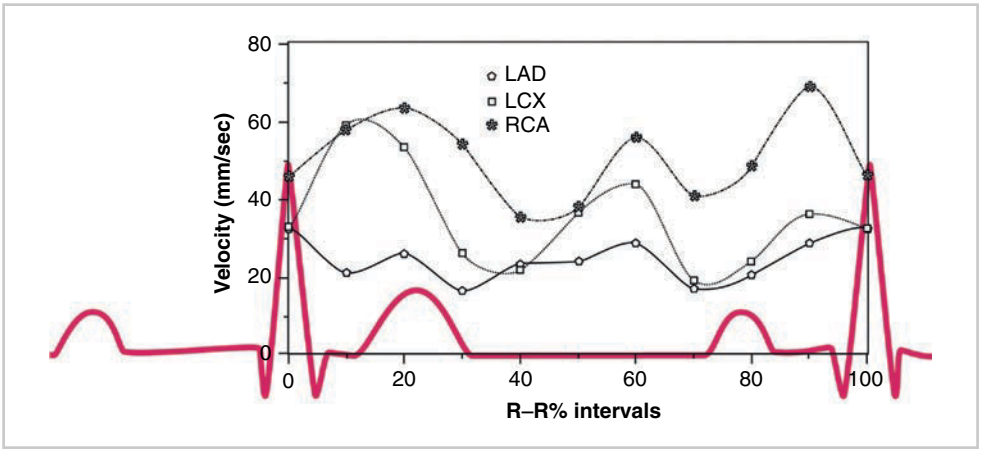

Figure 8.1. Coronary artery motion velocity profile of a patient with a baseline heart rate of 72 bpm. A biphasic pattern of rest periods was found during end systole (at 40–50% of the R–R interval) and mid-diastole (at 70–80% of the R–R interval). (Modified with permissino from Wolters Kluwer from Lu et al [1]).

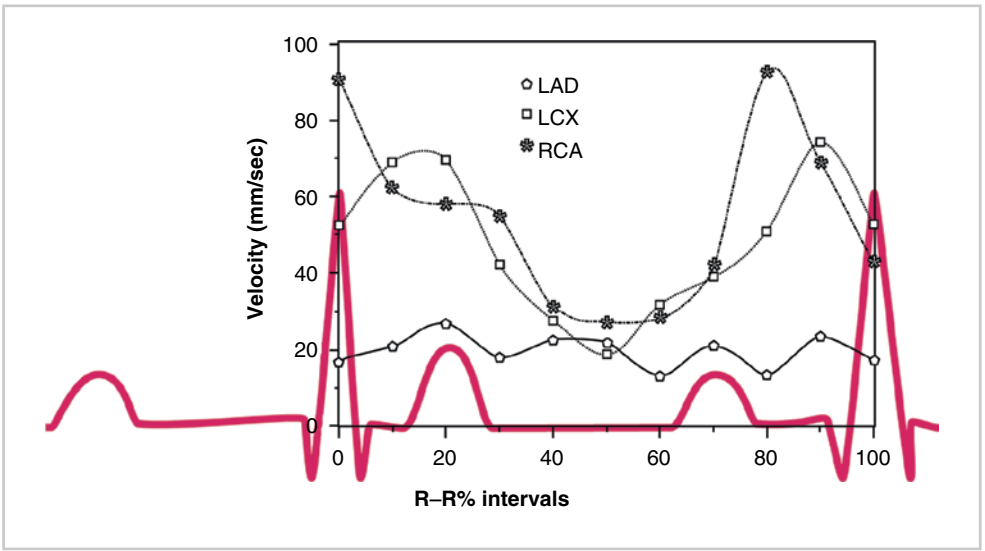

Figure 8.2. Coronary artery motion velocity profile of a patient with a baseline heart rate of 89 bpm. A monophasic rest period pattern was found near end systole (at 40–60% of the R–R interval). (Modified with permission from Wolters Kluwer from Lu et al [1]).

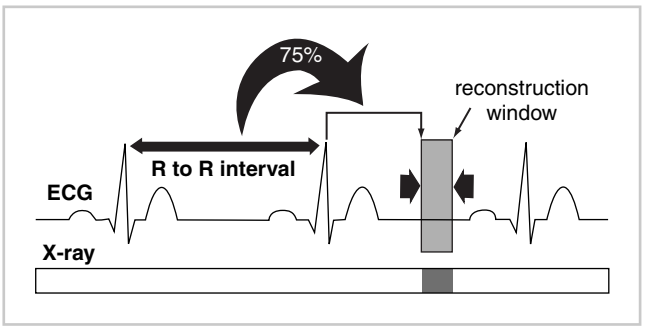

Figure 8.3. Prospective ECG-gating.

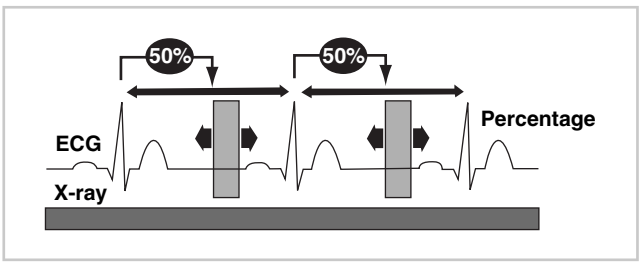

Figure 8.4. Retrospective ECG-gating.

Retrospective gating enables imaging at more rapid heart rates by employing multisegment reconstruction to increase the effective temporal resolution of the scanner. In addition, by overlapping data acquisition, errant reconstruction from premature heartbeats and variations in heart rate can be corrected through ECG-editing programs (Figure 8.5) [7].

Field of View

While the *scanned field of view* represents the entire object scanned within the gantry, the *displayed field of view* is defined as the angular size of the displayed scan on the 3-dimensional (3D) matrix. For a given CT application, the size of the matrix is 512×512, which limits the number of voxels that can be displayed within a particular field of view. For general thoracic CT applications, the entire chest is included in the field of view. However, with cardiac imaging applications, it is necessary to reduce the displayed field of to maximize *x*-axis and *y*-axis spatial resolution. Typically a field of view that encompasses the heart, pericardium, and great vessels is selected so that the *x*-axis and *y*-axis spatial resolution matches the *z*-axis resolution, which is related only to the collimated beam width. This resolution ranges from

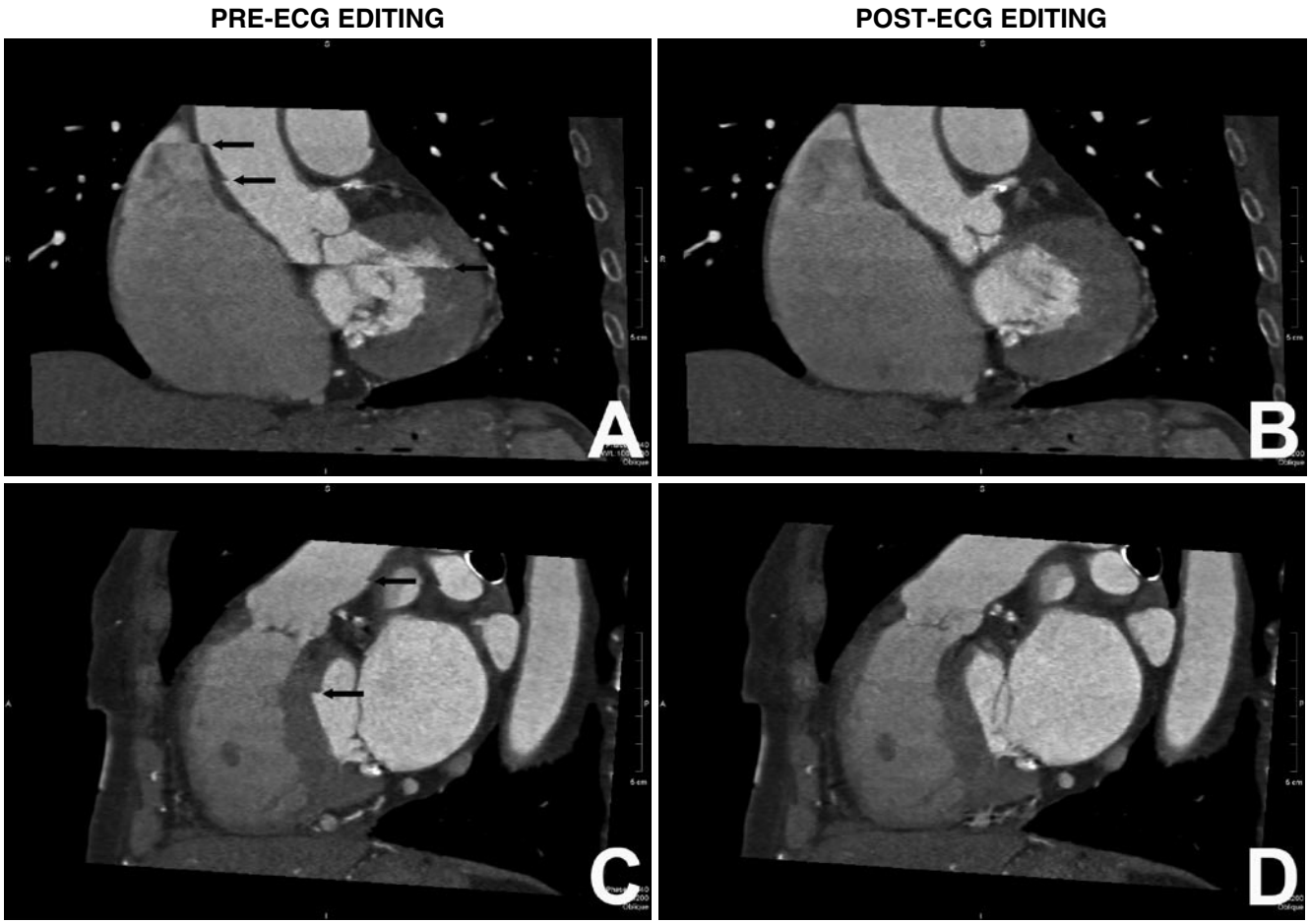

Figure 8.5. ECG editing to eliminate misregistration artifacts can be employed on retrospectively gated CT acquisitions. (**a**) Is an oblique coronal section taken at 40% of the R–R interval demonstrating stairstep-like misregistration artifacts (*arrows*) in a patient with atrial fibrillation undergoing a retrospectively gated 64-slice cardiac CT examination, in whom the R–R interval was notably irregular. (**c**) Is an oblique sagittal section at the same reconstruction interval demonstrating similar misregistration artifacts (*arrows*). (**b, d**) Demonstrate successful elimination of the artifacts in the same oblique coronal and sagittal planes using ECG editing to perform precise reconstruction at the end of the T wave (end systole).

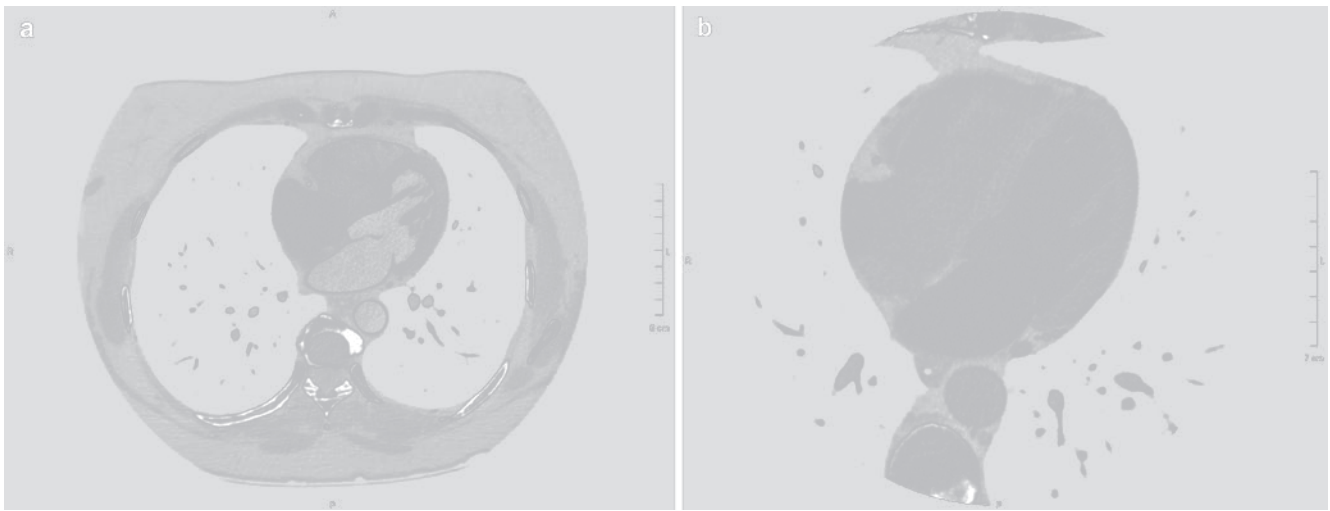

Figure 8.6. Axial projections of two gated cardiac CT examinations at different displayed fields of view. (**a**) Demonstrates a displayed field of view encompassing the entire chest. This will tend to limit image resolution in the *x* and *y* axes. (**b**) Demonstrates an appropriately limited field of view for a cardiac CT examination.

0.5 to 0.625 mm for most CT systems. Figure 8.6 demonstrates representative axial images from a gated thoracic CT exam with a larger field of view and a more refined field of view. It must be noted that use of a bowtie filter (to limit radiation to the patient) can limit the maximum field of view to 32 cm (not allowing X-ray beams to hit the lateral portions of the

chest and breast). This lowers radiation dose by 40% and limits the maximum scan field of view to 32 cm. Cardiac structures always fit within a 25 cm FOV, so this is becoming more typical practice to further reduce radiation exposure and limit incidental findings.

Convolution Kernel

The generation of interpretable cardiac CT images involves the application of a variety of reconstruction filters, the goal of which are to maximize signal-to-noise ratio and improve visualization of the object of interest. This image processing occurs on the CT scanner console and can be employed following acquisition of the raw CT data. The *convolution kernel* is defined as the image processing filter applied to the raw data to yield a final scan image. The sharpness of the final image is most directly influenced by the type of filter employed.

A *soft convolution kernel* will tend to smooth edges and reduce the amount of image noise. It can be advantageous to employ this kernel in obese patients where signal-to-noise ratio can be diminished secondary to attenuation from adipose tissue. *Sharp convolution kernels* tend to enhance edges at the cost of increased overall image noise. These sharp kernels can be used in patients with stents or heavily calcified vessels [8–10] to reduce blooming artifacts that can occur, as shown in Figure 8.7. For the majority of coronary CT imaging applications, a neutral convolution kernel is employed that balances image noise and edge detection.

Spiral Pitch

An important parameter for characterizing a spiral CT is the pitch. The pitch is defined as the table feed per gantry rotation divided by the width of the collimated beam. A pitch of greater than 1 implies there are gaps in data acquisition, while a pitch of less than 1 implies that there is overlap in data acquisition (Figure 8.8). Retrospectively gated multidetector cardiac CT data acquisitions are performed with a pitch of approximately 0.2, as cardiac gating is always necessary for motion-free images, and it is necessary to image an entire cardiac cycle at least once at each table position. Modern 64-slice CT scanners automatically determine pitch based on the scan length and heart rate. The

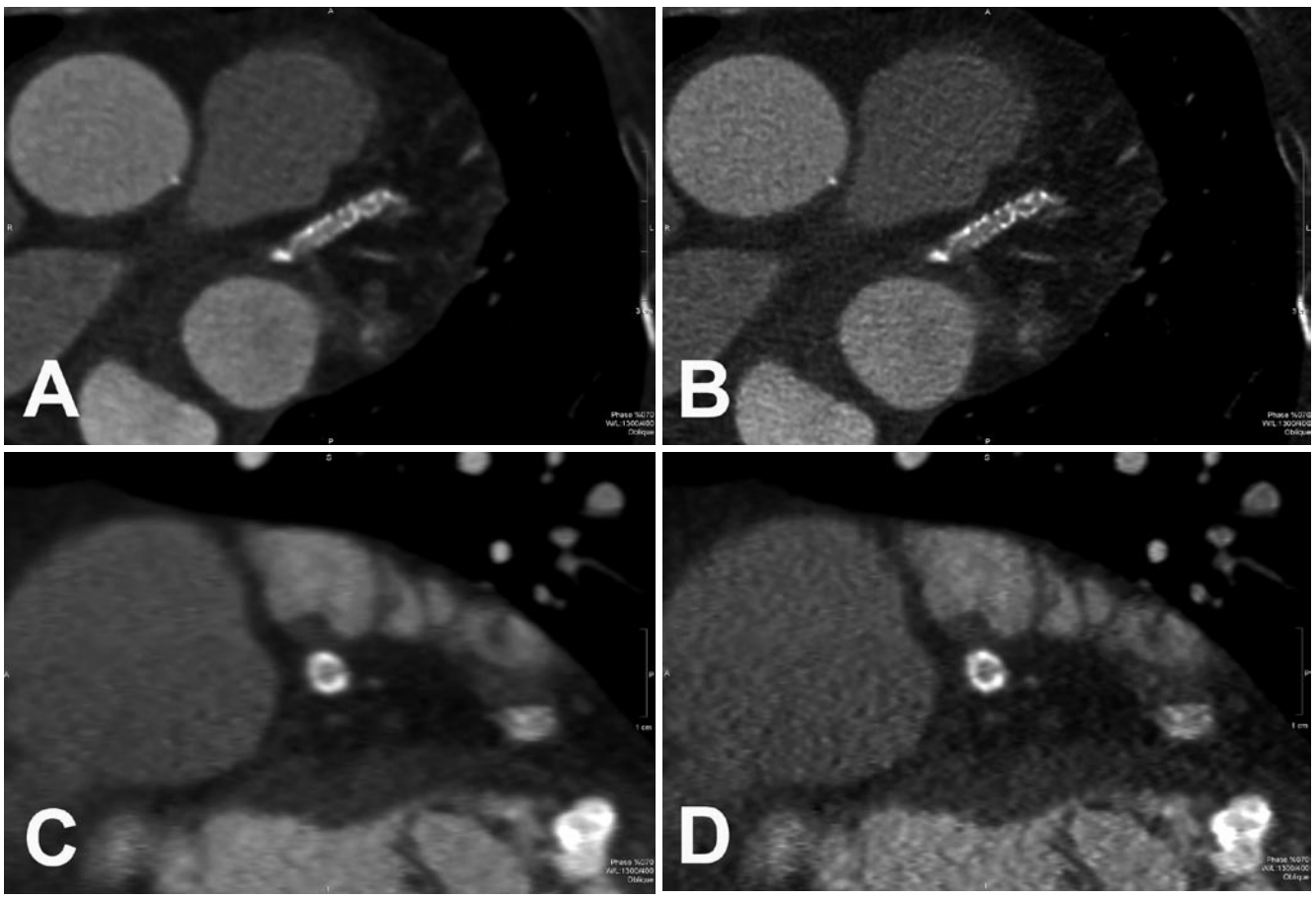

Figure 8.7. Sharp and smooth convolution kernels are employed to improve visualization of stents and calcified vessels while reducing blooming artifacts. (**a, c**) Depict long axis and short axis oblique thin-slice projections of an LAD stent using a standard smooth (B26f) kernel. (**b, d**) are similar projections using a sharp (B46f) convolution kernel. Blooming artifacts are reduced, and the edge of the stent is more clearly delineated at the expense of increased noise in the remainder of the image.

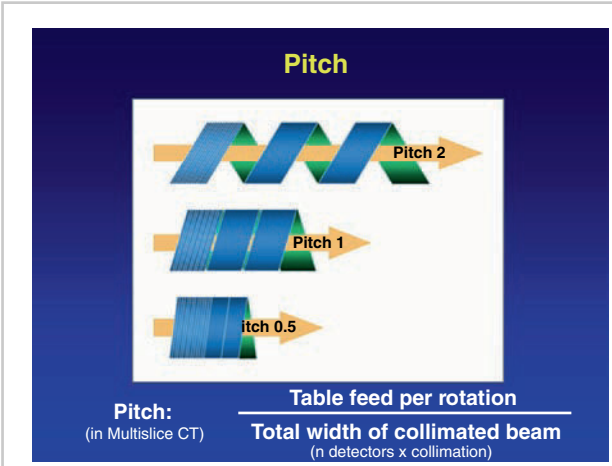

Figure 8.8. Pitch refers to the table feed per gantry rotation during a spiral acquisition divided by the width of the collimated beam. A pitch of exactly 1 (*central diagram*) implies that there are no data gaps and there is no overlap of data. When pitch is greater than 1 (*top diagram*), there are gaps in data acquisition, whereas when pitch is less than 1 (*bottom diagram*), there is data overlap. Retrospectively gated cardiac CT examinations are performed with a pitch of approximately 0.2.

major advantages of using a slower pitch is an improved temporal resolution due to increased data overlap while the major disadvantage is an increased radiation exposure. Multisegment reconstruction (discussed next) requires a decreased pitch compared to half-scan reconstruction [6].

Reconstruction of CT Data

With 64-detector CT systems, each revolution of the gantry enables imaging of 3.2–4.0 cm of the heart (depending on detector width). The reconstruction excludes the fan beam width (approximately 30°), so that approximately 210° of rotation are necessary to generate a single axial image. To cover the entire heart, the required length of most cardiac scans is 9–10 cm; this necessitates combining data from multiple table positions to yield a final volume of data. The greatest challenge in the reconstruction of this volumetric cardiac CT data is the maintenance of temporal uniformity: that is, one should be able to provide cardiac images at each table position from the same part of each cardiac cycle. A breakdown of temporal uniformity can lead to characteristic "stairstep" artifacts.

The most commonly used reconstruction algorithm in spiral cardiac CT is the *half-scan reconstruction method,* which involves the use of scan data from a single gantry rotation to generate an axial CT image. Using the half-scan method, the temporal resolution is approximately 60% of the rotational speed of the scanner (due to the fan beam width exclusion). For modern single source 64-slice CT scanners which have gantry rotation times ranging from 330 to 375 ms, the temporal resolution using the half-scan reconstruction method is approximately 165–200 ms. In patients with heart rates of 60 beats per minute (bpm) or less, the mid-diastolic diastasis period of minimal coronary

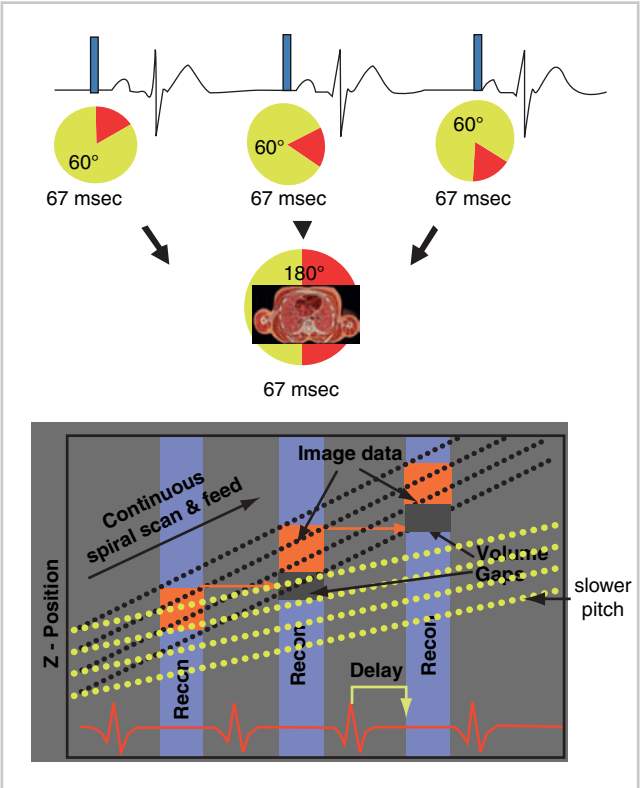

Figure 8.9. (**a**,**b**) Multisegment reconstruction of a CT acquisition involves the acquisition of data at a single table position over several cardiac cycles. The volumetric data are combined to yield a final summed volume. The major requirement for multisegment reconstruction is data overlap, which results in a slower pitch and higher radiation dose during the CT acquisition. Using this technique, effective temporal resolution can be improved to 67 ms for a scanner with a half-scan acquisition time of 200 ms.

motion is long enough to allow effective reconstructions in mid-diastole in the majority of patients.

In patients with heart rates faster than 80 bpm, the duration of the diastasis period decreases considerably and may be only 100–200 ms. This makes it nearly impossible to reconstruct motion-free images using the half-scan reconstruction method. In these cases, *multisegment reconstruction* may be utilized to improve the effective temporal resolution of the CT scanner. Multisegment reconstruction relies on additional data overlap with slower table movement and decreased pitch during CT acquisition [11, 12]. This overlap results in the same table position being available for imaging at multiple heart beats from multiple detectors (Figure 8.9). By combining views at a single table position from different subsequent gantry rotations, one simulated half-scan rotation is generated. This results in improved image quality with fewer motion artifacts. By combining images from three cardiac cycles, the effective temporal resolution can be improved to as much as 65 ms. Multisegment reconstruction relies heavily on a consistent R–R interval on the consecutive beats used to generate the final axial image. Irregularities from atrial fibrillation or sinus arrhythmia during breath holding may cause misregistration artifacts.

Postscan Related Postprocessing Parameters

After the scan has been completed and datasets have been generated, additional postprocessing techniques on a cardiac CT workstation are essential to accurately interpreting cardiac morphology as well as coronary artery anatomy and disease burden. The presence of an isotropic data set in which the spatial resolution is identical across all planes of examination facilitates manipulation of the data on a workstation.

The raw axial images are the most reliable for diagnosis, as they reflect the source data in the order the images were acquired. To assist the reader in processing large volumes of data and illustrating key findings, additional rendering techniques have been developed [13, 14]. These include the multiplanar reformatting, maximum intensity projection (MIP), the volume averaging (VA) and volume rendering (VR) techniques, and the curved multiplanar projection (CMP). All involve rendering data contained within a 3D slab (the thickness of which the user can change) of data as a single 2-dimensional (2D) projection.

Multiplanar Reformatting (MPR)

Multiplanar reformatting involves the selection of an arbitrary image plane in a cardiac CT volume. This technique requires an isotropic volumetric data set with equal spatial resolution in the X, Y, and Z axes. The plane may not conform to the conventional axial, coronal, and sagittal imaging planes and can be modified by the user, as shown in Figure 8.10. MPR is the mainstay for analysis of cardiac CT data sets and is the most reliable method for the reader to arrive at the correct diagnosis. It can be performed using a single slice or with differing numbers of stacked slices. When more than one slice is selected, a rendering option must be selected to display a composite image of the multiple slices.

Maximum Intensity Projection

The MIP involves the projection of data in a 3D slab so that only the voxels of highest HU are displayed on a 2D image (Figure 8.11). Initially developed by Rubin et al [15, 16] for use in peripheral CT angiography, the MIP is now used for nearly all CT angiography applications and is the mainstay of coronary artery interpretation. The MIP is ideal for the display of coronary artery images from a contrast CT examination as the maximum intensity in the coronary arteries is usually the intraluminal contrast. The coronary arteries are surrounded by low-attenuation epicardial fat, resulting in an angiogram-like image with excellent edge definition (Figure 8.11). Due the selection of the highest intensity voxels within a slab, the MIP tends to overestimate stenosis severity in calcified vessels and stented segments. Overreliance on MIPs can also lead the reader to overlook subtle findings in the coronary arteries. In general, readers should always reconfirm findings on MIP with the source axial data.

Volume Averaging and Volume Rendering

VA involves the projection of data in a 3D slab so that the intensity of all the voxels in the slab is averaged on a final 2D image (Figure 8.12). While edge definition is poorer than with MIP, VA enables the reader to "see through" a dense object in a slab and can be useful in interpreting stenoses in calcified vessels. When specific colors are assigned to specific ranges of HU in a 3D volumetric slab, this is termed VR; this is available on virtually every cardiac workstation. The relative position and 3D

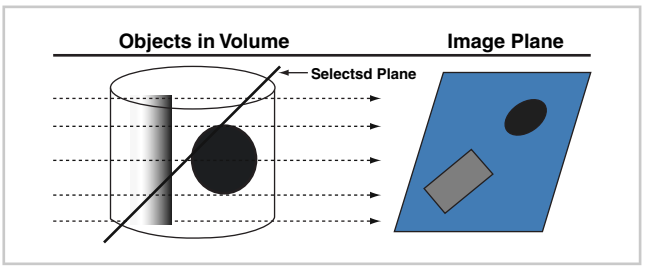

Figure 8.10. Multiplanar reformat projection (MPR).

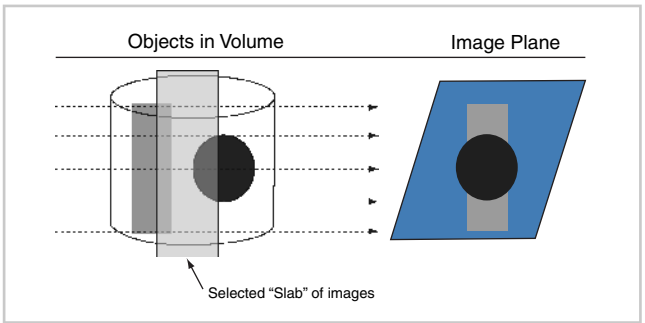

Figure 8.11. Maximum intensity projection.

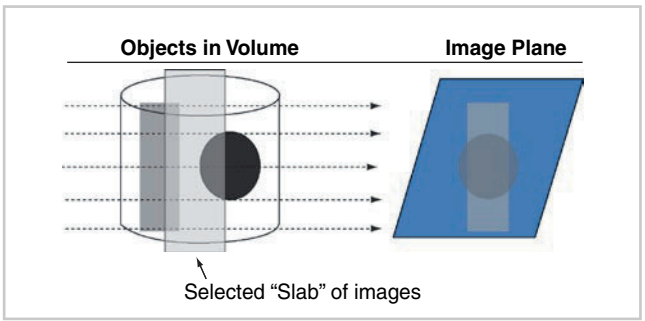

Figure 8.12. Volume averaging.

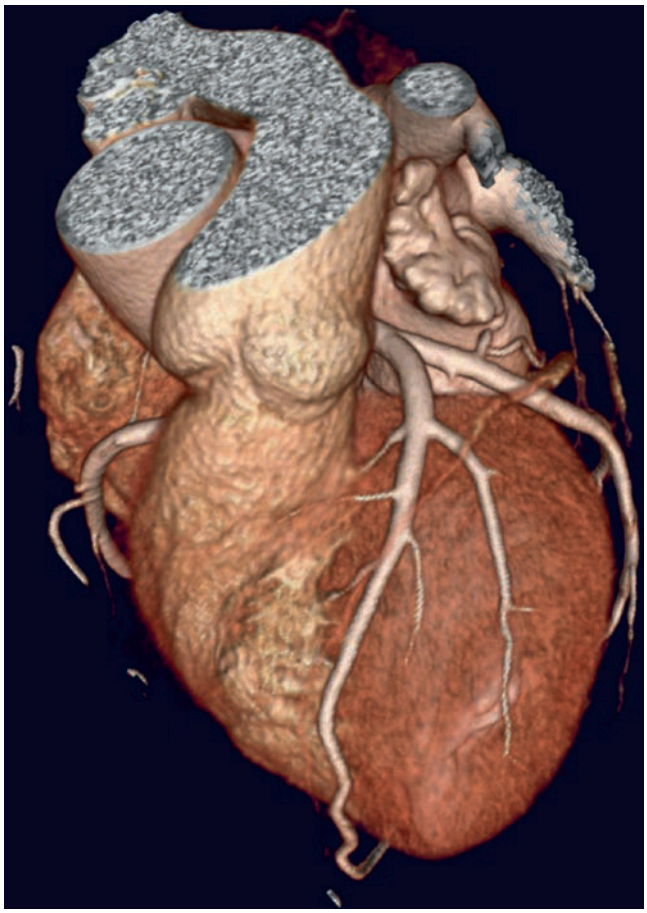

Figure 8.13. 3D volume rendering.

relationship of the coronary arteries, cardiac veins, and cardiac chambers is possible using 3D VR (Figure 8.13). The reader should never attempt to interpret stenoses purely on the basis of a 3D VR images: as calcium and intraluminal contrast have attenuation ranges that are near one another, significant coronary artery stenoses in calcified vessels can be misinterpreted.

Curved Multiplanar Projection

The CMP is a centerline method for analysis of vessels whereby a virtual plane is created using the center of the column of contrast visualized on a series of consecutive axial slices (Figure 8.14). A virtual plane in which the vessel is "stretched out" can then be displayed. CMP is useful for confirming and illustrating the appearance of stenoses identified using standard axial multiplanar projections. It is particularly useful for tortuous vessels and those vessels that cannot be easily tracked in a single plane or thin slab using MIP. The CMP is only as reliable as the accuracy of the centerline, and should not be used as a first-line assessment of coronary stenosis severity. Artifacts from inaccurate centerlines can lead to incorrect assessment of stenosis severity.

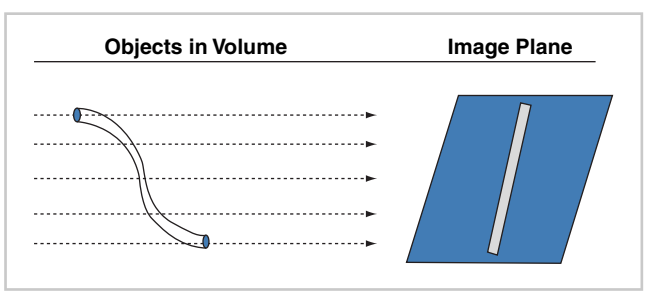

Figure 8.14. Curved planar reformat.

References

1. Lu B, Mao SS, Zhuang N, et al. Coronary artery motion during the cardiac cycle and optimal ECG triggering for coronary artery imaging. *Invest Radiol*. 2001;36(5):250–256.
2. Mao S, Lu B, Oudiz RJ, Bakhsheshi H, Liu SC, Budoff MJ. Coronary artery motion in electron beam tomography. *J Comput Assist Tomogr*. 2000;24(2):253–258.
3. Kim WY, Stuber M, Kissinger KV, Andersen NT, Manning WJ, Botnar RM. Impact of bulk cardiac motion on right coronary MR angiography and vessel wall imaging. *J Magn Reson Imaging*. 2001;14 (4):383–390.
4. Isma'eel H, Hamirani YS, Mehrinfar R, et al. Optimal phase for coronary interpretations and correlation of ejection fraction using late-diastole and end-diastole imaging in cardiac computed tomography angiography: implications for prospective triggering. *Int J Cardiovasc Imaging*. 2009;25(7):739–749.
5. Gurudevan SV, Narula J. Prospective electrocardiogram-gating: a new direction for CT coronary angiography? *Nat Clin Pract Cardiovasc Med*. 2008;5(7):366–367.
6. Flohr TG, Schaller S, Stierstorfer K, Bruder H, Ohnesorge BM, Schoepf UJ. Multi-detector row CT systems and image-reconstruction techniques. *Radiology*. 2005;235(3):756–773.
7. Cademartiri F, Mollet NR, Runza G, et al. Improving diagnostic accuracy of MDCT coronary angiography in patients with mild heart rhythm irregularities using ECG editing. *AJR Am J Roentgenol*. 2006; 186(3):634–638.
8. Ehara M, Kawai M, Surmely JF, et al. Diagnostic accuracy of coronary in-stent restenosis using 64-slice computed tomography: comparison with invasive coronary angiography. *J Am Coll Cardiol*. 2007;49(9): 951–959.
9. Nieman K, Cademartiri F, Raaijmakers R, Pattynama P, de Feyter P. Noninvasive angiographic evaluation of coronary stents with multislice spiral computed tomography. *Herz*. 2003;28(2):136–142.
10. Maintz D, Seifarth H, Flohr T, et al. Improved coronary artery stent visualization and in-stent stenosis detection using 16-slice computed-tomography and dedicated image reconstruction technique. *Invest Radiol*. 2003;38(12):790–795.
11. Kachelriess M, Ulzheimer S, Kalender WA. ECG-correlated image reconstruction from subsecond multi-slice spiral CT scans of the heart. *Med Phys*. 2000;27(8):1881–1902.
12. Ohnesorge B, Flohr T, Becker C, et al. Cardiac imaging by means of electrocardiographically gated multisection spiral CT: initial experience. *Radiology*. 2000;217(2):564–571.
13. Addis KA, Hopper KD, Iyriboz TA, et al. CT angiography: in vitro comparison of five reconstruction methods. *AJR Am J Roentgenol*. 2001;177(5):1171–1176.
14. Pavone P, Luccichenti G, Cademartiri F. From maximum intensity projection to volume rendering. *Semin Ultrasound CT MR*. 2001;22 (5):413–419.
15. Rubin GD, Dake MD, Napel S, et al. Spiral CT of renal artery stenosis: comparison of three-dimensional rendering techniques. *Radiology*. 1994;190(1):181–189.
16. Prokop M, Shin HO, Schanz A, Schaefer-Prokop CM. Use of maximum intensity projections in CT angiography: a basic review. *Radiographics*. 1997;17(2):433–451.

9

Coronary CT Angiography: Native Vessels

Stephan Achenbach

Introduction

Visualization of the coronary arteries has been the major focus of cardiac CT in the past years. Noninvasive "coronary CT angiography" has tremendous clinical potential for detecting or ruling out coronary artery stenoses in selected patients. In addition, imaging of coronary atherosclerotic plaque may play a potential role in risk stratification. However, spatial resolution and temporal resolution of CT imaging, even with the latest scanner generations, are not equal to invasive coronary angiography. Interpreters of coronary CT angiography data sets must be aware that artifacts can occur and may lead to false-positive and false-negative results. Diagnostic accuracy is impaired when image quality is reduced and image quality, in turn, is influenced by many factors such as the patient's heart rate, body weight, ability to cooperate, and extent of coronary calcification. Therefore, the clinical utility of coronary CT angiography significantly depends on the specific clinical situation and patient under investigation. The specific advantages and disadvantages of coronary CT angiography must be carefully considered before using this method in the workup of a patient with known or suspected coronary artery disease.

Imaging Protocol

Since the small dimensions and the rapid motion of the coronary vessels pose tremendous challenges for noninvasive imaging, high-end CT equipment and adequate imaging protocols must be used. Currently, 64-slice CT is considered the "state of the art" for coronary artery imaging, and newer technology, such as Dual Source CT and scanners that allow simultaneous acquisition of 256 or 320 cross-sections, may provide even further improved image quality.

A basic prerequisite for CT imaging of the coronary arteries is the patient's ability to understand and follow breathhold commands. Even slight respiratory motion during data acquisition will cause substantial artifact. Therefore, patients should be able to reliably hold their breath for approximately 10 s. Otherwise, coronary CT angiography should not be performed. Heart rate should be regular and preferably low (optimally below 60/min, even though this is not as strictly required for Dual Source CT) [1, 2]. Patients usually receive premedication with short acting beta blockers to lower the heart rate. Beta blockers can be administered orally approximately 1 h prior to scanning, or intravenously immediately before the scan. Sometimes, a combination of both is necessary. Nitrates should be given to all patients who have no contraindications in order to achieve coronary dilatation, which substantially improves image quality [1].

Typically, 50–100 mL of iodine-based, high concentration contrast agent are injected intravenously for coronary CT angiography. Recommended flow rates are 4–7 mL/s. Synchronization of contrast injection and data acquisition can be achieved either through a "bolus tracking" method or by using a separate "test bolus" acquisition to measure the contrast transit time. Subsequent data acquisition can follow various principles. *Retrospectively gated* scans are acquired in spiral mode and usually provide for higher image quality, more flexibility to choose the cardiac phase during which images are reconstructed, as well as the ability to reconstruct "functional" data sets throughout the cardiac cycle in order to analyze left ventricular function and regional wall motion. *Prospectively triggered* scans are associated with substantially lower radiation exposure and, especially in patients with truly low heart rates, do in many cases provide adequate image quality to assess the coronary lumen. Less flexibility to reconstruct data at different time instants in the cardiac cycle as well as greater susceptibility to artifacts caused by arrhythmia are trade-offs for the advantage of lower dose. Especially in young patients – in whom radiation dose may be of major concern – prospectively triggered scans should be strongly considered. However, it should be kept in mind that a fully diagnostic scan, not the lowest possible dose, is the major priority of data acquisition. If additional examinations result from a nondiagnostic or false-positive CT result, potential dose

savings are likely to be consumed by the added risks of additional procedures.

Typical data sets for coronary artery visualization by CT consist of approximately 200–300 thin (0.5–0.75 mm) transaxial cross-sections (Figure 9.1). In most cases, readers will interactively manipulate these data sets for interpretation on specific postprocessing workstations. Useful postprocessing tools include maximum intensity projections and multiplanar reconstructions (Figure 9.2). Three-dimensional renderings allow quite impressive visualization of the heart and coronary arteries, but they are not accurate for stenosis detection and play no role in data interpretation [3].

Typical Findings

In most cases, coronary CT angiography is performed to detect or rule out significant coronary artery stenoses (Figures 9.3 and 9.4). Coronary CT angiography does not allow exact quantification of coronary artery stenoses. In most cases, presence of a "significant" luminal stenosis is assumed when the diameter reduction of the coronary lumen appears to be more than 70%. Visual estimation of stenosis degree has no downsides as compared to quantitative approaches [4]. Stenosis severity in CT can appear to be less or more than invasive angiography – the typical margin of agreement is approximately ±20%. Stenoses that appear to be less than 50% in CT can be expected to be less than 70% in invasive angiography with a very high degree of certainty. In most cases, however, there is a tendency to *over*estimate, rather than underestimate, the degree of luminal stenosis in coronary CT angiography as compared to catheter-based invasive coronary angiography (Figure 9.5). Often, high-grade coronary artery stenoses appear as complete or near-complete interruptions of the coronary artery lumen in the CT data set – especially if image quality is not optimal (Figure 9.6). Categories of stenosis severity that are recommended for use in coronary CT angiography reports care listed in Table 9.1 [5]. The differentiation between complete coronary artery occlusions and high-grade stenoses can be difficult in coronary CT angiography. Very long lesions typically correspond to complete occlusions (Figure 9.7), while shorter lesions can either be secondary to high-grade luminal narrowing or to a complete occlusion with good distal filling via collateral flow. Since CT only shows a static image and flow in the coronary arteries cannot actually be seen, retrograde filling of a coronary artery segment cannot be differentiated from antegrade flow (Figure 9.8).

Insufficient image quality is most frequently the consequence of motion artifact (as a consequence of coronary movement or respiration), high image noise, or a combination of both. Additional problems can be caused by severe calcification, which causes partial volume effects (often referred to as "blooming") and aggravates motion artifacts (Figure 9.9). In some cases, artifacts render the entire data set or some coronary segments unevaluable. This has become less frequent with more modern scanners but can still occur, especially if data acquisition is not carefully and expertly performed. If artifacts caused by motion, calcium, or a combination of both cause misinterpretation, it will in most cases be overestimation of stenosis degree or a false-positive reading of a stenosis [6] (Figure 9.10). False-negative interpretations are less frequent.

Accuracy for Stenosis Detection

Clinical applications of coronary CT angiography will critically depend on its accuracy for detection of significant coronary artery stenoses. Numerous studies have assessed the accuracy of coronary CT angiography for stenosis detection in comparison to invasive, catheter-based coronary angiography. Using 40-slice CT [7–10], 64-slice CT [11–20], or Dual Source CT [2, 21–26], the sensitivity for the detection of coronary artery stenoses has ranged from 86 to 100% and specificity has been reported between 91 and 98 %. Accuracy values are not uniform across all patients. Several trials have demonstrated that high heart rates and extensive calcification negatively influence accuracy [6, 24–29]. Since degraded image will usually lead to false-positive rather than false-negative findings [6], specificity and positive predictive value will be affected worst (Figure 9.10).

Several analyses have clearly demonstrated superiority of 64-slice CT over previous technology [30–36] for the detection of coronary artery stenoses. No data are so far available for even more recent scanner generations. Several meta-analyses which were performed based on the results of smaller, single-center trials demonstrated high sensitivities (96–99% and 93–94%) for detecting individuals with at least one coronary artery stenosis (Table 9.2) [31–35]. Meijboom et al. put the diagnostic accuracy of coronary CT angiography in relation to the clinical presentation and pretest likelihood of coronary artery disease [36]. It was clearly shown that the diagnostic value of CT angiography was highest in patients with a relatively low pretest likelihood of disease and lowest in those patients in whom the

Figure 9.1. Normal anatomy of the coronary arteries in transaxial images. (**a**) Level of the left main origin from the aortic root. The bifurcation of the left main into the left anterior descending (*large arrow*) and left circumflex coronary artery (*small arrow*) can be seen. The *arrowheads* point at a coronary vein. (**b**) A few millimeters further distal, the left anterior descending coronary artery (*large arrow*) has given rise to a diagonal branch (*arrowhead*). (**c**) Level of the right coronary ostium. A short section of the right coronary artery is visible (*double arrows*). *Large arrow*: Mid left anterior descending coronary artery, *small arrow*: left circumflex coronary artery. (**d**) Mid-ventricular level. The left anterior descending coronary artery (*large arrow*), left circumflex coronary artery (*small arrow*), and right coronary artery can be seen (*double arrows*). (**e**) Distal segment of the right coronary artery (*double arrow*), which ends in the posterior descending artery (*small arrow*). The *arrowhead* points at a right ventricular branch.

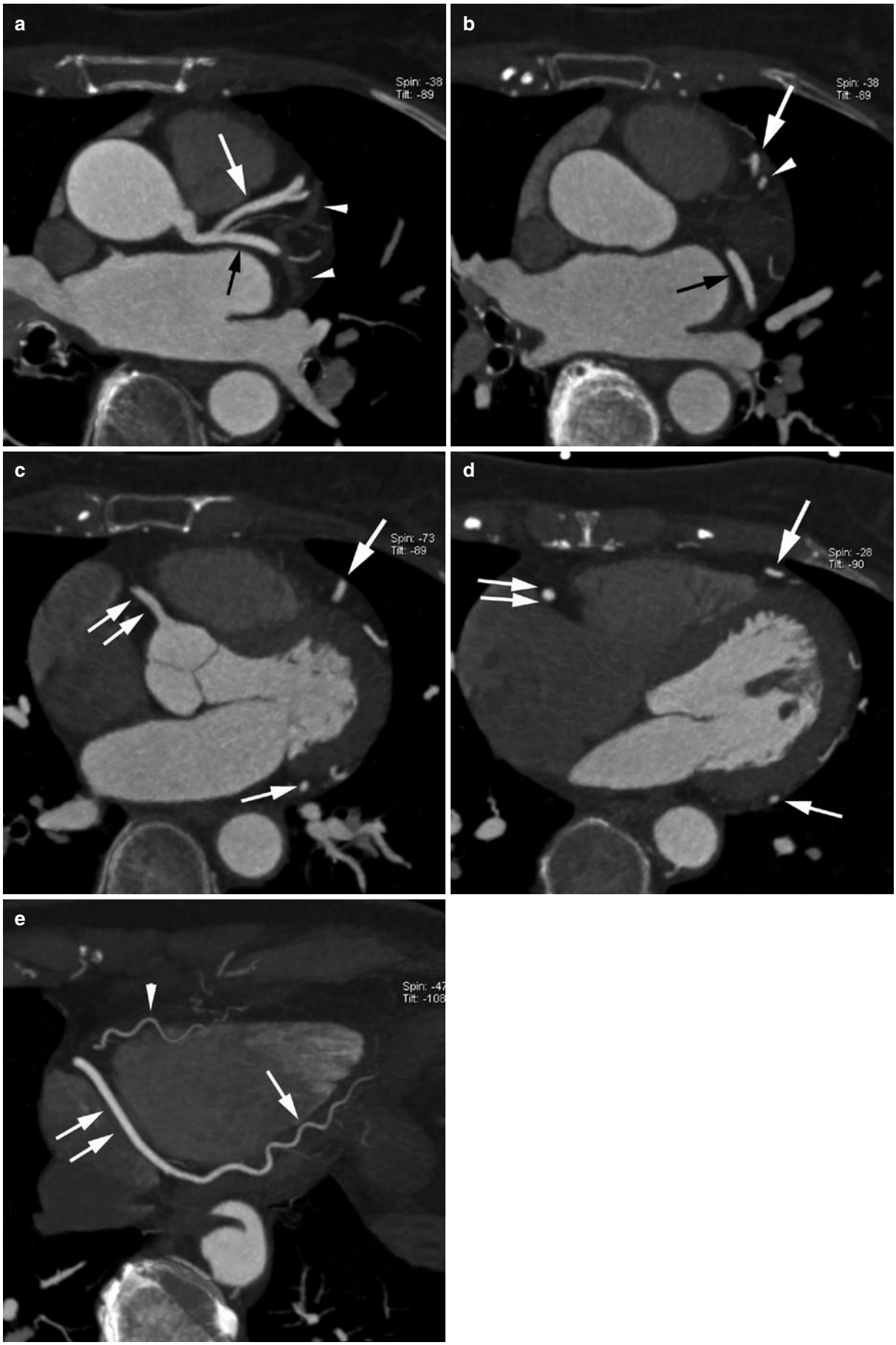
a
Spin: -38
Tilt: -89
b
Spin: -38
Tilt: -89
c
Spin: -73
Tilt: -89
d
Spin: -28
Tilt: -90
e
Spin: -47
Tilt: -108

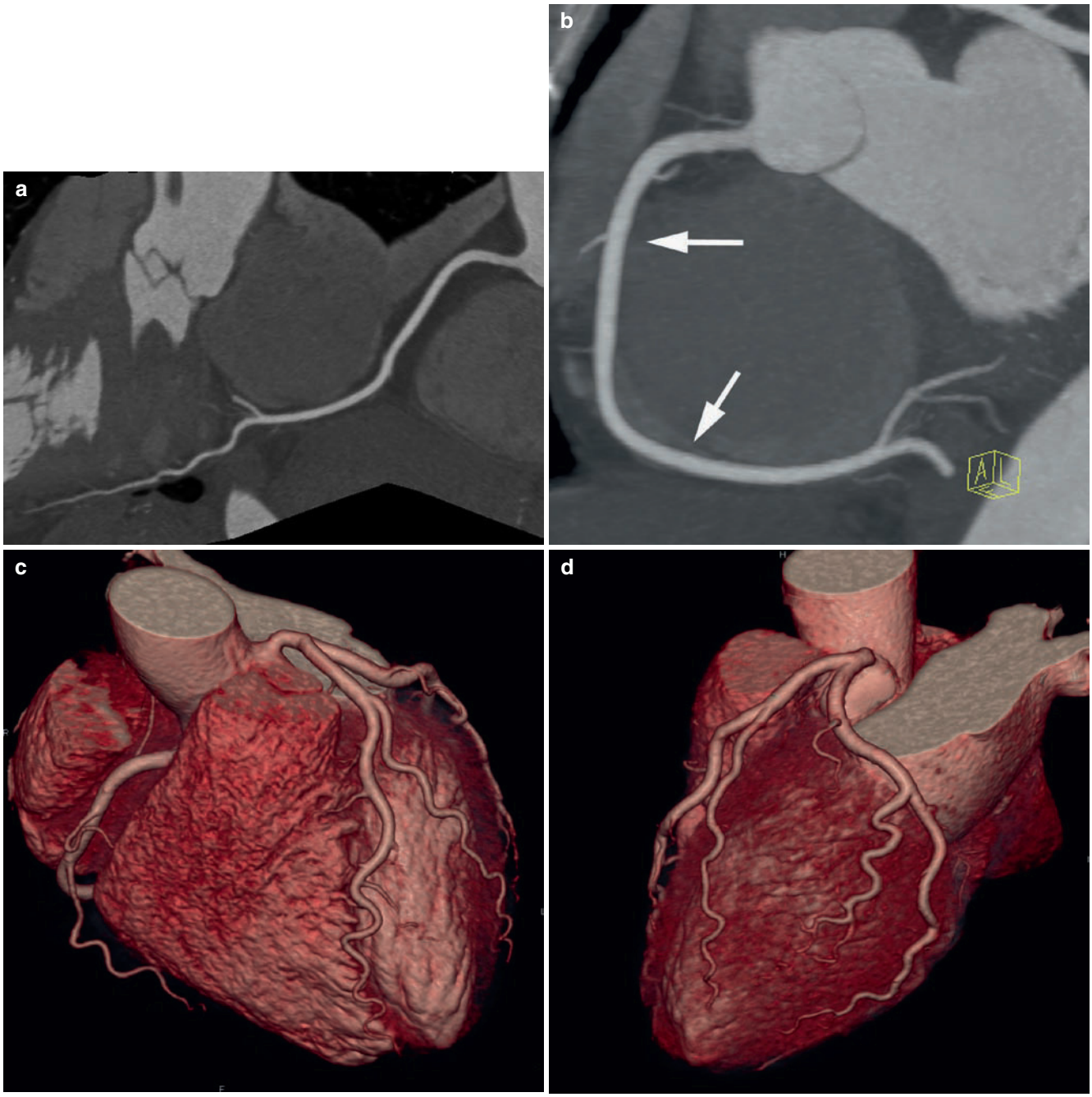

Figure 9.2. Same patient as in Figure 9.1. Various forms of postprocessing have been used to visualize longer segments of the coronary arteries. (**a**) Curved multiplanar reconstruction (curved MPR) of the right coronary artery. (**b**) Maximum intensity projection of the right coronary artery (*arrows*) in a double-oblique plane. (**c**, **d**) Three-dimensional, surface-weighted volume rendering technique reconstructions in two different angulations.

clinical presentation suggested a high likelihood that coronary stenoses would be present – most likely due to the more challenging conditions for imaging (Table 9.3). Based on these accuracy values, the clinical use of CT angiography will be most beneficial whenever the clinical situation implies a relatively low pretest likelihood of coronary disease, but still requires further workup to rule out significant coronary stenoses. In high-risk patients with a high likelihood of coronary artery stenoses, coronary CT angiography will be less useful: results are likely to be less accurate and clinically, noninvasive imaging in patients with a high likelihood of coronary artery stenoses is less attractive, because there it is relatively certain that treatment will include (interventional) revascularization which requires an invasive approach.

Several recent, large multicenter trials support the concept that CT performs well especially if disease is not severe and pretest likelihood for stenoses is relatively low [28, 37, 38] (Table 9.4). The "ACCURACY" trial studied 230 patients with suspected CAD [28]. Prevalence of disease was 25%,

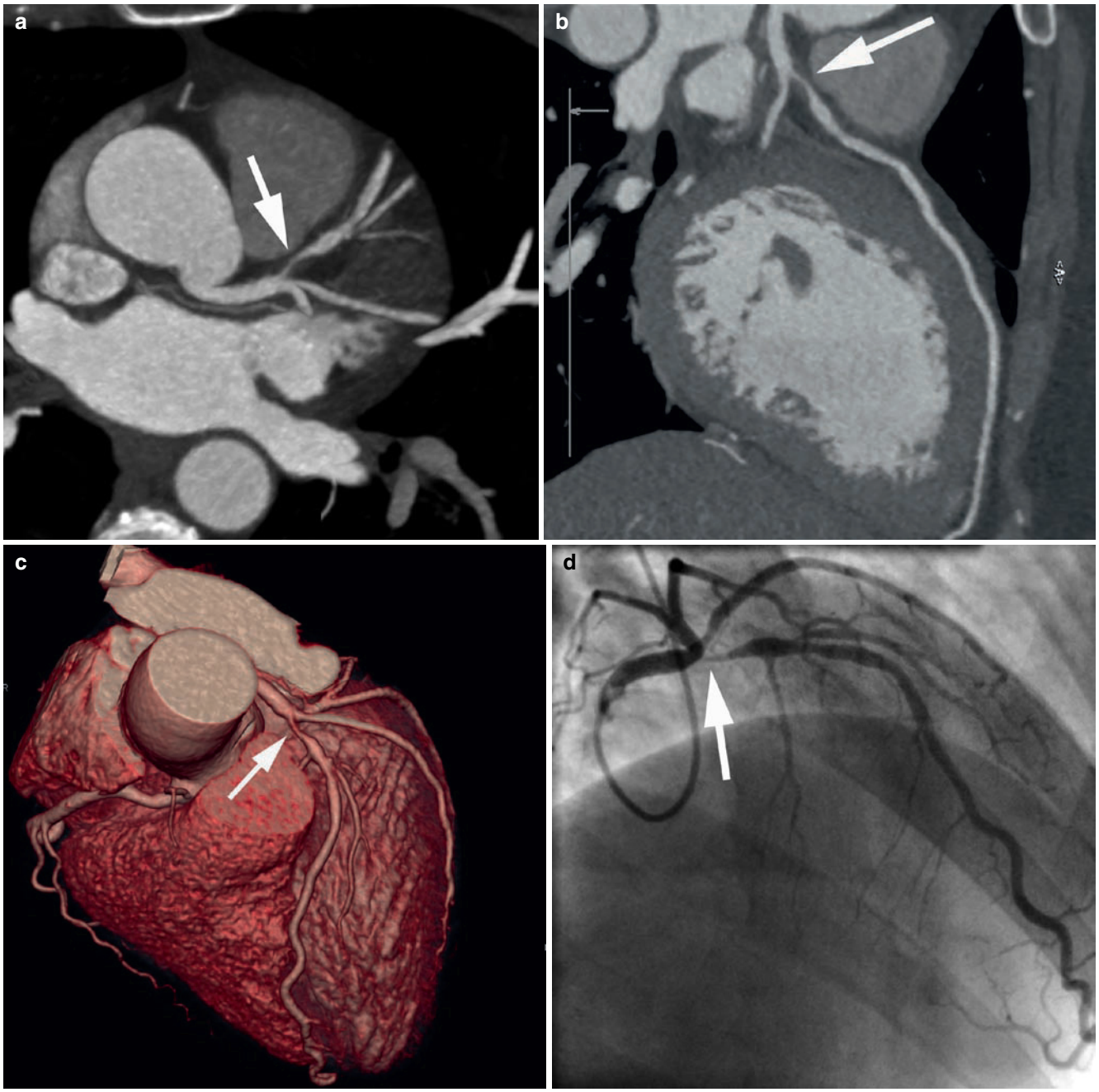

Figure 9.3. Coronary CT angiography in a patient with a very proximal, high-grade stenosis of the left anterior descending coronary artery. (**a**) Maximum intensity projection in a transaxial orientation. The stenosis of the left anterior descending coronary artery, just distal to the left main trifurcation, can be seen (*arrow*). (**b**) Curved multiplanar reconstruction of the left main and left anterior descending coronary artery (*arrow*: stenosis). (**c**) Three-dimensional reconstruction. (**d**) Invasive coronary angiogram.

and per-patient sensitivity and specificity for detecting individuals with at least one stenosis ≥50% were 95 and 83%. The negative predictive value was 99%, allowing CCTA to rule out stenoses with a high degree of certainty. On the other hand, the positive predictive value was only 64%, due to low prevalence of disease in this study. Meijboom et al. published a trial performed at three different sites, which enrolled 360 patients with stable ($n = 233$) or unstable symptoms ($n = 127$) but no previously known disease [38]. Again, 64 slice CT had a sensitivity of 99% for the identification of individuals with at least one coronary artery stenosis. On the other hand, the "Core64" trial studied a group of 291 patients with a different composition. Prevalence of obstructive disease was 56%, and 30% of the patients had previous myocardial infarction or coronary revascularization [37]. Consequently, accuracy was lower with a per-patient sensitivity of 85% and specificity of 90% (negative predictive value 83% and positive predictive value 91%). The results of these trials provide further evidence that CCTA can be highly reliable to rule out the presence of CAD but that its performance strongly depends on the type of patients evaluated.

Figure 9.4. Stenosis of the right coronary artery (*arrow*, **a**: invasive coronary angiogram). Three consecutive axial images (each 1-mm slice thickness) show normal coronary artery lumen proximal to the stenosis (*arrow*, **b**), absence of a contrast-enhanced lumen at the level of the stenosis (*arrow*, **c**), and reestablishment of a patent and normal coronary lumen distal to the stenosis (*arrow*, **d**). Same stenosis in curved multiplanar reconstructions (*arrows*, **e** and **f**), and in three-dimensional volume-rendered reconstruction (**g**, **h**).

Overall, the good diagnostic performance of coronary CT angiography in patients who are not at high likelihood of having coronary artery stenoses and especially the very high negative predictive value found for such patients indicate that CCTA may be a clinically useful tool in symptomatic patients who have a lower or intermediate likelihood of coronary disease, but require further workup to rule out significant coronary stenoses. A negative coronary CT angiography scan, if of high quality, will obviate the need for further testing. Indeed, several observational trials have clearly demonstrated that symptomatic patients, when coronary CT angiography was negative, had a very favorable clinical outcome even without further additional testing [39–44] and that downstream healthcare costs may be lower that with other diagnostic procedures [45].

Another situation in which the use of a noninvasive imaging technology to rapidly and reliably rule out coronary stenoses could be of tremendous clinical value is the setting of acute chest pain. Especially if the ECG is normal

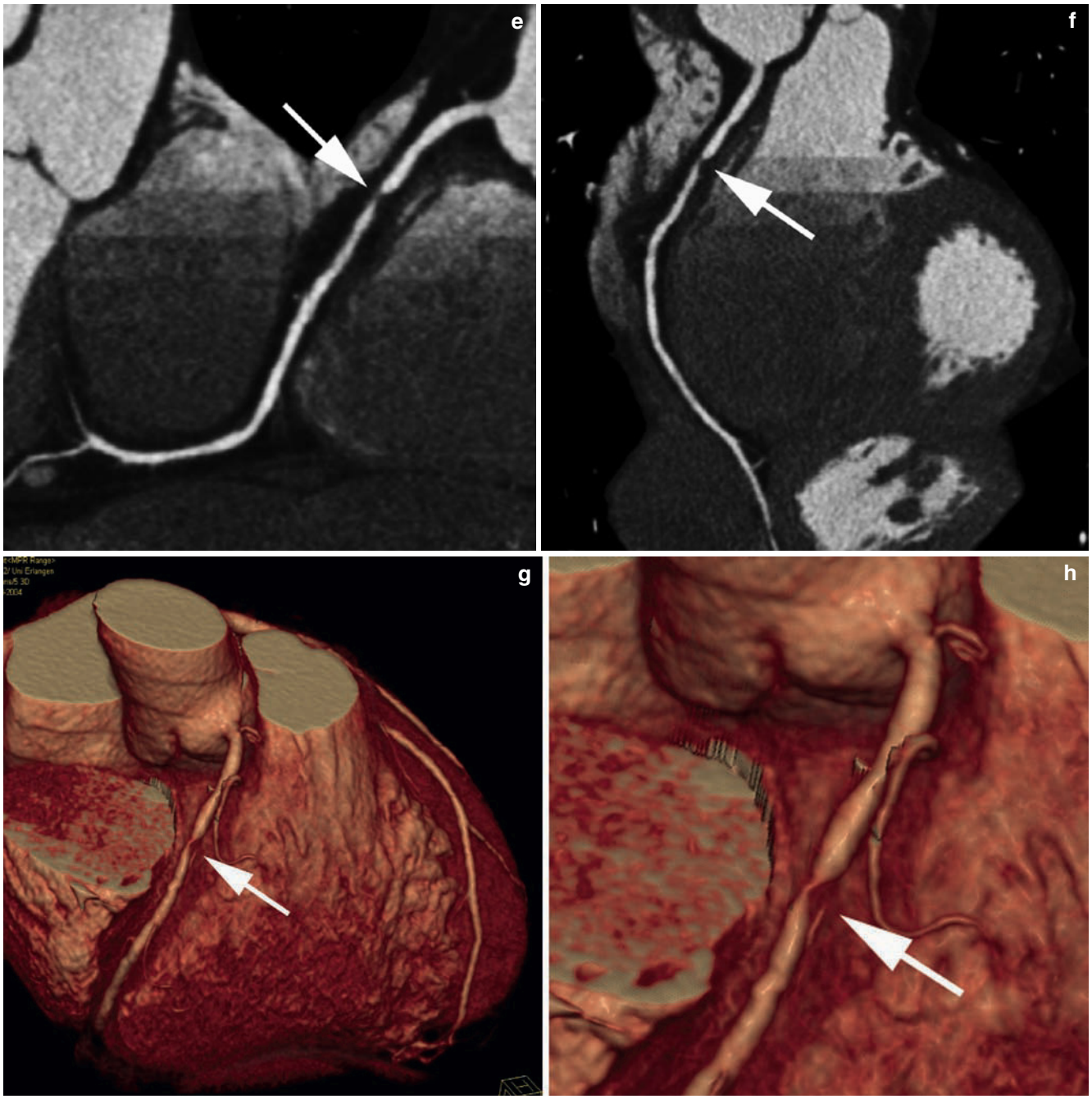

Figure 9.4. (Continued).

and myocardial enzymes are not elevated, the likelihood of coronary disease is low, but the possibility of myocardial infarction requires a rapid and definite diagnosis. In initial trials, CT angiography has been shown to be both accurate and safe to stratify patients with acute chest pain and absence of ECG changes as well as myocardial enzyme elevation [16, 46–50] (Figure 9.11). A potential cost advantage of incorporating CT angiography in the workup of low-likelihood acute chest pain patients as compared to the standard of care has been demonstrated [48], and the event rate in patients who were discharged based on a "negative" coronary CT angiogram after having been admitted with acute chest pain is extremely favorable [51, 52].

Coronary CT angiography and Ischemia

Coronary CT angiography, like invasive angiography, is a purely morphologic imaging modality and cannot demonstrate the functional relevance of stenoses (ischemia). Especially in the case of lesions with borderline degree of

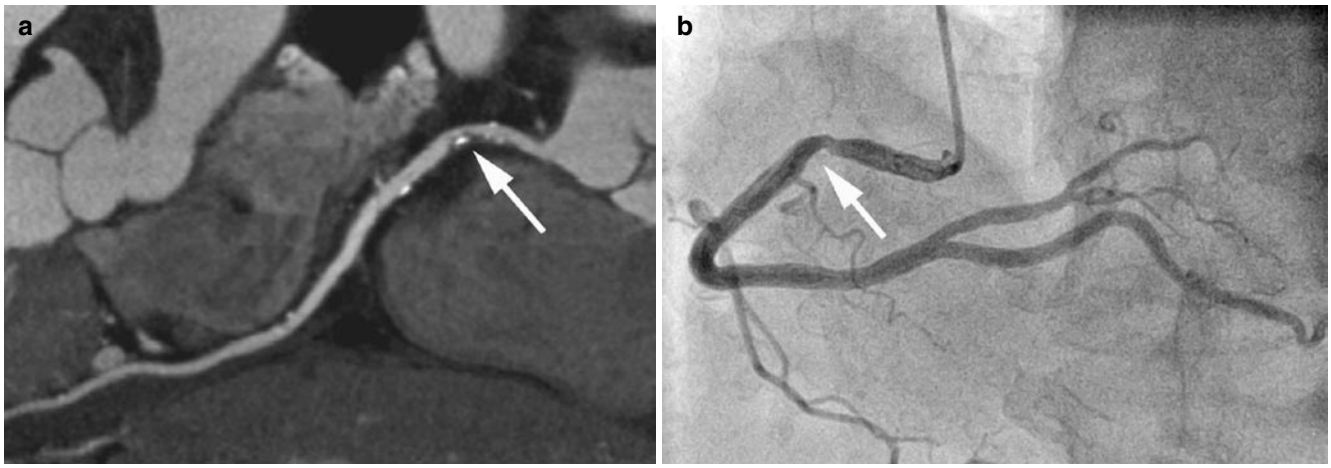

Figure 9.5. Frequently, the degree of luminal narrowing appears more severe in coronary CT angiography than in the invasive, catheter-based coronary angiogram. (**a)** Curved multiplanar reconstruction showing a stenosis in the proximal right coronary artery (*arrow*). (**b**) In the corresponding invasive angiogram, the stenosis appears less severe (*arrow*).

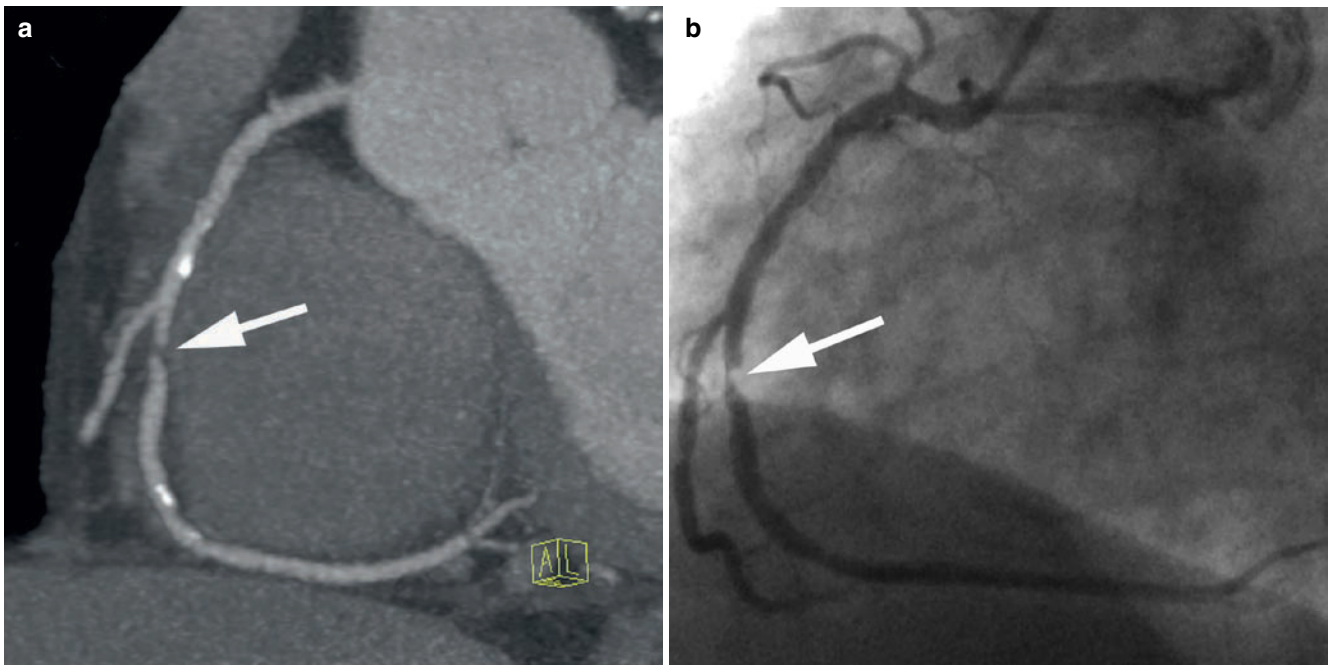

Figure 9.6. High-grade luminal stenoses often appear as complete interruption of the coronary artery lumen in coronary CT angiography. (**a**) Maximum Intensity Projection in a patient with a high-grade stenosis of the right coronary artery (*arrow*). At the site of the stenosis, the arterial lumen is completely interrupted. (**b**) Corresponding invasive coronary angiogram. A small residual lumen is present (*arrow*). The spatial resolution of CT is not sufficient to reliably visualize such small remaining lumina.

stenosis, this may be a limitation. Not surprisingly, coronary CT angiography is a better predictor of angiographic findings than testing for ischemia [53–55]. For example, an analysis of 114 patients with intermediate likelihood of coronary disease demonstrated that only 19 of 33 patients in whom stenoses were demonstrated by CCTA had ischemia in SPECT myocardial perfusion imaging. On the other hand, 28 of the 33 patients had obstructive coronary lesions in invasive coronary angiography. However, all 25 patients who received invasive angiography even though coronary CT angiography had ruled out the presence of obstructive stenoses had, in fact, a "negative" coronary angiogram [53]. Similarly, a comparison of SPECT and CT in 38 patients revealed that ruling out coronary artery stenoses by CT angiography had a negative predictive value of 94%, but detecting stenoses by CT only a positive predictive value of 32% to predict ischemia in myocardial perfusion imaging [56].

These results underscore that a "negative" coronary CT angiography result can reliably rule out the presence of coronary artery stenoses and the need for revascularization, and that it may therefore be a potential "gatekeeper" to avoid invasive angiograms. On the other hand, coronary CT angiography – like invasive angiography – should not be performed in an unselected patient population and is not

Table 9.1. Recommended categories of luminal stenosis severity for reporting coronary CT angiography[a]

Recommended quantitative stenosis grading
0 – Normal: Absence of plaque and no luminal stenosis
1 – Minimal: Plaque with <25% stenosis
2 – Mild: 25–49% stenosis
3 – Moderate: 50–69% stenosis
4 – Severe: 70–99% stenosis
5 – Occluded
Optional quantitative stenosis grading
0 – Normal: Absence of plaque and no luminal stenosis
1 – Mild: Plaque with <39% stenosis
2 – Moderate: 40–69% stenosis
3 – Severe: 70–99% stenosis
4 – Occluded

[a]Adapted from Raff et al [5]

for "screening" purposes. A positive CT scan by itself does not strongly predict the need for revascularization [56].

Coronary CT Angiography in the Context of Coronary Interventions

CT angiography may provide information that may be helpful in the context of coronary artery interventions. In addition to demonstrating the coronary lumen, CT imaging allows visualization of the amount and type of plaque, permits to quantify the amount of calcification, and can provide accurate, three-dimensional information on the angle of vessel bifurcations [57]. A recent publication described that coronary CT angiography allows accurate classification of coronary bifurcation lesions [58]. Older work, published by Mollet et al. in 2005, has demonstrated that CT angiography – by quantifying lesion length and degree of calcification – is more accurate than invasive angiography to predict the success of percutaneous treatment of chronic total coronary occlusions [59] (Figure 9.12).

Imaging of Coronary Atherosclerotic Plaque

Besides the detection of coronary artery stenoses, coronary CT angiography also allows the visualization of nonobstructive coronary atherosclerotic plaque. If image quality is sufficiently high, both calcified and noncalcified (a better term than *soft*) plaque components can be visualized (Figure 9.13). In data sets that have very high image quality and no artifacts, the sensitivity of coronary CT angiography to detect coronary artery segments affected by nonstenotic coronary atherosclerotic plaque has been reported to be between 80 and 90% [60]. Also, a number of studies have shown that plaque dimensions as well as the extent of coronary atherosclerotic remodeling can be estimated by coronary CT angiography [61–67] (Figure 9.14). However, measurements of plaque dimensions remain difficult, depend on sufficient image quality, and display a very high interobserver variability that has been reported to be as high as 37% [67, 68].

The presence and extent of coronary atherosclerotic plaque detected by coronary CT angiography has been shown to be associated with future cardiovascular events

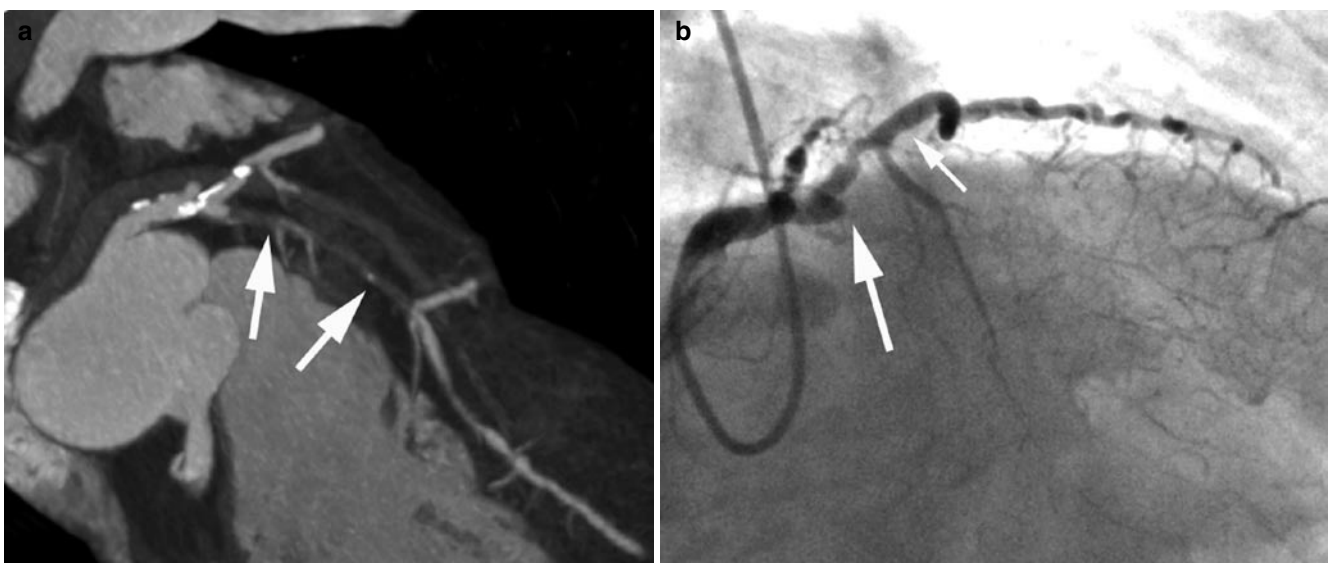

Figure 9.7. Total occlusion of the left anterior descending coronary artery. (**a**) Coronary CT angiography displays interruption of the coronary artery lumen over a long distance (*arrows*). (**b**) The invasive angiogram confirms proximal occlusion of the left anterior descending coronary artery (*large arrow*). The *small arrow* points at the diagonal branch.

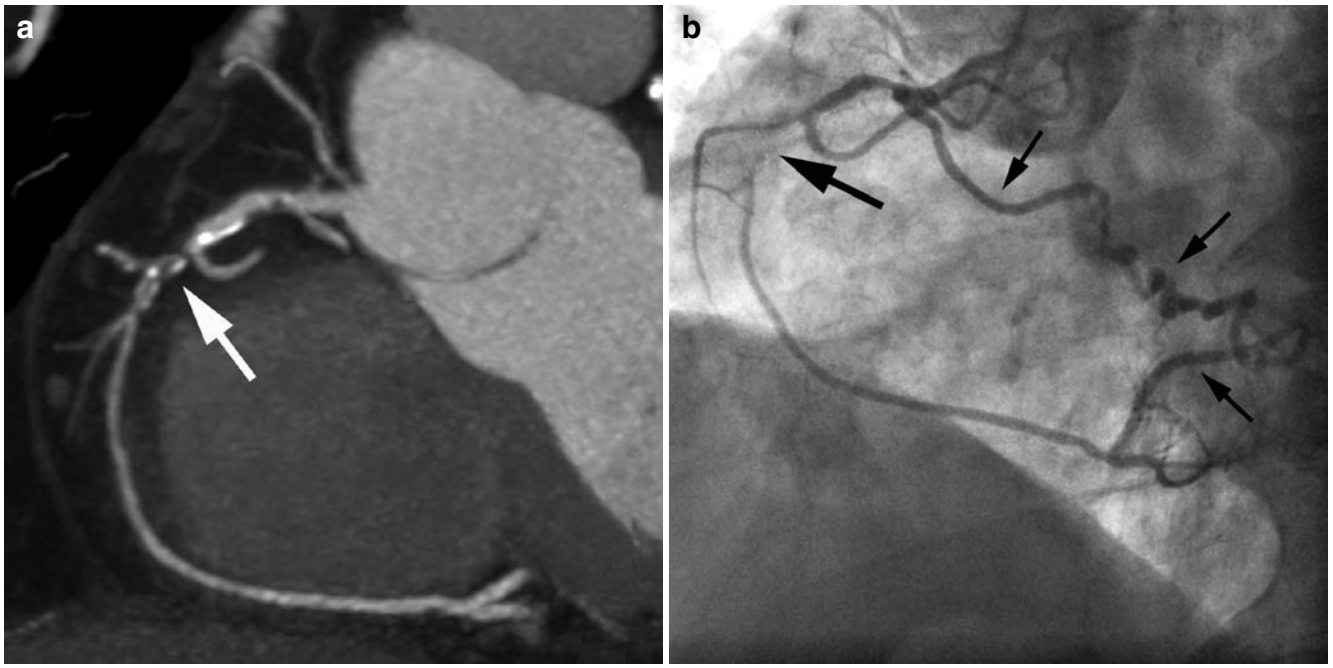

Figure 9.8. Coronary CT angiography cannot identify retrograde filling of a coronary artery via collaterals. (**a**) Maximum Intensity Projection of the right coronary artery showing lesion with severe impairment of the lumen (*arrow*). The distal vessel segments are filled with contrast. (**b**) Invasive coronary angiography shows chronic total occlusion of the proximal right coronary artery and retrograde filling of the mid and distal right coronary artery via a collateral vessel (Kugel's collateral).

in symptomatic patients in various studies. In a study performed by electron beam tomography (EBT) which included 2,538 patients who were followed for a mean period of 6 years, Ostrom et al. demonstrated that the presence of nonobstructive plaque in all three coronary arteries was associated with increased mortality (risk ratio 1.77 as compared to individuals without any detectable plaque). The presence of nonobstructive plaque in only one or two coronary vessels was not associated with an increased risk. Using 16-slice CT, Min et al. could demonstrate that the presence of coronary atherosclerotic plaque in at least five coronary artery segments in symptomatic patients was associated with increased mortality as compared to patients with detectable plaque in less than five segments [69]. Some information may be gained by analyzing plaque characteristics by CT. It has previously been shown that plaques with positive remodeling are associated with acute coronary syndromes. In a prospective study, Motoyama et al. demonstrated that plaques with positive remodeling and low CT attenuation were at particularly high risk for causing future cardiovascular events [70]. However, all of these data were obtained in patients who underwent coronary CT angiography for clinical reasons and who, consequently, were most likely symptomatic. In *asymptomatic* individuals, event rates are much lower. Consequently, it is more difficult to find a benefit of imaging for risk stratification. Currently, only one study is available which used coronary CT angiography for risk prediction in a healthy population. It included 1,000 Korean subjects aged 35–75 years [71]. 22% of individuals had detectable atherosclerosis, and coronary events – including revascularization – occurred exclusively in individuals with detectable plaque. However, most of these events were revascularizations triggered by the very fact that an atherosclerotic lesion had been detected and therefore do not necessarily indicate an impaired prognosis had CT not been performed. Appropriately, the authors of this study concluded that coronary CT angiography is not a useful screening tool in asymptomatic individuals.

Anomalous Coronary Arteries

Coronary CT angiography is an excellent tool to investigate patients with known or suspected congenital coronary artery anomalies (Figures. 9.15 and 9.16). Coronary CT angiography can classify both the origin and also the often complex course of anomalous coronary vessels [72–79]. While the necessity for contrast agent injection and radiation exposure are certain drawbacks of CT imaging as compared to MR, which is also a potential diagnostic tool in coronary artery anomalies, the ease of data acquisition and the predictability with which a high-resolution data set with optimal image quality for evaluation can be expected make coronary CT angiography a method of choice for the workup of known or suspected anomalous coronary vessels. Obviously, the use of low-dose image acquisition protocols is recommendable in the often young patients who undergo evaluation for anomalous coronary arteries.

Figure 9.9. Typical artifacts that can occur in coronary CT angiography. (**a**) Motion artifact due to rapid coronary artery movement. Here, the right coronary is affected. Motion causes blurring of the arterial contour (*large arrow*). It also causes low-density artifacts that, in this case, are outside the actual vessel cross-section (*small arrow*). Such artifacts are aggravated by the presence of calcium or other high-density material. (**b**) "misalignment" or "step" artifacts (*arrows*). Such artifacts can occur due to respiratory or other body motion or due to arrhythmias. (**c**) Severe calcification can render the coronary arteries uninterpretable regarding the presence of stenoses.

Guidelines and Recommendations

The possibility to perform noninvasive coronary angiography with CT is immensely attractive and care needs to be taken to avoid overutilization. Creating a "new layer" of testing in addition to currently available diagnostic procedures, without replacing other tests or, in the worst case, even leading to additional, unnecessary downstream testing must be avoided. Also, more than in other, established imaging modalities used in cardiology, the accuracy and clinical utility of coronary CT angiography depend on the expertise of the investigator. Finally, while there is rapidly accumulating evidence on accuracy, there are no data that link the use of CT angiography to improved outcomes. Consequently, official bodies and professional organizations have so far been reluctant to issue guidelines that would clearly support the use of CT imaging in the workup of coronary artery disease.

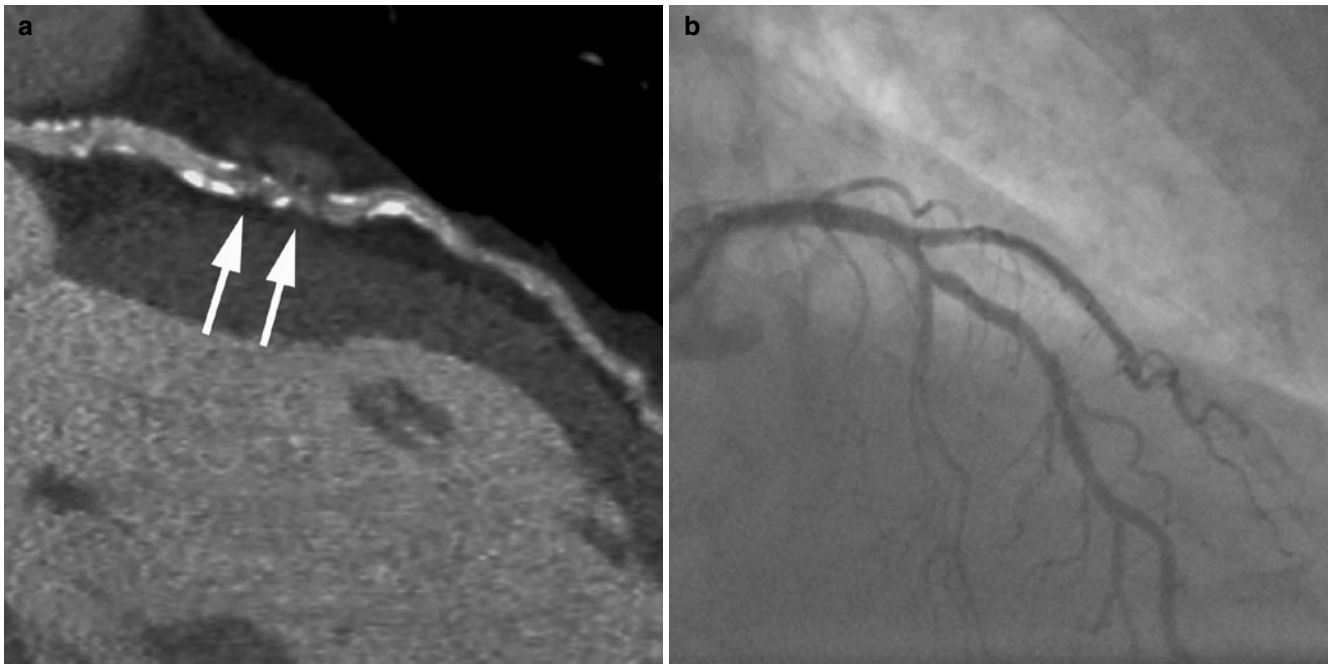

Figure 9.10. Artifacts typically lead to false-positive results of coronary CT angiography. (**a**) Calcification, slight motion and somewhat high image noise lead to a false-positive interpretation of the mid left anterior descending coronary artery (*arrows*). (**b**) Invasive angiography shows that no relevant stenosis is present.

The American Heart Association has issued a Scientific Statement on noninvasive coronary artery imaging [80].

Table 9.2. Results of meta-analyses that have evaluated the accuracy of coronary CT angiography for stenosis detection in comparison to invasive coronary angiography (*NPV* negative predictive value; *PPV* positive predictive value)

		Studies	Patients	Sensitivity (%)	Specificity (%)	NPV (%)	PPV (%)
Per-segment analysis							
Vanhoenacker et al [31]	16-slice CT	26	704	83	96	–	–
	64-slice CT	6	363	93	96	–	–
Hamon et al [32]	16-slice CT	16	1292	77	91	96	60
	64-slice CT	12	695	88	96	98	79
Abdulla et al [33]	64-slice CT	19	1,251	86	96	97	83
Gopalakrishnan et al [34]	16-slice CT	29	2,214	84	94	97	72
	40–64-slice CT	10	596	91	96	98	78
Mowatt et al [35]	64-slice CT	28	1,286	90	97	99	76
Per-patient analysis							
Vanhoenacker et al [31]	16-slice CT	26	704	97	81	–	–
	64-slice CT	6	363	99	93	–	–
Hamon et al [32]	16-slice CT	16	1292	95	69	92	79
	64-slice CT	12	695	97	90	96	93
Abdulla et al [33]	64-slice CT	13	875	98	91	94	97
Gopalakrishnan et al [34]	16-slice CT	29	2214	91	77	89	77
	40–64-slice CT	10	596	96	91	96	93
Mowatt et al [35]	64-slice CT	28	1,286	99	89	100	93

Table 9.3. Diagnostic performance of 64-slice CT depending on the clinical pretest likelihood of coronary artery disease in 254 patients[a]

Pretest probability[b]	*n*	Sensitivity	Specificity	Positive predicted value	Negative predicted value
High	105	98	74	93	89
Intermediate	83	100	84	80	100
Low	66	100	93	75	100

[a]Adapted from Meijboom et al [36]

[b]Estimated with the Duke Clinical Risk Score

Table 9.4. Diagnostic accuracy of 64-slice CT for the detection of patients with coronary artery stenoses in comparison to invasive coronary angiography in three multicenter trials

Author	Number of sites	Number of patients	Prevalence of obstructive CAD[a] (%)	Sensitivity	Specificity	Negative predictive value	Positive predictive value
Budoff [28]	16	230	25	95% (85–99%)	83% (76–88%)	99% (96–100%)	64% (53–75%)
Miller [37]	9	291	56	85% (79–90%)	90% (83–94%)	83% (75–89%)	91% (86–95%)
Meijboom [38]	3	360	68	99% (98–100%)	64% (55–73%)	97% (94–100%)	86% (82–90%)

[a]Presence of at least one stenosis of ≥50% diameter reduction

It contains the following comments concerning the use of coronary CT angiography for the detection of coronary artery stenoses:

> Neither coronary CT angiography nor coronary MR angiography should be used to screen for coronary artery disease in patients who have no signs or symptoms suggestive of coronary artery disease (Class III, level of evidence C) [80].

Figure 9.11. Typical findings of coronary CT angiography in patients with an acute coronary syndrome. (**a**) Coronary CT angiography (curved multiplanar reconstruction) shows three high-grade stenoses of the right coronary artery (*arrows*). (**b**) As frequently seen in acute coronary lesions, there is pronounced "positive remodeling" of the lesion, a consequence of plaque rupture with subsequent thrombus formation inside the vessel. (**c**) A cross-sectional view of the right coronary artery at the site of the lesion shows ring-like enhancement with a central filling defect. Similar to the pronounced positive remodeling shown in Figure 9.11B, this finding, when present, typically indicates an acute coronary lesion, but is not necessarily observed in all lesions associated with an acute coronary syndrome. (**d**) Invasive coronary angiogram.

The potential benefit of non-invasive coronary angiography is likely to be greatest and is reasonable for symptomatic patients who are at intermediate risk for coronary artery disease after initial risk stratification, including patients with equivocal stress-test results. (Class II, level of evidence B). Diagnostic accuracy favors coronary CT angiography over MR angiography for these patients (Class I, level of evidence B) [80].

In 2006, "Appropriateness Criteria" for cardiac CT and MR imaging were issued in the form of an Expert Consensus document. The *Appropriateness Criteria* list several situations in which coronary CT angiography is considered to be of clinical value (Table 9.5) [81]. Such situations include the use of CT coronary angiography to rule out coronary artery stenoses in patients who are symptomatic, but who have a noninterpretable or equivocal stress test, who are

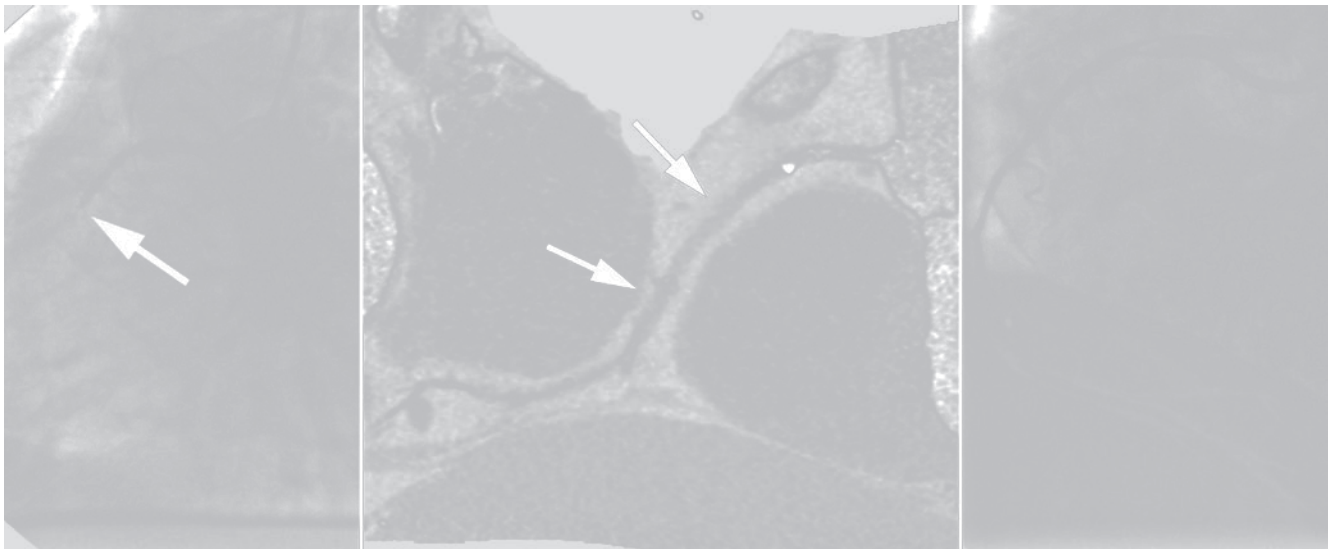

Figure 9.12. Chronic total coronary artery occlusion in coronary CT angiography. The preprocedural invasive coronary angiogram shows complete occlusion of the right coronary artery (*arrow* in *left panel*). Coronary CT angiography shows that the occluded segment is relatively long, but has very little calcification (*arrows*). Subsequent interventional revascularization is successful (*right panel*).

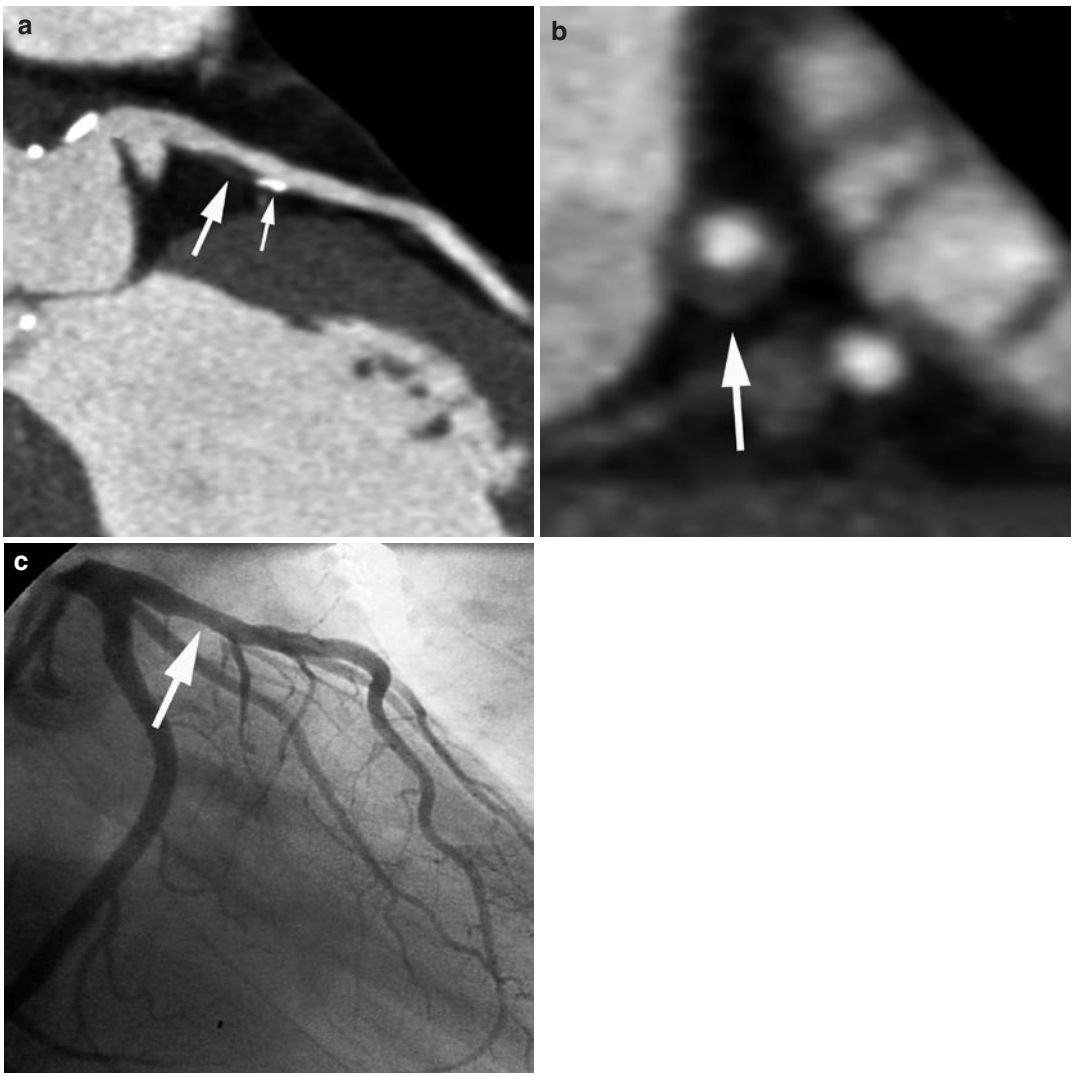

Figure 9.13. Visualization of nonobstructive coronary atherosclerotic plaque by CT. (**a**) Multiplanar reconstruction of the left anterior descending coronary artery. In the proximal vessel segment, a nonobstructive plaque which is partly calcified (*small arrow*) and partly noncalcified (*large arrow*) can easily be detected by CT. (**b**) Cross-sectional view of the plaque (*arrow*) shows its eccentric position. (**c**) Invasive coronary angiogram. Only a very slight luminal stenosis is present at the site of the plaque (*arrow*).

unable to exercise, or who have a noninterpretable ECG. Furthermore, the document considers the use of coronary CT angiography appropriate for patients with new onset heart failure and for patients who present witch acute chest pain and an intermediate pretest likelihood of coronary artery disease, but who have a normal ECG and absence of enzyme elevation (Table 9.3) [81]. Finally, the use of CT angiography is considered "appropriate" to evaluate patients with anomalous coronary arteries [81]. New *Appropriateness Criteria* for cardiac CT have been released in 2010, adding new appropriate uses to include coronary calcium scanning for asymptomatic persons and CTA for bypass graft evaluation, among others [82].

Limitations and Outlook

In spite of the impressive and continuously improving image quality, coronary CT angiography does not currently constitute a general replacement for invasive, catheter-based diagnostic coronary angiography. A lower spatial and temporal resolution as compared to invasive angiography, the requirement for regular and low heart rates, and the necessity for breathhold cooperation will preclude CT angiography in a relevant fraction of patients who require a workup for coronary artery disease. In addition, coronary CT angiography performs less well in patients with diffuse, severe disease, with substantial coronary calcification, or with small coronary arteries (as encountered, e.g., in some individuals with diabetes). For these cases and all situations where the need for a revascularization procedure is expected based on clinical grounds, an invasive approach and catheter-based angiography will remain the best diagnostic option.

Coronary CT angiography should only be performed by well-trained and experienced operators and only in individuals where fully diagnostic image quality can be expected. Its use should be limited to clinical situations where the expected

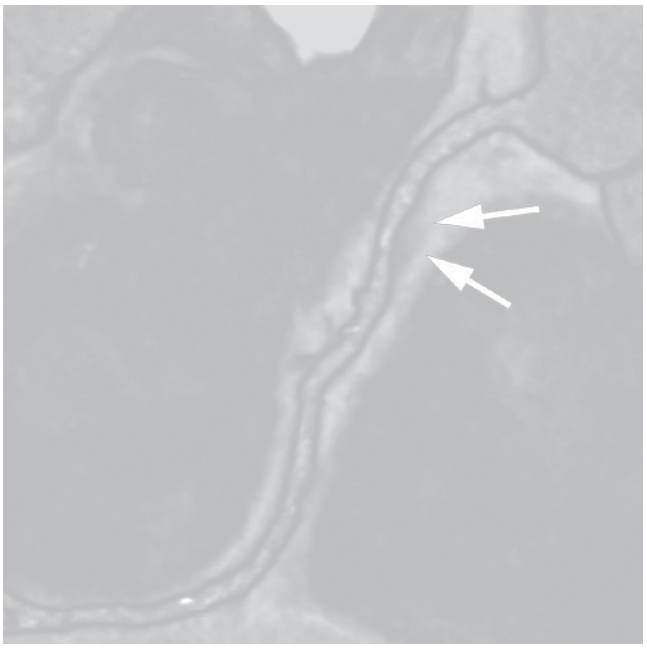

Figure 9.14. Pronounced positive remodeling of a nonobstructive, noncalcified coronary atherosclerotic plaque of the right coronary artery (*arrows*).

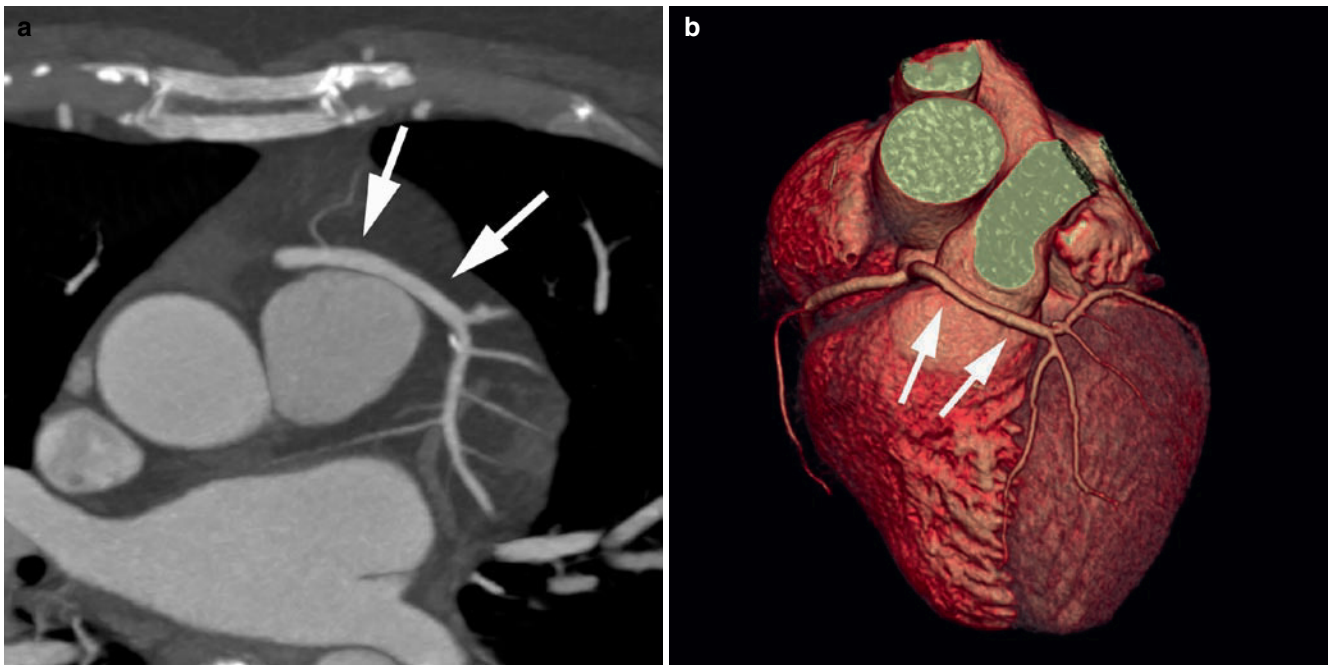

Figure 9.15. Visualization of a coronary anomaly by CT. Due to its three-dimensional nature, coronary CT angiography allows excellent delineation of the origin and course of anomalous coronary arteries. This patient has an anomalous left main coronary artery arising from the right coronary sinus and travelling anterior to the pulmonary artery, with subsequent division into the left anterior descending and left circumflex coronary artery. This infrequent anomaly is clinically harmless. (**a**) Two-dimensional CT image in transaxial orientation which shows the position of the anomalous left main coronary artery anterior to the pulmonary artery (*arrows*). (**b**) Three-dimensional reconstruction. The *arrows* point at the anomalous left main coronary artery.

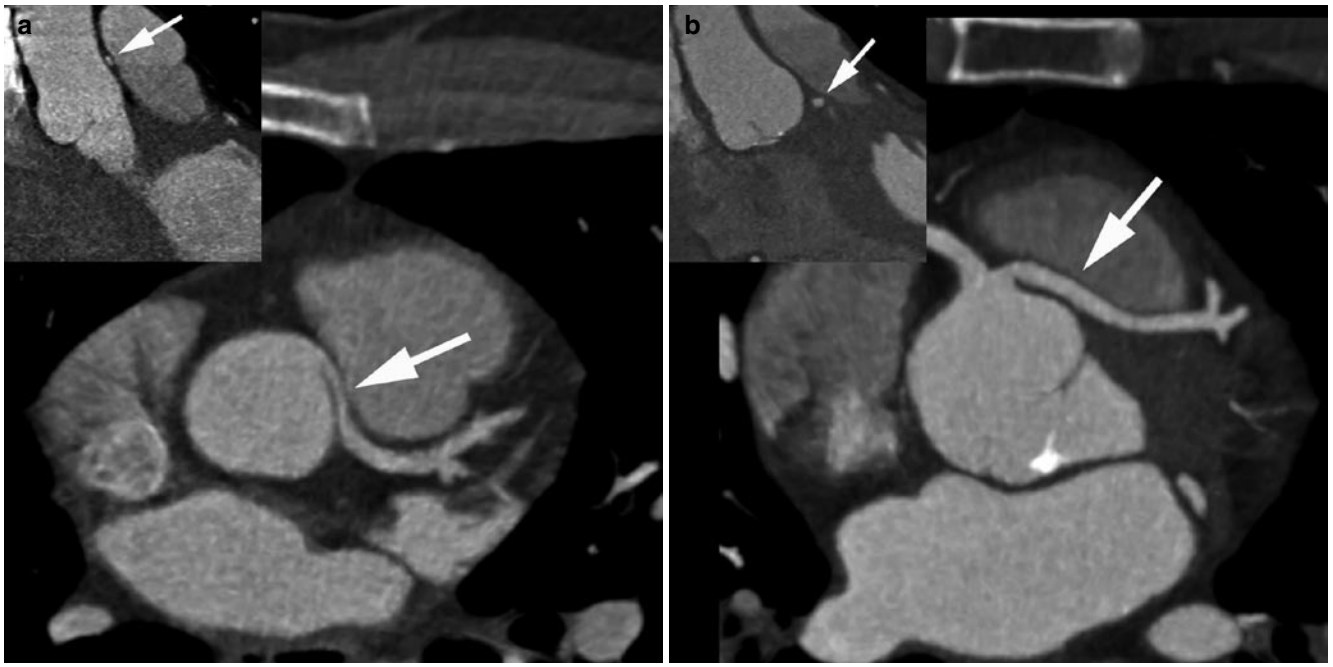

Figure 9.16. "Interarterial" vs. "subpulmonary" course of an anomalous left main coronary artery. (**a**) Patient with an anomalous left main coronary artery (*arrows*) that arises from the right coronary sinus and follows an "interarterial" course between the ascending aorta and right pulmonary artery. In this location (see *inset*), there is potential danger of ischemia due to kinking or compression of the left main coronary artery. Surgical correction, irrespective of symptoms, is frequently suggested. (**b**) Patient with an anomalous left main coronary which also arises from the right coronary sinus but then travels below the pulmonary artery, embedded in the septum ("subpulmonary" or "transseptal" course, see *arrows*). This anomaly is typically considered less harmful.

Table 9.5. "Appropriate" indications for CT coronary angiography according to an Expert Consensus Document[a]

Detection of CAD with prior test results – evaluation of chest pain syndrome
Uninterpretable or equivocal stress test result (exercise, perfusion, or stress echo)
Detection of CAD: symptomatic – evaluation of chest pain syndrome
Intermediate pretest probability of CAD, ECG uninterpretable or unable to exercise
Detection of CAD: symptomatic – acute chest pain
Intermediate pretest probability of CAD, no ECG changes and serial enzymes negative
Evaluation of coronary arteries in patients with new onset heart failure to assess etiology
Detection of CAD: symptomatic
Evaluation of suspected coronary anomalies

[a]Adapted from Hendel et al [81]

results are relevant to further management. Care needs to be taken to identify these situations and to target the utilization of coronary CT angiography towards those patients who benefit most. Continuously accumulating evidence will help better understand the clinical settings in which CT angiography is most useful. In addition, CT technology displays a truly impressive, ongoing evolution. The resulting measurable improvements in image quality are likely to translate into more stable, more diverse, and more widely accepted clinical applications of coronary CT angiography in the future.

References

1. Abbara S, Arbab-Zadeh A, Callister TQ, et al. SCCT guidelines for performance of coronary computed tomographic angiography: a report of the Society of Cardiovascular Computed Tomography Guidelines Committee. *J Cardiovasc Comput Tomogr*. 2009;3:190–204.
2. Achenbach S, Ropers U, Kuettner A, et al. Randomized comparison of 64-slice single- and dual-source computed tomography for the detection of coronary artery disease. *J Am Coll Cardiol Img*. 2008;1:177–186.
3. Ferencik M, Ropers D, Abbara S, et al. Diagnostic accuracy of image postprocessing methods for the detection of coronary artery stenoses by using multidetector CT. *Radiology*. 2007;243:696–702.
4. Cheng V, Gutstein A, Wolak S, et al. Moving beyond binary grading of coronary arterial stenoses on coronary computed tomographic angiography: insights for the imager and referring clinician. *JACC Cardiovasc Imaging*. 2008;1:472–474.
5. Raff GL, Abidov A, Achenbach S, et al. SCCT guidelines for the interpretation and reporting of coronary computed tomographic angiography. *J Cardiovasc Comput Tomogr*. 2009;3:122–136.
6. Hoffmann U, Moselewski F, Cury RC, et al. Predictive value of 16-slice multidetector spiral computed tomography to detect significant obstructive coronary artery disease in patients at high risk for coronary artery disease: patient-versus segment-based analysis. *Circulation*. 2004;110:2638–2643.
7. Lim MCL, Wong TW, Yaneza LO, De Larrazabal C, Lau JK, Boey HK. Non-invasive detection of significant coronary artery disease with multi-section computed tomography angiography in patients with suspected coronary artery disease. *Clin Radiol*. 2006;61:174–180.
8. Halon DA, Gaspar T, Adawi S, et al. Uses and limitations of 40 slice multi-detector row spiral computed tomography for diagnosing coronary lesions in unselected patients referred for routine invasive coronary angiography. *Cardiology*. 2007;108:200–209.
9. Watkins MW, Hesse B, Green CE, et al. Detection of coronary artery stenosis using 40-channel computed tomography with multisegment reconstruction. *Am J Cardiol*. 2007;99:175–181.
10. Grosse C, Globits S, Hergan K. Forty-slice spiral computed tomography of the coronary arteries: assessment of image quality and diagnostic accuracy in a non-selected patient population. *Acta Radiol*. 2007;48:36–44.
11. Ropers D, Rixe J, Anders K, et al. Usefulness of multidetector row computed tomography with 64 x 0.6 mm collimation and 330-ms rotation for the noninvasive detection of significant coronary artery stenoses. *Am J Cardiol*. 2006;97:343–348.

12. Fine JJ, Hopkins CB, Ruff N, Newton FC. Comparison of accuracy of 64-slice cardiovascular computed tomography with coronary angiography in patients with suspected coronary artery disease. *Am J Cardiol*. 2006;97:173–174.
13. Nikolaou K, Knez A, Rist C, et al. Accuracy of 64-MDCT in the diagnosis of ischemic heart disease. *AJR*. 2006;187:111–117.
14. Schlosser T, Mohrs OK, Magedanz A, et al. Noninvasive coronary angiography using 64-detector-row computed tomography in patients with a low to moderate pretest probability of significant coronary artery disease. *Acta Radiol*. 2007;48:300–307.
15. Mühlenbruch G, Seyfarth T, Soo CS, Pregalathan N, Mahnken AH. Diagnostic value of 64-slice multi-detector row cardiac CTA in symptomatic patients. *Eur Radiol*. 2007;17:603–609.
16. Meijboom WB, Mollet NR, Van Mieghem CA, et al. 64-slice computed tomography coronary angiography in patients with non-ST elevation acute coronary syndrome. *Heart*. 2007;93:1386–1392.
17. Herzog C, Zwerner PL, Doll JR, et al. Significant coronary artery stenosis: comparison on per-patient and per-vessel or per-segment basis at 64-section CT angiography. *Radiology*. 2007;244:112–120.
18. Ehara M, Surmely JF, Kawai M, et al. Diagnostic accuracy of 64-slice computed tomography for detecting angiographically significant coronary artery stenosis in an unselected consecutive patient population. *Circ J*. 2007;70:564–571.
19. Hausleiter J, Meyer T, Hadamitzky M, et al. Non-invasive coronary computed tomographic angiography for patients with suspected coronary artery disease: the coronary angiography by computed tomography with the use of a submillimeter resolution (CACTUS) trial. *Eur Heart J*. 2007;28:3034–3041.
20. Shabestari AA, Abdi S, Akhlaghpoor S, et al. Diagnostic performance of 64-channel multislice computed tomography in assessment of significant coronary artery disease in symptomatic subjects. *Am J Cardiol*. 2007;99:1656–1661.
21. Scheffel H, Alkadhi H, Plass A, et al. Accuracy of dual-source CT coronary angiography: first experience in a high pre-test probability population without heart rate control. *Eur Radiol*. 2006;16:2739–2747.
22. Heuschmid M, Burgstahler C, Reimann A, et al. Usefulness of noninvasive cardiac imaging using dual-source computed tomography in an unselected population with high prevalence of coronary artery disease. *Am J Cardiol*. 2007;100:587–592.
23. Ropers U, Ropers D, Pflederer T, et al. Influence of heart rate on the diagnostic accuracy of dual-source tomography computed angiography. *J Am Coll Cardiol*. 2007;50:2393–2398.
24. Leber AW, Johnson T, Becker A, et al. Diagnostic accuracy of dual-source multi-slice CT-coronary angiography in patients with an intermediate pretest likelihood for coronary artery disease. *Eur Heart J*. 2007;28:2354–2360.
25. Weustink AC, Meijboom WB, Mollet NR, et al. Reliable high-speed coronary computed tomography in symptomatic patients. *J Am Coll Cardiol*. 2007;50:786–794.
26. Alkadhi H, Scheffel H, Desbiolles L, et al. Dual-source computed tomography coronary angiography: influence of obesity, calcium load, and heart rate on diagnostic accuracy. *Eur Heart J*. 2008;29:766–776.
27. Gosthine S, Caussin C, Daoud B, et al. Non-invasive detection of coronary artery disease in patients with left bundle branch block using 64-slice computed tomography. *J Am Coll Cardiol*. 2006;48: 1929–1934.
28. Budoff MJ, Dowe D, Jollis JG, et al. Diagnostic performance of 64-multidetector row coronary computed tomographic angiography for evaluation of coronary artery stenosis in individuals without known coronary artery disease: results from the prospective multicenter ACCURACY (Assessment by Coronary Computed Tomographic Angiography of Individuals Undergoing Invasive Coronary Angiography) trial. *J Am Coll Cardiol*. 2008;52:1724–1732.
29. Vanhoenacker PK, Heijenbrok-Kal MH, Van Heste R, et al. Diagnostic performance of multidetector CT angiography for assessment of coronary artery disease: meta-analysis. *Radiology*. 2007;244:419–428.
30. Pugliese F, Mollet NR, Hunink MG, et al. Diagnostic performance of coronary CT angiography by using different generations of multisection scanners: single-center experience. *Radiology*. 2008;246:384–393.
31. Vanhoenacker PK, Heijenbrok-Kal MH, Van Heste R. et al Diagnostic performance of multidetector CT angiography for assessment of coronary artery disease: meta-analysis. *Radiology*. 2007;244:419–428.
32. Hamon M, Lepage O, Malagutti P, et al. Coronary arteries: diagnostic performance of 16- versus 64-section spiral CT compared with invasive coronary angiography – meta-analysis. *Radiology*. 2007;245:720–731.
33. Abdulla J, Abildstrom SZ, Gotzsche O, Christensen E, Kober L, Torp-Pedersen C. 64-multislice detection computed tomography coronary angiography as a potential alternative to conventional coronary angiography: a systematic review and meta-analysis. *Eur Heart J*. 2007;28:3042–3050.
34. Gopalakrishnan P, Wolson GT, Tak K. Accuracy of multislice computed tomography coronary angiography: a pooled estimate. *Cardiol Rev*. 2008;16:189–196.
35. Mowatt G, Cook JA, Hillis GS, et al. 64-Slice computed tomography angiography in the diagnosis and assessment of coronary artery disease: systematic review and meta-analysis. *Heart*. 2008;94:1386–1393.
36. Meijboom WB, van Mieghem CA, Mollet NR, et al. 64-slice computed tomography coronary angiography in patients with high, intermediate, or low pretest probability of significant coronary artery disease. *J Am Coll Cardiol*. 2007;50:1469–1475.
37. Miller JM, Rochitte CE, Dewey M, et al. Diagnostic performance of coronary angiography by 64-row CT. *N Engl J Med*. 2008;359:2324–2336.
38. Meijboom WB, Meijs MF, Schuijf JD, et al. Diagnostic accuracy of 64-slice computed tomography coronary angiography: a prospective, multicenter, multivendor study. *J Am Coll Cardiol*. 2008;52:2135–2144.
39. Danciu SC, Herrera CJ, Stecy PJ, Carell E, Saltiel F, Hines JL. Usefulness of multislice computed tomographic coronary angiography to identify patients with abnormal myocardial perfusion stress in whom diagnostic catheterization may be safely avoided. *Am J Cardiol*. 2007; 100:1605–1608.
40. Gilard M, Le Gal G, Cornily JC, et al. Midterm prognosis of patients with suspected coronary artery disease and normal multislice computed tomography findings. A prospective management outcome study. *Arch Intern Med*. 2007;165:1686–1689.
41. Lesser JR, Flygenring B, Knickelbine T, et al. Clinical utility of coronary CT angiography: coronary stenosis detection and prognosis in ambulatory patients. *Cath Cardiovasc Interv*. 2007;69:64–72.
42. Hadamitzky M, Freissmuth B, Meyer T, et al. Prognostic value of coronary computed tomographic angiography for prediction of cardiac events in patients with suspected coronary artery disease. *JACC Cardiovasc Imaging*. 2009;2:404–11.
43. Ostrom MP, Gopal A, Ahmadi N, et al. Mortality incidence and the severity of coronary atherosclerosis assessed by computed tomography angiography. *J Am Coll Cardiol*. 2008;52:1335–1343.
44. Gallagher AA, MJ CKM, Mehta LS, Wegner JH, Raff GH. Clinical effectiveness of coronary computed tomographic angiography in the triage of patients to cardiac catheterization and revascularization after inconclusive stress testing: results of a 2-year prospective trial. *J Nucl Cardiol*. 2009;16(5):701–13.
45. Min JK, Kang N, Shaw LJ, et al. Costs and clinical outcomes after coronary multidetector CT angiography in patients without known coronary artery disease: comparison to myocardial perfusion SPECT. *Radiology*. 2008;249:62–70.
46. Hoffmann U, Nagurney JT, Moselewski F, et al. Coronary multidetector computed tomography in the assessment of patients with acute chest pain. *Circulation*. 2006;114:2251–2260.
47. Gallagher MJ, Ross MA, Raff GL, Goldstein JA, O'Neill WW, O'Neil B. The diagnostic accuracy of 64-slice computed tomography coronary angiography compared with stress nuclear imaging in emergency department low-risk chest pain patients. *Ann Emerg Med*. 2007;49:125–136.
48. Goldstein JA, Gallagher MJ, O'Neill WW, Ross MA, O'Neil BJ, Raff GL. A randomized controlled trial of multi-slice coronary computed tomography for evaluation of acute chest pain. *J Am Coll Cardiol*. 2007;49:863–871.
49. Coles DR, Wilde P, Oberhoff M, Rogers CA, Karsch KR, Baumbach A. Multislice computed tomography coronary angiography in patients admitted with a suspected acute coronary syndrome. *Int J Cardiovasc Imaging*. 2007;23:603–614.

50. Hoffmann U, Bamberg F, Chae CU, et al. Coronary computed tomography angiography for early triage of patients with acute chest pain: The ROMICAT (rule out myocardial infarction using computer assisted tomography) trial. *J Am Coll Cardiol*. 2009;53:1642–1650.
51. Hollander JE, Chang AM, Shofer FS, et al. One-year outcomes following coronary computerized tomographic angiography for evaluation of emergency department patients with potential acute coronary syndrome. *Acad Emerg Med*. 2009;16(8):693–698.
52. Rubinshtein R, Halon DA, Gaspar T, et al. Usefulness of 64-slice cardiac computed tomographic angiography for diagnosing acute coronary syndromes and predicting clinical outcome in emergency department patients with chest pain of uncertain origin. *Circulation*. 2007;115:1762–1768.
53. Schuijf JD, Wijns W, Jukema JW, et al. Relationship between noninvasive coronary angiography with multi-slice computed tomography and myocardial perfusion imaging. *J Am Coll Cardiol*. 2006;48:2508–2514.
54. Hacker M, Jakobs T, Hack N, et al. Combined use of 64-slice computed tomography angiography and gated myocardial perfusion SPECT for the detection of functionally relevant coronary artery stenoses. First results in a clinical setting concerning patients with stable angina. *Nuklearmedizin*. 2007;46:29–35.
55. Hacker M, Jakobs T, Hack N, et al. Sixty-four slice spiral CT angiography does not predict the functional relevance of coronary artery stenoses in patients with stable angina. *Eur J Nucl Med Mol Imaging*. 2007;34:4–10.
56. Berman DS, Hachamovitch R, Shaw LJ, et al. Roles of nuclear cardiology, cardiac computed tomography, and cardiac magnetic resonance: Noninvasive risk stratification and a conceptual framework for the selection of noninvasive imaging tests in patients with known or suspected coronary artery disease. *J Nucl Med*. 2006;47:1107–1118.
57. Pflederer T, Ludwig J, Ropers D, Daniel WG, Achenbach S. Measurement of coronary artery bifurcation angles by multidetector computed tomography. *Invest Radiol*. 2006;41:793–798.
58. Van Mieghem CA, Thury A, Meijboom WB, et al. Detection and characterization of coronary bifurcation lesions with 64-slice computed tomography coronary angiography. *Eur Heart J*. 2007;28:1968–1976.
59. Mollet NR, Hoye A, Lemos PA, et al. Value of preprocedure multislice computed tomographic coronary angiography to predict the outcome of percutaneous recanalization of chronic total occlusions. *Am J Cardiol*. 2005;95:240–243.
60. Springer I. *Dewey M*. Comparison of multislice computed tomography with intravascular ultrasound for detection and characterization of coronary artery plaques: A systematic review. Eur J Radiol; 2008 [Epub ahead of print.].
61. Achenbach S, Moselewski F, Ropers D, et al. Detection of calcified and noncalcified coronary atherosclerotic plaque by contrast-enhanced, submillimeter multidetector spiral computed tomography: a segment-based comparison with intravascular ultrasound. *Circulation*. 2004;109:14–17.
62. Moselewski F, Ropers D, Pohle K, et al. Comparison of measurement of cross-sectional coronary atherosclerotic plaque and vessel areas by 16-slice multidetector computed tomography versus intravascular ultrasound. *Am J Cardiol*. 2004;94:1294–1297.
63. Sun J, Zhang Z, Lu B, et al. Identification and quantification of coronary atherosclerotic plaques: a comparison of 64-MDCT and intravascular ultrasound. *AJR Am J Roentgenol*. 2008;190:748–754.
64. Otsuka M, Bruining N, Van Pelt NC, et al. Quantification of coronary plaque by 64-slice computed tomography: a comparison with quantitative intracoronary ultrasound. *Invest Radiol*. 2008;43:314–321.
65. Petranovic M, Soni A, Bezzera H, et al. Assessment of nonstenotic coronary lesions by 64-slice multidetector computed tomography in comparison to intravascular ultrasound: evaluation of nonculprit coronary lesions. *J Cardiovasc Comput Tomogr*. 2009;3:24–31.
66. Achenbach S, Ropers D, Hoffmann U, et al. Assessment of coronary remodeling in stenotic and nonstenotic coronary atherosclerotic lesions by multidetector spiral computed tomography. *J Am Coll Cardiol*. 2004;43:842–847.
67. Leber AW, Becker A, Knez A, et al. Accuracy of 64-slice computed tomography to classify and quantify plaque volumes in the proximal coronary system: a comparative study using intravascular ultrasound. *J Am Coll Cardiol*. 2006;47:672–677.
68. Pflederer T, Schmid M, Ropers D, et al. Interobserver variability of 64-slice computed tomography for the quantification of non-calcified coronary atherosclerotic plaque. *Röfo*. 2007;179:953–957.
69. Min JK, Shaw LJ, Devereux RB, et al. Prognostic value of multidetector coronary computed tomographic angiography for prediction of all-cause mortality. *J Am Coll Cardiol*. 2007;50:1161–1170.
70. Motoyama S, Sarai M, Harigaya H, et al. Computed tomographic angiography characteristics of atherosclerotic plaques subsequently resulting in acute coronary syndrome. *J Am Coll Cardiol*. 2009;54:49–57.
71. Choi EK, Choi SI, Rivera JJ, et al. Coronary computed tomography angiography as a screening tool for the detection of occult coronary artery disease in asymptomatic individuals. *J Am Coll Cardiol*. 2008;52:357–365.
72. Ropers D, Moshage W, Daniel WG, et al. Visualization of coronary artery anomalies and their course by contrast-enhanced electron beam tomography and three-dimensional reconstruction. *Am J Cardiol*. 2001;87:193–197.
73. Deibler AR, Kuzo RS, Vohringer M, et al. Imaging of congenital coronary anomalies with multislice computed tomography. *Mayo Clin Proc*. 2004;79:1017–1023.
74. Datta J, White CS, Gilkeson RC, et al. Anomalous coronary arteries in adults: depiction at multi-detector row CT angiography. *Radiology*. 2005;235:812–818.
75. Schmid M, Achenbach S, Ludwig J, et al. Ropers D Visualization of coronary artery anomalies by contrast-enhanced multi-detector row spiral computed tomography. *Int J Cardiol*. 2006;111:430–435.
76. Kim SY, Seo JB, Do KJ, et al. Coronary artery anomalies: classification and ECG-gated multi-detector row CT findings with angiographic correlation. *Radiographics*. 2006;26:317–333.
77. Duran C, Kantarci M, Durur Subais I, et al. Remarkable anatomic anomalies of coronary arteries and their clinical importance: a multidetector computed tomography angiographic study. *J Comput Assist Tomogr*. 2006;30:939–948.
78. Kini S, Bis KG, Weaver L. Normal and variant coronary arterial and venous anatomy on high-resolution CT angiography. *AJR M J Roentgenol*. 2007;188:1665–1674.
79. Dodd JD, Ferencik M, Liberthson RR, et al. Congenital anomalies of coronary artery origin in adults: 64-MDCT appearance. *AJR Am J Roentgenol*. 2007;188:W138–W146.
80. Bluemke DA, Achenbach S, Budoff M, et al. Noninvasive coronary artery imaging: magnetic resonance angiography and multidetector computed tomography angiography: a scientific statement from the American Heart Association Committee on cardiovascular imaging and intervention of the council on cardiovascular radiology and intervention, and the councils on clinical cardiology and cardiovascular disease in the young. *Circulation*. 2008;118:586–606.
81. Hendel RC, Patel MR, Kramer CM, et al. ACCF/ACR/SCCT/SCMR/ASNC/NASCI/SCAI/SIR 2006 appropriateness criteria for cardiac computed tomography and cardiac magnetic resonance imaging: a report of the American College of Cardiology Foundation Quality Strategic Directions Committee Appropriateness Criteria Working Group, American College of Radiology, Society of Cardiovascular Computed Tomography, Society for Cardiovascular Magnetic Resonance, American Society of Nuclear Cardiology, North American Society for Cardiac Imaging, Society for Cardiovascular Angiography and Interventions, and Society of Interventional Radiology. *J Am Coll Cardiol*. 2006;48:1475–1497.
82. Taylor AJ, Cequeira M, Hodgson J, Mark D, Min J, O'Gara P, Pearson S, Rubin G. ACCF/SCCT/ACR/AHA/ASE/ASNC/SCAI/SCMR 2010 Appropriate Use Criteria for Cardiac Computed Tomography. *J Am Coll Cardiol*. 2010;55.

10

Coronary Angiography After Revascularization

Axel Schmermund, Annett Magedanz, Marco J. M. Schmidt, Thomas Schlosser, and Thomas Voigtländer

Background

As a result of the high prevalence of coronary artery disease in the Western world and increasingly also in the developing countries, coronary artery revascularization, albeit complex and expensive, is one of the most frequent medical procedures. It is estimated that annually worldwide approximately 800,000 patients undergo bypass surgery [1], and >1.5 million cardiac percutaneous interventions are performed. With the increasing success of these procedures and improved long-term results, it is no longer current practice to perform routine invasive follow-up examination after revascularization. Only patients with evidence of recurrent ischemia undergo coronary angiography. However, the decision to perform or withhold coronary angiography can be exceedingly difficult in patients who have a history of coronary artery revascularization. Commonly, the fact that coronary artery disease has been previously established will lead many physicians to liberally order invasive coronary angiography if their patients experience symptoms faintly reminiscent of angina pectoris. In this setting, coronary CT angiography increasingly plays a role for obtaining reliable information on coronary artery anatomy noninvasively.

Bypass Grafts

Venous Grafts: Anatomy and Natural History

Venous bypass grafts still represent the majority of all grafts used for bypass surgery. Due to differences in anatomy and surgical techniques, their patency rates are inferior to internal mammary artery grafts [1, 2]. Three modes of venous bypass graft degeneration have been described which occur at different time points after surgery. Within hours to weeks after surgery, technical deficiencies and thrombotic activation lead to early thrombotic occlusion in approximately 5–10% of the grafts [3]. Over the course of the following year, intimal hyperplasia and thrombosis appear to be the major mechanisms, accounting for an overall occlusion rate of 10–15% within the first year [3, 4]. Finally, after the first year, mechanisms known from native coronary artery atherosclerosis predominate. Bypass attrition between postoperative years 1 and 5 appears to be minimal. After year 5, atherothrombotic occlusion of venous grafts accounts for a reduced patency rate. It has traditionally been estimated to range between 40 and 60% at 10–12 years [3, 5]. However, data from the Veteran Affairs Cooperative Study indicate that venous grafts which are open 1 week after surgery have a patency rate of 68% after 10 years [1]. The presence of angiographic stenoses between 50 and 99% of graft diameter appears to be 17–22% at 10 years [1]. As opposed to native coronary arteries and arterial grafts, venous bypass grafts tend to develop an extensive thrombotic burden and occlude quite rapidly once a high-grade stenosis has formed.

Arterial Grafts: Anatomy and Natural History

The left internal mammary artery ("IMA") is most often used as arterial graft. Arterial vessels are by design much better adapted to systemic blood pressure values and shear stress than venous vessels, and this translates into improved patency rates [1, 2]. IMA grafts patent at 1 week after surgery had a 10-year patency rate of 88% in the Veterans Affairs Cooperative Study [1]. As with venous grafts, recipient vessel location and status influence graft survival. Survival is best for grafts to the left anterior descending coronary artery and a native vessel diameter ≥2 mm [1]. Interestingly, IMA grafts sewed to a recipient vessel with <50% diameter stenosis may have a very high rate of occlusion, probably due to competing flow through the native vessel [6]. Regarding CT imaging, the smaller lumen diameter of arterial grafts and frequent use of metal clips represent a challenge for diagnostic image quality.

Noninvasive CT Examination

Venous bypass grafts are typically larger in diameter than the native large epicardial coronary arteries (approximately 4–10 mm vs. 2–5 mm), and they are less subjected to cardiac motion. Accordingly, even with older-generation ("noncardiac") CT machines, investigators examined contrast enhancement along the course of the graft to establish bypass patency [7, 8]. Due to the inherent limitations of nongated scanning with relatively long acquisition times, overall diagnostic accuracy regarding bypass graft patency remained at approximately 90%, with better results for (larger) vein grafts than for the arterial grafts. It was not possible to identify potential nonocclusive high-grade bypass body stenoses, the distal anastomosis of the grafts, or the native coronary arterial run-off. The advent of electron-beam computed tomography (EBCT) as the first dedicated cardiac CT scanner and the development of noninvasive coronary angiography beginning in 1994 allowed for visualization of coronary bypass grafts and 3D representation of the graft vessels [9]. Still, however, image quality was in part insufficient for detailed analysis of small diameter grafts or the complex anatomy of native vessels and the anastomosis region. Also, artifacts related to metal clips and breathing / arrhythmias hampered image quality. Despite these limitations, EBCT bypass angiography was used for some years for detecting venous bypass graft occlusion or stenosis within the shaft body and proved to be helpful in a subset of patients with unspecific symptoms after bypass surgery.

With the later generations of multidetector CT angiography with 64 and more slices, shorter gantry rotation times, and reduced slice thickness, stenosis detection in more difficult situations such as in the bypass anastomosis region and in the visualization of arterial grafts surrounded by metal clips was greatly improved. Currently, arterial grafts and the anastomosis region of venous and arterial grafts can be analyzed with increased diagnostic yield [10–18] (Figure 10.1 and 10.2). Ropers et al. reported that even an analysis of native vessel disease progression appears to be possible [14] (Figure 10.3). Indeed, regarding the exclusion of high-grade stenoses, the negative predictive value was 100% for bypass grafts and 96–98% for the native coronary arteries (grafted or nongrafted).

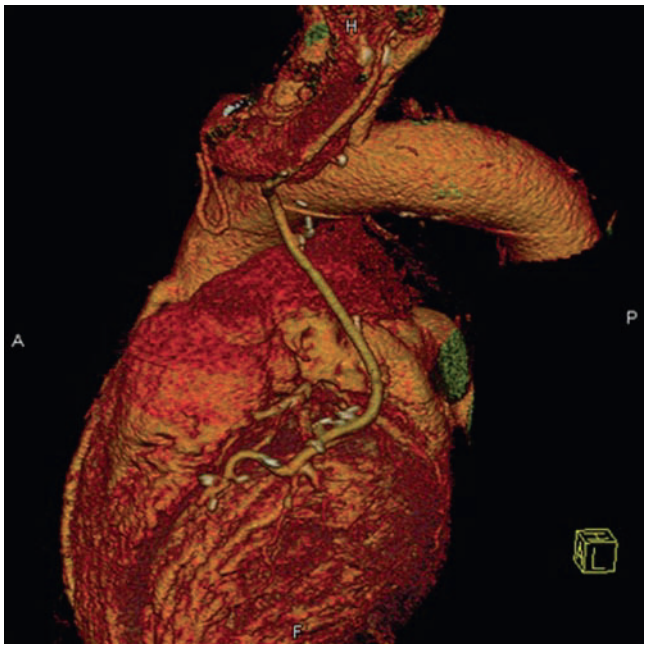

Figure 10.2. 64-row MDCT 3D image reconstruction shows a patent left internal mammary graft with two anostomoses to the first diagonal branch and left anterior descending coronary artery itself, respectively.

A meta-analysis by Hamon et al. comprised studies using 16- and 64-slice MDCT published up to May 2007 [10]. A total of 15 studies were included, 6 of which used 64-slice CT [11–16]. Table 10.1 gives an overview of the diagnostic performance of 64-slice MDCT in a total of 355 patients and 976 bypass grafts [10]. Between 87 and 100% of the grafts were fully assessable regarding the detection / exclusion of angiographically significant stenoses. In particular, a high negative predictive value was obtained in the studies, indicating

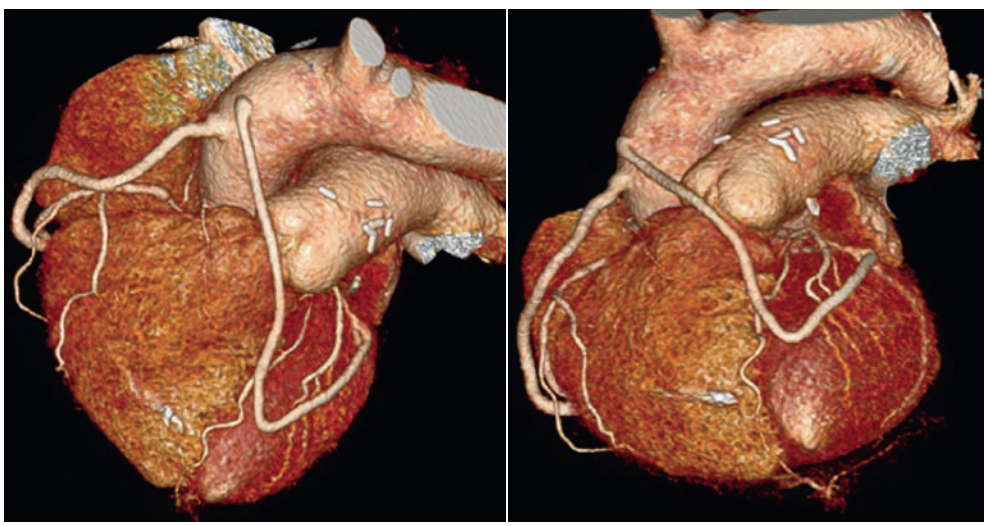

Figure 10.1. 64-row MDCT 3D image reconstruction shows two patent venous grafts coursing to a right coronary artery and an obtuse marginal branch (courtesy of Dr. Dieter Ropers, University Clinic Erlangen-Nürnberg, Germany).

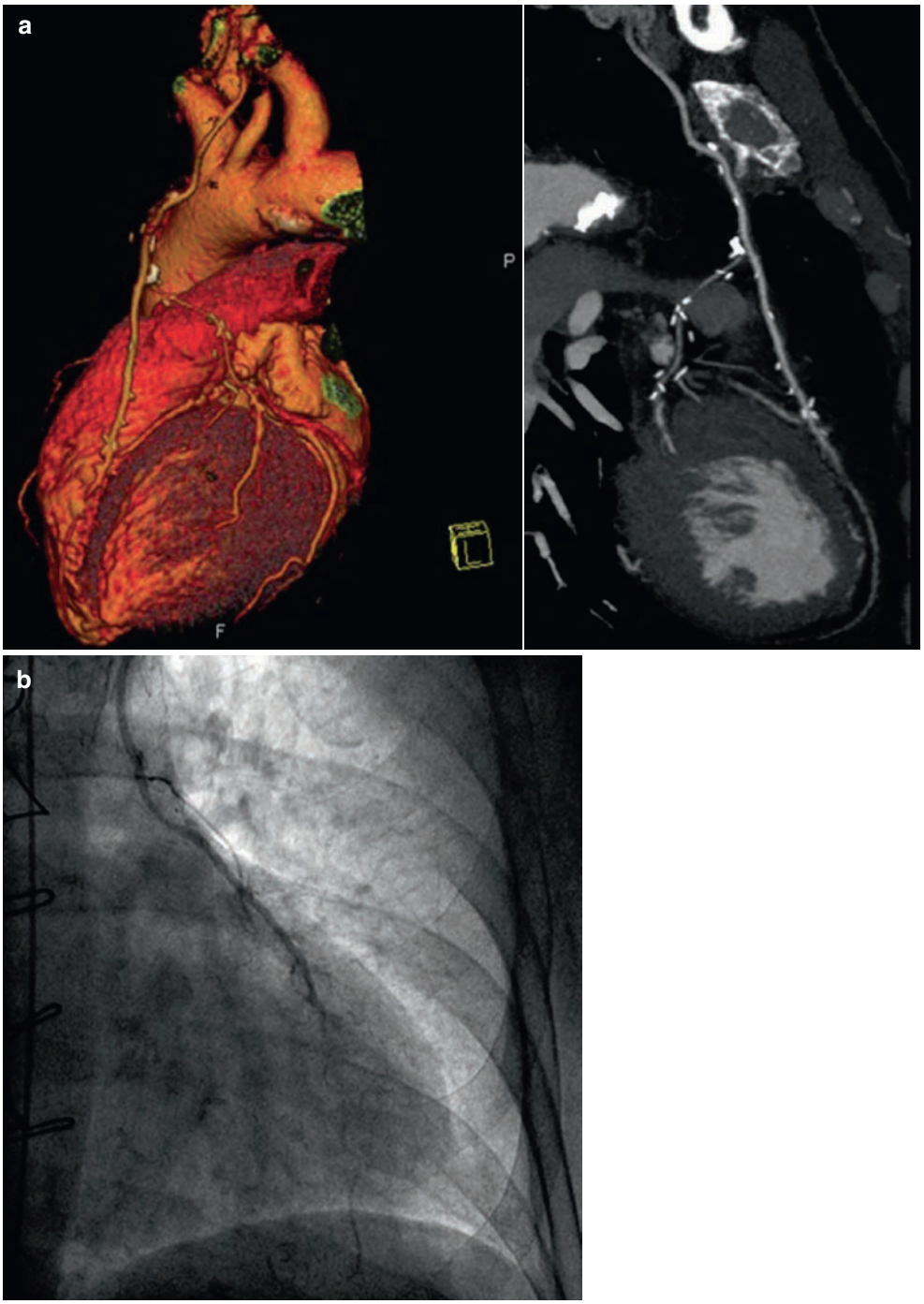

Figure 10.3. 64-row MDCT 3D image reconstruction (**a**) shows a patent left internal mammary graft to the left anterior descending coronary artery and the corresponding selective angiogram. Distal to the anastomosis, the left anterior descending coronary artery is occluded; see corresponding invasive angiographc image (**b**).

Table 10.1. Results of 64-slice MDCT examination of 976 bypass grafts as documented in a meta-analysis by Hamon et al [10]

Sensitivity (%)	Specificity (%)	Positive predictive value (%)	Negative predictive value (%)	Positive likelihood ratio	Negative likelihood ratio
98.1 (96.0,99.3)	96.9 (95.3,98.1)	94.1 (91.0,96.3)	99.1 (98.0,99.7)	24.7 (12.5,47.7)	0.03 (0.01,0.06)

Numbers in parentheses = 95% CI

the ability to reliably rule out high-grade stenoses or obstruction of the bypass grafts using 64-slice MDCT. Recently published studies have confirmed a negative predictive value for ruling out high-grade bypass graft stenoses ranging between 96 and 99% [17, 18]. However, depending on the anatomy, the distal anastomosis can still be challenging to examine, and the degree of stenosis tends to be overestimated [17]. The native coronary circulation can be assessed with high diagnostic yield despite previous bypass surgery [18]. However, similar as in a population with no previous bypass

surgery, heavy coronary calcification or a small native vessel diameter can render the CT analysis difficult.

Imaging Protocols

Noninvasive CT-based bypass graft evaluation is usually confined to patients with stable sinus rhythm. Most experts agree that consequential beta blocker should be undertaken with the aim of reaching heart rates ≤60–65 bpm. Although the most recent scanner generations may be less susceptible for motion artifacts, practical experience dictates that this approach yields superior visibility of coronary artery segments. For 64-slice MDCT, a temporal window of 60% of the RR-interval appears to be best suited [19]. Many experts also recommend the administration of oral or intravenous nitrates for vasodilation immediately prior to the scan. Specific scanning protocols with the various scanners are detailed elsewhere in this book.

Conclusions to Bypass Grafts

MDCT is increasingly used as a modality for the noninvasive assessment of bypass graft patency and stenoses [20]. As compared with invasive angiography, a sizeable proportion of currently approximately 5% of all grafts remains unassessable due to artifacts or anatomic complexity. However, this proportion has decreased with every advance in scanner technology and is likely to decrease further. At present, the reported values for sensitivity and specificity (irrespective of nonassessable grafts) are >95%. In particular, a high negative predictive value for ruling out significant stenoses can be achieved. This also holds true for the native coronary circulation in patients with previous bypass surgery. Considering recent advances in radiation reduction [21] and technological developments, MDCT can be viewed as being on its way to a standard clinical procedure for diagnosing bypass graft disease.

Coronary Stents

The vast majority of coronary interventions are currently performed in association with placement of a coronary stent to provide for scaffolding of the vessel wall [22, 23]. Most coronary stents are slotted tubes made of stainless steel. Such stents have been demonstrated to provide for less acute complications, increased patency rates, and reduced restenosis compared with conventional balloon angioplasty [22]. Long-term results of coronary stenting not only depend on the characteristics of the materials and stent design, but importantly also on the clinical scenario (unstable vs. stable patient), concomitant medical therapy, coronary anatomy, and specific lesion morphology. Whereas conventional bare metal stents are typically associated with clinically symptomatic restenosis in 20–30% of all patients, stents with active drug coating embedded in a polymer on the surface of the metal struts have a clinical restenosis rate <12% [23, 24]. Stent strut thickness may vary between 50 and 140 μm. Some stents have a closed cell design with comparably greater metal-to-surface ratio than stents with an open cell design. The weight of stents with common dimensions ranges from 8 to 16 mg. Further, some stents have radioopaque markers attached at the extreme portions to allow for better fluoroscopic visibility. These factors account for substantial differences in the appearance of different stents when evaluated by cardiac CT.

CT-based assessment of metal stents in large vessels with little motion such as the aorta and the renal and iliac arteries has demonstrated the potential to obtain images with diagnostic quality in the coronary arteries. However, coronary stents usually measure 2.5–4 mm in diameter and are constantly subjected to cardiac motion. Despite the recent improvements in image acquisition time, motion artifacts still play a role in the evaluation of stents with a small diameter. Virtually all coronary stents are made of metal and produce typical "blooming" artifacts. In combination with partial volume effects, this leads to decreased visibility of the stent lumen and underestimation of its diameter while at the same time, the outer diameter is overestimated. Detailed analysis of the inner-stent lumen is necessary to detect various degrees of intimal hyperplasia, the major mechanism of in-stent restenosis.

Because of the above noted limitations regarding the assessment of coronary stent morphology, early EBCT-studies used time-density curve analysis in regions of interest distal to the stent and in part compared these curves with the pattern in the aorta [25–27]. Only complete stent occlusion could be reliably detected, whereas high-grade and even subtotal stenoses were frequently not identified. This can be easily explained by the observation that even vessels with subtotal stenosis often display unimpeded contrast flow. Further, retrograde filling of an occluded vessel via collaterals is potentially problematic, if several cardiac cycles are needed to generate time-density curves with low temporal resolution.

In-vitro studies performed with different scanner generations have established the basic principles and issues of direct coronary stent imaging [28–31]. Clearly, the best possible spatial resolution is necessary (Figure 10.4). Usually, the visible artifacts include blooming ("thickening") of the stent struts with an apparent reduction of the visible stent lumen, increased attenuation values inside the stent lumen, and beamlike artifacts in the vicinity of the stent [28]. The density of the stents is inhomogeneous and depends on the distribution of the struts. Maximum values range from 600 to >1,500 Hounsfied Units (HU).

Recently, 2 meta-analyses of 16- and 64-row MDCT studies of coronary stents have been published regarding the diagnostic efficiency after stent implantation [32, 33]. On the basis of six studies using 64-row MDCT published in the years 2006 and 2007 [32], the proportion of stents with adequate diagnostic image quality ranged between only 58% and 100%. Excluding such segments/stents, pooled sensitivity and specificity regarding the detection of angiographically significant restenosis was 87% and 95%. Another

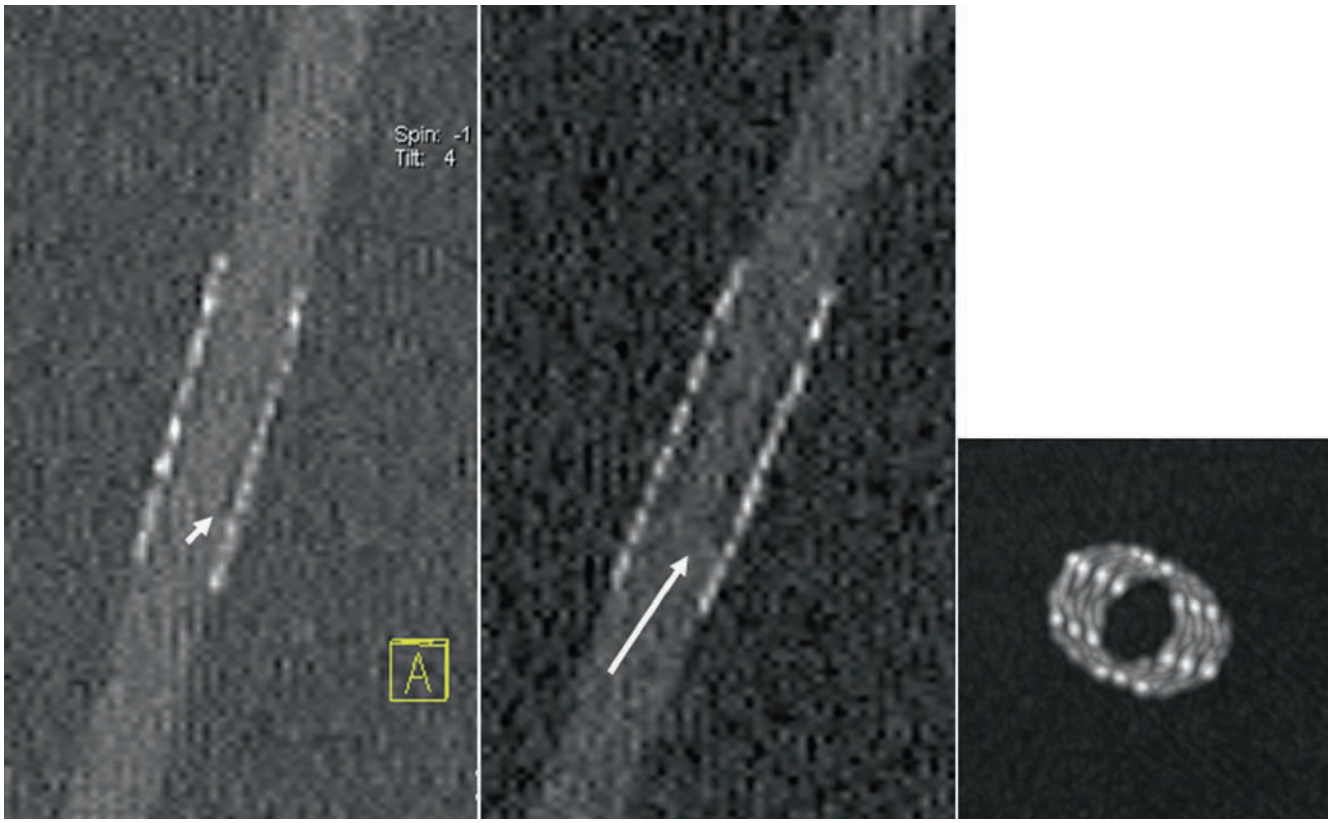

Figure 10.4. Ultra-high resolution images of a coronary stent using 64-row MDCT. The *two left panel* pictures show the stent mounted on a vessel model placed in a phantom with realistic attenuation values. The *short arrow* marks an artificial 30% in-stent restenosis (produced within the stented vessel model), the *longer arrow* a 50% restenosis in the same setting. The *right panel* shows a 3D reconstruction of the stent.

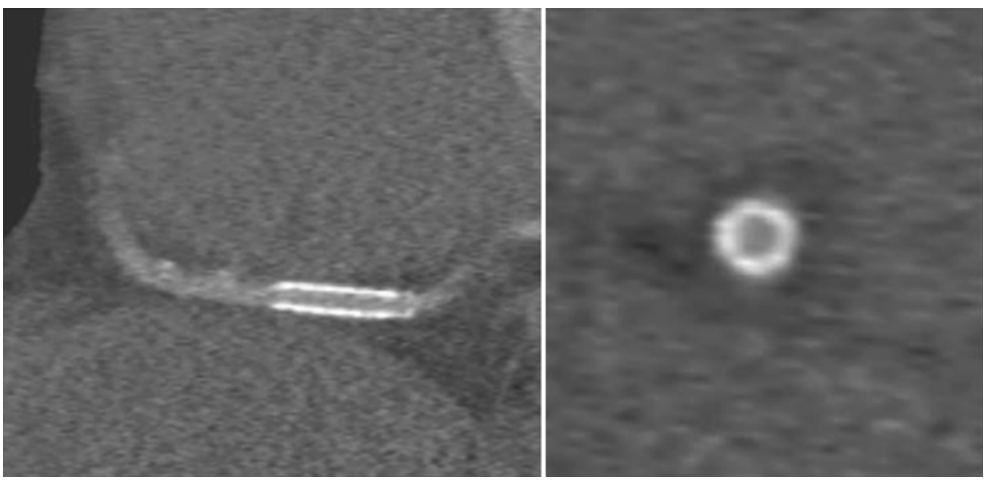

Figure 10.5. Patent stent in the distal right coronary artery.

meta-analysis comprised 14 studies using 64-row MDCT, including a total of 895 patients and 1,447 stents with a mean diameter of 3.1 mm [33]. Of these stents, 1,231 (91.4%) stents demonstrated an adequate diagnostic image quality. Overall sensitivity was 91%, and specificity was 91%. The positive predictive value was 68%, and the negative predictive value was 98%. Including nonassessable segments into the analysis, overall sensitivity and specificity decreased to 87% and 84%, with a positive predictive value of 53% and a negative predictive value of 97%, respectively.

Apart from stent materials and strut thickness, stent diameter is the most important factor influencing the ability to achieve diagnostic images. In fact, stents with a diameter ≥4.0 mm as encountered in large native coronary vessels or venous bypass grafts can be examined with quite good diagnostic accuracy [31]. Also, stents placed in the left main stem frequently measure ≥3.5 mm and can be examined quite accurately by using 64-row MDCT [34]. The thinner the struts of the usual metal stents are, the less beam hardening or blooming artifacts hamper image quality (Figure 10.5 and 10.6). At the extreme end of "CT-friendly" stents are bioabsorbable stents such as the magnesium stent [35]. It is hardly visible, so that the CT analysis resembles native coronary artery assessment [36, 37].

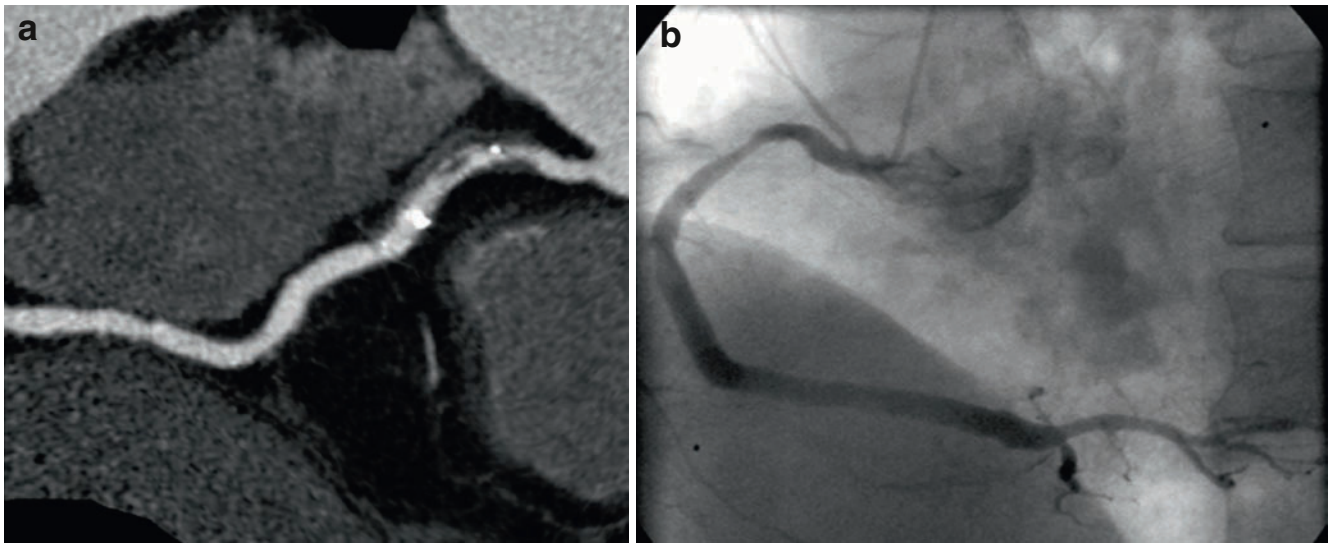

Figure 10.6. In-stent stenosis proximal right coronary artery. (**a**) 64-row MDCT. (**b**) Invasive angiographic representation.

Summary of Diagnostic Accuracy for Coronary Stent Evaluation

Because of the metal artifacts produced by the currently employed coronary stents, MDCT does not enable reliable visualization of the coronary stent lumen with the exception of large diameter stents (≥ 3.5–4.0 mm). At present, most coronary stents measure 3 mm in diameter and have relatively dense metal struts. With "blooming" and related artifacts, their lumen appears artificially small, precluding a reliable analysis. Thus, there are currently no accepted clinical applications for MDCT imaging of coronary stents. However, preliminary clinical data and, in particular, improvements in temporal and – to a lesser extent – spatial resolution allow for an optimistic perspective.

References

1. Goldman S, Zadina K, Moritz T, et al.; VA Cooperative Study Group #207/297/364. Long-term patency of saphenous vein and left internal mammary artery grafts after coronary artery bypass surgery: results from a Department of Veterans Affairs Cooperative Study. *J Am Coll Cardiol*. 2004;44:2149–2156.
2. Schwartz L, Kip KE, Frye RL, Alderman EL, Schaff HV, Detre KM; Bypass Angioplasty Revascularization Investigation. Coronary bypass graft patency in patients with diabetes in the Bypass Angioplasty Revascularization Investigation (BARI). *Circulation*. 2002;106:2652–2658.
3. Lytle BW, Loop FD, Cosgrove DM, Ratliff NB, Easley K, Taylor PC. Long-term (5 to 12 years) serial studies of internal mammary artery and saphenous vein coronary bypass grafts. *J Thorac Cardiovasc Surg*. 1985;89:248–258.
4. Shi Y, O'Brien JE Jr, Mannion JD, et al. Remodeling of autologous saphenous vein grafts. The role of perivascular myofibroblasts. *Circulation*. 1997;95:2684–2693.
5. Fitzgibbon GM, Kafka HP, Leach AJ, Keon WJ, Hooper GD, Burton JR. Coronary bypass graft fate and patient outcome: angiographic follow-up of 5, 065 grafts related to survival and reoperation in 1, 388 patients during 25 years. *J Am Coll Cardiol*. 1996;28:616–626.
6. Berger A, MacCarthy PA, Siebert U, et al. Long-term patency of internal mammary artery bypass grafts. Relationship with preoperative severity of the native coronary artery stenosis. *Circulation*. 2004; 110[suppl II]:II-36–II–40.
7. Brundage BH, Lipton MJ, Herfkens RJ, et al. Detection of patent coronary bypass grafts by computed tomography. A preliminary report. *Circulation*. 1980;61:826–831.
8. Daniel WG, Dohring W, Stender HS, Lichtlen PR. Value and limitations of computed tomography in assessing aortocoronary bypass graft patency. *Circulation*. 1983;67:983–987.
9. Achenbach S, Moshage W, Ropers D, Nossen J, Bachmann K. Noninvasive, three-dimensional visualization of coronary artery bypass grafts by electron beam tomography. *Am J Cardiol*. 1997;79: 856–861.
10. Hamon M, Lepage O, Malagutti P, et al. Diagnostic performance of 16- and 64-section spiral CT for coronary artery bypass graft assessment: meta-analysis. *Radiology*. 2008;247:679–686.
11. Malagutti P, Nieman K, Meijboom WB, et al. Use of 64-slice CT in symptomatic patients after coronary bypass surgery: evaluation of grafts and coronary arteries. *Eur Heart J*. 2007;28:1879–1885.
12. Pache G, Saueressig U, Frydrychowicz A, et al. initial experience with 64-slice cardiac CT: non-invasive visualization of coronary artery bypass grafts. *Eur Heart J*. 2006;27:976–980.
13. Dikkers R, Willems TP, Tio RA, Anthonio RL, Zijlstra F, Oudkerk M. The benefit of 64-MDCT prior to invasive coronary angiography in symptomatic post-CABG patients. *Int J Cardiovasc Imaging*. 2006;23:369–377.
14. Ropers D, Pohle FK, Kuettner A, et al. Diagnostic accuracy of noninvasive coronary angiography in patients after bypass surgery using 64-slice spiral computed tomography with 330-ms gantry rotation. *Circulation*. 2006;114:2334–2341.
15. Meyer TS, Martinoff S, Hadamitzky M, et al. Improved non-invasive assessment of coronary artery bypass grafts with 64-slice computed tomographic angiography in an unselected patient population. *J Am Coll Cardiol*. 2007;49:946–950.
16. Jabara R, Chronos N, Klein L, et al. Comparison of multidetector 64-slice computed tomographic angiography to coronary angiography to assess the patency of coronary artery bypass grafts. *Am J Cardiol*. 2007;99:1529–1534.
17. Feuchtner GM, Schachner T, Bonatti J, et al. Diagnostic performance of 64-slice computed tomography in evaluation of coronary artery bypass grafts. *AJR Am J Roentgenol*. 2007;189:574–580.
18. Nazeri I, Shahabi P, Tehrai M, Sharif-Kashani B, Nazeri A. Assessment of patients after coronary artery bypass grafting using 64-slice computed tomography. *Am J Cardiol*. 2009;103:667–673.

19. Desbiolles L, Leschka S, Plass A, et al. Evaluation of temporal windows for coronary artery bypass graft imaging with 64-slice CT. *Eur Radiol*. 2007;17:2819–2828.
20. Cademartiri F, Palumbo A, Maffei E, et al. Follow-up of internal mammary artery stent with 64-slice CT. *Int J Cardiovasc Imaging*. 2007;23:537–539.
21. Hermann F, Martinoff S, Meyer T, et al. Reduction of radiation dose estimates in cardiac 64-slice CT angiography in patients after coronary artery bypass graft surgery. *Invest Radiol*. 2008;43:253–260.
22. Colombo A, Stankovic G, Moses JW. Selection of coronary stents. *J Am Coll Cardiol*. 2002;40:1021–1033.
23. Trikalinos TA, Alsheikh-Ali AA, Tatsioni A, Nallamothu BK, Kent DM. Percutaneous coronary interventions for non-acute coronary artery disease: a quantitative 20-year synopsis and a network meta-analysis. *Lancet*. 2009;373:911–918.
24. Biondi-Zoccai G, Lotrionte M, Moretti C, et al. Percutaneous coronary intervention with everolimus-eluting stents (Xience V): systematic review and direct-indirect comparison meta-analyses with paclitaxel-eluting stents (Taxus) and sirolimus-eluting stents (Cypher). *Minerva Cardioangiol*. 2008;56:55–65.
25. Schmermund A, Haude M, Baumgart D, et al. Non-invasive assessment of coronary Palmaz-Schatz stents with contrast enhanced electron beam computed tomography. *Eur Heart J*. 1996;17:1546–1553.
26. Möhlenkamp S, Pump H, Baumgart D, et al. Minimally invasive evaluation of coronary stents with electron beam computed tomography: In vivo and in vitro experience. *Catheter Cardiovasc Interv*. 1999;48:39–47.
27. Pump H, Möhlenkamp S, Sehnert CA, et al. Coronary arterial stent patency: assessment with electron-beam CT. *Radiology*. 2000;214:447–452.
28. Maintz D, Juergens KU, Wichter T, Grude M, Heindel W, Fischbach R. Imaging of coronary artery stents using multislice computed tomography: in vitro evaluation. *Eur Radiol*. 2003;13:830–835.
29. Mahnken AH, Buecker A, Wildberger JE, et al. Coronary artery stents in multislice computed tomography: in vitro artifact evaluation. *Invest Radiol*. 2004;39:27–33.
30. Schlosser T, Scheuermann T, Ulzheimer S, et al. In-vitro evaluation of coronary stents and 64-detector-row computed tomography using a newly developed model of coronary artery stenosis. *Acta Radiol*. 2008;49:56–64.
31. Schlosser T, Scheuermann T, Ulzheimer S, et al. In vitro evaluation of coronary stents and in-stent stenosis using a dynamic cardiac phantom and a 64-detector row CT scanner. *Clin Res Cardiol*. 2007; 96:883–890.
32. Kumbhani DJ, Ingelmo CP, Schoenhagen P, Curtin RJ, Flamm SD, Desai MY. Meta-analysis of diagnostic efficacy of 64-slice computed tomography in the evaluation of coronary in-stent restenosis. *Am J Cardiol*. 2009;103:1675–1681.
33. Sun Z, Davidson R, Lin CHS. Multi-detector row CT angiography in the assessment of coronary in-stent restenosis: a systematic review. *Eur J Radiol*. 2009;69:489–495.
34. Van Mieghem CA, Cademartiri F, Mollet NR, et al. Multislice spiral computed tomography for the evaluation of stent patency after left main coronary artery stenting: a comparison with conventional coronary angiography and intravascular ultrasound. *Circulation*. 2006;114:645–653.
35. Erbel R, Di Mario C, Bartunek J, et al. Temporary scaffolding of coronary arteries with bioabsorbable magnesium stents: a prospective, non-randomised multicentre trial. *Lancet*. 2007;369:1869–1875.
36. Erbel R, Böse D, Haude M, et al. Absorbable coronary stents. New promising technology. *Herz*. 2007;32:308–319.
37. Maintz D, Burg MC, Seifarth H, et al. Update on multidetector coronary CT angiography of coronary stents: in vitro evaluation of 29 different stent types with dual-source CT. *Eur Radiol*. 2009;19:42–49.

Part IV

CT Angiography Assessment for Cardiac Pathology

11

Assessment of Cardiac Structure and Function by Computed Tomography Angiography

John A. Rumberger

Concept

Knowledge of cardiac ejection fractions [1], absolute ventricular volumes [2, 3], and location and extent of regional wall motion abnormalities provides valuable diagnostic and prognostic information, and noninvasive cardiac imaging has become the reference standard in routine clinical practice.

EBT (electron beam CT) was introduced in the early 1980s as the first viable CT scanner capable of measuring cardiac structure and function, but manufacturing was stopped in 2003, although scanners still function in a handful of centers.

High-resolution multi-detector CT (MDCT) scanners capable of quantitative imaging of the heart were introduced around 2002. Initially 16-slice scanners were validated but the current state of the art is 64+-slice scanners. This chapter discusses the use of 64+-slice MDCT for assessment of cardiac structure and function.

Current State of the Art

CT has traditionally oriented and displayed images parallel or at 90° angles to the long axis of the body (i.e., transaxial, coronal, and sagittal image planes). Such presentations oriented about the long axis of the body do not satisfy prior established presentations of cardiac images as they do not cleanly transect the ventricles, atria, or myocardial regions as supplied by the major coronary arteries.

The American Heart Association in 2002 [4] published standards of myocardial segmentation and nomenclature for tomographic imaging of the heart using noninvasive imaging modalities and divided the left ventricle (LV) into 17 segments. The nomenclature for image presentation for cardiac CT is: the short axis, horizontal long axis, and vertical long axis, as shown in Figure 11.1. These cardiac axes are very familiar to practitioners performing SPECT imaging; for those familiar with 2-dimensional echocardiography, these correspond to the short axis, apical four-chamber, and apical two-chamber views, respectively. These cardiac imaging planes are oriented at 90° angles relative to each other.

In order to employ CT to define the cardiac chambers and separate them from the surrounding myocardium, it is necessary to use intravenous contrast. In general, this can be accomplished with <100 mL of nonionic contrast, and it is possible to perform complete imaging of the heart chambers, the coronary arteries, and the proximal great vessels (aorta and pulmonary artery) in a single setting with a single injection of contrast. Methods for contrast administration for MDCT scanning of the heart are found elsewhere.

Orthogonal (short and various long axes) cardiac CT images after intravenous contrast allow for identification of nonopacified intracardiac thrombi (Figure 11.2a) and tumors (Figure 11.2b) including excellent resolution of the left atrium and the left atrial appendage (Figure 11.3), allowing localization of structures smaller than 1 mm [5, 6]. Cardiac CT can additionally be of assistance in defining thrombi or occult occlusion of the venae cavae and other right-sided structures. Cardiac CT can also be a primary method of defining intracardiac shunts such as those caused by inter-ventricular (Figure 11.4a) and inter-atrial (Figure 11.4b) congenital defects and other acquired defects post-infarction [7].

Cardiac CT can be used to quantitate left and right ventricular volumes [8–10], left and right atrial volumes, left and right ventricular muscle mass [11–14], regional left ventricular function, wall thickening and contractility [15–17], rates of diastolic filling of the right and left ventricles [16, 18, 19], post-infarction left and right ventricular remodeling [20–24], cardiac remodeling following cardiac [25] and lung transplantation [26], and ejection fraction [27–30] in patients with no contraindication to the use of iodinated contrast medium. Additional applications include quantitation of uni-valvular regurgitation [31] and assessment of infarct size [32, 33]. The majority of these validation studies was performed in the 1980s and 1990s using EBT and has been adapted and/or revalidated in studies using MDCT. In most instances, these quantitative aspects can be performed or at least well-approximated in patients

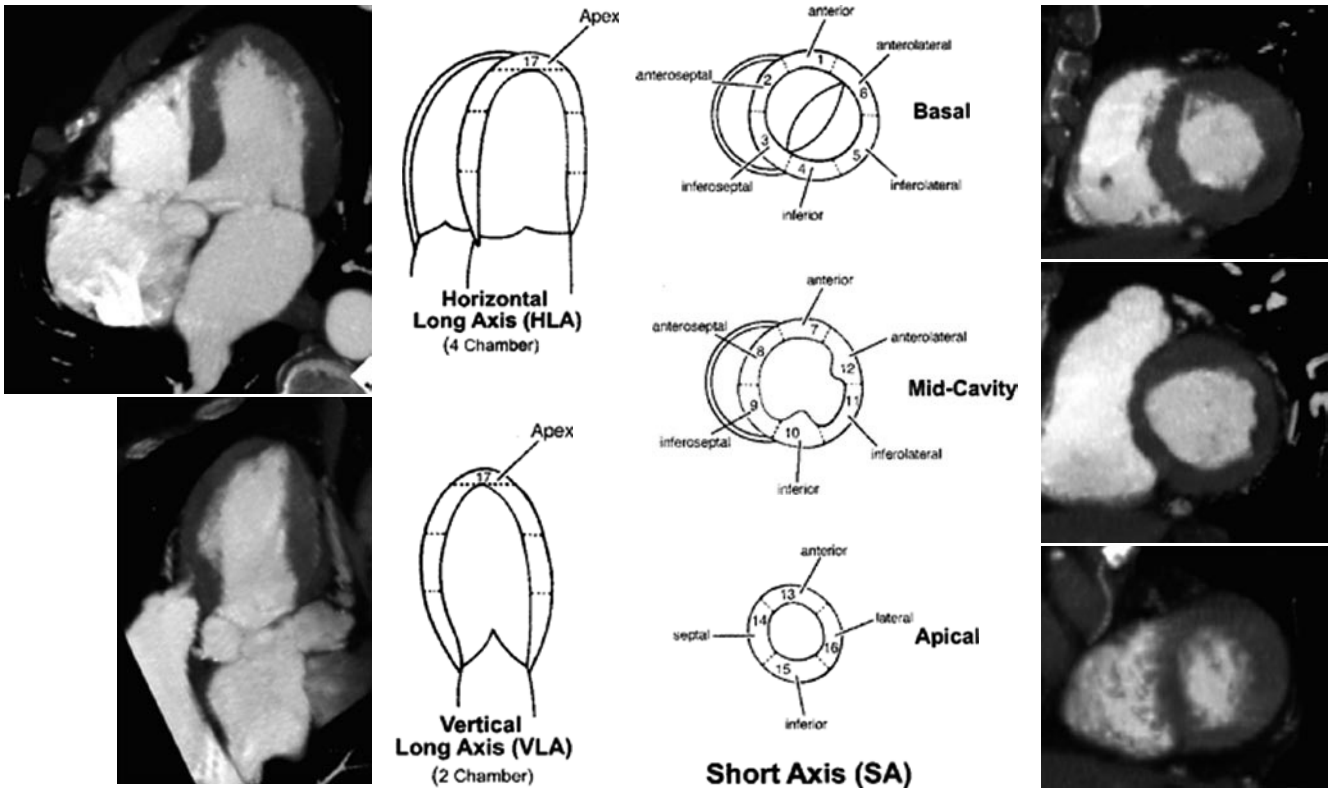

Figure 11.1. Standardized Presentation of the Heart in Cardiac CT. American Heart Association 17 segment model of the left ventricle (LV); the orthogonal imaging planes are the horizontal long axis, the vertical long axis, and the short axis. Adapted with permission of the American Heart Association [4]. Copyright 2002 American Heart Association, Inc.

with generally normal sinus rhythm. Since the number of cardiac cycles imaged per scan is single (256- and 320-slice scanners) or generally limited to <5 (64-slice scanners), quantitation may be limited in those patients with significant dysrhythmias, such as atrial fibrillation.

All available post-processing workstations can provide quantitative and often noninteractive (i.e., automatic) measurements of the LV in particular. Shown in Figure 11.5, a-e is the general outline of the procedure and subsequent display of the results. Table 11.1 shows validated norms for LV chamber size, wall thicknesses, ejection fraction, and ventricular volumes using cardiac CT. Reproducibility of CT in performing right and left ventricular volume and function measurements has also been established [34, 35].

Cardiac CT imaging using thin sections allows post-processing of images into end-diastolic and end-systolic short and "long" axis images at multiple ECG-phases to facilitate identification of structures and salient features of the ventricular anatomy (Figure11.6). Using short and long axis imaging also allows identification of infarct locations (Figure 11.7). Demonstrated in this latter example is a common CT finding in contrast-enhanced images from patients with remote myocardial infarction. The "negative" contrast noted in Figure 11.7 is actually due to lack of contrast opacification in the infarcted region causing "contrast rarefaction." Long axis (both vertical and horizontal) imaging of the left ventricle also allows for definition of basilar and apical infarcts, and true- and pseudo-apical aneurysms (Figure 11.8). Two-dimensional and three-dimensional reconstruction methods, possible in nearly an infinite number of imaging planes, also allows for postoperative assessment of left ventricular aneurysectomy (Figure 11.9). Global and regional details of the LV due to ischemic cardiomyopathy and hypertrophic cardiomyopathy using cardiac CT provide details commonly noted by other imaging methods. The right ventricle (RV) can also be imaged. Figure 11.10 shows a dilated RV in a patient with arrhythmogenic RV dysplasia, and Figure 11.11 shows fatty infiltration of the RV; cardiac CT can often be an alternative or a confirmatory method to MRI in the evaluation of such patients [36]. Biventricular consequences to congenital (Figure 11.12) and acquired heart disorders (Figure 11.13) can also be imaged.

Three-dimensional calipers available on all CT workstations allow for quantitative measures of ventricular dimensions in any axis (Figure 11.14a). Additionally, measures of ventricular muscle thicknesses can be done on all myocardial walls (Figure 11.14b). Measures of the aorta and other chambers such as the left atrium (Figure 11.14c) can also be helpful and augment data on ventricular volumes, muscle mass, and function by CT. Normal layers of fat on the epicardial surface of the heart and the outer surface of the pericardial sac provide natural contrast and permit the examiner to reliably identify the pericardium (Figure 11.15). Contrast-enhanced CT often allows separating chronic effusive pericarditis from gross pericardial thickening since the parietal and

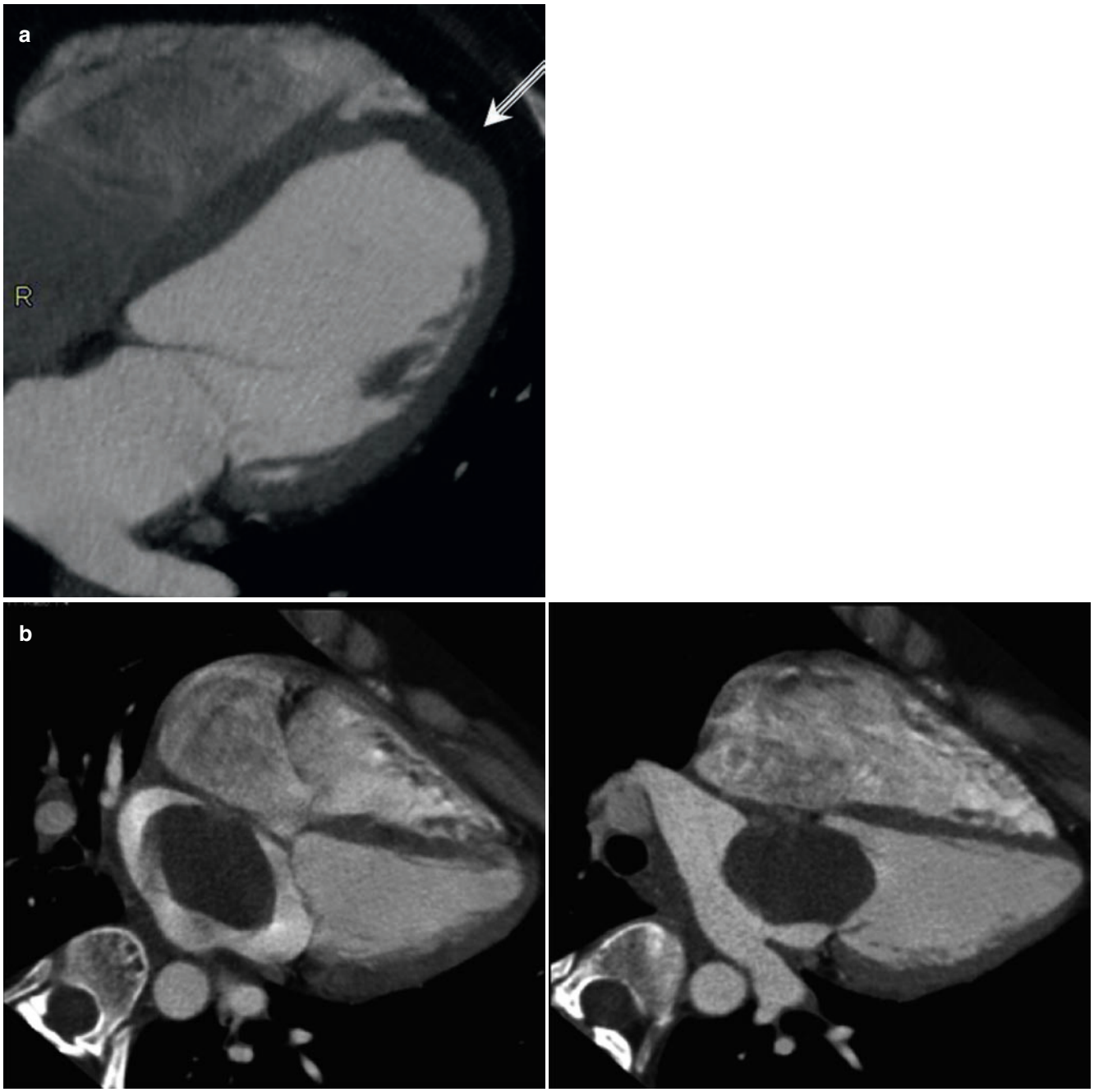

Figure 11.2. Examples of Nonopacified Cardiac Thrombus and Tumor. (**a**) Modified vertical long axis tomogram of the left ventricle (LV); the area noted by the arrow is a nonopacified thrombus at the LV apex. (**b**) Modified horizontal long axis image of the left atrium (LA)/LV; the nonopacified area in the LA chamber is a left atrial myxoma shown at end-systole and end-diastole: note that, during diastole, the myxoma prolapses through the mitral valve.

epicardial layers of the pericardium have their own blood supply. CT can be used to define the entire anatomy of the pericardium and may be of greatest value in localization of loculated effusions such as those confined to the posterior areas of the heart (which are difficult to define using surface 2-dimensional echocardiography). Tamponade can be identified with CT by right atrial or ventricular collapse or by indirect signs such as an inappropriately enlarged inferior vena cava or enlarged hepatic veins. High-resolution images can define the anatomic localization and extent of pericardial thickening. In the evaluation of a patient for constrictive pericarditis, CT can add considerably to the diagnosis. CT has an advantage over traditional echocardiography in that the entire cardiac volume is imaged very quickly, and then images of both 2-dimensional and 3-dimensional views can be rapidly generated. Contrast is usually not required to image the pericardium, as the natural delineation of the pericardial surface (usually 100 Hounsfield Units, HU) and adjacent air (<−700 HU) is dramatic. Calcified pericardial tissue is even easier to image, as the calcification is usually in the +300–400 HU range.

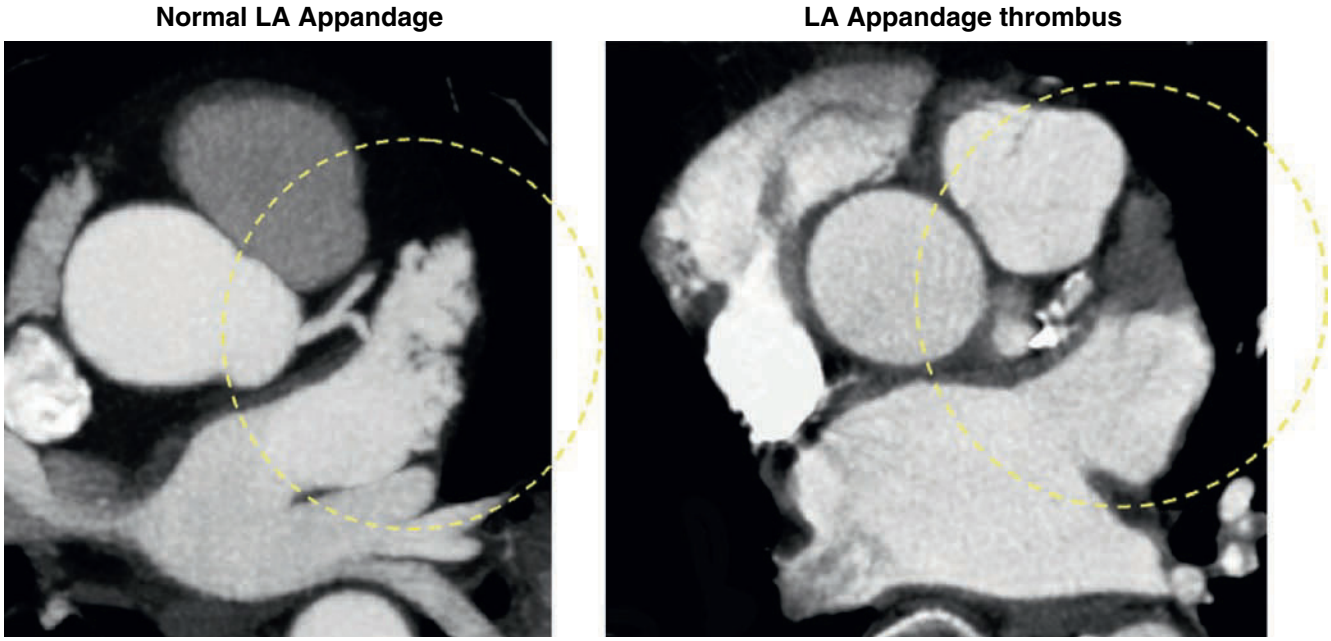

Figure 11.3. Definition of the left atrial appendage by Cardiac CT. *Left*: a normal LA (*left atrial*) appendage (*dotted circle*). *Right*: LA appendage with thrombus (*dotted circle*).

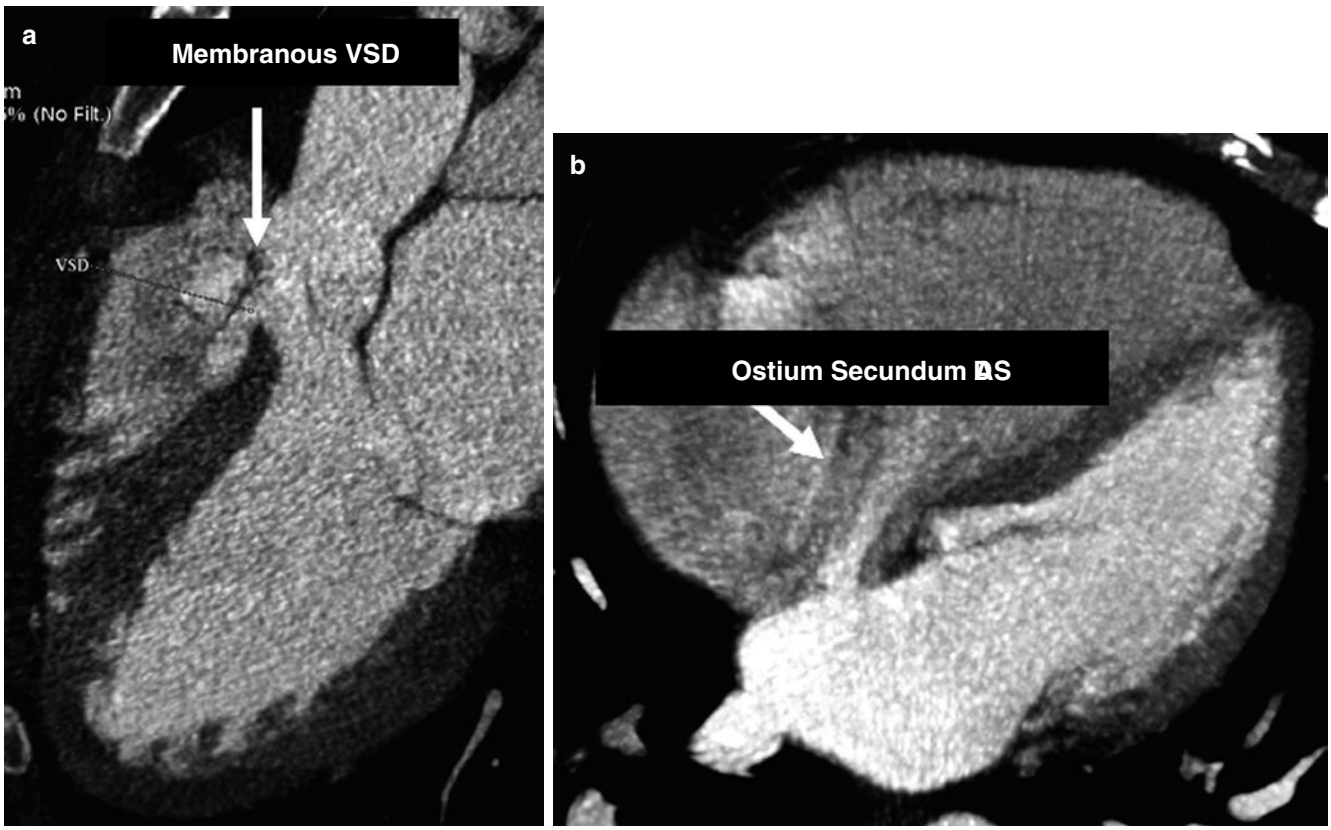

Figure 11.4. Examples of congenital intra-cardiac shunts as shown by Cardiac CT. (**a**) "Peri" membranous ventricular septal defect (VSD) as noted by the arrow. (**b**) Jet of contrast demonstrating a left to right shunt from an ostium secundum atrial septal defect (ASD) as noted by the arrow.

Indications

The mandate for a complete cardiac CT angiogram (CCTA) in routine clinical practice is to include quantitative cardiac structure and function as part of each evaluation performed for assessment of coronary plaque and lumen anatomy. However, quantitation of cardiac function using MDCT can only practically be performed using retrospective ECG-gating.

Prospective ECG-gating protocols provide static images of the heart and the coronary arteries and are appropriate if the indication for performing 64+-slice MDCT is solely

assessment of coronary artery anatomy. Prospectively gated MDCT can also provide general information about cardiac chamber sizes, general cardiac anatomy, and some evaluations of the pericardium, but cannot be used to quantitate LV and RV systolic or diastolic function. In such instances, if LV function is also desired for overall clinical assessment, then alternative methods are widely available such a gated SPECT, MRI, and 2-dimensional echocardiography. Although MRI and ultrasound provide no ionizing radiation exposure, SPECT imaging can result in radiation exposures up to 3–5 times that of cardiac CT.

Utilization of prospective ECG gating can significantly reduce the effective radiation dose to the patient using MDCT; however, if quantitation of LV function is also required, a retrospective gated cardiac CT can be performed with limited radiation by lowering the kV from 120 to 100 and application of ECG-dose (mA) modulation. A properly planned retrospective 64+slice cardiac CT can be

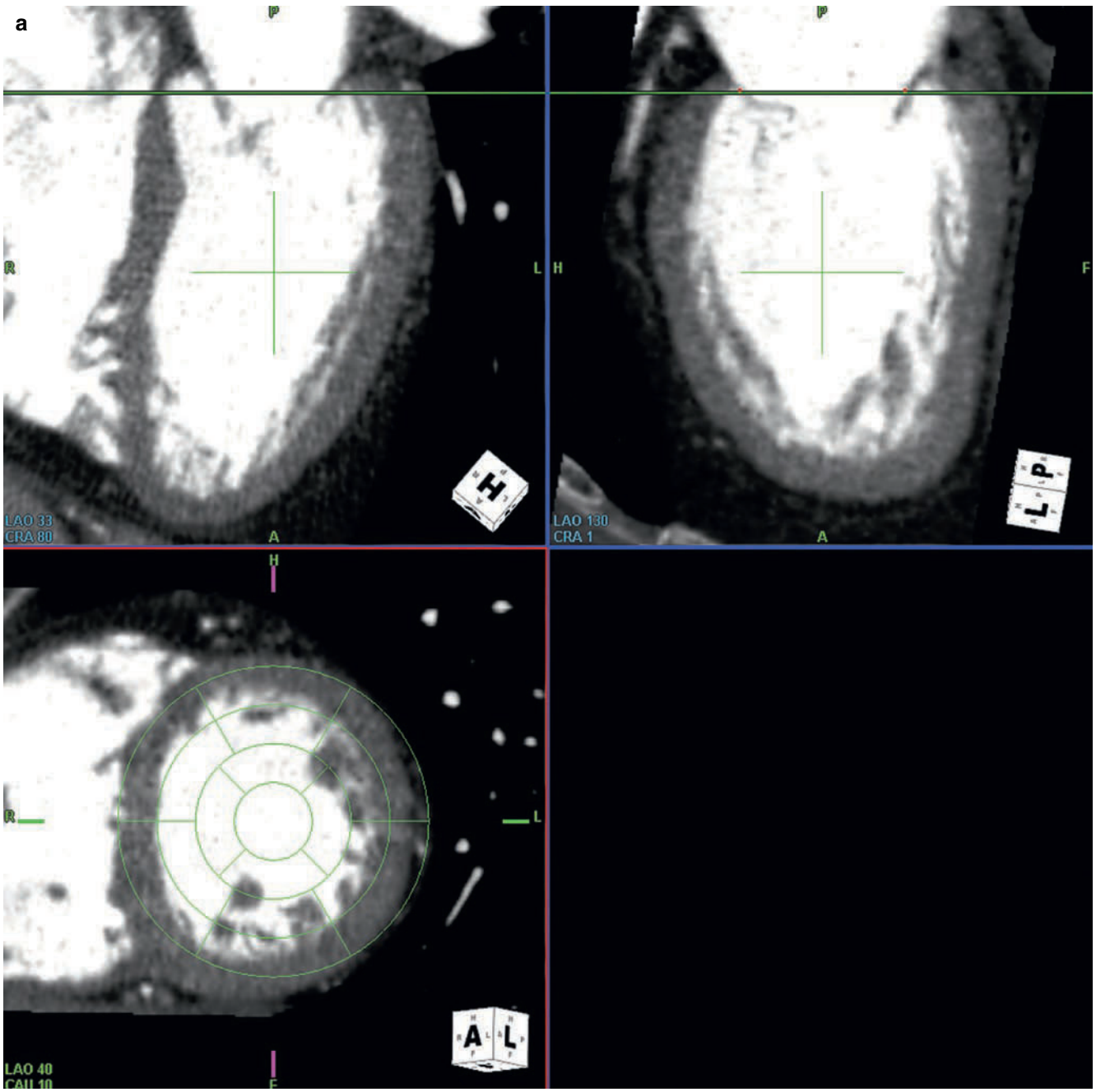

Figure 11.5. Quantitation of left ventricular (LV) function by Cardiac CT. (**a**) Horizontal long axis, vertical long axis, and short axis views of the LV; the line demonstrates the plane of the mitral valve: when performing quantitative analysis, it is necessary that the LV chamber be isolated. (**b**) Semi-quantitative edge definition of the cardiac endocardial surfaces using thresholding methods; from this information, the LV endocardial (chamber) volumes can be determined. (**c**) Semi-quantitative isolation of the LV myocardial epicardial and septal surfaces using thresholding methods; from this information the LV muscle mass and myocardial wall thicknesses can be determined. (**d**) Lower right of the figure: a color map of the myocardial surface systolic function is defined to provide definition of regional LV function. (**e**) LV chamber volume as a function of time during the cardiac cycle; from these data can be derived information on *EF* ejection fraction, *EDV* end-diastolic volume, *EDV* end-systolic volume, *SV* stroke volume, rates of systolic emptying (contractility), as well as rates of early and late diastolic filling (diastolic function).

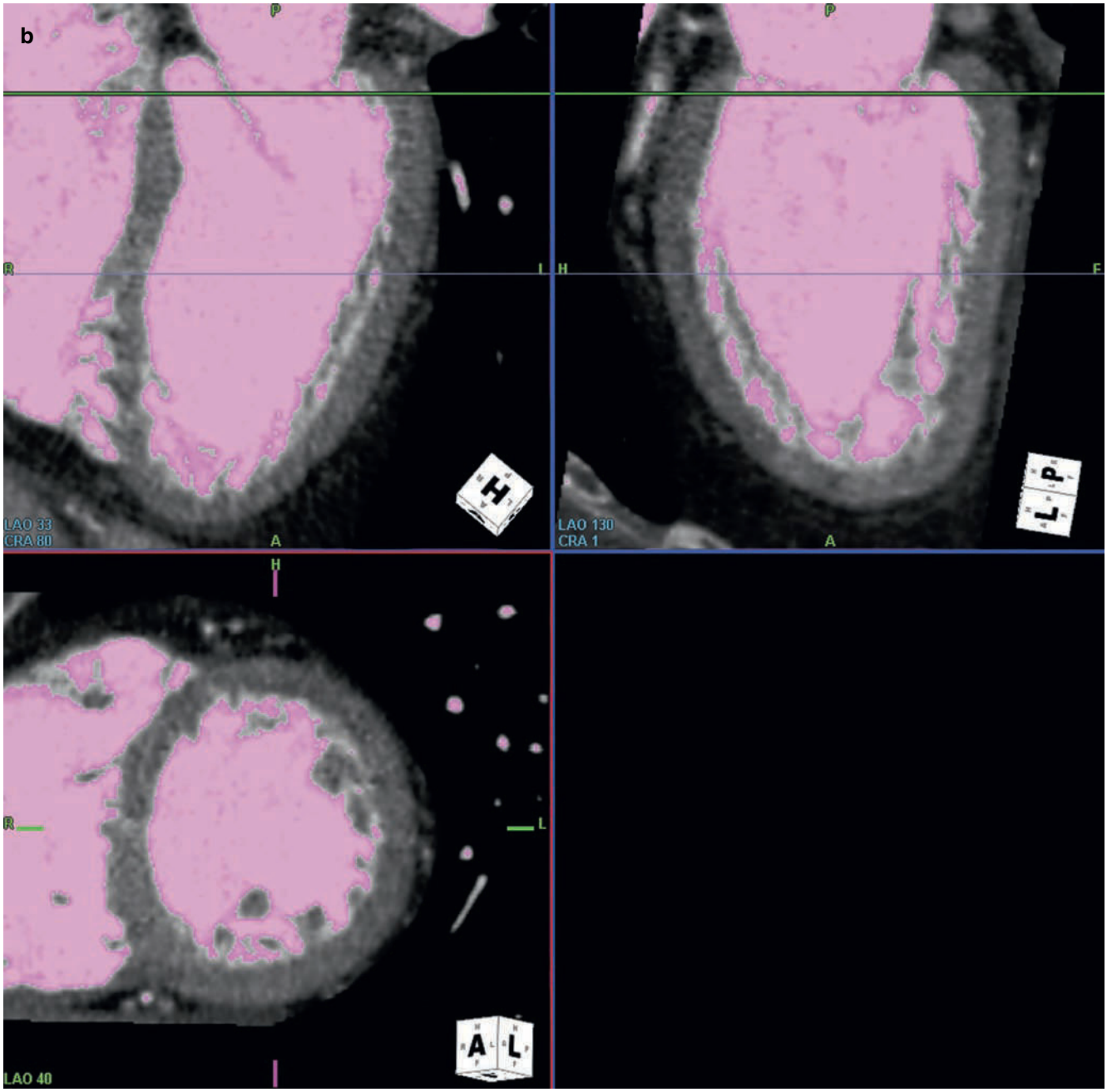

Figure 11.5. (Continued).

performed with effective patient radiation doses of 5–10 mSv vs. a prospectively gated MDCT scan, which can be done generally with effective radiation doses of 3–5 mSv (or slightly higher using 256-slice and 320-slice scanners).

Contraindications

The contraindications to performing a retrospectively gated MDCT for assessment of cardiac structure and function are the same as those for performing any cardiac CT examination. Beta-blockers are almost universally applied to get resting heart rates in the range of 60 beats/min. Individuals with reactive airways disease (e.g., emphysema, asthma) should only be given beta-blockers under controlled conditions. Intravenous contrast is also required, thus reduced renal function (e.g., creatinine >1.9 mg/dl) might suggest that an alternative method of evaluating the LV/RV should be considered, but there is no absolute contraindication for MDCT cardiac imaging in the presence of abnormal renal function. Issues of radiation exposure of the patient must be considered and risk vs. benefit defined by the referring physician. Patients unable to hold their breath for 15 s or who are uncooperative should be avoided for cardiac CT. The presence of various dysrhythmias (frequent PACs/PVCs) can make quantitation of LV function with MDCT difficult,

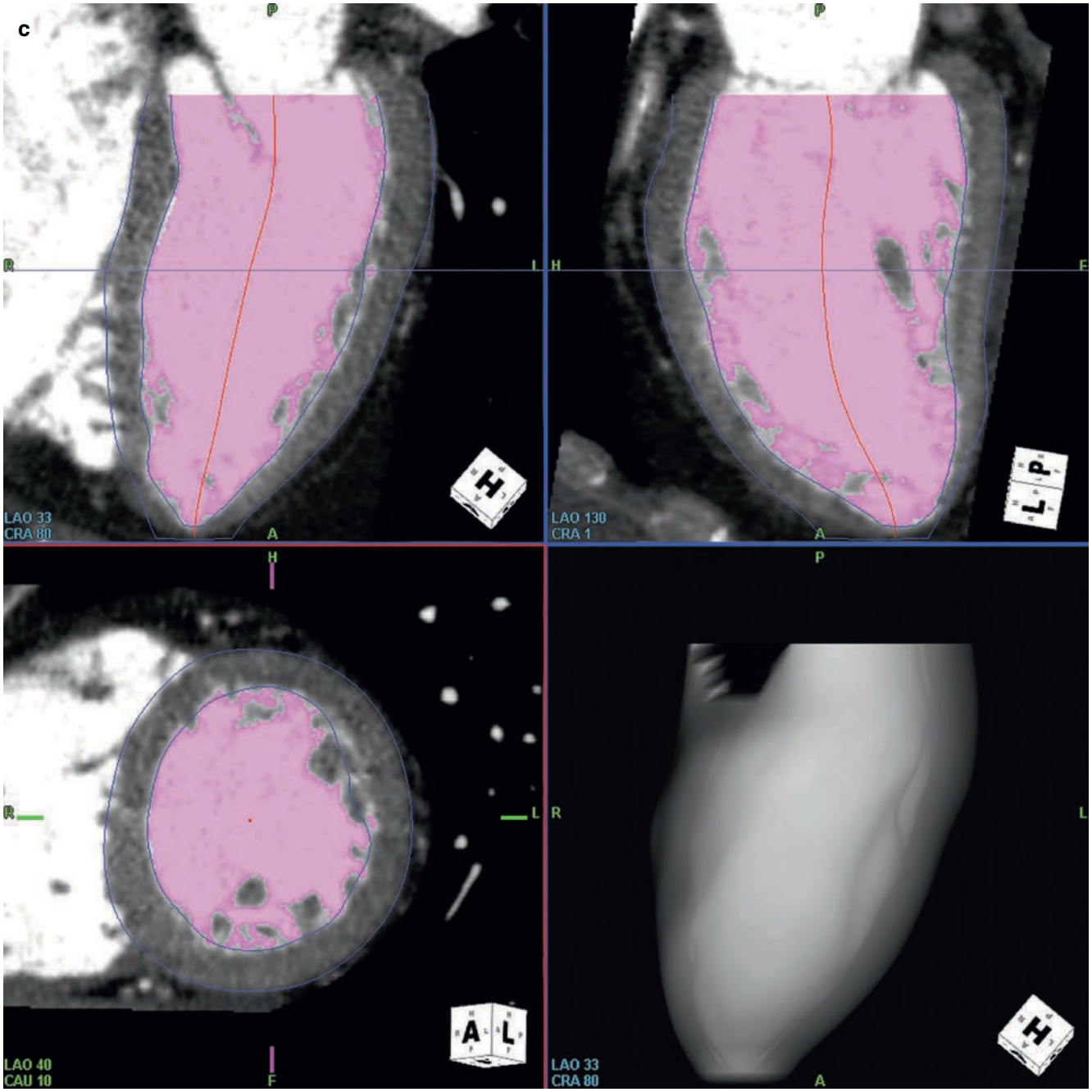

Figure 11.5. (Continued).

and individuals with pacemakers should have the ventricular rate set to 60 beats/min. The presence of atrial fibrillation is not a contraindication, but, with uncontrollable rapid ventricular response, will likely result in sub-optimal data.

Strengths

A properly planned 64+slice, retrospectively ECG-gated, MDCT examination can provide quantitative data on LV/RV systolic (and diastolic function) both globally and regionally. It can also provide quantitative data on chamber sizes, valve (both natural (Figure 11.16) and prosthetic) valve motion and cross-sectional areas, visualization of intra-cardiac shunts, definition of cardiac tumors and thrombi, quantitation of LV muscle mass, regional wall thicknesses and thickening, myocardial infarct size, and the gross physiologic consequences of pericardial effusions and pericardial constriction.

Limitations

Sub-optimal assessment of cardiac structures and function can occur due to cardiac dysrhythmias, inadequate heart rate control during imaging, and poor chamber contrast

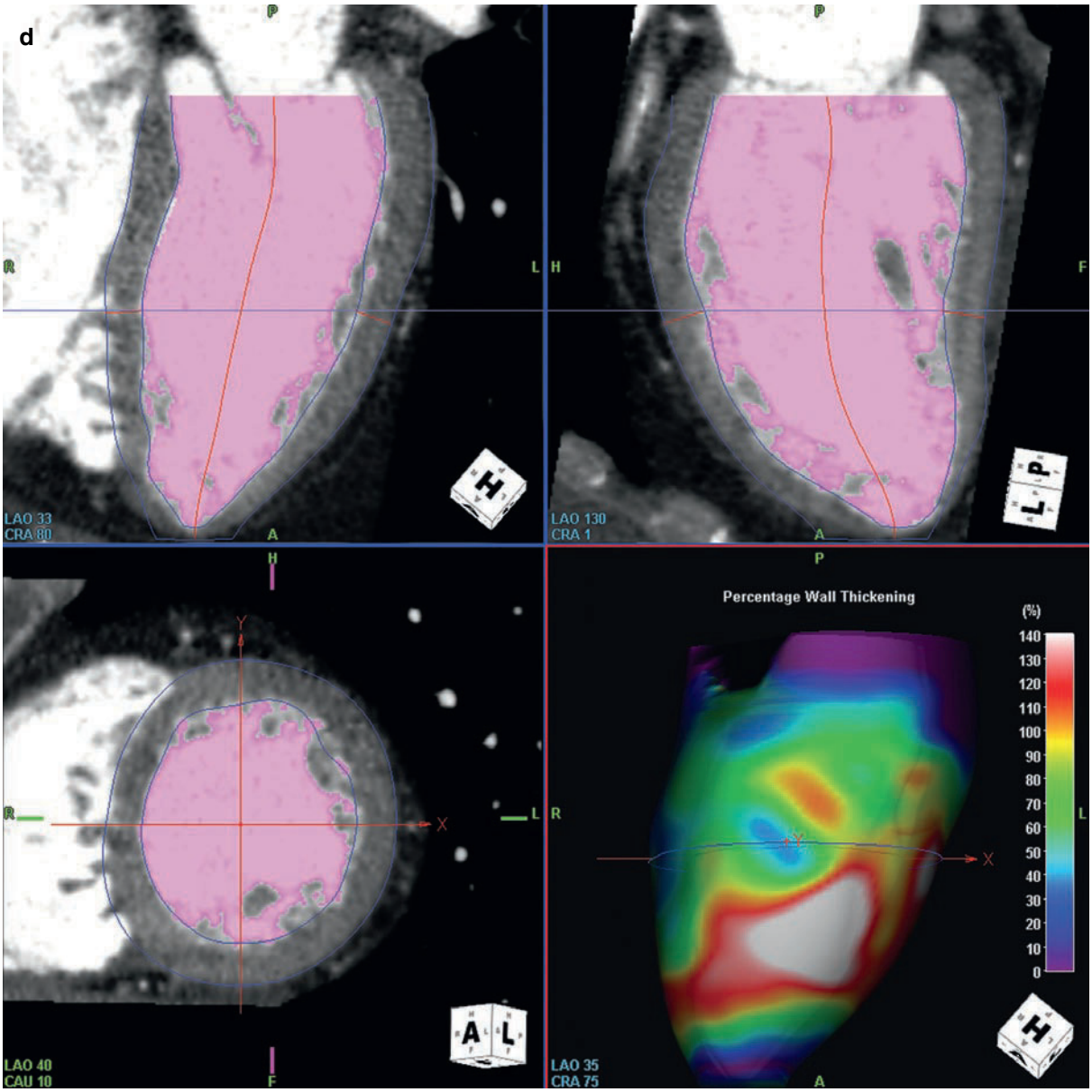

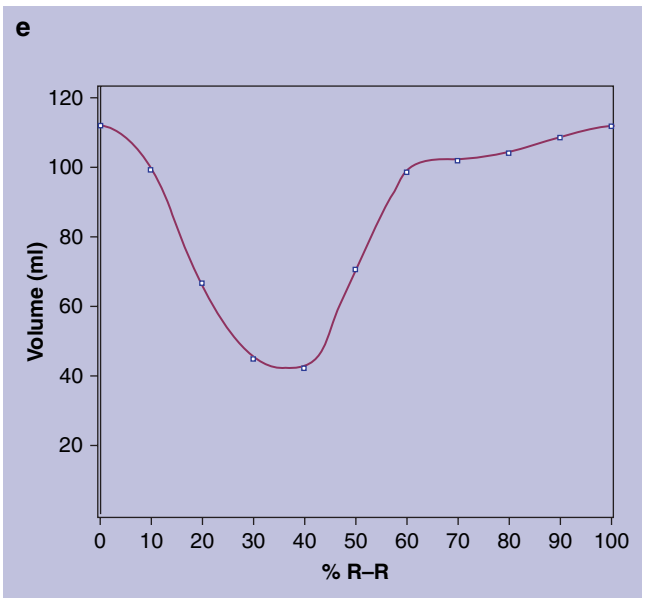

Figure 11.5. (Continued).

Table 11.1. Reference values for left ventricular size, function, and muscle mass for cardiac CT in adult women and men [30, 35]

Measurement	Women				Men			
	Reference range	Mildly abnormal	Moderately abnormal	Severely abnormal	Reference range	Mildly abnormal	Moderately abnormal	Severely abnormal
Septal wall thickness (mm)[a]	6–9	10–12	13–15	≥16	6–10	11–13	14–16	≥17
Posterior wall Thickness (mm)[a]	6–9	10–12	13–15	≥16	6–10	11–13	14–16	≥17
LV muscle Mass (gm)	66–155	156–176	177–187	>190	96–200	201–227	228–254	>260
LV diameter (mm)[a]	39–53	54–57	58–61	≥62	42–59	60–63	64–68	≥69
LV global EDV (mL)	60–110	111–122	123–136	≥140	70–160	161–190	191–210	≥210
LV global ESV (mL)	20–50	51–60	61–70	≥71	25–60	61–70	71–85	≥86
LV global EF (%)	≥55	45–54	30–44	<30	≥55	45–54	30–44	<30

[a]End-diastole, mid left ventricle; *EDV* end-diastolic volume; *ESV* end-systolic volume; *EF* ejection fraction

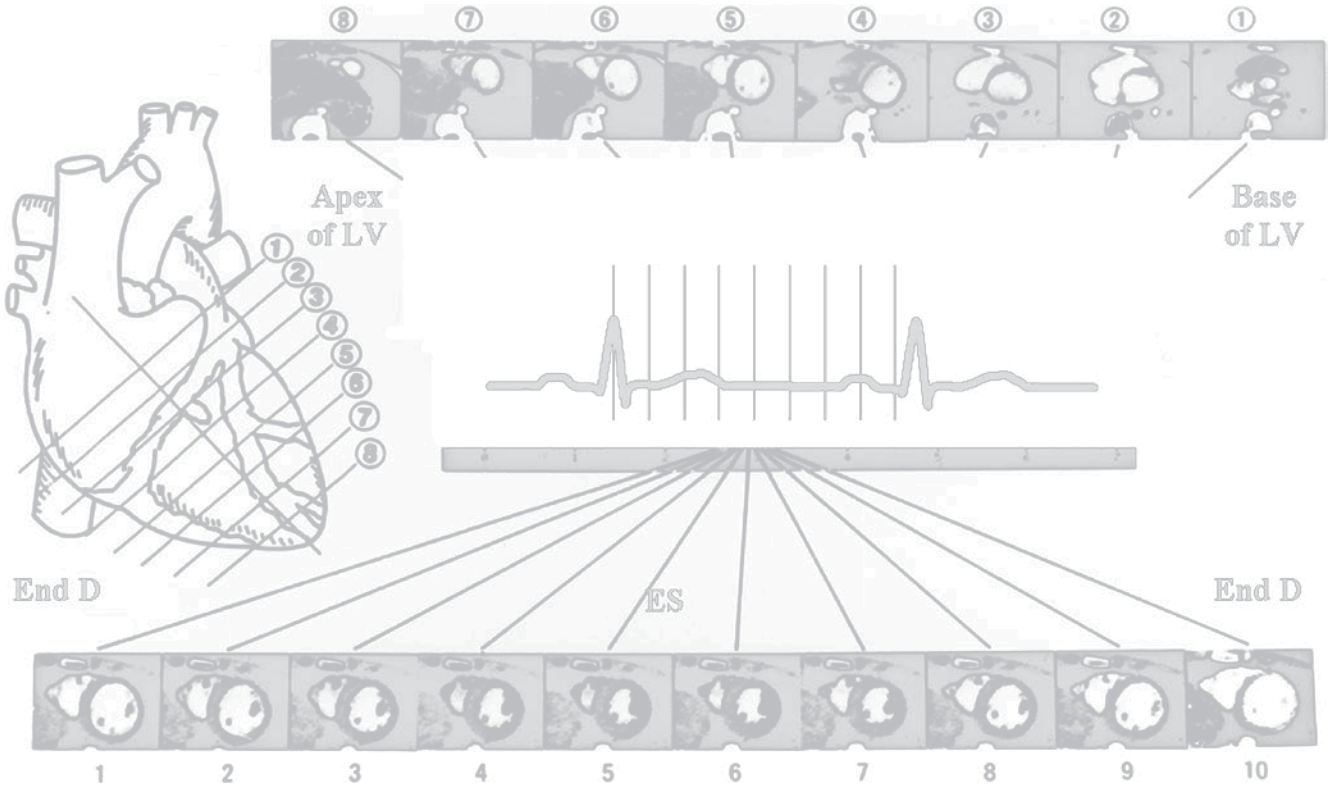

Figure 11.6. Example of LV short axis images from the apex to base of the heart and various ECG related phases defined from end-diastole (End D) to end-systole (ES) and back to end-diastole (end D) during a 10-phase ECG gated reconstruction of cardiac function using Cardiac CT.

timing/administration. Definition of end-diastole is straight-forward by noting the timing of the R-wave on the ECG and the appropriate CT reconstructed phase. Definition of end-systole is more difficult. Although using a 10-phase retrospective reconstruction usually assigns end-systole to the smallest chamber volume, recent data suggest that at least a 15 phase reconstruction might be more appropriate for timing of this event [37]. The number of phases reconstructed from a 64+-slice MDCT retrospectively ECG gated cardiac CT is a choice made by the physician, and going from a 10-phase to a 20-phase reconstruction only results in more images to review for analysis and the subsequent increase in file size and image storage requirements. Also, many of the available image processing workstations have a limit to the number of images that can be placed into active memory for review.

Comparison to Other Imaging Modalities

EBT and by inference 64+slice MDCT has been validated for assessment of cardiac function in comparison to SPECT imaging, MRI, contrast-ventriculography, and 2-dimensional echo.

Future Directions

The quantitation of cardiac structure and function by cardiac CT has been evolving for more than 25 years. Improvements in cardiac edge-detection methods have essentially eliminated the need to laboriously trace images from each tomographic plane and apply a modified

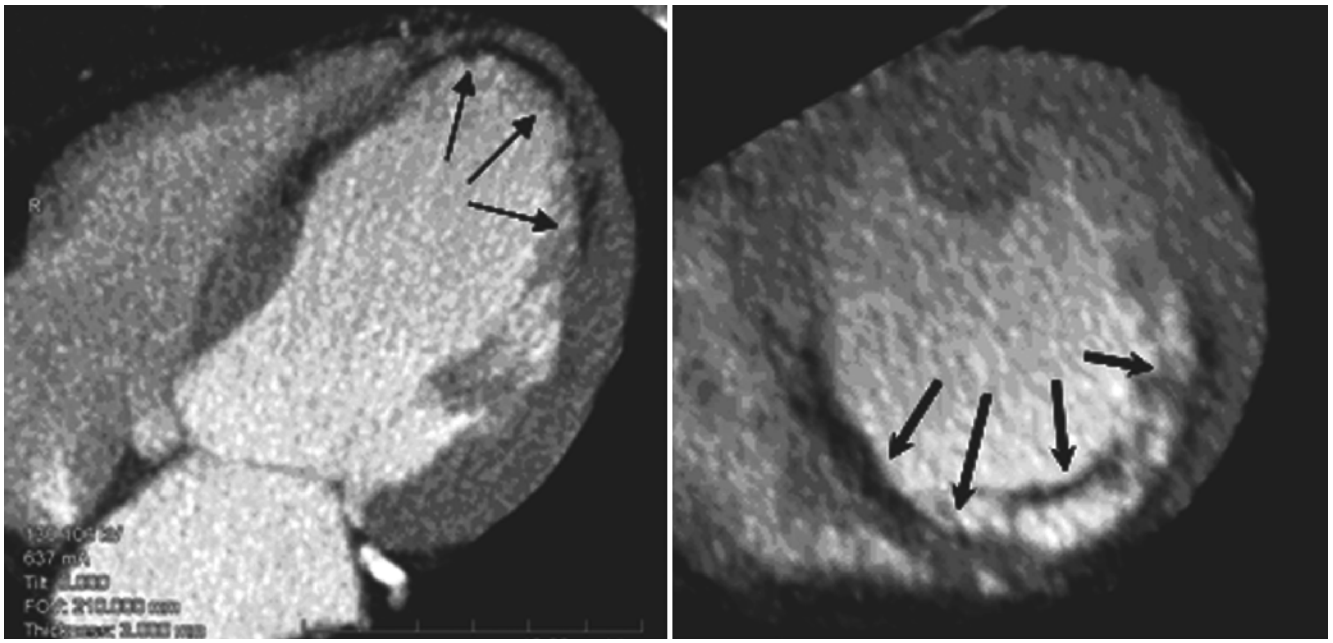

Figure 11.7. Vertical long axis and mid-LV short axis images of a patient with remote myocardial infarction. *Left*: vertical long axis; the *arrows* point to regions of transmural infarction in the lower septal wall, apex, and lateral wall. *Right*: mid-LV short axis; the *arrows* point to regions of transmural infarction in the inferior septum, inferior (*posterior*) wall, and lateral wall; using such presentations, estimates of myocardial infarction size can be estimated.

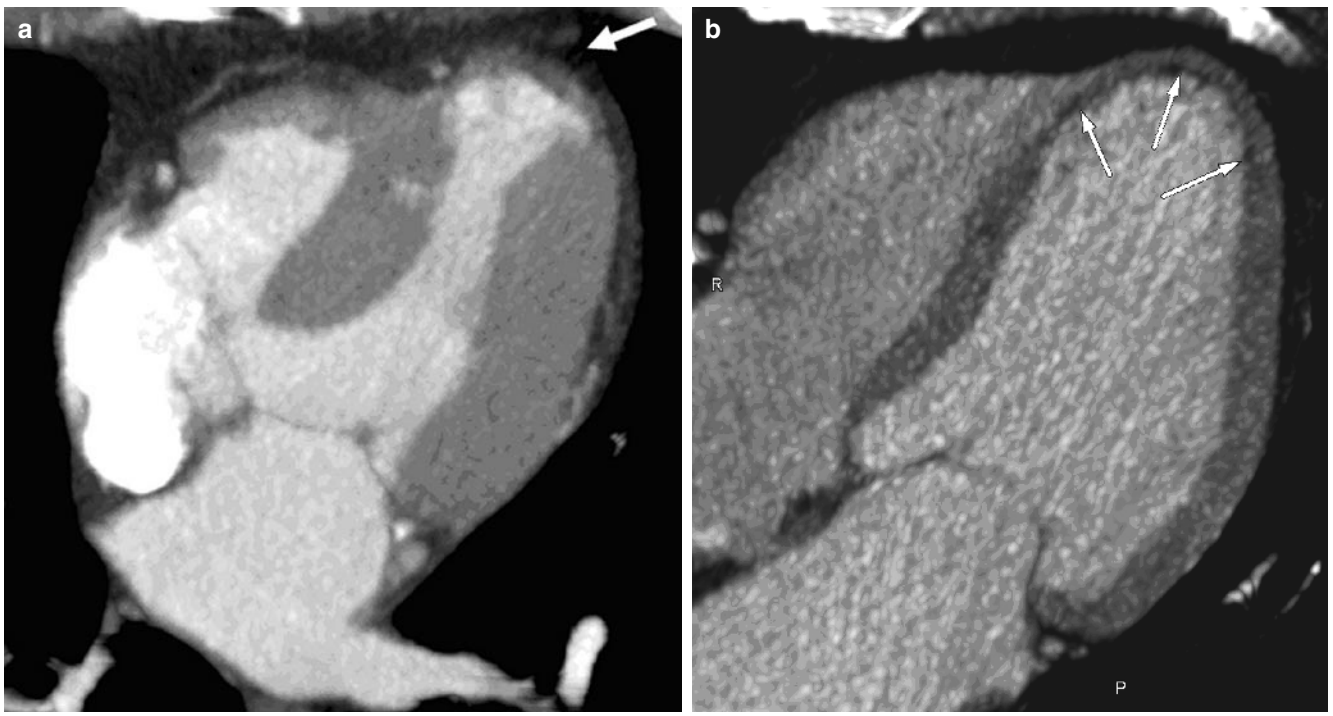

Figure 11.8. Examples of LV true aneurysm and infarction using Cardiac CT. (**a**) End-systolic long axis image of LV demonstrating LV apical aneurysm (*arrow*); (**b**) End-diastolic long axis image of LV demonstrating dilation of LV apex and thinning of myocardial with akinetic regional motion (*arrows*).

Simpson's (stack of coins) rule. All current workstations allow for straight-forward information on EF, regional wall thickening, regional wall motion, and LV volumes from 64+-slice MDCT cardiac examinations. Semi-quantitative information on left/right atrial volume/dimensions and RV volume/dimensions are also in development.

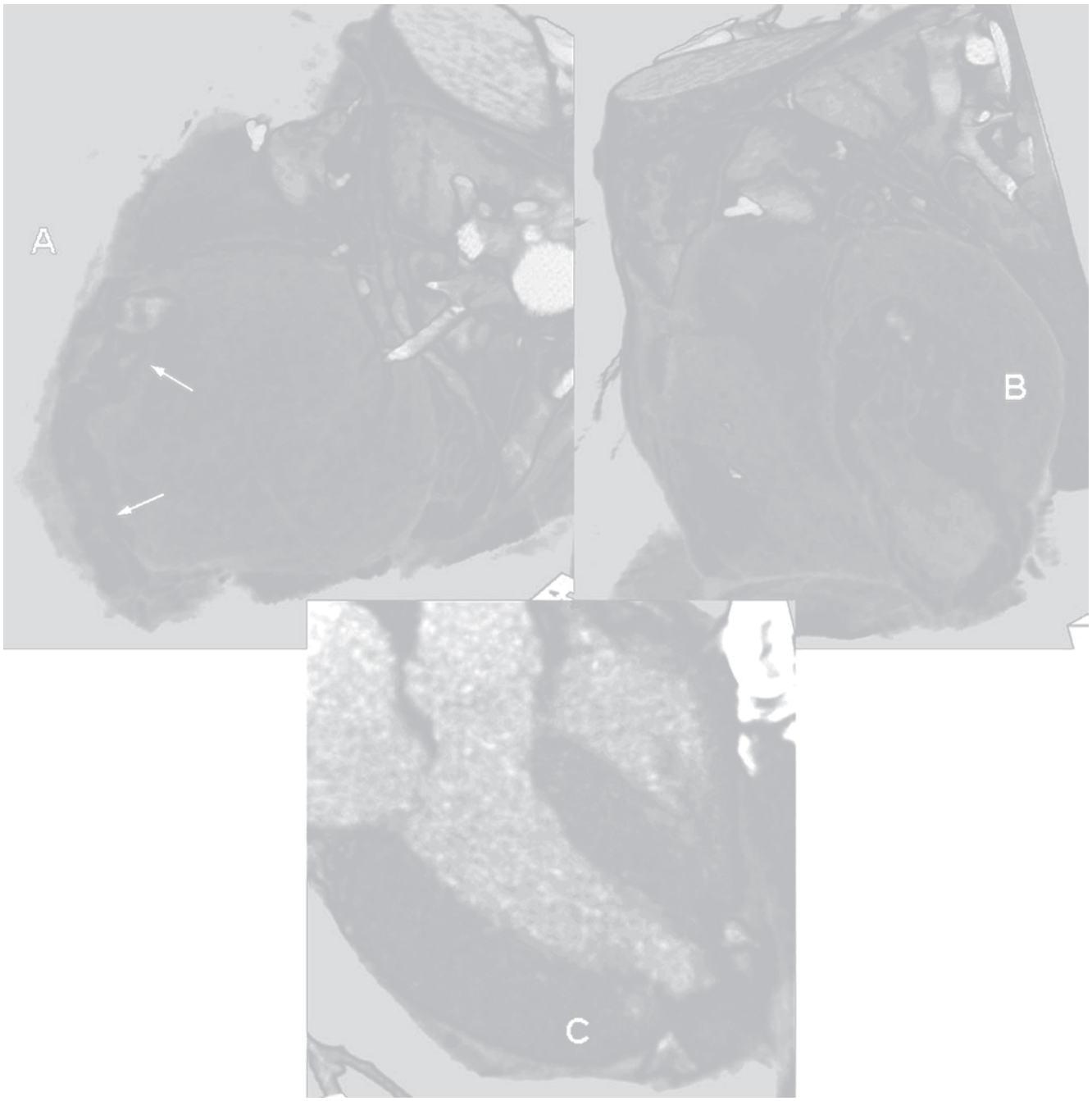

Figure 11.9. Cardiac CT Images of Patient after LV aneurysmectomy. (**a**, **b**) Volume rendering presentation from lateral and anterior views of the LV: the area of aneurysm repair is shown by the arrows. (**c**) A maximum intensity projection (2-dimensional) of the LV long axis showing the area of aneurysm repair: the two bright objects at the LV apex are surgical pledgets.

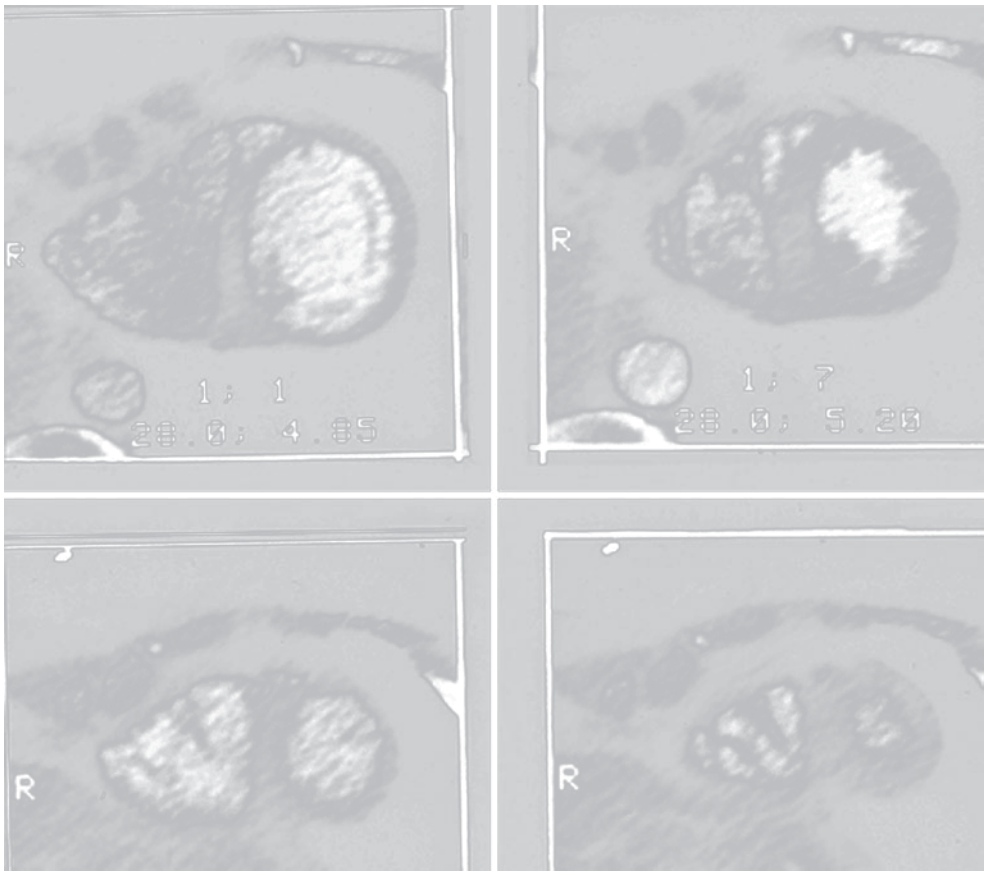

Figure 11.10. Short axis images of the LV (*right*) and RV (right ventricle, *left*) from an 18 year old woman with syncope and ARVD (arrhythmogenic RV dysplasia). Note the enlargement of the RV compared to the LV and the presence of wide trabeculations in the RV, both major criteria for diagnosis of ARVD.

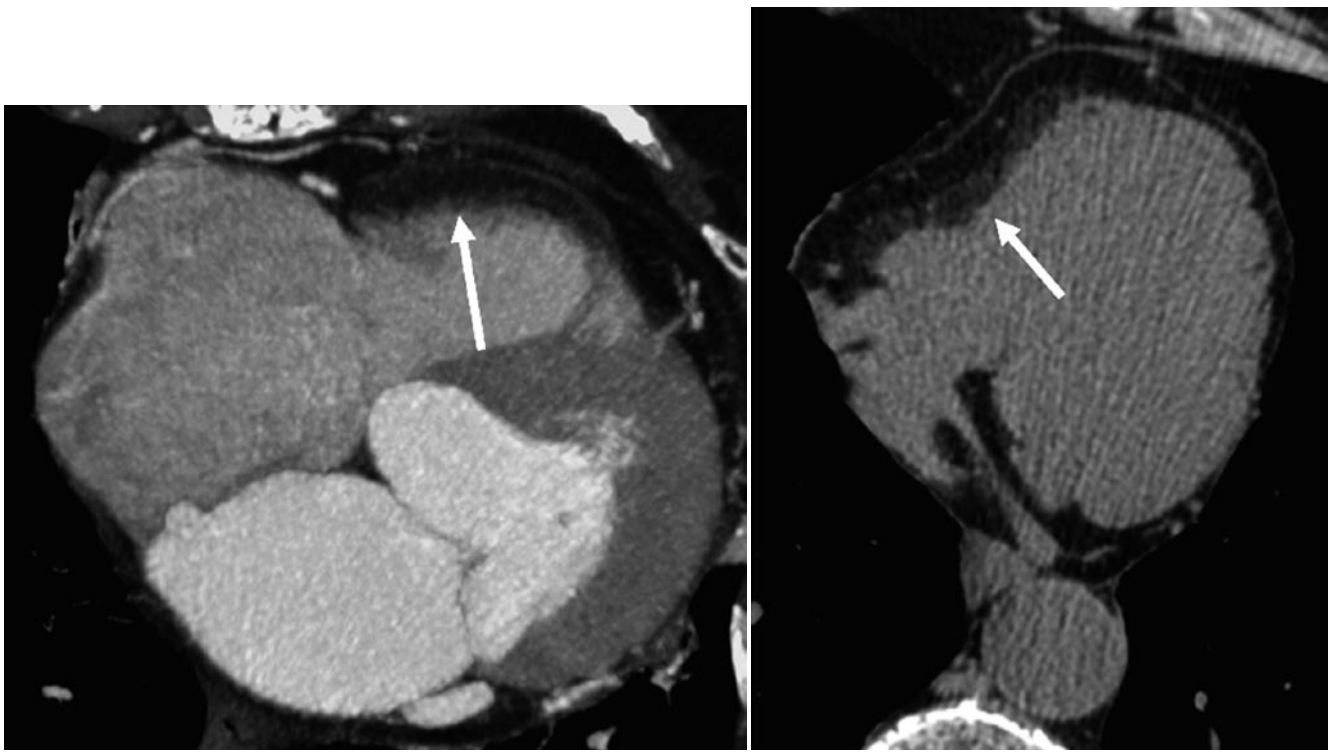

Figure 11.11. Cardiac CT Images of two patients with ARVD (arrhythmogenic right ventricular dysplasia). The *arrows* demonstrate "fatty infiltration" of the RV wall, a major diagnostic criteria for the diagnosis of ARVD.

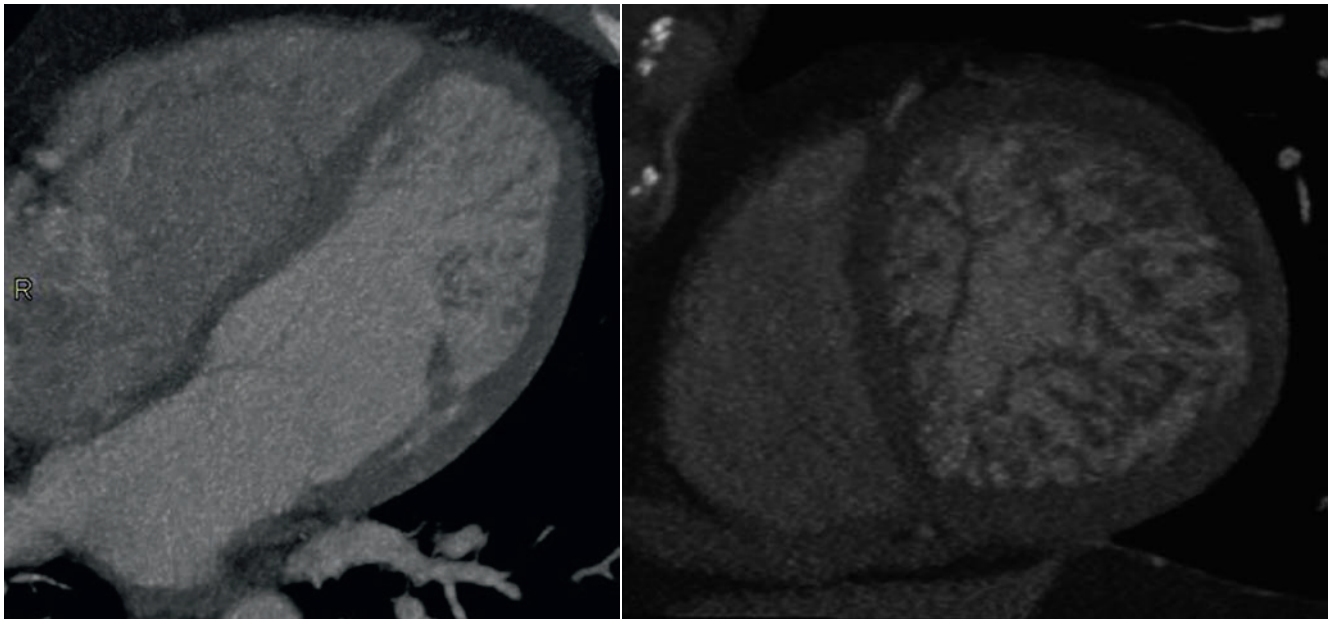

Figure 11.12. Cardiac CT in a patient with "non-compaction" of the LV. *Left*: Long axis showing dilation of the lower (apical) one half of the LV chamber. *Right*: a mid-LV short axis demonstrating dilation of the LV chamber and the presence of deep "sinusoids" (fenestrations) of the LV chamber.

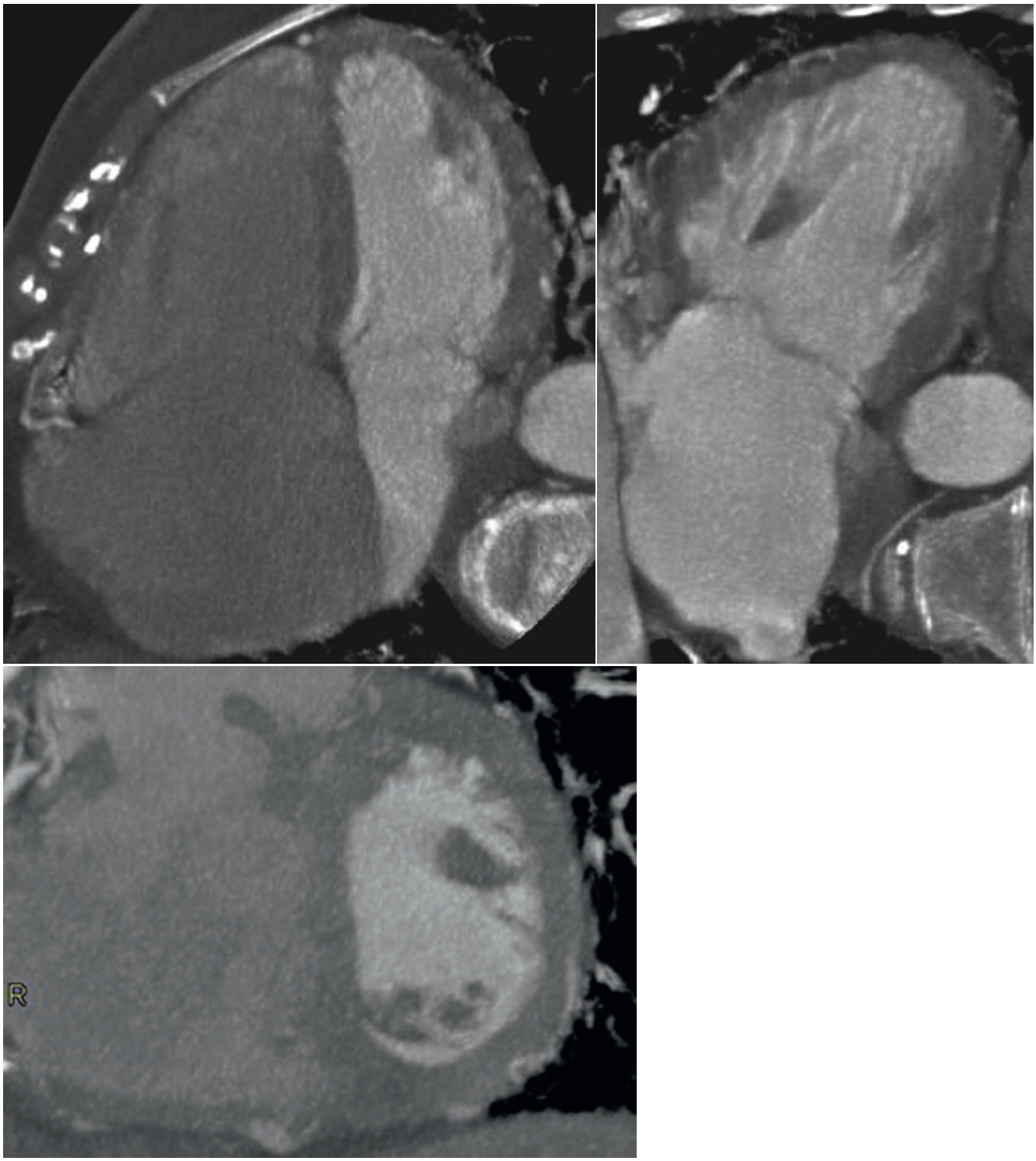

Figure 11.13. Cardiac CT of a patient with severe pulmonary hypertension as a consequence to severe, chronic mitral valve regurgitation. The horizontal (*left*) and vertical (*middle*) long axis images demonstrate the dilation of the RV and right atrium (RA)/left atrium; the short (*right*) axis image demonstrates a common characteristic of pulmonary hypertension and a "D" shaped interventricular septum (IVS).

Figure 11.14. Measurement of Cardiac and Chamber Dimensions in Cardiac CT. (**a**) Long axis and short axis dimensions of the left ventricular long axis and at mid ventricle short axis. (**b**) Measurements of septal, apical, and lateral wall thicknesses at end-diastole in a patient with severe cardiac hypertrophy. (**c**) Representative measurements of the aortic root and left atrium as measured mimicking a para-sternal measurement that might be done using 2-dimensional echocardiography (direction indicated by *arrow*).

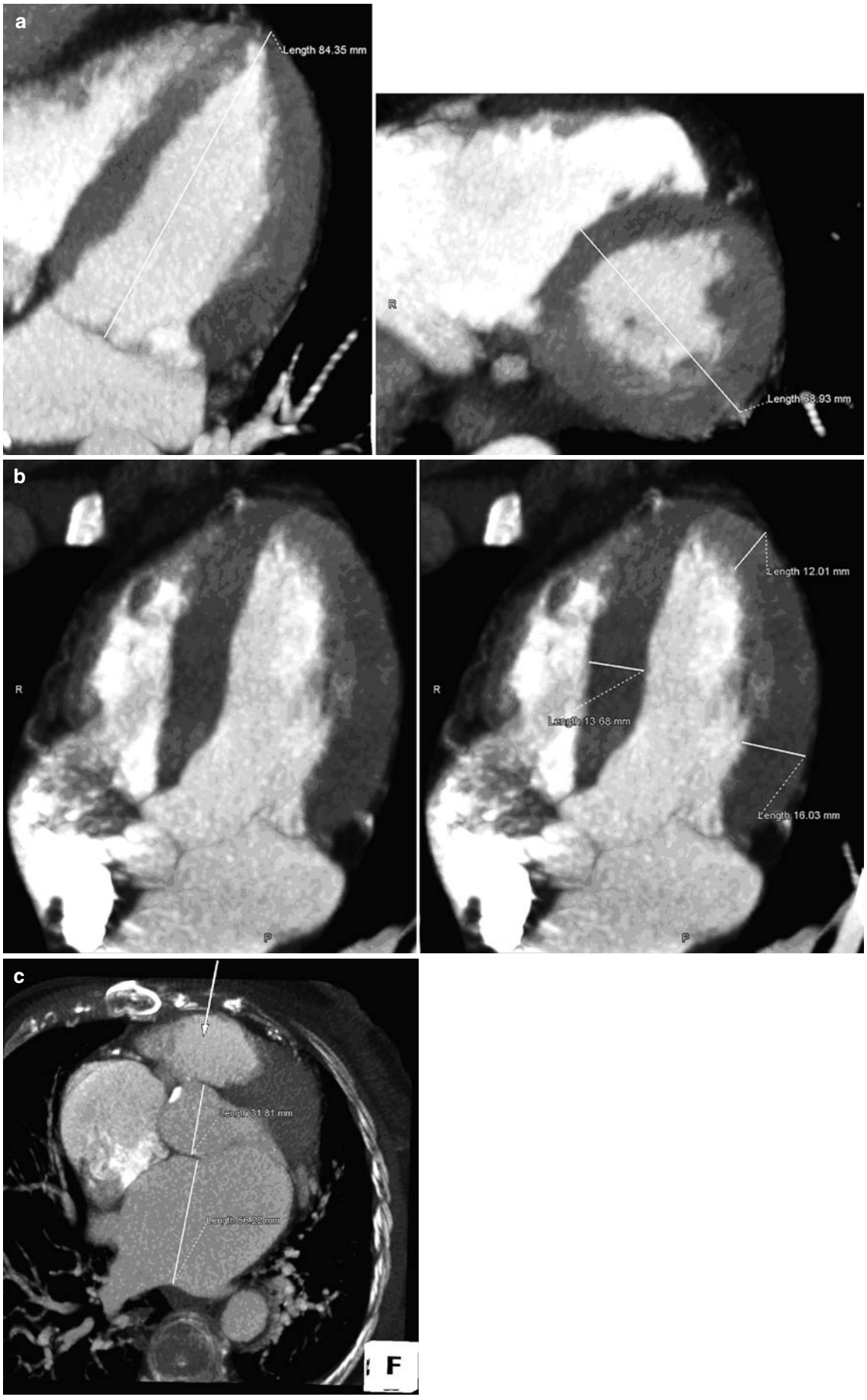
a
Length 84.35 mm
R
Length 68.93 mm
b
R
P
R
Length 12.01 mm
Length 13.68 mm
Length 16.03 mm
P
c
Length 31.81 mm
Length 56.22 mm
F

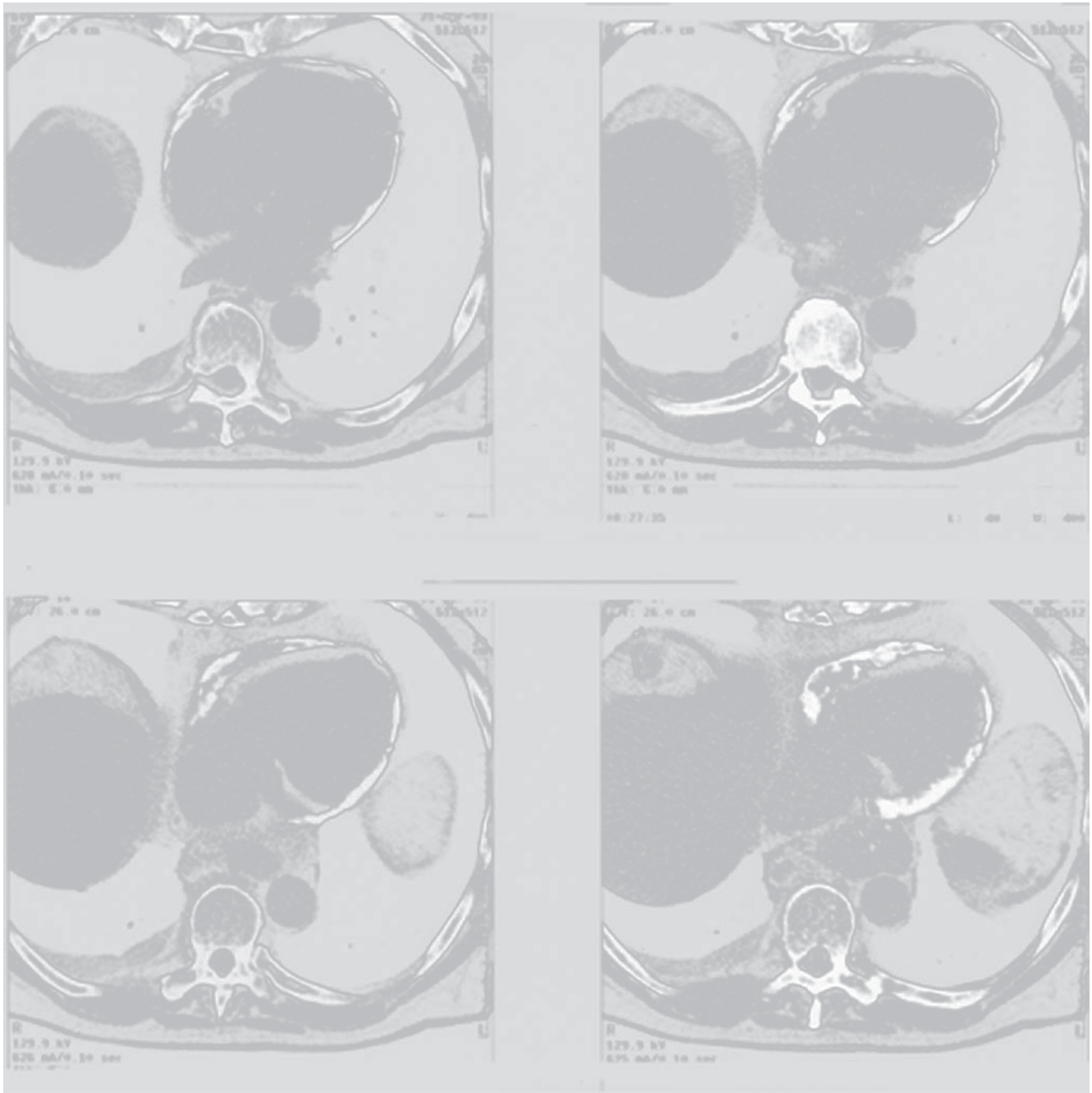

Figure 11.15. Evaluation of the pericardium by cardiac CT. (**a**) *Left* – Concentric, densely calcified pericardium in a patient with constrictive pericarditis as a consequence to tuberculosis. *Right* – Images from a patient with pericardial tamponade from a concentric pericardial effusion. (**b**) *Top Left*: Volume rendered image demonstrating entire cardiac volume; *Top Right*: Volume rendered image demonstrating only the cardiac epicardial surface; this was performed by changing the CT display window and level settings on the image presented in **b**, *top left; Bottom*: a maximum intensity projection of the horizontal cardiac long axis demonstrating the opacified cardiac chambers and the surrounding low intensity circumferential pericardial effusion.

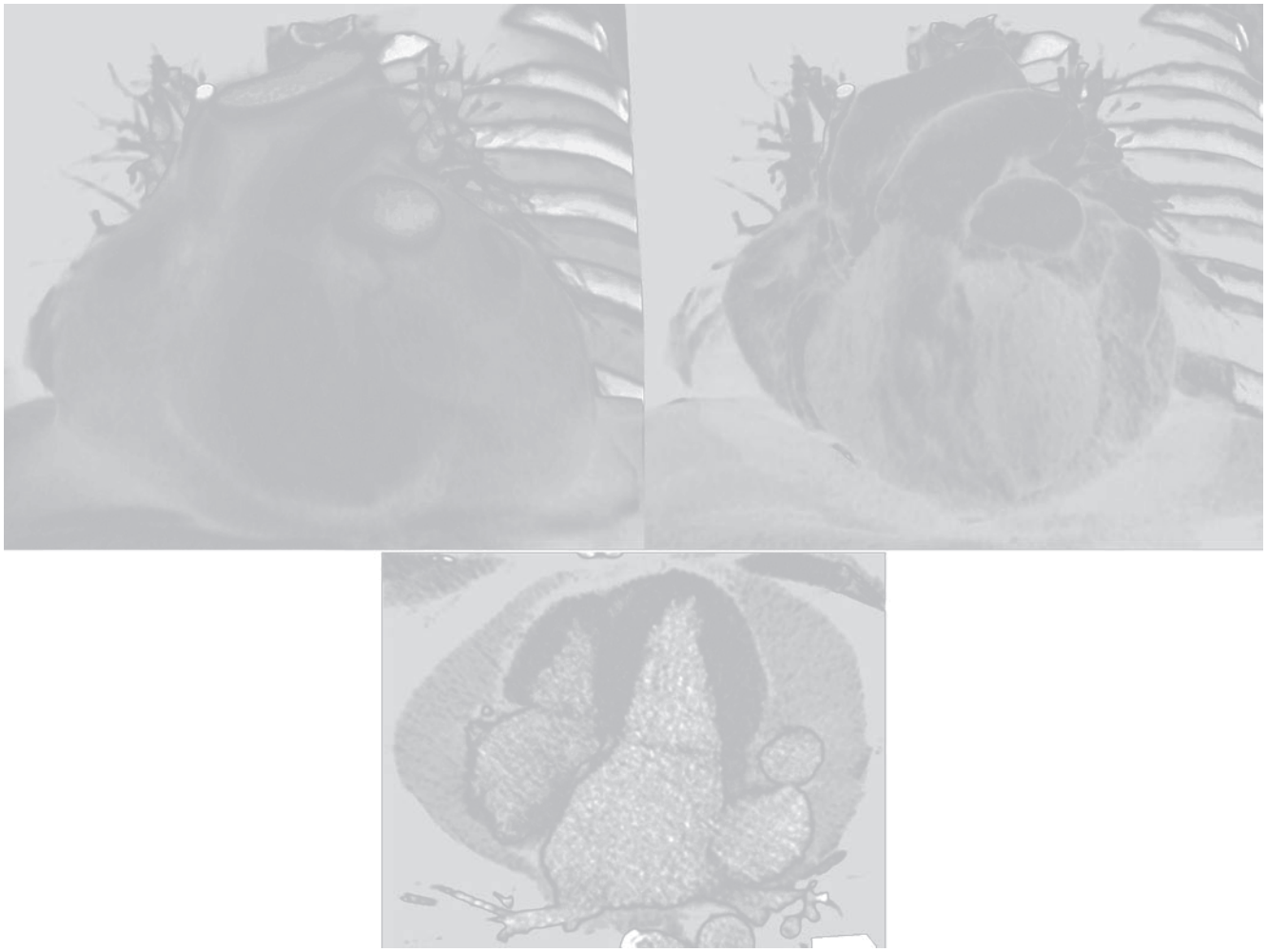

Figure 11.15. (Continued).

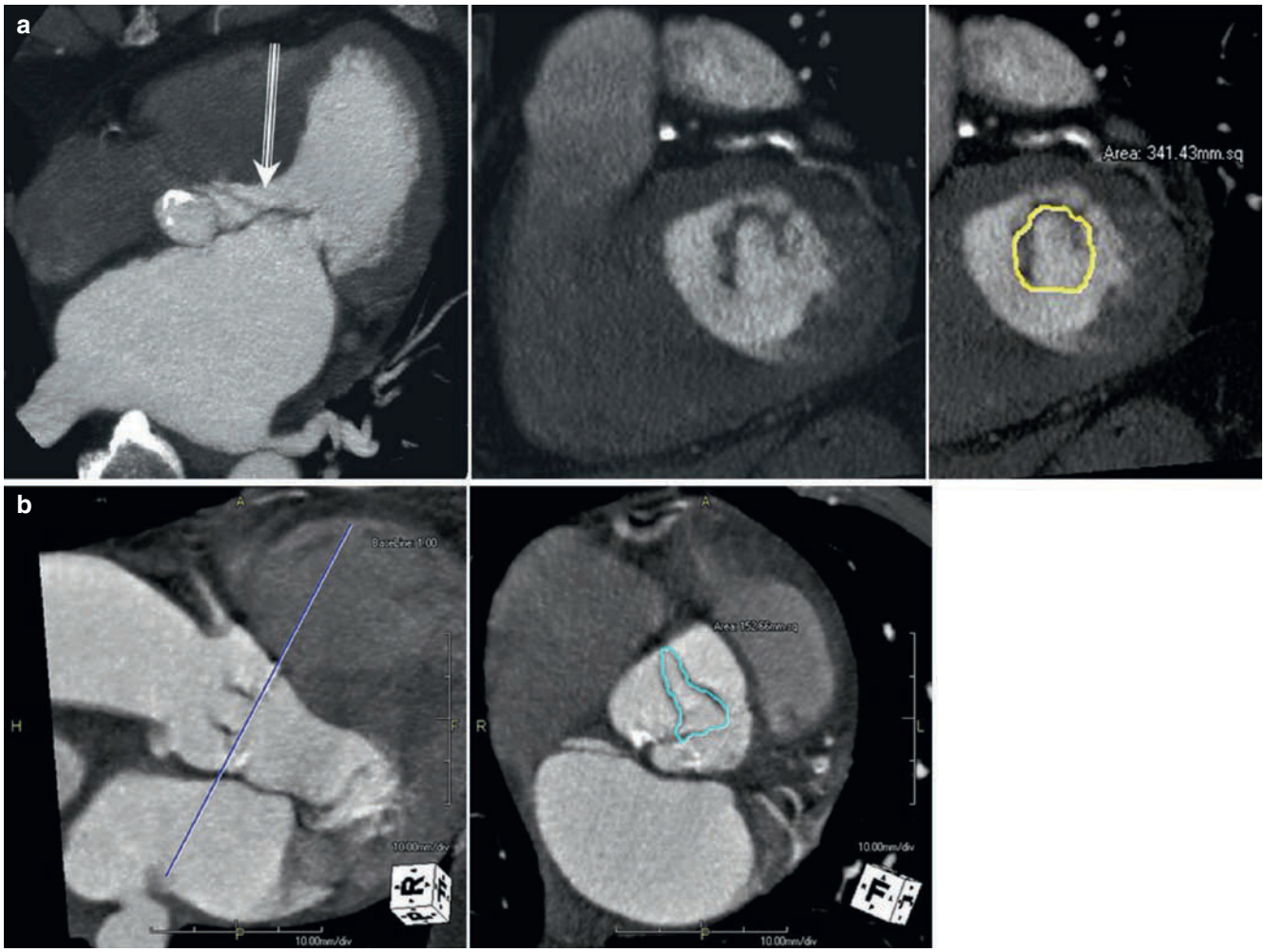

Figure 11.16. Evaluation of cardiac valve stenosis using cardiac CT. (**a**) LV long axis and short axis images demonstrating thickened mitral valve leaflets (*arrow*) and dilated left atrium and measurement of mitral valve area in a patient with moderate mitral valve stenosis. (**b**) Representative orthogonal views of the aortic valve and measurement of aortic valve area in a patient with known mild aortic valve stenosis.

References

1. Hammermeister KE, DeRouen TA, Dodge HT. Variables predictive of survival with coronary disease: selection by univariate and multivariate analyses from the clinical, electrocardiographic, exercise, arteriographic and quantitative angiographic evaluation. *Circulation*. 1979;59:421–450.
2. Norris RW, Barnaby PF, Brandt PWT. Prognosis after recovery from first acute myocardial infarction: determinant of reinfarction and sudden death. *Am J Cardiol*. 1984;53:408–413.
3. White HD, Norris RM, Brown MA, Brandt PWJ, Whitlock RML, Weld CJ. Left ventricular end-systolic volume as the major determinant of survival after recovery from myocardial infarction. *Circulation*. 1987;76:44–51.
4. Cerqueira MD, Weissman NJ, Dilsizian V, et al. Standardized myocardial segmentation and nomenclature for tomographic imaging of the heart – a statement for healthcare professions from the Cardiac Imaging Committee of the Council on Clinical Cardiology of the American Heart Association. *Circulation*. 2002;105:539–542.
5. Achenbach S, Sacher D, Ropers D, et al. Electron beam computed tomography for the detection of left atrial thrombi in patients with atrial fibrillation. *Heart*. 2004;90(12):1477–1478.
6. Meinel JF, Wang G, Jiang M, et al. Spatial variation of resolution and noise in multi-detector row spiral CT. *Acad Radiol*. 2003;10:607–610.
7. Paul JF, Mace L, Caussin C, et al. Multirow detector computed tomography assessment of intraseptal dissection and ventricular pseudoaneurysm in postinfarction ventricular septal defect. *Circulation*. 2001;104:497–498.
8. Reiter SJ, Rumberger JA, Feiring AJ, Stanford W, Marcus ML. Precision of right and left ventricular stroke volume measurements by rapid acquisition cine computed tomography. *Circulation*. 1986;74:890–900.
9. Yamamuro M, Tadamura E, Kubo S, et al. Cardiac functional analysis with multi-detector row CT and segmental reconstruction algorithm: comparison with echocardiography, SPECT, and MR imaging. *Radiology*. 2005;234:381–390.
10. Halliburton SS, Petersilka M, Schvartzman PR, Obuchowski N, White RD. Evaluation of left ventricular dysfunction using multiphasic reconstructions of coronary multi-slice computed tomography data in patients with chronic ischemic heart disease: validation against cine magnetic resonance imaging. *Int J Cardiovasc Imaging*. 2003;19:73–83.
11. Feiring AJ, Rumberger JA, Skorton DJ, et al. Determination of left ventricular mass in the dog with rapid acquisition cardiac CT scanning. *Circulation*. 1985;72:1355–1362.
12. Hajduczok Z, Weiss RM, Marcus ML, Stanford W. Determination of right ventricular mass in humans and dogs with ultrafast computed tomography. *Circulation*. 1990;82:202.

13. Kuroda T, Seward JB, Rumberger JA, Yanagi H, Tajik AJ. Left ventricular volume and mass: comparative study of 2-dimensional echocardiography and ultrafast computed tomography. *Echocardiography*. 1994;11:1–9.
14. Rumberger JA. Quantifying left ventricular regional and global systolic function using ultrafast computed tomography. *Am J Card Imaging*. 1991;5(1):29–37.
15. Feiring AJ, Rumberger JA, Reiter SJ, et al. Sectional and segmental variability of left ventricular function: Experimental and clinical studies using ultrafast computed tomography. *J Am Coll Cardiol*. 1988;12:415.
16. Lanzer P, Garrett J, Lipton MJ, et al. Quantitation of regional myocardial function by cine computed tomography: pharmacologic changes in wall thickness. *J Am Coll Cardiol*. 1986;8:682.
17. Feiring AJ, Rumberger JA. Ultrafast computed tomography analysis of regional radius-to-wall thickness ratios in normal and volume-overloaded human left ventricle. *Circulation*. 1992;85:1423–1432.
18. Rumberger JA, Weiss RM, Feiring AJ, et al. Patterns of regional diastolic function in the normal human left ventricle: An ultrafast-CT study. *J Am Coll Cardiol*. 1989;13:119–125.
19. Lipton MJ, Rumberger JA. The assessment of left ventricular systolic and diastolic function by ultrafast computed tomography. *Am J Card Imaging*. 1991;5:318–327.
20. Rumberger JA, Behrenbeck T, Breen JR, Reed JE, Gersh BJ. Non-parallel changes in global chamber volume and muscle mass during the first year following transmural myocardial infarction in man. *J Am Coll Cardiol*. 1993;21:673–682.
21. Hirose K, Reed JE, Rumberger JA. Serial changes in left and right ventricular systolic and diastolic mechanics during the first year after an initial left ventricular Q-wave myocardial infarction. *J Am Coll Cardiol*. 1995;25:1097–1104.
22. Hirose K, Shu NH, Reed JE, Rumberger JA. Right ventricular dilatation and remodeling the first year after an initial transmural wall myocardial infarction. *Am J Cardiol*. 1993;72:1126.
23. Chareonthaitawee P, Christian TF, Hirose K, Gibbons RJ, Rumberger JA. Relation of initial infarct size with the extent of left ventricular remodeling in the year after acute myocardial infarction. *J Am Coll Cardiol*. 1995;25:567–573.
24. Sehgal M, Hirose K, Reed JE, Rumberger JA. Regional left ventricular systolic thickening and thicknesses during the first year after initial Q-wave myocardial infarction: serial effects of ventricular remodeling. *Int J Cardiol*. 1996;53:45–54.
25. Vigneswaran WT, Rumberger JA, Rodeheffer RJ, Breen JF, McGregor CGA. Ventricular remodeling following orthotopic cardiac transplantation. *Mayo Clinic Proc*. 1996;71:735–742.
26. Rensing BJ, McDougall JC, Breen JR, Vigneswaran WT, McGregor CGA, Rumberger JA. Right and left ventricular remodeling after orthotopic single lung transplantation for end-stage emphysema. *J Heart Lung Transplant*. 1997;16:926–933.
27. Gerber T, Rumberger JA, Gibbons R, Behrenbeck T. Measurement of left ventricular ejection fraction by TC-99M sestamibi first-pass angiography in patients with myocardial infarction: comparison with electron beam computed tomography. *Am J Cardiol*. 1999;83:1022–1026.
28. Schuijf JD, Bax JJ, Jukema JW, et al. Noninvasive angiography and assessment of left ventricular function using multislice computed tomography in patients with type 2 diabetes. *Diabetes Care*. 2004;27:2905–2910.
29. Dirksen JS, Bax JJ, de Roos A, et al. Usefulness of dynamic multislice computed tomography of left ventricular function in unstable angina pectoris and comparison with echocardiography. *Am J Cardiol*. 2002;90:1157–1160.
30. Rumberger JA, Sheedy PF, Breen JF. Use of ultrafast (cine) X-ray of right and left ventricular volume measurements by electron-beam computed tomography in cardiac and cardiovascular imaging. In: Guiliani ER, Gersh BJ, McGoon MD, Dayes DL, Shaff HF, eds. *Mayo Clinic Practice of Cardiology*. 3rd ed. St. Louis: Mosby; 1996:303–324.
31. Rumberger JA, Reed JE. Quantitative dynamics of left ventricular emptying and filling as a function of heart size and stroke volume in pure aortic regurgitation and in normal subjects. *Am J Cardiol*. 1992;70:1045–1050.
32. Weiss RM, Stark CA, Rumberger JA, Marcus ML. Identification and quantitation of myocardial infarction or risk area size with cine-computed tomography. *Am J Card Imaging*. 1990;4:33–37.
33. Schmermund A, Gerber T, Behrenbeck T, et al. Myocardial infarct size by electron beam computed tomography: a comparison with ^{99m}Tc sestamibi. *Invest Radiol*. 1998;33:313–321.
34. Schmermund A, Breen JF, Sheedy PF, Rumberger JA. Reproducibility of right and left ventricular volume measurement by electron-beam CT in patients with congestive heart failure. *Int J Card Imaging*. 1998;14(3):201–209.
35. Lang RM et al. Recommendations for chamber quantification: a report from the American Society of Echocardiography's Guidelines and Standards Committee and the Chamber Quantification Writing Group, developed in conjunction with the European Association of Echocardiography, a branch of the European Society of Cardiology. *J Am Soc Echocardiogr*. 2005;18:1440–1463.
36. Soh EK, Villines TC, Feuerstein IM. Sixty-four-multislice computed tomography in a patient with arrhythmogenic right ventricular dysplasia. *J Cardiovasc Comput Tomogr*. 2008;2:191–192.
37. Bardo DME, Kachenoura N, Newby B, Lang RM, Mor-Avi V. Multidetector computed tomography evaluation of left ventricular volumes: Sources of error and guidelines for their minimization. *J Cardiovasc Comput Tomogr*. 2008;2:222–230.

12

Perfusion and Delayed Enhancement Imaging

Joao A. C. Lima and Ilan Gottlieb

Overview

A 54 year old male with diabetes and family history of CAD comes to a cardiologist for the first time for atypical chest pain. The patient reports "having to grasp for air" while in chest pain. A rest ECG is done at the office, in which nonspecific T wave changes were the only abnormality. Besides blood tests, the cardiologist orders an echocardiogram that shows reduced LV function and akinesis of the mid and apical anterior-septal walls, and a stress SPECT study that shows a perfusion defect in the same regions, with little reversibility on the rest images. Thinking this is most likely ischemic coronary disease, the cardiologist orders a cardiac MRI for viability evaluation prior to the invasive coronary angiography, which showed an occluded mid LAD artery with distal filling via collaterals. Given the presence of viability on the MRI scan, the patient successfully underwent PTCA of the mid-LAD lesion, and, two months later, LV function shows improvement and the patient is asymptomatic.

Cardiologists are familiar with relying on a number of different imaging modalities for a thorough assessment of cardiovascular disorders. Coronary anatomy evaluation is usually performed using invasive catheterization or more recently by noninvasive MDCT scans. Global and regional myocardial function as well as structural abnormalities can be assessed with echo, MRI, and MDCT. Subclinical atherosclerosis is usually assessed via detection of coronary calcium using MDCT or EBCT scanners or via measuring carotid intima-media thickness with ultrasound; while stress tests for ischemia detection and quantification are usually performed with nuclear SPECT or PET, echo stress, or stress MRI imaging. Finally, myocardial fibrosis for viability and prognosis assessment is usually detected and quantified by MRI and nuclear techniques.

From this list, myocardial fibrosis and perfusion are the only two assessments MDCT does not currently provide, but as will be discussed in this chapter, recent developments have demonstrated initial feasibility for MDCT to be a complete imaging modality, which, in a single scan, could provide a wide array of complementary information. Ideally, using one imaging modality to perform all these assessments during a single scan could have substantial economic implications, may serve to reduce patient anxiety, and improve workflow.

MDCT for Detection of Myocardial Fibrosis and Viability

The ability to distinguish dysfunctional but viable myocardium from nonviable tissue after acute or chronic ischemia has important implications for the therapeutic management of patients with coronary artery disease [1, 2]. Image-based characterization of myocardial scar morphology can identify those patients with hibernating myocardium who may achieve functional systolic recovery with revascularization [3]. The assessment of myocardial viability and infarct morphology with delayed contrast-enhanced MRI has been well validated over the past several years and is performed routinely by several clinical cardiac MRI centers.

The recent advent of MDCT technology has expanded its potential for a more comprehensive evaluation of cardiovascular diseases. While hypo-attenuation in the noncontrasted scan (due to fatty degeneration of the infarcted area) or during the contrast-enhanced coronary angiography scan has been shown to demonstrate areas of previous MI, it is largely underestimated by MDCT [4, 5]. Delayed MDCT myocardial imaging can accurately identify and characterize morphological features of acute and healed myocardial infarction, including infarct size, transmurality, and the presence of microvascular obstruction and collagenous scar (Figure 12.1) [6, 7]. Infarcted myocardial tissue by MDCT is characterized by well-delineated hyper-enhanced regions, whereas regions of microvascular obstruction by MDCT are characterized by hypo-enhancement on imaging early after MI [6, 7]. The mechanism of myocardial hyper-enhancement and hypo-enhancement in acutely injured myocardial territories after iodinated

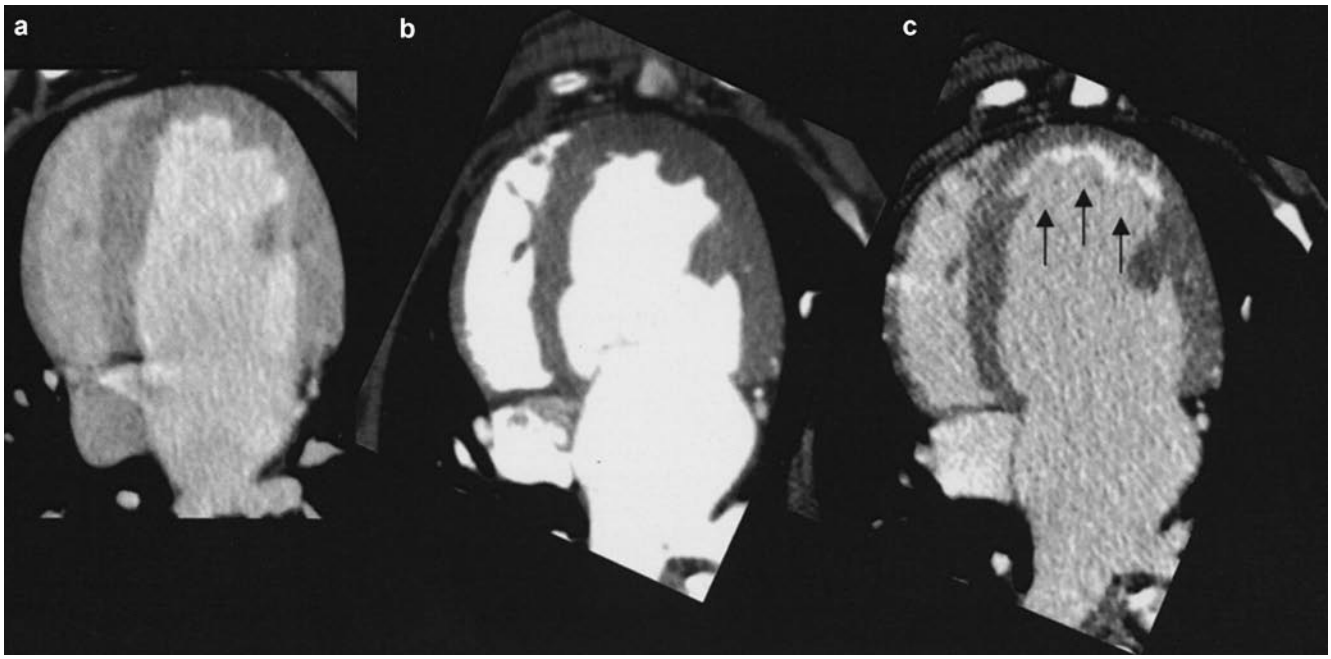

Figure 12.1. Typical contrast-enhanced myocardial MDCT images showing axial slices (**a**) at baseline (preinfarct) 5 min after contrast, (**b**) postinfarct during first-pass contrast injection, and (**c**) postinfarct 5 min after contrast injection. The infarcted region is represented by the subendocardial anterior hyperintense region (*arrows*).

contrast administration is similar to that proposed for delayed gadolinium-enhanced MRI [1]. Under conditions of normal myocyte function, sarcolemmal membranes serve to exclude iodine from the intracellular space. After myocyte necrosis, however, membrane dysfunction ensues, and iodine molecules are able to penetrate the cell. Because 75% of the total myocardial volume is intracellular, large increases in the volume of distribution are achieved, which results in marked hyper-enhancement relative to the non-injured myocytes. The mechanism of hyper-enhancement of healed myocardial infarction or collagenous scar is thought to be related to an accumulation of contrast media in the interstitial space between collagen fibers and thus an increased volume of distribution compared with that of tightly packed myocytes. The low signal intensity of microvascular obstruction regions despite restoration of normal flow through the infarct-related artery is explained by the death and subsequent cellular debris blockage of intramyocardial capillaries at the core of the damaged region. These obstructed capillaries do not allow contrast material to flow into the damaged bed, which results in a region of low signal intensity compared with normal myocardium. In minutes to hours, contrast material is able to penetrate this "no reflow" region, and the necrotic myocytes that reside in that myocardial territory then become hyper-enhanced as iodine is internalized by the cell. In weeks, the microvascular obstruction area is replaced by collagenous scar tissue, and the former dark area now become bright. Since the transmurality of delayed enhancement predicts functional recovery after revascularization [3], the better spatial resolution of MDCT as compared to CMR may influence the accuracy of viability assessment, but no study thus far has tested this hypothesis.

Ischemia Detection by MDCT

The notion that CT could provide information on myocardial perfusion has been documented in the past by investigators using electron beam CT [8]. However, the combination of a reliable coronary angiogram with stress-induced myocardial perfusion assessment had to wait until spiral CT technology progressed sufficiently to enable the acquisition of 64 slices simultaneously [9, 10]. Currently, the greatest limitations to CT coronary angiography are the presence of severely calcified coronary segments, stents, or other artifacts that limit luminal visualization. Patients with calcified arteries tend to be older and/or have advanced CAD. Their studies are challenging from a diagnostic viewpoint because vulnerable plaques and stenotic lesions may be hidden underneath large amounts of calcium accumulated in the outer portions of atherosclerotic plaques encompassing 1 or more segments. While progress in multidetector technology has improved our ability to study such patients, greater coverage and improved temporal resolution are unlikely to eliminate the problem, which is in large part intrinsic to the pathogenesis of atherosclerosis, namely, plaques grow outwardly first and tend to accumulate calcium as part of the healing process, therefore creating a natural shield to X-ray penetration. That is a particular limitation to the study of older persons, patients with advanced CAD, and patients who underwent coronary artery bypass graft surgery or multiple stent implantation, as well as patients with diseases such as chronic renal failure that accelerate plaque calcification.

Furthermore, coronary anatomic information is much more valuable when combined with a functional test, since some decisions regarding treatment are based on the

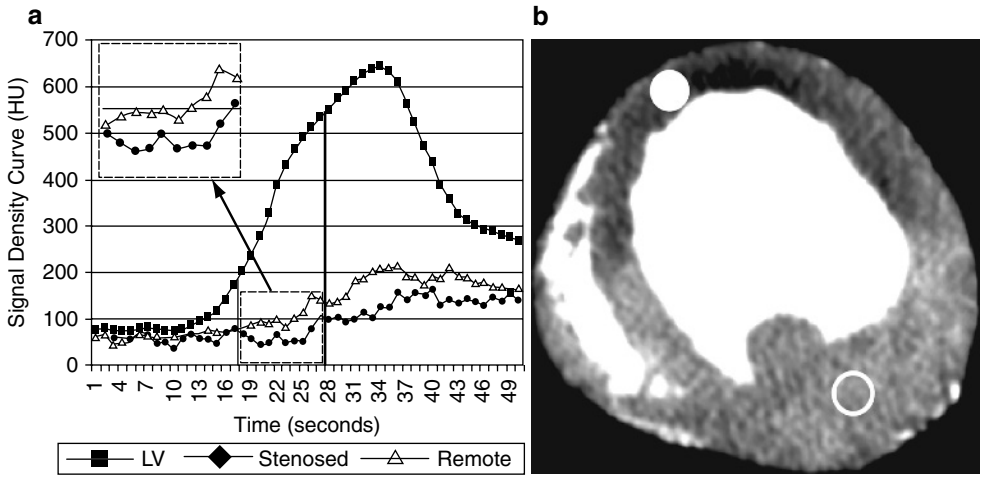

Figure 12.2. Myocardial enhancement upslope curves for the left ventricular cavity, remote and ischemic region (**a**). The usual timing of a coronary CT angiogram is shown as the region between the *vertical bars*. Following the contrast bolus with an ROI placed at the ischemic (*filled circle*) and remote (*open circle*), areas present a delta in myocardial enhancement intensity (**b**) that can be measured, as shown inside the *dashed box* (**a**).

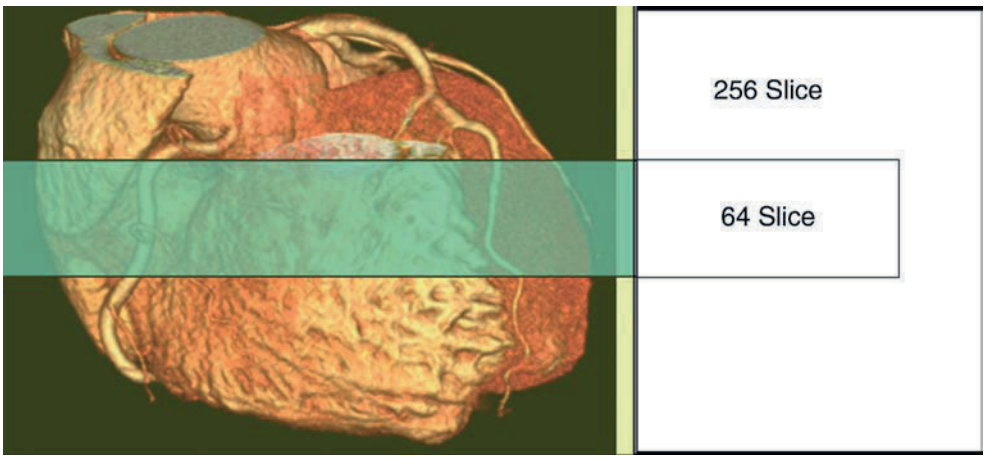

Figure 12.3. Schematic coverage of a 256-detector as compared to a 64-detector MDCT scanner.

detection of myocardial ischemia [11]. The poor correlation between anatomic modalities such as invasive coronary angiography [12, 13] and MDCT [14] with stress perfusion tests underscores the fact that one cannot substitute for the other.

Myocardial perfusion measurements by MDCT are derived from the upslope differences in contrast enhancement between the ischemic and remote areas (Figure 12.2). Current generation 64-detector scanners still have limited coverage of the heart, resulting in the base of the heart being scanned earlier in time than the apex, making comparisons in signal intensities between the two areas problematic. In this regard, the introduction of wide coverage MDCT technology that would allow the entire heart to be imaged in one gantry rotation (Figure 12.3) combined with the capability of programming such gated image acquisitions to occur only during specific portions of a given cardiac cycle (Figure 12.4) has created a brand new horizon of possibilities to reduce radiation exposure enough to enable the performance of combined angiography and myocardial perfusion assessment during stress, which, associated with the angiographic and delayed enhanced images, should provide a comprehensive cardiac assessment. Also, with more coverage, scan times will likely decrease, potentially reducing the amount of contrast material per scan. Such techniques would be ideal for the assessment of patients with chest pain who also have calcified coronaries, as well as the follow-up of patients with advanced heart disease, postcoronary artery bypass surgery, or multiple stent implantations.

Using iodine molecules as a tracer, current research has demonstrated that by measuring the concentration in time of the tracer in the myocardium, MDCT can determine absolute blood flow in different regions of the myocardium [9]. Recent attention to patients with chest pain but no obstructive epicardial CAD (syndrome X) has demonstrated that in a substantial proportion of these individuals microvascular processes can be identified by perfusion reserve measurements in association with traditional CAD risk factors such as hypercholesterolemia, hypertension, and smoking as well as with diabetes [15]. The possibility of quantifying epicardial coronary plaque while also assessing microvascular disease during maximal vasodilatation enables coronary MDCTA to characterize macrovascular atherosclerosis as well as microvascular dysfunction secondary to atherosclerosis or other disease processes. The capability of quantifying myocardial blood flow by contrast-enhanced MDCT could represent a "quantum leap" in our ability to assess and characterize the entire process of cardiac atherosclerosis.

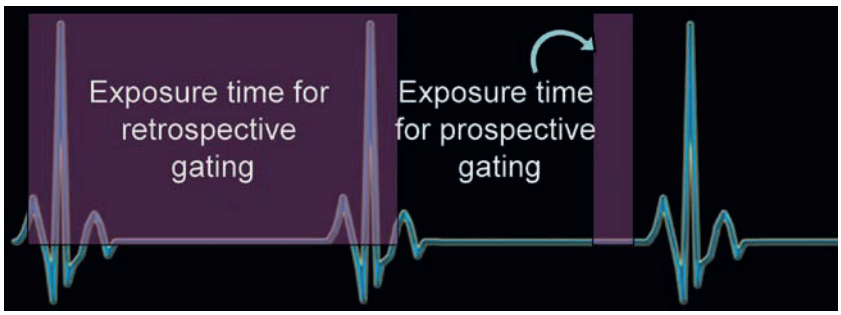

Figure 12.4. Schematic demonstration of the radiation exposure time differences between retrospective gating (single heart beat) and prospective triggering used in wide coverage MDCT scanners.

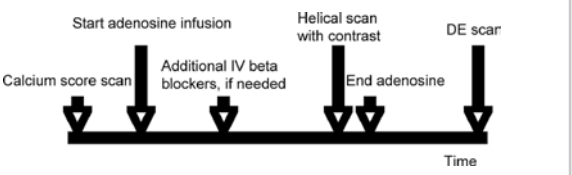

Figure 12.5. Proposed timeline for a comprehensive MDCT scan.

Integrating All Methodologies into One Examination

The number of scans to be performed varies for individual patients, depending on the clinical questions to be answered. For a comprehensive cardiac evaluation, in the future four consecutive scans should be performed, preferably with a wide coverage scanner (256 detectors or more) with acceptable radiation dose. The first one would be a low dose prospectively unenhanced calcium score scan (approximately 1–2 mSv) [16]. The second one would also be prospectively gated and contrasted scan for the acquisition of coronary angiography and morphology (approximately 3–4 mVs) [17]. The third would be a retrospectively gated scan stress perfusion study which could also evaluate LV function during maximum vasodilation (lasting 2–3 RR intervals – approximately 7–9 mSv) [18]. The fourth would be a low dose prospectively triggered delayed enhancement scan 5–10 minutes after the stress study (3–4 mSv) [19]. The final result would be calcium score, coronary anatomy, morphology, function, stress perfusion, and viability in a one stop shop scan that lasts approximately 20 minutes at a cost of about 14 to 19 mSv. Figure 12.5 shows a proposed timeline for a comprehensive cardiac evaluation.

Clinical Pearls: Delayed Enhancement

The optimal contrast dose to be used for DE images is still not defined, but studies in humans [5, 6] showed that the usual amount used for a 16-detector CCTA (120 to 140 ml) provide good enhancement.

For optimal contrast between the infarcted and the remote regions, the delayed enhanced scan should be done between 5–10 minutes after contrast injection [6].

Most of the studies done so far reconstructed the images in end-diastole for DE analysis.

The delayed enhancement pattern is important to differentiate between ischemic and nonischemic etiologies, the earlier being found as a wave front from the endocardium to the pericardium. Nonischemic cardiomyopathies can also result in myocardial scar that appears on DE images, but those tend to be patchy and do not follow the endocardium-to-epicardium pattern seen in ischemic cardiomyopathy [20].

Molecular size of the iodinated contrast material may affect the uptake of the tissue by that agent. Two trials used a smaller molecule with high iodine concentration (iomeprol) [5, 7] while another one used a larger molecule with a lower iodine concentration (iodixanol) [6]. It is still unclear which one is the best, if any, or whether other factors (such as ionic polarization) are important.

DE imaging by MDCT can be obtained both in patients with an acute MI as well as patients that had infarcts more than 6 months prior to imaging [5–7].

Microvascular obstruction can be imaged in the early phase after MI, and it is gradually replaced by fibrous tissue that appears bright on the DE images 2–4 weeks after the MI [21].

Clinical Pearls: Ischemia

Myocardial perfusion by MDCT is work in progress, and most of the published data is experimental.

Adenosine is the drug most often tested for stress perfusion in MDCT, due to its short onset and offset, safety profile, and proved efficacy in diverging blood from ischemic to nonischemic territories.

Since adenosine usually increases heart rate, aggressive beta-blockade should be pursued. Adequate hydration prior to the scan may potentially blunt the reflex increase in heart rate from the adenosine infusion

Nitroglycerin should not be given concomitantly to adenosine, since it can reverse the ischemic effects of the latter,

as well as decrease blood pressure and increase heart rate even further.

The visual contouring of the underperfused myocardial areas is the method currently being applied, but as new dedicated software becomes available, this will probably be done semi-automatically. Also, the best threshold for quantitatively discriminating ischemia from remote myocardium is still not defined.

The problem of balanced ischemia will potentially be solved with wide coverage MDCT scanners by allowing absolute quantification of myocardial blood flow.

Whether stress perfusion scans will be recommended to everyone or just selected patient populations (such as the ones with high calcium scores) is still under investigation.

References

1. Wu KC, Lima JA. Noninvasive imaging of myocardial viability: current techniques and future developments. *Circ Res*. 2003;93:1146–1158.
2. Pagley PR, Beller GA, Watson DD, Gimple LW, Ragosta M. Improved outcome after coronary bypass surgery in patients with ischemic cardiomyopathy and residual myocardial viability. *Circulation*. 1997; 96:793–800.
3. Kim RJ, Wu E, Rafael A, et al. The use of contrast-enhanced magnetic resonance imaging to identify reversible myocardial dysfunction. *N Engl J Med*. 2000;343:1445–1453.
4. Sanz J, Weeks D, Nikolaou K, et al. Detection of healed myocardial infarction with multidetector-row computed tomography and comparison with cardiac magnetic resonance delayed hyperenhancement. *Am J Cardiol*. 2006;98:149–155.
5. Mahnken AH, Koos R, Katoh M, et al. Assessment of myocardial viability in reperfused acute myocardial infarction using 16-slice computed tomography in comparison to magnetic resonance imaging. *J Am Coll Cardiol*. 2005;45:2042–2047.
6. Lardo AC, Cordeiro MA, Silva C, et al. Contrast-enhanced multidetector computed tomography viability imaging after myocardial infarction: characterization of myocyte death, microvascular obstruction, and chronic scar. *Circulation*. 2006;113:394–404.
7. Gerber BL, Belge B, Legros GJ, et al. Characterization of acute and chronic myocardial infarcts by multidetector computed tomography: comparison with contrast-enhanced magnetic resonance. *Circulation*. 2006;113:823–833.
8. Lerman LO, Siripornpitak S, Maffei NL, Sheedy PF II, Ritman EL. Measurement of in vivo myocardial microcirculatory function with electron beam CT. *J Comput Assist Tomogr*. 1999;23:390–398.
9. George RT, Jerosch-Herold M, Silva C, et al. Quantification of myocardial perfusion using dynamic 64-detector computed tomography. *Invest Radiol*. 2007;42:815–822.
10. George RT, Resar J, Silva C, et al. Combined computed tomography coronary angiography and perfusion imaging accurately detects the physiological significance of coronary stenoses in patients with chest pain. AHA Scientific Sessions 2006; Abstract 3264.
11. Smith SC Jr, Feldman TE, Hirshfeld JW Jr, et al. American College of Cardiology/American Heart Association Task Force on Practice Guidelines, ACC/AHA/SCAI Writing Committee to Update 2001 Guidelines for Percutaneous Coronary Intervention. ACC/AHA/SCAI 2005 guideline update for percutaneous coronary intervention: a report of the American College of Cardiology/American Heart Association Task Force on Practice Guidelines (ACC/AHA/SCAI Writing Committee to Update 2001 Guidelines for Percutaneous Coronary Intervention). *Circulation*. 2006;113:e166–e286.
12. Rodes-Cabau J, Candell-Riera J, Angel J, et al. Relation of myocardial perfusion defects and nonsignificant coronary lesions by angiography with insights from intravascular ultrasound and coronary pressure measurements. *Am J Cardiol*. 2005;96:1621–1626.
13. Ragosta M, Bishop AH, Lipson LC, et al. Comparison between angiography and fractional flow reserve versus single-photon emission computed tomographic myocardial perfusion imaging for determining lesion significance in patients with multivessel coronary disease. *Am J Cardiol*. 2007;99:896–902.
14. Schuijf JD, Wijns W, Jukema JW, et al. Relationship between noninvasive coronary angiography with multi-slice computed tomography and myocardial perfusion imaging. *J Am Coll Cardiol*. 2006;48: 2508–2514.
15. Buchthal SD, den Hollander JA, Merz CN, et al. Abnormal myocardial phosphorus-31 nuclear magnetic resonance spectroscopy in women with chest pain but normal coronary angiograms. *N Engl J Med*. 2000;342:829–835.
16. Detrano R, Guerci AD, Carr JJ, et al. Coronary calcium as a predictor of coronary events in four racial or ethnic groups. *N Engl J Med*. 2008;358:1336–1345.
17. George RT, Schuleri KH, Bluemke DA, Hare JM, Lima JA, Lardo AC. Prospectively ECG-gated multidetector computed tomography viability imaging accurately quantifies infarct size while lowering the radiation dose by an order of magnitude. *Circulation*. 2006;114 (supplement): II–818.
18. George R, Arbab-Zadeh A, Miller J, et al. Adenosine stress 64- and 256-row detector computed tomography angiography and perfusion imaging: a pilot study evaluating the transmural extent of perfusion abnormalities to predict atherosclerosis causing myocardial ischemia. *Circ Cardiovasc Imaging*. 2009;2:174–182.
19. Chang HJ, George RT, Schuleri KH, et al. Prospective electrocardiogram-gated delayed enhanced multidetector computed tomography accurately quantifies infarct size and reduces radiation exposure. *JACC Cardiovasc Imaging*. 2009;2:412–420.
20. Gottlieb I, Macedo R, Bluemke DA, Lima JA. Magnetic resonance imaging in the evaluation of non-ischemic cardiomyopathies: current applications and future perspectives. *Heart Fail Rev*. 2006;11: 313–323.
21. Wu KC, Kim RJ, Bluemke DA, et al. Quantification and time course of microvascular obstruction by contrast-enhanced echocardiography and magnetic resonance imaging following acute myocardial infarction and reperfusion. *J Am Coll Cardiol*. 1998;32:1756–1764.

13

Pericardial/Myocardial Disease Processes

Michael D. Shapiro, Ammar Sarwar, and Khurram Nasir

Introduction

While the current primary clinical use of contrast-enhanced cardiac computed tomography (CCT) remains the exclusion of coronary artery disease in low to intermediate risk symptomatic patients, this modality offers a unique opportunity to assess both the pericardium and myocardium. Given the associated contrast and radiation exposure, CCT presently serves as an adjunct to echocardiography and cardiac MRI for this purpose. However, CCT provides superb delineation of the pericardium and can precisely localize lesions as well aid in their characterization. Further, CCT can effectively evaluate morphology and function in various myocardial diseases, including the various cardiomyopathies. The volumetric nature of image acquisition with CCT provides an accurate and reproducible method for quantifying ventricular mass, volumes, and function. This chapter will discuss the application of CCT in the assessment of various myocardial and pericardial disease processes.

CT Imaging of Myocardial Disease

The World Health Organization defines the cardiomyopathies as diseases of myocardial tissue associated with cardiac dysfunction and subdivides them into four categories: dilated, restrictive, hypertrophic, and arrhythmogenic right ventricular cardiomyopathy (ARVC) [1].

Dilated cardiomyopathy is characterized by ventricular enlargement and decreased systolic function. Besides the reconstructed CT data at specific diastolic (and/or systolic) phases of the cardiac cycle for evaluation of the coronary arteries and cardiac morphology, a multiphase data set, which reconstructs the entire cardiac cycle at 5–10% intervals, allows for viewing images in cine mode. This multiphase reconstruction allows for assessment of left and right ventricular systolic function in any orientation, including all of the standard echocardiographic planes [2]. Thus, CCT can assess myocardial thickness, ventricular shape and volume, and global and regional ventricular function with excellent correlation to echocardiography and cardiac MRI [3, 4]. Additionally, patients with severely reduced left ventricular function are at risk for the development of mural thrombus. Given the inherently high contrast to noise ratio and excellent spatial resolution, CCT can readily identify such mural thrombi.

Restrictive cardiomyopathy is characterized by increased ventricular stiffness and associated diastolic dysfunction. Ventricular size and systolic function are usually normal, but the atria and systemic veins (superior and inferior vena cavae, hepatic veins, coronary sinus) are often dilated due to increased filling pressures. These features are easily depicted by CCT but are nonspecific. While CCT is not indicated solely for the evaluation of possible restrictive cardiomyopathy, it is useful in differentiating it from constrictive pericarditis. This distinction leads to important therapeutic consequences.

Hypertrophic cardiomyopathy is a genetic disorder of various sarcomeric proteins resulting in cardiac myocyte disarray and left ventricular hypertrophy with or without obstruction. This most commonly involves asymmetric septal hypertrophy, although other variants exist, including apical and mid-ventricular hypertrophy (Figure 13.1). In patients with dynamic left ventricular outflow obstruction, CCT delineates the systolic anterior motion of the anterior mitral valve leaflet on the multiphase images. While poor acoustic windows may limit echocardiography, CCT can reliably identify all areas of the myocardium and provide accurate measurements of wall thickness.

ARVC is an unusual cardiomyopathy characterized by abnormal right ventricular function, fatty or fibrous deposition of the right ventricular myocardium, and abnormal electrocardiographic changes, which predisposes these patients to sudden cardiac death. CCT has an advantage over echocardiography in its ability to visualize the right ventricle and thus to evaluate right ventricular morphology and systolic function, similar to MRI. However, MRI has superior tissue characterization capabilities and remains

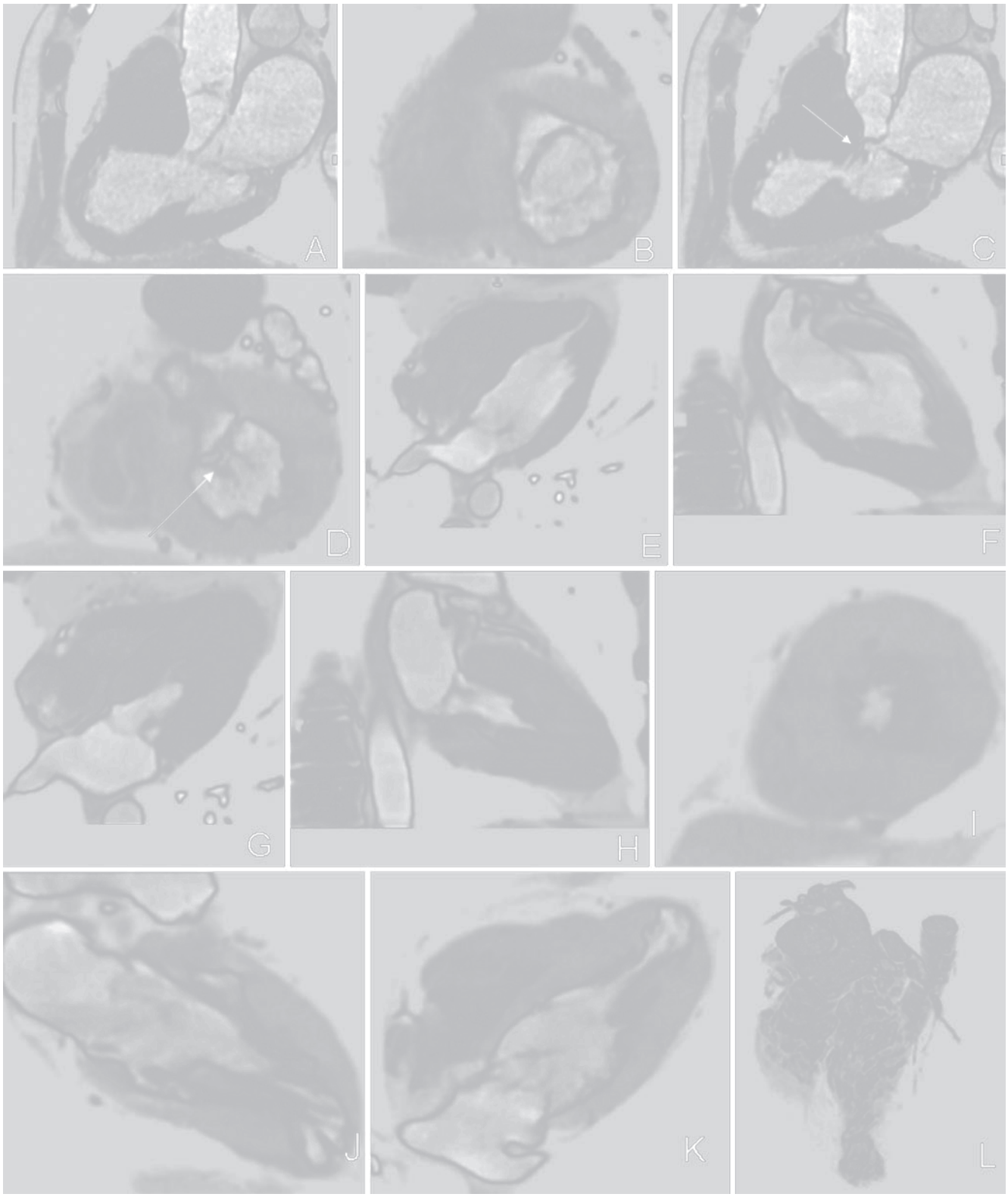

Figure 13.1. The most common form of hypertrophic cardiomyopathy manifests as asymmetric septal hypertrophy with or without obstruction. This three-chamber view in end-diastole (**a**) demonstrates abnormal thickening of the mid-and basal interventricular septum. The short-axis view in end-diastole (**b**) demonstrates normal mitral valve morphology and opening. In systole, the three-chamber view (**c**) demonstrates systolic anterior motion of the anterior mitral valve leaflet (*arrow*) causing a gradient across the left ventricular outflow tract. This is consistent with hypertrophic obstructive cardiomyopathy. The short-axis view in systole (**d**) also demonstrates systolic anterior motion of the mitral valve as well as incomplete coaptation of the leaflets (*arrow*), causing mitral regurgitation. In the apical form of hypertrophic cardiomyopathy, muscle thickening occurs predominantly at the apex of the left ventricle, as can be seen in end-diastolic images in the four-and two-chamber views (**e, f**). The corresponding end-systolic images demonstrate complete obliteration of the left ventricular apex (**g**, **h**). When the left ventricular hypertrophy primarily affects the mid-ventricular level, there can be mid-cavitary obliteration with an associated gradient at the level of obstruction. End-diastolic images in the short-axis (**i**), two-chamber (**j**), and four-chamber (**k**) views, and the 3-D volume-rendered image (**l**) demonstrate prominent thickening at the mid-ventricular level. The corresponding end-systolic images (**m–p**) demonstrate complete obliteration of the mid-cavity.

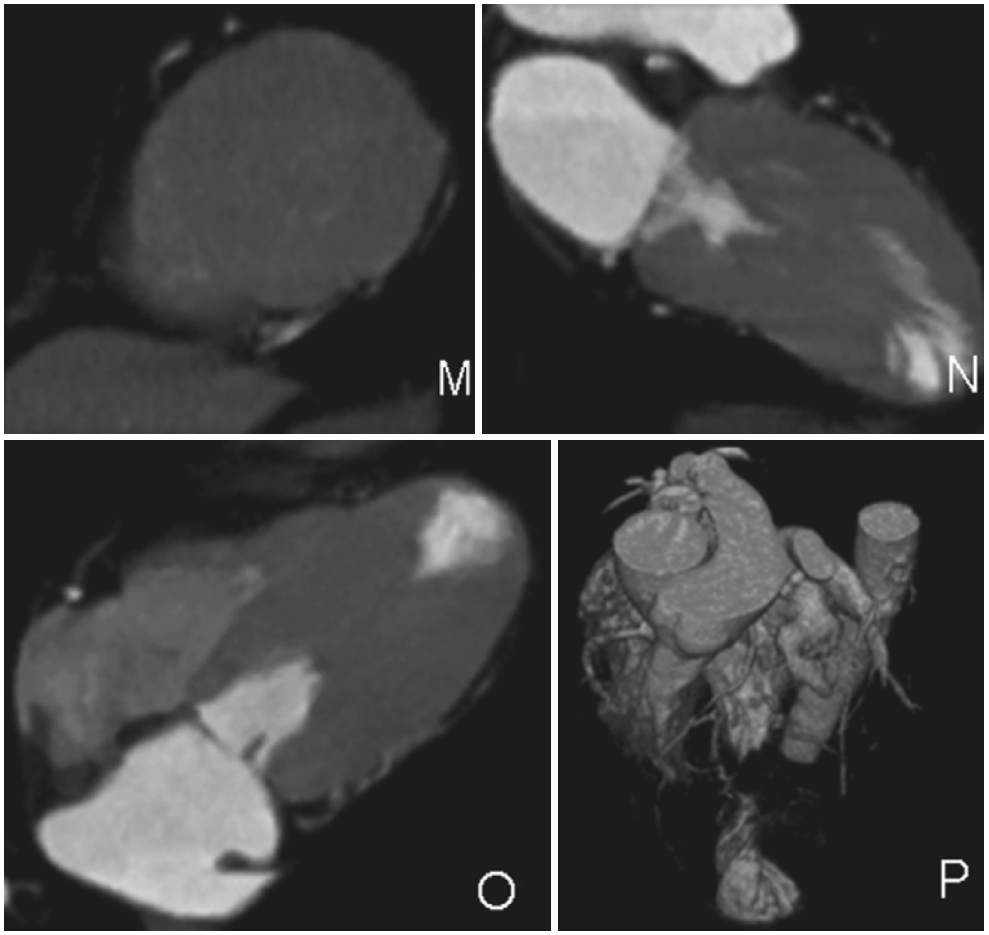

Figure 13.1 (continued)

the modality of choice for evaluating suspected ARVC. CCT becomes the modality of choice when metal objects or claustrophobia preclude MRI. When performing CCT in these patients, it is important to ensure adequate opacification of the right ventricle at the time of image acquisition. This can be achieved by either prolonging the contrast administration by several seconds (4–6 s) or by empirically utilizing a shorter delay time. Alternatively, placing a region of interest in the main pulmonary artery and triggering the scan at its peak opacification can consistently achieve preferential right-sided opacification. CCT can reliably characterize right ventricular dimensions as well as focal aneurysms of the myocardium, increased trabeculations, and/or areas of right ventricular dysfunction, all confirmatory findings in RV dysplasia. Importantly, CCT can also detect fatty infiltration as areas of hypoattenuation, confirmed by CT attenuation measurements. However, the finding of fat is sensitive but not specific for ARVC [5]. Hence, CCT findings must be correlated with clinical and electrocardiographic data to establish the diagnosis of ARVC.

Left ventricular noncompaction is a cardiomyopathy characterized by a 2-layered myocardium: a thin compacted layer and a thick noncompacted layer. The ratio of noncompacted to compacted myocardium has been reported to be 2.3:1 by cardiac MRI [6]. The hypertrabeculations of the noncompacted myocardium, as well as thrombi that may form within the recesses, are easily delineated with CCT due to its favorable contrast-to-noise ratio (Figure 13.2). Left ventricular noncompaction frequently manifests as a dilated cardiomyopathy with reduced left ventricular function, which can also be assessed by CCT. Clinically, noncompaction is associated with both heart failure and sudden death.

CT Imaging of Pericardial Disease

The pericardium is a double-layered membrane measuring <2 mm in thickness that forms a sac containing 10–50 mL of serous pericardial fluid, surrounding the heart and the origins of the great vessels (Figure 13.3) [7]. While echocardiography is conventionally used for the evaluation of pericardial diseases, CCT offers a number of distinct advantages. CCT provides a larger imaging field allowing assessment of concomitant pathology. In addition, CCT offers superior soft tissue contrast, and thus characterization of specific pericardial processes is sometimes possible. CCT is exquisitely sensitive to the detection of calcium and thus can be useful in identifying pericardial calcification, a finding that can be associated with constrictive pericarditis (Figure 13.4). One of the limitations of CCT in evaluating the pericardium, however, is its occasional difficulty in differentiating

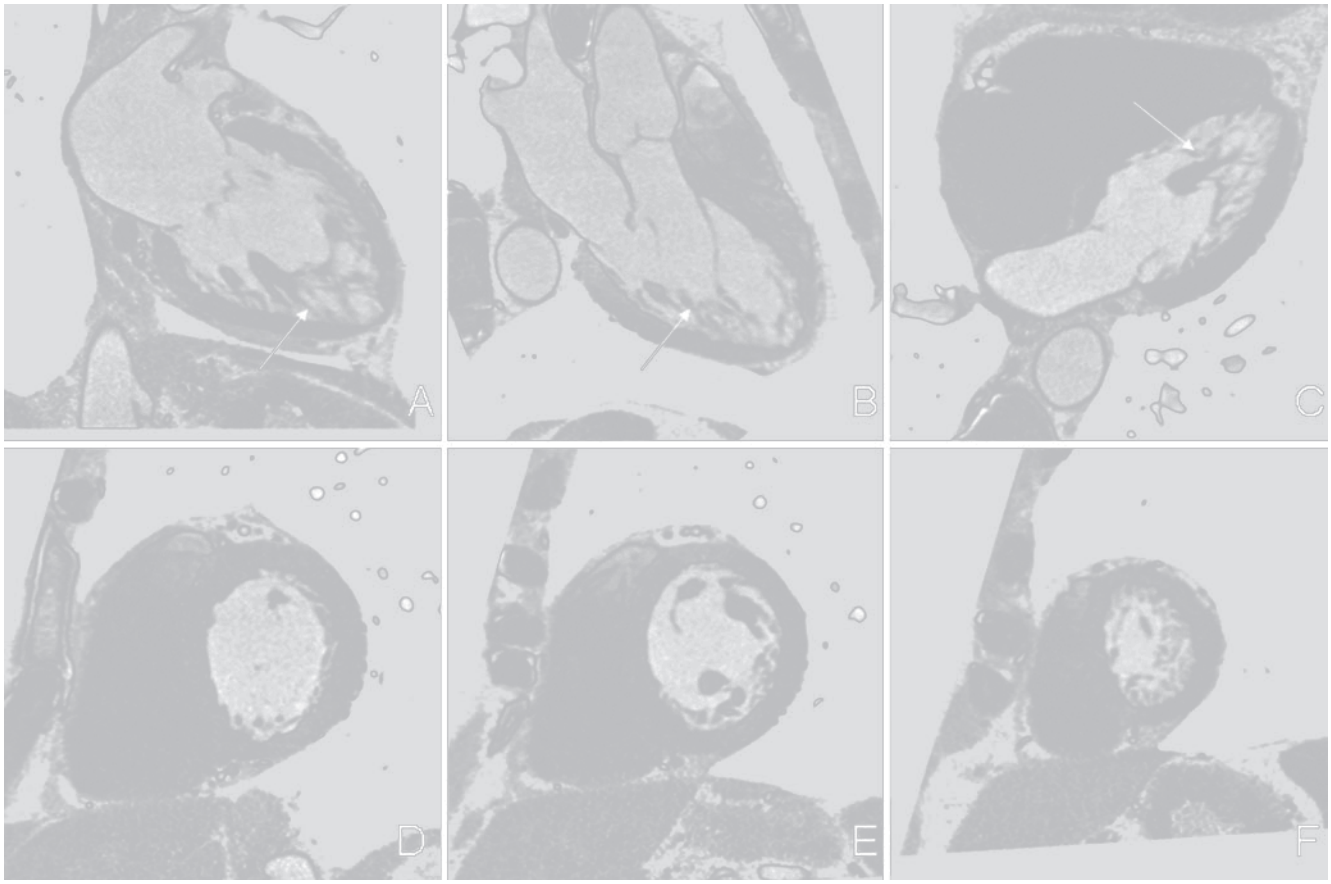

Figure 13.2. The morphological hallmark of left ventricular noncompaction is the presence of hypertrabeculations. These hypertrabeculations are often most prominent toward the left ventricular apex. End-diastolic images in the two-(**a**), three-(**b**), and four-chamber (**c**) views demonstrate these characteristically prominent trabeculations that form the noncompacted layer (*white arrows*). End-diastolic images in the short-axis view at the base (**d**), mid-ventricular (**e**), and apical levels (**f**) again demonstrate these hypertrabeculations, most prominently at the apex.

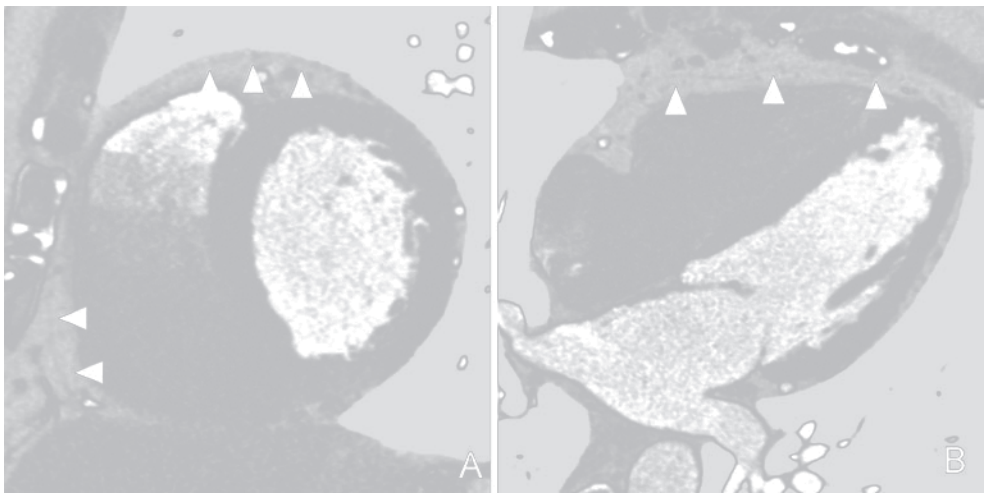

Figure 13.3. Due to its excellent spatial resolution, cardiac CT can image the pericardium, which is normally <2 mm thick. These short-axis (**a**) and four-chamber (**b**) views demonstrate the normal, thin pericardium (*white arrowheads*). The pericardium is often best visualized over the right side of the heart, as the more abundant epicardial fat located there provides good tissue contrast.

pericardial fluid from a thickened pericardium. To evaluate for pericardial inflammation, a noncontrast CT can be performed prior to the contrast-enhanced CT. Enhancement of the pericardium after contrast administration is indicative of pericardial inflammation, and may be seen in cases of pericarditis.

The current reference standard for the noninvasive evaluation of pericardial constriction is cardiac MRI. The characteristic anatomic changes associated with constrictive pericardial disease (elongated and narrow RV, enlargement of the right atrium and inferior cava, and pericardial thickening) are clearly identified with both MRI and CCT.

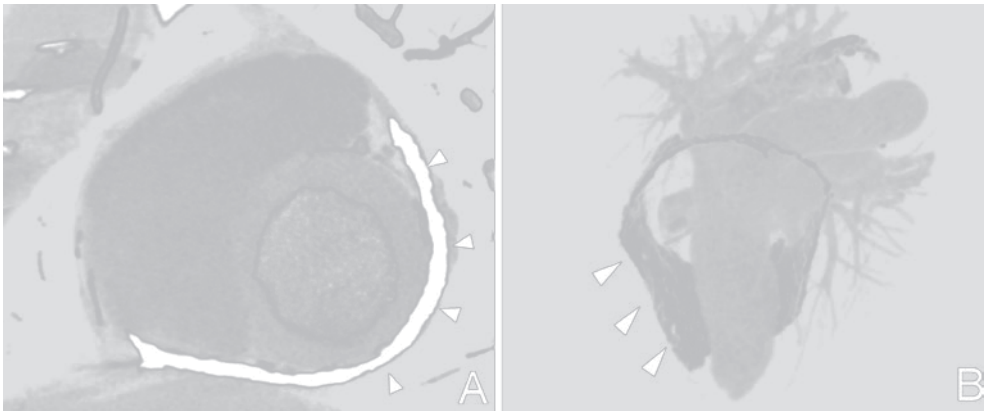

Figure 13.4. Cardiac CT is exquisitely sensitive for the detection of calcium. In this case of pericardial constriction, the patient was found to have a thickened, heavily calcified pericardium (*white arrowheads*) as noted on the short-axis view (**a**) and 3-D volume-rendered image (**b**). The volume-rendered image demonstrates circumferential pericardial calcification at the base.

However, since patients with true constrictive pericarditis typically present with orthopnea, it is often difficult for them to lie flat in the MRI scanner for up to one hour. CCT may offer another option for evaluating constrictive pericarditis, with short examination times representing one of its major advantages. The excellent spatial resolution of CCT allows for accurate measurement of pericardial thickness. A pericardial thickness >4 mm is considered pathological and, in the appropriate clinical context, is suggestive of pericardial constriction [8, 9]. However, it is important to note that neither pericardial calcification nor thickening is diagnostic of constrictive pericarditis. Besides these morphological characteristics, the demonstration of an early diastolic septal bounce on the multiphase cine images is suggestive of pericardial constriction [10].

The normal pericardium is a double-layered membrane that is <2 mm thick. A pericardial thickness >4 mm is considered pathological. Pericardial thickening may be found in the absence of constriction (e.g., acute pericariditis, uremia, collagen vascular diseases). Enhancement of the pericardium, indicative of pericardial inflammation, may be found in cases of pericarditis. Pericardial inflammation can be evaluated by performing CCT with and without contrast. The inflamed pericardium will demonstrate a significant increase in CT attenuation after contrast administration.

Rare individuals demonstrate a congenital absence of the pericardium. While this can present as a complete absence of pericardial tissue, most cases demonstrate only partial pericardial defects, typically on the left side (Figure 13.5a). Clues on CCT that suggest this diagnosis are rotation of the heart to the left, interposition of lung tissue in the aorta-pulmonary window, and bulging of the left atrial appendage through the pericardial defect. Infrequently, the left atrial appendage can be incarcerated in the defect requiring surgical enlargement or closure.

Echocardiography remains the modality of choice for the initial evaluation of pericardial effusion (Figure 13.5b). However, several findings make further evaluation with CCT useful, such as a loculated effusion, hemorrhagic effusion, or equivocal findings on echocardiography. Pericardial effusions may be characterized by CCT by measuring their CT attenuation. A CT attenuation close to water (e.g., 0 HU)

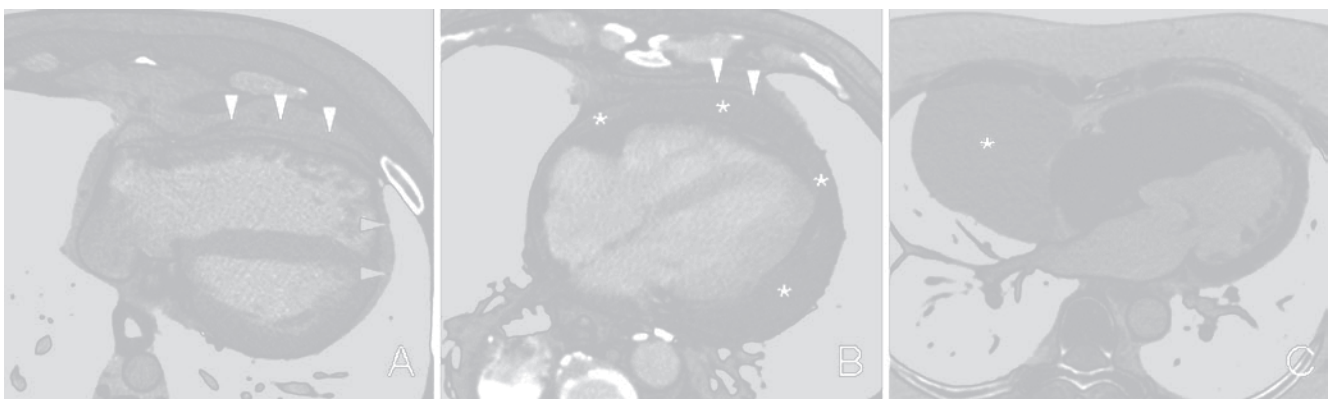

Figure 13.5. Partial absence of the pericardium (**a**). In this example, normal pericardium is found over the right ventricular free wall (*white arrowheads*), but there is absence of the pericardium over the right ventricular apex and left ventricle (*black arrowheads*). Pericardial effusions (*asterisks*) are often found in the context of pericarditis (**b**). In this case, the pericardium also enhanced after administration of iodinated contrast (*white arrowheads*), suggesting pericardial inflammation. Pericardial cysts (*asterisk*) are benign fluid-filled pericardial masses, typically found at the right cardiophrenic angle (**c**).

suggests a simple pericardial effusion. If the CT attenuation is greater than that of water, the effusion may represent hemorrhage, purulence, or a malignant process.

Pericardial masses include cysts and neoplasms. Pericardial cysts are congenital and are usually found at the right costophrenic angle [11].They tend to be smooth-walled simple cysts that do not enhance after contrast administration (Figure 13.5c). With regards to neoplasms, metastases are far more common than primary pericardial tumors. Neighboring structures, such as lung and breast, are most commonly the source of metastatic disease. Other findings associated with metastatic disease include pericardial effusion and an irregularly thickened pericardium [12]. Primary neoplasms of the pericardium occur infrequently and may be benign (fibroma, teratoma, lipoma, hemangioma) or malignant (mesothelioma, lymphoma, sarcoma, and liposarcoma) tumors [13].

Due to the volumetric nature of image acquisition, cardiac CT provides an accurate and reproducible method for assessing both myocardial and pericardial morphology and function. The excellent spatial resolution and contrast to noise ratio of CT allows for the detection of mural thrombi in patients with severely reduced left ventricular function. While echocardiography remains the primary noninvasive imaging modality for evaluation of the myocardium and pericardium, CCT serves as a valuable tool for further evaluation due to its inherently superb spatial resolution and soft tissue contrast. With further improvements in CCT technology, including refinements in temporal resolution and dramatic reductions in radiation exposure, CCT may play a larger role in the evaluation of patients with known or suspected diseases of the myocardium and pericardium.

References

1. Richardson P, McKenna W, Bristow M, et al. Report of the 1995 World Health Organization/International Society and Federation of Cardiology Task Force on the Definition and Classification of cardiomyopathies. *Circulation*. 1996;93:841–2.
2. Cerqueira MD, Weissman NJ, Dilsizian V, et al. Standardized myocardial segmentation and nomenclature for tomographic imaging of the heart: a statement for healthcare professionals from the Cardiac Imaging Committee of the Council on Clinical Cardiology of the American Heart Association. *Circulation*. 2002;105:539–42.
3. Annuar BR, Liew CK, Chin SP, et al. Assessment of global and regional left ventricular function using 64-slice multislice computed tomography and 2D echocardiography: a comparison with cardiac magnetic resonance. *Eur J Radiol*. 2008;65:112–119.
4. Halliburton SS, Petersilka M, Schvartzman PR, Obuchowski N, White RD. Evaluation of left ventricular dysfunction using multiphasic reconstructions of coronary multi-slice computed tomography data in patients with chronic ischemic heart disease: validation against cine magnetic resonance imaging. *Int J Cardiovasc Imaging*. 2003;19:73–83.
5. Tandri H, Bomma C, Calkins H, Bluemke DA. Magnetic resonance and computed tomography imaging of arrhythmogenic right ventricular dysplasia. *J Magn Reson Imaging*. 2004;19:848–58.
6. Petersen SE, Selvanayagam JB, Wiesmann F, et al. Left ventricular non-compaction: insights from cardiovascular magnetic resonance imaging. *J Am Coll Cardiol*. 2005;46:101–5.
7. Roberts WC, Spray TL. Pericardial heart disease: a study of its causes, consequences, and morphologic features. *Cardiovasc Clin*. 1976;7:11–65.
8. Soulen RL, Stark DD, Higgins CB. Magnetic resonance imaging of constrictive pericardial disease. *Amer J Cardiol*. 1985;55:480–4.
9. Spodick DH. Pericardial disease. *JAMA*. 1997;278:704.
10. Himelman RB, Lee E, Schiller NB. Septal bounce, vena cava plethora, and pericardial adhesion: informative two-dimensional echocardiographic signs in the diagnosis of pericardial constriction. *J Am Soc Echocardiogr*. 1998;1:333–50.
11. Oyama N, Oyama N, Komuro K, et al. Computed tomography and magnetic resonance imaging of the pericardium: anatomy and pathology. *Magn R*

14

Computed Tomography Evaluation in Valvular Heart Disease

Javier Sanz, Leticia Fernández-Friera, and Mario J. García

Introduction

Valvular heart disease (VHD) affects 2.5% of US adults and predominantly involves the left-sided cardiac structures. Regurgitant lesions are more common than stenoses, and mitral regurgitation (MR) is the most prevalent abnormality [1]. Doppler echocardiography is the initial imaging modality of choice, allowing for a complete diagnosis in the majority of patients [2]. In cases of poor acoustic window and/or disparate results regarding disease severity, additional tests may be required. Cardiac catheterization is a time-honored modality, but limited by its invasive nature. Magnetic resonance imaging (MRI) has become an excellent noninvasive alternative for both valvular insufficiency and stenosis [3]. Due to the need for radiation and contrast, computed tomography (CT) has a limited role for the evaluation of VHD as the primary indication. It may occasionally be employed as such when echocardiographic results are inconclusive and the patient is not a good candidate for MRI. However, CT is increasingly used for noninvasive coronary angiography, and useful information on valve anatomy and function can simultaneously be obtained from a coronary examination. Also, in patients with primary valve diseases, ruling out obstructive coronary artery disease is deemed a highly appropriate indication and may allow patients to forgo invasive coronary angiography.

General Considerations

A diagram summarizing the potential applications of CT for the evaluation of patients with VHD is shown in (Figure 14.1). Valvular assessment includes the detection of calcification in noncontrast scans and of other aspects of valvular anatomy and cardiac function using contrast enhancement. Quantification of valve calcification follows the same principles as coronary calcium scoring, and the "Agatston," volumetric and mass scores have been proposed. Electron-beam CT (EBCT) has been traditionally the reference standard for coronary calcium quantification, although multidetector CT (MDCT), particularly using scanners with ≥16 slices, has proven comparable in terms of accuracy and reproducibility. Regarding contrast-enhanced CT, detailed evaluation of valvular function and anatomy is possible for both regurgitant and, particularly, stenotic lesions (planimetry of the valve area). Visualization is usually better with MDCT due to its superior spatial resolution and the ability to image all phases of the cardiac cycle with the use of retrospective electrocardiographic (ECG) gating.

CT allows for accurate quantification of ventricular volumes, ejection fraction, and mass [4], all of which carry important prognostic and therapeutic implications in patients with VHD [2]. In isolated regurgitant lesions, the regurgitant volume (and fraction) can be derived from the

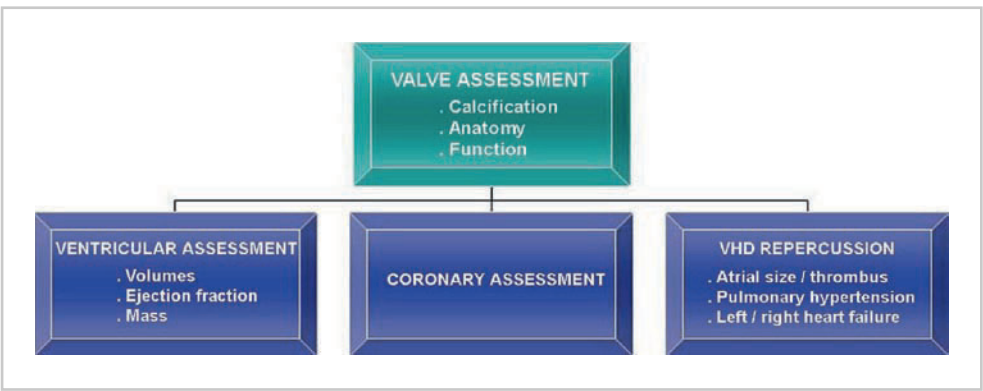

Figure 14.1. Comprehensive evaluation of valvular heart disease (VHD) with CT.

difference between the left and right stroke volumes [5]. Stenosis or regurgitation of the atrioventricular valves usually results in atrial enlargement. Significant regurgitation of any valve eventually causes ipsilateral ventricular dilatation, often accompanied by eccentric hypertrophy. Stenotic lesions of the semilunar (aortic and pulmonary) valves lead to concentric hypertrophy and later may also lead to ventricular dilatation. Poststenotic dilatation of the pulmonary trunk or the ascending aorta may be present as well.

CT can provide important information regarding hemodynamic repercussions of valvular lesions. Enlargement of the right heart chambers can be caused by tricuspid/pulmonary abnormalities or secondary pulmonary hypertension, and typically leads to posterior rotation of the cardiac axis (Figure 14.2). Pulmonary vein dilatation and interstitial and alveolar lung edema are all signs of increased left atrial pressures and left-sided heart failure. Similarly, dilatation of the pulmonary arteries, right heart chambers, superior and inferior vena cava, pleuro-pericardial effusions, and ascitis are suggestive of pulmonary hypertension and/or right ventricular heart failure [6].

CT coronary angiography for preoperative evaluation in VHD is increasingly used, and high accuracy for the detection of significant coronary stenoses has been reported, with slightly lower diagnostic yield in cases of aortic stenosis (AS) due to frequent aortic and coronary calcifications [7–10]. These studies have demonstrated high negative and moderate positive predictive value; thus, patients referred for valvular surgery without significant coronary stenoses by CT may safely avoid the need for invasive angiography [11]. On the other hand, patients with greater than mild degree of luminal stenosis (>50% on CCTA) or extensive calcifications (coronary calcium score >1,000) need to have a confirmatory catheterization. For this reason, it seems prudent to consider CT for this application only in selected patients with low or intermediate pretest probability.

Table 14.1. Imaging protocol

Scanning protocol (for a 256-slice scanner)	
Tube voltage (kV)	100–120
Tube output (mA)	500–800
Detector number	128
Detector collimation (mm)	0.6
ECG gating	Retrospective/prospective
Helical pitch[a]	0.16–0.18
Rotation time (ms)	270–330
Tube current modulation[a]	
(HR ≤ 65)	On
(HR > 65)	Off
Contrast protocol (370 mgI/mL)	
Contrast amount (mL)	80–100
Contrast infusion rate (mL/s)	4–5
Saline amount (mL)	50
Saline infusion rate (mL/s)	4–5
Image reconstruction	
Reconstruction filter	Intermediate
Slice width (mm)	0.6
Increment (mm)	0.3
Matrix	512 × 512
Reconstruction interval[a]	Every 10%
Image analysis: Axial images, MPR, MIP (cine loops and still frames)	

Typical scanning protocol for MDCT coronary angiography employed in our institution (Brilliance *iCT*®, Philips Medical Systems)

ECG electrocardiogram; *HR* heart rate; *MPR* multiplanar reformation; *MIP* maximum intensity projection

[a]If retrospective gating

A typical imaging protocol is summarized in Table 14.1. Contrast infusion is routinely followed by saline, resulting in a more compact bolus and easier evaluation of the right coronary artery; however, it may also impair the visualization of right chambers and valves. This can be overcome by employing a dual- or triple-phase injection protocols [12, 13]. Retrospective ECG gating is advantageous in patients with

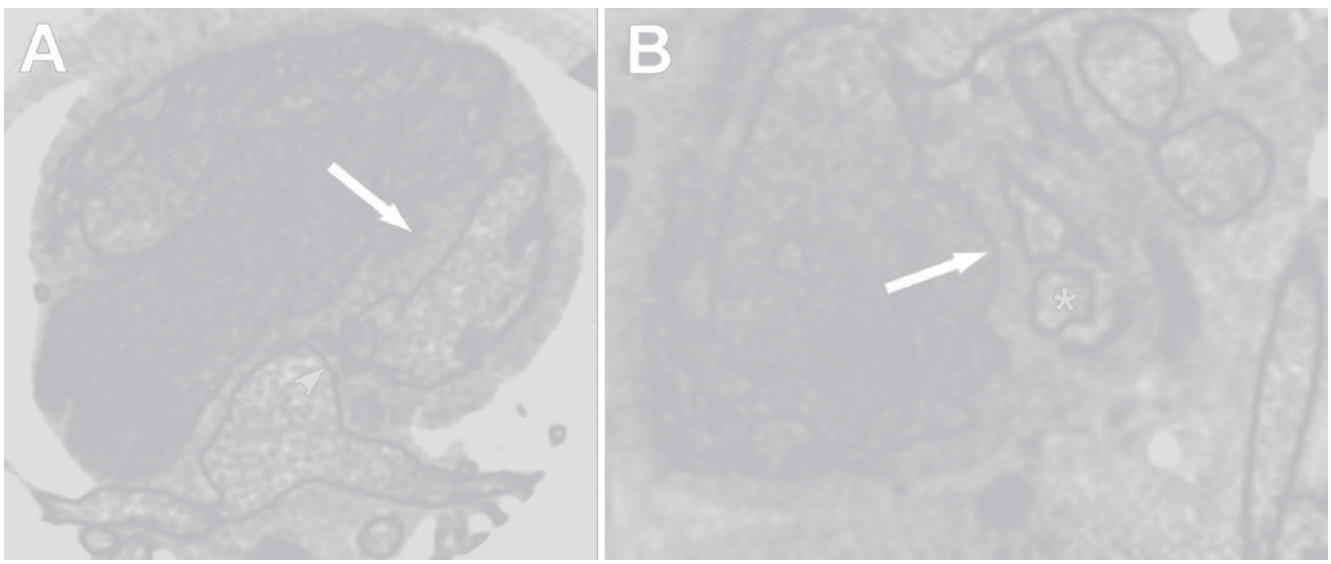

Figure 14.2. Four chamber (**a**) and short-axis (**b**) views of a contrast-enhanced CT scan in a young patient with congenital mitral stenosis ("parachute mitral valve"; *arrowhead* and *asterisk*) and secondary pulmonary hypertension. There is severe right ventricular hypertrophy and enlargement, together with abnormal interventricular septal bowing indicative of right ventricular pressure/volume overload (*arrows*).

VHD at the expense of higher radiation dose. ECG-based tube current modulation can be used, but it may limit the assessment of both ventricles and valves, particularly in obese patients and in the cardiac phases with lower output. If such evaluation is intended, it may be necessary to avoid its use.

Specific Valvular Abnormalities

Aortic Stenosis

Aortic stenosis (AS) is often accompanied by cusp calcification and tends to occur in patients with tri-leaflet valves above 65 years of age or in younger patients with congenital abnormalities (i.e., bicuspid valves). Severe calcification is associated with faster rate of stenosis progression and increased cardiac event rates [14]. Aortic valve calcification can be accurately quantified using CT (Figure 14.3), and interscan reproducibility is >90% [15–17]. The amount of calcification is directly correlated with the severity of AS [17–20], although the relationship is curvilinear (stenosis severity increases more rapidly at lower than higher calcium loads). The incremental value of the information derived from the aortic valve calcium score may be particularly useful in patients with low cardiac output and reduced transvalvular gradients.

Contrast-enhanced CT can precisely evaluate valve morphology, accurately differentiating tri-leaflet from bicuspid valves (Figures 14.4a, b). Planimetric determinations of the aortic valve area (Figure 14.4c) have shown excellent correlation with echocardiographic and invasive measurements [20–27].

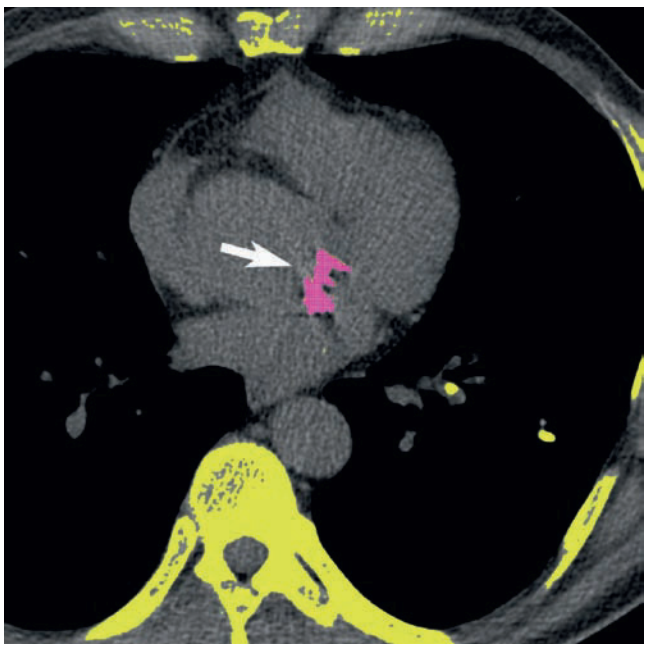

Figure 14.3. Axial, noncontrast CT image in a patient with moderate aortic stenosis, demonstrating the quantification of aortic valve calcium (*arrow*) using the same approach as for coronary calcium scoring. The valvular calcium score ("Agatston") was 2227.

Aortic Regurgitation

CT may be useful in evaluating the mechanism leading to aortic regurgitation (AR). AR caused by degenerative valve disease is characterized by thickened and/or calcified leaflets, and the area of lack of coaptation may be visualized in diastolic phase reconstructions centrally or at the commissures. In cases of AR secondary to enlargement of the aortic root, the regurgitant orifice is typically located centrally (Figure 14.5). Other etiologies that can be depicted include interposition of an intimal flap in cases of dissection, valve distortion or perforation in cases of endocarditis, or leaflet prolapse (observed in dissection and in Marfan syndrome). Regurgitant orifice areas measured by planimetry using MDCT correlate well with echocardiographic parameters of AR severity, such as the vena contracta width and the ratio of regurgitant jet to left ventricular outflow tract height, and allow for the detection of moderate and severe AR with high accuracy [28–30].

Mitral Stenosis

As in the case of aortic valve calcification, the presence of calcium in the mitral annulus is associated with systemic

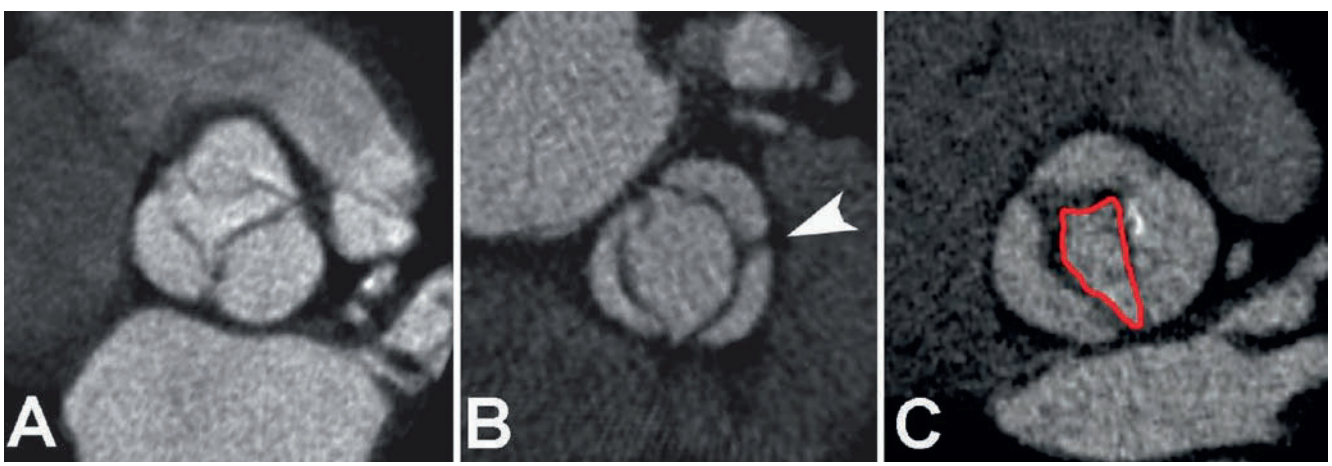

Figure 14.4. Double-oblique systolic reconstructions of contrast-enhanced CT scans showing a tri-leaflet (**a**) and a bicuspid aortic valve (the *arrowhead* indicates the fusion of the right and left coronary sinuses; (**b**) Planimetry of the valve can be performed subsequently (*red contour*, (**c**). The figure shows a bicuspid aortic valve with moderate stenosis (valve area = 1.2 cm^2).

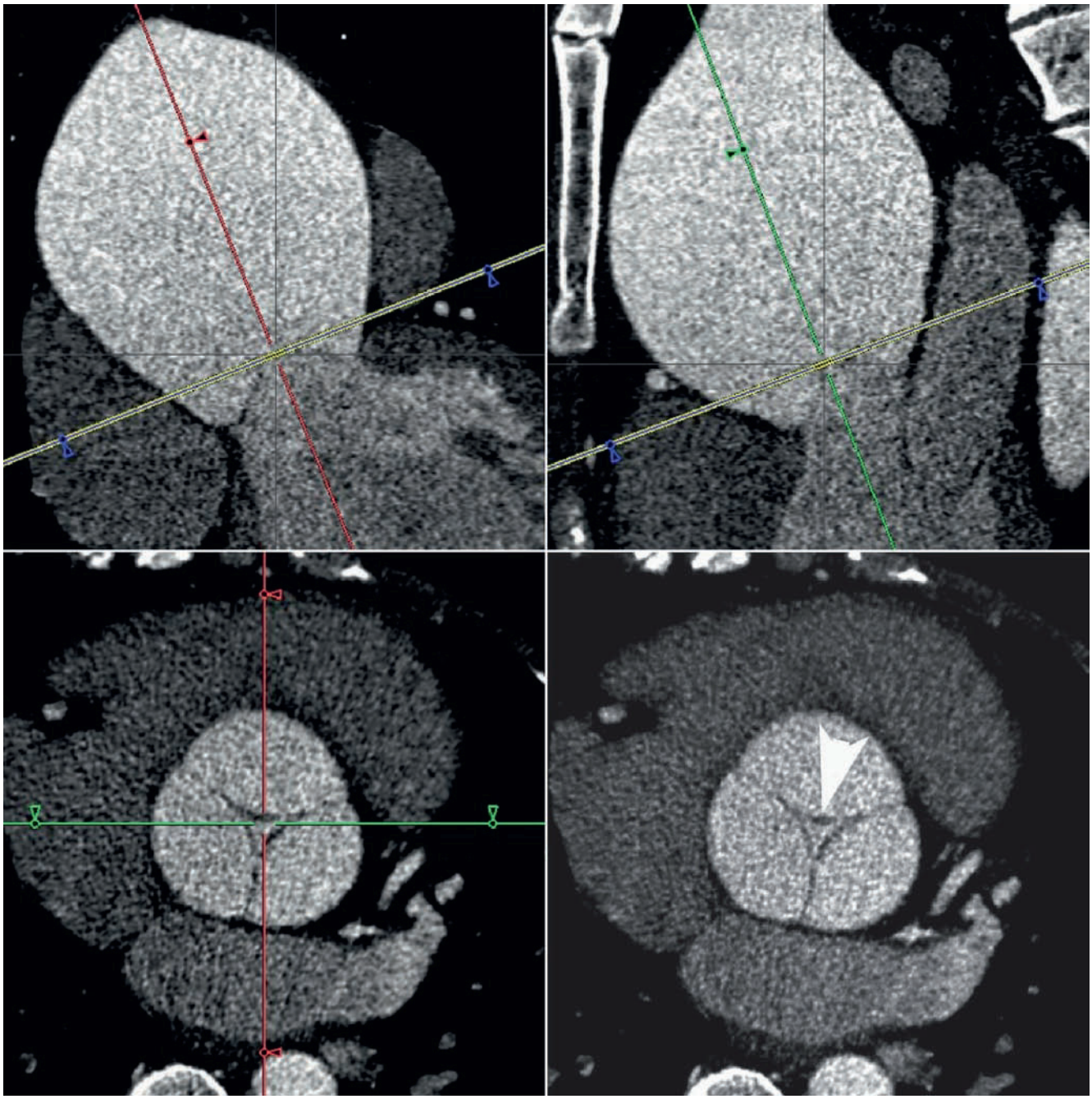

Figure 14.5. Contrast-enhanced MDCT in a patient with an aneurysmal dilated aorta and aortic insufficiency. The valvular plane (*yellow line*) is oriented perpendicular to two orthogonal planes aligned with the ascending aorta (*red* and *green lines*). A large, central area of insufficient leaflet coaptation during diastole (*right lower panel*; *arrowhead*) can be visualized.

atherosclerosis and carries negative prognostic implications. The amount of mitral annular calcium can also be quantified with CT (Figure 14.6), although reproducibility appears to be somewhat lower [15]. In rheumatic mitral stenosis (MS) calcification can extend to the leaflets, commissures, subvalvular apparatus, or even the left atrial wall. MS is often accompanied by marked atrial enlargement involving the appendage. The presence or/absence of thrombus in the left atrial appendage can be determined after contrast administration with very high sensitivity although lower specificity (since slow flow may impair opacification), which may be increased by adding delayed imaging [31, 32]. Planimetry of mitral valve opening by CT provides accurate assessment of MS severity (Figure 14.7) [33].

Mitral Regurgitation

In patients with mitral valve prolapse, CT can demonstrate the presence of leaflet thickening or the degree and location of prolapse (Figure 14.8). In cases of MR secondary to annular enlargement (often accompanying dilated cardiomyopathy), dimensions of the annulus can be accurately quantified, and a central area of insufficient leaflet coaptation may be observed.

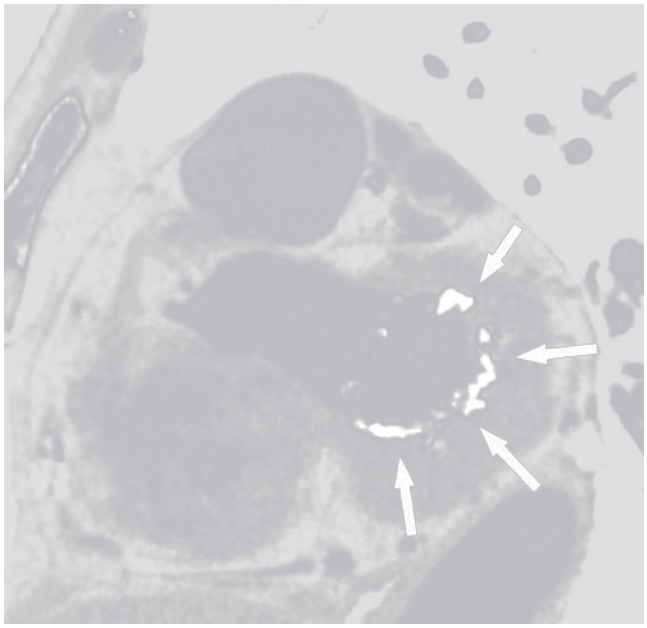

Figure 14.6. Short-axis view at the level of the mitral valve, showing extensive annular calcification (*arrows*).

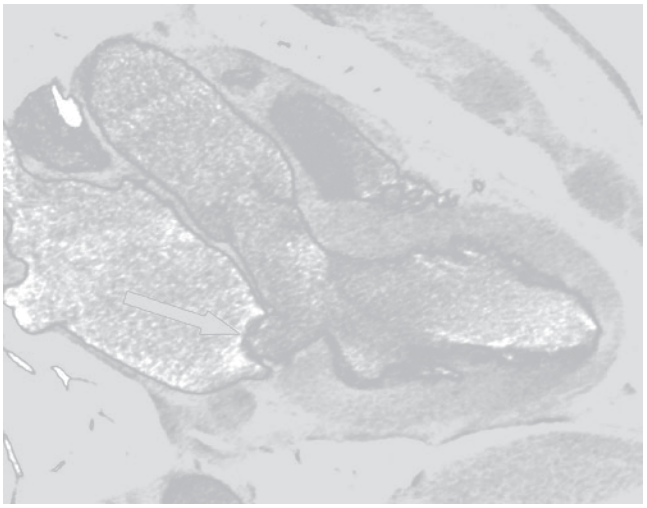

Figure 14.8. End-systolic three-chamber view of the left ventricle demonstrating prolapse of the posterior mitral leaflet (*arrow*).

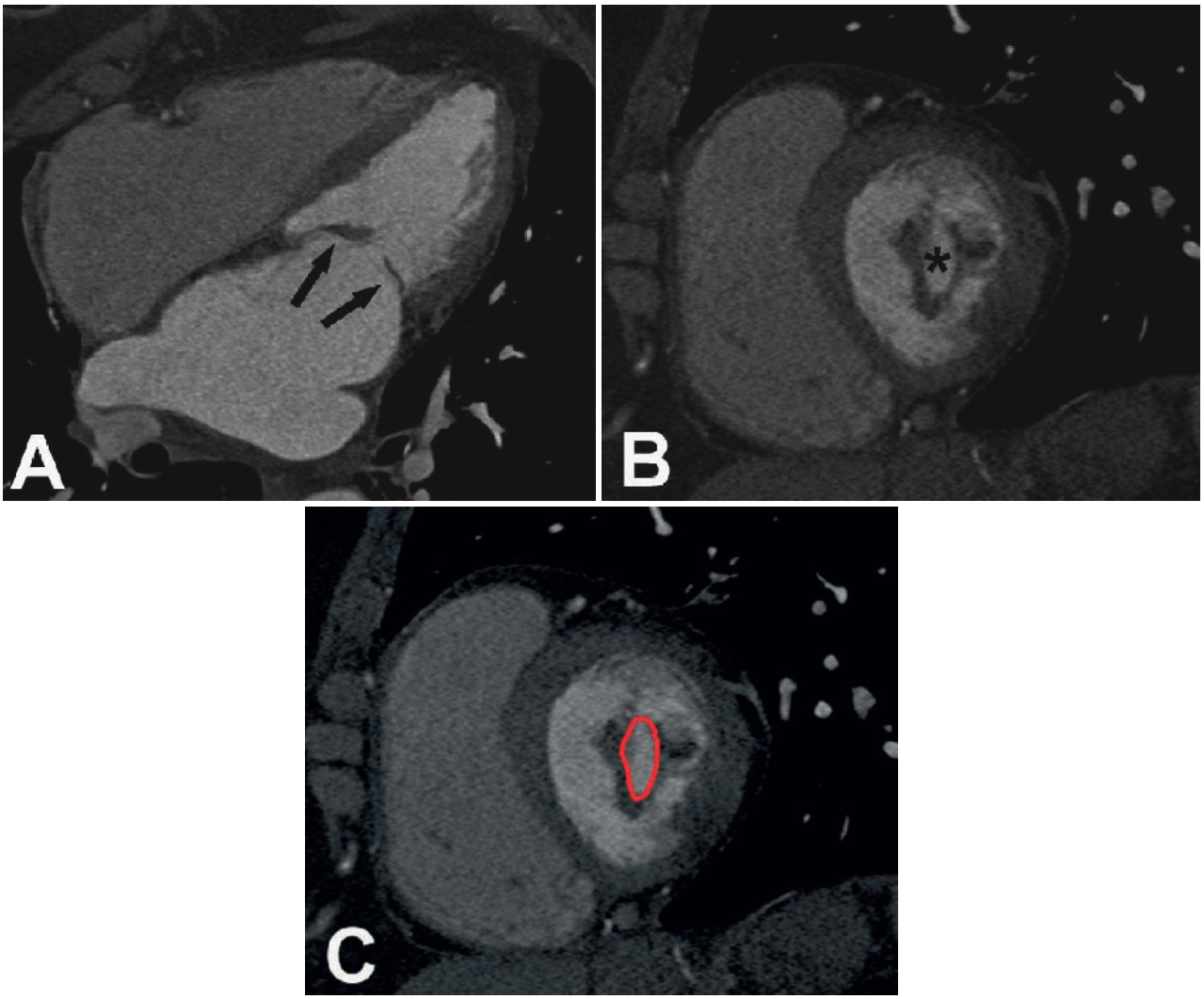

Figure 14.7. Contrast-enhanced CT scan in the four-chamber and short-axis views (**a** and **b**, respectively) from a patient with rheumatic mitral stenosis. The typical thickening and restricted dome-shaped opening of the leaflets can be observed (*arrows* and *asterisk*). Planimetry of the valve (**c**) demonstrated moderate stenosis (*red contour*; area = 1.3 cm^2).

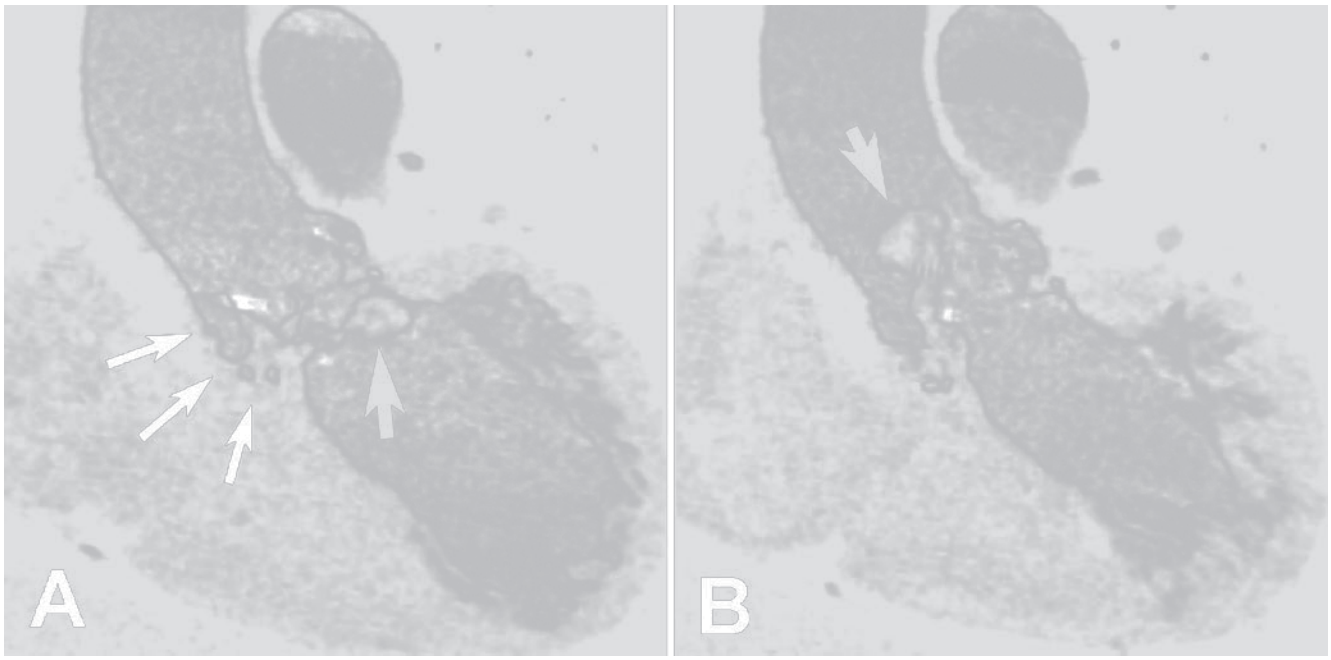

Figure 14.9. Diastolic (**a**) and systolic (**b**) reconstructions of a contrast-enhanced MDCT study in a patient with a bioprosthesis in the aortic position. A large, mobile vegetation that prolapses into the ascending aorta in systole can be noted (*black arrows*). In addition, perivalvular thickening and fluid-filled collections can be noted (*white arrows*) indicating the presence of a perivalular abscess.

Although quantifying MR degree may be difficult, preliminary data suggest that planimetry of the regurgitant orifice by CT correlates well with echocardiographic grading of severity [34]. An alternative approach validated for EBCT includes quantification of cardiac output with the flow mode by the indicator dilution method, and volumetric left ventricular calculations in the cine mode. The regurgitant fraction is obtained from the difference between these two measurements [35].

Infective Endocarditis

The diagnosis of infective endocarditis often relies on the visualization of vegetations, and transthoracic and transesophageal echocardiography are usually superior to CT due to higher temporal resolution. Vegetations are often mobile and tend to be in the atrial aspect in atrioventricular valves and the ventricular aspect in semilunar valves (Figure 14.9). CT can be particularly useful in the demonstration of perivalvular abscesses as fluid-filled collections (Figure 14.9) that may retain contrast in delayed imaging [36]. In a recent study, MDCT correctly identified 26 out of 27 (96%) patients with valvular vegetations and 9 out of 9 (100%) patients with abscesses, which were better characterized by MDCT than with transesophageal echocardiography [37]. In patients with aortic valve endocarditis with highly mobile vegetations, CT may be especially attractive as an alternative to invasive coronary angiography for preoperative evaluation.

Prosthetic Valves

Many of the aforementioned features of native VHD apply also to the evaluation of cardiac bioprostheses. CT is particularly useful for the evaluation of some types of mechanical valves. In prosthesis with two discs, these should open symmetrically (Figure 14.10). In those with a single disc, the angle of opening can also be measured [38]. Finally, heterografts and homografts can be evaluated completely, including the distal anastomosis and the patency of the coronary arteries if these were reimplanted.

Imaging Pearls

Plan ahead; this will allow for imaging protocol optimization if valvular evaluation will be attempted.

If simultaneous assessment of the right heart structures is intended, the contrast protocol should be optimized (Figure 14.11). An initial bolus of 80–100 mL followed by a mixture of contrast and saline (1:1) at 4–5 mL/s will result in adequate coronary evaluation and sufficient right-heart opacification without excessive enhancement. Alternatively, a second infusion of contrast administered at a slower rate (2–3 mL/s) can be employed [12, 13].

Quantification of ventricular end-systolic volumes and the degree of MR and AS requires adequate image quality during systole. It may be necessary to avoid tube current modulation in these cases. Alternatively, the maximal tube output can be timed to end-systole, which will provide adequate depiction of mitral closure and aortic opening, as well as potentially motionless coronary images (particularly at higher heart rates).

If the whole thoracic aorta needs to be imaged (i.e., in cases of aneurysm with associated AR) and the coronary evaluation is not required, using thicker detector collimation will enable reductions in radiation dose and breath-

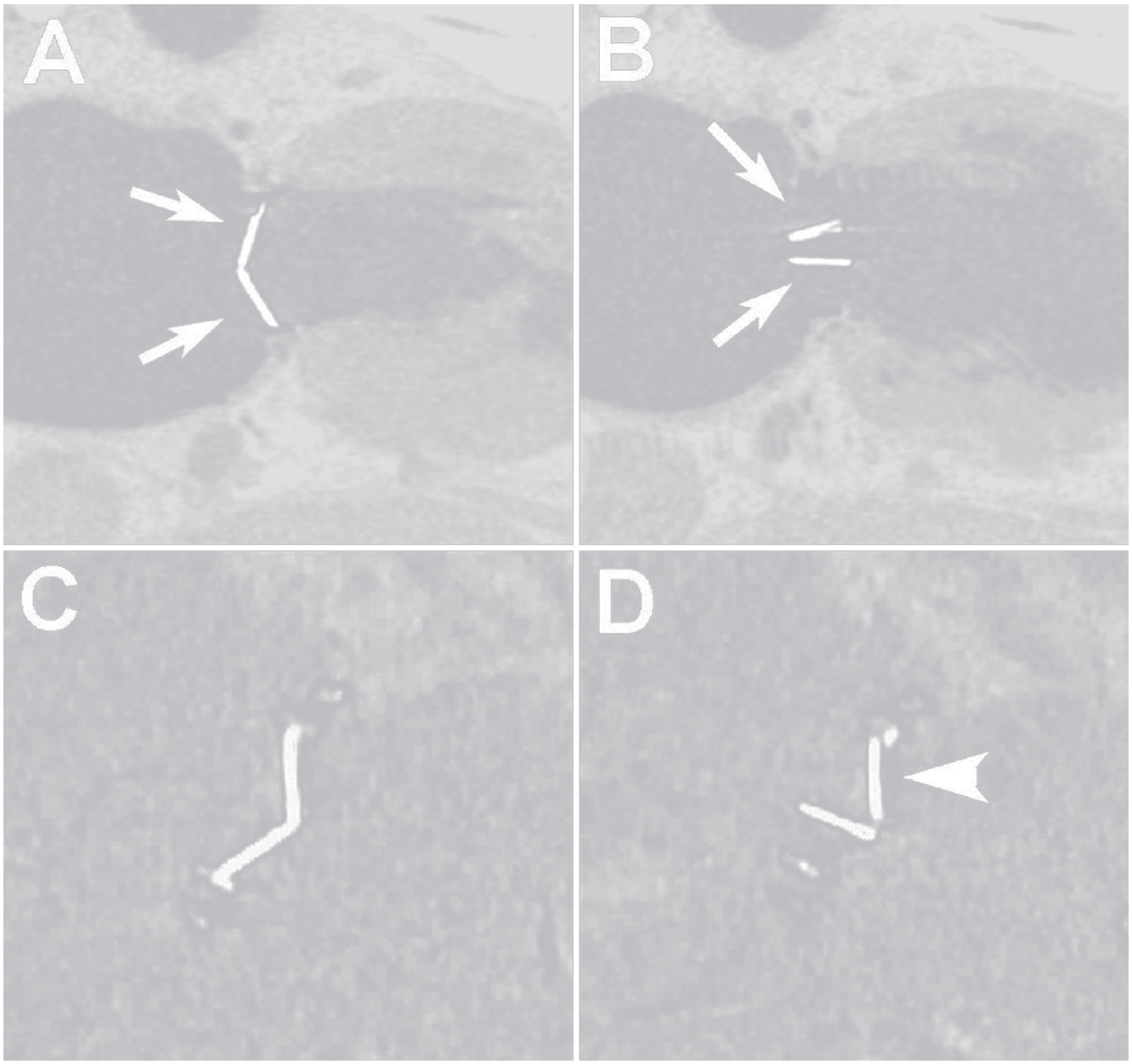

Figure 14.10. Evaluation of mechanical prostheses by CT. The *top row* shows contrast-enhanced images (systole (**a**) diastole (**b**)) of a normal-functioning mechanical prosthesis in the mitral position. The two discs close and open completely and symmetrically (*white arrows*) during the cardiac cycle. Comparable systolic (**c**) and diastolic (**d**) reconstructions of a noncontrast CT evaluation of a dysfunctional mitral prosthesis. One of the discs does not open in diastole (*white arrowhead*). Subsequent surgical intervention demonstrated prosthetic thrombosis.

hold duration. Most patients with VHD can tolerate beta blockers for optimal coronary evaluation. However, caution and smaller doses are recommended in cases with severe degrees of left ventricular dysfunction/dilatation, AS, AR, or pulmonary hypertension.

Atrial fibrillation is common in patients with VHD. It may lead to decrease in image quality and accuracy of valvular and ventricular assessment, although this is typically more significant for evaluation of the coronary arteries.

For the evaluation of ventricular or valvular function with MDCT, reconstructions at every 10% of the RR interval are usually sufficient. In specific cases, a more detailed evaluation of the valve can be obtained by reconstructing images at smaller intervals (i.e., every 5%) in the cardiac phase of interest (for example, during systole for AS) [39]. The combination of cine loops and still frames facilitates the detection of valvular abnormalities.

Variability of the quantification of aortic valve calcium is lowest in mid-diastole [40]. Aortic valvular "Agatston" score ≥1,100 resulted in respective sensitivity and specificity of 93% and 82% for the diagnosis of severe AS [17]. A score >3,700 has a positive predictive value of near 100% [23].

The optimal plane to perform planimetry of the valvular area is parallel to the annulus as determined from two orthogonal double-oblique views perpendicular to the valve plane. The optimal level of that plane is the one showing the smallest area during the phase of maximum valve opening (Figure 14.5).

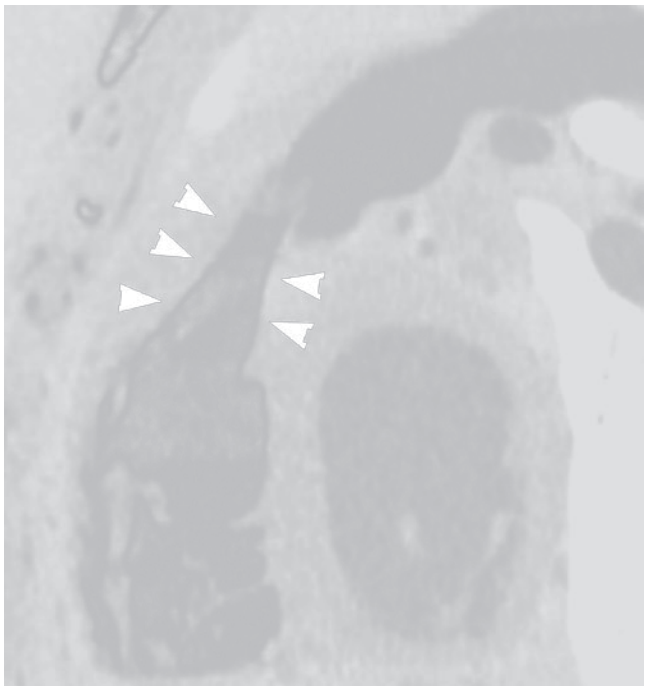

Figure 14.11. Contrast-enhanced CT in a patient with pulmonary infundibula stenosis (*arrowheads*). The contrast protocol was optimized to provide adequate opacification of right heart chambers.

Quantification of the regurgitant volume/fraction from the difference in right and left stroke volumes is only accurate for isolated regurgitant lesions.

A score evaluating leaflet mobility and thickening, subvalvular thickening and calcification, as well as the presence of left atrial thrombus may determine whether MS can be treated percutaneously or surgically. CT can provide useful information of all of these features.

The mitral valve is divided into the anterolateral commissure, posteromedial commissure, anterior leaflet, and posterior leaflet. The leaflets are subdivided into three segments each (A1, A2, and A3; and P1, P2, and P3, from lateral to medial). Determination of which segments are affected and to what degree determines in part the likelihood of successful surgical repair in mitral valve prolapse.

Sharper reconstruction filters and increasing window level of the image display facilitates evaluation of mechanical prosthetic valves (Figure 14.10).

References

1. Nkomo VT, Gardin JM, Skelton TN, Gottdiener JS, Scott CG, Enriquez-Sarano M. Burden of valvular heart diseases: a population-based study. *Lancet*. 2006;368(9540):1005–1011.
2. Bonow RO, Carabello BA, Chatterjee K, et al. 2008 Focused update incorporated into the ACC/AHA 2006 guidelines for the management of patients with valvular heart disease: a report of the American College of Cardiology/American Heart Association Task Force on Practice Guidelines (Writing Committee to Revise the 1998 Guidelines for the Management of Patients With Valvular Heart Disease): endorsed by the Society of Cardiovascular Anesthesiologists, Society for Cardiovascular Angiography and Interventions, and Society of Thoracic Surgeons. *Circulation*. 2008;118(15):e523–e661.
3. Cawley PJ, Maki JH, Otto CM. Cardiovascular magnetic resonance imaging for valvular heart disease: technique and validation. *Circulation*. 2009;119(3):468–478.
4. Orakzai SH, Orakzai RH, Nasir K, Budoff MJ. Assessment of cardiac function using multidetector row computed tomography. *J Comput Assist Tomogr*. 2006;30(4):555–563.
5. Reiter SJ, Rumberger JA, Stanford W, Marcus ML. Quantitative determination of aortic regurgitant volumes in dogs by ultrafast computed tomography. *Circulation*. 1987;76(3):728–735.
6. Boxt LM. CT of valvular heart disease. *Int J Cardiovasc Imaging*. 2005;21(1):105–113.
7. Gilard M, Cornily JC, Pennec PY, et al. Accuracy of multislice computed tomography in the preoperative assessment of coronary disease in patients with aortic valve stenosis. *J Am Coll Cardiol*. 2006;47(10):2020–2024.
8. Meijboom WB, Mollet NR, Van Mieghem CA, et al. Pre-operative computed tomography coronary angiography to detect significant coronary artery disease in patients referred for cardiac valve surgery. *J Am Coll Cardiol*. 2006;48(8):1658–1665.
9. Reant P, Brunot S, Lafitte S, et al. Predictive value of noninvasive coronary angiography with multidetector computed tomography to detect significant coronary stenosis before valve surgery. *Am J Cardiol*. 2006;97(10):1506–1510.
10. Scheffel H, Leschka S, Plass A, et al. Accuracy of 64-slice computed tomography for the preoperative detection of coronary artery disease in patients with chronic aortic regurgitation. *Am J Cardiol*. 2007;100(4):701–706.
11. Russo V, Gostoli V, Lovato L, et al. Clinical value of multidetector CT coronary angiography as a preoperative screening test before non-coronary cardiac surgery. *Heart*. 2007;93(12):1591–1598.
12. Litmanovich D, Zamboni GA, Hauser TH, Lin PJ, Clouse ME, Raptopoulos V. ECG-gated chest CT angiography with 64-MDCT and tri-phasic IV contrast administration regimen in patients with acute non-specific chest pain. *Eur Radiol*. 2008;18(2):308–317.
13. Takakuwa KM, Halpern EJ. Evaluation of a "triple rule-out" coronary CT angiography protocol: use of 64-Section CT in low-to-moderate risk emergency department patients suspected of having acute coronary syndrome. *Radiology*. 2008;248(2):438–446.
14. Rosenhek R, Binder T, Porenta G, et al. Predictors of outcome in severe, asymptomatic aortic stenosis. *N Engl J Med*. 2000;343(9):611–617.
15. Budoff MJ, Takasu J, Katz R, et al. Reproducibility of CT measurements of aortic valve calcification, mitral annulus calcification, and aortic wall calcification in the multi-ethnic study of atherosclerosis. *Acad Radiol*. 2006;13(2):166–172.
16. Koos R, Mahnken AH, Kuhl HP, et al. Quantification of aortic valve calcification using multislice spiral computed tomography: comparison with atomic absorption spectroscopy. *Invest Radiol*. 2006;41(5):485–489.
17. Messika-Zeitoun D, Aubry MC, Detaint D, et al. Evaluation and clinical implications of aortic valve calcification measured by electron-beam computed tomography. *Circulation*. 2004;110(3):356–362.
18. Koos R, Kuhl HP, Muhlenbruch G, Wildberger JE, Gunther RW, Mahnken AH. Prevalence and clinical importance of aortic valve calcification detected incidentally on CT scans: comparison with echocardiography. *Radiology*. 2006;241(1):76–82.
19. Koos R, Mahnken AH, Sinha AM, Wildberger JE, Hoffmann R, Kuhl HP. Aortic valve calcification as a marker for aortic stenosis severity: assessment on 16-MDCT. *AJR Am J Roentgenol*. 2004;183(6):1813–1818.
20. Shavelle DM, Budoff MJ, Buljubasic N, et al. Usefulness of aortic valve calcium scores by electron beam computed tomography as a marker for aortic stenosis. *Am J Cardiol*. 2003;92(3):349–353.
21. Alkadhi H, Wildermuth S, Plass A, et al. Aortic stenosis: comparative evaluation of 16-detector row CT and echocardiography. *Radiology*. 2006;240(1):47–55.
22. Bouvier E, Logeart D, Sablayrolles JL, et al. Diagnosis of aortic valvular stenosis by multislice cardiac computed tomography. *Eur Heart J*. 2006;27(24):3033–3038.
23. Cowell SJ, Newby DE, Burton J, et al. Aortic valve calcification on computed tomography predicts the severity of aortic stenosis. *Clin Radiol*. 2003;58(9):712–716.

24. Feuchtner GM, Dichtl W, Friedrich GJ, et al. Multislice computed tomography for detection of patients with aortic valve stenosis and quantification of severity. *J Am Coll Cardiol*. 2006;47(7):1410–1417.
25. Feuchtner GM, Muller S, Bonatti J, et al. Sixty-four slice CT evaluation of aortic stenosis using planimetry of the aortic valve area. *AJR Am J Roentgenol*. 2007;189(1):197–203.
26. LaBounty TM, Sundaram B, Agarwal P, Armstrong WA, Kazerooni EA, Yamada E. Aortic valve area on 64-MDCT correlates with transesophageal echocardiography in aortic stenosis. *AJR Am J Roentgenol*. 2008;191(6):1652–1658.
27. Lembcke A, Thiele H, Lachnitt A, et al. Precision of forty slice spiral computed tomography for quantifying aortic valve stenosis: comparison with echocardiography and validation against cardiac catheterization. *Invest Radiol*. 2008;43(10):719–728.
28. Alkadhi H, Desbiolles L, Husmann L, et al. Aortic regurgitation: assessment with 64-section CT. *Radiology*. 2007;245(1):111–121.
29. Feuchtner GM, Dichtl W, Muller S, et al. 64-MDCT for diagnosis of aortic regurgitation in patients referred to CT coronary angiography. *AJR Am J Roentgenol*. 2008;191(1):W1–W7.
30. Jassal DS, Shapiro MD, Neilan TG, et al. 64-slice multidetector computed tomography (MDCT) for detection of aortic regurgitation and quantification of severity. *Invest Radiol*. 2007;42(7):507–512.
31. Kim YY, Klein AL, Halliburton SS, et al. Left atrial appendage filling defects identified by multidetector computed tomography in patients undergoing radiofrequency pulmonary vein antral isolation: a comparison with transesophageal echocardiography. *Am Heart J*. 2007;154(6):1199–1205.
32. Hur J, Kim YJ, Lee HJ, et al. Left atrial appendage thrombi in stroke patients: detection with two-phase cardiac CT angiography versus transesophageal echocardiography. *Radiology*. 2009;251(3):683–690.
33. Messika-Zeitoun D, Serfaty JM, Laissy JP, et al. Assessment of the mitral valve area in patients with mitral stenosis by multislice computed tomography. *J Am Coll Cardiol*. 2006;48(2):411–413.
34. Alkadhi H, Wildermuth S, Bettex DA, et al. Mitral regurgitation: quantification with 16-detector row CT–initial experience. *Radiology*. 2006;238(2):454–463.
35. Lembcke A, Borges AC, Dushe S, et al. Assessment of mitral valve regurgitation at electron-beam CT: comparison with Doppler echocardiography. *Radiology*. 2005;236(1):47–55.
36. Gilkeson RC, Markowitz AH, Balgude A, Sachs PB. MDCT evaluation of aortic valvular disease. *AJR Am J Roentgenol*. 2006;186(2):350–360.
37. Feuchtner GM, Stolzmann P, Dichtl W, et al. Multislice computed tomography in infective endocarditis: comparison with transesophageal echocardiography and intraoperative findings. *J Am Coll Cardiol*. 2009;53(5):436–444.
38. Konen E, Goitein O, Feinberg MS, et al. The role of ECG-gated MDCT in the evaluation of aortic and mitral mechanical valves: initial experience. *AJR Am J Roentgenol*. 2008;191(1):26–31.
39. Abbara S, Pena AJ, Maurovich-Horvat P, et al. Feasibility and optimization of aortic valve planimetry with MDCT. *AJR Am J Roentgenol*. 2007;188(2):356–360.
40. Ruhl KM, Das M, Koos R, et al. Variability of aortic valve calcification measurement with multislice spiral computed tomography. *Invest Radiol*. 2006;41(4):370–373.

15

Assessment of Cardiac and Thoracic Masses

Jabi E. Shriki, Patrick M. Colletti, and William D. BoswellJr

Overview

Excellent spatial and contrast resolution make cardiovascular computed tomographic angiography (CCTA) an ideal method for the detection and evaluation of cardiac masses and masses adjacent to the heart. Suspended respiration and cardiac gating techniques employed with CCTA enhance delineation of planes between masses and normal structures. While many cardiac masses are well demonstrated with nongated CT, two approaches to cardiac gating may be applied: prospective ECG triggering and retrospective ECG gating [1]. The ability to freeze cardiac motion enables clearer evaluation of tissue attenuation and enhancement characteristics of normal myocardium and of masses.

Precontrast imaging may help to identify features of masses such as calcifications, which appear as foci of punctuate or coarse hyperattenuation, typically in the range of 130 Hounsfield units (HU), and hemorrhage, which may have a more modest and ill-defined hyperattenuation relative to normal myocardium. Precontrast low attenuation may be helpful for characterizing myxomas or cystic features of masses. Comparison of pre- and postcontrast images is also useful in quantifying the amount of enhancement. Tumor enhancement may occur in a later phase and may not be well-seen in the arterial phase, during which CCTA is usually performed; this is however, dependent on the degree of vascularity within the tumor. However, optimal opacification of the left atrium and left ventricle will allow clear delineation of masses that extend into the chambers of the left heart. The amount of iodinated contrast agent required for satisfactory CT evaluation of cardiac masses depends on patient mass, with 0.5–1.0 g of iodine per kilogram body mass as the usual dose [2]. Using standard low-osmolality contrast agents with concentrations of 300–400 mg iodine/mL, typically 100 mL of contrast agent is administered at 4–5 mL/s via a programmable injector system. This is followed by a bolus flush of 50 mL of normal saline [3].

Timing the CT image acquisition to the contrast agent bolus arrival for most left atrial and left ventricular masses is identical to timing used for coronary artery CT examinations [4]. Optimal left atrial appendage enhancement may, however, be somewhat difficult, since the left atrial appendage may opacify somewhat more slowly or heterogeneously. In addition, there may be considerable variability in circulation time from patient to patient, particularly in patients with cardiac tumors or thrombi. The time between peripheral contrast injection and appearance of contrast in the aorta can be determined using a small volume test contrast agent bolus of 20 mL and rapid, repeated imaging of a single transaortic plane [5]. Alternatively, with bolus tracking, a HU threshold may be set such that the volume acquisition is triggered to begin once a certain HU value is detected in the ascending aorta. A uniform, programmed injection requires 10–25 s for delivery of intravenous contrast agent and up to 50 additional seconds for the saline flush. One potential pitfall in employing automatic bolus detection in cardiac masses is that it is possible to inadvertently place the bolus detection region-of-interest (ROI) within a chamber or a vessel which contains internal thrombus or tumor. Such an error results may result in failure to detect the bolus as shown in (Figure 15.1).

Opacification of the right heart with contrast may be more challenging. Without appropriate acquisition timing for right heart visualization, there may be insufficient contrast for delineation of right atrial and right ventricular endocardial borders. Excessive contrast within the right heart may result in streaking and obscuration of subtle masses. Optimal timing and technique for right heart examination usually differs from that used for routine CCTA. In most patients, optimal right ventricular opacification is achieved by placing the ROI for bolus tracking in the main pulmonary artery. Right ventricular delineation in congenital heart disease with transposition or other abnormal great vessel relationships requires some a priori

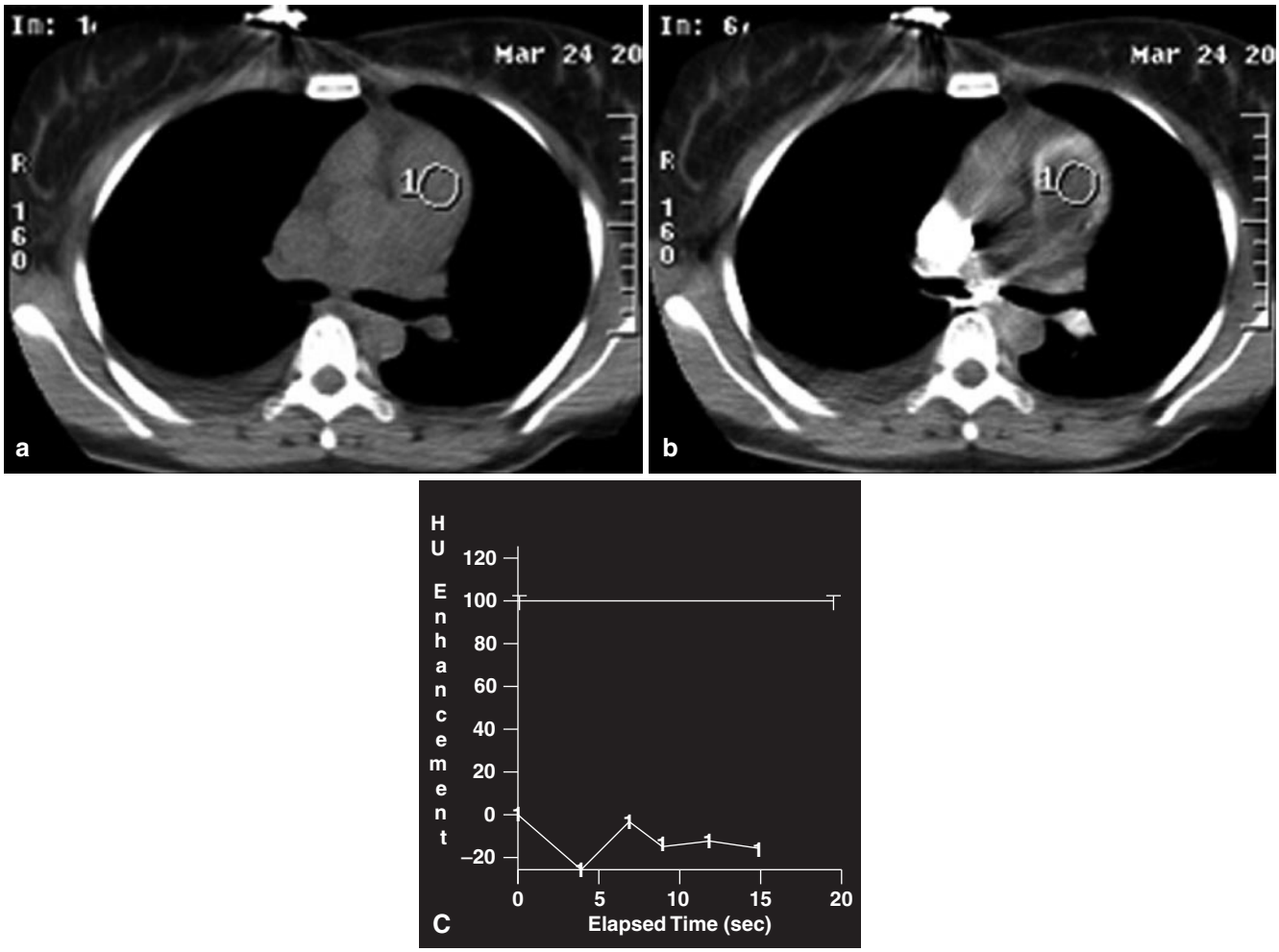

Figure 15.1. (**a**, **b**) Pitfall of automated bolus detection. Automatic bolus detection fails due to tumor replacing the blood pool in the selected region-of-interest (ROI) in the main pulmonary artery. The enhancement curve (**c**) shows that the preset attenuation threshold is not met, due to placement of the ROI in the mass within the pulmonary artery.

knowledge of the anatomy and relevant surgical history to select the correct region for timing prescription. When opacification of multiple chambers is needed, more complex injection protocols can be utilized with multiphasic contrast administration, including injection of mixtures of saline and contrast [6].

One advantage cardiac magnetic resonance imaging (CMR) holds over cardiac CT for cardiac masses is the ability to obtain excellent contrast for both the right ventricle and left ventricle in the same examination due to the ability to image the heart in multiple phases of contrast administration, with no radiation dose. Further investigations are needed to determine how to reliably achieve sufficient contrast in both ventricles with CCTA.

Clinical [7–19] and imaging [20–28] features of cardiac masses are summarized in Tables 15.1–15.4.

Table 15.1. Benign cardiac neoplasms

	Location	Features
Myxoma (40% of all benign tumors) (Figure 15.16)	LA septum 75%; RA 18%; ventricles 7%; multiple 5%	10% calcified; frequent systemic emboli; may protrude through mitral valve during diastole
Fibroelastoma	Arise from valves; project into aorta or MPA	Derived from endocardium; may be multiple; often an incidental finding at surgery
Lipoma	Varies	Encapsulated adipose tissue (fat attenuation); asymptomatic; negative CT density; 25% are multiple; consider tuberous sclerosis; should not be confused with fat in paracardiac folds
Lipomatous hypertrophy	Atrial septum; protrudes into RA	Fat attenuation
Fibroma	Myocardium	Well-delineated, calcified; enhance minimally
Hemangioma	Myocardium	Calcifications; delayed enhancement
Lymphangioma	Myocardium	Diffuse proliferation; minimally enhancing
Paraganglioma, dysembryoma, pheochromocytoma	Paracardiac; AV groove	Sympathetic plexus; hyper-enhancing; correlate with urinary catecholamines; alpha-and beta-blockade for surgery
Teratoma	Pericardial; attach to the aorta or PAroots	Multicystic; frequently calcify; moderate enhancement

Table 15.2. Cystic cardiac masses

	Location	Features
Pleuro-pericardial cyst	75% in right paracardiac angle	Asymptomatic (avascular/calcified); unilocular, sharply marginated, 20–40 HU; may communicate with pericardium; change shape with body position
Echinococcal cysts	Myocardial or pericardial	(Avascular/calcific rim); nearly always also in liver, lung, eyes, brain
Tuberculoma	Myocardial or pericardial	Calcified; constrictive pericarditis
Hematoma	Posterior recesses at the aortic root or left atrium	Acutely hyper-dense; may calcify; traumatic or postsurgical
Thrombosed coronary aneurysm	Course of coronary arteries	Calcified rim; thrombus

Table 15.3. Malignant cardiac tumors

	Location	Features
Metastasis (20×as common as primary tumor) (Figure 15.2)	Pericardial; intravascular; intramyocardial	Seen in 10% of end-stage cancers; lung (36%), breast (7%), esophagus (6%); lymphoma, melanoma, Kaposi's sarcoma, leukemia (20%); modes of dissemination: direct or lymphatic; hematogenous; direct venous extension (pulmonary veins or inferior vena cava)
Lung, breast, melanoma, sarcoma, leukemia, thyroid, kidney	Pericardial; direct or lymphatic; hematogeno us; direct venous extension	Lung cancer may extend to the left atrium along the pulmonary veins
Renal, urothelial, hepatocellular, adrenal, retroperitoneal sarcoma	Extend up the inferior vena cava to the right atrium	Enhancing intravascular mass; primary tumor identified
Lymphoma	Pericardium; myocardium; commonly basal in location	May infiltrate epicardial fat; 50% associated with HIV
Angiosarcoma (Figure 15.1)	Pericardium; RV, RA, myocardium	Angiosarcoma of the pericardium or right ventricle is most common; poor prognosis; distribution is similar to lymphoma
Osteosarcoma	RA, RV	Ossification
Rhabdomyosarcoma, fibrosarcoma	Myocardium	Most common primary cardiac malignancy in infants and children. Always involves the myocardium; pericardial involvement is typically in the form of nodular masses rather than sheet-like spread
Mesothelioma	Pericardium	Intrapericardial mass; effusions;constrictive physiology

Table 15.4. Other cardiac masses

	Location	Features
Endomyocardial fibrosis	Pericardium; myocardium	Thickened pericardium; thickened myocardium with patchy enhancement restrictive and constrictive physiology
Erdheim-Chester disease (nonlangherans fibrosis)	Pericardium; myocardium	Thickened pericardium; thickened myocardium with patchy enhancement restrictive and constrictive physiology
RA thrombus (Figure 15.12)	Right atrium	Associated with indwelling catheters and devices
RV thrombus	Right ventricle	Associated with severe coagulopathy; dilated cardiomyopathy
LA thrombus (Figure 15.11)	Left atrium	Seen in atrial fibrillation and mitral stenosis; attached to posterior or superior atrial wall; may be calcified
LV thrombus (Figure 15.8)	Left ventricle	Common complication of myocardial infarction (20–40% of anterior MIs); contiguous to akinetic myocardium; most common at the apex
Vegetations	Valves; catheters	EKG-triggered cine views of valves helpful

Interpreting Cardiac Masses: Key Descriptors

Location

Lesion location relative to the heart should be noted and may provide a hint as to the nature of a particular mass. Masses related to the heart itself which are cardiac in origin have a unique differential diagnosis. Masses immediately adjacent to the heart and intimately involving the pericardium should be described as pericardial (Figure 15.2). Masses which are external to the heart should be described as paracardial (within the mediastinum, adjacent to the heart). For lesions that are within the mediastinum, a separate set of diagnostic possibilities should be included in the differential. A full discussion of mediastinal masses, however, is beyond the scope of this text. Although some tumors may violate planes and make identification of the organ of origin difficult, in most cases, cardiac masses, pericardial masses, and mediastinal masses can be separated.

Chamber Involvement

The chamber of origin and location within the chamber should be noted. For example a mass in the left atrium attached along the interatrial septum has a higher chance of being an atrial myxoma. A mass in the left atrial appendage has a higher probability of being a thrombus. Some authors have suggested that, on imaging, metastases are more common in the right heart. However, this could be due to the earlier detection of right heart masses, since the wall of the right ventricle is thinner than the wall of the left ventricle. A mass in the left ventricle may be neoplastic, if it

Figure 15.2. Twenty-two-year-old female with a primary pericardial primitive neuroectodermal tumor. Images obtained are obtained as part of a postcontrast nongated CT scan of the chest. Transverse and oblique four-chamber views are shown (**a–d**). In this case, the tumor was causing restriction of cardiac motion, and as a result artifacts due to cardiac motion are mild. There is heavy neoplastic infiltration of the atrioventricular groove with invasion of the right atrium and ventricle (*black arrowheads*).

is felt to be arising from the wall. A mass at the apex of the left ventricle, which appears separate from the wall, has a higher probability of being a thrombus. Attention should be given to associated wall motion abnormalities or aneurysms. Severe metastatic involvement of the myocardial wall may result in a wall motion abnormality. However, a thrombus may present as a mass closely associated with a wall motion abnormality such as dyskinetic aneurysmal segment. Transiently, thrombi with a peripheral origin, such as deep vein thrombi, may be seen in the right atrium and right ventricle (Figure 15.3). A mass which arises from the crista terminalis of the right atrium may be a prominent network of Chiari. Elastofibromas are common lesions which occur along the valve surfaces, but are usually small and not well-seen on CCTA. Valvular vegetations may rarely grow to a size where they may mimic a cardiac mass, although this diagnosis should be considered in some cases where a mass is closely related to a valve. An example of

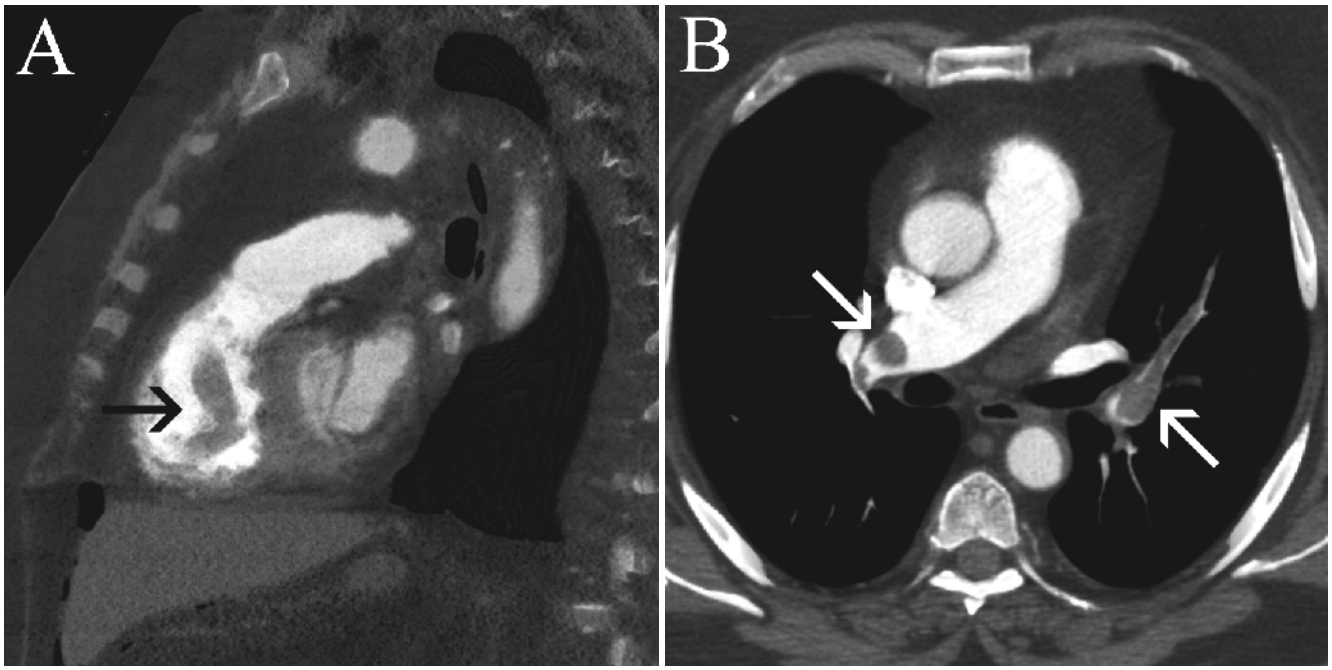

Figure 15.3. Forty-four-year-old female with shortness of breath. The sagittal, minimum intensity projection (MinIP) view shows a vermiform, low-attenuation filling defect (*black arrow*, (**a**)), representing a thrombus in the right ventricle, which had likely migrated from the lower extremities or from the pelvic venous system. MinIP views are useful in demonstrating low attenuation structures, when surrounded by relatively high attenuation. A transverse view on the same study shows multiple, separate pulmonary emboli (*white arrows*, (**b**)).

valvular pathology mimicking a cardiac mass is caseous mitral annular calcification, where an ovoid mass of caseous calcifications develops in close proximity to the mitral annulus as a result of liquefactive necrosis of mitral valvular calcifications (Figure 15.4).

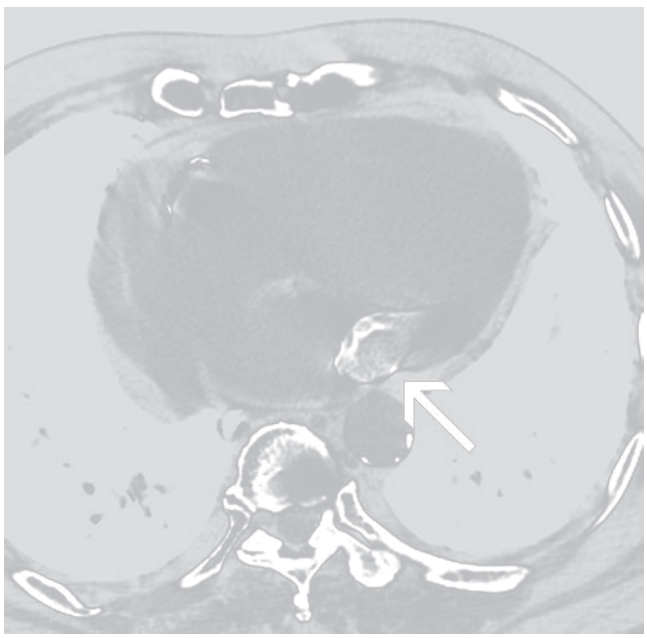

Figure 15.4. Eighty-one-year-old male with caseous mitral annular calcifications. A mass was seen near the region of the mitral annulus on echocardiography. CT was performed for further evaluation. A noncontrast, transverse image shows the classic morphology of caseous mitral annular calcifications, with central homogeneous hyperattenuation representing liquified calcifications and denser, peripheral shell-like calcifications (*white arrow*).

Lesion Morphology

Masses should also be described as intramural (within the myocardial wall) or intracameral (within the cardiac chamber). Metastatic and malignant primary tumors usually have a significant intramural component or a very broad-based attachment to the wall of the myocardium, whereas benign masses are more commonly pedunculated and intracameral, often having a narrow attachment. Although there are exceptions to this rule, this rubric is commonly helpful in identifying pedunculated masses as benign. Thrombi which are adherent to the internal wall of the ventricle are, however, an important exception to this rule. Lesion shape is less helpful as both benign and malignant masses may be lobulated or appear round.

Attenuation

Attenuation can be characterized by HU measurement. Care should be taken to ensure that cardiac gating is adequate as the presence of motion may alter or artifactually elevate measured attenuation. Attenuation values from −100 to −10 HU are generally associated with fatty masses such as intracardiac lipomas or lipomatous hyperplasia of the interatrial septum. Cystic masses will tend to have attenuation values between −10 and 10 HU. Calcifications have an attenuation value of 130 HU or greater. Coarse calcifications may be seen in myxomas, although many other lesions may calcify, including some thrombi and many treated metastases. Attenuation relative to muscle or specifically myocardium is frequently used to describe lesions as hypoattenuating or

hyperattenuating. Frequently, attenuation relative to the blood pool is also described, although it should be noted that patients with anemia may have depressed precontrast attenuation of vascular structures.

Enhancement

Enhancement should be reported with respect to the degree of enhancement and to the phase at which enhancement is seen. Lesions which show no or minimal enhancement are more likely to be benign. This is true of thrombi, which usually show no enhancement. Myxomas usually show minimal or mild postcontrast enhancement. Angiosarcomas, the most common malignant primary neoplasm of the heart, may have very avid enhancement, to the extent that the borders of these masses may be indistinguishable from contrast within the chamber of the heart. Other neoplastic lesions, including metastases, may show more modest enhancement.

Involvement of Other Vascular Structures

Numerous masses may invade the heart from the great vessels. Tumors of the upper abdomen may grow into the right atrium via the inferior vena cava (Figure 15.5). Hepatocellular carcinoma, adrenocortical carcinoma, and renal

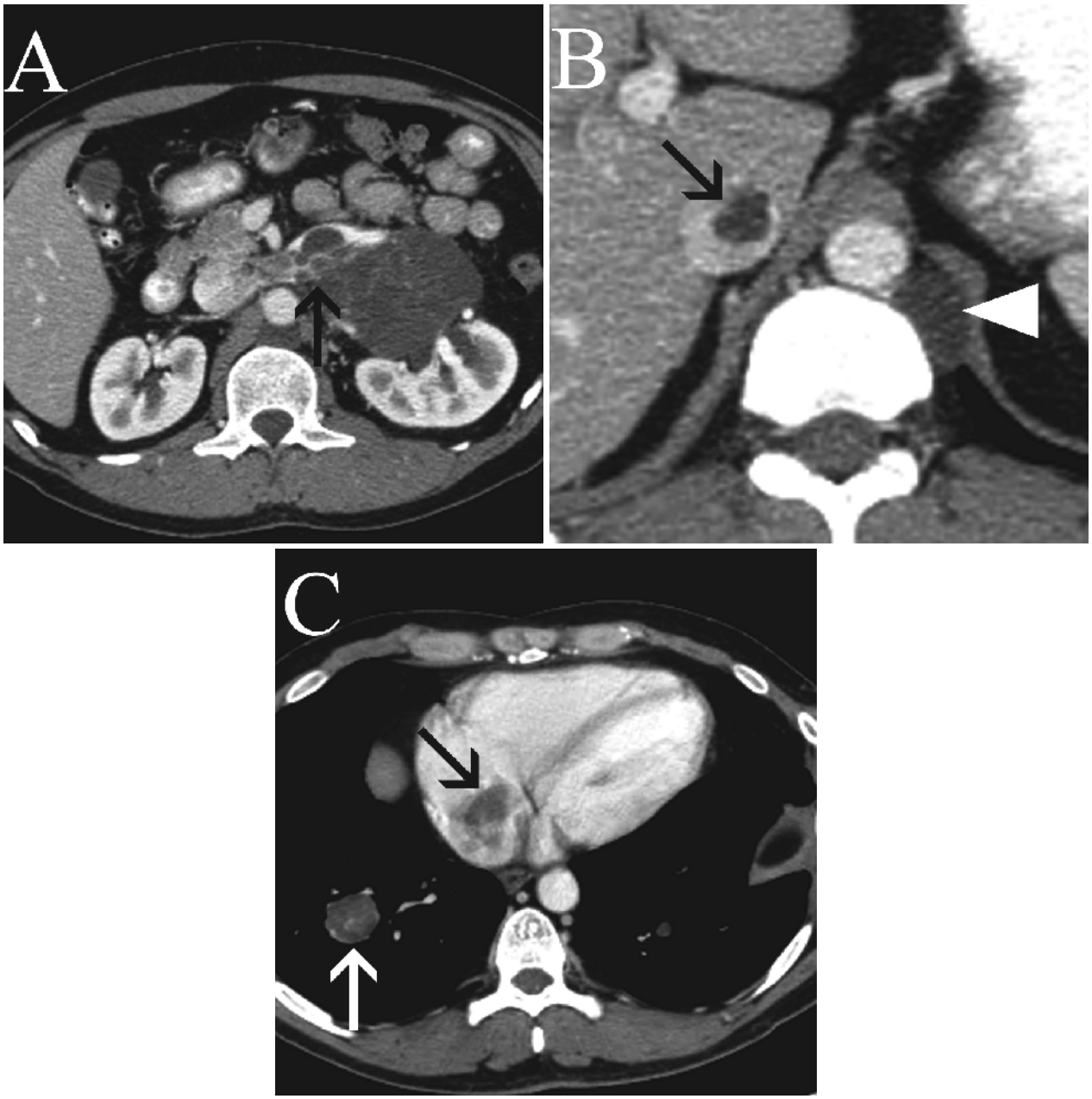

Figure 15.5. Twenty-four-year-old male with retroperitoneal malignant germ cell tumor**.** Postcontrast CT images are obtained of the abdomen in the portal venous phase and are shown from caudal (**a**) to cranial (**c**). There is extensive left periaortic lymphadenopathy, with invasion of tumor into the left renal vein (*black arrow* on (**a**)). There is also extension of tumor into the IVC and right atrium (*black arrows* on **b**, **c**, respectively). Note other sites of metastatic disease including a right lower lobe metastasis (*white arrow*, (**c**)) and a left retrocrural lymph node (*white arrowhead*, (**b**)). This tumor exhibits a common appearance of metastatic disease from germ cell tumor with low internal attenuation.

cell carcinoma are among the most common tumors of the upper abdomen to invade into the right atrium. Bronchogenic carcinomas may invade into the heart through the pulmonary veins and present as a left atrial mass. Mediastinal tumors and bronchogenic carcinomas that involve the mediastinum may also grow into the heart via the superior vena cava. Tumors of the mediastinum may also grow directly into the heart with external myocardial invasion. Thrombi along catheters may also track along venous structures, most commonly the superior vena cava.

Lesion Number

Multiple lesions are more likely to be due to metastatic disease or to multiple thrombi. Metastatic disease typically appears as multiple lesions in the wall in different locations. Multiple thrombi may be encountered as well, especially when masses are located in characteristic locations, such as the left atrial appendage or the left ventricular apex.

Commonly Encountered Masses

Although a complete discussion of all cardiac masses is beyond the scope of this chapter, familiarity with the most common causes of cardiac masses assists in arriving at the correct diagnosis.

Thrombi

Thrombi are the most common cause of intracardiac masses. On precontrast CT, thrombi may either present as hypoattenuating or hyperattenuating masses, relative to blood pool (Figures 15.6 and 15.7). Attenuation relative to blood pool is influenced by the patient's hematocrit, since more anemic patients will have relatively lower attenuation of blood pool. The degree of attenuation within a thrombus may be dependent on thrombus age. Most thrombi will show no enhancement after administration of contrast. However, some chronic thrombi, described as being more organized, have been reported to have some peripheral enhancement after contrast administration [29]. This is most commonly seen in the setting of chronic thrombi adherent to the wall, and has been reported mostly on magnetic resonance imaging (MRI). On CCTA, essentially no contrast enhancement will be shown within thrombi. In the case of small thrombi, HUs may be elevated after administration of contrast when comparison between pre- and postcontrast CCTA is made, although this is more likely related to pseudoenhancement, whereupon beam hardening effects cause false elevation of attenuation values due to adjacent hyperattenuating structures or contrast. On MRI, thrombi are most commonly dark on all sequences. Thrombi can also be recognized by the characteristic locations in which they occur, including at the left ventricular apex and in the left atrial appendage.

Ventricular thrombi can be recognized by their characteristic location, most commonly at the apex of the left ventricle (Figure 15.8). Morphologically, they may either present as one or many ovoid structures within the chamber or may appear pedunculated (Figure 15.9). Many thrombi may also be flat and layered against the endocardial surface of the left ventricular wall. Association with an underlying wall motion abnormality, such as an area of aneurysm formation or an area of infarction, is also an important hint to the correct diagnosis. Ventricular thrombi

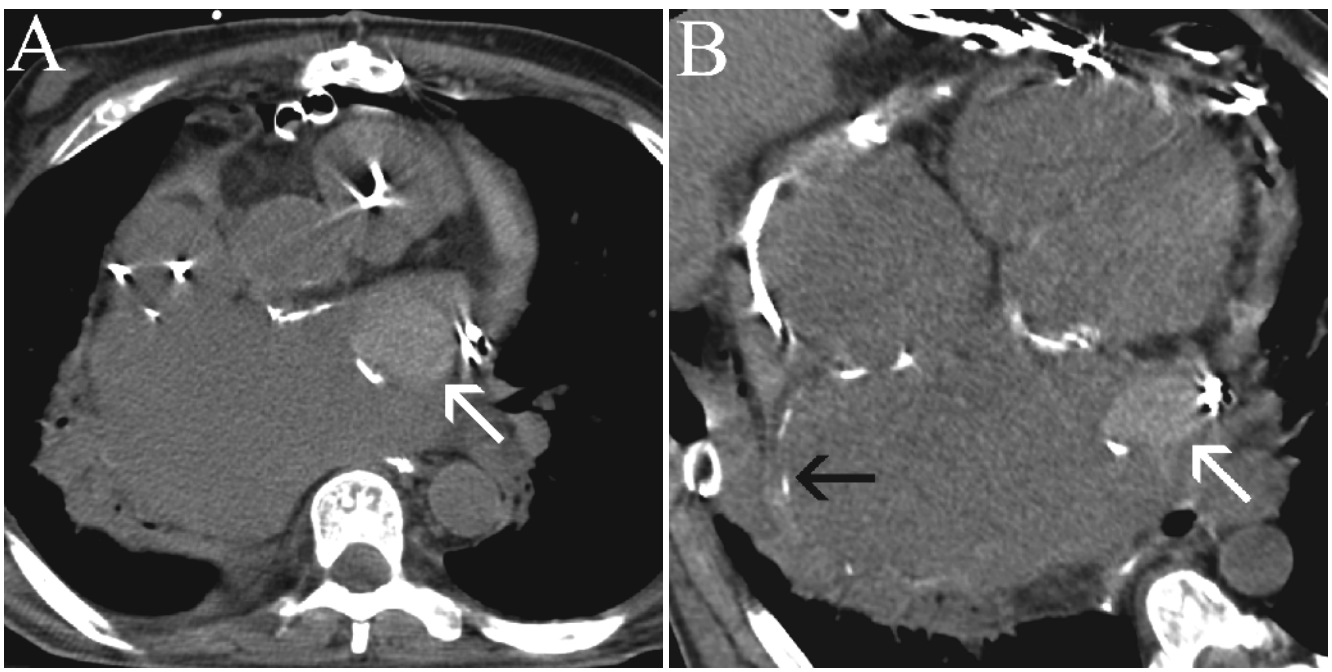

Figure 15.6. Fifty-six-year-old male with rheumatic heart disease and a hyperattenuating left atrial appendage thrombus. Oblique MPR views are shown from a noncontrast scan (**a**, **b**). A focal mass with hyperattenuation is present in the left atrial appendage, which was also seen on echocardiogram (not shown) and was consistent with an atrial thrombus (*white arrows*). Note the presence of atrial wall calcifications (*black arrow*), which are encountered commonly in the setting of rheumatic heart disease. The left atrium massively enlarged and forms the right heart border (**a**).

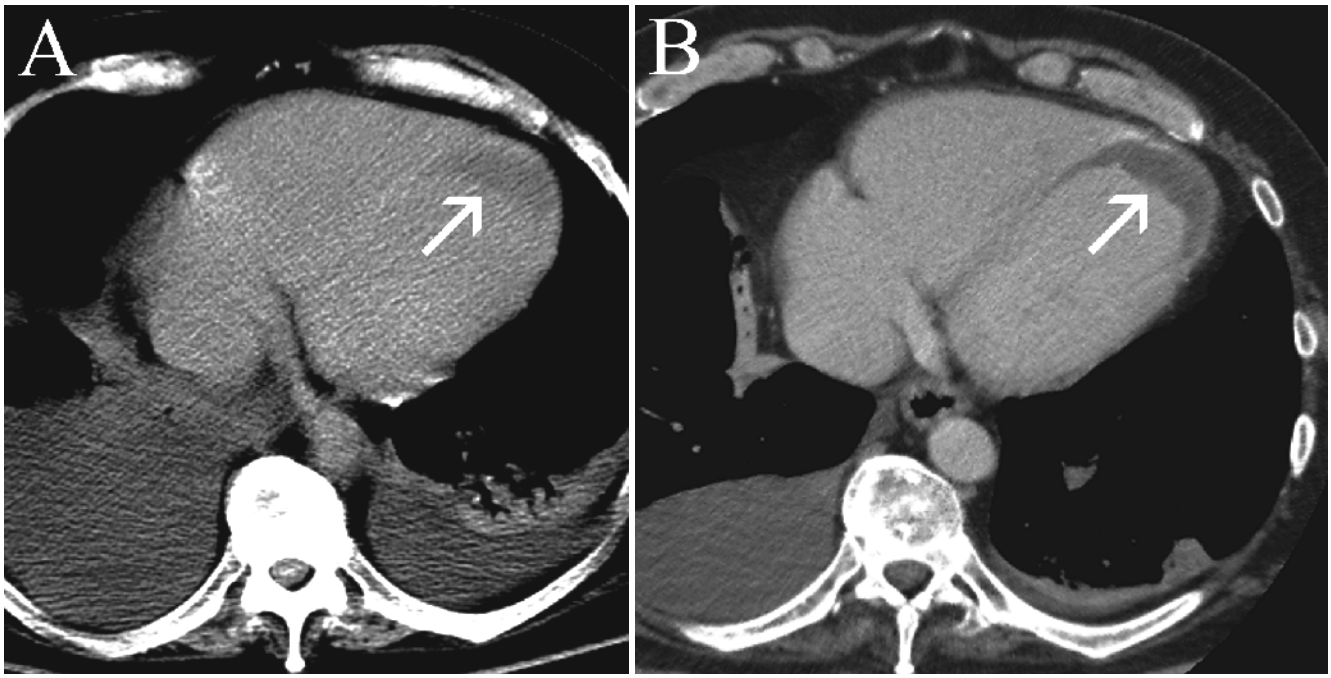

Figure 15.7. Sixty-two-year-old male admitted with a recent myocardial infarction with a hypoattenuating left ventricular thrombus. A transverse, noncontrast view (**a**) obtained to evaluate the extent of pleural effusion demonstrates an area of low attenuation at the left ventricular apex (*white arrow*). A thrombus was suspected. A repeat scan 1 week later obtained with a small amount of intravenous contrast (**b**) demonstrates clear delineation of the large thrombus at the left ventricular apex (*white arrow*).

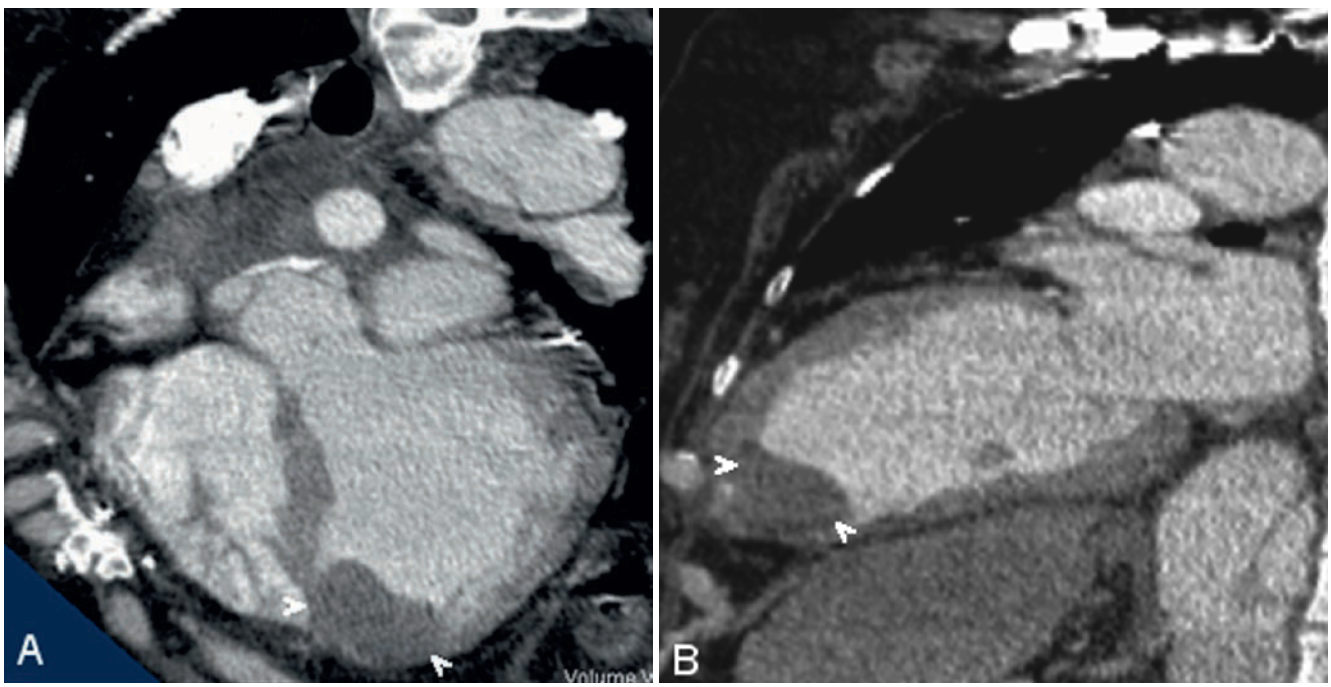

Figure 15.8. Forty-five-year-old woman with a recent myocardial infarction. Four-chamber (**a**) and two-chamber (**b**) views from a cardiac CT show a left ventricular apical aneurysm with thrombus (*white arrowheads*).

have been reported in up to one third of transmural infarctions [30], and are associated much more commonly with apical and anterior infarctions, in comparison to inferior wall infarctions [30, 31]. Visualization of multiple thrombi is not uncommon in the postinfarction setting.

Atrial thrombi can be very problematic to confidently diagnose. Patients at risk for having atrial thrombi commonly have enlarged atria with heterogeneous enhancement as a result of circulatory stasis within the left atrium. This smoke-like enhancement can be especially prominent in the left atrial appendage, and, in patients with severe atrial enlargement, poor opacification of the chamber and appendage may make exclusion of thrombus very difficult (Figure 15.10). As a result, TEE is still considered

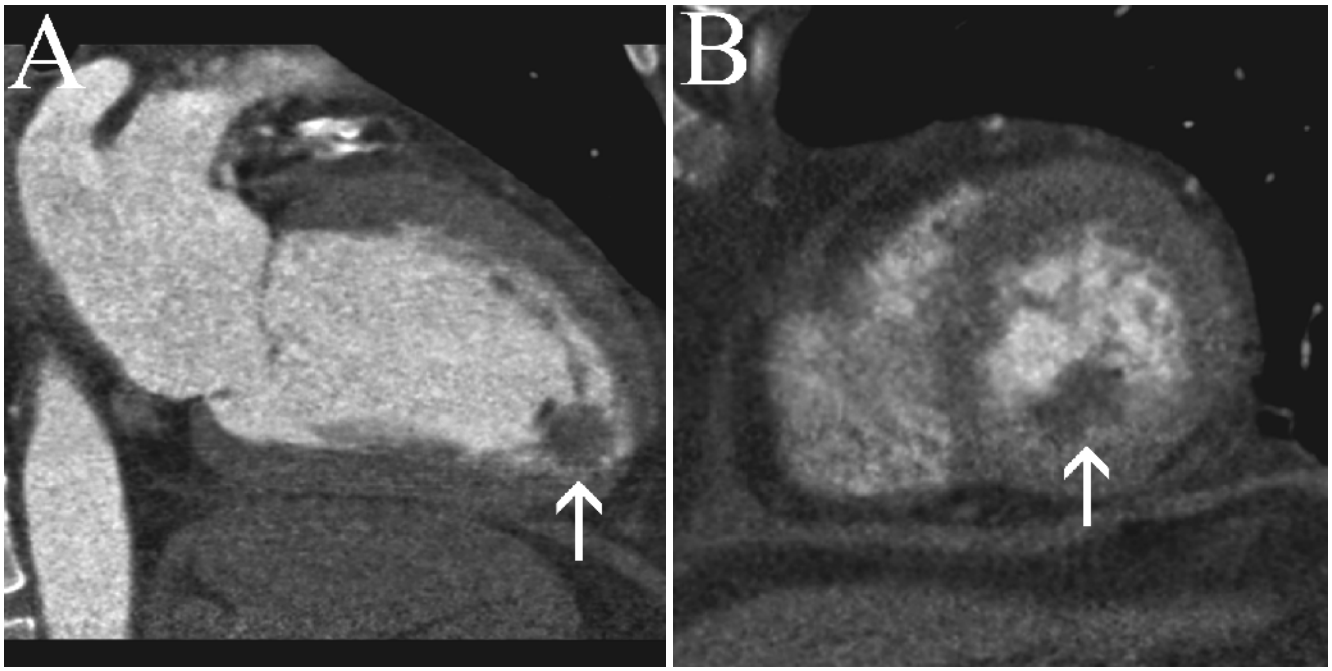

Figure 15.9. Fifty-five-year-old male with a mass at the ventricular apex on transthoracic echocardiogram. Images from a cardiac CT scan obtained in the two-chamber (**a**) and short axis (**b**) planes are shown. A mobile, intracameral, low attenuating, nonenhancing, apical mass is seen consistent with a thrombus. A small area of apical septal late gadolinium enhancement was demonstrated on the patient's CMR (not shown).

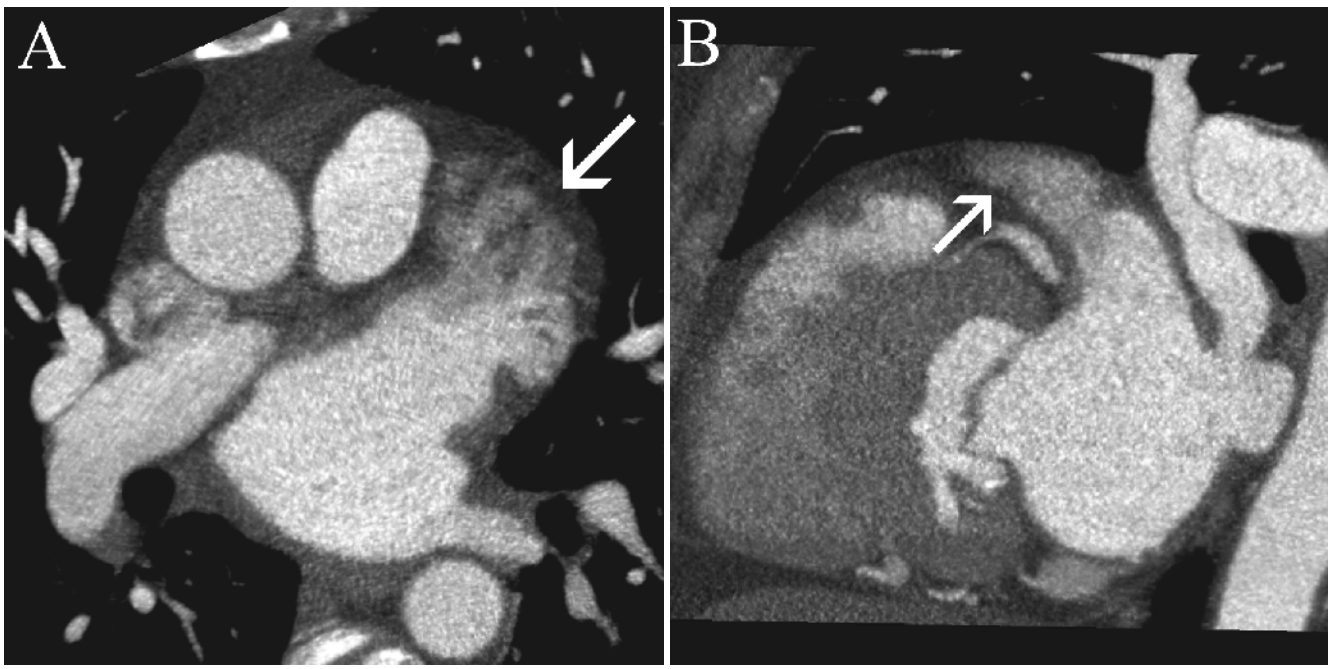

Figure 15.10. Forty-seven-year-old female with atypical chest pain. Orthogonal MPR views of the left atrium from a CCTA (**a**, **b**) demonstrate left atrial enlargement with heterogeneous enhancement of the left atrial appendage. No thrombus was identified on echocardiography. Heterogeneous opacification of the left atrial appendage is a significant pitfall in the identification or exclusion of atrial thrombi on CCTA.

the gold standard for the evaluation of a thrombus in the left atrium or left atrial appendage. Imaging protocols with a delayed phase or with the patient in the prone position have been reported as techniques for improved opacification of the atrial appendage, although these techniques are not yet widely employed [32, 33]. When a nonenhancing filling defect is clearly delineated by contrast, however, a left atrial appendage thrombus can be more easily diagnosed (Figure 15.11). Differentiation from other cardiac masses is usually made on the clinical basis in patients with known atrial enlargement and dysfunction. Right atrial thrombi may form in the atrial appendage, and can be difficult to delineate due to the inherently homogeneous opacification of the normal right heart (Figure 15.12). There are however lower risks of thrombus development in the right atrial appendage, since this structure tends to be flatter and more

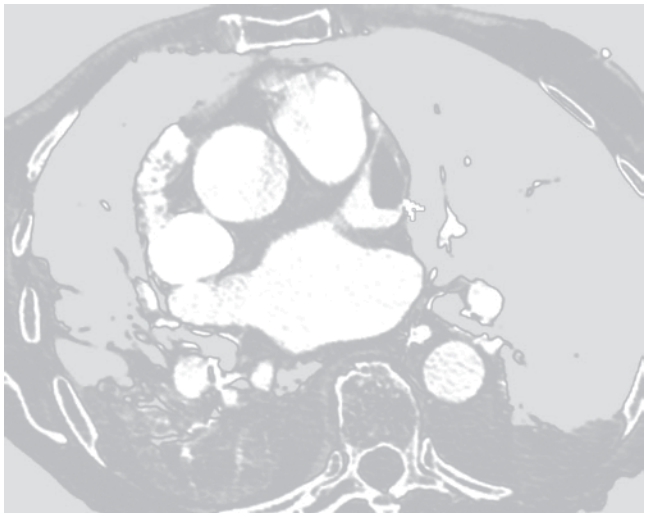

Figure 15.11. Forty-eight-year-old female with left atrial enlargement and atrial fibrillation. On a contrast-enhanced CT scan, a filling defect is clearly identified in the left atrial appendage (*white arrowhead*). When such a defect is clearly delineated by contrast as in this case, thrombus can be more definitively identified.

broad-based, compared to the left atrial appendage, which is a more lobulated or tubular structure and has a neck. These morphologic differences make the left atrial appendage more prone to the development of thrombi compared to the right atrial appendage.

Metastatic Disease

Metastatic lesions are the most common cause of a neoplastic mass in the heart. Metastatic disease has been reported as more common in the right heart, but this may be due to the earlier recognition of metastatic lesions in the right ventricle, since the wall is thinner than that of the left ventricular wall. Most metastatic lesions are isoattenuating to the myocardium on precontrast CT imaging. Contrast enhancement of metastatic lesions is somewhat variable depending on the degree of vascularity of the neoplasm. Most metastases enhance less than the myocardium initially after administration of contrast, but will slowly accumulate and retain contrast. Metastases may also show retention of contrast on late-phase imaging. This pattern of enhancement may be less well-characterized on CT, since multiphasic imaging with CT is uncommonly performed (Figure 15.13). It should also be noted that the optimal phase for CCTA during coronary arterial enhancement is earlier than the optimal phase for demonstrating myocardial wall enhancement. As a result, the differential enhancement between a metastatic lesion and normal myocardium may not be as clearly seen on CCTA (Figure 15.14). The most common morphology of cardiac metastatic disease is an intramural mass or a mass with a broad-based attachment, in contradistinction to benign masses, which tend to be intracameral and have a narrow attachment. Many metastases which invade the heart from the adjacent mediastinal or pericardial spaces may, however, involve the epicardium first, and subsequently invade into the myocardium. Metastatic disease to the heart is found in up to 10% of patients with a primary at the time of autopsy [34]. Although numerous primary tumor sites have been reported to be metastatic to the heart, the lung is the most common site of a primary tumor, occurring in up to 36.7% of patients [35]. Melanoma is, however, an important source of hematogenous disease to the heart from a distant primary site that does not first involve the

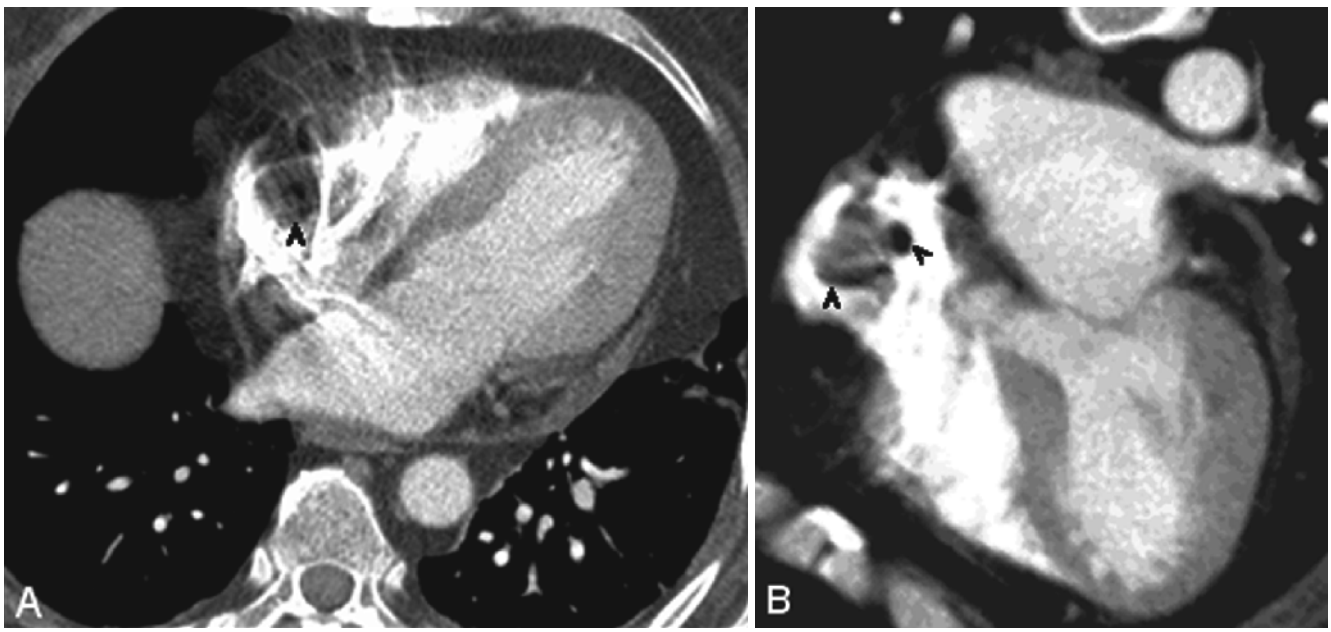

Figure 15.12. Thirty-eight-year-old female with recent resection of gastric carcinoma. Transverse (**a**) and four-chamber (**b**) views are shown from a CT scan of the chest. There is some heterogeneous opacification of the right atrium with some streaking, although the thrombus can be seen through these artifacts (*black arrowheads*). The patient also had a large parenchymal hepatic hematoma, related to her recent surgery, which may have contributed to the development of a right atrial thrombus. CMR (not shown) showed features consistent with a thrombus, and this structure resolved on subsequent studies.

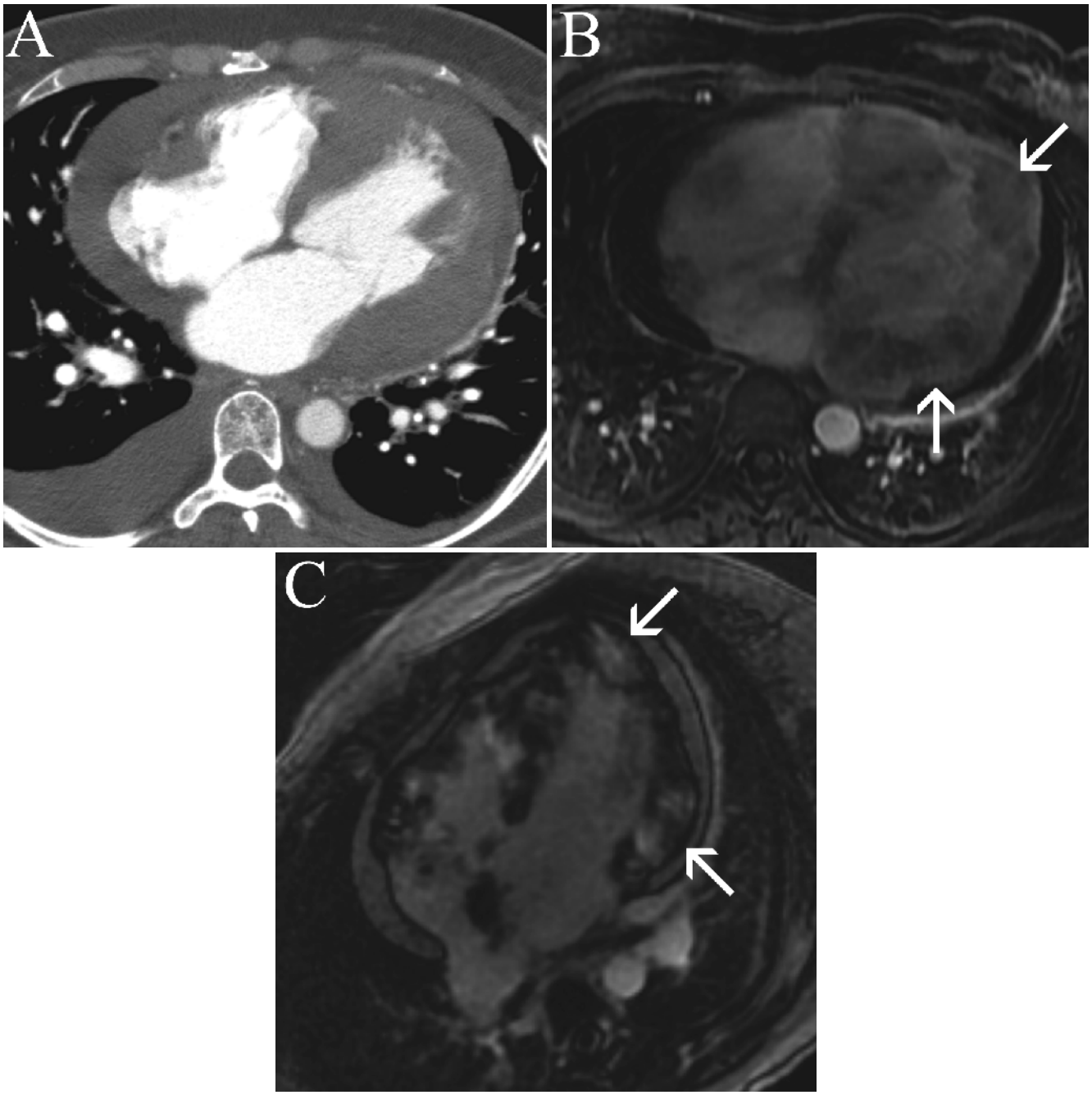

Figure 15.13. Forty-five-year-old female with metastatic melanoma. A transverse view from a contrast-enhanced CT scan (**a**) shows irregular thickening of the ventricular walls and a moderate-sized pericardial effusion. The ventricular metastases are not well-delineated due to the early phase of contrast administration, which was in part, due to the patient's poor cardiac function. A postcontrast CMR sequence obtained at 70 s after intravenous injection of gadolinium (**b**) demonstrates areas of relatively decreased enhancement related to the perfused myocardium (*white arrows*). A delayed, four-chamber view obtained 10 min after contrast administration (**c**) demonstrates late enhancement within the cardiac metastases (*white arrows*).

mediastinum [36]. An example of metastases involving the right ventricle is shown in Figure 15.15.

Myxomas

Myxomas are the most common benign neoplasm of the heart and comprise 50% of all primary cardiac masses. Myxomas characteristically occur in the atrial, and are more commonly left atrial rather than right atrial, with a reported predominance of 80% compared to 20% in the right atrium. Masses which arise in the atria may also prolapse into the ventricular chambers [14]. Myxomas have also, however, been reported to occur in both ventricles. The most common imaging appearance is that of a lobulated mass with precontrast hypoattenuation relative to blood pool and relative to myocardium. Masses are commonly lobulated in appearance and predominantly intracameral. The most common site of attachment for either right or left atrial myxomas is at the fossa ovalis, which can

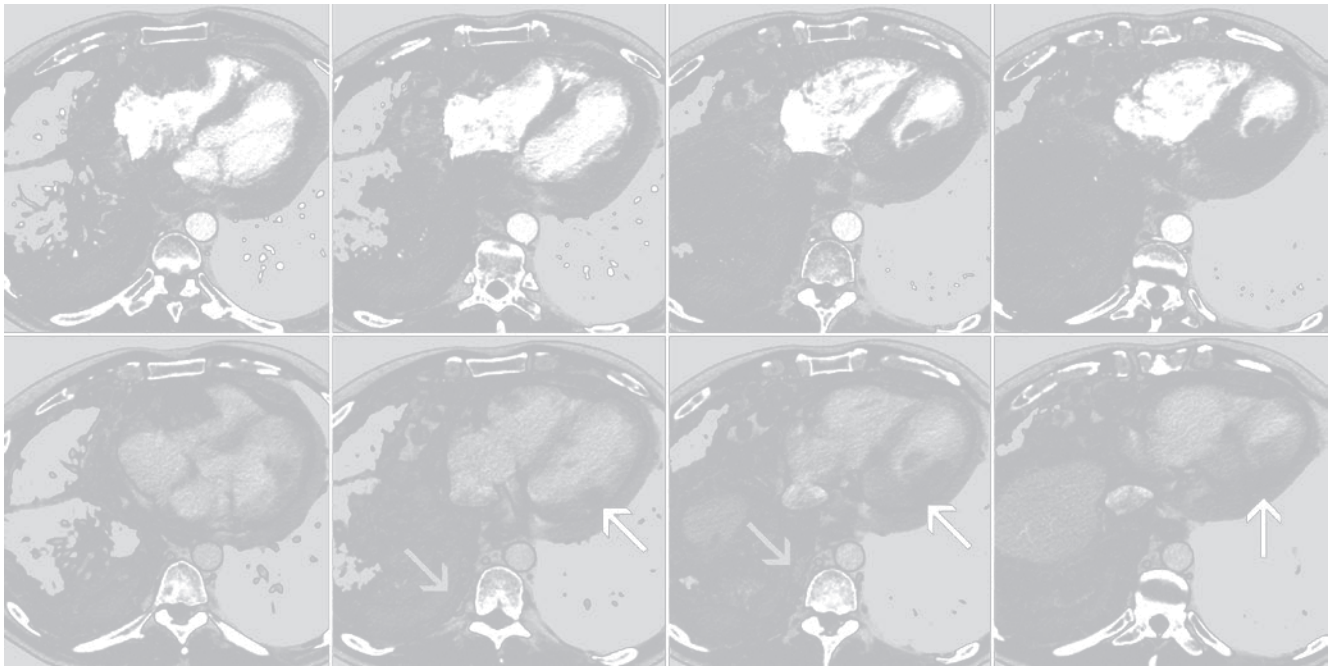

Figure 15.14. Fifty-six-year-old male with high-grade urothelial malignancy and cardiac metastases. Transverse views from an arterial phase of a postcontrast CT scan (*top row*) faintly show metastases to the left ventricular myocardium (*white arrows*). These areas of hypoenhancement are better seen in the portal venous phase images (*bottom row*), where the myocardium is more well-enhanced. Note that other metastases are also better seen on the later phase study, including pleural metastases (*black arrows*).

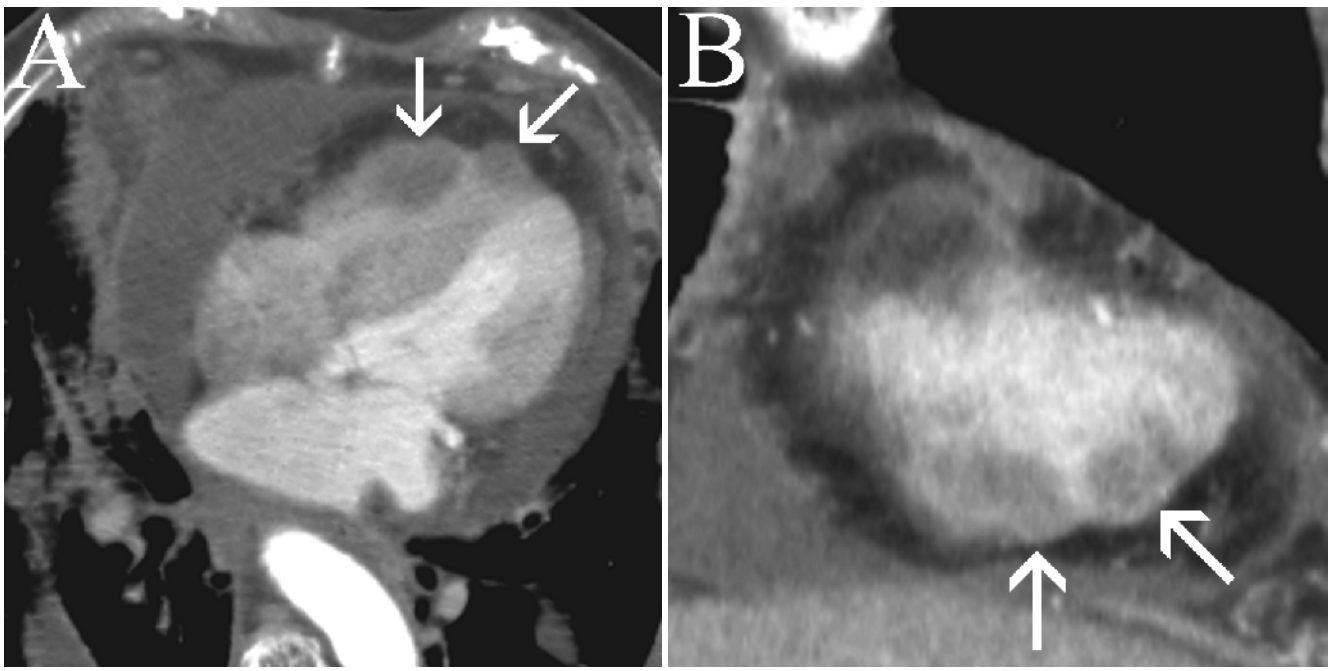

Figure 15.15. Forty-eight-year-old female with right ventricular metastases due to thymic carcinoma. Transverse (**a**) and coronal (**b**) views from a postcontrast CT scan show large masses arising from the wall of the right ventricle, with broad-based attachments to the ventricular wall, consistent with metastatic disease.

be helpful in arriving at the correct diagnosis [9]. Correct identification of the site of attachment is also helpful in presurgical planning. Atrial myxomas commonly demonstrate punctate or coarse calcifications, which is also useful in establishing the diagnosis. Precontrast hypoattenuation is commonly seen relative to blood pool and normal myocardium (Figure 15.16). Rarely, atrial myxomas may be diffusely and densely calcified [17].

The classic triad of clinical symptoms reported with myxomas includes constitutional symptoms, manifestations of obstructive valvular disease, and embolic phenomenon. Constitutional symptoms include fever, malaise, weight loss, and anemia, among others. These symptoms are likely related to an autoimmune response, initiated by the tumor [37]. Cardiac-related symptoms of atrial myxomas vary depending on the chamber of involvement. Atrial

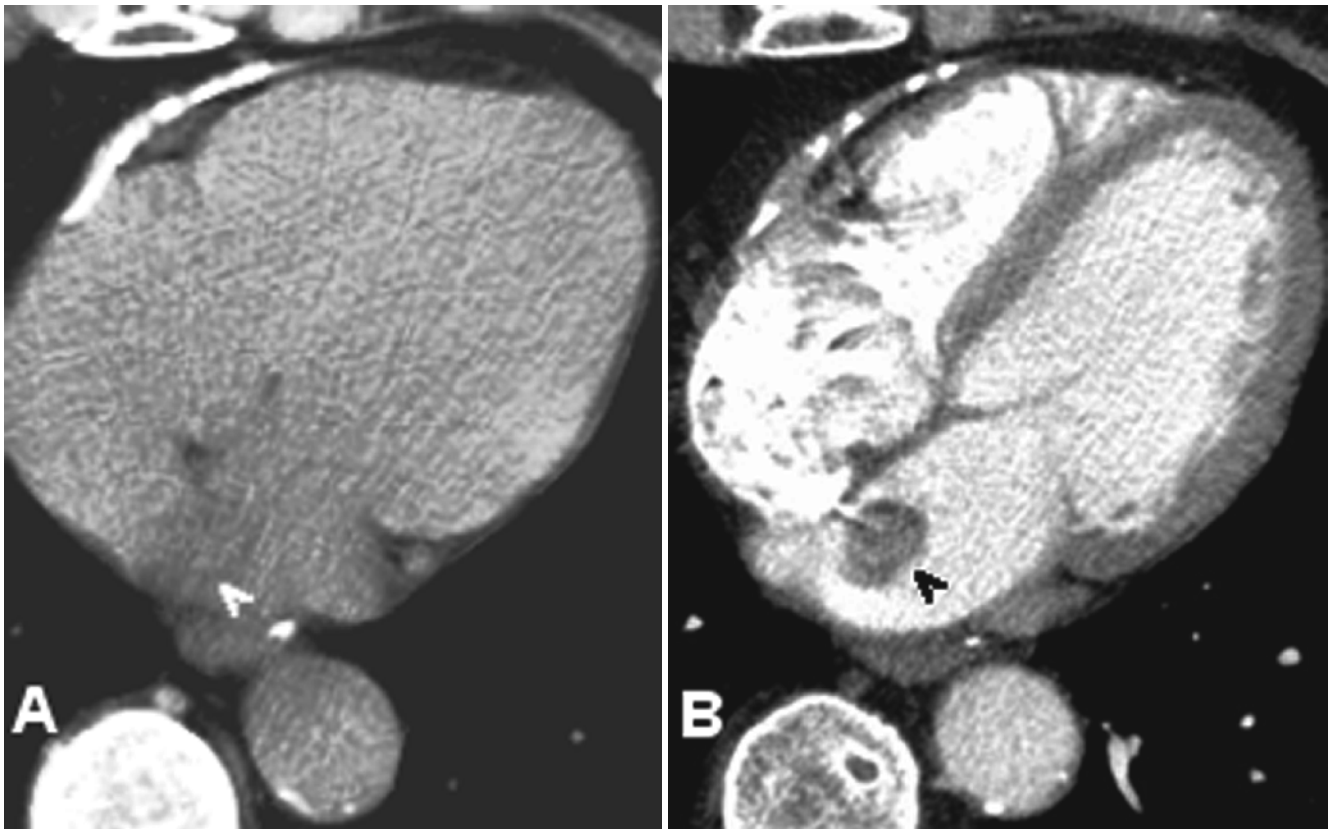

Figure 15.16. Fifty-two-year-old male with a left atrial mass. A precontrast CT scan (**a**) demonstrates the low attenuation left atrial mass. The postcontrast study (**b**) shows no enhancement, and delineates the pedunculated nature of the mass, which arises from the region of the fossa ovalis, consistent with left atrial myxoma.

myxomas have been commonly reported to mimic mitral valve disease and rheumatic heart disease by clinical presentation [38]. Involvement of other valves may, however, produce manifestations of aortic, pulmonic, or tricuspid valvular disease. Embolization is another common feature of myxomas, and may occur to either the pulmonic or systemic circulation, depending on the chamber of involvement. Up to 35% of left atrial myxomas and up to 10% of right atrial myxomas may develop emboli, although this difference could be related to the more apparent manifestations of systemic emboli [39].

A genetic predisposition to myxomas has been postulated and suggested by case reports of families with multiple members with myxomas and in patients with several myxomas [40]. Notably, Carney's Syndrome may be associated with atrial myxomas in two thirds of patients in addition to other manifestations including mammary myxoid fibroadenomas, pigmented cutaneous lesions, endocrine disorders, testicular tumors, and schwannomas [41].

Cardiac Sarcomas

Cardiac sarcomas comprise the most common primary malignant tumors of the heart, but are a rare entity overall, with a prevalence at autopsy as low as 0.0001% [42]. Metastases to the heart outnumber malignant primary lesions by 20–40 to 1. Among subtypes of sarcoma, angiosarcomas are most common, comprising approximately 37%. This tumor subtype in particular tends to occur commonly in the right atrium. Other subtypes tend to arise most commonly from the left atrium, although all types of sarcomas may occur in any chamber [13]. For most cardiac sarcomas, survival is reported as very poor, with metastases commonly detected shortly after clinical presentation [10].

On CCTA and CMR, angiosarcomas may show areas of hemorrhage and necrosis and may appear heterogeneous. Avid enhancement is commonly seen (Figure 15.17), and tumors may be difficult to delineate from the ventricular chamber on later phases due to bright enhancement. Venous lakes and linear vascular structures within masses may be seen, resulting in what has been likened to a "sun-ray pattern" [43]. Two morphological appearances of angiosarcomas have been reported, including a focal mass arising from the myocardium itself or a diffuse infiltrating process involving the myocardium and pericardium [44, 45]. Undifferentiated sarcomas are tumors with no specific histological staining patterns. The nature and definition of tumors in this category has changed over time as histological techniques have improved. Similar to angiosarcomas, these tumors may either present as a focal mass or as a diffusely infiltrative myocardial and pericardial process. The common site of origin is the left atrium, with a predisposition reported at 80% [13]. A propensity for valvular

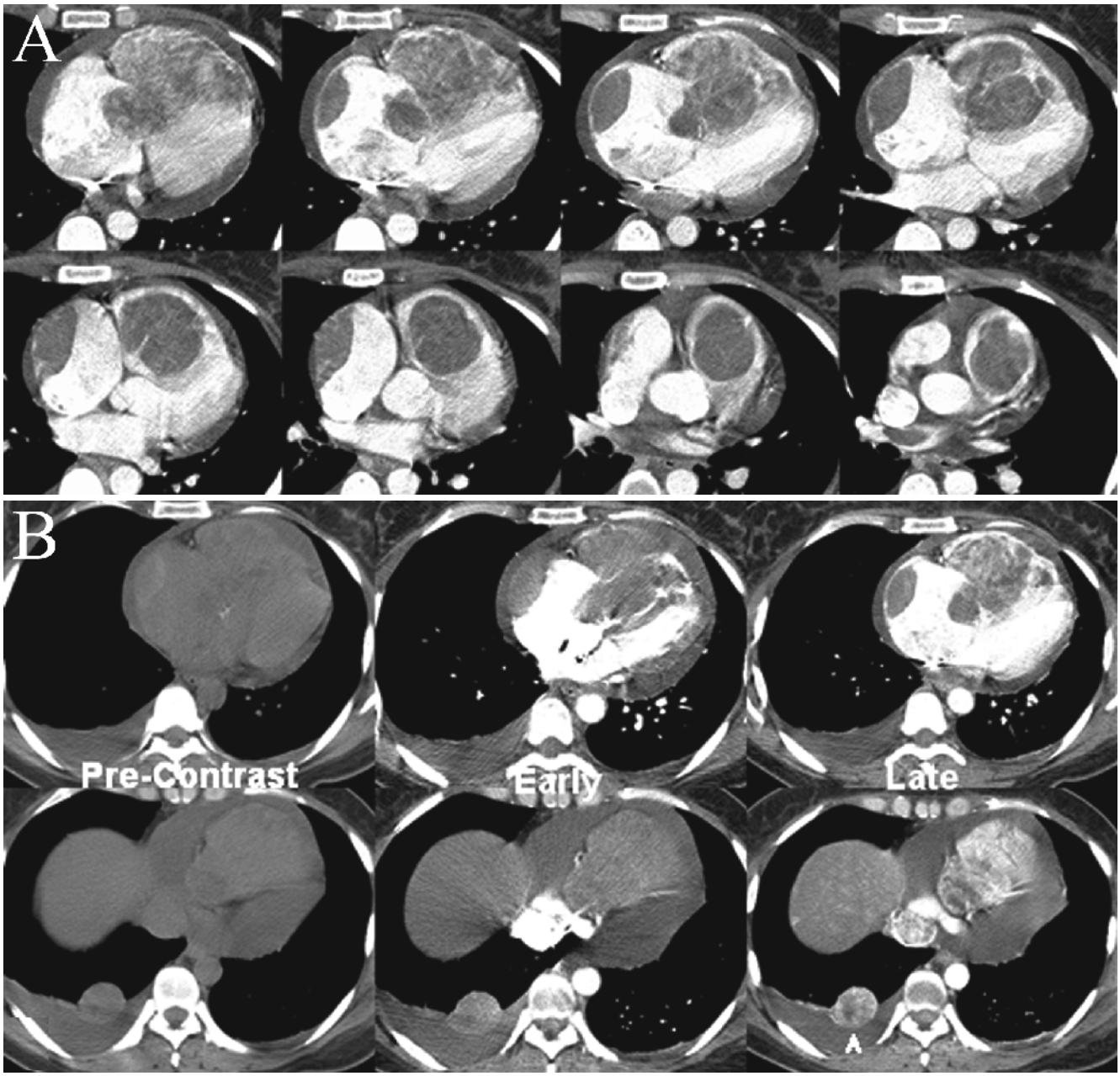

Figure 15.17. (**a, b**) Thirty-three-year-old female with angiosarcoma. Sequential precontrast, early, and late contrasted images demonstrate vascular enhancement within the angiosarcoma. Note the enhancing right lower lobe pulmonary nodule (*arrowhead*), consistent with a metastasis.

involvement has also been reported [46–48]. Rhabdomyosarcomas are very uncommon in adults, but are the most common form of cardiac sarcomas and the most common primary cardiac malignancy in pediatric populations [13]. Embryonal rhabdomyosarcomas occur in pediatric patients, whereas tumors in adults tend to be more pleomorphic [49]. Osteosarcomas of the heart are rare neoplasms, and are distinguished by their propensity to form dense calcifications [50], although some tumors of this type may demonstrate only minimal calcification [13]. Other tumor subtypes include leiomyosarcoma, fibrosarcoma, and liposarcoma, although these are even rarer than the aforementioned neoplasms.

Cardiac Lymphoma

Cardiac lymphoma is a very rare entity, and in a series of 533 cardiac tumors and cysts, it accounted for only 1.3% of tumors [11]. These tumors are rare since there are no true intracardiac lymph nodes. Tumors likely arise from primitive, totipotential mesenchymal cells, and usually consist of high grade B-cell lymphoma. Strictly defined, cardiac lymphoma includes lymphoma involving the heart and pericardium without other areas of lymphomatous involvement. Anecdotal reports suggest that there is increased risk for cardiac lymphoma in AIDS and in other immune deficiency states [51]. Given the rarity of this entity, the radiologic

findings are not well-established, although reports indicate that tumors are usually relatively isoattenuating on CT and isointense on CMR, with heterogeneous enhancement after contrast administration [52].

Lipoma

Cardiac lipomas are the second most common cause of a benign cardiac neoplasm, after myxomas. Lipomas are easily recognized as benign by the homogeneous, precontrast attenuation consistent with fat, which demonstrate essentially no enhancement after contrast administration. Tumors are soft and may be large at the time of initial diagnosis. Symptoms are usually due to mass effect, although commonly cardiac lipomas are detected incidentally and prior to onset of clinical manifestations. Some tumors may encase coronary arteries, resulting in mass effect and displacement, making resection difficult [53]. Although there is seldomly diagnostic uncertainty, some entities may mimic lipomas, including lipomatous hypertrophy of the interatrial septum (Figure 15.18). Rarely, lipomatous metaplasia within chronic myocardial infarctions may be misdiagnosed as a lipoma [54].

Papillary Fibroelastoma

Papillary fibroelastomas, also known as Lambl excrescences, are avascular masses comprised of fronds of dense connective tissue. These masses may be either reactive in nature or may be related to a hamartoma [55]. The true prevalence of this entity is not known, and these tumors have been postulated to be under-recognized and under-diagnosed due to their small size. Most sources refer to these lesions as the third most common benign neoplasms behind myxomas and lipomas. Ninety percent of papillary fibroelastomas occur on the valves, with the aortic valve being the most common location. When associated with the atrioventricular valves, these tumors tend to occur along the atrial side, which may help to differentiate these lesions from thrombi [56]. Associated valvular dysfunction is common, although many of these lesions are detected incidentally [57]. An additional, common presentation is embolic phenomenon, which may occur to the systemic or pulmonary circulation [58]. These tumors are, however, uncommonly reported on CCTA, and as a result no characteristic CCTA features of this entity have emerged.

Pediatric Cardiac Masses

In pediatric patients who present with cardiac masses, a separate set of diagnostic possibilities should be considered. Pediatric patients will less commonly present for CCTA evaluation, due to radiation concerns. Additionally, since there is sparse literature on CCTA in pediatric patients, the typical appearances of many masses are difficult to delineate. However, some familiarity with masses which may present in pediatric patients is useful to physicians involved in cardiac imaging.

In infants and children, the most common masses encountered are rhabdomyomas. These masses tend to be in the wall of the ventricles, and the vast majority of these masses are multiple. A strong association with tuberous sclerosis is present, although many patients do not manifest other signs of tuberous sclerosis until many years later. Spontaneous regression of tumors is common, although

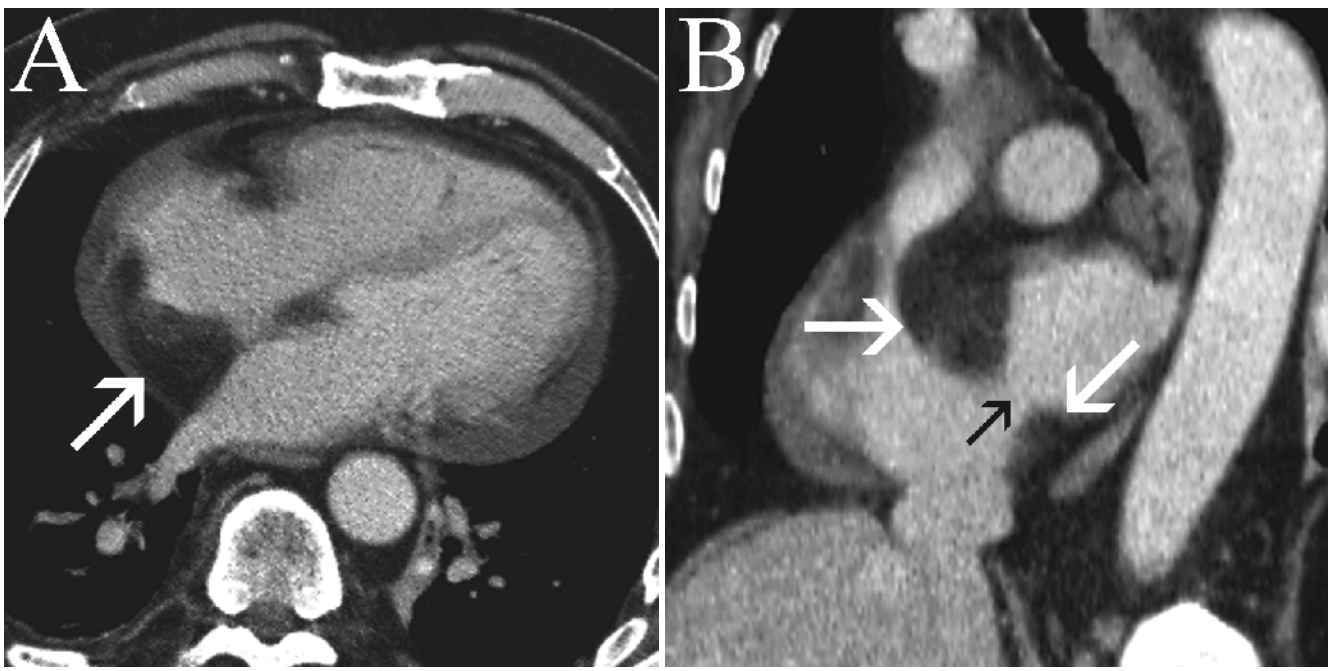

Figure 15.18. Seventy-eight-year-old male with lipomatous hypertrophy of the interatrial septum. Images from a CT scan of the chest obtained in the transverse plane (**a**) and in the short axis plane of the heart (**b**) show lipomatous hypertrophy in the wall of the interatrial septum (*white arrows*). Note the characteristic sparing of the region of the fossa ovalis (*black arrow*).

the initial clinical presentation may be severe [59]. Cardiac fibroma constitutes the second most common mass in the heart, and is usually seen as a large, solitary mass. Some of these may grow to an enormous size. Symptoms may include heart failure, chest pain, arrhythmias, and sudden cardiac death [60]. Myxomas are very rare in the pediatric population, but have been reported in large series in older pediatric patients and adolescents [17]. As described earlier, the most common malignant neoplasm in pediatric patients is a cardiac rhabdomyosarcoma, which often has embryonal features at histology. Additional rare tumors are encountered in pediatric populations including cardiac angiomas, cardiac teratomas, and Purkinje cell tumors.

Mimics of Cardiac Masses

Several normal structures in the heart may mimic a mass even to an experienced reader. Misidentification of normal structures as masses can lead to unnecessary biopsies, surgeries, and subsequent morbidity. Notably, in the right atrium, a prominent crista terminalis may mimic a cardiac mass. When a small and reticulated mass is present along this structure in the right atrium, a network of Chiari may be present. Uncommonly, prominence of the Eustachian valve or juxtacaval lipomatous tissue may mimic a lower right atrial mass. Usually, the contrast timing for the right ventricle is such that some saline is being injected at the time of scanning of the heart. However, in some cases, unopacified blood flow entering the right atrium from the inferior vena cava may simulate a mass when the right atrium is otherwise filled with contrast. In the left atrium, the "coumadin ridge," located between the atrial appendage ostium and the superior pulmonary vein, may appear mass-like.

References

1. Desjardins B, Kazerooni EA. ECG-gated cardiac CT. *Am J Roentgenol*. 2004;182:993–1010.
2. Newhouse JH, Murphy RX. Tissue distribution of soluble contrast: effect of dose variation and changes with time. *Am J Roentgenol*. 1981; 136:463–467.
3. Cademartiri F, Mollet N, van der Lugt A, et al. Non-invasive 16-row multislice CT coronary angiography: usefulness of saline chaser. *Eur Radiol*. 2004;14:178–183.
4. Awai K, Hiraishi K, Hori S. Effect of contrast material injection duration and rate on aortic peak time and peak enhancement at dynamic CT involving injection protocol with dose tailored to patient weight. *Radiology*. 2004;230(1):142–150.
5. Cademartiri F, Nieman K, van der Lugt A, et al. Intravenous contrast material administration at 16-detector row helical CT coronary angiography: test bolus versus bolus-tracking technique. *Radiology*. 2004;233:817–823.
6. Bae KT, Tran HQ, Heiken JP. Uniform vascular contrast enhancement and reduced contrast medium volume achieved by using exponentially decelerated contrast material injection method. *Radiology*. 2004; 231:732–736.
7. Boyd DB. Computerized transmission tomography of the heart using scanning electron beams. In: Higgins CH, ed. *Computed Tomography of the Heart and Great Vessels*. Mount Kisco, New York: Futura; 1983:45–55.
8. Newhouse JH. Fluid compartment distribution of intravenous iothalamate in the dog. *Invest Radiol*. 1977;12:364–367.
9. Prichard RW. Tumors of the heart. *Arch Pathol*. 1951;51:98–128.
10. Glancy DL, Morales JB, Roberts WC. Angiosarcoma of the heart. *Am J Cardiol*. 1968;21:413–419.
11. McAllister HA, Fenoglio JJ Jr. *Tumors of the Cardiovascular System: Atlas of Tumor Pathology, Second Series*. Washington, DC: Armed Forces Institute of Pathology; 1978.
12. Lund JT, Ehman RL, Julsrud PR, et al. Cardiac masses: assessment by MR imaging. *AJR Am J Roentgenol*. 1989;152(3):469–473.
13. Burke AP, Cowan D, Virmani R. Primary sarcomas of the heart. *Cancer*. 1992;69:387–395.
14. Tazelaar HD, Locke TJ, McGregor CG. Pathology of surgically excised primary cardiac tumors. *Mayo Clin Proc*. 1992;67(10):957–965.
15. Lam KY, Dickens P, Chan AC. Tumors of the heart. A 20-year experience with a review of 12,485 consecutive autopsies. *Arch Pathol Lab Med*. 1993;117(10):1027–1031.
16. Marx GR. Cardiac tumors. In: Emmanouilides GC, Gutgesell HP, Riemenschneider TA, Allen HD, eds. *Moss and Adams Heart Disease in Infants, Children, and Adolescents: Including the Fetus and Young Adult*. 5th ed. Vol 2. Baltimore: Williams & Wilkins; 1995:1773–1786.
17. Burke A, Virmani R. *Tumors of the Heart and Great Vessels: Atlas of Tumor Pathology*. Fasc 16, ser 3. Washington, DC: Armed Forces Institute of Pathology; 1996.
18. Takach TJ, Reul GJ, Ott DA, Cooley DA. Primary cardiac tumors in infants and children: immediate and long-term operative results. *Ann Thorac Surg*. 1996;62(2):559–564.
19. Ludomirsky A. Cardiac tumors. In: Bricker JT, Fisher DJ, eds. *The Science and Practice of Pediatric Cardiology*. 9th ed. Vol 2. Baltimore: Williams & Wilkins; 1998:1885–1893.
20. Araoz PA, Eklund HE, Welch TJ, Breen JF. CT and MR imaging of primary cardiac malignancies. *Radiographics*. 1999;19(6):1421–1434.
21. Chiles C, Woodard PK, Gutierrez FR, Link KM. Metastatic involvement of the heart and pericardium: CT and MR imaging. *RadioGraphics*. 2000;20:1073–1103.
22. Grebenc ML, Rosado de Christenson ML, Burke AP, Green CE, Galvin JR. Primary cardiac and pericardial neoplasms: radiologic–pathologic correlation. *Radiographics*. 2000;20:1073–1103; quiz 1110–1071;1112.
23. GrebencML, Rosado-de-Christenson ML, Green CE, Burke AP, Galvin JR. Cardiac myxoma: imaging features in 83 patients. *Radiographics.* 2002; 2(3):673–689.
24. Piazza N, Chughtai T, Toledano K, et al. Primary cardiac tumours: eighteen years of surgical experience on 21 patients. *Can J Cardiol*. 2004; 20(14):1443–1448.
25. Tatli S, Lipton MJ. CT for intracardiac thrombi and tumors. Int J Cardiovasc Imaging 2005;21(1):115–131.
26. Butany J, Nair V, Naseemuddin A, et al. Cardiac tumours: diagnosis and management. *Lancet Oncol*. 2005;6(4):219–228.
27. Leipsic JA, Heyneman LE, Kim RJ. Cardiac masses and myocardial diseases. In: McAdams HP, Reddy GP, eds. *Cardiopulmonary Imaging Syllabus – 2005*. Leesburg, VA: American Roentgen Ray Society; 2005: 1–13.
28. Sparrow PJ, Kurian JB, Jones TR, Sivananthan MU. MR imaging of cardiac tumors. *Radiographics*. 2005;25:1255–1276.
29. Barkhausen J, Hunold P, Eggebrecht HH, et al. Detection and characterization of intracardiac thrombi on MR imaging. *AJR*. 2002;179: 1539–1542.
30. Weinreich DJ, Burke JF, Ferrel JP. Left ventricular mural thrombi complicating acute myocardial infarction long-term follow-up with serial echocardiography. *Ann Intern Med*. 1984;100(6):789–794.
31. Asinger RW, Mikell FL, Elsperger J, Hodges M. Incidence of left ventricular thrombosis after acute transmural myocardial infarction: serial evaluation by two-dimensional echocardiography. *NEJM*. 1981; 305(6):297–302.
32. Hur J, Kim YJ, Nam JE, et al. Thrombus in the left atrial appendage in stroke patients: detection with cardiac CT angiography–a preliminary report. *Radiology*. 2008;249(1):81–87.
33. Hur J, Kim YJ, Lee HJ, et al. Left atrial appendage thrombi in stroke patients: detection with two-phase cardiac CT angiography

versus transesophageal echocardiography. *Radiology*. 2009;251(3): 683–690.
34. Abraham KP, Reddy V, Gattuso P. Neoplasms metastatic to the heart: review of 3314 consecutive autopsies. *Am J Cardiovasc Pathol*. 1990; 3:195–198.
35. Klatt EC, Heitz DR. Cardiac metastases. *Cancer*. 1990;65:1456–1459.
36. MacGee W. Metastatic and invasive tumours involving the heart in a geriatric population: a necropsy study. *Virchows Arch A Pathol Anat Histopathol*. 1991;419:183–189.
37. Bjessmo S, Ivert T. Cardiac myxoma: 40 years' experience in 63 patients. *Ann Thorac Surg*. 1997;63:697–700.
38. Markel ML, Waller BF, Armstrong WF. Cardiac myxoma: a review. *Medicine*. 1987;66:114–125.
39. Castells E, Ferran V, Octavio-de-Toledo MC. Cardiac myxomas: surgical treatment, long-term results and recurrence. *J Cardiovasc Surg*. 1993;34:49–53.
40. Carney JA. Differences between nonfamilial and familial cardiac myxoma. *Am J Surg Pathol*. 1985;9:53–55.
41. Carney JA, Gordon H, Carpenter PC, Shenoy BV, Go VW. The complex of myxomas, spotty pigmentation and endocrine overactivity. *Medicine*. 1985;64:270–283.
42. McCallister HA Jr. Primary tumors of the heart and pericardium. *Curr Probl Cardiol*. 1979;4:1–51.
43. Yahata S, Endo T, Honma H, et al. Sunray appearance on enhanced magnetic resonance image of cardiac angiosarcoma with pericardial obliteration. *Am Heart J*. 1994;127:468–471.
44. Bruna J, Lockwood M. Primary heart angiosarcoma detected by computed tomography and magnetic resonance imaging. *Eur Radiol*. 1998;8:66–68.
45. Jannigan DT, Husain A, Robinson NA. Cardiac angiosarcomas: a review and a case report. *Cancer*. 1986;57:852–859.
46. Herhusky MJ, Gregg SB, Virmani R, Chun PKC, Bender H, Gray GF Jr. Cardiac sarcoma presenting as metastatic disease. *Arch Pathol Lab Med*. 1985;109:943–945.
47. Ludomirsky A, Vargo TA, Murphy DJ, Gresik MV, Ott DA, Mullins CE. Intracardiac undifferentiated sarcoma in infancy. *J Am Coll Cardiol*. 1985;6:1362–1364; Abstract 37.
48. Itoh K, Matsumura T, Egawa Y, et al. Primary mitral valve sarcoma in infancy. *Pediatr Cardiol*. 1998;19:174–177.
49. Hwa J, Ward C, Nunn G, et al. Primary interventricular cardiac tumors in children: contemporary diagnostic and management options. *Pediatr Cardiol*. 1994;15:233–237.
50. Chaloupka JC, Fishman EK, Siegelman SS. Use of CT in the evaluation of primary cardiac tumors. *Cardiovasc Intervent Radiol*. 1986;9: 132–135.
51. Holladay AO, Siegel RJ, Schwartz DA. Cardiac malignant lymphoma in acquired immune deficiency syndrome. *Cancer*. 1997;70(8): 2203–2207.
52. Dorsay TA, Ho VB, Roviera MJ, Armstrong MA, Brissette MD. Primary cardiac lymphoma: CT and MR findings. *J Comput Assist Tomogr*. 1993; 17:978–981.
53. Hananouchi GI, Goff WB. Cardiac lipoma: six-year follow-up with MRI characteristics, and a review of the literature. *Magn Reson Imaging*. 1990;8(6):825–828.
54. Banks KP, Lisanti CJ. Incidental finding of a lipomatous lesion involving the myocardium of the left ventricular wall. *AJR*. 2004;182: 261–262.
55. Rubin MA, Snell JA, Tazelaar HD, Lack EE, et al. Cardiac papillary fibroelastoma: an immunohistochemical investigation and unusual clinical manifestations. *Mod Pathol*. 1995;8:402–407.
56. Klarich KW, Enriquez-Sarano M, Gura GM, et al. Papillary fibroelastoma: echocardiographic characteristics for diagnosis and pathologic correction. *J Am Coll Cardiol*. 1997;30:784–790.
57. Edward FH, Hale D, Cohen A, et al. Primary cardiac valve tumors. *Ann Thorac Surg*. 1991;52:1127–1131.
58. McFadden PM, Lacy JR. Intracardiac papillary fibroelastoma: an occult cause of embolic neurologic deficit. *Ann Thorac Surg*. 1987;43: 667–669.
59. Bosi G, Lintermans JP, Pellegrino PA, et al. The natura history of cardiac rhabdomyoma with and without tuberous sclerosis. *Acta Pediatr*. 1996;85:928–931.
60. Turi GK, Albala A, Fenoglio JJ Jr. Cardiac fibromatosis: an ultrastructural study. *Hum Pathol*. 1980;11:577–579.

Part V

CT Vascular Angiography

16

CT Angiography of the Peripheral Arteries

Jabi E. Shriki, Thomas-Duythuc To, and Leonardo C. Clavijo

Introduction

Computed tomographic (CT) angiography is a useful modality in imaging the peripheral arterial tree and has become an integral component of many cardiovascular imaging practices. Large portions of the arterial system can be easily imaged with excellent spatial resolution, low radiation dose, and minimal risks to the patient. Additionally, the skill set of 3D data manipulation in evaluation of coronary arteries and vascular structures elsewhere in the body can be translated into skills useful in the interpretation of peripheral studies. Advancements in CT angiography, including scanners with 64 row detectors and higher, have made submillimeter isotropic voxel resolution possible, enabling more detailed visualization of arterial structures. Simultaneous increases in computational speed and widespread availability of dedicated 3D workstations make visualization and evaluation of peripheral arterial anatomy much more facile.

Acquisition and Scanning Techniques

Special Considerations Regarding Peripheral CT Angiography

Several technical considerations should be recognized in making the transition from cardiac to peripheral vascular CT angiography. First, while the coronary arteries are usually briskly opacified along with the aorta even in the presence of stenosis, the peripheral vasculature may have a variable relationship with aortic opacification. In patients with severe atherosclerotic disease and multiple stenoses or aneurysms, optimal opacification may be achieved much later than aortic enhancement. In other thoracic, abdominal, and neuroimaging applications, higher detector row CT scanners provide a number of advantages. However, for peripheral CT angiography, the high speed of scanning with multidetector row CT scanners may result in outpacing of the bolus of contrast, with images obtained prior to arrival of the contrast bolus into the area of interest. As a result, the timing of scanning for peripheral CT angiography has separate considerations that differ from scanning other, more proximal, body parts (Figure 16.1).

Also, the reconstructed field of view for peripheral applications is frequently larger in transverse axial dimension than that employed for cardiac CT. This occurs because of the necessarily larger field of view needed to encompass the vascular anatomy when performing a peripheral CT angiogram from the pelvis to the lower extremities. As a result, images may have lower in-plane spatial resolution.

Figure 16.1. A 3D reconstruction demonstrating that the run-off vessels are less well opacified than the popliteal arteries, likely related to slight outpacing of the contrast bolus by the speed of the scanner.

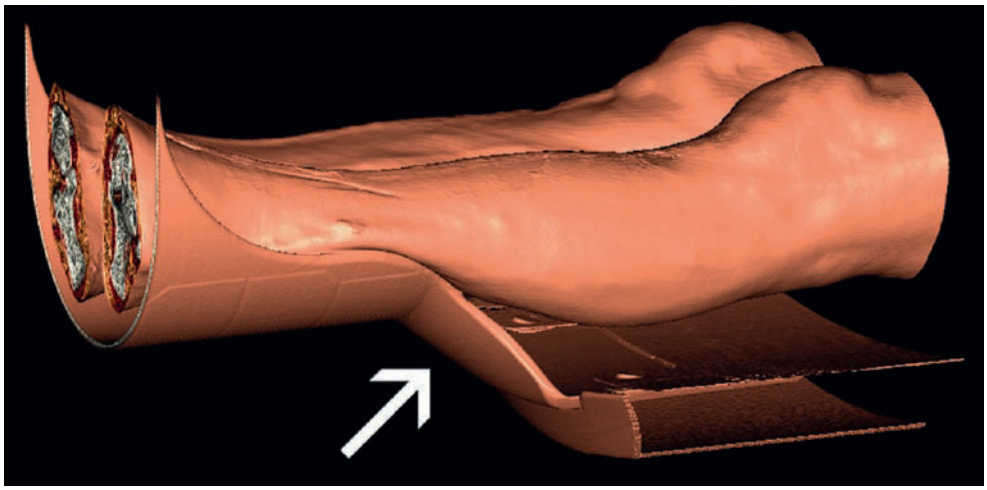

Figure 16.2. Reconstructed, volume projections can demonstrate the soft tissue anatomy. The lower extremities should be closely apposed to one another in order to minimize the dimensions of the reconstructed field of view. In this case, this is achieved by use of a table extension (*white arrow*).

This loss of in-plane resolution may be offset by the use of separate, reconstructed fields of view for each lower extremity or for different parts of the anatomy scanned. When imaging the lower extremities, the feet should be kept straight and apposed to one another as closely as possible, so that the reconstructed field of view closely matches the anatomy being imaged. This can be achieved by binding the feet into a table extension or harness, which is usually attachable or built into the table (Figure 16.2).

An additional consideration is the larger craniocaudal extent of the anatomy imaged in peripheral CT angiography compared to cardiac CT. As a result, data sets may be much larger for comparable slice thickness. For example, whereas a cardiac CT single phase reconstruction at 0.5 mm may comprise 100–200 or more images, a peripheral CT angiogram including the entirety of the lower extremities might include several hundred images, due to the larger craniocaudal extent included. As a result, thicker slices may be evaluated initially, whereas thin slices may be used adjunctively and in a more limited role for problem solving. Alternatively, some 3D workstations have options for subvolume selection, which enables evaluation of the arterial tree in a piecemeal fashion, allowing larger data sets to be evaluated, with enhanced multiplanar reformatting capabilities.

Contrast Administration

Rapid rates of contrast administration are critical in obtaining optimal vascular opacification. Consequently, a more central, large bore venous access line, 18 gauge catheter in the antecubital fossa, is highly preferable to a smaller or more peripheral venous access site. Most studies for peripheral CT angiography report contrast rates of 3.5–4.0 cc/s as optimal [1–3]. Since the area scanned in imaging the peripheral arterial tree is significantly larger in craniocaudal extent compared to the coronary tree, a more prolonged bolus of contrast, with a slightly slower rate is preferable to ensure homogeneous, persistent, bright opacification of the peripheral arteries. This injection rate is slightly slower than the rate employed for imaging the heart which may be as high as 5–6 cc/s [4], since the aim of peripheral CT angiography is a sustained peak of bright opacification, whereas in coronary CT prolongation of peak contrast opacification is a less important factor. Patients are usually given a formulation of intravenous contrast with 300–400 mg of iodine/mL, with 120–180 cc/s of contrast given depending on each patient's body surface area [5]. The total amount of contrast, however, may be reduced when scanners with higher numbers of detectors are used [6, 7]. Higher iodine concentrations have been demonstrated to have higher attenuation levels when the aortic enhancement is measured on scans [8]. Larger amounts of contrast are needed in patients who are taller or are more obese [5].

Administration of a saline chaser is useful in ensuring both a higher degree of opacification and prolongation of the plateau of attenuation once the peak is obtained. A saline chaser is also useful in diminishing the total amount of contrast needed for optimal opacification [9, 10]. Saline injection can also clear the residual central contrast from the venous system. Dense central venous contrast can impede imaging of the proximal upper extremity arterial system due to resultant streaking from stasis of contrast in the superior vena cava, brachiocephalic veins, or other venous structures. When imaging the upper extremities, contrast injection should be made via the contralateral extremity to avoid this pitfall.

Optimal timing for acquisition varies significantly in each patient. In patients with normal cardiac function, a rapid acquisition of images may outpace the bolus of contrast. In patients with depressed cardiac function or arterial pathology which may inhibit brisk outflow, including stenoses or aneurysms, the scanning time should be prolonged to ensure that the region of interest (ROI) scanned is optimally opacified and that scanning is not performed before arrival of the contrast bolus [11]. At our institution, in patients with suspected atherosclerotic disease, the lower extremities are scanned twice, with a second acquisition beginning just

above the knees and immediately after the first acquisition. This second acquisition enhances visualization of arterial structures, although there may be significant venous contamination at the time of a second scan, which may make 3D reconstructions somewhat difficult to evaluate.

Several techniques for ensuring optimal timing may be employed. A timing bolus utilizes injection of a small amount of contrast with serial images through a ROI in order to predict the timing of bolus arrival. This is somewhat problematic in evaluating the peripheral arterial tree, since different portions of the arterial tree may be opacified at different times, depending on the degree of upstream disease. This technique necessitates two separate injections, although this usually only minimally increases the total amount of contrast, since only a small amount is given for the initial injection. This technique may help in preparing the patient for the common clinical manifestations such as sensory warmth and a metallic taste which commonly ensue after contrast administration.

Alternatively, bolus tracking can be utilized with a single contrast injection. With this technique, a ROI within the aorta is serially scanned during the injection of contrast. When the attenuation value reaches a particular, preset threshold, scanning of the remainder of the field of view is initiated. At our institution, for peripheral CT angiography of the lower extremities, an attenuation value of 180 Hounsefield units (HU) is employed and the ROI is placed in the infrarenal aorta. The ROI is sized to include approximately one half the diameter of the aorta at this level. Different vendor-specific protocols are available for automated contrast monitoring. For slower scanners, a lower threshold (100 HU) may be used to ensure that the speed of scanning matches arrival of the contrast bolus [12]. A significant limitation of the bolus tracking technique is that the ROI may be placed within an area of thrombus or in the false lumen of an aortic dissection. If this is the case, opacification may not occur or may occur in a portion of the vessel that is outside the ROI. Technologists should be instructed to visually monitor the images obtained during bolus tracking for appearance of the bolus of contrast. Close monitoring for optimal vascular enhancement may limit some of these failures in automated bolus detection.

Preset timing of contrast is less commonly employed at most institutions, especially for imaging peripheral arteries. This technique may be especially problematic in patients with atherosclerotic disease and in patients with low cardiac output where the bolus will be circulated through the arteries more slowly. For the upper extremities, scanning may be initiated 20 s after the start of contrast injection. For the lower extremities, scanning may be initiated 50 s after the beginning of injection [13].

Techniques for Evaluating Studies

Several studies have demonstrated an excellent accuracy of CT in comparison to conventional digital subtraction angiography (DSA), based solely on evaluation of transverse images [14, 15]. In many early studies, the transverse axial data set was evaluated alone. The transverse plane of the body is in a relatively perpendicular axis to the long arteries of the extremities, resulting in views which approximate the short axis plane of much of the vascular tree with minimal technical manipulation of data sets. Additionally, final review of studies at a dedicated 3D workstation is commonly employed. Key images for demonstrating stenoses or other vascular pathology, detected by the interpreting physician, are subsequently also sent to the picture archiving and communication system (PACS) for further correlation by the referring physician and to illustrate important findings.

In addition to evaluation of transverse axial data sets, review of long and short axis views utilizing multiplanar reformatted views (MPR), thick maximum intensity projection views (MIP, Figure 16.3), and curvilinear plane reformatted views (CPR, Figure 16.4) likely results in a more thorough assessment of the peripheral vascular tree and in improved sensitivity and specificity [16]. Review of the transverse axial views is the usual starting point for most readers. Reformatting the data along the plane of the vessel utilizing MPR views introduces few artifacts, as long as scans are obtained using isotropic voxels. MIP views generally demonstrate the higher attenuation values within a thick slab of the data set, and are useful for demonstrating the course of a tortuous vessel when enhanced with contrast. MIP views are also useful for demonstrating other high attenuation structures such as stents (Figure 16.5a), surgical clips, calcifications, and osseous structures. CPR images introduce some potential artifacts, as computer algorithms select the center line to be followed. User-directed CPR images may be created, but are commonly time consuming and require some expertise to create. Unlike evaluation of the coronary arteries, CPR images are less susceptible to artifacts in the large vessels of the extremities, where arteries course in relatively straight planes. 3D views are usually demonstrated with a lit projection and are helpful in demonstrating anatomic relationships, though they are problematic for demonstrating or grading stenoses (Figure 16.5b).

Newer tools enable color-coding of vessels to bring attention to areas of plaque. Also, techniques are available for characterization of atherosclerotic lesions with respect to attenuation values in order to classify lesions as fatty, fibrous, or calcified. These tools may be used adjunctively to the techniques described earlier, but have yet to be rigorously evaluated or validated.

Validation of Peripheral CT Angiography

Advancement in CT technology has been rapid, with the recent advent of isotropic voxel imaging and multidetector CT. As a result of the rapid development of new CT techniques, the pace of technological advancement has surpassed the rate at which newer technologies are

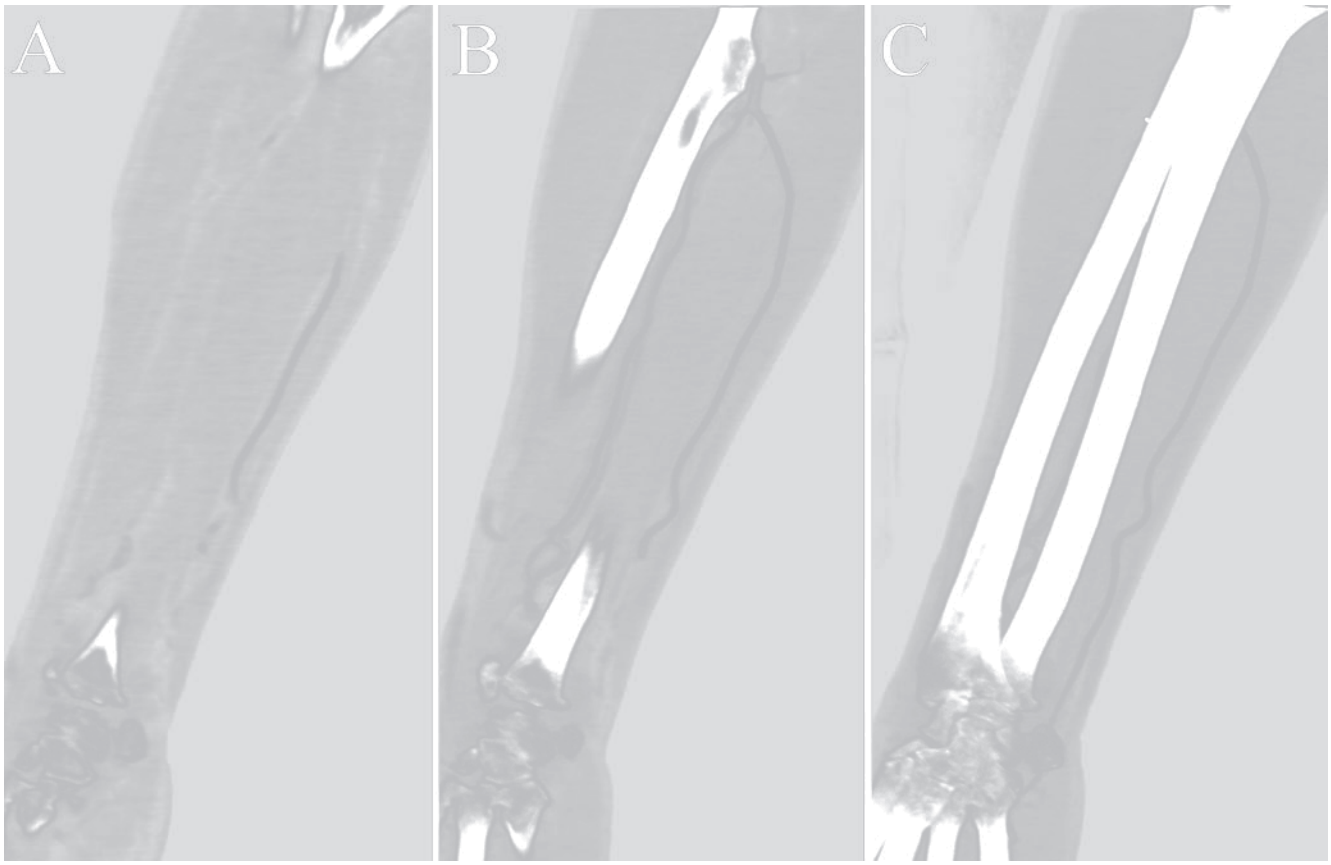

Figure 16.3. A reformatted view through the radial artery is shown (**a**). On the progressively thicker maximum intensity projection (MIP) views obtained with a thickness of 2 cm (**b**) and 4 cm (**c**), a greater length of the arterial anatomy is demonstrated. MIP views are also useful for demonstrating high attenuation structures such as bones and stents.

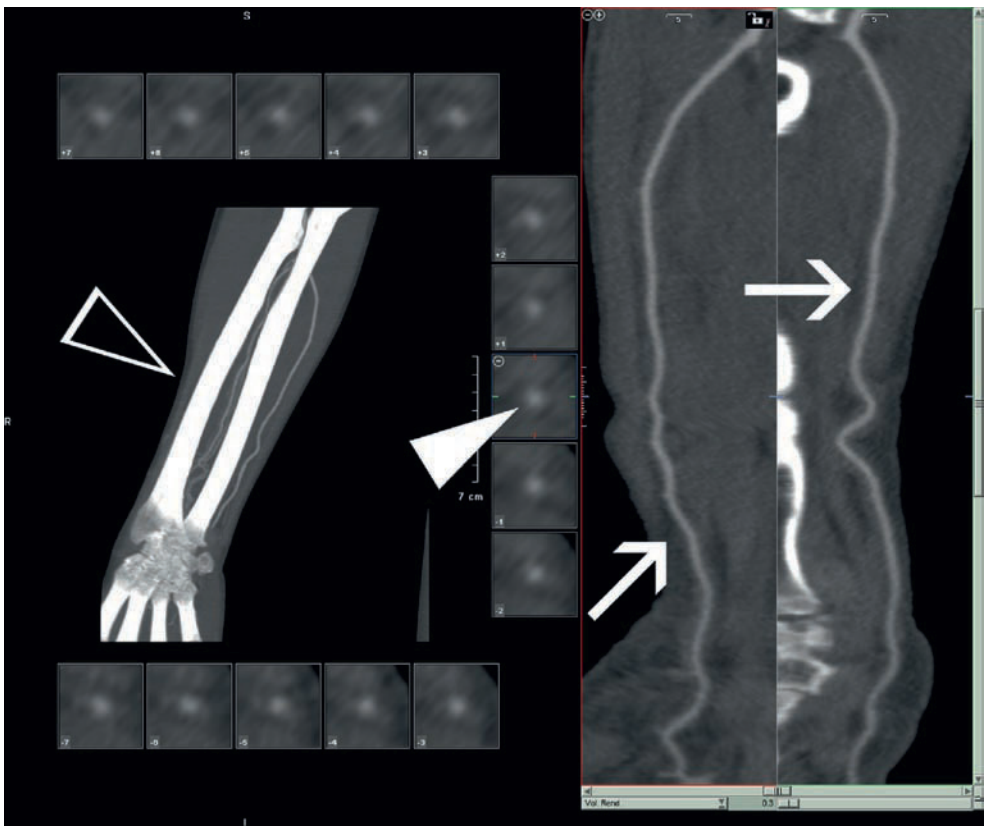

Figure 16.4. Curved planar reformatted views show the long axis, orthogonal (*white arrows*) and short axis (*closed arrowhead*) of arterial structures. This is contrasted with the MIP multiplanar reformatted (MPR) view (*open arrowhead*).

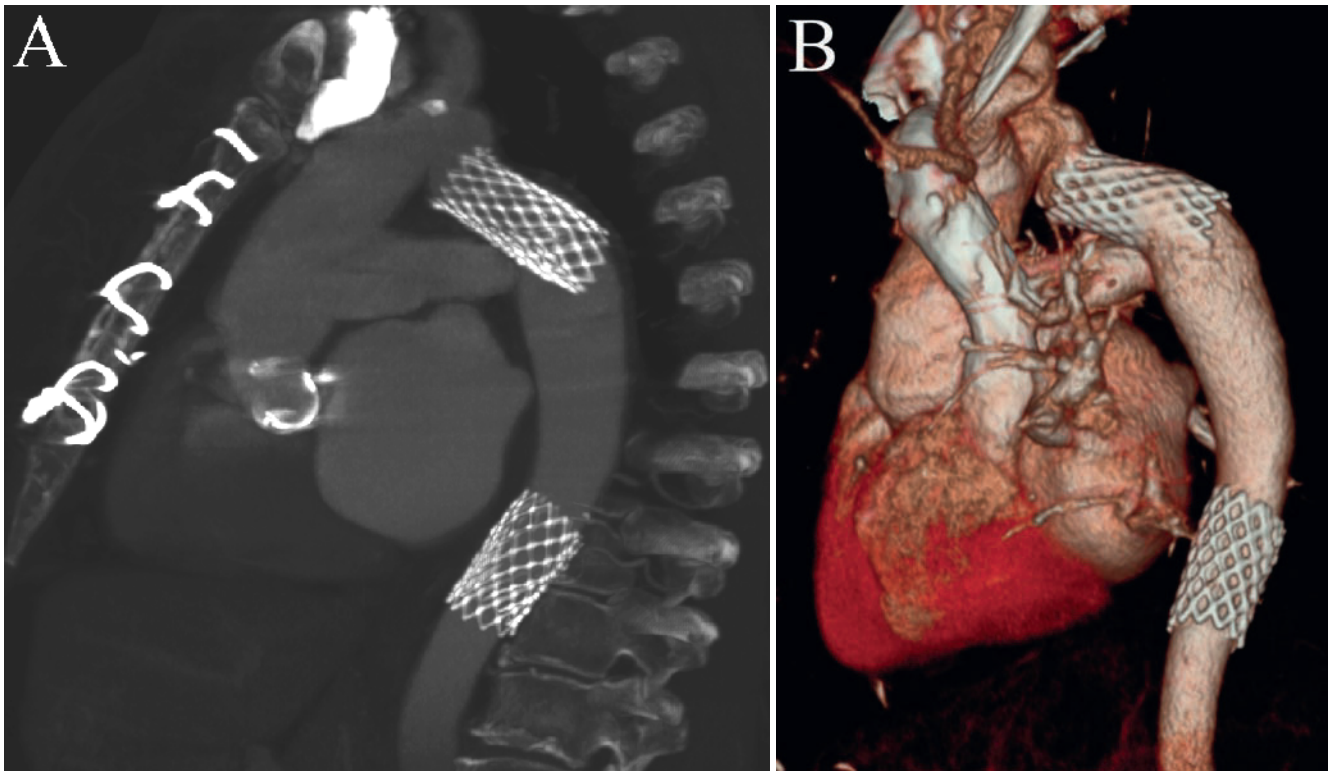

Figure 16.5. The thick, MIP view (**a**) demonstrates the aortic stents. They are also well-seen on the volume rendered view (**b**) in this patient who is status post aortic stenting after repair for aortic coarctation and a bicuspid aortic valve.

validated. For this reason, large multicenter studies and metaanalyses likely underestimate the accuracy of CT angiography as a tool.

Large studies have, however, demonstrated several significant advantages of CT angiography in comparison to DSA, including a fourfold lower radiation dose and a much lower risk of complications. Moreover, studies have shown an excellent accuracy for the diagnosis of atherosclerotic disease and excellent correlation with DSA [17]. Diagnostic CT angiography performs comparably to DSA and favorably compared to duplex ultrasound and MR angiography for the evaluation in patients with chronic peripheral arterial disease (PAD) and in patients with traumatic vascular injuries [16].

A study evaluating CT angiography with 64-row detector scanners for the detection of peripheral vascular disease evaluated 840 segments of the systemic arteries in 28 patients with lower extremity claudication. This study found an overall diagnostic accuracy of 98% in the detection of lesions with a degree of stenosis of 50% or higher. The sensitivity and specificity for detecting stenosis by CT angiography were 99 and 98%, respectively [18]. Moreover, the use of advanced imaging tools, including 3D reconstructions and MPR views, provide detailed visualization of stenotic lesions, normal, or previously revascularized lower extremity arteries along with nearby extravascular structures. Augmenting axial images with reformatted views has been shown to improve accuracy of interpretation [19].

Role of Peripheral CT Angiography to the Vascular Physician

The most important application of CT angiography for the vascular interventional specialist is pre-procedure planning, including: selection of patients best treated with endovascular intervention vs. open surgical procedures, identification of vascular access sites, pre-procedure selection of appropriate angiographic views, and pre-procedural lesion characterization (thrombus burden, dissection, calcification, tortuosity, etc.). CT angiography also provides valuable information in tailoring the most appropriate endovascular therapy, including: thrombolysis, laser or orbital atherectomy, reentry device, distal embolic protection device, balloon angioplasty, self-expanding or balloon expandable stents, and covered stents (Table 16.1).

Patients who undergo intervention for PAD have a higher incidence of vascular access site complications compared to patients who undergo percutaneous coronary intervention [20]. Patients with atherosclerotic disease commonly have a high burden of diffuse, often densely calcified atherosclerotic plaques. As a result, vascular access selection is one of the

Table 16.1. Advantages of CT angiography in patients with peripheral arterial disease (PAD) prior to endovascular

Interventions
Selection of patients for endovascular vs. open surgical revascularization
Vascular access selection
Lesion characterization (thrombus, degree of calcification, lesion length, vessel size)
Arterial vascular inflow and outflow
Selection of interventional angiographic views and angulations
Equipment selection based on lesion characteristics and vessel size (thrombolysis, sheaths, wires, balloons, stents, atherectomy, distal embolic protection)
Decreased contrast use
Decreased radiation exposure
Evaluation of extravascular arterial disease (popliteal entrapment and popliteal cystic disease)

most important steps to ensure safe and successful peripheral interventions and remains a great challenge. The atherosclerotic burden in some patients may prevent adequate hemostasis and may predispose to vascular access complications. CT angiography offers an overall view of the arterial system and, therefore, may allow for identification of the most appropriate access site for peripheral interventions. In patients with severe, diffuse disease, alternative access sites or techniques (brachial, popliteal, antegrade, bypass grafts) may be utilized. CT angiography also helps in the decision to use distal embolic protection devices, especially in cases where there is heavy atherosclerotic burden, soft or unstable plaque, or thrombus. The choice of an appropriate device for the protection against distal embolization may be guided by vessel anatomy, tortuosity, and landing zone anatomy.

Normal Peripheral Arterial Anatomy

Symptomatic manifestations of arterial diseases may appear in the distal extremities, but may arise from disease which is proximal and remote to the site of symptoms. Since disease anywhere in the arterial tree may produce symptoms, knowledge of normal anatomy of the entire arterial tree is necessary in order to interpret peripheral CT angiography.

Upper Extremities

The normal upper extremity arterial supply begins with the subclavian arteries. The left subclavian artery typically arises directly from the aortic arch. The right subclavian artery most commonly arises from the brachiocephalic or innominate artery. In 15% of patients, the innominate artery also gives of the left common carotid artery – a variant described as bovine arch branching. In these patients, the left common carotid artery commonly arises as the first vessel off of the innominate, although it may arise more cranially as a trifurcation vessel of the innominate artery [21].

Other commonly encountered variants of aberrant origination of the right subclavian artery exist. An aberrant right subclavian artery may either arise from a left sided aortic arch, as the last major vessel from the arch (left arch with aberrant right subclavian artery, Figure 16.6). In the case of a right aortic arch, the left subclavian artery may arise as the

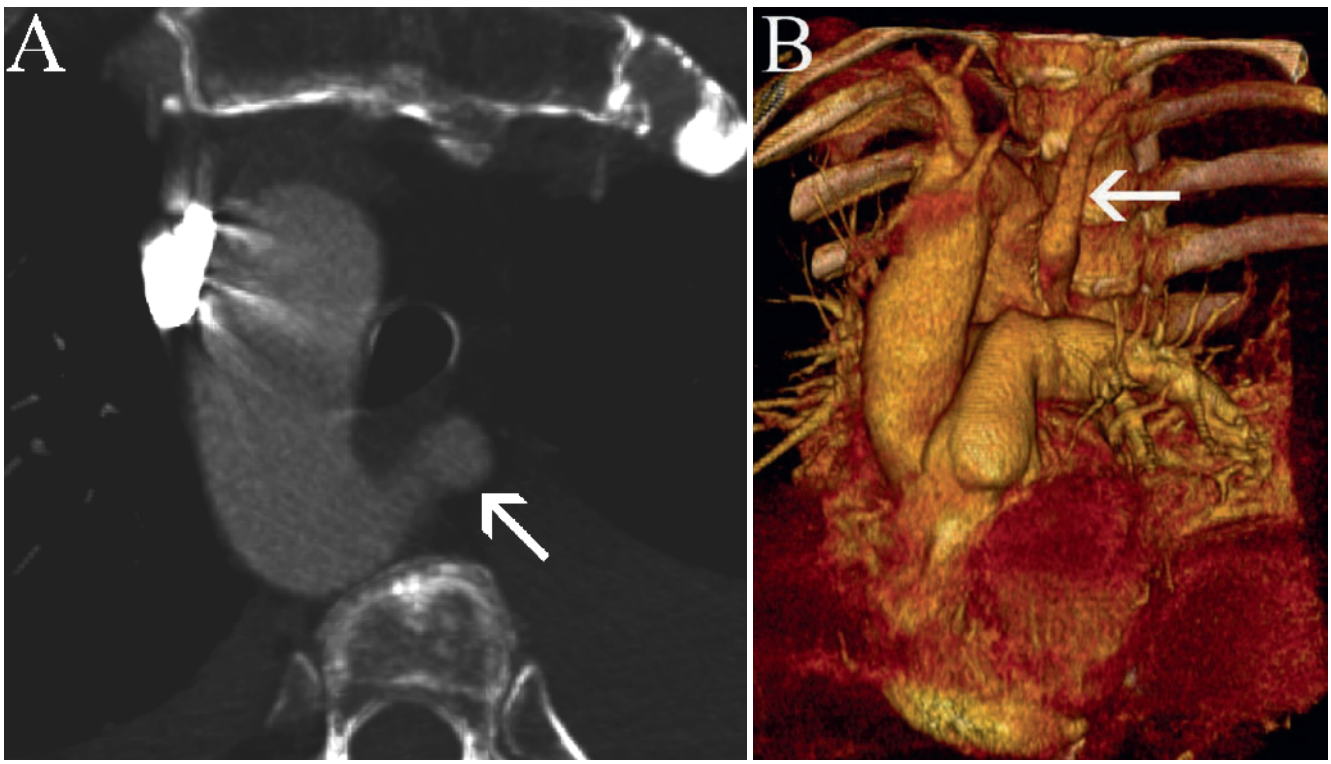

Figure 16.6. On this CT scan of the chest performed to evaluate for an etiology of shortness of breath, a right-sided aortic arch with an aberrant left subclavian artery (*white arrow*) is incidentally noted. This is shown on the transverse view (**a**) and volume rendered (**b**) view.

last major vessel from the arch (right arch with aberrant left subclavian artery). In either case, the aberrant subclavian artery commonly takes a course posterior to the esophagus, and may produce dysphagia. Dysphagia lusoria is commonly used as a term for dysphagia which results from either an aberrant subclavian artery or from a double aortic arch [22]. In addition, an aberrant subclavian artery may arise from a dilated trunk, termed a diverticulum of Kommerel. This is a true aneurysm which likely results from an embryological remnant of a separate, incompletely formed aortic arch. Both the double aortic arch and the right arch with an aberrant left subclavian artery represent vascular rings. In the latter case, the ring is completed by the ligamentum arteriosum. Atherosclerotic complication rates resulting from aberrant subclavian arteries are likely similar to rates of atherosclerotic complications observed in normal arteries.

Anatomically, the subclavian artery is divided into proximal, middle, and distal portions. The proximal portion of the subclavian artery is defined as the portion medial to the anterior scalene muscle. The mid portion of the subclavian artery is located posterior to the anterior scalene muscle and usually contains the most cranial portion of the subclavian arch. The distal portion of the subclavian artery lies lateral to the lateral border of the anterior scalene muscle and ends at the lateral border of the first rib.

The vertebral artery is usually the first vessel that arises from the subclavian artery and most commonly arises from the first portion of the subclavian artery, usually within 1.2–2.5 cm of the vessel origin. The other vessels include the internal mammary artery (Figure 16.7), thyrocervical trunk, and costocervical trunk. These vessels also most commonly arise from the first portion of the subclavian artery and are usually clustered near the medial border of the anterior scalene muscle.

At the lateral border of the first rib, the subclavian artery changes name to become the axillary artery. The axillary artery predominantly feeds the upper chest wall and the proximal portion of the upper extremity. In the case of axillary artery occlusion, collateral flow may be provided through chest wall and scapular collaterals when the axillary artery is occluded proximal to the origin of the subscapular artery. By definition, the axillary artery ends at the lateral border of the teres major, where it changes name to the brachial artery. An important relationship exists between the axillary artery and the brachial plexus, which surrounds the axillary artery.

The brachial artery is the main vessel to the upper extremity. Most commonly, the brachial artery gives off a profunda branch in the upper portion of the upper extremity. Below the elbow, the brachial artery usually bifurcates into a radial artery laterally and an ulnar artery medially. In 15% of patients, the brachial artery gives off the radial artery proximal to the elbow as it courses in the upper arm. There is a close relationship with the median nerve which runs just medial to the brachial artery.

Lower Extremity

The aortic bifurcation most commonly occurs at the level of the L4 vertebral body, although some patients may have an unusually high aortic bifurcation as a normal variant. The common iliac arteries are usually 4–5 cm in length, although the right common iliac artery is usually slightly longer than the left. The common iliac arteries course

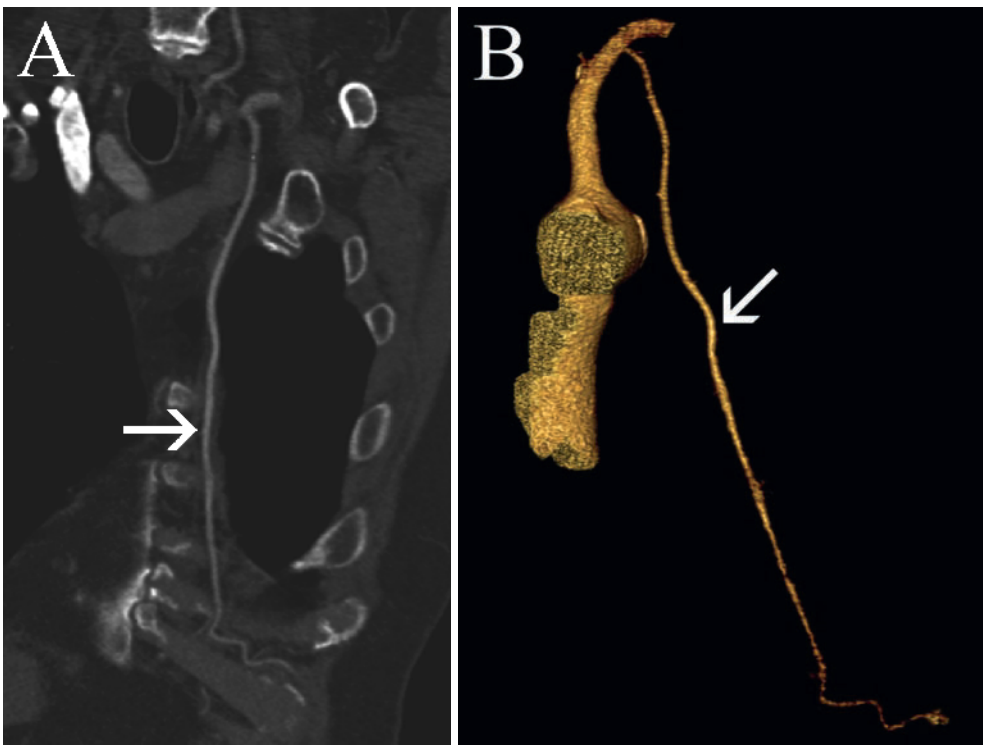

Figure 16.7. CT angiography is useful in demonstrating the internal mammary arteries in patients in whom aortocoronary bypass is planned. The course of the left internal mammary artery (*white arrows*) is demonstrated on the curved plane reformatted view (**a**) and also on the volume rendered view (**b**). In evaluating the subclavian artery and its branches, injection of contrast should be made via the contralateral extremity in order to ensure that streaking from dense venous contrast does not occur.

medial to the psoas muscles and beneath the ureters to the inferior pelvic brim before bifurcating into external and internal branches. Accessory renal arteries may rarely arise from the common iliac arteries, especially when a pelvic or ptotic kidney is present.

The internal iliac artery runs posteriorly from the common iliac artery, and subsequently gives off anterior and posterior divisions. The main branch of the posterior division is the superior gluteal artery, which runs out the sciatic foramen. The posterior division also usually gives rise to an iliolumbar artery, which may be an important source of endoleaks in patients who undergo abdominal aortic aneurysm repair. The anterior division gives off several important branches including the internal pudendal artery and the uterine artery in women. The external iliac artery courses more anteriorly in comparison to the internal iliac artery. At the inguinal ligament, it changes name to become the common femoral artery. Vascular landmarks for the inguinal ligament are the origins of the circumflex iliac artery and inferior epigastric artery.

The common femoral artery, which begins below the inguinal ligament, is a short vessel which usually has a length of 4 cm and gives off the superficial femoral artery and deep femoral artery at approximately the level of the lesser trochanter of the femur. Most commonly, there is also a slightly more lateral branch given off at the same level, which is the circumflex femoral artery. The term "superficial femoral artery" is still used commonly by physicians, whereas anatomists favor the name "femoral artery." There has been some shift in nomenclature among physicians to refer to the femoral artery and drop the descriptor "superficial" because of the accompanying vein. The "superficial" femoral vein, which accompanies the artery, is part of the deep venous system, and, despite its name, it is not part of the superficial venous system. Rarely, this may be a source of confusion when thrombi of the vein are reported.

The femoral artery courses anteromedially in the thigh. In the middle third of the thigh, the femoral artery enters the adductor canal or eponymously, Hunter's canal. This is a frequent site of atherosclerotic disease. At the junction of the middle and lower third of the thigh, the femoral artery exits the adductor canal and changes name to the popliteal artery. The popliteal artery is a common site of several unique diseases including cystic adventitial disease and popliteal artery entrapment syndrome. Knee dislocation injuries may damage the popliteal artery. Around the level of the knee, the popliteal artery gives off medial and lateral genicular branches. These branches may serve as important collaterals for reconstitution of the popliteal artery from profunda to genicular collateral pathways in the setting of femoral artery occlusion.

The popliteal artery continues behind the knee and gives off the anterior tibial artery. In most patients, the anterior tibial artery gives off the dorsalis pedis artery which courses along the dorsal aspect of the foot. The other main branch of the popliteal artery is the tibioperoneal trunk. This divides into the posterior tibial artery and peroneal artery. The peroneal artery runs in the deep compartment of the lower portion of the lower extremity and usually terminates above the ankle. The posterior tibial artery runs posterior to the medial maleolus of the ankle and frequently can be palpated at this point. The plantar arch is an arcade of vessels which may be primarily served by either the dorsalis pedis artery or the posterior tibial artery. The main vessel supplying the plantar arch should be noted and included in CT angiography reports.

Abnormalities and Diseases of the Peripheral Arteries

Vascular Variants

Several variants of normal anatomy have been described, but are uncommon. Moreover, variants which contribute to clinically significant arterial disease are rare. CT has an advantage in demonstrating 3D anatomy of muscular and osseous anatomy in comparison to conventional angiography. As a result, CT is useful in demonstrating relationships between the arterial anatomy and osseous and muscular structures. Some variants may not cause significant vascular pathology. Rarely, for example, the external iliac artery may be absent, and the common femoral artery arises from the internal iliac artery (Figure 16.8). This is, however, not a common variant, and would not be expected to cause clinically significant manifestations of arterial disease [23].

Rarely, the main lower extremity artery may arise from the internal iliac artery, and course posteriorly to the ischial tuberosity. This variant is known as a persistent sciatic artery. The anomalous course of the artery along the ischial tuberosity can result in premature atherosclerotic disease (Figure 16.9) and also in formation of aneurysms (Figure 16.10). Typically occlusion or aneurysm formation occurs where the artery courses behind the ischial tuberosity. This is thought to occur due to repetitive underlying trauma due to impaction of the ischial tuberosity onto the artery [24].

For variants where abnormal muscular anatomy may contribute to pathology, the arterial tree may be better imaged with MRI. MRI has several potential advantages over CCTA, including better resolution of soft tissue structures such as musculature and joints. Non-contrast MR angiography techniques also permit imaging with the extremity in different positions, without the use of ionizing radiation.

Atherosclerotic Disease

Atherosclerosis is by far the most common disease of the peripheral arterial tree [25]. At times, patients may present with concomitant cerebrovascular disease and coronary atherosclerotic disease, although some patients with atherosclerotic disease may present with peripheral ischemia as their initial symptom. In patients with other signs of

Figure 16.8. (**a, b**) An unusual variant is shown in which there is congenital absence of the external iliac artery. The internal iliac artery (*white arrow*) in this case takes a course posteriorly to give off the anterior and posterior divisions, before continuing anteriorly to give off the common femoral artery.

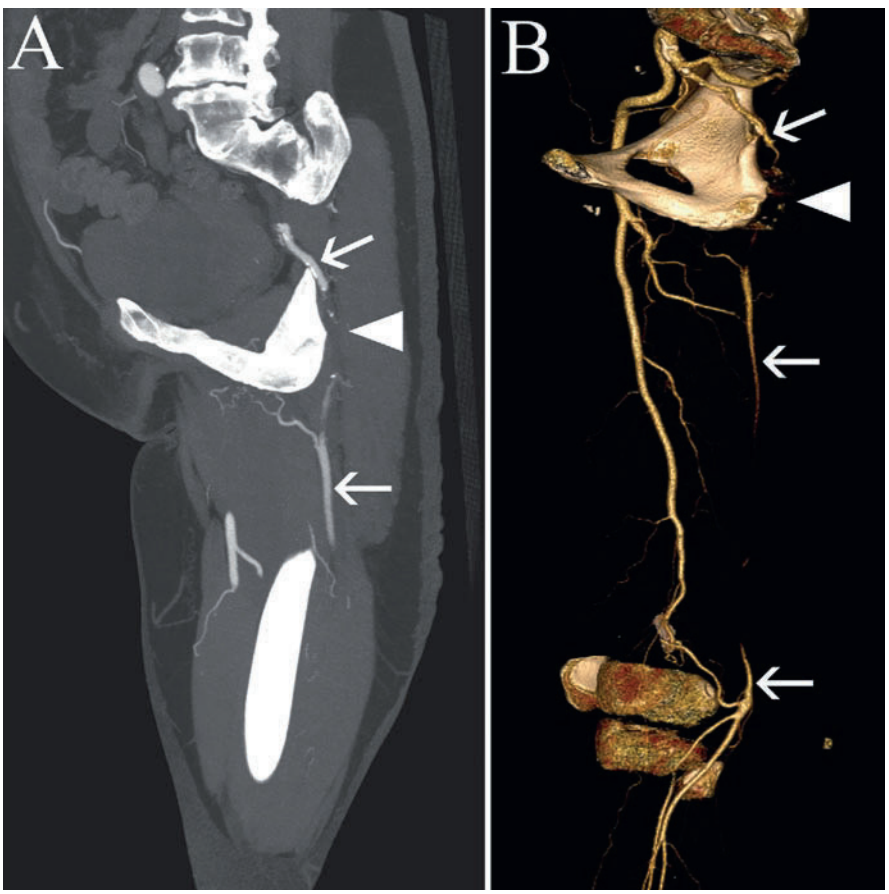

Figure 16.9. (**a, b**) Images of the right lower extremity are shown in a patient with bilateral persistent sciatic arteries. Note that the persistent sciatic artery (*white arrows*) is occluded at the level of the ischial tuberosity (*white arrowhead*). There is also, a second, long segment of probable occlusion of the persistent sciatic artery in the thigh. There is, however, reconstitution of the vessel via large profunda collaterals after both occlusions.

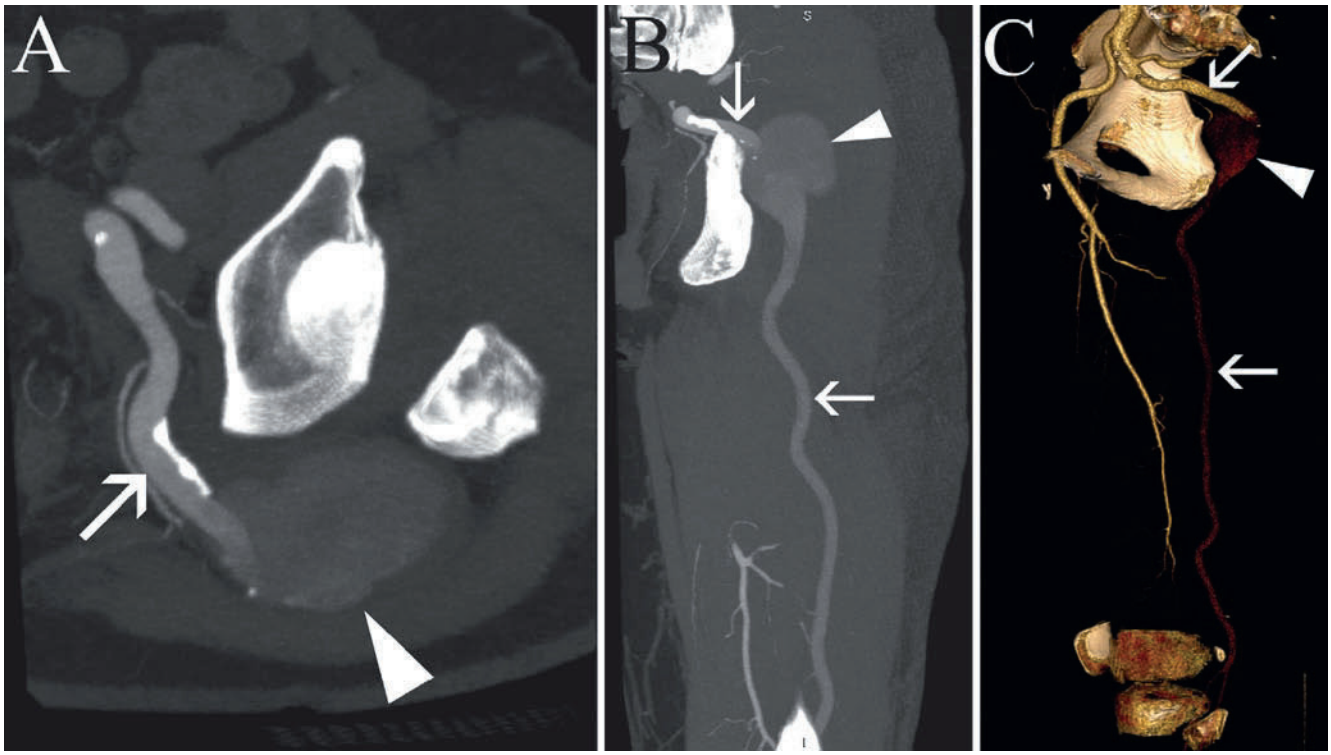

Figure 16.10. (Same patient as in Figure 16.9) (**a–c**) Images of the left lower extremity are shown in a patient with bilateral persistent sciatic arteries (*white arrows*). Note the presence of a large aneurysm extending just above the ischial tuberosity (*white arrowhead*). Note also that the vessel is less well opacified distal to the aneurysm, due to stagnant flow.

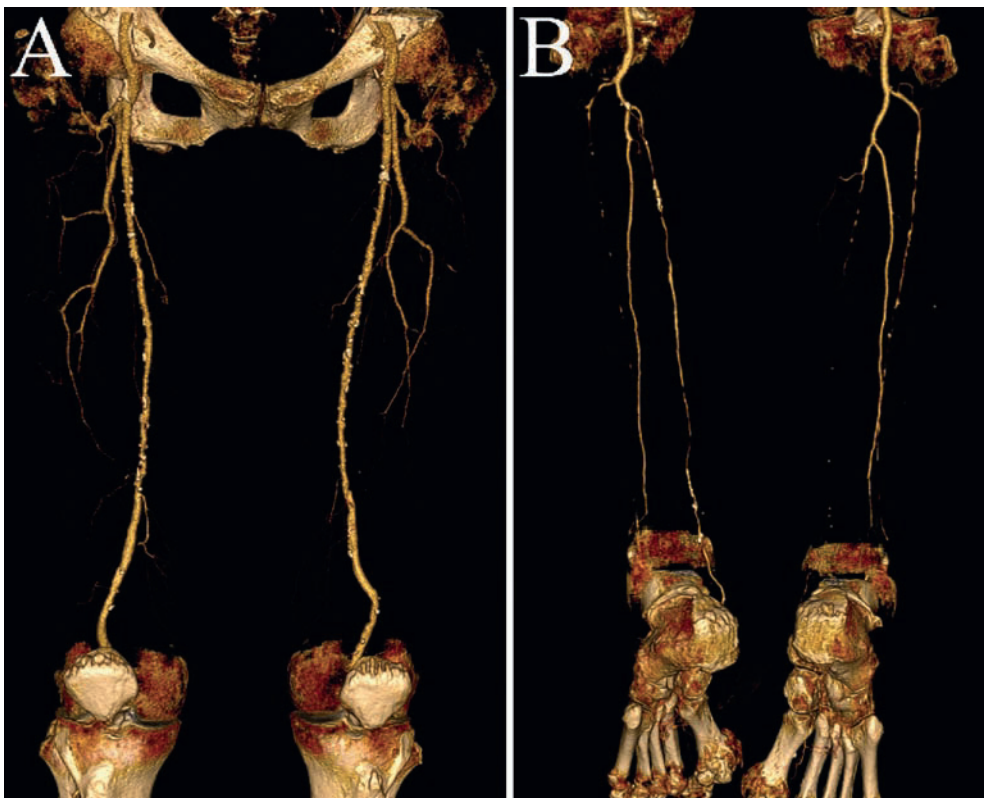

Figure 16.11. (**a, b**) Multifocal atherosclerosis is demonstrated on these volume-rendered views of the lower extremities. The femur, tibia, and fibula have been subtracted from the field of view in order to better demonstrate the arterial anatomy.

atherosclerotic disease, PAD may significantly contribute to worsening morbidity and mortality. Patients with PAD have a four to fivefold increase in risk of myocardial infarction or stroke [26, 27].

Peripheral vascular disease or PAD, also called peripheral artery occlusive disease (PAOD), is a common condition in 10–25% of patients over the age of 55. The incidence increases with age at a rate of 0.3% per year in men aged 40–55 and at

a rate of 1% per year in men over the age of 75. Up to 70–80% of affected individuals are symptomatic, although only a minority of patients will eventually require revascularization. Twenty-five percent of patients with PAD, however, will require some medical or surgical treatment [28, 29].

Peripheral CT angiography demonstrates atherosclerosis at a very early stage in the disease process. Plaques may be calcified or non-calcified, and may not cause stenosis until very late in the disease process (Figure 16.11). Densely calcified atherosclerotic plaques in the peripheral arterial tree may somewhat degrade CT angiography image quality, although this is less of a concern when imaging the extremities compared to the coronary arteries due to the larger caliber of vessels and the lower potential for motion and other artifacts. Low attenuation plaques, likely related to an early phase of plaque evolution, may also be seen [30].

Atherosclerotic plaques may be present throughout the vascular tree. Typically aortic atherosclerotic disease begins in the infrarenal aorta and becomes more severe closer to the aortic bifurcation. A rarer variant in some patients with atherosclerotic disease is the development of arborified, endoaortic calcified plaques, which predominantly protrude into the lumen, and are usually most pronounced in the juxtamesenteric and juxtarenal aorta. This variant has been termed a coral reef aorta (Figure 16.12) [31].

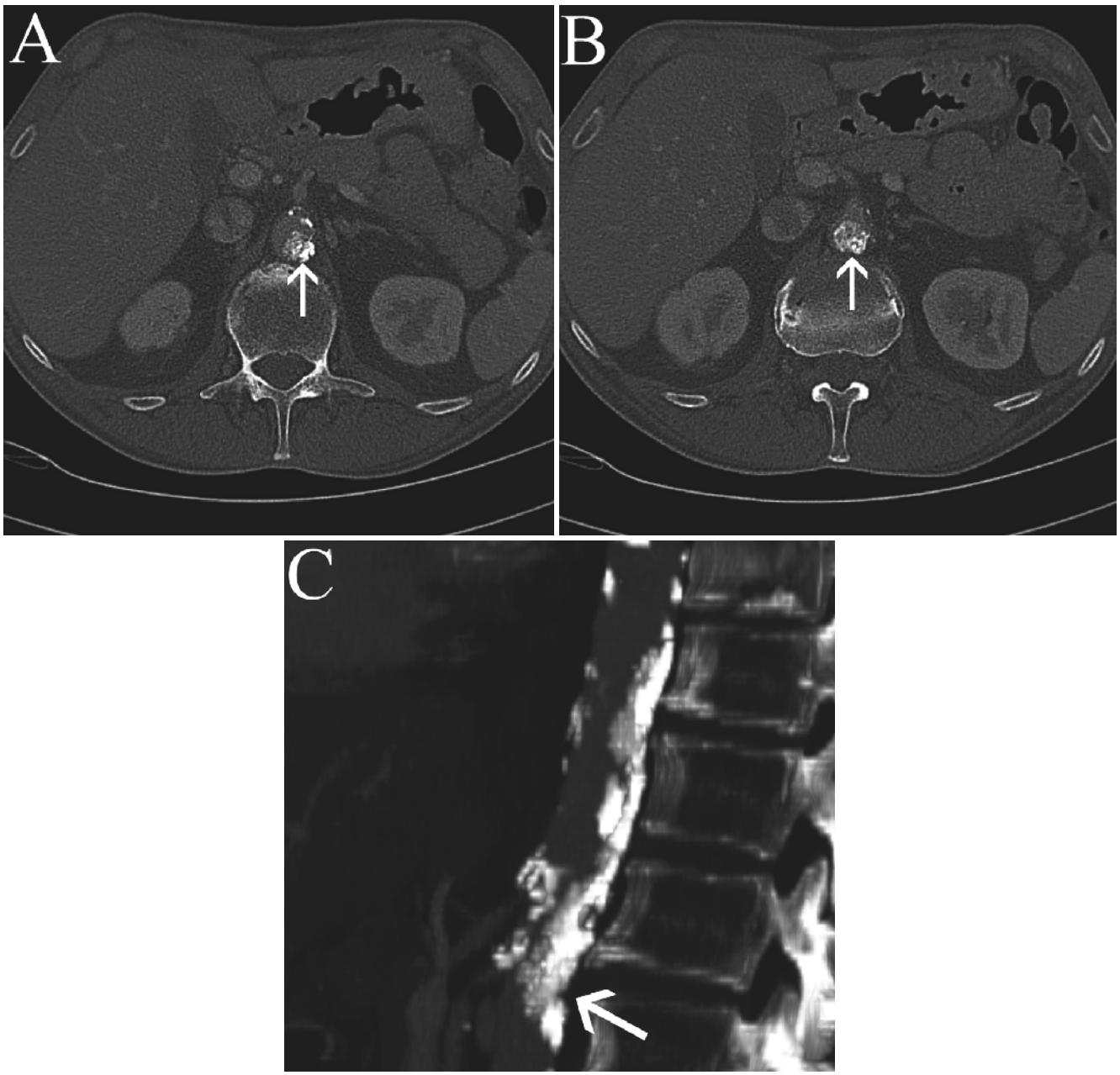

Figure 16.12. Views from a CT angiogram of the abdomen are shown with transverse (**a, b**) and sagittal (**c**) images shown. A coral reef aorta is present with dense endoaortic calcific proliferation. Densely calcified, endoluminal, arborified plaques are present (*white arrows*) in the juxtamesenteric aorta.

Recognition of this variant of atherosclerotic disease is important since patients with endoaortic calcific proliferation are at higher risk for postcatheterization embolic phenomenon. It has been suggested that endovascular interventions which necessitate crossing of the juxtamesenteric aorta should be avoided in patients with a "coral reef aorta." [32, 33]

In the peripheral tree, atherosclerotic disease may be multifocal and consists of mixed attenuation plaques. CT angiography is useful in demonstrating stenoses of 50% or greater, which may contribute to patient symptoms. Specific features of each plaque which should be described include location of lesions, degree of stenosis, and length of plaque. When CT angiography is used for plaque characterization, descriptors for plaque attenuation may be added, with reporting of plaques as calcified, non-calcified, or mixed. Specific criteria for intervention have also been delineated, based on the degree of patient symptoms [34].

Atherosclerotic disease may cause a number of symptoms depending on the site of involvement. Several syndromes have been characterized based on the distribution of atherosclerotic disease. For example, subclavian steal syndrome results from proximal stenosis in the subclavian artery (Figure 16.13). As a result of stenosis, the distal subclavian artery may receive collateral flow from the vertebral arteries. Reversal of flow through the ipsilateral vertebral artery commonly ensues. Patients present with symptoms related to vertebrobasilar insufficiency. These symptoms are commonly worsened during exercise of the upper extremity, which results in increased flow to the extremity and worsened steal. Leriche's syndrome is a constellation of symptoms which results from aortic and bilateral iliac artery disease, including gluteal and lower extremity claudication, penile impotence, and lower extremity atrophy.

Grafts and Stents in the Arterial Tree

In addition to being a noninvasive modality with excellent spatial resolution, CT angiography has several other advantages in the evaluation of the treated vascular system. In comparison to MRI and MR angiography, CT angiography is advantageous for visualization of stents. On MRI, stents may be visualized only as artifacts and the internal lumen may be nonvisualized due to susceptibility effects. Other metallic structures including surgical clips may also induce artifacts on MRI including signal void and failure of fat saturation, whereas artifacts from surgical devices are less significant on CT.

Stents in peripheral arterial structures are typically very well-seen using thick, maximum intensity projection images (Figure 16.14). This allows visualization of stent struts and exclusion of strut fractures. Stents are easily depicted as high attenuation structures, and contrast opacification has no adverse effects on visualization of stents. In the short axis view, stent struts are frequently seen as regularly spaced, hyperattenuating foci at the rim of the artery, commonly in a hexagonal array (Figure 16.15). Because of the relatively high attenuation of stent material, and because of the phenomenon of "blooming" on CT, a very bright stent may appear to be outside the confines of the wall of a vessel. The limitations of stent depiction on coronary CT are less significant in evaluation of the peripheral arterial tree due to the larger internal diameter of stents commonly employed in the peripheral vessels and to the absence of motion and other artifacts which can limit the evaluability of coronary stents.

Graft material is also well-evaluated on CT. Bypass grafts are commonly recognized as long, smooth tubes connected to the native vasculature on 3D, colored, lit projections (Figure 16.16). On axial views, the excluded, unopacified, native lumen is frequently visible. The connections between graft material and lumen may be enlarged and irregular, as

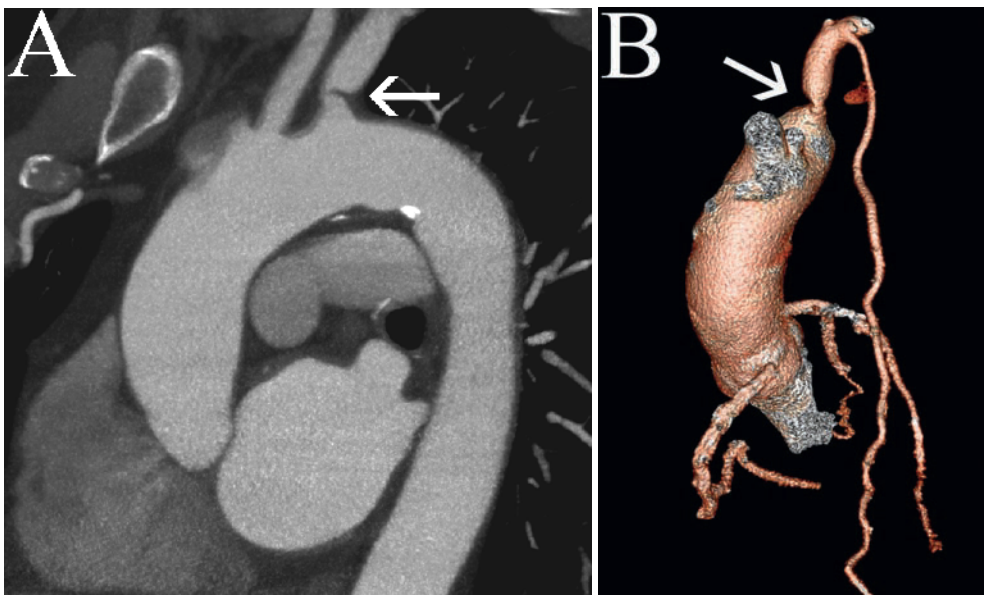

Figure 16.13. Images from a CT angiogram are shown in a patient with known coronary artery disease and concomitant symptoms of subclavian steal. The oblique sagittal (**a**) and volume-rendered (**b**) views show a focal, shelf-like area of narrowing near the origin of the left subclavian artery (*white arrows*). In this case, identification of this stenosis was useful as an explanation of the patient's symptoms. Preoperative identification of subclavian stenosis is also important in patients in whom aortocoronary bypass is planned, as this condition may impede optimal flow through the internal mammary artery.

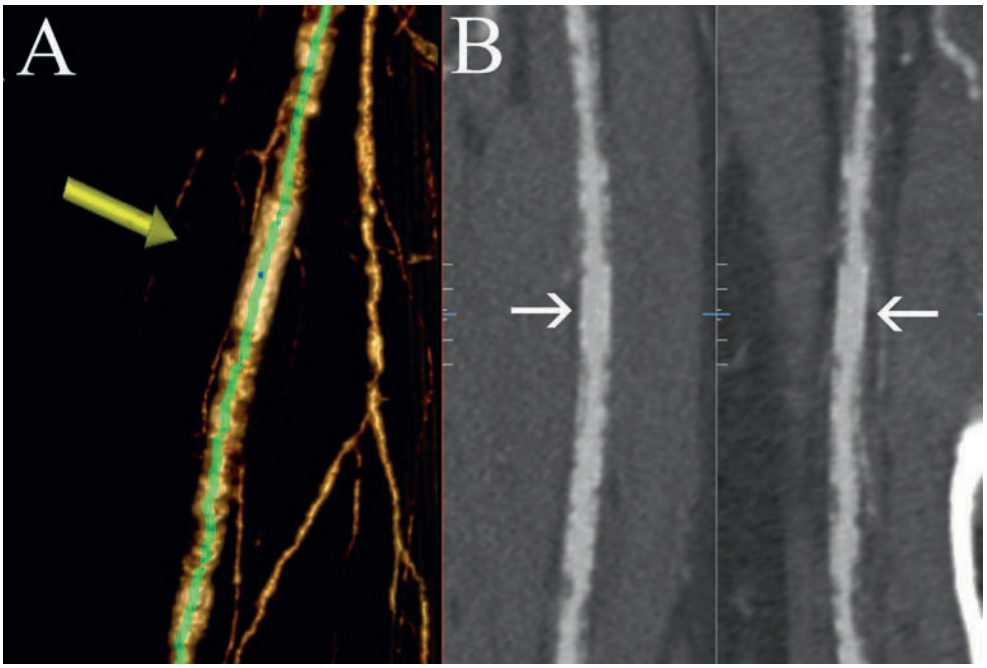

Figure 16.14. Stents are well-depicted on CT angiography. In this case, the stent is seen on the volume rendered view (*yellow arrow*, **a**) and also on the orthogonal, curved plane reformatted views (*white arrows*, **b**).

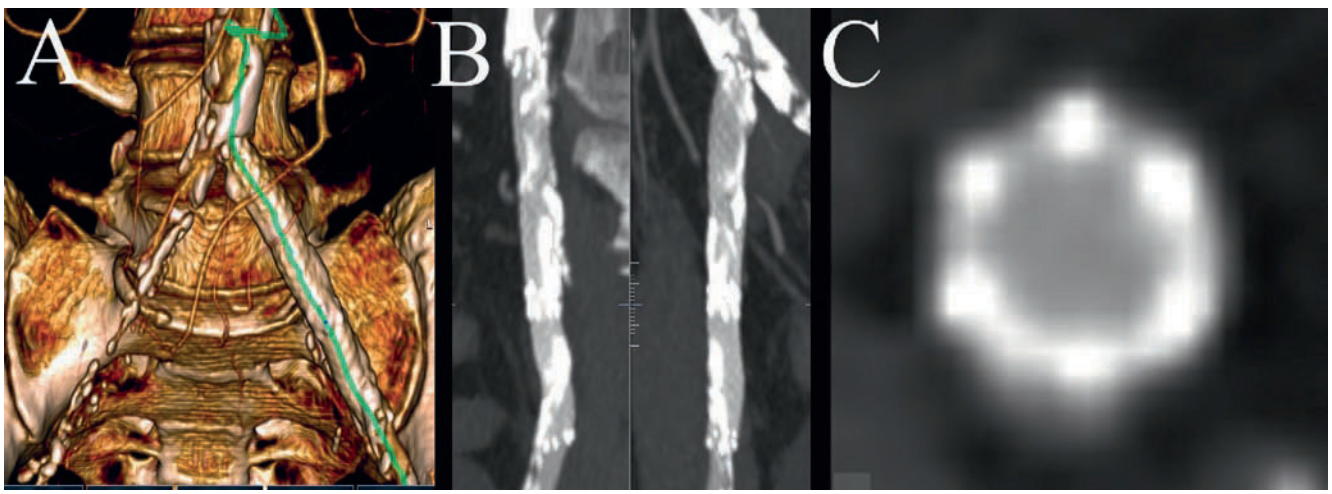

Figure 16.15. A stent is the left common iliac artery is shown. The stent is present on the volume rendered view (**a**) and also on the curved plane reformatted views (**b**). Note that, in the short axis of the vessel (**c**), the stent is seen as a hexagonal array of hyperattenuating struts.

a result of the patch angioplasty frequently performed at anastomoses. Grafts commonly are comprised of either interposed veins or polyfluorotetraethylene (PTFE). In some cases, where increased torsional effects are anticipated and may compromise grafts, re-enforced graft material is commonly employed, and such grafts are typically depicted as corrugated on CT angiography (Figure 16.17).

Trauma

CT angiography as a modality has multiple features that make it ideal for imaging of the arterial tree in the setting of trauma. First, intimal flaps and abnormalities of the wall of the artery are better depicted by CT compared to MR angiography, and may be better seen than on ultrasound. CT angiography is also useful in demonstrating the entire arterial tree in a less time-intensive fashion than ultrasound. Concomitant posttraumatic deformities to the muscles and bones may also be simultaneously demonstrated (Figure 16.18).

Several signs of arterial injury may be present on CT and include vessel nonopacification, abrupt vessel occlusion, pseudoaneurysm formation, intimal flap formation, or arteriovenous fistula. Traumatic injury to vessels may ensue after blunt or penetrating trauma and in association with fractures which may displace vessels [16].

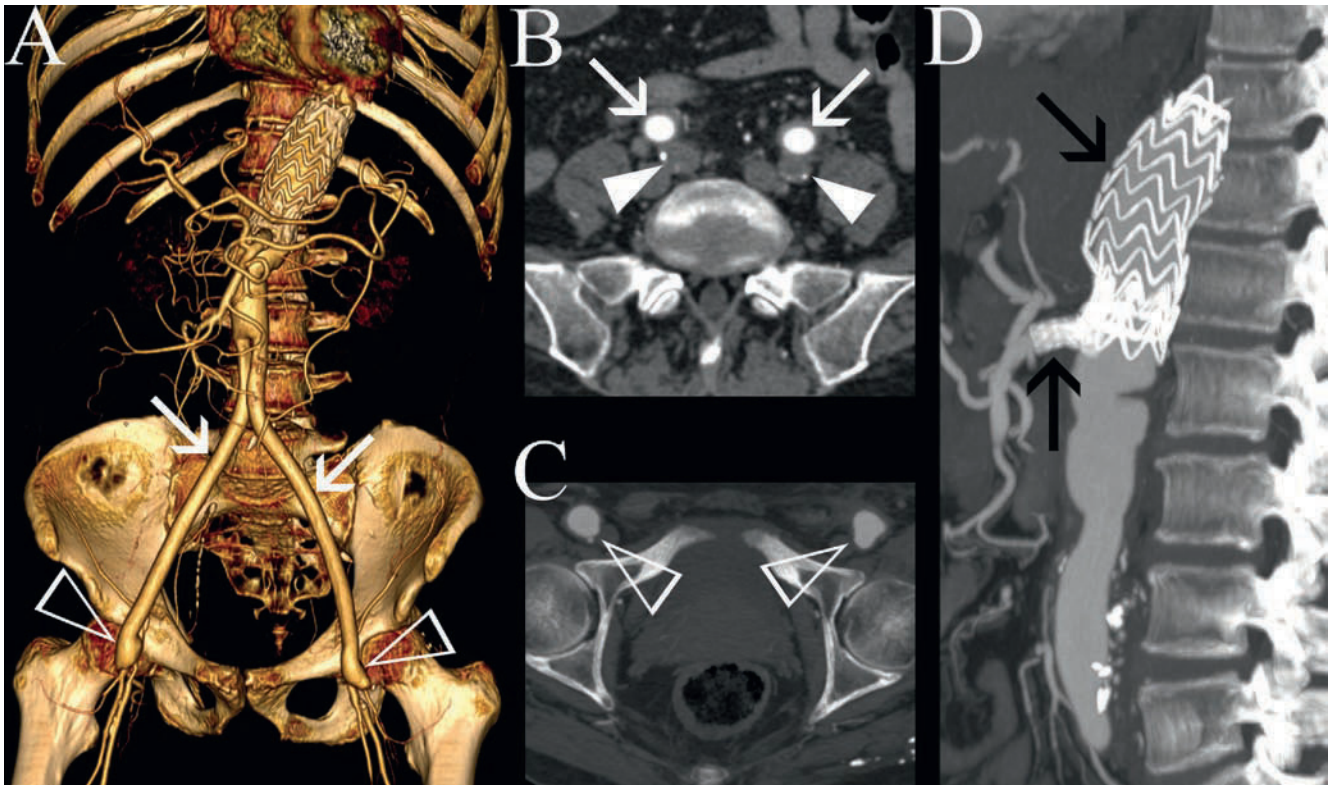

Figure 16.16. Bilateral, aortofemoral bypass grafts are present (*white arrows*) and are seen as unusually smooth appearing structures in the vascular tree. The occluded, native vessels are visualized on the transverse view (**b**, *white arrowheads*), but are not visualized on the volume rendered view (**a**), since the native arteries are not opacified. Enlargement and irregularity may be present at anastomotic sites (*white, open arrowheads*, **c**). Note that the patient also has aortic and celiac stents (*black arrows*, **d**).

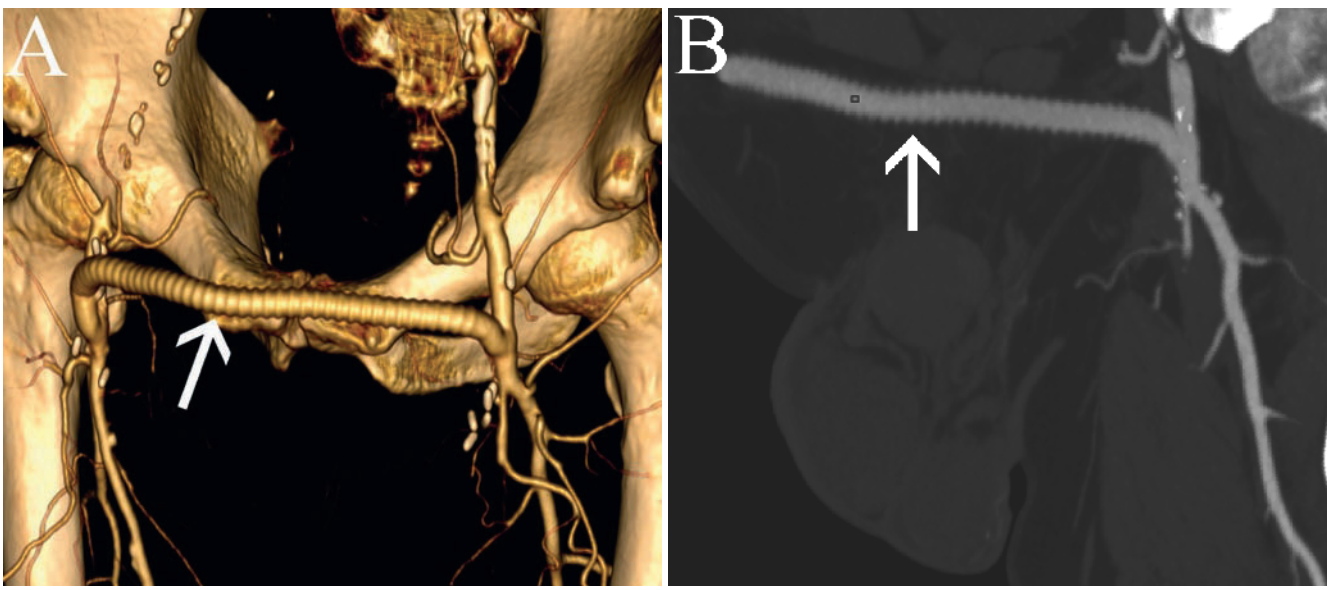

Figure 16.17. A bifemoral bypass graft (*white arrows*) is evident with a typical, corrugated appearance, which is well seen on the volume rendered view (**a**) and the curved planar reformatted view (**b**).

Fibromuscular Dysplasia

Although fibromuscular dysplasia is a common cause of stenosis in the renal or carotid arteries, it is less commonly encountered elsewhere in the peripheral arterial tree. When involving the peripheral arteries, fibromuscular dysplasia most commonly occurs in the external iliac artery, which is the third most common site of fibromuscular dysplasia. As in other parts of the body, the classification system for fibromuscular dysplasia is based on the layer of the artery

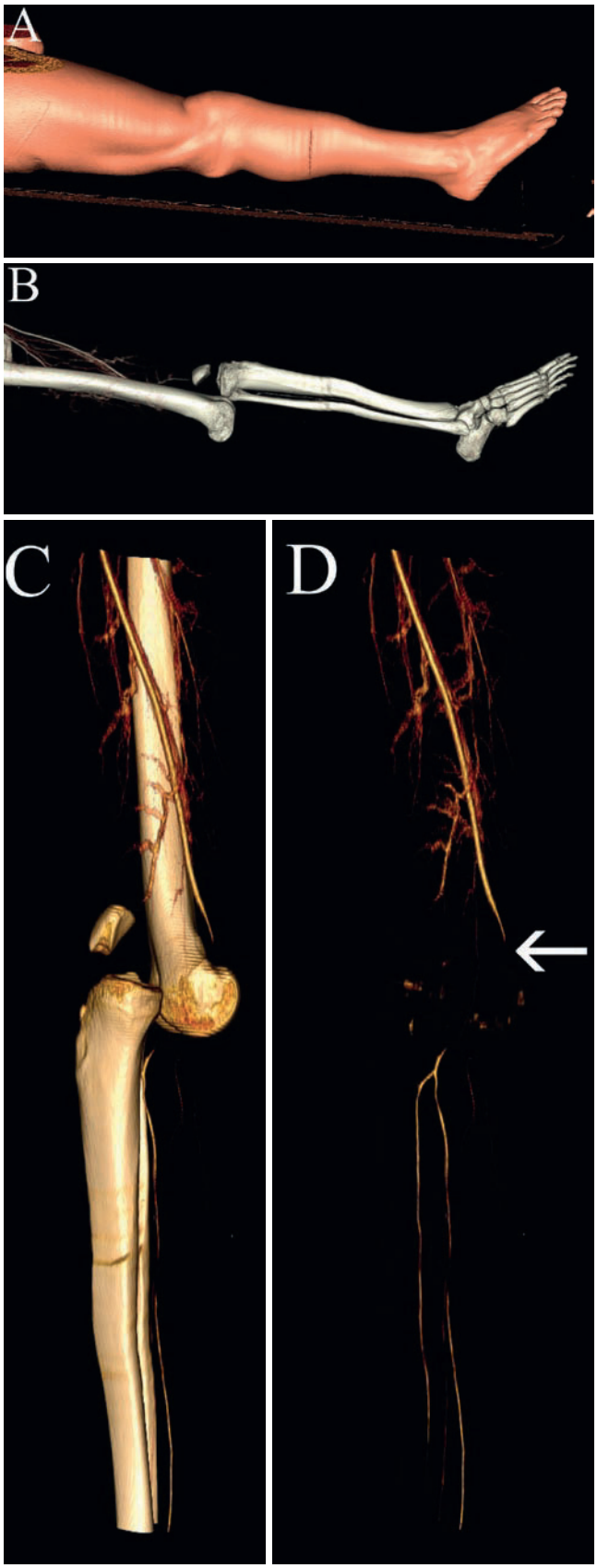

Figure 16.18. CT angiography is useful in the setting of trauma. A surface-rendered view (**a**) shows the deformity in the outer contour of the extremity. CT angiography simultaneously demonstrates osseous structures, demonstrating a dislocation at the knee (**b, c**). The osseous structures may be subtracted, however, in order to better demonstrate the underlying arterial anatomy (**d**). In this case, resultant occlusion of the popliteal artery is also present (*white arrow*, **d**).

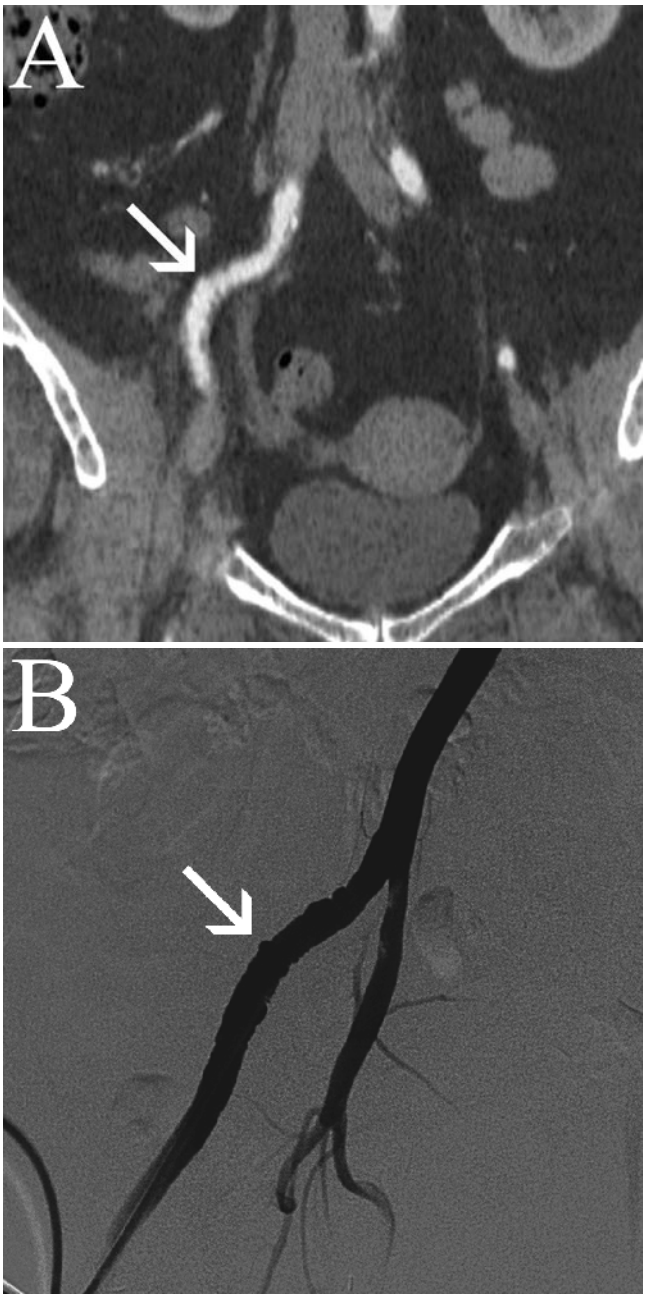

Figure 16.19. Fibromuscular dysplasia is shown in the external iliac artery, which is the third most common site for this entity, following the internal carotid and renal arteries. The classic, beaded appearance of the external iliac artery (*white arrow*) is demonstrated on a reformatted view from the patient's abdominal CT (**a**), but is more clearly demonstrated on the conventional angiography (**b**) due to the higher spatial resolution.

involved, with medial fibroplasia being the most common form. The most typical appearance of fibromuscular dysplasia is apparent beading of the vessel and is due to several, closely approximated web-like areas of narrowing with intervening out-pouchings of the vessel (Figure 16.19) [35]. Other forms of fibromuscular dysplasia may have a variety of appearances [36]. Conventional angiography may have an advantage in demonstrating this entity compared with CT, due to the inherently higher spatial resolution of conventional angiographic images.

Other Diseases of the Systemic Arteries

Cystic adventitial disease is a rare entity, which may affect any artery adjacent to a joint and presents as a smooth narrowing in a patient without atherosclerotic disease. The narrowing is accompanied by cystic structures along the course of the artery. The most common artery affected is the popliteal. MRI is the preferred modality for depicting the cysts which occur along the vessel, although low attenuation cysts are commonly observed on CT [37, 38].

Popliteal artery entrapment syndrome can occur due to a number of abnormalities of the relationship between the popliteal artery and the muscles of the popliteal space. The most common abnormal muscle in this case is the medial head of the gastrocnemius, although a number of abnormal relationships have been described. This syndrome usually causes some degree of fixed narrowing of the popliteal artery, although there is commonly a dynamic component of narrowing usually during plantar flexion or dorsiflexion. Repetitive trauma to the artery as a result of the abnormal relationship to the muscle may cause aneurysmal dilatation, thrombosis, or thromboembolism. MRI is useful in demonstrating popliteal artery entrapment syndrome, where an abnormal muscular slip courses medial to the popliteal artery. In this case, the lower extremity may need to be imaged in several positions including dorsiflexion and plantarflexion [37]. This is also more easily performed with MR angiography since MR angiography is less sensitive to optimal vascular opacification and images can be obtained at different time-points. Also, as non-contrast means of performing MRA become more robust, some vascular pathology may be imaged without the administration of contrast.

Since the common femoral artery is a common site of vascular access, it is subject to a higher rate of iatrogenic complications including chiefly pseudoaneurysm and arteriovenous fistula formation. Because of the focal nature of these complications, and because the portion of the artery involved is frequently very superficial, ultrasound with doppler is usually an adequate modality for the diagnosis and follow-up of femoral artery complications which may ensue after catheterization. On the other hand, when a deep or retroperitoneal hematoma is suspected, CT may be a more robust technique than ultrasound.

Other Modalities for Imaging the Peripheral Arteries

Advancements in imaging of the peripheral arteries have occurred in virtually every modality. As a result, the decision between modalities is more complex. Ankle-brachial index measurement is an adequate means of making an initial diagnosis of PAD [34]. Further evaluation with ultrasound is also useful in demonstrating atherosclerotic disease. Complete evaluation of the entire extremity with ultrasound is, however, very time-intensive and detection of disease is technologist-dependent. Detection and measurement of stenoses with ultrasound is also dependent on technical factors, such as the angle of insonation employed. Evaluation of the pelvic vasculature by ultrasound is much more difficult, and portions of the vasculature may not be easily demonstrated at ultrasound due to overlying bowel gas and osseous structures. In very obese patients, ultrasound may be significantly limited. An additional limitation of ultrasound is in the detection of disease distal to high-grade stenosis.

MRI and MR angiography have several advantages in patients including the ability to perform imaging without contrast. Contrast-independent MR angiography techniques have advanced dramatically, although there is still considerable variability between institutions and MR technology. In particular, the adequacy of particular MR sequences for imaging the arterial tree are dependent on the scanner, sequences, and vendor-specific techniques used. MR angiography has significant limitations in evaluating the post-surgical arterial tree, due to artifacts such as failure of fat saturation and susceptibility artifacts due to surgical clips, stents, or other foreign material. MR angiography is also contraindicated in patients with pacemakers. In the past, MR has been preferable in patients with renal disease due to relatively lower nephrotoxicity of gadolinium, compared to iodinated contrast media. However, the recent recognition of nephrogenic systemic fibrosis as a complication of gadolinium administration has decreased the utility of MR angiography in patients with chronic, severe renal disease [39]. Gadolinium should generally not be given to patients with a creatinine clearance of 30 cc/min or less. In patients who are already dialysis-dependent, iodinated contrast may be a better choice. CT has an advantage to MR angiography in superior spatial resolution and depiction of smaller vessels.

Radiation Dose in Peripheral CT Angiography

The radiation dose in CT angiography remains high and is increasingly a consideration in most CT applications. Concerns of radiation are somewhat mitigated by the fact that there are less radiosensitive tissues in the extremities. When imaging the extremities, breast and abdominal shielding can easily be employed with no compromise to image quality. Shielding significantly decreases scatter and is under-utilized in patients undergoing CT in general, including peripheral CT angiography.

The radiation dose for conventional angiography is, however, much higher than for CT angiography [40]. This is in contradistinction to radiation doses in the heart, where catheterization results in lower radiation doses compared to CT. One study found that for a 16-slice CT scanner, the average radiation dose for a peripheral CT angiogram was 3.0 mSv in men, whereas the radiation dose for a conventional angiogram had an average of 11.0 mSv. Other studies

have shown similar results, with CT angiography generally found to have a fourfold lower radiation dose in comparison with peripheral angiography [41]. Although peripheral CT angiography has a relatively low radiation dose and relatively less radiosensitive tissues are exposed, the risks of radiation should not be taken lightly.

References

1. Rubin GD, Schmidt AJ, Logan LJ, Sofilos MC. Multi-detector row CT angiography of lower extremity arterial inflow and runoff: initial experience. *Radiology*. 2001;221:146–158.
2. Ofer A, Nitecki SS, Linn S, et al. Multidetector CT angiography of peripheral vascular disease: a prospective comparison with intraarterial digital subtraction angiography. *Am J Roentgenol*. 2003;180:719–724.
3. Jakobs TF, Wintersperger BJ, Becker CR. MDCT-imaging of peripheral arterial disease. *Semin Ultrasound CT MR*. 2004;25:145–155.
4. Johnson PT, Pannu HK, Fishman EK. IV contrast infusion for coronary artery CT angiography: literature review and results of a Nationwide Survey. *Am J Roentgenol*. 2009;192:W214–W221.
5. Bae KT, Seeck BA, Hildebolt CF, et al. Contrast enhancement in cardiovascular MDCT: effect of body weight, height, body surface area, body mass index, and obesity. *Am J Roentgenol*. 2008;190:777–784.
6. Fleischmann D. Aorto-popliteal bolus transit time in peripheral CT angiography: can fast acquisition outrun the bolus? *Eur Radiol*. 2003;13:S268.
7. Heuschmid M, Krieger A, Beierlein W, et al. Assessment of peripheral arterial occlusive disease: comparison of multislice-CT angiography (MS-CTA) and intraarterial digital subtraction angiography (IA-DSA). *Eur J Med Res*. 2003;8:389–396.
8. Cademartiri F, Mollet NR, Van der Lugt A, et al. Intravenous contrast material administration at helical 16–detector row CT coronary angiography: effect of iodine concentration on vascular attenuation. *Radiology*. 2005;236:661–665.
9. Orlandini FA, Boini S, Iochum-Duchamps S, et al. Assessment of the use of a saline chaser to reduce the volume of contrast medium in abdominal CT. *Am J Roentgenol*. 2006;187:511–515.
10. Cademartiri F, Mollet NR, Van der Lugt A, et al. Non-invasive 16-row multislice CT coronary angiography: usefulness of saline chaser. *Eur Radiol*. 2004;14(2):178–183.
11. Becker CR, Wintersperger B, Jakobs TF. Multi-detector-row CT angiography of peripheral arteries. *Semin Ultrasound CT MR*. 2003; 24:268–279.
12. Fleischmann D. Use of high concentration contrast media: principles and rationale – vascular district. *Eur J Radiol*. 2003;45:S88–S93.
13. Miller-Thomas MM, West OC, Cohen AM. Diagnosing traumatic arterial injury in the extremities with CT angiography: pearls and pitfalls. *Radiographics*. 2005;25:S133–S142.
14. Lawrence JA, Kim D, Kent KC, et al. Lower extremity spiral CT angiography versus catheter angiography. *Radiology*. 1995;194:903–908.
15. Rieker O, Duber C, Schmiedt W, et al. Prospective comparison of CT angiography of the legs with intraarterial digital subtraction angiography. *AJR Am J Roentgenol*. 1996;166:269–276.
16. Otah KE, Takase K, Igarashi K, et al. MDCT compared with digital subtraction angiography for assessment of lower extremity arterial occlusive disease: importance of reviewing cross-sectional images. *AJR Am J Roentgenol*. 2004;182:201–209.
17. Willman JK, Baumert T, Chandler P. Aortoiliac and lower extremity assessed with 16 detector row CT angiography respective comparison with distal subtraction angiography. *Radiology*. 2005;236:1083–1093.
18. Shareghi S, Gopal A, Gul K, et al. Diagnostic accuracy of 64 multidetector computed tomographic angiography in peripheral vascular disease. *Catheter Cardiovasc Interv*. 2010;75(1):23–31.
19. Fishman EK, Ney DR, Heath DG, et al. Volume rendering versus maximum intensity projection in CT angiography: what works best, when, and why. *Radiographics*. 2006;26:905–922.
20. Shammas MW, Lemke JH, Dipple EG. In-hospital complications of peripheral vascular interventions using fractionated heparin as the primary anticoagulant. *J Invasive Cardiol*. 2003;15:242–246.
21. Lippert H, Pabst R. Aortic arch. In: Lippert H (Ed.), *Arterial Variations in Man: Classification and Frequency*. Munich, Germany: JF Bergmann; 1985:3–10.
22. Janssen M, Baggen MGA, Veen HF, et al. Dysphagia lusoria: clinical aspects, manometric findings, diagnosis, and therapy. *Am J Gastroenterol*. 2000;95:1411–1416.
23. Koyama T, Tadanori T, Kitanaka Y, et al. Congenital anomaly of the external iliac artery: a case report. *J Vasc Surg*. 2003;37(3):683–685.
24. Brantley SK, Rigdon EE, Raju S. Persistent sciatic artery: embryology, pathology, and treatment. *J Vasc Surg*. 1993;18(2):242–248.
25. Mesurolle B, Qanadli SD, El Hajjam M, Goeau-Brissonniere OA, Mignon F, Lacombe P. Occlusive arterial disease of abdominal aorta and lower extremities: comparison of helical CT angiography with transcatheter angiography. *Clin Imaging*. 2004;28:252–260.
26. Ness J, Aronow WS. Prevalence of coexistence of coronary artery disease, ischemic stroke, and peripheral arterial disease in older persons, mean age 80 years, in an academic hospital-based geriatrics practice. Brief reports. *J Am Geriatr Soc*. 1999;47(10): 1255–1256.
27. Newman AB, Shemanski L, Manolio TA, et al. Ankle-arm index as a predictor of cardiovascular disease and mortality in the cardiovascular health study. *Arterioscler Thromb Vasc Biol*. 1999;19: 538–545.
28. "Peripheral arterial disease prevention and prevalence". Peripheral Arterial Disease; 1 Nov 2007. Available at: http://www.3-rx.com/ab/more/peripheral-arterial-disease-prevention-and-prevalence/. Retrieved on 03.09.09.
29. Sharrett AR. "Peripheral arterial disease prevalence". Peripheral Arterial Disease; 21 Sep 2007. http://www.health.am/vein/more/peripheral-arterial-disease-prevalence/. Retrieved on 03.09.09.
30. Cordeiro M, Lima J. Atherosclerotic plaque characterization by multidetector row computed tomography angiography. *J Am Coll Cardiol*. 2006;47(8):C40–C47.
31. Rosenberg GD, Killewich LA. Case report: blue toe syndrome from a "coral reef" aorta. *Ann Vasc Surg*. 1995;9(6):561–564.
32. Levien LJ, Veller MG. Popliteal artery entrapment syndrome: more common than previously recognized. *J Vasc Surg*. 1999;30(4):587–598.
33. Qvarfordt PG, Reilly LM, Sedwitz MM, Ehrenfeld WK, Stoney RJ. "Coral reef" atherosclerosis of the suprarenal aorta: a unique clinical entity. *J Vasc Surg*. 1984;1(6):903–909.
34. Hirsch AT, Haskal ZJ, Hertzer NR, et al. ACC/AHA guidelines for the management of patients with peripheral arterial disease (lower extremity, renal, mesenteric, and abdominal aortic). *J Vasc Interv Radiol*. 2006;17(9):1383–1398.
35. Walter JF, Stanley JC, Mehigan JT, et al. External iliac artery fibrodysplasia. *Am J Roentgenol*. 1978;31(1):125–128.
36. Sauer L, Reilly LM, Goldstone J, et al. Clinical spectrum of symptomatic external iliac fibromuscular dysplasia. *J Vasc Surg*. 1990;12(4):488-495; discussion 495–496.
37. Elias DA, White LM, Rubenstein JD, et al. Pictorial essay, clinical evaluation and MR imaging features of popliteal artery entrapment and cystic adventitial disease. *Am J Roentgenol*. 2003;180:627–632.
38. Tsolakis IA, Walvatne CS. Cystic adventitial disease of the popliteal artery: diagnosis and treatment. *Eur J Vasc Endovasc Surg*. 1998;15(3): 188–194.
39. Sadowski EA, Bennett LK, Chan MR, et al. Nephrogenic systemic fibrosis: risk factors and incidence estimation. *Radiology*. 2007; 243:148–157.
40. Kocinaja D, Cioppaa AA, Ambrosinia GT, et al. Radiation dose exposure during cardiac and peripheral arteries catheterization. *Int J Cardiol*. 2006;113(2):283–284.
41. Martin ML, Tay KH, Borys F, et al. Multidetector CT angiography of the aortoiliac system and lower extremities: a prospective comparison with digital subtraction angiography. *Am J Roentgenol*. 2003; 180:1085–1091.

17

Aortic, Renal, and Carotid CT Angiography

Matthew J. Budoff and Mohit Gupta

Introduction

Computed tomographic angiography of other vascular beds is significantly easier to perform and interpret than coronary studies. There is no cardiac motion to contend with, so gating is most often not necessary. The exception is the ascending aorta, where pseudodissections (an appearance of a dissection caused by motion of the aortic root – Figure 17.1) have plagued earlier studies with single slice CT, due to motion artifacts [1]. Non-gated modes allow for very fast acquisition, and interpretation is significantly less complicated. Without ECG gating or breath-holding, artifacts, such as misregistration, do not occur, improving image quality compared to cardiac studies. Most of the large vessels of interest (carotid, renal, mesenteric) have significantly larger diameters than those of coronary arteries, as well as less tortuous courses. Renal and carotid arteries are usually straight structures, so reconstructions are significantly less complicated than coronary imaging. Also, due to the increased speed of newer systems (electron beam tomography (EBT) and 16+ row MDCT), venous enhancement is less common, so it is easier to see the arteries without superimposed contrast-filled structures (venous contamination). This is another reason why CT is most often superior to magnetic resonance imaging in these other vascular beds. Of course, the requirements of radiation (more significant for carotid imaging due to radiation-sensitive organs such as thyroid and orbits) and contrast (more significant for renal artery imaging due to the frequent coexistence of renal insufficiency and renal artery stenosis) make magnetic resonance more attractive for selective cases. In regard to the aorta, CT angiography can diagnose aneurysm, dissection, and wall abnormalities such as ulceration, calcification, or thrombus throughout the full length of the aorta as well as involvement of branch vessels.

Disease of the aorta or great vessels can present with a broad clinical spectrum of symptoms and signs. The accepted diagnostic gold standard, selective digital subtraction angiography, is now being challenged by state-of-the-art CT angiography (CTA) and MR angiography (MRA). Currently, in many centers, cross-sectional imaging modalities are being used as the first line of diagnosis to evaluate the vascular system, and conventional angiography is reserved for therapeutic intervention.

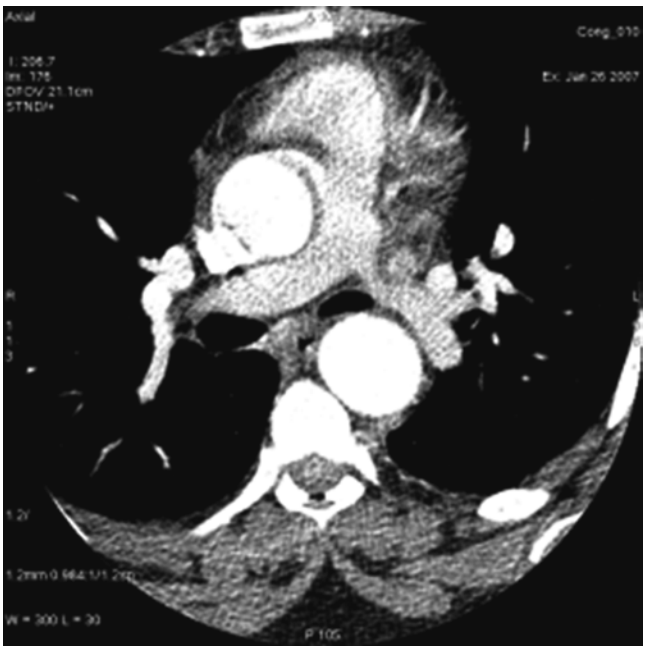

Figure 17.1. Axial view of pseudo-dissection of aorta, caused by motion artifact in an ungated computed tomography (CT) scan of the chest.

Principles of Imaging

In aortic imaging, the volume coverage capabilities of MDCT come to full use without having to compromise on resolution or detail [2, 3]. With the current configuration of 64-row (or greater) CT scanners, the entire abdominal aorta and the iliac arteries can be covered within seconds and with isotropic resolution (Chap. 1). Interrogation of

the dataset can now be made in the anteroposterior (coronal) and lateral (sagittal) planes, which has been the convention with invasive angiography.

Larger collimation (more detectors) reduces contrast, as the imaging territory is covered in a shorter period of time. With up to 320 detectors, volume coverage per rotation is as great as 160 mm. The typical distance needed for the abdominal aorta is on the order of 400 mm, so two to three rotations would cover the entire abdomen. With rotation speeds <500 ms, that could be accomplished in 1–2 s. There is no ECG gating (therefore no registration or collimation issues), and contrast requirements are minimal (30–40 cc per study). Another technique to minimize contrast is use of saline to flush the contrast through the system (Chap. 2). The saline chaser offers two significant benefits with CTA imaging. One is that the contrast is forced from the tubing and extremity veins into the central circulation, allowing for a reduction in the total dose of contrast. A second benefit is that the contrast sitting in the vein during imaging can cause partial volume (beam hardening) artifacts. Moving the contrast out of the venous system is important for cardiac imaging (where the scatter from the superior vena cava can cause artifacts in the right atrium and right coronary artery), carotid imaging (obscuring the proximal brachiocephalic artery or carotid base), and pulmonary imaging. With fast imaging, the venous circulation does not fill, reducing venous contamination (large vein obscuring smaller arteries), which could be problematic in renal beds and runoff studies, often seen with MRI.

CT Technique

Understanding the principles of CTA techniques is essential to acquire diagnostic images consistently. This section reviews current CTA methods used in the evaluation of great vessels. The following broad approach is a guide to CT scan acquisition for various scanners. For peripheral imaging, where ECG gating is not required, 16–320 slice scanners are more than adequate to image the entire volume. Also, there is not the need for speed (temporal resolution or rotation speed) that is required for cardiac work.

1. Intravenous injection of 35–70 mL of a nonionic contrast agent (300–370 mg I/mL), decreasing with scanners with higher numbers of detectors.
2. Monophasic or biphasic injection rate: most commonly a monophasic injection at 4 mL/s (followed by a saline bolus). Three phase injections (pure contrast, followed by mixed contrast saline, followed by pure saline) are more important and common with cardiac applications.
3. Scan delay determined by test injection (10 mL at 4 mL/s) or by automated triggering (to achieve imaging to coincide with contrast arrival in the aortic root close to the area of interest). The scan delay should be determined near the start of the section you are imaging (transverse aorta for carotids, abdominal aorta for renals or runoffs).
4. Pitch:
   - *For 16-detector MDCT*: 16 × 0.625 mm detector configuration with 1.25 mm reconstruction thickness and pitch = 1.7 (table speed 17.5 mm/rotation divided by 10 mm detector coverage (16 × 0.625 = 10 mm)), reconstructed retrospectively with 0.37 mm interval for 3D and MPR
   - *For 64-detector MDCT*: 64 × 0.625 mm detector configuration with 0.625–1.25 mm reconstruction thickness and pitch = 1(moving the table 40 mm and covering 40 mm with each rotation) up to a pitch of 1.375 (table speed 55 mm/rotation divided by 40 mm detector width), reconstructed retrospectively with 0.3 mm interval for 3D and MPR. (The 40 mm of detector width coverage per rotation used is currently available in the GE and Phillips 64 systems. Siemens single or dual source has 19.2–38.4 mm of collimation, increasing with Philips 256 (128 detectors of 0.625 mm allowing 80 mm of coverage per rotation, and the Toshiba 320 allows 160 mm of coverage per rotation).

Thus, large areas can be scanned with minimal contrast use. The most common protocols employed increase the image acquisition time from 100 ms per image to 200–300 ms per image, to improve tissue penetration and reduce image noise. Still, at most 50–60 mL of contrast is all that is necessary to complete a thoracic and abdominal aortic study.

Aortic Imaging

The speed and ease of modern CTA make it the technique of choice for diagnosing chronic and acute aortic pathologic findings such as intramural hematoma, aneurysm, traumatic injuries, atherosclerosis, and dissection (Figure 17.2). With the current configuration of 64-row CT scanners, the entire abdominal aorta and the iliac arteries can be covered with isotropic resolution. Moreover, the high scan speed allows substantial reduction of the amount of contrast material used in earlier studies, hence reducing the adverse effects.

Aortic Dissection

The superior temporal resolution of current MDCT systems significantly improves imaging of the aorta, because motion artifacts are eliminated in the ascending aorta. CT is often considered a superior method over other imaging methods for identification of aortic dissection, as the intimal flap is usually well delineated, even in branches of the aorta. The 3D nature and the ability to see the outer wall, false lumen, and presence of clot make this technique superior to even invasive angiography for evaluation of dissection (Figure 17.3). The extent of the dissection including the proximal entry and distal re-entry sites, involvement of adjacent branch vessels, and potential comprise of the true lumen are thoroughly

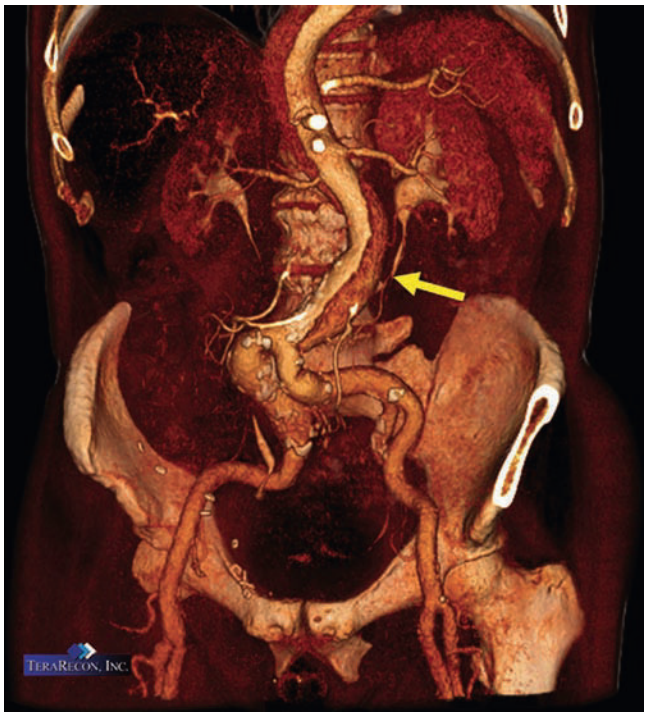

Figure 17.2. A volume-rendered image depicting an aortic dissection involving the abdominal aorta (*arrow*), starting below the renal arteries and ending prior to the iliac arteries (courtesy of TeraRecon, Inc.).

Figure 17.3. Spiral aortic dissection seen on a sagittal view of a gated 64-multidetector computed tomography (MDCT) cardiac scan.

evaluated. The ability to visualize the great vessels into the transverse aorta, neck, and arms makes CT significantly more robust than transthoracic and transesophageal echocardiographic imaging and significantly better tolerated by patients. Transthoracic echocardiography visualizes the aortic root well, but is poor at imaging the mid-ascending and descending thoracic aorta. Transesophageal echocardiography is minimally invasive and but does not image the distal ascending thoracic aorta or arch well. Because imaging protocols for MDCT can be performed in under 10 min (significantly shorter than MR or transesophageal echocardiography), even unstable patients can be evaluated and triaged quickly. With use of flow modes (usually used for timing of contrast), assessing luminal flow in the true and false lumens is possible. Simultaneous evaluation of the coronary arteries and pulmonary arteries (triple rule out) can be accomplished with cardiac gating applied.

Thoracic Imaging

Diseases of the thoracic aorta present a diagnostic challenge. Many aortic conditions, such as aneurysms, typically cause no symptoms and often go clinically unrecognized until a life threatening complication occurs. CT is the primary means of imaging the lung, thoracic trauma (blunt and penetrating), aneurysms, and aortic dissections [4]. CT is playing an increasingly important role in the diagnosis and management of thoracic aortic pathology [5, 6]. Once aortic disease is detected, a comprehensive evaluation of the entire thoracic aorta is indicated to demonstrate the maximal aortic diameter and to detect associated disease in other segments of the aorta. In the situation of an acute life-threatening event, CT can provide extensive information concerning the heart, aorta, and great vessels with a single scan protocol (Figure 17.4). In addition, during the same examination, the brain and spinal canal can be evaluated, if necessary. The entire global CT examination (head, cervical spine, chest, abdomen, and pelvis) can be completed on modern MDCT systems with scan times of 20 s and exam times that are <15 min [7].

Thoracic aortic imaging is the one area where gating the cardiac cycle (similar to CTA applications) is important [8]. The reduction in motion artifact provided by ECG gating is especially relevant to axial data from the ascending aorta. The evaluation of aneurysms of the ascending thoracic aorta and the assessment of possible type A aortic dissection is improved with this methodology due to effective elimination of motion artifacts [9] (Figure 17.1). Moreover, the possibility of applying ECG-controlled X-ray tube dose modulation is an authentic step forward for reducing radiation exposure rates.

Comparison to Other Methods

Although MRI and transesophageal echocardiography can provide exquisite and unique information, the robust nature of CT often makes it the imaging modality of choice. Advantages are the ability to image the entire aorta and beyond, demonstration of surrounding structures and organs, quantitative measures of aneurysm size and location, and a rapid examination time. Limitations are the negative effects of iodinated contrast on renal function,

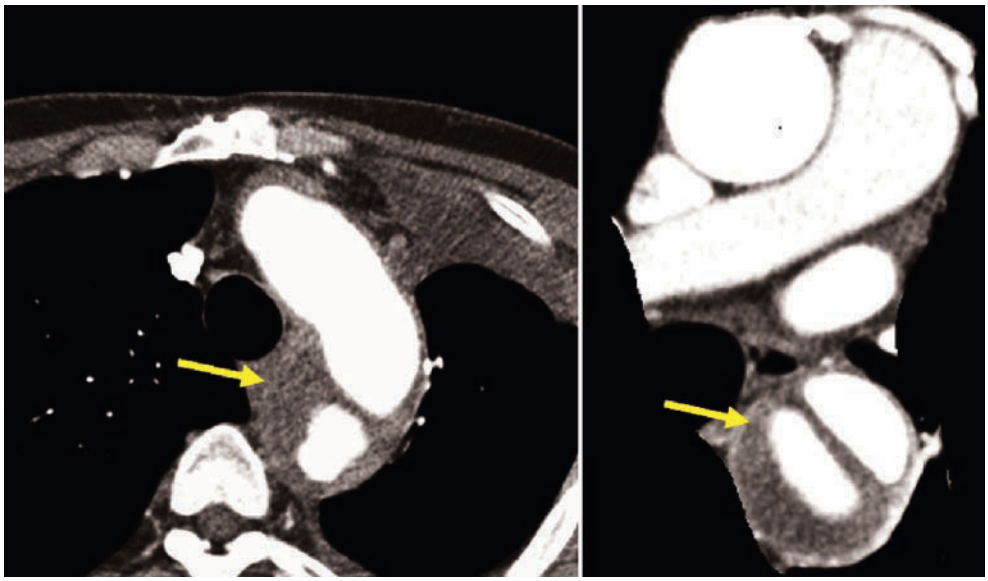

Figure 17.4. Thoracic aortic dissection extending into the transverse aorta (*left*) and descending thoracic aorta (*right*). The intramural thrombus is easily identified by the arrow.

the rare adverse reactions to iodinated contrast, and the inability to directly measure blood flow (useful to determine true and false lumens). A current MDCT protocol for CT angiography provides high-resolution arterial phase images from the thoracic inlet to the femoral arteries. This coverage incorporates the entire aorta, as well as the organs of the chest, abdomen, and pelvis. Beyond classifying dissections as involving the ascending (Stanford type A) or descending (type B), CT can demonstrate associated findings critical to patient care such as mediastinal hematoma, pericardial effusions, pseudoaneurysm formation, and active extravasation of contrast from the aorta. Quantitative measurement of aneurysm size, location, and relation to branch vessels can be used for planning operative or intravascular repair and for monitoring post-procedure anatomy. The necessity for precise and quantitative measurements with CT has become more critical with the continued advancements in endovascular repair with stent-grafts [10, 11].

CT angiography is less operator-dependent than transesophageal echocardiography, allows complete organ visualization, and is faster and more convenient for patients than magnetic resonance imaging and digital subtraction angiography. The latter issues are especially important with severely ill patients. In the setting of blunt and penetrating trauma, CT of the chest can be extremely useful in diagnosis and as an aid to surgical management [12]. Another major advantage over MR is that these examinations are performed in critically ill patients who may require mechanical ventilation, invasive monitoring, intravenous infusion pumps, and cardiac pacing.

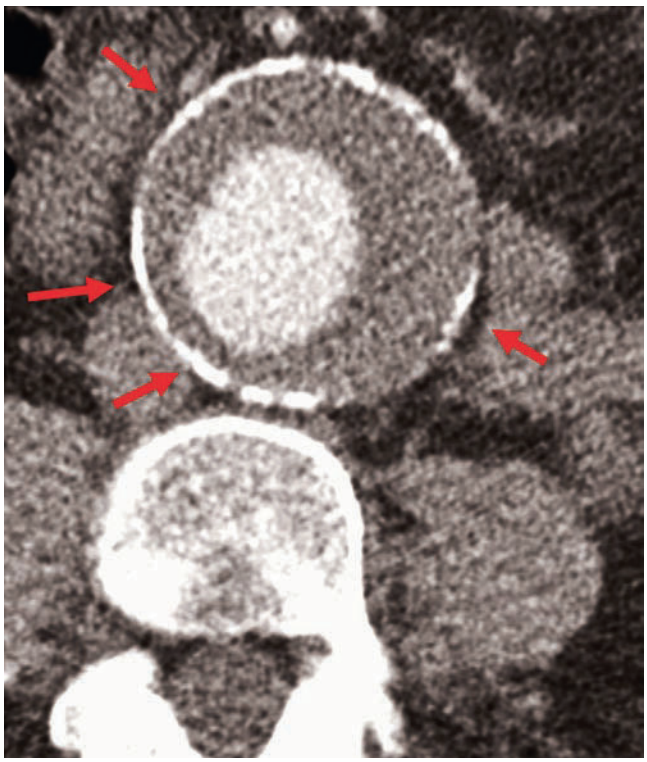

Figure 17.5. Aortic wall calcification (*arrow*) and aneurysm on an axial image at the level of abdominal aorta.

Abdominal Aorta

Aortic aneurysm is associated with risk for sudden death due to aortic dissection or rupture and can occur associated with connective tissue disorders or acquired cardiovascular disease [13]. The ability to measure the diameter, wall thrombus, and calcification makes this an ideal modality for sequential following of patients and to make an accurate assessment for surgical planning or medical therapy (Figure 17.5). Aortic endovascular stenting is gaining acceptance as an alternative to traditional open surgical repair for abdominal aortic aneurysms. CT

imaging is the predominant method used for preoperative planning to assess the feasibility of endovascular aortic stenting and also to select the appropriate aortic stent graft. The abdominal aorta is usually scanned before and following intravenous contrast enhancement, which enables detection of calcification of the arterial wall which will be partly obscured following contrast enhancement. It also provides a baseline for evaluating any vascular injury with hemorrhage or thrombus that will be seen on the post-contrast acquisition. 3D sagittal and coronal reconstructions are routinely performed (Figures 17.6 and 17.7). Maximum intensity projection (MIP) provides images similar to conventional angiography and is useful to visualize calcification and the relationship of the aneurysm to adjacent vessels.

Common Indications for CTA of Abdominal Aorta

1. Detection and depiction of atherosclerotic occlusive disease or aneurysmal dilatation of the abdominal aorta and iliac arteries.
2. Preoperative assessment of aortoiliac aneurysms to determine whether open repair or stent grafting is indicated.
3. Preoperative measurement of the aneurysm for selecting the appropriate stent graft.
4. Follow-up for the size and progression or regression of abdominal aortic aneurysms.
5. Diagnose the presence and severity of complications following aortic stent-graft placement including endoleaks, aneurysm expansion, rupture, pseudoaneurysm, thrombus, and graft migration) [14].
6. Detection and depiction of aortic dissection.
7. Detect the presence of aortic aneurysm rupture.

Accurate measurements of the aortic root diameter can be made easily and the extent of the aneurysm defined. Luminal thrombus is easily identified by differences in tissue density during contrast enhancement. The tomographic format of CT provides excellent definition of the relationship of aortic aneurysms to adjacent structures. Leakage of blood from the aneurysm or stent may be recognizable with contrast enhancement of surrounding tissues.

The 2D images (axial data), maximal intensity projection, and multiplanar imaging allow accurate measurement of length, location, and diameter of aneurysms. The involvement of branch vessels (renals, mesenterics, iliacs, etc.) is also easily assessed with minimal contrast requirements. CT angiography has become the first-line modality for evaluation for planning stent-graft deployment (Figure 17.7) and post-procedural assessment (Figure 17.8). Cephalocaudal coverage from the celiac trunk to the proximal thighs provides a suitable study volume to detect aortic disease. Although the preoperative assessment requires a true early arterial phase to investigate all preoperative necessities (e.g., aortic neck diameters, angle and distance from the renal arteries), the postoperative study requires a biphasic scan protocol, allowing a more detailed inspection of the perigraft space to rule out possible endoleaks. High-resolution, thin slice protocols are preferable, especially for the post-processing task.

Several studies have demonstrated the accuracy of CT for the diagnosis of aortic diseases. Stueckle et al [15] compared conventional angiography to CTA in the diagnosis of morphologic changes in the abdominal aorta and its branches in 52 patients who underwent both MDCT and invasive angiography before surgical treatment. All CT examinations were performed after administration of 100 mL contrast medium with a collimation of 4×1 mm and a pitch of 7. All aneurysms, occlusions, stenoses, and calcifications were diagnosed correctly by CTA in axial and multiplanar projections (sensitivity 100%; specificity 100%).

The degree of stenosis was overestimated in three cases when using axial projections. 3D volume-rendered CTA showed a sensitivity of 91% for aneurysms, 82% for stenoses, 75% for occlusions, and 77% for calcifications. The specificity was 100% in all cases. With increased detector systems, imaging improves. Multislice CT angiography is similar to invasive angiography for abdominal vessels if multiplanar projections are used.

Nihan et al [16] described 25 patients (22 preoperative and 3 postoperative) who underwent EBT angiography prior to surgery, with results compared to surgical findings. Among the 22 preoperatively evaluated patients, 17 patients had thoracic and/or abdominal aorta aneurysm with or without associated mural thrombus and calcified arteriosclerotic plaques, and four had dissection in the thoracic and abdominal aorta. The findings by CTA correlated with the surgical findings in all cases. In one preoperative patient, interventional angiography resulted in the misdiagnosis of occlusion in the proximal part of the abdominal aorta, but EBA showed tortuosity and division anomaly of the abdominal aorta which could not be evaluated by interventional angiography because of technical limitations. There was one postoperative case of a patient with Marfan's syndrome who was found to have a pseudoaneurysm surrounding a graft in the ascending thoracic aorta with contrast extending from the pseudoaneurysmal space to the right atrium. These findings were in addition to that found on conventional invasive angiography. These findings demonstrated that CTA is a highly accurate imaging method in all kinds of thoracic and abdominal aorta diseases in the preoperative and postoperative period with excellent 3D images competitive in quality with interventional angiography. In some instances, CT angiography images give more information about the aortic diseases due to visualization of lumen, thrombus, and wall disease simultaneously, as compared to interventional angiography.

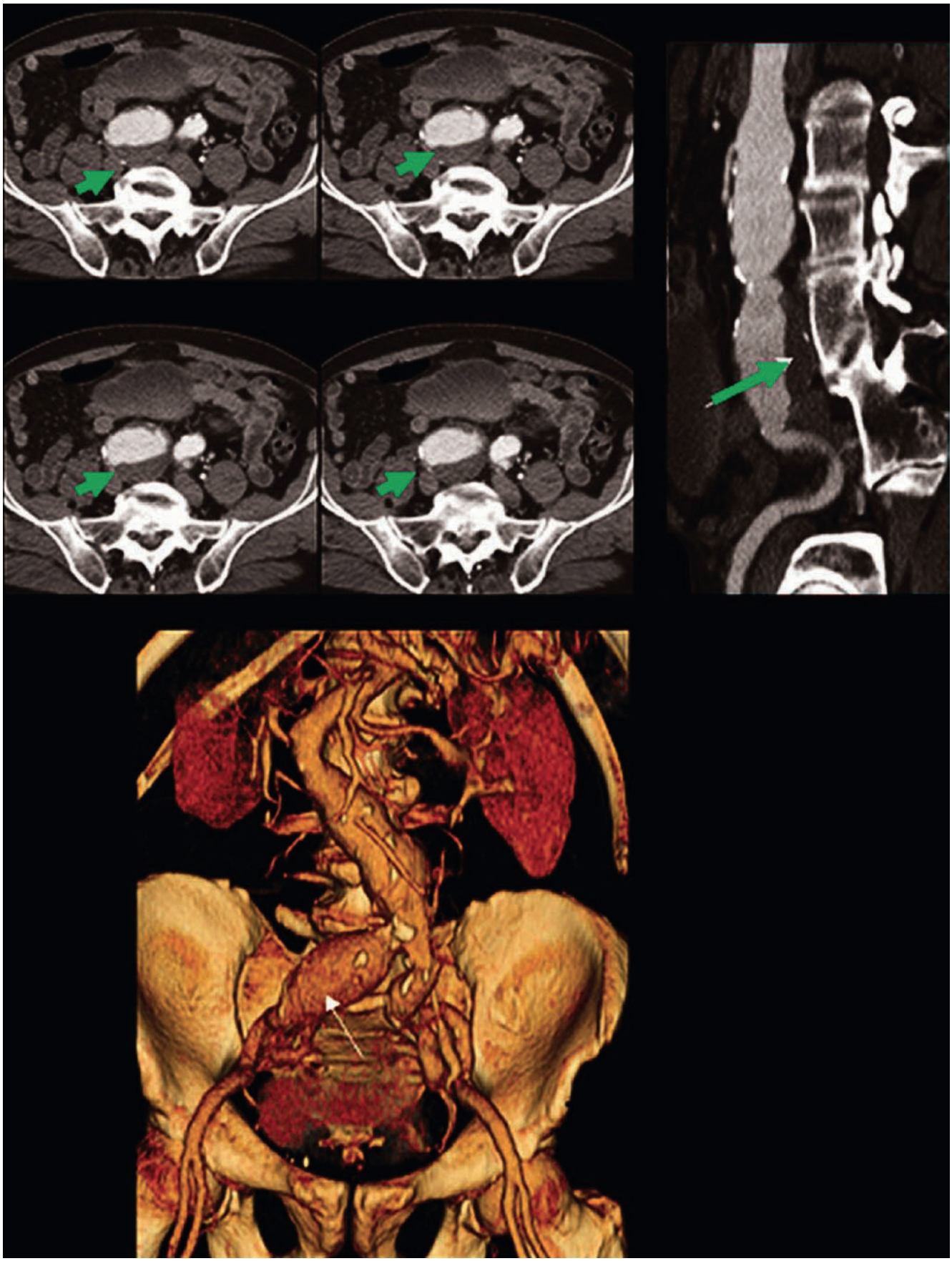

Figure 17.6. A representation of the 2D axial images (*top left*), curved multiplanar reformat (*top right*), and volume-rendered images (*bottom*) of a patient with an abdominal aortic aneurysm. The iliacs and femoral bifurcations can be seen best in their true anatomic 3D orientation with the volume-rendered image. The thrombus, however, is only visible on the 2D images and curved MIP image (*green arrows*). The *white arrow* demonstrates the iliac aneurysm.

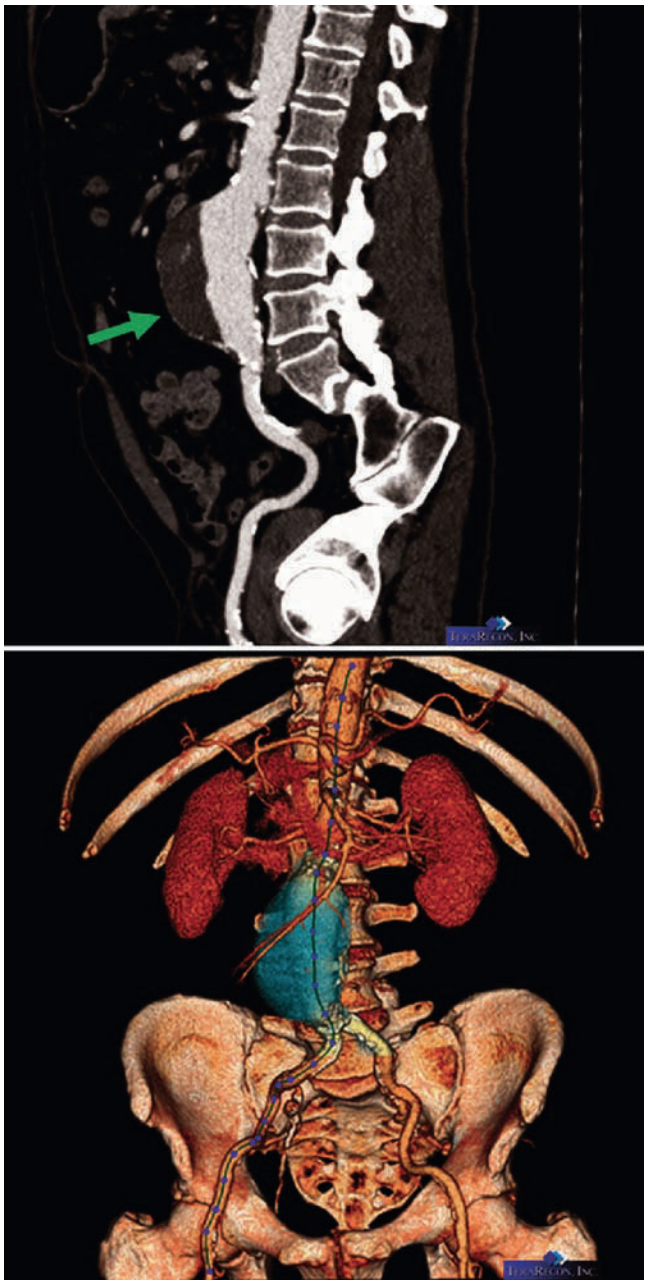

Figure 17.7. Abdominal aortic aneurysm with large intramural thrombus, seen on maximal intensity projection image (*top*, *green arrow*) and volume-rendered (*bottom*, *blue structure*) (courtesy of TeraRecon, Inc.).

Comparison to Other Modalities

Like CT, MRA of the abdomen is always acquired as part of a routine lower extremity runoff procedure most commonly performed for symptoms of claudication.

With CT, the renals can be routinely evaluated during an abdominal aorta study. For MR, the evaluation of the renal arteries for characterizing potential renal artery stenosis in patients with hypertension must be done as a separate procedure, with different imaging protocols. This is also true for evaluation of a potential renal donor. In these patients, dedicated abdominal MRA acquisition is required with

Figure 17.8. A patient status post repair of a thoracic aortic aneurysm. The stent can be seen without scatter artifact or partial volume effect (courtesy of TeraRecon, Inc.).

greater contrast enhancement, which is not feasible when the legs and feet must also be imaged at the same time. This is because there is a limit on the total volume of gadolinium, which is usually 30–45 mL for an adult. An abdominal MRA performed for the indications listed previously is often scanned as part of the same procedure as a thoracic MRA, as it is for CT.

Conclusion

The simultaneous acquisition of multiple thin collimated slices in combination with enhanced gantry rotation speed offers thin slice coverage of extended volumes without any loss in spatial resolution. Early limitations of four slice scanners required restricting the scan volume and focusing on dedicated abdominal vessel territories in order to provide high spatial resolution (1–2 mm), while 16+ detector-row technology now enables full abdominal coverage from the diaphragm to the groin without compromise of spatial resolution. This technique enables the evaluation of the whole arterial visceral vasculature (e.g., hepatic vessels, mesenteric vessels, renal arteries) and the aortic-iliac axis in a single data acquisition. Higher detectors allow faster volume coverage (lowering contrast requirements, while slightly raising radiation requirements).

Renal and Mesenteric Arteries

Renal vasculature is very commonly imaged to rule out renovascular hypertension. Although renal artery duplex sonography is often the first examination performed, there are a number of well-recognized limitations, most important being the challenge of optimally visualizing these vessels in obese patients. Catheter angiography has been the traditional gold standard for renal artery evaluation; however, improvements in spatial resolution and image quality of cross-sectional techniques have allowed MR and CT angiography to replace this invasive examination in most circumstances. Current 64+ channel CT systems permit rapid acquisition of large volumes of submillimeter data with isotropic resolution (equal resolution in the X, Y, and Z dimension), allowing 3D data to be reconstructed in any plane. MRA has also benefited from a number of recent developments, including improvements in gradient hardware and the recent introduction of parallel imaging, both of which permit reduced acquisition times and improved spatial resolution; however thicker slices with MRA require acquisition in the plane of interest, making scanning protocols much more complicated.

CTA, combined with abdominal/parenchymal imaging, is a first-line diagnostic test in patients with suspected abdominal vascular emergencies, such as acute mesenteric ischemia, and an excellent tool to assess a wide variety of vascular abnormalities of the abdominal viscera. Important indications for directed renal artery imaging comprise the assessment of patients with suspected renal vascular hypertension to exclude hemodynamically significant renal artery stenosis as well as a complete preoperative assessment for renal transplant candidates. A wide range of functional techniques are now available with CTA, which may help us to identify patients who would or would not benefit from renal artery revascularization [17]. MDCT angiography of the renal arteries is performed with a high-resolution protocol (thickness as thin as 0.5–0.625 mm). Achieving adequate coverage to encompass the entire kidneys and the origins of accessory renal arteries is easily accomplished in a scan of <3 s duration, or as part of the aortic evaluation (described previously). With adequate selection of acquisition parameters (thin collimation), high spatial-resolution volumetric datasets for subsequent 2D and 3D reformation can be acquired (Figure 17.9). Whereas fast acquisitions allow a reduction of total contrast volume in the setting of CTA, this is not the case when CTA is combined with a second-phase abdominal MDCT acquisition for parenchymal (e.g., hepatic) imaging. Renal CTA is an accurate and reliable test for visualizing vascular anatomy (Figure 17.10) and renal artery stenosis, and therefore a viable alternative to MRA in the assessment of patients with renovascular hypertension and in potential living related renal donors.

Figure 17.9. A volume-rendered image of the abdominal aorta and vessels (including exquisite detail of the mesenteric and iliac arteries) using 64-detector MDCTA.

Methods

Routine clinical practice follows the rule of thumb that the injection duration should match the acquisition time. Biphasic injection protocols, with an initially high injection rate followed by a slower continuing injection phase, ensure optimal opacification of the renal arteries (Chap. 2). Note that high-concentration contrast material requires only moderate injection flow rates (maximum of 4.5 mL/s) to achieve high iodine administration rates [18].

By using a half-second MDCT scanner and a 1 mm nominal section thickness, Willmann et al [19] obtained excellent quality CT angiograms (92 and 99% sensitivity and specificity, respectively) for the detection of hemodynamically significant arterial stenosis of aortoiliac and renal arteries. When compared to MRA, there is no statistically significant difference between 3D MRA and MDCT angiography in the

Figure 17.10. Renal artery aneurysm.

detection of hemodynamically significant arterial stenosis of the aortoiliac and renal arteries. This study also demonstrated that patient acceptance of the CT study is higher than either invasive angiography or MRA.

Tepe et al used 3D EBT angiography to evaluate renal artery lesions as well as vascular variants that are crucial to detect before surgery [20]. Forty patients underwent EBT (GE-Imatron, C 150 ultrafast CT scanner, San Francisco, CA) of the renal arteries. The study demonstrated that both maximal intensity projection (MIP) and volume-rendered images were excellent in demonstrating stenosis of the renal arteries. Accessory and main renal arteries were easily depicted, and stenosis was shown with high accuracy. In this study, among 40 renal angiography patients, 21 had stenosis of the renal arteries with different percent-ages. A total of 12 accessory renal arteries (five left, seven right) were detected. CT, with its noninvasive volume rendering (VR) and MIP techniques, is easy to apply and is functional and accurate for neoplasms, renal vascular anatomy, and renal artery stenosis.

While most vascular beds have demonstrated an advantage of MIP imaging over VR for accurate stenosis detection (especially coronary artery imaging), renal vasculature seems more amenable to quantitation with VR. One study specifically compared overall image quality and vascular delineation on MIP and VR images. The authors found that all main and accessory renal arteries depicted at invasive angiography were also demonstrated on MIP and VR images [21]. VR performed slightly better than MIP for quantification of stenoses >50% (VR: $r^2 = 0.84$, $p < 0.001$; MIP: $r^2 = 0.38$, $p = 0.001$) and significantly better for severe stenoses (VR: $r^2 = 0.83$, $p < 0.001$; MIP: $r^2 = 0.21$, $p = 0.1$). For detection of stenosis, VR yielded a substantial improvement in positive predictive value (VR: 95 and 90%; MIP: 86 and 68% for stenoses >50 and 70%, respectively). Image quality obtained with VR was not significantly better than that with MIP; however, vascular delineation on VR images was significantly better (Figure 17.11). The VR technique of renal MRA enabled more accurate detection and quantification of renal artery stenosis than did MIP, with significantly improved vascular delineation.

Another study evaluated findings in 50 main and 11 accessory renal arteries [22]. All arteries depicted on conventional angiograms were visualized on MIP and VR images. Receiver operating characteristic (ROC) analysis for MIP and VR images demonstrated excellent discrimination for the diagnosis of stenosis of at least 50% (area under the ROC curve, 0.96–0.99). While in this study, sensitivity was not significantly different for VR and MIP (89% vs. 94%, $p > 0.1$), and specificity was greater with VR (99% vs. 87%, $p = 0.008$–0.08). Stenosis of at least 50% was overestimated with CT angiography in four accessory renal arteries, but three accessory renal arteries not depicted at conventional angiography were depicted at CT angiography. In the evaluation of renal artery stenosis, CT angiography with VR is faster and more accurate than CT angiography with MIP. Accessory arteries not depicted with conventional angiography were depicted with both CT angiographic algorithms.

Figure 17.11. A volume-rendered electron beam tomography (EBT) study of the renal arteries, depicting a high-grade stenosis of the left renal artery (*arrow*). The left kidney also opacifies less (*darker color*) than the right kidney, suggesting decreased blood flow and significance of the visualized stenosis.

CT angiography is a highly reliable technique for detection of renal artery stenosis as well as for morphologic assessment and can surpass conventional angiography in terms of diagnostic accuracy and reduced exposure to iodinated contrast (Figure 17.11). In patients with renal insufficiency, color-coded duplex ultrasound or gadolinium-enhanced MRA should remain the initial examination performed, depending on local expertise and availability. However, new warnings regarding systemic fibrosis with gadolinium make this agent contraindicated in patients with glomerular filtration rates of <30 mg/mL/mm^2.

Mesenteric Vasculature

MDCT angiography has become a valuable minimally invasive tool for the visualization of normal vascular anatomy and its variants as well as for pathologic conditions affecting the mesenteric vessels (Figures 17.12 and 17.13) [19, 23, 24]. Indications for MDCT angiography include not only acute and chronic ischemia, aneurysm, and dissection, but also preoperative vascular assessment for patients undergoing liver lesion embolization as well as in the setting of liver transplantation [25, 26]. Protocols for typical aortic imaging (described previously) are used to image the mesenteric vasculature. Mesentric CTA has been facilitated by rapid image acquisition with 64 slice scanners, which reduce artifact from respiratory variation. This allows visualization of lesions at the mesenteric orifice and evaluation of distal reconstitution. Mesenteric CTA can assist in the evaluation of abdominal pain by ruling out other intra-abdominal pathology. Multiple axial images and rotational views may be necessary to evaluate mesenteric lesions at the aortic orifice.

The reconstructed images allow for easy evaluation of all abdominal vasculature. VR is most often used, predominantly due to the complex anatomy, making MIP imaging more

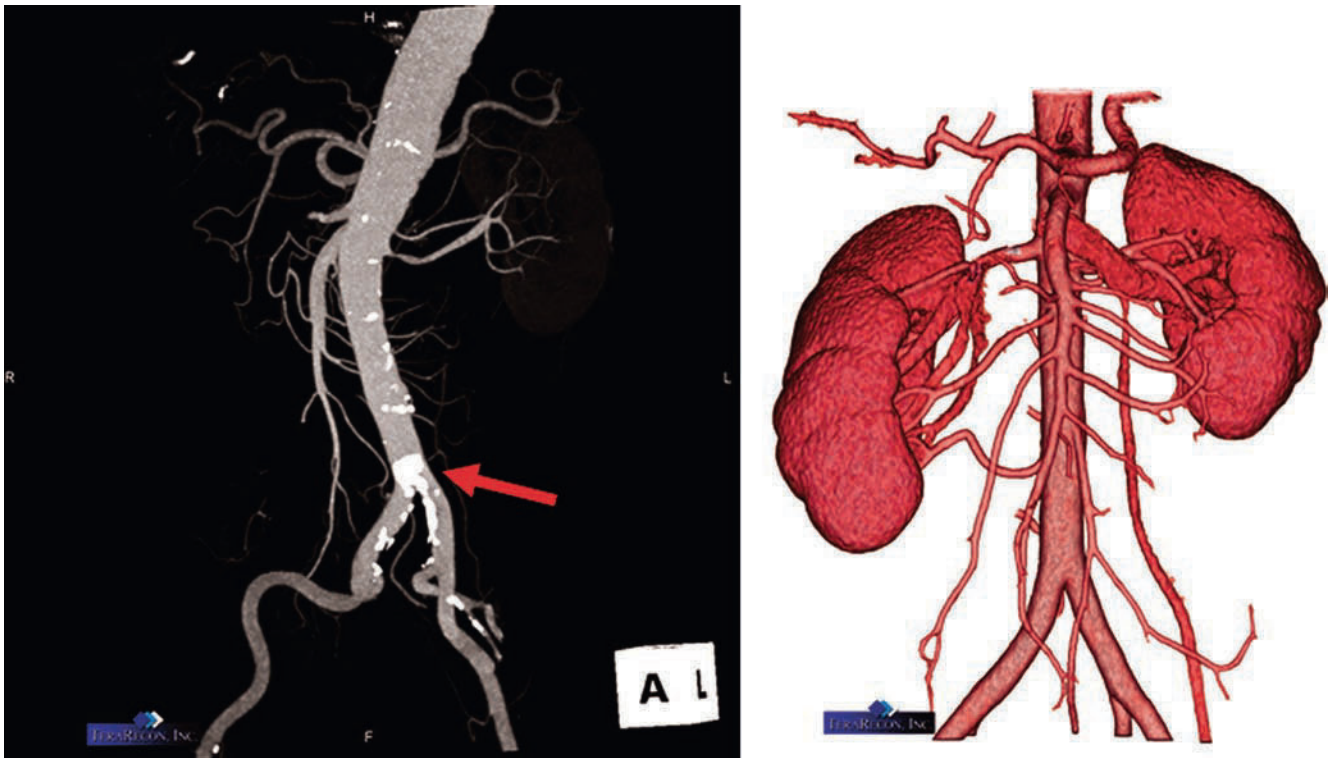

Figure 17.12. Maximal intensity projection of the abdominal aorta, demonstrating severe calcifications at the iliac bifurcation (*arrow*, *left image*). The *right* image demonstrates a normal arterial bed in another patient, displayed using volume rendering (VR) (courtesy of TeraRecon, Inc.).

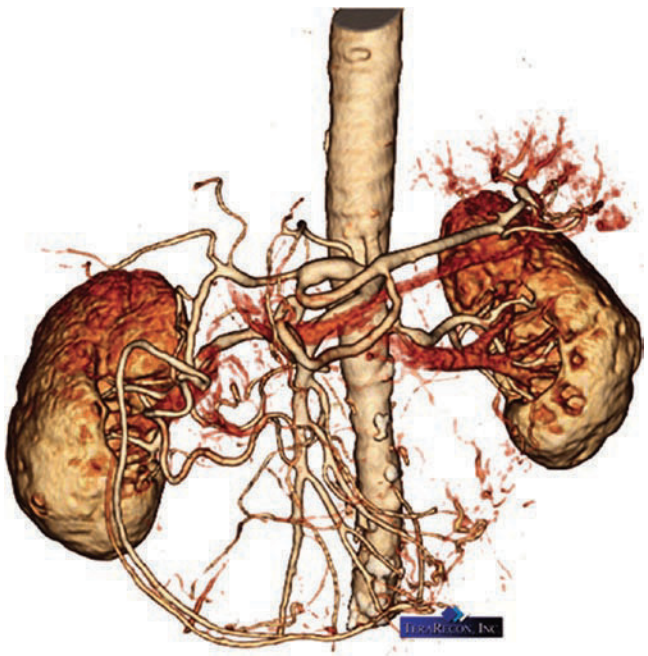

Figure 17.13. 3D image demonstrating the ability of CT to visualize the abdominal arteries, including the gastric arteries in this case. Reconstruction performed on Aquarius Workstation, TeraRecon, San Mateo, CA (courtesy of TeraRecon, Inc.).

difficult (Figure 17.13). Since the arteries are highly tortuous, leaving the 2D plane often (and traveling both caudally and cranially at different times), these vessels pose the most challenge with axial interpretations. With coronary imaging, the arteries run cranial to caudal, without significant exception. Thus, interpreting with MIP or axial imaging is fairly straightforward, as the operator needs to systematically go from the most cranial images to the most caudal to follow the respective arteries. With mesenteric imaging, the arteries commonly turn both cranially and caudally, and VR makes visualization of the entire dataset with one reconstruction possible. No studies of the diagnostic potential of the different reconstruction methods have been reported.

CTA and contrast-enhanced MRA are excellent noninvasive screening techniques for patients suspected of having mesenteric ischemia of all causes. CTA has higher spatial resolution and faster acquisition times, allowing assessment of the peripheral visceral branches and the inferior mesenteric artery with greater accuracy than contrast-enhanced MRA. In addition, it allows the identification of calcified plaques. Contrast-enhanced MRA is therefore our clear second choice in this clinical setting, but the lack of radiation and iodinated contrast agents make it the technique of choice for children and patients with azotemia [27].

Carotid Artery CT Angiography

Ischemic cerebrovascular events are often due to atherosclerotic narrowing of the carotid bifurcation (Figure 17.14) [28]. Carotid bifurcation disease contributes to stroke, transient ischemic attacks, or amaurosis figax through sudden occlusion, and cerebral or ocular embolization. Invasive angiography is the current reference standard for

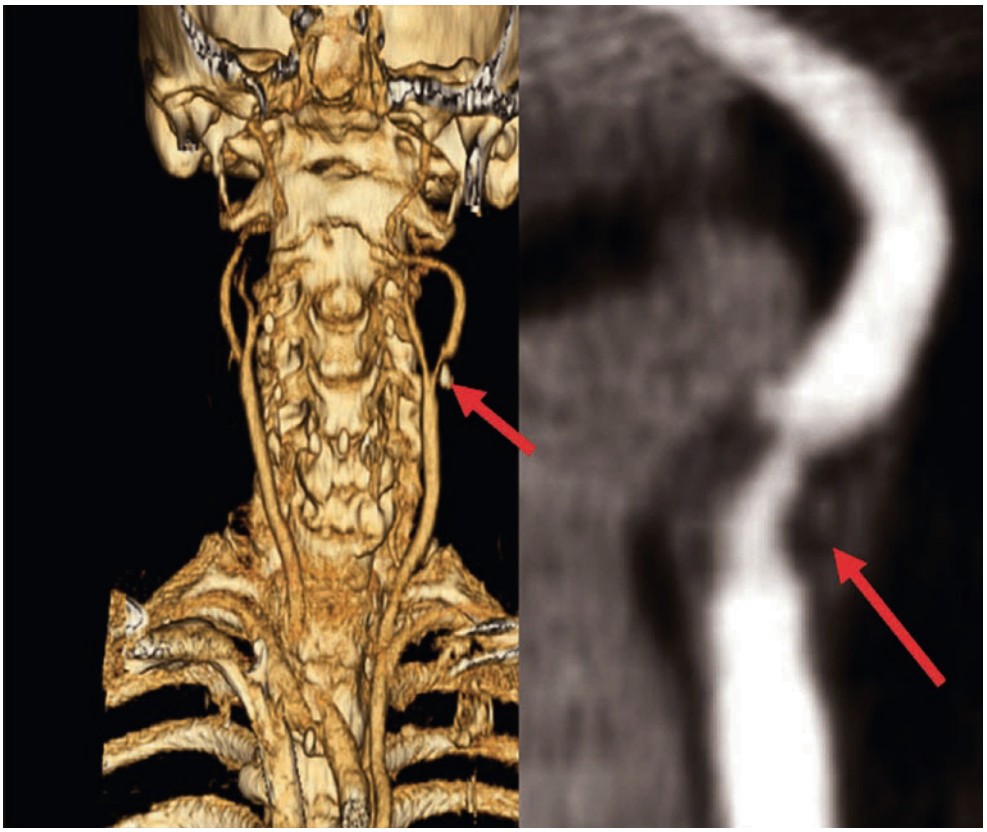

Figure 17.14. Two patients with carotid stenosis at the bifurcation. The *left image* is a volume-rendered image, with a high-grade stenosis at the proximal portion of the internal carotid, with a dense calcification also seen (*arrow*). The *right image* demonstrates a maximal intensity projection image of the same region, with a tight stenosis and thrombus present (*arrow*).

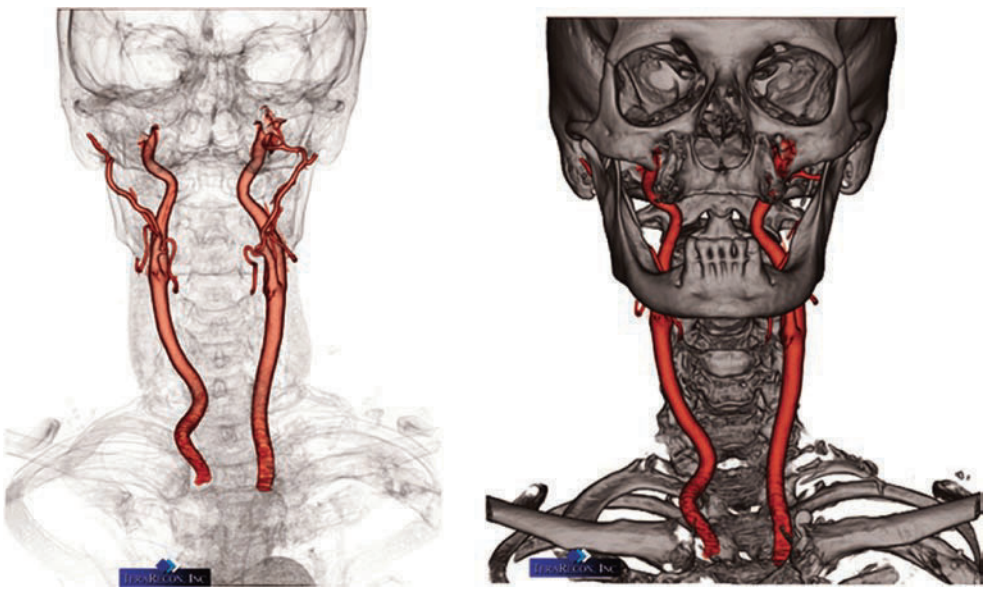

Figure 17.15. 3D images of normal carotid arteries bilaterally (courtesy of TeraRecon, Inc.).

the evaluation of obstructive carotid artery disease. CT angiography is a robust technique in assessing carotid artery stenosis, allowing excellent visualization of the lumen of the carotid artery using intravenous contrast (Figure 17.15). Subsequent refinement of magnetic resonance imaging, ultrasound, and CT techniques has led to changes in clinical practice whereby many centers have now abandoned conventional X-ray angiography in place of safer imaging modalities [29]. CT angiography offers details of the entire relevant neurovascular axis by excluding significant carotid disease and intracranial disease [30].

Coupling non-contrast-enhanced cranial CT imaging with CT perfusion imaging and CTA of the entire cerebrovascular axis is both safe and feasible [31]. Current practice is to use CTA to facilitate patient triage and provide specific information to rule out large vessel stenosis in patients with transient ischemic attacks, suspected stroke, or in patients with carotid bruits and (Figure 17.16) [29].

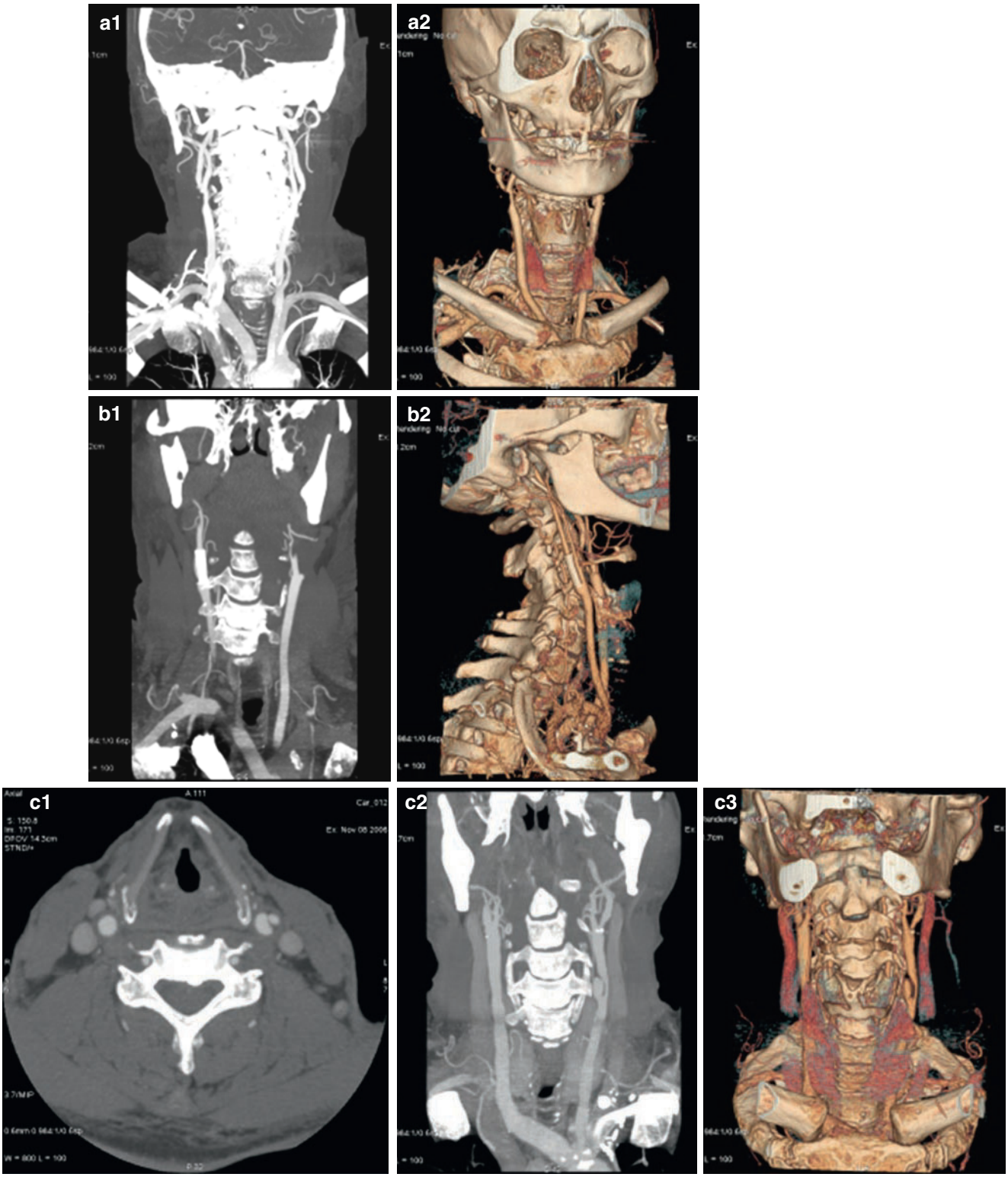

Figure 17.16. (**a**1) Right external carotid artery stenosis. (**a**2) Volume rendered image of right external carotid artery stenosis. (**b**1) Coronal view of right internal carotid artery (ICA) stent. (**b**2) Volume rendered image of right ICA stent. (**c**1) Axial view of left carotid artery dissection. (**c**2) Coronal view of left carotid artery dissection. (**c**3) Volume rendered image of left carotid artery dissection.

Common indications include evaluation of patients with carotid bruits, symptoms of vertebral insufficiency, borderline carotid ultrasound examinations, or insufficient MRA examinations of the carotid system. Many vascular surgeons will not operate based upon carotid ultrasound, requiring confirmation with either CTA or invasive angiography. This chapter will address the clinical applications of CT angiography of the carotid and vertebral arteries.

The North American Symptomatic Carotid Endarterectomy Trial and European Carotid Surgery Trial demonstrated a large reduction in strokes by performing carotid endarterectomy [29, 32, 33] in symptomatic patients with a stenosis of more than 70%, Thus, an accurate assessment of carotid disease is

important. Furthermore, endarterectomy in patients with a symptomatic moderate carotid stenosis of 50–69% produced a moderate reduction in the risk of stroke [33]. Randoux et al [34] prospectively compared gadolinium-enhanced MRA and CTA with invasive angiography for use in detecting atheromatous stenosis and plaque morphology at the carotid bifurcation in 22 patients. There was significant correlation between CTA, enhanced MRA, and invasive angiography. Severe internal carotid artery (ICA) stenoses were detected with high sensitivity and specificity: 100 and 100%, respectively, with CT angiography; 93 and 100%, respectively, with enhanced MRA.

Apart from a hemodynamically significant luminal stenosis, complexities in extracranial carotid artery plaque morphology, including surface irregularities/ulcerations due to plaque rupture, calcification, fibrous cap thinning, intraplaque hemorrhage, and the presence of necrotic core, have also been shown to increase the risk of thromboembolic events. Out of all the modalities, luminal surface irregularities and ulcerations are most frequently seen at CTA. CTA allows for rapid acquisition of imaging data that can be reconstructed into 2D and 3D images with cross-sectional views that are able to accurately depict plaque morphology. MIP techniques allow for data to be reconstructed into images that closely resemble conventional catheter-based angiograms that can be rotated 360° to be viewed from any angle. This helps to delineate the unstable plaques which are less stenotic but at high risk of producing symptomatic embolization or carotid occlusion. Most studies suggest that CT angiography is the best modality for analyzing plaque morphology. Saba et al [35] evaluated the carotid arteries of 237 patients by MDCT and Ultrasound Doppler, and correlated the findings with the surgical results. MDCT was proven to be better than Doppler, with the surgical confirmation underlining a 93.8% sensitivity and 98.6% specificity for MDCT. Detection of ulcerated plaques may prove to be important, since it has been suggested that the presence of plaque ulceration is a risk factor for embolism [36]. However, the inability of invasive angiography to depict plaque ulceration is well documented [37,38], partly because of the limited number of views that are typically obtained. In the case in which CT angiography depicted an ulceration that was not depicted at gadolinium-enhanced MRA, this could be due to a lack of spatial resolution at gadolinium-enhanced MRA.

The eventual ability to preemptively identify asymptomatic plaques with the high likelihood to produce symptoms is the most practical goal of CTA imaging technique, allowing appropriate intervention prior to a disabling or fatal neurologic event. CT angiography and gadolinium-enhanced MRA have both proved reliable and fast techniques to evaluate the degree of ICA stenosis [38]. CT angiography has some substantial benefits, including its accuracy and lack of invasiveness [39], and improved spatial and temporal resolution as compared with MRA.

Methods for Carotid CT Angiography

Carotid CT angiographic images are obtained with patients placed in the supine position with the head tilted back as far as possible to avoid inclusion of dental hardware. Spiral data can be acquired with a 0.5–0.625 mm slice thickness starting at the seventh cervical vertebra and proceeding as far cephalad as required. Some centers suggest starting at the CT parameters including a field of view (FOV) of 15 cm and a section thickness of 1 mm. With a power injector, 30–40 mL of nonionic contrast medium is injected at a rate of 2.5 mL/s into an antecubital vein. Administration of each bolus was followed immediately by a 20 mL saline flush. The acquisition is initiated after the start of the administration of contrast medium, the time of which was determined by a test of circulation time.

In general, good image quality is essential. A CT angiographic image of good quality is easily obtained if the patient does not move during the study. Given the faster scan times with increased detector systems, this is even easier. A breath-hold acquisition is not necessary. Compared with invasive angiography and CTA, a major limitation of gadolinium-enhanced MRA is spatial resolution. By using automatic triggering with detection of the contrast material bolus, it is fairly straightforward to selectively obtain an arterial phase image. Previous studies [40] have shown that a combination of optimal tracking volume placement and adjustment of tracking volume size ensures optimal sensitivity to the contrast material bolus. By choosing a 20 mm tracker volume placed in the aortic arch, bolus arrival was always detected. Careful timing is very important, with arterial enhancement being critical. It is vital to make sure that there is no venous filling when images are obtained. Obtaining images too early will lead to nonenhanced images, and obtaining images late allows for venous enhancement. Large jugular veins filled with contrast in close proximity to the carotid arteries can make the interpretation of carotid arteries more difficult.

Transverse source images are reconstructed in 1 mm increments by using a small FOV (15 cm). These parameters allowed a spatial resolution of $0.3 \times 0.3 \times 0.6$ mm. Total coverage is approximately 18 cm. The images are then analyzed with axial images and maximal intensity projection or curved multiplanar reconstruction. Total post-processing time is now done in real time (<1 min). Precision of length and degree of stenosis is reported to depend more on measurement technique than on acquisition parameters [41]. The accuracy of stenosis measurement depends on the scanning plane, which ideally should be perpendicular to the carotid artery used to obtain magnified transverse oblique images. Most authors consider maximal intensity projection or curved multiplanar reconstructions the most accurate techniques for measurements. VR is considered the least accurate technique for measurement. Given that a large proportion of patients with carotid artery disease will be evaluated for potential carotid artery stenting, CT imaging should focus on the assessment of the following: (1) stenosis severity, (2) disease within the aortic arch and at the origin of the common carotid arteries, (3) size of the common carotid artery at lesion location, (4) size of the distal ICA, and (5) the presence of contralateral disease.

Comparison to MR

Gadolinium-enhanced MRA is an appropriate technique for evaluating ICA stenosis [42–44]. Clinically relevant stenosis and occlusions of the ICA were correctly detected with good sensitivity and specificity and good interobserver agreement. Most studies with gadolinium-enhanced MRA demonstrate overestimation of the degree of stenosis [43–45]. Artifacts due to excessive section thickness, necessary with current MR systems, cause a partial volume effect [46, 47]. The signal loss can also be explained by the presence of hemodynamic modifications. The decreased flow caused by stenosis leads to a reduced concentration of contrast agent in the distal arterial lumen, which may also explain why overestimation of stenosis with gadolinium-enhanced MRA can occur [48], especially for evaluating the degree of stenosis in small-vessel lumens.

Plaques that are more prone to disruption, fracture, or fissuring may be associated with a higher risk of embolization, occlusion, and consequent ischemic neurologic events [45]. Plaque irregularities are more frequent at CT angiography than at invasive angiography or contrast-enhanced MRA.

In general, studies demonstrate that MRA sometimes performs inferiorly to CT angiography, mainly due to lower spatial resolution. MR has been postulated to demonstrate inflammation, and MRI-derived measurements of fibrous-cap and lipid-core thickness have the potential for identifying vulnerable carotid plaques in vivo, although this application is still very experimental [46]. CT does not have the same potential for demonstrating flow or inflammation.

Invasive angiography has long been considered the standard for evaluation of carotid stenosis but has well-known risks and limitations. Invasive angiography allows only a limited number of views, which can lead to an underestimation of the degree of stenosis by as much as 40% [47] when compared with histologic correlation. Invasive angiography is also a relatively expensive technique that uses numerous resources. Finally and perhaps most importantly, there is a small but definite risk of major complications secondary to the procedure itself. The Asymptomatic Carotid Atherosclerosis Study Committee reported a 1.2% risk of persisting neurologic deficit or death following invasive angiography, while the surgical risk was 1.5%. The risks associated with CT angiography are markedly lower with similar or lower radiation exposures and no catheter-induced risks.

MRA is adequate to replace invasive angiography in most patients. However, it has been proved that CT angiography is highly accurate and can also replace invasive angiography [31, 48]. In contrast to the other two modalities, CT angiography allows direct visualization of arterial wall and atheromatous plaque, making the measurement of stenosis much easier. Almost all authors consider that calcified plaque is a limitation of CT angiography. This can be minimized by using multiplanar volume reconstruction to visualize the entire bifurcation initially with a large-volume reconstruction. By reducing volume reconstruction, we can clearly visualize the residual lumen at the maximal part of stenosis, even when circumferential calcified plaques are present. Moreover, CT angiography is able to differentiate mural calcifications and contrast material because attenuation of intraluminal contrast and calcifications are not similar. Therefore, calcifications should not be considered limitations of CT angiography [48]. Also, carotid arteries tend to calcify less than either coronary or peripheral arteries (perhaps due to the fact that carotid arteries are more elastic and less muscular), so dense circumferential calcifications occur less frequently in this vascular bed.

CTA has been shown to have a pooled sensitivity of 95% and specificity of 98% for the detection of >70% stenoses, even if only older scanners are used. Differentiation between lipid, fibrous, and calcified plaques may be possible. Carotid CTA has come of age and can be used to quantify stenoses more precisely than ultrasound, to detect tandem stenoses, and for the workup of acute stroke patients. The newer scanners, with prospective triggering and use of 100 kVp, have the additional advantage of a very low radiation profile, allowing for minimal risk to the patient and maximum visualization of the arteries in question.

Imaging the Vertebral Artery

Although conventional intra-arterial angiography remains the gold standard method for imaging the vertebral artery, noninvasive modalities such as ultrasound, multislice computed tomographic angiography, and magnetic resonance angiography are constantly improving and are playing an increasingly important role in diagnosing vertebral artery pathology in clinical practice. Normal anatomy, normal variants, and a number of pathologic entities such as vertebral atherosclerosis, arterial dissection, arteriovenous fistula, subclavian steal syndrome, and vertebrobasilar dolichoectasia can be seen.

Summary

During the past decade, we have been witness to a tremendous development in the field of CT imaging. CTA has gained remarkably by improvements in scan time and image quality, replacing diagnostic angiography in many cases of peripheral, carotid, and renal angiography. These vascular beds do not suffer from motion artifacts, so imaging with CT is ideal. CTA is less expensive, less invasive, and allows simultaneous visualization of large anatomic areas from multiple angles using 3D display. Nevertheless, along with exciting advances, MDCT also carries some emerging and important issues such as increased patient radiation exposure and continued exposure to iodinated contrast.

References

1. Rooholamini SA, Stanford W. Ultrafast computed tomography in the diagnosis of aortic aneurysms and dissections. In: Stanford W, Rum-berger J, eds. *Ultrafast Computed Tomography in Cardiac Imaging: Principles and Practice*. Mount Kisco, NY: Futura Publishing; 1992:287–310.
2. Katz DS, Hon M. CT angiography of the lower extremities and aortoiliac system with a multi-detector row helical CT scanner: promise of new opportunities fulfilled. *Radiology*. 2001;221:7–10.
3. Kim JK, Park SY, Kim HJ, et al. Living donor kidneys: usefulness of multi-detector row CT for comprehensive evaluation. *Radiology*. 2003;229:869–876.
4. Fishman JE. Imaging of blunt aortic and great vessel trauma. *J Thorac Imaging*. 2000;15(2):97–103.
5. Kouchoukos NT, Dougenis D. Surgery of the thoracic aorta. *N Engl J Med*. 1997;336(26):1876–1888.
6. Rubin GD. Helical CT angiography of the thoracic aorta. *J Thorac Imaging*. 1997;12(2):128–149.
7. Rubin GD, Shiau MC, Leung AN, Kee ST, Logan LJ, Sofilos MC. Aorta and iliac arteries: single versus multiple detector-row helical CT angiography. *Radiology*. 2000;215(3):670–676.
8. Gotway MB, Dawn SK. Thoracic aorta imaging with multislice CT. *Radiol Clin North Am*. 2003;41:521–543.
9. Roos JE, Willmann JK, Weishaupt D, et al. Thoracic aorta: motion artifact reduction with retrospective and prospective electrocardiography assisted multi-detector row CT. *Radiology*. 2002;222:271–277.
10. Galla JD, Ergin MA, Lansman SL, et al. Identification of risk factors in patients undergoing thoracoabdominal aneurysm repair. *J Card Surg*. 1997;12:292–299.
11. Semba CP, Kato N, Kee ST, et al. Acute rupture of the descending thoracic aorta: repair with use of endovascular stent-grafts. *J Vasc Interv Radiol*. 1997;8(3):337–342.
12. Zinck SE, Primack SL. Radiographic and CT findings in blunt chest trauma. *J Thorac Imaging*. 2000;15(2):87–96.
13. Lu B, Dai RP, Jing BL, et al. Electron beam tomography with three-dimensional reconstruction in the diagnosis of aortic diseases. *J Cardiovasc Surg*. 2000;41:659–668.
14. Hobo R, Buth J. Secondary interventions following endovascular abdominal aortic aneurysm repair using current endografts. A EUROSTAR report. *J Vasc Surg*. 2006;43(5):896–902.
15. Stueckle CA, Haegele KF, Jendreck M, et al. Multislice computed tomography angiography of the abdominal arteries: comparison between computed tomography angiography and digital subtraction angiography findings in 52 cases. *Australas Radiol*. 2004;48(2):142–147.
16. Nihan E, Levent A, Sekup A. Assessment of aortic diseases with electron beam tomographic angiography. *EBT Symp*. 2003;11–15.
17. Glockner JF, Vrtiska TJ. Renal MR and CT angiography: current concepts. *Abdom Imaging*. 2007;32:407–420.
18. Fleischmann D. Multiple detector-row CT angiography of the renal and mesenteric vessels. *Eur J Radiol*. 2003;45(suppl 1):S79–S87.
19. Willmann JK, Wildermuth S, Pfammatter T, et al. Aortoiliac and renal arteries: prospective intraindividual comparison of contrast-enhanced three-dimensional MR angiography and multi-detector row CT angiography. *Radiology*. 2003;226:798–811.
20. Tepe SM, Memisoglu E, Kural AR. Three-dimensional noninvasive contrast-enhanced electron beam tomography angiography of the kidneys: adjunctive use in medical and surgical management. *Clin Imaging*. 2004;28(1):52–58.
21. Mallouhi A, Schocke M, Judmaier W, et al. 3D MR angiography of renal arteries: comparison of volume rendering and maximum intensity projection algorithms. *Radiology*. 2002;223(2):509–516.
22. Johnson PT, Halpern EJ, Kuszyk BS, et al. Renal artery stenosis: CT angiography – comparison of real-time volume-rendering and maximum intensity projection algorithms. *Radiology*. 1999;211(2):337–343.
23. Laghi A, Iannaccone R, Catalano C, et al. Multislice spiral computed tomography angiography of mesenteric arteries. *Lancet*. 2001;358:638–639.
24. Lawler LP, Fishman EK. Celiomesenteric anomaly demonstration by multidetector CT and volume rendering. *J Comput Assist Tomogr*. 2001;25:802–804.
25. Erbay N, Raptopoulos V, Pomfret EA, et al. Living donor liver transplantation in adults: vascular variants important in surgical planning for donors and recipients. *Am J Roentgenol*. 2003;181:109–114.
26. Byun JH, Kim TK, Lee SS, et al. Evaluation of the hepatic artery in potential donors for living donor liver transplantation by computed tomography angiography using multidetector-row computed tomography: comparison of volume rendering and maximum intensity projection techniques. *J Comput Assist Tomogr*. 2003;27:125–131.
27. Shih MP, Hagspiel KD. CTA and MRA in mesenteric ischemia: part 1, role in diagnosis and differential diagnosis. *AJR Am J Roentgenol*. 2007;188(2):452–461.
28. Kannel WB. Current status of the epidemiology of brain infarction associated with occlusive arterial disease. *Stroke*. 1971;2:295–318.
29. North American Symptomatic Carotid Endarterectomy Trial Collaborators. Beneficial effect of carotid endarterectomy in sympto-matic patients with high-grade carotid stenosis. *N Engl J Med*. 1991;325:445–453.
30. Smith WS, Roberts HC, Chuang NA, et al. Safety and feasibility of a CT protocol for acute stroke: combined CT, CT angiography, and CT perfusion imaging in 53 consecutive patients. *Am J Neuroradiol*. 2003;24:688–690.
31. Na DG, Ryoo JW, Lee KH, et al. Multiphasic perfusion computed tomography in hyperacute ischemic stroke: comparison with diffusion and perfusion magnetic resonance imaging. *J Comput Assist Tomogr*. 2003;27:194–206.
32. European Carotid Surgery Trialists Collaborative Group. MRC European Carotid Surgery Trial: interim results for symptomatic patients with severe (70–99%) or with mild (0–29%) carotid stenosis. *Lancet*. 1991;337:1235–1243.
33. Barnett HJ, Taylor DW, Eliasziw M, et al. Benefit of carotid endarterectomy in patients with symptomatic moderate or severe stenosis: North American Symptomatic Carotid Endarterectomy Trial Collaborators. *N Engl J Med*. 1998;339:1415–1425.
34. Randoux B, Marro B, Koskas F, et al. Carotid artery stenosis: prospective comparison of CT, three-dimensional gadolinium-enhanced MR, and conventional angiography. *Radiology*. 2001;220(1):179–185.
35. Saba L, Caddeo G, Sanfilippo R, et al. CT and ultrasound in the study of ulcerated carotid plaque compared with surgical results: potentialities and advantages of multidetector row CT angiography. *Am J Neuroradiol*. 2007;28(6):1061–1066.
36. Hatsukami TS, Ferguson MS, Beach KW, et al. Carotid plaque morphology and clinical events. *Stroke*. 1997;28:95–100.
37. Comerota AJ, Katz ML, White JV, Grosh JD. The preoperative diagnosis of the ulcerated carotid atheroma. *J Vasc Surg*. 1990;11:505-510.
38. Runge VM, Kirsch JE, Lee C. Contrast-enhanced MR angiography. *J Magn Reson Imaging*. 1993;3:233–239.
39. Marro B, Zouaoui A, Koskas F, et al. Computerized tomographic angiography scan following carotid endarterectomy. *Ann Vasc Surg*. 1998;12:451–456.
40. Castillo M, Wilson JD. CT angiography of the common carotid artery bifurcation: comparison between two techniques and conventional angiography. *Neuroradiology*. 1994;36:602–604.
41. Cinat M, Lane CT, Pham H, Lee A, Wilson SE, Gordon I. Helical CT angiography in the preoperative evaluation of carotid artery stenosis. *J Vasc Surg*. 1998;28:290–300.
42. Leclerc X, Martinat P, Godefroy O, et al. Contrast-enhanced three-dimensional fast imaging with steady-state precession (FISP) MR angiography of supraaortic vessels: preliminary results. *Am J Neuroradiol*. 1998;19:1405–1413.
43. Slosman F, Stolpen AH, Lexa FJ, et al. Extracranial atherosclerotic carotid artery disease: evaluation of non-breath-hold three-dimensional gadolinium-enhanced MR angiography. *Am J Roentgenol*. 1998;170:489–495.

44. Scarabino T, Carriero A, Magarelli N, et al. MR angiography in carotid stenosis: a comparison of three techniques. *Eur J Radiol*. 1998;28:117–125.
45. Cronqvist M, Stahlberg F, Larsson EM, Lonntoft M, Holtas S. Evaluation of time-of-flight and phase-contrast MRA sequences at 1.0 T for diagnosis of carotid artery disease. I. A phantom and volunteer study. *Acta Radiol*. 1996;37:267–277.
46. Remonda L, Heid O, Schroth G. Carotid artery stenosis, occlusion, and pseudo-occlusion: first-pass, gadolinium-enhanced, three-dimensional MR angiography – preliminary study. *Radiology*. 1998;208:95–102.
47. Levy RA, Prince MR. Arterial-phase three-dimensional contrast-enhanced MR angiography of the carotid arteries. *Am J Roentgenol*. 1996;167:211–215.
48. Randoux B, Marro B, Marsault C. Carotid artery stenosis: competiton between CT angiography and MR angiography. *Am J Neuroradiol*. 2004;25(4):663–664.

18

Assessment of Pulmonary Vascular Disease

Tae Young Choi and Ronald J. Oudiz

Pulmonary vascular diseases span a variety of disease entities including pulmonary arterial hypertension (PAH), pulmonary venous hypertension, pulmonary embolism, pulmonary arteriovenous malformation, pulmonary arterial stenosis, pulmonary arterial aneurysm, pulmonary veno-occlusive disease (PVOD), and pulmonary capillary hemangiomatosis (see Sect. 18.1.2). In this chapter, we briefly review pulmonary hypertension (PH) and pulmonary embolism (PE), including their cardiac computed tomography (CT) findings.

Pulmonary Hypertension

PH is characterized by an elevation in resting pulmonary arterial pressure with accompanying right ventricular failure. PAH refers to a disease of the precapillary pulmonary circulation which is the result of a complex process intrinsic to the pulmonary vasculature. This process leads to a progressive increase in pulmonary vascular resistance and right ventricular (RV) afterload, and usually results in right-sided cardiac failure. PAH is hemodynamically defined as a mean pulmonary artery pressure greater than 25 mmHg at rest, with a normal pulmonary artery wedge pressure measured at right heart catheterization [1]. PAH is a progressive and life-threatening condition with a poor prognosis if untreated. Most patients with PAH present with exertional dyspnea that progresses over months to years. Exertional angina, syncope, and peripheral edema appear in more severe PH with impaired right heart function. The diagnosis of PAH is often delayed due to the nonspecific symptoms and subtle findings on physical examination.

Methods of Detecting PH

The chest radiographic findings of PH are dilatation of the central pulmonary artery, pruning of the peripheral arteries, and right-sided cardiac chamber enlargement [2, 3]. The chest radiograph may suggest an underlying cause for PH and is thus recommended in the workup of suspected PH. Transthoracic echocardiography (TTE) is often used as a first-line screening test to exclude or identify patients with severe PH by estimating systolic pulmonary artery (PA) pressure and looking for evidence of the cardiac hemodynamic perturbations seen with PAH, such as right-sided cardiac and great vessel chamber enlargement and dysfunction, flattening of the interventricular septum, and pericardial effusion. Echocardiography is also useful for evaluating congenital heart disease (CHD) and left-sided heart disease. Right-sided heart catheterization (RHC), the most accurate test for determining mean pulmonary arterial pressure, remains the gold standard by which the diagnosis of PH is made, and hemodynamic severity is calculated. RHC is required not only to confirm the presence and the severity of PH, but also to exclude left-sided heart disease, potentially correctable intracardiac left-to-right shunting, and to perform acute vasodilator testing.

Because the signs and symptoms of PH are nonspecific and there is no reliable noninvasive test for its detection, patients often undergo CT as part of their diagnostic workup. CT is able to evaluate the lung tissue (for interstitial or emphysematous changes), pulmonary artery (calcification, dilation, embolism, patent ductus), pulmonary veins, right ventricle (hypertrophy, dysplasia), right atrium (enlargement, clot), septum (atrial and ventricular septal defects) and IVC simultaneously, along with left sided chambers and coronaries, making it a potential one stop shop for PH patients.

It is important to be aware of the CT findings that may suggest the diagnosis of PH, such as an enlarged main pulmonary artery (Figure 18.1). Radiographically, PH is said to be more likely when the main pulmonary artery diameter (MPAD) is ≥29 mm (sensitivity 69%, specificity 100%) [4, 5] and/or the ratio of the main pulmonary artery to ascending aorta diameter is >1 [6]. Others have reported that the most specific CT findings for the presence of PH were both a MPAD ≥29 mm and segmental artery-to-bronchus ratio of >1:1 in three or four lobes (specificity 100%) [7]. In

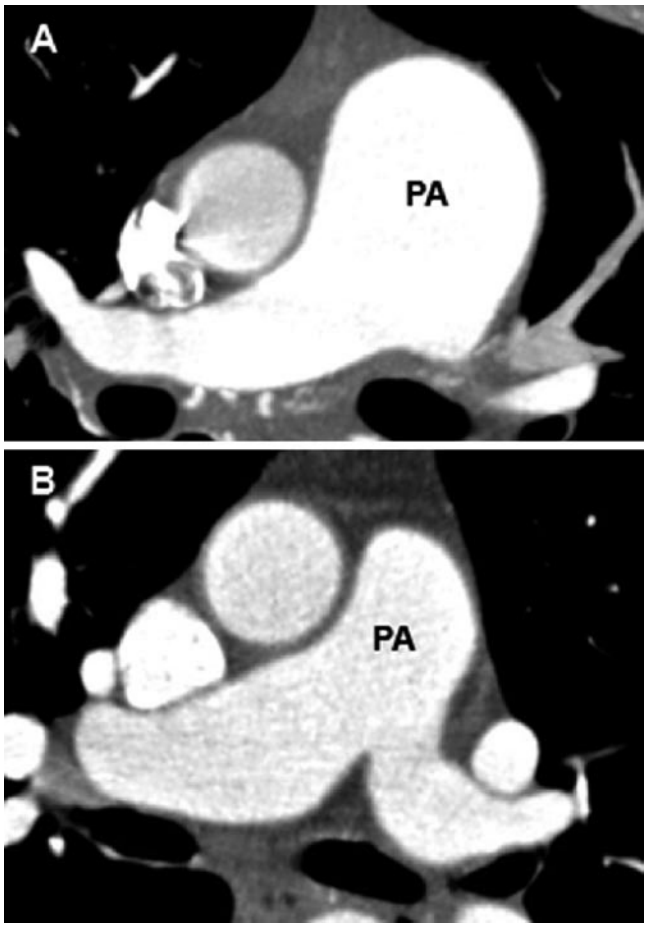

Figure 18.1. Electron beam CT scan in a 22-year-old woman (**a**) and 64 slice multidetector CT (MDCT) in a 40-year-old man (**b**), both with pulmonary hypertension (PH). Pulmonary arteries (PA) are enlarged and tapering distally, with an increased main PA to aorta ratio.

addition, the MPAD correlates with the severity of PH; two studies have defined the upper limit of normal for MPAD as 32 mm [4, 8]. An additional feature of PH is rapid tapering or "pruning" of the distal pulmonary vessels (Figure 18.1).

The presence of calcification in the pulmonary arteries suggests more severe disease [9], as does pericardial thickening and/or effusion [10]. Some studies have reported that hypertrophy of the bronchial artery occurs frequently in patients with idiopathic PAH (IPAH) and Eisenmenger's syndrome [11, 12]. These studies also reported that pulmonary artery thromboses and aneurysms were common in patients with CHD as compared to patients with IPAH, while dilation and mural calcification was seen in similar frequency in both groups [11].

It is generally accepted that in patients with chronic, unrepaired systemic-to-pulmonary shunts the CT findings can appear very similar to those found in precapillary PH such as IPAH and PAH associated with connective tissue disease, portal hypertension, and HIV infection. Commonly, right (or pulmonic) ventricular hypertrophy is seen, with right ventricular enlargement and associated right atrial enlargement (Figure 18.2).

As the right ventricle enlarges, the interventricular septum becomes flattened (Figure 18.3) and eventually convex

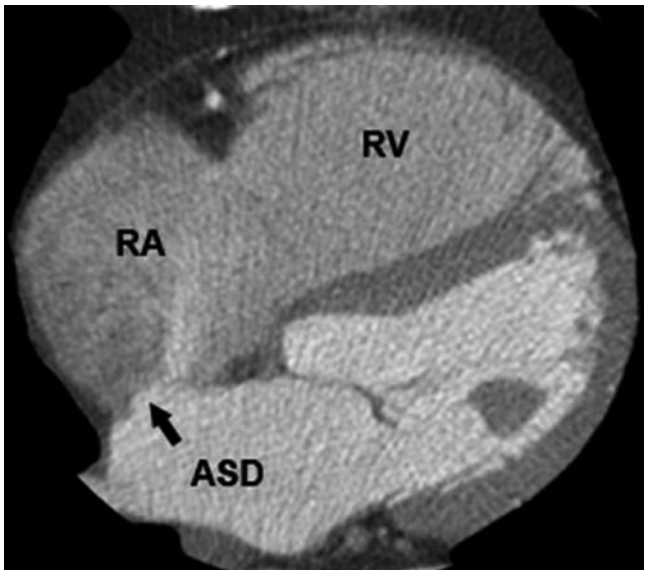

Figure 18.2. Sixty-four slice MDCT in a 44-year-old man with secondum atrial septal defect (ASD) (*black arrow*) and PH demonstrating right atrial (RA) and right ventricular (RV) enlargement.

Figure 18.3. Sixty-four slice MDCT in a 31-year-old man with sinus venosum atrial septal defect (ASD) and PH demonstrating right atrial dilation and right ventricular hypertrophy, and flattening of the interventricular septum (*black arrow*), indicating high right sided pressures.

to the left side [13–15], and thus septal flattening is a commonly noted cardiac abnormality found in patients with PH [16]. If cine-CT is performed, reduced right ventricular systolic function may also be present. The presence of retrograde opacification of the inferior vena cava or hepatic vein during contrast-enhanced CT may be a nonspecific sign of significant PH and/or right ventricular dysfunction [17] (Figure 18.4).

Although CT imaging of the great vessels is a simple and straightforward noninvasive methodology, it has not gained widespread acceptance as a screening test for PH [1]. Table 18.1 summarizes the CT findings of PH. Many of the typical CT findings of PH are not confined to a particular subset of a disease process, but rather reflect the end

Figure 18.4. Sixty-four slice MDCT in a 26-year-old man with anolamous pulmonary venous return and PH demonstrating right atrial dilation and right ventricular hypertrophy, and dilated inferior vena cava with swirling of white contrast (*black arrow*), indicating severe tricuspid regurgitation.

Table 18.1. Summary of CT findings in pulmonary hypertension

Pulmonary arteries
Enlarged proximal vessels
Pruning of the distal vessels
Calcification of the proximal pulmonary arteries
Thrombosis
Aneurysms
Heart
RA, RV, and IVC dilation
RV hypertrophy
Decreased RV systolic function
Flattened interventricular septum ("D-shaped" and undersized left ventricle)
Pericardial thickening and/or effusion
Others
Hypertrophy of bronchial arteries
Segmental bronchial artery to bronchus ratio >1:1 in three or four lobes
Retrograde opacification of the inferior vena cava or hepatic vein

result of the chronic hemodynamic effect of PH upon cardiovascular anatomy. Thus, while all PH is not due to CHD, and all CHD does not result in PH, we will attempt to demonstrate the typical findings of PH in selected cases.

Classification of PH

The proceedings of the Fourth World Symposium on PH held in 2008 in Dana Point, California, contain a comprehensive diagnostic classification of PAH, which was slightly revised from the previous (2003) version. The current Dana Point classification is listed in Table 18.2 [18] with major changes in italics.

Table 18.2. Updated clinical classification of pulmonary hypertension (World Symposium of PH, 2008, Dana Point, CA)[a]

1. Pulmonary arterial hypertension (PAH)
   - 1.1. Idiopathic PAH
   - 1.2. *Heritable*
     - 1.2.1. *BMPR2 mutation(familial or isolated)*
     - 1.2.2. *ALK1, endoglin (with or without hereditary hemorrhagic telangiectasia)*
     - 1.2.3. *Unknown*
   - 1.3. Drug- and toxin-induced
   - 1.4. Associated with
     - 1.4.1. Connective tissue diseases
     - 1.4.2. HIV infection
     - 1.4.3. Portal hypertension
     - 1.4.4. Congenital heart diseases
     - 1.4.5. *Schistosomiasis*
     - 1.4.6. *Chronic hemolytic anemia*
   - 1.5. Persistent pulmonary hypertension of the newborn
   - 1.6. *Pulmonary veno-occlusive disease (PVOD) and/or pulmonary capillary hemangiomatosis (PCH)*
2. Pulmonary hypertension owing to left heart disease
   - 2.1. *Systolic dysfunction*
   - 2.2. *Diastolic dysfunction*
   - 2.3. Valvular disease
3. Pulmonary hypertension owing to lung diseases and/or hypoxia
   - 3.1. Chronic obstructive pulmonary disease
   - 3.2. Interstitial lung disease
   - 3.3. *Other pulmonary diseases with mixed restrictive and obstructive pattern*
   - 3.4. Sleep-disordered breathing
   - 3.5. Alveolar hypoventilation disorders
   - 3.6. Chronic exposure to high altitude
   - 3.7. Developmental abnormalities
4. *Chronic thromboembolic pulmonary hypertension (CTEPH)*
5. *Pulmonary hypertension with unclear multifactorial mechanisms*
   - 5.1. *Hematologic disorders: myeloproliferative disorders, splenectomy*
   - 5.2. *Systemic disorders: sarcoidosis, pulmonary Langerhans cell histiocytosis, lymphangioleiomyomatosis, neurofibromatosis, vasculitis*
   - 5.3. *Metabolic disorders: glycogen storage disease, Gaucher disease, thyroid disorders*
   - 5.4. *Others: tumoral obstruction, fibrosing mediastinitis, chronic renal failure on dialysis*

ALK1 activin receptor-like kinase type1; *BMPR2* bone morphogenetic protein receptor type2; *HIV* human immunodeficiency virus

[a]Reproduced with permission from Elsevier from Simonneau et al [18]

Idiopathic and Heritable PAH

IPAH refers to PAH without a demonstrable etiology which is sporadic disease (neither familial nor an identifiable risk factor). The incidence of IPAH is rare, with an estimated incidence of 1–2 cases per million people per year worldwide [19]. The disorder is approximately four times more frequent in women [20, 21], presenting most commonly in the third decade in women and in the fourth decade in men [19]. There appears to be no racial or ethnic predisposition [19]. When PAH occurs in a familial context, germline mutations in the bone morphogenetic protein receptor type 2 (*BMPR2*) gene, a member of the transforming growth factor β signaling family, can be detected in approximately 70% of cases [22, 23]. Mutations in activin receptor-like kinase type 1 (ALK-1 or endoglin), also members of the transforming growth factor β signaling family, have also been identified in patients with familial PAH, predominantly with coexisting hereditary hemorrhagic telangiectasia. Because *BMPR2* mutations have also been detected

in 11–40% of apparently idiopathic cases with no family history [24, 25], the distinction between idiopathic and familial *BMPR2* mutations may in fact be artificial. Interestingly, in up to 30% of families with PAH, no *BMPR2* mutation has been identified. Thus, heritable forms of PAH include IPAH with germline mutations and familial cases with or without identified germline mutations [26, 27]. Genetic testing is not mandatory in heritable PAH, and in fact it is recommended that genetic testing be performed only after genetic counseling takes place, with a discussion of the risks, benefits, and limitations of such testing [28].

PAH Associated with Connective Tissue Diseases

The prevalence of PAH has been well established for patients with systemic sclerosis (SSc). Two recent prospective studies using echocardiography as a screening method and right heart catheterization for confirmation found a prevalence of PAH in SS of between 7 and 12% [29, 30]. It has been reported that the prevalence of PAH in systemic lupus erythematosis and mixed connective tissue disease remains unknown; although its incidence is greater than IPAH, it occurs less frequently than in SSc [31–34]. In the absence of fibrotic lung disease, PAH has also been reported infrequently in Sjögren syndrome [35], polymyositis [36], and rheumatoid arthritis [37]. Approximately one half of patients with PH and connective tissue diseases will die within 1 year if untreated [38]. PH is also a frequent complication of idiopathic pulmonary fibrosis (IPF) and is associated with a two to threefold increase in mortality [39], whereas in patients with sarcoidosis, mortality is nearly doubled [40]. It is increasingly being recognized that PH in patients with IPF is the sequela of a "primary" occlusive pulmonary vasculopathy, rather than being purely secondary to fibrotic destruction of the vascular bed [41].

Congenital Heart Disease

PH related to CHD results from the effects of a long-standing abnormal increase in pulmonary blood flow which leads to pathologic changes in the pulmonary vasculature, particularly in the smaller vessels. This results in increased pulmonary vascular resistance, which in turn has deleterious effects upon the heart and larger pulmonary vascular structures. Direct shunts can increase pulmonary blood flow and pressure (patent ductus arteriosis) (Figure 18.5).

Eisenmenger syndrome is defined as CHD with an initially large systemic-to-pulmonary shunt that induces progressive pulmonary vascular disease and PAH resulting in reversal of the shunt and central cyanosis [42, 43]. Eisenmenger syndrome represents the most advanced form of PAH associated with CHD (Figure 18.6). It has been reported that a large proportion of patients with CHD develop some degree of PAH [44–46]. The prevalence of PAH associated with congenital systemic-to-pulmonary shunts in Europe and North America has been estimated to range between 1.6 and 12.5 cases per million adults, with 25–50% of this population affected by Eisenmenger syndrome [47].

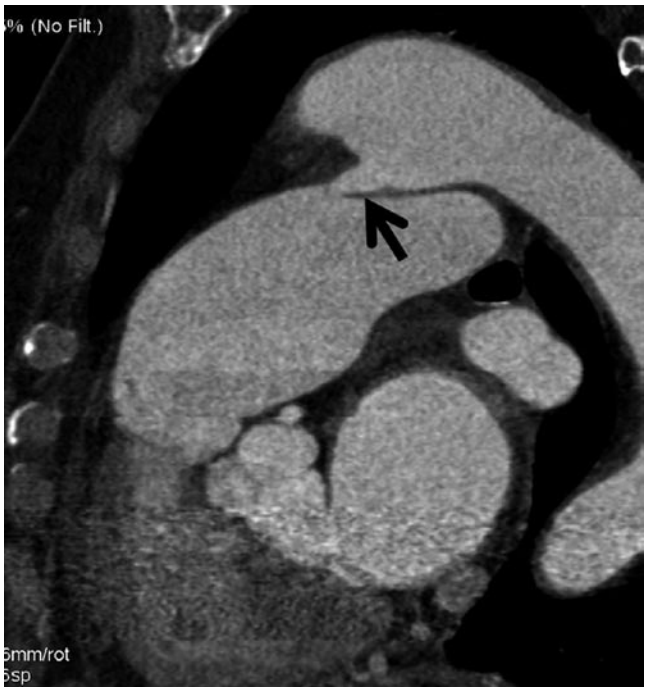

Figure 18.5. Sixty-four slice MDCT in a 20-year-old woman with patent ductus arteriosis (*black arrow*), seen well in this sagittal view with resultant dilation of the main pulmonary artery.

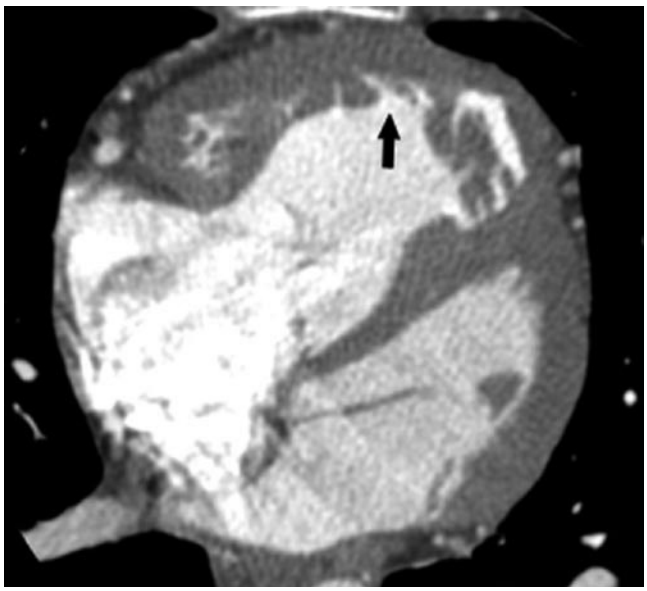

Figure 18.6. CT scan in a 22-year-old woman with Eisenmenger syndrome due to ASD and PH. Right cardiac chambers are enlarged with marked right ventricular hypertrophy (*black arrow*).

Schistosomiasis

The mechanism of PH in patients with schistosomiasis is probably multifactorial, and includes mechanical obstruction, local vascular inflammation related to eggs, and portal

hypertension [48, 49]. These cases can have a similar clinical presentation to IPAH [50], with similar histopathologic findings [51], and thus similar radiographic appearance.

Chronic Hemolytic Anemia

The prevalence of PAH in sickle cell disease (SCD) is not clearly established. The largest study revealed that 32% of patients with SCD had PH as defined by a Doppler-derived tricuspid regurgitation jet velocity ≥2.5 m/s [52]. The mechanism of PAH in SCD also remains uncertain. One hypothesis is that chronic hemolysis results in high rates of nitric oxide consumption producing a state of resistance to nitric oxide bioactivity, which results in less activity of smooth muscle guanosine monophosphate, a potent vasovasodilator/antiproliferative mediator [53, 54].

Pulmonary Veno-Occlusive Disease and Pulmonary Capillary Hemangiomatosis

PVOD accounts for a small number of PH cases. Because of its nonspecific findings of clinical features, laboratory data, and radiological manifestations, it is not easy to distinguish PVOD from IPAH, chronic thromboembolic disease, and other pulmonary diseases. The incidence is not clear, but the estimated annual incidence rate is 0.1–0.2 cases of PVOD per million persons in the general population [55, 56]. The prognosis of PVOD is poor, and the only curative therapy is lung transplantation. The CT findings of the disease may present smooth septal thickening, diffuse or mosaic ground-glass opacities, multiple small nodules, and pleural effusion [57–61]. PVOD and PCH also show the presence of crackles and clubbing on physical examination, hemosiderin-laden macrophages on bronchoalveolar lavage [62], and a lower carbon monoxide diffusing capacity and PaO_2 [61]. Although they may present similarly to IPAH, given the current evidence of different radiological, histopathologic findings and clinical outcomes, PVOD and PCH are classified separately.

PH Due to Lung Diseases and/or Hypoxia

A subcategory of lung disease characterized by a mixed obstructive and restrictive pattern includes chronic bronchiectasis, cystic fibrosis [63], and a newly identified syndrome characterized by the combination of pulmonary fibrosis, mainly of the lower zones of the lung, and emphysema, mainly of the upper zones of the lung [64]. The prevalence of PH in all of these conditions remains largely unknown. However, in a recent retrospective study of 998 patients with chronic obstructive pulmonary disease who underwent right heart catheterization, only 1% had severe PH (mean PA pressure >40 mmHg) [65]. In the syndrome of combined pulmonary fibrosis and emphysema, the prevalence of PH is almost 50% [64].

Pulmonary Embolism

PE is an obstruction of a pulmonary artery caused by a blood clot, air, fat, or tumor tissue. The most common cause of the obstruction is a blood clot (thrombus) usually from a peripheral vein. Most patients with deep vein thrombosis (DVT) develop PE. The average annual incidence of venous thromboembolism (VTE) in the United States is 1/1,000, with about 250,000 incident cases occurring annually [66–68]. The challenge in understanding the real disease is that an additional equal number of patients are diagnosed with PE at autopsy [66, 69]. It is estimated that between 650,000 and 900,000 fatal and nonfatal VTE events occur in the US annually. Left untreated, PE has a high mortality rate and accounts for 5–10% of all in-hospital deaths. The classic triad of signs and symptoms of PE (hemoptysis, dyspnea, chest pain) are neither sensitive nor specific, and many patients with PE are initially asymptomatic; most patients who have symptoms often have atypical and/or nonspecific symptoms, such as dyspnea, tachypnea, and chest pain.

Diagnostic Workup of PE

Many diagnostic tests have been suggested for the evaluation of patients with suspected VTE. These include the history and physical examination to the electrocardiogram, chest radiography, echocardiography, ventilation-perfusion scintigraphy, pulmonary angiography, CT and MR angiography, lower-extremity venography, and sonography. Although the diagnostic accuracy of laboratory tests such as D-dimer has increased (a negative result in combination with a low-probability clinical assessment provides reasonable certainty for excluding PE), radiologic imaging plays an important role in the diagnosis of PE, especially with the development of multidetector CT (MDCT) and increased use of CT pulmonary angiography.

Although normal chest X-ray findings are observed in 24% of patients with PE, an elevated hemidiaphragm can be observed in 28–41% of patients with acute PE. An elevated hemidiaphragm, consolidation, pleural effusion, or atelectasis occurs in about two-third of patients with acute PE. Especially in massive PE (Figure 18.7), local hyperlucency is seen when a lobar or segmental artery is occluded (Westermark sign), and engorgement of a major hilar artery (Fleischner sign) can be detected [70, 71]. Abrupt tapering or termination of a pulmonary vessel (knuckle sign), a pleural-based density or costophrenic density (Hampton's hump), and alveolar or interstitial pulmonary edema may occur. Most of the above chest X-ray findings are nonspecific. Nuclear scintigraphy (ventilation-perfusion or V/Q scanning) is useful if multidetector CT angiography (MDCTA) is not available. The V/Q scan in a patient with an acute PE will demonstrate an area distal to thrombus that is not properly perfused, altering the V/Q ratio.

Pulmonary angiography, the gold standard for diagnosing PE, is being replaced in many institutions with MDCTA,

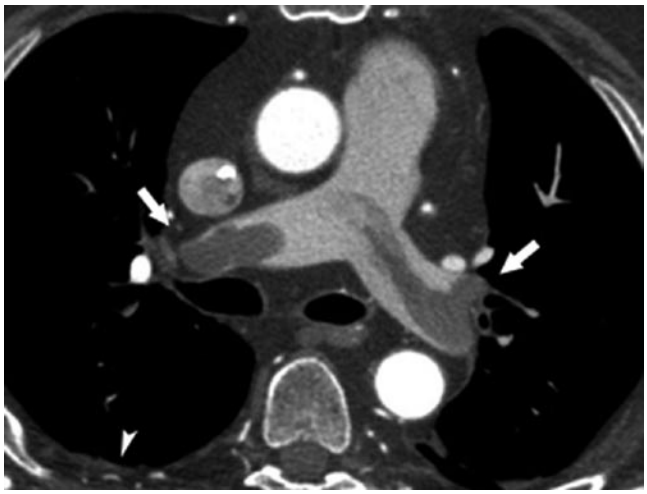

Figure 18.7. Sixty-four slice MDCT in a patient with pulmonary embolism (PE). An axial section at the level of the main pulmonary artery shows the filling defect (*white arrows*) of bilaterally enlarged pulmonary arteries with massive thromo-emboli. A small amount of right pleural effusion (*white arrowhead*) is observed.

which is less invasive, easier to perform, and has high sensitivity (83–100%) and specificity (89–97%) [72–74]. The PIOPED studies (large multicenter trials for CCTA in suspected PE) report negative predictive values as high as 99%.

The newest noninvasive method for the evaluation and diagnosis of PE is MRI. Although not as extensively studied as other imaging techniques, it can be utilized for the patients with renal dysfunction or an iodine contrast allergy. CT angiographic findings are shown (Figs. 18.7 and 18.8).

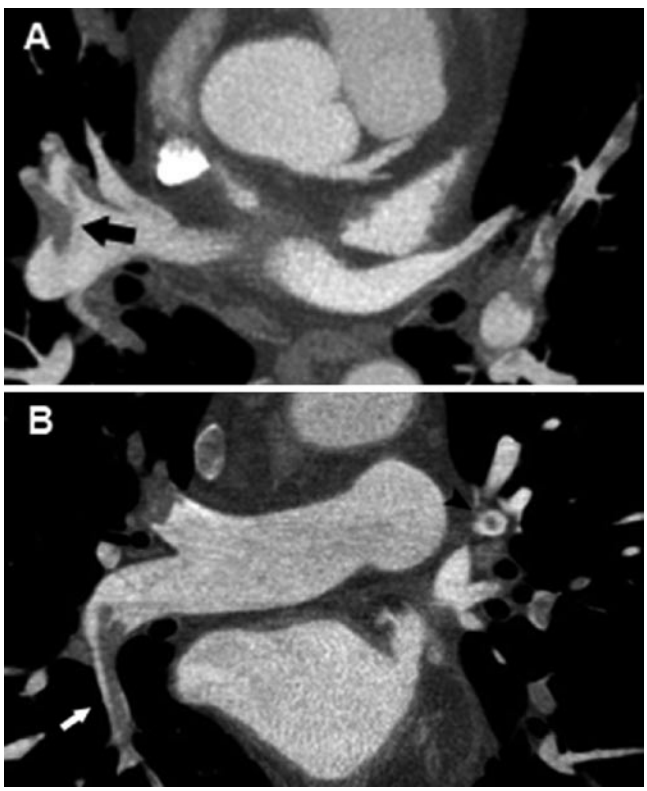

Figure 18.8. Sixty-four slice MDCT in a 58-year-old man with multiple bilateral PE. (**a**) "Saddle embolus" (*black arrow*) at the bifurcation of right pulmonary artery (PA). (**b**) "Tram line" (*white arrow*) and "ring shape" (*black arrowhead*) features of emboli at both peripheral PAs.

Chronic Thromboembolic PH

Chronic thromboembolic pulmonary hypertension (CTEPH) represents a frequent cause of PH (Figure 18.8). The incidence of CTEPH is uncertain; however, it is known to occur in up to 4% of patients after an acute PE [75, 76]. It is strongly recommended that patients with suspected or confirmed CTEPH be referred to a center with expertise in the management of this disease to consider the feasibility of performing pulmonary thromboendarterectomy, currently the only curative treatment. The decision depends on the location of the obstruction (central vs. more distal pulmonary arteries), the correlation between hemodynamic findings, and the degree of mechanical obstruction.

References

1. McLaughlin VV, Archer SL, Badesch DB, et al. ACCF/AHA 2009 expert consensus document on pulmonary hypertension a report of the American College of Cardiology Foundation Task Force on Expert Consensus Documents and the American Heart Association developed in collaboration with the American College of Chest Physicians; American Thoracic Society, Inc.; and the Pulmonary Hypertension Association. *J Am Coll Cardiol*. 2009;53:1573–1619.
2. Fleischner FG. Pulmonary embolism. *Clin Radiol*. 1962;13:169–182.
3. Simon M, Sasahara AA, Cannilla JE. The radiology of pulmonary hypertension. *Semin Roentgenol*. 1967;2:368–388.
4. Kuriyama K, Gamsu G, Stern RG, Cann CE, Herfkens RJ, Brundage BH. CT-determined pulmonary artery diameters in predicting pulmonary hypertension. *Invest Radiol*. 1984;19:16–22.
5. Kuo PC, Plotkin JS, Johnson LB, et al. Distinctive clinical features of portopulmonary hypertension. *Chest*. 1997;112:980–986.
6. Ng CS, Wells AU, Padley SP. A CT sign of chronic pulmonary arterial hypertension: the ratio of main pulmonary artery to aortic diameter. *J Thorac Imaging*. 1999;14:270–278.
7. Tan RT, Kuzo R, Goodman LR, et al. Utility of CT scan evaluation for predicting pulmonary hypertension in patients with parenchymal lung disease. *Chest*. 1998;113:1250–1256.
8. Edwards PD, Bull RK, Coulden R. CT measurement of main pulmonary artery diameter. *Br J Radiol*. 1998;71:1018–1020.
9. Chatterjee K, De Marco T, Alpert JS. Pulmonary hypertension: hemodynamic diagnosis and management. *Arch Int Med*. 2002;162:1925–1933.
10. Baque-Juston MC, Wells AU, Hansell DM. Pericardial thickening or effusion in patients with pulmonary artery hypertension: a CT study. *AJR Am J Roentgenol*. 1999;172:361–364.
11. Perloff JK, Hart EM, Greaves SM, Miner PD, Child JS. Proximal pulmonary arterial and intrapulmonary radiologic features of Eisenmenger syndrome and primary pulmonary hypertension. *Am J Cardiol*. 2003;92:182–187.
12. Griffin N, Allen D, Wort J, et al. Eisenmenger syndrome and idiopathic pulmonary arterial hypertension: do parenchymal lung changes reflect aetiology? *Clin Radiol*. 2007;62:587–595.
13. Van Der Meer RW, Pattynama PM, Van Strijen MJ, et al. Right ventricular dysfunction and pulmonary obstruction index at helical CT: prediction of clinical outcome during 3-month follow-up in patients with acute pulmonary embolism. *Radiology*. 2005;235:798–803.
14. Reid JH, Murchison JT. Acute right ventricular dilatation: a new helical CT sign of massive pulmonary embolism. *Clin Radiol*. 1998;53:694–698.
15. Bossone E, Duong-Wagner TH, Paciocco G, et al. Echocardiographic features of primary pulmonary hypertension. *J Am Soc Echocardiogr*. 1999;12:655–662.
16. Ryan T, Petrovic O, Dillon JC, Feigenbaum HF, Conley HJ, Armstrong W. An echocardiographic index for separation of right ventricular volume and pressure overload. *J Am Coll Cardiol*. 1985;5:918–924.

17. Yeh BM, Kurzman P, Foster E, Qayyum A, Joe B, Coakley F. Clinical relevance of retrograde inferior vena cava or hepatic vein opacification during contrast-enhanced CT. *Am J Roentgenol*. 2004;183:1227–1232.
18. Simonneau G, Robbins IM, Beghetti M, et al. Updated clinical classification of pulmonary hypertension. *J Am Coll Cardiol*. 2009;54:S43–S54.
19. Rich S, Dantzker DR, Ayres SM, et al. Primary pulmonary hypertension: a national prospective study. *Ann Intern Med*. 1987;107:216–223.
20. Loyd JE, Butler MG, Foroud TM, Conneally PM, Phillips JA, Newman JH. Genetic anticipation and abnormal gender ratio at birth in familial primary pulmonary hypertension. *Am J Respir Crit Care Med*. 1995;152:93–97.
21. Loyd JE, Primm RK, Newman JH. Familial primary pulmonary hypertension: clinical patterns. *Am Rev Respir Dis*. 1984;129:194–197.
22. Cogan JD, Pauciulo MW, Batchman AP, et al. High frequency of BMPR2 exonic deletions/ duplications in familial pulmonary arterial hypertension. *Am J Respir Crit Care Med*. 2006;174:590–598.
23. Aldred MA, Vijayakrishnan J, James V, et al. BMPR2 gene rearrangements account for a significant proportion of mutations in familial and idiopathic pulmonary arterial hypertension. *Hum Mutat*. 2006; 27:212–213.
24. Machado RD, Aldred MA, James V, et al. Mutations of the TGF- β type II receptor BMPR2 in pulmonary arterial hypertension. *Hum Mutat*. 2006;27:121–132.
25. Thomson JR, Machado RD, Pauciulo MW, et al. Sporadic primary pulmonary hypertension is associated with germline mutations of the gene encoding BMPR-II, a receptor member of the TGF-β family. *J Med Genet*. 2000;37:741–745.
26. Chaouat A, Coulet F, Favre C, et al. Endoglin germline mutation in a patient with hereditary haemorrhagic telangiectasia and dexfenfluramine associated pulmonary arterial hypertension. *Thorax*. 2004;59: 446–448.
27. Trembath RC, Thomson JR, Machado RD, et al. Clinical and molecular genetic features of pulmonary hypertension in patients with hereditary hemorrhagic telangiectasia. *N Engl J Med*. 2001;345:325–334.
28. McGoon M, Gutterman D, Steen V, et al. Screening, early detection, and diagnosis of pulmonary arterial hypertension: ACCP evidence based clinical practice guidelines. *Chest*. 2004;126:14S–34S.
29. Hachulla E, Gressin V, Guillevin L, et al. Early detection of pulmonary arterial hypertension in systemic sclerosis: a French nationwide prospective multicenter study. *Arthritis Rheum*. 2005;52:3792–3800.
30. Mukerjee D, St George D, Coleiro B, et al. Prevalence and outcome in systemic sclerosis associated pulmonary arterial hypertension: application of a registry approach. *Ann Rheum Dis*. 2003;62: 1088–1093.
31. Tanaka E, Harigai M, Tanaka M, Kawaguchi Y, Hara M, Kamatani N. Pulmonary hypertension in systemic lupus erythematosus: evaluation of clinical characteristics and response to immunosuppressive treatment. *J Rheumatol*. 2002;29:282–287.
32. Asherson RA, Higenbottam TW, Dinh Xuan AT, Khamashta MA, Hughes GR. Pulmonary hypertension in a lupus clinic: experience with twenty-four patients. *J Rheumatol*. 1990;17:1292–1298.
33. Burdt MA, Hoffman RW, Deutscher SL, Wang GS, Johnson JC, Sharp GC. Long-term outcome in mixed connective tissue disease: longitudinal clinical and serologic findings. *Arthritis Rheum*. 1999;42:899–909.
34. Jaïs X, Launay D, Yaici A, et al. Immunosuppressive therapy in lupus- and mixed connective tissue disease-associated pulmonary arterial hypertension: a retrospective analysis of twenty-three cases. *Arthritis Rheum*. 2008;58:521–531.
35. Launay D, Hachulla E, Hatron PY, Jaïs X, Simonneau G, Humbert M. Pulmonary arterial hypertension: a rare complication of primary Sjögren syndrome: report of 9 new cases and review of the literature. *Medicine (Baltimore)*. 2007;86:299–315.
36. Bunch TW, Tancredi RG, Lie JT. Pulmonary hypertension in polymyositis. *Chest*. 1981;79:105–107.
37. Dawson JK, Goodson NG, Graham DR, Lynch MP. Raised pulmonary artery pressures measured with Doppler echocardiography in rheumatoid arthritis patients. *Rheumatology (Oxford)*. 2000;39:1320–1325.
38. Coghlan JG, Handler C. Connective tissue associated pulmonary arterial hypertension. *Lupus*. 2006;15:138–142.
39. Lettieri CJ, Nathan SD, Barnett SD, et al. Prevalence and outcomes of pulmonary arterial hypertension in advanced idiopathic pulmonary fibrosis. *Chest*. 2006;129:746–752.
40. Nunes H, Humbert M, Capron F, et al. Pulmonary hypertension associated with sarcoidosis: mechanisms, haemodynamics and prognosis. *Thorax*. 2006;61:68–74.
41. Zisman DA, Karlamangla AS, Ross DJ, et al. High-resolution chest CT findings do not predict the presence of pulmonary hypertension in advanced idiopathic pulmonary fibrosis. *Chest*. 2007;132:773–779.
42. Eisenmenger V. Die angeborene defecte der kammersheidewand das herzen. *Z Klin Med*. 1897;132:131.
43. Wood P. The Eisenmenger syndrome or pulmonary hypertension with reversed central shunt. *Br Med J*. 1958;2:701–709.
44. Daliento L, Somerville J, Presbitero P, et al. Eisenmenger syndrome: factors relating to deterioration and death. *Eur Heart J*. 1998;19: 1845–1855.
45. Besterman E. Atrial septal defect with pulmonary hypertension. *Br Heart J*. 1961;23:587–598.
46. Hoffman JI, Rudolph AM. The natural history of ventricular septal defects in infancy. *Am J Cardiol*. 1965;16:634–653.
47. Galiè N, Manes A, Palazzini M, et al. Management of pulmonary arterial hypertension associated with congenital systemic-to pulmonary shunts and Eisenmenger's syndrome. *Drugs*. 2008;68:1049–1066.
48. Shaw AP, Ghareed A. The pathogenesis of pulmonary schistosomiasis in Egypt with special reference to Ayerza's disease. *J Pathol Bacteriol*. 1938;46:401–424.
49. de Cleva R, Herman P, Pugliese V, et al. Prevalence of pulmonary hypertension in patients with hepatosplenic Mansonic schistosomiasis – prospective study. *Hepatogastroenterology*. 2003;50:2028–2030.
50. Lapa MS, Ferreira EV, Jardim C, Martins Bdo C, Arakaki JS, Souza R. Clinical characteristics of pulmonary hypertension patients in two reference centers in the city of Sao Paulo]. *Rev Assoc Med Bras*. 2006;52:139–143.
51. Chaves E. The pathology of the arterial pulmonary vasculature in Manson's schistosomiasis. *Chest*. 1966;50:72–77.
52. Gladwin MT, Sachdev V, Jison ML, et al. Pulmonary hypertension as a risk factor for death in patients with sickle cell disease. *N Engl J Med*. 2004;350:886–895.
53. Reiter CD, Wang X, Tanus-Santos JE, et al. Cell-free hemoglobin limits nitric oxide bioavailability in sickle-cell disease. *Nat Med*. 2002;8:1383–1389.
54. Gladwin MT, Lancaster JR Jr, Freeman BA, Schechter AN. Nitric oxide's reactions with hemoglobin: a view through the SNO-storm. *Nat Med*. 2003;9:496–500.
55. Mandel J, Mark EJ, Hales CA. Pulmonary veno-occlusive disease. *Am J Respir Crit Care Med*. 2000;162:1964–1973.
56. Frazier AA, Franks TJ, Mohammed TL, Ozbudak IH, Galvin JR. From the Archives of the AFIP: pulmonary veno-occlusive disease and pulmonary capillary hemangiomatosis. *Radiographics*. 2007;27:867–882.
57. Holcomb BW Jr, Loyd JE, Ely EW, Johnson J, Robbins IM. Pulmonary veno-occlusive disease: a case series and new observations. *Chest*. 2000;118:1671–1679.
58. Resten A, Maitre S, Humbert M, et al. Pulmonary hypertension: CT of the chest in pulmonary veno-occlusive disease. *Am J Roentgenol*. 2004;183:65–70.
59. Lantuéjoul S, Sheppard MN, Corrin B, Burke MM, Nicholson AG. Pulmonary veno-occlusive disease and pulmonary capillary hemangiomatosis: a clinicopathologic study of 35 cases. *Am J Surg Pathol*. 2006;30:850–857.
60. Ozsoyoglu AA, Swartz J, Farver CF, Mohammed TL. High resolution computed tomographic imaging and pathologic features of pulmonary veno-occlusive disease: a review of three patients. *Curr Probl Diagn Radiol*. 2006;35:219–223.
61. Montani D, Achouh L, Dorfmuller P, et al. Pulmonary venoocclusive disease: clinical, functional, radiologic, and hemodynamic characteristics and outcome of 24 cases confirmed by histology. *Medicine(Baltimore)*. 2008;87:220–233.
62. Rabiller A, Jaïs X, Hamid A, et al. Occult alveolar haemorrhage in pulmonary veno-occlusive disease. *Eur Respir J*. 2006;27:108–113.

63. Fraser KL, Tullis DE, Sasson Z, Hyland RH, Thornley KS, Hanly PJ. Pulmonary hypertension and cardiac function in adult cystic fibrosis: role of hypoxemia. *Chest*. 1999;115:1321–1328.
64. Cottin V, Nunes H, Brillet PY, et al. Combined pulmonary fibrosis and emphysema: a distinct underrecognised entity. *Eur Respir J*. 2005;26: 586–593.
65. Chaouat A, Bugnet AS, Kadaoui N, et al. Severe pulmonary hypertension and chronic obstructive pulmonary disease. *Am J Respir Crit Care Med*. 2005;172:189–194.
66. Silverstein MD, Heit JA, Mohr DN, Petterson TM, O'Fallon WM, Melton LJ III. Trends in the incidence of deep vein thrombosis and pulmonary embolism: a 25-year population-based study. *Arch Intern Med*. 1998;158:585–593.
67. Tapson VF. Acute pulmonary embolism. *N Engl J Med*. 2008;358: 1037–1052.
68. Heit JA. The epidemiology of venous thromboembolism in the community. *Arterioscler Thromb Vasc Biol*. 2008;28:370–372.
69. Sandler DA, Martin JF. Autopsy proven pulmonary embolism in hospital patients: are we detecting enough deep vein thrombosis? *J R Soc Med*. 1989;82:203–205.
70. Stein PD, Terrin ML, Hales CA, et al. Clinical, laboratory, roentgenographic and electrocardiographic findings in patients with acute pulmonary embolism and no pre-existing cardiac or pulmonary disease. *Chest*. 1991;100:598–603.
71. Stein PD, Willis PW III, DeMets DL, Greenspan RH. Plain chest roentgenogram in patients with acute pulmonary embolism and no preexisting cardiac or pulmonary disease. *Am J Noninvas Cardiol*. 1987; 1:171–176.
72. Stein PD, Fowler SE, Goodman LR, et al. Multidetector computed tomography for acute pulmonary embolism. *N Engl J Med*. 2006;354: 2317–2327.
73. Qanadli SD, Hajjam ME, Mesurolle B, et al: Pulmonary embolism detection. Prospective evaluation of dual-section helical CT versus selective pulmonary arteriography in 157 patients. *Radiology*. 2000; 217:447–455.
74. Winer-Muram HT, Rydberg J, Johnson MS, et al. Suspected acute pulmonary embolism: Evaluation with multi-detector row CT versus digital subtraction pulmonary arteriography. *Radiology*. 2004;233: 806–815.
75. Tapson VF, Humbert M. Incidence and prevalence of chronic thromboembolic pulmonary hypertension: from acute to chronic pulmonary embolism. *Proc Am Thorac Soc*. 2006;3:564–567.
76. Pengo V, Lensing AW, Prins MH, et al. Incidence of chronic thromboembolic pulmonary hypertension after pulmonary embolism. *N Engl J Med*. 2004;350:2257–2264.

Part VI

Multidisciplinary Topics

19

Comparative Use of Radionuclide Stress Testing, Coronary Artery Calcium Scanning, and Noninvasive Coronary Angiography for Diagnostic and Prognostic Cardiac Assessment

Daniel S. Berman, Leslee J. Shaw, James K. Min, Aiden Abidov, Guido Germano, Sean W. Hayes, John D. Friedman, Louise E.J. Thomson, Xingping Kang, Piotr J. Slomka, and Alan Rozanski

Single-photon emission computed tomography (SPECT) or positron emission tomography (PET) myocardial perfusion scintigraphy (MPS) is a well-established noninvasive imaging modality that is a core element in evaluation of patients with stable chest pain syndromes. Stress SPECT MPS is the most commonly utilized stress imaging technique for patients with suspected or known coronary artery disease (CAD) and has a robust evidence base including the support of numerous clinical guidelines.

By comparison, cardiac computed tomography (CT) is a more recently developed method, providing noninvasive approaches for imaging coronary atherosclerosis and coronary artery stenosis. After being in use for well over a decade, noncontrast CT for imaging the extent of coronary artery calcification (CAC) has an extensive evidence base supporting its use in CAD prevention. Contrast-enhanced CT for noninvasive CT coronary angiography (CCTA) is relatively new, but has a rapidly growing evidence base regarding diagnosing obstructive CAD and assessing risk.

It is likely that noncontrast CT or CCTA for assessment of extent of atherosclerosis will become an increasing part of mainstream cardiovascular imaging practices as a first-line test. In some patients, further ischemia testing with MPS will be required. Similarly, MPS will continue to be widely used as a first-line test, and, in some patients, further anatomic definition of atherosclerosis with CT will also be appropriate. This review also provides a synopsis of the available literature on imaging that integrates both CT and MPS in strategies for the assessment of asymptomatic patients for their atherosclerotic coronary disease burden and risk as well as symptomatic patients for diagnosis and guiding management. We propose possible risk-based strategies through which imaging might be used to identify asymptomatic candidates for more intensive prevention and risk factor modification strategies as well as symptomatic patients who would benefit from referral to invasive coronary angiography (ICA) for consideration of revascularization.

Introduction

Radionuclide stress testing has long been an essential component in physicians' diagnostic and prognostic assessment for patients presenting with signs or symptoms suggestive of CAD. In recent years, coronary CT has emerged as a complementary and potential alternative technique to MPS for the evaluation of patients with CAD symptoms [1, 2]. Coronary CT can be used to noninvasively quantify the degree of coronary artery calcification, identify atherosclerotic plaque, and evaluate the degree of coronary luminal narrowing. These new applications are forcing a re-evaluation of existing paradigms for the diagnosing and risk stratification of patients with suspected CAD. Concurrent with recent improvements in coronary CT technology and increase in its utilization, a growing evidence base has emerged which has clarified the potential roles of CAC scanning and CCTA in cardiac populations. In this review, we will provide an overview the current use of MPS, CAC scanning, and CCTA, and evaluate their potential complementary uses for optimizing the clinical assessment of patients with suspected or known CAD or subjects for whom screening for atherosclerosis may be beneficial.

Stress Myocardial Perfusion Scintigraphy

Stress MPS is most commonly performed using SPECT (approximately 7 million studies per year in the US), with increasing application of PET in recent years [3]. By comparison, 3 million stress echo procedures are performed annually. The diagnostic and prognostic applications of MPS have become part of standard clinical guidelines for assessment of patients with suspected or known CAD [4–6]. The Appropriate Use Criteria (AUC) for MPS have recently been revised, and these guidelines are increasingly

being applied as standards for quality assessment of cardiac imaging practice [7].

Prognostic Assessment Using MPS

The diagnostic applications of noninvasive cardiac testing have remained relatively constant over the last 30 years and are thus not reviewed here. By contrast, the prognostic applications of MPS have evolved continuously. MPS has been consistently shown to be an effective tool for risk-stratification as well as for predicting benefit from revascularization, reflecting, in part, the increasing recognition that anatomic findings by themselves often do not provide sufficient information to guide the management of patients with known CAD.

Prognostic Significance of Normal and Equivocal MPS Studies

For purposes of prognostic risk assessment, MPS is performed using either exercise or pharmacologic stress. A normal exercise MPS study at an "adequate" level of achieved stress – conventionally defined as achieving >85% of maximal predicted heart rate – or a normal pharmacologic stress MPS study generally identifies patients as being at low term risk for future cardiac events [4, 8]. A meta-analysis of 19 studies (n=39,173) determined that a normal or low risk stress MPS was associated with an annual cardiac event rate of only 0.6% (25–75th percentile=0.5–0.9%) [9]. Among patients without comorbidities, a normal stress MPS study defines a low risk of cardiac events across the spectrum of CAD likelihood, during short-term follow-up (2–3 years) [8]. The presence of a normal stress MPS study also generally signifies a low risk of cardiac events among patients with known CAD, although the risk is higher in these patients than in those without known CAD [10].

Studies indicate that the risk of cardiac events among patients with normal MPS studies and various comorbidities may be increased to 1–3% per year, a level of patient risk that is generally considered as an "intermediate" range relative to therapeutic decision-making. Subgroups of patients with relatively higher risk despite a normal stress MPS study include those who have peripheral arterial disease, diabetes [11], atrial fibrillation [12], dyspnea or heart failure symptoms [13], those requiring pharmacologic stress [8], patients with chronic kidney disease [14], and the elderly [15].

Given these considerations, the risk of adverse cardiac events should not be defined by stress MPS results in isolation. Rather, prognostic assessment should also take into account patients' baseline clinical risk. For pharmacologic stress, this concept has been illustrated in a large adenosine-tested population [16], in which the risk was highest among insulin dependent diabetics, intermediate among noninsulin dependent diabetics, and lowest – but not as low as with exercise MPS – among the remaining patients. In addition to baseline characteristics, the patient's response to stress needs to be considered. The findings of exercise hypotension or evidence of chronotropic incompetence may also signify an increased risk even in the presence of a normal scan [17]. Similarly, the finding of transient ischemic dilation (TID) of the left ventricle is associated with an elevated risk, even in the presence of an otherwise completely normal scan [18] (Figure 19.1).

Early data suggested that there is little difference between the presence of a normal MPS study and an equivocal MPS study, wherein the amount of observed defect reversibility is too small to consider the study diagnostic of abnormality. This is because an equivocal study falls within the "flat" portion of the exponential curve that relates ischemia to the likelihood of cardiac events. Beginning with work by Staniloff et al [19], various studies have confirmed comparably low cardiac event rates among patients who had normal vs. equivocal MPS results. More recently, however, 18,200 patients were followed-up for a mean of 2.7 years [20], and those patients with equivocal SPECT interpretation [5] had a slightly but significantly higher rate of cardiac death compared to those with normal scans. This finding suggests that the use of the equivocal scan category may be an aid to clinicians in avoiding misclassification of patients with high risk anatomic findings (see section on Limitations of MPS in this chapter.)

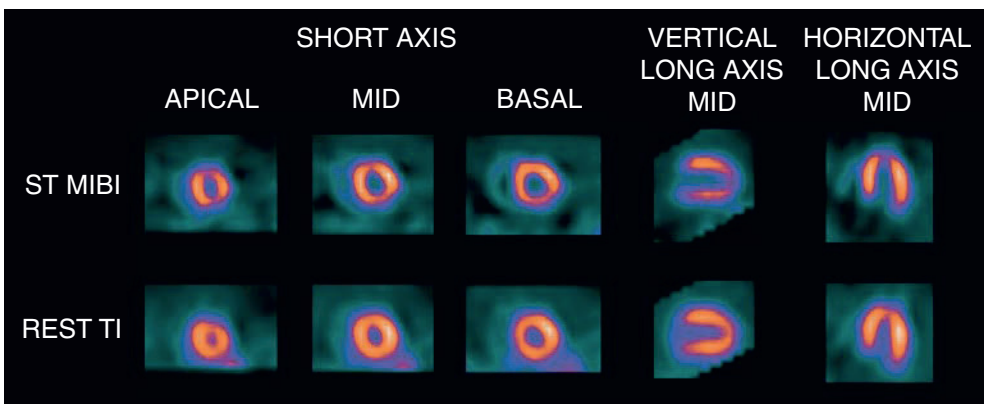

Figure 19.1. Exercise myocardial perfusion ingle photon emission computed tomography (SPECT) in a 67-year-old diabetic woman with shortness of breath and no known coronary artery disease (CAD). The imaging shows normal perfusion and transient ischemic dilation (TID) (1.40). Invasive coronary angiography (ICA) revealed severe three vessel disease (70–90% stenosis).

Prognostic Significance of Mildly and Severely Abnormal Stress-Rest MPS Studies

A moderately to severely abnormal MPS study is associated with elevated risk of cardiac events. Observational data have shown that event, and the majority of these patients are thus referred to coronary angiography [21]. Distinction should be made, in this regard, concerning assessment of left ventricular (LV) function vs. that of the amount of ischemic myocardium. Both are prognostic predictors but, as a general concept, while the overall magnitude of stress perfusion defects and ejection fraction (EF) are among the strongest predictors of mortality, *the magnitude of ischemia is the stronger predictor of benefit from revascularization [*22].

While the decision to pursue very aggressive management is generally straightforward in the presence of moderate to severe ischemia, selecting optimal management among patients with only mild inducible ischemia is often challenging. In general, data suggest that patients with mild perfusion abnormalities have only mildly elevated risk of cardiac events and do not clearly benefit from coronary revascularization procedures [22]. However, if one of more non-perfusion high risk variables are seen on MPS, referral to ICA in patients with mild perfusion abnormalities is reasonable in certain clinical settings. The high-risk scintigraphic abnormalities were shown below (Table 19.1), among which one of the most important is TID of the left ventricle post-stress [18], which is strongly associated with severe proximal coronary stenosis as noted earlier, even for patients with normal perfusion results, TID is associated with an elevated risk of cardiac events [18]. Increased lung uptake on the post-stress study, related to elevated pulmonary capillary wedge pressure during stress, is another high risk MPS finding [23].

LV size, EF, and stress-induced wall motion abnormalities, findings from the ECG-gated MPS examination, confer further information regarding patient risk. A post-stress EF <35% has been noted to be a high risk marker signifying worsening event-free survival [2, 4] as has an increase in LV end-systolic volume [24]. Normal limits for men and women for EF and end-systolic volume have been reported [25]. The presence of stunned myocardium on gated MPS study (represented by post-stress decrease in wall motion in association with relatively normal wall motion and/or perfusion on rest MPS imaging) may also signify the presence of a regionally-severe stenosis subtending the region of LV dysfunction [26].

Table 19.1. "High risk" MPS patterns

Extensive and/or severe reversible myocardial perfusion defects
TID of the left ventricular (LV)
Transient lung reuptake following stress (or thallium studies)
Ischemia in the setting of clinically unheralded myocardial infarction
Substantially reduced exercise LVEF on post-stress MPS or fall in LVEF between post stress and rest gated MPS study
Pattern of stunned myocardium on post stress MPS

As with normal MPS studies, mild ischemia in the setting of significant comorbidities, such as diabetes [16], atrial fibrillation [27], or peripheral arterial disease, also increases overall event risk, and the risk associated with mild ischemia on MPS may be accentuated in the presence of various non-scintigraphic signs and symptoms. These would include the induction of exercise chest pain [28], particularly if it occurs early during early stress testing or is prolonged following it, the occurrence of ischemia in association with low exercise effort, the elicitation of relative hypotension, and the induction of marked ST segment abnormalities during or following stress testing.

Exercise vs. Pharmacologic Stress for Use with MPS

Exercise is the preferred method of stress testing for MPS, as it provides the clinician with insight into these various non-scintigraphic factors associated with patient outcomes [4]. In addition, exercise helps to define patients' capabilities for physical work and provides documentation of ischemic thresholds that may be important for serial monitoring of anti-ischemic therapies. Nonetheless, with the aging of the US population and increasing comorbidities, many patients are unable to achieve an adequate level of stress during exercise and require pharmacologic stress imaging. By 2009, approximately 50% of stress MPS studies were performed with pharmacologic stress.

Multiple issues are specifically pertinent to pharmacologic stress. Pharmacologic MPS may be employed using a vasodilator or inotropic pharmacologic stress. Vasodilator agents are given using a brief infusion of intravenous (IV) adenosine or dipyridamole and, more recently, regadenoson, a new A2A agonist administered by rapid injection over 10 s using a single-use pre-filled syringe [29]. These agents produce maximal coronary hyperemia by their induction of maximal coronary arteriolar dilation. In patients with hemodynamically significant stenosis, coronary blood flow cannot increase to the extent noted in normal segments. Unlike exercise-induced perfusion abnormalities which are tightly associated with true ischemia and associated regional wall motion abnormalities, heterogeneity of myocardial perfusion without production of ischemia generally occurs with the use of the vasodilators. In patients with collateral-dependent total coronary occlusion or critical stenosis, however, the vasodilator-induced hyperemia may be associated with a coronary steal in which the pressure falls in the collateral vessels, causing a true decrease in blood flow to the zones supplied by the collateralized vessels. The decrease in blood flow in such instances results in true ischemia, including induction of regional wall motion abnormalities, ischemic ECG response or TID of the left ventricle. When ST segment deviations occur during infusion of IV adenosine, it may signify worsening event-free survival [30]. Chest pain following vasodilator infusion, however, is considered nondiagnostic as it may be a side effect of the drug unrelated to ischemia.

Semiquantitative Analysis of MPS Studies

It should be evident from this discussion that quantification of the amount of ischemia on stress-rest MPS is highly important for accurate prognostic assessment. Accordingly, nuclear cardiology reports should routinely specify the extent and severity of inducible myocardial ischemia, its location, and provide an overall estimation of the percent myocardium at risk. While subjective terms such as mildly, moderately, and severely abnormal are commonly used, they do not adequately express the degree of abnormality on MPS studies. To achieve a greater uniformity of test interpretation, a 17-segment model is recommended as a way to provide a semiquantitative analysis of MPS [31]. The recommended approach uses a 5 point scoring (0 = normal, 4 = absent tracer uptake), and summed stress, summed rest, and summed difference scores are used to provide global indices of the extent and severity of hypoperfusion [22, 32]. These global indices have been consistently shown to be strong predictors of risk with SPECT [33, 34] and more recently with PET [35, 36].

Due to the unit-less nature of the summed stress score and its dependence on the particular scoring system employed (e.g., 17 vs. 20 segment), we have recently developed a normalized summed score calculated by dividing the summed score by the maximal score possible and multiplying by 100 [22]. For the 17 segment, 5 score system, the maximal score is 68, and for the 20 segment system, the score is 80. The result is that a % myocardium abnormal for stress, ischemic, and rest perfusion defects can be reported. It has been shown that this % myocardium ischemic has similar prognostic implications for 17 and 20 segment score approaches [37]. This score can function with any segmental scoring system, and provides the clinician with a number that is intuitively understood. We now employ this % myocardium approach routinely in all of our clinical reporting as well as in all prognostic manuscripts. Observational data suggest that in general when 5–10% of the myocardium is abnormal at stress, risk is intermediate [22, 37]. When >10% of the myocardium is involved, the data suggest that these patients are at high. When >10% of the myocardium is *ischemic* (reversible defects), there is likely to be a benefit, in terms of improved outcome, from coronary revascularization [22] (Figures 19.2 and 19.3).

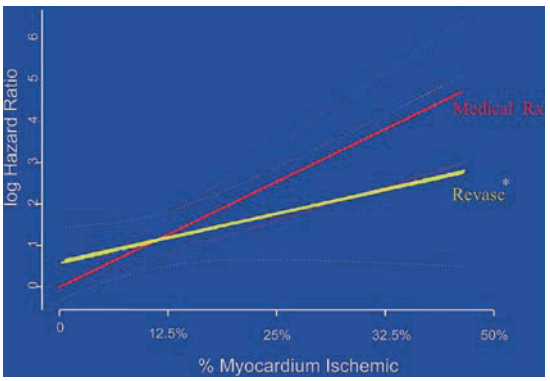

Figure 19.2. Relationship between % myocardium ischemic and log of the hazard ratio in 10,647 patients treated either with medical therapy (*dashed line*) or early revascularization (<60 days post-SPECT MPS; *solid line*) based on multivariable modeling. In the setting of little or no ischemia, medical therapy is associated with superior survival; with increasing amounts of ischemia a progressive survival benefit with revascularization over medical therapy is present. Ninety-five percent confidence intervals are shown by the closely *dotted lines* (* indicates $p < 0.001$) (adapted with permission of Wolters Kluwer from Hachamovitch et al [22]).

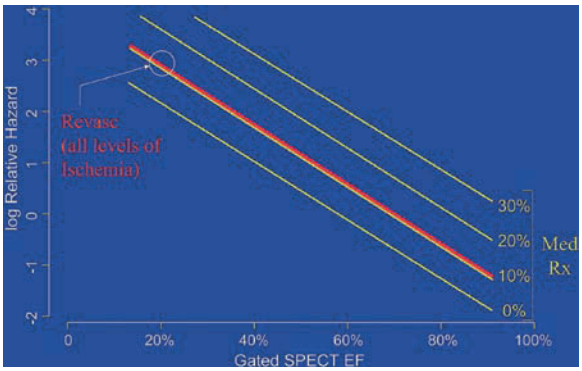

Figure 19.3. Relationship between gated SPECT EF and log of the hazard ratio in 5,366 patients based on multivariable modeling. *Solid lines* represent predicted survival for 0, 10, 20, and 30% myocardium ischemic in patients treated medically. *Dashed lines* represent predicted survival for patients treated with revascularization for all values of % myocardium ischemic. Overall, risk increased with decreasing ejection fraction (EF). For any value of EF, however, risk also increased as % myocardium ischemic increased, indicating an incremental value for % myocardium ischemic over EF. Compared to risk in patients treated medically, risk in patients undergoing early revascularization was independent of the % myocardium ischemic present (as evidenced by a *single (red) line* representing survival after revascularization for all degrees of ischemia). Risk in the early revascularization patients was similar to the risk of medically treated patients with 10% myocardium ischemic, throughout the range of EF (adapted with the kind permission of Springer Science + Business Media from Hachamovitch et al [44]).

Quantitative Analysis of MPS

An important advantage of the nuclear cardiology methods over stress echocardiography and current clinical use of rest/stress cardiac magnetic resonance imaging is the ability to objectively quantify perfusion defects and the magnitude of ischemia. Multiple commercially available software packages provide automatic or semiautomatic quantitation of perfusion defects with SPECT or PET myocardial perfusion imaging, providing objectivity as well as improved reproducibility of the quantitative measurements [38–42].

Slomka et al [38, 43] have developed the measurement of the total perfusion deficit (TPD) (Figure 19.4), providing an objective assessment of global stress and rest myocardial perfusion abnormality that incorporates the extent and severity of perfusion defect. Stress, rest, and ischemic TPDs are in essence computed, normalized summed stress, rest, and differences scores [43] – the semiquantitative scores used in most of the prognostic literature on nuclear cardiology. The automatic TPD measurement was found to

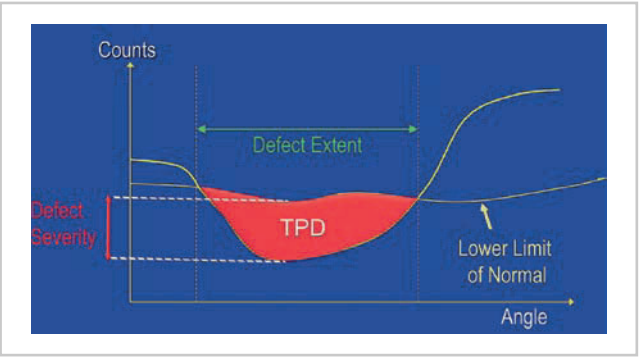

Figure 19.4. The concept of total perfusion deficit (TPD). A circumferential profile for one short axis slice is shown with corresponding normal limits. The areas below the normal limit curve but above the circumferential profile curve for a given slice define perfusion deficit in a given slice. These areas are computed for all circumferential profiles in the myocardium and summed forming TPD (adapted with the kind permission of Springer Science + Business Media from Berman et al [38]).

be superior to expert visual analysis of perfusion defects measurement in detecting angiographically significant CAD [43].

Beyond measurements of the magnitude of perfusion defects, the objective quantitative analysis software packages all provide measurements of LV EF and end-diastolic volume, complementing the perfusion measurements for assessment of prognosis.

Predicting Benefit from Revascularization with MPS

In a large single center registry of 10,627 patients without prior CAD who underwent SPECT MPS, a "proof-of-principle" question was asked: Can imaging identify appropriate and beneficial treatment strategies and at what threshold of abnormality does therapeutic efficacy shift [22]? After adjusting for differences between medically treated and revascularized patients – including propensity score adjustment to correct for differences in referral patterns to treatment options – patients with extensive myocardial ischemia by SPECT MPS exhibited a clear survival benefit with myocardial revascularization for the intermediate-term occurrences of cardiac death (Figure 19.2). By contrast, among those with no myocardial ischemia, the cardiac death rate was higher with myocardial revascularization than with medical therapy. The "cross-over point" at which myocardial ischemia tipped the balance towards myocardial revascularization appeared to be more than 10% ischemic myocardium. Thus, this study provided valuable insight into potential linkage between cardiac imaging results, patient treatment, and patient clinical outcomes. A subsequent registry study by this group extended these results by examining the role of LVEF in prediction of risk and prediction of survival benefit from therapy assignment on the basis of MPS results [44], showing that the 10% ischemia threshold for prediction of revascularization benefit held across the range of EF. While EF predicts risk of cardiac death, the extent of ischemia is the strongest predictor of survival benefit with revascularization.

Shortly after these results were published, the results of the Clinical Outcomes Utilizing Revascularization and Aggressive Drug Evaluation (COURAGE) trial [45] were reported, casting doubt as to whether coronary anatomic assessment alone is sufficient to determine whether patients are likely to benefit from revascularization. Even patients with advanced angiographic disease showed no difference in hard event rates when being assigned to an optimal medical therapy (OMT) strategy vs. OMT combined with percutaneous coronary intervention (PCI). Subsequently, a nonrandomized nuclear substudy of the COURAGE trial [46] examined the influence of ischemia on outcomes. Ischemia was defined quantitatively by the objectively determined TPD at stress and rest (Figure 19.4). This was study of 314 patients in whom both pre- and 6–18 month post-randomization SPECT MPS was performed. Patients assigned to PCI and OMT demonstrated significantly greater ischemia reduction when compared to patients receiving OMT alone (PCI + OMT: 33% ($n = 159$); OMT alone: 19% ($n = 155$); $p = 0.0004$). Ischemia reduction ≥5% was also more frequent in the PCI + OMT group compared with the OMT alone group (33.3 vs. 19.8%, respectively, $p = 0.004$) (Figure 19.5). The study also showed that ischemia reduction, by OMT or OMT + PCI, was associated with improved long-term outcomes. However, some patients in the OMT alone group demonstrated dramatic ischemia reduction (Figure 19.6). Importantly, among the relatively smaller subset of patients with "moderate-to-severe pretreatment ischemia," a significantly greater proportion showed significant ischemia reduction (≥5% reduction in ischemic myocardium) with a strategy of PCI + OMT as opposed to OMT (78 vs. 52%; $p = 0.007$). Hence, despite the lack of improved survival with PCI + OMT vs. OMT alone in the main COURAGE study [45], the substudy suggests that PCI + OMT appears to be a superior approach to reduce ischemic burden, particularly in patients with extensive ischemia. Thus, the COURAGE substudy provides supportive evidence that imaging of myocardial ischemia could affect patient outcomes through guiding decisions for revascularization.

Of importance, the COURAGE results are not generalizable to patients who have left main CAD (these patients were excluded from COURAGE) as well as to patients being considered for CABG as their revascularization procedure. Hence, a new randomized clinical trial is currently under review: the ISCHEMIA trial (the International Study of Comparative Health Effectiveness with Medical and Invasive Approaches) proposes to incorporate moderate to severe imaging evidence of ischemia as an inclusion criterion. If funded, this trial promises to further clarify the initially reported results and allow us to better understand what constitutes optimal patient management. Such future study should also differentiate cohorts for PCI and CABG and characterize the type and completeness of medical therapy.

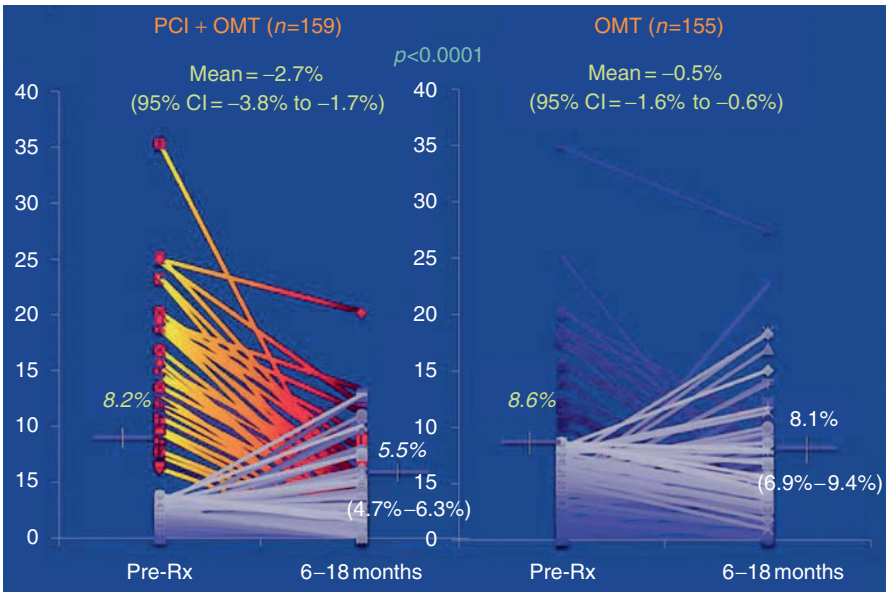

Figure 19.5. Comparison of inducible ischemia with myocardial perfusion scintigraphy (MPS) pretreatment and after 6–18 months of optimal medical therapy (OMT) with or without percutaneous coronary intervention (PCI) (adapted with permission of the Wolters Kluwer from Shaw et al [46]).

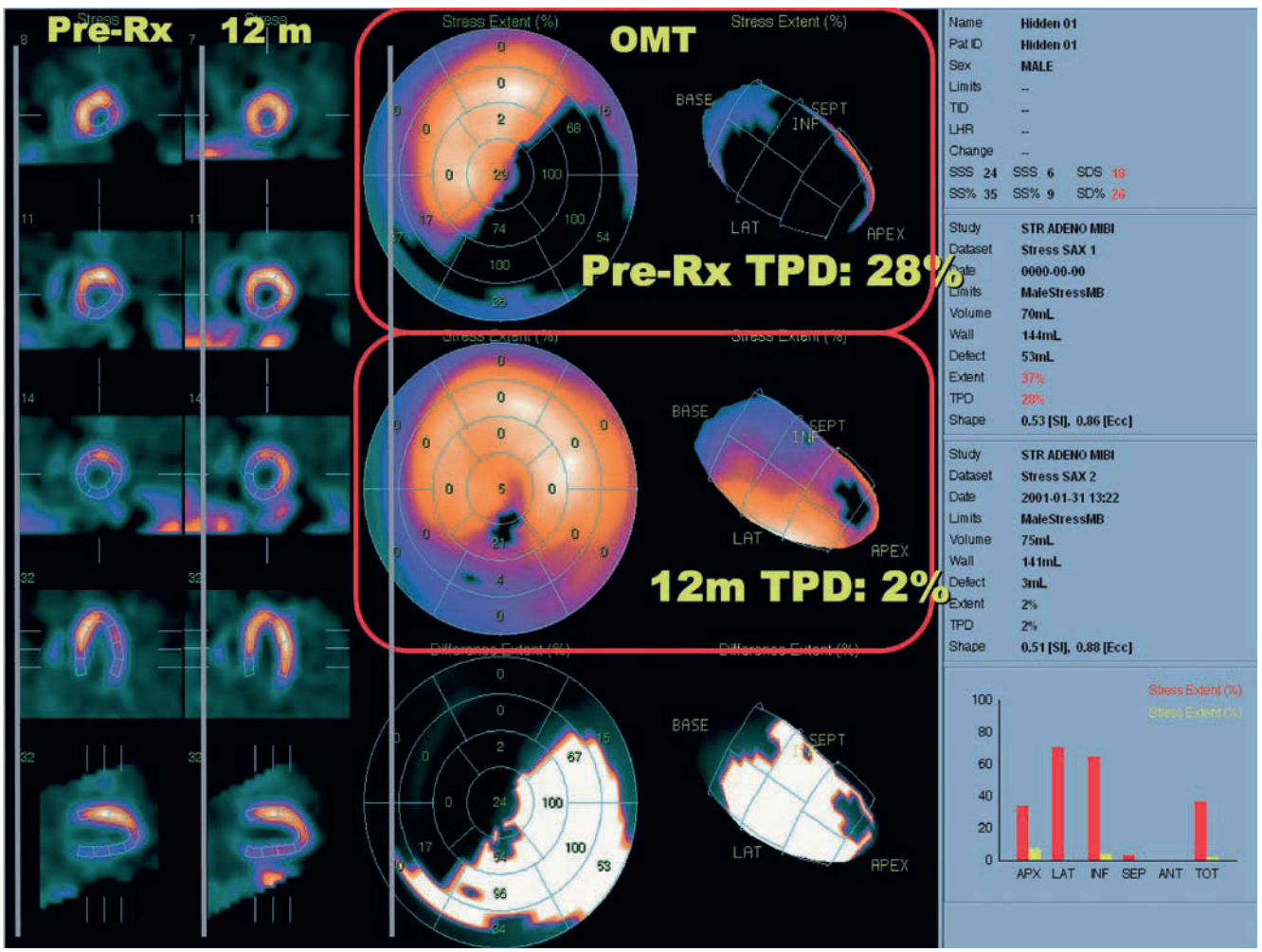

Figure 19.6. An illustrative case of a COURAGE patient enrolled in the substudy. The pretreatment stress images are in the first column while the 12 month follow-up images are in the second column. A severe and extensive perfusion defect is seen in the pretreatment with near complete resolution on the post-treatment study. The polar plots for the first and second studies are also noted in the center of this slide. The stress TPD for the baseline study was 28% of the myocardium, while the second study following 12 months of aggressive medical intervention resulted in a dramatic decline to a TPD of only 2%.

Limitations of MPS

While assessment of perfusion on MPS has high sensitivity for detecting ischemia, it may underestimate the extent of ischemia [47, 48]. Of interest, in a recent study of 101 patients who underwent MPS and ICA and were found to have significant obstruction of the left main coronary artery, only 55% of the patients were identified as being at high risk on the basis of ≥10% myocardium ischemia [48]. However, when ancillary findings such as TID, increased lung uptake, and stress-induced wall motion abnormalities were taken into account, 87% of patients with left main CAD were identified as being at high risk (Figure 19.7). Moreover, none of the patients with left main CAD had completely normal (non-equivocal) MPI studies – underscoring the importance of the category of "equivocal" in reporting MPS examinations [20]. It is also possible for MPS to be normal in a patient with severe and extensive CAD. This phenomenon may be due to "balanced ischemia," a hypothetical circumstance in which patients with severe disease in all coronary arteries may not manifest a regional perfusion defect on MPS [49, 50]. However, this phenomenon, if present, must be relatively uncommon, since no study to date has contradicted the observation of low cardiac event rates among patients with a normal stress MPS study, assuming an adequate heart rate achieved for exercise studies and the absence of medications that could impede maximal vasodilation with dipyridamole or adenosine, such as caffeine and the absence of major comorbidities.

Early data suggest that coronary flow reserve measurements – currently possible with PET myocardial perfusion studies and potentially possible with SPECT studies and novel gamma cameras – may improve risk classification in patients with minor perfusion defects [35]. It is possible that these quantitative coronary flow reserve measurements will provide information regarding endothelial function abnormalities, at a stage of CAD before hemodynamically significant coronary stenosis has occurred. In general, however, a limitation of the MPS methods is that they do not provide assessments of the subclinical atherosclerotic burden that can be obtained from non-contrast cardiac CT as discussed in the following Section.

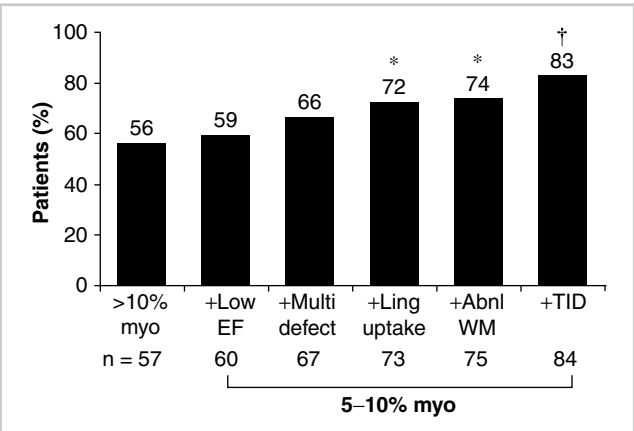

Figure 19.7. Detection rates of left main CAD in patients with high risk of abnormality by perfusion and nonperfusion data on gated myocardial perfusion SPECT. *$p < 0.05$ and †$p < 0.001$ vs. >10% myocardium at stress, respectively. *% myo* % of myocardium; *EF* ejection fraction; *Multi* multi vessel; *Abnl WM* abnormal wall motion; *TID* transient ischemic dilation (adapted with the kind permission of Springer Science + Business Media from Berman et al [48]).

Cardiac CT

CT Coronary Calcium Scanning

Chronologically, noncontrast ECG-gated cardiac CT evolved before CCTA as the initial clinically relevant application of cardiac CT; it has enabled the accurate measurement of coronary artery calcification, opening up the opportunity for improved assessment of patients with subclinical coronary atherosclerosis. CAC is thought to develop in the body's attempt to contain and stabilize inflamed coronary plaque [51]. In general, evidence of CAC reflects a more advanced stage of plaque development. CAC is considered pathognomonic of coronary atherosclerosis. A quantitative relationship has been demonstrated between CAC and histopathologic evidence of coronary plaque area: Calcified plaque assessment correlates with pathologic assessment of the total amount of calcified plus noncalcified plaque [52]. As such, CAC serves as an indirect but proportional marker for global atherosclerotic burden.

Substantial study has now established the prognostic value of CAC imaging, and also characterized estimators of risk following consideration of CAC distribution according to age, gender, and other clinical variables [53–55]. Initial studies were performed in ethnically narrow populations, but, recently, follow-up of 6,722 patients from four ethnic groups in the Multi-Ethnic Study of Atherosclerosis (MESA) registry [56] demonstrated that the CAC score is a significant predictor of both major cardiac events (cardiac death or myocardial infarction) and any coronary events in all ethnic groups (Figure 19.8). Moreover, a new analysis of the data from the same study [57] demonstrates that risk stratification based on standard absolute cutoff points of CAC score (<100, 100–400, and >400 Agatston units) performed much better than age-sex-race/ethnicity–specific percentiles in terms of model fit and discrimination (Figure 19.9).

Limitations of CAC Scanning

While CAC scanning is effective in predicting risk, to date there is little objective data to indicate that aggressive treatment of patients with subclinical atherosclerosis defined by CAC reduces subsequent cardiac events. In a randomized clinical trial, a part of the St. Francis Heart Study showed a trend to less progression of the CAC score in patients treated with statins vs. a control group, but failed to reach statistical significance [58]. There is a recent trend toward recommendation of CAC testing for asymptomatic patients,

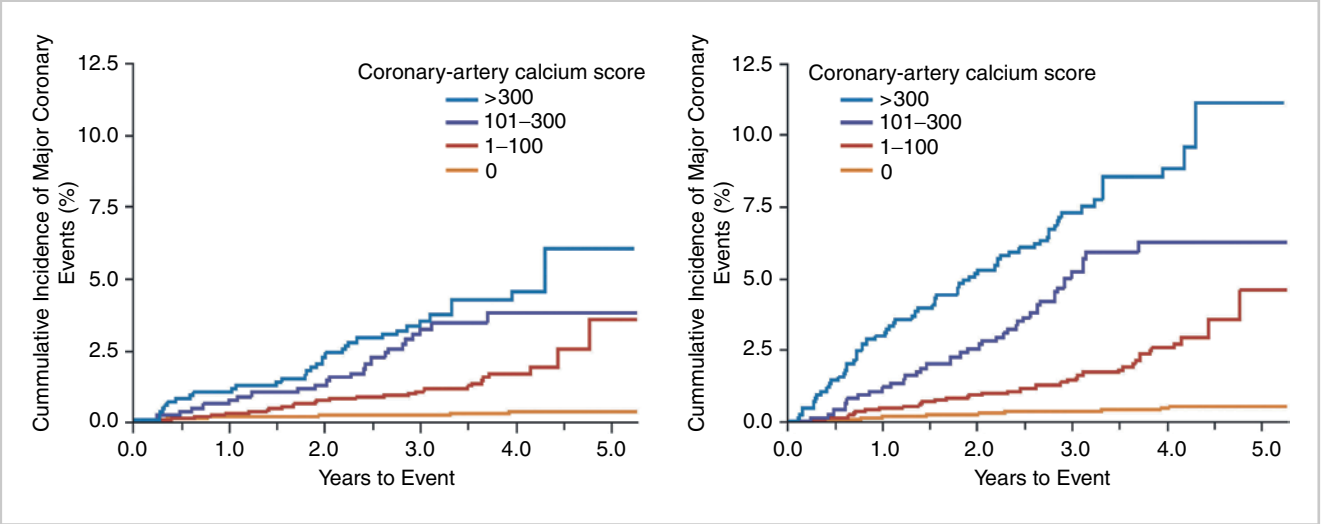

Figure 19.8. Unadjusted Kaplan–Meier cumulative-event curves for coronary events among participants with CAC Scores of 0, 1–100, 101–300, and >300. A shows the rates for major coronary events (myocardial infarction and death from coronary heart disease), and B shows the rates for any coronary event. The differences among all curves are statistically significant ($p < 0.001$) (adapted with permission from Detrano et al [56]. Copyright © 2008 Massachusetts Medical Society. All rights reserved).

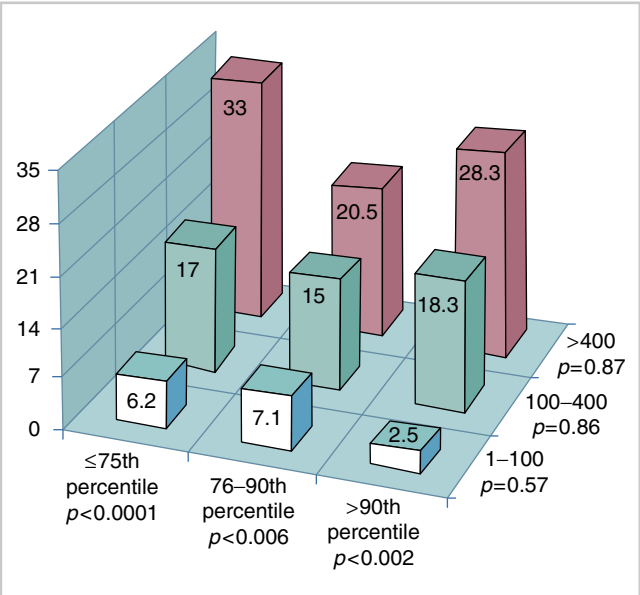

Figure 19.9. Rates of Incident CAD/1,000 Person Years at Risk by Joint Categories of Absolute CAC Group and Age-Sex-Race/Ethnicity–Specific Percentiles Displays the rates of incident CAD/1,000 person years at risk by joint categories of absolute CAC group and age-, sex-, and race/ethnicity-specific percentiles. Within a particular level of age-, sex-, and race/ethnicity-specific percentile, there remains a clear trend of increasing risk across levels of the absolute CAC groups. In contrast, once absolute CAC category is fixed, there is no increasing trend across levels of age-, sex-, and race/ethnicity-specific categories (adapted with permission of Elsevier from Budoff et al [57]).

at least those at intermediate clinical risk, and for aggressive treatment of those with prognostically important amounts of CAC [53, 54]. A randomized trial assessing the effects of CAC scanning on patient outcomes is being considered. While uncommon, some patients with only non-calcified plaque may develop an acute coronary syndrome (ACS).

CCTA: Diagnostic and Prognostic Impact in Different Clinical Populations

While considered possible since the initial description by Hounsfield of computed tomography [59], the era of CCTA did not begin to grow significantly until 1998 when the first multislice computed tomography (MSCT) scanners with four detector rows and rotation times of less than 0.5 s became clinically available [60]. For practical purposes, the introduction of the 16-slice MSCT scanners in 2001 marked the start of the rapid growth phase of CCTA [61]. This development allowed routine visualization of even small coronary segments, sparking interest. By 2005, four major manufacturers were offering 64-slice scanners, providing CT angiograms with true 3D data in isotropic voxels of ~0.5 mm and complete studies in 5–10 heartbeats. Since then, CCTA has been increasingly applied in clinical practice. However, the extent to which it will be used in preference to stress imaging methods in patients with atypical angina or other symptoms indicating an intermediate likelihood of CAD has not yet been determined.

Comparisons of CCTA to Invasive Angiography

Numerous studies of the diagnostic accuracy of the CCTA have been performed comparing CCTA to ICA. These studies have limitations such as referral bias. Nevertheless, on the basis of a large body of evidence, CCTA is considered the most accurate noninvasive test for the detection and exclusion of CAD as defined by ICA, based on published meta-analyzes. Recently, three large multicenter trials regarding the accuracy of CCTA for detecting CAD by ICA have been published [62–64]. A recent

prospective, multicenter, multivendor study conducted with "real-world" analysis – no patients or segments were excluded because of impaired image quality attributable to either coronary motion or calcifications – involved 360 symptomatic patients with acute and stable anginal syndromes who were between 50 and 70 years of age and were referred for diagnostic conventional ICA, which was compared with CCTA [64]. In this population of patients with intermediate-to-high and high pretest likelihood of CAD, CCTA was reliable for ruling out significant CAD. Specificity of the CCTA in this study was lower than in most other reports, probably due to the inclusion of all the segments and patients despite observed artifacts. An important recently published prospective multicenter trial (ACCURACY: Assessment by Coronary Computed Tomographic Angiography of Individuals Undergoing Invasive Coronary Angiography) [62] investigated 230 symptomatic patients with intermediate-to-high and high likelihood of CAD who were referred for the ICA. In this study, 64-slice CCTA demonstrated high diagnostic accuracy for detection of obstructive coronary stenosis at both thresholds of 50 and 70% stenosis. The authors also concluded that the 99% negative predictive value at the patient and vessel level observed in this study establishes CCTA as an effective noninvasive alternative to ICA to rule out obstructive CAD. In this study, the prevalence of obstructive CAD was 12.5%. Similar high diagnostic accuracy of the CCTA compared to ICA was demonstrated in the CACTUS (Coronary Angiography by Computed Tomography with the use of a Submillimeter resolution) trial [65] that included 243 patients with an intermediate pretest probability for CAD. In a subsequent multicenter trial, the CORE 64 (The Coronary Artery Evaluation using 64-Row Multidetector Computed Tomography Angiography) study, the overall accuracy was similar, but with somewhat lower negative predictive value [63].

Initial Applications of CCTA

In patients with an intermediate likelihood of CAD, the clinical implications of a normal CCTA study are generally clear: the high negative predictive value implies that the symptoms leading to testing are very unlikely to be due to obstructive CAD. The clinical implications of the abnormal CCTA study are often, however, less clear. While the coronary angiographic correlations have been excellent, the correlations between CCTA and functional measures of ischemia have been much lower. In the studies to date in which both SPECT MPS and CCTA have been performed, less than 50% of the patients with CCTA studies showing ≥50% stenosis demonstrated ischemia by SPECT-MPS (Figure 19.11) [66]. Since a stenosis of ≥70% severity is now more widely required as an angiographic criterion for the need for revascularization, it would be of interest to see the relationship between CCTA and ischemia using this angiographic cutoff point. However, given the lack of excellent correlation between angiographic stenosis and coronary flow reserve, the current "gold standard" for hemodynamic significance [67, 68], it is likely that a substantial proportion of such lesions, even with the ≥70% stenosis criterion, will not demonstrate ischemia. In a study of 292 patients undergoing MPS and CCTA within 6 months, we have shown that less than 50% of lesions with between 70–89% stenosis on CCTA demonstrated ischemia on MPS as assessed by TPD (Figure 19.10) [69].

CCTA is a relatively new modality in the armamentarium of advanced cardiac imaging. Thus, prognostic data available still cover either relatively small populations or provide a limited (either short- or mid-term) follow-up length. Nevertheless, initial publications in this field demonstrate powerful predictive value of CCTA, with excellent prognosis in those patients who have no evidence of atherosclerosis on their index scan [70, 71].

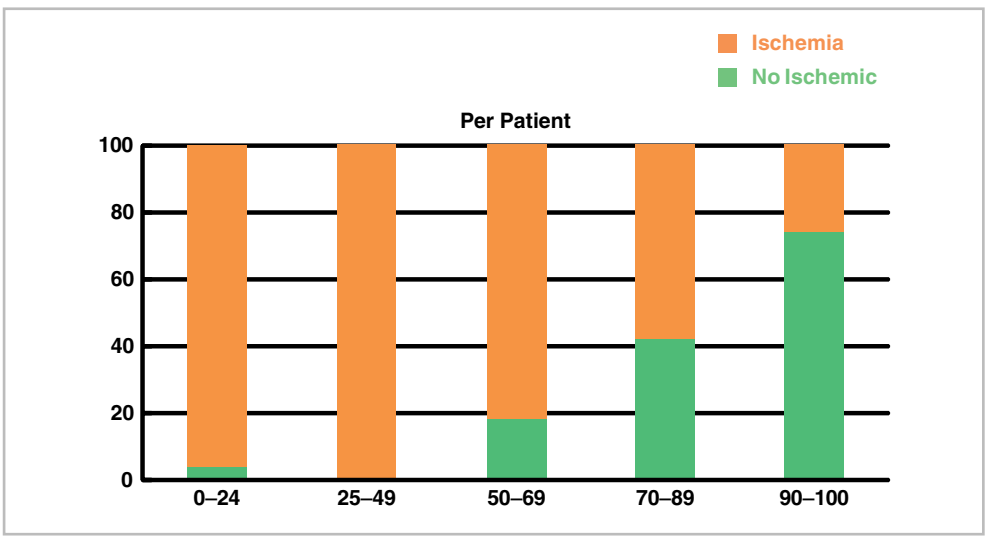

Figure 19.10. Prevalence of ischemia on SPECT MPI in patient groups defined by maximal stenosis detected during CCTA. Bars represent percent of individuals in each stenosis category with ischemia, defined by TPD ≥5%, on SPECT MPI. The numbers in parentheses represent number of individuals in each stenosis category. In a per-patient analysis, prevalence of ischemia increased in proportion to stenosis severity with $p = 0.001$ across all categories of stenosis severity. (adapted with permission of Springer from Tamarappoo et al [69]).

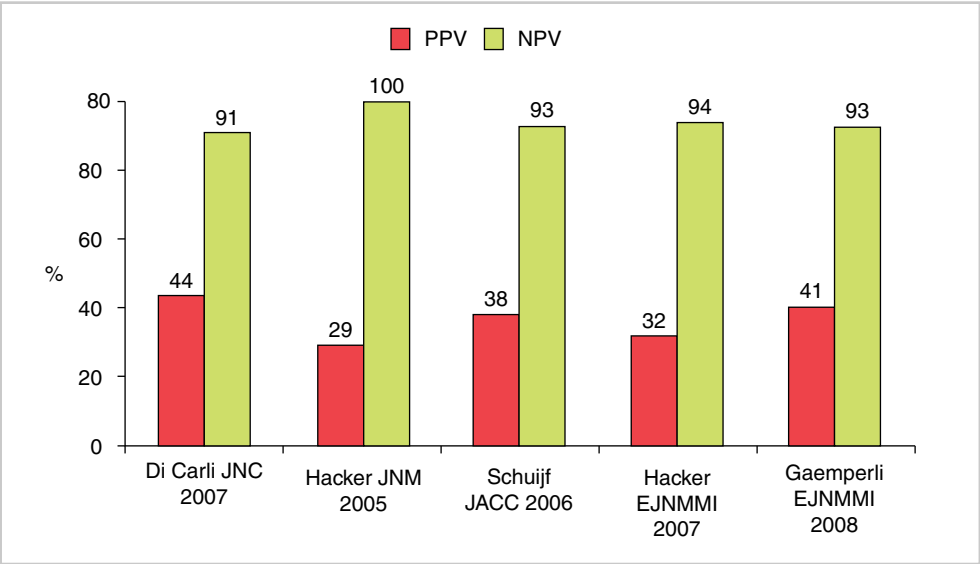

Figure 19.11. Available to-date studies demonstrating positive and negative predictive values of the CCTA stenosis ≥50% in predicting MPS ischemia (adapted with the kind permission of Spring Science + Business Media from Hachamovitch and Di Carli [134]).

Recently, more detailed analysis of the larger population ($n = 1{,}127$) has shown that in patients with chest pain CCTA identifies increased risk for all-cause death [72]. In this population, a negative CCTA was associated with extremely low all-cause mortality. Notably, the CCTA predictors of death included proximal left anterior descending artery stenosis and number of vessels with ≥50 and ≥70% stenosis. Of importance, there was an appropriate increase in the death rate associated with each step of increased risk when the CCTA was assessed by the Duke CAD Prognostic Index (Figure 19.12).

This risk predictive ability of CCTA-identified coronary artery stenosis appears to be above and beyond that of atherosclerosis detection by CAC. In a recent prospective study of 432 patients undergoing both CCTA and CAC and followed for almost 2 years, both CCTA findings of obstructive coronary artery stenosis as well as increasing CAC scores were associated with the development of major adverse cardiac events. After adjustment of demographics, risk factors, and baseline CAC score, CCTA findings – including presence of any coronary artery stenosis ≥50%, increasing numbers of coronary segments exhibiting stenosis ≥50%, increasing number of coronary segments with any plaque, and increasing number of coronary segments with noncalcified plaque – were independently predictive of adverse events [73].

Of importance also is a significant additive prognostic value of the combined CCTA and MPS results; in a recent communication in this field, presence of both abnormal CCTA and MPS carried a substantially worse prognosis than any one of these tests alone (Figure 19.13) [74]. In this European study, 541 patients who had both MPS and CCTA were followed-up for a median of 672 days; hard event rate in patients with none or mild CAD as defined by CCTA (<50% stenosis) was 1.8 vs. 4.8% per year in patients with significant CAD (≥50% stenosis). A normal MPS (SSS <4) and abnormal

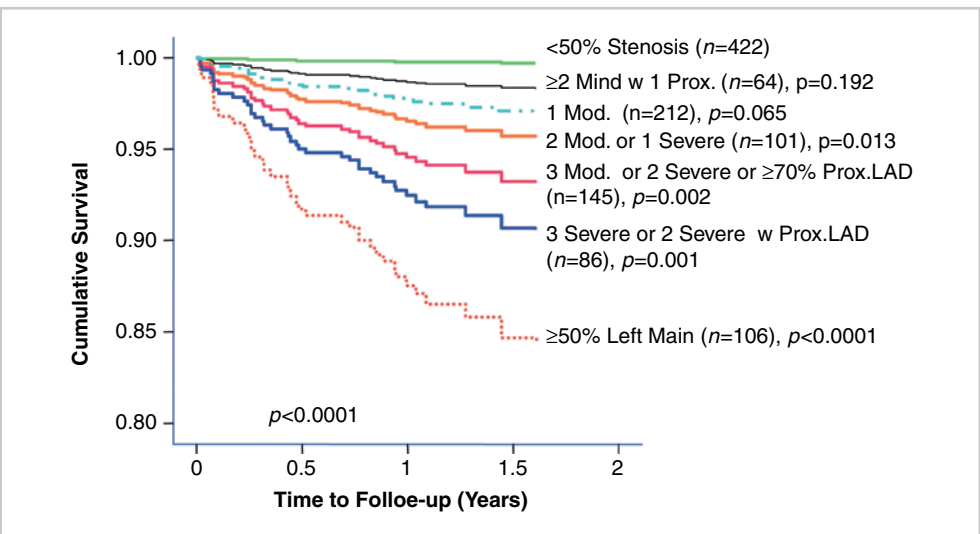

Figure 19.12. Cumulative survival in patients exhibiting plaque by the Duke Prognostic Coronary Artery Disease Index. Risk-adjusted $p < 0.001$ (controlling for age, family history, and dyslipidemia). *LAD* left anterior descending artery; *Mild (30–49%), Mod (50–69%)* moderate; *Severe (≥70%), Prox* proximal (adapted with permission of Elsevier from Min et al [71]).

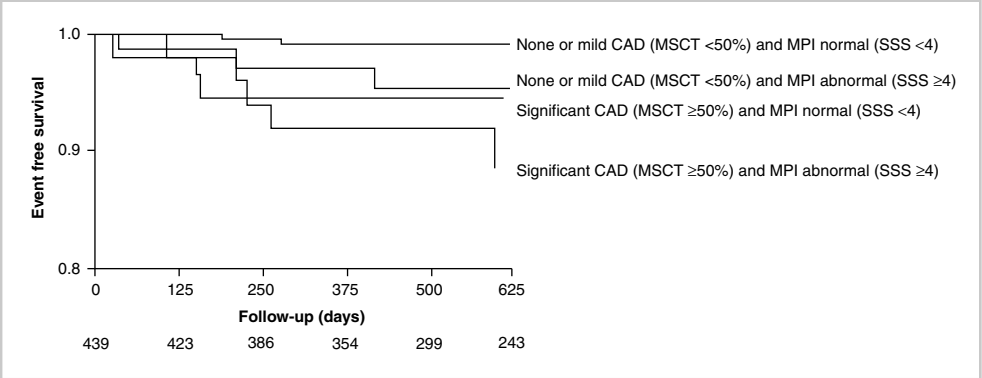

Figure 19.13. Kaplan–Meier curves for hard events (all-cause mortality and nonfatal myocardial infarction) in patients with a normal MPI (SSS <4) and none or mild CAD (<50% stenosis) on multislice computed tomography (MSCT), in patients with an abnormal MPI (SSS ≥4) and with none or mild CAD (<50% stenosis) on MSCT, in patients with a normal MPI (SSS <4) and significant CAD (MSCT ≥50% stenosis), and, finally, in patients with an abnormal MPI (SSS ≥4) and significant CAD (MSCT ≥50% stenosis). *MPI* myocardial perfusion imaging; *SSS* summed stress score. (Log Rank *p*-value < 0.005) (adapted with permission of Elsevier from van Werkhoven et al [75]).

MPS (SSS ≥4) were associated with an event rate of 1.1 and 3.8% per year, respectively. CCTA and MPS findings were associated with synergistic prognostic impact, and their combined utilization resulted in significantly improved prediction of cardiac events ($p < 0.005$) [74].

Limitations of CCTA

While the negative predictive value (NPV) of CCTA has been consistently shown to be very high, the positive predictive value for obstructive CAD at ICA is less impressive due to the lower resolution of the method (0.4 vs. 0.2 mm for ICA). Furthermore, the positive predictive value of CCTA findings for ischemia by MPS is poor; i.e., there are many sources of false-positive CCTA studies, including dense coronary calcium, coronary artery motion, arrhythmia, patient motion, breathing, and technical sources of error.

Hybrid CT/SPECT and CT/PET

Interest in combining the functional information provided by MPS with the anatomical information provided by CT has led to the development of new hybrid CT SPECT equipment that allows for essentially simultaneous assessment of both anatomic and perfusion parameters. SPECT/CT systems are now available from multiple manufacturers.

For PET, hybrid PET/CT has become the standard for almost all commercially available PET machines, linking the high resolution of CT with the functional richness of PET. In the future, it is possible that SPECT systems with dramatic increases in sensitivity as well as increases in spatial resolution could become available, with the potential of rapid, dynamic SPECT and routine absolute quantifications of coronary flow [76]. In some form, it is predicted that hybrid systems will play an increasingly important role for combined anatomic/functional imaging in the future.

Currently, however, the place of hybrid imaging for CCTA and MPS with PET or SPECT remains unclear. While it is likely that tests of anatomy and function will prove to be complementary in a substantial proportion of patients undergoing imaging tests [75, 77], whether these tests are most effectively applied sequentially or simultaneously is yet to be defined. If hybrid approaches with acceptably low radiation burden become widely available and if combined testing is not prohibitively expensive, the potential of the combined approach will have the greatest opportunity to be realized. Since it is usually not possible to determine which patients require both anatomic assessment of the coronary arteries and assessment of myocardial perfusion, the combination of CCTA and MPS in a single setting is not likely to become common. Most likely, such combination could be selectively performed in the subset of patients with equivocal findings on one of the exams using software for image registration and fusion [77] to resolve diagnostic discrepancies between these two techniques. However, the combination of CAC scanning with MPS, made possible as a routine with PET/CT or SPECT/CT systems, could prove to be a commonly performed combined study, providing information both for guiding the need and intensity of medical therapy/risk factor modification, including the need for treatment of ischemia and possible revascularization.

Complementary Aspects of the Imaging Technologies

As noted in earlier, each of the imaging modalities that we have reviewed offers salient strengths and weaknesses. CAC scanning can be used to estimate the total magnitude of atherosclerotic burden and predict patient outcomes, but it is a nonspecific means for predicting the presence or severity of angiographically significant stenoses. MPS is a useful test for diagnosing the presence of angiographically significant CAD among patients with intermediate CAD likelihood, and is a highly effective test for predicting prognosis and benefit from revascularization and for assessing myocardial viability, but MPS cannot predict the underlying burden of atherosclerotic plaque. Rather, we have previously demonstrated that within stress test populations, a normal MPI study may often still be associated with substantial subclinical atherosclerosis (Figure 19.14) [78].

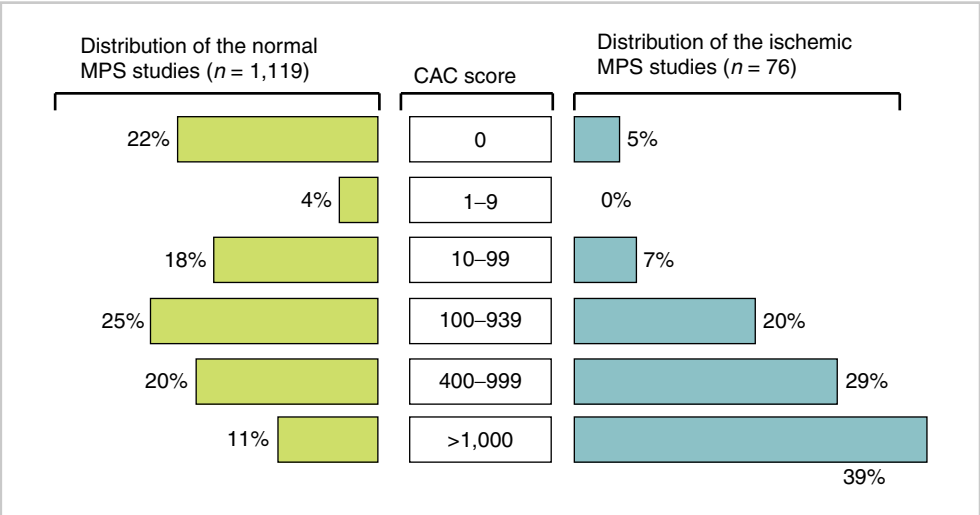

Figure 19.14. Distribution of CAC scores for the 1,119 patients manifesting a normal MPS (*left*) and the 76 patients with an ischemic MPS (*right*) (adapted with permission of Elsevier from Berman et al [78]).

In our experience, even when CAC scores exceed 1,000 in our stress test patients, ~80% of these patients will have a normal MPS study [78], indicating that extensive atherosclerosis can commonly be present without resulting in inducible myocardial ischemia. CCTA is effective in determining the presence and magnitude of angiographically significant CAD and it useful for diagnosis in patients with a intermediate likelihood of CAD. CCTA may also have future use in evaluating coronary plaque morphology [79], but it has not yet been widely used for assessment of myocardial ischemia.

The availabilities of all three tests (MPS, CAC, CCTA) provide physicians with the ability to evaluate the magnitude of atherosclerotic burden and coronary stenoses noninvasively and to define the functional significance of coronary lesions. The challenge is to define the appropriate clinical synergy among these tests. In the current era of rapidly escalating medical expenditures, consideration of medical costs must be carefully weighed in determining the potential attractiveness of logically conceived paradigms for incorporating these three technologies into a new schema for the diagnostic or prognostic evaluation of patients with suspected CAD. A second issue is the consideration of cumulative radiation exposure. Recent data have focused increased concern on the potential long-term effects of low-dose radiation [80]. With patients being evaluated at earlier ages and potentially being followed for decades, it may be reasonable to assume that radiation exposure will play an increasing role in choice of testing strategies.

As CAC scanning and CCTA mature in their applications, it will become increasingly important for physicians to understand how these newer and older technologies compare to each other and can be used in complementary fashion for the clinical management of patients with suspected or known CAD. Already, emerging data have begun to formulate an evidence base that physicians can rely upon to make more informed decisions regarding patient management. Accordingly, we will now review the complementary aspects of imaging technologies for common management decisions, such as how and who to screen for CAD, how to best perform diagnostic testing among patients with an intermediate pretest likelihood of CAD, and the use of testing for risk stratification purposes. In addition to these common uses, we will compare the use of various imaging modalities as they relate to other commonplace cardiologic issues, including the assessment of patients with acute chest pain, the evaluation of myocardial viability and work-up of patients with heart failure, selection of patients for implantable cardioverter-defibrillator (ICD) placement, and the guidance for cardiac resynchronization therapy (CRT).

Screening for CAD

Screening for CAD is sometimes applied in mandatory fashion to certain segments of the public and to individuals with increased CAD risk factor burden. For years, exercise ECG was advocated as a means of screening such individuals, followed by MPS study for those who have a positive ECG response. More recently, CAC scanning has emerged as a new means for initially screening, but controversy exists as to which asymptomatic subjects are candidates. Some investigators have suggested that the need for CAC scanning be based on the Framingham Risk Score (FRS) [81]. The FRS assesses individuals' 10-year risk of cardiac events based on subject age, gender, history of smoking and diabetes, and measurements of blood pressure and LDL, HDL, and triglyceride. Subjects are arbitrarily divided into groups based on their 10 year FRS risk: "low" if it is under 6%, "intermediate" if it is 6–20%, and "high" if it is >20%. CAC scanning has been recommended for those with intermediate FRS risk [54, 82, 83].

Various studies, however, have suggested that the FRS is not an effective screening tool for predicting the presence or absence of CAC in stress test populations [84, 85]. Thus, caution should be used on relying even on a low FRS to exclude the potential utility of CAC scanning in asymptomatic patients who are candidates for stress testing. A recent consensus statement has suggested that tests of atherosclerosis

such as CAC scanning or carotid intimal-medial thickness could be become a routine means of evaluating all men over age 45 and women over age 55 as to their long-term risk of adverse cardiac events risk based on the degree of their underlying atherosclerotic burden, as recommended by the SHAPE (Society for Heart Attack Provention and Eradication) Guidelines (Figure 19.15) [86]. In patients with extensive coronary atherosclerosis, generally accepted as an Agatston CAC score of ≥400, stress myocardial perfusion imaging is considered appropriate [87]. This triaging aspect of CAC testing is based on a documented threshold relationship between the magnitude of CAC and the likelihood of inducible myocardial ischemia. He et al [88] were the first to evaluate the interrelationship between CAC scores and the likelihood of inducible myocardial ischemia. In their study of 370 asymptomatic patients undergoing both CAC scanning and MPS, among those with CAC scores ≤100, only ~1% had an abnormal MPS. For higher CAC scores, the rate of abnormal MPS increased progressively, such that nearly half of patients with a CAC score >400 had inducible ischemia on MPS. In a larger study involving 1,195 consecutively tested patients without a prior CAD diagnosis who underwent both CAC scanning and MPS, ischemia was low among not only patients with a CAC score <100 but also for CAC sores between 100 and 400 (Figure 19.16) [78]. Each of these studies has been in agreement for an increase in MPS ischemia for those with CAC scores>400, but the studies have differed concerning the observed rate of ischemia among those with

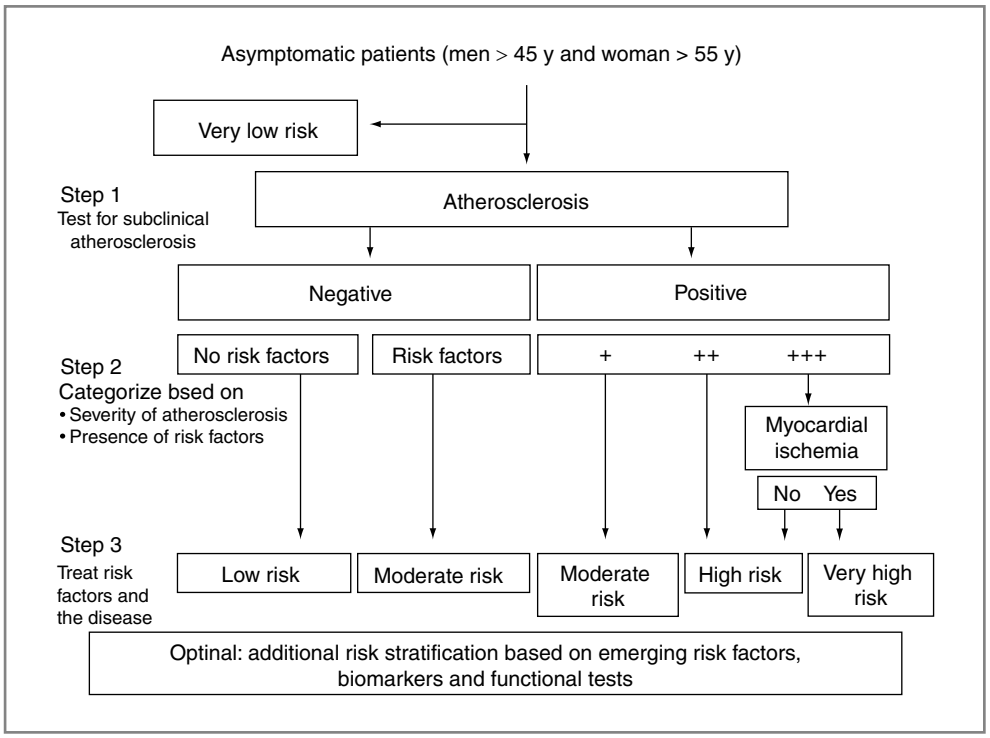

Figure 19.15. An approach to screening for atherosclerosis advocated by the Association for the Eradication of Heart Attacks (AHEA) (*Y* years) (adapted with permission of Elsevier from Naghavi et al [86]).

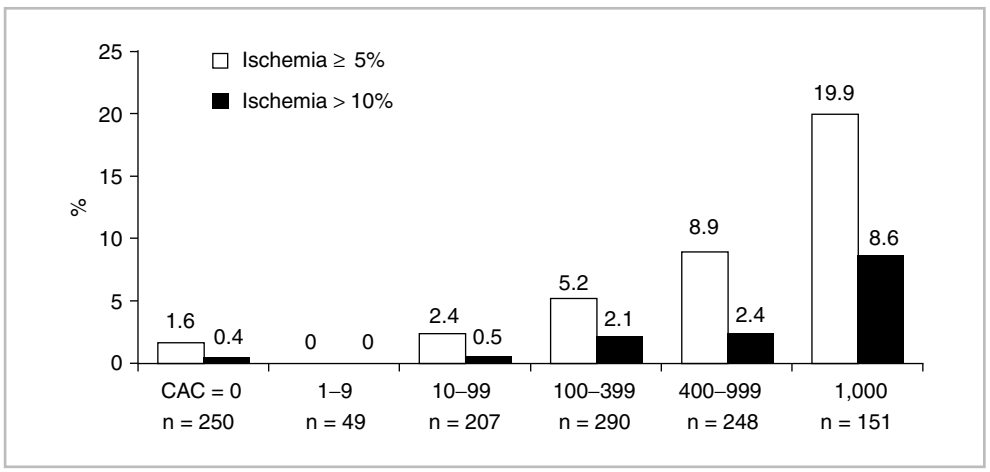

Figure 19.16. The frequency of an ischemic MPS (≥5% ischemic myocardium) (*gray bars*) and of a moderate to severe ischemia (>10% ischemic myocardium) (*black bars*) for patients divided into six CAC score groupings (adapted with permission of Elsevier from Berman et al [78]).

CAC scores between 100 and 400. Most likely, the difference between these studies may relate to various selection biases or differences in interpretive criteria for MPS studies. Subsequent data indicate that the threshold CAC sore for referring patients for stress testing might vary according to ancillary clinical data. For instance, the threshold value for inducible ischemia may be lowered to 100–400 based on data observed among patients with metabolic syndrome or diabetes [89], and other data indicate that the CAC threshold for ischemia is much higher in asymptomatic individuals compared to patients with a typical or typical angina [90]. By contrast, a poor correlation between LDL or HDL levels and CAC sores in clinical populations has been shown [91], suggesting that cholesterol variables are not likely to serve as a triage factor in selection for MPS study following CAC scanning. The intensity of medical management is then guided by a combination of risk factors and the CAC score. The use of CCTA in further evaluation of asymptomatic patients with extensive CAC has not yet been documented to be useful.

Diagnostic Testing

Screening should be distinguished from the test evaluation of patients with symptoms. In the symptomatic patient, testing is considered to be in the "diagnostic mode." In the symptomatic patient, the first question that arises is "what is the cause of the symptoms" (i.e., establishing the diagnosis). For risk assessment, the short-term as well as the long-term risk needs to be considered, in order to appropriately guide the management decisions, which chiefly deal with whether revascularization needs to be considered. In patients presenting with stable chest pain symptoms, the first question that arises is ascertaining a diagnosis: Is the chest pain due to CAD? The first step in diagnostic assessment is determining patients' pretest likelihood of angiographically significant CAD based on the Bayesian analysis of patients' age, gender, risk factors, and symptoms, as initially suggested by the classic work of Diamond et al [92, 93] and what degree of intensity of medical therapy is warranted. CCTA is growing rapidly in this diagnostic application. For a recent update on the clinical applications of CCTA, the AUC for CCTA are expected to be published by mid 2010.

Evaluation of Patient with Acute Chest Pain

Almost 6 million individuals are evaluated each year for acute chest pain in the emergency department (ED) [94]. Despite standardized protocols and high vigilance, between 2 and 6% of patients are erroneously discharged with missed myocardial infarction [95]. For patients with normal or nondiagnostic initial ECGs on presentation to the ED, an important clinical problem is to distinguish those with acute coronary syndromes requiring hospital admission from those who may be safely discharged.

Because most patients presenting with acute chest pain subsequently "rule out" for acute ischemic syndromes, chest pain units have been instituted for the acute evaluation of chest pain patients presenting to the ED. Because of the relationship to closure of a coronary artery, SPECT MPS is an effective means of detecting patients with acute ischemic syndromes. Tc-99m sestamibi or tetrofosmin SPECT MPS, with injection during chest pain, has been shown to reduce clinical indecision in the acute evaluation of chest pain. A number of studies have demonstrated a role for SPECT MPS in the initial evaluation of these patients. A normal rest Tc-99m sestamibi or tetrafosmin SPECT MPS study has a 99% negative predictive value [96, 97]. A prospective, randomized, controlled multicenter trial examined whether incorporating acute rest SPECT MPS into an ED evaluation strategy of patients presenting with suspected acute ischemia improved initial ED triage [98]. A significant reduction in hospitalization was noted in patients with normal SPECT MPS studies.

Use of CCTA in the Evaluation of Acute Chest Pain

Proponents of CCTA advocate its potential usefulness in this patient subgroup, highlighting the high NPV of CCTA to successfully identify individuals in whom no obstructive CAD exists and who bear a favorable prognosis. More recently, CCTA has also been assessed for the work-up of acute chest pain. A single-center randomized study of 197 individuals presenting with acute chest pain to the ED compared a CCTA-based diagnostic evaluation strategy to "standard of care" algorithms which employed MPS [99]. In contrast to individuals undergoing standard of care assessment, individuals undergoing CCTA experienced reduced diagnostic time in the ED (3.4 vs. 15.0 h, $p < 0.01$) and fewer repeat evaluations for chest pain. These findings translated to lower costs for a CCTA-based evaluation by almost $300 per patient.

Subsequently, the CT-STAT (Coronary Computed Tomography for Systemic Triage of Acute Chest Pain Patients to Treatment) trial, a multicenter randomized trial comparing CCTA to rest/stress MPS in patients with chest pain in ED, was performed (Late Breaking Clinical Trial, AHA, 2009) also demonstrated more rapid time to diagnosis and lower costs with CCTA vs. the standard of care, with equal safety. In a related study, 368 patients presenting to the ED with acute chest pain underwent 64-slice CCTA after initially negative troponin measurements and electrocardiograms [100]. CCTA results were blinded to the caring physician. One-half of the study patients had no evidence of CAD by CCTA, with a NPV of 100% for ACS in a 6-month follow-up. By contrast, the presence of any plaque on CCTA scan possessed 100% sensitivity for ACS detection, although the specificity for ACS detection was low (54%). Specificity for ACS detection was improved by restriction of the diagnosis of CAD to those with ≥50% stenosis by CCTA, findings which were incremental to Thrombolysis in Myocardial Infarction risk scores. While these early data are favorable, further

study is still needed in larger cohorts to verify the safety and effectiveness of a CCTA-based evaluation of acute chest pain patients.

Of note, the presence of nonobstructive coronary artery plaque portends a low but nonzero risk, congruent with the data observed in the stable chest pain population, and is therefore an imperfect stand-alone instrument for triaging individuals with possible ACS. On the basis of the available information, the CCTA and MPS approaches appear to be similarly effective in this application at the present time.

Evaluation of Patients with Stable Chest Pain

By convention, patients are commonly divided into three CAD likelihood groups: low (<15%), intermediate (15–85%), and high (>85%). Symptomatic patients with a low likelihood of CAD (<15%) generally require only primary prevention and no testing, similar to asymptomatic patients with a low 10-year risk. This might apply, for example, to a 30-year-old with no risk factors for CAD experiencing nonanginal chest discomfort. By contrast, value of noninvasive diagnostic testing is greatest in patients with an intermediate likelihood of disease.

CCTA as the Initial Test

A trend in diagnostic testing may be the potential increased use of CCTA as opposed to stress testing as the first line for evaluating diagnostic patients, at least among those with a low intermediate pretest likelihood of CAD. An approach to the symptomatic patient with an intermediate pretest likelihood of CAD, based on using CCTA as the initial test, is shown in Figure 19.17 [101]. After the CCTA, the need for further testing and therapy would be guided by the post-test likelihood of CAD and the extent and severity of the observed disease. If the CCTA is normal (no stenosis, no coronary calcium), primary prevention would be appropriate. It is likely that the relatively high NPV – the definitive ability to rule out CAD – will become a principal driving force in the initial application of CCTA. On the other hand, if critical proximal stenoses are observed (e.g., >90%), direct referral to selective coronary angiography would appear to be appropriate.

It must be recognized that currently CCTA is almost purely *anatomic* in its information. While providing important information for guiding medical management and establishing diagnosis, it is limited in the information regarding need for revascularization. Thus, if a coronary stenosis is defined by CCTA but the anatomy is not "compelling" regarding the need for revascularization, referral for stress ischemia testing (e.g., MPS) would appear appropriate to determine the need to consider coronary revascularization.

Stress Imaging as the Initial Test

An alternate approach in this intermediate likelihood group would be to perform ischemia testing with MPS as the initial test with consideration of CCTA when the results of MPS are uncertain (Figure 19.18). With this approach, patients with extensive ischemia would be referred to ICA. Patients with 5–10% ischemia would be further assessed for the presence of ancillary high risk markers (low EF, TID, etc; Table 19.1) or high risk conditions (advanced age, diabetes mellitus, atrial fibrillation, pharmacologic stress, and dyspnea). Those with one or more of these high risk markers or conditions would be candidates for ICA. In those

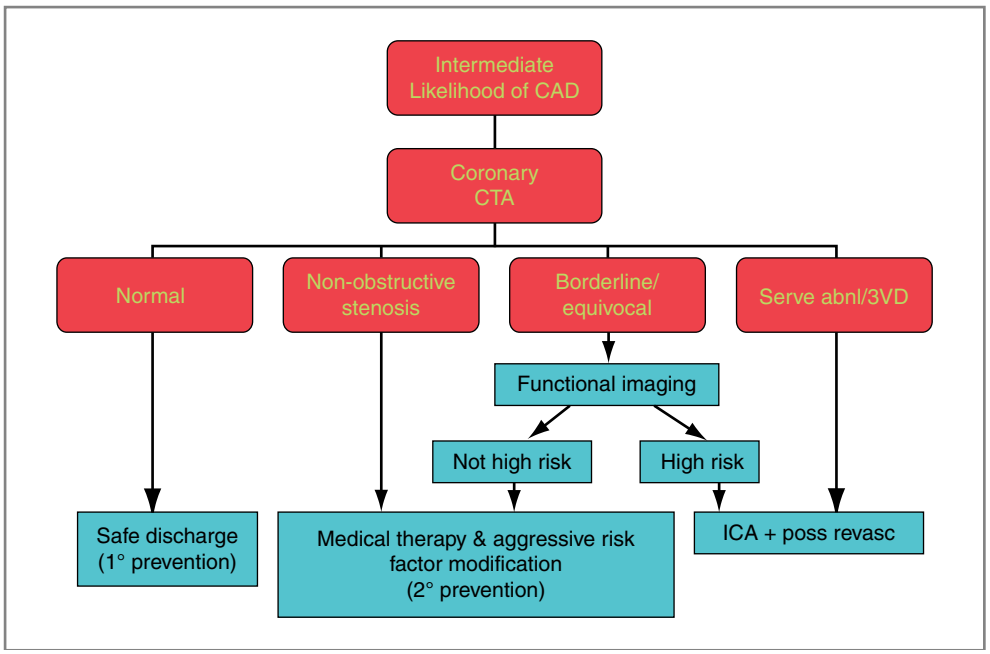

Figure 19.17. CCTA approach to diagnosis and management of CAD in symptomatic patients with an intermediate pretest likelihood of CAD. *Abnl* abnormal; *revasc* revascularization (adapted with the kind permission of Springer Science + Business Media from Schuijf et al [101]).

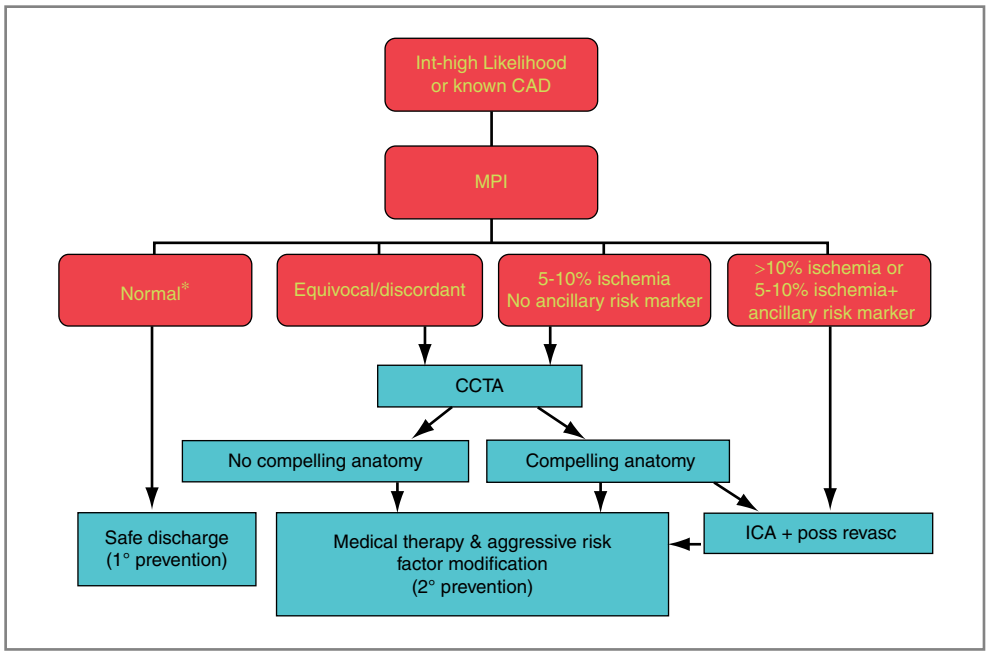

Figure 19.18. MPI approach to diagnosis and management of CAD in *symptomatic* patients with an intermediate pretest likelihood of CAD (* indicates with normal MPI in patients not already identified as requiring maximal medical therapy using secondary prevention guidelines, consider atherosclerosis imaging.) *ICA* invasive coronary angiography; *poss revasc* possible revascularization .

with 5–10% ischemia and none of the high risk markers or conditions, consideration is given to the performance of CCTA. CCTA is also considered in patients with equivocal MPS or in whom the MPS results and the results of stress testing are markedly discordant (e.g., severe ST depression with a normal MPS study). The reason for suggesting the use of CCTA in these patients is that a small percentage of patients with left main CAD might be missed by MPS in the absence of absolute flow measurements [48].

Another group in whom CCTA might be commonly employed is in patients with equivocal nuclear results or in whom there is a marked discordance in the clinical or ECG results and the nuclear results. Usefulness of CCTA in patients with equivocal or nondiagnostic MPS was most recently demonstrated by Abidov et al [102]

Patient Risk Stratification and Guiding Patient Management

In contrast to patients with an intermediate likelihood of CAD, patients with a high likelihood of CAD are generally considered by their clinicians to have CAD and are treated accordingly. Therefore, these patients are usually not referred for noninvasive imaging to establish a diagnosis. If symptoms are limiting, they are directly sent for ICA. In many circumstances, particularly when symptoms are relieved with medical therapy and when there are comorbidities, however, there is a need to assess the extent and severity of ischemia in order to guide the decision for revascularization based on prognostic considerations. There is no evidence at this time to support the use of CCTA for these patients. In contrast, there is evidence that patients deemed to have a high (>85%) likelihood of CAD or those with known CAD frequently benefit from MPS for purposes of determining the need for consideration of revascularization. In these patients, when symptoms are well controlled medically, the question is one of prognosis and potential benefit from revascularization rather than diagnosis [1, 74]. Hachamovitch et al [6] have demonstrated that initial testing with MPS rather than direct coronary angiography, in patients with a high likelihood of CAD and without limiting symptoms, may be cost-effective and appropriate. After nuclear testing, those with extensive ischemia would be sent for catheterization. Those with no ischemia or minimal ischemia may become candidates for CAC scanning if they are not already identified as requiring maximal medical therapy for prevention. Those with mild to moderate ischemia might be candidates for CCTA, to be certain that high-risk angiographic disease such as left main stenosis was not present. Another group of these patients in whom CCTA might prove to be effective is the group with equivocal nuclear results or when there is a marked discordance in the clinical or the ECG results and the nuclear results. Using CCTA as an initial test in patients with a high pretest likelihood of CAD would not appear to be reasonable, since it would be expected that over 75% of them would have abnormal CCTA studies, many if not most of whom would require further testing.

Of note, however, is that CCTA is extremely accurate in assessing bypass graft patency, and can be an effective tool in guiding the need for and approach to ICA. CCTA can also be used to assess the patency of coronary artery stents, providing they are of sufficient size [103]. In stents that are less than 3 mm in diameter, the frequency of diagnostic test results is decreased.

Applications of Nuclear Cardiology Beyond Rest/Stress MPS

Assessment of Myocardial Viability and Chronic Heart Failure

Cardiac SPECT or PET methods can be effectively used to distinguish viable but nonfunctioning myocardium that can be improved with revascularization from nonviable myocardium. In this setting, viable myocardium is defined as regions exhibiting resting regional wall motion abnormality associated with radionuclide, echocardiographic, or cardiac MRI evidence that the abnormally contracting myocardium is not scar. With SPECT, radionuclide techniques commonly employed to assess myocardial viability include indices of regional myocardial perfusion and cell membrane integrity (nitroglycerin augmented resting Tc-99m agent studies) [104, 105] and indices of regional cellularity as defined by the potassium space (redistribution thallium-201 imaging) [106, 107]. With PET, a measure of glucose metabolism using F-18-fluorodeoxyglucose (FDG) PET is the most common viability approach used [108–110]. Due to the more common availability of Echocardiography (Echo) and SPECT methods, the approaches of SPECT MPS and low-dose dobutamine echo are often chosen as methods to assess myocardial viability. In centers with expertise in cardiac FDG PET, PET appears to be more accurate for detecting myocardial viability than the SPECT methods [3]. While there are few comparative studies, it is widely held that the PET approach is highly competitive with late enhancement by cardiac MRI as a method for guiding management of patients with ischemic cardiomyopathy [111, 112]. When extensive myocardial viability is found with any of the available modalities, improvement in ventricular function after successful revascularization is common, whereas function usually does not improve in patients with no or small amounts of viable myocardium. Although delayed contrast enhancement during coronary CT angiography can assess myocardial scarring, the approach provides less contrast between the infarct zone and the normal zone than cardiac MRI [113]. In general, at the present time there is little evidence supporting the use of cardiac CT in clinical assessment of myocardial viability.

Selection of Patients for ICD Placement

The selection of patients for implantable cardioverter-defibrillator (ICD) placement is based on EF and clinical findings; however, many patients with low EF prove not to have needed the ICD, while many patients with normal EF suffer from sudden cardiac death. Iodine-123 radiolabeled metaiodobenzylguanidine (^{123}I-MIBG), an analog of the false nerve transmitter guanethidine that accumulates in the presynaptic terminals of sympathetic nerves may provide an improved method for this selection. For cardiac applications, the heart-to-mediastinum ratio of MIBG is measured, with the mediastinum serving as a background measurement for standardization [114].

In patients with chronic heart failure (CHF), studies have consistently shown that decreased cardiac uptake of MIBG is a strong predictor of prognosis [115–119]. A recent international phase III multicenter trial, AdreView Myocardial Imaging for Risk Evaluation in Heart Failure (ADMIRE-HF) [120], has provided preliminary evidence that MIBG might be useful in assessing prognosis in heart failure patients [121]. In ADMIRE-HF, adverse events of CHF progression, life-threatening arrhythmias, or cardiac death were more than twice as frequent in patients with lower heart-to-mediastinum (H/M) ratios than in those with higher ratios ($p < 0.0001$), and the incidence of death was ten times greater in the lowest 10% vs. the highest 20% cardiac uptake groups. Thus, cardiac ^{123}I-MIBG imaging has the potential to lead to better selection of patients for ICD placement. Based on the consistent literature findings and the results of the ADMIRE-HF study, FDA approval of the agent is expected in the near future.

Assessment of Left Ventricular Dyssynchrony: Guidance for CRT

A recent randomized trial automatic defibrillator implantation with cardiac resynchronization therapy (MADIT-CRT) [122] has shown that CRT combined with ICD placement is associated with lower mortality than ICD alone in patients with low LVEF and wide QRS. However, as with ICD placement, the selection of patients who might benefit from CRT is also not highly effective at this time. Assessment of ventricular dyssynchrony may improve the selection of patients who benefit from CRT. Due to the 4D nature of the datasets, resting gated SPECT or PET MPS studies can be used to assess ventricular dyssynchrony [123, 124]. Studies have shown that an assessment of inter- and intraventricular dyssynchrony can be effectively performed by means of phase analysis on gated SPECT [125–129] or gated blood pool SPECT [130, 131]. Studies have reported that responders and nonresponders from CRT therapy can be distinguished by phase analysis [128, 132, 133]. Patients with broad dispersion of phase angles are more likely to respond to CRT. In small single-center trials, sensitivity/specificity for predicting response to CRT have been reported as 70 per 74% [128] and 83 per 81% [132]. In comparison to tissue Doppler imaging by Echo, the SPECT methods have the advantage of providing true 3D onset of contraction data for the entire left ventricle. Additionally, the methods of analysis are automatic, thus providing high reproducibility. Prospective trials are needed to compare the value of SPECT vs. Echo in predicting benefit from CRT as well as to determine whether this assessment is superior to the standard criterion of prolonged QRS duration for selecting patients for CRT.

Applications of CCTA in CAD Beyond Assessment of Coronary Stenosis

Ruling Out Ischemic Cardiomyopathy

When patients present with CHF and evidence of cardiomyopathy of uncertain origin, normal coronary arteries on CCTA may often be a definitive way of ruling out CAD as the cause. Alternatively, if a patient with CHF is found to have no stress or rest abnormalities on MPS, the likelihood of CAD as the cause of CHF can also be considered to be low. Thus, in the appropriate setting, a normal CCTA or SPECT or PET MPS (or cardiac MRI) might obviate the need for ICA in a patient with CHF of unknown etiology.

Summary

CAC scanning and CCTA have emerged as new means of evaluating atherosclerotic disease burden, plaque morphology, and degree of anatomic stenosis in the coronary vasculature on a noninvasive basis. While these technologies are not likely to replace the use of MPS, which remains the mainstay of functional evaluation among patients with suspected CAD, they are likely to both modify and complement the future use of MPS study in diagnostic populations. Increasing evidence indicates that CAC scanning can play a pivotal role in screening and evaluation of asymptomatic patients, and this application has recently begun to be reimbursed in some locations and by some insurance plans. In addition, CAC scanning may prove to add useful information in triaging which patients may benefit from diagnostic stress testing. CAC scanning may also be useful in patients who have had normal MPS studies as the amount of atherosclerosis could guide the intensity of their subsequent medical management. In symptomatic patients with an intermediate pretest likelihood of CAD, CCTA is likely to be increasingly used instead of MPS due to its ability to rule out CAD more definitively. Patients with normal CCTA or critical stenosis and symptoms will have clear management pathways. In some patients with abnormal CCTA but no critical stenosis, the MPS may be indicated to evaluate the magnitude of ischemia. In patients with a high likelihood of CAD or known CAD, MPS is likely to remain the mainstay of assessment, unless the symptoms are of such degree that the patients would be sent directly to ICA. In patients with a high likelihood of CAD but no limiting symptoms, initial testing with MPS is more likely than CCTA to be able to effectively guide management, improving the selection of patients in need of ICA. In all of the applications, it is anticipated that additional downstream testing will be both necessary and appropriate in a small proportion of patients after either MPS or cardiac CT has been performed as the initial test. In assessment of myocardial viability, the SPECT or PET methods have been well validated and there is currently little application of CCTA.

References

1. Berman DS, Hachamovitch R, Shaw LJ, et al. Roles of nuclear cardiology, cardiac computed tomography, and cardiac magnetic resonance: assessment of patients with suspected coronary artery disease. *J Nucl Med*. 2006;47:74–82.
2. Berman DS, Hachamovitch R, Shaw LJ, et al. Roles of nuclear cardiology, cardiac computed tomography, and cardiac magnetic resonance: noninvasive risk stratification and a conceptual framework for the selection of noninvasive imaging tests in patients with known or suspected coronary artery disease. *J Nucl Med*. 2006;47:1107–1118.
3. Bengel FM, Higuchi T, Javadi MS, Lautamaki R. Cardiac positron emission tomography. *J Am Coll Cardiol*. 2009;54(1):1–15.
4. Klocke FJ, Baird MG, Lorell BH, et al. ACC/AHA/ASNC guidelines for the clinical use of cardiac radionuclide imaging-executive summary. A Report of the American College of Cardiology/American Heart Association Task Force on Practice Guidelines (ACC/AHA/ASNC Committee to Revise the 1995 Guidelines for the Clinical Use of Cardiac Radionuclide Imaging). *Circulation*. 2003;108:1404–1418.
5. Berman DS, Hachamovitch R, Shaw LJ, Hayes S, Germano G. Nuclear cardiology. In: Fuster V, OR RA, Walsh RA, Poole-Wilson P, eds. *Hurst's The Heart*. 12th ed. New York: McGraw-Hill Companies; 2008:544–576.
6. Hachamovitch R, Hayes SW, Friedman JD, Cohen I, Berman DS. Stress myocardial perfusion SPECT is clinically effective and cost-effective in risk-stratification of patients with a high likelihood of CAD but no known CAD. *J Am Coll Cardiol*. 2004;43:200–208.
7. Hendel RC, Berman DS, Di Carli MF, et al. ACCF/ASNC/ACR/AHA/ASE/SCCT/SCMR/SNM 2009 Appropriate use criteria for cardiac radionuclide imaging. A report of the American College of Cardiology Foundation Appropriate Use Criteria Task Force, the American Society of Nuclear Cardiology, the American College of Radiology, the American Heart Association, the American Society of Echocardiography, the Society of Cardiovascular Computed Tomography, the Society for Cardiovascular Magnetic Resonance, and the Society of Nuclear Medicine Endorsed by the American College of Emergency Physicians. *J Am Coll Cardiol*. 2009;53(23):2201–2229.
8. Hachamovitch R, Hayes S, Friedman JD, et al. Determinants of risk and its temporal variation in patients with normal stress myocardial perfusion scans: what is the warranty period of a normal scan? *J Am Coll Cardiol*. 2003;41(8):1329–1340.
9. Shaw LJ, Iskandrian AE. Prognostic value of gated myocardial perfusion SPECT. *J Nucl Cardiol*. 2004;11(2):171–185.
10. Gibbons RJ, Abrams J, Chatterjee K, et al. ACC/AHA 2002 guideline update for the management of patients with chronic stable angina – summary article: a report of the American College of Cardiology/American Heart Association Task Force on Practice Guidelines (Committee on the Management of Patients With Chronic Stable Angina). *Circulation*. 2003;107(1):149–158.
11. Kang X, Berman DS, Lewin HC, et al. Incremental prognostic value of myocardial perfusion single photon emission computed tomography in patients with diabetes mellitus. *Am Heart J*. 1999;138(6 pt 1):1025–1032.
12. Santos MM, Abidov A, Hayes SW, et al. Prognostic implications of myocardial perfusion SPECT in patients with atrial fibrillation [abstract]. *J Nucl Med*. 2002;43:98P.
13. Abidov A, Rozanski A, Hachamovitch R, et al. Complaints of dyspnea among patients referred for cardiac stress testing. *New Engl J Med*. 2005;353:1889–1898.
14. Hakeem A, Bhatti S, Dillie KS, et al. Predictive value of myocardial perfusion single-photon emission computed tomography and the impact of renal function on cardiac death. *Circulation*. 2008;118(24):2540–2549.
15. Hachamovitch R, Kang X, Amanullah AM, et al. Prognostic implications of myocardial perfusion single-photon emission computed tomography in the elderly. *Circulation*. 2009;120(22):2197–2206.
16. Berman DS, Kang X, Hayes SW, et al. Adenosine myocardial perfusion single-photon emission computed tomography in women compared with men. Impact of diabetes mellitus on incremental prognostic value and effect on patient management. *J Am Coll Cardiol*. 2003;41(7):1125–1133.

17. Azarbal B, Hayes SW, Lewin HC, Hachamovitch R, Cohen I, Berman DS. The incremental prognostic value of percentage of heart rate reserve achieved over myocardial perfusion single-photon emission computed tomography in the prediction of cardiac death and all-cause mortality: superiority over 85% of maximal age-predicted heart rate. *J Am Coll Cardiol*. 2004;44:423–430.
18. Abidov A, Bax JJ, Hayes SW, et al. Transient ischemic dilation ratio of the left ventricle is a significant predictor of future cardiac events in patients with otherwise normal myocardial perfusion SPECT. *J Am Coll Cardiol*. 2003;42:1818–1825.
19. Staniloff HM, Forrester JS, Berman DS, Swan HJ. Prediction of death, myocardial infarction, and worsening chest pain using thallium scintigraphy and exercise electrocardiography. *J Nucl Med*. 1986;27(12): 1842–1848.
20. Abidov A, Hachamovitch R, Hayes SW, et al. Are shades of gray prognostically useful in reporting myocardial perfusion single-photon emission computed tomography? *Circulation Imaging*. 2009;2:290–298.
21. Mowatt G, Vale L, Brazzelli M, et al. Systematic review of the effectiveness and cost-effectiveness, and economic evaluation, of myocardial perfusion scintigraphy for the diagnosis and management of angina and myocardial infarction. *Health Technol Assess*. 2004;8(30):iii-iv, 1–207.
22. Hachamovitch R, Hayes SW, Friedman JD, Cohen I, Berman DS. Comparison of the short-term survival benefit associated with revascularization compared with medical therapy in patients with no prior coronary artery disease undergoing stress myocardial perfusion single photon emission computed tomography. *Circulation*. 2003;107(23):2900–2907.
23. Kaminek M, Myslivecek M, Skvarilova M, et al. Increased prognostic value of combined myocardial perfusion SPECT imaging and the quantification of lung Tl-201 uptake. *Clin Nucl Med*. 2002;27(4):255–260.
24. Sharir T, Germano G, Kavanagh PB, et al. Incremental prognostic value of post-stress left ventricular ejection fraction and volume by gated myocardial perfusion single photon emission computed tomography, *Circulation*. 1999;100:1035–1042.
25. Sharir T, Kang X, Germano G, et al. Prognostic value of poststress left ventricular volume and ejection fraction by gated myocardial perfusion SPECT in women and men: gender-related differences in normal limits and outcomes. *J Nucl Cardiol*. 2006;13:495–506.
26. Sharir T, Bacher-Stier C, Dhar S, et al. Identification of severe and extensive coronary artery disease by postexercise regional wall motion abnormalities in Tc-99m sestamibi gated single-photon emission computed tomography. *Am J Cardiol*. 2000;86(11):1171–1175.
27. Abidov A, Hachamovitch R, Rozanski A, et al. Prognostic implications of atrial fibrillation in patients undergoing myocardial perfusion single-photon emission computed tomography. *J Am Coll Cardiol*. 2004;44(5):1062–1070.
28. Klein J, Chao SY, Berman DS, Rozanski A. Is 'silent' myocardial ischemia really as severe as symptomatic ischemia? The analytical effect of patient selection biases. *Circulation*. 1994;89(5):1958–1966.
29. Cerqueira MD, Nguyen P, Staehr P, Underwood R, Iskandrian AE. Effects of age, gender, obesity, and diabetes on the efficacy and safety of the selective A2A agonist regadenoson versus adenosine in myocardial perfsuion imaging. *J Am Coll Cardiol Img*. 2008;1:307–316.
30. Abbott BG, Afshar M, Berger AK, Wackers FJ. Prognostic significance of ischemic electrocardiographic changes during adenosine infusion in patients with normal myocardial perfusion imaging. *J Nucl Cardiol*. 2003;10(1):9–16.
31. Cerqueira MD, Weissman NJ, Dilsizian V, et al. Standardized myocardial segmentation and nomenclature for tomographic imaging of the heart: a statement for healthcare professionals from the Cardiac Imaging Committee of the Council on Clinical Cardiology of the American Heart Association. *Circulation*. 2002;105(4):539–542.
32. Berman DS, Kiat H, Friedman JD, et al. Separate acquisition rest thallium-201/stress technetium-99m sestamibi dual-isotope myocardial perfusion single-photon emission computed tomography: a clinical validation study. *J Am Coll Cardiol*. 1993;22(5):1455–1464.
33. Berman DS, Hachamovitch R, Kiat H, et al. Incremental value of prognostic testing in patients with known or suspected ischemic heart disease: a basis for optimal utilization of exercise technetium-99m sestamibi myocardial perfusion single-photon emission computed tomography [published erratum appears in *J Am Coll Cardiol*. 1996; 27(3):756]. *J Am Coll Cardiol*. 1995;26(3):639–647.
34. Hachamovitch R, Berman DS, Kiat H, et al. Exercise myocardial perfusion SPECT in patients without known coronary artery disease: incremental prognostic value and use in risk stratification. *Circulation*. 1996;93(5):905–914.
35. Herzog BA, Husmann L, Valenta I, et al. Long-term prognostic value of 13N-ammonia myocardial perfusion positron emission tomography added value of coronary flow reserve. *J Am Coll Cardiol*. 2009;54(2): 150–156.
36. Dorbala S, Hachamovitch R, Curillova Z, et al. Incremental prognostic value of gated Rb-82 positron emission tomography myocardial perfusion imaging over clinical variables and rest LVEF. *JACC Cardiovasc Imaging*. 2009;2(7):846–854.
37. Berman DS, Abidov A, Kang X, et al. Prognostic validation of a 17-segment score derived from a 20-segment score for myocardial perfusion SPECT interpretation. *J Nucl Cardiol*. 2004;11:414–423.
38. Berman DS, Kang X, Gransar H, et al. Quantitative assessment of myocardial perfusion abnormality on SPECT myocardial perfusion imaging is more reproducible than expert visual analysis. *J Nucl Cardiol*. 2009;16:45–53.
39. Slomka PJ, Berman DS, Germano G. Quantification of serial changes in myocardial perfusion. *J Nucl Med*. 2004;45(12):1978–1980.
40. Garcia EV. Quantitative myocardial perfusion single-photon emission computed tomographic imaging: quo vadis? (Where do we go from here?). *J Nucl Cardiol*. 1994;1(1):83–93.
41. Ficaro E, Kritzman J, Corbett J. Development and clinical validation of normal Tc-99m sestamibi database: comparison of 3D-MSPECT to CEqual [abstract]. *J Nucl Med*. 1999;40(5):125P.
42. Mahmarian JJ, Cerqueira MD, Iskandrian AE, et al. Regadenoson induces comparable left ventricular perfusion defects as adenosine: a quantitative analysis from the ADVANCE MPI 2 trial. *JACC Cardiovasc Imaging*. 2009;2(8):959–968.
43. Slomka PJ, Nishina H, Berman DS, et al. Automated quantification of myocardial perfusion SPECT using simplified normal limits. *J Nucl Cardiol*. 2005;12(1):66–77.
44. Hachamovitch R, Rozanski A, Hayes SW, et al. Predicting therapeutic benefit from myocardial revascularization procedures: are measurements of both resting left ventricular ejection fraction and stress-induced myocardial ischemia necessary? *J Nucl Cardiol*. 2006; 13:768–778.
45. Boden WE, O'Rourke RA, Teo KK, et al. Optimal medical therapy with or without PCI for stable coronary disease. *N Engl J Med*. 2007;356(15):1503–1516.
46. Shaw LJ, Berman DS, Maron DJ, et al. Optimal medical therapy with or without percutaneous coronary intervention to reduce ischemic burden: results from the Clinical Outcomes Utilizing Revascularization and Aggressive Drug Evaluation (COURAGE) trial nuclear substudy. *Circulation*. 2008;117(10):1283–1291.
47. Lima RS, Watson DD, Goode AR, et al. Incremental value of combined perfusion and function over perfusion alone by gated SPECT myocardial perfusion imaging for detection of severe three-vessel coronary artery disease. *J Am Coll Cardiol*. 2003;42:64–70.
48. Berman DS, Kang X, Slomka PJ, et al. Underestimation of extent of ischemia by gated SPECT myocardial perfusion imaging in patients with left main coronary artery disease. *J Nucl Cardiol*. 2007;14: 521–528.
49. Abdulla A, Maddahi J, Garcia E, et al. Slow regional clearance of myocardial thallium-201 in the absence of perfusion defect: Its contribution to detection of individual coronary artery stenoses and mechanisms for its occurence. *Circulation*. 1985;71:72–79.
50. Ragosta M, Bishop AH, Lipson LC, et al. Comparison between angiography and fractional flow reserve versus single-photon emission computed tomographic myocardial perfusion imaging for determining lesion significance in patients with multivessel coronary disease. *Am J Cardiol*. 2007;99(7):896–902.

51. Demer LL, Tintut Y. Vascular calcification: Pathobiology of a multifaceted disease. *Circulation*. 2008;117:2938–2948.
52. Rumberger JA, Simons DB, Fitzpatrick LA, Sheedy PF, Schwartz RS. Coronary artery calcium area by electron-beam computed tomography and coronary atherosclerotic plaque area. A histopathologic correlative study. *Circulation*. 1995;92(8):2157–2162.
53. Greenland P, Bonow RO, Brundage BH, et al. ACCF/AHA 2007 clinical expert consensus document on coronary artery calcium scoring by computed tomography in global cardiovascular risk assessment and in evaluation of patients with chest pain: a report of the American College of Cardiology Foundation Clinical Expert Consensus Task Force (ACCF/AHA Writing Committee to Update the 2000 Expert Consensus Document on Electron Beam Computed Tomography). *Circulation*. 2007;115(3):402–426.
54. Budoff MJ, Achenbach S, Blumenthal RS, et al. Assessment of coronary artery disease by cardiac computed tomography: a scientific statement from the American Heart Association Committee on Cardiovascular Imaging and Intervention, Council on Cardiovascular Radiology and Intervention, and Committee on Cardiac Imaging, Council on Clinical Cardiology. *Circulation*. 2006;114(16):1761–1791.
55. Yan LL, Liu K, Daviglus ML, et al. Education, 15-year risk factor progression, and coronary artery calcium in young adulthood and early middle age: the Coronary Artery Risk Development in Young Adults study. *JAMA*. 2006;295(15):1793–1800.
56. Detrano R, Guerci AD, Carr JJ, et al. Coronary calcium as a predictor of coronary events in four racial or ethnic groups. *N Engl J Med*. 2008;358(13):1336–1345.
57. Budoff MJ, Nasir K, McClelland RL, et al. Coronary calcium predicts events better with absolute calcium scores than age-sex-race/ethnicity percentiles: MESA (multi-ethnic study of atherosclerosis). *J Am Coll Cardiol*. 2009;53(4):345–352.
58. Arad Y, Goodman KJ, Roth M, Newstein D, Guerci AD. Coronary calcification, coronary disease risk factors, C-reactive protein, and atherosclerotic disease events: the St. Francis Heart Study. *J Am Coll Cardiol*. 2005;46:158–165.
59. Hounsfield GN. Computerized transverse axial scanning (tomography). 1. Description of system. *Br J Radiol*. 1973;46(552):1016–1022.
60. Achenbach S, Giesler T, Ropers D, et al. Detection of coronary artery stenoses by contrast-enhanced, retrospectively electrocardiographically-gated, multislice spiral computed tomography. *Circulation*. 2001;103(21):2535–2538.
61. Nieman K, Cademartiri F, Lemos PA, Raaijmakers R, Pattynama PM, de Feyter PJ. Reliable noninvasive coronary angiography with fast submillimeter multislice spiral computed tomography. *Circulation*. 2002;106(16):2051–2054.
62. Budoff MJ, Dowe D, Jollis JG, et al. Diagnostic performance of 64-multidetector row coronary computed tomographic angiography for evaluation of coronary artery stenosis in individuals without known coronary artery disease: results from the prospective multicenter ACCURACY (Assessment by Coronary Computed Tomographic Angiography of Individuals Undergoing Invasive Coronary Angiography) trial. *J Am Coll Cardiol*. 2008;52(21):1724–1732.
63. Miller JM, Rochitte CE, Dewey M, et al. Diagnostic performance of coronary angiography by 64-row CT. *N Engl J Med*. 2008;359(22):2324–2336.
64. Meijboom WB, Meijs MF, Schuijf JD, et al. Diagnostic accuracy of 64-slice computed tomography coronary angiography: a prospective, multicenter, multivendor study. *J Am Coll Cardiol*. 2008;52(25):2135–2144.
65. Hausleiter J, Meyer T, Hadamitzky M, et al. Non-invasive coronary computed tomographic angiography for patients with suspected coronary artery disease: the Coronary Angiography by Computed Tomography with the Use of a Submillimeter resolution (CACTUS) trial. *Eur Heart J*. 2007;28(24):3034–3041.
66. Di Carli MF, Hachamovitch R. New technology for non-invasive evaluation of coronary artery disease. *Circulation*. 2007;115:1464–1480.
67. Fearon WF, Tonino PA, De Bruyne B, Siebert U, Pijls NH. Rationale and design of the fractional flow reserve versus angiography for multivessel evaluation (FAME) study. *Am Heart J*. 2007;154(4):632–636.
68. Tonino PA, De Bruyne B, Pijls NH, et al. Fractional flow reserve versus angiography for guiding percutaneous coronary intervention. *N Engl J Med*. 2009;360(3):213–224.
69. Tamparappoo BK, Gutstein A, Cheng VY, et al. Assessment of the relationship between stenosis severity and distribution of coronary artery stenoses on multislice computed tomographic angiography and myocardial ischemia detected by single photon emission computed tomography. *J Nucl cardiol*. 2010 in press.
70. Gaemperli O, Valenta I, Schepis T, et al. Coronary 64-slice CT angiography predicts outcome in patients with known or suspected coronary artery disease. *Eur Radiol*. 2008;18(6):1162–1173.
71. Pundziute G, Schuijf JD, Jukema JW, et al. Prognostic value of multislice computed tomography coronary angiography in patients with known or suspected coronary artery disease. *J Am Coll Cardiol*. 2007;49(1):62–70.
72. Min JK, Shaw LJ, Devereux RB, et al. Prognostic value of multidetector coronary computed tomographic angiography for prediction of all-cause mortality. *J Am Coll Cardiol*. 2007;50(12):1161–1170.
73. van Werkhoven JM, Schuijf JD, Gaemperli O, et al. Incremental prognostic value of multi-slice computed tomography coronary angiography over coronary artery calcium scoring in patients with suspected coronary artery disease. *Eur Heart J*. 2009;30(21):2622–2629.
74. Berman DS, Hachamovitch R, Shaw LJ, Hayes SW, Germano G. Nuclear cardiology. In: AR FV, O'Rourke RA, Roberts R, King SB, Wellens HJJ, eds. *Hurst's The Heart*. 11th ed. New York: McGraw-Hill Companies; 2004:563–597.
75. van Werkhoven JM, Schuijf JD, Gaemperli O, et al. Prognostic value of multislice computed tomography and gated single-photon emission computed tomography in patients with suspected coronary artery disease. *J Am Coll Cardiol*. 2009;53(7):623–632.
76. Gambhir SS, Berman DS, Ziffer J, et al. A novel high sensitivity rapid-acquisition single-photon cardiac imaging camera. *J Nucl Med*. 2009;50:635–643.
77. Slomka PJ, Cheng VY, Dey D, et al. Quantitative analysis of myocardial perfusion SPECT anatomically guided by coregistered 64-slice coronary CT angiography. *J Nucl Med*. 2009;50:1621–1630.
78. Berman DS, Wong ND, Gransar H, et al. Relationship between stress-induced myocardial ischemia and atherosclerosis measured by coronary calcium tomography. *J Am Coll Cardiol*. 2004;44:923–930.
79. Motoyama S, Sarai M, Harigaya H, et al. Computed tomographic angiography characteristics of atherosclerotic plaques subsequently resulting in acute coronary syndrome. *J Am Coll Cardiol*. 2009;54(1):49–57.
80. Einstein AJ, Moser KW, Thompson RC, Cerqueira MD, Henzlova MJ. Radiation dose to patients from cardiac diagnostic imaging. *Circulation*. 2007;116(11):1290–1305.
81. Expert Panel on Detection, Evaluation, and Treatment of High Blood Cholesterol In Adults. *JAMA*. 2001;285(19):2486–2497.
82. Greenland P, Bonow RO, Brundage BH, et al. Computed tomography: ACC/AHA writing committee to update the 2000 clinical expert consensus document on electron-beam computed tomography for the diagnosis and prognosis for coronary artery disease. *J Am Coll Cardiol*. 2007;49(3):378–402.
83. Hecht HS, Budoff MJ, Berman DS, Ehrlich J, Rumberger JA. Coronary artery calcium scanning: clinical paradigms for cardiac risk assessment and treatment. *Am Heart J*. 2006;151(6):1139–1146.
84. Grover SA, Coupal L, Hu XP. Identifying adults at increased risk of coronary disease. How well do the current cholesterol guidelines work? *JAMA*. 1995;274(10):801–806.
85. Nasir K, Michos ED, Blumenthal RS, Raggi P. Detection of high-risk young adults and women by coronary calcium and National Cholesterol Education Program Panel III guidelines. *J Am Coll Cardiol*. 2005;46(10):1931–1936.
86. Naghavi M, Falk E, Hecht HS, et al.; Force ftST. From vulnerable plaque to vulnerable patient-Part III: executive summary of the Screening for Heart Attack Prevention and Education (SHAPE) Task Force Report. *Am J Cardiol*. 2006;98:2–15.

87. Hendel RC, Berman DS, Di Carli MF, et al. ACCF/ASNC/ACR/AHA/ASE/SCCT/SCMR/SNM 2009 appropriate use criteria for cardiac radionuclide imaging: a report of the American College of Cardiology Foundation Appropriate Use Criteria Task Force, the American Society of Nuclear Cardiology, the American College of Radiology, the American Heart Association, the American Society of Echocardiography, the Society of Cardiovascular Computed Tomography, the Society for Cardiovascular Magnetic Resonance, and the Society of Nuclear Medicine: endorsed by the American College of Emergency Physicians. *Circulation*. 2009;119:e561–e587.
88. He ZX, Hedrick TD, Pratt CM, et al. Severity of coronary artery calcification by electron beam computed tomography predicts silent myocardial ischemia. *Circulation*. 2000;101(3):244–251.
89. Wong ND, Rozanski A, Gransar H, et al. Metabolic syndrome and diabetes are associated with an increased likelihood of inducible myocardial ischemia among patients with subclinical atherosclerosis. *Diabetes Care*. 2005;28:1445–1450.
90. Rozanski A, Gransar H, Wong ND, et al. Use of coronary calcium scanning for predicting inducible myocardial ischemia: influence of patients' clinical presentation. *J Nucl Cardiol*. 2007;14(5):669–679.
91. Hecht HS, Superko HR, Smith LK, McColgan BP. Relation of coronary artery calcium identified by electron beam tomography to serum lipoprotein levels and implications for treatment. *Am J Cardiol*. 2001;87(4):406–412.
92. Diamond GA, Forrester JS. Analysis of probability as an aid in the clinical diagnosis of coronary-artery disease. *N Engl J Med*. 1979;300(24):1350–1358.
93. Diamond GA, Staniloff HM, Forrester JS, Pollock BH, Swan HJ. Computer-assisted diagnosis in the noninvasive evaluation of patients with suspected coronary artery disease. *J Am Coll Cardiol*. 1983;1(2 pt 1):444–455.
94. McCaig LF, Burt CW. *National Hospital Ambulatory Medical Care Survey: 2003 Emergency Department Summary: Advance Data from Vital and Health Statistics, No. 358*. Hyattsville, MD: National Center for Health Statistics; 2005.
95. Pope JH, Aufderheide TP, Ruthazer R, et al. Missed diagnoses of acute cardiac ischemia in the emergency department. *N Engl J Med*. 2000;342(16):1163–1170.
96. Conti A, Gallini C, Costanzo E, et al. Early detection of myocardial ischaemia in the emergency department by rest or exercise (99m)Tc tracer myocardial SPET in patients with chest pain and non-diagnostic ECG. *Eur J Nucl Med*. 2001;28(12):1806–1810.
97. Miller TD, Christian TF, Hopfenspirger MR, Hodge DO, Hauser MF, Gibbons RJ. Prognosis in patients with spontaneous chest pain, a nondiagnostic electrocardiogram, normal cardiac enzymes, and no evidence of severe resting ischemia by quantitative technetium 99m sestamibi tomographic imaging. *J Nucl Cardiol*. 1998;5(1):64–72.
98. Udelson JE, Spiegler EJ. Emergency department perfusion imaging for suspected coronary artery disease: the ERASE Chest Pain Trial. *Md Med*. 2001;suppl:90–94.
99. Goldstein JA, Gallagher MJ, O'Neill WW, Ross MA, O'Neil BJ, Raff GL. A randomized controlled trial of multi-slice coronary computed tomography for evaluation of acute chest pain. *J Am Coll Cardiol*. 2007;49(8):863–871.
100. Hoffmann U, Bamberg F, Chae CU, et al. Usefulness of coronary CT angiography in the early triage of patients with acute chest pain [abstract]. *Circulation*. 2008;118:S655.
101. Schuijf JD, Jukema JW, van der Wall EE, Bax JJ. The current status of multislice computed tomography in the diagnosis and prognosis of coronary artery disease. *J Nucl Cardiol*. 2007;14(4):604–612.
102. Abidov A, Gallagher M, Chinnaiyan K, Mehta L, Wegner J, Raff G. Clinical effectiveness of coronary computed tomographic angiography in the triage of patients to cardiac catheterization and revascularization after inconclusive stress testing: results of a two-year prospective trial. *J Nucl Cardiol*. 2009;16(5):701–713.
103. Kalra MK, Brady TJ. Current status and future directions in technical developments of cardiac computed tomography. *J Cardiovasc Comput Tomogr*. 2008;2:71–80.
104. Hayes SW, Berman DS, Germano G. Stress testing and imaging protocols. In: Germano G, Berman DS, eds. *Clinical Gated Cardiac SPECT*. 2nd ed. Oxford, UK: Blackwell Publishing; 2006:47–68.
105. Sciagra R, Bisi G, Santoro GM, et al. Comparison of baseline-nitrate technetium-99m sestamibi with rest-redistribution thallium-201 tomography in detecting viable hibernating myocardium and predicting postrevascularization recovery. *J Am Coll Cardiol*. 1997;30(2):384–391.
106. Pohost GM, Zir LM, Moore RH, McKusick KA, Guiney TE, Beller GA. Differentiation of transiently ischemic from infarcted myocardium by serial imaging after a single dose of thallium-201. *Circulation*. 1977;55(2):294–302.
107. Gutman J, Berman DS, Freeman M, et al. Time to completed redistribution of thallium-201 in exercise myocardial scintigraphy: relationship to the degree of coronary artery stenosis. *Am Heart J*. 1983;106(5 pt 1):989–995.
108. Tillisch J, Brunken R, Marshall R, et al. Reversibility of cardiac wall-motion abnormalities predicted by positron tomography. *N Engl J Med*. 1986;314(14):884–888.
109. Di Carli MF, Asgarzadie F, Schelbert HR, et al. Quantitative relation between myocardial viability and improvement in heart failure symptoms after revascularization in patients with ischemic cardiomyopathy. *Circulation*. 1995;92(12):3436–3444.
110. Beanlands RS, Nichol G, Huszti E, et al. F-18-fluorodeoxyglucose positron emission tomography imaging-assisted management of patients with severe left ventricular dysfunction and suspected coronary disease: a randomized, controlled trial (PARR-2). *J Am Coll Cardiol*. 2007;50(20):2002–2012.
111. Wu YW, Tadamura E, Yamamuro M, et al. Comparison of contrast-enhanced MRI with (18)F-FDG PET/201Tl SPECT in dysfunctional myocardium: relation to early functional outcome after surgical revascularization in chronic ischemic heart disease. *J Nucl Med*. 2007;48(7):1096–1103.
112. Schinkel AF, Poldermans D, Elhendy A, Bax JJ. Assessment of myocardial viability in patients with heart failure. *J Nucl Med*. 2007;48(7):1135–1146.
113. Nieman K, Cury RC, Ferencik M, et al. Differentiation of recent and chronic myocardial infarction by cardiac computed tomography. *Am J Cardiol*. 2006;98(3):303–308.
114. Dobrucki LW, Sinusas AJ. Cardiovascular molecular imaging. *Semin Nucl Med*. 2005;35(1):73–81.
115. Agostini D, Verberne HJ, Burchert W, et al. I-123-mIBG myocardial imaging for assessment of risk for a major cardiac event in heart failure patients: insights from a retrospective European multicenter study. *Eur J Nucl Med Mol Imaging*. 2008;35(3):535–546.
116. Cohen-Solal A, Esanu Y, Logeart D, et al. Cardiac metaiodobenzylguanidine uptake in patients with moderate chronic heart failure: relationship with peak oxygen uptake and prognosis. *J Am Coll Cardiol*. 1999;33(3):759–766.
117. Merlet P, Valette H, Dubois-Rande JL, et al. Prognostic value of cardiac metaiodobenzylguanidine imaging in patients with heart failure. *J Nucl Med*. 1992;33(4):471–477.
118. Nakata T, Miyamoto K, Doi A, et al. Cardiac death prediction and impaired cardiac sympathetic innervation assessed by MIBG in patients with failing and nonfailing hearts. *J Nucl Cardiol*. 1998;5(6):579–590.
119. Wakabayashi T, Nakata T, Hashimoto A, et al. Assessment of underlying etiology and cardiac sympathetic innervation to identify patients at high risk of cardiac death. *J Nucl Med*. 2001;42(12):1757–1767.
120. Jacobson AF, Lombard J, Banerjee G, Camici PG. 123I-mIBG scintigraphy to predict risk for adverse cardiac outcomes in heart failure patients: design of two prospective multicenter international trials. *J Nucl Cardiol*. 2009;16(1):113–121.
121. Jacobson A. The prognostic significance of 123I-mIBG myocardial scintigraphy in heart failure patients: Results from the Prospective Multicenter International ADMIRE-HF Trial (Abstract No.09-LB-65168-ACC). American College of Cardiology, 2009: Presentation.

122. Moss AJ, Hall WJ, Cannom DS, et al. Cardiac-resynchronization therapy for the prevention of heart-failure events. *N Engl J Med*. 2009;361(14):1329–1338.
123. Henneman MM, van der Wall EE, Ypenburg C, et al. Nuclear imaging in cardiac resynchronization therapy. *J Nucl Med*. 2007;48(12): 2001–2010.
124. Ypenburg C, Westenberg JJ, Bleeker GB, et al. Noninvasive imaging in cardiac resynchronization therapy – Part 1: selection of patients. *Pacing Clin Electrophysiol*. 2008;31(11):1475–1499.
125. Van Kriekinge SD, Nishina H, Ohba M, Berman DS, Germano G. Automatic global and regional phase analysis from gated myocardial perfusion SPECT imaging: application to the characterization of ventricular contraction in patients with left bundle branch block. *J Nucl Med*. 2008;49(11):1790–1797.
126. Chen J, Garcia EV, Folks RD, et al. Onset of left ventricular mechanical contraction as determined by phase analysis of ECG-gated myocardial perfusion SPECT imaging: development of a diagnostic tool for assessment of cardiac mechanical dyssynchrony. *J Nucl Cardiol*. 2005;12(6):687–695.
127. Chen J, Faber TL, Cooke CD, Garcia EV. Temporal resolution of multiharmonic phase analysis of ECG-gated myocardial perfusion SPECT studies. *J Nucl Cardiol*. 2008;15(3):383–391.
128. Henneman MM, Chen J, Dibbets-Schneider P, et al. Can LV dyssynchrony as assessed with phase analysis on gated myocardial perfusion SPECT predict response to CRT? *J Nucl Med*. 2007;48(7):1104–1111.
129. Trimble MA, Velazquez EJ, Adams GL, et al. Repeatability and reproducibility of phase analysis of gated single-photon emission computed tomography myocardial perfusion imaging used to quantify cardiac dyssynchrony. *Nucl Med Commun*. 2008;29(4):374–381.
130. Nichols KJ, Van Tosh A, De Bondt P, Bergmann SR, Palestro CJ, Reichek N. Normal limits of gated blood pool SPECT count-based regional cardiac function parameters. *Int J Cardiovasc Imaging*. 2008;24(7): 717–725.
131. Van Kriekinge SD, De Bondt P, Vanderheyden M, Willems R, Berman DS, Germano G. Gated blood pool SPECT assessment of changes in ventricular function and dyssynchrony in patients responding to cardiac resynchronization therapy. *J Nucl Med*. 2009;50:170P.
132. Boogers MM, Van Kriekinge SD, Henneman MM, et al. Quantitative gated SPECT-derived phase analysis on gated myocardial perfusion SPECT detects left ventricular dyssynchrony and predicts response to cardiac resynchronization therapy. *J Nucl Med*. 2009;50:718–725.
133. Yamamoto A, Takahashi N, Munakata K, et al. Global and regional evaluation of systolic and diastolic left ventricular temporal parameters using a novel program for ECG-gated myocardial perfusion SPECT – validation by comparison with gated equilibrium radionuclide angiography and speckle-tracking radial strain from echocardiography. *Ann Nucl Med*. 2007;21(2):115–121.
134. Hachamovitch R, Di Carli MF. Nuclear cardiology will remain the "gatekeeper" over computed tomography (CT) angiography. *J Nucl Cardiol*. 2007;14:634–644.

20

Cardiovascular Magnetic Resonance Imaging: Overview of Clinical Applications

Jerold S. Shinbane, Jabi E. Shriki, Antreas Hindoyan, and Patrick M. Colletti

Introduction

Technologic advances in cardiovascular magnetic resonance imaging (CMR) and cardiovascular computed tomography angiography (CCTA) allow these modalities to comprehensively visualize cardiovascular structures and function. The decision to perform CMR vs. CCTA requires knowledge of the individual strengths and limitations of these imaging techniques, the specific details of a patient's medical history, and the clinical questions which need to be answered. In many clinical scenarios, echocardiography is performed as an initial study to assess cardiovascular substrates, with CMR or CCTA performed when further cardiovascular characterization is necessary and a noninvasive approach is preferable. Given the rapid evolution of these technologies, appropriateness criteria have been developed for specific cardiovascular indications [1].

The strengths of CMR include evaluation of tissue characteristics, myocardial perfusion, ventricular function, myocardial metabolism, viability, shunts, valvular function, flow velocities, and peripheral vasculature without the need for iodinated contrast media or X-ray irradiation. Paramagnetic contrast agents have greatly expanded the applications of CMR. The paramagnetic element gadolinium, when attached to a chelating agent like DTPA, provides a means for contrast enhancement allowing assessment of perfusion and delayed enhancement to detect acutely infarcted myocardium and chronic myocardial scar. CMR spectroscopy provides noninvasive assessment of myocardial metabolism allowing a mechanistic understanding of myocardial function when using ^{31}P to depict the high energy phosphates, phosphocreatine and ATP, and inorganic phosphate to evaluate intracellular pH.

In comparisons to CMR, the strengths of CCTA technologies currently include a greater ability to characterize coronary vasculature, shorter study times, and the ability to image patients with pacemakers, defibrillators, and other devices incompatible or problematic within a CMR system. As opposed to data acquisition with CCTA as one axial imaging sequence leading to one comprehensive 3D data cube, CMR requires multiple views and MR imaging sequences. CT also allows quantification of coronary artery calcium for risk stratification. Both CCTA and CMR technologies are advancing rapidly, and therefore future applications may lead to changes in these strengths and limitations.

Patient Selection and Preparation

While there is considerable effort focused on reducing the radiation exposure with CCTA techniques, the lack of ionizing radiation is an important strength of CMR. This issue is especially important in young patients, who may be at increased long term risk of malignancy [2]. As opposed to iodinated contrast agents used in CCTA, which enhance vascular structures by increasing CT Hounsfield Units, gadolinium-based contrast agents are paramagnetic and change the magnetic properties of water in close proximity to the contrast agent.

The relative safety of gadolinium-based contrast agents is a significant strength of MR. Iodinated contrast agents are associated with a significant incidence of acute side effects including allergic reaction, hypotension, bronchospasm, and pulmonary edema along with acute and chronic nephropathy. Recently though, gadolinium-based contrast agents have been associated with both worsening renal function and nephrogenic systemic fibrosis in patients with moderate to severe renal dysfunction, particularly in patients on dialysis [3, 4]. CMR techniques such as black blood imaging and bright blood imaging allow for differentiation of vasculature without the injection of a contrast agent. CMR imaging sequences and technology continue to rapidly evolve with 3D real time acquisition and increased field strengths to 3 T with attendant increased signal to noise ratio, but can be limited by field inhomogeneity and specific absorption rate limits [5–7]. The effects and safety

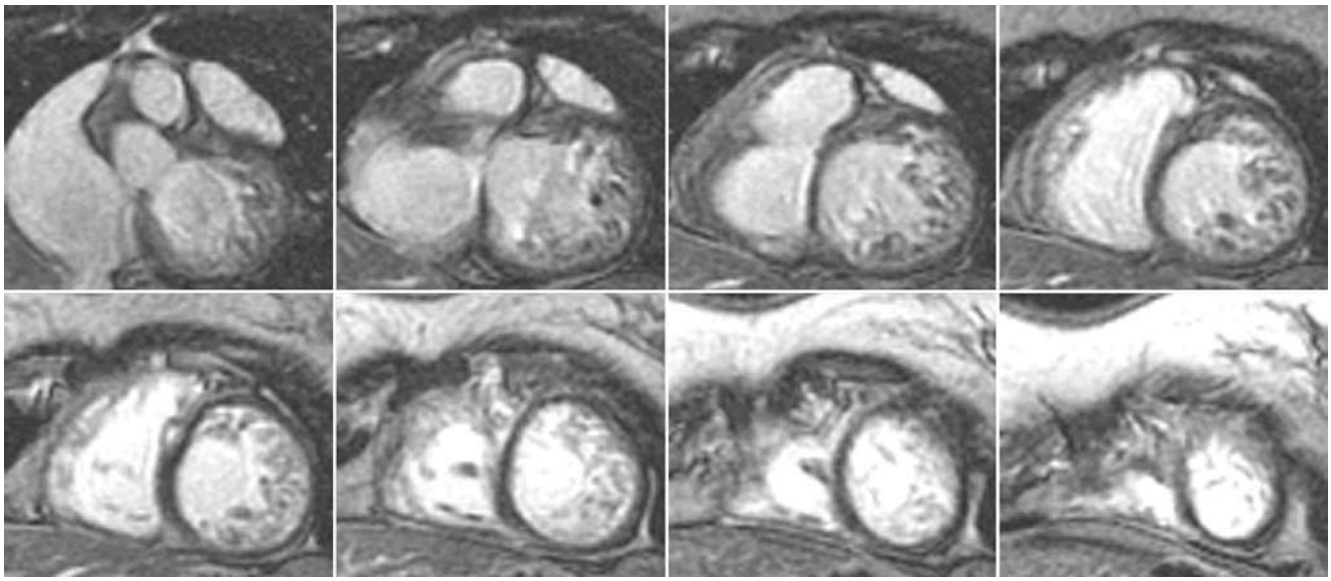

Figure 20.1. Short axis, delayed enhancement views show deep trabeculation in a case of ventricular noncompaction. Delayed enhancement images were obtained with an inversion time chosen to null myocardial signal, which would normally suppress or darken myocardium. In this case, there is bright signal from contrast in the blood pool interdigitating into the bands of noncompacted myocardium.

of field strengths greater than 3 T require further investigation [8, 9].

Patient size and body habitus are also important in deciding which imaging modality to employ. Image quality can be compromised in patients with an increased body mass index with CCTA and may require increased radiation exposure for adequate imaging [10]. This limitation is less significant with CMR, although there are limitations in MR access due to extreme patient size related to magnet bore diameter and table weight limits.

Prior to CMR, patients require a complete history for ferromagnetic prosthetic implants, devices, or depositions. These may have relative or absolute contraindications to MR imaging. It is important to ensure that patients with susceptible devices are not exposed to the MR environment. Most prosthetic heart valves and annuloplasty rings can be safely scanned, but specific details of compatibility need to be assessed individually prior to patient study [11]. Cardiac devices such as pacemakers and implantable cardiac defibrillators are almost always considered absolute contraindications for MRI, although there is some controversy regarding the MRI of patients with these devices, with some preliminary data suggesting that imaging may not be absolutely contraindicated in this setting [12, 13]. Detailed knowledge of patient, device, scanner, scanning protocol, alternative imaging techniques and importance of the clinical question are important factors in determination of individualized risk vs. benefit of performance of an MR study [14]. Pacemaker technologies have been engineered to be MR compatible for 1.5 T scanners with preliminary investigation in process [15].

Although study times for CMR have decreased due to advances in technology as well as efficiency of labs in performing protocols, studies are still significantly longer than those achieved with CCTA with scanning times on the order of seconds. The patient's ability to lie still in a supine position and comply with breath hold commands is important to both technologies, but can be more easily achieved with CCTA given the short study times. Claustrophobia is a common consideration in imaging some patients, although, with appropriate premedication, this is seldom a cause for premature termination of an examination [16, 17]. Larger bore magnets, open magnets, and visual devices allowing patients to see out of the magnet may make this even less of an issue in the future.

During image acquisition, special attention needs to be focused on electrocardiographic recording for monitoring and gating, as the MR environment can interfere with sensing of the QRS complex. Attention to skin prep, lead placement, and ECG vector can improve the ability to perform ECG gating, which is especially important when stress imaging is being considered [18, 19]. Due to acoustic noise associated with scanning, auditory protection with ear plugs is necessary [20].

Coronary Artery Visualization

CMR techniques can visualize coronary arteries for the assessment of coronary artery disease [21–23]. Additionally, CMR can assess patency and stenoses of coronary artery bypass grafts [24]. Advances in technique have improved the ability to visualize coronary arteries with respiratory gating, but issues of cardiac, coronary artery, and respiratory motion as well as problems with assessment of small caliber vessels still remain [24–27]. Techniques to minimize these issues and allow for coronary artery imaging include whole heart imaging with respiratory gating, and 3D

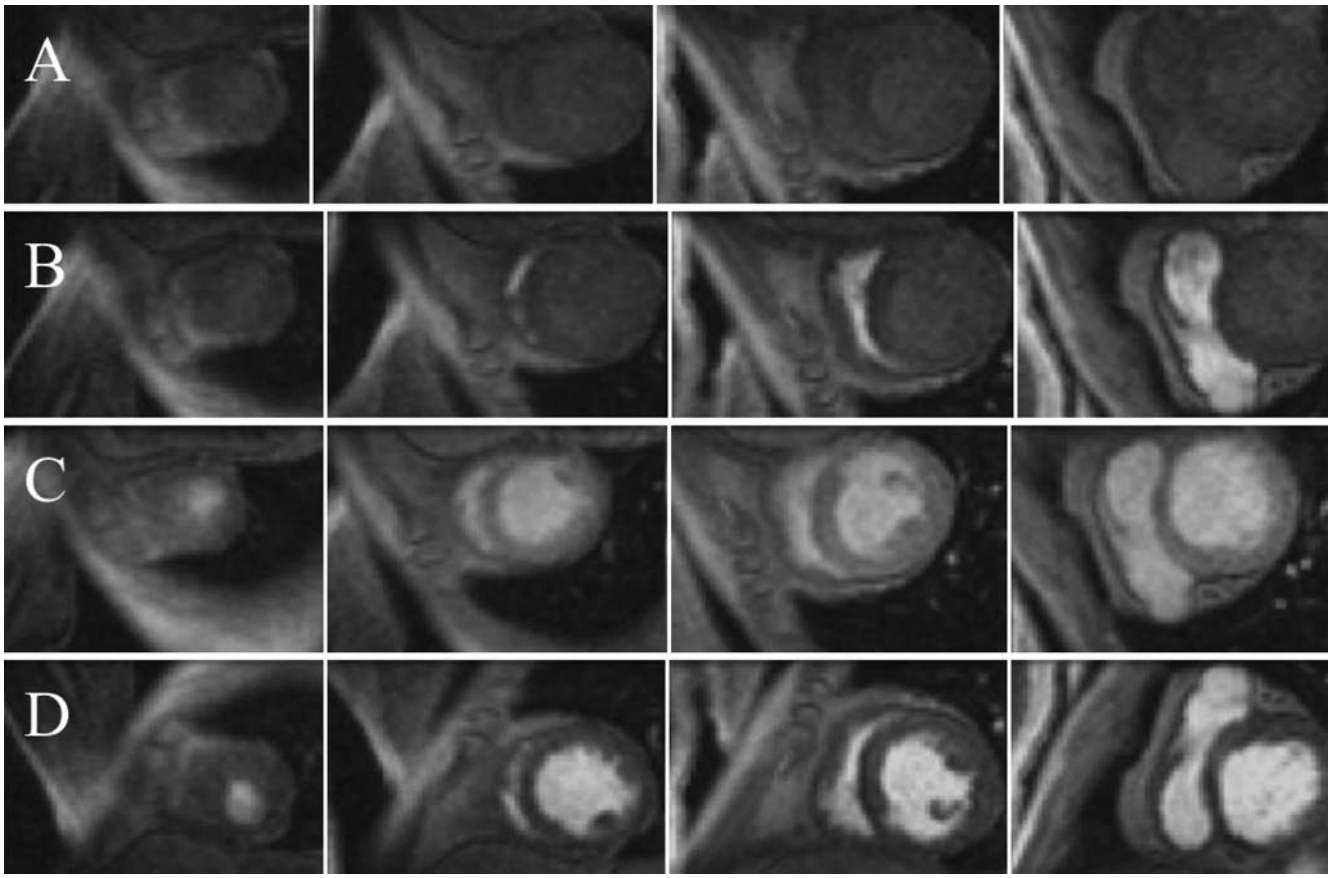

Figure 20.2. First pass myocardial perfusion study with serial short axis images demonstrating the progression of gadolinium enhancement. (**a**) Pregadolinium. (**b**) Right ventricular enhancement. (**c**) Right and left ventricular enhancement. (**d**) Left ventricular myocardial enhancement.

techniques have improved the ability to visualize the coronary arteries [23].

Since myocardial infarction can occur due to plaque rupture and thrombosis in coronary arteries without obstructive disease, there is a need to attempt to characterize plaques potentially at higher risk for rupture [28, 29]. Both CCTA and CMR can assess tissue characteristics of coronary artery plaque, but identification of vulnerable plaques requires further study [30]. CMR can assess tissue characteristics of vessel wall and atheromas, with assessment of fibrous tissue, fat, and calcified lesion components, but requires continued investigation to identify characteristics of vulnerable plaques [31, 32]. CMR can assess for vascular remodeling with changes in wall thickness and lumen size [33]. Noncalcified plaque detection and quantification between CMR and CT have been comparable, but CMR provides greater information on tissue characteristics [34].

Anomalous coronary arteries can be diagnosed with CMR [21, 35]. In addition to definition of anatomy of anomalous coronary artery origin, CMR can also assess functional significance through perfusion imaging [36]. CCTA has historically proven to more optimally assess coronary arteries, but advances in technology are improving CMR techniques [37].

CMR is also useful in the assessment and understanding of microvascular coronary artery disease. Phosphorus-31 nuclear magnetic resonance spectroscopy has provided a window into the assessment of myocardial metabolism through assessment of myocardial high-energy phosphates. This tool has allowed insight into mechanisms of chest pain in the absence of obstructive coronary artery disease [38]. Studies have demonstrated direct evidence of metabolic abnormalities consistent with ischemia in women with chest pain without obstructive coronary artery disease, and proven essential in forwarding the understanding of microvascular coronary artery disease [39].

Characterization of Cardiomyopathic Processes

CMR can characterize cardiac structures and function by reproducibly assessing right and left ventricular volumes, ejection fraction, wall thickness, and wall motion [40–45]. The ability to comprehensively assess ejection fraction, wall motion, perfusion, and viability is a great strength of CMR in the characterization of myocardial substrates associated with coronary artery disease as well as other myopathic

disease processes. Evaluation with assessment of multiple components including coronary anatomy, ventricular function, rest perfusion, adenosine or dobutamine perfusion, and delayed enhancement provides comprehensive evaluation of ischemic heart disease with high accuracy [22].

CMR also provides excellent imaging of intraventricular structures such as trabeculae and is helpful in the diagnosis of ventricular noncompaction (Figure 20.1) [46]. A ratio of noncompacted to compacted myocardium of greater than 2.3 by echocardiography, CMR, or CCTA is useful in differentiating ventricular noncompaction from other conditions including hypertrophic cardiomyopathy, dilated cardiomyopathy, hypertensive heart disease, and hypertrophy associated with aortic stenosis.

The performance of rest and stress first pass imaging as well as delayed enhancement imaging are practical strengths of CMR over CCTA and are important to characterization of ischemia, myocardial infarction, and ischemic cardiomyopathy. First-pass perfusion imaging of the heart, obtained immediately after injection of gadolinium, can be performed with CMR and is useful for evaluating for perfusion abnormalities at rest and during pharmacologic stress with adenosine or dobutamine (Figures 20.2 and 20.3) [47–50]. CMR perfusion correlates with invasive fractional flow reserve and offers prognostic information important to risk stratification [48, 51]. Dobutamine CMR can be used to assess for ischemia and demonstrated a higher diagnostic accuracy than dobutamine echocardiography [52]. Additionally, dobutamine CMR is helpful in the assessment of patients with poor echo windows [53]. Dobutamine CMR can also assess for functional improvement after revascularization of ischemic cardiomyopathy [54]. The use of CMR assessment of response to percutaneous coronary intervention with first pass imaging evaluated in the baseline state and with dipyridamole has been reported [55]. CCTA adenosine stress perfusion is achievable but in an earlier state of study [56].

With delayed enhancement images, obtained approximately 10 min after gadolinium-based contrast administration, gadolinium clears from normal myocardium, but enhances areas of fibrosis or inflammation [57]. Delayed enhancement imaging using iodinated contrast agent with CCTA is also able to image fibrosis associated with myocardial infarction, but is currently less well established and limited by the overall radiation exposure required to perform the additional delayed imaging [58]. Interpretation of gadolinium delayed contrast enhancement has become more complex as it has been recognized to occur in a variety of cardiovascular disease processes associated with fibrosis or inflammation. Interpretation of delayed enhancement requires correlation of the individual patient's medical history and the posed clinical question with the pattern of delayed enhancement. The sensitivity and specificity delayed enhancement patterns for particular disease processes requires greater investigation.

Delayed gadolinium enhancement may be useful in assessing a variety of cardiomyopathic processes. Infarct related delayed contrast enhancement typically occurs in the anatomic distribution of coronary arteries. There is a subendocardial delayed enhancement pattern with increasing degrees of transmural extension depending on the

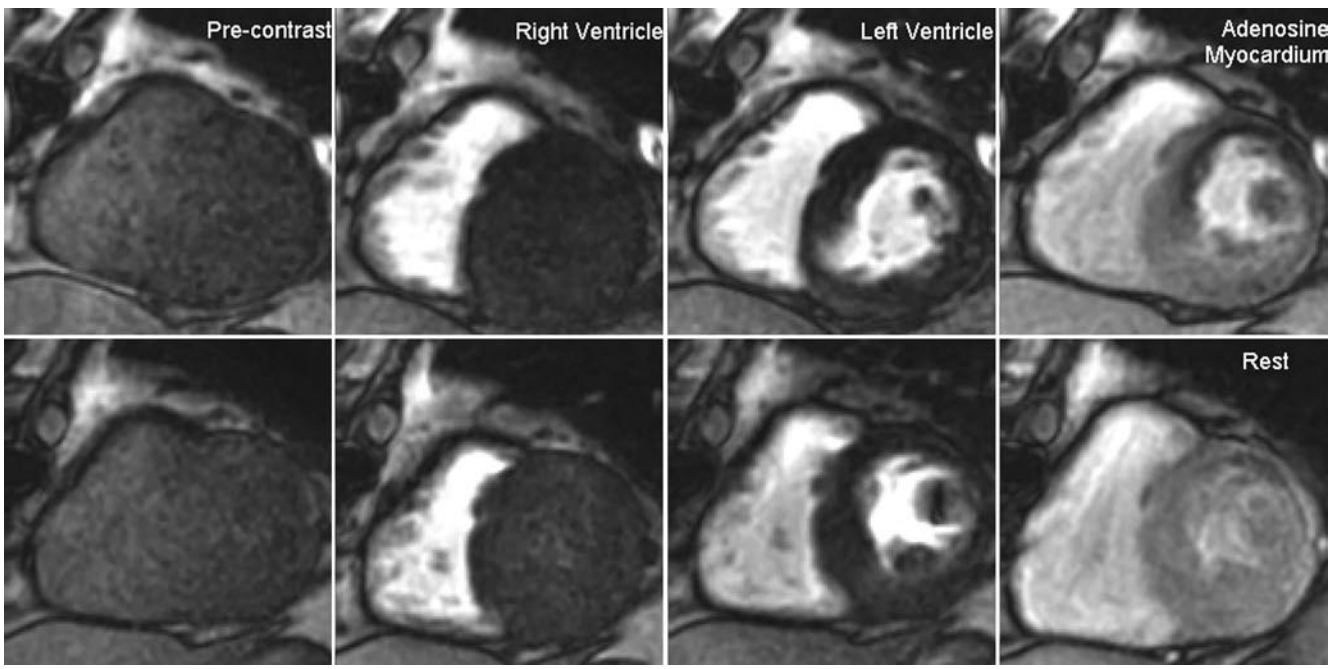

Figure 20.3. First-pass perfusion imaging demonstrating resting normal perfusion (*lower panels*) and adenosine perfusion imaging with evidence of ischemia. Note that resting images (*bottom row*) demonstrate normal perfusion throughout the left ventricle. After administration of adenosine (*top row*), an area of decreased signal intensity is demonstrated in a subendocardial distribution involving the anteroseptal, anterior, and anterolateral walls. This is consistent with an area of ischemia in the distribution of the left anterior descending coronary artery.

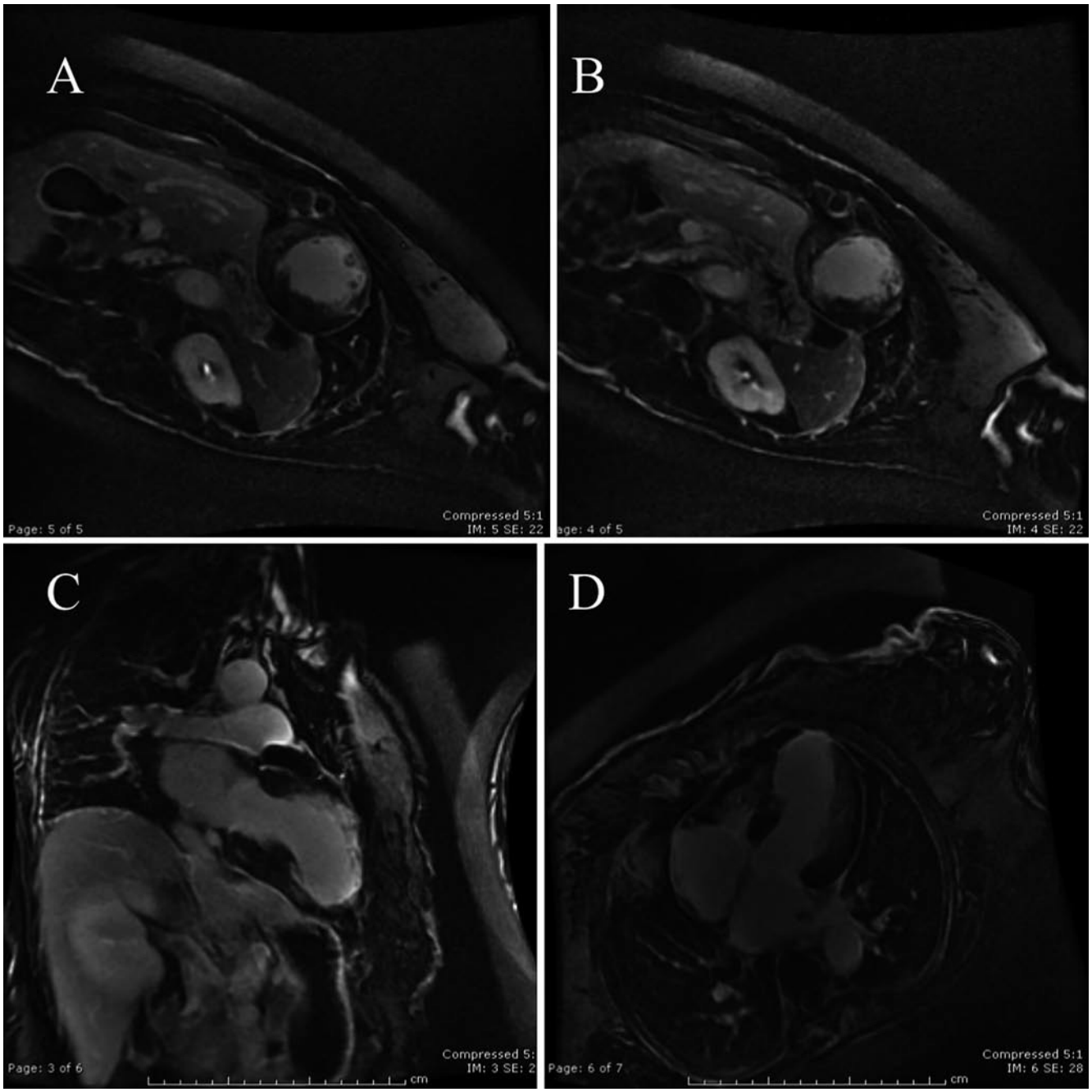

Figure 20.4. Delayed gadolinium enhancement views showing a myocardial infarct with extensive involvement of the mid anteroseptal, anterior and anterolateral walls, and the apex. (**a**, **b**) Short axis views. (**c**) 2 Chamber view. (**d**) 4 Chamber view.

extent of infarct (Figures 20.4 and 20.5) [59]. There may be areas of peri-infarct tissue heterogeneity, representing areas of viable myocardium and fibrosis. These heterogeneous areas may increase the propensity for the development of ventricular tachycardia (Figure 20.6) [60]. Microvascular obstruction is usually depicted as a subendocardial nonenhancing area due to tissue necrosis which is completely surrounded by delayed enhancement [61].

In ischemic cardiomyopathy, gadolinium delayed enhancement images can assess for areas of viability prior to potential revascularization. Specifically, in patient with ischemic cardiomyopathy, delayed hyperenhancement correlates with lack of viability defined by thallium single photon emission computed tomography [62]. Soon after acute myocardial infarction, gadolinium delayed enhancement CMR images can assess infarct size in comparison to other clinical indices of infarct size [63]. The degree of wall thickening correlates with degree of myocardial nonenhancement on delayed images after recent myocardial infarction and predicts improvement in wall thickening as assessed by study at a later time [64].

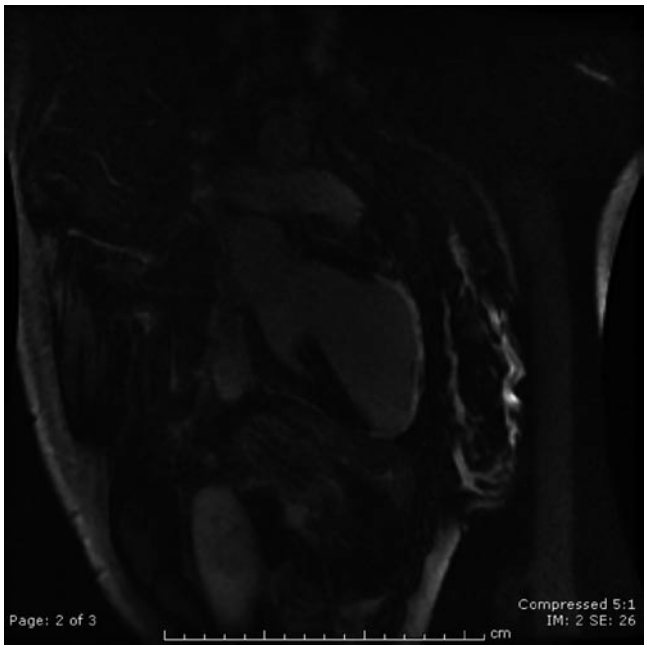

Figure 20.5. Delayed gadolinium enhancement 2 chamber view demonstrating transmural myocardial infarction involving the mid to distal left anterior descending coronary artery distribution.

Delayed contrast enhancement may be useful in differentiating ischemic from nonischemic dilated cardiomyopathy. A delayed enhancement subendocardial to transmural infarct pattern is consistent with ischemic cardiomyopathy while other patterns are not consistent with infarct including subepicardial and mid-wall fibrosis [59]. Mid-wall fibrosis in dilated cardiomyopathy has been associated with worse prognosis and ventricular arrhythmias [65, 66]. The presence and degree of gadolinium enhancement can predict remodeling response to beta-blockers in both ischemic and nonischemic cardiomyopathy [66].

Delayed enhancement imaging is also useful in the assessment of other cardiomyopathic processes, including hypertrophic cardiomyopathy and arrhythmogenic right ventricular cardiomyopathy (ARVC). In hypertrophic cardiomyopathy, the assessment for regional wall thickness, indexed ventricular mass, ejection fraction, valvular information, and hemodynamic data including gradients can be performed (Figure 20.7)[67–71]. The presence, extent, and pattern of gadolinium delayed enhancement provides additional prognostic significance related to ventricular arrhythmias in hypertrophic cardiomyopathy [72]. In comparison to nonischemic dilated cardiomyopathy, the dilated phase of hypertrophic cardiomyopathy has a greater extent of delayed enhancement predominantly in the septal and anterior walls [73]. Preoperative and follow-up studies may be useful in patients undergoing surgical myocardial resection or coronary artery septal embolization [69, 74]. In the setting of ARVC, delayed contrast enhancement of the right ventricle and left ventricle may be identified, in addition to right ventricular intramyocardial fat, increased right ventricular trabeculation, abnormal right ventricular size or shape, and regional and global function (Figure 20.8) [75, 76].

Delayed gadolinium enhancement may also be useful in the assessment of inflammatory and infiltrative processes. In cardiac amyloid, the typical delayed enhancement pattern is a patchy subendocardial pattern (Figure 20.9) [77]. Tissue characteristics seen on CMR may help to differentiate amyloid from hypertrophic cardiomyopathy [78].

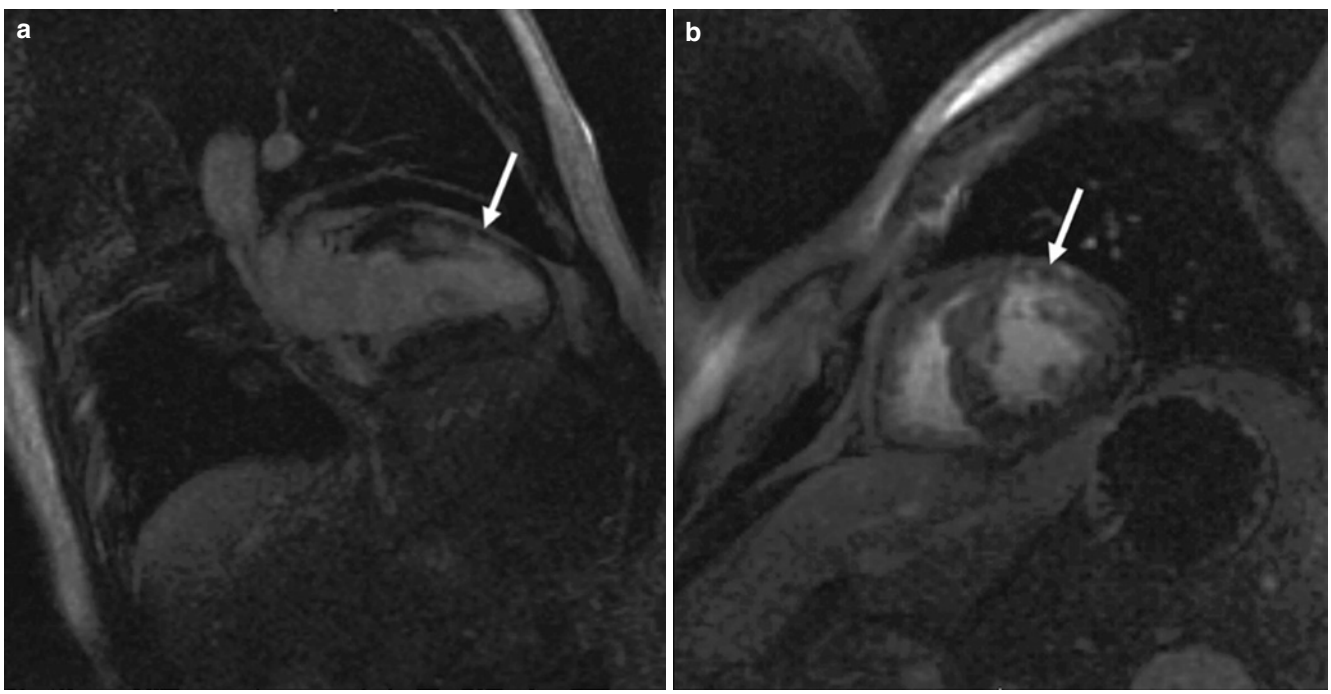

Figure 20.6. Delayed gadolinium enhancement images demonstrate a myocardial infarction in the left anterior descending coronary artery territory. Portions of the infarct are transmural, although most of the distribution is subendocardial, with hetereogeneity of signal ("*gray zone*") (*arrows*) in areas between grossly infarcted tissue and normal myocardium. (**a**) 2 Chamber view. (**b**) Short axis view.

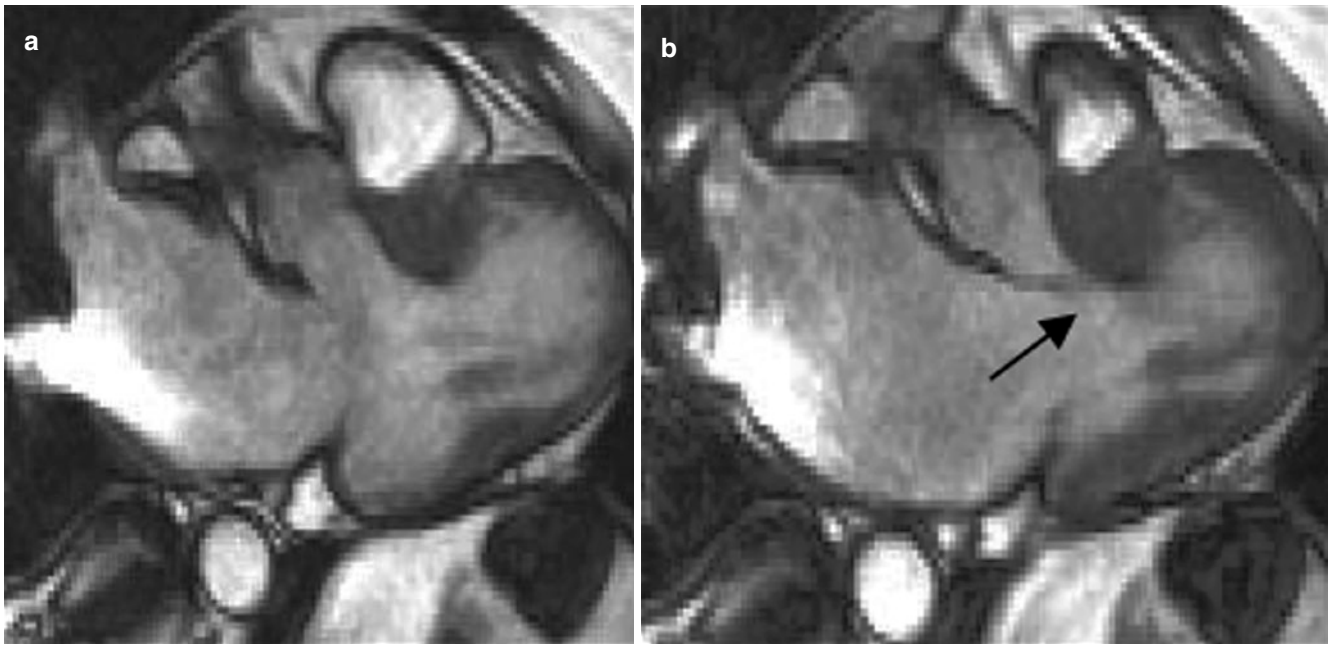

Figure 20.7. Patient with hypertrophic cardiomyopathy during ventricular diastole (**a**) and ventricular systole (**b**) demonstrating systolic anterior motion of the mitral valve (*arrow*).

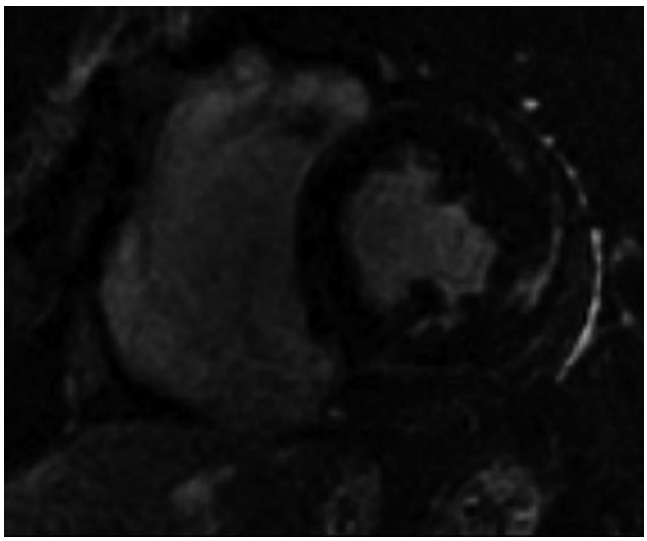

Figure 20.8. Short axis delayed gadolinium enhancement view demonstrating right ventricular enlargement as well as left ventricular delayed contrast enhancement in arrhythmogenic right ventricular cardiomyopathy.

Figure 20.9. Short axis delayed gadolinium enhancement view demonstrating contrast enhancement associated with cardiac amyloid.

Gadolinium enhanced CMR can identify inflammation and fibrosis associated with cardiac sarcoidosis [79]. In sarcoid, mid-wall delayed enhancement often involves the basal septum, especially the right ventricular side of the basal septum (Figure 20.10) [80]. Transmural enhancement correlates with wall motion abnormalities which may represent fibrogranulomatous tissue involvement [81]. Additionally, changes associated with treatment of cardiac sarcoidosis with steroids have been reported [82]. Gadolinium enhancement associated with the inflammatory process in Chagas disease has also been reported [83]. In Chagas disease, the extent of myocardial fibrosis correlates with disease severity, and delayed enhancement imaging can detect involvement in the early asymptomatic phase of disease [84]. Delayed gadolinium enhancement can be seen in acute and

chronic myocarditis and can help differentiate acute myocardial infarction from acute myocarditis, with delayed enhancement imaging pattern demonstrating a nonsubendocardial distribution (Figure 20.11) [85, 86]. Delayed enhancement can additionally be seen in the pericardium associated with pericarditis (Figure 20.12).

Although it may be frequently difficult to discern whether areas of gadolinium enhancement are related to myocardial infarctions or other causes of cardiomyopathy, subendocardial involvement with variable degrees of transmurality are more suggestive of infarctions, especially when in the expected vascular distribution of a coronary artery. Midwall, subepicardial, or nodular enhancement patterns should raise suspicion that other processes may be causing the abnormality.

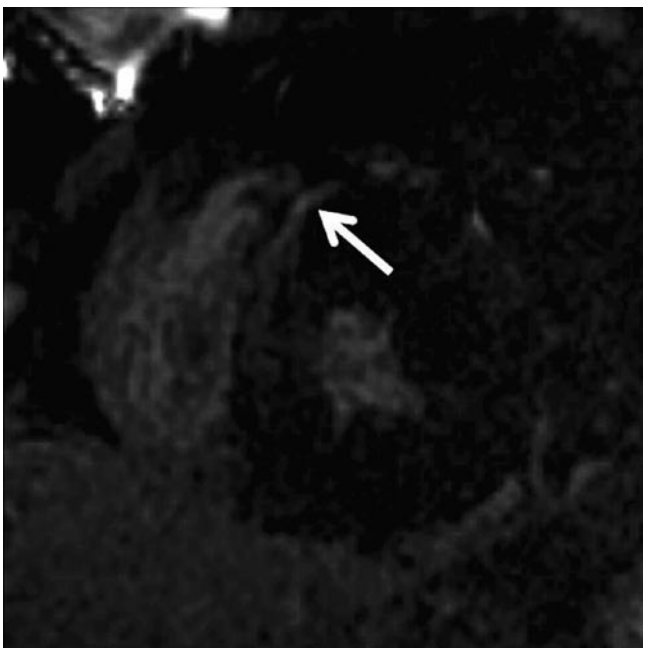

Figure 20.10. Short axis delayed gadolinium enhancement view demonstrating cardiac sarcoidosis with involvement of the right ventricular side of the basal septum (*arrow*).

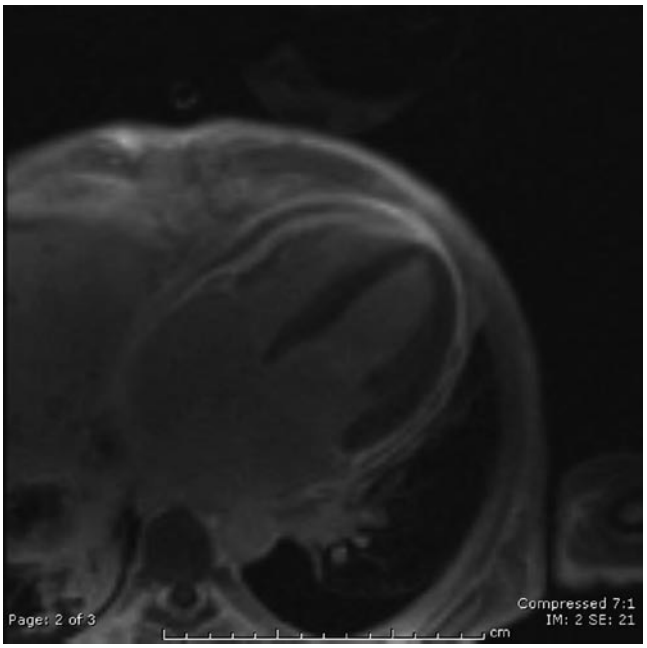

Figure 20.12. A 4 chamber view demonstrating pericardial delayed enhancement associated with pericarditis.

Cardiac Masses

Assessment with CMR is useful in the diagnosis and characterization of cardiac masses due to the ability to comprehensively assess tissue characteristics of a mass, as well as involvement of a mass in relation to surrounding cardiac and thoracic structures (Figure 20.13). With the use of multiple pulse sequences with emphasis on T1 and T2 weighting, proton density, and perfusion imaging, CMR is especially useful in assessment of tissue characteristics of masses [87]. Mass location, tissue characteristics, and presence of pericardial or pleural involvement are important factors for evaluating and staging benign or malignant cardiac neoplasms when findings are compared to actual histologic examination [88].

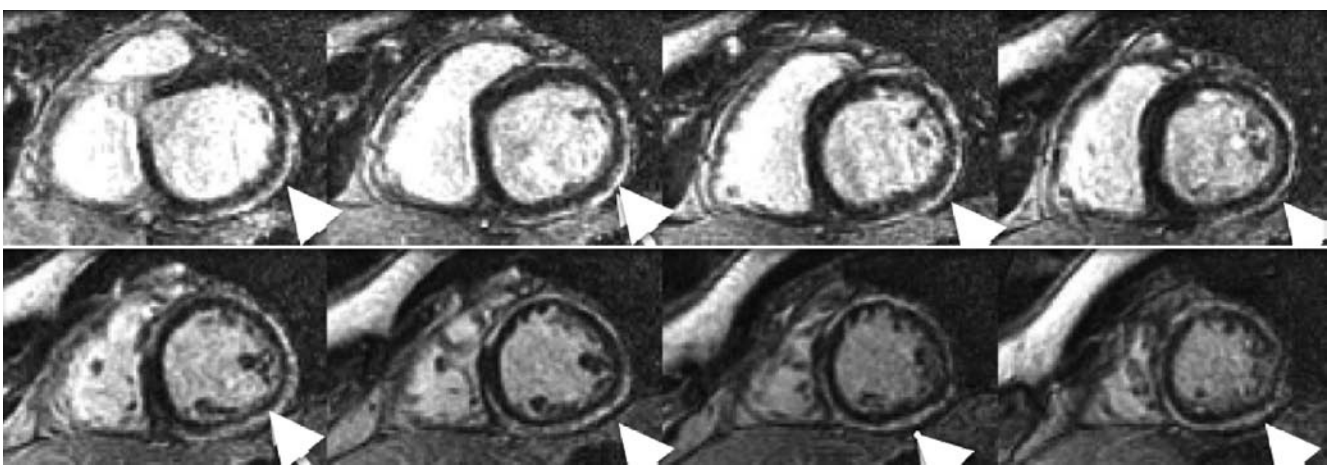

Figure 20.11. Short axis delayed gadolinium enhancement images demonstrate subepicardial enhancement (*arrowheads*) consistent with myocarditis.

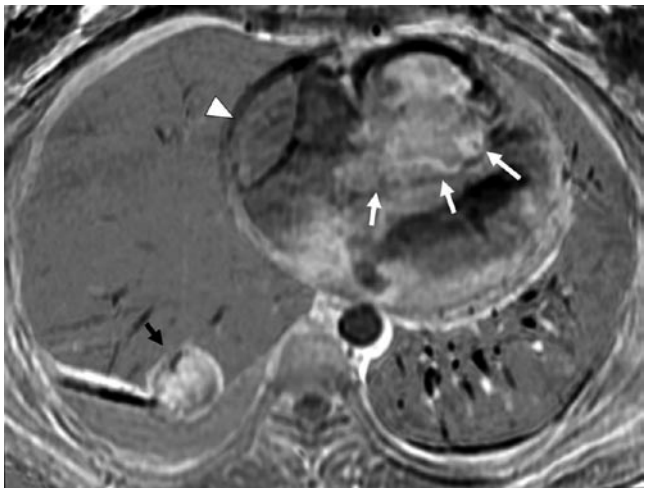

Figure 20.13. A large, broad-based mass is present arising from the right ventricle (*white arrows*). There is also an enhancing mass in the right atrium (*arrowhead*) with an elliptical border with the right atrial lumen. A right lower lobe enhancing mass is present (*black arrow*), likely representing a metastasis. A right pleural effusion is also present. This mass was a cardiac angiosarcoma.

Benign tumors, primary malignant tumors, and metastatic malignant tumors, have been identified with CMR, including fibromas, lipomas, myxomas, mesotheliomas, sarcomas, lymphomas, melanomas, and metastatic carcinomas (Figures 20.14 and 20.15) [89–100]. Tumor mimicks can also be identified including lipomatous hypertrophy of the interatrial septum, prominent crista terminalis, Chiari network, and thrombus (Figure 20.16) [91, 100, 101].

Congenital Heart Disease

The ability of CMR to provide comprehensive assessment of cardiovascular structure and function, as well as an extra-cardiac thoracic structure, makes it useful in the diagnosis, facilitation of treatment, and follow-up of patients with congenital heart disease. CMR can comprehensively assess simple and complex congenital heart disease in the native state or after surgical treatment (Figures 20.17 and 20.18) [102–118].

In addition to cardiac structure, ventricular function is extremely important in patients with congenital heart disease, with worse prognosis with ventricular dysfunction late after surgical repair of such anomalies as tetralogy of Fallot [119]. Baseline as well a dobutamine stress CMR can assess ventricular function, and has been used to assess right ventricular dysfunction in patients with chronic right ventricular pressure overload secondary to congenital heart disease [113, 120]. Additionally, cardiac shunts can be accurately assessed over the spectrum of pulmonary to systemic shunt ratios [108].

CMR is useful in preprocedure planning for surgical approaches to congenital heart disease [114]. Studies can also provide information important to the preprocedural planning of interventional cardiology procedures, such as atrial septal defect closure, with ability to assess such factors as defect size and rim characteristics [117]. Postsurgical imaging is important for the follow-up of surgically treated congenital heart disease, with reports demonstrating the utility of postsurgical follow-up for tetralogy of Fallot, Mustard's operation for transposition of the great vessels, and follow-up of arterial switch for transposition of the great vessels [106, 110, 118]. Delayed enhancement imaging can be used to assess for the degree and location of fibrosis associated with congenital surgical procedures [121].

In addition to congenital aortic lesions such as coarctation of the aorta, CMR can diagnose acquired vascular and valvular heart disease including aneurysm, dissection, and wall abnormalities such as penetrating ulcers, calcification, or thrombus with ability to assess all aortic segments

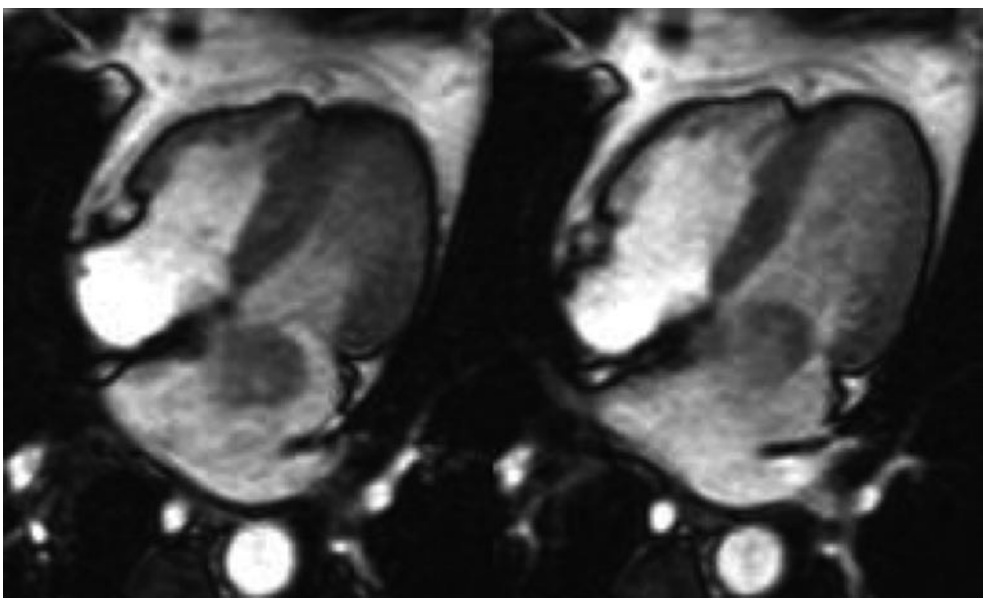

Figure 20.14. A 4 chamber image in ventricular systole and diastole demonstrating a large left atrial myxoma.

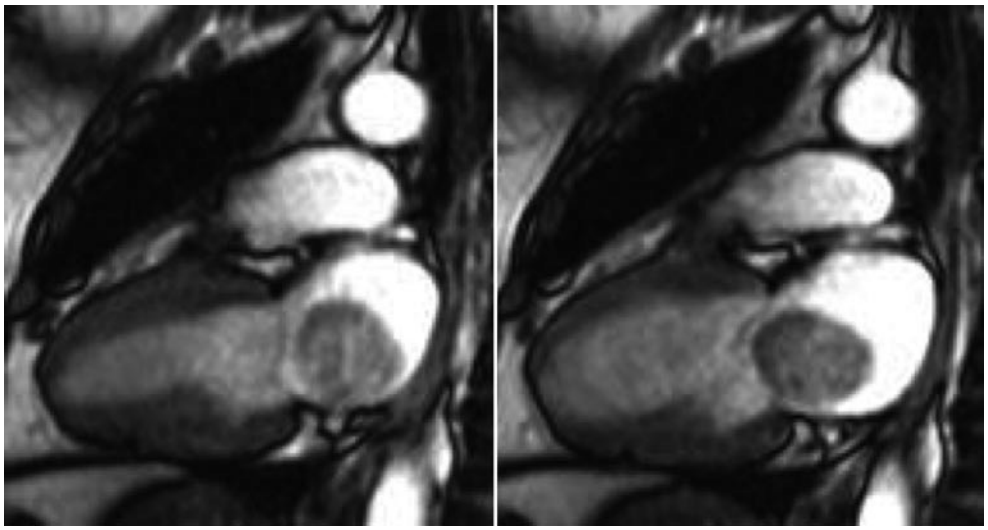

Figure 20.15. Large atrial myxoma on a 2 chamber view which obstructs the mitral valve during atrial systole.

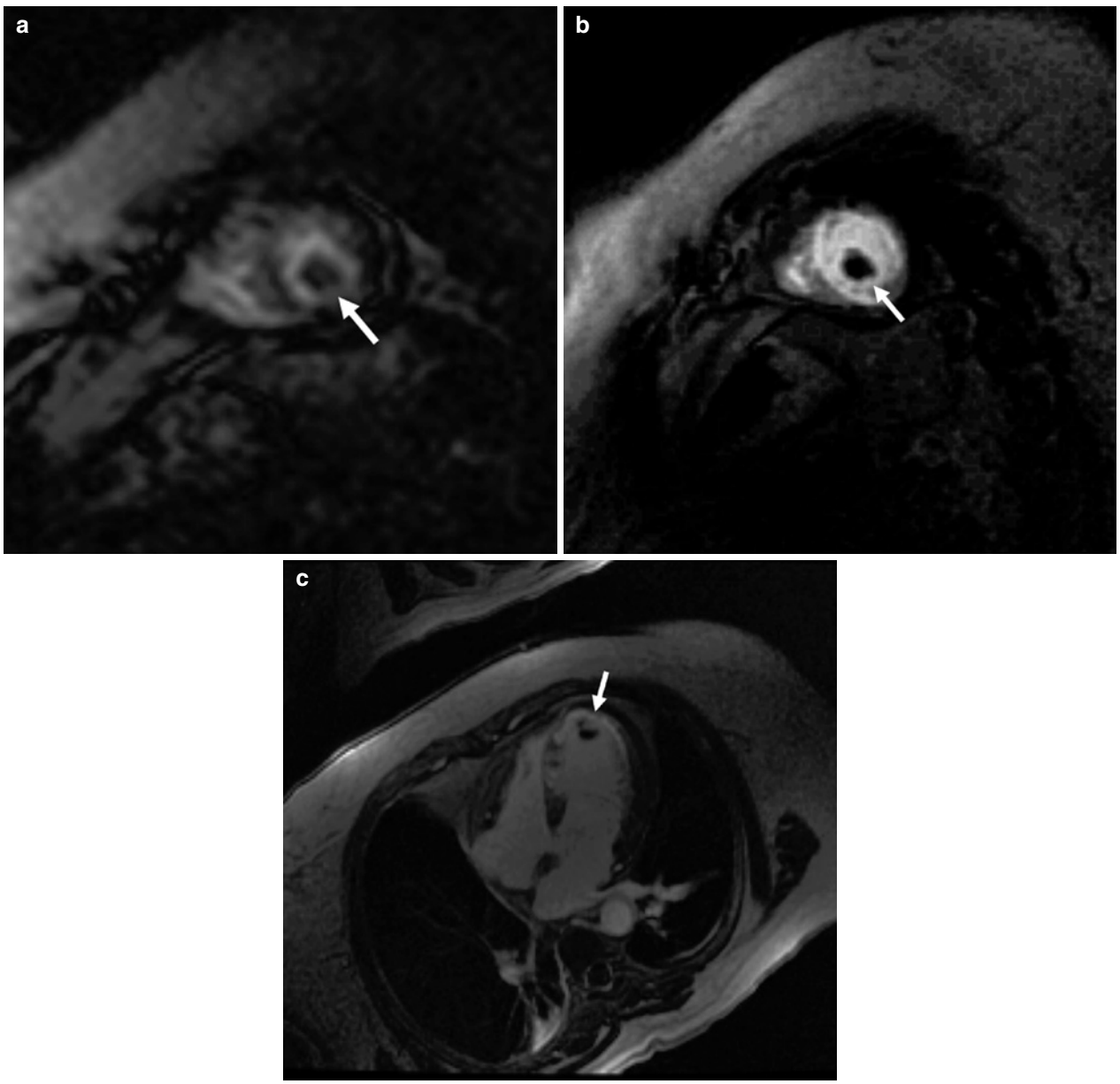

Figure 20.16. Chronic myocardial infarction with apical aneurysm and an apical thrombus (*arrows*). (**a**) Short axis first pass perfusion image. (**b**) Short axis functional image. (**c**) Delayed gadolinium enhancement 4 chamber view.

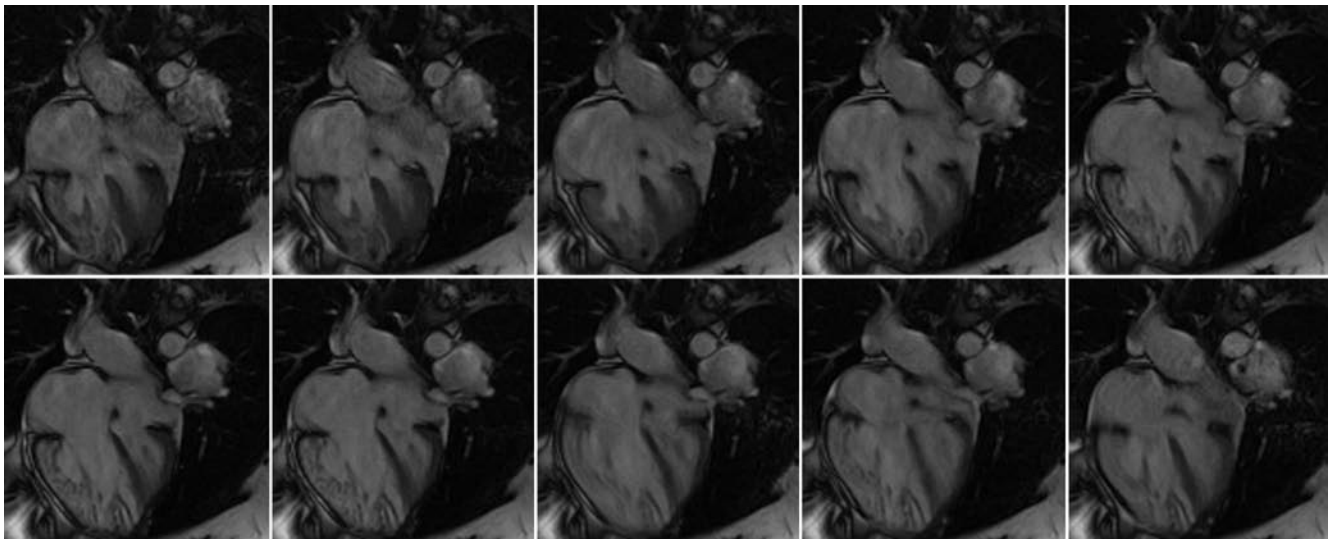

Figure 20.17. CMR 4 chamber images demonstrating a large secundum atrial septal defect, with right ventricular enlargement and hypertrophy and right atrial enlargement.

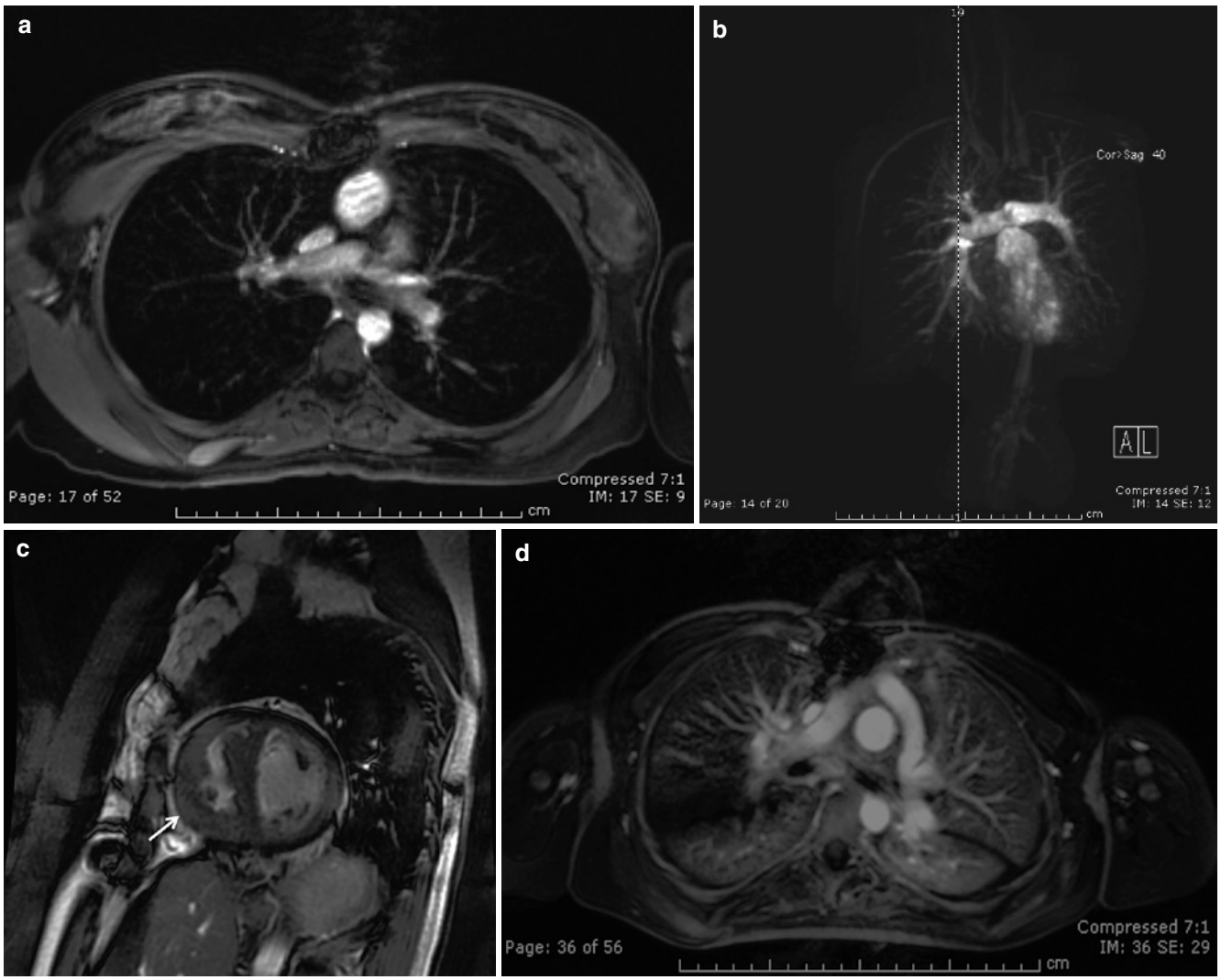

Figure 20.18. Transposition of the great arteries (D-type), status post previous atrial baffle procedure in childhood, with subsequent pulmonary artery banding procedure in preparation for an arterial switch operation. (**a**) An axial view demonstrates the anterior position of the aorta. (**b**) MR angiogram status post pulmonary artery banding. (**c**) Due to the pulmonary artery banding, there is hypertrophy of the previously thin morphologic left ventricular myocardium in the venous position (*arrow*). (**d**) After arterial switch, the neoaorta is now located posteriorly to the main pulmonary artery.

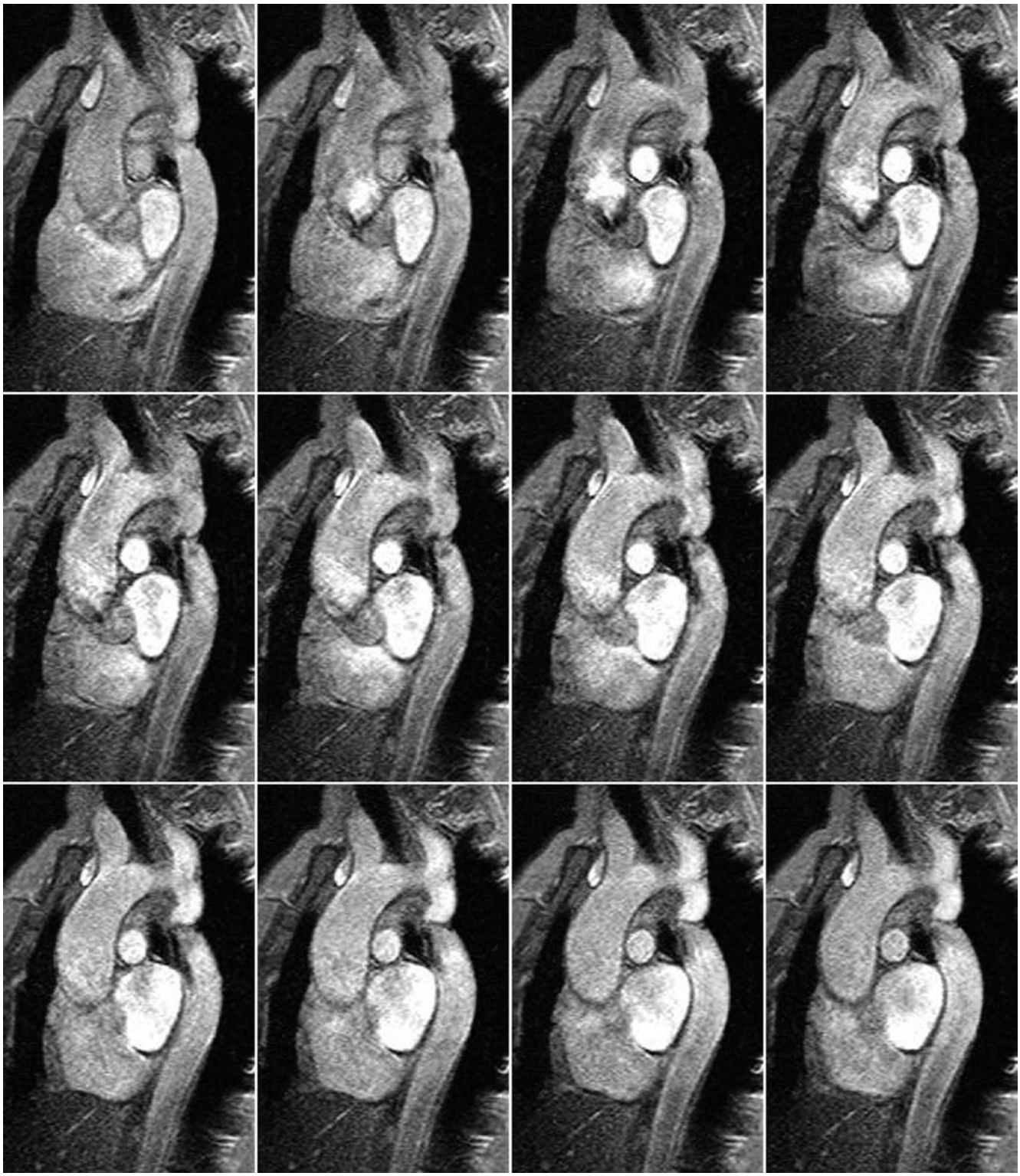

Figure 20.19. Serial sagittal slices demonstrating coarctation of the aorta.

(Figures 20.19 and 20.20) [122]. CMR can characterize valves for thickening, stensosis, and regurgitation, and can assess for such abnormalities as significant aortic valve stenosis, with measurement of pressure gradients velocity–time integral and valve dimensions which correlate well with echocardiogram (Figure 20.21) [123].

Imaging approaches that are faster and more operator-independent should increase the utility of CMR for the assessment of congenital heart disease [116, 124]. Real time cardiac catheterization guided by magnetic resonance in compatible lab settings is being investigated for use in the assessment of congenital heart disease [125].

Figure 20.20. Magnetic resonance aortogram demonstrating multifocal plaques, bilateral renal artery stenosis (*upper arrows*), and a saccular aneurysm of infrarenal aorta (*lower arrow*).

Figure 20.21. Mild aortic regurgitation with an eccentric jet.

Cardiac Electrophysiology Applications

Due to the comprehensive nature of CMR, it has been shown to be useful in cardiac electrophysiology in the assessment for structural and functional abnormalities associated with electrophysiologically-related disease processes. The major limitation to assessment of patients with electrophysiologic issues is the preexistence of devices including pacemakers and implantable cardiac defibrillators. Issues reported have included pacemaker malfunction and lead heating [126–128]. As discussed previously, some studies question whether scanning of patients with pacemakers using 1.5 T systems is an absolute contraindication [12, 13].

Diagnosis and characterization of ischemic and nonischemic dilated cardiomyopathy is essential to risk stratification of patients for the primary prevention of sudden cardiac death. Due to multiple trials which have demonstrated benefit to placement of an implantable cardiac defibrillator based on severity of cardiac systolic dysfunction, the quantitative assessment of function in dilated ischemic and nonischemic cardiomyopathy has become an important issue. As previously detailed, CMR can characterize cardiac structure and function by reproducibly assessing ventricular volumes, ejection fraction, wall thickness, and wall motion. The use of the extent and location of myocardial infarct scar as criteria for prophylactic defibrillator placement is now being investigated [129].

Other applications relate to the assessment of arrhythmogenic substrates and involve myopathy of the right ventricle. Right ventricular morphology and function can be challenging to assess by modalities such as echocardiography due to the complex shape of the right ventricle, and therefore 3D tomographic modalites such as CMR are useful, providing reproducible assessment of right ventricular size and function [45]. ARVC is associated with ventricular arrhythmias and sudden cardiac death [130, 131]. The diagnosis is challenging to make and involves multiple possible diagnostic factors, including clinical symptoms, family history, ECG findings, results of electrophysiology study, and structural/functional abnormalities of the right ventricle. Imaging for abnormalities associated with ARVC can be missed with multiple imaging modalities. CMR has become the diagnostic modality most commonly used to assess for ARVC, as CMR can differentiate tissue characteristics between fat and myocardium, as well as providing assessment of right ventricular size, shape, and function.

The initial focus of CMR identification of ARVC related to characterization of intramyocardial fat, but intramyocardial fat may also be present in normal subjects [132]. Initially, there was over-diagnosis of ARVC, partially due to focus on fat involvement and thinning of the right ventricle [133]. More recent focus has been on right ventricular size, shape, and function, with assessment on global and regional right ventricular wall motion abnormalities, scalloping of the ventricle, increased trabeculation, and delayed enhancement associated with fibrofatty infiltrates [134]. Delayed enhancement can be seen due to fibrofatty infiltrates in ARVC, but can be challenging to asses due to the thin wall of the right ventricle [135]. Delayed enhancement can be seen also in the left ventricle in ARVC with CMR (Figure 20.8). ARVC may mimic Brugada syndrome; therefore, CMR can be useful as part of the work-up for Brugada syndrome, assessing for structural abnormalities associated with right ventricular cardiomyopathy [136]. Study

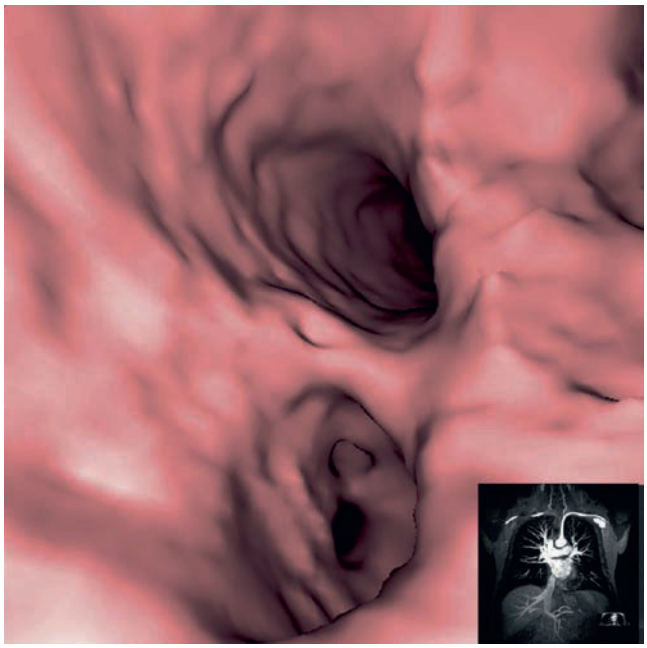

Figure 20.22. Endovascular view of the left upper and left lower pulmonary veins obtained from reconstruction of a MR angiogram (*lower right panel*) for use with integration with electroanatomic mapping to facilitate atrial fibrillation ablation.

with CMR for assessment of structural changes associated with Brugada syndrome has only demonstrated subtle anatomic findings in comparison to normal volunteers [137]. As CMR is contraindicated in patients with implantable cardiac defibrillators, comprehensive diagnosis needs to be performed in patients suspected of having ARVC prior to device placement.

Assessment of atrial anatomy is important to the understanding and treatment of supraventricular arrhythmias. Detailed assessment of left atrial anatomy is particularly important for ablation techniques for atrial fibrillation. Techniques for atrial fibrillation ablation are in evolution, and involve either segmental catheter ablation of the pulmonary veins or circumferential electrical isolation of the pulmonary veins [138–140]. CMR can characterize the left atrial volume and function, as well as location, shape, complexity, and individual venous variation to help in the preoperative planning, procedural facilitation, and postoperative follow-up for atrial fibrillation ablation procedures (Figure 20.22) [141–146]. Similar to CCTA, the integration of real time catheter-based electroanatomic maps with 3D CMR angiography images obtained preprocedure facilitates the performance of ablation procedures [147–149]. Integration of intracardiac echo and CMR images can allow for mapping and ablation with real time localization of esophageal position and catheter tissue contact (Figure 20.23) [150]. CMR delayed enhancement imaging can visualize radiofrequency energy applications after atrial fibrillation ablation as well as for other types of atrial and ventricular ablation procedures [151]. Assessment of degree of atrial myopathy is a predictor of success [152]. The use of real time CMR in an MR compatible electrophysiology laboratory is a goal which could allow real time assessment of ablation lesions during ablation procedures [153].

Similar to cardiovascular CCTA, CMR has been used to diagnose and provide surveillance for pulmonary vein stenosis, a potential complication of atrial fibrillation ablation [154–156]. In addition to providing roadmaps for ablation, preprocedure studies can serve as templates to assess for changes in pulmonary vein anatomy on postprocedure studies. As the time course of pulmonary vein stenosis continues to be defined, CMR may become a useful tool for the long term follow-up for possible pulmonary vein stenosis [157].

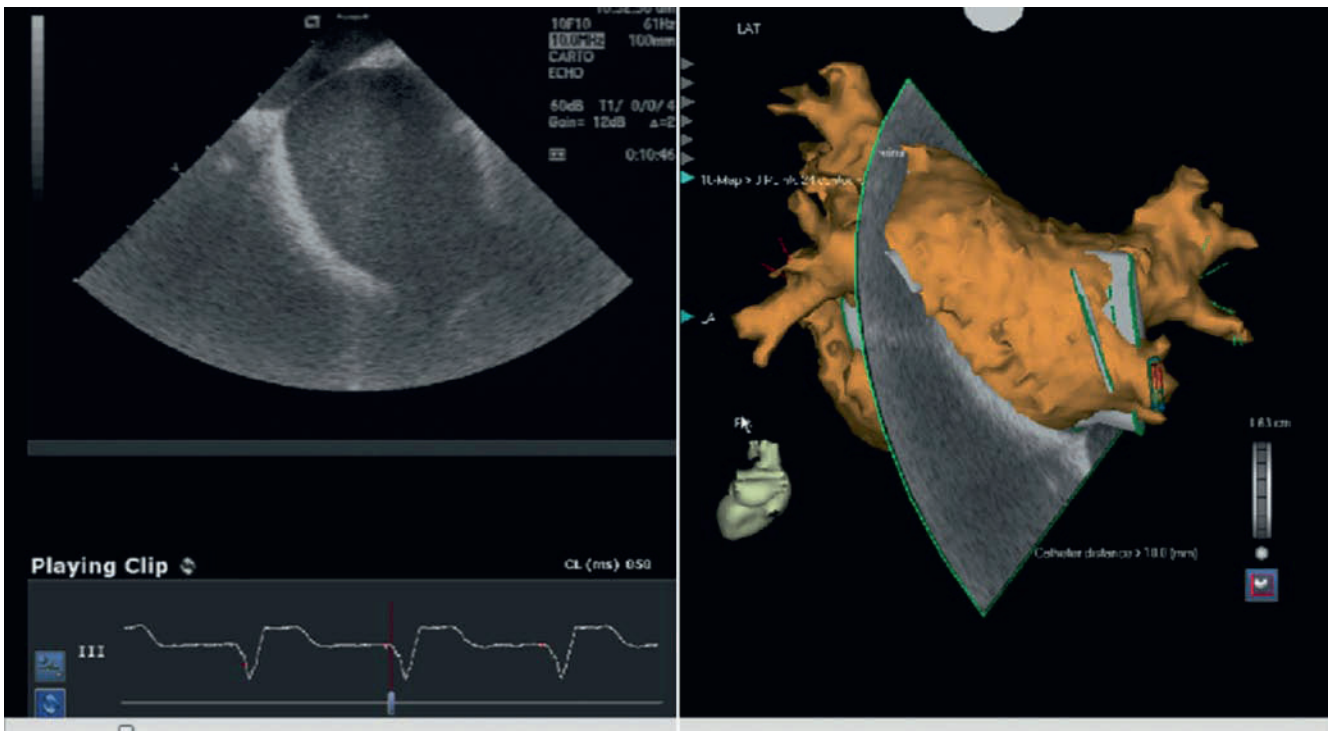

Figure 20.23. Volume rendered MR angiogram integration with intracardiac echo images for atrial fibrillation ablation.

An important component of imaging related to atrial fibrillation therapies is evaluation for atrial thrombus. Although CMR can identify atrial appendage thrombi, the technology can misidentify poor contrast filling of the appendage as thrombus and can overestimate the size of thrombi [158, 159]. CMR studies show low diagnostic accuracy for detection of atrial thrombi, related to limitations in spatial resolution [160]. CMR has been shown to be useful for the planning and follow-up of left atrial appendage occluder devices for stroke prophylaxis. CMR can quantify the left atrial appendage with appendage orifice diameter and appendage long-axis diameter, and can assess for device location in relation to the appendage after placement [161].

CMR can assess factors important to decisions related to cardiac resynchronization therapy (CRT) in patients with depressed left ventricular function, ventricular conduction abnormalities, and congestive heart failure. The coronary venous system can be imaged with CMR [162–164]. CCTA though provides more practical evaluation of coronary venous branch anatomy on a routine basis, and CMR cannot be used in situations where an existing device may be upgraded to a biventricular device due to MR/device potential interactions. CMR is useful in the assessment of dyssynchrony and factors predicting effect of CRT [165–167]. CMR also offers information about infarct location and morphology using delayed gadolinium contrast enhancement imaging. Myocardial infarct scar location and size have been associated with prediction of response to CRT, as an increased percent of myocardium infarcted as well as posterolateral infarct scar location lead to nonresponse (Figure 20.24) [165, 168–170]. CMR can identify anatomy limiting the ability to perform pacing and defibrillator procedures related to the coronary venous system, such as presence of a left-sided superior vena cava with a connection to an aneurysmal coronary sinus without presence of a right-sided superior vena cava (Figure 20.25).

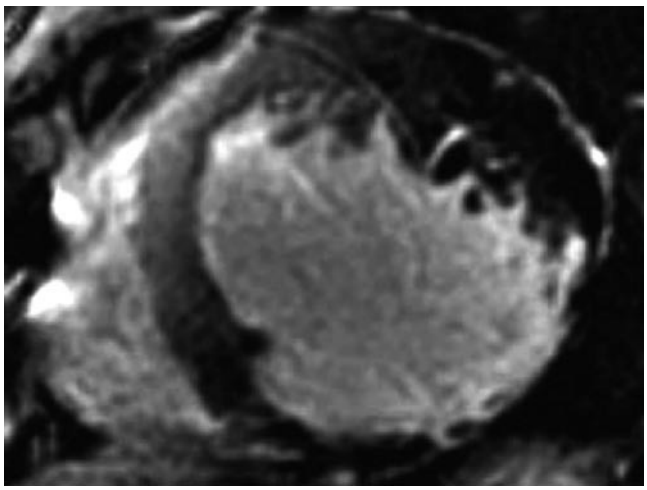

Figure 20.24. Transmural inferolateral myocardial infarction on a delayed gadolinium enhancement short axis view, which may limit left ventricular lead placement in cardiac resynchronization therapy.

Summary

Both CCTA and CMR are robust imaging modalities for characterization of cardiovascular substrates. Decisions related to performing CMR vs. CCTA require information including patient age, allergy history, clinical stability to be in the MR environment for the amount of time necessary for study given the limitations to patient monitoring, history of claustrophobia, history of ferromagnetic devices, implant or deposits, devices, renal function, cardiac rhythm and rate, strengths and limitations of other imaging modalities, and the posed clinical question. CMR provides assessment for the diagnosis and treatment of cardiovascular disease, including cardiovascular structure, function, tissue characterization, myocardial perfusion, and metabolism. Applications include the assessment of coronary artery disease, myocardial substrates, congenital heart disease, thoracic vasculature, valvular function, masses, and assessment of electrophysiologically-relevant substrates. Advances in technology will continue to lead to novel clinical and research applications.

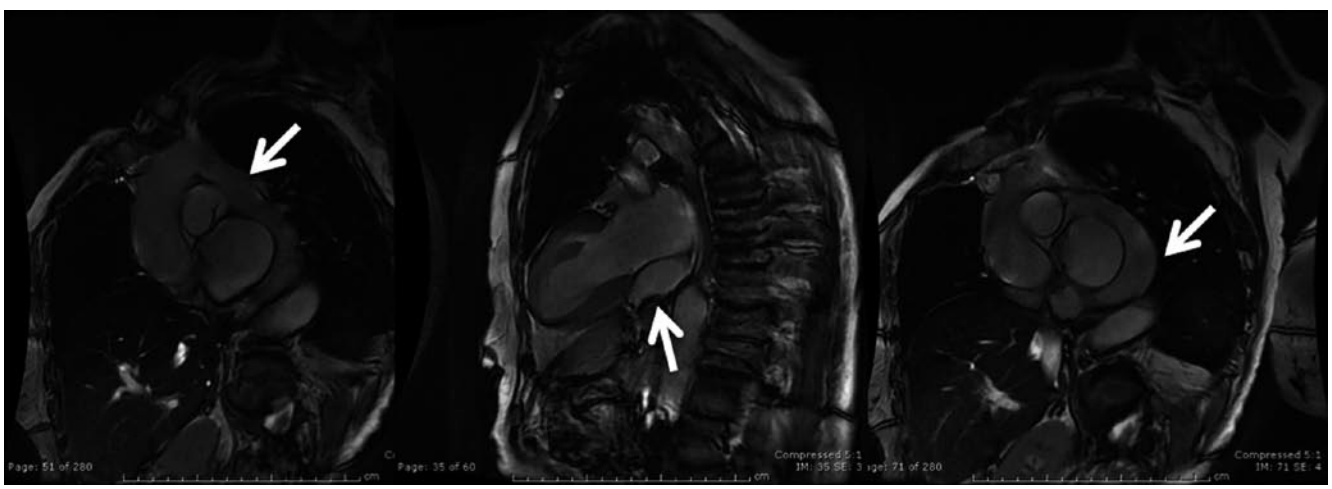

Figure 20.25. Left-sided superior vena cava connection to an aneurysmal coronary sinus. A right-sided superior vena cava was not present. This anatomy can be challenging for transvenous placement of pacemaker and implantable cardiac defibrillator leads.

References

1. Hendel RC, Patel MR, Kramer CM, et al. ACCF/ACR/SCCT/SCMR/ASNC/NASCI/SCAI/SIR 2006 appropriateness criteria for cardiac computed tomography and cardiac magnetic resonance imaging: a report of the American College of Cardiology Foundation Quality Strategic Directions Committee Appropriateness Criteria Working Group, American College of Radiology, Society of Cardiovascular Computed Tomography, Society for Cardiovascular Magnetic Resonance, American Society of Nuclear Cardiology, North American Society for Cardiac Imaging, Society for Cardiovascular Angiography and Interventions, and Society of Interventional Radiology. *J Am Coll Cardiol*. 2006;48(7):1475–1497.
2. Einstein AJ, Henzlova MJ, Rajagopalan S. Estimating risk of cancer associated with radiation exposure from 64-slice computed tomography coronary angiography. *JAMA*. 2007;298(3):317–323.
3. Ergun I, Keven K, Uruc I, et al. The safety of gadolinium in patients with stage 3 and 4 renal failure. *Nephrol Dial Transplant*. 2006;21(3):697–700.
4. Sadowski EA, Bennett LK, Chan MR, et al. Nephrogenic systemic fibrosis: risk factors and incidence estimation. *Radiology*. 2007;243(1):148–157.
5. Nayak KS, Cunningham CH, Santos JM, Pauly JM. Real-time cardiac MRI at 3 tesla. *Magn Reson Med*. 2004;51(4):655–660.
6. McGee KP, Debbins JP, Boskamp EB, Blawat L, Angelos L, King KF. Cardiac magnetic resonance parallel imaging at 3.0 Tesla: technical feasibility and advantages. *J Magn Reson Imaging*. 2004;19(3):291-297.
7. Gharib AM, Elagha A, Pettigrew RI. Cardiac magnetic resonance at high field: promises and problems. *Curr Probl Diagn Radiol*. 2008;37(2):49–56.
8. Kangarlu A, Burgess RE, Zhu H, et al. Cognitive, cardiac, and physiological safety studies in ultra high field magnetic resonance imaging. *Magn Reson Imaging*. 1999;17(10):1407–1416.
9. Schneider JE, Lanz T, Barnes H, et al. Ultra-fast and accurate assessment of cardiac function in rats using accelerated MRI at 9.4 Tesla. *Magn Reson Med*. 2008;59(3):636–641.
10. Raff GL, Gallagher MJ, O'Neill WW, Goldstein JA. Diagnostic accuracy of noninvasive coronary angiography using 64-slice spiral computed tomography. *J Am Coll Cardiol*. 2005;46(3):552–557.
11. Shellock FG. Prosthetic heart valves and annuloplasty rings: assessment of magnetic field interactions, heating, and artifacts at 1.5 Tesla. *J Cardiovasc Magn Reson*. 2001;3(4):317–324.
12. Martin ET, Coman JA, Shellock FG, Pulling CC, Fair R, Jenkins K. Magnetic resonance imaging and cardiac pacemaker safety at 1.5-Tesla. *J Am Coll Cardiol*. 2004;43(7):1315–1324.
13. Gimbel JR. Magnetic resonance imaging of implantable cardiac rhythm devices at 3.0 tesla. *Pacing Clin Electrophysiol*. 2008;31(7):795–801.
14. Shinbane JS, Colletti PM, Shellock FG. MR in patients with pacemakers and ICDs: defining the issues. *J Cardiovasc Magn Reson*. 2007;9(1):5–13.
15. Sutton R, Kanal E, Wilkoff BL, et al. Safety of magnetic resonance imaging of patients with a new Medtronic EnRhythm MRI SureScan pacing system: clinical study design. *Trials*. 2008;9:68.
16. Francis JM, Pennell DJ. Treatment of claustrophobia for cardiovascular magnetic resonance: use and effectiveness of mild sedation. *J Cardiovasc Magn Reson*. 2000;2(2):139–141.
17. Eshed I, Althoff CE, Hamm B, Hermann KG. Claustrophobia and premature termination of magnetic resonance imaging examinations. *J Magn Reson Imaging*. 2007;26(2):401–404.
18. Chia JM, Fischer SE, Wickline SA, Lorenz CH. Performance of QRS detection for cardiac magnetic resonance imaging with a novel vectorcardiographic triggering method. *J Magn Reson Imaging*. 2000;12(5):678–688.
19. Dimick RN, Hedlund LW, Herfkens RJ, Fram EK, Utz J. Optimizing electrocardiograph electrode placement for cardiac-gated magnetic resonance imaging. *Invest Radiol*. 1987;22(1):17–22.
20. Counter SA, Olofsson A, Grahn HF, Borg E. MRI acoustic noise: sound pressure and frequency analysis. *J Magn Reson Imaging*. 1997;7(3):606–611.
21. Budoff MJ, Achenbach S, Duerinckx A. Clinical utility of computed tomography and magnetic resonance techniques for noninvasive coronary angiography. *J Am Coll Cardiol*. 2003;42(11):1867–1878.
22. Plein S, Greenwood JP, Ridgway JP, Cranny G, Ball SG, Sivananthan MU. Assessment of non-ST-segment elevation acute coronary syndromes with cardiac magnetic resonance imaging. *J Am Coll Cardiol*. 2004;44(11):2173–2181.
23. Yang Q, Li K, Liu X, et al. Contrast-enhanced whole-heart coronary magnetic resonance angiography at 3.0-T: a comparative study with X-ray angiography in a single center. *J Am Coll Cardiol*. 2009;54(1):69–76.
24. Stauder NI, Klumpp B, Stauder H, et al. Assessment of coronary artery bypass grafts by magnetic resonance imaging. *Br J Radiol*. 2007;80(960):975–983.
25. Kessler W, Achenbach S, Moshage W, et al. Usefulness of respiratory gated magnetic resonance coronary angiography in assessing narrowings > or = 50% in diameter in native coronary arteries and in aortocoronary bypass conduits. *Am J Cardiol*. 1997;80(8):989–993.
26. Achenbach S, Kessler W, Moshage WE, et al. Visualization of the coronary arteries in three-dimensional reconstructions using respiratory gated magnetic resonance imaging. *Coron Artery Dis*. 1997;8(7):441–448.
27. So NM, Lam WW, Li D, Chan AK, Sanderson JE, Metreweli C. Magnetic resonance coronary angiography with 3D TrueFISP: breath-hold versus respiratory gated imaging. *Br J Radiol*. 2005;78(926):116–121.
28. Naghavi M, Libby P, Falk E, et al. From vulnerable plaque to vulnerable patient: a call for new definitions and risk assessment strategies: Part I. *Circulation*. 2003;108(14):1664–1672.
29. Naghavi M, Libby P, Falk E, et al. From vulnerable plaque to vulnerable patient: a call for new definitions and risk assessment strategies: part II. *Circulation*. 2003;108(15):1772–1778.
30. Yeon SB, Sabir A, Clouse M, et al. Delayed-enhancement cardiovascular magnetic resonance coronary artery wall imaging: comparison with multislice computed tomography and quantitative coronary angiography. *J Am Coll Cardiol*. 2007;50(5):441–447.
31. Nikolaou K, Becker CR, Muders M, et al. Multidetector-row computed tomography and magnetic resonance imaging of atherosclerotic lesions in human ex vivo coronary arteries. *Atherosclerosis*. 2004;174(2):243–252.
32. Fayad ZA, Fuster V, Nikolaou K, Becker C. Computed tomography and magnetic resonance imaging for noninvasive coronary angiography and plaque imaging: current and potential future concepts. *Circulation*. 2002;106(15):2026–2034.
33. Kim WY, Stuber M, Bornert P, Kissinger KV, Manning WJ, Botnar RM. Three-dimensional black-blood cardiac magnetic resonance coronary vessel wall imaging detects positive arterial remodeling in patients with nonsignificant coronary artery disease. *Circulation*. 2002;106(3):296–299.
34. Viles-Gonzalez JF, Poon M, Sanz J, et al. In vivo 16-slice, multidetector-row computed tomography for the assessment of experimental atherosclerosis: comparison with magnetic resonance imaging and histopathology. *Circulation*. 2004;110(11):1467–1472.
35. Post JC, van Rossum AC, Bronzwaer JG, et al. Magnetic resonance angiography of anomalous coronary arteries. A new gold standard for delineating the proximal course? *Circulation*. 1995;92(11):3163–3171.
36. Bunce NH, Rahman SL, Keegan J, Gatehouse PD, Lorenz CH, Pennell DJ. Anomalous coronary arteries: anatomic and functional assessment by coronary and perfusion cardiovascular magnetic resonance in three sisters. *J Cardiovasc Magn Reson*. 2001;3(4):361–369.
37. Sato Y, Matsumoto N, Komatsu S, et al. Anomalous origin of the right coronary artery: depiction at whole-heart coronary magnetic resonance angiography. *Int J Cardiol*. 2008;127(2):274–275.
38. Buchthal SD, den Hollander JA, Merz CN, et al. Abnormal myocardial phosphorus-31 nuclear magnetic resonance spectroscopy in women with chest pain but normal coronary angiograms. *N Engl J Med*. 2000;342(12):829–835.
39. Johnson BD, Shaw LJ, Buchthal SD, et al. Prognosis in women with myocardial ischemia in the absence of obstructive coronary disease: results from the National Institutes of Health-National Heart, Lung,

and Blood Institute-Sponsored Women's Ischemia Syndrome Evaluation (WISE). *Circulation*. 2004;109(24):2993–2999.
40. Cranney GB, Lotan CS, Dean L, Baxley W, Bouchard A, Pohost GM. Left ventricular volume measurement using cardiac axis nuclear magnetic resonance imaging. Validation by calibrated ventricular angiography. *Circulation*. 1990;82(1):154–163.
41. Rumberger JA, Behrenbeck T, Bell MR, et al. Determination of ventricular ejection fraction: a comparison of available imaging methods. The Cardiovascular Imaging Working Group. *Mayo Clin Proc*. 1997;72(9):860–870.
42. Scharhag J, Schneider G, Urhausen A, Rochette V, Kramann B, Kindermann W. Athlete's heart: right and left ventricular mass and function in male endurance athletes and untrained individuals determined by magnetic resonance imaging. *J Am Coll Cardiol*. 2002; 40(10):1856–1863.
43. Rominger MB, Bachmann GF, Pabst W, Rau WS. Right ventricular volumes and ejection fraction with fast cine MR imaging in breath-hold technique: applicability, normal values from 52 volunteers, and evaluation of 325 adult cardiac patients. *J Magn Reson Imaging*. 1999; 10(6):908–918.
44. Ioannidis JP, Trikalinos TA, Danias PG. Electrocardiogram-gated single-photon emission computed tomography versus cardiac magnetic resonance imaging for the assessment of left ventricular volumes and ejection fraction: a meta-analysis. *J Am Coll Cardiol*. 2002; 39(12):2059–2068.
45. Grothues F, Moon JC, Bellenger NG, Smith GS, Klein HU, Pennell DJ. Interstudy reproducibility of right ventricular volumes, function, and mass with cardiovascular magnetic resonance. *Am Heart J*. 2004; 147(2):218–223.
46. Petersen SE, Selvanayagam JB, Wiesmann F, et al. Left ventricular non-compaction: insights from cardiovascular magnetic resonance imaging. *J Am Coll Cardiol*. 2005;46(1):101–105.
47. Cheng AS, Pegg TJ, Karamitsos TD, et al. Cardiovascular magnetic resonance perfusion imaging at 3-tesla for the detection of coronary artery disease: a comparison with 1.5-tesla. *J Am Coll Cardiol*. 2007; 49(25):2440–2449.
48. Jahnke C, Nagel E, Gebker R, et al. Prognostic value of cardiac magnetic resonance stress tests: adenosine stress perfusion and dobutamine stress wall motion imaging. *Circulation*. 2007;115(13):1769–1776.
49. Dall'Armellina E, Morgan TM, Mandapaka S, et al. Prediction of cardiac events in patients with reduced left ventricular ejection fraction with dobutamine cardiovascular magnetic resonance assessment of wall motion score index. *J Am Coll Cardiol*. 2008;52(4):279–286.
50. Kuijpers D, Ho KY, van Dijkman PR, Vliegenthart R, Oudkerk M. Dobutamine cardiovascular magnetic resonance for the detection of myocardial ischemia with the use of myocardial tagging. *Circulation*. 2003;107(12):1592–1597.
51. Costa MA, Shoemaker S, Futamatsu H, et al. Quantitative magnetic resonance perfusion imaging detects anatomic and physiologic coronary artery disease as measured by coronary angiography and fractional flow reserve. *J Am Coll Cardiol*. 2007;50(6):514–522.
52. Nagel E, Lehmkuhl HB, Bocksch W, et al. Noninvasive diagnosis of ischemia-induced wall motion abnormalities with the use of high-dose dobutamine stress MRI: comparison with dobutamine stress echocardiography. *Circulation*. 1999;99(6):763–770.
53. Hundley WG, Morgan TM, Neagle CM, Hamilton CA, Rerkpattanapipat P, Link KM. Magnetic resonance imaging determination of cardiac prognosis. *Circulation*. 2002;106(18):2328–2333.
54. Samady H, Choi CJ, Ragosta M, Powers ER, Beller GA, Kramer CM. Electromechanical mapping identifies improvement in function and retention of contractile reserve after revascularization in ischemic cardiomyopathy. *Circulation*. 2004;110(16):2410–2416.
55. Al-Saadi N, Nagel E, Gross M, et al. Improvement of myocardial perfusion reserve early after coronary intervention: assessment with cardiac magnetic resonance imaging. *J Am Coll Cardiol*. 2000;36(5):1557–1564.
56. Blankstein R, Shturman LD, Rogers IS, et al. Adenosine-induced stress myocardial perfusion imaging using dual-source cardiac computed tomography. *J Am Coll Cardiol*. 2009;54(12):1072–1084.
57. Kim RJ, Fieno DS, Parrish TB, et al. Relationship of MRI delayed contrast enhancement to irreversible injury, infarct age, and contractile function. *Circulation*. 1999;100(19):1992–2002.
58. Gerber BL, Belge B, Legros GJ, et al. Characterization of acute and chronic myocardial infarcts by multidetector computed tomography: comparison with contrast-enhanced magnetic resonance. *Circulation*. 2006;113(6):823–833.
59. McCrohon JA, Moon JC, Prasad SK, et al. Differentiation of heart failure related to dilated cardiomyopathy and coronary artery disease using gadolinium-enhanced cardiovascular magnetic resonance. *Circulation*. 2003;108(1):54–59.
60. Schmidt A, Azevedo CF, Cheng A, et al. Infarct tissue heterogeneity by magnetic resonance imaging identifies enhanced cardiac arrhythmia susceptibility in patients with left ventricular dysfunction. *Circulation*. 2007;115(15):2006–2014.
61. Lardo AC, Cordeiro MA, Silva C, et al. Contrast-enhanced multidetector computed tomography viability imaging after myocardial infarction: characterization of myocyte death, microvascular obstruction, and chronic scar. *Circulation*. 2006;113(3):394–404.
62. Ansari M, Araoz PA, Gerard SK, et al. Comparison of late enhancement cardiovascular magnetic resonance and thallium SPECT in patients with coronary disease and left ventricular dysfunction. *J Cardiovasc Magn Reson*. 2004;6(2):549–556.
63. Ingkanisorn WP, Rhoads KL, Aletras AH, Kellman P, Arai AE. Gadolinium delayed enhancement cardiovascular magnetic resonance correlates with clinical measures of myocardial infarction. *J Am Coll Cardiol*. 2004;43(12):2253–2259.
64. Ichikawa Y, Sakuma H, Suzawa N, et al. Late gadolinium-enhanced magnetic resonance imaging in acute and chronic myocardial infarction. Improved prediction of regional myocardial contraction in the chronic state by measuring thickness of nonenhanced myocardium. *J Am Coll Cardiol*. 2005;45(6):901–909.
65. Assomull RG, Prasad SK, Lyne J, et al. Cardiovascular magnetic resonance, fibrosis, and prognosis in dilated cardiomyopathy. *J Am Coll Cardiol*. 2006;48(10):1977–1985.
66. Bello D, Shah DJ, Farah GM, et al. Gadolinium cardiovascular magnetic resonance predicts reversible myocardial dysfunction and remodeling in patients with heart failure undergoing beta-blocker therapy. *Circulation*. 2003;108(16):1945–1953.
67. Dong SJ, MacGregor JH, Crawley AP, et al. Left ventricular wall thickness and regional systolic function in patients with hypertrophic cardiomyopathy. A three-dimensional tagged magnetic resonance imaging study. *Circulation*. 1994;90(3):1200–1209.
68. Devlin AM, Moore NR, Ostman-Smith I. A comparison of MRI and echocardiography in hypertrophic cardiomyopathy. *Br J Radiol*. 1999; 72(855):258–264.
69. Schulz-Menger J, Strohm O, Waigand J, Uhlich F, Dietz R, Friedrich MG. The value of magnetic resonance imaging of the left ventricular outflow tract in patients with hypertrophic obstructive cardiomyopathy after septal artery embolization. *Circulation*. 2000;101(15):1764–1766.
70. Teraoka K, Hirano M, Ookubo H, et al. Delayed contrast enhancement of MRI in hypertrophic cardiomyopathy. *Magn Reson Imaging*. 2004;22(2):155–161.
71. Moon JC, McKenna WJ, McCrohon JA, Elliott PM, Smith GC, Pennell DJ. Toward clinical risk assessment in hypertrophic cardiomyopathy with gadolinium cardiovascular magnetic resonance. *J Am Coll Cardiol*. 2003;41(9):1561–1567.
72. Bello D, Fieno DS, Kim RJ, et al. Infarct morphology identifies patients with substrate for sustained ventricular tachycardia. *J Am Coll Cardiol*. 2005;45(7):1104–1108.
73. Matoh F, Satoh H, Shiraki K, et al. Usefulness of delayed enhancement magnetic resonance imaging to differentiate dilated phase of hypertrophic cardiomyopathy and dilated cardiomyopathy. *J Card Fail*. 2007;13(5):372–379.
74. White RD, Obuchowski NA, Gunawardena S, et al. Left ventricular outflow tract obstruction in hypertrophic cardiomyopathy: presurgical and postsurgical evaluation by computed tomography magnetic resonance imaging. *Am J Card Imaging*. 1996;10(1):1–13.

75. Casolo G, Di Cesare E, Molinari G, et al. Diagnostic work up of arrhythmogenic right ventricular cardiomyopathy by cardiovascular magnetic resonance (CMR). Consensus statement. *Radiol Med*. 2004; 108(1–2):39–55.
76. Casolo G, Di Cesare E, Molinari G, et al. Diagnostic work up of arrhythmogenic right ventricular cardiomyopathy by cardiovascular magnetic resonance (CMR). Consensus statement. *Radiol Med (Torino)*. 2004;108(1–2):39–55.
77. Maceira AM, Joshi J, Prasad SK, et al. Cardiovascular magnetic resonance in cardiac amyloidosis. *Circulation*. 2005;111(2):186–193.
78. Fattori R, Rocchi G, Celletti F, Bertaccini P, Rapezzi C, Gavelli G. Contribution of magnetic resonance imaging in the differential diagnosis of cardiac amyloidosis and symmetric hypertrophic cardiomyopathy. *Am Heart J*. 1998;136(5):824–830.
79. Nemeth MA, Muthupillai R, Wilson JM, Awasthi M, Flamm SD. Cardiac sarcoidosis detected by delayed-hyperenhancement magnetic resonance imaging. *Tex Heart Inst J*. 2004;31(1):99–102.
80. Smedema JP, Snoep G, van Kroonenburgh MP, et al. Evaluation of the accuracy of gadolinium-enhanced cardiovascular magnetic resonance in the diagnosis of cardiac sarcoidosis. *J Am Coll Cardiol*. 2005;45(10):1683–1690.
81. Tadamura E, Yamamuro M, Kubo S, et al. Effectiveness of delayed enhanced MRI for identification of cardiac sarcoidosis: comparison with radionuclide imaging. *AJR Am J Roentgenol*. 2005;185(1):110–115.
82. Shimada T, Shimada K, Sakane T, et al. Diagnosis of cardiac sarcoidosis and evaluation of the effects of steroid therapy by gadolinium-DTPA-enhanced magnetic resonance imaging. *Am J Med*. 2001;110(7):520–527.
83. Bocchi EA, Kalil R, Bacal F, et al. Magnetic resonance imaging in chronic Chagas' disease: correlation with endomyocardial biopsy findings and gallium-67 cardiac uptake. *Echocardiography*. 1998;15(3):279–288.
84. Rochitte CE, Oliveira PF, Andrade JM, et al. Myocardial delayed enhancement by magnetic resonance imaging in patients with Chagas' disease: a marker of disease severity. *J Am Coll Cardiol*. 2005;46(8): 1553–1558.
85. De Cobelli F, Pieroni M, Esposito A, et al. Delayed gadolinium-enhanced cardiac magnetic resonance in patients with chronic myocarditis presenting with heart failure or recurrent arrhythmias. *J Am Coll Cardiol*. 2006;47(8):1649–1654.
86. Laissy JP, Hyafil F, Feldman LJ, et al. Differentiating acute myocardial infarction from myocarditis: diagnostic value of early- and delayed-perfusion cardiac MR imaging. *Radiology*. 2005;237(1):75–82.
87. Grizzard JD, Ang GB. Magnetic resonance imaging of pericardial disease and cardiac masses. *Magn Reson Imaging Clin N Am*. 2007;15(4): 579–607; vi.
88. Hoffmann U, Globits S, Schima W, et al. Usefulness of magnetic resonance imaging of cardiac and paracardiac masses. *Am J Cardiol*. 2003; 92(7):890–895.
89. Brechtel K, Reddy GP, Higgins CB. Cardiac fibroma in an infant: magnetic resonance imaging characteristics. *J Cardiovasc Magn Reson*. 1999; 1(2): 159–161.
90. Kamiya H, Ohno M, Iwata H, et al. Cardiac lipoma in the interventricular septum: evaluation by computed tomography and magnetic resonance imaging. *Am Heart J*. 1990;119(5):1215–1217.
91. Salanitri JC, Pereles FS. Cardiac lipoma and lipomatous hypertrophy of the interatrial septum: cardiac magnetic resonance imaging findings. *J Comput Assist Tomogr*. 2004;28(6):852–856.
92. Matsuoka H, Hamada M, Honda T, et al. Morphologic and histologic characterization of cardiac myxomas by magnetic resonance imaging. *Angiology*. 1996;47(7):693–698.
93. Watanabe AT, Teitelbaum GP, Henderson RW, Bradley WG Jr. Magnetic resonance imaging of cardiac sarcomas. *J Thorac Imaging*. 1989;4(2): 90–92.
94. Inoko M, Iga K, Kyo K, et al. Primary cardiac angiosarcoma detected by magnetic resonance imaging but not by computed tomography. *Intern Med*. 2001;40(5):391–395.
95. Tahara T, Takase B, Yamagishi T, et al. A case report on primary cardiac non-Hodgkin's lymphoma: an approach by magnetic resonance and thallium-201 imaging. *J Cardiovasc Magn Reson*. 1999;1(2):163–167.
96. Schrem SS, Colvin SB, Weinreb JC, Glassman E, Kronzon I. Metastatic cardiac liposarcoma: diagnosis by transesophageal echocardiography and magnetic resonance imaging. *J Am Soc Echocardiogr*. 1990;3(2): 149–153.
97. Mousseaux E, Meunier P, Azancott S, Dubayle P, Gaux JC. Cardiac metastatic melanoma investigated by magnetic resonance imaging. *Magn Reson Imaging*. 1998;16(1):91–95.
98. Testempassi E, Takeuchi H, Fukuda Y, Harada J, Tada S. Cardiac metastasis of colon adenocarcinoma diagnosed by magnetic resonance imaging. *Acta Cardiol*. 1994;49(2):191–196.
99. Weinsaft JW, Kim HW, Shah DJ, et al. Detection of left ventricular thrombus by delayed-enhancement cardiovascular magnetic resonance prevalence and markers in patients with systolic dysfunction. *J Am Coll Cardiol*. 2008;52(2):148–157.
100. Gaudio C, Di Michele S, Cera M, Nguyen BL, Pannarale G, Alessandri N. Prominent crista terminalis mimicking a right atrial mixoma: cardiac magnetic resonance aspects. *Eur Rev Med Pharmacol Sci*. 2004; 8(4):165–168.
101. Patane S, Marte F, Di Bella G, Coglitore S. A large left atrial thrombus mimicking an atrial tumour. *Int J Cardiol*. 2009;133(2):e58–e59.
102. Fratz S, Hess J, Schuhbaeck A, et al. Routine clinical cardiovascular magnetic resonance in paediatric and adult congenital heart disease: patients, protocols, questions asked and contributions made. *J Cardiovasc Magn Reson*. 2008;10(1):46.
103. Nishimura T, Fujii T. Double-chambered right ventricle demonstrated by magnetic resonance imaging before cardiac catheterization–case report. *Angiology*. 1988;39(3 pt 1):259–262.
104. Rees S, Somerville J, Warnes C, et al. Comparison of magnetic resonance imaging with echocardiography and radionuclide angiography in assessing cardiac function and anatomy following Mustard's operation for transposition of the great arteries. *Am J Cardiol*. 1988; 61(15):1316–1322.
105. Theissen P, Kaemmerer H, Sechtem U, et al. Magnetic resonance imaging of cardiac function and morphology in patients with transposition of the great arteries following Mustard procedure. *Thorac Cardiovasc Surg*. 1991;39(suppl 3):221–224.
106. Greenberg SB, Faerber EN, Balsara RK. Tetralogy of Fallot: diagnostic imaging after palliative and corrective surgery. *J Thorac Imaging*. 1995;10(1):26–35.
107. Watanabe H, Hayashi JI, Sugawara M, Yagi N. Complete unilateral anomalous connection of the left pulmonary veins to the coronary sinus with unroofed coronary sinus syndrome: a case report. *Thorac Cardiovasc Surg*. 1999;47(3):193–195.
108. Arheden H, Holmqvist C, Thilen U, et al. Left-to-right cardiac shunts: comparison of measurements obtained with MR velocity mapping and with radionuclide angiography. *Radiology*. 1999;211(2): 453–458.
109. Hahm JK, Park YW, Lee JK, et al. Magnetic resonance imaging of unroofed coronary sinus: three cases. *Pediatr Cardiol*. 2000;21(4): 382–387.
110. Helbing WA, de Roos A. Clinical applications of cardiac magnetic resonance imaging after repair of tetralogy of Fallot. *Pediatr Cardiol*. 2000;21(1):70–79.
111. Ferrari VA, Scott CH, Holland GA, Axel L, Sutton MS. Ultrafast three-dimensional contrast-enhanced magnetic resonance angiography and imaging in the diagnosis of partial anomalous pulmonary venous drainage. *J Am Coll Cardiol*. 2001;37(4):1120–1128.
112. Geva T, Greil GF, Marshall AC, Landzberg M, Powell AJ. Gadolinium-enhanced 3-dimensional magnetic resonance angiography of pulmonary blood supply in patients with complex pulmonary stenosis or atresia: comparison with x-ray angiography. *Circulation*. 2002;106(4): 473–478.
113. Tulevski II, van der Wall EE, Groenink M, et al. Usefulness of magnetic resonance imaging dobutamine stress in asymptomatic and minimally symptomatic patients with decreased cardiac reserve from congenital heart disease (complete and corrected transposition of the great arteries and subpulmonic obstruction). *Am J Cardiol*. 2002;89(9):1077–1081.

114. Haramati LB, Glickstein JS, Issenberg HJ, Haramati N, Crooke GA. MR imaging and CT of vascular anomalies and connections in patients with congenital heart disease: significance in surgical planning. *Radiographics.* 2002;22(2):337–347; discussion 348–339.
115. Razavi RS, Hill DL, Muthurangu V, et al. Three-dimensional magnetic resonance imaging of congenital cardiac anomalies. *Cardiol Young*. 2003;13(5):461–465.
116. Sorensen TS, Korperich H, Greil GF, et al. Operator-independent isotropic three-dimensional magnetic resonance imaging for morphology in congenital heart disease: a validation study. *Circulation*. 2004; 110(2):163–169.
117. Durongpisitkul K, Tang NL, Soongswang J, Laohaprasitiporn D, Nanal A. Predictors of successful transcatheter closure of atrial septal defect by cardiac magnetic resonance imaging. *Pediatr Cardiol*. 2004;25(2):124–130.
118. Taylor AM, Dymarkowski S, Hamaekers P, et al. MR coronary angiography and late-enhancement myocardial MR in children who underwent arterial switch surgery for transposition of great arteries. *Radiology*. 2005;234(2):542–547.
119. Ghai A, Silversides C, Harris L, Webb GD, Siu SC, Therrien J. Left ventricular dysfunction is a risk factor for sudden cardiac death in adults late after repair of tetralogy of Fallot. *J Am Coll Cardiol*. 2002;40(9): 1675–1680.
120. Robbers-Visser D, Luijnenburg SE, van den Berg J, et al. Safety and observer variability of cardiac magnetic resonance imaging combined with low-dose dobutamine stress-testing in patients with complex congenital heart disease. Int J Cardiol Sep 8 2009 [Epub].
121. Harris MA, Johnson TR, Weinberg PM, Fogel MA. Delayed-enhancement cardiovascular magnetic resonance identifies fibrous tissue in children after surgery for congenital heart disease. *J Thorac Cardiovasc Surg*. 2007;133(3):676–681.
122. Hartnell GG. Imaging of aortic aneurysms and dissection: CT and MRI. *J Thorac Imaging*. 2001;16(1):35–46.
123. Caruthers SD, Lin SJ, Brown P, et al. Practical value of cardiac magnetic resonance imaging for clinical quantification of aortic valve stenosis: comparison with echocardiography. *Circulation*. 2003;108(18): 2236–2243.
124. Razavi R, Hill DL, Keevil SF, et al. Cardiac catheterisation guided by MRI in children and adults with congenital heart disease. *Lancet*. 2003;362(9399):1877–1882.
125. Geva T, Marshall AC. Magnetic resonance imaging-guided catheter interventions in congenital heart disease. *Circulation*. 2006;113(8): 1051–1052.
126. Lauck G, von Smekal A, Wolke S, et al. Effects of nuclear magnetic resonance imaging on cardiac pacemakers. *Pacing Clin Electrophysiol*. 1995;18(8):1549–1555.
127. Vahlhaus C, Sommer T, Lewalter T, et al. Interference with cardiac pacemakers by magnetic resonance imaging: are there irreversible changes at 0.5 Tesla? *Pacing Clin Electrophysiol*. 2001;24(4 pt 1):489–495.
128. Achenbach S, Moshage W, Diem B, Bieberle T, Schibgilla V, Bachmann K. Effects of magnetic resonance imaging on cardiac pacemakers and electrodes. *Am Heart J*. 1997;134(3):467–473.
129. Kadish AH, Bello D, Finn JP, et al. Rationale and design for the defibrillators to reduce risk by Magnetic Resonance Imaging Evaluation (DETERMINE) trial. *J Cardiovasc Electrophysiol*. 2009;20(9): 982–987.
130. Corrado D, Thiene G, Nava A, Rossi L, Pennelli N. Sudden death in young competitive athletes: clinicopathologic correlations in 22 cases. *Am J Med*. 1990;89(5):588–596.
131. Tabib A, Loire R, Chalabreysse L, et al. Circumstances of death and gross and microscopic observations in a series of 200 cases of sudden death associated with arrhythmogenic right ventricular cardiomyopathy and/or dysplasia. *Circulation*. 2003;108(24):3000–3005.
132. di Cesare E. MRI assessment of right ventricular dysplasia. *Eur Radiol*. 2003;13(6):1387–1393.
133. Bomma C, Rutberg J, Tandri H, et al. Misdiagnosis of arrhythmogenic right ventricular dysplasia/cardiomyopathy. *J Cardiovasc Electrophysiol*. 2004;15(3):300–306.
134. Bluemke DA, Krupinski EA, Ovitt T, et al. MR Imaging of arrhythmogenic right ventricular cardiomyopathy: morphologic findings and interobserver reliability. *Cardiology*. 2003;99(3):153–162.
135. Tandri H, Saranathan M, Rodriguez ER, et al. Noninvasive detection of myocardial fibrosis in arrhythmogenic right ventricular cardiomyopathy using delayed-enhancement magnetic resonance imaging. *J Am Coll Cardiol*. 2005;45(1):98–103.
136. Wilde AA, Antzelevitch C, Borggrefe M, et al. Proposed diagnostic criteria for the Brugada syndrome: consensus report. *Circulation*. 2002; 106(19):2514–2519.
137. Papavassiliu T, Wolpert C, Fluchter S, et al. Magnetic resonance imaging findings in patients with Brugada syndrome. *J Cardiovasc Electrophysiol*. 2004;15(10):1133–1138.
138. Nakagawa H, Aoyama H, Beckman KJ, et al. Relation between pulmonary vein firing and extent of left atrial-pulmonary vein connection in patients with atrial fibrillation. *Circulation*. 2004;109(12): 1523–1529.
139. Pappone C, Rosanio S, Oreto G, et al. Circumferential radiofrequency ablation of pulmonary vein ostia: a new anatomic approach for curing atrial fibrillation. *Circulation.* 2000;102(21):2619–2628.
140. Oral H, Knight BP, Ozaydin M, et al. Segmental ostial ablation to isolate the pulmonary veins during atrial fibrillation: feasibility and mechanistic insights. *Circulation*. 2002;106(10):1256–1262.
141. Hauser TH, McClennen S, Katsimaglis G, Josephson ME, Manning WJ, Yeon SB. Assessment of left atrial volume by contrast enhanced magnetic resonance angiography. *J Cardiovasc Magn Reson*. 2004; 6(2):491–497.
142. Lickfett L, Kato R, Tandri H, et al. Characterization of a new pulmonary vein variant using magnetic resonance angiography: incidence, imaging, and interventional implications of the "right top pulmonary vein". *J Cardiovasc Electrophysiol*. 2004;15(5):538–543.
143. Kato R, Lickfett L, Meininger G, et al. Pulmonary vein anatomy in patients undergoing catheter ablation of atrial fibrillation: lessons learned by use of magnetic resonance imaging. *Circulation*. 2003;107(15): 2004–2010.
144. Mansour M, Holmvang G, Sosnovik D, et al. Assessment of pulmonary vein anatomic variability by magnetic resonance imaging: implications for catheter ablation techniques for atrial fibrillation. *J Cardiovasc Electrophysiol*. 2004;15(4):387–393.
145. Nori D, Raff G, Gupta V, Gentry R, Boura J, Haines DE. Cardiac magnetic resonance imaging assessment of regional and global left atrial function before and after catheter ablation for atrial fibrillation. *J Interv Card Electrophysiol*. 2009;26:109–117.
146. Mahabadi AA, Samy B, Seneviratne SK, et al. Quantitative assessment of left atrial volume by electrocardiographic-gated contrast-enhanced multidetector computed tomography. *J Cardiovasc Comput Tomogr*. 2009;3(2):80–87.
147. Dickfeld T, Calkins H, Zviman M, et al. Anatomic stereotactic catheter ablation on three-dimensional magnetic resonance images in real time. *Circulation*. 2003;108(19):2407–2413.
148. Dickfeld T, Calkins H, Zviman M, et al. Stereotactic magnetic resonance guidance for anatomically targeted ablations of the fossa ovalis and the left atrium. *J Interv Card Electrophysiol*. 2004;11(2): 105–115.
149. Bertaglia E, Brandolino G, Zoppo F, Zerbo F, Pascotto P. Integration of three-dimensional left atrial magnetic resonance images into a real-time electroanatomic mapping system: validation of a registration method. *Pacing Clin Electrophysiol*. 2008;31(3):273–282.
150. Aleong R, Heist EK, Ruskin JN, Mansour M. Integration of intracardiac echocardiography with magnetic resonance imaging allows visualization of the esophagus during catheter ablation of atrial fibrillation. *Heart Rhythm*. 2008;5(7):1088.
151. Peters DC, Wylie JV, Hauser TH, et al. Detection of pulmonary vein and left atrial scar after catheter ablation with three-dimensional navigator-gated delayed enhancement MR imaging: initial experience. *Radiology*. 2007;243(3):690–695.
152. Oakes RS, Badger TJ, Kholmovski EG, et al. Detection and quantification of left atrial structural remodeling with delayed-enhancement

magnetic resonance imaging in patients with atrial fibrillation. *Circulation*. 2009;119(13):1758–1767.
153. Lardo AC, McVeigh ER, Jumrussirikul P, et al. Visualization and temporal/spatial characterization of cardiac radiofrequency ablation lesions using magnetic resonance imaging. *Circulation*. 2000; 102(6): 698–705.
154. Robbins IM, Colvin EV, Doyle TP, et al. Pulmonary vein stenosis after catheter ablation of atrial fibrillation. *Circulation*. 1998;98(17): 1769–1775.
155. Taylor GW, Kay GN, Zheng X, Bishop S, Ideker RE. Pathological effects of extensive radiofrequency energy applications in the pulmonary veins in dogs. *Circulation*. 2000;101(14):1736–1742.
156. Dill T, Neumann T, Ekinci O, et al. Pulmonary vein diameter reduction after radiofrequency catheter ablation for paroxysmal atrial fibrillation evaluated by contrast-enhanced three-dimensional magnetic resonance imaging. *Circulation*. 2003;107(6):845–850.
157. Arentz T, Jander N, von Rosenthal J, et al. Incidence of pulmonary vein stenosis 2 years after radiofrequency catheter ablation of refractory atrial fibrillation. *Eur Heart J*. 2003;24(10):963–969.
158. Ohyama H, Hosomi N, Takahashi T, et al. Comparison of magnetic resonance imaging and transesophageal echocardiography in detection of thrombus in the left atrial appendage. *Stroke*. 2003;34(10): 2436–2439.
159. Ohyama H, Mizushige K, Hosomi N. Magnetic resonance imaging of left atrial thrombus. *Heart*. 2002;88(3):233.
160. Mohrs OK, Nowak B, Petersen SE, et al. Thrombus detection in the left atrial appendage using contrast-enhanced MRI: a pilot study. *AJR Am J Roentgenol*. 2006;186(1):198–205.
161. Mohrs OK, Schraeder R, Petersen SE, et al. Percutaneous left atrial appendage transcatheter occlusion (PLAATO): planning and follow-up using contrast-enhanced MRI. *AJR Am J Roentgenol*. 2006;186(2): 361–364.
162. Younger JF, Plein S, Crean A, Ball SG, Greenwood JP. Visualization of coronary venous anatomy by cardiovascular magnetic resonance. *J Cardiovasc Magn Reson*. 2009;11(1):26.
163. Rasche V, Binner L, Cavagna F, et al. Whole-heart coronary vein imaging: a comparison between non-contrast-agent- and contrast-agent-enhanced visualization of the coronary venous system. *Magn Reson Med*. 2007;57(6):1019–1026.
164. Nezafat R, Han Y, Peters DC, et al. Coronary magnetic resonance vein imaging: imaging contrast, sequence, and timing. *Magn Reson Med*. 2007;58(6):1196–1206.
165. Bilchick KC, Dimaano V, Wu KC, et al. Cardiac magnetic resonance assessment of dyssynchrony and myocardial scar predicts function class improvement following cardiac resynchronization therapy. *JACC Cardiovasc Imaging*. 2008;1(5):561–568.
166. Chalil S, Stegemann B, Muhyaldeen S, et al. Intraventricular dyssynchrony predicts mortality and morbidity after cardiac resynchronization therapy: a study using cardiovascular magnetic resonance tissue synchronization imaging. *J Am Coll Cardiol*. 2007;50(3):243–252.
167. England B, Lee A, Tran T, et al. Magnetic resonance criteria for future trials of cardiac resynchronization therapy. *J Cardiovasc Magn Reson*. 2005;7(5):827–834.
168. Bleeker GB, Kaandorp TA, Lamb HJ, et al. Effect of posterolateral scar tissue on clinical and echocardiographic improvement after cardiac resynchronization therapy. *Circulation*. 2006;113(7):969–976.
169. Chalil S, Stegemann B, Muhyaldeen SA, et al. Effect of posterolateral left ventricular scar on mortality and morbidity following cardiac resynchronization therapy. *Pacing Clin Electrophysiol*. 2007;30(10): 1201–1209.
170. White JA, Yee R, Yuan X, et al. Delayed enhancement magnetic resonance imaging predicts response to cardiac resynchronization therapy in patients with intraventricular dyssynchrony. *J Am Coll Cardiol*. 2006;48(10):1953–1960.

21

Computed Tomographic Angiography in the Assessment of Congenital Heart Disease

Christopher P. Learn and Stephen C. Cook

Introduction

The adult congenital heart disease (CHD) population is becoming increasingly prevalent. Approximately 6 per 1,000 live births in the United States are affected by complex CHD, and as many as 75 per 1,000 live births have simple lesions such as ventricular septal defects [1]. Improved medical and surgical care has decreased early and late mortality resulting in the increased number of patients surviving well into adulthood with both simple and complex forms of CHD. As a result of these improvements, the number of adult survivors with CHD surpassed the number of pediatric patients with CHD in the year 2000. Currently, it is estimated there are approximately 800,000 adults with CHD in the United States [2].

Given the wide diversity of congenital lesions, the variety of surgical palliative techniques developed, subsequent modifications, and innovative transcatheter techniques, optimal noninvasive imaging is essential to the assessment of this complex patient population. Finally, as a result of rapid improvements, evaluation of the optimal noninvasive imaging tool has become an active and ongoing field of study in this expanding patient population.

Prior to the introduction of cardiovascular magnetic resonance (CMR) imaging and cardiovascular computed tomographic angiography (CCTA), transthoracic echocardiography (TTE) and cardiac catheterization were the mainstay imaging modalities in the diagnosis and evaluation of the patient with complex CHD [3]. Advances in TTE imaging and its widespread availability provided physicians with a technique to supplant cardiac catheterization as the predominant imaging modality for CHD in children. In the hands of a skilled technologist, TTE provides noninvasive information regarding complex CHD while avoiding radiation and intravenous contrast exposure associated with serial cardiac catheterizations.

Both TTE and catheterization have their disadvantages with regards to imaging the adult with CHD. Anatomic windows for ultrasound are often limited by chest wall deformities (e.g., pectus deformities, spinal abnormalities) and postsurgical changes. Increased chest wall diameter due to somatic growth or obesity requires lower ultrasound frequencies to achieve adequate penetration, at the cost of decreased spatial resolution, precluding complete assessment of the adolescent or young adult with simple or complex CHD [4]. Transesophageal echocardiography may avoid some of these pitfalls at the expense of perceived invasiveness by the patient, limited assessment of anterior structures (e.g., conduits), associated sedation risks, and the need for increased operator expertise.

As a result of advances in alternative imaging modalities (e.g., CMR and CCTA), the number of diagnostic cardiac catheterization cases has decreased dramatically. However, the decrease in diagnostic procedures has now been exceeded by the number of catheter-based closure devices. These are performed routinely in this patient population for a number of late-onset complications associated with a variety of defects [5]. Despite the evolution in transcatheter technology, this procedure carries the inherent risks of trauma to vascular structures [6] and sedation or general anesthesia often required for prolonged procedural times. Of note, physicians performing these technically challenging procedures should be mindful of radiation exposure as fluoroscopy time alone is a poor predictor of radiation-induced skin injuries [7].

Magnetic resonance imaging allows for a three-dimensional assessment of the heart as well as delineation of extra-cardiac structures without ionizing radiation. The benefits of CMR in the evaluation of the adult CHD patient are diverse including quantification of both left and right ventricular size and systolic function, shunt quantification, evaluation of valvular disease; and assessment of myocardial perfusion and fibrosis [8]. Despite these numerous applications and advantages, a complete examination, including acquisition times, for the young adult with complex CHD is often prolonged and may not be tolerated by a patient with claustrophobia, heart failure, cyanosis, or orthopnea. Further, signal void artifact often associated with prior transcatheter interventions may preclude a complete CMR examination [9]. Finally, CMR is contraindicated

in patients with implantable cardioverter defibrillators and/or pacemakers.

Concurrently, there have been numerous advances (e.g., reduced scan times; higher spatial/temporal resolution) in the field of cardiovascular CT [10]. Consequently, CCTA provides a suitable alternative to CMR that offers an accurate assessment of intra- and extra-cardiac anatomy of patients with both simple and complex CHD while overcoming the limitations of CMR. Further CCTA allows for accurate quantification of volume and function comparable to CMR [11]. In contrast to CMR, acquisition time is brief. Therefore, this technique should be strongly considered in patients with poor echocardiographic windows and contraindications to CMR.

Unfortunately, CCTA is not without disadvantages. This technique still requires exposure to ionizing radiation as well as nephrotoxic contrast. Importantly, patients with CHD have many potential sources of ongoing radiation exposure that often begin in infancy and continue throughout life. Serial chest X-rays, nuclear scans, CT scans, and diagnostic/therapeutic catheterizations are performed as a result of prior corrective or palliative interventions [12]. Therefore, physicians who perform and/or refer patients for this procedure should be familiar with radiation exposure and techniques available to reduce radiation exposure at the time of CCTA examination.

CT Imaging Protocol

Foremost in performing an appropriately executed CCTA examination in the adolescent or young adult with simple or complex CHD is methodical pre-study planning. Repeating a study due to suboptimal technique exposes the patient to unnecessary risk (e.g., radiation exposure, contrast exposure). Collaboration with a specialist in adult CHD may avoid many potential pitfalls. Prior to the initiation of a study, the diagnostic indication, the original anatomic defects, operative course as well as postsurgical anatomic changes should be completely understood. With this knowledge, the appropriate extent of anatomic coverage and timing of contrast administration will provide the information necessary from the images acquired at the time of the examination.

Cardiac Anatomy: A Sequential Approach

CHD is highly variable in its complexity and anatomic arrangements. Attempts to adequately describe complicated lesions have led to a nuanced taxonomy of eponyms, synonymous, and near-synonymous terms. For instance, even the basic terms of "left" and "right" can lead to confusion. By convention, they refer to morphologic characteristics of a cardiac chamber rather than position within the chest.

To lessen clinical confusion and facilitate academic study, various systematic schemata have developed. Van Praagh's "segmental approach" [13] describes each of the three main segments of cardiac anatomy – the atria, ventricles, and great arteries – in series. This is analogous to the construction of a home, where each segment builds off the prior with the atria serving as the foundation. The sequence is often abbreviated by a sequence of three letters (X,Y,Z) where the first letter describes visceral-atrial situs, the second ventricular looping, and the third the relationships of the great arteries. This analysis is often recommended, particularly for the evaluation of those with complex CHD as it provides a systematic approach that can be applied to each patient.

Atrial Situs

Atrial situs usually follows the positioning of the unpaired abdominal viscera. For instance, the normal arrangement is situs *solitus* (S,y,z) where the morphologic right atrium, systemic venous return, and liver are on the right side of the patient. The morphologic left atrium, pulmonary venous return, stomach, and spleen are on the left side. The morphology of the atrial appendage provides important clues to determine right or left-sidedness (Figure 21.1).

The mirror image of this arrangement–with the morphologic right atrium and liver on the patient's left and the morphologic left atrium, stomach, and spleen on the patient's right– is situs *inversus*. (I,y,z) Cases of both atria having characteristics of either the left or right atrium (atrial isomerism) are described as *ambiguous* (A,y,z).

Bronchial morphology may further assist in determining atrial situs as there is good correlation between atrial and bronchial morphology. The first branch of the right mainstem bronchus courses above (eparterial) the right pulmonary artery. Alternatively, the first branch of the left mainstem bronchus courses below (hyparterial) the left pulmonary artery (Figure 21.2). This bronchial configuration would indirectly suggest atrial situs.

Ventricular Looping

Typically, the morphologic right ventricle is to the right and anterior of the left ventricle. This arrangement is called "*D-loop*" (x,D,z) and results from rightward or dextro-looping of the primitive heart early in fetal development. If the primitive heart developed in a leftward (levo-) fashion, it can result in the left ventricle anterior and rightward of the right ventricle or "*L-loop*"(x,L,z).

Features that often distinguish the morphologic right ventricle include the presence of coarse trabeculae and a prominent moderator band, tricuspid valve attachments to the septum and free wall, and absence of fibrous continuity between the tricuspid valve and semilunar valve. In contrast, the morphologic left ventricle has a smooth septal surface and fibrous continuity between the mitral and semilunar valves.

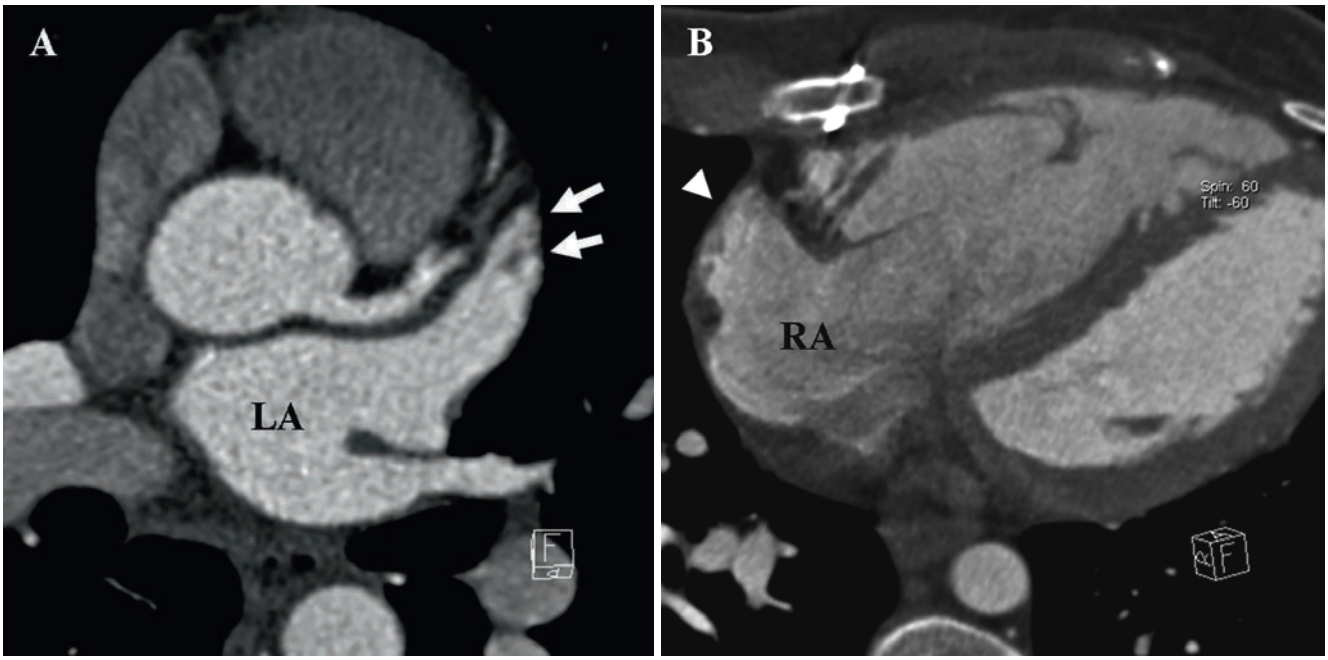

Figure 21.1. Oblique axial view (**a**) demonstrates the features of a morphologic left atrium (LA), including its finger-like appearance and pectinate muscles (*arrows*). In contrast, the oblique coronal view (**b**) demonstrates a broad-based triangular appendage (*arrowhead*) suggestive of a right atrial appendage. *RA* right atrium.

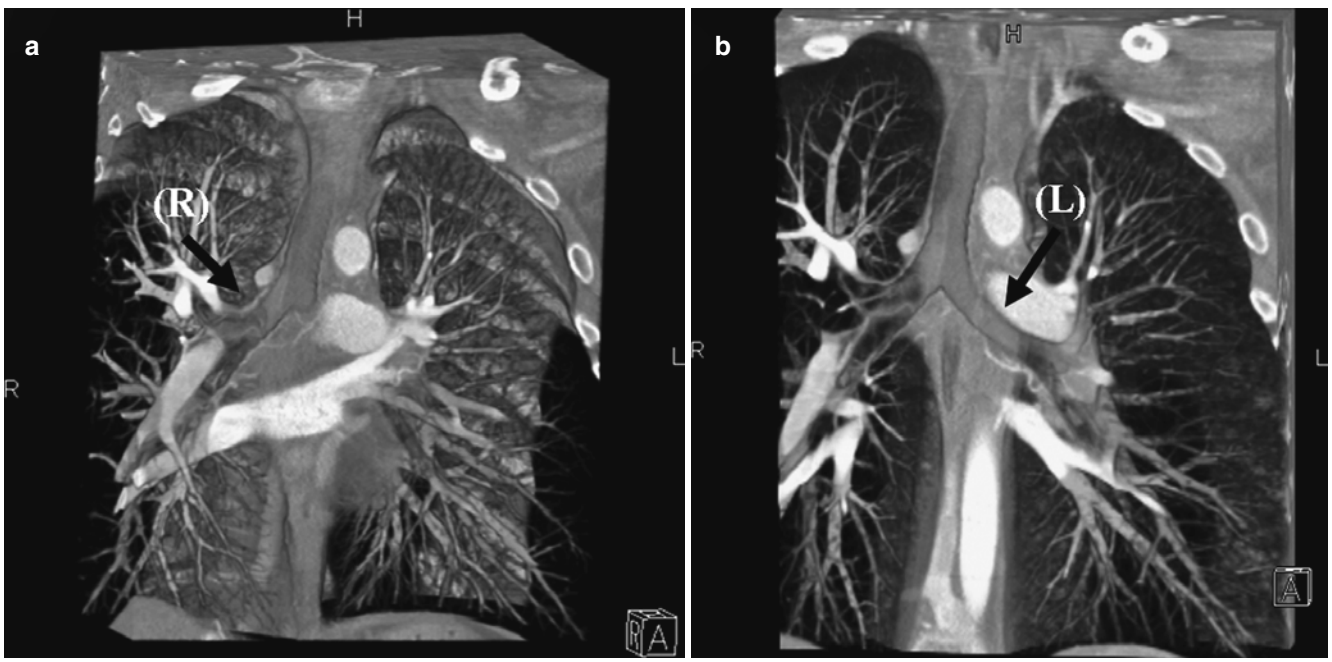

Figure 21.2. Volume-rendered three-dimensional reconstructions (**a, b**) demonstrating pulmonary situs solitus. The pulmonary artery of the morphologic right lung travels anteriorly to the bronchus (R; *arrow*). The pulmonary artery of the morphologic left lung travels over its main bronchus (L; *arrow*) and posterior to the upper lobe bronchus.

Semilunar Valve Relationships

Van Praagh described six potential relationships of the aortic and pulmonary valves. Each variant is defined by the position of the aortic valve relative to the pulmonary valve. In the normal relationship, *solitus* (x,y,S), the aortic valve is rightward and posterior of the pulmonary valve. If the aortic valve is leftward and posterior, it is termed *inversus* (x,y,I). When the aortic valve is rightward and anterior, it is *D-malposition* (x,y,D), and when the aortic valve is leftward and anterior, it is *L-malposition* (x,y,L). Uncommonly, the aortic valve can lie directly *anterior* (x,y,A) or directly *posterior* (x,y,P) of the pulmonary valve.

Concordant/Discordant Relationships

Anderson et al. [14] proposed an alternate means of describing complicated CHD. Their approach places greater emphasis on the connections between the different segments.

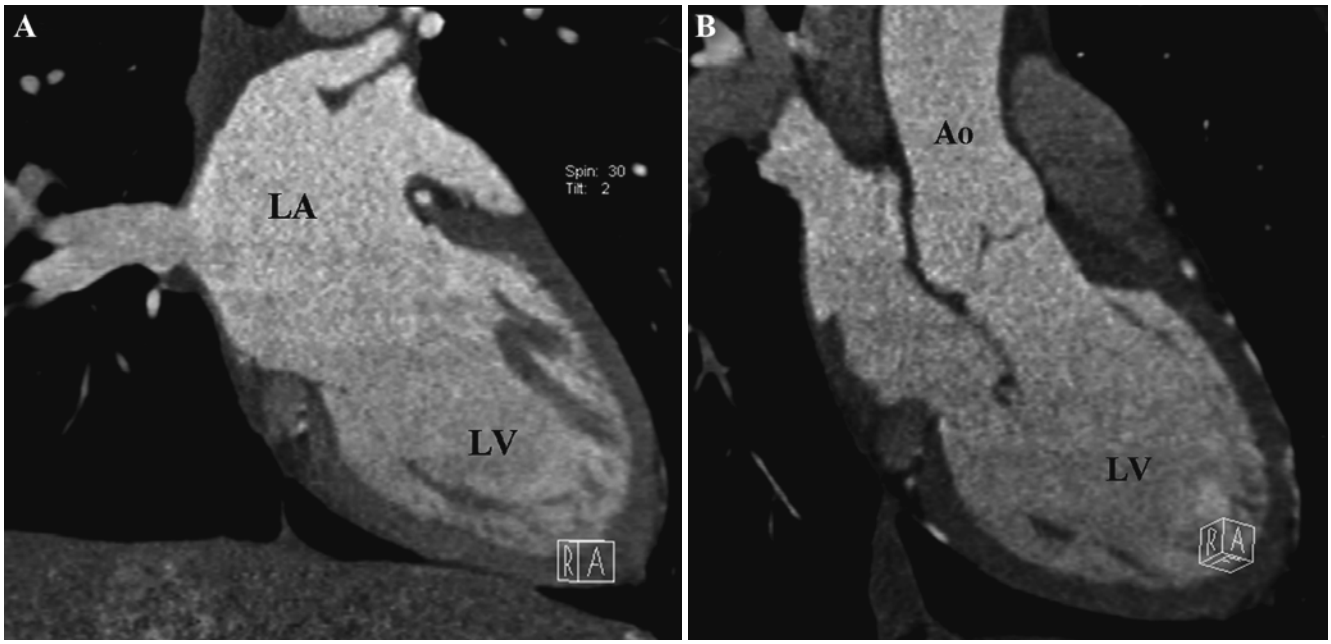

Figure 21.3. Atrioventricular and ventriculoarterial concordance. The oblique coronal view (**a**) demonstrates atrioventricular concordance between the left atrium (LA) and left ventricle (LV). The oblique coronal view (**b**) demonstrates ventriculoarterial concordance between the LV and the aorta (Ao).

Segments can be *concordant* (normally related; Figure 21.3) or *discordant*. For instance, if the right atrium connects normally via a tricuspid valve to the right ventricle, there is *atrioventricular concordance*. If the right ventricle then gives rise to the pulmonary artery, there is *ventriculoarterial concordance*. In d-transposition of the great arteries (d-TGA), where the right ventricle gives rise to the aorta, there is *ventriculoarterial discordance*. Additionally, atrioventricular connections can also be *absent* (e.g., tricuspid atresia) or *double-committed* (connected to both ventricles equally or to one more than the other).

Venous Abnormalities

Systemic Venous Abnormalities

Systemic venous anomalies include bilateral superior vena cavae (presence/absence of a bridging innominate vein), a unilateral left superior vena cava (SVC) (communicating with an enlarged coronary sinus), and interrupted inferior vena cava (often with continuation via the azygous or hemiazygous veins).

Pulmonary Venous Abnormalities

Abnormal pulmonary venous return is described as being total or partial. In total anomalous venous return (TAPVR), all four pulmonary veins drain anomalously. If at least one of the veins drains inappropriately, it is described as partial (PAPVR). Abnormal pulmonary venous return is often associated with a sinus venosus atrial septal defect (ASD).

There are four variants of TAPVR: supracardiac, cardiac, infracardiac and mixed. *Supracardiac*-type is the most common with the pulmonary veins connecting to the systemic venous circulation via the SVC, innominate vein, or azygos vein. *Cardiac*-type describes the pulmonary veins draining to the coronary sinus or similar vein to the right atrium. In patients with the *infracardiac*-type, the pulmonary veins drain into the portal or hepatic veins. *Mixed* is any combination of the above venous abnormalities.

If any of these is associated with any degree of obstruction, particularly common in the infracardiac-type, this can lead to severe pulmonary congestion in infancy. Therefore, surgical palliation is often required in the newborn period. Late-onset complications following surgical correction include stenosis at the site of reanastomosis of one or more of the pulmonary veins.

The utility of CCTA has been well described in the evaluation of the pulmonary veins before and after radiofrequency ablation [15]. Therefore, this technique is ideally suited to evaluate the pulmonary venous anatomy in the adult CHD patient with native disease (PAPVR with sinus venosus atrial septal defect) as well as the patient who presents with increasing dyspnea to determine the presence/absence of stenosis after prior palliative repair (Figure 21.4).

Cor Triatriatum

Cor triatriatum occurs when the common pulmonary venous chamber is partially separated by a membrane from the left atrium. This rare defect is thought to occur as a result of failure of the common pulmonary vein to become incorporated into the left atrium. This "pulmonary venous chamber" may drain to the left atrium indirectly via an anomalous channel [16]. Commonly associated defects include ASD or patent foramen ovale, sinus venosus, ASD, PAPVR, and persistent left SVC. Without surgical correction, a highly restrictive

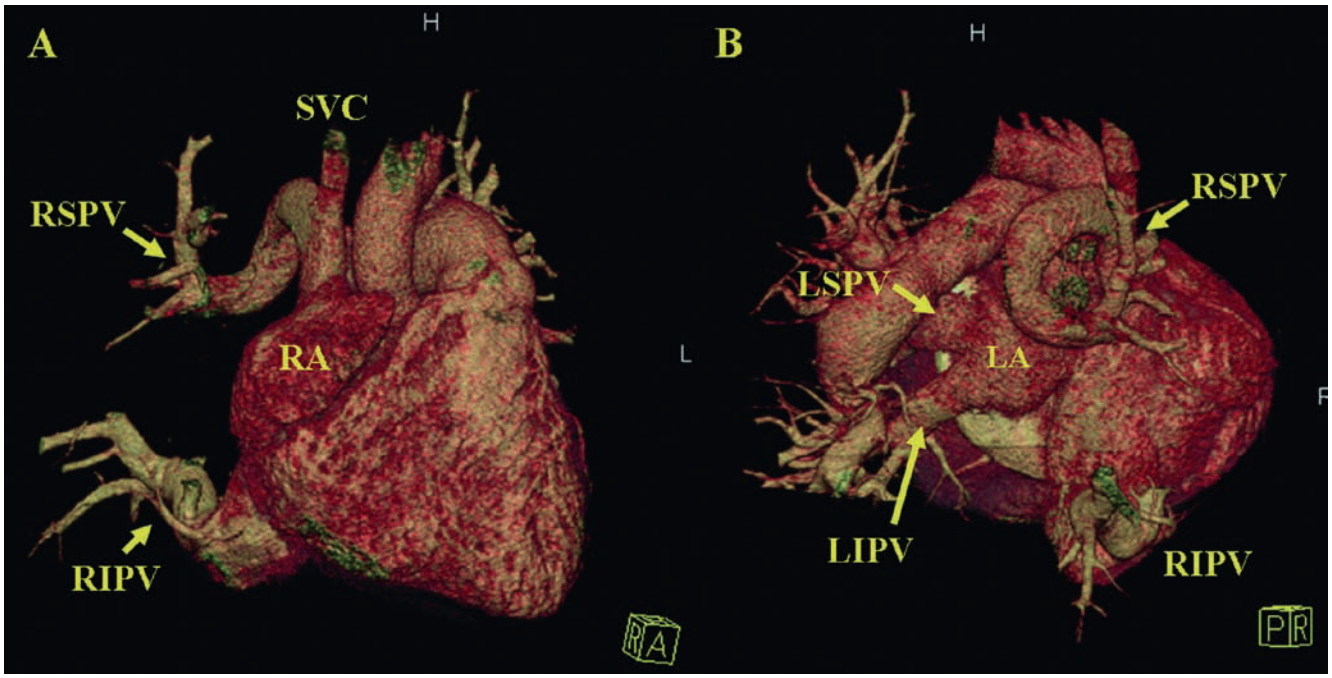

Figure 21.4. Volume rendered three dimensional reconstructions demonstrate anomalous return of the right superior pulmonary vein (RSPV) to the superior vena cava (SVC) and right inferior pulmonary vein (RIPV) to the inferior vena cava (**a**). Note the normal return of the left pulmonary veins to the left atrium (**b**). *LA* left atrium; *LIPV* left inferior pulmonary vein; *LSPV* left superior pulmonary vein; *RA* right atrium.

communication between the pulmonary venous confluence and the left atrium is associated with high mortality during infancy. In contrast, the patient with mild or no obstruction may not present until later in adult life.

Hence, improvements in spatial and temporal resolution of CCTA provide the capability of defining not only the anatomy of the atria and the pulmonary veins but also a thin membrane to establish the diagnosis of cor triatriatum. Further, this technique is also appropriate for the postoperative assessment in the patient with co-existing lesions as there are no reports of recurrence of a left atrial membrane following resection.

Congenital Heart Defects: Simple Lesions

Atrial Septal Defects

Defects in atrial septation are among the most common congenital heart defects. They are classified by their anatomic location. The two most common variants, secundum and primum, are true defects within the atrial septum. The sinus venous defect is not a true defect in the atrial septum but rather a deficiency in the wall separating the pulmonary veins from the right atrium. This results in a left-to-right shunt similar to the primum and secundum ASDs. The coronary sinus ASD shares a similar aberration and physiologic outcome. Here, there is a deficiency in the wall separating the coronary sinus from the left atrium (Figure 21.5).

Of these, ostium secundum defects or *secundum ASDs*, are the most common variant. Ostium primum defects or *primum ASDs* are the next most common. As the primum portion of the atrial septum is contiguous with the

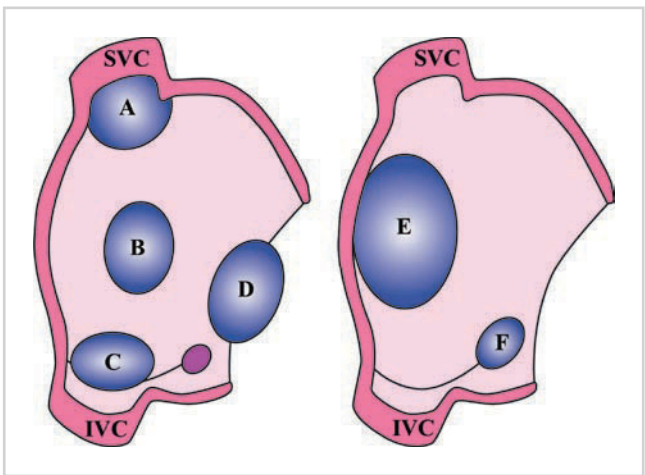

Figure 21.5. Atrial septal defects: *A* indicates the superior sinus venosus atrial septal defect (ASD); *B*, secundum ASD; *C*, inferior sinus venosus ASD; *D*, ostium primum ASD or partial atrioventricular septal defect; *E*, secundum ASD without posterior septal rim; and *F*, coronary sinus ASD. *SVC* superior vena cava; *IVC* inferior vena cava (reprinted with permission of Wolters Kluwer from Webb and Gatzoulis [17]).

atrioventricular valves and intraventricular septum, they are often classified within the spectrum of atrioventricular septal defects (AVSD or atrioventricular canal defects).

Sinus venous ASDs are rare and account for approximately 5–10% of all ASDs [17]. They most often occur at the junction of the SVC and the right atrium. A defect in this area creates a connection between the right upper pulmonary veins and the right atrium. Less commonly, they can involve the junction of the IVC and the right lower pulmonary veins. *Coronary sinus defects* are often described as an "unroofing" of the coronary sinus, allowing drainage from the coronary sinus to the left atrium. Technically, these defects do not involve the atrial septum but share

similar physiologic implications to anatomic defects of the atrial septum.

The clinical implications of ASDs are influenced by the degree of shunting that occurs at the level of the defect. The magnitude of shunting is further determined by the size of the defect and the difference in pressure between the left and right atria. In most patients, left atrial pressure exceeds right atrial pressure, resulting in shunting of oxygen-rich pulmonary venous return to the right atrium. These patients may not develop symptoms of volume loading of the right heart (e.g., dyspnea; exercise intolerance) until adolescence or young adulthood.

Indications for ASD closure should include right atrial and ventricular enlargement in the setting of an ASD more than 10 mm in diameter or a ratio of pulmonary to systemic blood flow (Qp:Qs) of greater than 1.5:1 [17]. Of note, ASDs can allow systemic venous thrombi to bypass the pulmonary circulatory bed and reach this systemic circulation under certain conditions. As stated previously, left atrial pressure typically exceeds right atrial pressure, so flow across the defect is typically left-to-right. Right atrial pressure can transiently exceed left atrial pressure during changes in intrathoracic pressure such as Valsalva maneuvers. This type of environment can ultimately set the stage for a paradoxical embolus. Therefore, this should be considered as an indication for closure.

Rarely, an untreated persistent left-to-right atrial shunt can lead to increased pulmonary vascular resistance. In the setting of pulmonary hypertension, right atrial pressure can exceed left atrial pressure, resulting in the shunting of oxygen-poor systemic venous return to the left atrium. Here, a complete evaluation of the defect should include not only a noninvasive assessment of the anatomy of the defect but also a hemodynamic cardiac catheterization prior to surgical and/or transcatheter closure to determine if the defect can be safely closed.

Prior to the advent of atrial septal occlusion devices performed in the cardiac catheterization laboratory [18], the treatment of choice had largely been surgical management. Currently, secundum defects can now be managed with fewer complications and shorter inpatient hospital stay compared to conventional surgical management [19]. The success of percutaneous closure is determined by the presence of adequate rims of atrial tissue to secure the device.

Again, the improved spatial resolution of multidetector CT provides an enhanced assessment of the adequacy of atrial rims than conventional electron beam CT [20]. Complete CT assessment prior to percutaneous closure of a secundum ASD should include an assessment of the pulmonary venous anatomy, dimensions of the defect, and description of the presence/absence of the superior, inferior and retroaortic rims (Figure 21.6). Assessment of a device postimplantation, particularly in the symptomatic patient, should include the orientation of the device within the defect, impingement on surrounding structures such as the atrioventricular or semilunar valves, pulmonary veins, and pericardial effusion [21].

Due to the association of anomalous pulmonary venous drainage with the sinus venosus ASD, this defect cannot be addressed percutaneously. Similarly, the primum ASD lies in close proximity to the atrioventricular valves. Therefore, this defect is not amenable to percutaneous closure. As the primum defect is often classified within the spectrum of AVSD, a cleft mitral valve is commonly encountered with this defect. Following surgical repair, patients should be monitored for residual shunts and stenosis and/or regurgitation of the atrioventricular valves.

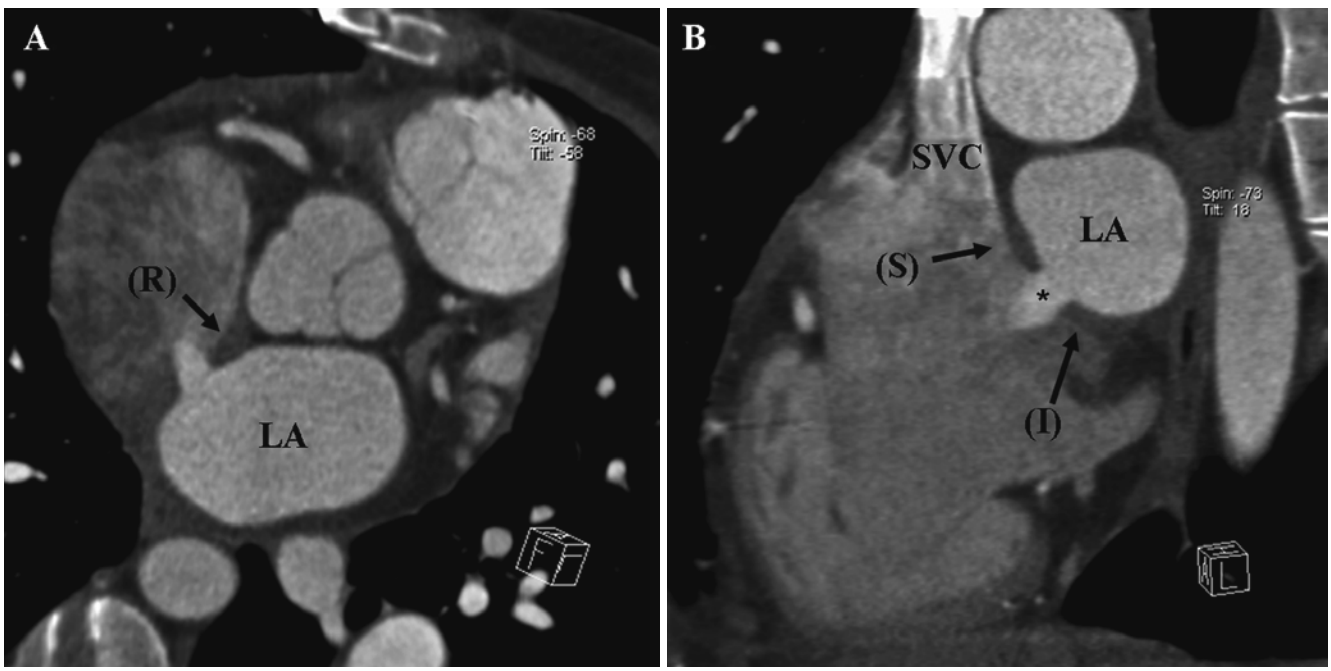

Figure 21.6. Oblique axial (**a**) and sagittal (**b**) views demonstrate the anatomy of the atrial septal defect as well as anatomic information regarding surrounding rims that are often helpful in the pre-interventional assessment to determine suitability for transcatheter closure. (*I*) inferior rim; *LA* left atrium; (*R*) retroaortic rim; (*S*) superior rim; *SVC* superior vena cava.

Atrial Isomerism

Atrial isomerism is defined as a duplication of the structures typical of either the left or right side of the body. This is often reported in patients with heterotaxy syndrome. This syndrome is associated with intestinal abnormalities, poorly functioning or absent splenic tissue, and complex CHD [22].

In right atrial isomerism, both atria have the broad-based atrial appendages typical of the right atrium and receive systemic venous return (SVC, inferior vena cava and coronary sinus). This is typically associated bilateral trilobed lungs, a large liver spanning the abdomen, and asplenia.

Left atrial isomerism is characterized by both atria having narrow based atrial appendages and receiving the ipsilateral pulmonary veins. This is associated with bilateral bilobed lungs, interruption of the inferior vena cava, a midline liver, and polysplenia.

Ventricular Septal Defects

As with ASDs, defects in the ventricular septum are among the most common CHD lesions. They too are described by their position within the septum. The ventricular septum is divided into four regions: *inlet, membranous, outlet* and *muscular.* The *inlet* septum is the region of the septum that divides the annuli of the mitral and tricuspid valves. The *muscular* septum extends from the inlet towards the apex of the heart. Defects in the *perimembranous* septum extend from under the aortic valve towards the septal leaflet of the tricuspid valve. *Outlet* ventricular septal defects (VSDs) are in the area of the septum adjacent to both the aortic and pulmonary valves.

The presentation and management of the patient with VSD is often dependent on the size and location of the defect. Smaller defects located in the muscular septum may undergo spontaneous closure. Occasionally, aneurysmal tissue from the tricuspid valve may result in spontaneous VSD closure (perimembranous-type). Small defects that restrict the volume of blood flow, and pressure between the left and right ventricles may be of little hemodynamic consequence. However, larger nonrestrictive defects expose the right ventricle and pulmonary artery bed to the systemic pressure of the left ventricle. Unrepaired, these patients will develop pulmonary vascular changes similar to those with pulmonary hypertension within the first or second year of life (e.g., medial hypertrophy, vascular endothelial changes). Ultimately, there is a decrease in the degree in left-to-right shunting and reversal of shunt (right-to-left) consistent with Eisenmenger physiology. Therefore, this group benefits from timely surgical referral to avoid the progressive and irreversible changes of pulmonary vascular disease. Other considerations for surgical referral include interference with atrioventricular or semilunar valve function despite restrictive physiology at the level of the defect.

Ongoing advances in transcatheter techniques now provide an alternative method to address defects located in the perimembranous and muscular portion of the interventricular septum [23, 24]. This technique has been demonstrated to be safe and effective when performed in experienced centers.

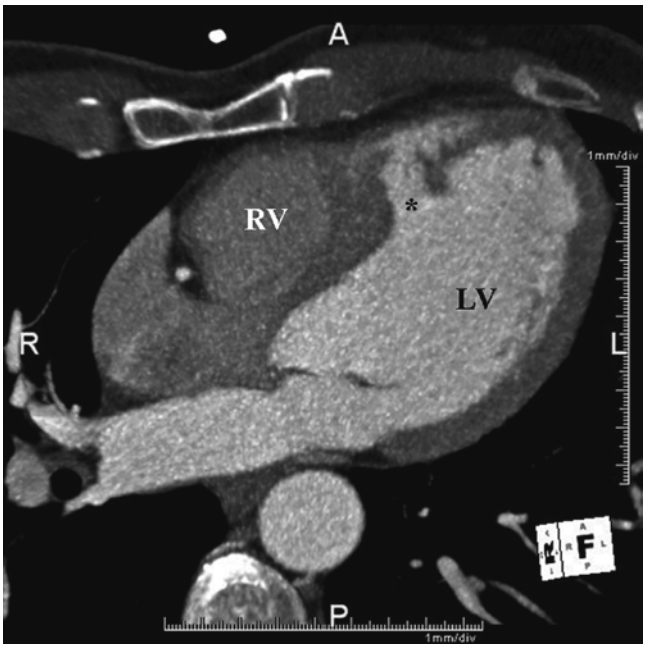

Figure 21.7. An oblique axial image demonstrates a restrictive, muscular ventricular septal defect (VSD; *asterisk*) as a result of a prominent moderator band present in the body of the right ventricle (RV) precluding a significant left-to-right shunt. *LV* left ventricle.

However, the most significant late-onset complication in the perimembranous closure group includes complete atrioventricular block necessitating careful evaluation during follow-up evaluation.

Although the natural history of VSD is excellent, it is often dependent on the size and location of the defect, associated defects, prior surgical repair, timing of surgical repair, and presence of pulmonary vascular disease. Following either surgical or percutaneous device closure, CCTA has utility in assessing the adequacy of closure via the detection of residual defects (Figure 21.7). It may also be useful in the pre-catheterization assessment to evaluate defect size as well as relationship of the defect to surrounding anatomic structures to determine suitability for percutaneous closure.

Atrioventricular Septal Defects

An atrioventricular septal defect (AVSD) is defined by a defect that involves the primum portion of the atrial septum, a common atrioventricular valve, and the inlet portion of the ventricular septum [25]. This defect commonly occurs in patients with Down syndrome.

There are many terms used to further classify the various anatomic features and "balance" of the ventricles associated with the AVSD. A *complete atrioventricular canal defect* (CAVC) has a single defect involving both the atrial and ventricular septum and a common AV valve. An *incomplete AV canal defect* lacks either the atrial or ventricular component. A *balanced* AVSD occurs when the left and right ventricles are of equal size. Here, the common AV valve is symmetrically located over both ventricles. An *unbalanced* AVSD occurs when one of the ventricles is significantly smaller than the other. As a result of the common AV valve, the aorta has

"sprung forward" resulting in a "gooseneck" deformity of the left ventricular outflow tract. This may have clinical implications at the time of surgical repair as abnormal attachments from the common AV valve to the left ventricular outflow tract (LVOT) may create significant LVOT obstruction.

Most adult patients with this diagnosis will have undergone prior surgical palliation in infancy. The long-term prognosis following complete AVSD repair is reasonable. However, common late-onset complications associated with this lesion include left and right AV valve insufficiency, residual atrial or ventricular level shunt, and LVOT obstruction. Therefore, CCTA obtained to evaluate this defect should assess for each of these late onset complications.

Aortic Abnormalities

Patent Ductus Arteriosus

The ductus arteriosus is a vascular connection between the proximal left pulmonary artery and aorta that is essential for fetal circulation. Before birth, the ductus arteriosus allows much of the oxygenated blood from the placenta to bypass the pulmonary vascular bed and supply the systemic circulation via the descending aorta. It typically closes spontaneously within a week following birth. Beyond this time, if the vessel remains patent, a shunt now exists between the systemic and pulmonary vascular beds. This may be beneficial in certain CHDs, e.g., pulmonary atresia or hypoplastic left heart syndrome (HLHS), where the duct can provide a stable source of blood flow to either the pulmonary or systemic circulation. In an otherwise normal circulation, a patent ductus arteriosus (PDA) may have serious sequela that is often determined by the size of the ductus. As pulmonary vascular resistance falls, there is an increase in the degree of left-to-right shunt. While a trivial or small PDA is often of little hemodynamic consequence, a large PDA can expose the pulmonary vascular bed to an excessive volume of pulmonary blood flow and systemic arterial pressure. Untreated, a large ductus can lead to pulmonary hypertension even after the duct is closed.

While surgical ligation of a ductus is a straight forward surgical procedure, catheter-based techniques have now become the procedure of choice for the majority of PDAs [26]. Pre-intervention CCTA may be useful to demonstrate the size, shape, and course of the duct as well as its diameter at the pulmonary and aortic ends as these factors may impact upon the type of occluder device chosen at the time of intervention (Figure 21.8).

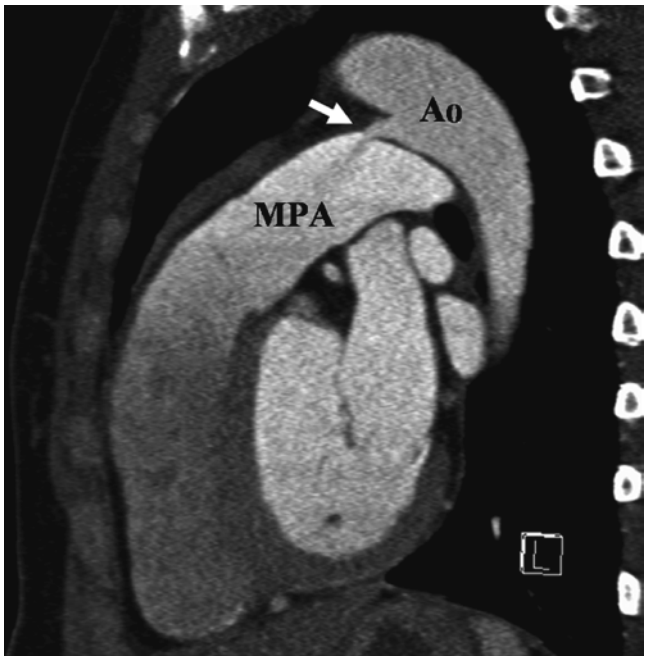

Figure 21.8. Oblique sagittal view demonstrates a small patent ductus ateriosus (*arrow*) *Ao* aorta; *MPA* main pulmonary artery.

Aortopulmonary Window

The aortopulmonary (AP) window is a rare congenital defect defined as a direct communication between the pulmonary artery and the ascending aorta. While physiologically similar to a large PDA, they are distinct in that this defect is the result of incomplete division of the common arterial trunk [27]. Commonly associated defects include ASD, VSD, and tetralogy of Fallot (TOF). Patients diagnosed in infancy often undergo repair with a pericardial or Dacron patch. Unrepaired, the adult patient may present with a continuous murmur and left heart enlargement (small AP window) or, more likely, pulmonary hypertension, cyanosis, and Eisenmenger physiology in the patient with the large AP window. In the patient with unoperated AP window, CCTA should inspect and confirm not only the presence of a window but also associated lesions. For those with repaired AP windows, CCTA, when indicated, should evaluate the aortic and pulmonary artery architecture.

Coarctation of the Aorta/Interrupted Aortic Arch

Coarctation of the aorta (CoA) is defined as a focal narrowing of the aorta. Most commonly the area of narrowing is just distal to the origin of the left subclavian artery at the insertion of the ductus arteriosus. This "juxtaductal" tissue of the aorta has characteristics similar to ductal tissue leading to further constriction in the postnatal period. Yet, this single theory does not explain the pathophysiology of coarctation entirely as a diffuse form of coarctation characterized by hypoplasia of the transverse arch is also encountered.

CoA may occur in isolation (simple CoA) or in conjunction with associated with other abnormalities (complex CoA). Complex CoA is often associated with bicuspid aortic valve (BAV), mitral valve abnormalities, VSDs, intracranial aneurysms, and Turner syndrome.

Discovered in infancy, coarctation is most often repaired surgically. Surgical techniques have evolved since the 1940s.

The subclavian flap technique, interposition jump graft, and patch aortoplasty are less commonly employed compared to the end-to-end and extended end-to-end anastomoses. Each technique has specific advantages, disadvantages, and associated long-term complications. Native lesions identified in the adolescent or young adult are often treated with balloon angioplasty, including stent placement if the patient is of near adult size [28].

Late-onset complications include arterial hypertension, recoarctation, aortic aneurysm, accelerated atherosclerosis and sudden cardiac death, left ventricular failure, cerebrovascular accident, and ruptured aortic aneurysm [29]. Therefore, noninvasive evaluation of the patient with history of surgical and/or transcatheter repair of CoA should include CCTA.

CCTA, when obtained to assess this congenital lesion, provides a wealth of information including precise measurements of the entire aortic arch, anatomy and severity of the coarctation segment, presence/absence of arch hypoplasia, and description of collateral vessels bypassing the region of stenosis [30]. CCTA offers significant advantages in the assessment of the patient with coarctation who has undergone prior transcatheter therapy. As a result of late-onset complications, namely recoarctation and aneurysm at the site of prior palliative repairs, many young adults have undergone transcatheter repairs. Although CMR is often the examination of choice in the adult CHD population, many transcatheter devices including stents create significant signal void artifact precluding an accurate assessment of the anatomy of interest. In contrast, CCTA provides an accurate assessment of the lumen of the stented segment and surrounding anatomic structures without artifact. Lastly, as prior natural history studies have suggested that myocardial infarction secondary to accelerated atherosclerosis is the most common cause of death, the coronary arteries should be closely inspected at the time of examination.

Interruption of the aortic arch is defined by complete disruption in continuity of the aortic arch [31]. This defect is further characterized by the location of the defect (types A–C) and often associated with other important defects including VSD, AVSD, PDA, BAV, subaortic stenosis, transposition of the great arteries, and double-outlet right ventricle (DORV). Surgical therapy is required to restore continuity of the aortic arch and concomitant defects. However, late-onset complications include restenosis at the site of prior surgical repair. Therefore, CCTA has a role in the assessment of this population, similar to the CoA group, to depict the anatomy of the aorta and arch, late postoperative complications as well as evaluation of those who may have undergone transcatheter interventions to address prior complications.

Congenital Valvular Disease

Bicuspid Aortic Valve/Valvar Aortic Stenosis

A BAV is perhaps the most common congenital heart abnormality, affecting slightly more than 1% of the general population [1]. The term BAV is actually a misnomer. Typically, the valve apparatus is still composed of three cusps, yet two of the cusps remained fused together. The resulting valve is functionally bicuspid. Most commonly, this fusion is along the commissures between the leaflets associated with the right and left coronary arteries.

A BAV is often discovered after a murmur is appreciated on routine examination. Mild degrees of stenosis may be well tolerated and never warrant intervention. With increasingly severe degrees of stensosis, left ventricular hypertrophy and enlargement ensues and accounts for approximately 50% of aortic valve replacement in adults. Additional late onset complications associated with the BAV include aortic regurgitation and aortic root dilation.

Congenital aortic stenosis is associated with trileaflet aortic valves (often with a disproportionately small aortic valve annulus) or with severely dysplastic leaflets, including the functionally unicuspid valve. Rheumatic heart disease accounts for a significant proportion of acquired aortic valve stenosis in the pediatric population.

Transthoracic echocardiography is the primary noninvasive modality in the evaluation of aortic valvular disease. This technique provides an assessment of the valve (degree of stenosis/regurgitation), ventricular size and function, and aorta (poststenotic dilatation). Although echocardiography remains the mainstay of assessing aortic valvular disease, CCTA has gained utility in the assessment of the aortic valve while overcoming the limitations of ultrasound. In patients with poor acoustic windows (e.g., obesity, pulmonary disease, chest wall deformities), CCTA provides an accurate assessment of valve morphology, dimensions, and presence/absence of calcification. Further, CCTA estimates of valve area correlate highly with TEE dimensions [32]. Importantly, CCTA allows for accurate assessment of poststenotic aortic root dilation that may not be appreciated with transthoracic imaging. Complementary three-dimensional volume-rendered reconstructions performed with off-line analysis may provide insight of the entire aortic root and have potential impact that is helpful with upcoming surgical planning. While BAV can occur in isolation, it is also associated with an increased risk of coarctation, interrupted aortic arch [33], and coronary artery anomalies [34]. The advantages of this technique have been well defined in the assessment of the thoracic aorta and should also be considered in the evaluation of the patient with combined arch and valvular disease.

Subvalvar Aortic Stenosis

Subvalvar aortic stenosis is most often caused by a fibrous membrane or ring of tissue. This can occur in isolation or in association with a VSD, CoA, Shone complex, PDA, left SVC, and valvular aortic stenosis. The degree of stenosis may remain stable, but most tend to progress over time. In contrast to valvar aortic stenosis, this lesion is not amenable to catheter-based interventions. If the degree of obstruction below the level of the valve becomes significant, the lesion must be addressed surgically with resection of

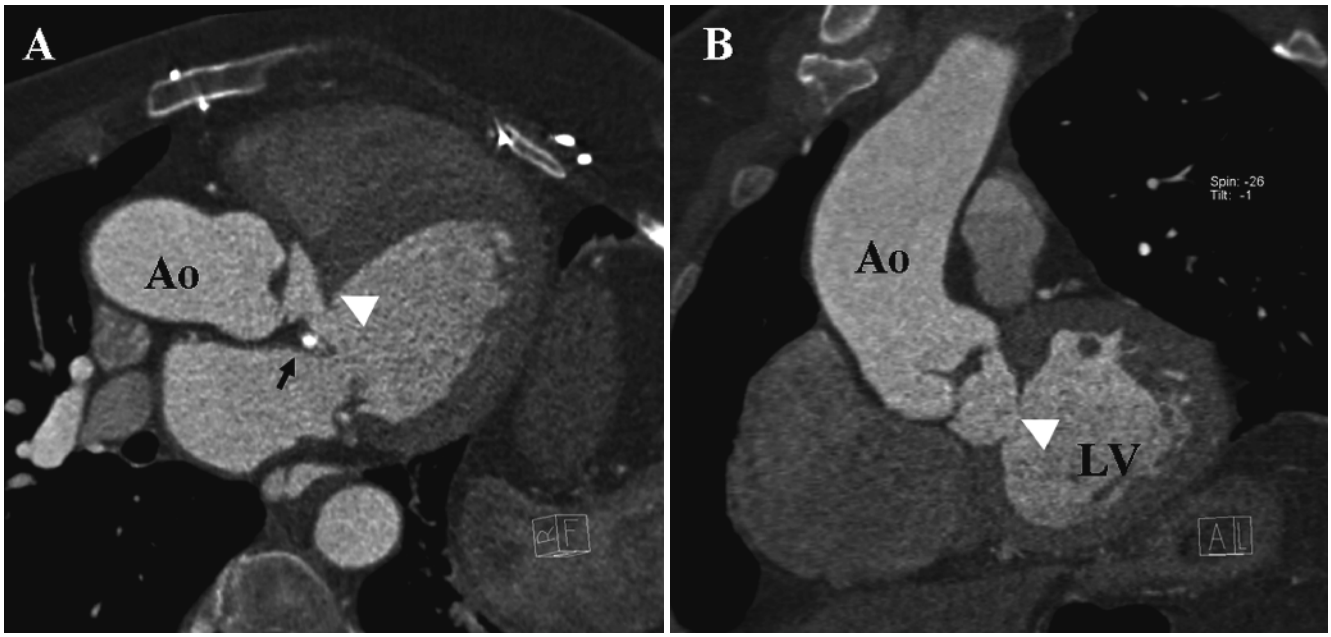

Figure 21.9. Oblique axial (**a**) and sagittal (**b**) views demonstrating a discrete subaortic membrane (*arrowhead*) in a patient with a bicuspid aortic valve and coarctation of the aorta. Note the calcified anterior leaflet of the mitral valve. *Ao* aorta; *LV* left ventricle.

the membrane. There is a significant risk of recurrence despite surgical intervention. Due to the recurrence of this lesion, a history of this defect and/or associated defects commonly associated with a subaortic membrane should prompt close inspection of the left ventricular outflow tract in patients undergoing CCTA examinations with both simple and complex CHD (Figure 21.9).

Supravalvar Aortic Stenosis

Supravalvar stenosis is defined as stenosis immediately above the level of the sinuses of Valsalva. This is an uncommon occurrence in the general population and is highly associated with Williams Syndrome (7q11.23 deletion syndrome). Associated lesions include aortic valve abnormalities, Shone complex, and coronary artery abnormalities. Theoretically, these patients are presumed to be at risk of premature atherosclerosis as the coronary arteries are continuously exposed to supranormal pressures. Indications for surgical repair in the symptomatic patient include a mean gradient >50 mmHg (peak instantaneous gradient >70 mmHg) by Doppler echocardiography. CCTA may assist in the initial diagnosis of this defect, but, more importantly, this technique may provide insight into the coronary artery anatomy and late outcomes in this population that has not been well established.

Pulmonary Stenosis

Congenital pulmonary stenosis is usually an isolated defect, but it may also occur in combination with subvalvar stenosis. A wide variety of malformations of the valve can be present including small valve annulus, thickened valves, fused valve leaflets, abnormal movement or doming of the valve during systole, or even ridges of dysplastic tissue. This obstruction leads to poststenotic dilation of the main pulmonary artery and right ventricular hypertrophy. Right ventricular hypertrophy leads to a dynamic narrowing of the right ventricular outflow tract and further increase in degree in obstruction.

Severe or critical pulmonary stenosis may require balloon valvuloplasty in infancy. Balloon valvuloplasty is recommended in the symptomatic adult with a peak instantaneous Doppler gradient > 50mmHg. Surgical therapy is recommended for patients with severe pulmonary stenosis, a hypoplastic pulmonary valve annulus, severe pulmonary insufficiency, and sub/supravalvar pulmonary stenosis. Surgery is also reserved for patients with severely dysplastic valves that are not necessarily amenable to transcatheter therapies.

Because of the anterior position of the pulmonary valve and the right ventricular outflow tract, these structures are difficult to completely visualize with echocardiography, especially in patients following prior cardiac surgery. CCTA is well suited to image this patient population to completely delineate the right ventricular outflow tract, pulmonary valve annulus, and distal structures including the branch pulmonary arteries. Pre-interventional assessment of pulmonary valve anatomy and dimensions may even predict suitability for balloon valvuloplasty. Lastly, CCTA provides quantification of right ventricular size and function in the postinterventional setting in the patient with residual pulmonary stenosis/regurgitation.

Congenital Heart Defects: Moderate/ Severe Complexity

Tetralogy of Fallot

TOF is the most common heart defect that results in cyanosis after the newborn period. The tetrad consists of: a malalignment VSD, subpulmonary stenosis, overriding aorta, and right ventricular hypertrophy. Although the exact embryologic origin of TOF is yet to be determined, anterior and superior displacement of the infundibular septum accounts for the first three features of this defect. Right ventricular hypertrophy is a consequence of subpulmonary stenosis.

TOF is also associated with other abnormalities including ASDs, left SVC to coronary sinus, and a right aortic arch. Associated coronary artery anomalies include the left anterior descending arising from the right coronary artery (RCA), circumflex arising from the RCA, a large conus branch, and single coronary artery system.

The repair of TOF typically involves resection of subpulmonic (e.g., infundibular) obstruction and patch closure of the VSD. Relief of the right ventricular outflow tract obstruction may occur via a variety of techniques. Patients with a restrictive pulmonary valve annulus may require a longitudinal incision of the pulmonary valve with subsequent augmentation with patch material (transannular patch) and augmentation of the pulmonary arteries when indicated. In more severe forms (e.g. pulmonary atresia), a right ventricular-to-pulmonary artery conduit is performed to establish continuity between the right ventricle and pulmonary arteries. Following these repairs, there is significant residual pulmonary insufficiency. This is often well tolerated until adolescence and young adulthood. The evolution of noninvasive imaging (CMR and CCTA) has illustrated progressive right ventricular enlargement and systolic dysfunction as a consequence of lifelong pulmonary insufficiency. Therefore, symptomatic patients with these findings should be referred for surgical pulmonary valve replacement. Finally, novel techniques are currently under investigation (Melody® Transcatheter Pulmonary Valve, Medtronic, Fridley, MN) to address pulmonary insufficiency via a transcatheter approach while simultaneously avoiding the risks associated with re-operation in this complex group of patients [35].

Noninvasive imaging studies obtained routinely or in anticipation of pulmonary valve replacement should assess right and left ventricular volumes and function, anatomy of the right ventricular outflow tract, presence/absence of residual ventricular septal defect, and anatomy of the proximal and distal branch pulmonary arteries. CCTA may provide accurate anatomic as well as functional data including those who have undergone complex interventions (Figure 21.10).

Lastly, progressive aortic root dilation is frequently demonstrated in the adult tetralogy population despite adequate surgical repair [36]. This process may be due to an inherent aortopathy rather than a sequelae of the intracardiac defects [37]. Therefore, CCTA assessment of the adolescent or adult patient with TOF should include close inspection of the aortic anatomy at the time of examination.

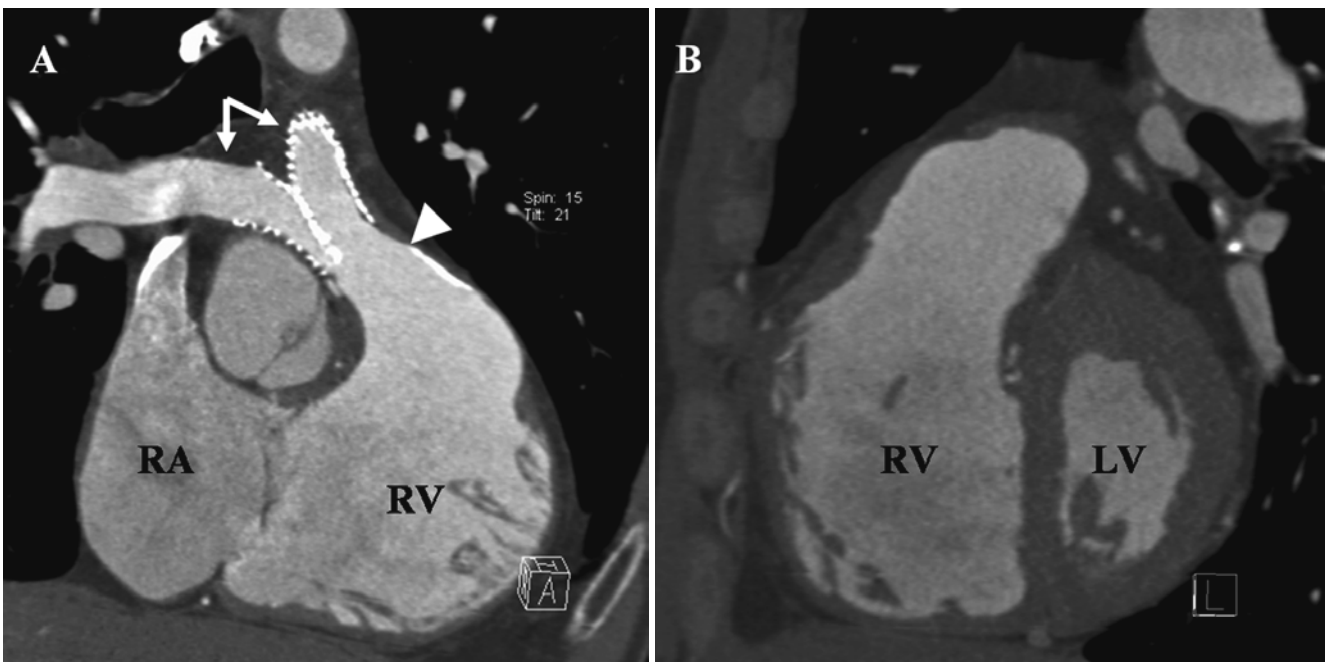

Figure 21.10. The oblique coronal (**a**) and sagittal (**b**) views demonstrate the long-term complications associated with tetralogy of Fallot. Lifelong pulmonary insufficiency is a consequence associated with prior surgical palliations (*arrowhead*) that results in a dilated right ventricle (RV) when compared to the size of the left ventricle (LV). Prior palliative procedures often result in branch pulmonary artery stenosis often requiring transcatheter therapy (*arrows*). *RA* right atrium.

Double-Outlet Right Ventricle

When both great arteries are intimately associated with the right ventricle (>50%), this anatomic relationship is described as double-outlet right ventricle (DORV). DORV is not a single congenital defect, but rather a continuum of defects best understood by the relationship by the relationship between the great vessels and the position of the VSD. The location of the VSD further corresponds with each specific physiologic subtype [38].

The location of the VSD may be *subaortic, subpulmonic, doubly-committed* (a single defect lying inferior to both the aorta and pulmonary artery) or *remote* from the great arteries. The relationship of the great arteries is defined by the position of the aorta relative to the pulmonary artery. Although normal relationships may exist, typically, the aorta lies *rightward and posterior* to the pulmonary artery. Alternatively, the aorta may lie side by side or *rightward and anterior* to the pulmonary artery with the subpulmonic variant (d-TGA physiology) of DORV.

Pulmonary stenosis is commonly observed in DORV, occurring in approximately 70% of cases [39, 40]. Other associated anomalies include secundum ASDs, relative hypoplasia of the left ventricle, mitral valve anomalies (atrioventricular attachments to the septum), a persistent left SVC, and coronary artery anomalies. CoA or arch hypoplasia commonly occurs in the subpulmonary variant of DORV (Taussig-Bing anomaly). Although these associated defects are relatively uncommon, when present, they create a significant impact on the physiology of the underlying defect as well as surgical management options.

Given the variety of anatomic relationships and associated features, surgical palliative approaches to repair of DORV are diverse. Repairs typically include closure of the VSD such that blood flow is routed ("tunneled") to restore continuity between the left ventricle and the aorta (subaortic DORV). An arterial switch procedure may be performed to restore left ventricular-aortic continuity in patients with DORV with subpulmonary VSD. Associated features such as ASDs and atrioventricular valve chordae are addressed simultaneously. In some cases, biventricular repair is not always possible, and a single ventricle palliation is performed (e.g., staged Fontan procedure).

Late outcomes of DORV are similar to TOF, but are further determined by the underlying anatomy and type of surgical palliation. Complications include obstruction of the right ventricular-to-pulmonary artery conduit, stenosis of interventricular tunnels, subaortic stenosis, and neoaortic root dilation. CCTA is suitable in the pre-operative assessment of this lesion as it accurately describes the three-dimensional relationship of the VSD to surrounding structures such as the great arteries and coronary arteries. Further, it provides an accurate assessment of postoperative anatomic changes including vital conduits that are at increased risk of calcification/stenosis.

Transposition of the Great Arteries

Transposition of the great arteries (TGA) is one of the most common, severe congenital heart lesions and is often lethal to affected infants without intervention. Although TGA may occur in any number of complex CHDs (e.g., DORV), it is most commonly used to describe isolated ventriculoarterial discordance. In other words, the right ventricle gives rise to the aorta and coronary arteries, and the left ventricle gives rise to the pulmonary artery (Figure 21.11).

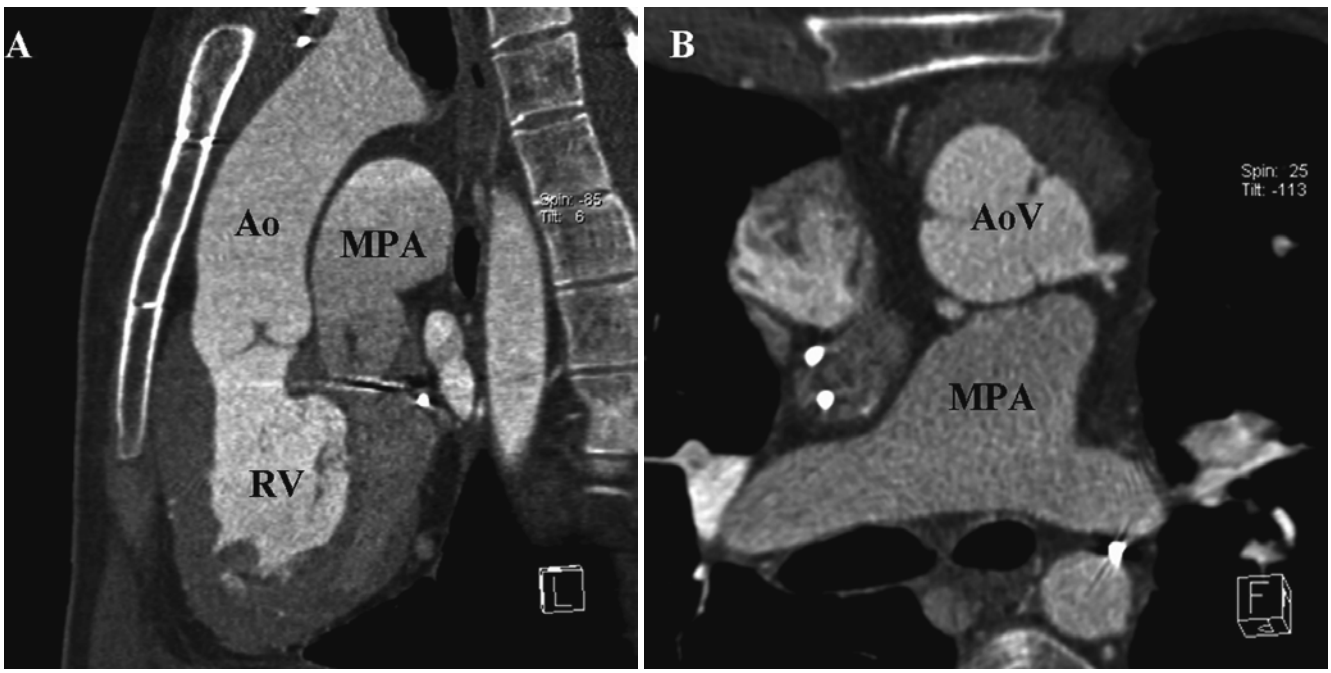

Figure 21.11. An oblique sagittal view (**a**) demonstrates ventriculoarterial discordance between the right ventricle (RV) and the aorta (Ao) in a patient with d-transposition of the great arteries status-post Mustard repair. The oblique axial view (**b**) displays the anterior-posterior relationship of the great vessels. *AoV* aortic valve; *MPA* main pulmonary artery.

TGA is often described as dextro or d-TGA. This name arises from the most common anatomic relationship of the aortic and pulmonary valves resulting in this anatomic relationship [22]. Here, the aorta is transposed with the pulmonary artery such that the aorta is anterior and rightward of the pulmonary artery. Recall that, the prefixes of d- and l- describe only the anatomic position of the aortic and pulmonary valves and not the arrangement of the remainder of the segmental cardiac anatomy. Associated defects include VSD (perimembranous, muscular), left ventricular outflow tract obstruction, CoA, and coronary artery abnormalities.

The physiology of d-TGA is often described as two circulations "in parallel" in contrast to the circulation that occurs "in series." The systemic venous return passes through the right atrium and right ventricle, then to the aorta and systemic circulation without ever reaching the lungs. Similarly, the pulmonary venous return enters the left atrium and left ventricle only to return to the pulmonary arterial bed.

Without a substantial mixing lesion, this parallel circulation is not sustainable and can quickly result in death. Continuous prostaglandin infusion can maintain patency of the ductus arteriosus and facilitate mixing. In the absence of a significant atrial or ventricular septal defect, a balloon atrial septostomy may be necessary to stabilize an infant until definitive surgical repair can be performed. Prior to the availability of balloon septostomy, a surgical excision of atrial tissue without cardio-pulmonary bypass was performed (the Blalock-Hanlon procedure).

Before the advent of improved coronary artery surgical techniques, redirecting blood at the atrial level was associated with lower mortality than attempting to switch the aorta and pulmonary arties to their typical anatomic positions. The Mustard and the Senning procedures baffle systemic venous return to the right ventricle and pulmonary venous return to the left ventricle. This allows oxygen-poor blood to reach the lungs via the morphologic left ventricle, and oxygen-rich blood reaches the systemic circulation via the morphologic right ventricle.

While the redirection of atrial blood flow restores a normal circulation, there are negative late sequelae. The superior and inferior systemic baffles that redirect venous return from the SVC and IVC (respectively) to the morphologic left ventricle can develop baffle leaks and/or stenosis. Similarly, the pulmonary venous baffle may develop stenosis as well. Further, the morphologic right ventricle is not well suited to tolerate systemic pressures lifelong. This ultimately leads to hypertrophy, dilation, and failure.

With advances in coronary artery surgical techniques, the arterial switch procedure allows the aorta and pulmonary arteries to be moved to restore ventriculoarterial concordance. This requires excision and mobilization of the proximal coronary and surrounding "buttons" of aortic tissue along with Lecompte maneuver to bring the pulmonary artery to the anterior position. Challenges of this technique include the variety of coronary artery anomalies associated with this defect.

In the patient with a Mustard or Senning palliation, CCTA is valuable to assess not only the complex anatomy and associated postoperative changes encountered with this population, but also the late onset complications such as baffle obstruction and residual hemodynamic lesions (Figure 21.12). Although CMR is frequently performed to assess quantification of RV volumes and function, CCTA may be utilized to quantify this data in this population as well.

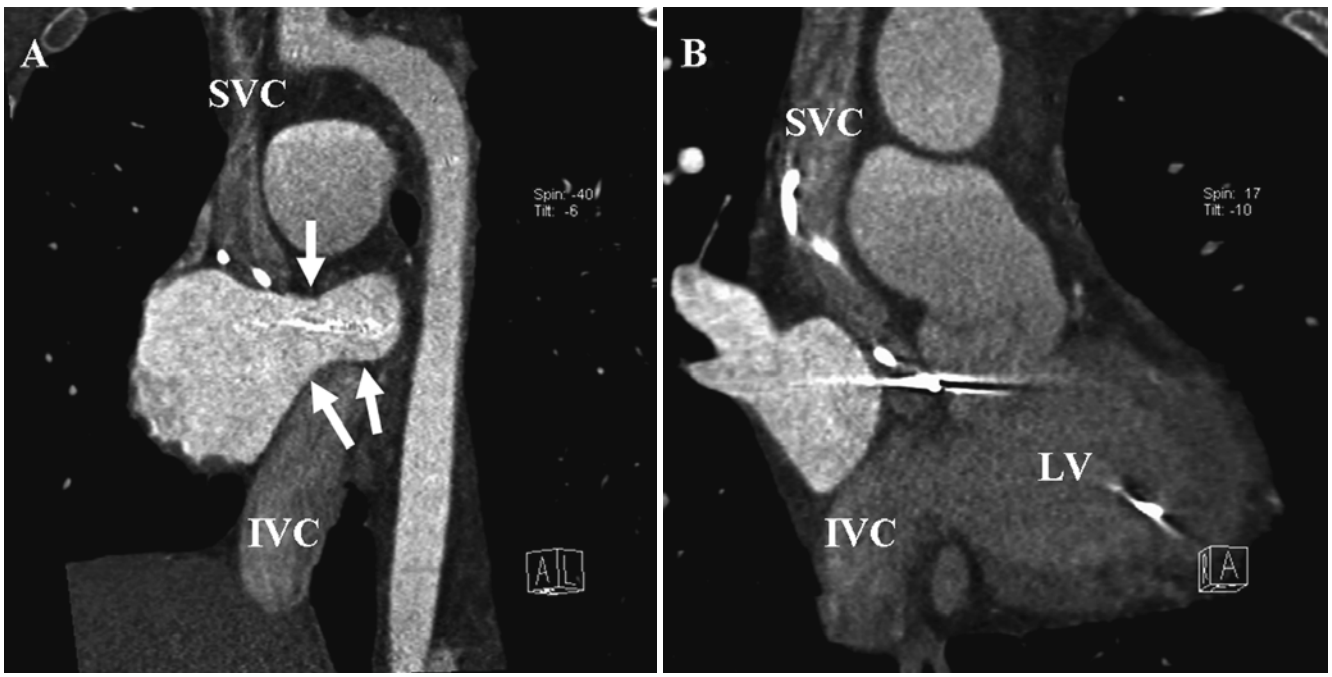

Figure 21.12. An oblique sagittal view (**a**) further demonstrates the anatomic appearance of the pulmonary venous baffle (*arrows*). The presence of pacing leads and contrast opacification in the systemic right ventricle challenge the ability to interpret the presence of systemic venous baffle obstruction (oblique coronal view; **b**). Secondary findings such as a prominent azygous vein may suggest the presence of this anomaly.

In the patient who has undergone an arterial switch procedure, CCTA is ideal to assess the coronary arteries for stenosis or early calcification [41]. In addition, when performed in this surgical subgroup, one should inspect the pulmonary arteries to determine the degree of branch pulmonary stenosis present after the Lecompte maneuver. Lastly, the neo-aorta should be closely evaluated as this group is at risk for dilation long-term.

Congenitally Corrected Transposition of the Great Arteries

In congenitally corrected transposition of the great arteries (ccTGA), there is both atrioventricular and ventriculoarterial discordance. Here, the systemic venous return courses from the right atrium through the mitral valve and morphologic left ventricle, ultimately reaching the pulmonary arterial bed via the pulmonary valve. Similarly, pulmonary venous return courses from the left atrium through the tricuspid valve into a morphologic right ventricle and ultimately the systemic circulation via the aortic valve. The term "congenitally corrected" has been accepted such that, in the absence of associated abnormalities, oxygen-poor systemic venous return reaches the lungs and oxygen-rich pulmonary venous return reaches the aorta via the morphologic left and right ventricles, respectively.

Patients with ccTGA frequently demonstrate a normal (levocardia) or midline (mesocardia) position of the heart within the chest. However, 20% of patients demonstrate the heart in the right chest (dextrocardia). Commonly encountered associated anomalies include VSD, pulmonary stenosis/atresia, and tricuspid valve abnormalities (dysplasia, Ebstein malformation). The most common late complications associated with this late condition include tricuspid regurgitation, right ventricular enlargement and dysfunction, congestive heart failure, and complete atrioventricular (AV) block [42]. With the increasing number of patients requiring pacemaker therapy as a result of AV block, CCTA may be beneficial to assess anatomic and functional (RV) data in this patient population (Figure 21.13). Further, this may be an ideal tool to assess the coronary venous anatomy to facilitate lead placement at the time of pacemaker implantation.

Truncus Arteriosus

In truncus arteriosus, a common aorticopulmonary trunk arising from the base of the heart is present that then gives rise to the coronary arteries, pulmonary arteries, and aorta. The truncal valve is often trileaflet (69%), and regurgitation of this valve is not uncommon. The classification scheme presented here, Collete and Edwards, defines truncus arteriosus by the relationship of the pulmonary arteries [43]. A Type I truncus has a short common arterial trunk that gives rise to an aorta and a main pulmonary artery. Type II is defined by the absence of a main pulmonary artery segment. The left and right branch pulmonary arteries arise in close proximity to one another from the ascending truncal artery. In type III, there is no main pulmonary artery segment, and the left and right pulmonary arteries arise separately at a distance from one another. Type IV is defined by the absence of pulmonary arteries. Here, the lungs are supplied by AP collateral vessels. This is more accurately classified as pulmonary atresia, and no longer considered with the spectrum of common arterial trunk.

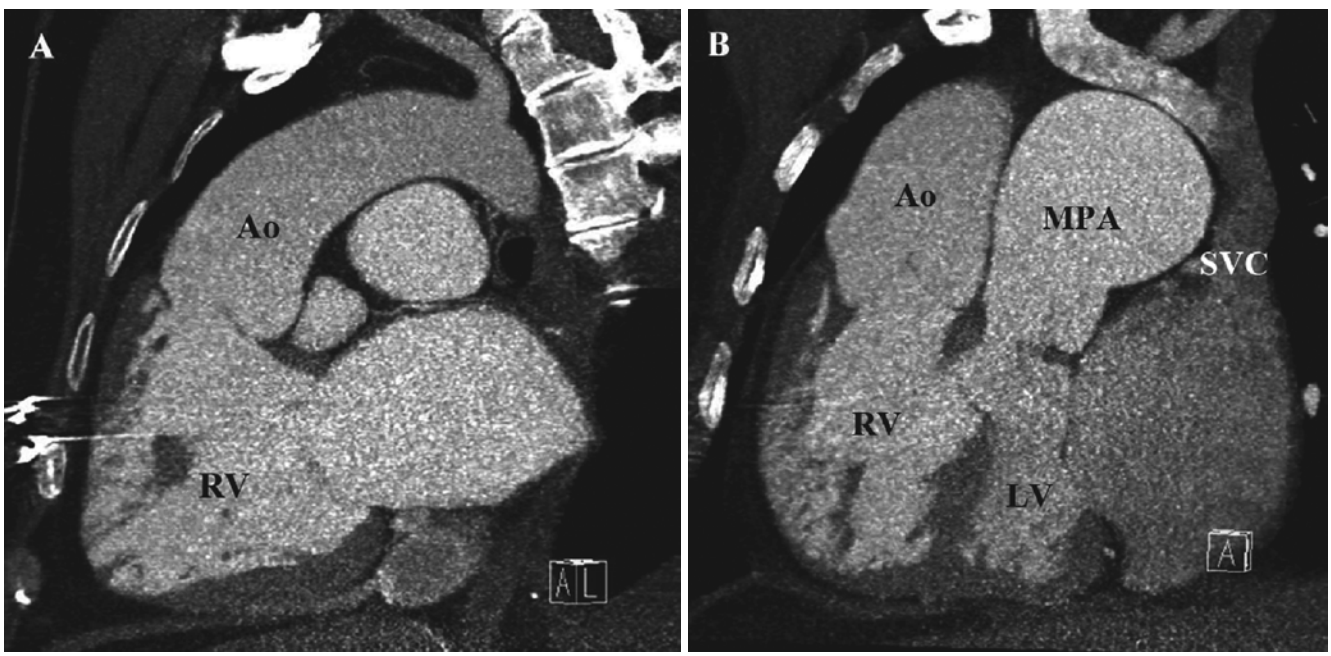

Figure 21.13. The oblique sagittal (**a**) and coronal (**b**) images display the underlying anatomy and demonstrate ventriculoarterial discordance.

Associated anomalies include CoA and interruption of the aorta. Other commonly associated defects include ASD, aberrant subclavian artery, and persistent left SVC to coronary sinus.

This defect presents in the newborn period necessitating surgical palliation. Surgical repair of truncus typically utilizes a conduit from the right ventricle to either the main pulmonary artery segment (Type I) or anastomosis to the branch pulmonary arteries (Types II and III). The long-term survival following initial successful repair continues to improve and therefore the number of adolescents and adults with this complex lesion will continue to grow. For this reason, it is imperative to recognize the late-onset complications associated with this defect. Each CCTA evaluation should closely inspect the right ventricle-pulmonary artery conduit to determine the presence/absence of stenosis or calcification, anatomy of the proximal and distal branch pulmonary arteries, neo-aortic root dilatation, and ventricular volumes and function.

Single Ventricle Lesions

Among the most complex congenital heart lesions are those with severe hypoplasia or atresia of the left or right ventricle. Consequently, these patients are reliant on a single ventricle and associated shunts to perfuse both the pulmonary and systemic vascular beds. The full spectrum of single ventricle lesions is beyond the scope of this text. Nonetheless, the more common variations are *tricuspid atresia* and hypoplastic left heart syndrome (HLHS). Despite the wide variation in single ventricle pathology, the surgical palliations ultimately share a similar physiologic goal.

As its name suggests, tricuspid atresia is defined by the absence of a tricuspid valve. Initially, blood returning to the right atrium passes through an ASD to the left heart and mixes with pulmonary venous return. The right ventricle is often atretic and receives blood via a ventricular septal defect. If there is ventriculoarterial concordance, the pulmonary arteries are often small and rely on ductal flow for an adequate source of pulmonary blood flow. Alternatively, if there is ventriculoarterial discordance, the aorta arises from the rudimentary right ventricle, and, upon occasion, there may be aortic obstruction requiring ductal patency.

HLHS describes a variety of left-sided abnormalities that are insufficient to meet the demands of the systemic circulation. They are further qualified by stenosis or atresia of mitral and aortic valves [e.g., mitral stenosis and aortic stenosis (MS/AS), mitral stenosis and aortic atresia (MS/AA), mitral and aortic atresia (MA/AA)]. If the ascending aorta is sufficiently atretic, the carotid and coronary arteries rely upon retrograde ductal blood flow to these vital structures.

In most cases of univentricular physiology, either the systemic or pulmonary bed relies upon patency of the ductal artery. If the ductal artery constricts or becomes stenotic, the results can be catastrophic. Ductal patency can be maintained with a continuous infusion of prostaglandin and more recently stents delivered via cardiac catheterization. Often a surgical shunt must be created to maintain a more durable blood supply.

Modern congenital heart surgery can be traced to 1944 with the creation of a systemic to pulmonary shunt conceived of by Helen Taussig, performed by Alfred Blalock with assistance of Vivian Thomas [44]. The original or *classic Blalock-Taussig shunt (c-BTS)* is a direct anastomosis of the subclavian artery to the ipsilateral pulmonary artery. Adaptations in this surgical technique lead to the development of the *modified BT shunt (m-BTS)*, an artificial (e.g., Gore-Tex) graft that connects the subclavian artery to the pulmonary artery without disrupting the integrity of the subclavian artery from the affected arm (Figure 21.14) [45].

Modified BT shunts are often utilized in the early palliation of hypoplastic left heart disease to augment pulmonary blood flow after the main pulmonary artery has been fashioned to reconstruct the aortic arch. An alternative strategy to augment pulmonary blood flow is the *Sano shunt*, a conduit located between the right ventricle and the pulmonary artery.

Other systemic to pulmonary arterial shunts include the *Waterston shunt* (ascending aorta to right pulmonary artery), the *Potts shunt* (descending aorta to left pulmonary artery), and the *Cooley shunt* (early ascending aorta to right pulmonary artery within the pericardium). Currently, modern *central shunts* utilize an artificial graft between the ascending aorta and the main pulmonary artery.

Although stable sources of pulmonary blood flow, systemic to pulmonary arterial shunts often lead to distortion of the pulmonary artery architecture, as the blood flow is often directed towards one pulmonary artery. As pulmonary vascular resistance decreases with age, congestive heart failure may develop as a result of excessive pulmonary blood flow. Most importantly, these shunts may become kinked, occluded, narrowed, or thrombosed, compromising pulmonary blood supply.

Alternatively, there are circumstances where complete repair is not immediately feasible or must be delayed. Here, surgical banding of the pulmonary arteries is often utilized as an initial palliation. Restricting the diameter of the pulmonary arteries can protect the pulmonary vascular bed from excessive blood flow and pressure. Surgical bands can be placed around either the main pulmonary artery (MPA) or the proximal branch left and right branch pulmonary arteries. Unfortunately, banding can cause negative sequelae, particularly if the band was placed on a young patient who later effectively outgrows the size of the band. Occasionally, the band may migrate distally, occluding one pulmonary artery, and this results in unopposed pulmonary arterial flow to the opposite branch. Poststenotic dilation may result in the band that is placed too tightly. Structures proximal to this band gradient are also exposed to increased afterload, and, as a result, pulmonary valve regurgitation, right ventricular enlargement and dysfunction, and tricuspid valve insufficiency may ensue.

As patients grow and pulmonary vascular resistance drops, BT shunts often become less physiologically

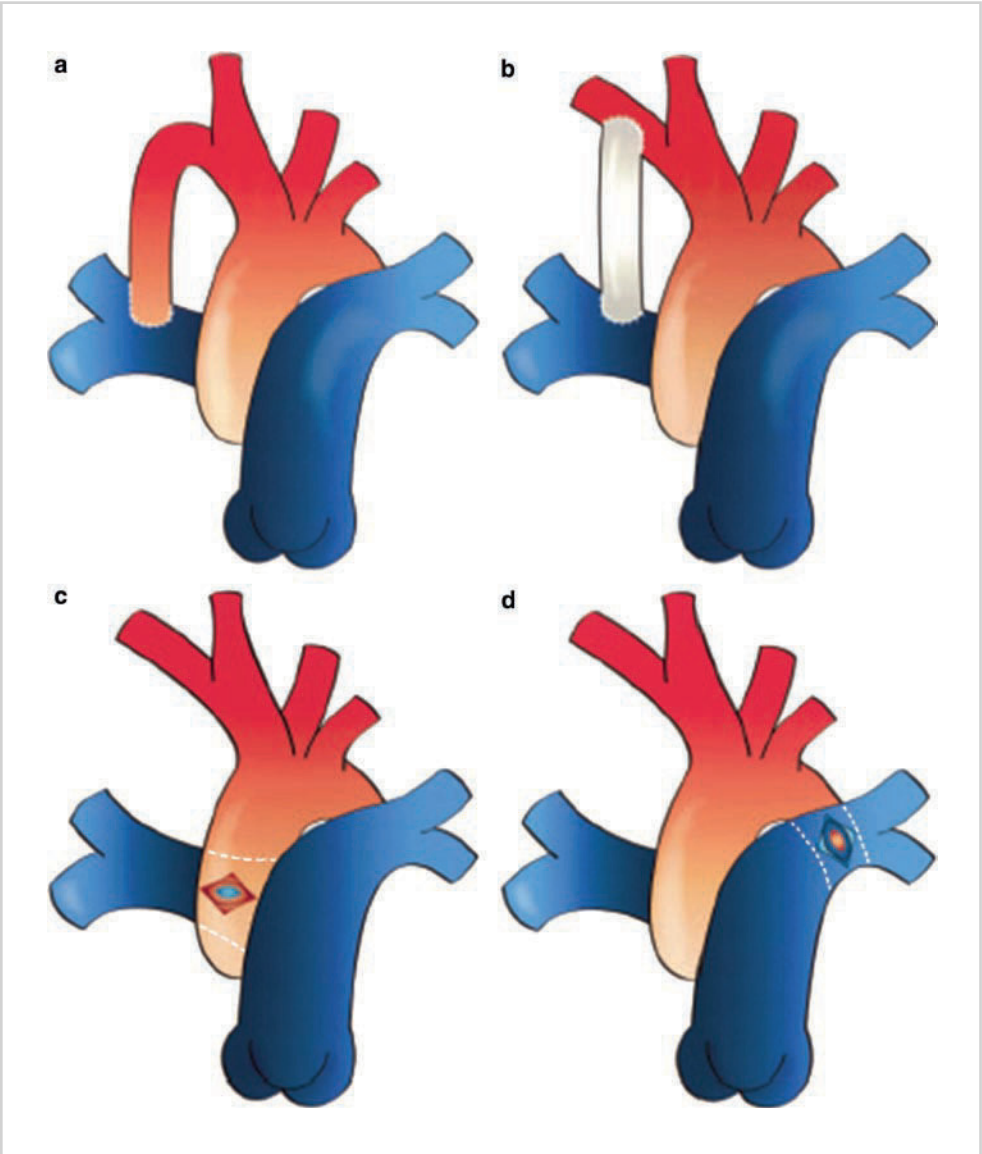

Figure 21.14. Aortopulmonary shunts. (**a**) the classic Blalock-Taussig shunt; (**b**) a modified Blalock-Taussig shunt; (**c**) a Waterston shunt; and (**d**) the Potts shunt. (reprinted with permission of Wolters Kluwer from Khairy et al. [45].

favorable. The *Glenn shunt (bidirectional)* is an end-to-side anastomosis of the SVC to the undivided pulmonary artery. It is most often performed as the second stage in a series of staged palliations in the surgical management of HLHS, at approximately 4–6 months of age. The third stage, the *Fontan procedure,* is the final palliative procedure that establishes continuity of the systemic venous return (SVC, IVC) to the pulmonary arteries via a variety of conduits (intracardiac, extracardiac). The Glenn and Fontan shunts cannot be safely performed in infancy as pulmonary vascular resistance must first fall substantially before it is exceeded by systemic venous pressure to drive blood forward through the veno-arterial shunt.

The Fontan procedure has undergone significant evolution and variations since its inception in 1971 [46]. Earlier techniques utilized an atriopulmonary (atrial-to-pulmonary artery) anastomosis. Late-onset complications including atrial arrhythmias, compression of the pulmonary veins, and thrombus as a result of severe atrial enlargement prompted surgical revision of this technique. More recently, surgical techniques utilize conduits made of artificial or pericardial tissue to direct and improve systemic venous flow to the pulmonary arteries via intracardiac (lateral tunnel) or extracardiac routes. Occasionally, a fenestration is placed within the conduit of the high-risk Fontan patient to serve as a "pop-off" for systemic venous return, thus allowing for maintenance of cardiac output via a right-to-left shunt. If pulmonary vascular resistance remains low postoperatively, these can be later closed percutaneously.

CCTA imaging is promising in the assessment of the single ventricle patient to assess late-onset complications [47]. However, there are limitations of this technique in the adolescent and young adult who have undergone single ventricle palliation. The low-cardiac output, frequent collaterals, and asymmetric blood flow between the left and

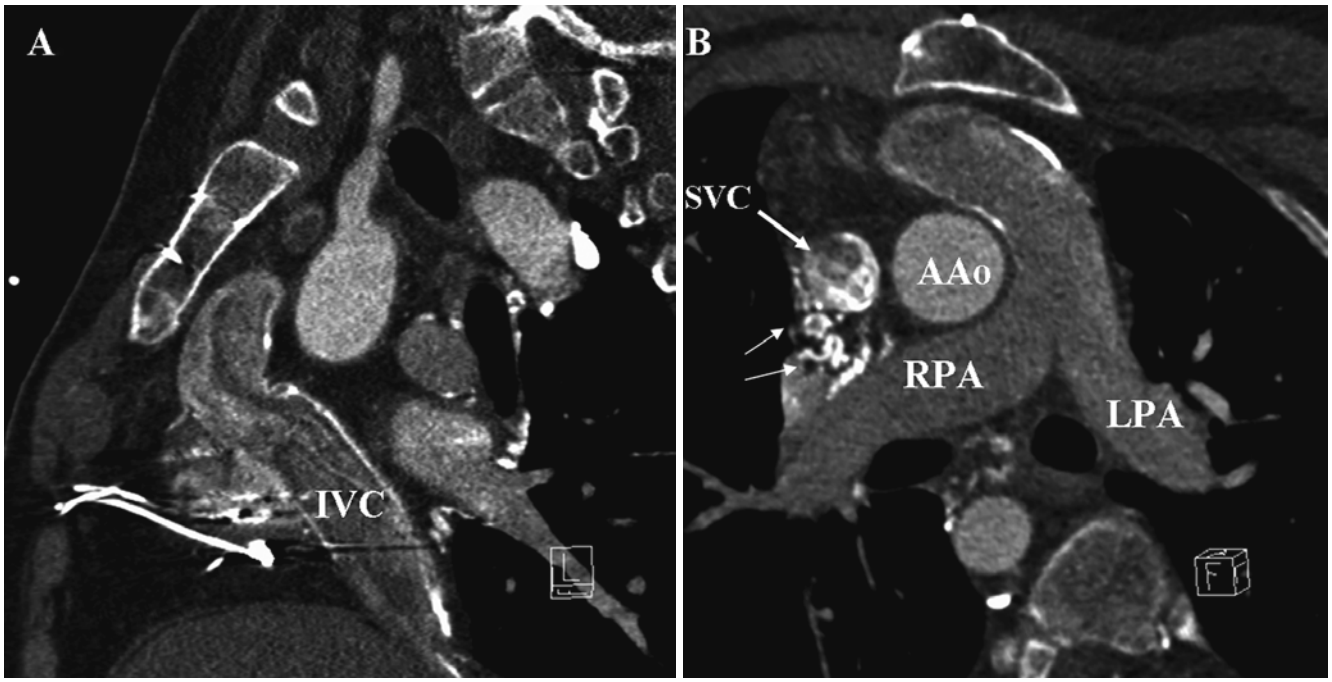

Figure 21.15. Oblique sagittal (**a**) and axial (**b**) views demonstrate the challenges of accurately defining Fontan anatomy. Despite an accurate timing bolus, this is a low-cardiac output state leading to accumulation of contrast in the superior vena cava (SVC) and poor opacification of desired anatomic structures. In addition, collaterals (*arrows*) may create a "steal phenomenon," resulting in poor contrast opacification. Further, incomplete opacification of the inferior vena cava (IVC) diminishes diagnostic accuracy to assess for thombus in this segment of the cavopulmonary anastomosis. *AAo* ascending aorta; *LPA* left pulmonary artery; *RPA* right pulmonary artery.

right lungs that results from prior cavopulmonary anastomoses create technical challenges for an accurate gated CCTA examination (Figure 21.15). Dual-injection strategies are recommended to overcome these limitations and completely assess the cavopulmonary anastomosis [48]. However, this has only been reported with success in the pediatric population, and so may not be practical in adults with CHD where there is a higher incidence of chronic venous insufficiency. Due to these limitations, CMR is often the imaging modality of choice unless otherwise contraindicated.

Summary

Adults with CHD represent a large and diverse group of patients with both simple and complex disease. Physicians who care for this population are not only challenged by the unique needs of this rapidly growing number of patients but also identifying an ideal noninvasive tool to accurately assess the needs of this patient group. Although CMR has been recognized as the noninvasive imaging tool of choice in this patient population, advances in CCTA clearly demonstrate the value of this modality for this patient population. However, it is imperative for imaging specialists to have a thorough understanding and respect for the growing field of complex CHD where collaboration with adult congenital specialists may provide key insight to a successfully executed CCTA examination.

References

1. Hoffman JI, Kaplan S. The incidence of congenital heart disease. *J Am Coll Cardiol*. 2002;39(12):1890–1900.
2. Warnes CA, Liberthson R, Danielson GK, et al. Task force 1: the changing profile of congenital heart disease in adult life. *J Am Coll Cardiol*. 2001;37(5):1170–1175.
3. Ho VB. ACR appropriateness criteria on suspected congenital heart disease in adults. *J Am Coll Radiol*. 2008;5(2):97–104.
4. Pinto NM, Marino BS, Wernovsky G, et al. Obesity is a common comorbidity in children with congenital and acquired heart disease. *Pediatrics*. 2007;120(5):e1157–e1164.
5. Kim MS, Klein AJ, Carroll JD. Transcatheter closure of intracardiac defects in adults. *J Interv Cardiol*. 2007;20(6):524–545.
6. Chue CD, Hudsmith LE, Stumper O, De Giovanni J, Thorne SA, Clift P. Femoral vascular access complications in adult congenital heart disease patients: audit from a single tertiary center. *Congenit Heart Dis*. 2008;3(5):336–340.
7. Balter S, Moses J. Managing patient dose in interventional cardiology. *Catheter Cardiovasc Interv*. 2007;70(2):244–249.
8. Knauth Meadows A, Ordovas K, Higgins CB, Reddy GP. Magnetic resonance imaging in the adult with congenital heart disease. *Semin Roentgenol*. 2008;43(3):246–258
9. Cook SC, Raman SV. Multidetector computed tomography in the adolescent and young adult with congenital heart disease. *J Cardiovasc Comput Tomogr*. 2008;2(1):36–49.
10. Otero HJ, Steigner ML, Rybicki FJ. The "post-64" era of coronary CT angiography: understanding new technology from physical principles. *Radiol Clin North Am*. 2009;47(1):79–90.
11. Raman SV, Cook SC, McCarthy B, Ferketich AK. Usefulness of multidetector row computed tomography to quantify right ventricular size and function in adults with either tetralogy of Fallot or transposition of the great arteries. *Am J Cardiol*. 2005;95(5):683–686.
12. Hoffmann A, Engelfriet P, Mulder B. Radiation exposure during follow-up of adults with congenital heart disease. *Int J Cardiol*. 2007; 118(2):151–153.

13. Van Praagh R. Terminology of congenital heart disease. Glossary and commentary. *Circulation*. 1977;56(2):139–143.
14. Tynan MJ, Becker AE, Macartney FJ, Jimenez MQ, Shinebourne EA, Anderson RH. Nomenclature and classification of congenital heart disease. *Br Heart J*. 1979;41(5):544–553.
15. Lacomis JM, Wigginton W, Fuhrman C, Schwartzman D, Armfield DR, Pealer KM. Multi-detector row CT of the left atrium and pulmonary veins before radio-frequency catheter ablation for atrial fibrillation. *Radiographics*. 2003;23 Spec No:S35-S48; discussion S48–S50.
16. Geva T, Van Praagh S. Anomalies of the pulmonary veins. In: Allen HD, Driscoll DJ, Shaddy RE, Feltes TF, eds. *Moss and Adams' Heart Disease in Infants, Children, and Adolescents: Including the Fetus and Young Adults*. Vol 2. 7th ed. Philadelphia, PA: Lippincott Williams & Wilkins; 2008:761–792.
17. Webb G, Gatzoulis MA. Atrial septal defects in the adult: recent progress and overview. *Circulation*. 2006;114(15):1645–1653.
18. King TD, Thompson SL, Steiner C, Mills NL. Secundum atrial septal defect. Nonoperative closure during cardiac catheterization. *JAMA*. 1976;235(23):2506–2509.
19. Du ZD, Hijazi ZM, Kleinman CS, Silverman NH, Larntz K. Comparison between transcatheter and surgical closure of secundum atrial septal defect in children and adults: results of a multicenter nonrandomized trial. *J Am Coll Cardiol*. 2002;39(11):1836–1844.
20. Gade CL, Bergman G, Naidu S, Weinsaft JW, Callister TQ, Min JK. Comprehensive evaluation of atrial septal defects in individuals undergoing percutaneous repair by 64-detector row computed tomography. *Int J Cardiovasc Imaging*. 2007;23(3):397–404.
21. Zaidi AN, Cheatham JP, Raman SV, Cook SC. Multislice computed tomographic findings in symptomatic patients after amplatzer septal occluder device implantation. *J Interv Cardiol*. 2009;22(1): 92–97.
22. Applegate KE, Goske MJ, Pierce G, Murphy D. Situs revisited: imaging of the heterotaxy syndrome. *Radiographics*. 1999;19(4):837-852; discussion 853–834.
23. Butera G, Carminati M, Chessa M, et al. Transcatheter closure of perimembranous ventricular septal defects: early and long-term results. *J Am Coll Cardiol*. 2007;50(12):1189–1195.
24. Holzer R, Balzer D, Cao QL, Lock K, Hijazi ZM. Device closure of muscular ventricular septal defects using the Amplatzer muscular ventricular septal defect occluder: immediate and mid-term results of a U.S. registry. *J Am Coll Cardiol*. 2004;43(7):1257–1263.
25. Craig B. Atrioventricular septal defect: from fetus to adult. *Heart*. 2006;92(12):1879–1885.
26. Grifka RG. Transcatheter PDA closure: equipment and technique. *J Interv Cardiol*. 2001;14(1):97–107.
27. Bertolini A, Dalmonte P, Bava GL, Moretti R, Cervo G, Marasini M. Aortopulmonary septal defects. A review of the literature and report of ten cases. *J Cardiovasc Surg (Torino)*. 1994;35(3):207–213.
28. Rao PS. Coarctation of the aorta. *Curr Cardiol Rep*. 2005;7(6): 425–434.
29. Cohen M, Fuster V, Steele PM, Driscoll D, McGoon DC. Coarctation of the aorta. Long-term follow-up and prediction of outcome after surgical correction. *Circulation*. 1989;80(4):840–845.
30. Sebastia C, Quiroga S, Boye R, Perez-Lafuente M, Castella E, Alvarez-Castells A. Aortic stenosis: spectrum of diseases depicted at multisection CT. *Radiographics*. 2003;23 Spec No:S79–S91.
31. Yang DH, Goo HW, Seo DM, et al. Multislice CT angiography of interrupted aortic arch. *Pediatr Radiol*. 2008;38(1):89–100.
32. Feuchtner GM, Muller S, Bonatti J, et al. Sixty-four slice CT evaluation of aortic stenosis using planimetry of the aortic valve area. *AJR Am J Roentgenol*. 2007;189(1):197–203.
33. Duran AC, Frescura C, Sans-Coma V, Angelini A, Basso C, Thiene G. Bicuspid aortic valves in hearts with other congenital heart disease. *J Heart Valve Dis*. 1995;4(6):581–590.
34. Roberts WC. The congenitally bicuspid aortic valve. A study of 85 autopsy cases. *Am J Cardiol*. 1970;26(1):72–83.
35. Lurz P, Bonhoeffer P, Taylor AM. Percutaneous pulmonary valve implantation: an update. *Expert Rev Cardiovasc Ther*. 2009;7(7):823–833.
36. Niwa K, Siu SC, Webb GD, Gatzoulis MA. Progressive aortic root dilatation in adults late after repair of tetralogy of Fallot. *Circulation*. 2002;106(11):1374–1378.
37. Tan JL, Davlouros PA, McCarthy KP, Gatzoulis MA, Ho SY. Intrinsic histological abnormalities of aortic root and ascending aorta in tetralogy of Fallot: evidence of causative mechanism for aortic dilatation and aortopathy. *Circulation*. 2005;112(7):961–968.
38. Bashore TM. Adult congenital heart disease: right ventricular outflow tract lesions. *Circulation*. 2007;115(14):1933–1947.
39. Chang DS, Barack BM, Lee MH, Lee HY. Congenitally corrected transposition of the great arteries: imaging with 16-MDCT. *AJR Am J Roentgenol*. 2007;188(5):W428–W430.
40. Hagler DJ. Double-outlet right ventricle and double-outlet left ventricle. In: Allen HD, Driscoll DJ, Shaddy RE, Feltes TF, eds. *Moss and Adams' Heart Disease in Infants, Children, and Adolescents: Including the Fetus and Young Adults*. Vol 2. 7th ed. Philadelphia, PA: Lippincott Williams & Wilkins; 2008.
41. Ou P, Celermajer DS, Marini D, et al. Safety and accuracy of 64-slice computed tomography coronary angiography in children after the arterial switch operation for transposition of the great arteries. *JACC Cardiovasc Imaging*. 2008;1(3):331–339.
42. Graham TP Jr, Bernard YD, Mellen BG, et al. Long-term outcome in congenitally corrected transposition of the great arteries: a multiinstitutional study. *J Am Coll Cardiol*. 2000;36(1):255–261.
43. Collett RW, Edwards JE. Persistent truncus arteriosus; a classification according to anatomic types. *Surg Clin North Am*. 1949;29(4): 1245–1270.
44. Blalock A, Taussig HB. The surgical treatment of malformations of the heart in which there is pulmonary stenosis or pulmonary atresia. *JAMA*. 1945;128(3):198–202.
45. Khairy P, Poirier N, Mercier LA. Univentricular heart. *Circulation*. 2007;115(6):800–812.
46. Fontan F, Baudet E. Surgical repair of tricuspid atresia. *Thorax*. 1971;26(3):240–248.
47. Spevak PJ, Johnson PT, Fishman EK. Surgically corrected congenital heart disease: utility of 64-MDCT. *AJR Am J Roentgenol*. 2008;191(3):854–861.
48. Greenberg SB, Bhutta ST. A dual contrast injection technique for multidetector computed tomography angiography of Fontan procedures. *Int J Cardiovasc Imaging*. 2008;24(3):345–348.

22

CT Imaging: Cardiac Electrophysiology Applications

Jerold S. Shinbane, Marc J. Girsky, Leslie A. Saxon, Michael K. Cao, David A. Cesario, and Matthew J. Budoff

An understanding of detailed 3-D cardiac anatomy is important to the field of cardiac electrophysiology. Cardiovascular computed tomographic angiography (CCTA) can comprehensively assess cardiovascular structure and function relevant to the assessment, treatment, and follow-up of patients with electrophysiologically-related disease processes. CCTA provides 3-D visualization of cardiac chambers, coronary vessels, and thoracic vasculature including structures particularly important to cardiac electrophysiology, such as the coronary veins, pulmonary veins, and left atrium. This comprehensive technology is extremely useful for the identification and characterization of cardiovascular substrates relevant to cardiac electrophysiology, and has great relevance to treatment of arrhythmias through preprocedure planning, procedural facilitation, and procedural follow-up.

Particular attention to details of patient preparation and image acquisition and processing are important to optimizing CCTA studies in patients who may have irregular rhythms due to premature atrial contractions, premature ventricular contractions, or other arrhythmias including atrial fibrillation. Medications to control heart rate and rhythm as well as pacemaker reprogramming to regularize rhythms may be useful. Acquisition protocols which compensate for irregular beats through deletion of short R-R intervals and analysis of mid-diastolic phases of the R-R interval with an absolute rather than relative time from the preceding R wave can improve image quality [1].

The indication for the CCTA study is important to providing the correct field of view as well as the region of interest for maximum contrast opacification. The contrast circulation time and the injection protocol are important factors to take into account to achieve maximal opacification of the region or regions of interest. Assessment of right ventricular function as well as coronary venous anatomy requires protocols providing adequate contrast enhancement to these structures, while still opacifying other cardiac structures and coronary arterial anatomy (Figure 22.1). Multiphase injection protocols with varying degrees of contrast, diluted contrast, and saline administered at variable speeds of delivery are used to optimally opacify structures for various electrophysiology indications.

As patients undergoing CCTA often undergo electrophysiology procedures requiring fluoroscopy, techniques to limit radiation dose are extremely important. Dose reductions can be achieved through limitation of field of view to essential structures and use of dose limiting imaging protocols. Dose modulation with retrospective gating or prospective gating can be used in some circumstances, but these techniques are limited in the setting of irregular rhythms. In some settings, such as imaging for atrial fibrillation ablation, the use of nongated images for merge with electrophysiology systems can be considered, which substantially decreases radiation dose.

Cardiovascular Substrates Associated with Sudden Cardiac Death

Sudden cardiac death is associated with a variety of cardiovascular structural or primary electrophysiologic abnormalities, often with the first manifestation of disease being sudden death. Vascular anatomies associated with sudden cardiac death can be identified by CCTA, and include anomalous coronary arteries, severe coronary artery disease, critical aortic stenosis, aortic aneurysm, and aortic dissection [2–7]. Cine CCTA can characterize cardiomyopathic substrates through reproducible volumetric measurement of ventricular volumes and ejection fraction (Figure 22.2), ventricular wall thickness, and ventricular regional wall motion, and can directly visualize coronary arteries, which may potentially facilitate differentiation between ischemic and nonischemic cardiomyopathy [8–11]. CCTA can identify and characterize cardiomyopathic processes associated with ventricular arrhythmias and sudden cardiac death, including dilated ischemic and nonischemic cardiomyopathy, hypertrophic cardiomyopathy, arrhythmogenic right ventricular cardiomyopathy, and ventricular noncompaction [10, 12–17].

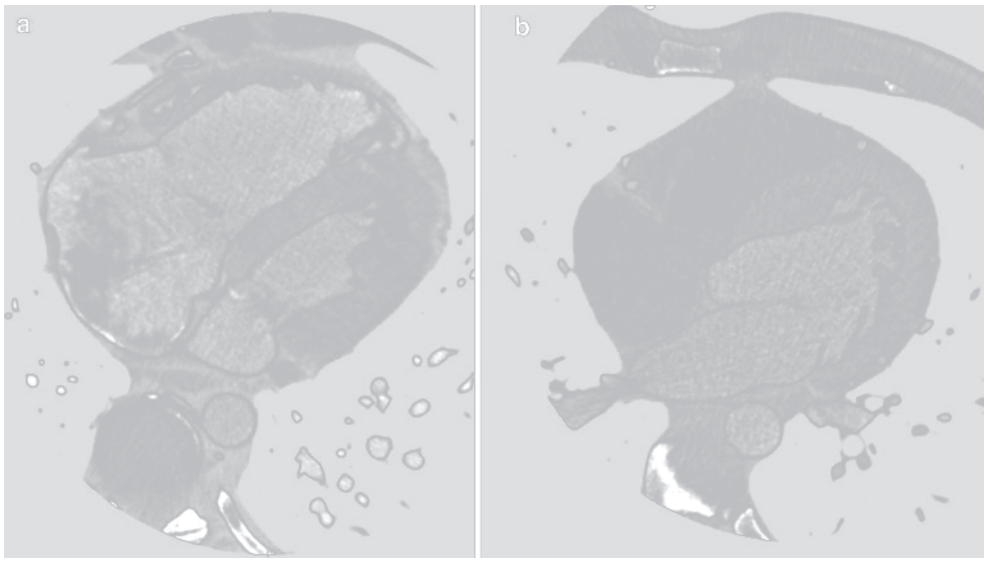

Figure 22.1. Axial views demonstrating a contrast injection timing protocol for contrast enhancement of the right ventricle and left ventricle, useful for assessment of right ventricular pathology (**a**), and a protocol for contrast enhancement of the left ventricle, useful for coronary artery assessment without streak artifacts in the superior vena cava (**b**).

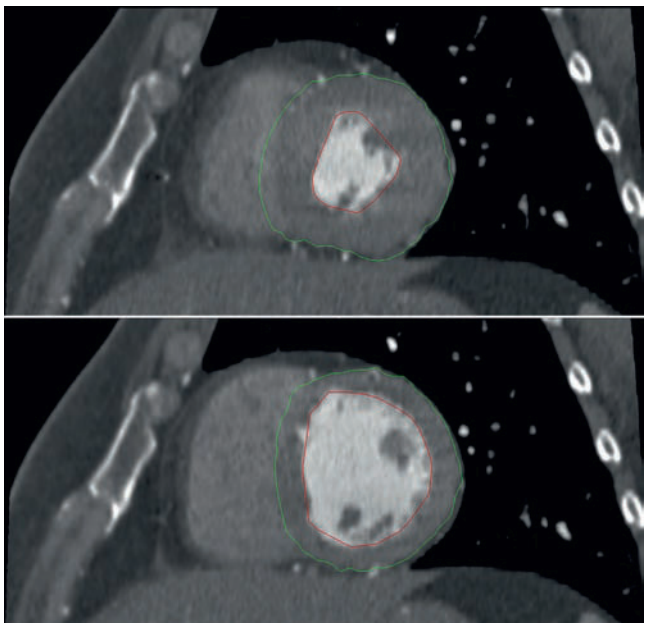

Figure 22.2. Short-axis view demonstrating ventricular end-systole (*upper panel*) and ventricular end-diastole (*lower panel*). Endocardial contours (*red lines*) and epicardial contours (*green lines*) are used to volumetrically assess left ventricular chamber size, myocardial mass, and function.

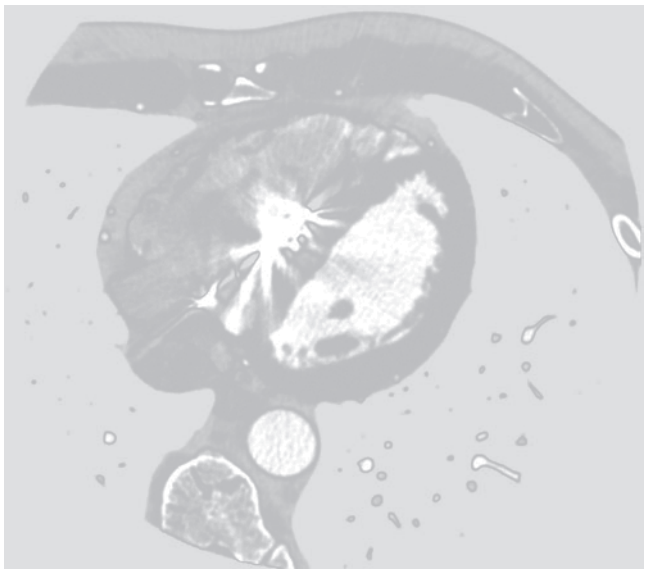

Figure 22.3. CCTA axial view demonstrating fibrofatty replacement of right ventricular myocardium, low-attenuation trabeculations, and right ventricular free wall scalloping in arrhythmogenic right ventricular cardiomyopathy. A right ventricular defibrillation lead is present with beam hardening artifact.

The diagnosis of arrhythmogenic right ventricular cardiomyopathy involves criteria including clinical history, family history, ECG abnormalities, and electrophysiologic testing results [18]. Although cardiovascular magnetic resonance (CMR) imaging has been the diagnostic imaging modality of choice, CCTA can visualize the anatomic features associated with arrhythmogenic right ventricular cardiomyopathy, such as epicardial and myocardial fat, low-attenuation trabeculations, right ventricular free wall scalloping, right ventricular enlargement, and global and regional right ventricular wall motion abnormalities [13, 19–22]. This process can involve both ventricles as visualized by CCTA [20, 23]. CCTA is particularly useful in the assessment of patients with pre-existing cardiac devices limiting the use of magnetic resonance imaging (Figure 22.3).

Electrophysiologic Mapping and Radiofrequency Catheter Ablation

Atrial Fibrillation Ablation

Atrial fibrillation ablation requires a detailed understanding of an individual patient's cardiovascular anatomy through 3-D characterization of the relationships between the left atrium, the surrounding cardiac structures, and extracardiac thoracic structures. A preprocedure study serves as a roadmap for procedural planning, a 3-D data set for intraprocedure electroanatomic mapping and ablation, and a template for the follow-up of atrial remodeling and assessment for complications including pulmonary vein stenosis.

The causes of atrial fibrillation are multiple, and include induction of atrial fibrillation by premature atrial foci from the pulmonary veins [24]. Catheter-based techniques for treatment of atrial fibrillation have focused on segmental ablation or complete circumferential electrical isolation of the pulmonary veins. The goals of these techniques are: (1) ablation or isolation of ectopic pulmonary vein foci so that these foci cannot trigger atrial fibrillation, (2) ablation of other ectopic atrial foci, and (3) long linear lesions providing pathways of preferential electrical conduction [25–28]. There are a variety of approaches to catheter-based ablation for atrial fibrillation. Percutaneous catheter-based approaches access the left atrium via either a single or double transseptal technique depending on the number of left atrial catheters used.

CCTA characterization of the left atrium and pulmonary veins is achieved through multiple modalities of evaluation including multiplane 2-D views, 3-D volumetric reconstructions, virtual endocardial views, and volumetric quantification of the atria. Pulmonary venous anatomy demonstrates great variability regarding vein number, location, size, shape, and os complexity (Figures 22.4–22.6). CCTA can visualize these pulmonary vein characteristics and can define the relationship between veins as well as between the left upper pulmonary vein and left atrial appendage [29–33]. Workstation software can be used to quantify characteristics of the pulmonary vein ostia, including area, maximum diameter, minimum diameter, and eccentricity. Key to these measurements is identification the left atrial/pulmonary vein interface, determination of the

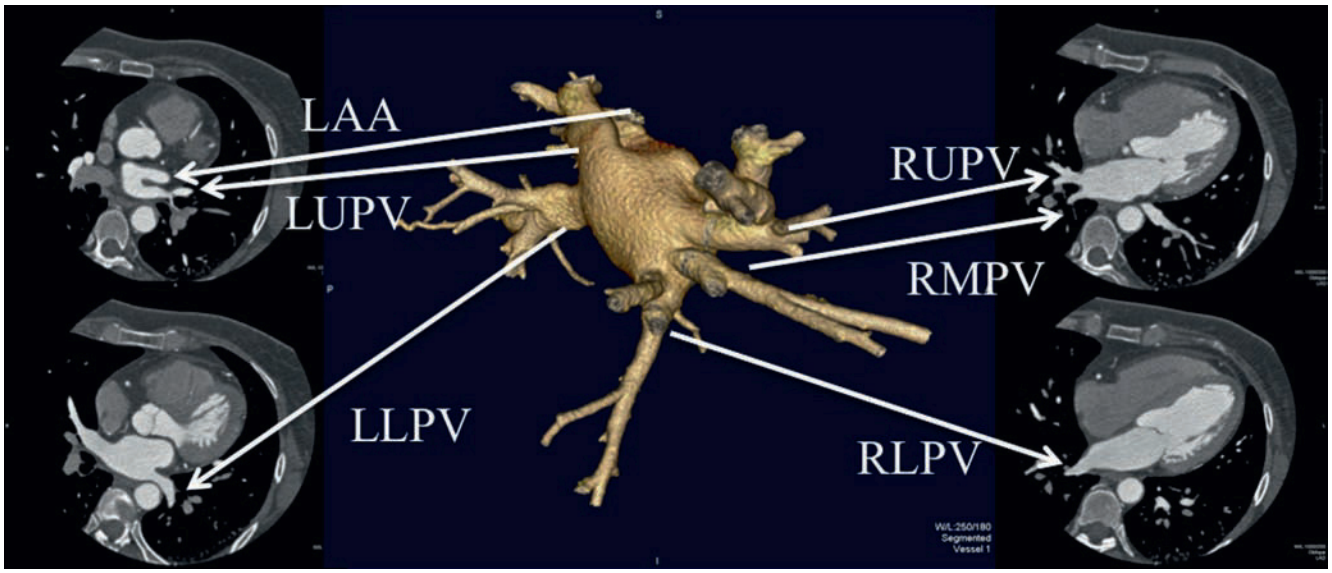

Figure 22.4. Characterization of the left atrium and pulmonary veins demonstrated through 2-D axial views and 3-D volumetric reconstruction, demonstrating 2 left-sided pulmonary veins and variant anatomy with 3-right sided pulmonary veins. *LAA* left atrial appendage; *LUPV* left upper pulmonary vein; *LLPV* left lower pulmonary vein; *RUPV* right upper pulmonary vein; *RMPV* right middle pulmonary vein; and *RLPV* right lower pulmonary vein.

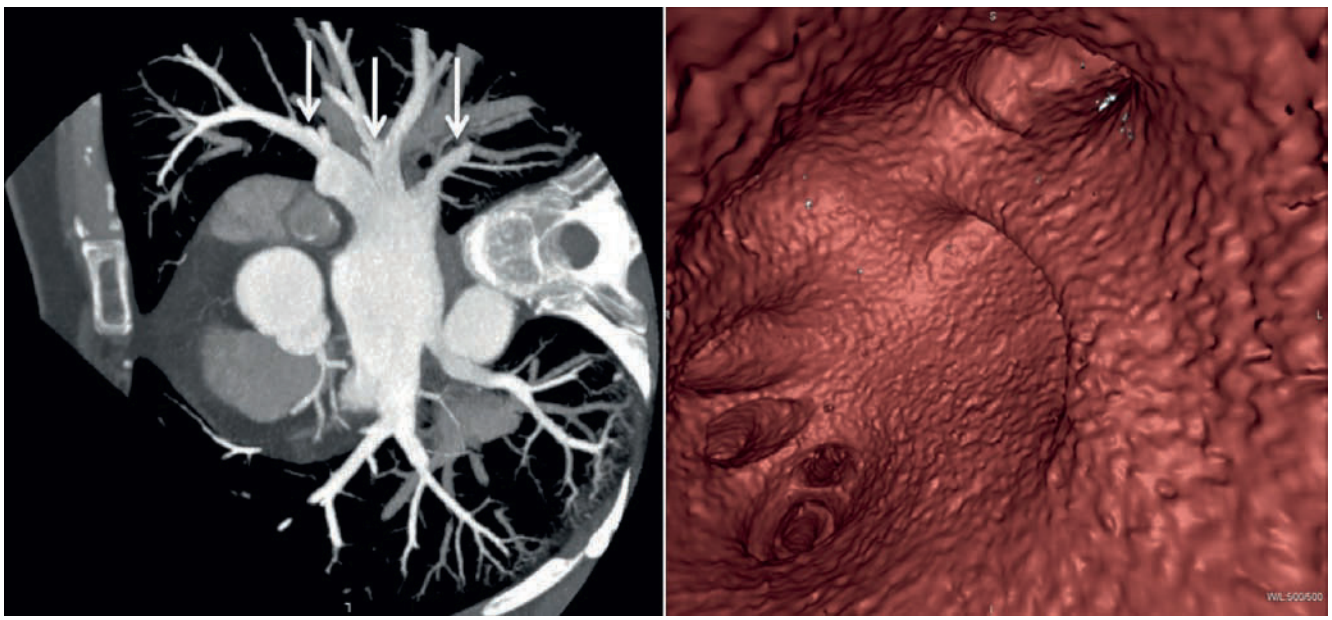

Figure 22.5. Characterization of the left atrium and pulmonary veins demonstrated through double oblique thick MIP (*left panel*), and a 3-D endocardial view demonstrating 3-right sided pulmonary veins (*right panel*).

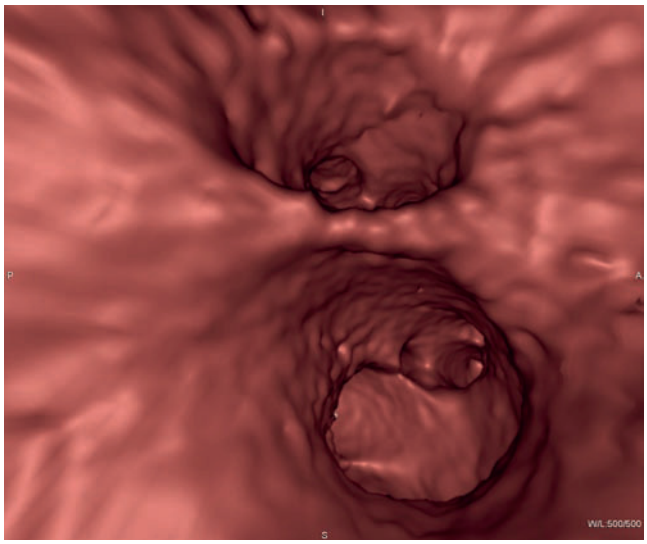

Figure 22.6. Characterization of the relationship between and os characteristics of a right upper and right middle pulmonary veins on a 3-D endocardial view.

long axis of the vein at the os, and recognition that the vein os is often an ovoid shape rather than circular (Figure 22.7). Additionally, atrial anatomy can be defined, including patent foramen ovale, atrial septal defects, and atrial masses.

Factors related to atrial size and thoracic pathology as visualized by CCTA are important to decisions to proceed with atrial fibrillation ablation. Left atrial volume is an important predictor of procedural success with atrial fibrillation ablation, as recurrence of atrial fibrillation is associated with an increased left atrial volume (Figures 22.8 and 22.9). CCTA measured atrial volume of greater than 135 cc has been associated with a higher recurrence rate [34]. CCTA left atrial volume reference values have been determined [35], and provide better accuracy of left atrial size than echo determined left atrial diameter [36–38]. Incidental thoracic findings visualized on CCTA have also been demonstrated to influence decisions regarding proceeding with atrial fibrillation ablation [39].

The recognition of atrial thrombi is extremely important prior to consideration of atrial fibrillation ablation. The left atrial appendage is a complicated multilobed tube-like structure with an intricate array of pectinate muscles (Figure 22.10). The contractile function of the appendage in the setting of atrial myopathy and atrial fibrillation is often depressed with decreased flow velocity. These factors make the appendage difficult to fill with contrast during CCTA study, and therefore difficult to analyze for thrombi, as filling defects can be due to inadequate filling or thrombi (Figure 22.11) [40–42].

CCTA has been shown be able to rule out thrombus, with transesophageal echo as the gold standard comparison. In patients with preprocedure non-gated CCTA prior to atrial fibrillation ablation, the sensitivity is high for ruling out thrombus, especially in lower risk patients (age <52 and CHADS2 score <1), but specificity remains more limited [43]. The specificity and positive predictive value of CCTA to identify thrombi is low though, as some patients have filling defects which are due to appendage filling issues rather than thrombus, and inter-observer variability is high [43–49]. Delayed CCTA images, allowing more time for left atrial appendage filling, may improve appendage filling [50]. Imaging in the prone position may decrease false positive results [51]. The left atrial appendage/ascending aorta Hounsfield Unit ratio is inversely related to the degree of spontaneous echo contrast and thrombus [52]. A left atrial appendage/ascending aorta Hounsfield Unit ratio of greater than 0.75 has shown 100% negative predictive value [47]. The use of CCTA to assess for atrial thrombus requires further investigation of imaging techniques and analysis criteria. Until further study, transesophageal echo will remain the gold-standard study for atrial thrombus assessment.

Thoracic anatomy relevant to ablation includes the relationship of the esophagus and aorta to the posterior left atrium and pulmonary veins (Figures 22.12 and 22.13). Left atrial-esophageal fistula has been reported as a fatal complication of atrial fibrillation ablation [53]. There is variability of the course of the esophagus and degree of contact between the posterior left atrium/pulmonary veins and the esophagus. The relationship between the posterior left atrium and the esophagus can be visualized prior to ablation. Barium swallow has also been used during CCTA to better visualize the esophagus [54–56]. Esophageal motility, change of the position of the esophagus with respiration, patient position, and timing of the CCTA in relation to the procedure can cause change in the spatial relationship of the esophagus to the posterior left atrium at the time of the ablation procedure. The relationship of the coronary vasculature to the left atrium is also important, especially

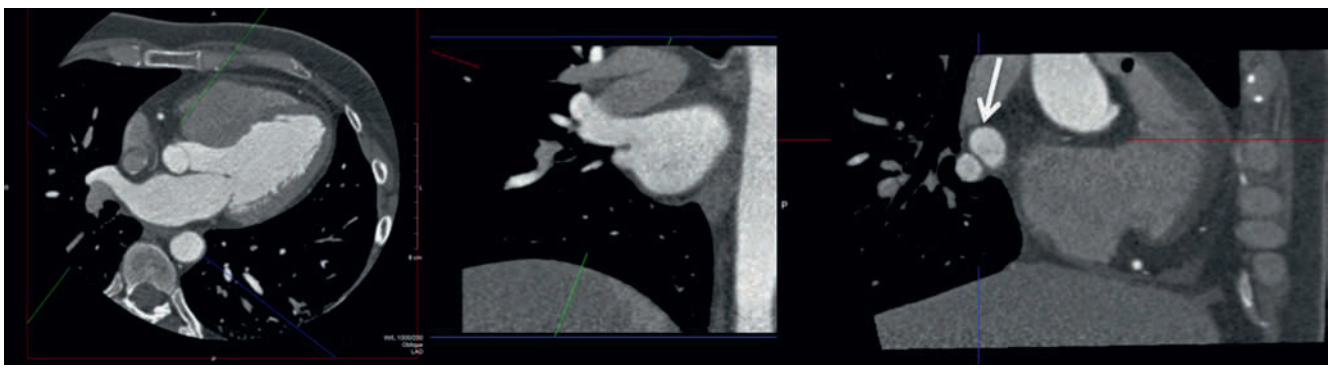

Figure 22.7. Identification the left atrial/pulmonary vein interface, determination of the long axis of the vein at the os, and en face visualization of an ovoid pulmonary vein os.

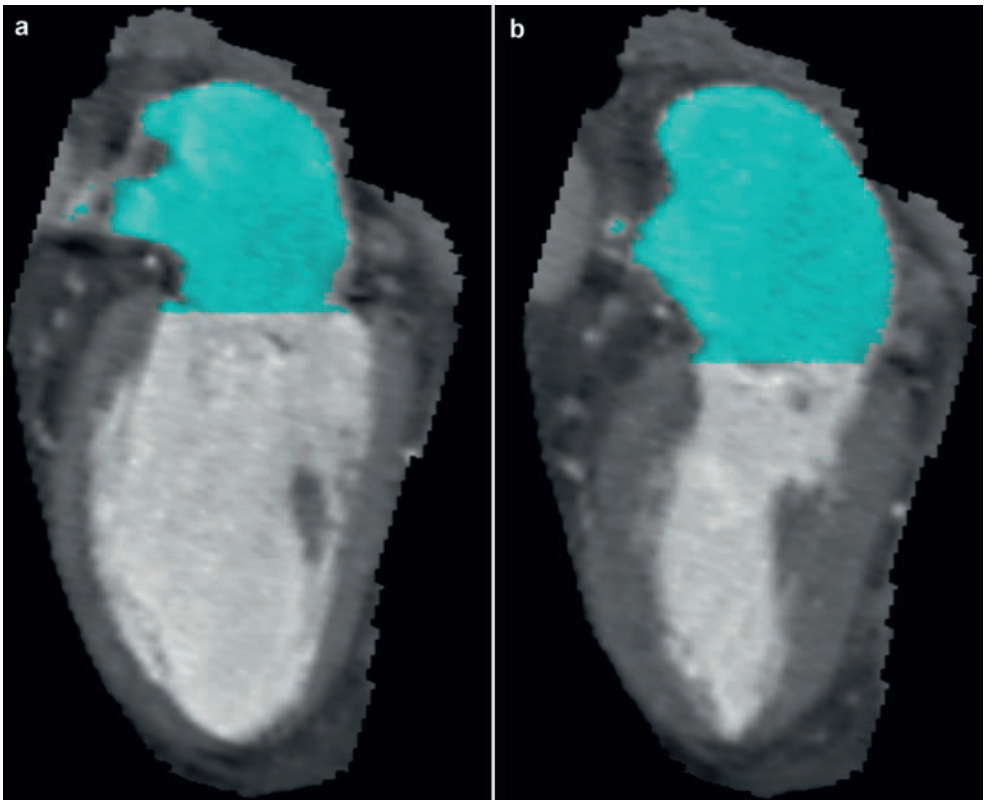

Figure 22.8. Assessment of left atrial volume during atrial systole (**a**) and diastole (**b**).

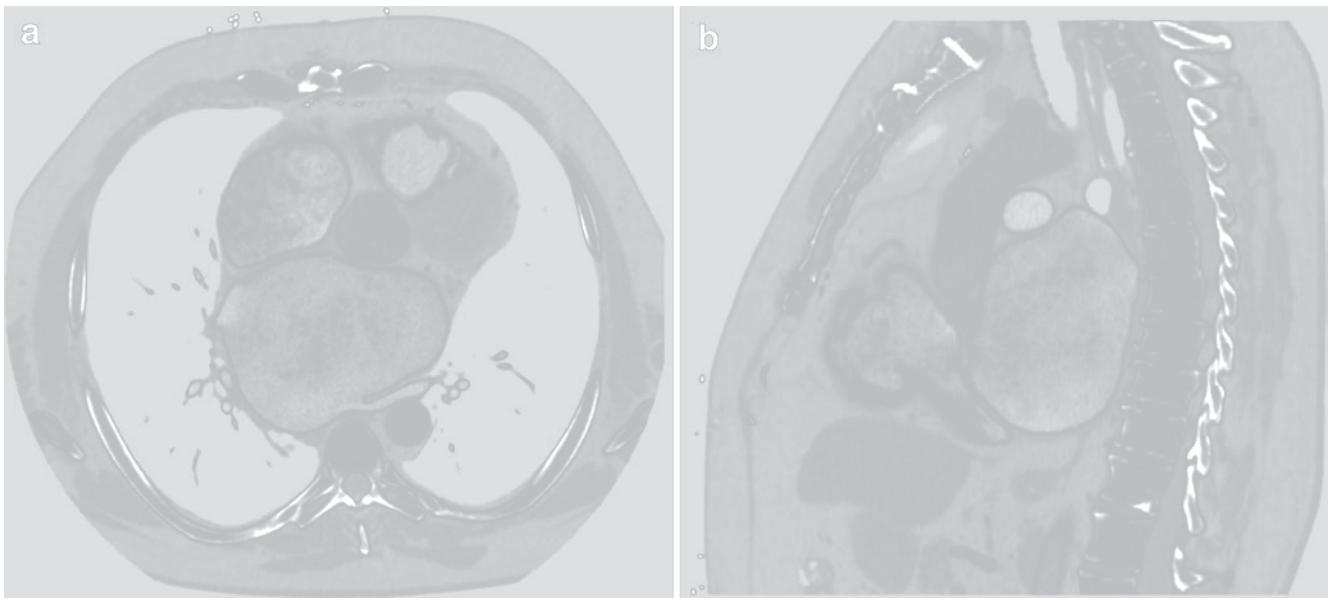

Figure 22.9. Axial (**a**) and sagittal (**b**) views demonstrating profound atrial enlargement in a patient with atrial fibrillation. The left atrial volume was greater than 450 cc.

the relationship between the coronary veins, circumflex coronary artery, and the posterior left atrium/AV groove in order to avoid coronary artery complications (Figure 22.14) [57]. Additionally, the relationship of the bronchi and pulmonary veins can be characterized by CCTA, and is important to avoid complications with ablation [58].

Electroanatomic mapping with CCTA image integration has revolutionized catheter-based therapies by allowing for electrical mapping and ablation to occur on a 3-D map of the patient's individual endocardial left atrial anatomy. The process involves importation of the unprocessed DICOM images into the electrophysiology mapping system, use of edge detection software to define cardiac vascular structures, and editing down to structures relevant to ablation including the left atrium and in some electrophysiology laboratories the aorta and esophagus (Figure 22.15). Subsequently, a separate catheter-based anatomic map is created using landmark points in the left atrium followed

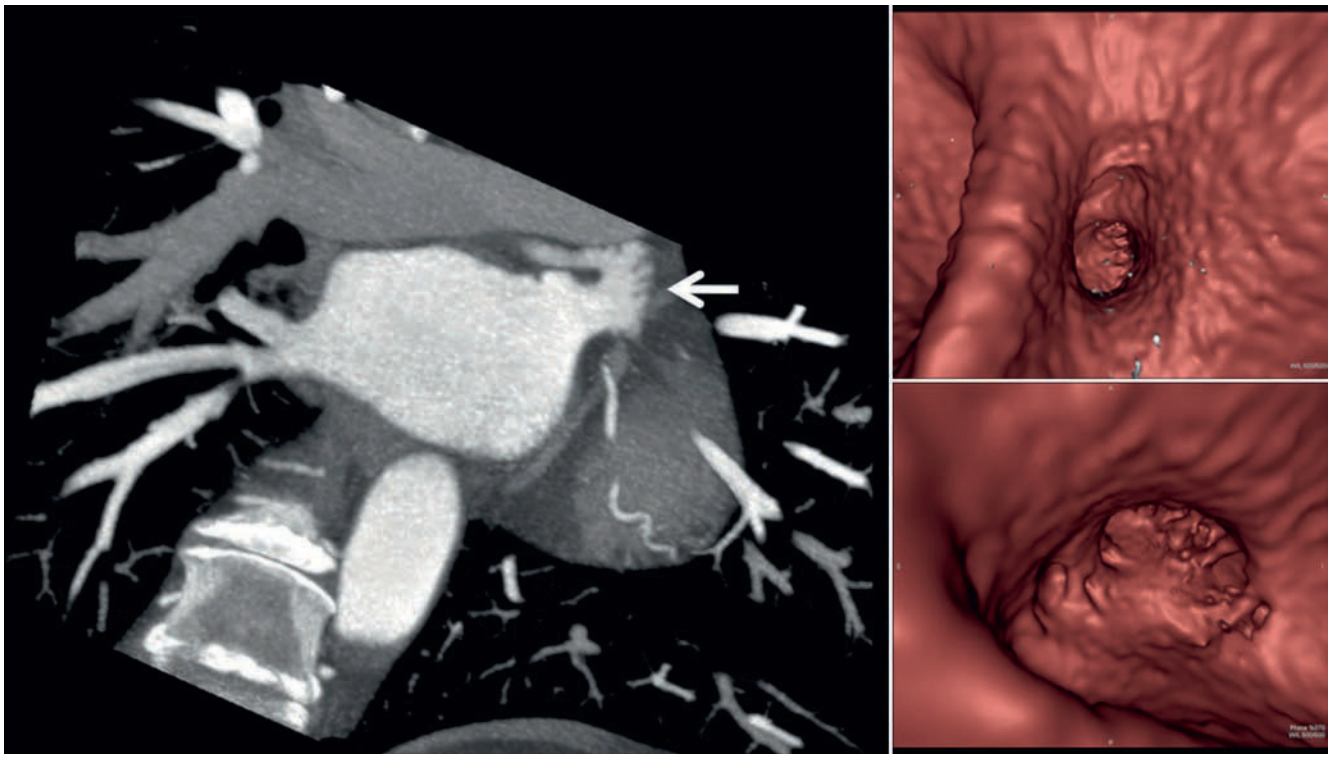

Figure 22.10. Double oblique 2-D view (*left panel*) showing the complex anatomy of the left atrial appendage with a multilobed tube-like structure with an intricate array of pectinate muscles (*arrow*). Endocardial views (*right panels*) show the relationship of the left atrial appendage os to the "coumadin ridge" and the appendage os shape.

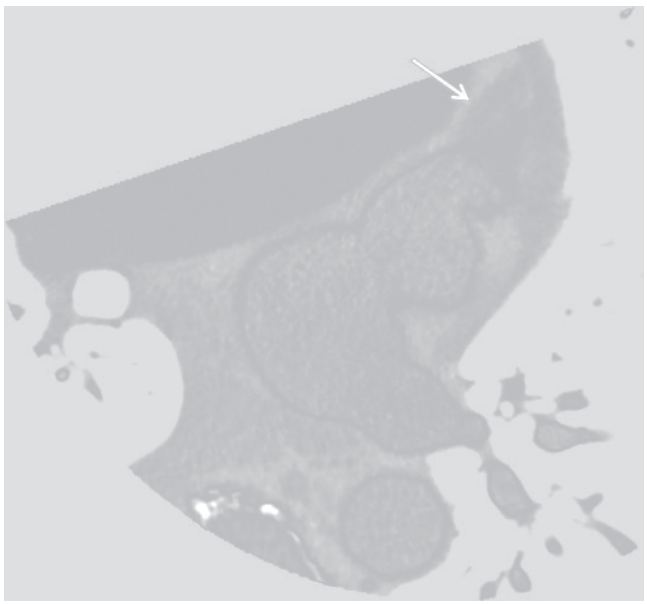

Figure 22.11. Double oblique 2-D view demonstrating a filling defect in the left atrial appendage with a differential diagnosis of incomplete filling of the appendage versus thrombus.

by registration of surface points defining the endocardium of the left atrium. This anatomic catheter-based map is then integrated with the CCTA images with assessment of markers of successful integration defined by an acceptable catheter to endocardium distance, which has been demonstrated to be feasible and accurate (Figure 22.16) [59, 60]. If registration is inadequate, catheter-based points are edited and new points registered to ensure that the atrial endocardial surface has been adequately mapped. Atrial size is important to integration techniques as greater misregisration occurs with larger atrial size [61].

Electroanatomic mapping with image integration allows mapping of arrhythmia electrical activation and propagation, definition of electrically silent areas, assessment of catheter position in the atrium, and documentation of radiofrequency applications on the 3-D CCTA reconstruction (Figures 22.17 and 22.18). The localization of the ablation catheter tip on this endocardial left atrial reconstruction helps to ensure that radiofrequency applications are placed in the atrium and not in the pulmonary veins or ostia to avoid pulmonary vein stenosis. Subsequent to ablation, mapping using this system can be performed to ensure electrical isolation of the pulmonary veins. Ablation guided by integration of preprocedure CCTA with real time catheter-based electroanatomic maps can increase the efficacy of and decrease complications associated with atrial fibrillation ablation. This technique has been shown to increase restoration of sinus rhythm and decrease recurrence of atrial fibrillation compared to electroanatomic mapping alone [62, 63].

Pulmonary vein stenosis is a potential complication of atrial fibrillation ablation (Figure 22.19) [64, 65]. The incidence of stenoses is dependent on technique, definition of significant stenosis, and degree of surveillance [66]. Pulmonary vein stenoses can occur when ablation lesions are applied directly to the pulmonary veins [67]; therefore, imaging technologies which can visualize the atrial/pulmonary

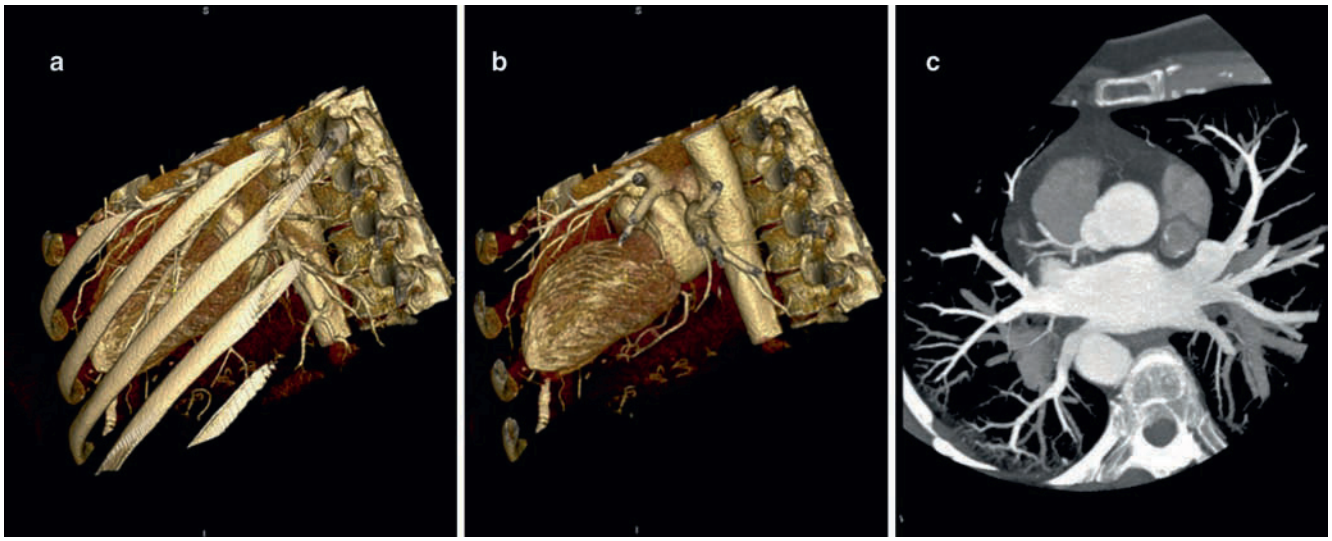

Figure 22.12. 3-D reconstructions (**a, b**) demonstrating the relationship of the aorta to the posterior left atrium and left lower pulmonary vein. A double oblique view (**c**) demonstrating the relationship of the esophagus and aorta to the posterior left atrium and pulmonary veins.

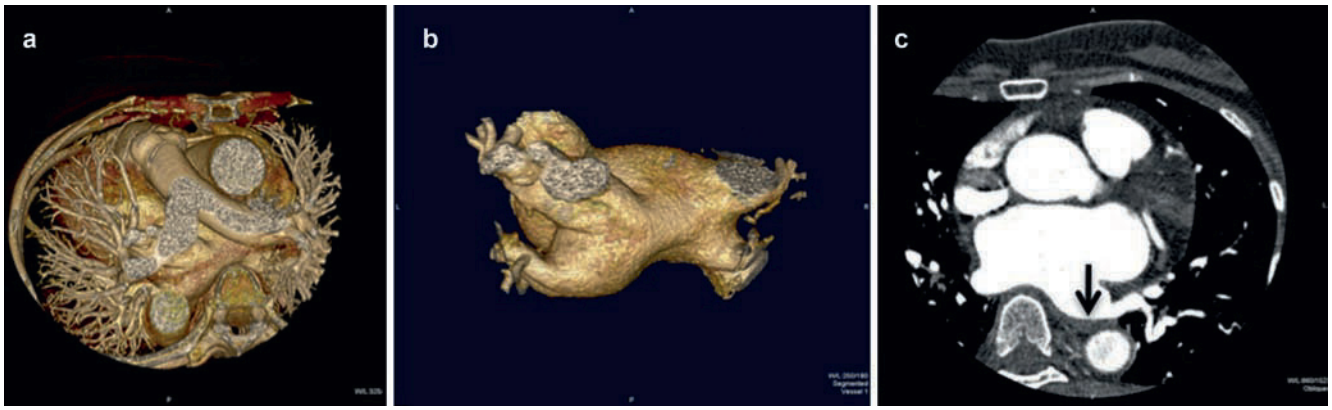

Figure 22.13. 3-D reconstructions (**a, b**) demonstrating the relationship of the aorta to the posterior left atrium and left lower pulmonary vein. A 2-D axial view (**c**) demonstrates the relationship of the esophagus and aorta to the posterior left atrium and pulmonary veins. In this case, the esophagus (*arrow*) is "sandwiched" between spine and aorta at the level of the left lower pulmonary vein.

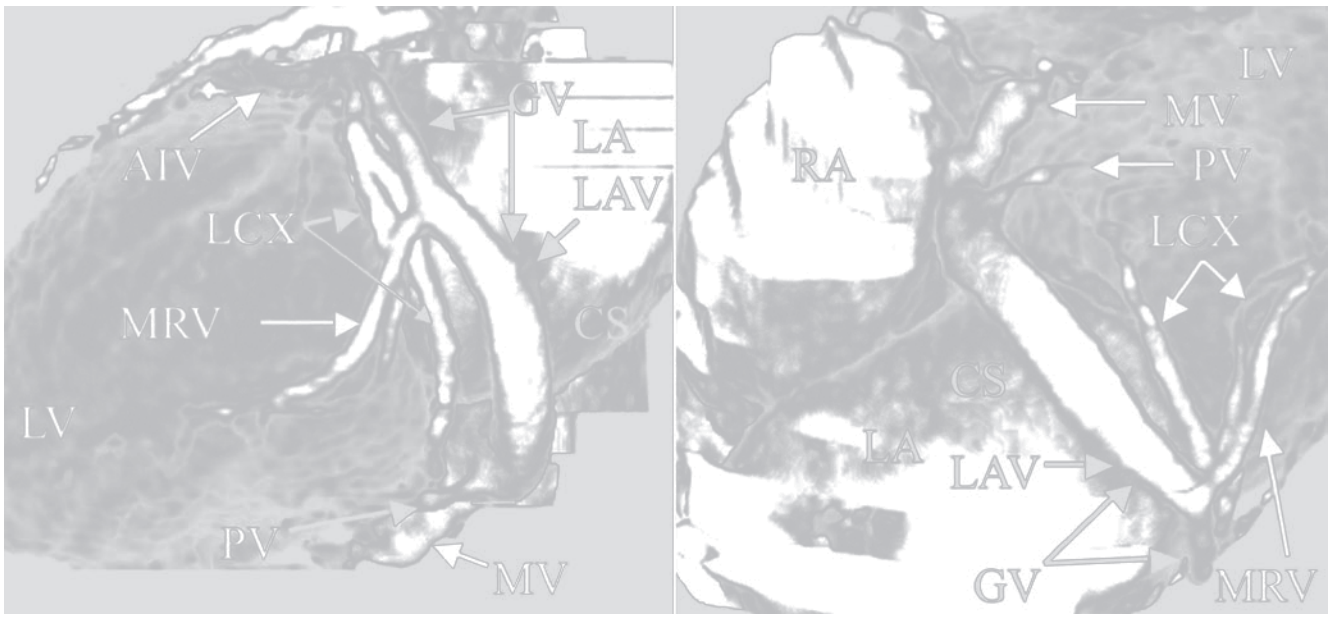

Figure 22.14. The left-lateral view (*left panel*) and diaphragmatic view (*right panel*) of the heart. The left circumflex coronary artery and coronary veins are clearly displayed. The great cardiac vein is seen overlying the left circumflex coronary artery for a short (<30 mm) segment. The marginal vein is dominant, and the posterior vein is small in size. *AIV* anterior interventricular vein; *CS* coronary sinus; *GV* great cardiac vein; *LA* left atrium; *LAV* left atrial vein; *LCX* left circumflex coronary artery; *LV* left ventricle; *MV* middle cardiac vein, *MRV* marginal vein, *PV* posterior vein (reprinted with permission of Elsevier from Mao et al [77].

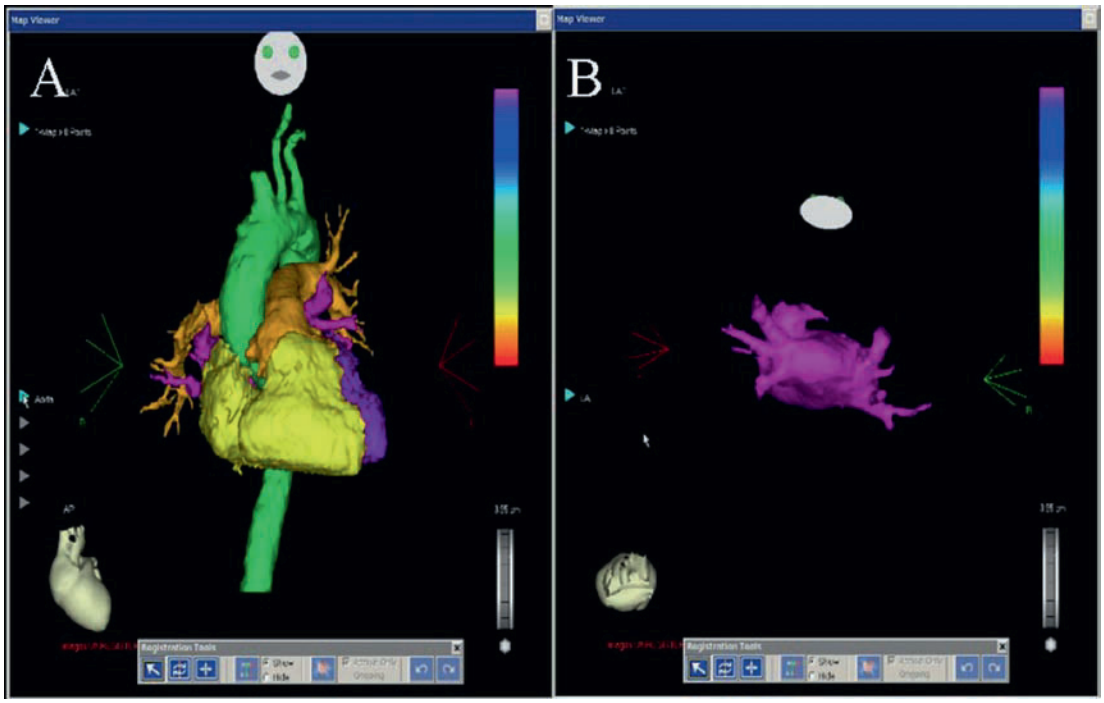

Figure 22.15. Initial image processing for electroanatomic mapping with CCTA image integration showing segmentation of vascular structures (**a**) with the aorta (*green*), pulmonary arteries (*orange*), right atrium and right ventricle (*yellow*) edited out, with the left atrium (*purple*) subsequently rotated to demonstrate the posterior left atrium (**b**).

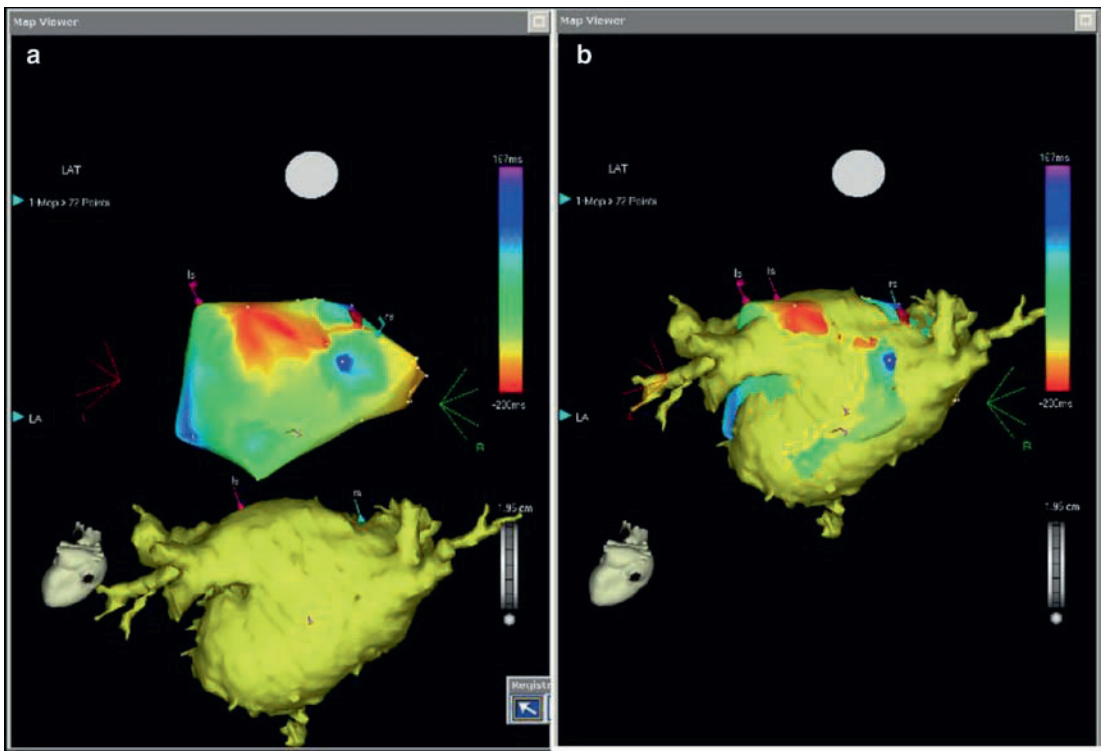

Figure 22.16. Image processing for electroanatomic mapping with CCTA image integration with a catheter-based anatomic map of the left atrium (**a**, *upper image*) and the 3-D volume rendered CT image of the left atrium (**a**, *lower image*) with integration of these images (**b**).

vein interface are important to applying ablation lesions within the atria rather than the pulmonary veins. CCTA integration with catheter-based mapping has also been shown to decrease the incidence of pulmonary vein stenosis [63]. The baseline preprocedure study can serve as a template for assessment of pulmonary vein stenosis and can identify pre-existing pulmonary vein stenoses due to other etiologies preventing misdiagnosis of ablation related stenosis [68].

Recurrence of atrial fibrillation or occurrence of atrial flutter can occur after atrial fibrillation ablation procedures. Achieving uninterrupted ablation lines around pulmonary veins and uninterrupted linear lesions within the

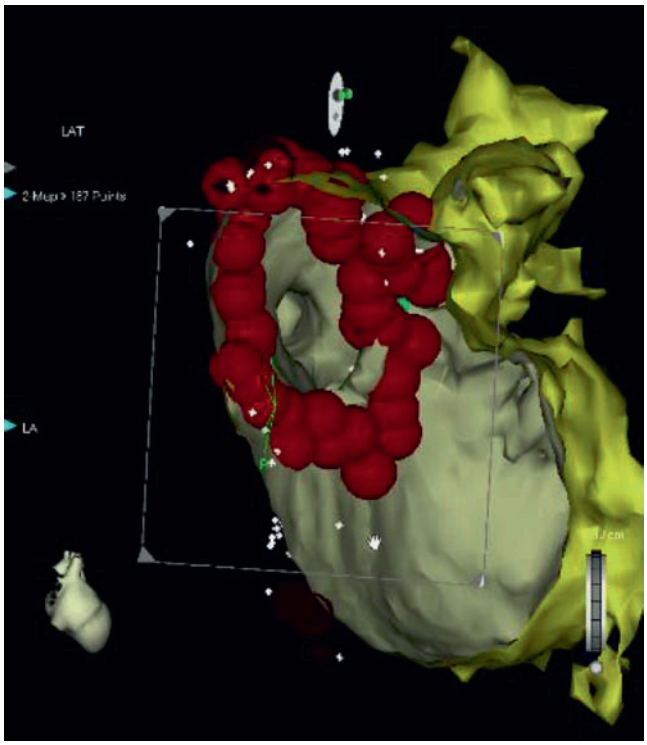

Figure 22.17. Electroanatomic mapping with image integration demonstrating an endocardial view of the left upper pulmonary vein after radiofrequency catheter isolation of the vein with encircling radiofrequency energy applications (*red spheres*).

atrium is important to the performance of atrial fibrillation ablation procedures, as gaps within these lesion lines can lead to unsuccessful isolation. Gaps within ablation lines can also serve as substrate for postablation left atrial flutter circuits, using the gap as a substrate for reentry [26, 69]. Image integration allows for registration of the position of ablation lesions, therefore facilitating creation of continuous ablation lines.

Although CCTA can identify the position of the esophagus in relation to the left atrium before ablation, additional techniques are used in the electrophysiology laboratory to help avoid the complication of atrial esophageal fistula. Integrated imaging can be used to identify the position of the esophagus during ablation [56]. Esophageal temperature probes and intracardiac echo can be used to help avoid esophageal complications such as atrial esophageal fistulas [70, 71]. CCTA or CMR image integration with catheter-based intracardiac maps can be additionally integrated with real time intracardiac echocardiography, providing real time visualization of the esophagus as well as visualization of transseptal puncture, appendage thrombi, ablation catheter contact and lesion depth, pulmonary vein stenosis, and pericardial effusion (Figures 22.20 and 22.21) [71–75]. Multimodal imaging with integration of CCTA images and real-time fluoroscopy is also being preliminarily investigated [76].

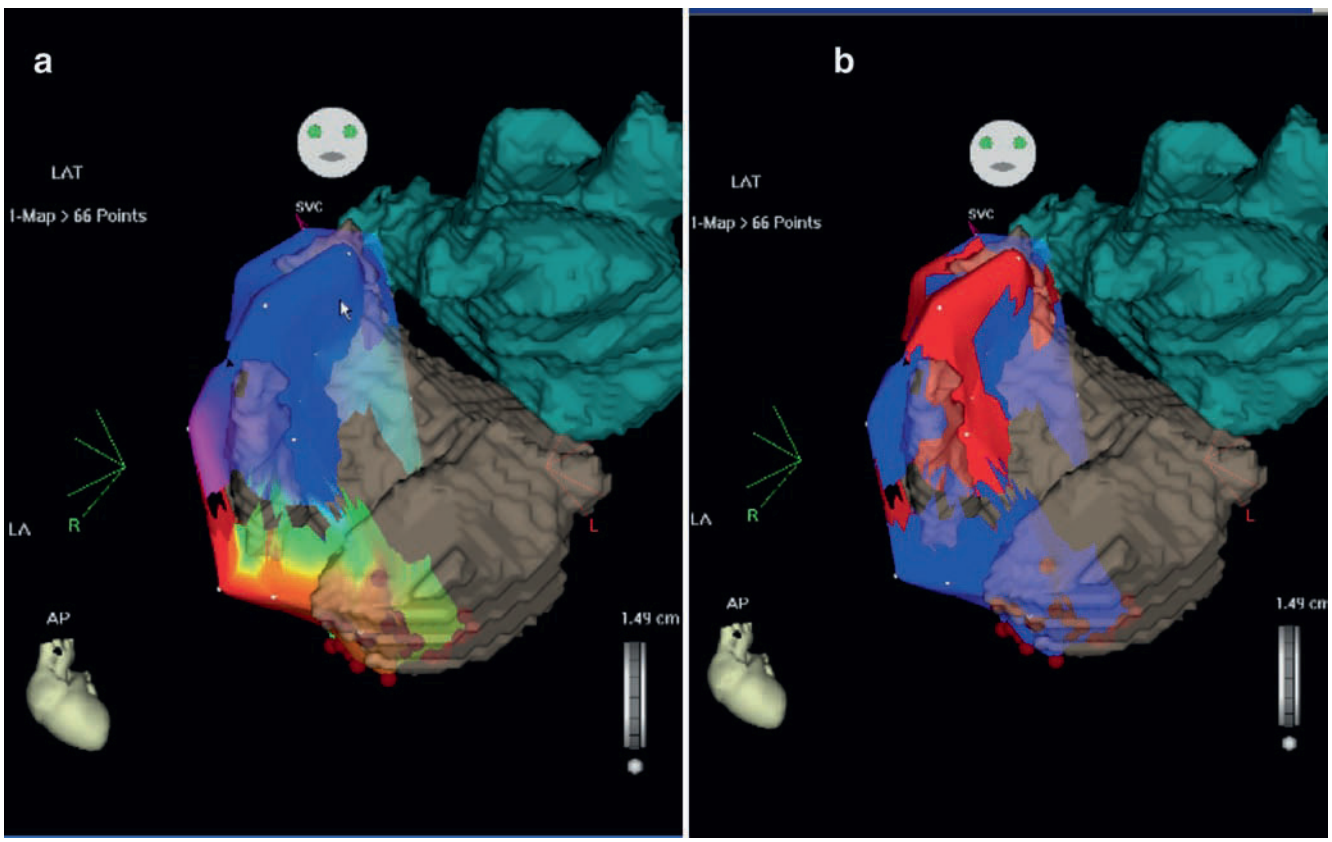

Figure 22.18. Electroanatomic mapping with image integration demonstrating mapping of arrhythmia electrical activation (**a**) and arrhythmia wavefront propogation (**b**).

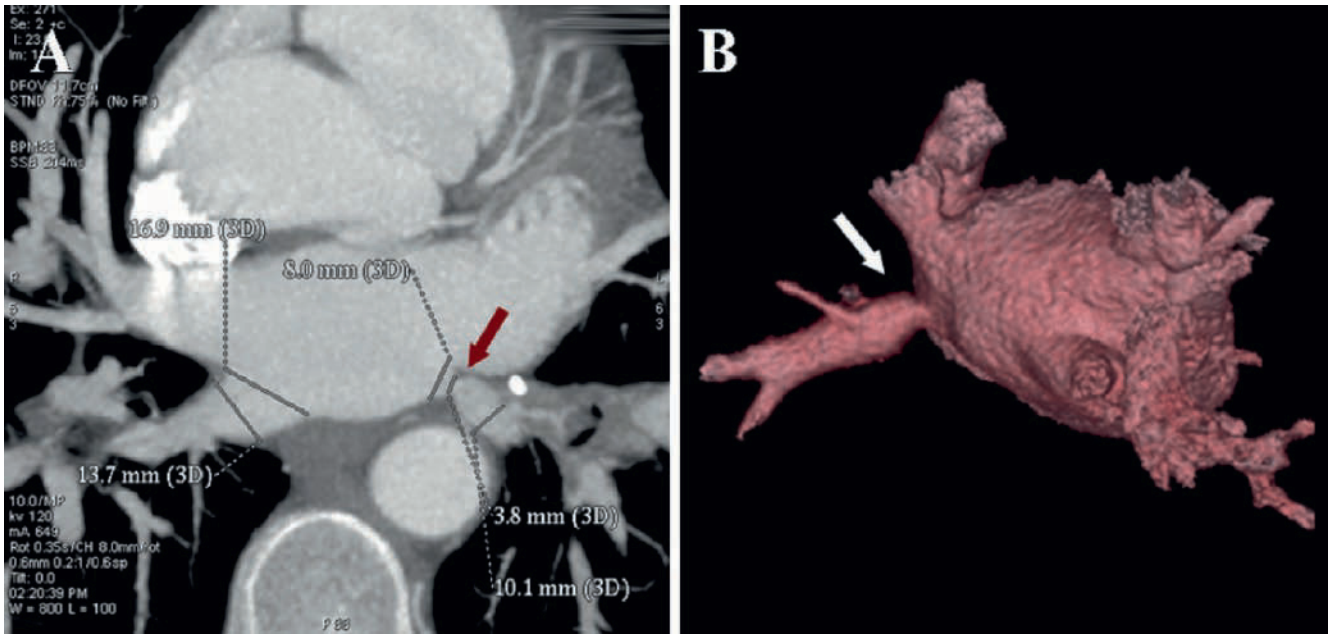

Figure 22.19. 2-D (**a**) and 3-D (**b**) volume rendered images demonstrating pulmonary vein stenosis of a left lower pulmonary vein (courtesy of Dr. Jeffrey Schussler, Baylor University Medical Center, Dallas, TX).

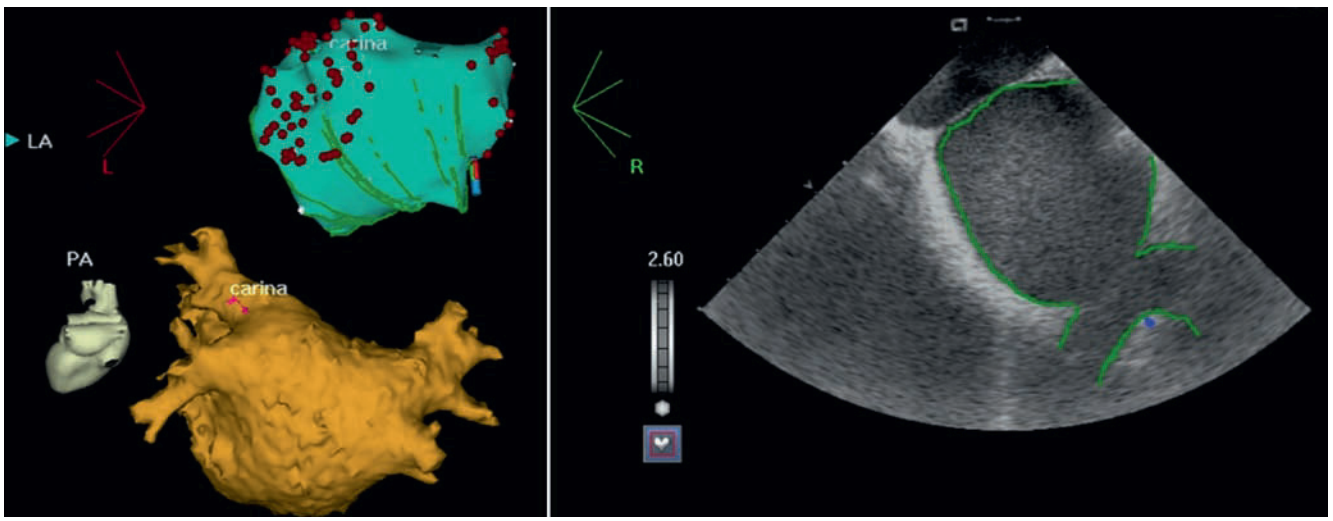

Figure 22.20. Components of electroanatomic mapping with CCTA and intracardiac echo image integration, with a catheter-based anatomic map (*upper left image*), CCTA (*lower left image*), and intracardiac echo (*right image*).

Cardiac Resynchronization Therapy

CCTA can visualize the coronary venous system and may potentially play an important role in the evolution of cardiac resynchronization therapy (CRT) (Figure 22.22) [77–79]. CRT is used to optimize cardiac function through resynchronization of ventricular contraction in patients with dilated ischemic and nonischemic cardiomyopathy, ventricular conduction abnormalities, and moderate to severe heart failure [80–82]. With CRT, a chronic pacing lead is placed in a branch vessel of the coronary venous system to achieve left ventricular pacing. As opposed to the right atrial and right ventricular leads, which can be actively fixated in many positions in their respective chambers, placement of the coronary venous lead can be challenging, as lead position is limited by the individual confines and variation of the existing coronary venous anatomy.

Coronary venous imaging can provide roadmaps for CRT coronary venous lead placement, with potential avoidance of a percutaneous approach in the setting of inadequate coronary venous anatomy. CCTA can provide detailed assessment of the coronary venous anatomy, with coronary sinus diameter, branch vessel 3-D location relative to the left ventricle, branch vessel diameter, and branch vessel angulation off of the coronary sinus/great cardiac vein (Figure 22.23) [77]. CCTA can also visualize structures which could limit access

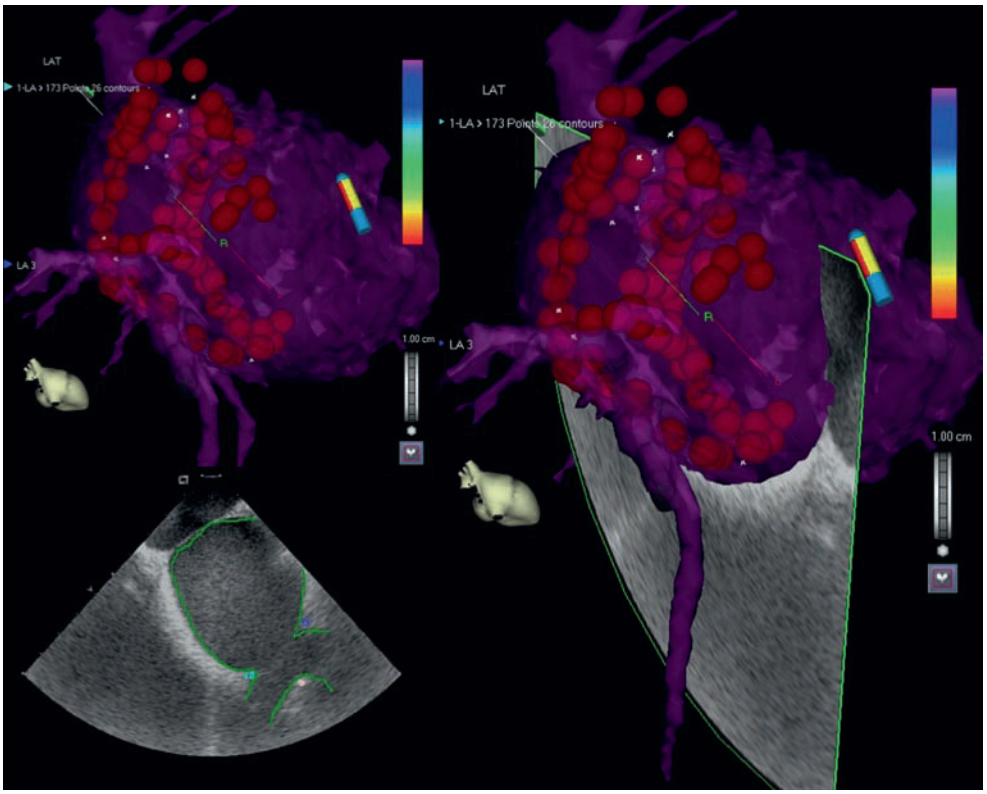

Figure 22.21. Electroanatomic mapping with CCTA and intracardiac echo image integration demonstrating an endocardial view after radiofrequency catheter pulmonary vein isolation with encircling radiofrequency energy applications (*red spheres*).

Figure 22.22. 3-D volume rendered image demonstrating visualization of the coronary venous system including the coronary sinus (*double white arrow*), a middle cardiac vein (*black arrow*), and a posterolateral vein (*single white arrow*).

to the coronary venous system, such as a prominent Thebesian valve covering the coronary sinus os (Figure 22.24) [83]. Other abnormalities, such as coronary sinus diverticula (Figure 22.25) and a left superior vena cava to coronary sinus connection (Figure 22.26), can be identified. Visualization of the phrenic nerve and its relation to the coronary venous anatomy may be important to the avoidance of diaphragmatic pacing (Figure 22.27) [84]. In cases where the coronary venous anatomy is not amenable to a venous approach to left ventricular lead placement, CCTA can facilitate planning of approach to epicardial lead placement (Figure 22.28).

Further research is required to assess the use of CCTA images comprehensively for facilitation of CRT. Preliminary data suggest that preprocedure knowledge of the 3-D coronary venous anatomy can facilitate procedures through decreased procedure time and utilization of guide catheters [85]. The assessment of correlation between CCTA visualized sites of coronary venous branch veins and echo derived area of latest mechanical activation has been associated with acute response to CRT, with lack of response associated with disparity in location between these sites [86].

The CMR literature has shown that the amount of and location of myocardial infarct scar visualized with CMR delayed gadolinium enhancement imaging is important to CRT response. The percent total scar predicted response to CRT, with greater response in patients with less than 15% percent total scar and poor response in patients with posterolateral scar [87–89]. Delayed contrast enhancement imaging of myocardial infarction has been performed with CCTA, but requires further study regarding optimal image acquisition analysis [90–94]. Comprehensive analysis of factors important to response to CRT including coronary venous anatomy, 3-D global and regional ventricular function, and delayed enhancement requires further assessment for CRT planning and facilitation to maximize CRT response.

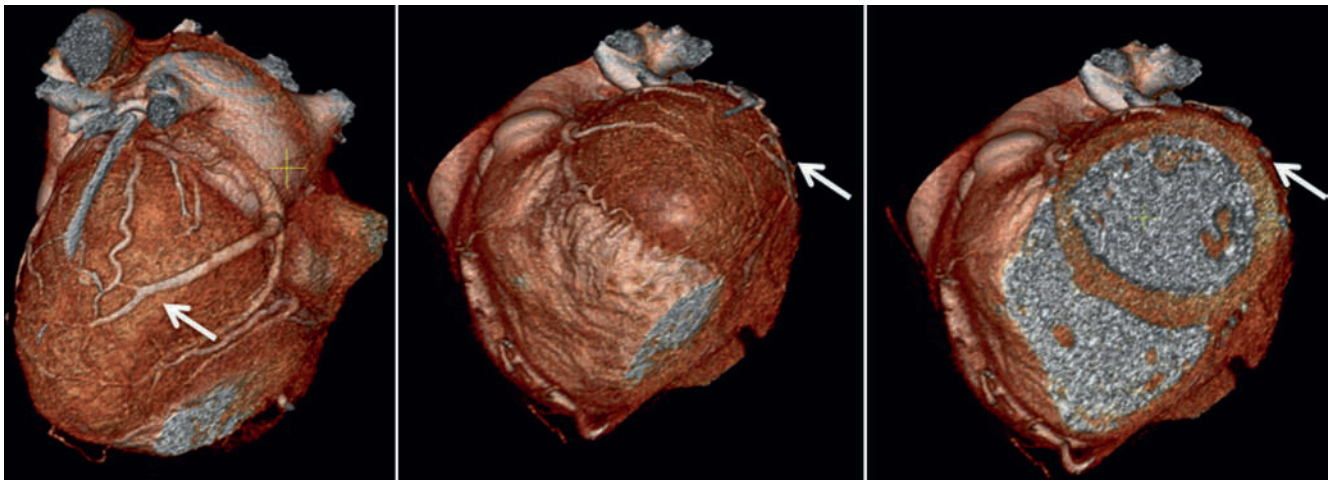

Figure 22.23. CCTA 3-D views demonstrating localization of the myocardial segment associated with the distal portion of the posterolateral vein.

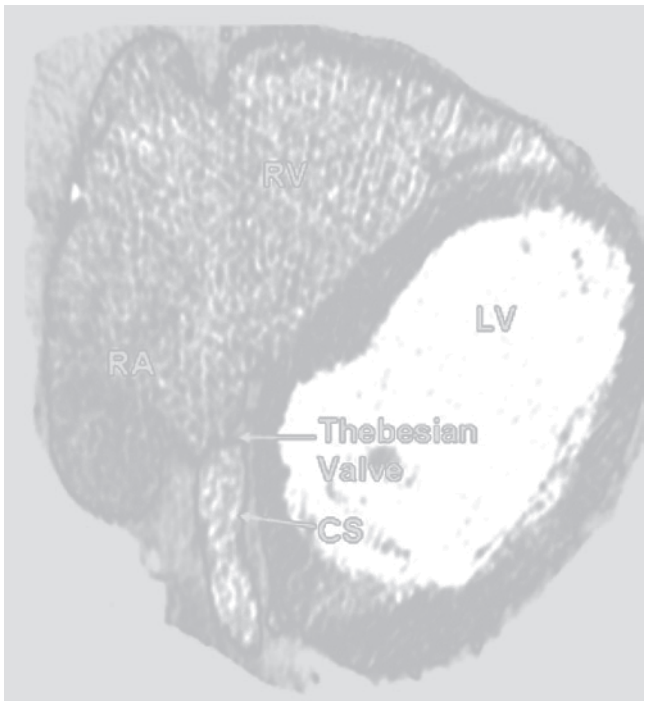

Figure 22.24. Axial images at the coronary sinus os level demonstrating a prominent Thebesian valve. *CS* coronary sinus; *RA* right atrium; *RV* right ventricle; *LV* left ventricle (reprinted with permission of John Wiley and Sons from Shinbane et al [83]).

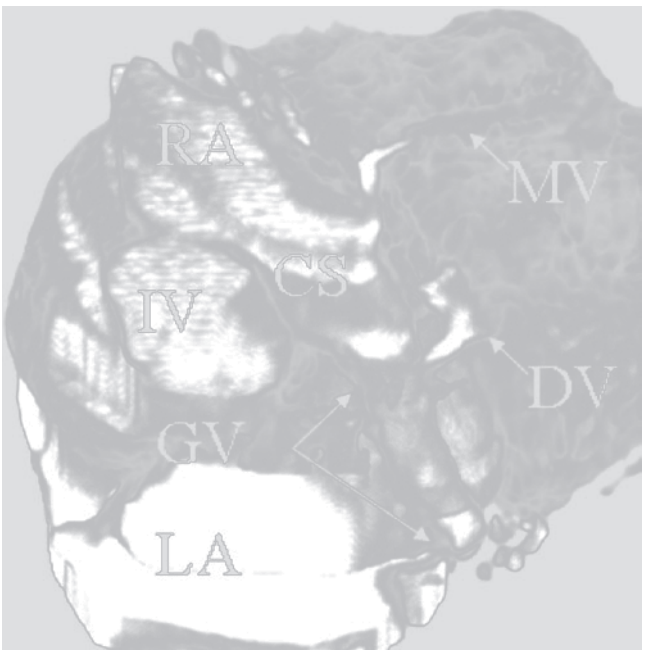

Figure 22.25. CCTA demonstrating a coronary sinus diverticulum (*arrow*). *CS* coronary sinus; *DV* diverticulum; *GV* great cardiac vein; *IV* inferior vena cava; *LA* left atrium; *MV* marginal vein; *RA* right atrium.

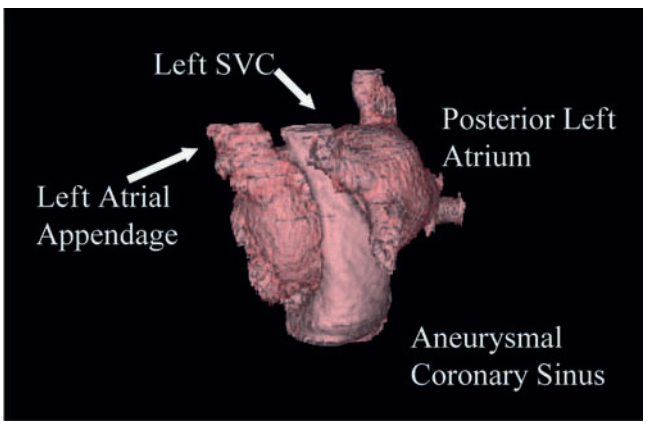

Figure 22.26. 3-D volume rendered view demonstrating a left superior vena cava with connection to an aneurysmal coronary sinus. A right-sided superior vena cava was not present.

Summary

CCTA provides comprehensive assessment important to the diagnosis and treatment of electrophysiologically-relevant cardiovascular disease. The ability to rapidly analyze cardiovascular structures relevant to cardiac electrophysiology as well as use of image sets to facilitate ablation and device procedures has advanced the field of cardiac electrophysiology. The role of advanced cardiac imaging in the diagnosis and treatment of electrophysiologic disease will continue to expand, with a greater spectrum of applications related to identification of arrhythmogenic substrates and the mapping and ablation of a greater spectrum of arrhythmias.

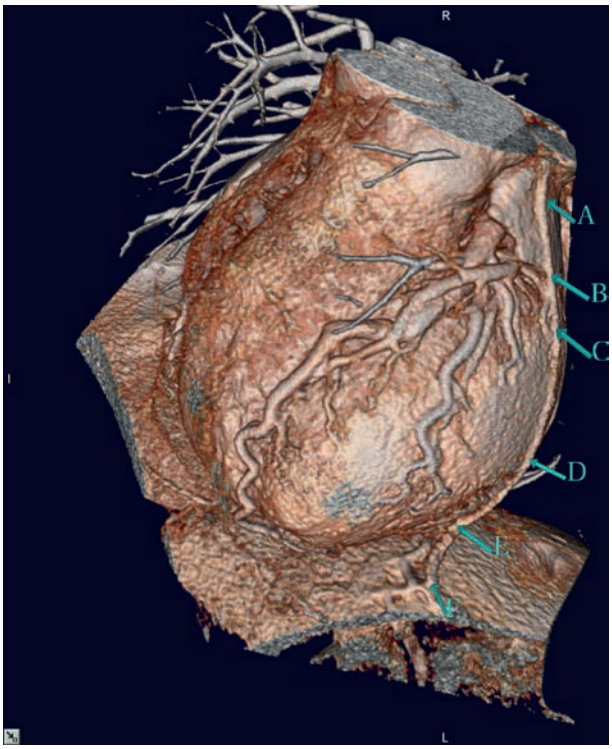

Figure 22.27. 3-D volume rendered image showing visualization of the course (**a–e**) of the left phrenic nerve (reprinted with permission of Elsevier from Matsumoto et al [84]).

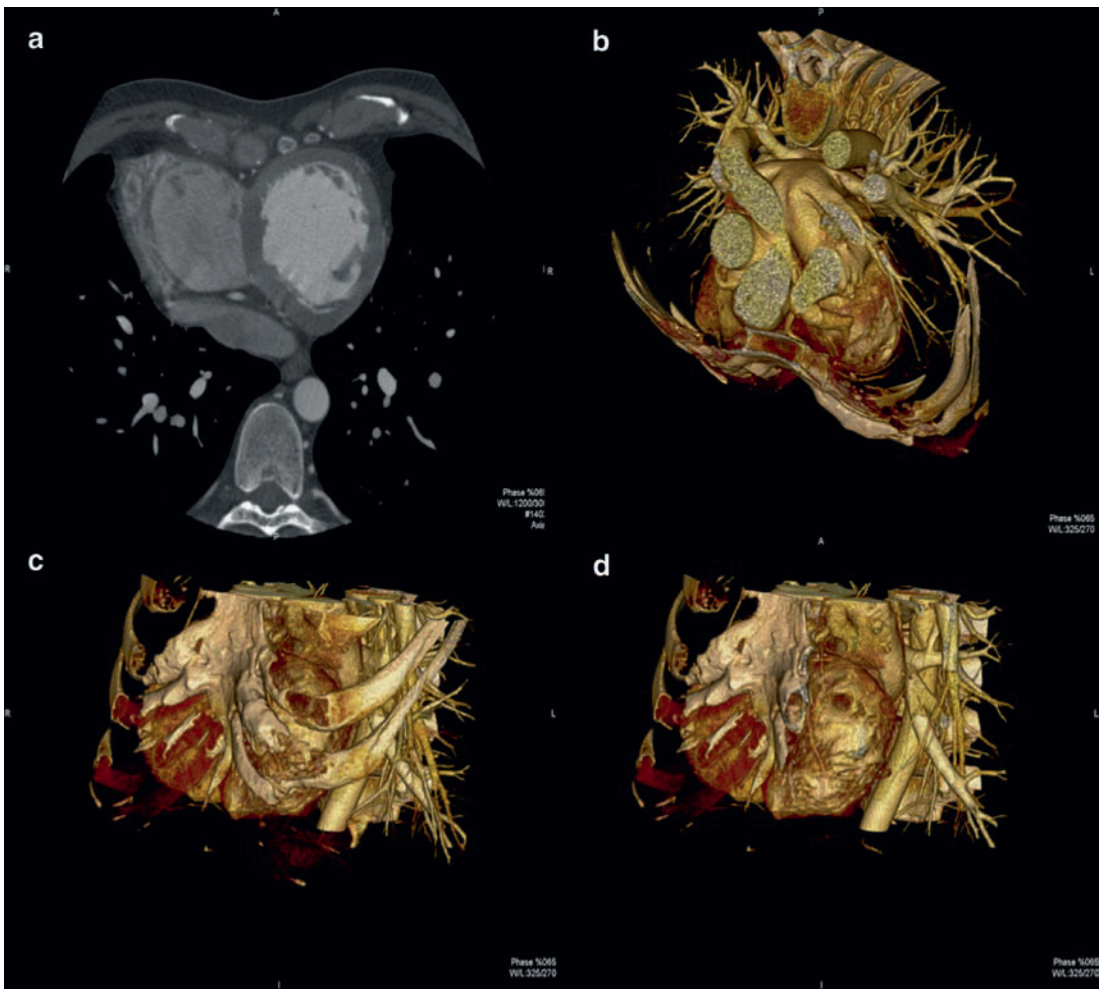

Figure 22.28. 2-D (**a**) and 3-D (**b–d**) views demonstrating anterior rotation of the left ventricle and relation to skeletal structures useful to planning a minimally invasive approach to epicardial left ventricular lead placement in a patient with coronary venous anatomy not amenable to a percutaneous approach to cardiac resynchronization therapy.

References

1. Matsutani H, Sano T, Kondo T, et al. ECG-edit function in multidetector-row computed tomography coronary arteriography for patients with arrhythmias. *Circ J*. 2008;72(7):1071–1078.
2. Duran C, Kantarci M, Durur Subasi I, et al. Remarkable anatomic anomalies of coronary arteries and their clinical importance: a multidetector computed tomography angiographic study. *J Comput Assist Tomogr*. 2006;30(6):939–948.
3. Shabestari AA, Abdi S, Akhlaghpoor S, et al. Diagnostic performance of 64-channel multislice computed tomography in assessment of significant coronary artery disease in symptomatic subjects. *Am J Cardiol*. 2007;99(12):1656–1661.
4. Schuijf JD, Pundziute G, Jukema JW, et al. Diagnostic accuracy of 64-slice multislice computed tomography in the noninvasive evaluation of significant coronary artery disease. *Am J Cardiol*. 2006;98(2):145–148.
5. Ropers D, Rixe J, Anders K, et al. Usefulness of multidetector row spiral computed tomography with 64- x 0.6-mm collimation and 330-ms rotation for the noninvasive detection of significant coronary artery stenoses. *Am J Cardiol*. 2006;97(3):343–348.
6. Laissy JP, Messika-Zeitoun D, Serfaty JM, et al. Comprehensive evaluation of preoperative patients with aortic valve stenosis. Usefulness of multi-detector cardiac computed tomography. *Heart*. 2007;93(9):1121–1125.
7. Shiga T, Wajima Z, Apfel CC, Inoue T, Ohe Y. Diagnostic accuracy of transesophageal echocardiography, helical computed tomography, and magnetic resonance imaging for suspected thoracic aortic dissection: systematic review and meta-analysis. *Arch Intern Med*. 2006;166(13):1350–1356.
8. Kim TH, Ryu YH, Hur J, et al. Evaluation of right ventricular volume and mass using retrospective ECG-gated cardiac multidetector computed tomography: comparison with first-pass radionuclide angiography. *Eur Radiol*. 2005;15(9):1987–1993.
9. Butler J, Shapiro MD, Jassal DS, et al. Comparison of multidetector computed tomography and two-dimensional transthoracic echocardiography for left ventricular assessment in patients with heart failure. *Am J Cardiol*. 2007;99(2):247–249.
10. Cornily JC, Gilard M, Le Gal G, et al. Accuracy of 16-detector multislice spiral computed tomography in the initial evaluation of dilated cardiomyopathy. *Eur J Radiol*. 2007;61(1):84–90.
11. Andreini D, Pontone G, Pepi M, et al. Diagnostic accuracy of multidetector computed tomography coronary angiography in patients with dilated cardiomyopathy. *J Am Coll Cardiol*. 2007;49(20):2044–2050.
12. Shiozaki AA, Santos TS, Artega E, Rochitte CE. Images in cardiovascular medicine. Myocardial delayed enhancement by computed tomography in hypertrophic cardiomyopathy. *Circulation*. 2007;115(17):e430–e431.
13. Bomma C, Dalal D, Tandri H, et al. Evolving role of multidetector computed tomography in evaluation of arrhythmogenic right ventricular dysplasia/cardiomyopathy. *Am J Cardiol*. 2007;100(1):99–105.
14. Hamamichi Y, Ichida F, Hashimoto I, et al. Isolated noncompaction of the ventricular myocardium: ultrafast computed tomography and magnetic resonance imaging. *Int J Cardiovasc Imaging*. 2001;17(4):305–314.
15. Mohrs OK, Magedanz A, Schlosser T. Noncompaction of the left ventricular myocardium detected by 64-slice multidetector computed tomography. *Clin Cardiol*. 2007;30(1):48.
16. Kirsch J, Williamson EE, Araoz PA. Non-compaction visualization using ECG-gated dual-source CT. *Int J Cardiol*. 2007;118(2):e46–e47.
17. Ito H, Dajani KA. A case with noncompaction of the left ventricular myocardium detected by 64-slice multidetector computed tomography. *J Thorac Imaging*. 2009;24(1):38–40.
18. McKenna WJ, Thiene G, Nava A, et al. Diagnosis of arrhythmogenic right ventricular dysplasia/cardiomyopathy. Task Force of the Working Group Myocardial and Pericardial Disease of the European Society of Cardiology and of the Scientific Council on Cardiomyopathies of the International Society and Federation of Cardiology. *Br Heart J*. 1994;71(3):215–218.
19. Kimura F, Sakai F, Sakomura Y, et al. Helical CT features of arrhythmogenic right ventricular cardiomyopathy. *Radiographics*. 2002;22(5):1111–1124.
20. Wu YW, Tadamura E, Kanao S, et al. Structural and functional assessment of arrhythmogenic right ventricular dysplasia/cardiomyopathy by multi-slice computed tomography: comparison with cardiovascular magnetic resonance. *Int J Cardiol*. 2007;115(3):e118–e121.
21. Soh EK, Villines TC, Feuerstein IM. Sixty-four-multislice computed tomography in a patient with arrhythmogenic right ventricular dysplasia. *J Cardiovasc Comput Tomogr*. 2008;2(3):191–192.
22. Omichi C, Sugiyabu Y, Kakizawa Y, Endo M. Three-dimensional image of arrhythmogenic right ventricular dysplasia/cardiomyopathy reconstructed with 64-multislice computed tomography. *Heart Rhythm*. 2008;5(11):1631–1632.
23. Matsuo S, Sato Y, Nakae I, et al. Left ventricular involvement in arrhythmogenic right ventricular cardiomyopathy demonstrated by multidetector-row computed tomography. *Int J Cardiol*. 2007;115(3):e129–e131.
24. Haissaguerre M, Jais P, Shah DC, et al. Spontaneous initiation of atrial fibrillation by ectopic beats originating in the pulmonary veins. *N Engl J Med*. 1998;339(10):659–666.
25. Marine JE, Dong J, Calkins H. Catheter ablation therapy for atrial fibrillation. *Prog Cardiovasc Dis*. 2005;48(3):178–192.
26. Haissaguerre M, Hocini M, Sanders P, et al. Catheter ablation of long-lasting persistent atrial fibrillation: clinical outcome and mechanisms of subsequent arrhythmias. *J Cardiovasc Electrophysiol*. 2005;16(11):1138–1147.
27. Tamborero D, Mont L, Molina I, et al. Selective segmental ostial ablation and circumferential pulmonary veins ablation. Results of an individualized strategy to cure refractory atrial fibrillation. *J Interv Card Electrophysiol*. 2007;19(1):19–27.
28. Oral H, Pappone C, Chugh A, et al. Circumferential pulmonary-vein ablation for chronic atrial fibrillation. *N Engl J Med*. 2006;354(9):934–941.
29. Schwartzman D, Bazaz R, Nosbisch J. Catheter ablation to suppress atrial fibrillation: evolution of technique at a single center. *J Interv Card Electrophysiol*. 2003;9(2):295–300.
30. Scharf C, Sneider M, Case I, et al. Anatomy of the pulmonary veins in patients with atrial fibrillation and effects of segmental ostial ablation analyzed by computed tomography. *J Cardiovasc Electrophysiol*. 2003;14(2):150–155.
31. Wood MA, Wittkamp M, Henry D, et al. A comparison of pulmonary vein ostial anatomy by computerized tomography, echocardiography, and venography in patients with atrial fibrillation having radiofrequency catheter ablation. *Am J Cardiol*. 2004;93(1):49–53.
32. Jongbloed MR, Dirksen MS, Bax JJ, et al. Atrial fibrillation: multidetector row CT of pulmonary vein anatomy prior to radiofrequency catheter ablation–initial experience. *Radiology*. 2005;234(3):702–709.
33. Kaseno K, Tada H, Koyama K, et al. Prevalence and characterization of pulmonary vein variants in patients with atrial fibrillation determined using 3-dimensional computed tomography. *Am J Cardiol*. 2008;101(11):1638–1642.
34. Helms AS, West JJ, Patel A, et al. Relation of left atrial volume from three-dimensional computed tomography to atrial fibrillation recurrence following ablation. *Am J Cardiol*. 2009;103(7):989–993.
35. Stolzmann P, Scheffel H, Leschka S, et al. Reference values for quantitative left ventricular and left atrial measurements in cardiac computed tomography. *Eur Radiol*. 2008;18(8):1625–1634.
36. Hof I, Arbab-Zadeh A, Scherr D, et al. Correlation of left atrial diameter by echocardiography and left atrial volume by computed tomography. *J Cardiovasc Electrophysiol*. 2009;20(2):159–163.
37. Christiaens L, Lequeux B, Ardilouze P, et al. A new method for measurement of left atrial volumes using 64-slice spiral computed tomography: comparison with two-dimensional echocardiographic techniques. *Int J Cardiol*. 2009;131(2):217–224.
38. Mahabadi AA, Samy B, Seneviratne SK, et al. Quantitative assessment of left atrial volume by electrocardiographic-gated contrast-enhanced multidetector computed tomography. *J Cardiovasc Comput Tomogr*. 2009;3(2):80–87.

39. Wissner E, Wellnitz CV, Srivathsan K, Scott LR, Altemose GT. Value of multislice computed tomography angiography of the thorax in preparation for catheter ablation for the treatment of atrial fibrillation: the impact of unexpected cardiac and extracardiac findings on patient care. *Eur J Radiol*. 2008;72(2):284–288.
40. Shinbane JS. Cardiovascular computed tomographic angiography in patients with atrial fibrillation: challenges of anatomy, physiology, and electrophysiology. *J Cardiovasc Comput Tomogr*. 2008;2(3):181–182.
41. Garcia MJ. Detection of left atrial appendage thrombus by cardiac computed tomography: a word of caution. *JACC Cardiovasc Imaging*. 2009;2(1):77–79.
42. Saremi F, Channual S, Gurudevan SV, Narula J, Abolhoda A. Prevalence of left atrial appendage pseudothrombus filling defects in patients with atrial fibrillation undergoing coronary computed tomography angiography. *J Cardiovasc Comput Tomogr*. 2008;2(3):164–171.
43. Martinez MW, Kirsch J, Williamson EE, et al. Utility of nongated multidetector computed tomography for detection of left atrial thrombus in patients undergoing catheter ablation of atrial fibrillation. *JACC Cardiovasc Imaging*. 2009;2(1):69–76.
44. Achenbach S, Sacher D, Ropers D, et al. Electron beam computed tomography for the detection of left atrial thrombi in patients with atrial fibrillation. *Heart*. 2004;90(12):1477–1478.
45. Shapiro MD, Neilan TG, Jassal DS, et al. Multidetector computed tomography for the detection of left atrial appendage thrombus: a comparative study with transesophageal echocardiography. *J Comput Assist Tomogr*. 2007;31(6):905–909.
46. Hur J, Kim YJ, Nam JE, et al. Thrombus in the left atrial appendage in stroke patients: detection with cardiac CT angiography–a preliminary report. *Radiology*. 2008;249(1):81–87.
47. Patel A, Au E, Donegan K, et al. Multidetector row computed tomography for identification of left atrial appendage filling defects in patients undergoing pulmonary vein isolation for treatment of atrial fibrillation: comparison with transesophageal echocardiography. *Heart Rhythm*. 2008;5(2):253–260.
48. Tang RB, Dong JZ, Zhang ZQ, et al. Comparison of contrast enhanced 64-slice computed tomography and transesophageal echocardiography in detection of left atrial thrombus in patients with atrial fibrillation. *J Interv Card Electrophysiol*. 2008;22(3):199–203.
49. Gottlieb I, Pinheiro A, Brinker JA, et al. Diagnostic accuracy of arterial phase 64-slice multidetector CT angiography for left atrial appendage thrombus in patients undergoing atrial fibrillation ablation. *J Cardiovasc Electrophysiol*. 2008;19(3):247–251.
50. Hur J, Kim YJ, Lee HJ, et al. Left atrial appendage thrombi in stroke patients: detection with two-phase cardiac CT angiography versus transesophageal echocardiography. *Radiology*. 2009;251(3):683–690.
51. Tani T, Yamakami S, Matsushita T, et al. Usefulness of electron beam tomography in the prone position for detecting atrial thrombi in chronic atrial fibrillation. *J Comput Assist Tomogr*. 2003;27(1):78–84.
52. Kim YY, Klein AL, Halliburton SS, et al. Left atrial appendage filling defects identified by multidetector computed tomography in patients undergoing radiofrequency pulmonary vein antral isolation: a comparison with transesophageal echocardiography. *Am Heart J*. 2007;154(6):1199–1205.
53. Pappone C, Oral H, Santinelli V, et al. Atrio-esophageal fistula as a complication of percutaneous transcatheter ablation of atrial fibrillation. *Circulation*. 2004;109:2724–2726.
54. Lemola K, Sneider M, Desjardins B, et al. Computed tomographic analysis of the anatomy of the left atrium and the esophagus. Implications for left atrial catheter ablation. *Circulation*. 2004;110:3655–3660.
55. Cury RC, Abbara S, Schmidt S, et al. Relationship of the esophagus and aorta to the left atrium and pulmonary veins: implications for catheter ablation of atrial fibrillation. *Heart Rhythm*. 2005;2(12):1317–1323.
56. Piorkowski C, Hindricks G, Schreiber D, et al. Electroanatomic reconstruction of the left atrium, pulmonary veins, and esophagus compared with the "true anatomy" on multislice computed tomography in patients undergoing catheter ablation of atrial fibrillation. *Heart Rhythm*. 2006;3(3):317–327.
57. Lemola K, Mueller G, Desjardins B, et al. Topographic analysis of the coronary sinus and major cardiac veins by computed tomography. *Heart Rhythm*. 2005;2(7):694–699.
58. Wu MH, Wongcharoen W, Tsao HM, et al. Close relationship between the bronchi and pulmonary veins: implications for the prevention of atriobronchial fistula after atrial fibrillation ablation. *J Cardiovasc Electrophysiol*. 2007;18(10):1056–1059.
59. Kistler PM, Earley MJ, Harris S, et al. Validation of three-dimensional cardiac image integration: use of integrated CT image into electroanatomic mapping system to perform catheter ablation of atrial fibrillation. *J Cardiovasc Electrophysiol*. 2006;17(4):341–348.
60. Sra J, Krum D, Hare J, et al. Feasibility and validation of registration of three-dimensional left atrial models derived from computed tomography with a noncontact cardiac mapping system. *Heart Rhythm*. 2005;2(1):55–63.
61. Heist EK, Chevalier J, Holmvang G, et al. Factors affecting error in integration of electroanatomic mapping with CT and MR imaging during catheter ablation of atrial fibrillation. *J Interv Card Electrophysiol*. 2006;17(1):21–27.
62. Kistler PM, Rajappan K, Jahngir M, et al. The impact of CT image integration into an electroanatomic mapping system on clinical outcomes of catheter ablation of atrial fibrillation. *J Cardiovasc Electrophysiol*. 2006;17(10):1093–1101.
63. Martinek M, Nesser HJ, Aichinger J, Boehm G, Purerfellner H. Impact of integration of multislice computed tomography imaging into three-dimensional electroanatomic mapping on clinical outcomes, safety, and efficacy using radiofrequency ablation for atrial fibrillation. *Pacing Clin Electrophysiol*. 2007;30(10):1215–1223.
64. Robbins IM, Colvin EV, Doyle TP, et al. Pulmonary vein stenosis after catheter ablation of atrial fibrillation. *Circulation*. 1998;98(17):1769–1775.
65. Packer DL, Keelan P, Munger TM, et al. Clinical presentation, investigation, and management of pulmonary vein stenosis complicating ablation for atrial fibrillation. *Circulation*. 2005;111(5):546–554.
66. Dong J, Vasamreddy CR, Jayam V, et al. Incidence and predictors of pulmonary vein stenosis following catheter ablation of atrial fibrillation using the anatomic pulmonary vein ablation approach: results from paired magnetic resonance imaging. *J Cardiovasc Electrophysiol Aug*. 2005;16(8):845–852.
67. Sigurdsson G, Troughton RW, Xu XF, et al. Detection of pulmonary vein stenosis by transesophageal echocardiography: comparison with multidetector computed tomography. *Am Heart J*. 2007;153(5):800–806.
68. Wongcharoen W, Tsao HM, Wu MH, et al. Preexisting pulmonary vein stenosis in patients undergoing atrial fibrillation ablation: a report of five cases. *J Cardiovasc Electrophysiol Apr*. 2006;17(4):423–425.
69. Chae S, Oral H, Good E, et al. Atrial tachycardia after circumferential pulmonary vein ablation of atrial fibrillation: mechanistic insights, results of catheter ablation, and risk factors for recurrence. *J Am Coll Cardiol*. 2007;50(18):1781–1787.
70. Malamis AP, Kirshenbaum KJ, Nadimpalli S. CT radiographic findings: atrio-esophageal fistula after transcatheter percutaneous ablation of atrial fibrillation. *J Thorac Imaging*. 2007;22(2):188–191.
71. Aleong R, Heist EK, Ruskin JN, Mansour M. Integration of intracardiac echocardiography with magnetic resonance imaging allows visualization of the esophagus during catheter ablation of atrial fibrillation. *Heart Rhythm*. 2008;5(7):1088.
72. Jongbloed MR, Bax JJ, van der Wall EE, Schalij MJ. Thrombus in the left atrial appendage detected by intracardiac echocardiography. *Int J Cardiovasc Imaging*. 2004;20(2):113–116.
73. den Uijl DW, Tops LF, Tolosana JM, et al. Real-time integration of intracardiac echocardiography and multislice computed tomography to guide radiofrequency catheter ablation for atrial fibrillation. *Heart Rhythm*. 2008;5(10):1403–1410.
74. Ren JF, Marchlinski FE, Callans DJ. Left atrial thrombus associated with ablation for atrial fibrillation: identification with intracardiac echocardiography. *J Am Coll Cardiol*. 2004;43(10):1861–1867.
75. Saliba W, Thomas J. Intracardiac echocardiography during catheter ablation of atrial fibrillation. *Europace*. 2008;10 Suppl 3:iii42–47.

76. Knecht S, Skali H, O'Neill MD, et al. Computed tomography-fluoroscopy overlay evaluation during catheter ablation of left atrial arrhythmia. *Europace*. 2008;10(8):931–938.
77. Mao S, Shinbane JS, Girsky MJ, et al. Coronary venous imaging with electron beam computed tomographic angiography: three-dimensional mapping and relationship with coronary arteries. *Am Heart J*. 2005;150(2):315–322.
78. Jongbloed MR, Lamb HJ, Bax JJ, et al. Noninvasive visualization of the cardiac venous system using multislice computed tomography. *J Am Coll Cardiol*. 2005;45(5):749–753.
79. Van de Veire NR, Schuijf JD, De Sutter J, et al. Non-invasive visualization of the cardiac venous system in coronary artery disease patients using 64-slice computed tomography. *J Am Coll Cardiol*. 2006; 48(9):1832–1838.
80. Saxon LA, De Marco T, Schafer J, Chatterjee K, Kumar UN, Foster E. Effects of long-term biventricular stimulation for resynchronization on echocardiographic measures of remodeling. *Circulation*. 2002; 105(11):1304–1310.
81. Abraham WT, Fisher WG, Smith AL, et al. Cardiac resynchronization in chronic heart failure. *N Engl J Med*. 2002;346(24):1845–1853.
82. St John Sutton MG, Plappert T, Abraham WT, et al. Effect of cardiac resynchronization therapy on left ventricular size and function in chronic heart failure. *Circulation*. 2003;107(15):1985–1990.
83. Shinbane JS, Girsky MJ, Mao S, Budoff MJ. Thebesian valve imaging with electron beam CT angiography: implications for resynchronization therapy. *Pacing Clin Electrophysiol*. 2004;27(11):1566–1567.
84. Matsumoto Y, Krishnan S, Fowler SJ, et al. Detection of phrenic nerves and their relation to cardiac anatomy using 64-slice multidetector computed tomography. *Am J Cardiol*. 2007;100(1):133–137.
85. Girsky MJ, Shinbane JS, Ahmadi N, Flores F, Mao S, Budoff MJ. Three-Dimensional coronary venous imaging with computed tomographic angiography facilitates cardiac resynchronization therapy. *J Am Coll Cardiol*. 2009;53:A265.
86. Van de Veire NR, Marsan NA, Schuijf JD, et al. Noninvasive imaging of cardiac venous anatomy with 64–slice multi-slice computed tomography and noninvasive assessment of left ventricular dyssynchrony by 3-dimensional tissue synchronization imaging in patients with heart failure scheduled for cardiac resynchronization therapy. *Am J Cardiol*. 2008;101(7):1023–1029.
87. White JA, Yee R, Yuan X, et al. Delayed enhancement magnetic resonance imaging predicts response to cardiac resynchronization therapy in patients with intraventricular dyssynchrony. *J Am Coll Cardiol*. 2006;48(10):1953–1960.
88. Bleeker GB, Kaandorp TA, Lamb HJ, et al. Effect of posterolateral scar tissue on clinical and echocardiographic improvement after cardiac resynchronization therapy. *Circulation*. 2006;113(7):969–976.
89. Chalil S, Stegemann B, Muhyaldeen SA, et al. Effect of posterolateral left ventricular scar on mortality and morbidity following cardiac resynchronization therapy. *Pacing Clin Electrophysiol*. 2007;30(10):1201–1209.
90. Lardo AC, Cordeiro MA, Silva C, et al. Contrast-enhanced multidetector computed tomography viability imaging after myocardial infarction: characterization of myocyte death, microvascular obstruction, and chronic scar. *Circulation*. 2006;113(3):394–404.
91. Chiou KR, Liu CP, Peng NJ, et al. Identification and viability assessment of infarcted myocardium with late enhancement multidetector computed tomography: comparison with thallium single photon emission computed tomography and echocardiography. *Am Heart J*. 2008;155(4):738–745.
92. Mahnken AH, Koos R, Katoh M, et al. Assessment of myocardial viability in reperfused acute myocardial infarction using 16-slice computed tomography in comparison to magnetic resonance imaging. *J Am Coll Cardiol*. 2005;45(12):2042–2047.
93. Sato A, Hiroe M, Nozato T, et al. Early validation study of 64-slice multidetector computed tomography for the assessment of myocardial viability and the prediction of left ventricular remodelling after acute myocardial infarction. *Eur Heart J*. 2008;29(4):490–498.
94. Habis M, Capderou A, Ghostine S, et al. Acute myocardial infarction early viability assessment by 64-slice computed tomography immediately after coronary angiography: comparison with low-dose dobutamine echocardiography. *J Am Coll Cardiol*. 2007;49(11):1178–1185.

23

An Interventionalist's Perspective: Diagnosis of Cardiovascular Disease

Jeffrey M. Schussler

Introduction

Coronary computed tomographic angiography (CCTA) has become one of the diagnostic tests of choice for the determination of the presence and severity of coronary atherosclerosis. With its high specificity, CCTA can be an extremely helpful test in determining which patients do *not* require cardiac catheterization. Given this fact, it seems somewhat counter-intuitive that the interventional cardiology community has embraced this technology. One would theorize that a strong *noninvasive angiography* program would reduce volume and divert patients away from the catheterization lab. In fact, centers where CCTA is available do not appear to have lead to a reduction in invasive volumes [1].

CCTA can also help interventionalists plan percutaneous coronary intervention (PCI) strategies, alerting them to the presence of left main or multi-vessel disease, length and severity of lesions, presence and amount of calcification, tortuosity, coronary variants, and anomalies. Additionally, it has a wide range of utility after revascularization including follow-up after PCI to evaluate stent patency, and after coronary artery bypass grafting (CABG) to evaluate graft patency.

Invasive Cardiac Catheterization

Invasive cardiac catheterization, the "gold standard" diagnostic technique for the evaluation of coronary artery disease (CAD), has been used for clinical evaluation of coronary stenosis since the 1960s [2–4]. However, it has several well known drawbacks. There is a certain degree of inter-observer variation when describing degree of stenosis [5]. Quantitative coronary angiography (QCA), which is not used routinely in clinical practice, is helpful but does not eliminate this error [6, 7].

Since coronary angiography only allows for the definition of the lumen of the coronary only, the wall of the coronary artery remains nonvisualized unless intravascular ultrasound is used [8, 9]. This leads to under-identification of the presence of disease in patients with minimal disease, and can contribute to underestimation of plaque burden due to compensatory expansion of the coronary arteries [10–13]. These relatively minor stenoses can be the cause of future acute coronary syndromes and myocardial infarction [14].

There is a small but inherent risk of complication associated with invasive evaluation of the coronary arteries. This is due to the need to directly instrument the coronary artery as well as the obligate arterial access. The risk of major complications such as death is approximately 0.1% [15, 16], with a combined risk of all major complications (e.g., stroke, renal failure, or major bleeding) of ≤2 % [17, 18]. Minor complications such as local pain, ecchymosis, or hematoma at the access site can be higher, and are frequently a source of delayed discharge and patient dissatisfaction [19].

Invasive coronary angiography is considered the "gold standard" for definitive cardiac evaluation in patients with chest pain [17]. As it is such a powerful tool, it has even been suggested that invasive angiography should be the test of choice in inpatients with chest pain [20]. Angiography has been shown to be better able to detect the presence of atherosclerotic coronary disease than functional tests, reduces early returns to the emergency department, and has an overall higher level of patient satisfaction [21]. Invasive angiography has even been suggested as the screening test of choice in the primary prevention of CAD [22]. However, due to the aforementioned risks, it often is used as second line in patients who have low-to-moderate presumed risk or after performing functional testing [23].

Coronary Evaluation

Determination of Coronary Atherosclerosis Prior to Invasive Evaluation and Intervention

With its high specificity and negative predictive value, CCTA has the ability to exclude the majority of patients who have no significant disease. In patients with chest pain who have no

observable coronary disease by CCTA, there is a nearly 100% chance that they will not have the need for further cardiac evaluation, and will have no cardiac events up to 3 years (Figure 23.1) [24]. It is also accurate enough to determine which arteries have high-grade lesions, and which have minimal disease (Figure 23.2) [25–28]. This can mean the difference between planning an intervention on a single proximal vessel or on the expectation of a difficult multiple vessel intervention [29, 30]. CCTA may also allow for improved planning of clopidogrel loading prior to catheterization. If surgical disease is discovered on CCTA, a "loading dose" of clopidogrel may be withheld, reducing a delay in revascularization (Figure 23.3). It can

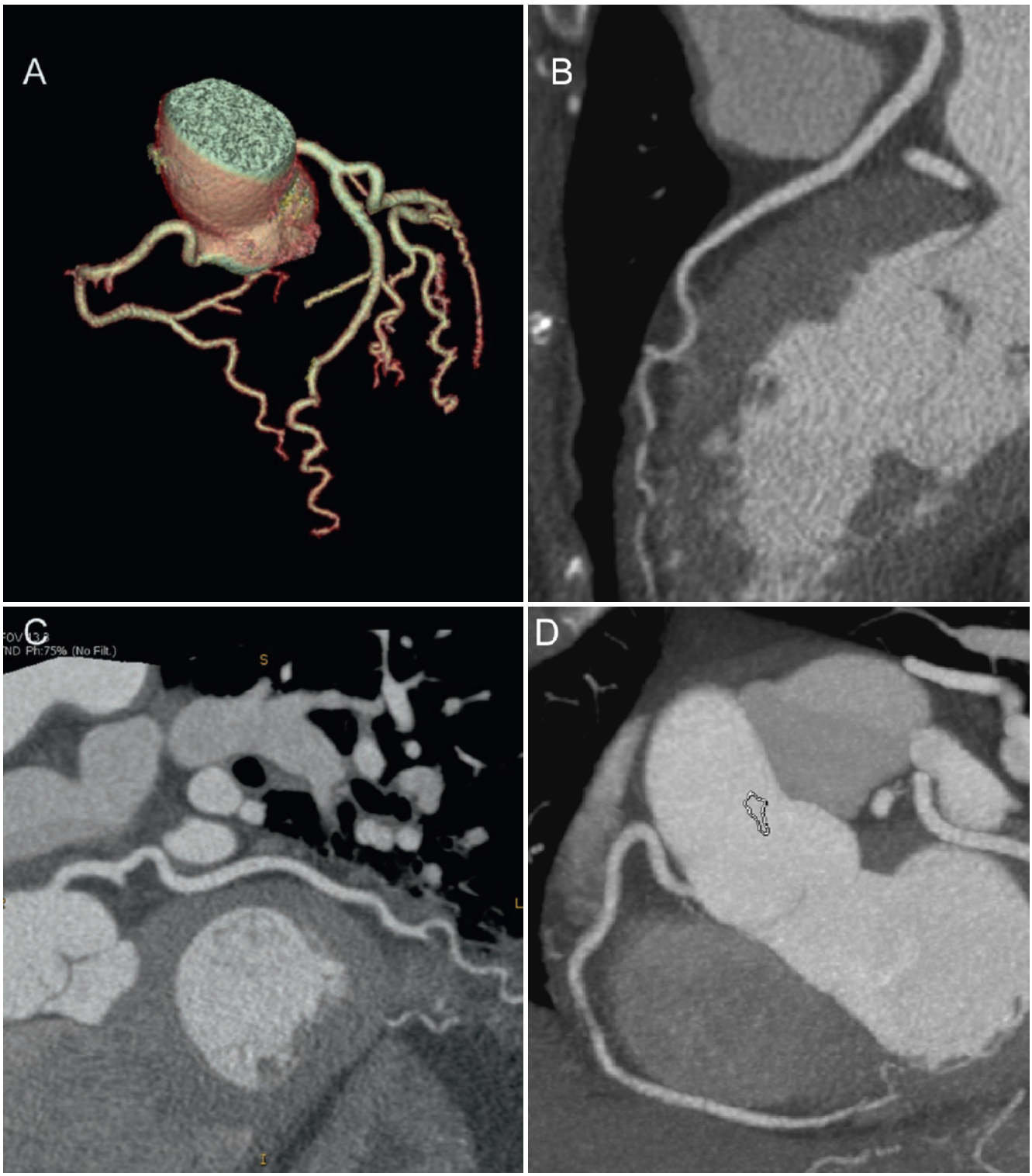

Figure 23.1. Normal CCTA in a 55 year old woman with risk factors for coronary disease and chest pain. A three dimensional view of the coronary anatomy (**a**) demonstrates a right dominant system without coronary anomalies. Individual curved reformatted images of the left anterior descending (**b**), left circumflex (**c**), and right coronary artery (**d**) demonstrate no plaque in any of the arterial tree.

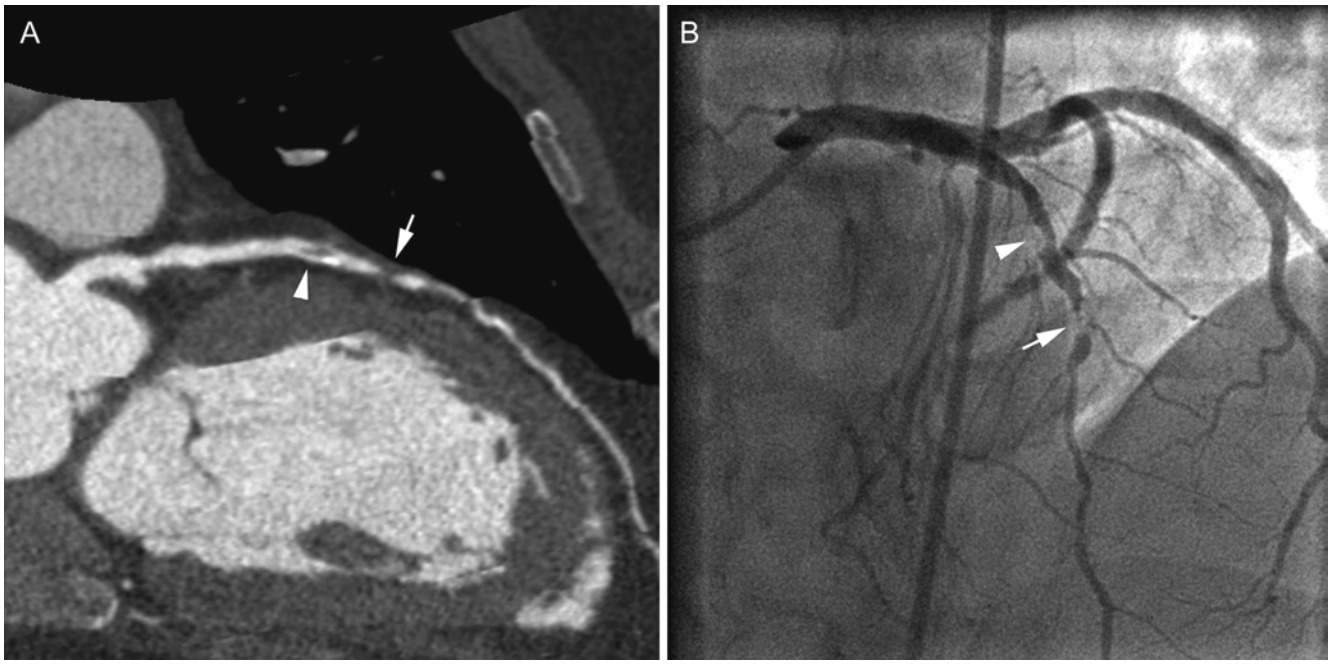

Figure 23.2. Patient with chest pain referred for CCTA. A high-grade lesion is seen in the mid left anterior descending (**a**, *arrow*). More moderate plaque is noted proximal to the lesion (**a**, *arrowhead*). The same lesions are seen on the follow-up invasive angiogram (**b**).

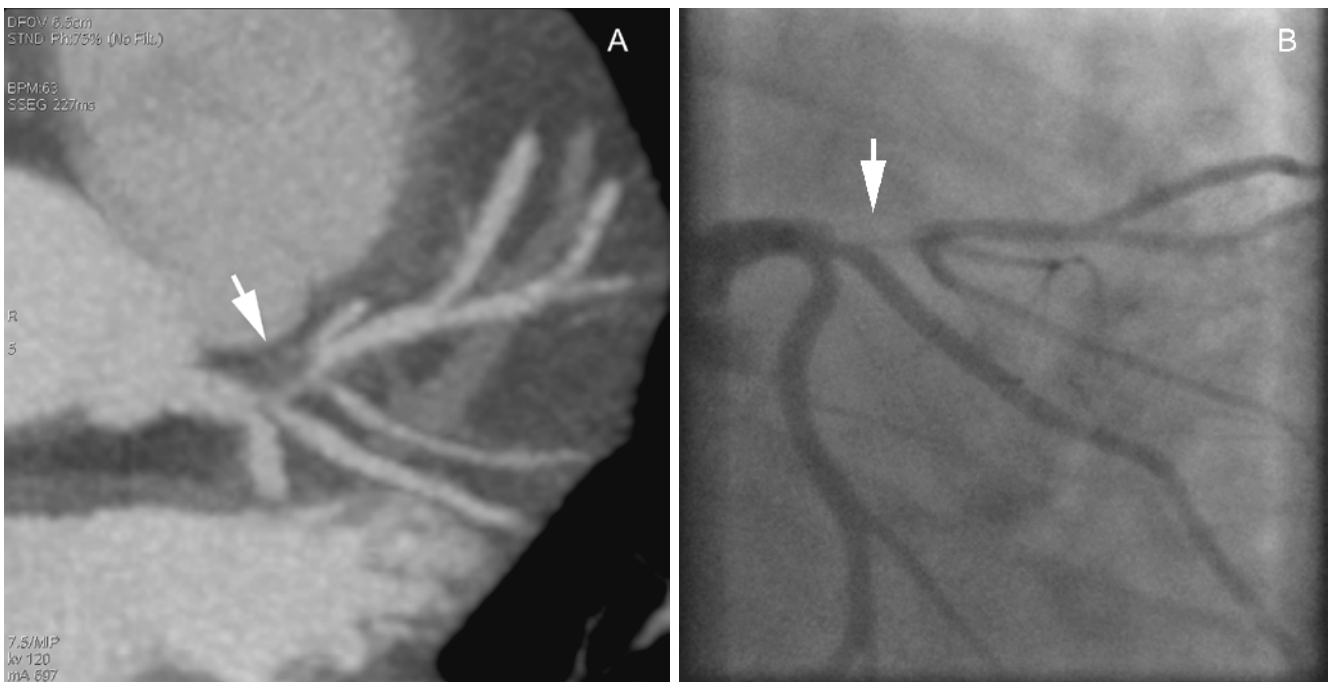

Figure 23.3. CCTA demonstrating a high-grade noncalcified plaque involving the ostium of the left anterior descending (LAD) and distal left main (**a**, *arrow*). The invasive angiogram (**b**) is shown for comparison. Based on the findings of the CCTA scan, it was felt that the location of the plaque was unfavorable for PCI as there would be a high risk for compromise of the left circumflex, ramus intermedius (RI), and first diagonal branches. This was less apparent on invasive angiography. A surgical consultation was obtained, and the patient went on to successful bypass of the LAD, diagonal, and RI.

also allow for a "preview" of the coronary anatomy for planning of stent placement, including stent sizing prior to diagnostic catheterization (Figure 23.4) CCTA may be helpful to identify the location of the ostia of the coronary arteries. Even in cases where true anomalies are not present, it can be helpful to know that a patient has an "anterior takeoff" of a right coronary, as this may lead to use of specific types of catheters for the engagement of that artery (Figure 23.5).

Total Occlusions

Since the bolus of contrast reaches the arteries simultaneously, it is difficult to distinguish high-grade lesions from totally occluded coronaries. Newer data suggest that when occlusions are found, CCTA may be helpful in defining the length of stenosis, complexity of the plaque, and therefore give insight into the potential ease or difficulty in

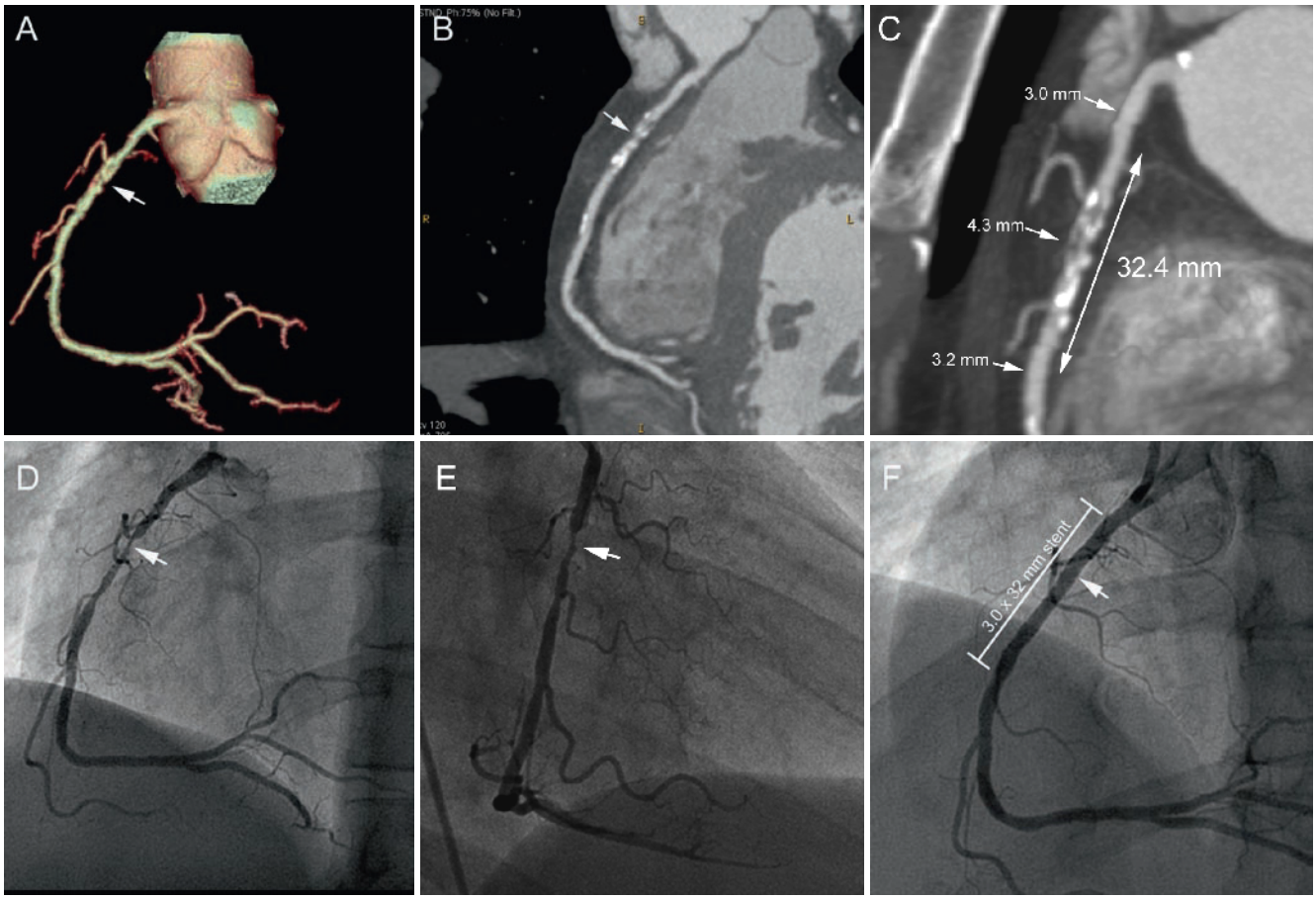

Figure 23.4. CCTA of a patient with cardiac risk factors and chest pain. A CCTA (**a**, **b**, *arrows*) demonstrates a high grade lesion in the proximal right coronary artery. The severity is suggested by the complex nature of the plaque, with both soft and calcific portions, as well as the compensatory expansion of the artery within the most severe area (**c**). The length and the extent of plaque were evident from the CCTA (**c**). Invasive coronary angiogram confirmed the high grade lesion in the right coronary artery (**d**, **e**, *arrows*). A stent was selected (**f**) to cover not only the high grade area (*arrow*), but also the more moderate plaque proximal and distal to the most severe portions of the lesion (**f**). (Reprinted with permission from Bhella, Hassan, and Schussler.).

undertaking complex percutaneous revascularization of these lesions [31–33] (Figure 23.6).

Left Main Disease

The presence of severe left main disease is potentially dangerous if not known prior to diagnostic angiography. Placement of a catheter into a diseased left main coronary artery can cause dramatic reduction of coronary blood flow, and can even result in death during diagnostic angiography [34, 35]. In a situation where left main disease is discovered on the CCTA, plans can be made to use smaller diagnostic catheters, or even have an intra-aortic balloon pump stationed close at hand. Left main disease identified on the CCTA allows preparation for the potential hemodynamic compromise of engaging a catheter in a severely diseased left main coronary. It is important to remember that CCTA cannot give hemodynamic information. It is prudent to proceed to invasive evaluation if noninvasive angiography suggests significant left main stenosis (Figure 23.7).

Plaque Evaluation

CCTA, like intravascular ultrasound (IVUS), has the ability to visualize plaque and to roughly quantify its amount [36–38]. It is well known that patients with minimal CAD may still have events due to plaque which is not fully defined by invasive coronary angiography. These types of nonstenotic plaques are detectable by CCTA, and there is ongoing research assessing definition of unstable plaque using CCTA [39–41] (Figure 23.8). Glagov remodeling of coronary atherosclerotic lesions can be appreciated on CCTA. As the plaque intrudes on the lumen of the artery, compensatory expansion of the artery occurs, which is seen on CCTA, but not by conventional angiography [42, 43]. Artery remodeling is often a clue that the stenosis seen by CCTA is severe (Figure 23.9).

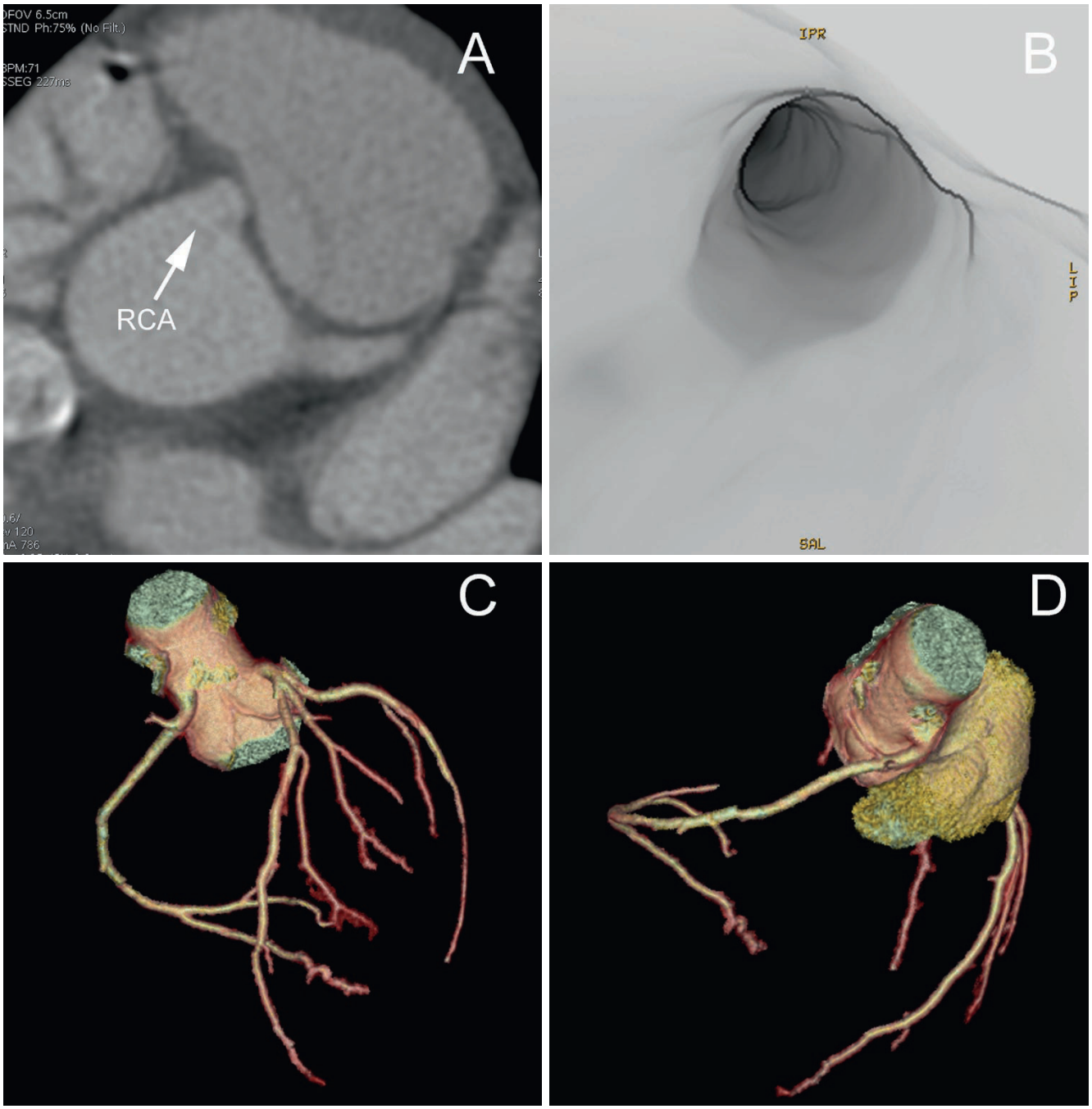

Figure 23.5. CCTA of a patient with an "anterior" takeoff of the right coronary artery (RCA). The axial images (**a**) demonstrate the ostium of the right coronary artery slightly higher and more anterior than normally seen. The location on the axial "clock-face" of the aortic root is approximately "1 o'clock" rather than the normal "10–12 o'clock" seen in most coronary trees. This is not truly anomalous and has no impact on the function of the artery. The ostium (**b**) has a normal round orifice. Three dimensional views (**c**) show the high-anterior takeoff in relation to the cusp and the left main. The pulmonary outflow (**d**) does not impinge on the artery. This artery would be best catheterized using a modified Amplatz-type catheter rather than a typical Judkins-right catheter.

Post Intervention Evaluation by CCTA

Post-PCI Evaluation

CCTA can be used for evaluation of stent patency. Imaging through stents (especially in smaller arteries) can be problematic due to a significant amount of beam hardening artifact due to the scatter of X-rays by the metallic stents. It is important to use appropriate window and threshold levels to obtain adequate images. In-stent restenosis, a process that is brought on by smooth muscle cell migration and neointimal hyperplasia, has also been successfully evaluated by CCTA [44–46] (Figure 23.10).

Post-Bypass Evaluation

There are excellent data to support the use of CCTA in the evaluation of post- CABG patients [47–49]. In some

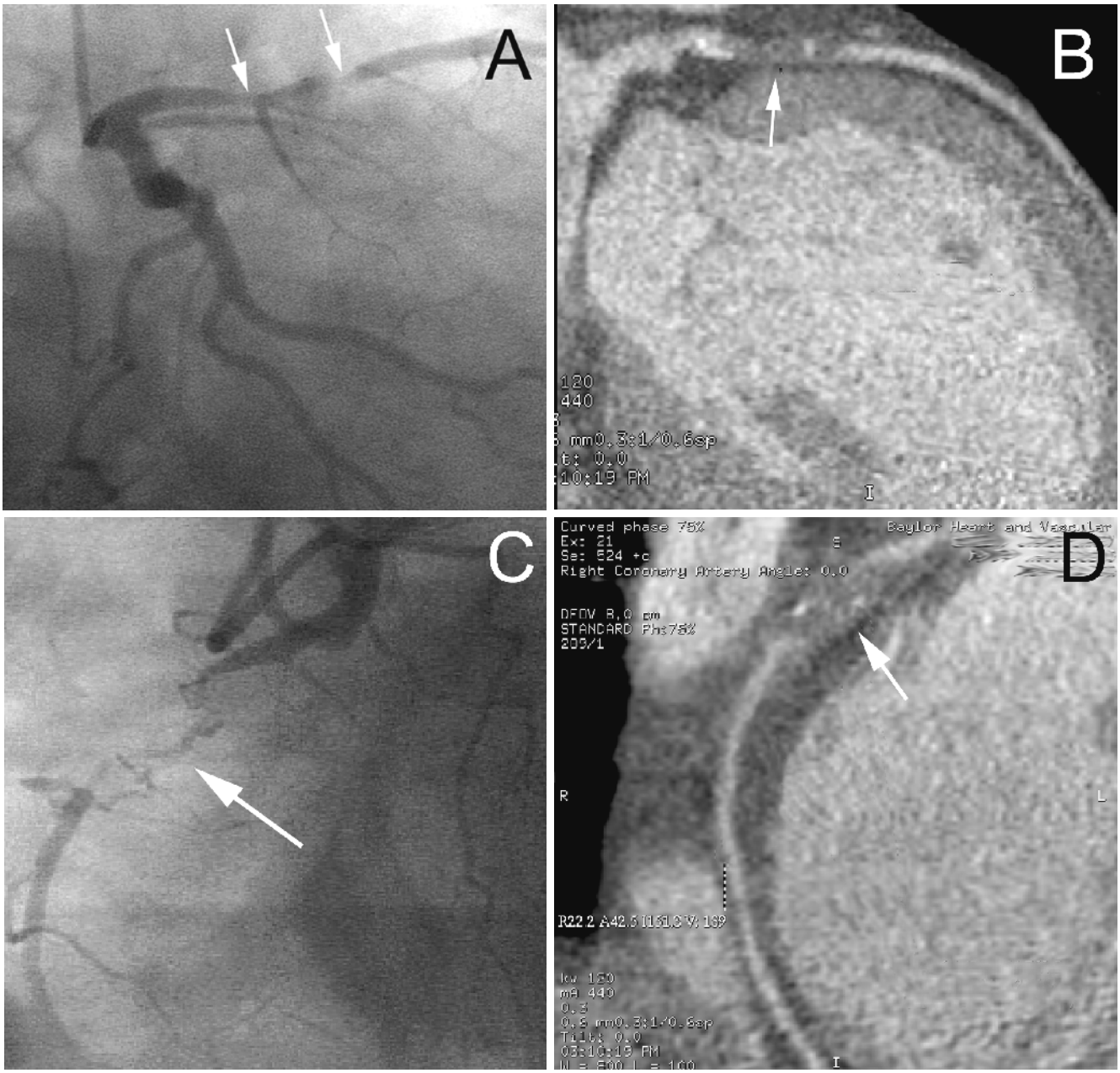

Figure 23.6. High-grade lesion in the left anterior descending, demonstrated by invasive angiography (**a**) and CCTA (**b**). The lesion has the same CCTA characteristics as a complete occlusion with bridging collaterals (**c**, **d**). There is paucity of contrast, compensatory expansion, and a large plaque burden. Complete occlusions cannot be easily distinguished from very high-grade stenoses base on CCTA.

respects, the imaging of bypass grafts is easier as there is less movement of the grafts and greater contrast between the contrast in the grafts and the surrounding tissue. Visualization of graft patency is often more easily performed using 3D views rather than axial or even MPR views. For many newer post-bypass studies, CCTA has become the test of choice to evaluate graft patency rather than traditional invasive evaluation [50–53] (Figure 23.11). It is important to alert the technologist that the study is to be performed with attention to bypass grafts so that more of the ascending aorta is visualized. Slice thickness may be increased to reduce radiation. Imaging can be performed on conduits with metallic proximal connectors, but there may be some hardening artifact when many metallic clips are present [52, 54, 55].

Patients are sometimes referred for invasive catheterization with a history of CABG surgery, without information regarding the types of grafts or which arteries were bypassed. It can then be a challenging and time-consuming task to find all of the grafts at cardiac catheterization. CCTA can be helpful, not only by delineating which grafts are patent, but by providing a "roadmap" as to the number of grafts, their origins, as well as the location of the anastamoses with native vessels prior to invasive angiography.

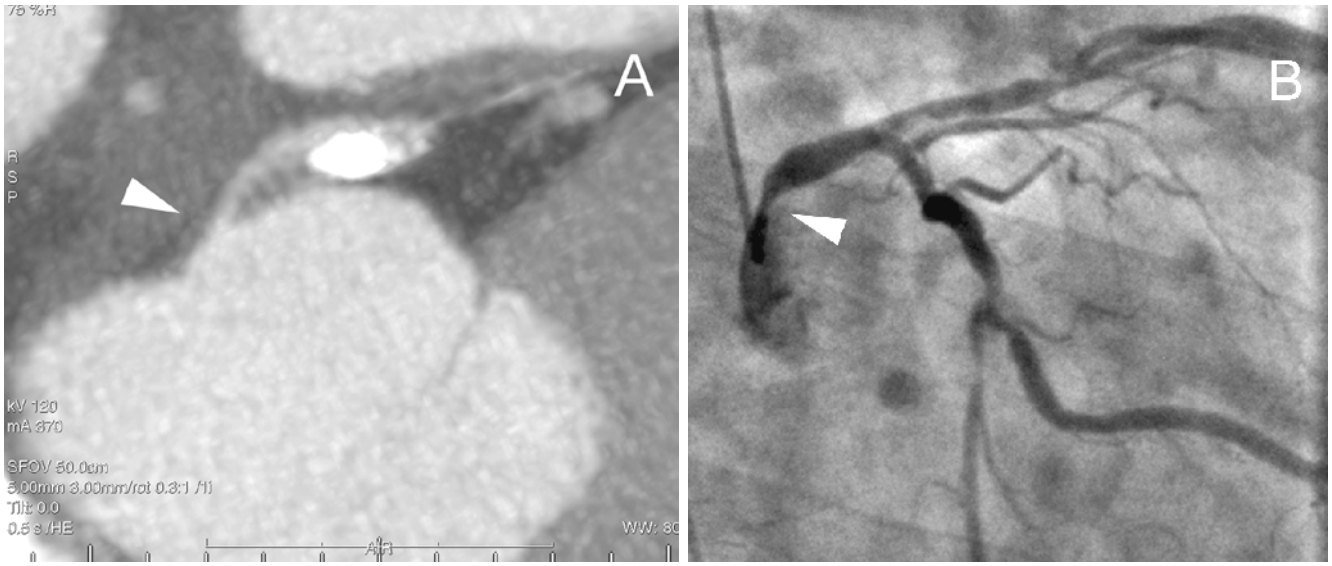

Figure 23.7. High-grade stenosis of the left main coronary artery seen by CCTA (**a**, *arrowhead*). The corresponding invasive coronary angiogram is seen (**b**, *arrowhead*), demonstrating a severe angiographic stenosis. There was immediate "damping" of the pressure tracing upon engagement of a 4-French diagnostic catheter. The noninvasive study was so dramatically abnormal that it prompted the operator to deliberately choose a smaller French-sized catheter than normal, and have an intra-aortic balloon pump in the room prior to catheterization. (Reprinted with permission from Schussler et al).

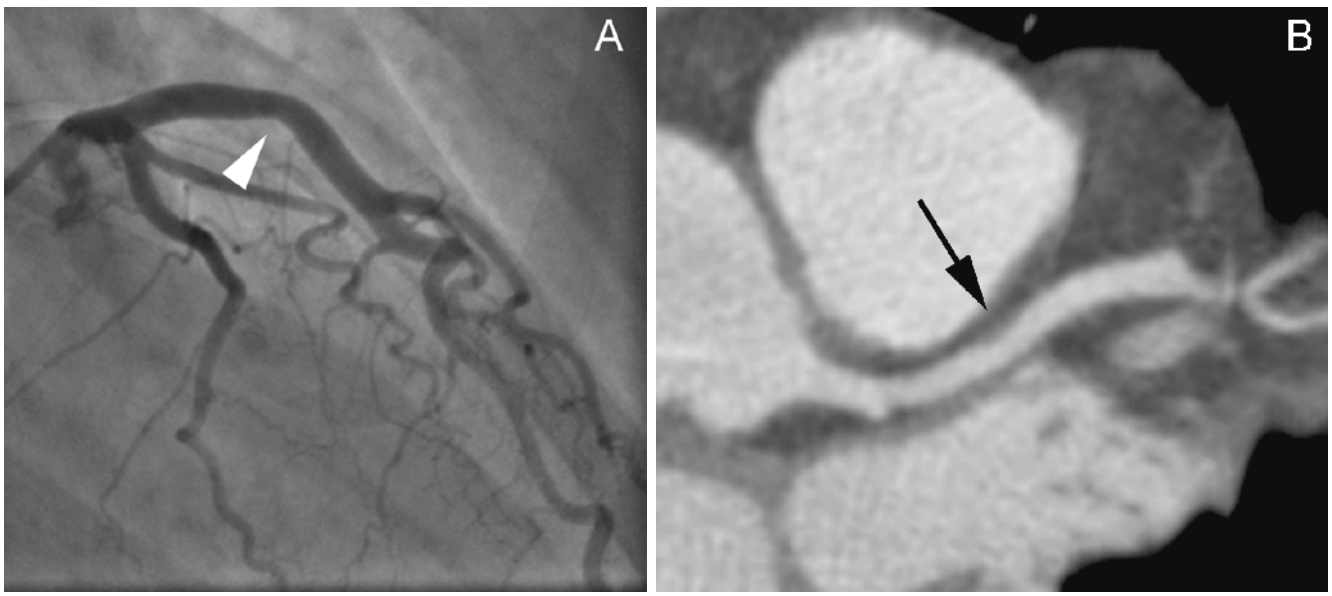

Figure 23.8. Essentially "normal" coronary angiogram in a 33-year-old woman. A "luminal irregularity" (**a**, *white arrowhead*) in the left anterior descending artery corresponds to a non-calcified plaque (**b**, *black arrow*) seen by CCTA. It is possible that by defining asymptomatic, sub-clinical plaque in younger patients, they may be prescribed statin therapy long before they would otherwise have been treated.

Even though evaluation of bypass grafts is relatively straightforward with CCTA, it has to be kept in mind that, in most cases, the clinical situation will warrant evaluating not only the status of the patient's bypass grafts, but also that of the native coronary arteries either distal to the bypass insertion site or of those coronary arteries that did not receive a bypass graft. Frequently, evaluation of native arteries in patients with bypass grafts tends to be difficult or even impossible with CCTA because of the often pronounced calcification that exists in the native coronary arteries of CABG patients [56, 57].

Evaluation of the Noncoronary Cardiac Surgery Patient

There is growing literature to support a strategy of noninvasive coronary angiography in patients with only low or moderate risk for coronary disease, prior to noncoronary cardiac surgery [58–61]. With congenital heart disease, coronary anomalies, or cardiac masses, it may actually be more advantageous to perform a CCTA, as it gives additional structural information which is relevant to the case

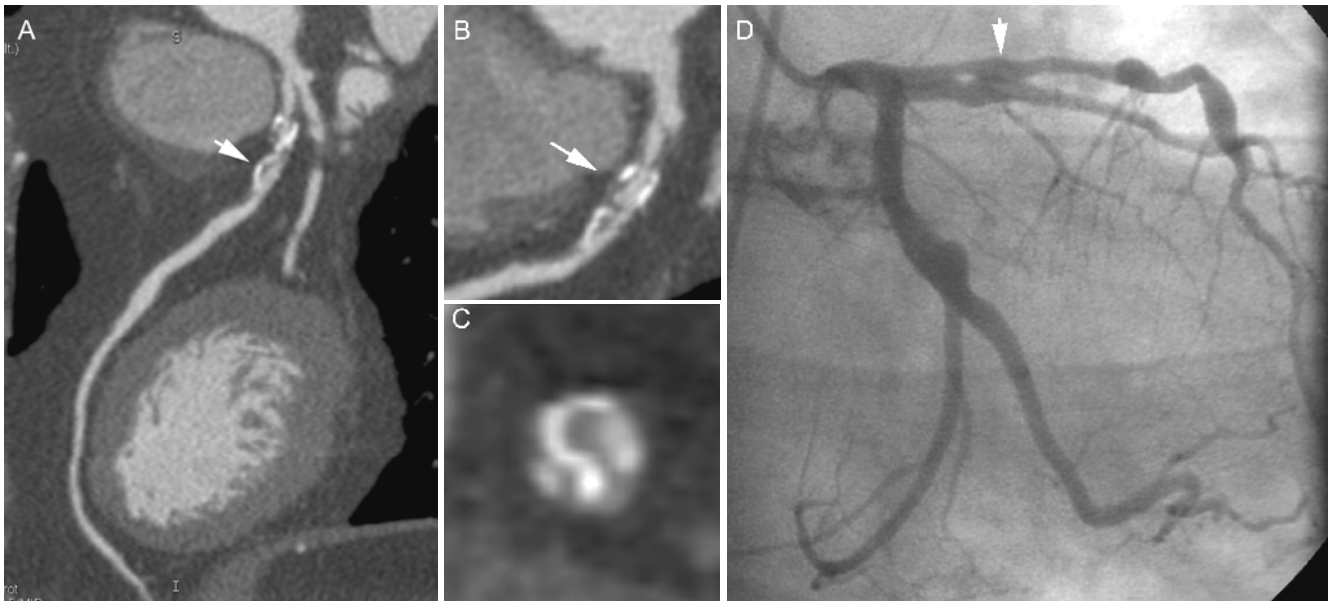

Figure 23.9. CCTA and invasive angiogram in a man with chest pain. The proximal LAD has a complex, high-grade stenosis (**a**, *arrow*). Closer and cross-sectional views of the plaque (**b**, *arrow*; **c**) show that it is made up of soft and calcified plaque, and there is expansion of the artery when compared to more proximal reference sections. Invasive angiography (**d**, *arrow*) may have more difficulty demonstrating the severity of plaque burden due to the compensatory expansion.

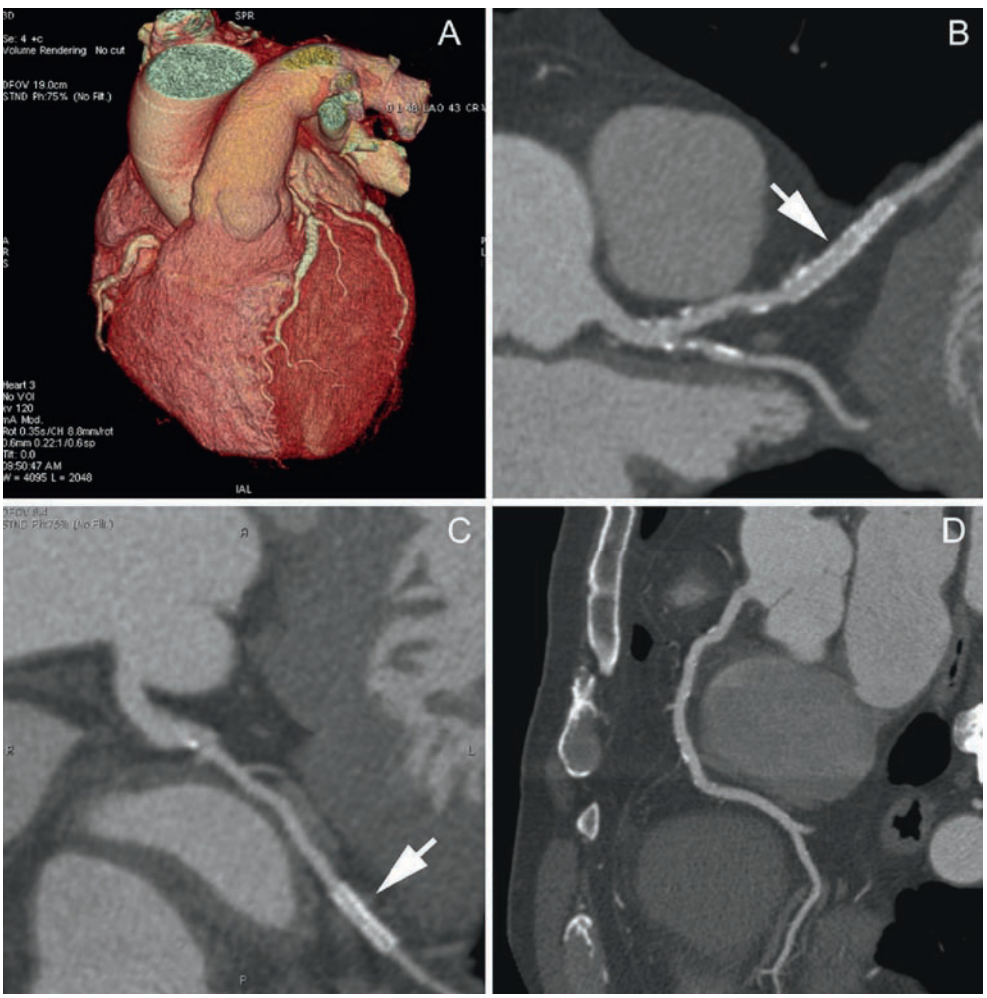

Figure 23.10. A CCTA of a patient with previous stents placed in the left anterior descending (LAD) and left circumflex (LCx), now having chest pain. Three dimensional image (**a**) show the location of the stents. The curved reformatted CT images demonstrate patency of the LAD stent (**b**, *arrow*) and the LCx stent (**c**, *arrow*). The right coronary artery has only minimal disease (**d**). No further cardiac testing was needed with this patient.

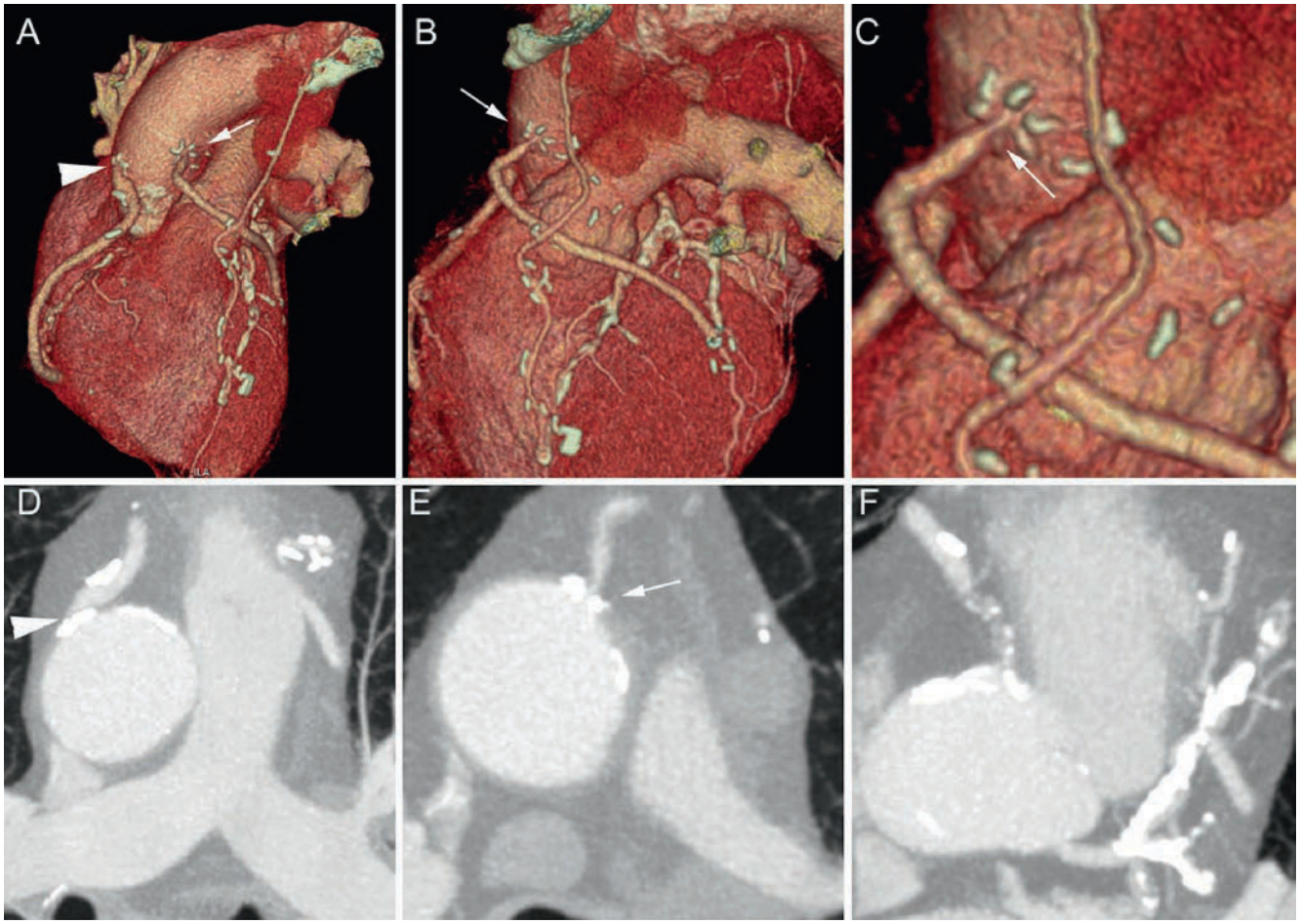

Figure 23.11. CCTA to evaluate a patient with previous coronary artery bypass graft surgery. This patient's anastamoses were fashioned using nitinol clips. There is a patent saphenous vein graft (SVG) to the right coronary (**a**, **d**, *arrowhead*). A SVG to the circumflex system (**b**, **c**, **e**, *arrow*) demonstrates a narrowing at the ostium of the graft. The proximal native circulation is shown to have occlusion of the proximal RCA and calcific plaque of the proximal LAD and LCx (**f**).

[62–64]. Conceivably, CCTA technology could advance to the point where the decision to *proceed* even with coronary revascularization could be made without any invasive tests being performed (Figure 23.12).

Conclusion

Interventional cardiologists should embrace CCTA as a helpful addition to their armamentarium to diagnose and help combat cardiovascular disease. There are many situations in which the use of CCTA is not only complementary, but *better* than its invasive counterpart in the evaluation of the cardiac patient. It can be an enormous aid in the planning of interventional procedures, and can give additional information which invasive angiography cannot. In the future, with additional improvements in resolution and reduction in radiation exposure, there may come a time when all patients will have CCTA as a prelude to an invasive procedure.

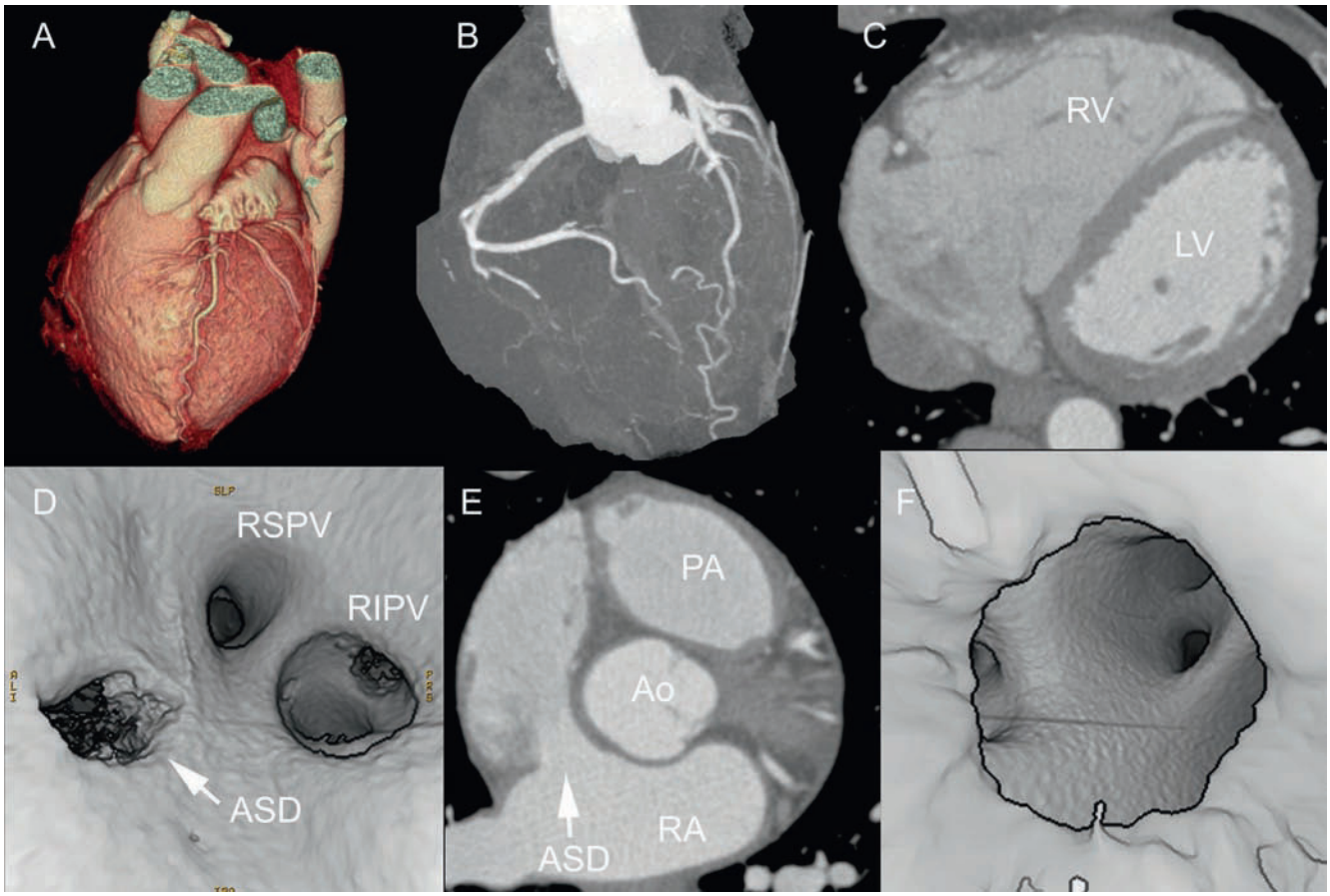

Figure 23.12. CCTA performed in a young patient who is to undergo atrial septal defect (ASD) closure. The 3D and MIP views (**a**, **b**) show no significant coronary disease. This was confirmed with review of the axial and reformatted images (not pictured). Axial image of the heart (**c**) clearly shows enlargement of the right ventricle (RV) compared to the left ventricle (LV), which is a sign of the chronicity of the volume overload of the right heart from the ASD. The ASD is shown from an "internal" view (**d**, *arrow*). This also allows for the evaluation of the size and location of the pulmonary veins (*RSPV* right superior pulmonary vein, *RIPV* right inferior pulmonary vein), which can alter management from percutaneous to surgical closure. An "internal" view of the ASD as seen from the right atrium shows the location of the left sided pulmonary veins across the left atrium (**f**). (Reprinted with permission from Rese et al).

References

1. Auseon AJ, Advani SS, Bush CA, Raman SV. Impact of 64-slice multidetector computed tomography on other diagnostic studies for coronary artery disease. *Am J Med*. 2009;122:387–391.
2. Weidner W, MacAlpin R, Hanafee W, Kattus A. Percutaneous transaxillary selective coronary angiography. *Radiology*. 1965;85:652–657.
3. Selinger H. Selective coronary cine-angiography. *W V Med J*. 1966; 62:336–337.
4. Spellberg RD, Unger I. The percutaneous femoral artery approach to selective coronary arteriography. *Circulation*. 1967;36:730–733.
5. Banerjee S, Crook AM, Dawson JR, Timmis AD, Hemingway H. Magnitude and consequences of error in coronary angiography interpretation (the ACRE study). *Am J Cardiol*. 2000;85:309–314.
6. Goldberg RK, Kleiman NS, Minor ST, Abukhalil J, Raizner AE. Comparison of quantitative coronary angiography to visual estimates of lesion severity pre and post PTCA. *Am Heart J*. 1990;119:178–184.
7. Herrington DM, Siebes M, Walford GD. Sources of error in quantitative coronary angiography. *Cathet Cardiovasc Diagn*. 1993;29:314–321.
8. Nissen SE, Gurley JC. Application of intravascular ultrasound for detection and quantitation of coronary atherosclerosis. *Int J Card Imaging*. 1991;6:165–177.
9. Topol EJ, Nissen SE. Our preoccupation with coronary luminology. The dissociation between clinical and angiographic findings in ischemic heart disease. *Circulation*. 1995;92:2333–2342.
10. Yamashita T, Colombo A, Tobis JM. Limitations of coronary angiography compared with intravascular ultrasound: implications for coronary interventions. *Prog Cardiovasc Dis*. 1999;42:91–138.
11. Arnett EN, Isner JM, Redwood DR, et al. Coronary artery narrowing in coronary heart disease: comparison of cineangiographic and necropsy findings. *Ann Intern Med*. 1979;91:350–356.
12. Glagov S, Weisenberg E, Zarins CK, Stankunavicius R, Kolettis GJ. Compensatory enlargement of human atherosclerotic coronary arteries. *N Engl J Med*. 1987;316:1371–1375.
13. Stiel GM, Stiel LS, Schofer J, Donath K, Mathey DG. Impact of compensatory enlargement of atherosclerotic coronary arteries on angiographic assessment of coronary artery disease. *Circulation*. 1989;80:1603–1609.
14. Macieira-Coelho E, Cantinho G, da Costa BB, et al. Minimal residual coronary obstructions in patients who suffered a first myocardial infarction. A prospective study comparing coronary angiography and exercise thallium scintigraphy. *Clin Cardiol*. 1993;16:879–82.
15. Kennedy JW, Baxley WA, Bunnel IL, et al. Mortality related to cardiac catheterization and angiography. *Cathet Cardiovasc Diagn*. 1982;8:323–340.
16. Noto TJ Jr, Johnson LW, Krone R, et al. Cardiac catheterization 1990: a report of the Registry of the Society for Cardiac Angiography and Interventions (SCA&I). *Cathet Cardiovasc Diagn*. 1991;24:75–83.
17. Scanlon PJ, Faxon DP, Audet AM, et al. ACC/AHA guidelines for coronary angiography. A report of the American College of Cardiology/American Heart Association Task Force on practice guidelines (Committee on Coronary Angiography). Developed in collaboration with the Society for Cardiac Angiography and Interventions. *J Am Coll Cardiol*. 1999;33:1756–1824.
18. Heuser RR. Outpatient coronary angiography: indications, safety, and complication rates. *Herz*. 1998;23:21–26.

19. Ammann P, Brunner-La Rocca HP, Angehrn W, Roelli H, Sagmeister M, Rickli H. Procedural complications following diagnostic coronary angiography are related to the operator's experience and the catheter size. *Catheter Cardiovasc Interv*. 2003;59:13–18.
20. deFilippi CR, Rosanio S, Tocchi M, et al. Randomized comparison of a strategy of predischarge coronary angiography versus exercise testing in low-risk patients in a chest pain unit: in-hospital and long-term outcomes. *J Am Coll Cardiol*. 2001;37:2042–2049.
21. Wyer PC. Predischarge coronary angiography was better than exercise testing for reducing hospital use after low-risk chest pain. *ACP J Club*. 2002;136:8.
22. Gandelman G, Bodenheimer MM. Screening coronary arteriography in the primary prevention of coronary artery disease. *Heart Dis*. 2003;5:335–344.
23. Patel MR, Dehmer GJ, Hirshfeld JW, Smith PK, Spertus JA. ACCF/SCAI/STS/AATS/AHA/ASNC 2009 Appropriateness Criteria for Coronary Revascularization: a report by the American College of Cardiology Foundation Appropriateness Criteria Task Force, Society for Cardiovascular Angiography and Interventions, Society of Thoracic Surgeons, American Association for Thoracic Surgery, American Heart Association, and the American Society of Nuclear Cardiology Endorsed by the American Society of Echocardiography, the Heart Failure Society of America, and the Society of Cardiovascular Computed Tomography. *J Am Coll Cardiol*. 2009;53:530–553.
24. Fazel P, Peterman MA, Schussler JM. Three-year outcomes and cost analysis in patients receiving 64-slice computed tomographic coronary angiography for chest pain. *Am J Cardiol*. 2009;104:498–500.
25. Stein PD, Yaekoub AY, Matta F, Sostman HD. 64-slice CT for diagnosis of coronary artery disease: a systematic review. *Am J Med*. 2008;121:715–725.
26. Mowatt G, Cook JA, Hillis GS, et al. 64-Slice computed tomography angiography in the diagnosis and assessment of coronary artery disease: systematic review and meta-analysis. *Heart*. 2008;94:1386–1393.
27. Meijboom WB, Meijs MF, Schuijf JD, et al. Diagnostic accuracy of 64-slice computed tomography coronary angiography: a prospective, multicenter, multivendor study. *J Am Coll Cardiol*. 2008;52:2135–2144.
28. Budoff MJ, Dowe D, Jollis JG, et al. Diagnostic performance of 64-multidetector row coronary computed tomographic angiography for evaluation of coronary artery stenosis in individuals without known coronary artery disease: results from the prospective multicenter ACCURACY (Assessment by Coronary Computed Tomographic Angiography of Individuals Undergoing Invasive Coronary Angiography) trial. *J Am Coll Cardiol*. 2008;52:1724–1732.
29. Otsuka M, Sugahara S, Umeda K, et al. Utility of multislice computed tomography as a strategic tool for complex percutaneous coronary intervention. *Int J Cardiovasc Imaging*. 2008;24:201–210.
30. Van Mieghem CA, Thury A, Meijboom WB, et al. Detection and characterization of coronary bifurcation lesions with 64-slice computed tomography coronary angiography. *Eur Heart J*. 2007;28:1968–1976.
31. Rieber J, Sheth TN, Mooyaart EA, et al. Assessment of the presence and extent of coronary collateralization by coronary computed tomographic angiography in patients with total occlusions. *Int J Cardiovasc Imaging*. 2009;25:331–337.
32. Van Mieghem CA, van der Ent M, de Feyter PJ. Percutaneous coronary intervention for chronic total occlusions: value of preprocedural multislice CT guidance. *Heart*. 2007;93:1492.
33. Mollet NR, Hoye A, Lemos PA, et al. Value of preprocedure multislice computed tomographic coronary angiography to predict the outcome of percutaneous recanalization of chronic total occlusions. *Am J Cardiol*. 2005;95:240–243.
34. Curtis MJ, Traboulsi M, Knudtson ML, Lester WM. Left main coronary artery dissection during cardiac catheterization. *Can J Cardiol*. 1992;8:725–728.
35. Devlin G, Lazzam L, Schwartz L. Mortality related to diagnostic cardiac catheterization. The importance of left main coronary disease and catheter induced trauma. *Int J Card Imaging*. 1997;13:379–384. discussion 85–86.
36. Andreini D, Pontone G, Bartorelli AL, et al. Comparison of feasibility and diagnostic accuracy of 64-slice multidetector computed tomographic coronary angiography versus invasive coronary angiography versus intravascular ultrasound for evaluation of in-stent restenosis. *Am J Cardiol*. 2009;103:1349-1358.
37. Wijpkema JS, Tio RA, Zijlstra F. Quantification of coronary lesions by 64-slice computed tomography compared with quantitative coronary angiography and intravascular ultrasound. *J Am Coll Cardiol*. 2006;47:891. author reply-2.
38. Hammer-Hansen S, Kofoed KF, Kelbaek H, et al. Volumetric evaluation of coronary plaque in patients presenting with acute myocardial infarction or stable angina pectoris-a multislice computerized tomography study. *Am Heart J*. 2009;157:481–487.
39. Kunita E, Fujii T, Urabe Y, et al. Coronary plaque stabilization followed by Color Code Plaque(TM) analysis with 64-slice multidetector row computed tomography. *Circ J*. 2009;73(4):772–775.
40. Kunimasa T, Sato Y, Sugi K, Moroi M. Evaluation by multislice computed tomography of atherosclerotic coronary artery plaques in non-culprit, remote coronary arteries of patients with acute coronary syndrome. *Circ J*. 2005;69:1346–1351.
41. Inoue F, Sato Y, Matsumoto N, Tani S, Uchiyama T. Evaluation of plaque texture by means of multislice computed tomography in patients with acute coronary syndrome and stable angina. *Circ J*. 2004;68:840-844.
42. Tanaka M, Tomiyasu KI, Fukui M, et al. Evaluation of characteristics and degree of remodeling in coronary atherosclerotic lesions by 64-detector multislice computed tomography (MSCT). *Atherosclerosis*. 2009;203(2):436–441.
43. Funabashi N, Asano M, Komuro I. Non-calcified plaques of coronary arteries with obvious outward remodeling demonstrated by multislice computed tomography. *Int J Cardiol*. 2006;109:264.
44. Dehghani P, Marcuzzi D, Cheema AN. Use of multislice CT coronary angiography to assess degree of left main stent overhang into the aorta. *Heart*. 2009;95:708.
45. Nakamura K, Funabashi N, Uehara M, et al. Impairment factors for evaluating the patency of drug-eluting stents and bare metal stents in coronary arteries by 64-slice computed tomography versus conventional coronary angiography. *Int J Cardiol*. 2008;130:349–356.
46. Hecht HS, Zaric M, Jelnin V, Lubarsky L, Prakash M, Roubin G. Usefulness of 64-detector computed tomographic angiography for diagnosing in-stent restenosis in native coronary arteries. *Am J Cardiol*. 2008;101:820–824.
47. Jabara R, Chronos N, Klein L, et al. Comparison of multidetector 64-slice computed tomographic angiography to coronary angiography to assess the patency of coronary artery bypass grafts. *Am J Cardiol*. 2007;99:1529–1534.
48. Chiurlia E, Menozzi M, Ratti C, Romagnoli R, Modena MG. Follow-up of coronary artery bypass graft patency by multislice computed tomography. *Am J Cardiol*. 2005;95:1094–1097.
49. Meyer TS, Martinoff S, Hadamitzky M, et al. Improved noninvasive assessment of coronary artery bypass grafts with 64-slice computed tomographic angiography in an unselected patient population. *J Am Coll Cardiol*. 2007;49:946–950.
50. Gao C, Liu Z, Li B, et al. Comparison of graft patency for off-pump and conventional coronary arterial bypass grafting using 64-slice multidetector spiral computed tomography angiography. *Interact Cardiovasc Thorac Surg*. 2009;8:325–329.
51. Marini D, Agnoletti G, Brunelle F, Sidi D, Bonnet D, Ou P. Cardiac CT angiography after coronary artery surgery in children using 64-slice CT scan. *Eur J Radiol*. 2009;71(3):492–497.
52. Schussler JM, White CH, Fontes MA, Master SA, Hamman BL. Spyder proximal coronary vein graft patency over time: the SPPOT study. *Heart Surg Forum*. 2009;12:E49–E53.
53. Schachner T, Feuchtner GM, Bonatti J, et al. Evaluation of robotic coronary surgery with intraoperative graft angiography and postoperative multislice computed tomography. *Ann Thorac Surg*. 2007;83:1361–1367.
54. Peterman MA, Hamman BL, Schussler JM. 64-Slice CT angiography of saphenous vein graft anastomoses fashioned with interrupted nitinol clips. *Ann Thorac Surg*. 2007;83:1204.
55. Schussler JM, Hamman BL. Multislice cardiac computed tomography of symmetry bypass connector. *Heart*. 2004;90:1480.

56. Malagutti P, Nieman K, Meijboom WB, et al. Use of 64-slice CT in symptomatic patients after coronary bypass surgery: evaluation of grafts and coronary arteries. *Eur Heart J*. 2007;28:1879–1885.
57. Nazeri I, Shahabi P, Tehrai M, Sharif-Kashani B, Nazeri A. Assessment of patients after coronary artery bypass grafting using 64-slice computed tomography. *Am J Cardiol*. 2009;103:667–673.
58. Gilard M, Cornily JC, Pennec PY, et al. Accuracy of multislice computed tomography in the preoperative assessment of coronary disease in patients with aortic valve stenosis. *J Am Coll Cardiol*. 2006;47:2020–2024.
59. Scheffel H, Leschka S, Plass A, et al. Accuracy of 64-slice computed tomography for the preoperative detection of coronary artery disease in patients with chronic aortic regurgitation. *Am J Cardiol*. 2007;100:701–706.
60. Weinberg L, Spanger MC, Harley I, Story DA, Hall A. Multislice computed tomography coronary angiography: risk stratification of patients in the perioperative period. *Anaesth Intensive Care*. 2008;36:308–323.
61. Berbarie RF, Aslam MK, Kuiper JJ, et al. Preoperative exclusion of significant coronary artery disease by 64-slice CT coronary angiography in a patient with a left atrial myxoma. *Proc (Bayl Univ Med Cent)*. 2006;19:121.
62. Tandon A, Allison RB, Grayburn PA, Hamman BL, Schussler JM. Preoperative visualization of a muscular ventricular septal defect by 64-slice cardiac computed tomography. *Proc (Bayl Univ Med Cent)*. 2008;21:281.
63. Gibbs WN, Hamman BL, Roberts WC, Schussler JM. Diagnosis of congenital unicuspid aortic valve by 64-slice cardiac computed tomography. *Proc (Bayl Univ Med Cent)*. 2008;21:139.
64. Berbarie RF, Dockery WD, Johnson KB, Rosenthal RL, Stoler RC, Schussler JM. Use of multislice computed tomographic coronary angiography for the diagnosis of anomalous coronary arteries. *Am J Cardiol*. 2006;98:402–406.

24

CCTA: Cardiothoracic Surgery Applications

Jerold S. Shinbane, Mark J. Cunningham, Craig J. Baker, and Vaughn A. Starnes

Introduction

Cardiovascular computed tomographic angiography (CCTA) has great relevance for cardiothoracic surgical procedures, providing information essential to decisions regarding proceeding with surgical intervention, presurgical planning, as well as assessment for surgical efficacy and complications. In addition to visualization cardiovascular anatomy, CCTA provides a 3-D view of the relationships between thoracic skeletal, vascular, visceral, and cardiac structures (Figure 24.1). The spectrum of approaches to cardiovascular surgery has expanded to minimally invasively procedures [1, 2]. CCTA 3-D full field of view images with use of editing software enables visualization of multidimensional planes important to achieving access to target structures while avoiding important vascular and visceral thoracic structures for planning of these minimally invasive procedures.

Imaging Related to Coronary Artery Disease

CCTA has particular significance to planning of reoperation for coronary artery disease, as the number of prior operations incrementally increases risk. At re-operation, the majority of adverse events occur during sternotomy or prebypass dissection including injury to bypass grafts and great vessels [3, 4]. CCTA can demonstrate structures coursing immediately posterior to the sternum which may require special precautions (Figure 24.2 and 24.3). High risk features on CCTA include the right ventricle or aorta less than 1 cm from the chest wall and coronary artery bypass grafts coursing across the midline less than 1 cm from the sternum [5]. Preoperative CCTA assessment of the relationship of cardiovascular structures to the sternum has been used to plan

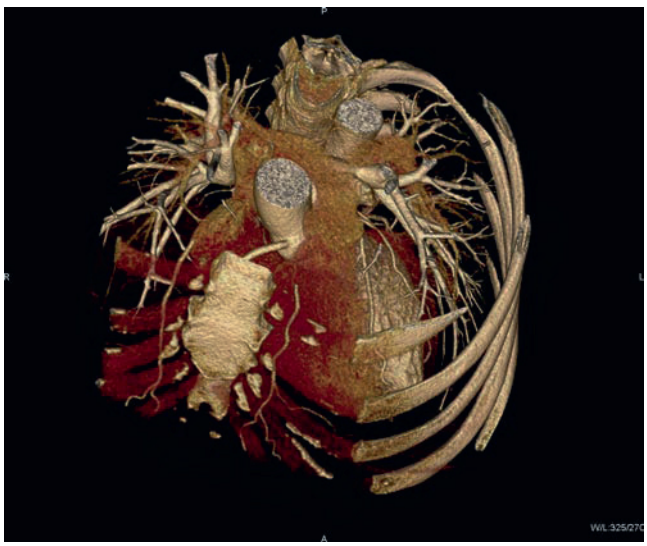

Figure 24.1. A 3-D reconstruction demonstrating the relationships between thoracic skeletal, vascular, visceral, and cardiac structures.

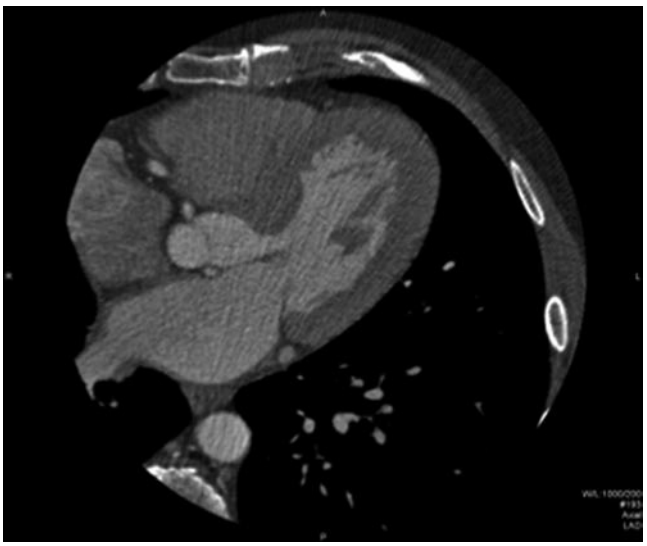

Figure 24.2. A 2-D axial view showing the right ventricle coursing immediately posterior to the sternum.

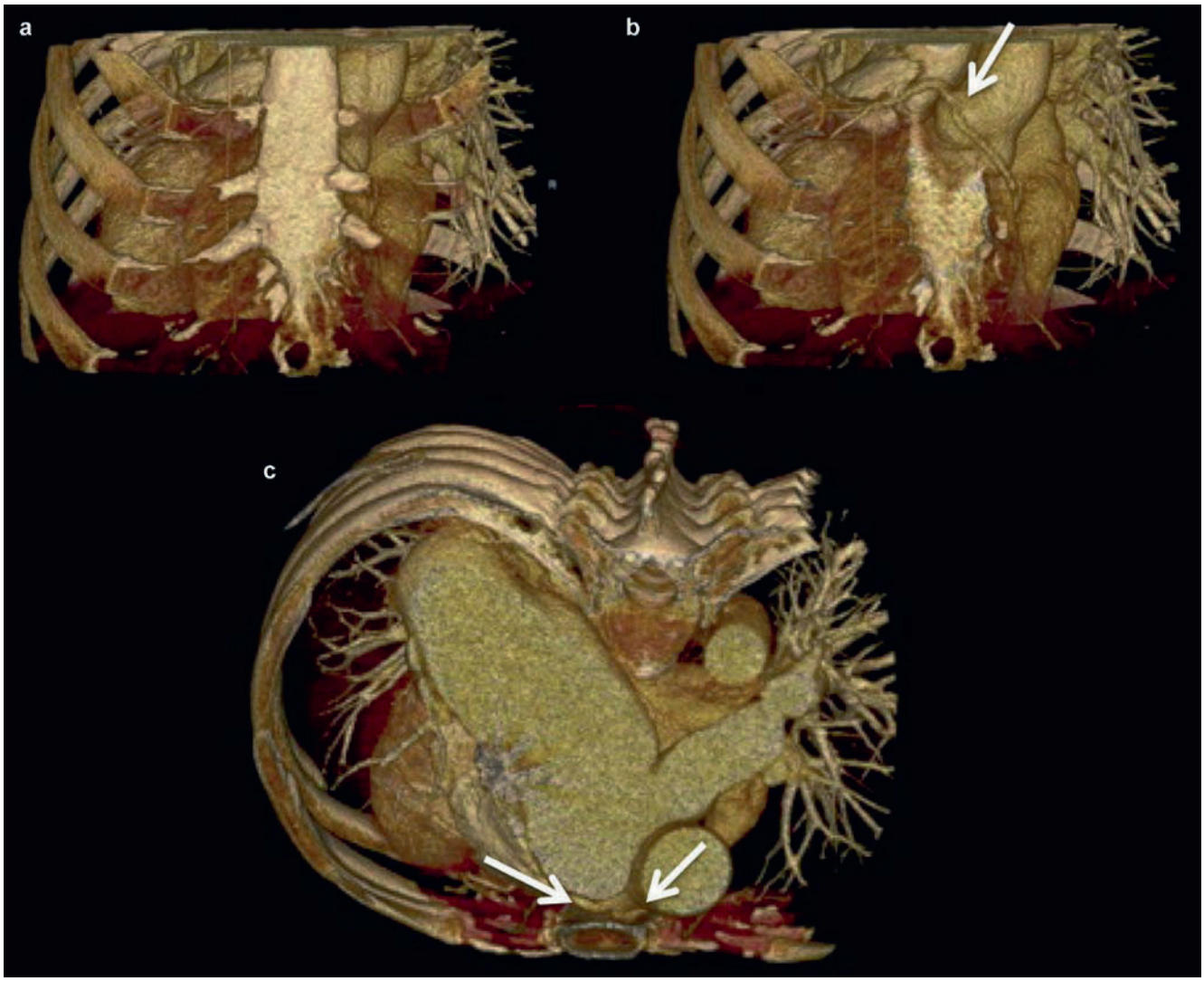

Figure 24.3. Anomalous coronary arteries (*arrows*) coursing in close proximity to the sternum. (**a**) 3-D volume rendered view demonstrating sternum. (**b**) 3-D volume rendered view with sternum partially edited to demonstrating the anomalous coronary circulation. (**c**) 3-D volume rendered view demonstrating the relation of coronary arteries to sternum.

alternate approaches in patients with high risk sternotomy anatomy, including: cancelation of surgery, nonsternotomy incisional approach, deep hypothermic cardiac arrest, initiation of peripheral cardiopulmonary bypass, and peripheral vascular dissection and exposure prior to midline sternotomy [5, 6]. Skeletal defects, traumatic injury, metastatic disease, abscess, and osteomyelitis in the sternum can also be identified (Figures 24.4 and 24.5).

In the setting of initial surgery as well as re-operation for obstructive coronary artery disease, the use of CCTA to define native coronary anatomy has limitations due to calcification of native coronary arteries and inability to define collateral flow; therefore invasive coronary artery remains the gold standard. CCTA though can be useful in assessing graft location and graft patency (Figure 24.6). CCTA may be useful prior to redo of coronary artery bypass graft surgery in situations where cardiac catheterization was unable to completely define graft anatomy, particularly as to whether a graft was occluded vs. unable to be cannulated at cardiac catheterization. CCTA in both the native as well as operated setting can define the location and patency of the left and right internal mammary arteries (Figure 24.7). Depending on the field of view, CCTA can assess for subclavian artery stenoses. If only graft location is required, increased slice thickness could be performed to decrease radiation dose. Clip artifacts may make assessment of grafts more challenging, particularly at the anastamosis site with the native coronary artery (Figure 24.8).

In the setting of coronary artery disease associated with severe ischemic cardiomyopathy, challenging decisions relate to transplant vs. high risk coronary artery bypass surgery, often with additional decisions as to valvular repair or replacement and ventricular aneurysmectomy. Assessment of myocardial viability has become important to the preprocedure decision-making process. Cardiovascular magnetic resonance imaging (CMR) has played an important role in this assessment due to the ability to assess for infarct related fibrosis as well as regional contractility [7–10]. Infarct related

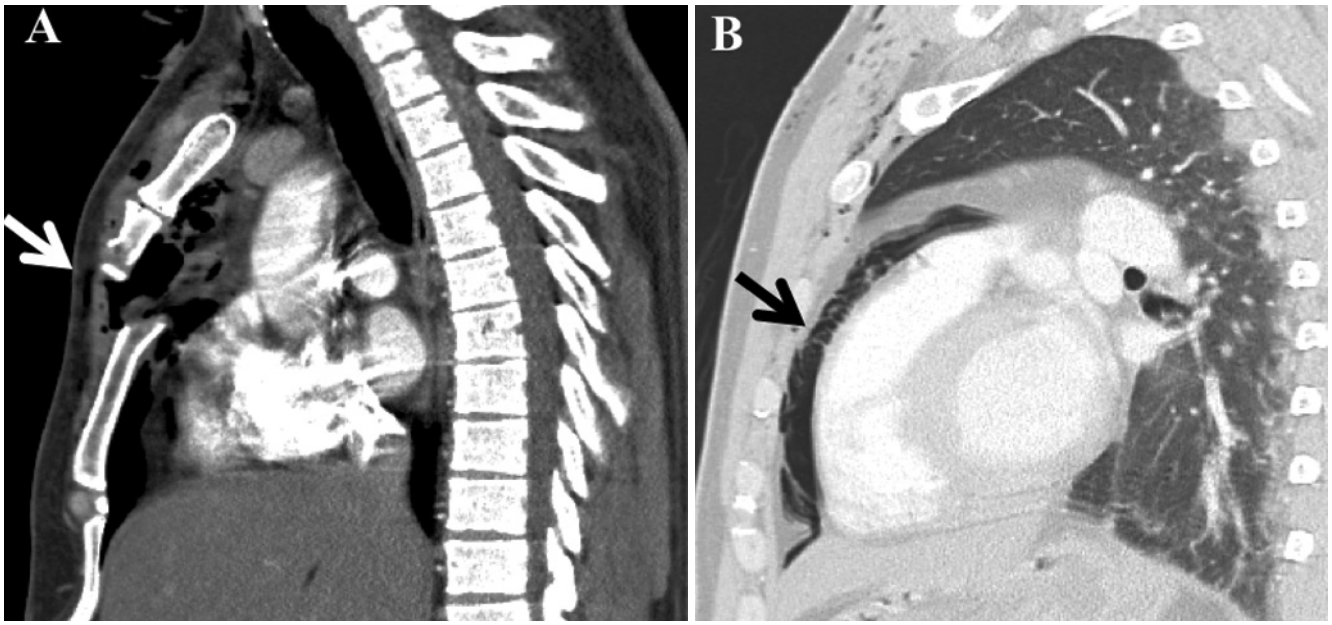

Figure 24.4. Sagittal views demonstrating traumatic injury to the chest. (**a**) Demonstration of sternal fracture (*arrow*). (**b**) Demonstration of pneumopericardium (*arrow*).

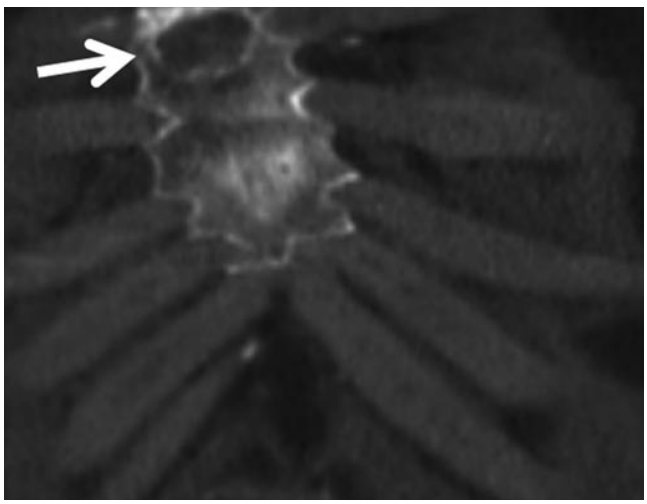

Figure 24.5. Sternal metastasis in a patient with aortic dissection.

Figure 24.6. CCTA 3-D view showing a left internal mammary artery to the left anterior descending coronary artery (*black arrow*), saphenous vein graft to an obtuse marginal branch (*double black arrow*), saphenous vein graft to a diagonal artery (*white arrow*), and saphenous vein graft to the posterior descending artery (*double white arrow*).

fibrosis can be defined quantitatively as percent myocardium infarcted, with additional definition of segmental location and transmurality of infarcted myocardium. Additionally, assessment of ventricular volumes, wall motion, myocardial perfusion, valvular function, and ventricular thrombus can be performed. These images can also be used for decision-making regarding viability and ventricular dimensions for planning of coronary artery bypass surgery and aneurysmectomy (Figure 24.9).

More recently, CCTA delayed enhancement imaging has been shown to reliably demonstrate fibrosis associated with myocardial infarction. In animal models, delayed contrast imaging has been shown to correlate with acute and chronic infarct shape and transmurality including assessment for necrosis in the acute setting [11]. This technique requires reimaging 10–15 mins after administration of iodinated contrast and therefore requires additional radiation. The technique has been demonstrated to correlate with thallium SPECT assessment of viability [12]. In the setting of acute myocardial infarction, CCTA delayed enhancement correlates with CMR assessment of viability [13]. Delayed enhancement imaging can also be performed immediately after cardiac catheterization without contrast reinjection (Figure 24.10). In this setting, CCTA delayed enhancement was associated with increased subsequent heart failure admissions and correlated with low dose dobutamine assessment of viability [14, 15]. As techniques evolve, CCTA delayed enhancement imaging may

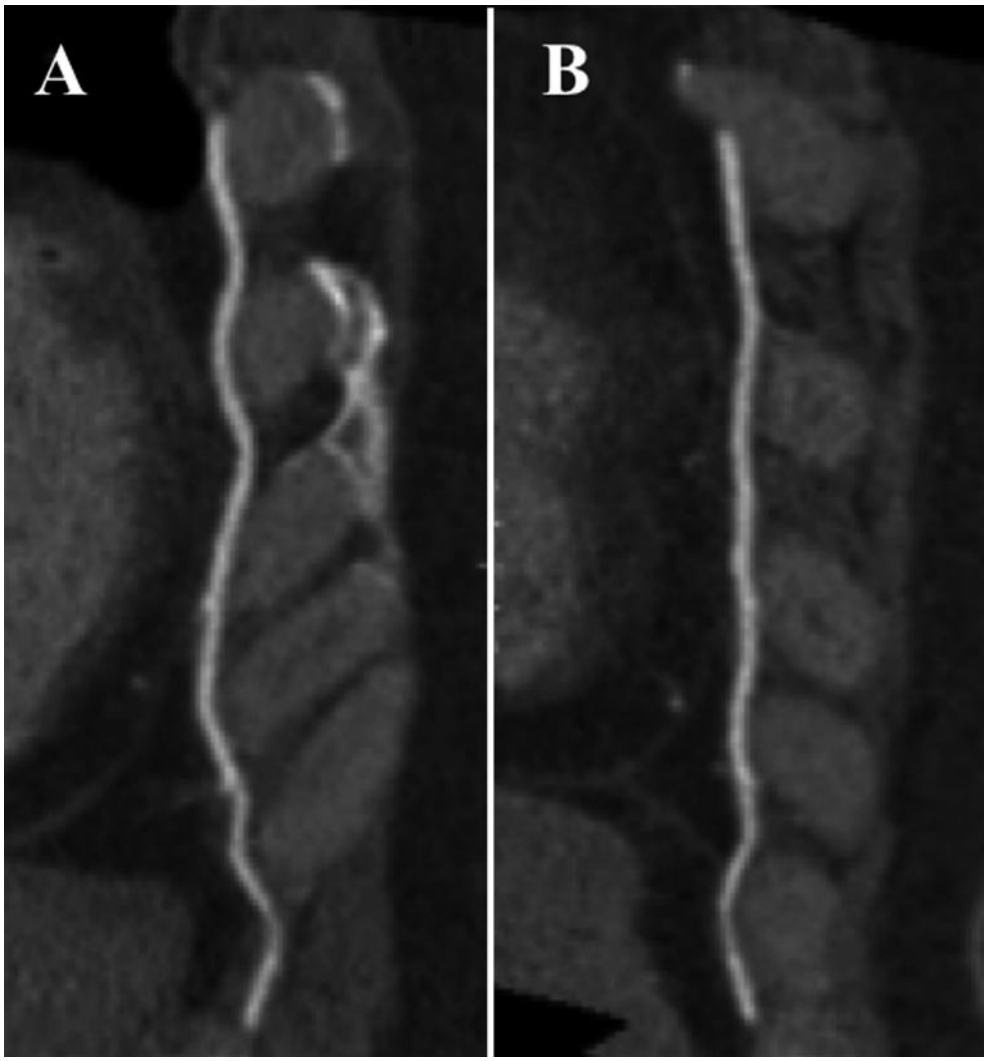

Figure 24.7. CCTA visualization of the left (**a**) and right (**b**) internal mammary arteries.

ultimately serve in a similar capacity to CMR for preoperative decision-making and planning.

Imaging Related to Valvular Disease

The role of CCTA in procedures for valvular disease includes open surgical, minimally invasive, and percutaneous approaches. Preliminary data suggest that CCTA can provide preoperative assessment of valvular and coronary artery anatomy, allowing for valvular surgery without the need for invasive cardiac catheterization in some clinical scenarios. The high negative predictive value of CCTA allows patients without obstructive disease on CCTA to proceed with valve surgery without invasive coronary angiography [16–18]. In addition to ruling out obstructive coronary artery disease, CCTA can be used to quantitatively assess valve area with planimetry in aortic stenosis comparable to that achieved with echo and cardiac catheterization [19–22]. Aortic annulus size as well as degree of calcification correlates with echo and surgical findings [23]. In the setting of aortic regurgitation, assessment can be made of the regurgitant orifice [24]. Additionally, CCTA may be used for assessment of the optimal incision site when a minimally invasive approach is contemplated. Special considerations and limitations to CCTA imaging techniques exist, as acute beta blockade and sublingual nitroglycerin may be contraindicated as part of the CCTA imaging protocol in patients with severe to critical aortic stenosis.

Percutaneous approaches to aortic valve disease include a transfemoral retrograde aortic approach or a transapical approach [25]. In transcatheter aortic valve replacement, CCTA can provide detailed information important to placement including aortic root dimensions, morphology of the aortic annulus, distance from the aortic annulus to the coronary artery ostia, and visualization of calcified plaques close the left main ostium (Figure 24.11) [26, 27]. Postoperatively, CCTA can define placement of the prosthetic valve and the relation of valve to the left main. In one study, in 50% of cases, the prosthetic valve extended into the left main ostium and valvular calcium was within 5 mm of the os [28]. Peripheral CCTA can provide assessment of factors limiting a transfemoral retrograde aortic approach, due to the large French size of the introducers. Factors

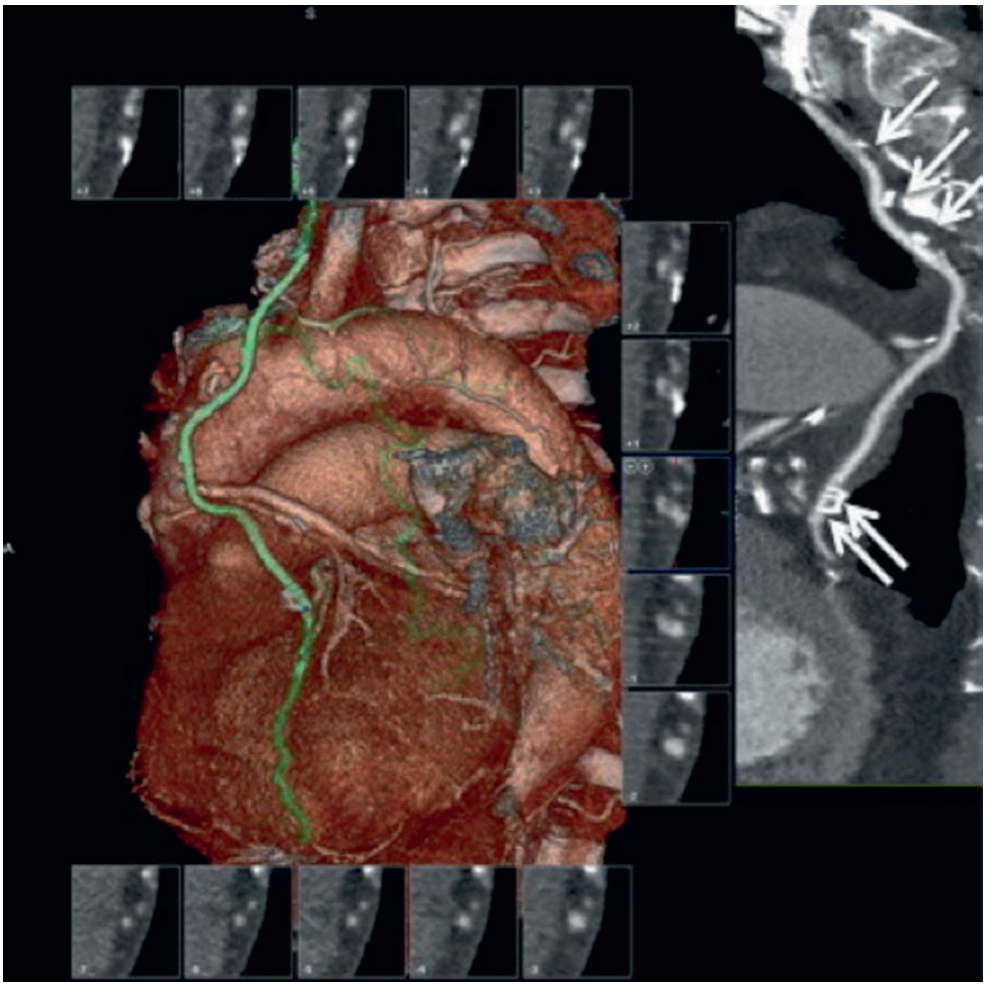

Figure 24.8. Surgical clip artifacts (*white arrows*) with a clip (*double white arrow*) obscuring the anastamosis of the left internal mammary artery graft to the left anterior descending coronary artery.

limiting placement via a transfemoral approach include small luminal diameter of the ilio-femoral arterial system, significant vessel calcification, and severe angulation between the common and external iliac arteries [29].

Regarding mitral valve procedures, CCTA can assess mitral valve geometry, tenting height, and leaflet tethering related to functional mitral regurgitation in patients with congestive heart failure [30]. In percutaneous mitral valve annuloplasty, the relationships between the mitral annulus, coronary venous anatomy, and coronary arteries are important to procedural decision-making. CCTA can provide important 3-D information on these relationships, particularly in regard to the relationship of the coronary sinus/great cardiac vein to the mitral annulus as well as the 3-D relationships between the circumflex coronary artery, coronary sinus/great cardiac vein, and mitral annulus to avoid injury to the circumflex coronary artery [31, 32].

Endocarditis involving the aortic valve and aortic root can provide particularly challenging scenarios for cardiac catheterization due to large aortic vegetations, aortic pseudo-aneurysms, and aortic root abscesses. CCTA can define the extent of infection regarding abscess, pseudo-aneurysms, and the fistula location as well as providing assessment of coronary artery anatomy (Figure 24.12) [33]. As these patients are sometimes critically ill, heart rate control may be difficult, but images may still be diagnostic. Prosthetic valve function can be viewed similarly to fluoroscopic views in order to assess mechanical valve motion as well as the presence of thrombus/vegetation (Figure 24.13).

Aortic Imaging

CCTA and CMR diagnosis of acute and chronic aortic disease is well-established. These technologies can visualize dissection, intramural hematoma, penetrating ulcer, aortic aneurysm, and aortic rupture, detailing dissection flap entry and exit site, location and extent of true and false lumen, dissection into branch vessels, involvement of the sinuses of Valsalva, dissection into the coronary arteries, and dissection into the pericardium [34–36]. CCTA can assess coronary artery anatomy when cardiac catheterization is high risk or unachievable due to aortic pathology, such as severe atherosclerotic disease with large atheromas, thrombi, aneurysms, or dissections (Figure 24.14 and 24.15). Similarly, in settings of trauma where rapid assessment for thoracic and coronary artery traumatic abnormalities is vital, CCTA may be useful [37–39]. CCTA provides assessment of vascular dimensions for endograft sizing and placement important to endovascular aneurysm repair [40]. The presence and

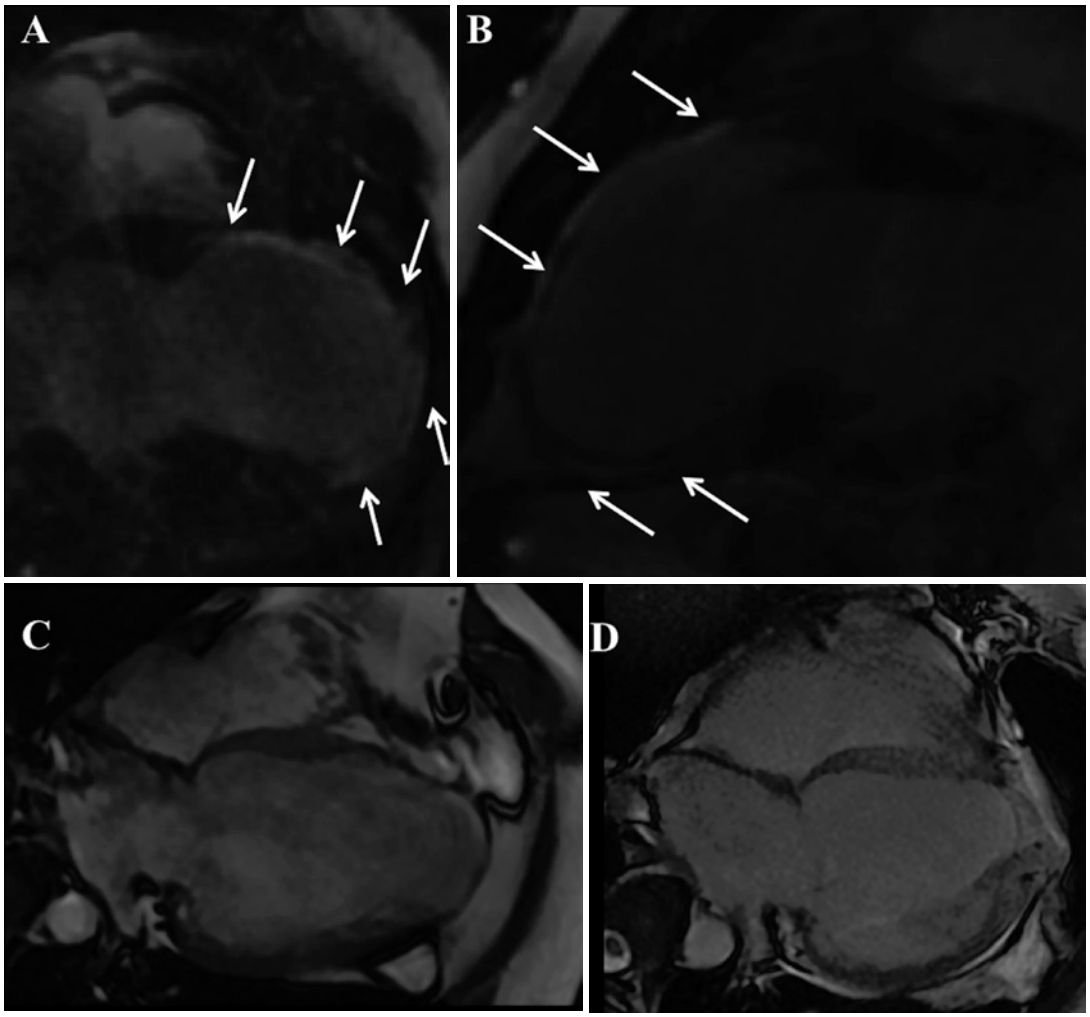

Figure 24.9. Presurgical assessment in a patient with ischemic cardiomyopathy showing transmural mid to distal anterior and inferior wall myocardial infarctions (*arrows*) on delayed gadolinium enhancement views with viability of basal segments of these walls and of the lateral territory. (**a**) 4 chamber delayed gadolinium enhanced view. (**b**) 2 chamber view delayed gadolinium enhanced view. The patient underwent coronary artery bypass graft surgery and ventricular aneurysmectomy. (**c**) Presurgical steady state free precession 4 chambers view. (**d**) Postsurgical steady state free precession 4 chambers view.

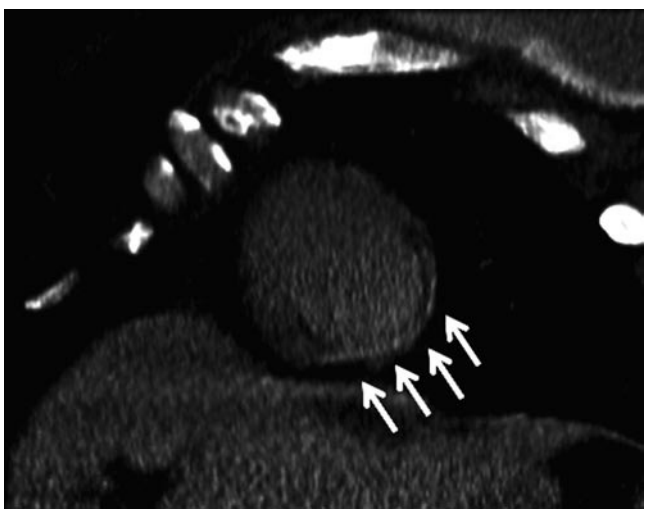

Figure 24.10. Delayed enhancement imaging performed immediately after cardiac catheterization without contrast reinjection, demonstrating inferior and inferolateral delayed enhancement on a short axis view.

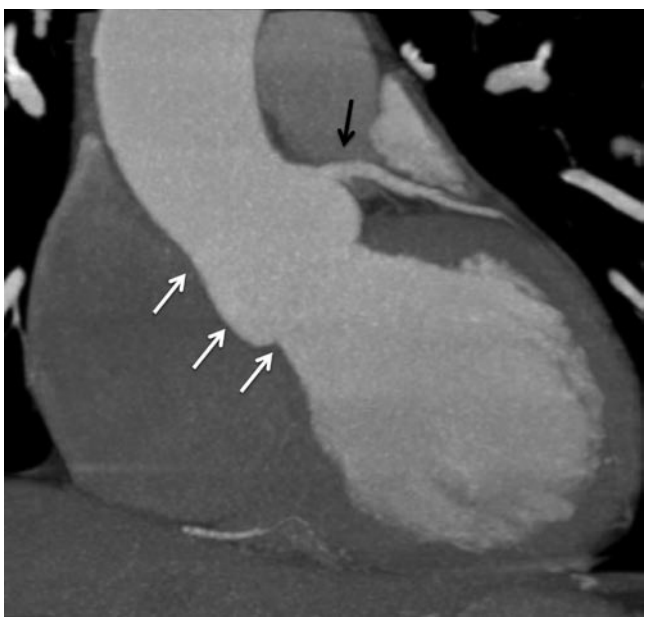

Figure 24.11. Double-oblique view in the plane of the aortic root demonstrating the relationship of the aortic annulus, sinuses of Valsalva, sinotubular junction (*white arrows*, caudal to cranial), and left main coronary artery ostium (*black arrow*).

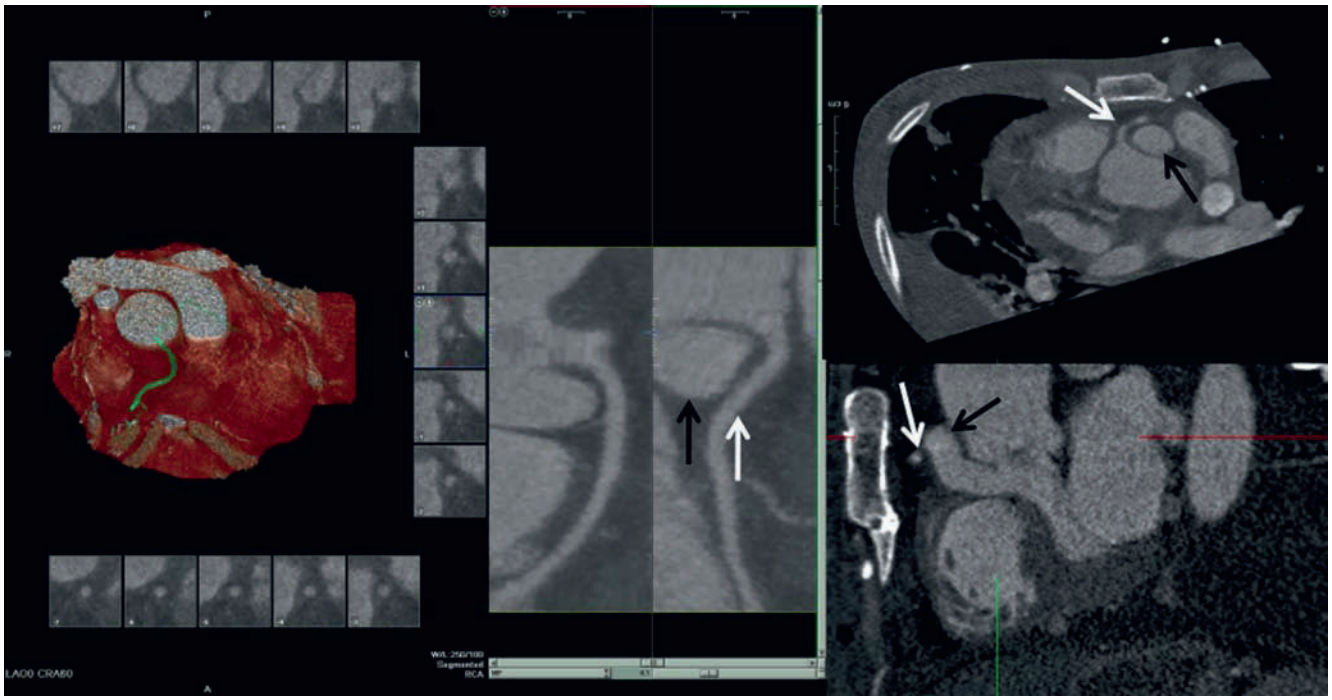

Figure 24.12. Multiplane views showing the relationship of an aortic pseudoaneurysm (*black arrows*) to the right coronary artery (*white arrows*) in a patient with aortic valve endocarditis.

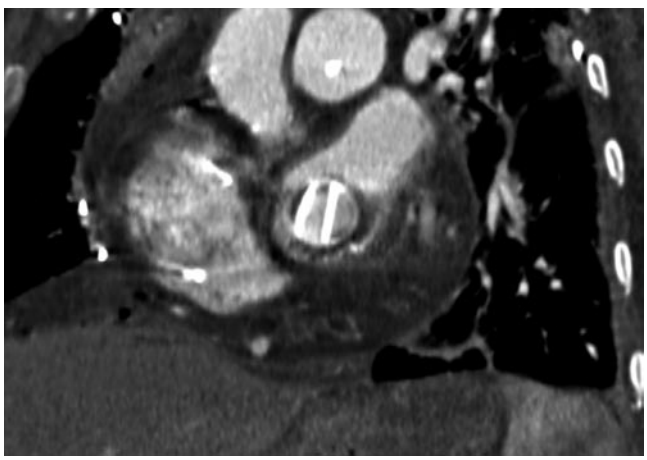

Figure 24.13. Functional images demonstrating an immobile anterior leaflet of a mechanical prosthetic mitral valve due to thrombus.

degree of atherosclerosis, calcification, and thrombus can be important to cross clamp decisions related to multiple types of cardiothoracic procedures. CCTA can also be useful in the assessment of infected aortic aneurysms, with findings including saccular structure, contiguous soft tissue masses, contrast enhancement, fluid, gas, and adjoining bone destruction [41].

Pericardial Disease

Assessment for constrictive pericarditis is challenging and often involves multiple modalities of imaging including echocardiography as well as invasive cardiac catheterization to assess hemodynamic elements. CT can be helpful in assessing pericardial thickness by cardiac region as well as the degree of calcification [42–44]. Surgical complications often relate to coronary artery damage related to dissecting the pericardium away from the coronary arteries. CCTA can define the relationship between the pericardium and coronary arteries, including areas of pericardial thickening, pericardial calcification, as well as tethering of coronary arteries on dynamic images (Figure 24.16).

Decisions regarding percutaneous vs. surgical approaches to drain pericardial fluid collections can be facilitated by CT assessment of the location, extent, and tissue characteristics of the pericardial effusion [45]. A percutaneous approach may be limited by the complexity of the effusion with loculation or effusion tissue attenuation consistent with blood, proteinaceous material, or thrombus as well as the accessibility to the effusion determined by the relation to skeletal and thoracic structures (Figure 24.17).

Congenital Heart Disease

In native or operated congenital heart disease, CCTA is useful for determining anatomy and physiology important to surgical planning, particularly in patients with pacemakers and devices, as CMR is limited in use in these settings [46, 47]. Decisions regarding the use of CCTA vs. CMR depend on multiple factors, including the age of the patient, need for assessment of small vessel anatomy, and presence of either pacemakers or ICDs. The associated radiation with CCTA is a major issue, although techniques to minimize dose are being advanced [48, 49]. CCTA definition of thoracic and abdominal situs, rotational abnormalities of thoracic vasculature, atrial and ventricular septal defects, shunts and

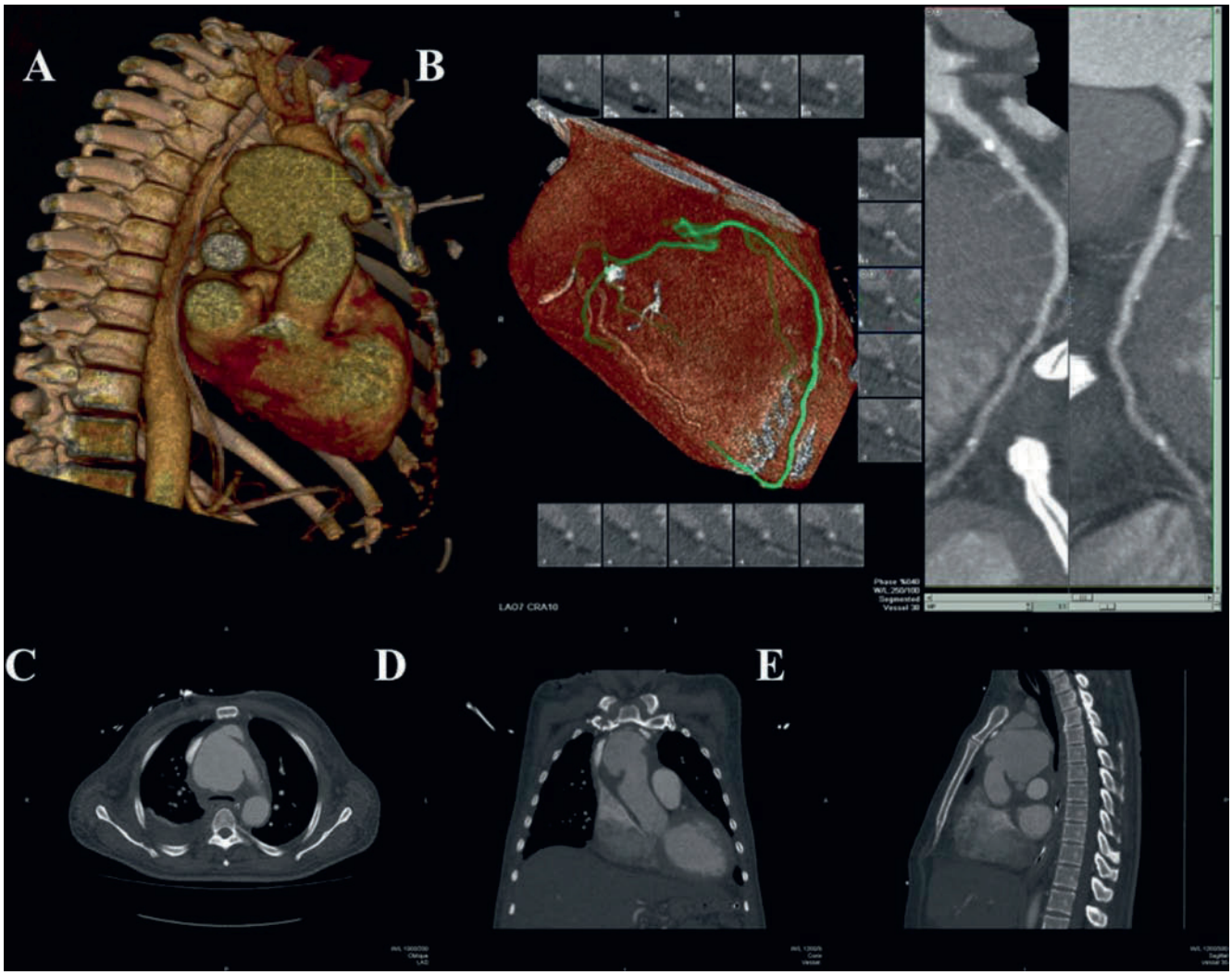

Figure 24.14. A large aortic aneurysm which may impede invasive cardiac catheterization, with multiomodal views including (**a**) 3-D view; (**b**) Curved multiplanar reformat view visualizing the left anterior descending coronary artery; (**c**) Axial view; (**d**) Coronal view; (**e**) Sagittal view.

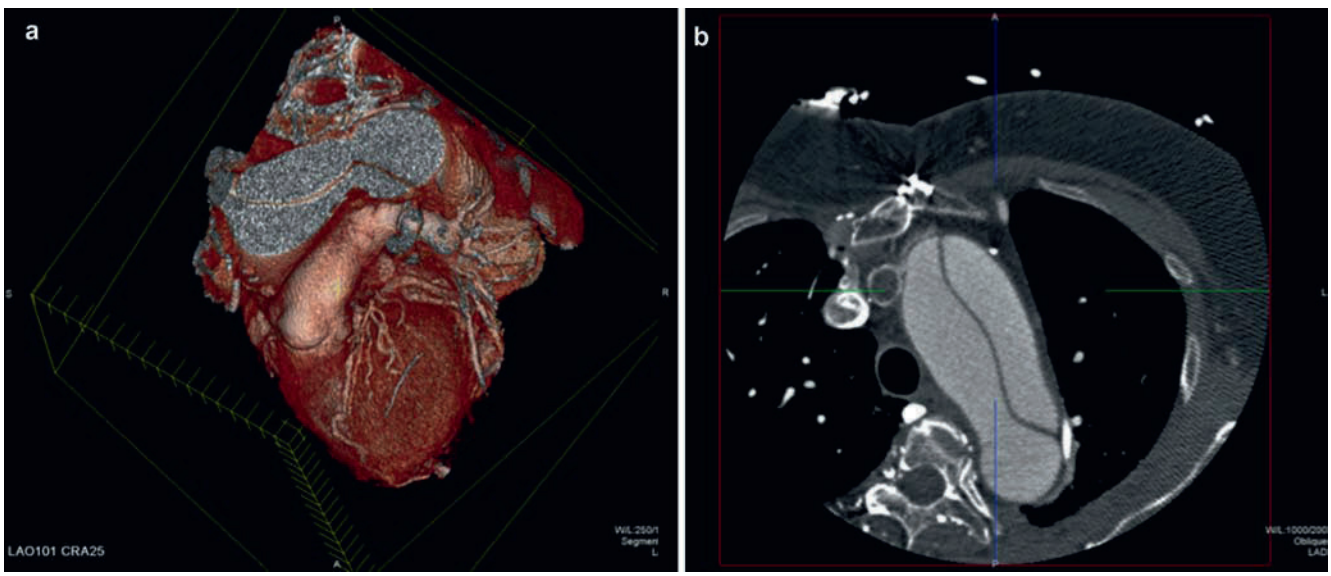

Figure 24.15. Aortic dissection making cardiac catheterization challenging for assessment for coronary artery disease. (**a**) 3-D view. (**b**) double-oblique 2-D views of an aortic dissection.

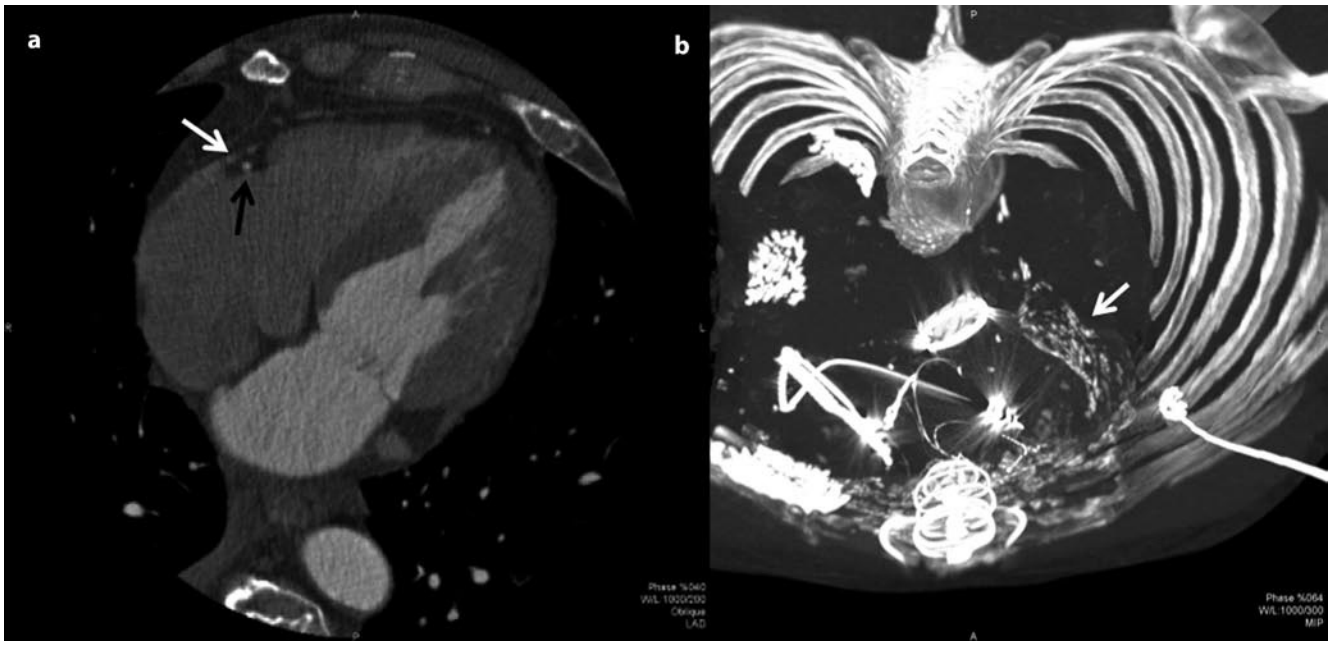

Figure 24.16. (**a**) Oblique 2-D image demonstrating the relationship of the right coronary artery (*black arrows*) to thickened pericardium (*white arrows*) prior to pericardiectomy in a patient with constrictive pericarditis. (**b**) Calcific constrictive pericarditis (*white arrow*) in a patient with rheumatic heard disease, mitral valve replacement, and a dual chamber pacemaker.

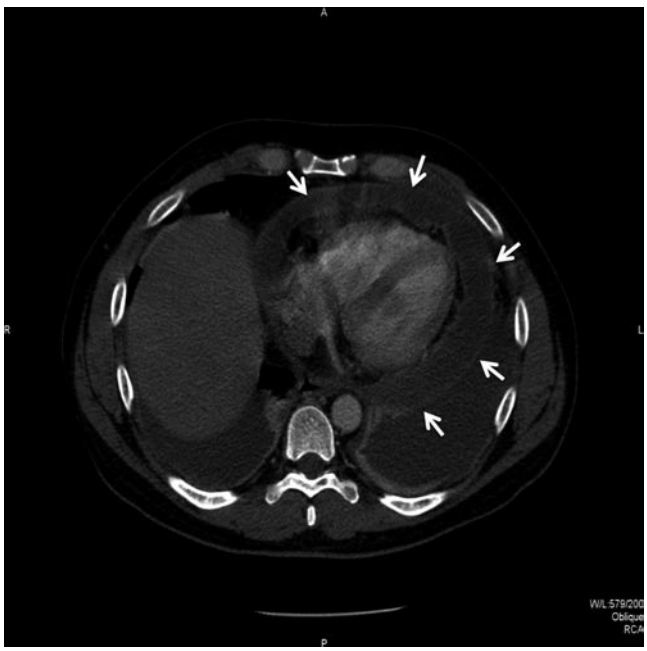

Figure 24.17. A large circumferential effusion with tissue attenuation, consistent proteinaceous material, and complexity of structure which required open surgical dissection.

fistulas, and anomalous vessels, including large vessel and small vessel anatomy, can be achieved in one 3-D data set (Figure 24.18). Examples of CCTA assessment include reimplanted coronary arteries related to procedures such as arterial switch for transposition of the great arteries [50, 51], pulmonary artery dimensions and assessment of pulmonary artery stenosis in children with congenital heart disease with associated decreased pulmonary blood flow [52], aortpulmonary collateral vessels in patients with pulmonary atresia and ventricular septal defects [53], pulmonary venous anatomy in critically ill infants [54], right ventricular function and postoperatively in patients with such conditions as tetralogy of Fallot and transposition of the great vessels [55], stents and baffles related to transposition of the great artery procedures [56], evaluation and post surgical follow-up for coarctation the aorta and patent ductus arteriosus [57–59], and shunts associated with atrial and ventricular septal defects [60].

In younger patients, where coronary artery disease is unlikely, coronary artery anomalies can lead to ischemia, infarction, and sudden cardiac death. Decisions regarding potential surgical therapy for correction depend on identification of anomalies at potential high risk for these events. Multiple factors help to determine whether or not a surgical intervention is necessary. CCTA can define absence of an artery, anomalous origin, and course in relation to arterial and cardiac chamber structures (Figure 24.19) [61–63]. The characteristics of the coronary artery os are important, especially the relationship to the aorta and the shape of the coronary artery os, including a slit-like orifice. Additional factors defining risk include artery take-off from the contralateral cusp, presence of an interarterial course, and anomalous arteries arising from other structures such as the pulmonary artery. Anomalous coronary arteries are often associated with other congenital abnormalities which can be comprehensively diagnosed. Although invasive cardiac catheterization can define anomalous coronary anatomy, often the arteries are difficult to locate and cannulate, and the os characteristics can be changed by the presence of a coronary artery catheter. CCTA can also define coronary artery fistula anatomy, including origin, course, and distal entry site as well as the characteristics of the entry site with either multiple small vessels or a single vessel [64].

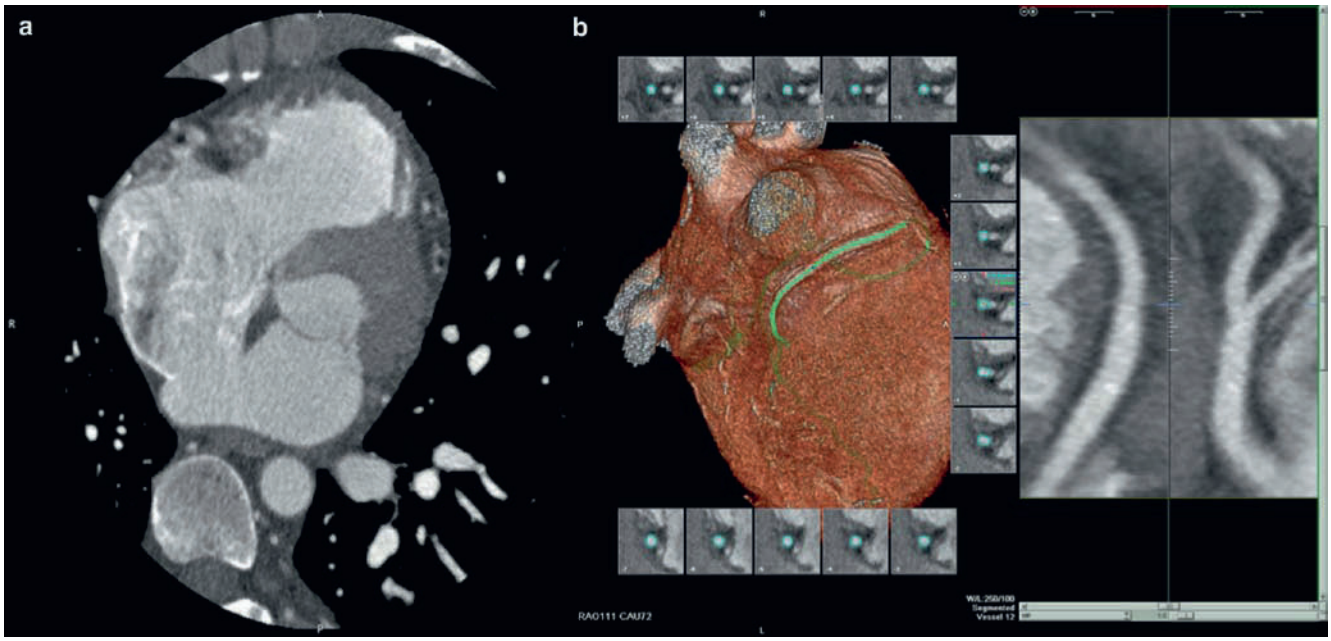

Figure 24.18. Presurgical assessment for repair of atrial septal defect. (**a**) 2-D axial view showing a large secundum atrial septal defect. (**b**) Curved multiplanar reformat demonstrating no evidence of obstructive coronary artery disease in the right coronary artery segment shown.

Figure 24.19. Anomalous coronary artery anatomy with a single coronary ostium arising from the right coronary cusp giving off a left main taking a retroaortic course and a right coronary artery. (**a**) 3D reconstruction of the coronary arteries. (**b**) Double-oblique maximal intensity projection.

Summary

The spectrum of cardiothoracic surgical options continues to expand. CCTA can facilitate surgical procedures and requires continued investigation to define optimal procedural approaches to coronary artery, valvular, and aortic pathology. Although the cardiothoracic surgeon may not necessarily be the CCTA reading physician, detailed knowledge of the images and workstation software capabilities is essential for the surgeon to attain a 3-D understanding of an individual patient's cardiothoracic presurgical anatomy. A close working relationship with the imager as well as direct viewing of multimodal images are import to the comprehensive utilization of data to define approaches to particular cardiovascular disease processes.

References

1. Nifong LW, Chitwood WR, Pappas PS, et al. Robotic mitral valve surgery: a United States multicenter trial. *J Thorac Cardiovasc Surg*. 2005;129(6):1395–1404.
2. Kim BS, Soltesz EG, Cohn LH. Minimally invasive approaches to aortic valve surgery: Brigham experience. *Semin Thorac Cardiovasc Surg*. 2006;18(2):148–153.
3. Roselli EE, Pettersson GB, Blackstone EH, et al. Adverse events during reoperative cardiac surgery: frequency, characterization, and rescue. *J Thorac Cardiovasc Surg*. 2008;135(2):316–323.
4. Sabik JF 3rd, Blackstone EH, Houghtaling PL, Walts PA, Lytle BW. Is reoperation still a risk factor in coronary artery bypass surgery? *Ann Thorac Surg*. 2005;80(5):1719–1727.
5. Kamdar AR, Meadows TA, Roselli EE, et al. Multidetector computed tomographic angiography in planning of reoperative cardiothoracic surgery. *Ann Thorac Surg*. 2008;85(4):1239–1245.
6. Gasparovic H, Rybicki FJ, Millstine J, et al. Three dimensional computed tomographic imaging in planning the surgical approach for

redo cardiac surgery after coronary revascularization. *Eur J Cardiothorac Surg*. 2005;28(2):244–249.
7. Kim RJ, Wu E, Rafael A, et al. The use of contrast-enhanced magnetic resonance imaging to identify reversible myocardial dysfunction. *N Engl J Med*. 2000;343(20):1445–1453.
8. Klein C, Nekolla SG, Bengel FM, et al. Assessment of myocardial viability with contrast-enhanced magnetic resonance imaging: comparison with positron emission tomography. *Circulation*. 2002; 105(2):162–167.
9. Kuhl HP, Beek AM, van der Weerdt AP, et al. Myocardial viability in chronic ischemic heart disease: comparison of contrast-enhanced magnetic resonance imaging with (18)F-fluorodeoxyglucose positron emission tomography. *J Am Coll Cardiol*. 2003;41(8):1341–1348.
10. Selvanayagam JB, Kardos A, Francis JM, et al. Value of delayed-enhancement cardiovascular magnetic resonance imaging in predicting myocardial viability after surgical revascularization. *Circulation*. 2004;110(12):1535–1541.
11. Lardo AC, Cordeiro MA, Silva C, et al. Contrast-enhanced multidetector computed tomography viability imaging after myocardial infarction: characterization of myocyte death, microvascular obstruction, and chronic scar. *Circulation*. 2006;113(3):394–404.
12. Chiou KR, Liu CP, Peng NJ, et al. Identification and viability assessment of infarcted myocardium with late enhancement multidetector computed tomography: comparison with thallium single photon emission computed tomography and echocardiography. *Am Heart J*. 2008;155(4):738–745.
13. Mahnken AH, Koos R, Katoh M, et al. Assessment of myocardial viability in reperfused acute myocardial infarction using 16-slice computed tomography in comparison to magnetic resonance imaging. *J Am Coll Cardiol*. 2005;45(12):2042–2047.
14. Sato A, Hiroe M, Nozato T, et al. Early validation study of 64-slice multidetector computed tomography for the assessment of myocardial viability and the prediction of left ventricular remodelling after acute myocardial infarction. *Eur Heart J*. 2008;29(4):490–498.
15. Habis M, Capderou A, Ghostine S, et al. Acute myocardial infarction early viability assessment by 64-slice computed tomography immediately after coronary angiography: comparison with low-dose dobutamine echocardiography. *J Am Coll Cardiol*. 2007;49(11): 1178–1185.
16. Gilard M, Cornily JC, Pennec PY, et al. Accuracy of multislice computed tomography in the preoperative assessment of coronary disease in patients with aortic valve stenosis. *J Am Coll Cardiol*. 2006;47(10):2020–2024.
17. Meijboom WB, Mollet NR, Van Mieghem CA, et al. Pre-operative computed tomography coronary angiography to detect significant coronary artery disease in patients referred for cardiac valve surgery. *J Am Coll Cardiol*. 2006;48(8):1658–1665.
18. Scheffel H, Leschka S, Plass A, et al. Accuracy of 64-slice computed tomography for the preoperative detection of coronary artery disease in patients with chronic aortic regurgitation. *Am J Cardiol*. 2007;100(4):701–706.
19. Tanaka H, Shimada K, Yoshida K, Jissho S, Yoshikawa J, Yoshiyama M. The simultaneous assessment of aortic valve area and coronary artery stenosis using 16-slice multidetector-row computed tomography in patients with aortic stenosis comparison with echocardiography. *Circ J*. 2007;71(10):1593–1598.
20. Lembcke A, Kivelitz DE, Borges AC, et al. Quantification of aortic valve stenosis: head-to-head comparison of 64-slice spiral computed tomography with transesophageal and transthoracic echocardiography and cardiac catheterization. *Invest Radiol*. 2009;44(1):7–14.
21. Laissy JP, Messika-Zeitoun D, Serfaty JM, et al. Comprehensive evaluation of preoperative patients with aortic valve stenosis: usefulness of cardiac multidetector computed tomography. *Heart*. 2007; 93(9):1121–1125.
22. Habis M, Daoud B, Roger VL, et al. Comparison of 64-slice computed tomography planimetry and Doppler echocardiography in the assessment of aortic valve stenosis. *J Heart Valve Dis*. 2007;16(3): 216–224.
23. Willmann JK, Weishaupt D, Lachat M, et al. Electrocardiographically gated multi-detector row CT for assessment of valvular morphology and calcification in aortic stenosis. *Radiology*. 2002;225(1):120–128.
24. Alkadhi H, Wildermuth S, Bettex DA, et al. Mitral regurgitation: quantification with 16-detector row CT–initial experience. *Radiology*. 2006;238(2):454–463.
25. Webb JG, Pasupati S, Humphries K, et al. Percutaneous transarterial aortic valve replacement in selected high-risk patients with aortic stenosis. *Circulation*. 2007;116(7):755–763.
26. Tops LF, Wood DA, Delgado V, et al. Noninvasive evaluation of the aortic root with multislice computed tomography implications for transcatheter aortic valve replacement. *JACC Cardiovasc Imaging*. 2008;1(3):321–330.
27. Akhtar M, Tuzcu EM, Kapadia SR, et al. Aortic root morphology in patients undergoing percutaneous aortic valve replacement: evidence of aortic root remodeling. *J Thorac Cardiovasc Surg*. 2009; 137(4):950–956.
28. Wood DA, Tops LF, Mayo JR, et al. Role of multislice computed tomography in transcatheter aortic valve replacement. *Am J Cardiol*. 2009;103(9):1295–1301.
29. Kurra V, Schoenhagen P, Roselli EE, et al. Prevalence of significant peripheral artery disease in patients evaluated for percutaneous aortic valve insertion: preprocedural assessment with multidetector computed tomography. *J Thorac Cardiovasc Surg*. 2009; 137(5):1258–1264.
30. Delgado V, Tops LF, Schuijf JD, et al. Assessment of mitral valve anatomy and geometry with multislice computed tomography. *JACC Cardiovasc Imaging*. 2009;2(5):556–565.
31. Mao S, Shinbane JS, Girsky MJ, et al. Coronary venous imaging with electron beam computed tomographic angiography: three-dimensional mapping and relationship with coronary arteries. *Am Heart J*. 2005;150(2):315–322.
32. Choure AJ, Garcia MJ, Hesse B, et al. In vivo analysis of the anatomical relationship of coronary sinus to mitral annulus and left circumflex coronary artery using cardiac multidetector computed tomography: implications for percutaneous coronary sinus mitral annuloplasty. *J Am Coll Cardiol*. 2006;48(10):1938–1945.
33. Feuchtner GM, Stolzmann P, Dichtl W, et al. Multislice computed tomography in infective endocarditis: comparison with transesophageal echocardiography and intraoperative findings. *J Am Coll Cardiol*. 2009;53(5):436–444.
34. Hayter RG, Rhea JT, Small A, Tafazoli FS, Novelline RA. Suspected aortic dissection and other aortic disorders: multi-detector row CT in 373 cases in the emergency setting. *Radiology*. 2006;238(3):841–852.
35. Yoshida S, Akiba H, Tamakawa M, et al. Thoracic involvement of type A aortic dissection and intramural hematoma: diagnostic accuracy–comparison of emergency helical CT and surgical findings. *Radiology*. 2003;228(2):430–435.
36. Yoshikai M, Ikeda K, Itoh M, Noguchi R. Detection of coronary artery disease in acute aortic dissection: the efficacy of 64-row multidetector computed tomography. *J Card Surg*. 2008;23(3):277–279.
37. Smayra T, Noun R, Tohme-Noun C. Left anterior descending coronary artery dissection after blunt chest trauma: assessment by multidetector row computed tomography. *J Thorac Cardiovasc Surg*. 2007;133(3):811–812.
38. Sato Y, Matsumoto N, Komatsu S, et al. Coronary artery dissection after blunt chest trauma: depiction at multidetector-row computed tomography. *Int J Cardiol*. 2007;118(1):108–110.
39. Scaglione M, Pinto A, Pinto F, Romano L, Ragozzino A, Grassi R. Role of contrast-enhanced helical CT in the evaluation of acute thoracic aortic injuries after blunt chest trauma. *Eur Radiol*. 2001;11(12):2444–2448.
40. Higashiura W, Sakaguchi S, Tabayashi N, Taniguchi S, Kichikawa K. Impact of 3-dimensional-computed tomography workstation for precise planning of endovascular aneurysm repair. *Circ J*. 2008; 72(12):2028–2034.
41. Lin MP, Chang SC, Wu RH, Chou CK, Tzeng WS. A comparison of computed tomography, magnetic resonance imaging, and digital subtraction angiography findings in the diagnosis of infected aortic aneurysm. *J Comput Assist Tomogr*. 2008;32(4):616–620.

42. Suh SY, Rha SW, Kim JW, et al. The usefulness of three-dimensional multidetector computed tomography to delineate pericardial calcification in constrictive pericarditis. *Int J Cardiol*. 2006; 113(3):414–416.
43. von Erffa J, Daniel WG, Achenbach S. Three-dimensional visualization of severe pericardial calcification in constrictive pericarditis using multidetector-row computed tomography. *Eur Heart J*. 2006;27(3):275.
44. Kameda Y, Funabashi N, Kawakubo M, et al. Heart in an eggshell–eggshell appearance calcified constrictive pericarditis demonstrated by three-dimensional images of multislice computed tomography. *Int J Cardiol*. 2007;120(2):269–272.
45. Rifkin RD, Mernoff DB. Noninvasive evaluation of pericardial effusion composition by computed tomography. *Am Heart J*. 2005; 149(6):1120–1127.
46. Cook SC, Dyke PC 2nd, Raman SV. Management of adults with congenital heart disease with cardiovascular computed tomography. *J Cardiovasc Comput Tomogr*. 2008;2(1):12–22.
47. Shinbane JS, Colletti PM, Shellock FG. MR in patients with pacemakers and ICDs: defining the issues. *J Cardiovasc Magn Reson*. 2007;9(1):5–13.
48. Hoffmann A, Engelfriet P, Mulder B. Radiation exposure during follow-up of adults with congenital heart disease. *Int J Cardiol*. 2007;118(2):151–153.
49. Saad MB, Rohnean A, Sigal-Cinqualbre A, Adler G, Paul JF. Evaluation of image quality and radiation dose of thoracic and coronary dual-source CT in 110 infants with congenital heart disease. *Pediatr Radiol*. 2009;39(7):668–676.
50. Oztunc F, Baris S, Adaletli I, et al. Coronary events and anatomy after arterial switch operation for transposition of the great arteries: detection by 16-row multislice computed tomography angiography in pediatric patients. *Cardiovasc Intervent Radiol*. 2009; 32(2):206–212.
51. Ou P, Celermajer DS, Marini D, et al. Safety and accuracy of 64-slice computed tomography coronary angiography in children after the arterial switch operation for transposition of the great arteries. *JACC Cardiovasc Imaging*. 2008;1(3):331–339.
52. Hayabuchi Y, Mori K, Kitagawa T, Inoue M, Kagami S. Accurate quantification of pulmonary artery diameter in patients with cyanotic congenital heart disease using multidetector-row computed tomography. *Am Heart J*. 2007;154(4):783–788.
53. Maeda E, Akahane M, Kato N, et al. Assessment of major aortopulmonary collateral arteries with multidetector-row computed tomography. *Radiat Med*. 2006;24(5):378–383.
54. Hirsch R, Gottliebson W, Crotty E, Fleck R, Strife J. Computed tomography angiography with three-dimensional reconstruction for pulmony venous definition in high-risk infants with congenital heart disease. *Congenit Heart Dis*. 2006;1(3):104–110.
55. Raman SV, Cook SC, McCarthy B, Ferketich AK. Usefulness of multidetector row computed tomography to quantify right ventricular size and function in adults with either tetralogy of Fallot or transposition of the great arteries. *Am J Cardiol*. 2005;95(5):683–686.
56. Cook SC, McCarthy M, Daniels CJ, Cheatham JP, Raman SV. Usefulness of multislice computed tomography angiography to evaluate intravascular stents and transcatheter occlusion devices in patients with d-transposition of the great arteries after mustard repair. *Am J Cardiol*. 2004;94(7):967–969.
57. Hu XH, Huang GY, Pa M, et al. Multidetector CT angiography and 3D reconstruction in young children with coarctation of the aorta. *Pediatr Cardiol*. 2008;29(4):726–731.
58. Pinilla I, Bret M, Cuesta E, Borches D, Oliver JM, Gomez-Leon N. Role of computed tomography and magnetic resonance imaging in aortobronchial fistula diagnosis following aortic coarctation reparative surgery. Report of two cases. *J Cardiovasc Surg*. (Torino) 2006;47(2): 221–227.
59. Morgan-Hughes GJ, Marshall AJ, Roobottom C. Morphologic assessment of patent ductus arteriosus in adults using retrospectively ECG-gated multidetector CT. *AJR Am J Roentgenol*. 2003; 181(3):749–754.
60. Funabashi N, Asano M, Sekine T, Nakayama T, Komuro I. Direction, location, and size of shunt flow in congenital heart disease evaluated by ECG-gated multislice computed tomography. *Int J Cardiol*. 2006;112(3):399–404.
61. Sato Y, Inoue F, Matsumoto N, et al. Detection of anomalous origins of the coronary artery by means of multislice computed tomography. *Circ J Mar*. 2005;69(3):320–324.
62. de Jonge GJ, van Ooijen PM, Piers LH, et al. Visualization of anomalous coronary arteries on dual-source computed tomography. *Eur Radiol*. 2008;18(11):2425–2432.
63. Datta J, White CS, Gilkeson RC, et al. Anomalous coronary arteries in adults: depiction at multi-detector row CT angiography. *Radiology*. 2005;235(3):812–818.
64. Dodd JD, Ferencik M, Liberthson RR, et al. Evaluation of efficacy of 64-slice multidetector computed tomography in patients with congenital coronary fistulas. *J Comput Assist Tomogr*. 2008; 32(2):265–270.

25

Orientation and Approach to Cardiovascular Images

Yasmin Hamirani, Antreas Hindoyan, and Jerold S. Shinbane

Introduction

Cardiovascular computed tomographic angiography (CCTA) allows for the comprehensive analysis of a variety of cardiovascular diseases. Reading CCTA scans in many ways is easier than interpreting invasive cardiac angiography or echocardiography, as the data are obtained as one 3D data cube in the axial plane. The focus of this chapter is to orient the reader to viewing and analyzing CCTA images.

Axial Images

The axial view (Figures 25.1–25.34) is the primary view for the identification and assessment of cardiovascular anatomy, with other 2D and 3D views used for confirmation of the findings noted. In the axial plane, the thorax is imaged in serial slices, either cranio-caudally or, in some cases, caudal to cranial. Thinner slices enable the reader to examine what is contained in a slice with greater clarity and detail than thicker slices. Just as slices of bread can be stacked in sequence to reconstitute the original loaf, the axial slices of the thorax can be aligned in sequence to reconstruct cardiovascular structures, using an advanced post-processing workstation.

Cardiac axial images are routinely acquired with a small field of view (FOV), allowing increased resolution of data analyzed for cardiac disease. However, all CT systems have multiple FOV settings to allow for imaging of the entire chest, not just the cardiac field. For an evaluation of the cardiac structures and the coronary arteries, a small FOV is recommended. CCTA uses a 512 × 5 12 matrix, with each pixel representing a certain amount of data. With a smaller FOV (i.e., 15 cm), each pixel represents more data (better spatial resolution). If the FOV is enlarged (i.e., 30 cm), this halves the resolution in each voxel, as 512 pixels are each divided into portions to constitute 30 cm. The small FOV focuses on the field of interest without degrading the image quality prior to transfer to the workstation, allowing the physician to zoom in on smaller structures during image analysis.

The axial slices are viewed cranio-caudally. The reader should visualize the patient in the supine position with the patient's feet coming out towards the reader. For orientation to the patient's right and left side, think of "shaking hands" with the image, with the patient's right being the reader's left and vice versa. The sternum (anterior) and spine (posterior) can also be used to orient the reader in the axial plane. The reader should never try to analyze a structure using one axial slice. Assessment of adjacent axial slices to establish anatomic continuity should be performed for comprehensive identification of a structure.

The images should be assessed for contrast timing and dose, in order to gauge the adequacy of contrast enhancement of the left ventricle, aortic root, and coronary arteries. If the right ventricle appears more enhanced than the left ventricle, the images may have been acquired too early after contrast administration. Additionally, the presence of significant contrast in the superior vena cava can cause "streak artifact," which could make interpretation of the mid right coronary artery difficult.

The reader needs to use a systematic and comprehensive method for analyzing images rather than immediately focusing on the most prominent findings. When reviewing axial images in a methodical manner, one may first focus on the noncoronary structures. Components of analysis should include: the cardiac and thoracic situs, abdominal situs (if views extend to this level), the size and architecture of aorta and branch vessels at all visualized levels, the size and architecture of the main pulmonary artery and pulmonary artery branches, 3D relationships between the aorta and pulmonary arteries, anomalous thoracic vascular anatomy, location/number/course of the pulmonary veins, atrioventricular and ventriculoarterial concordance, continuity of the atrial septum, continuity of the ventricular septum, the presence of filling defects in the left atrial appendage, atria and ventricles, other cardiac masses, gross valvular structure, myocardial thickness and tissue attenuation, and pericardial thickness and presence of effusion. Additional

assessment of appropriately windowed full field of view images need to be performed to assess thoracic structure including: skeletal structure, pulmonary vascular structures for presence of pulmonary artery filling defects, lung parenchyma, presence of thoracic masses, and assessment of abdominal structures which may be in the field of view.

Next, attention may be focused on coronary vascular structures. Prior to assessment for coronary arterial atherosclerotic disease on the axial slices, the origins and course of the coronary arteries should be assessed. Viewing the aortic root in the axial plane as a "clock face," the right coronary artery is seen arising from the right coronary cusp at approximately 11:30 on the "clock face" and the left main coronary artery arises off of the left coronary cusp at approximately 3:30 on the "clock face." The cusps should be assessed for any anomalous origin of the coronary arteries. The course and termination of the arteries should be assessed with evaluation for an anomalous course as well as an intramyocardial course. The coronary artery dominance should also be evaluated.

Beginning at the most cranial slices, maximum intensity projections can be viewed at 5 mm slice thickness. This helps with visualization of the longitudinal course of the vessels, with one limitation being that the brightest pixel dominates the image. Therefore, in the presence of heavily calcified segments, one might miss a noncalcified plaque causing a significant narrowing of the coronary vessel. Adjusting the slice thickness back to 0.5 mm, each coronary artery segment can be followed, assessing for the presence of calcified, mixed, and noncalcified plaque in the vessels of mild, moderate, or severe grades. The coronary artery calcium images should also be referenced as they demonstrate the presence and location of calcium without contrast in the coronary arteries.

In the axial view, the vessels are followed in the plane of image acquisition. If the CT system used does not provide true isotropic voxels due to limited z axis resolution, the axial view provides the most pristine images, as manipulation in other planes does not have the same resolution. Each individual artery should be followed through the cranial to caudal axial slices rather than attempting to view multiple arteries on one axial slice. The left main coronary artery, left anterior descending coronary artery, circumflex coronary artery, and right coronary artery are analyzed individually along with their branches. The posterior descending artery can be visualized either coming from the right coronary artery or circumflex, running in the posterior interventricular groove.

In the axial view, a patent artery usually appears as a circle or linear segment, depending on the orientation of the artery to the axial plane. Assessing areas where the coronary arteries turn or are tortuous can be challenging using the axial views. The right coronary artery, due to excessive motion, may have a "cashew nut" like shape or appear as a double image. As one courses from cranial to caudal following a particular artery, a different phase of the R-R interval may need to be chosen in order to minimize motion artifact. As the axial views do not follow the in-plane course of the coronary arteries, other views including 3D, double oblique, and curved multiplanar reformatted (MPR) views are employed to follow the course of the artery being analyzed. With curved MPR views, a centerline is created and the artery "straightened out" and viewed as a cylinder. As there are potential artifacts with all of these additional techniques, the axial slices should always be used to confirm or exclude any potential lesions that might be seen with other reconstructions.

Coronal and Sagittal Images

In the coronal and sagittal views (Figures 25.35–25.67 and Figures 25.68–25.131), multiple stacks of images are viewed at once. Within a single breath hold using a 64 slice scanner with 0.625 mm thick slices, 40 mm of heart is acquired in one heart beat. Three to four heartbeats are required to cover the whole heart. The data sets are then aligned. In most cases, thin collimation lines seen on the coronal images separate them. If the data sets are not aligned properly, step artifact is seen, which is important to identify since it may appear as a stenosis on reconstructed views. This artifact would not be present using scanners which have an acquisition volume which can image the heart in one gantry rotation. Also, in the coronal and sagittal views, the homogeneity of contrast, measured as Hounsfield units (HU), can be assessed in the descending aorta measured cranial to caudal on a slice which demonstrates the aorta. If the HUs decrease significantly as the aorta descends, the distal coronary arteries may be less well opacified and more difficult to analyze.

With coronal images, the heart is viewed from anterior to posterior while scrolling through multiple stacks of images. Small pericardial effusions can be appreciated on coronal images with the fluid layering in the pericardial space just above the diaphragm. The HU cursor, if placed on the effusion, can confirm that the attenuation of the fluid is near water attenuation (0 HU). In coronal images on anterior slices, the sternum is visualized. Thickened image sets using maximum intensity projection views can be used to follow the course of right and left internal mammary arteries on both sides of the sternum for patency as well as to assess whether or not they have been used as arterial bypass grafts in a patient with history of coronary artery bypass graft surgery. The mid segment of right coronary artery is best visualized in the coronal image plane. With sagittal images, the heart can be viewed by scrolling through the chest from left to right on multiple stacks of images. Sagittal images are helpful for viewing the aortic arch as well as the origin of venous grafts.

Double Oblique Views

The axial, coronal, or sagittal views can be used as a starting point to rotate an image slice out of these standard planes through the 3D CCTA data cube. Use of oblique views allows the reader to follow the course of each coronary artery, which is especially useful for tortuous segments. The optimal assessment plane for the most proximal

segment of a coronary artery can be identified and then rotated 360°. The oblique plane is the moved at small increments to identify each subsequent segment of the artery. Additionally, starting from the standard axial, coronal, and sagittal planes, oblique views can be displayed allowing vascular structures to be measured en face, such as at various levels of the aorta (aortic annulus, sinus of Valsalva, sinotubular junction, ascending, arch, and descending aorta), pulmonary arteries, pulmonary vein ostia, and atrial and ventricular septal defects. As these structures often have ovoid rather than circular shapes, the maximum and minimum diameters as well as the area of the structure can be quantified.

Curved Multiplanar Reformatted Views

Curved MPR images can be used to evaluate an entire coronary artery in one view. The reader can choose the plane of a specific artery, which is displayed as a "curved surface" from within the 3D volume. This view also creates cross sectional cuts of each coronary arterial segment. The thickness of the cross sectional cuts can be adjusted using workstation software. All other structures are automatically eliminated, including the side branches, and separate reconstructions can be rendered for every side branch. With MPR images, uncertainties as to the true center of the vessel may be of concern, causing the computer to create the appearance of a stenosis by following an area of dense calcium rather than the vessel lumen. Additionally, the centerline can jump from the coronary artery to follow an adjacent coronary vein. The centerline can be viewed in order to ensure that it remains within the vessel of analysis. Keeping this limitation in mind, curved MPR is an extremely useful tool to evaluate CCTA data. While constructing curved MPR images, cross sectional images of each artery are obtained allowing comparison of the segment of interest (coronary artery stenosis) to the segments above and below it as a reference. Additionally, the long axis has a luminal view that can be rotated the 360° around its central axis in order to assess eccentric plaques and stenoses.

Volume Rendered 3D Images

The volume rendered technique relies on identifying all pixels above a certain threshold with various degrees of attenuation. The results are most similar to invasive coronary angiography, with no change in the true anatomic course or relationship of coronary arteries with other structures, and the coronary arteries seen as relatively smooth structures with 3D landmarks present. The image can be rotated, allowing the interpreter some flexibility in visualizing the segment from multiple angles. A stenotic coronary artery segment will look darker as well as narrowed on volume rendered images. The 3D volume rendered images in CCTA help in identification of coronary anomalies as well as to assess the dominance of the coronary arterial tree. In patients with previous coronary artery bypass graft surgery, the origin of grafts from the aorta can be counted and the course of grafts can be followed to a particular native vessel. Stumps of occluded grafts can also be easily identified.

Although the 3D images are intuitive regarding orientation to cardiovascular structures, the automatic editing software can edit out parts of the coronary arteries, mimicking stenoses. One method to avoid this automatic over editing would be hand-editing, which is cumbersome and time-consuming. Myocardial bridging can also appear as coronary artery occlusion as the artery courses intramyocardially from the epicardium. Due to issues related to the reconstruction, the volume rendered images are not used as the primary modality to document the presence of stenosis. Confirmation of coronary artery findings using other modalities is essential.

Endovascular 3D views can also be obtained to assess such structures as the pulmonary veins. This technique is extremely dependent on filtering and therefore, although useful for assessing the 3D structures from an endovascular perspective, can be problematic regarding use for anatomic measurements. Instead, 2D measurements in the appropriate plane should be used.

Functional Views

For retrospectively gated studies, functional views can be reformatted for assessment of left ventricular volumes and function, and, depending on the techniques used, right ventricular and left atrial volumes and function. End-diastolic measurements of ventricular wall thickness can be obtained on short axis views. The aortic valve and mitral valve anatomy and motion can be assessed regarding valve cusp number, valve excursion, valve apposition, and valve prolapse. Functional image sets can be formatted following the traditional echo views, but with the ability to view motion through the entire cardiac volume in these views. Functional views can also be viewed in oblique planes for dynamic analysis of specific structures.

Conclusion

CCTA provides the ability to use multiple planes of images to document abnormalities of the thoracic vasculature, heart, and the coronary vessels. Although axial images are most commonly relied on for final interpretation, other planes and reconstruction modalities, if used with a thorough knowledge of their strengths and limitations, are important to analysis. The employment of these modalities in an organized approach coupled with an understanding of the spatial relationships between cardiovascular structures allow for comprehensive diagnosis of cardiovascular pathology. The images that follow in this chapter will help the reader orient to CCTA axial, coronal, and sagittal views.

2D Orientation Images Sets

AAO ascending aorta; *AV* aortic valve; *DAO* descending aorta; Diag diagonal; *IAS* interatrial septum; *IPV* inferior pulmonary vein; *IVC* inferior vena cava; *IVS* interventricular septum; *LA* left atrium; *LAA* left atrial appendage; L*AD* left anterior descending coronary artery; *LCX* left circumflex coronary artery; *LIMA* left internal mammary artery; *LM* left main coronary artery; *LS* left sinus of Valsalva; *LV* left ventricle; *MV* mitral valve; *PA* pulmonary artery; *RA* right atrium; *RAA* right atrial appendage; *RCA* right coronary artery; *RIMA* right internal mammary artery; *RV* right ventricle; *SPV* superior pulmonary vein; *SVC* superior vena cava..

Orientation to Axial Images

Figures 25.1–25.34. Serial axial CT angiography images beginning at the level of the pulmonary artery with slices proceeding in a cranial to caudal direction.

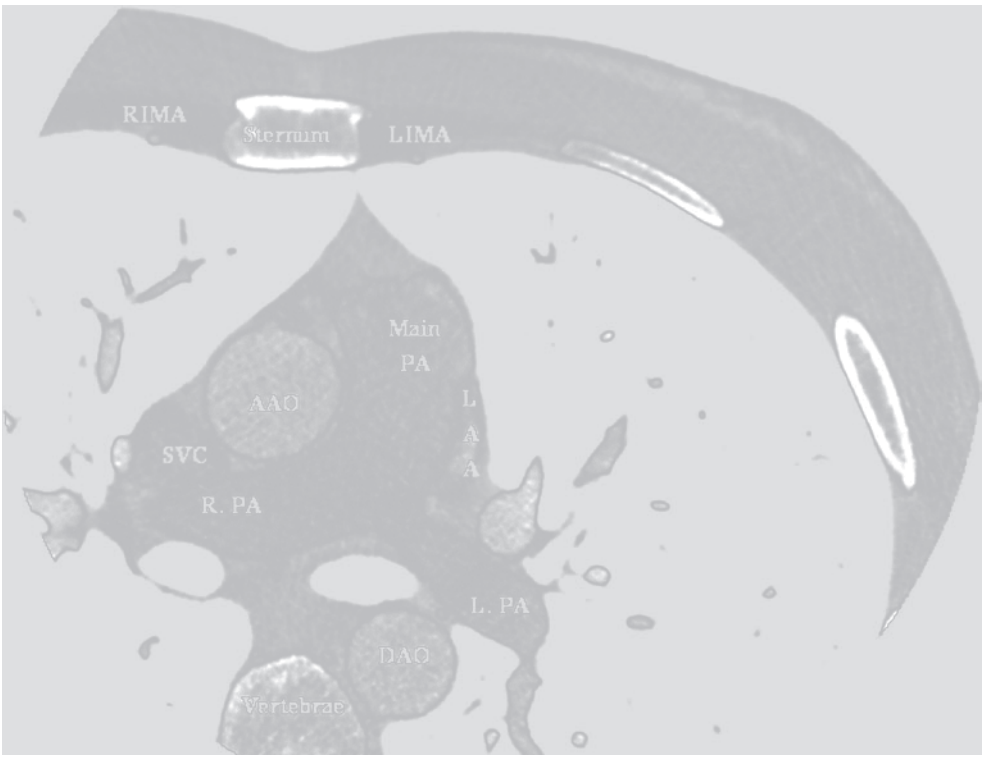

Figure 25.1.

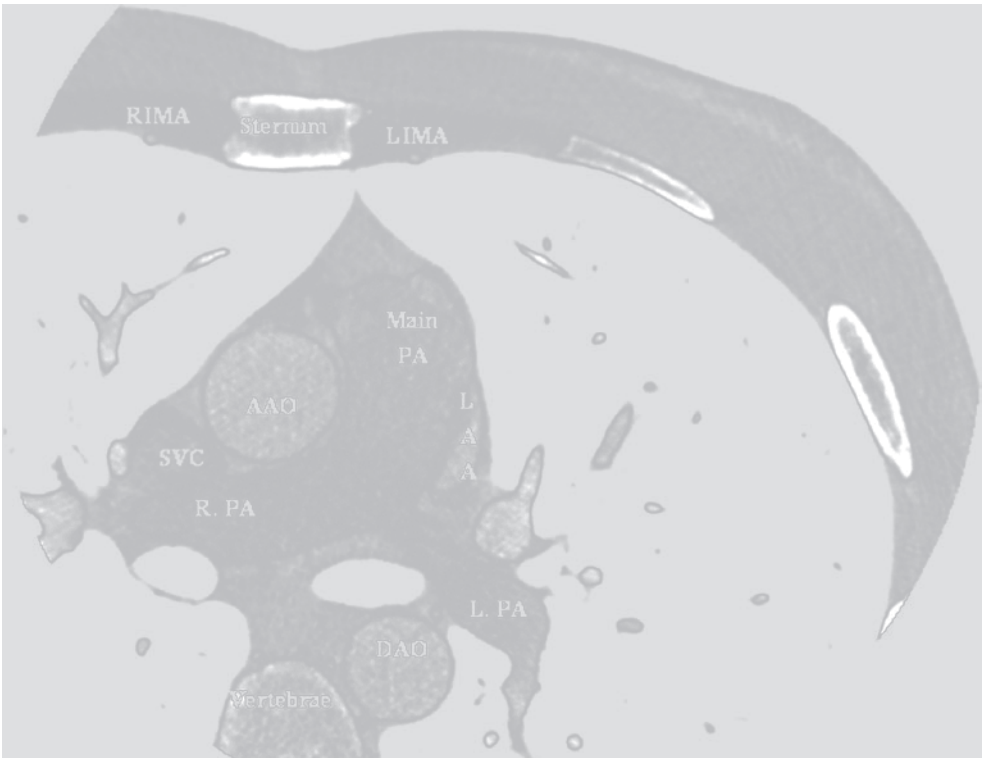

Figure 25.2.

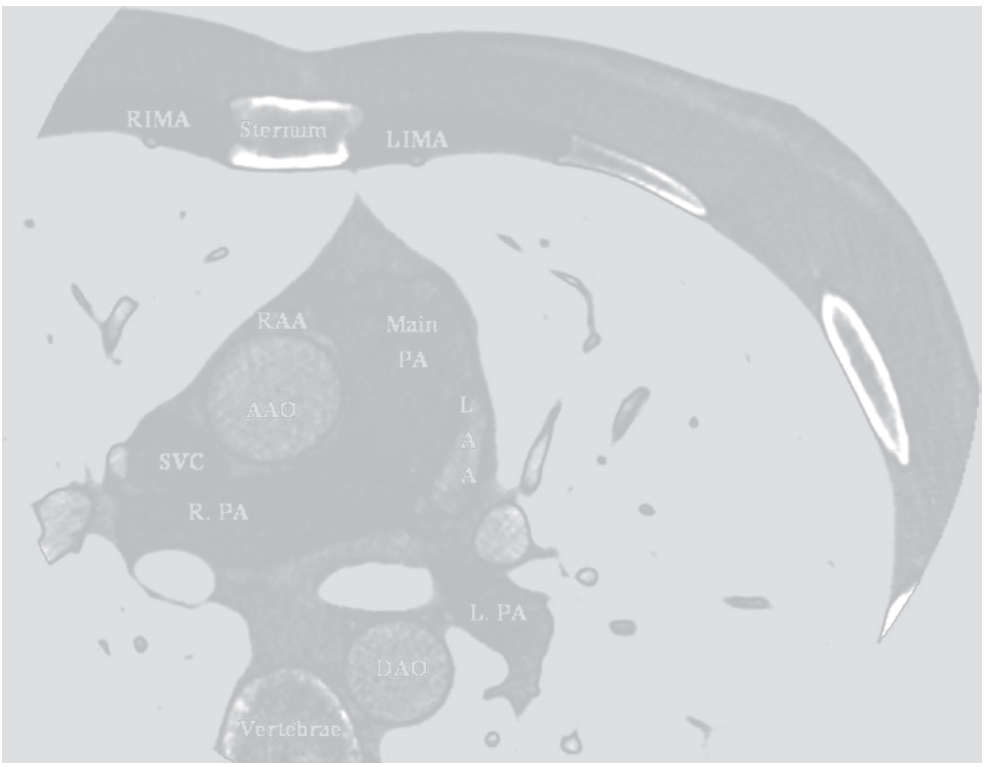

Figure 25.3.

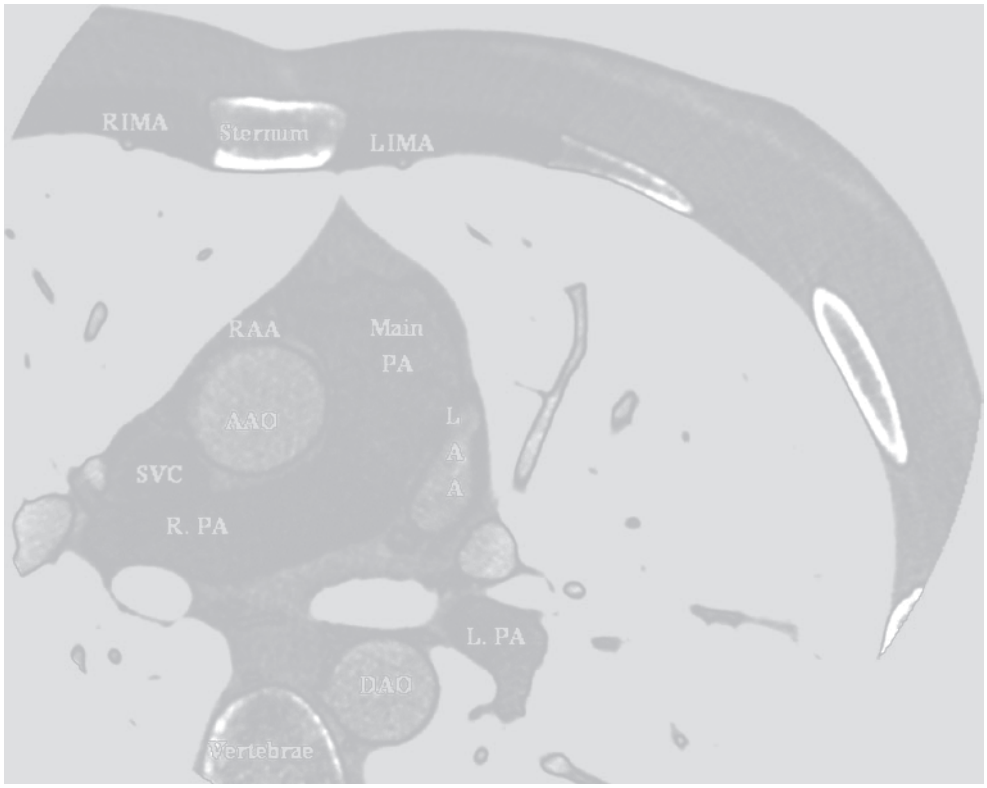

Figure 25.4.

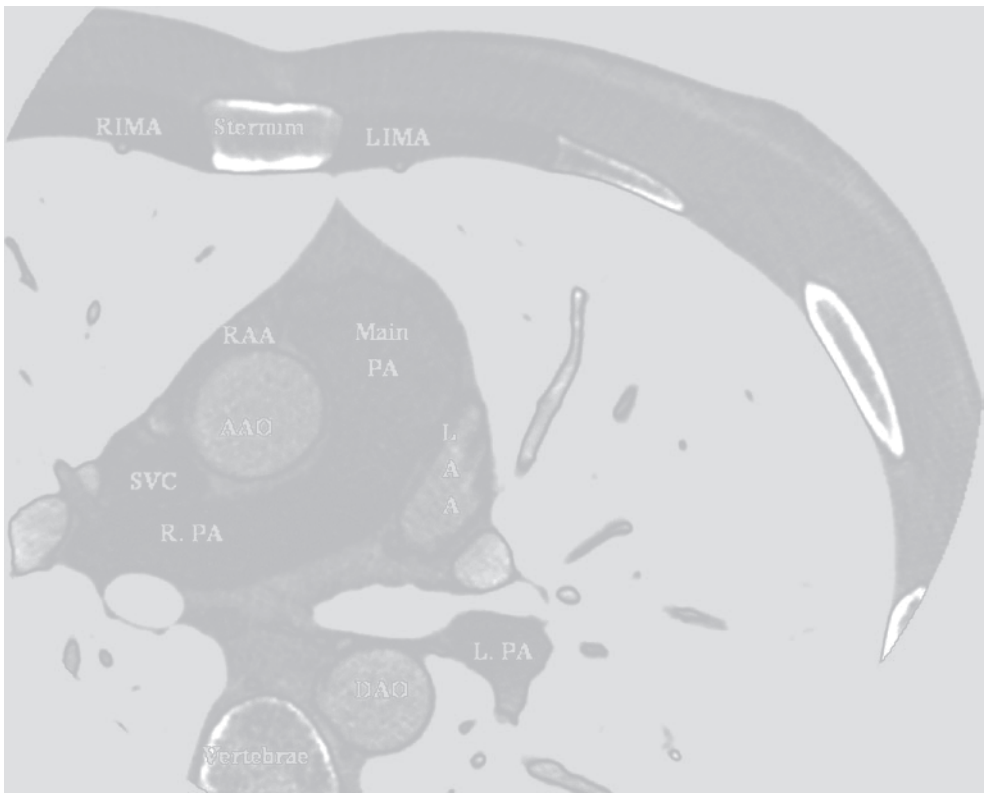

Figure 25.5.

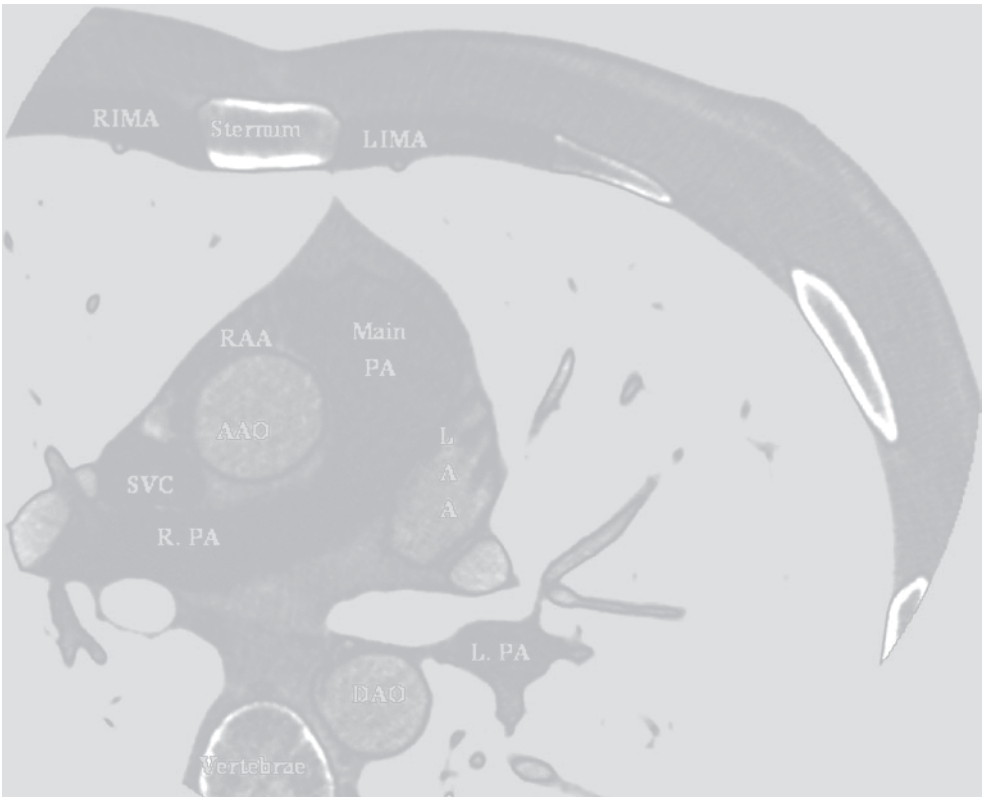

Figure 25.6.

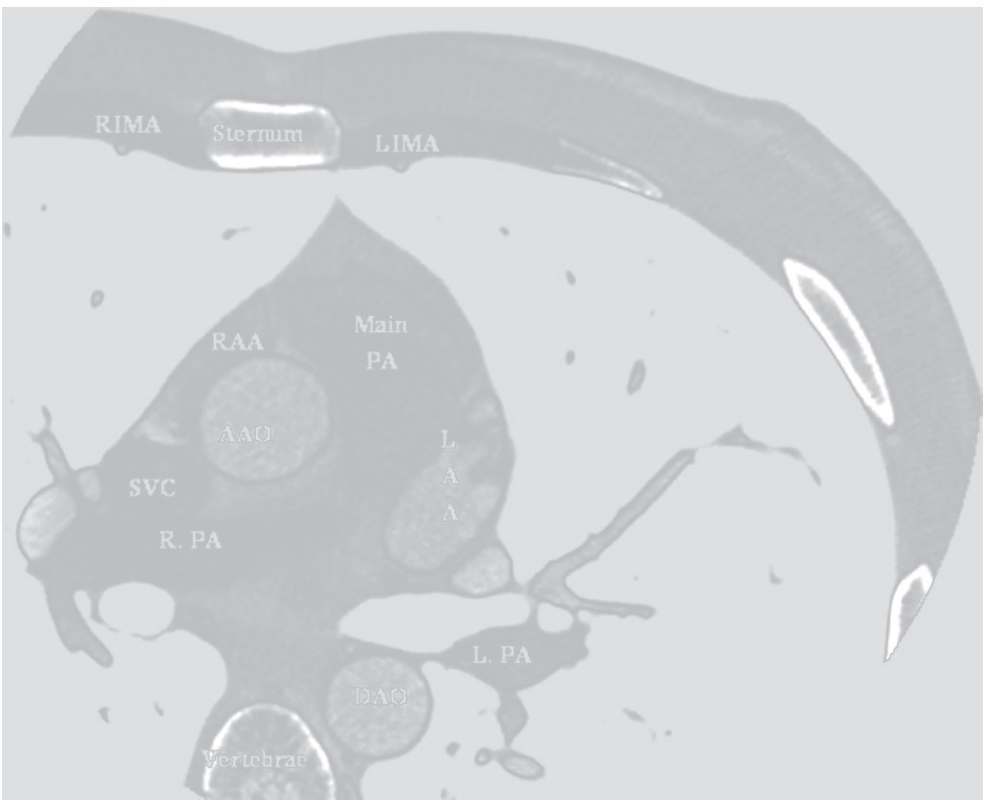

Figure 25.7.

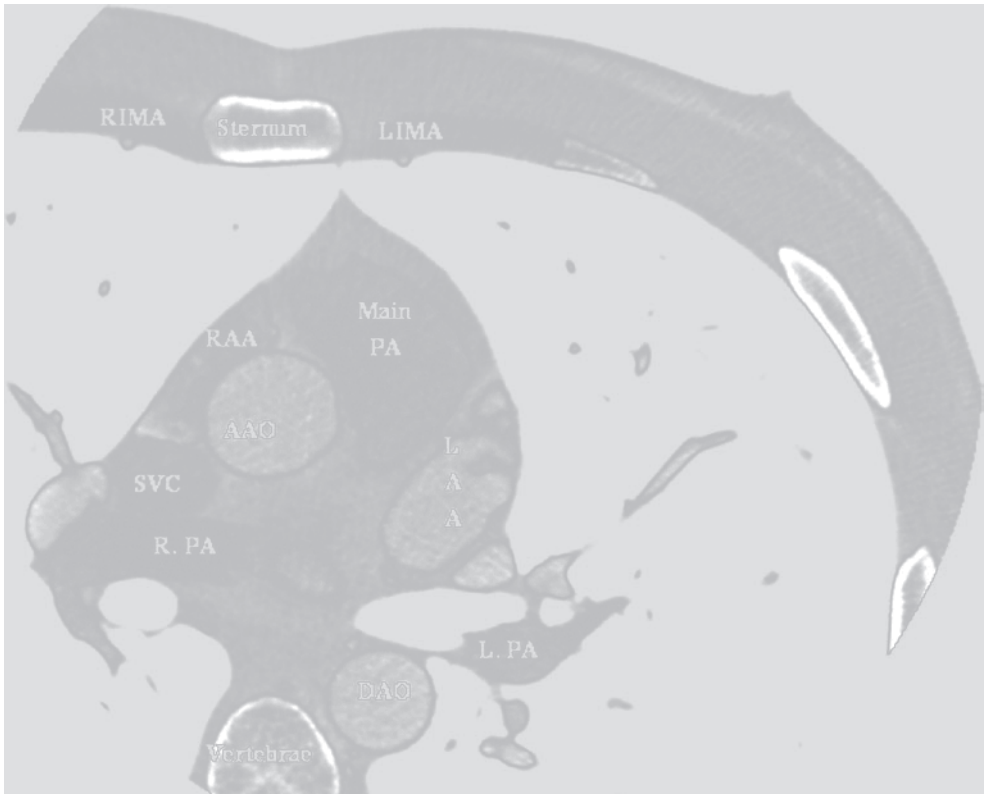

Figure 25.8.

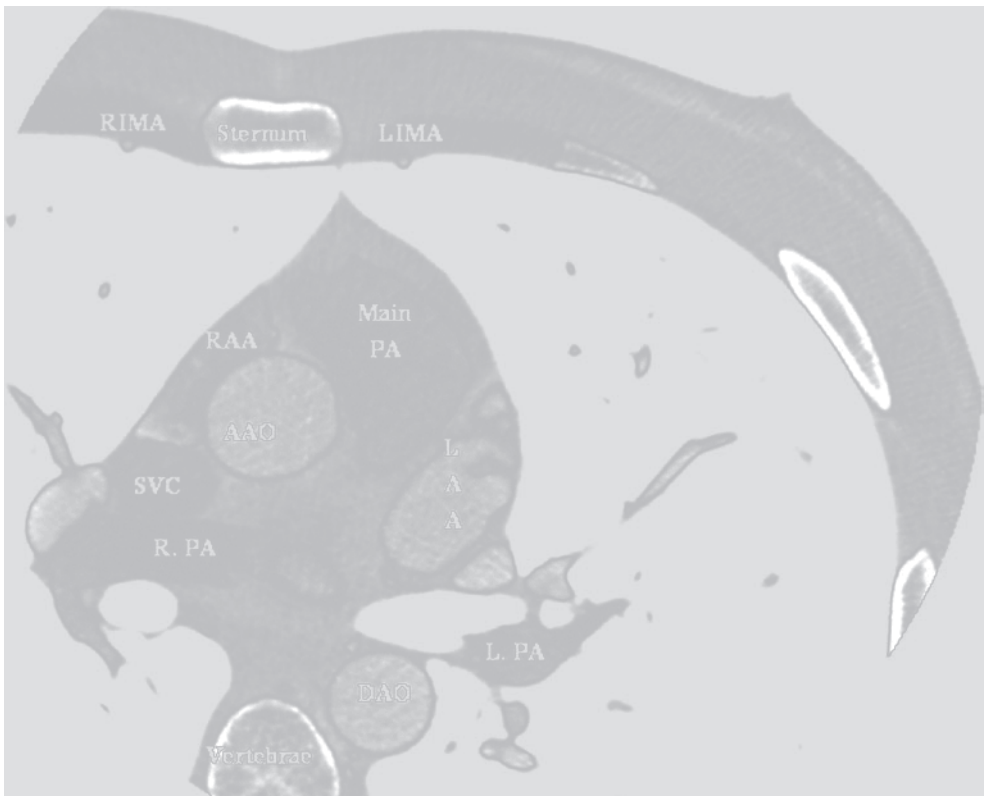

Figure 25.9.

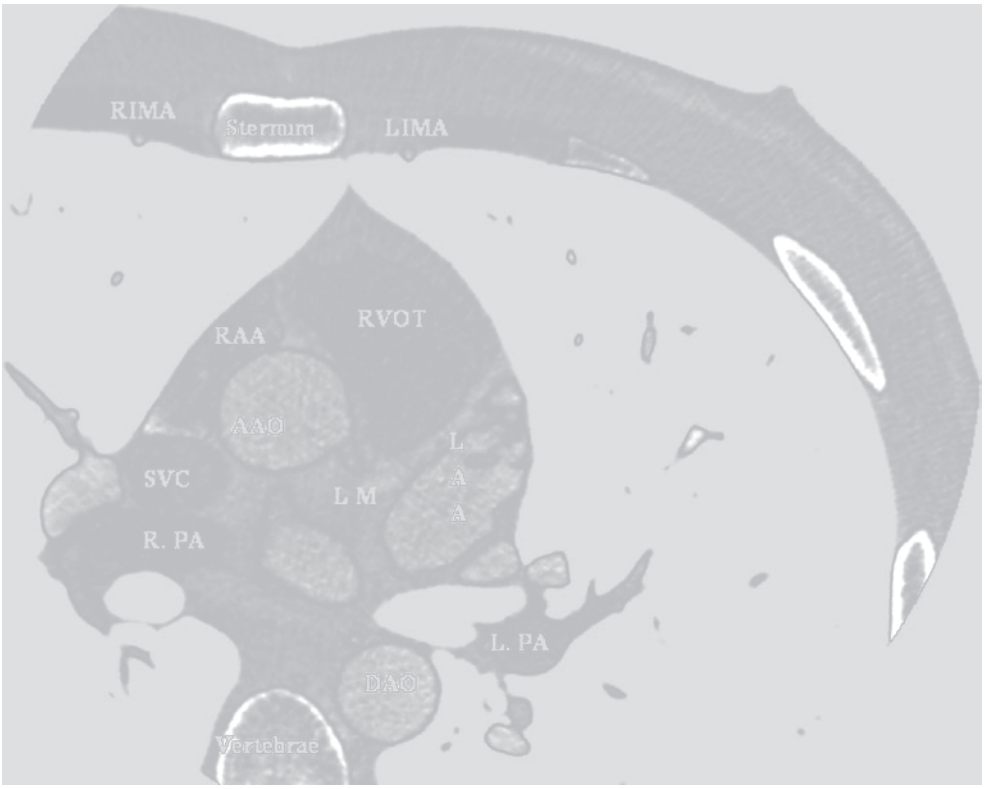

Figure 25.10.

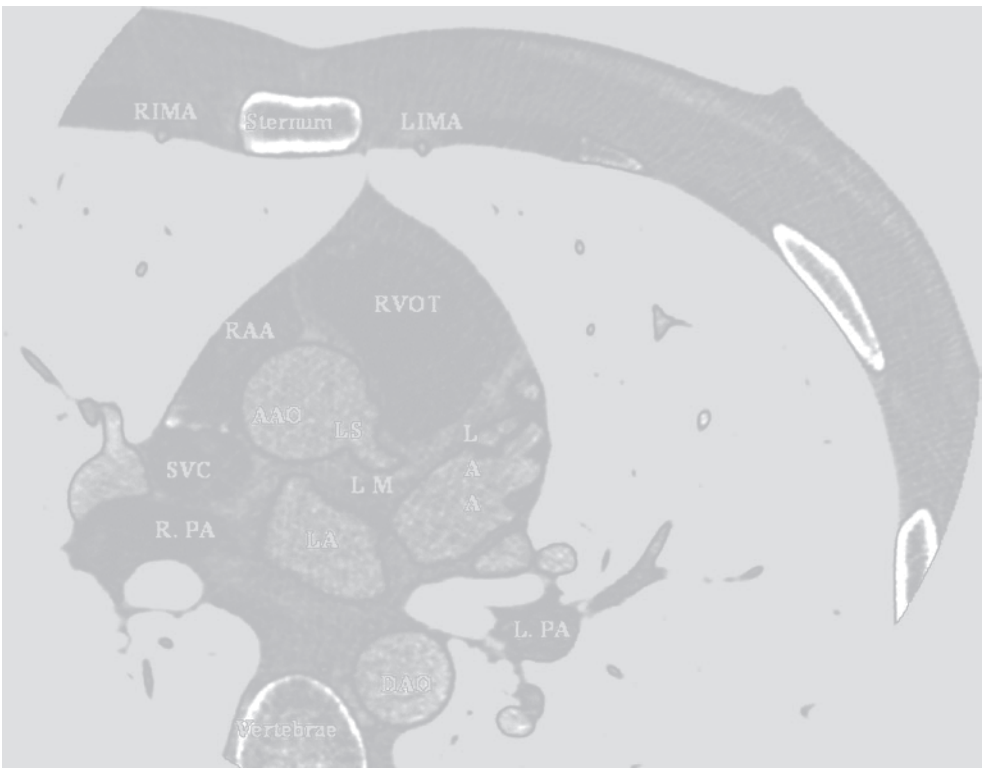

Figure 25.11.

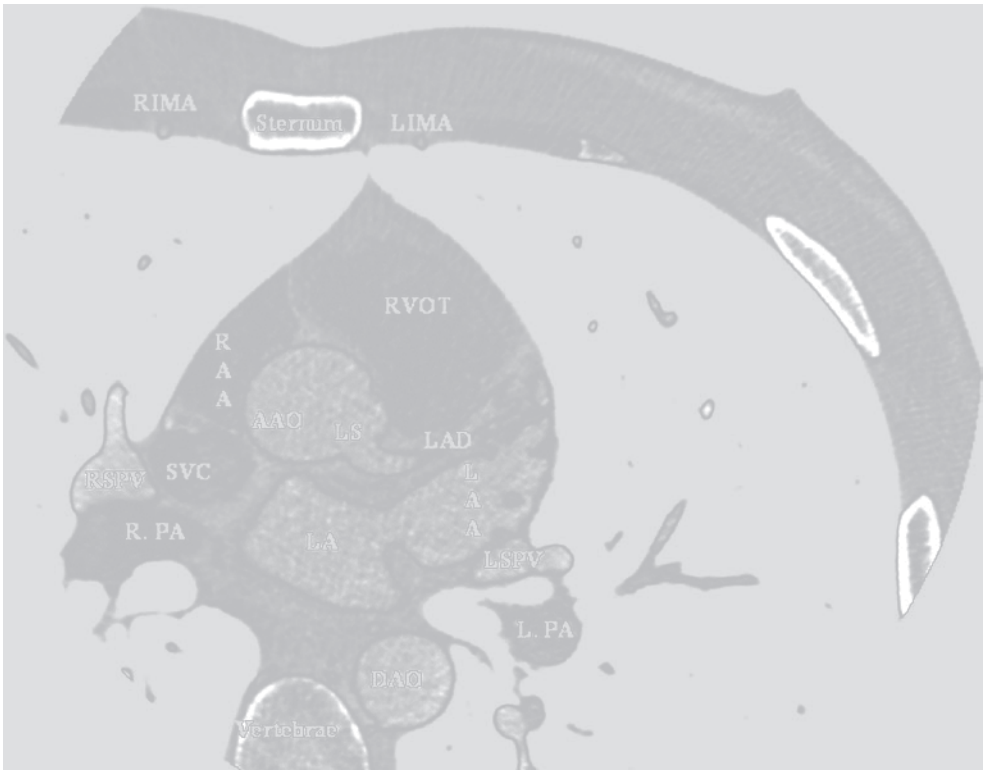

Figure 25.12.

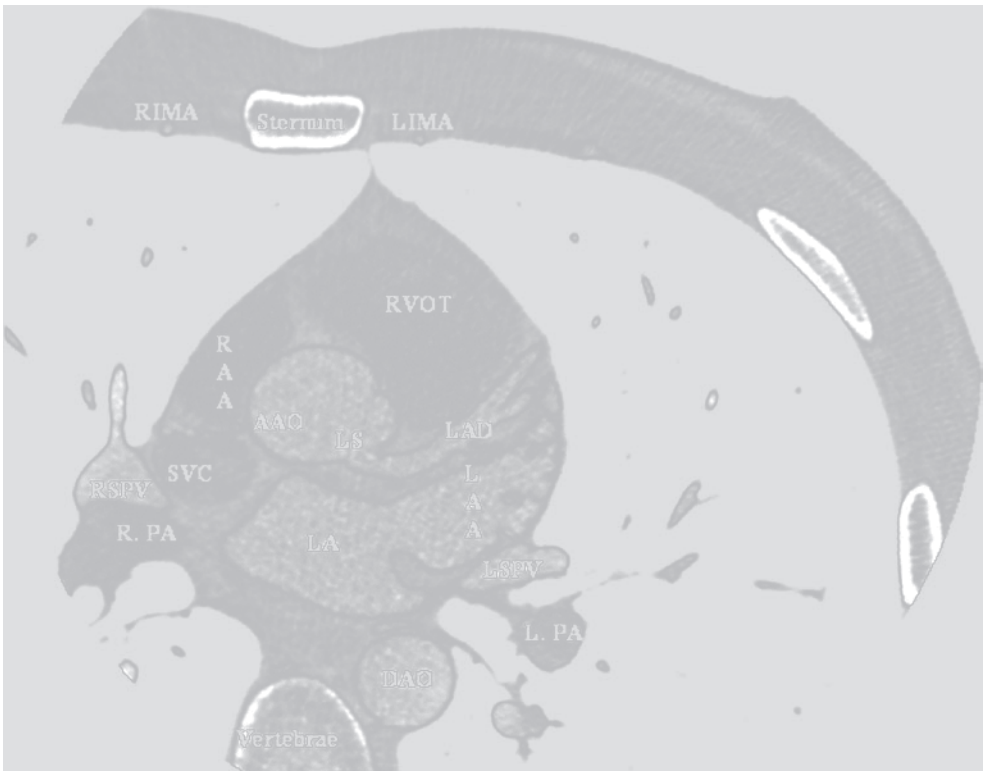

Figure 25.13.

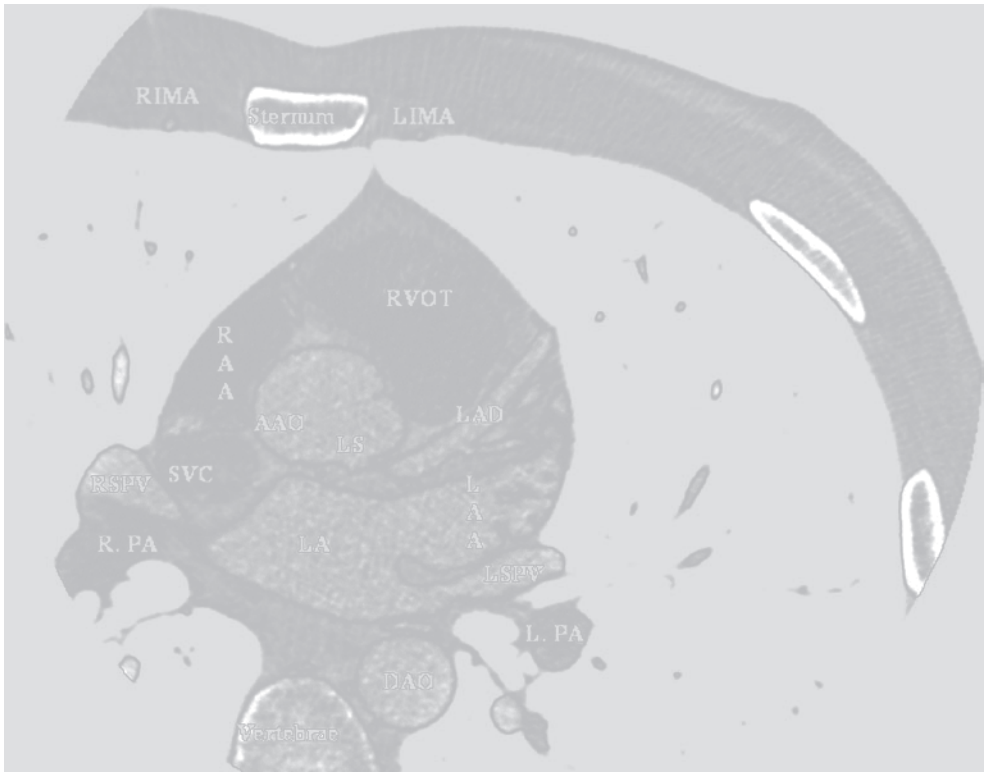

Figure 25.14.

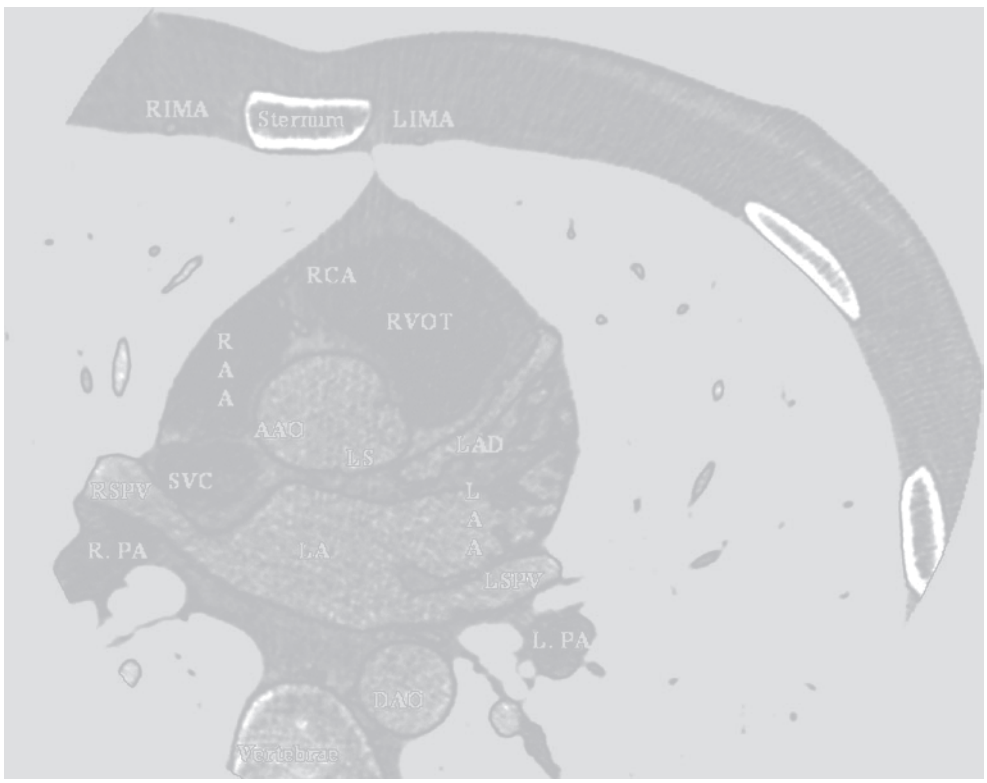

Figure 25.15.

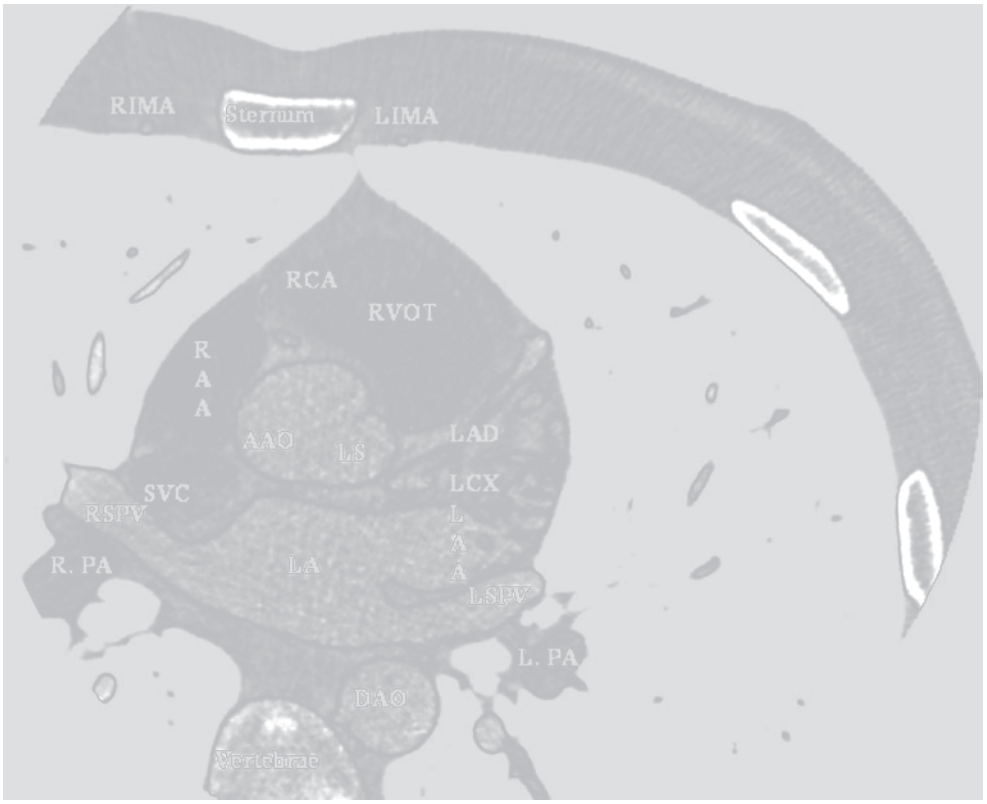

Figure 25.16.

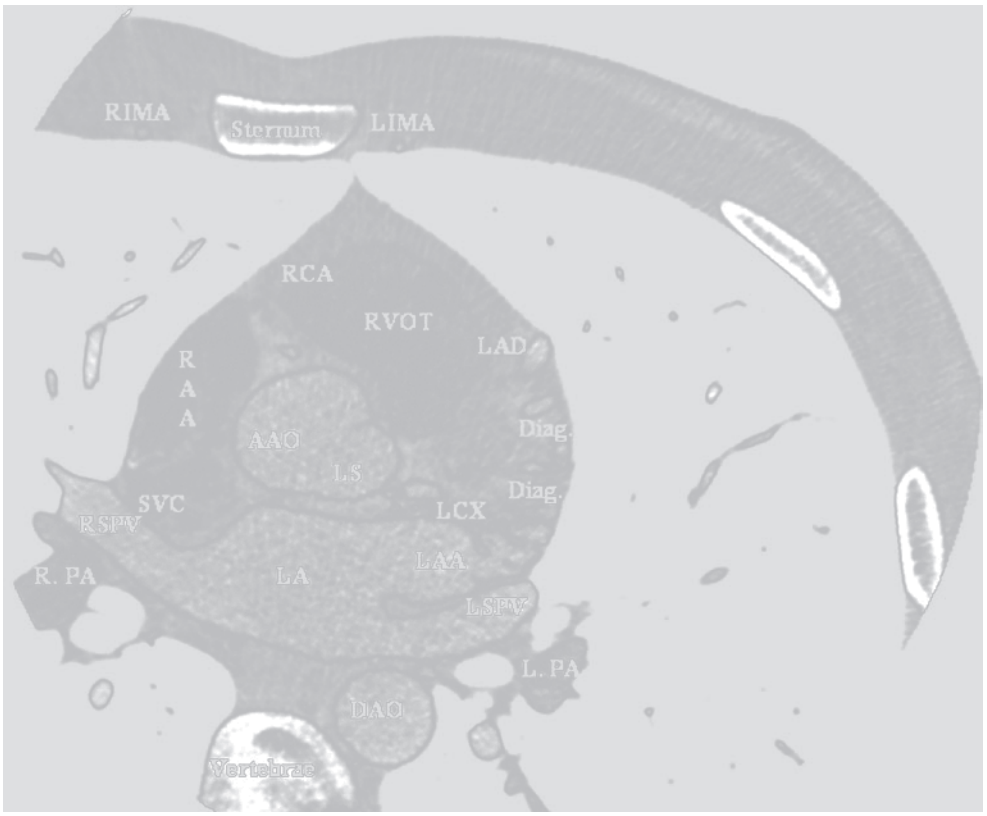

Figure 25.17.

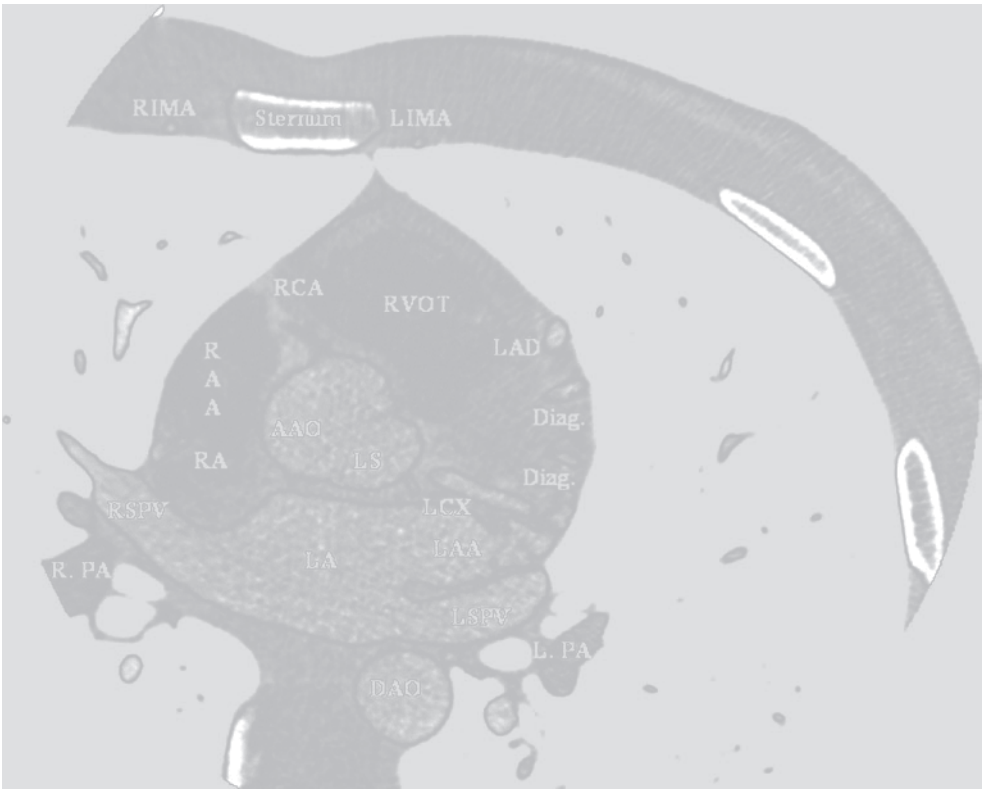

Figure 25.18.

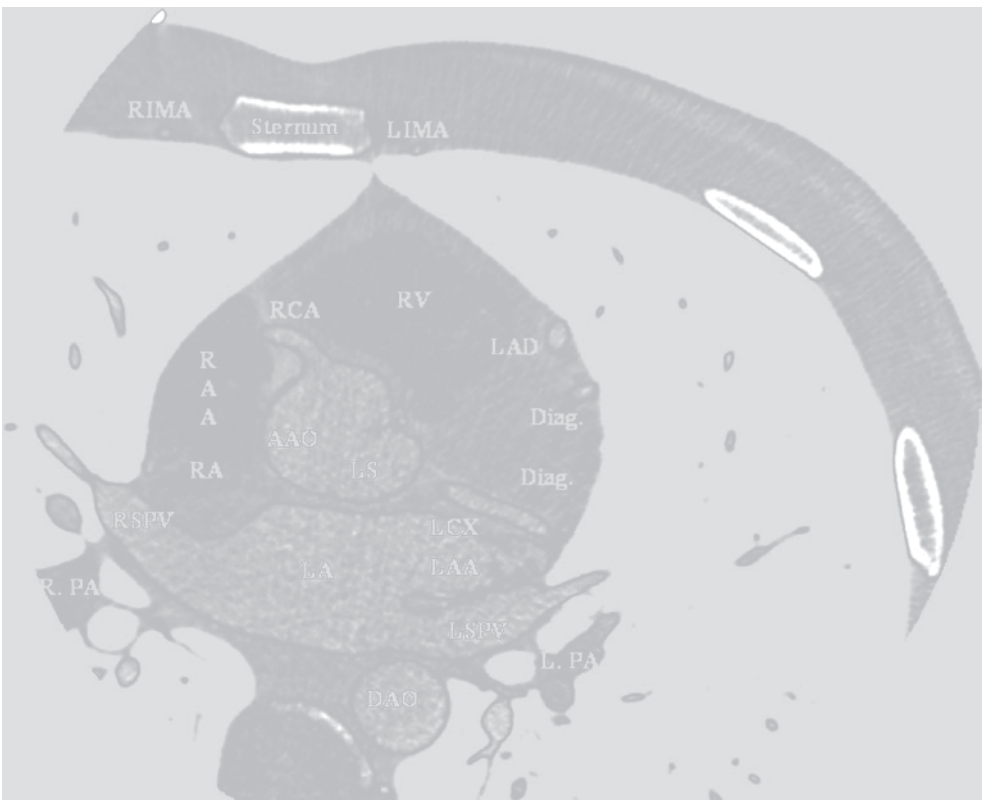

Figure 25.19.

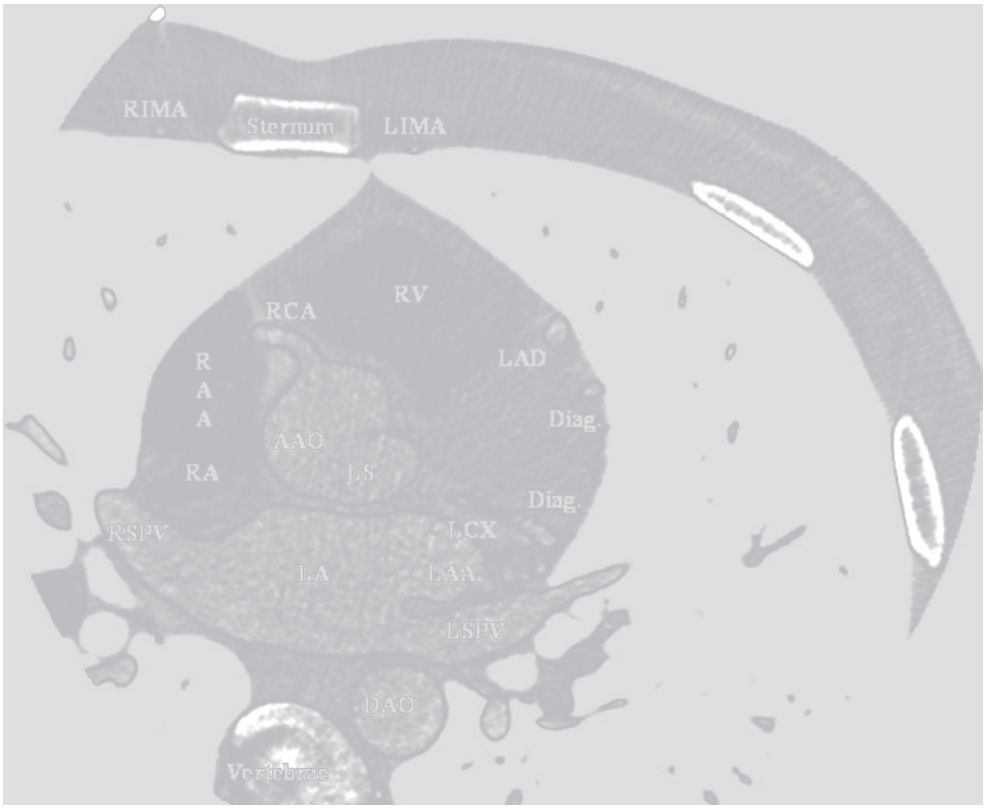

Figure 25.20.

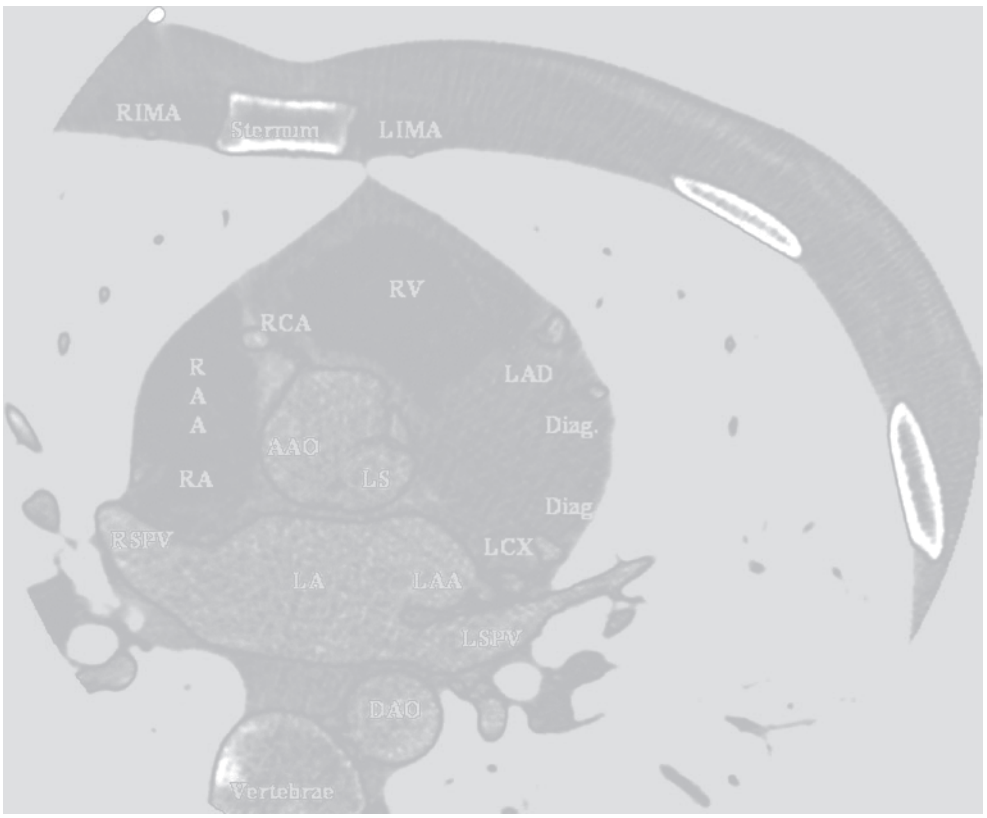

Figure 25.21.

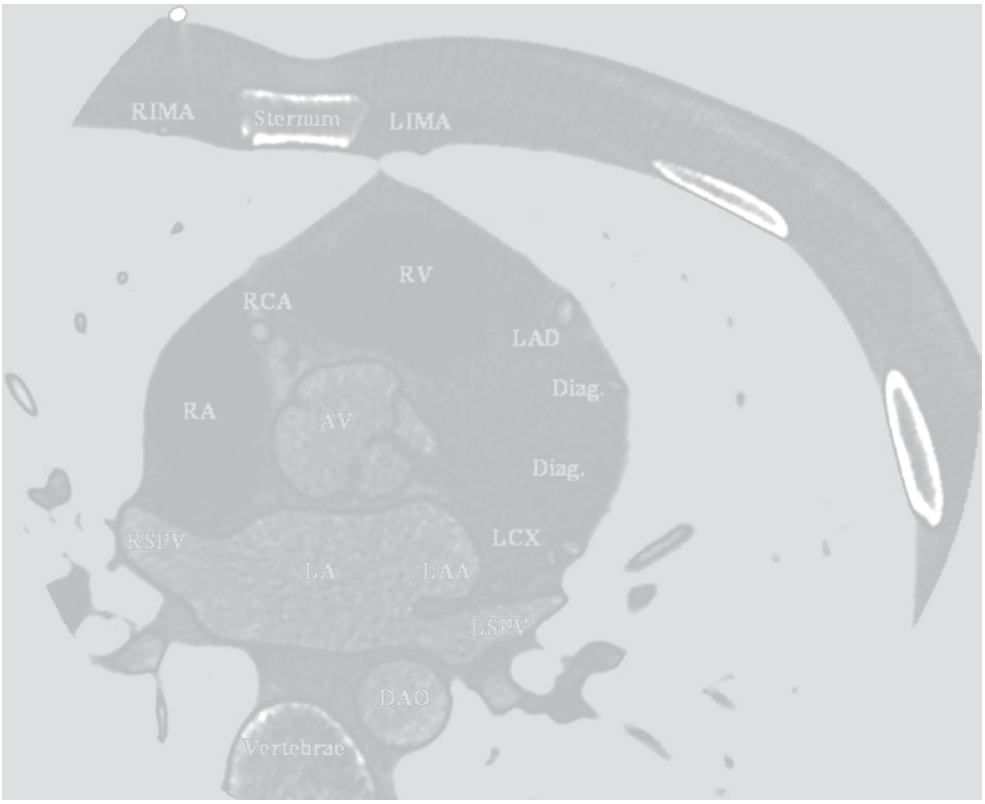

Figure 25.22.

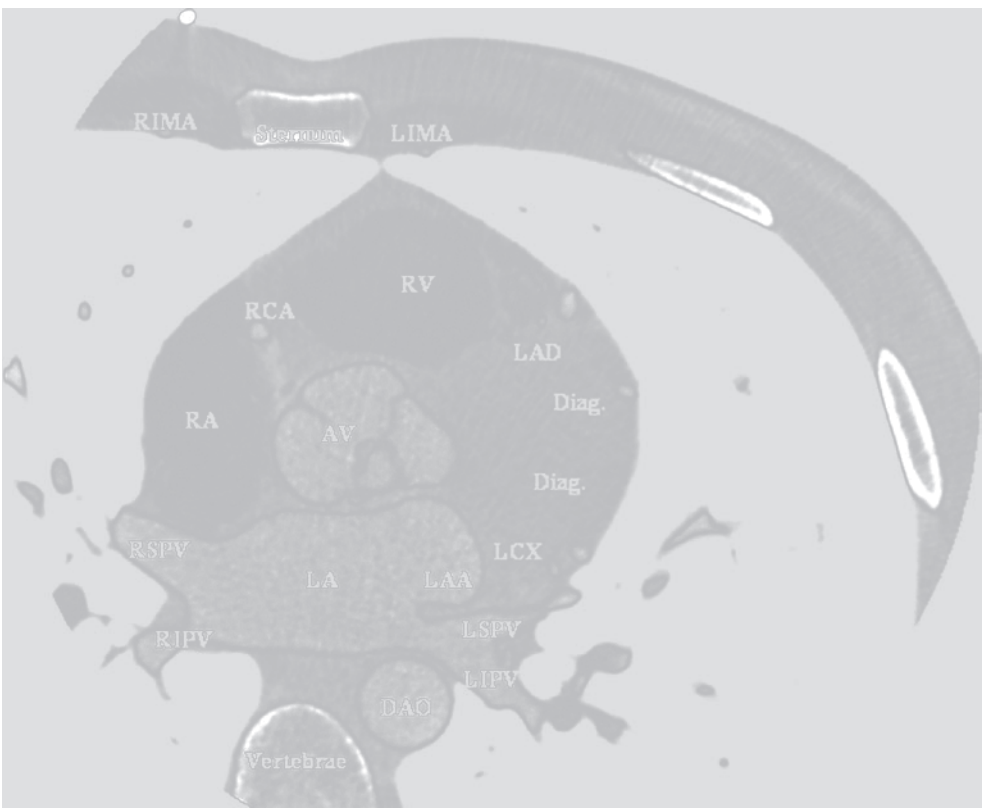

Figure 25.23.

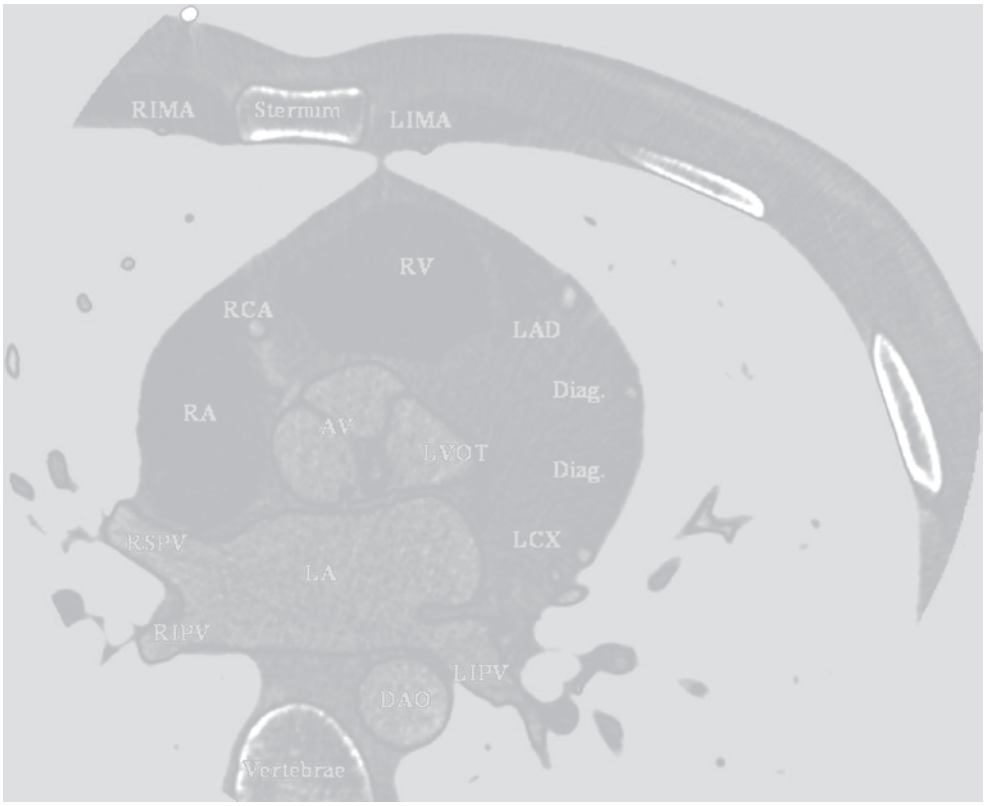

Figure 25.24.

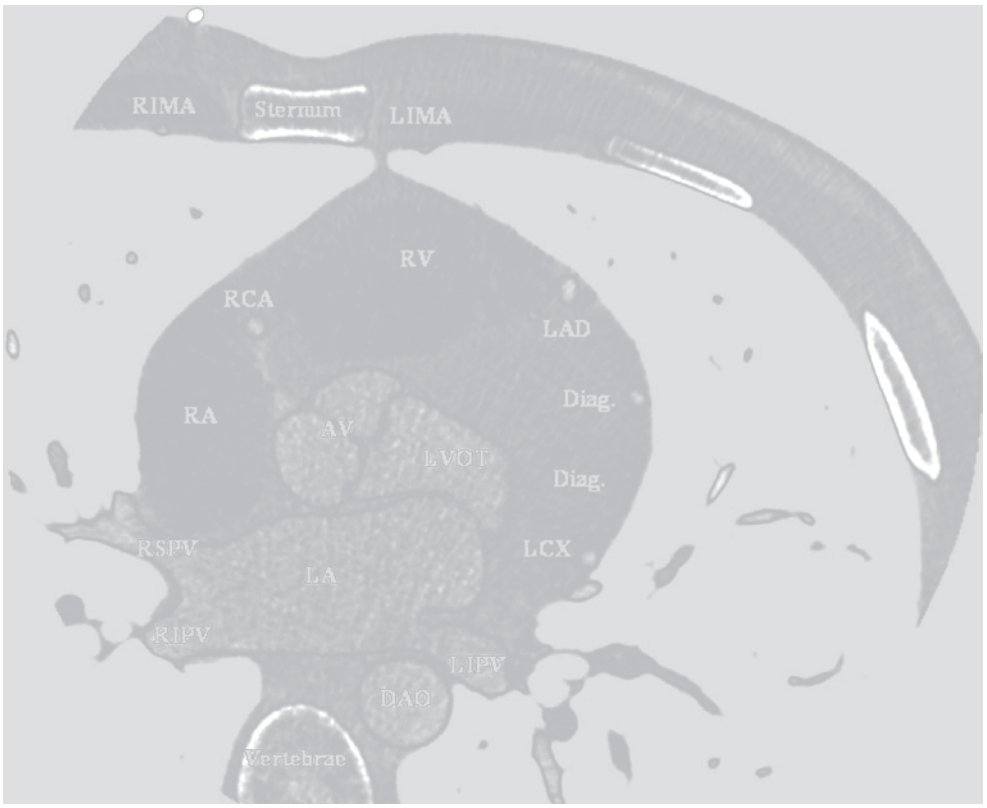

Figure 25.25.

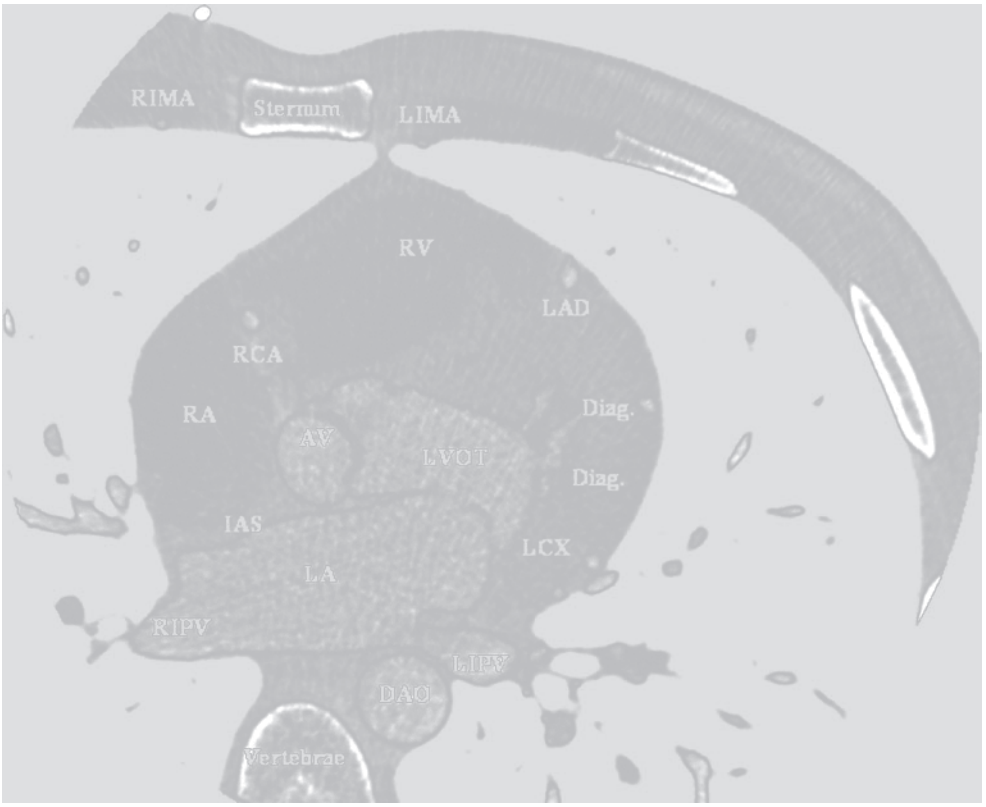

Figure 25.26.

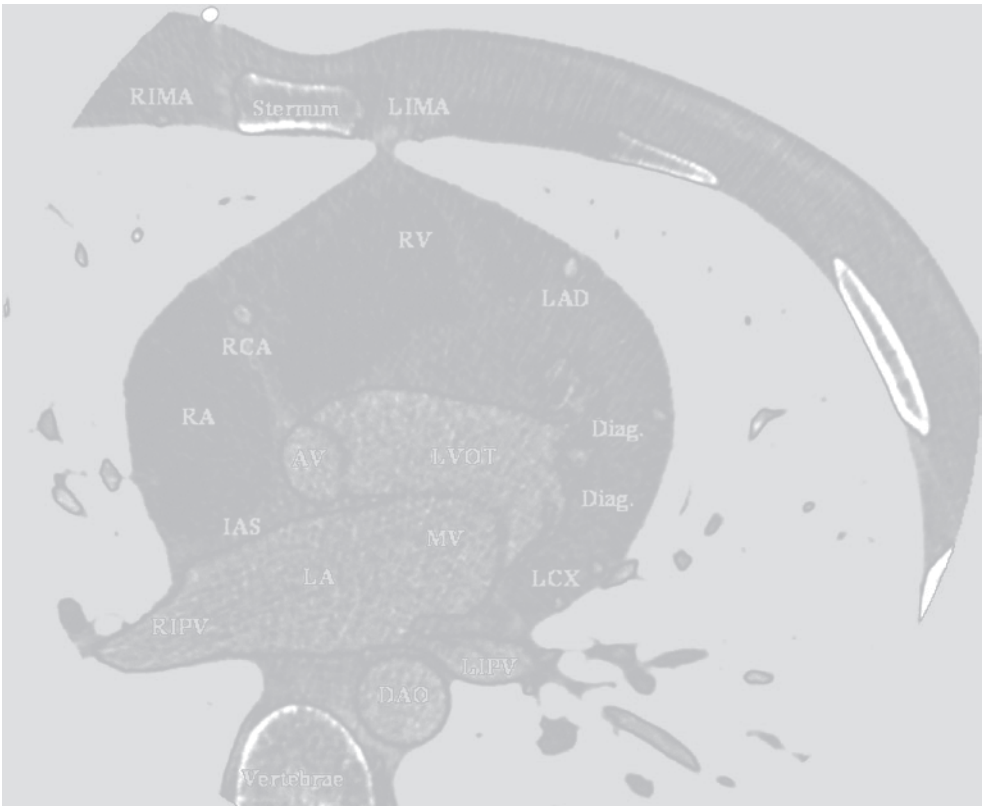

Figure 25.27.

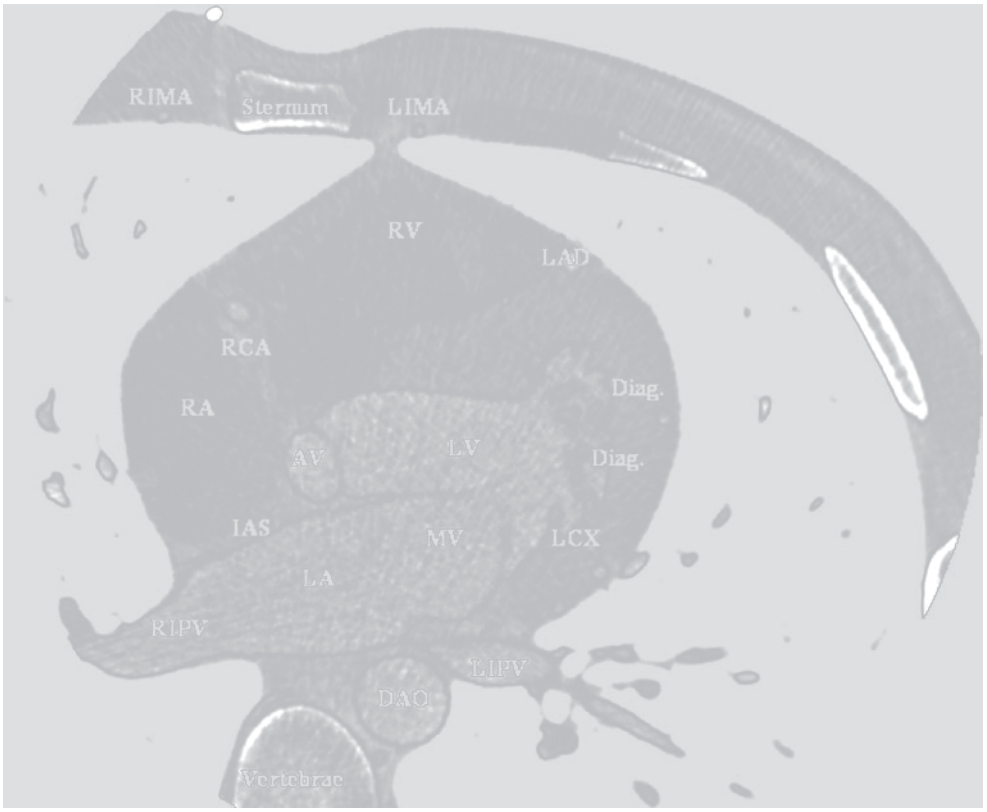

Figure 25.28.

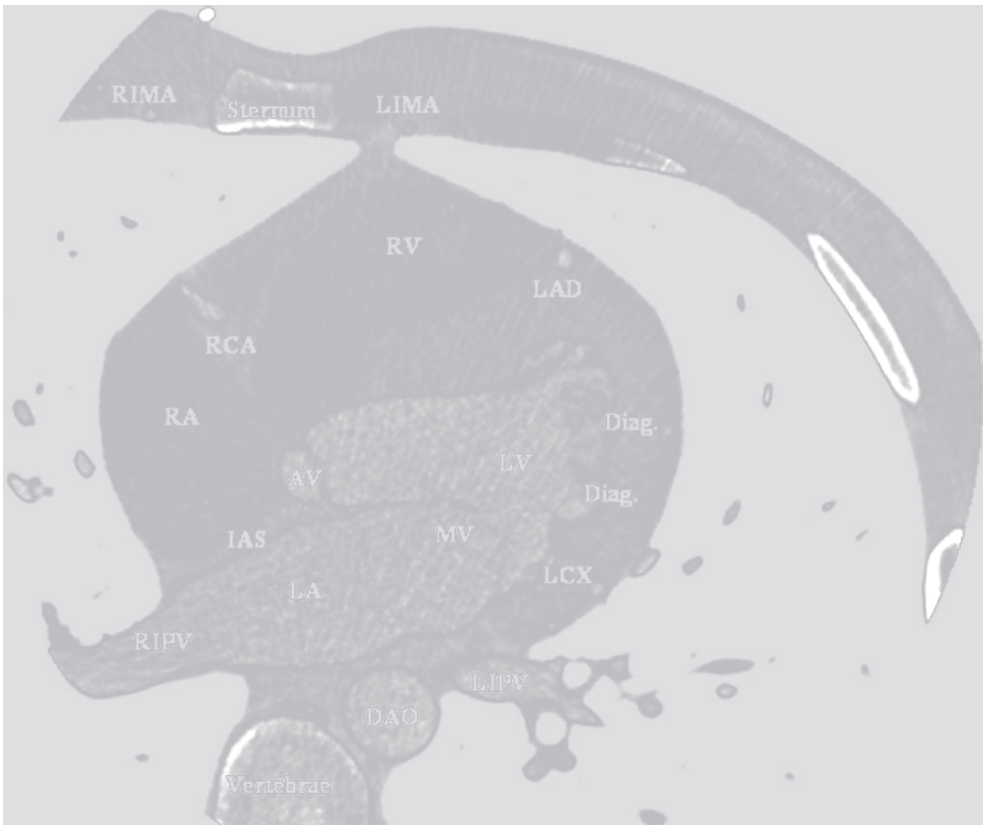

Figure 25.29.

Figure 25.30.

Figure 25.31.

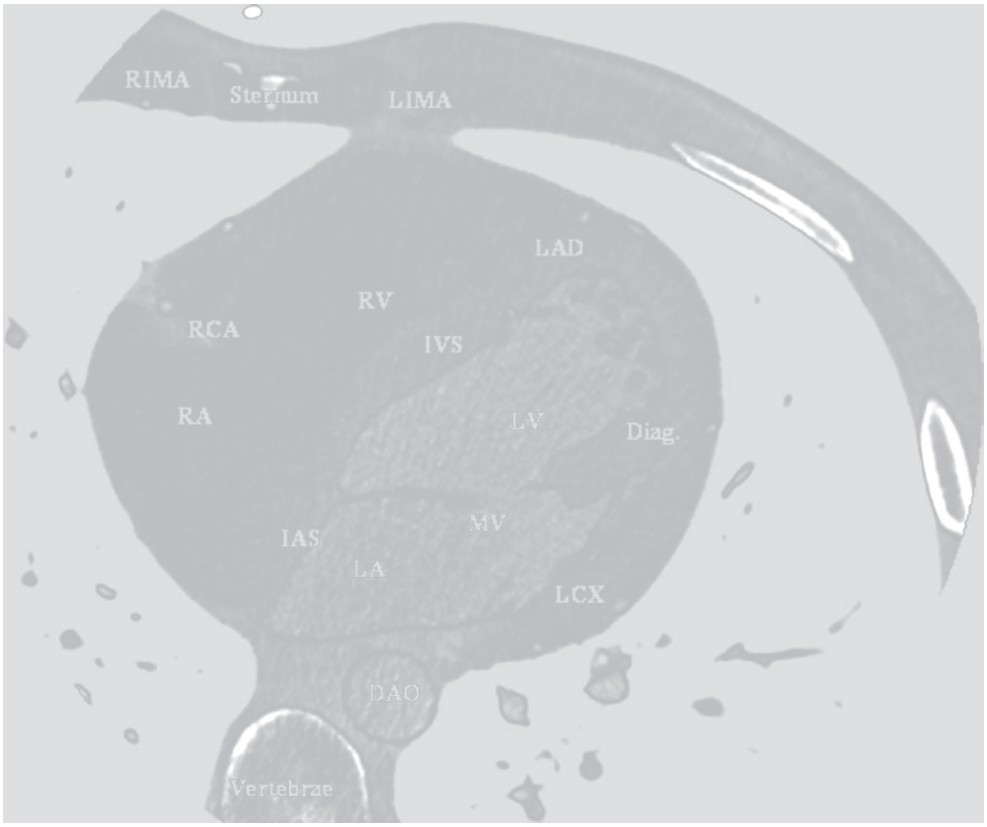

Figure 25.32.

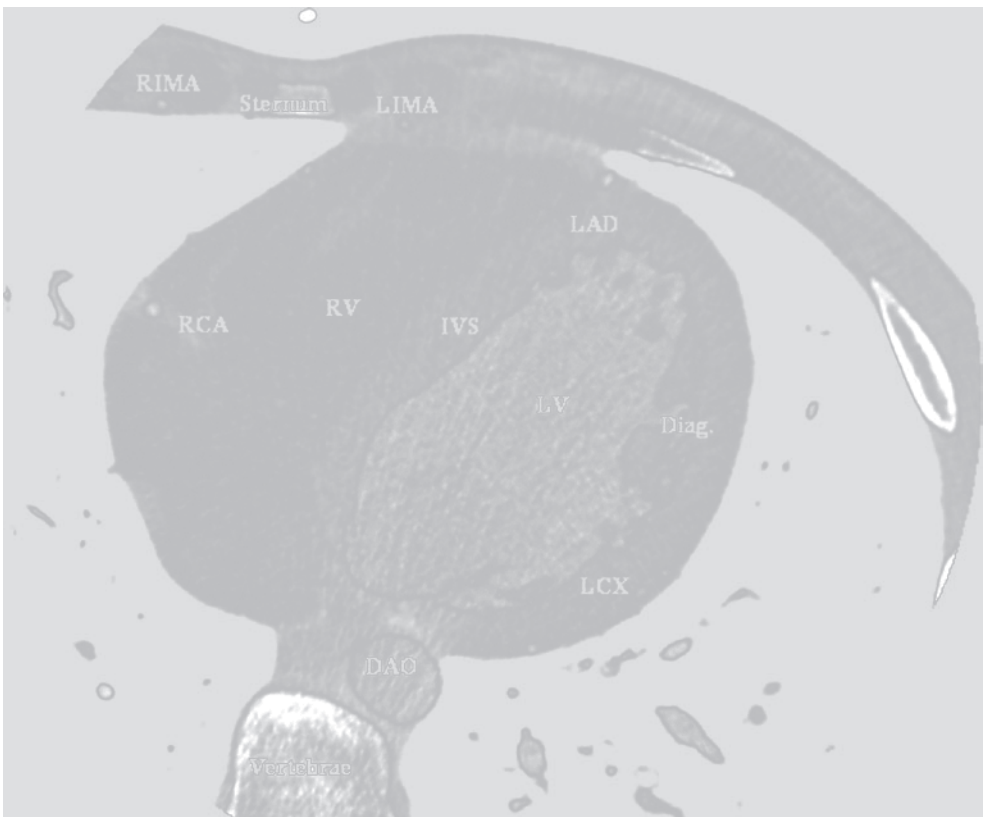

Figure 25.33.

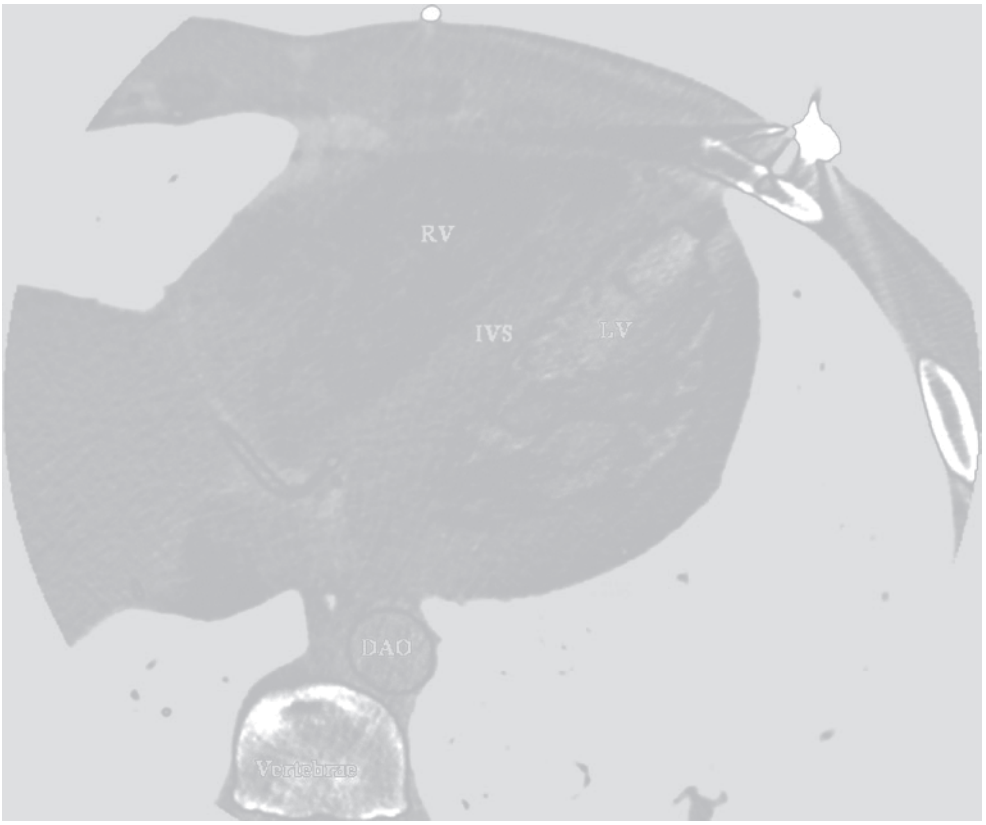

Figure 25.34.

Orientation to Coronal Images

Figures 25.35–25.67. Serial coronal CT angiography images beginning at the level of the sternum with slices proceeding in an anterior to posterior direction..

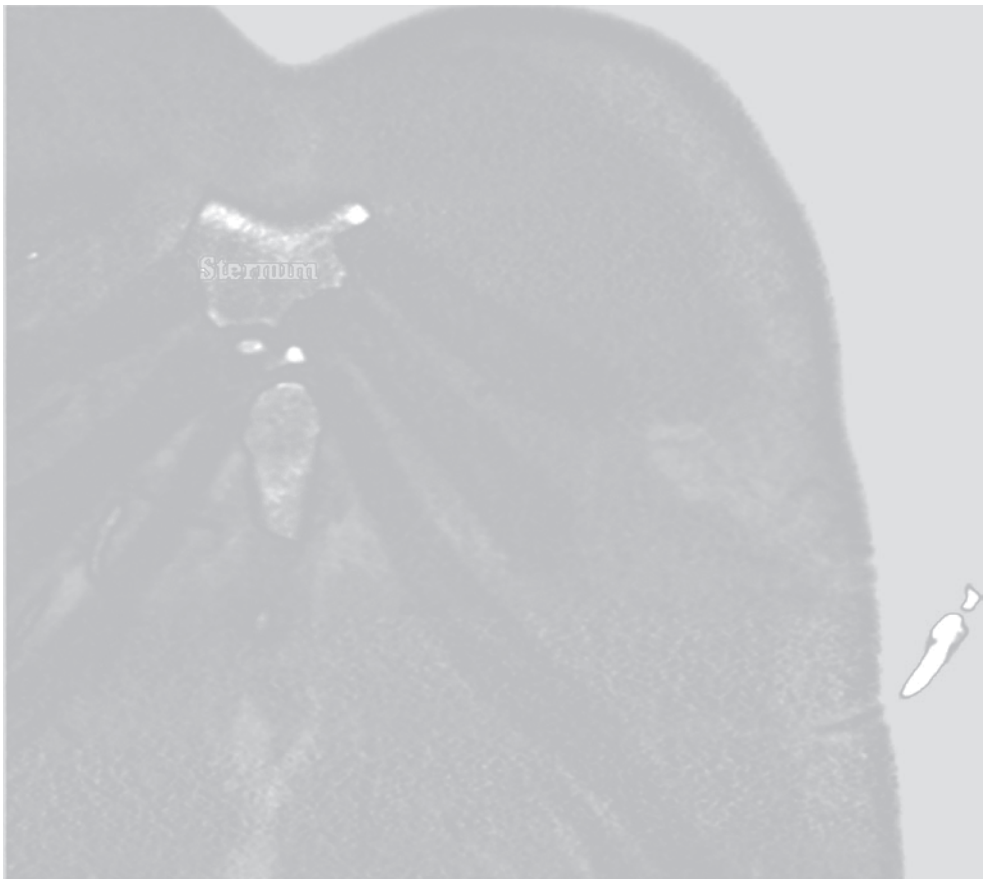

Figure 25.35.

Figure 25.36.

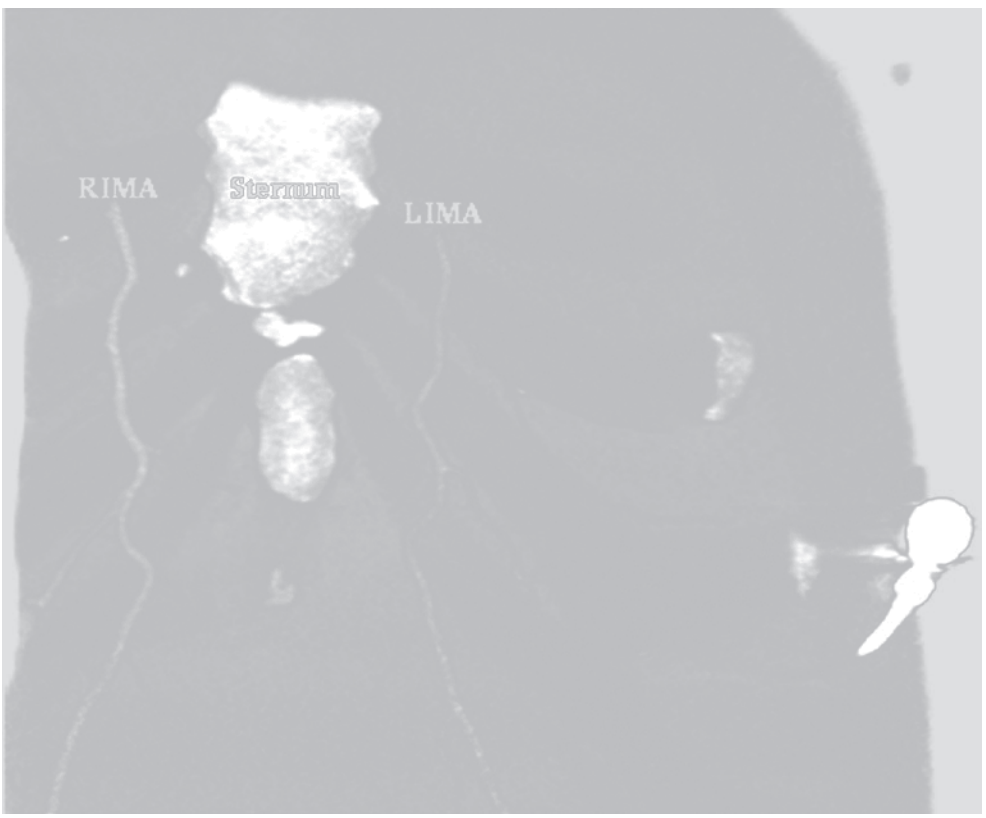

Figure 25.37.

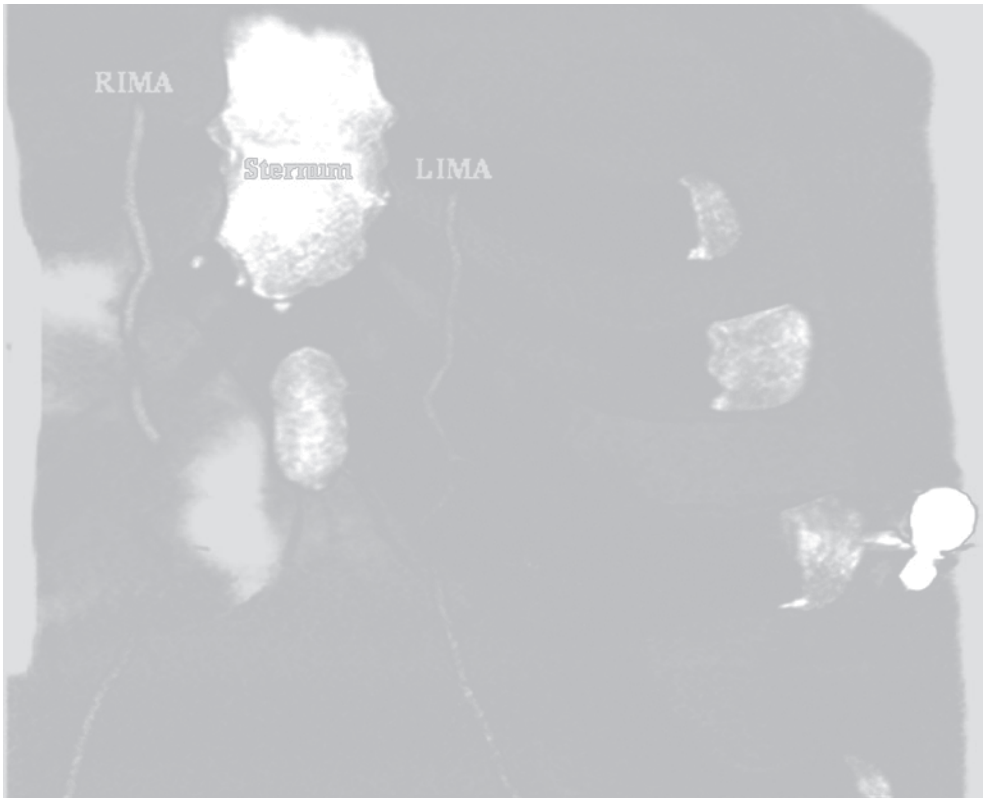

Figure 25.38.

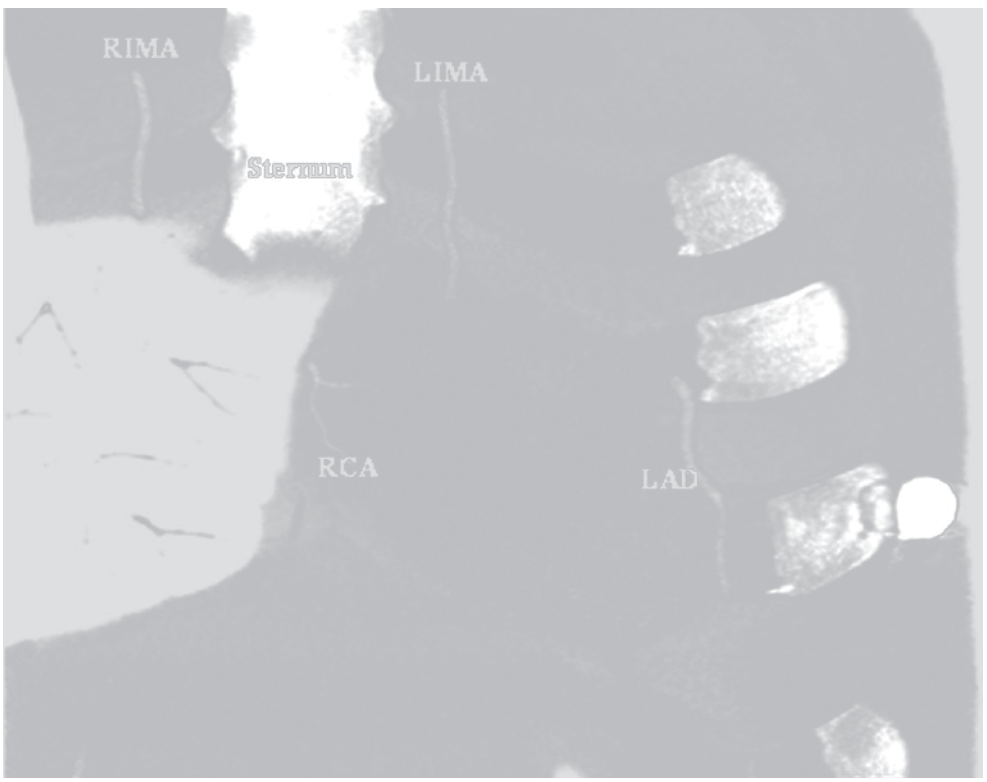

Figure 25.39.

Figure 25.40.

Figure 25.41.

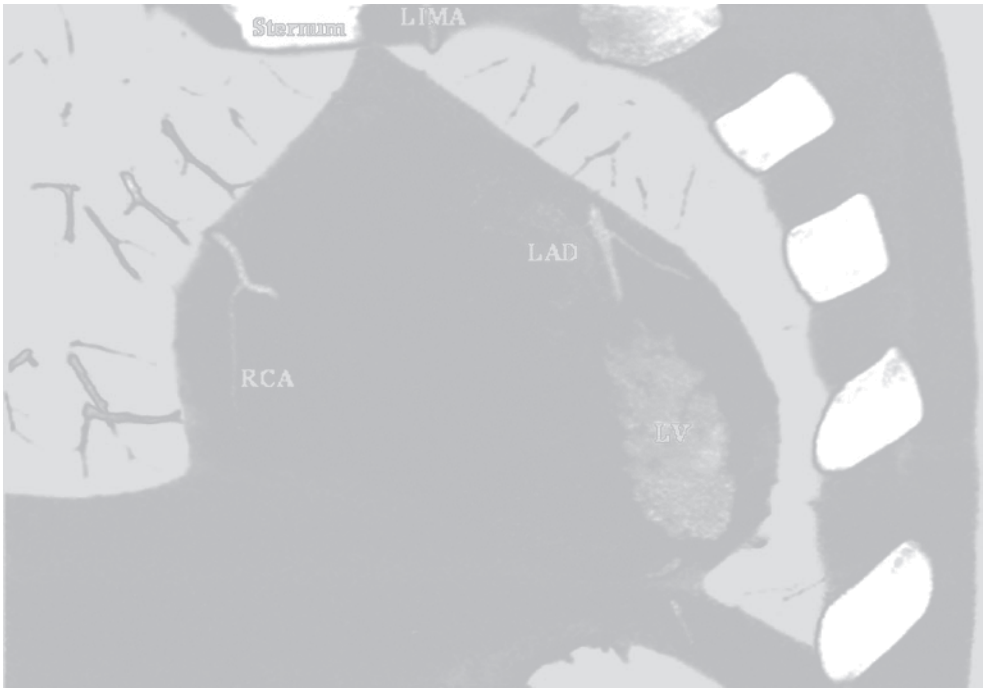

Figure 25.42.

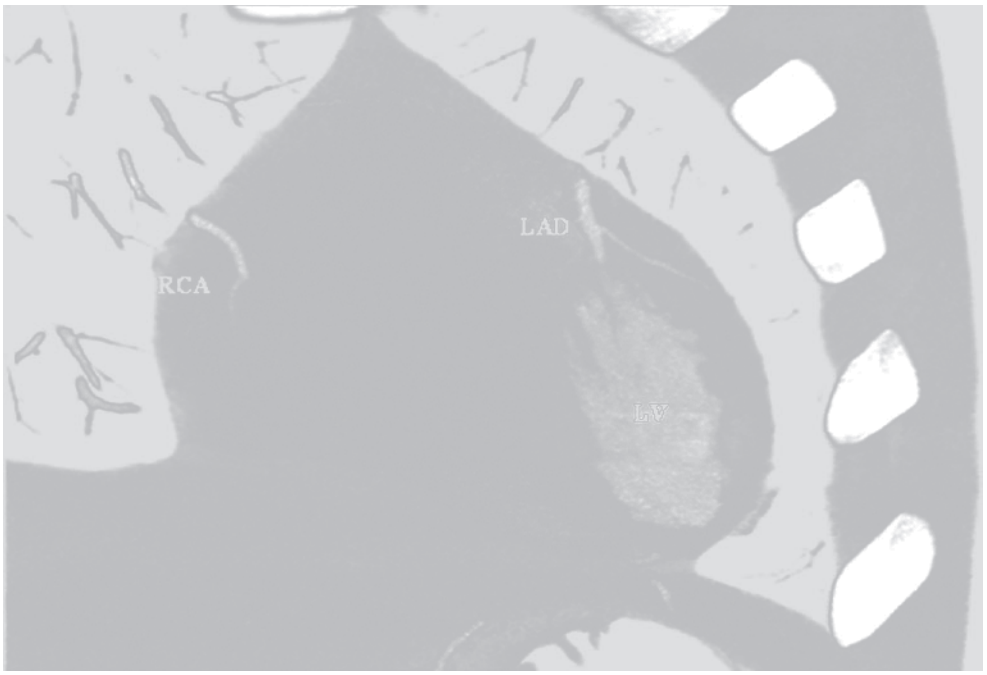

Figure 25.43.

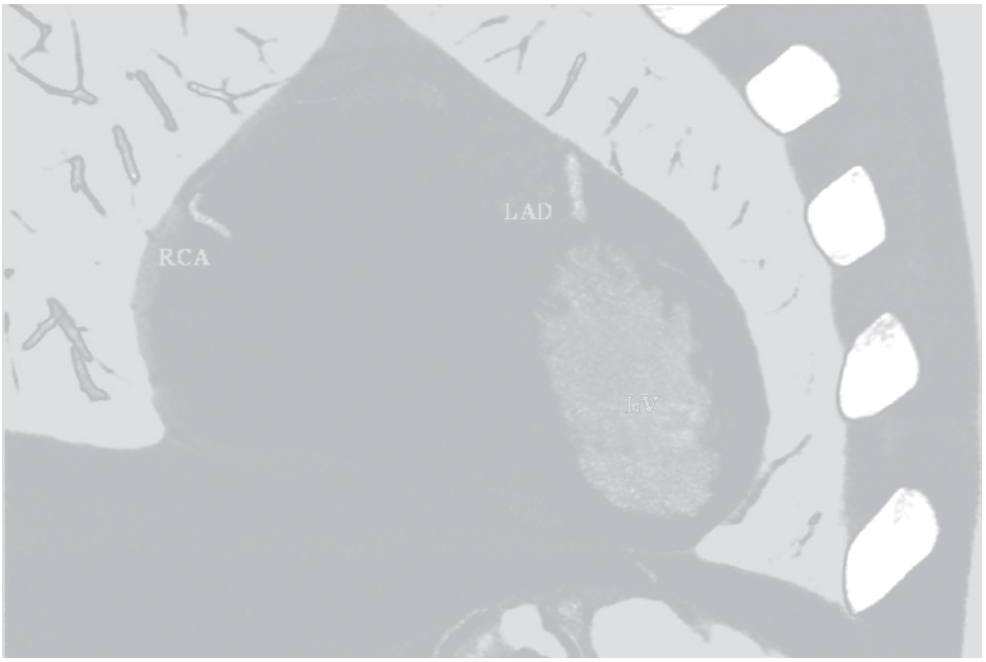

Figure 25.44.

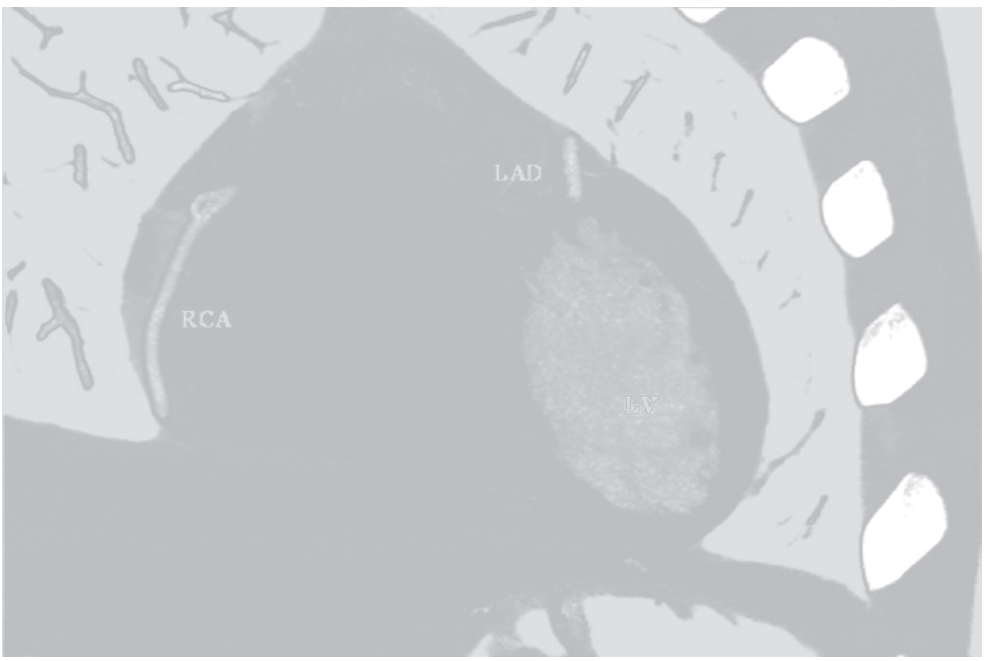

Figure 25.45.

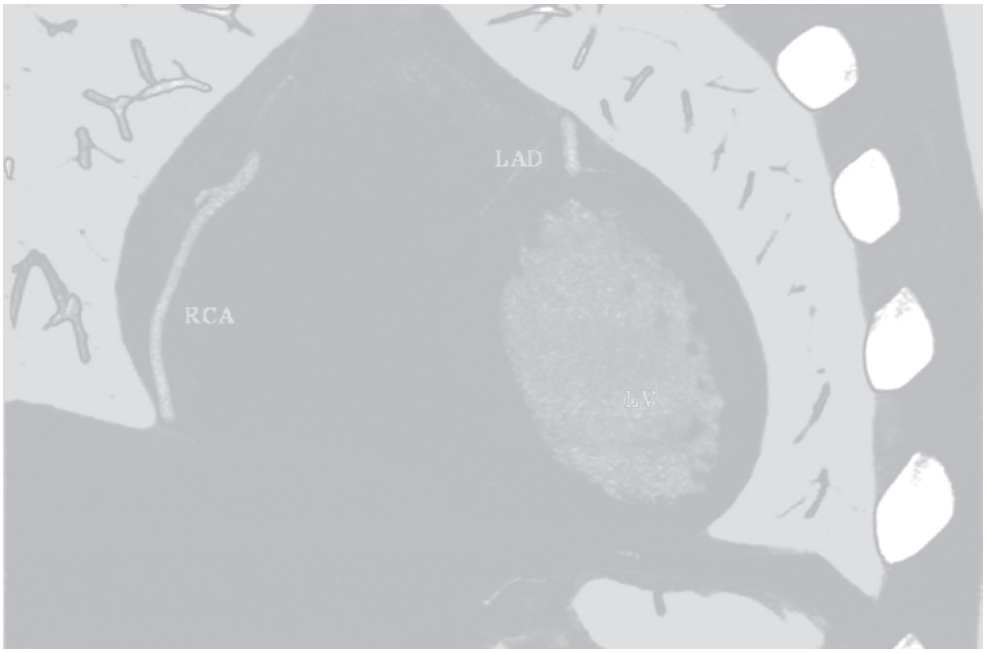

Figure 25.46.

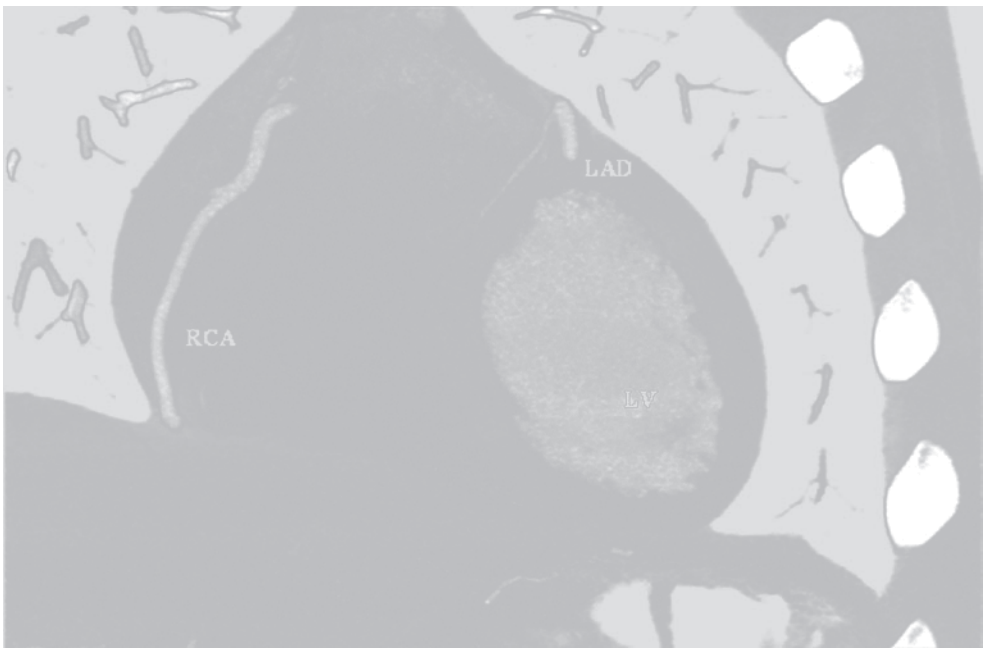

Figure 25.47.

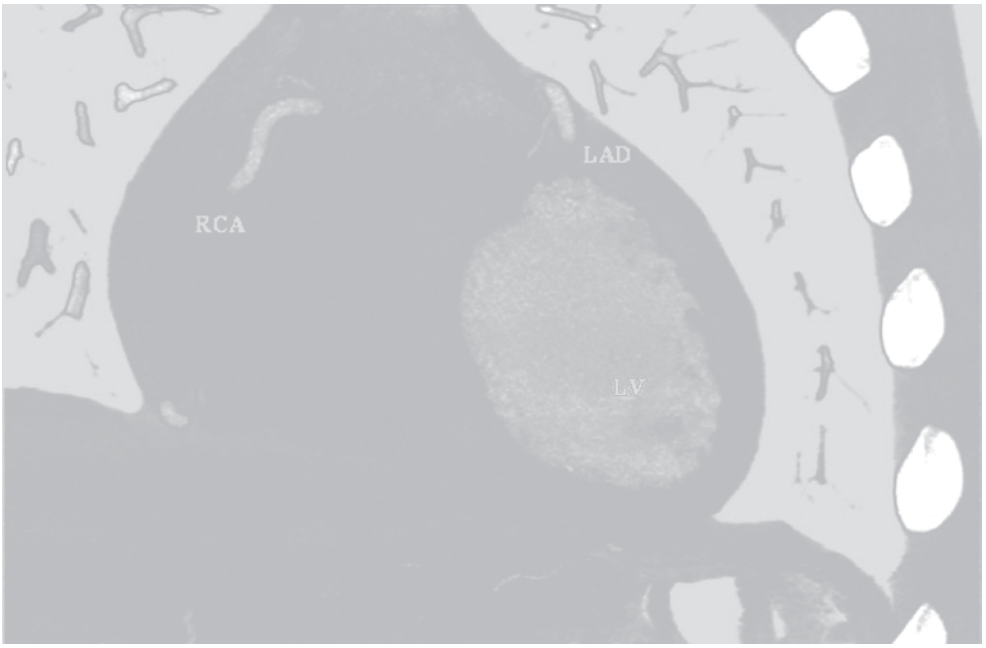

Figure 25.48.

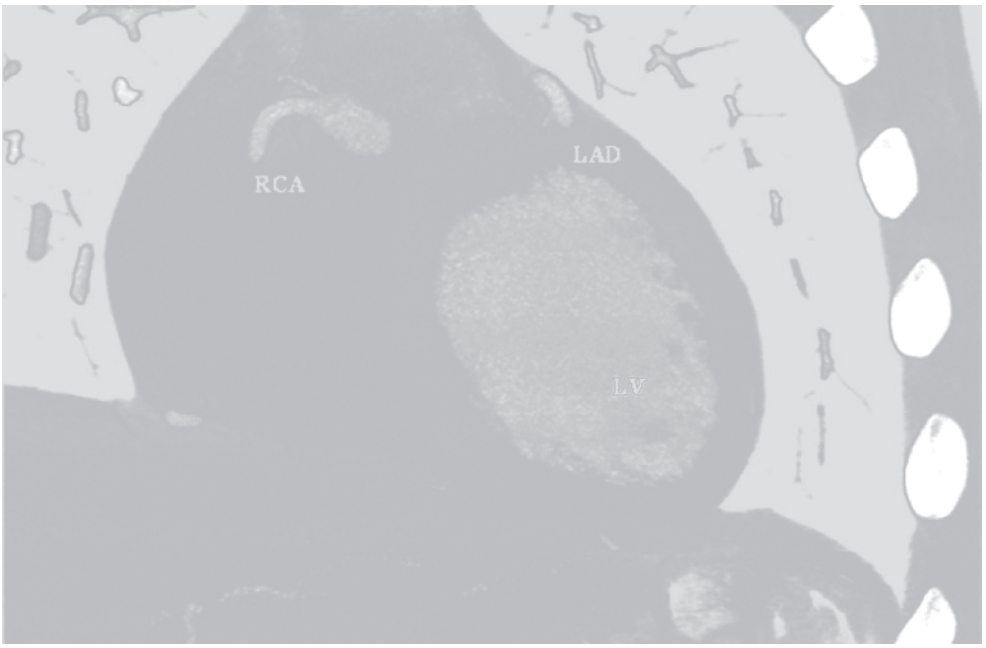

Figure 25.49.

Figure 25.50.

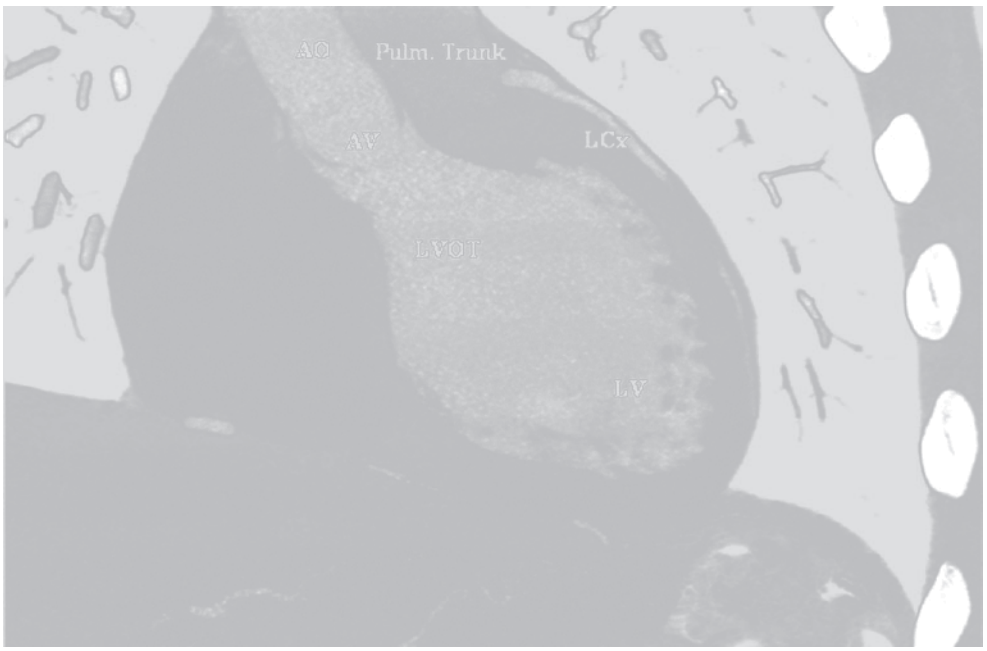

Figure 25.51.

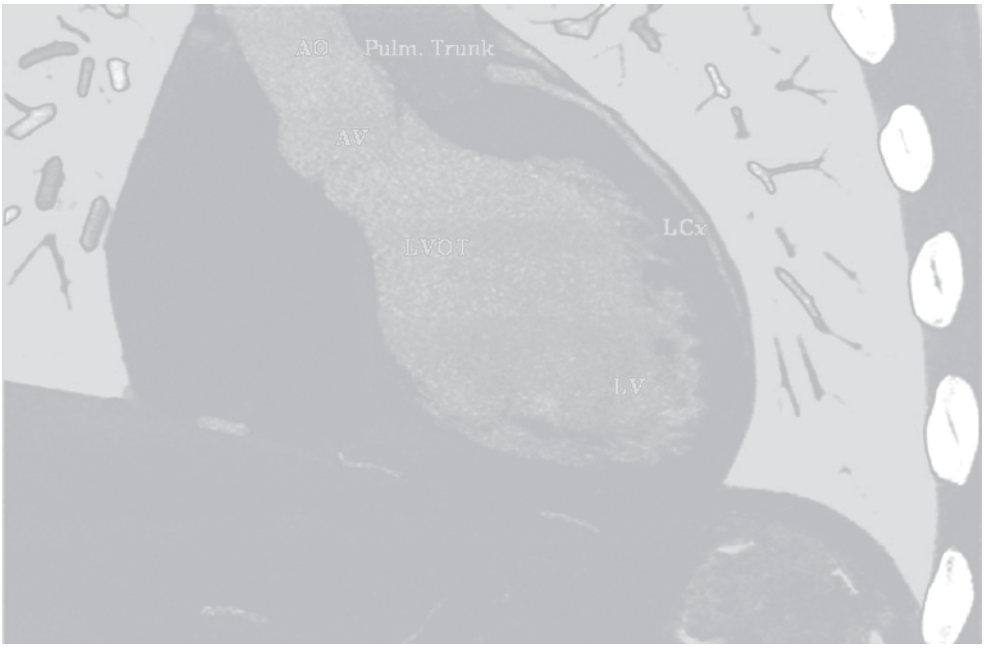

Figure 25.52.

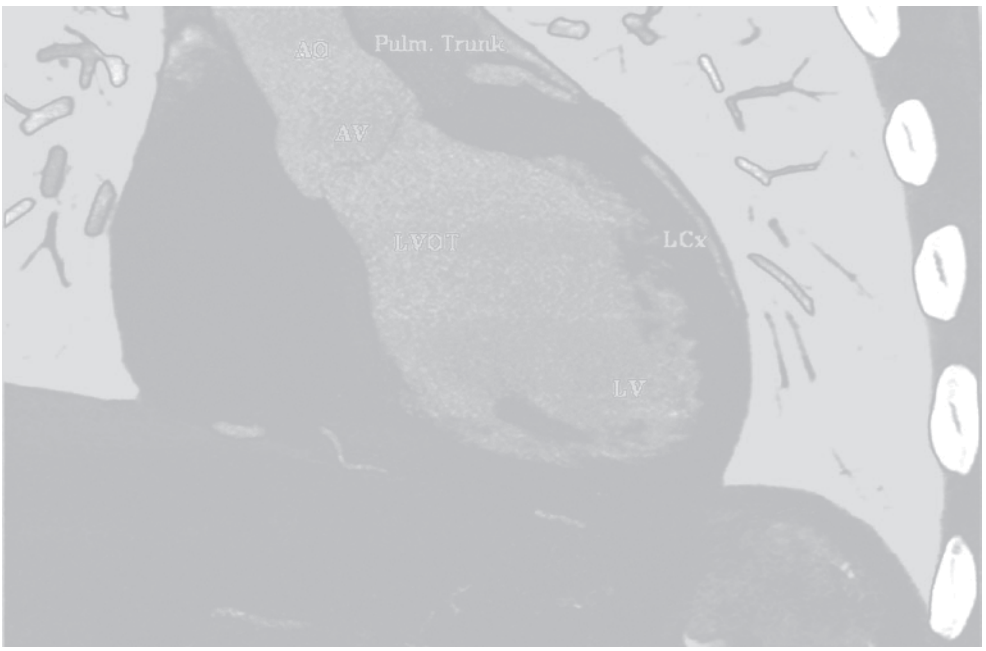

Figure 25.53.

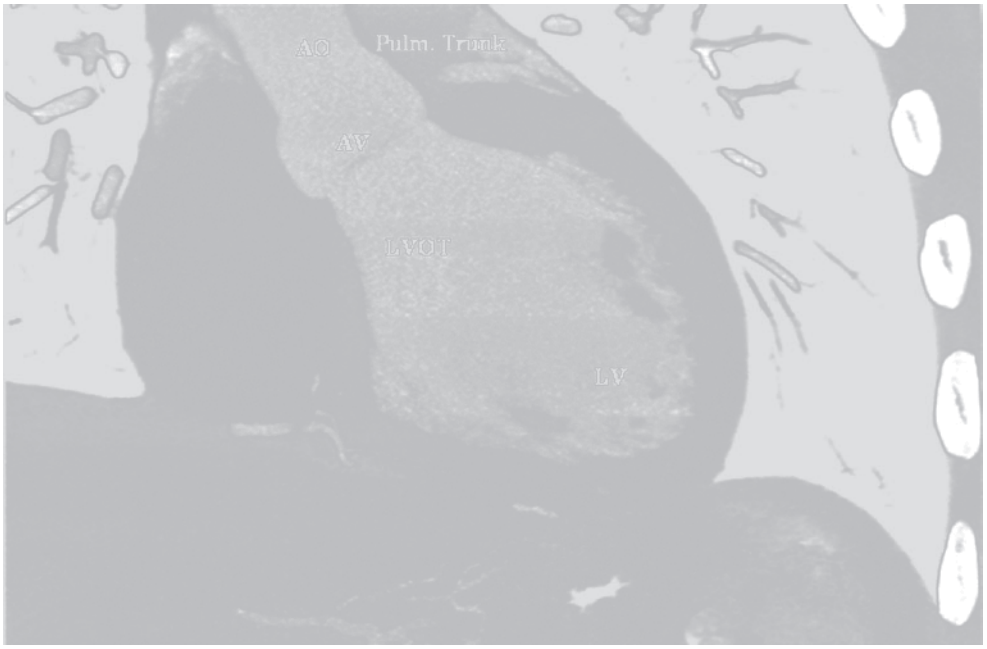

Figure 25.54.

Figure 25.55.

Figure 25.56.

Figure 25.57.

Figure 25.58.

Figure 25.59.

Figure 25.60.

Figure 25.61.

Figure 25.62.

Figure 25.63.

Figure 25.64.

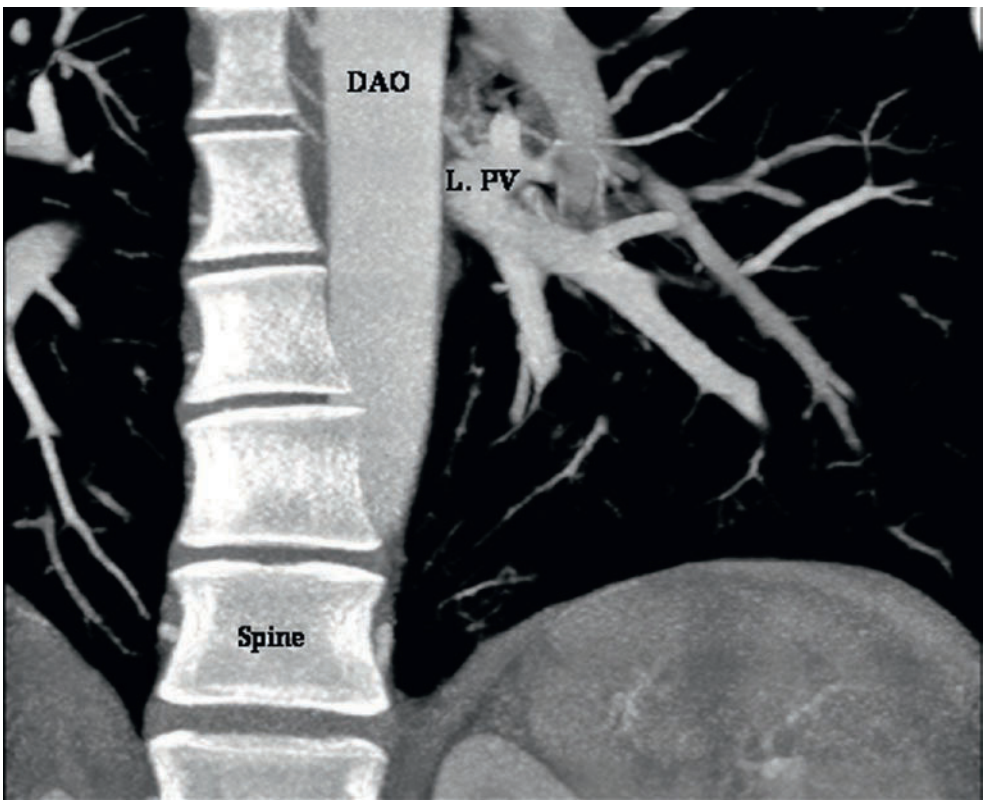

Figure 25.65.

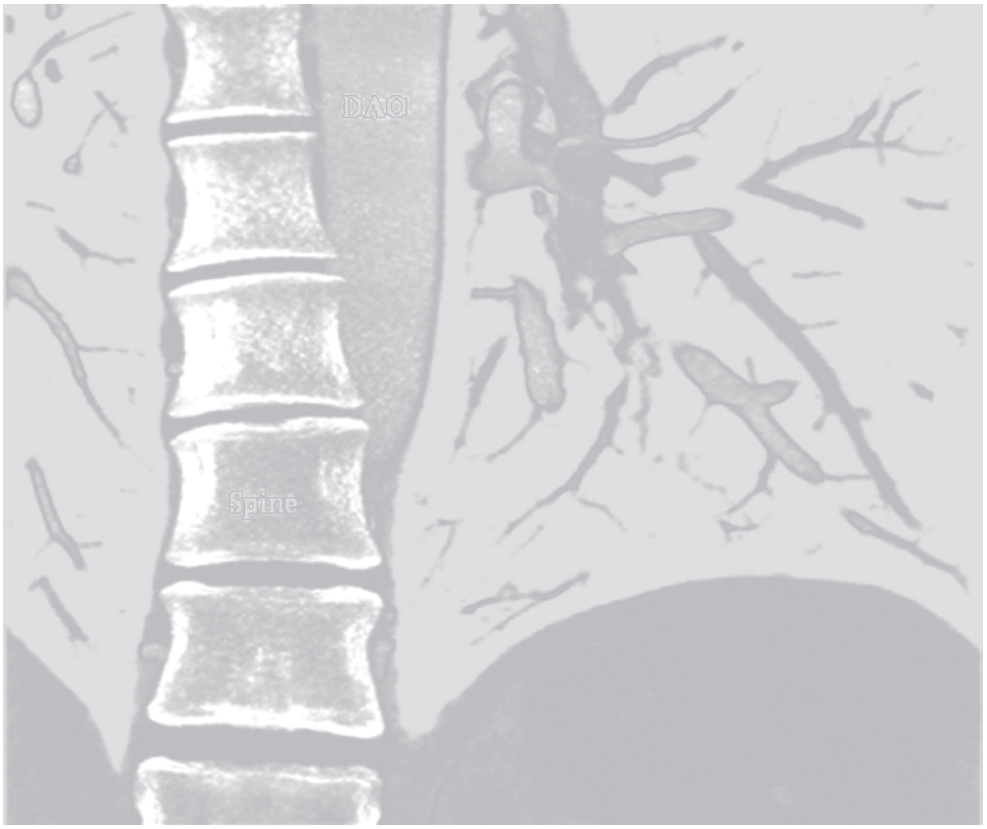

Figure 25.66.

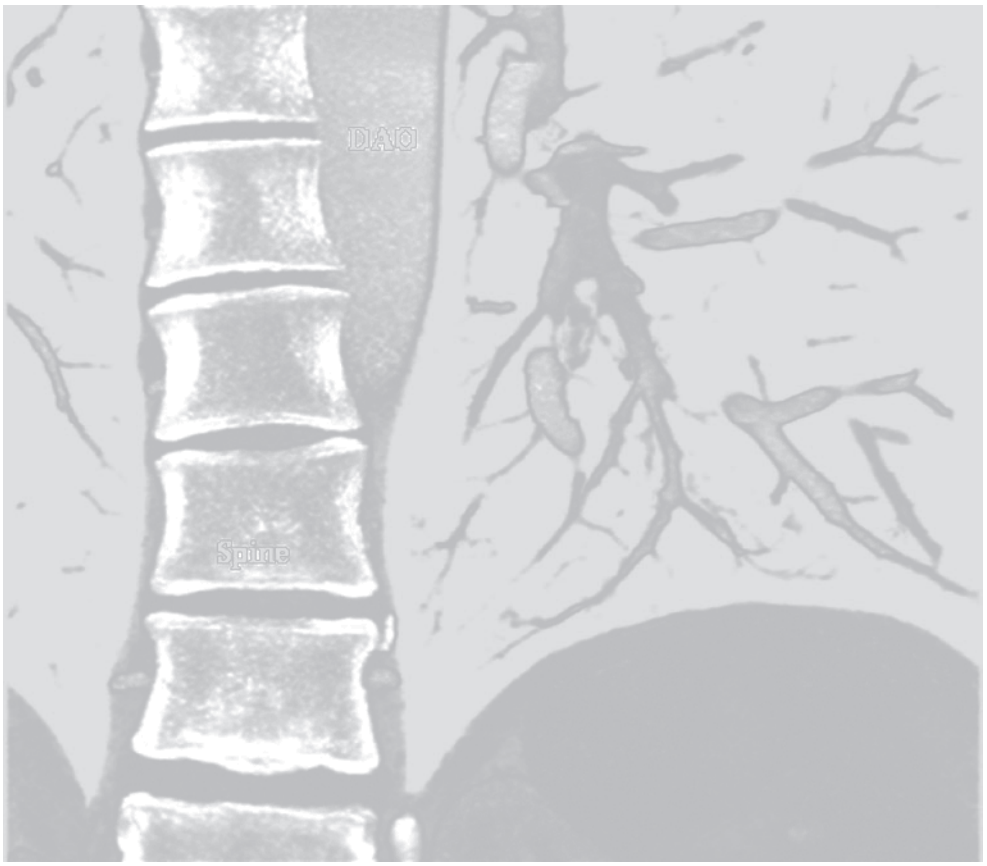

Figure 25.67.

Orientation to Sagittal Images

Figures 25.68–25.131. Serial sagittal CT angiography images beginning at the level of the left ventricular apex with slices proceeding in a left to right direction.

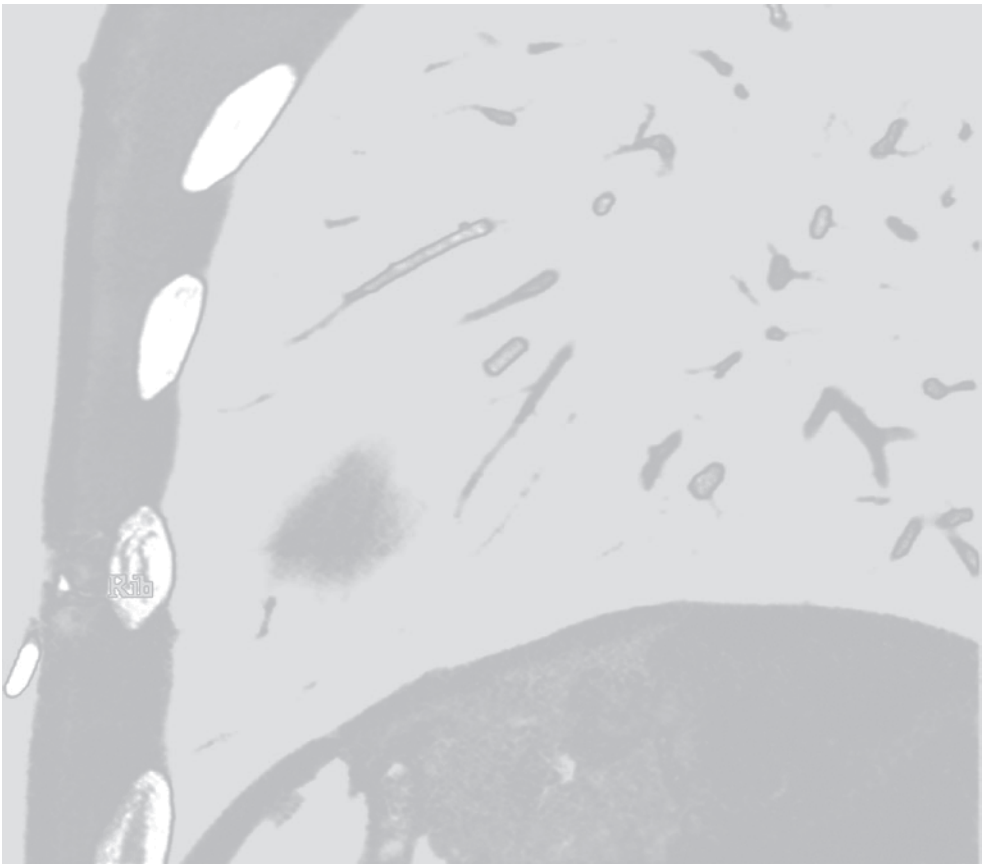

Figure 25.68.

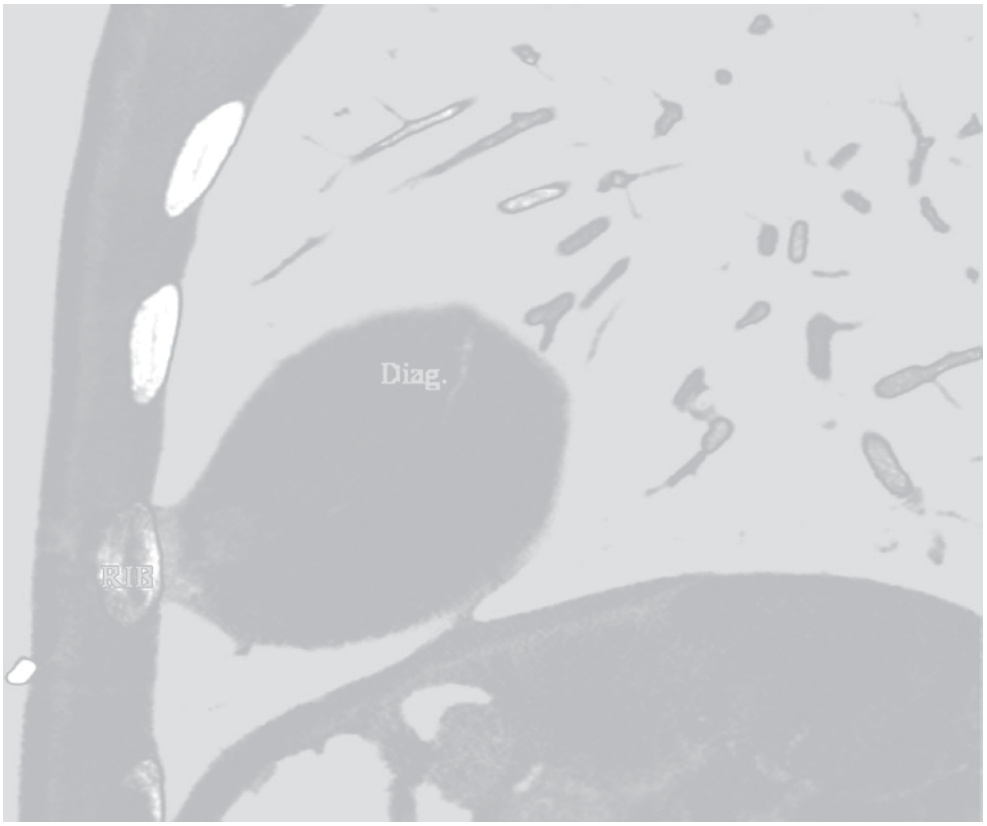

Figure 25.69.

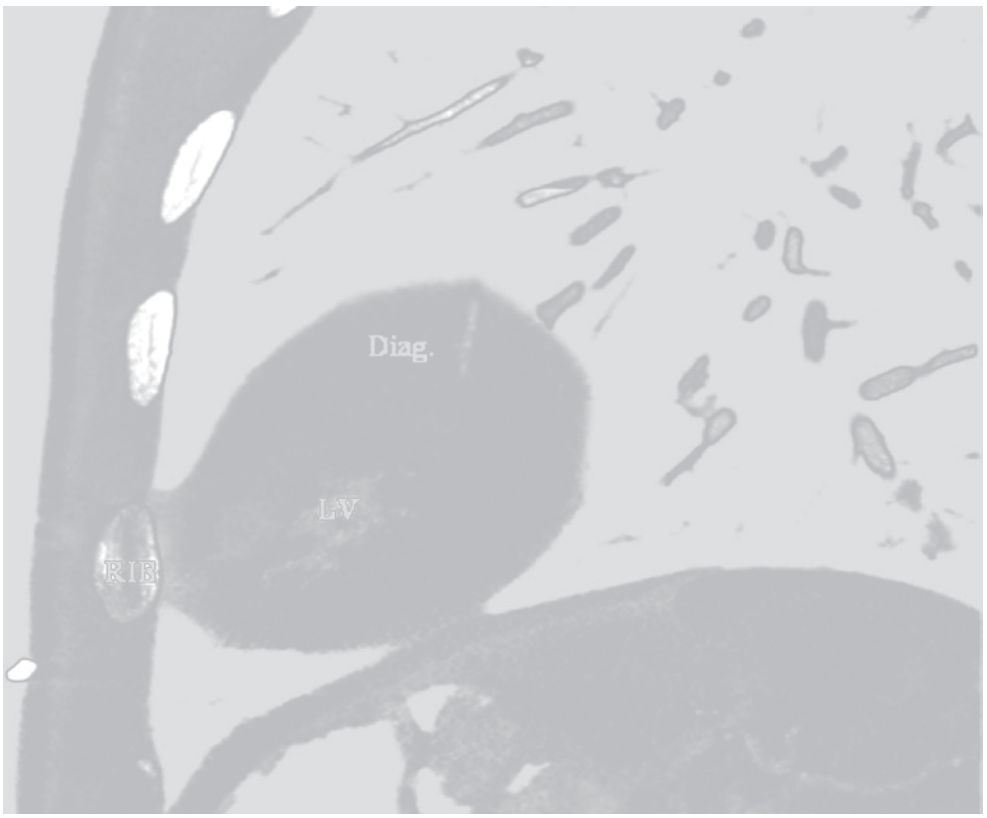

Figure 25.70.

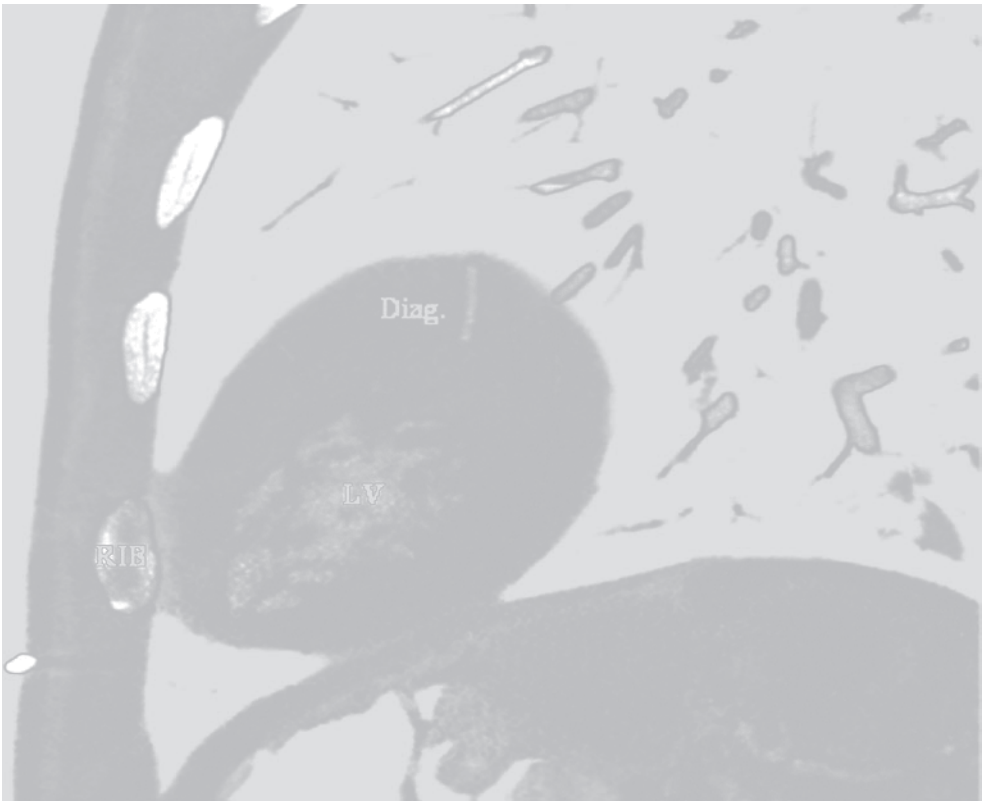

Figure 25.71.

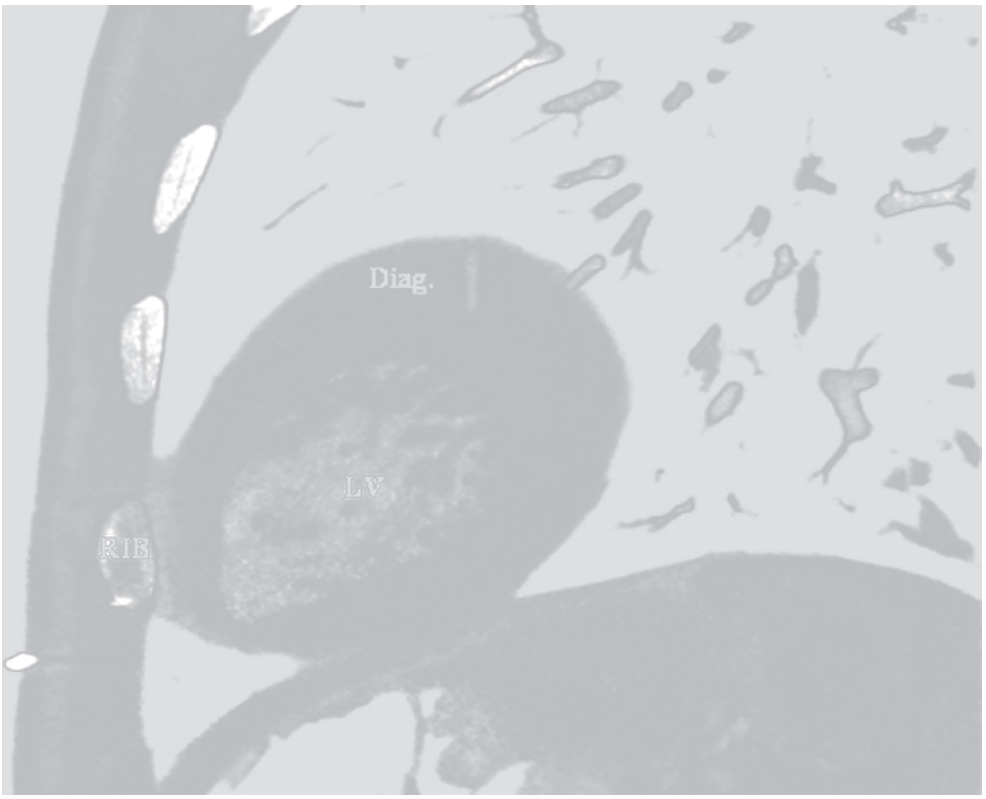

Figure 25.72.

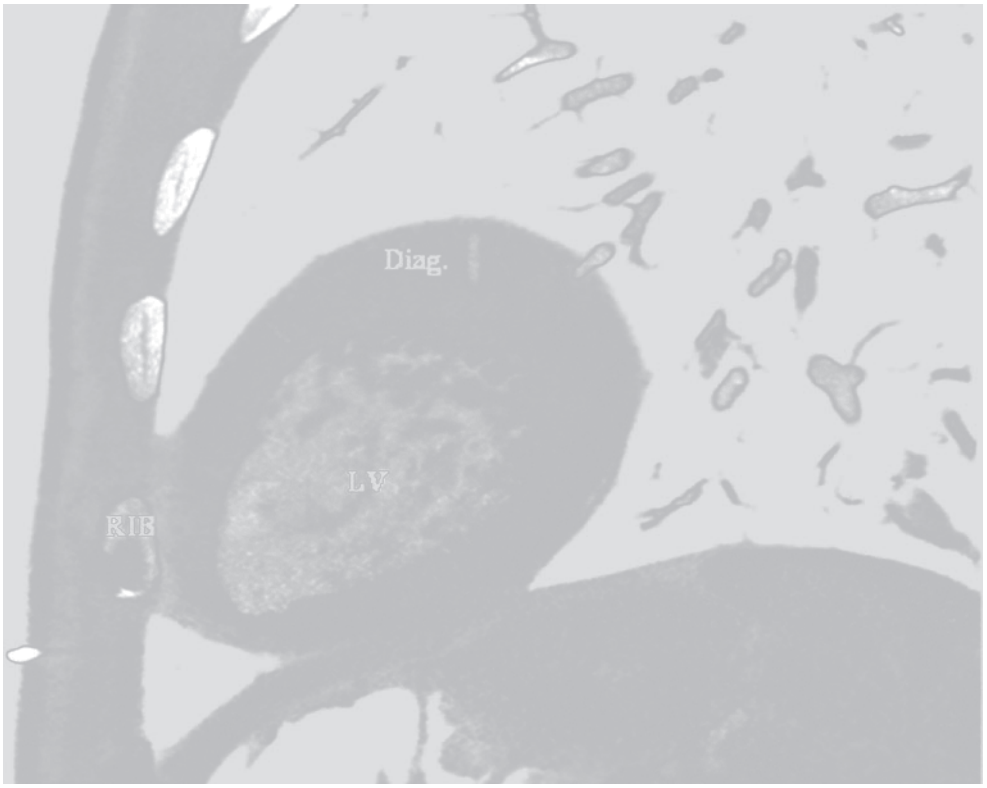

Figure 25.73.

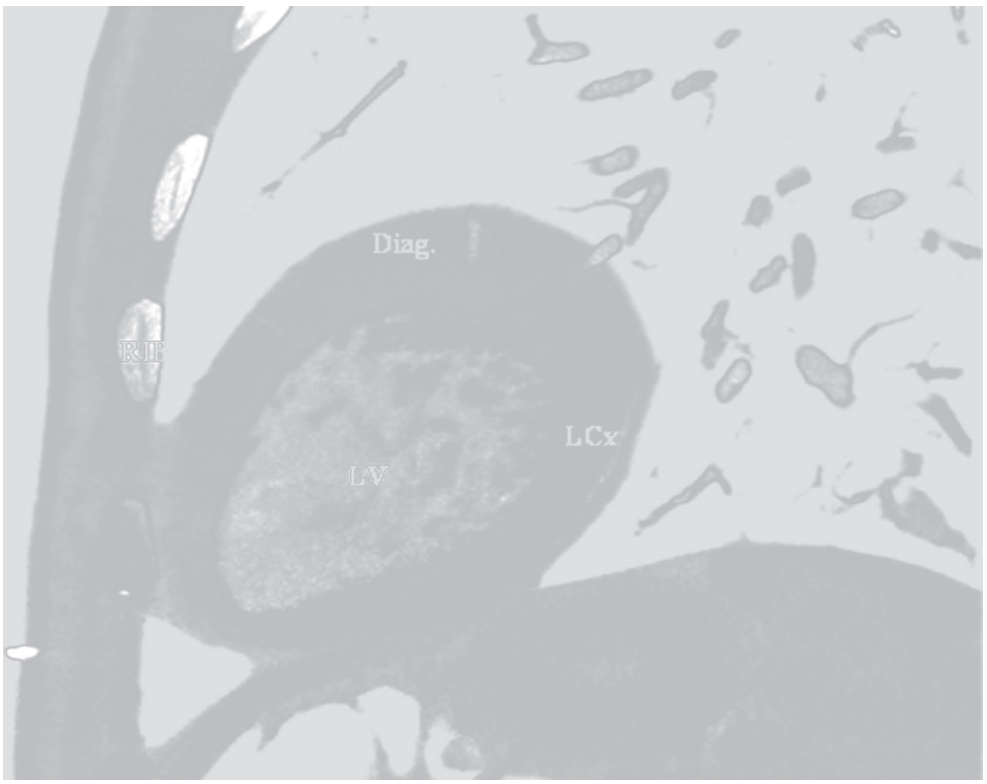

Figure 25.74.

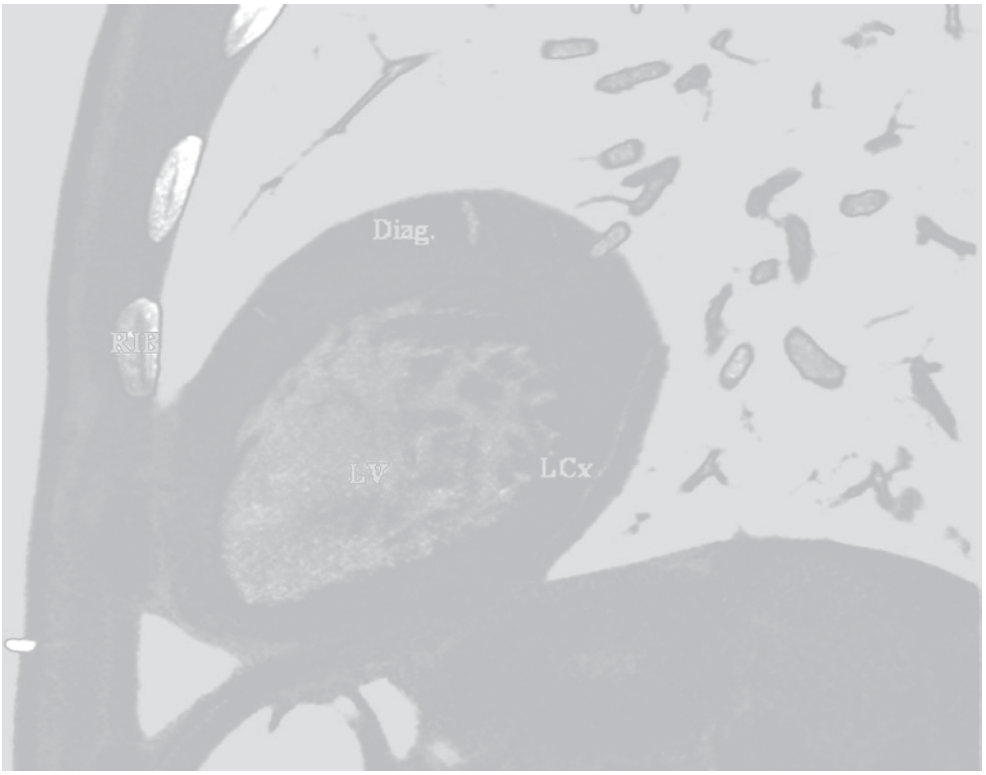

Figure 25.75.

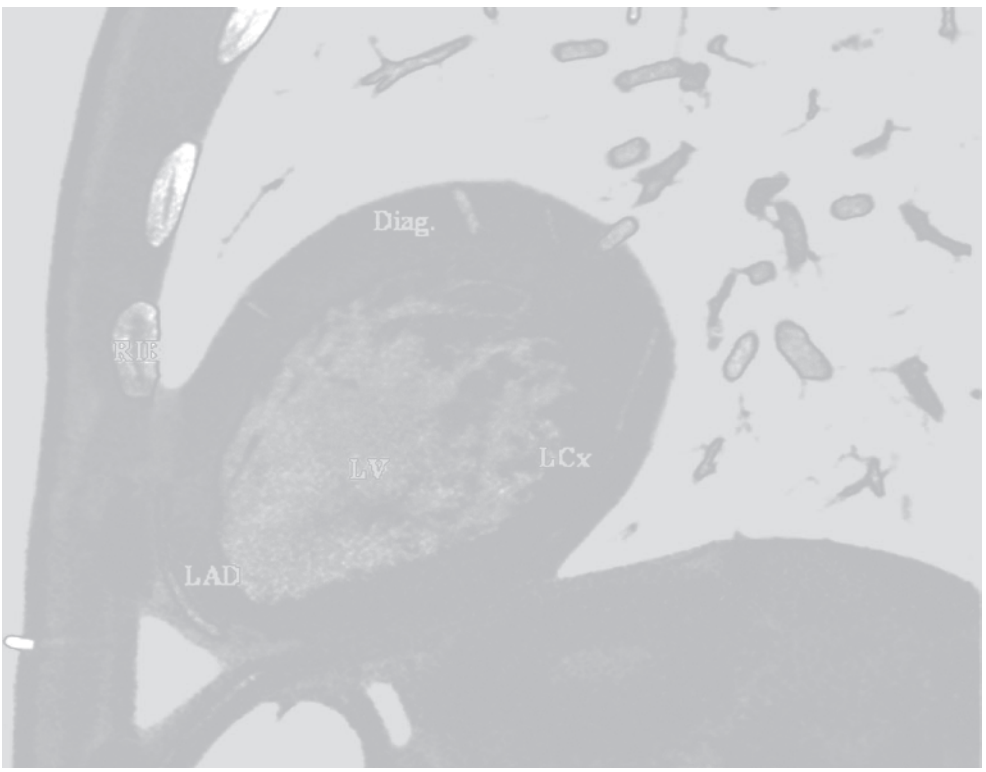

Figure 25.76.

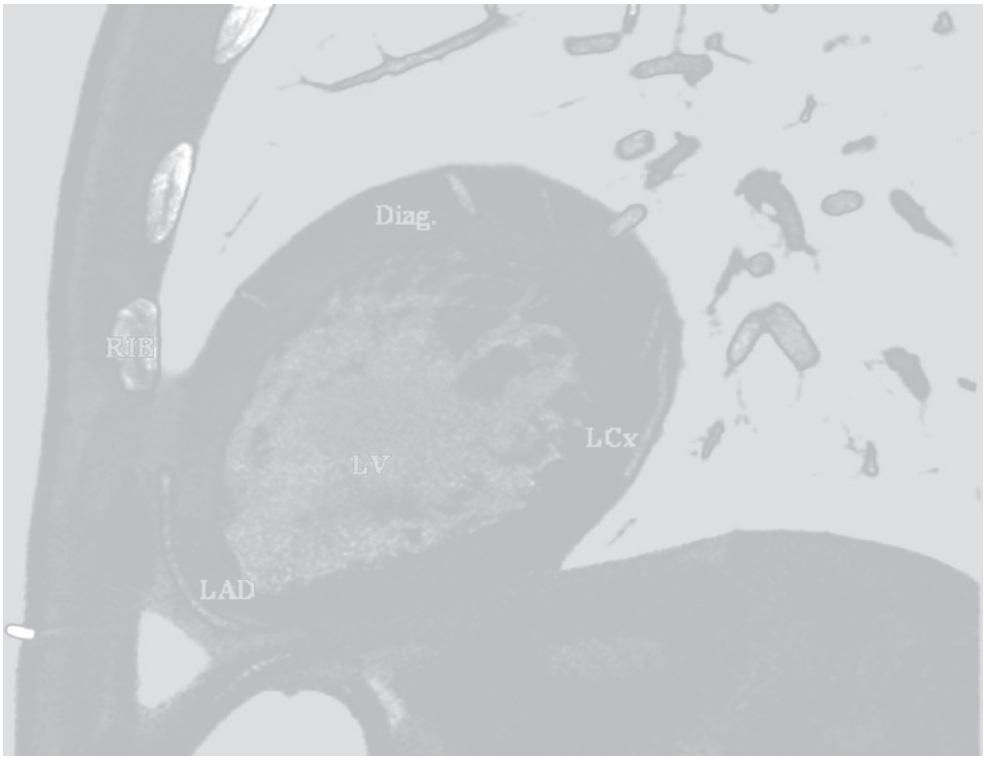

Figure 25.77.

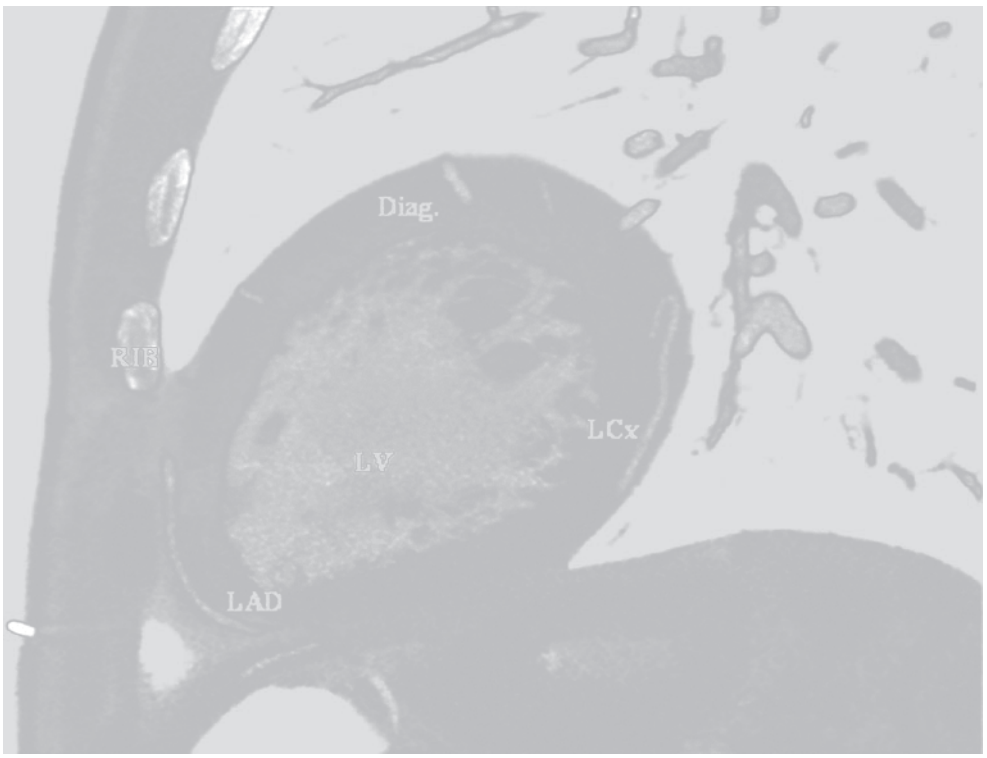

Figure 25.78.

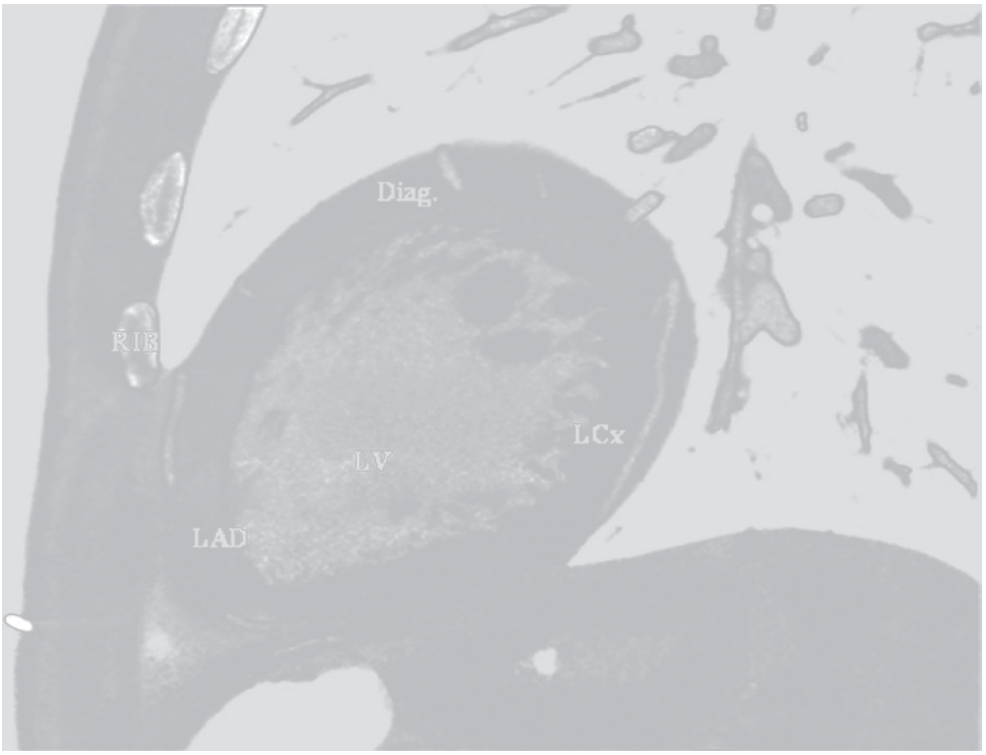

Figure 25.79.

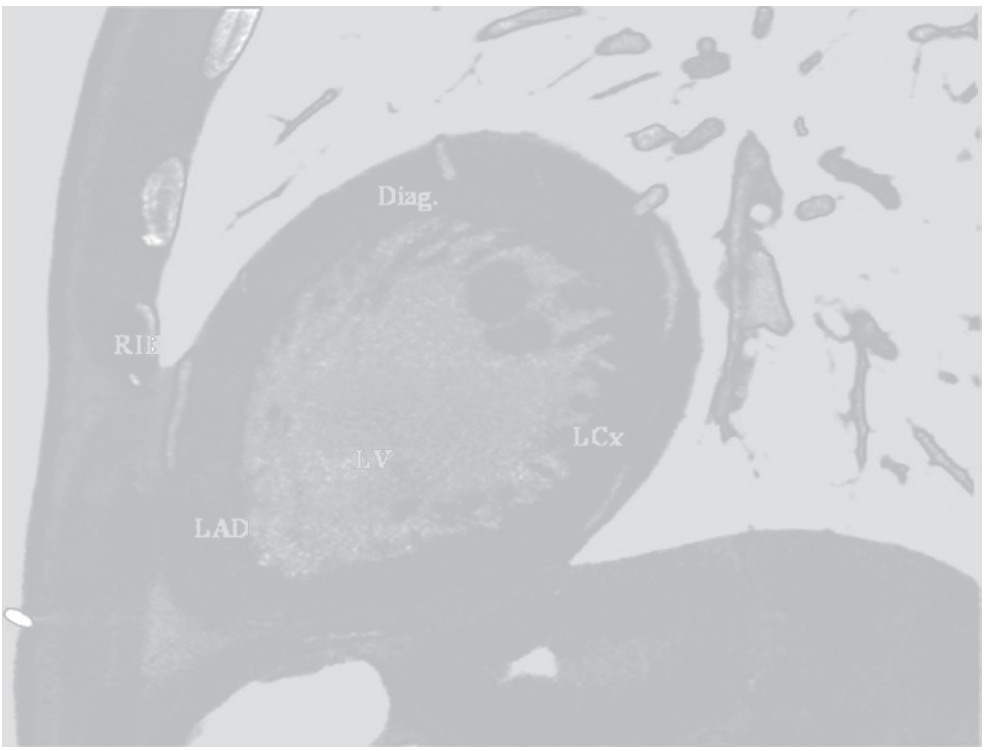

Figure 25.80.

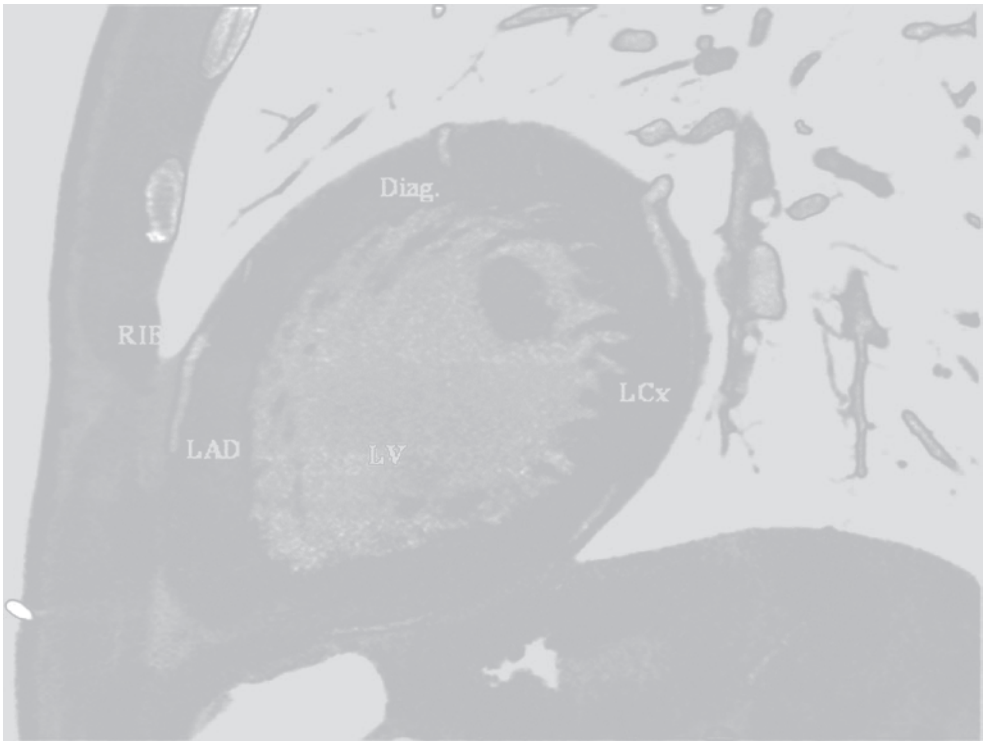

Figure 25.81.

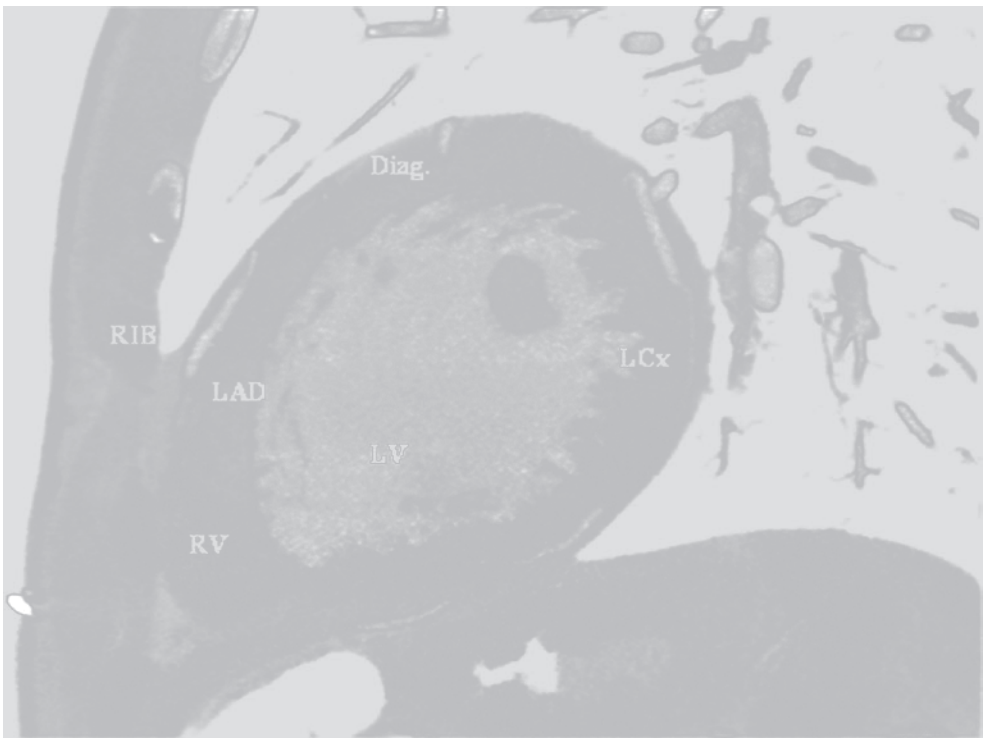

Figure 25.82.

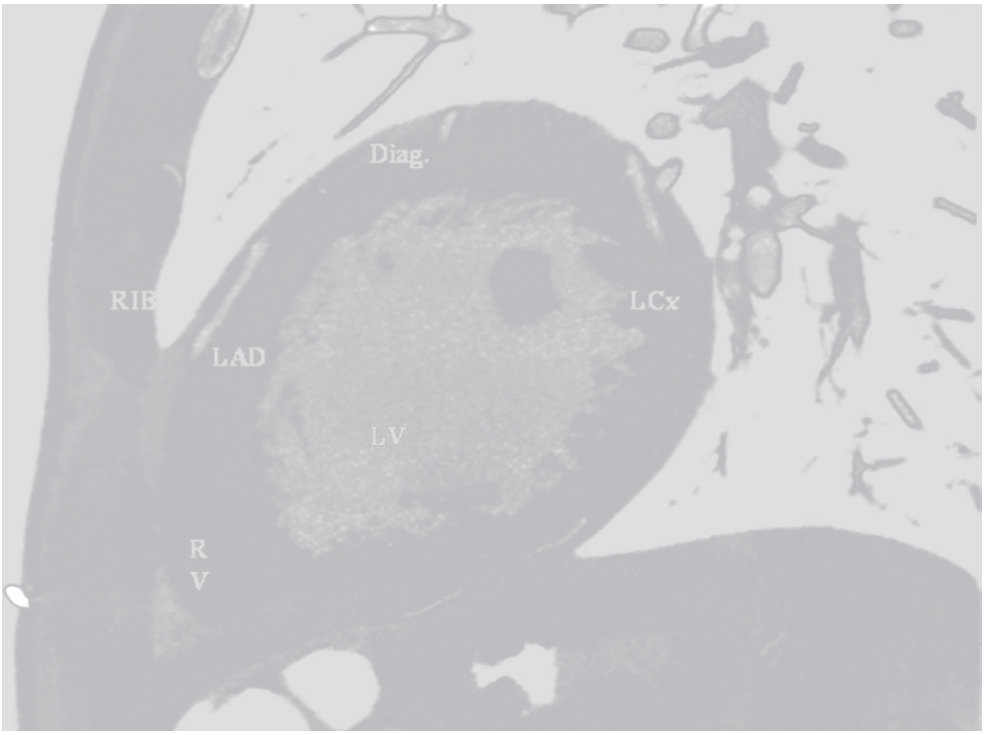

Figure 25.83.

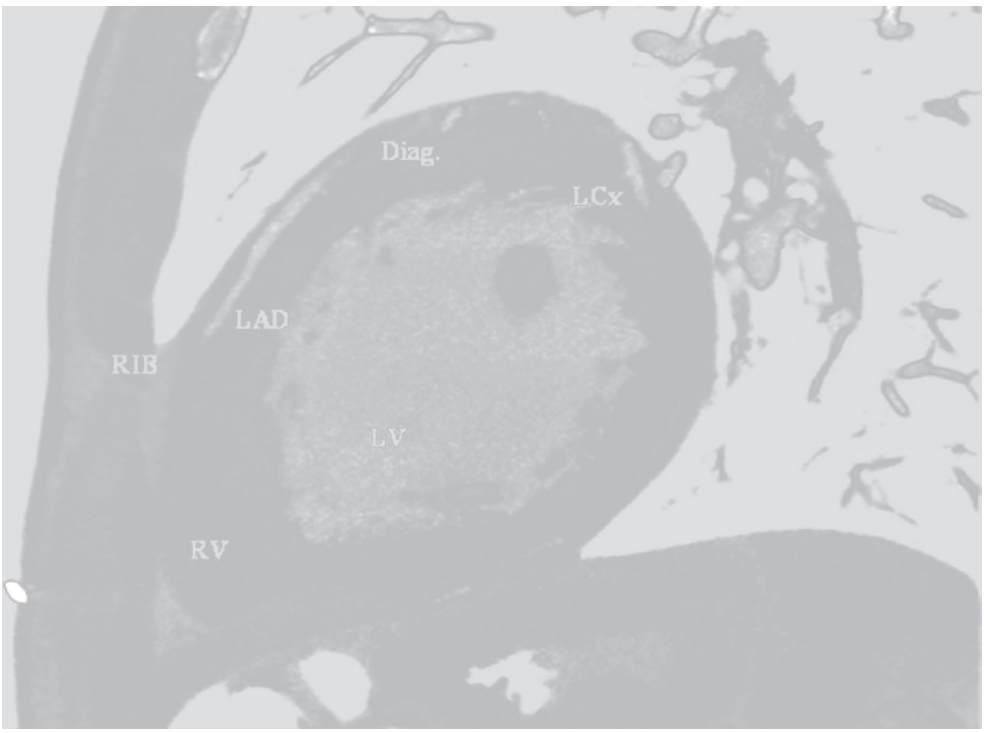

Figure 25.84.

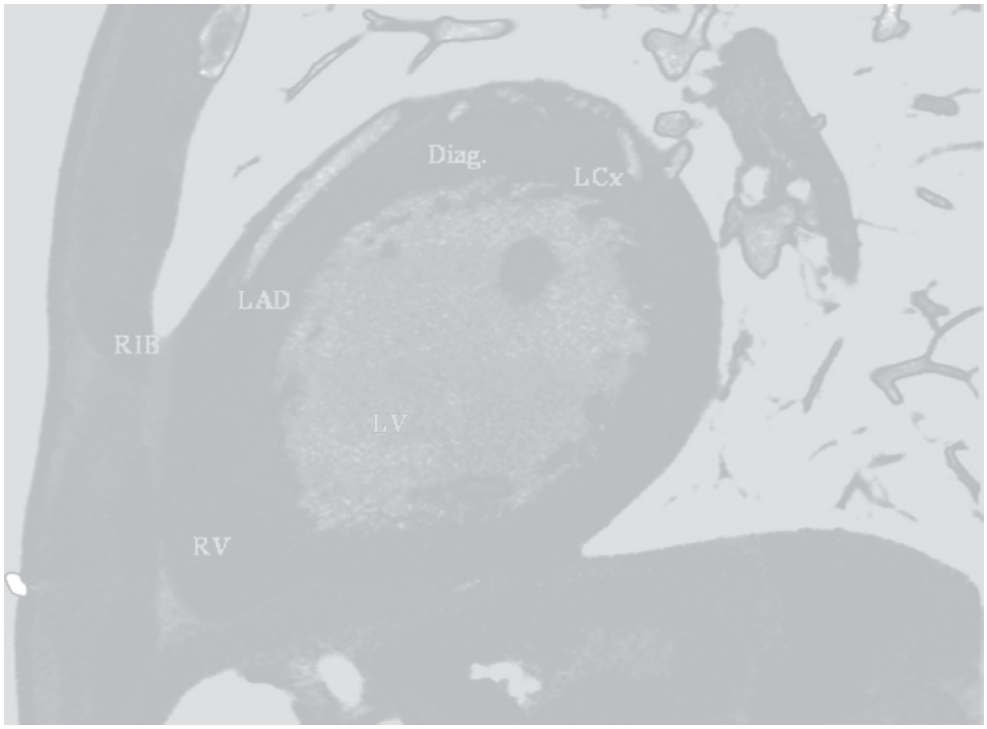

Figure 25.85.

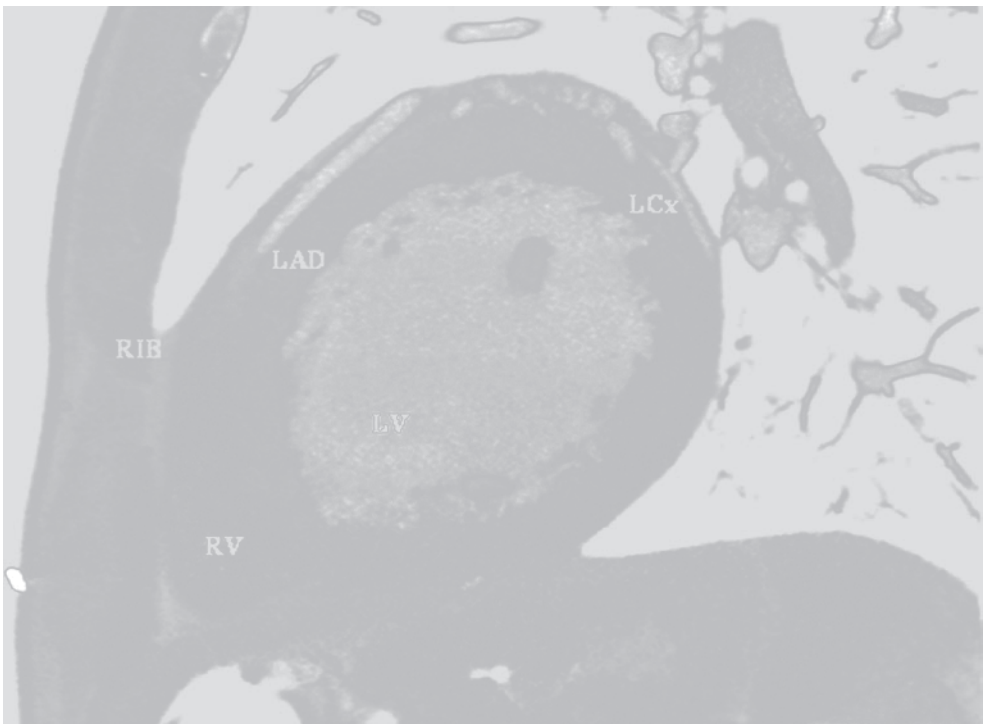

Figure 25.86.

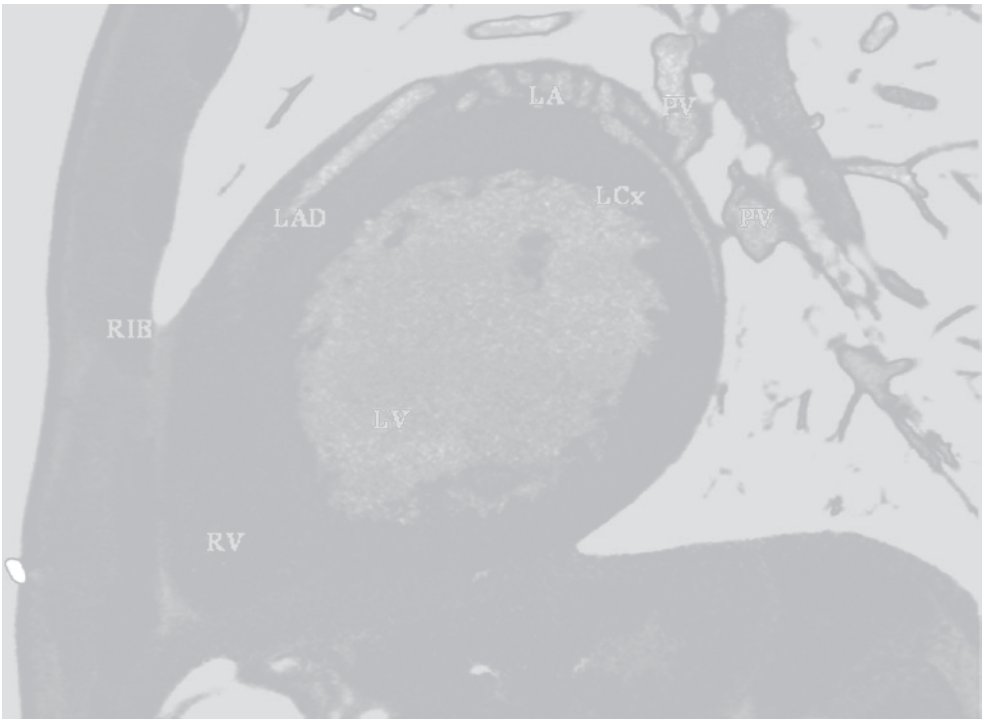

Figure 25.87.

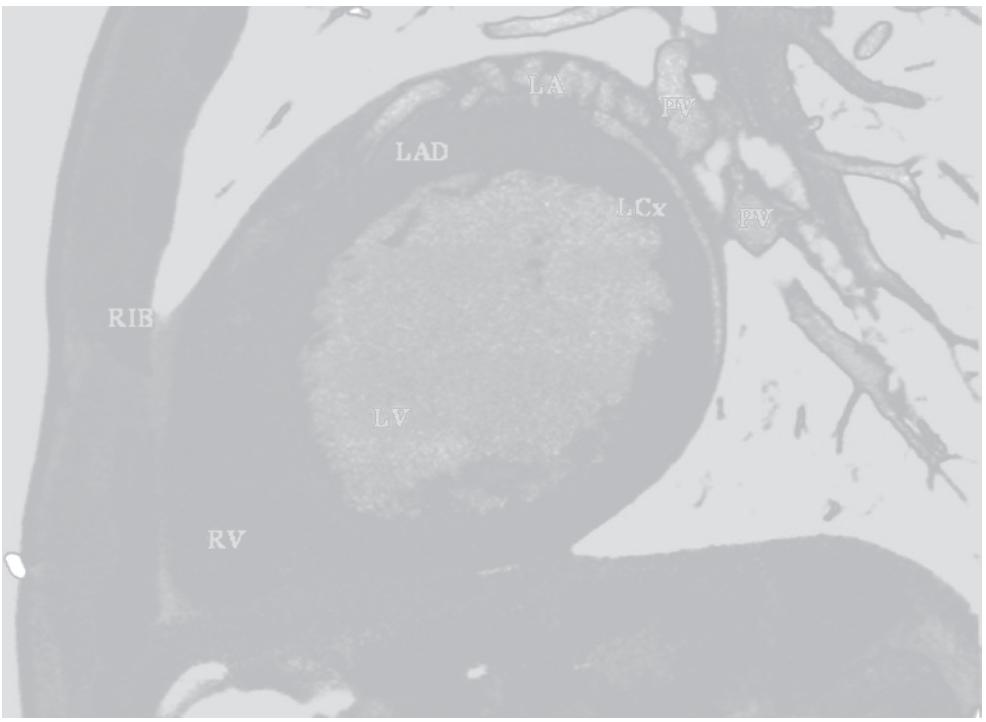

Figure 25.88.

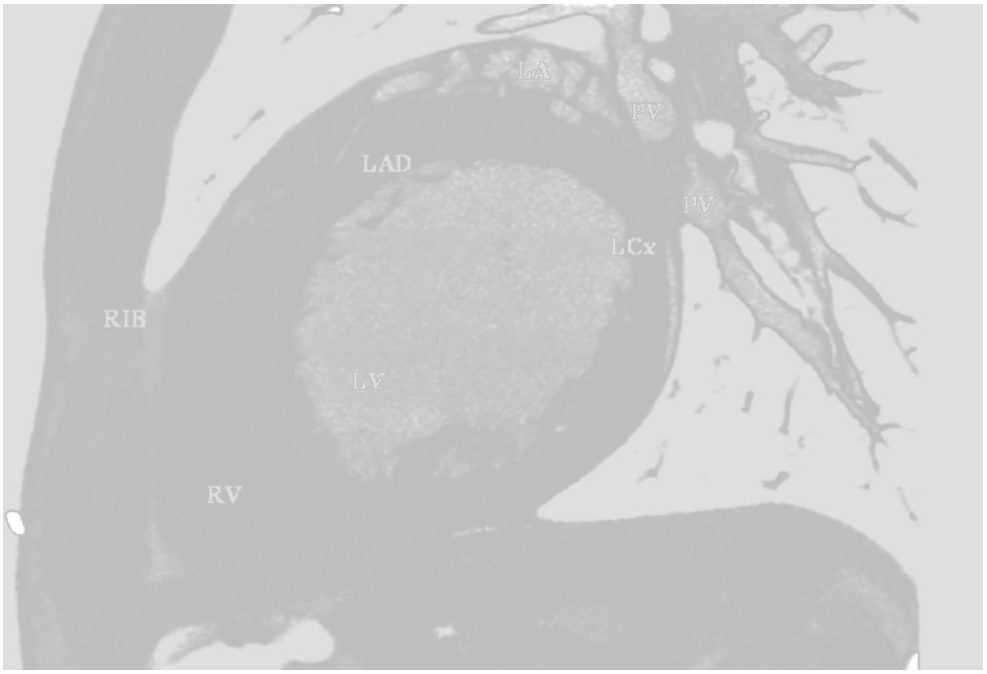

Figure 25.89.

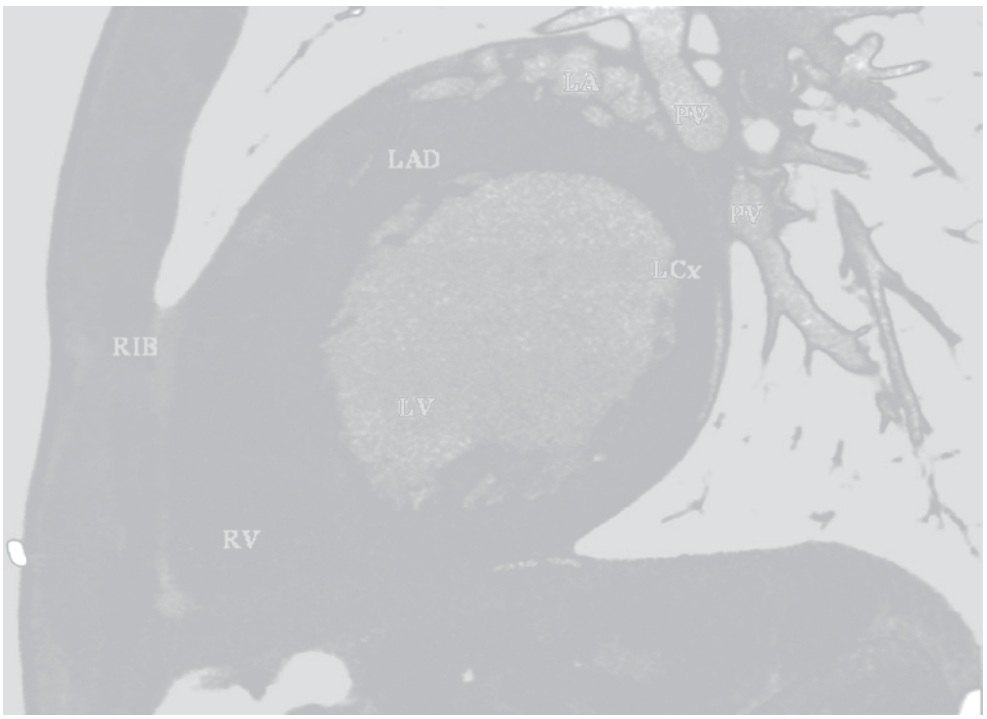

Figure 25.90.

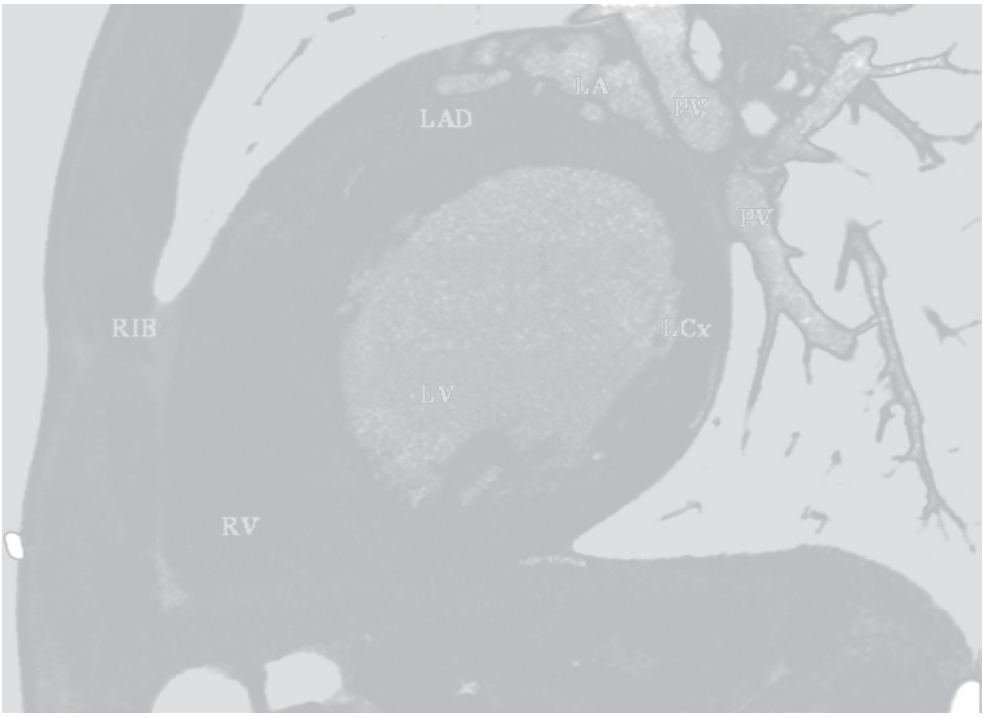

Figure 25.91.

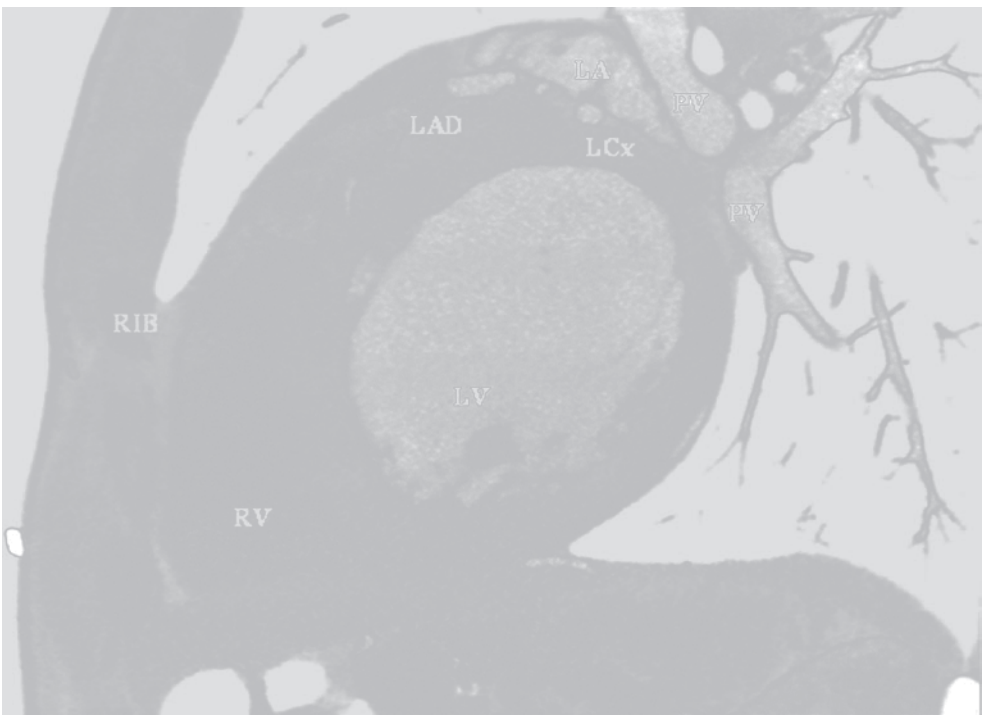

Figure 25.92.

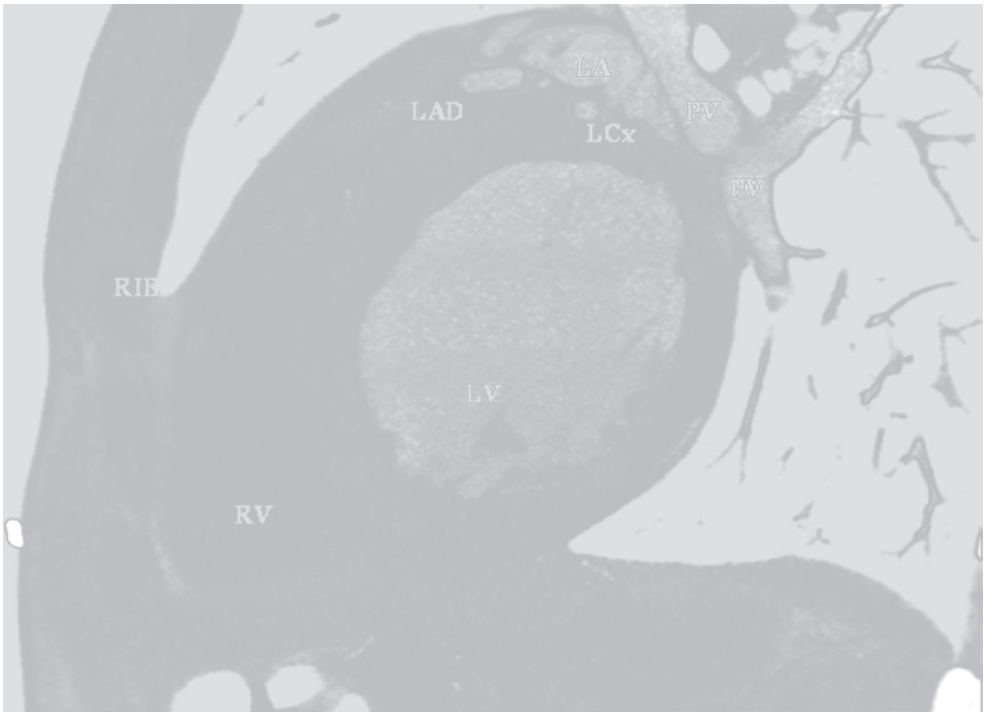

Figure 25.93.

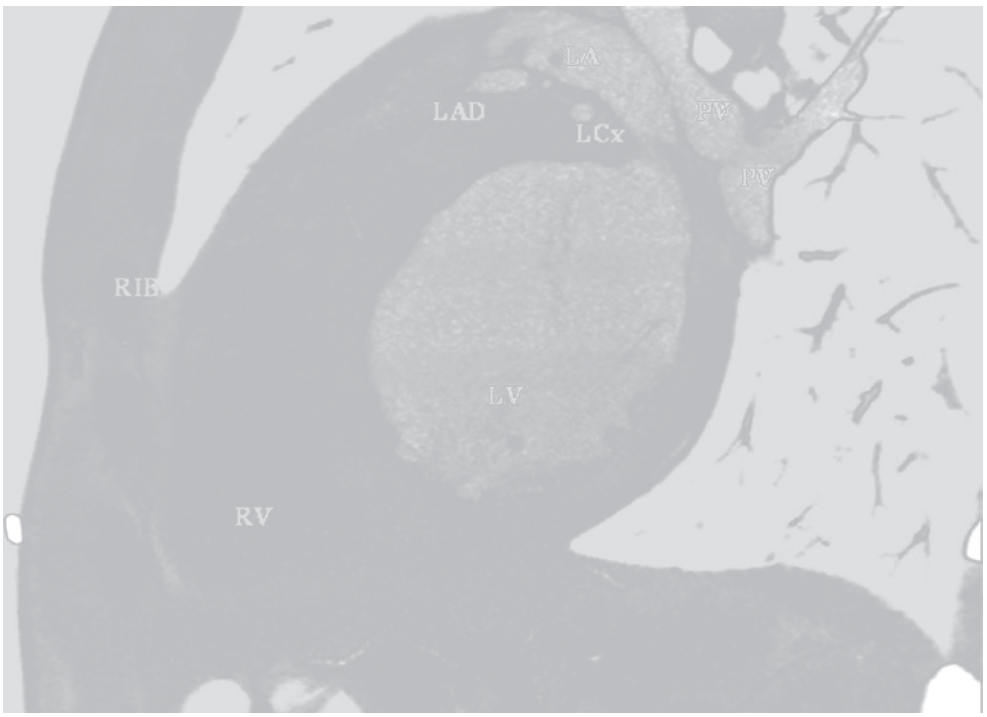

Figure 25.94.

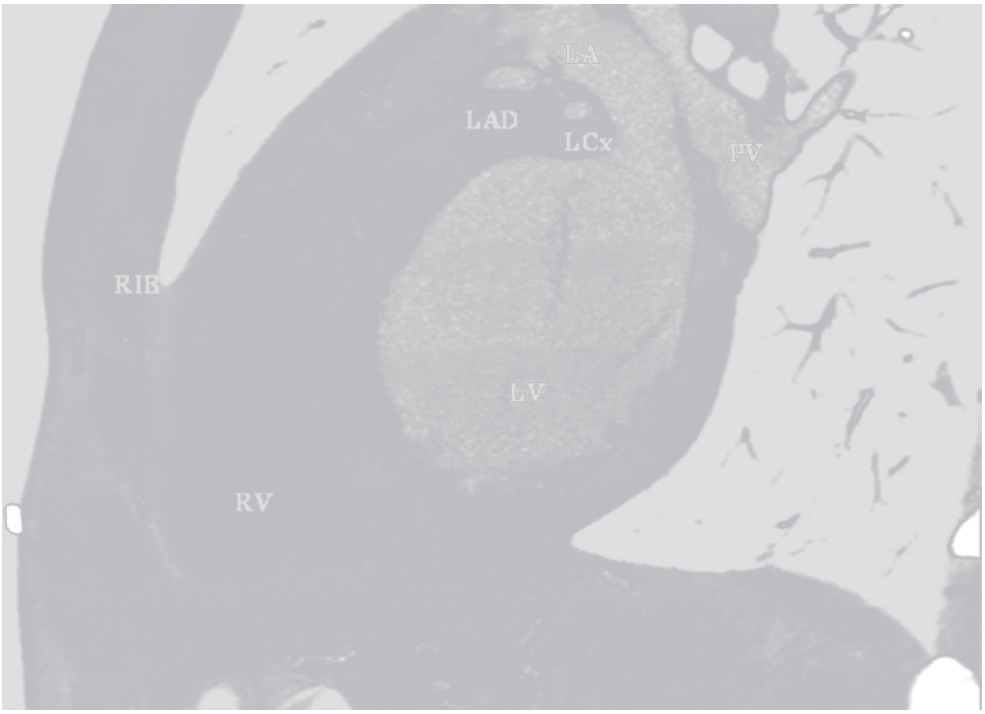

Figure 25.95.

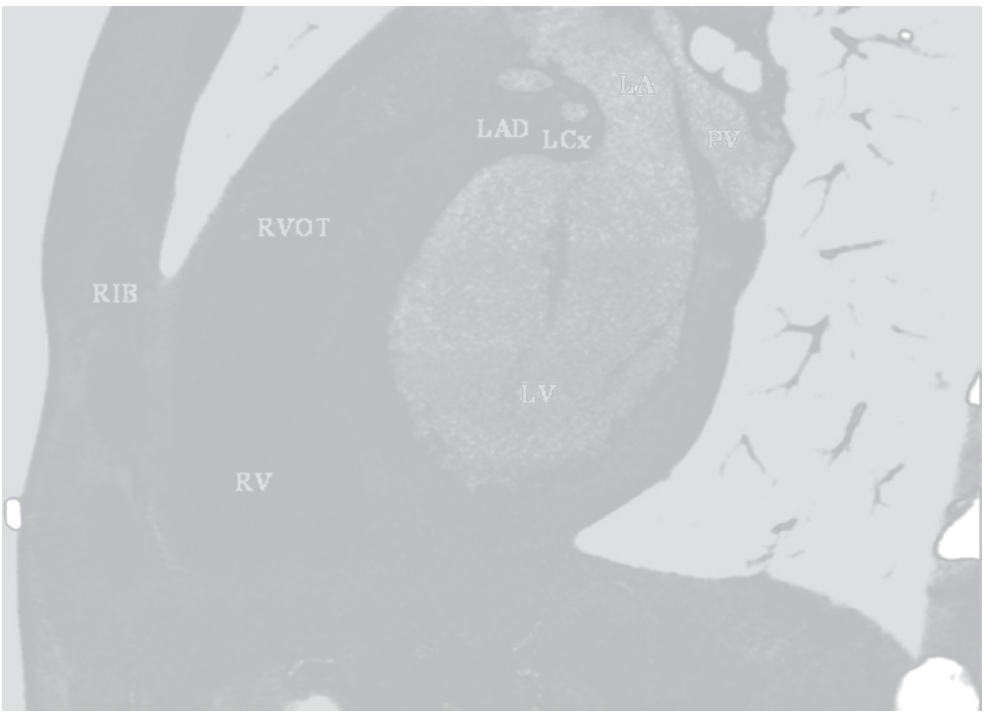

Figure 25.96.

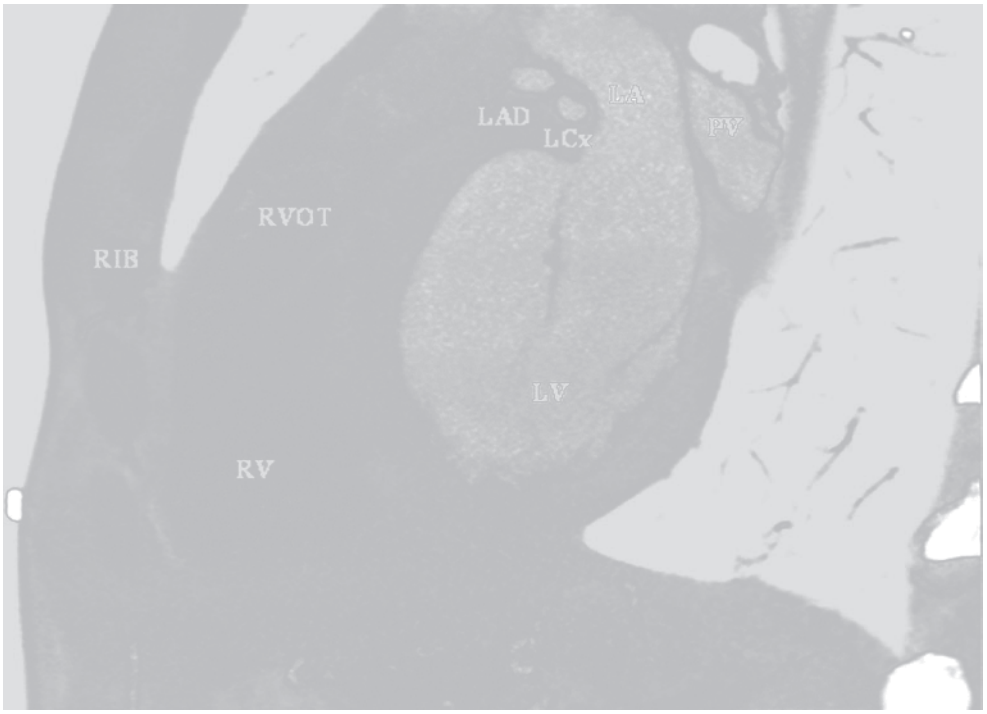

Figure 25.97.

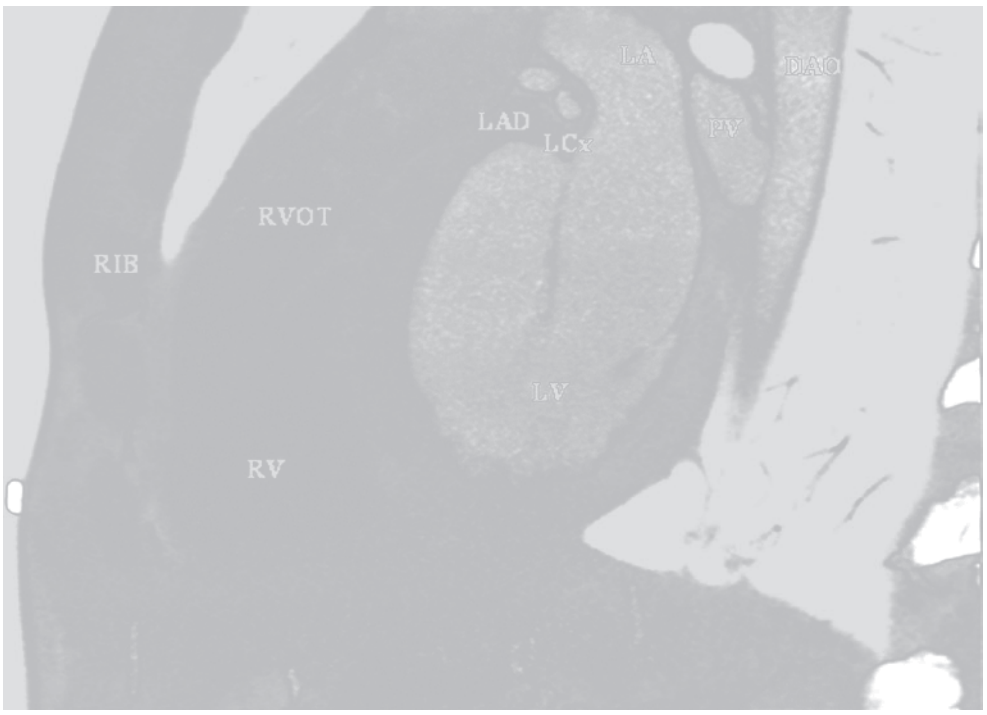

Figure 25.98.

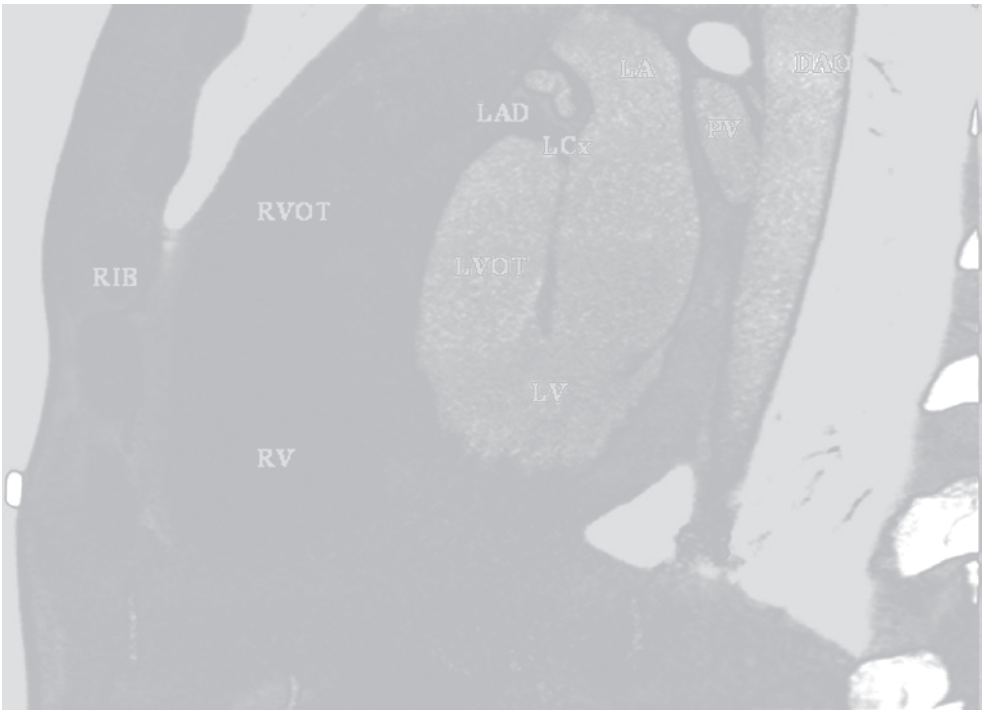

Figure 25.99.

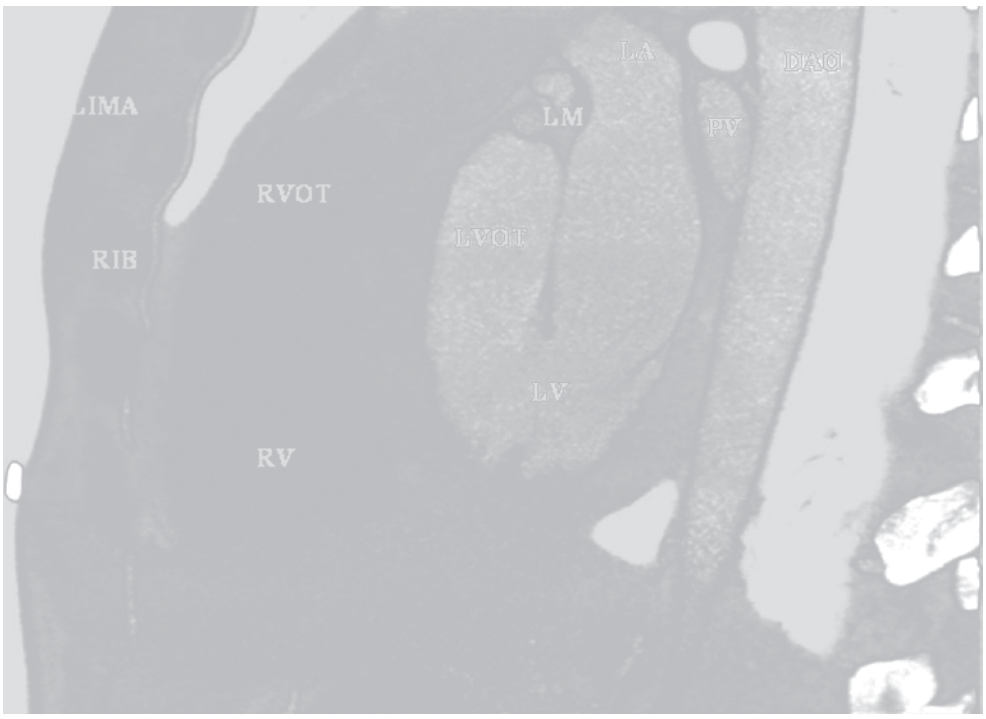

Figure 25.100.

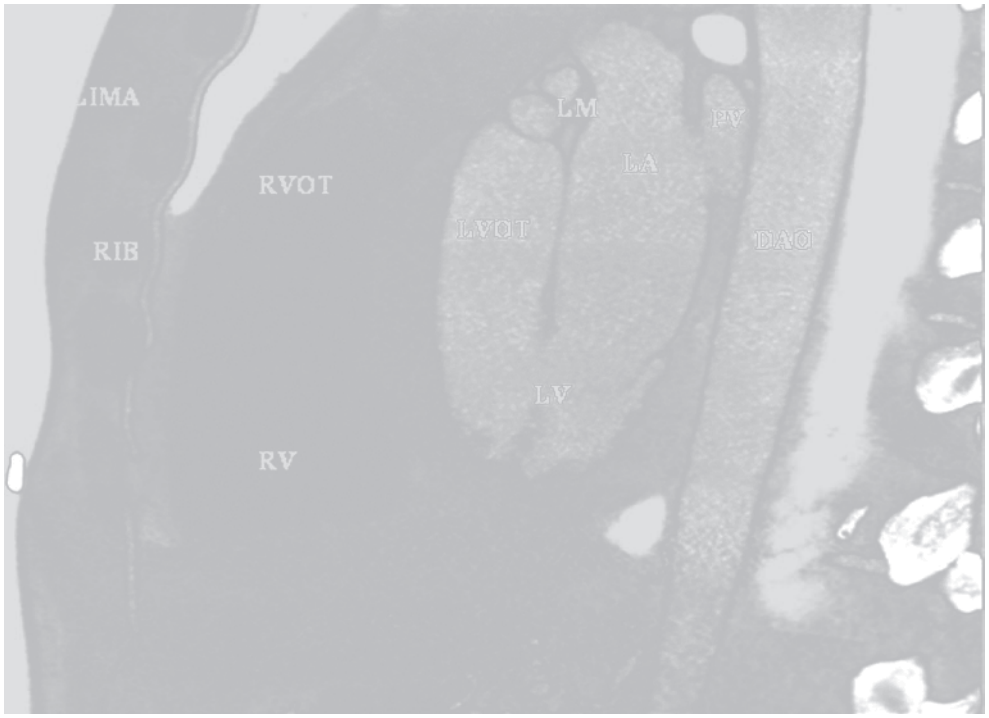

Figure 25.101.

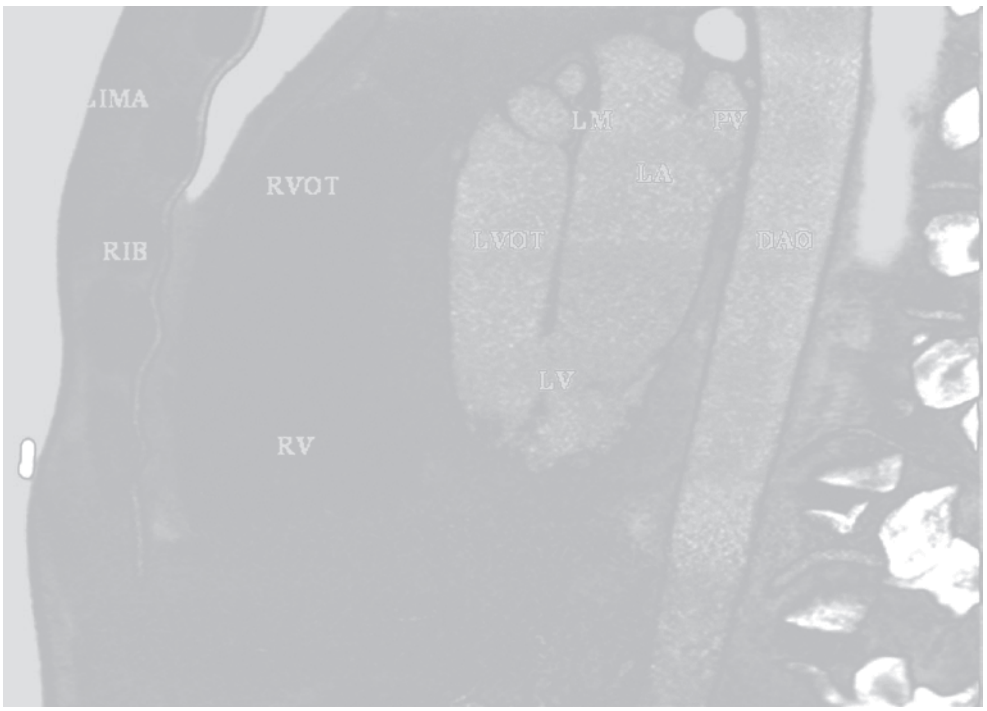

Figure 25.102.

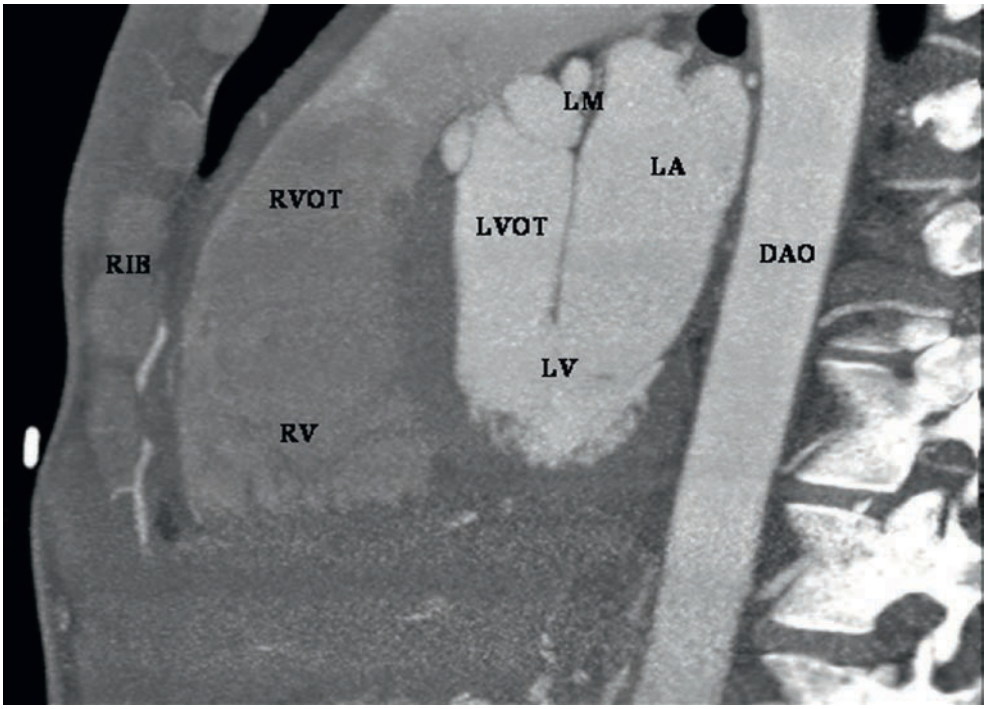

Figure 25.103.

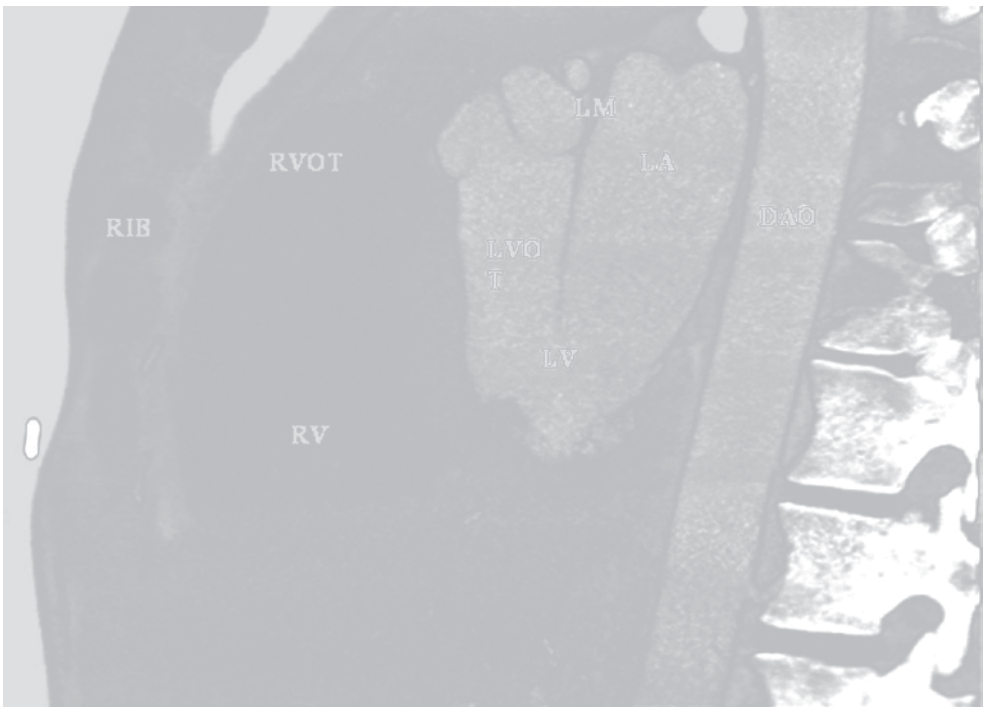

Figure 25.104.

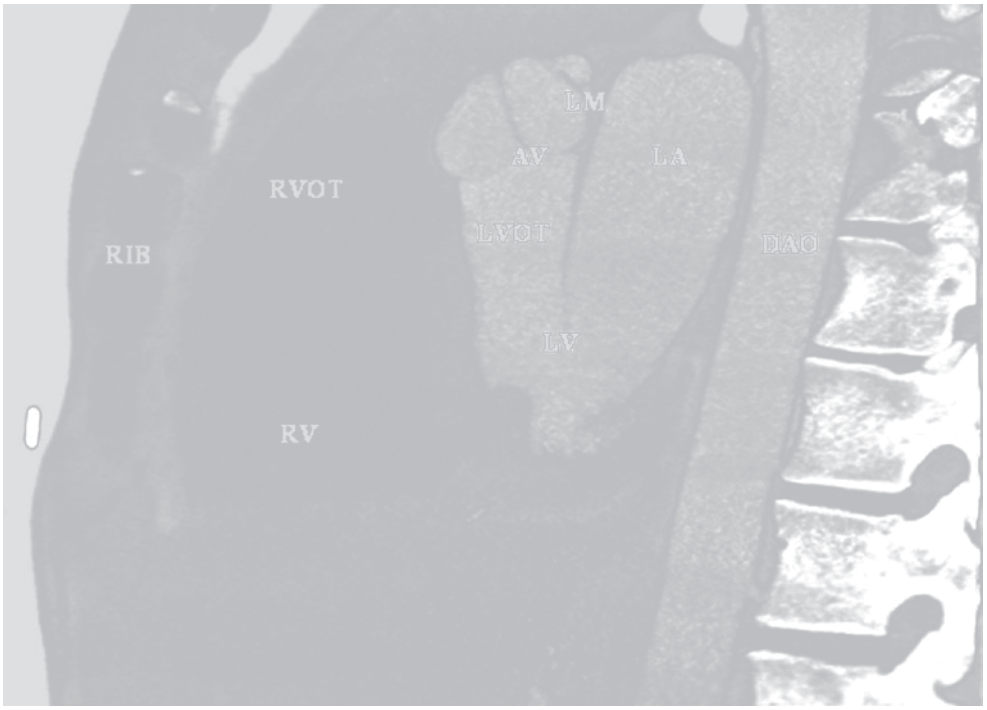

Figure 25.105.

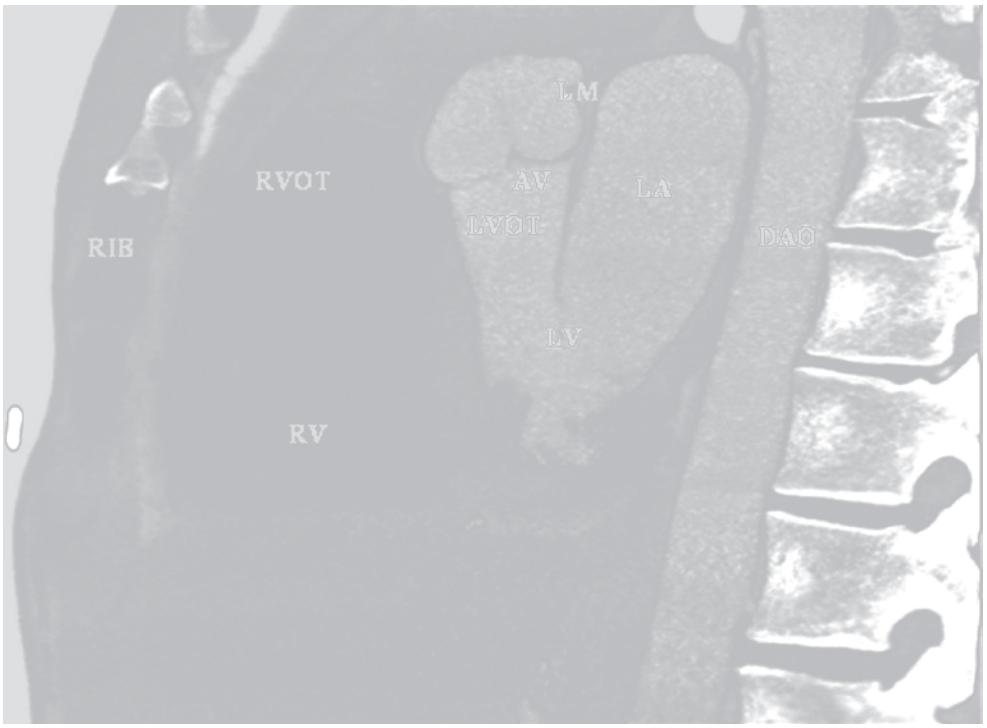

Figure 25.106.

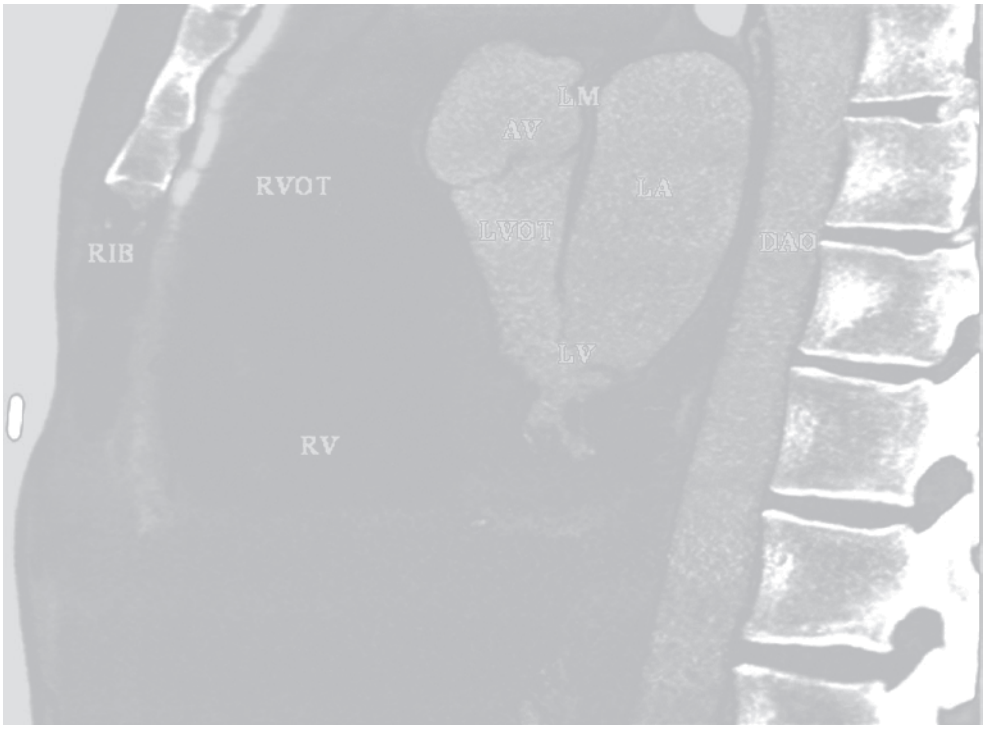

Figure 25.107.

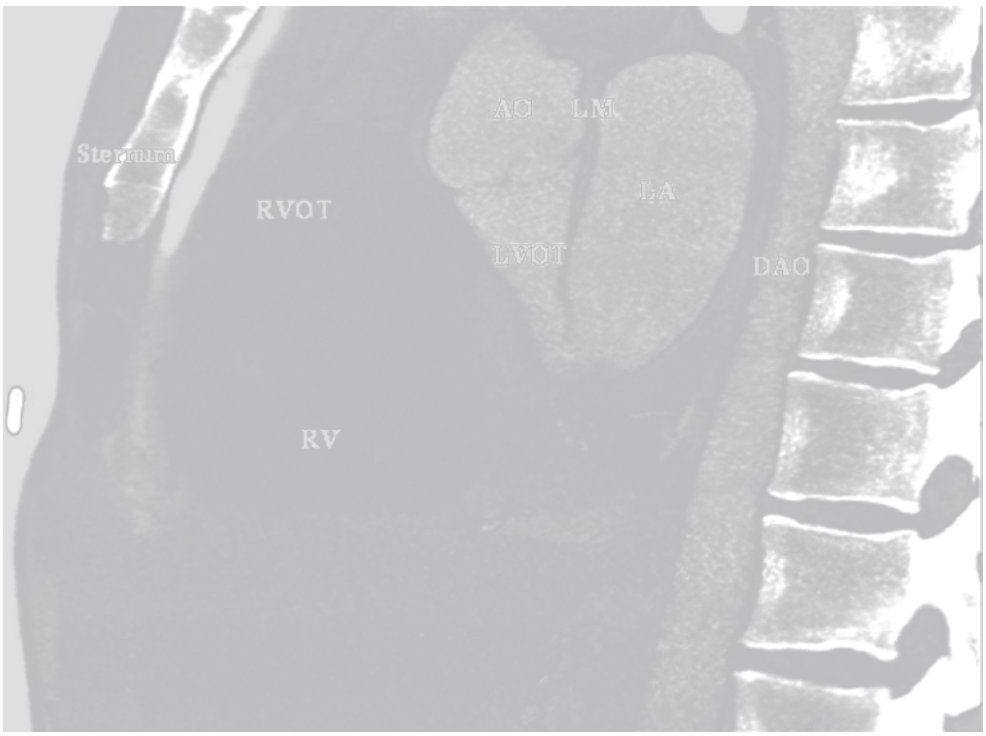

Figure 25.108.

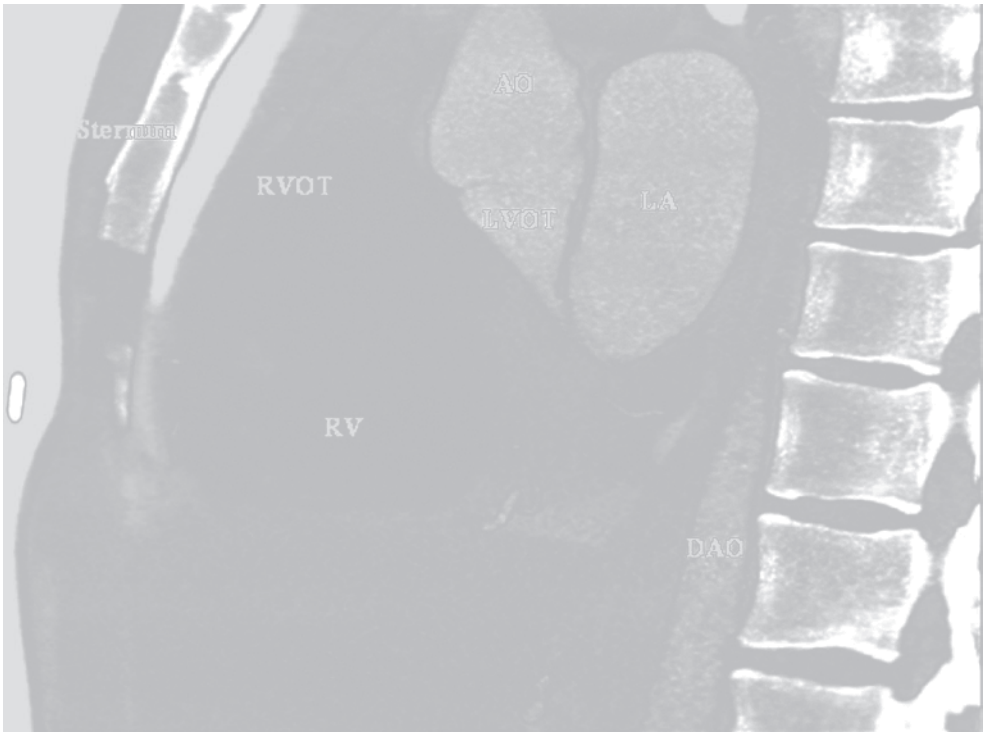

Figure 25.109.

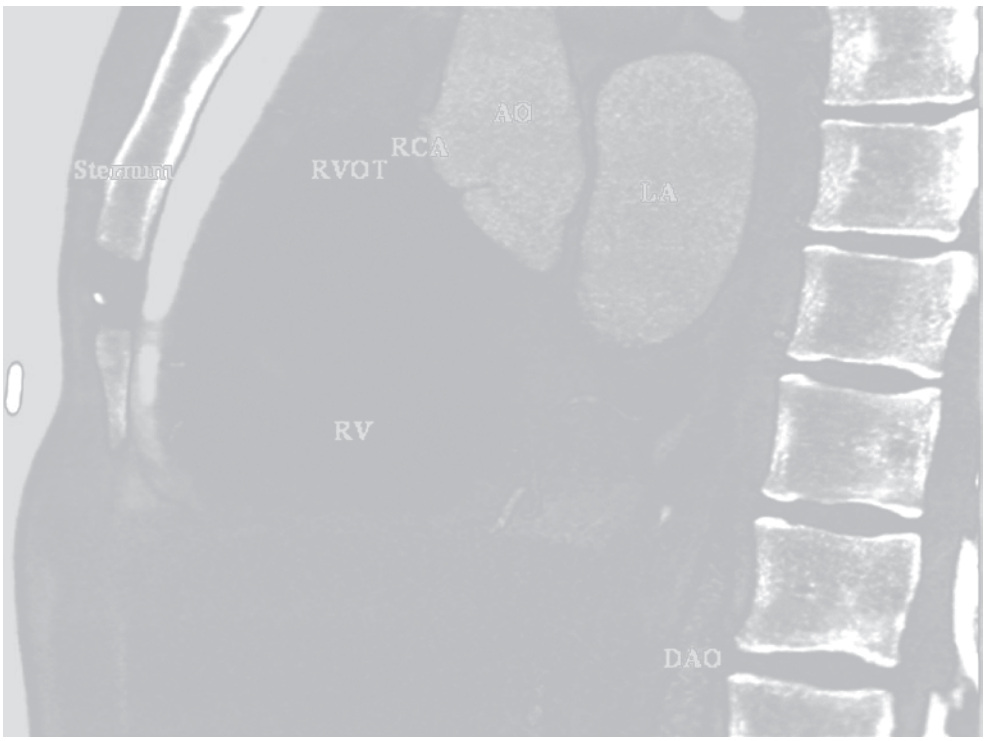

Figure 25.110.

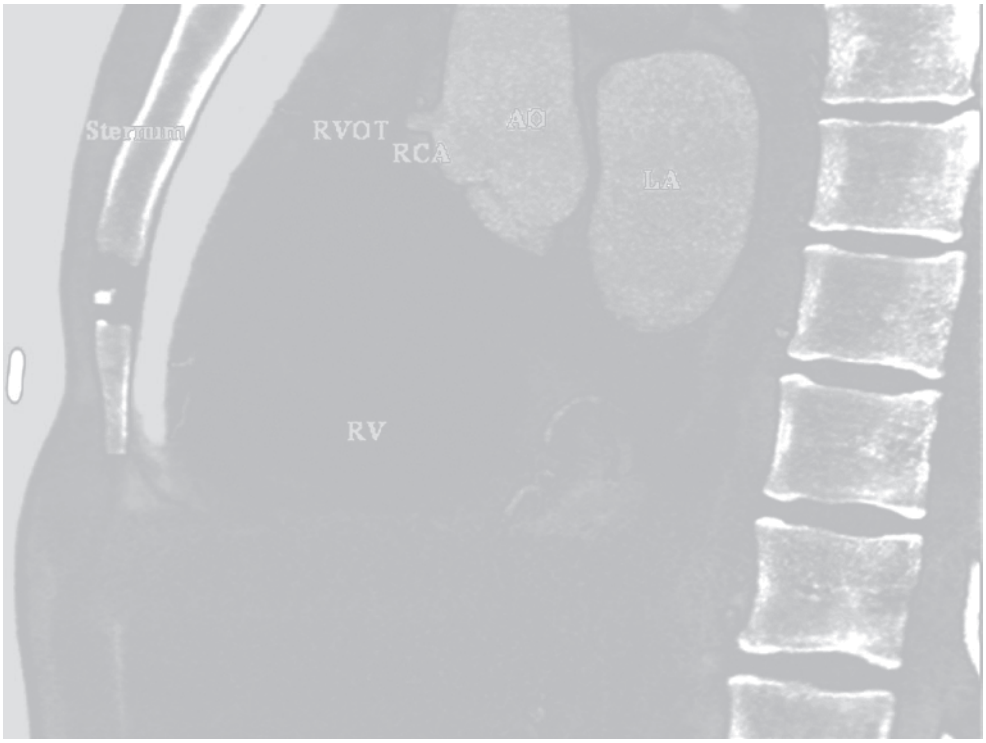

Figure 25.111.

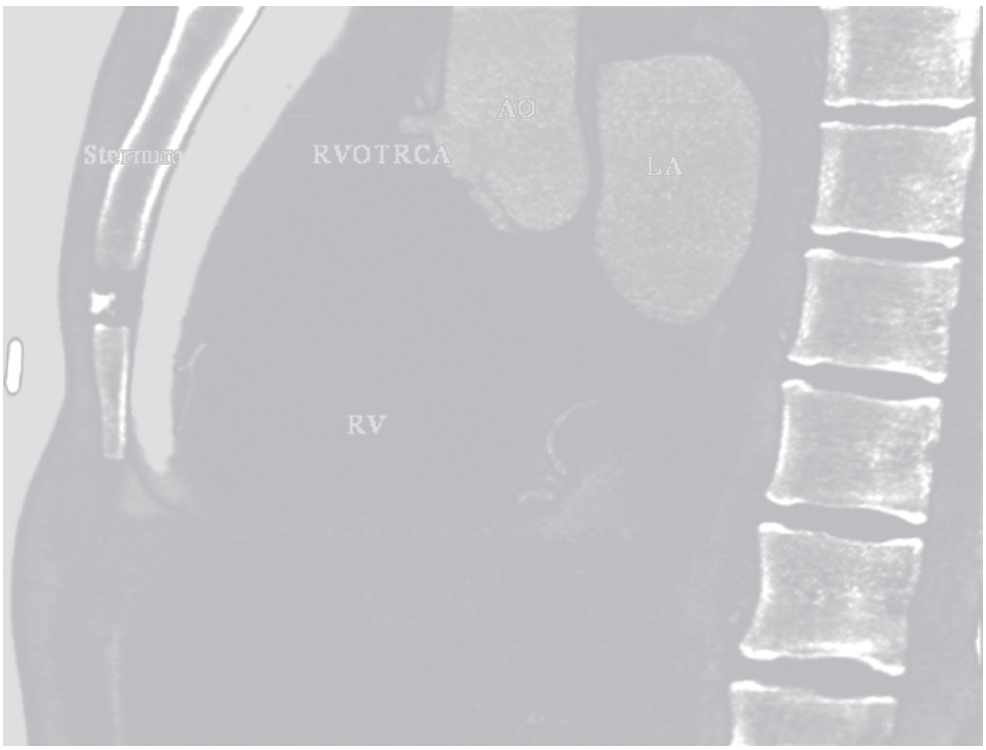

Figure 25.112.

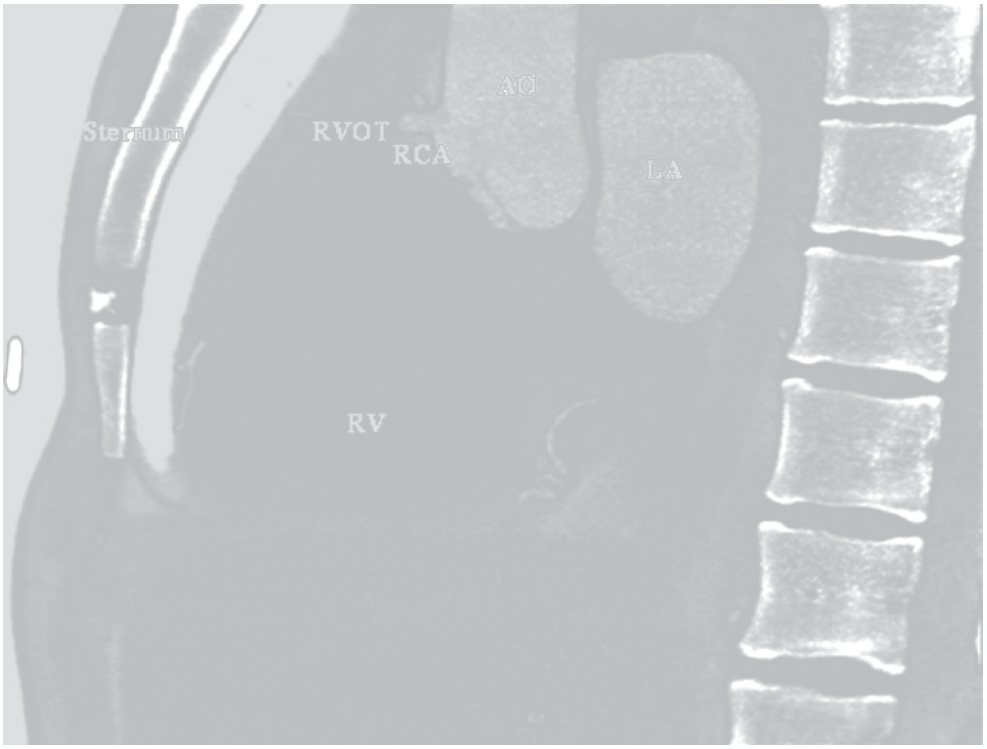

Figure 25.113.

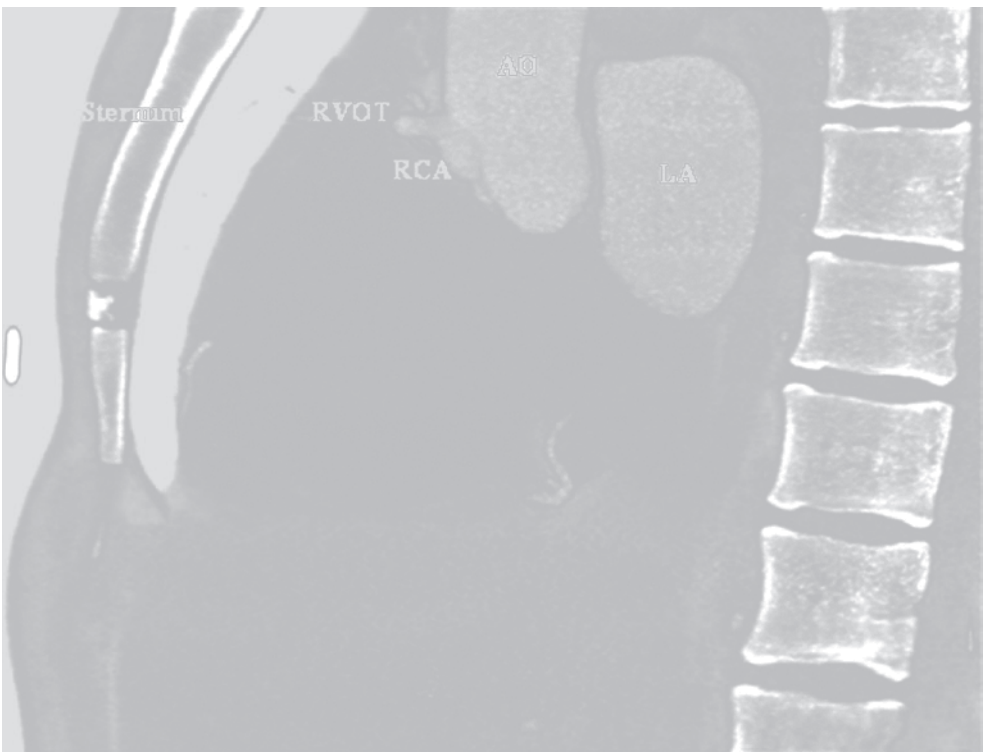

Figure 25.114.

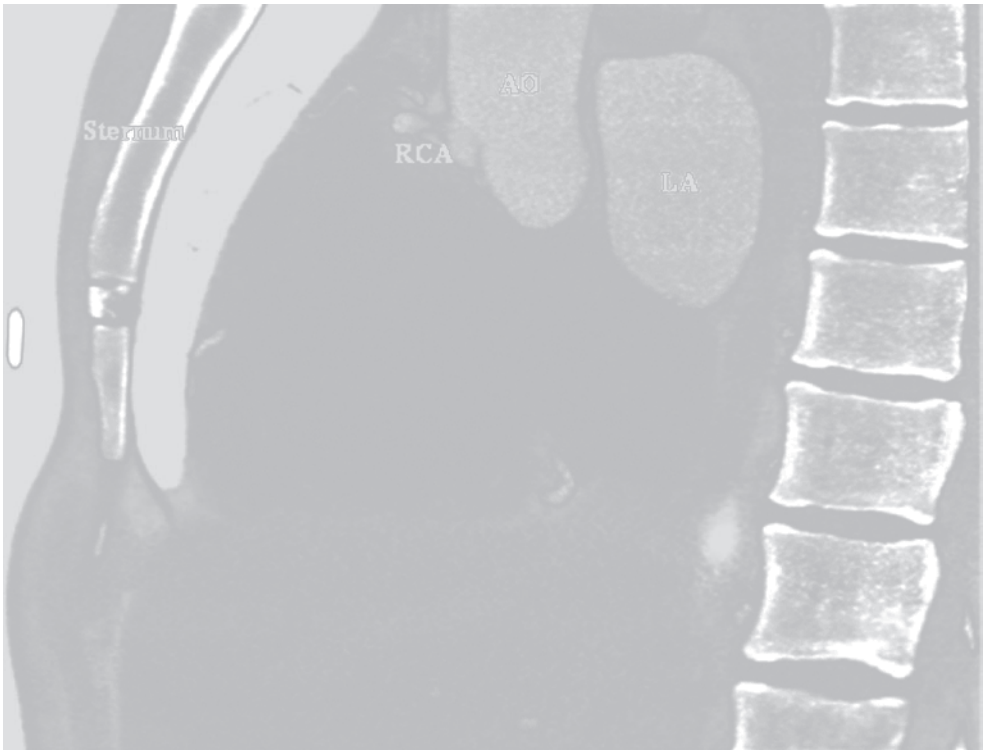

Figure 25.115.

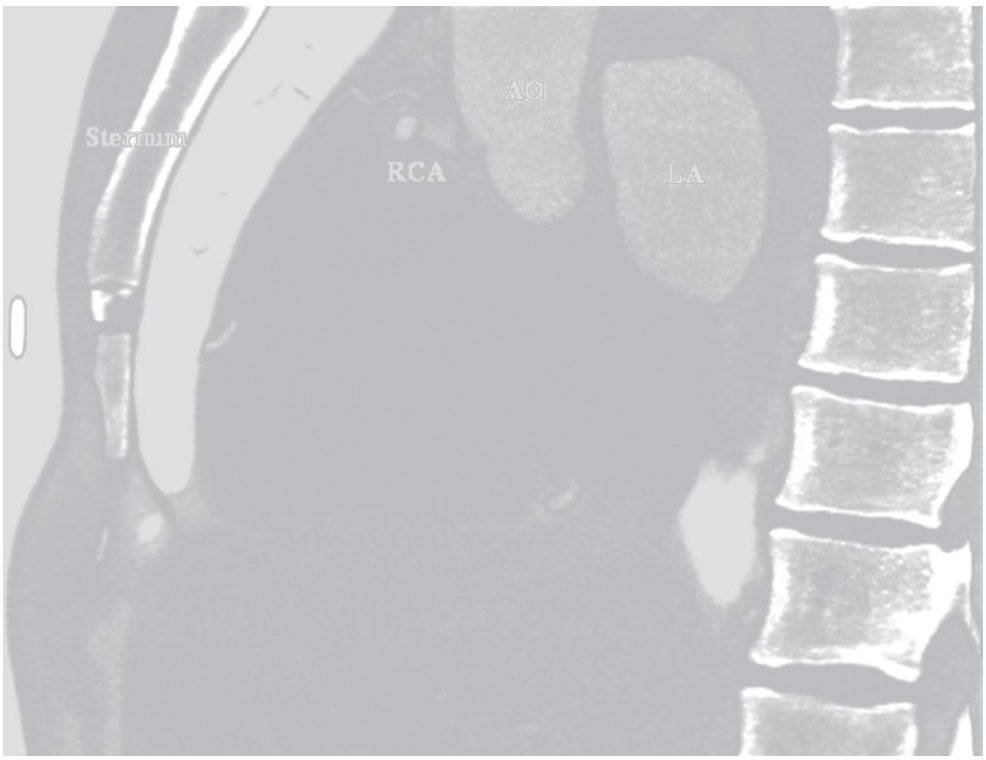

Figure 25.116.

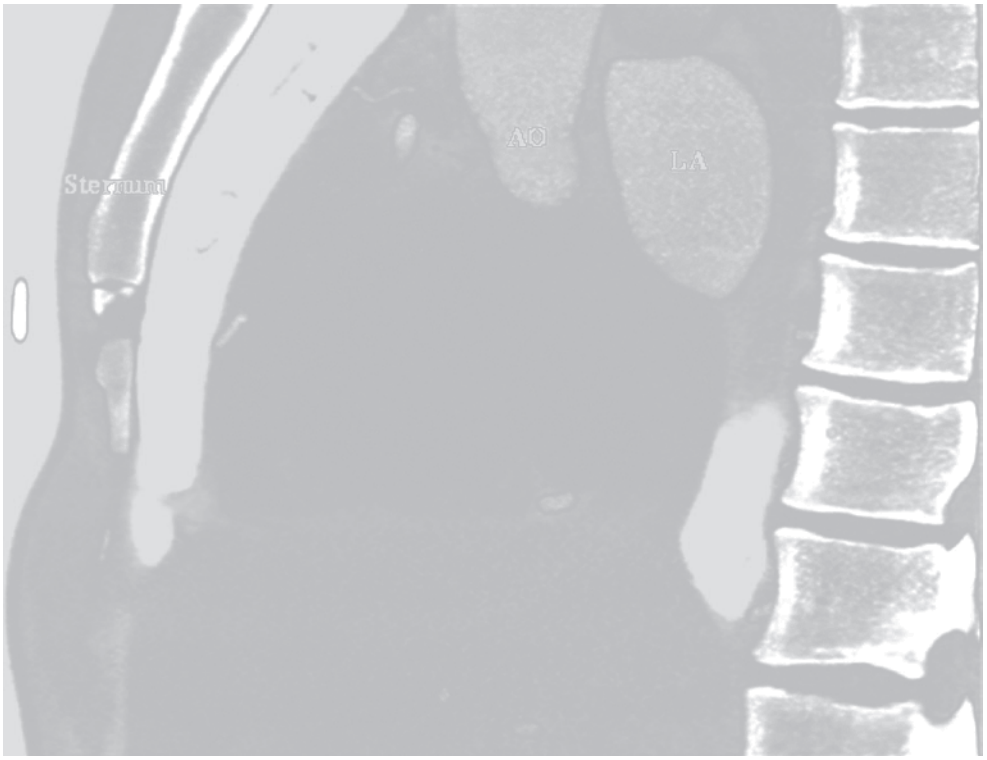

Figure 25.117.

Figure 25.118.

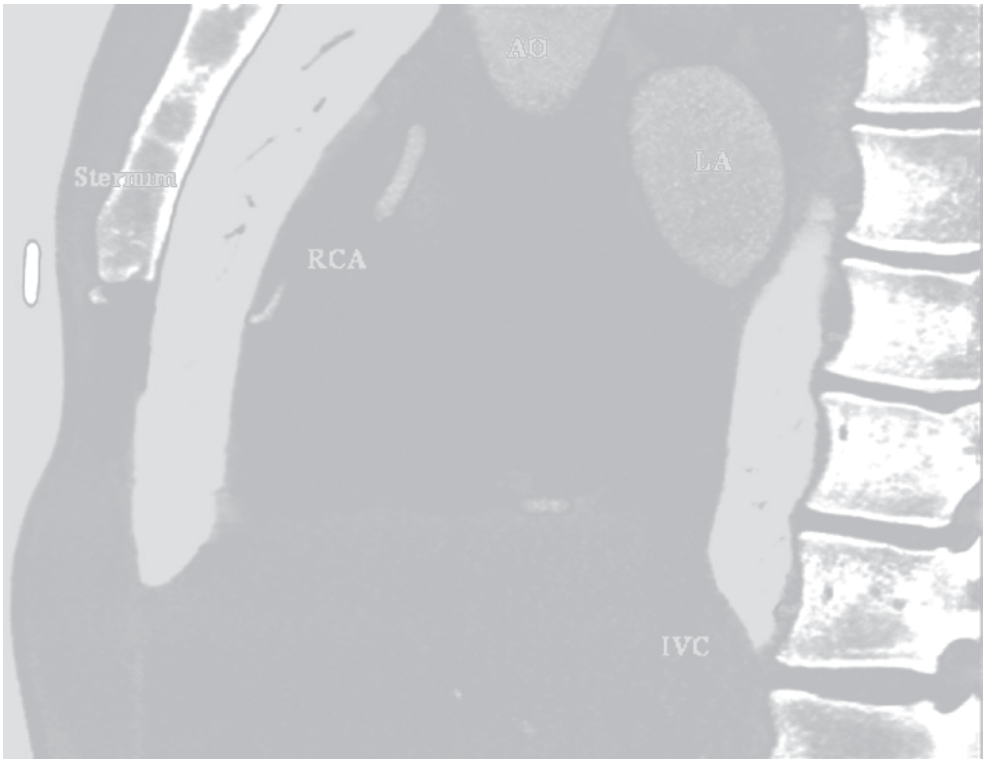

Figure 25.119.

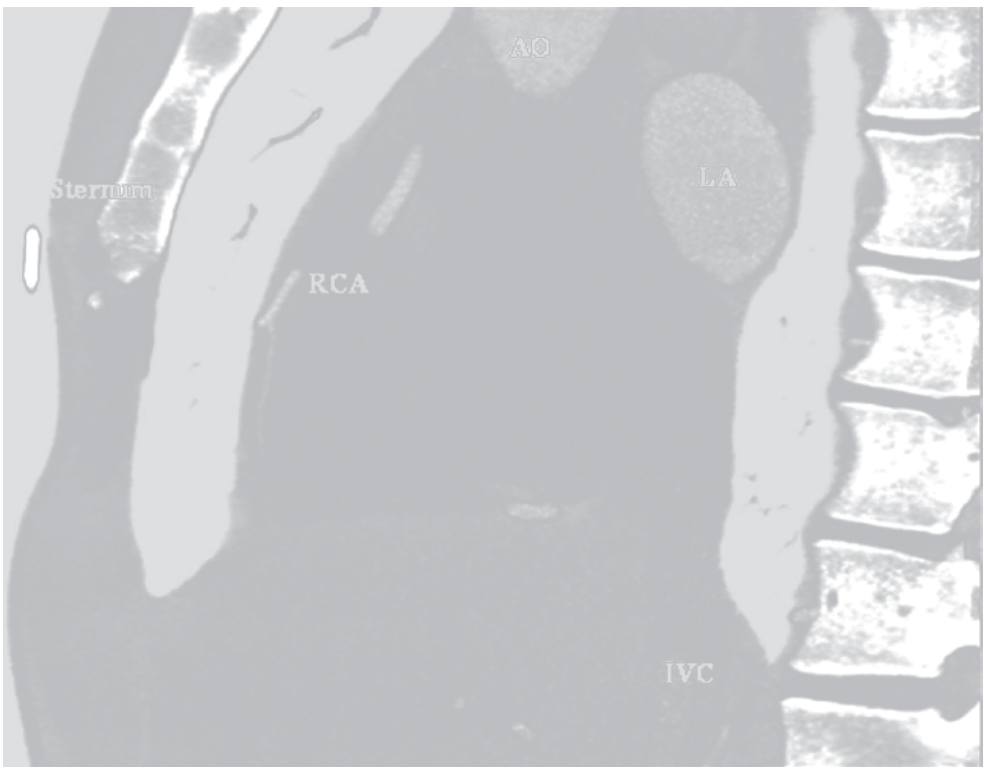

Figure 25.120.

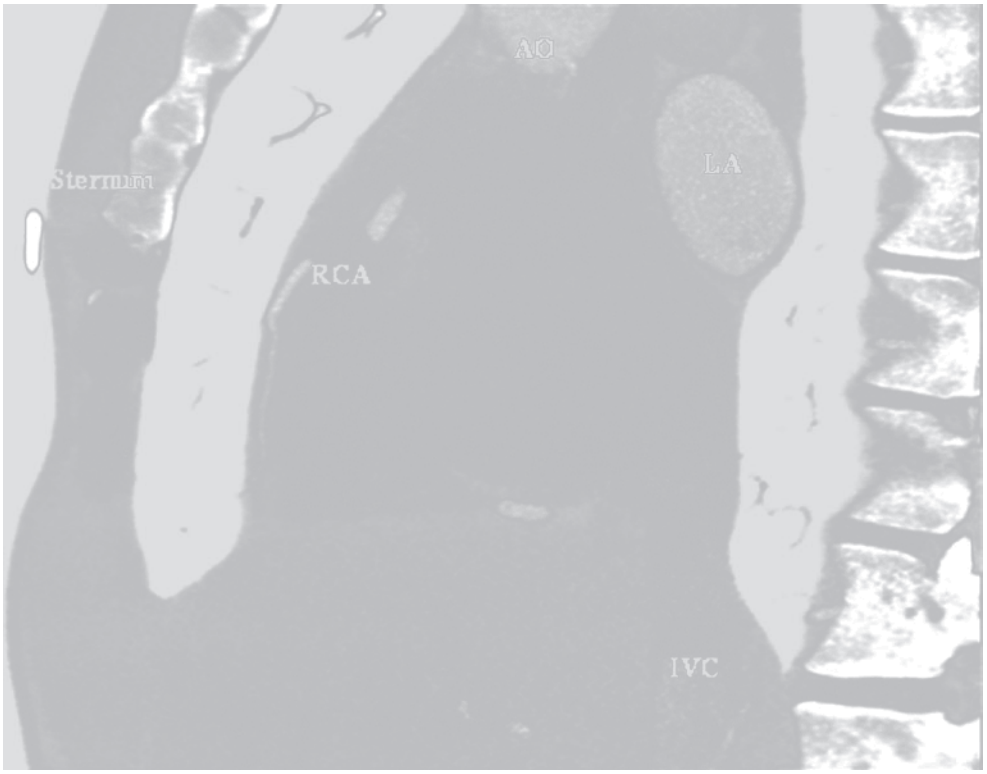

Figure 25.121.

Figure 25.122.

Figure 25.123.

Figure 25.124.

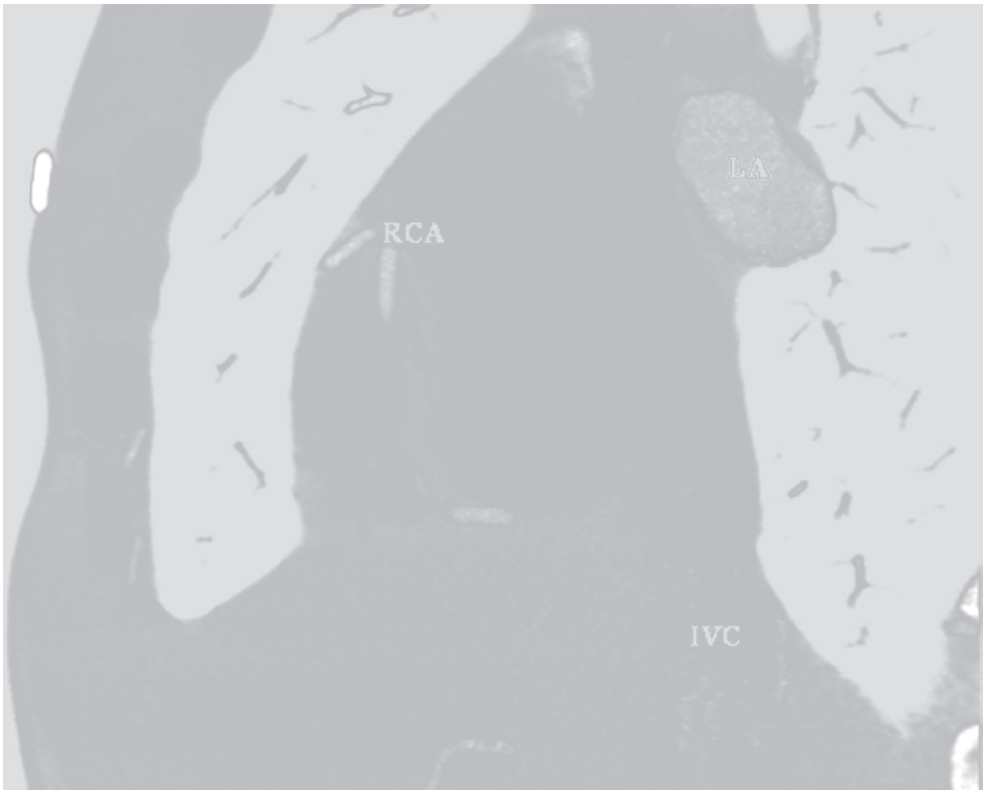

Figure 25.125.

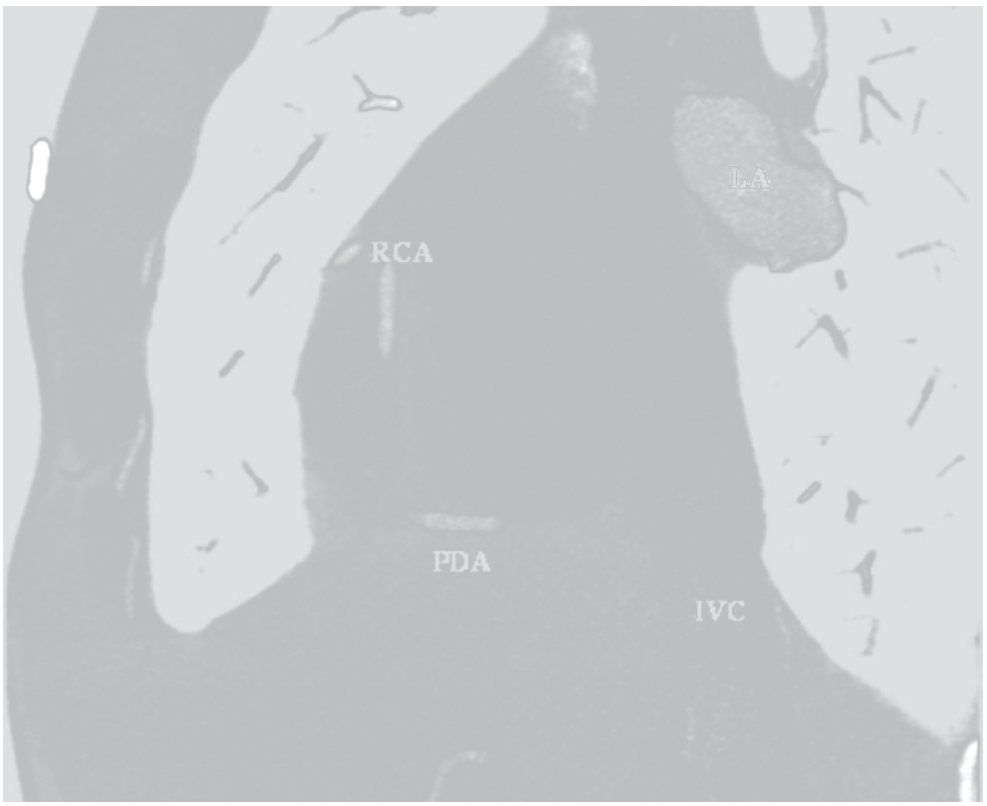

Figure 25.126.

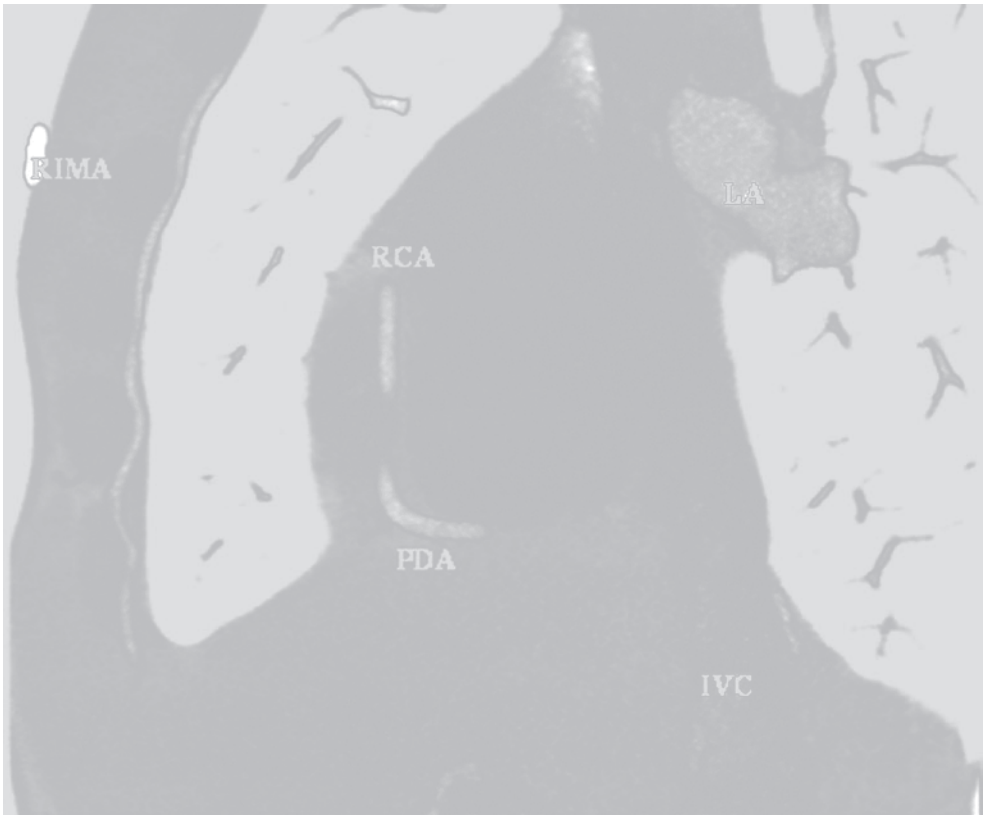

Figure 25.127.

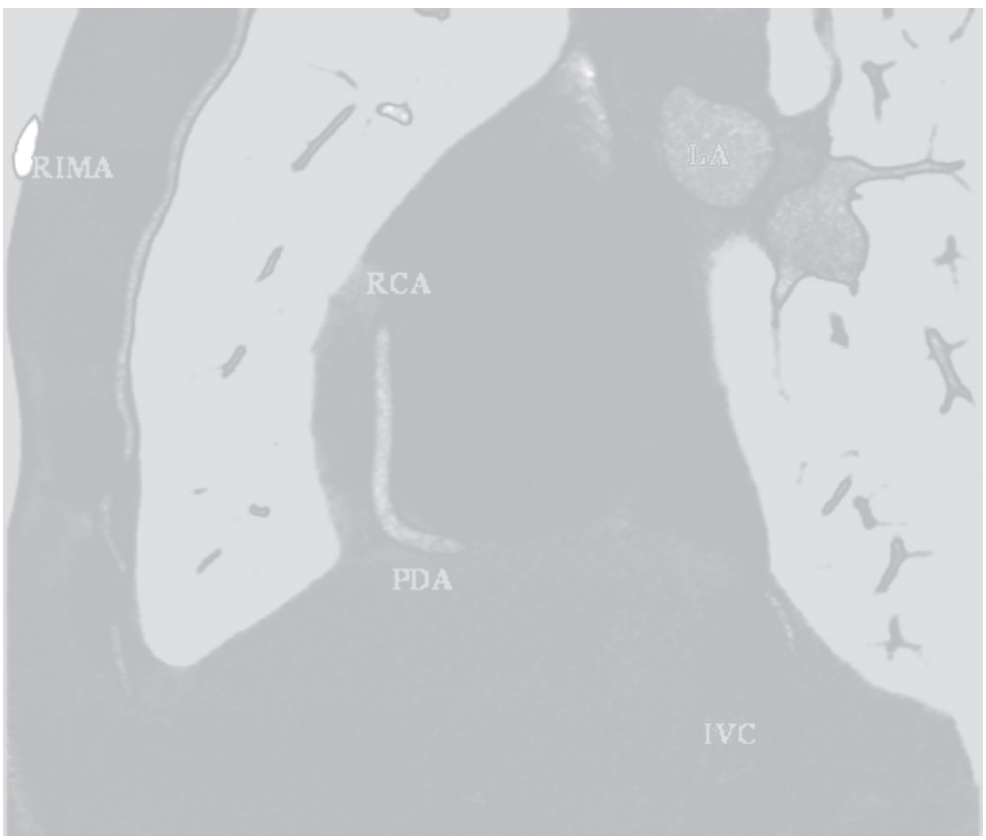

Figure 25.128.

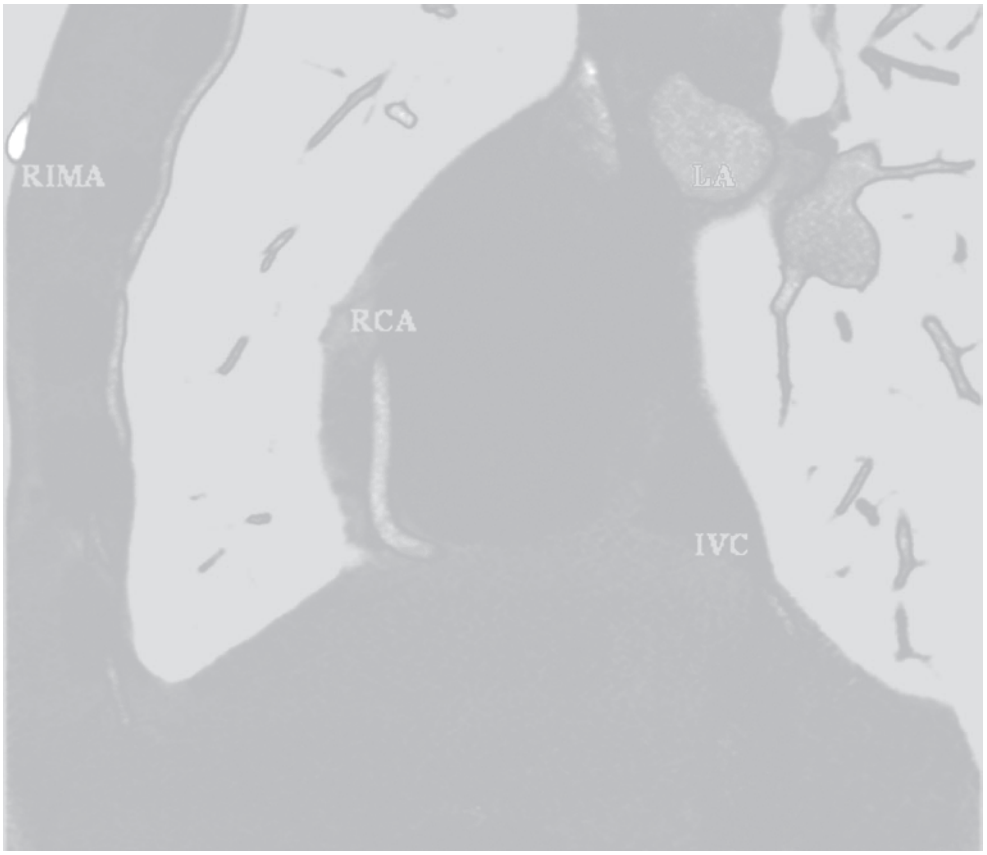

Figure 25.129.

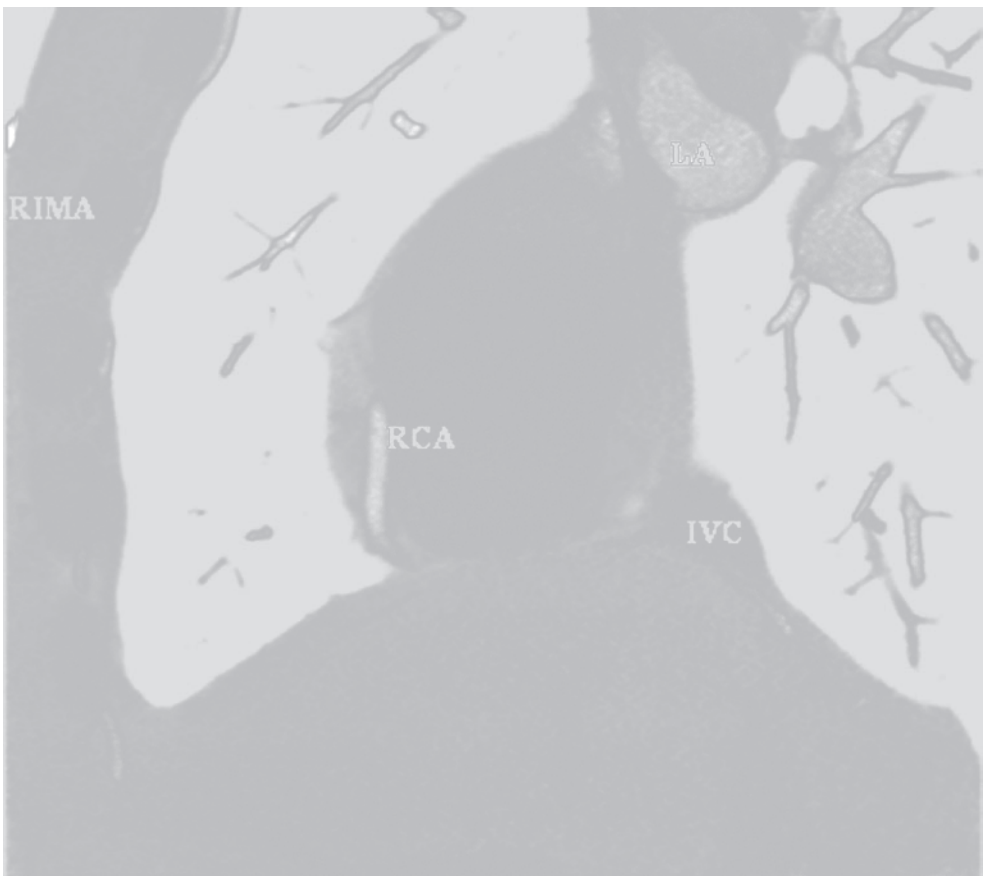

Figure 25.130.

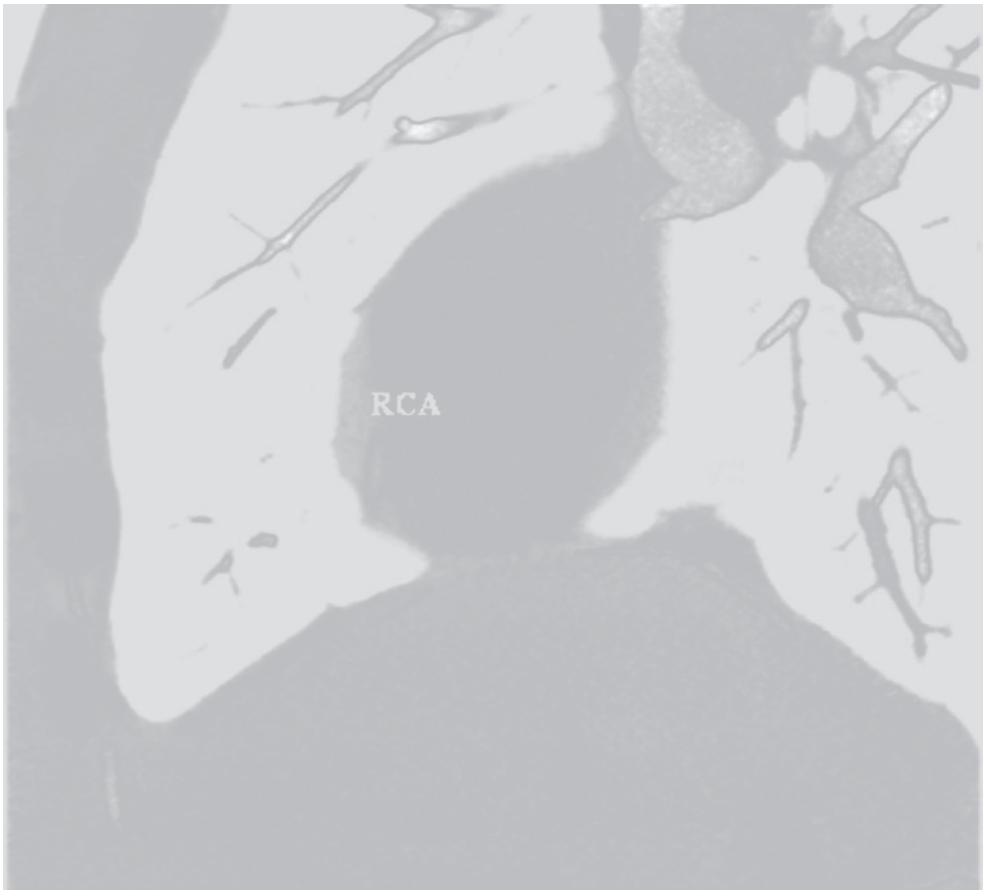

Figure 25.131.

Index